nagra.

Arbeitsbericht NAB 16-25

Thermo-hydro-chemical (THC) behaviour of a Spanish bentonite after dismantling Heater #1 and Heater #2 of the FEBEX in-situ test at the Grimsel Test Site

July 2018

A.M. Fernández, D.M. Sánchez-Ledesma, A. Melón, L. M. Robredo, J.J. Rey, M. Labajo, M.A. Clavero, S. Fernández & A.E. González

Ciemat

National Cooperative for the Disposal of Radioactive Waste

Hardstrasse 73
P.O. Box 280
5430 Wettingen
Switzerland
Tel. +41 56 437 11 11

www.nagra.ch

nagra.

Arbeitsbericht NAB 16-25

Thermo-hydro-chemical (THC) behaviour of a Spanish bentonite after dismantling Heater #1 and Heater #2 of the FEBEX in-situ test at the Grimsel Test Site

July 2018

A.M. Fernández, D.M. Sánchez-Ledesma, A. Melón, L. M. Robredo, J.J. Rey, M. Labajo, M.A. Clavero, S. Fernández & A.E. González

Ciemat

KEYWORDS

Bentonite, THC, Pore water, Mineralogy, Crystallochemistry, CEC, Redox, Microbiology, Hydrocarbons

National Cooperative for the Disposal of Radioactive Waste

Hardstrasse 73
P.O. Box 280
5430 Wettingen
Switzerland
Tel. +41 56 437 11 11

www.nagra.ch

Nagra Arbeitsberichte ("Working Reports") present the results of work in progress that have not necessarily been subject to a comprehensive review. They are intended to provide rapid dissemination of current information.
This report was prepared on behalf of Nagra. The viewpoints presented and conclusions reached are those of the author(s) and do not necessarily represent those of Nagra.

"Copyright © 2018 by Nagra, Wettingen (Switzerland) / All rights reserved.
All parts of this work are protected by copyright. Any utilisation outwith the remit of the copyright law is unlawful and liable to prosecution. This applies in particular to translations, storage and processing in electronic systems and programs, microfilms, reproductions, etc."

Summary

Bentonites are an essential component of the multi-barrier system securing the long-term safety of the final disposal of nuclear waste. The efficiency of engineering such clay barrier relies on its physical and chemical confinement properties: low permeability, low diffusivity, high retention and swelling capacity. Therefore, an important issue for performance assessment purposes is to have confidence in and demonstrate the long-term preservation of these properties over periods of e.g. hundreds of thousands of years under real repository conditions.

One possible scientific approach used to tackle the problem of predicting long-term clay barrier behaviour is through the analysis of results from experiments conducted in underground research laboratories (URL) at real scale and under realistic conditions. The FEBEX in-situ test project provided the opportunity to understand and quantify the processes taking place in the near-field and to evaluate the behaviour of the compacted FEBEX bentonite after 18 years of running the experiment.

From a geochemical point of view, the bentonite's function to isolate the canisters from water and retard the migration of radionuclides means also maintaining a suitable chemical environment for canister integrity and radionuclide retention over time, buffering possible alteration/deterioration processes of the bentonite.

The dismantling of the second part of the FEBEX in-situ test allowed quantifying the modifications of the bentonite due to changing physico-chemical conditions and different types of perturbations over time: a) interactions with granitic groundwater (saturation phase), b) heat (desaturation phase due to heating), c) perturbations linked to the interactions between the bentonite and engineered solid materials (concrete, iron, C-steels and other metals, organics, etc.), and d) interactions with different gases produced and consumed in the system (CO_2, H_2, CH_4, etc.) due to mineral dissolution/precipitation, microbiological reactions and corrosion processes.

In this report, the impact of different perturbations were described in terms of 1) modifications in pore water chemistry and redox conditions, which may affect the smectite's structural stability and speciation of dissolved ions, 2) dissolution and redistribution of primary mineral phases and precipitation/neoformation of secondary minerals, 3) clay mineral alteration or modifications of the clay mineral properties (especially cation exchange capacity, cation exchange population, crystallochemical structure, layer charge and swelling ability), and transport properties through modifications in porosity, permeability and tortuosity due to cementation processes

Some specific reactions observed in laboratory and large scale experiments over time were also detected in the FEBEX in-situ experiment. These reactions are: dissolution/precipitation, cation exchange, metal corrosion, gas production, hydrocarbon oxidation and Mg accumulation at the heater interface.

The global data analysed from samples obtained after the dismantling operations of Heater #1 in 2002 and Heater #2 in 2015, indicated that no significant structural changes in the smectite occured. The whole bentonite barrier preserved its main physico-chemical properties unaltered (CEC, layer charge, water adsorption capacity and total and external surface area) and the alterations observed were restricted to localized zones, mainly at the bentonite/shotcrete (< 6.25 – 12.5 cm) and bentonite/heater (< 5 – 10 cm) interfaces.

Table of Contents

Summary I

Table of Contents III

List of Tables VI

List of Figures X

1 Introduction 1
1.1 The FEBEX Project 1
1.2 Test configuration during FEBEX I 2
1.3 Dismantling of Heater #1 and test configuration afterwards (FEBEX II) 5
1.4 Dismantling Heater #2: concept 9
1.5 Gas and water sampling during the FEBEX in-situ test 13

2 Objectives of the THC studies in the FEBEX in-situ test 15

3 Materials 17
3.1 The bentonite 17
3.2 Sampling during the dismantling of Heater #1 17
3.3 Sampling during the dismantling of Heater #2 20

4 Methodology 31
4.1 Sub-sampling at the laboratory 32
4.2 Physical properties 34
4.3 Mineralogical analysis: XRD, SEM, TEM, FTIR and thermal analysis 35
4.4 Geochemical analysis of the bentonite samples 36
4.4.1 Chemical analysis by X-Ray fluorescence 36
4.4.2 Poorly crystalline and free silica, aluminium and iron 37
4.4.3 Fe(II)-Fe_{total} in the samples at contact with the liner and heater 38
4.4.4 Total carbon, total inorganic carbon and total sulphur 38
4.5 Physico-chemical characterization 38
4.5.1 Layer charge 38
4.5.2 Cation exchange capacity 39
4.5.3 Cation exchange population 39
4.5.4 Zeta potential and size of colloid clay particles 39
4.5.5 BET and external surface area 41
4.5.6 Total surface area 41
4.5.7 Water adsorption isotherms 41
4.5.8 Soluble salts by aqueous leaching 42
4.6 Pore water chemistry 42
4.7 Water chemical analyses 45

5 Results 47
5.1 Visual aspects 47
5.2 Water content and dry density 52
5.3 Mineralogical analyses 55
5.3.1 X-Ray diffraction 55
5.3.1.1 Total fraction from retrieved samples after dismantling of Heater #2 55
5.3.1.2 Oriented clay mineral aggregates from retrieved samples after dismantling of Heater #2 58
5.3.1.3 X-Ray diffraction from retrieved samples after dismantling of Heater #1 60
5.3.2 FTIR analyses 63
5.3.3 Thermal analyses 74
5.3.4 TEM analyses 86
5.4 Geochemical analysis of the bentonite samples 112
5.4.1 Composition of the bentonite by X-Ray fluorescence 112
5.4.2 Analysis of the < 2 µm fraction by XRF 116
5.4.3 Total carbon and total sulphur 117
5.4.4 Poorly crystalline and free silica, aluminium and iron 121
5.5 Physico-chemical characterization 124
5.5.1 Layer charge 124
5.5.2 Cation exchange capacity 127
5.5.3 Cation exchange population 129
5.5.4 Zeta potential and size of colloid clay particles 138
5.5.5 External surface area 143
5.5.6 Total surface area 153
5.5.7 Water adsorption isotherms 154
5.5.8 Soluble salts by aqueous leaching 157
5.6 Pore water chemistry 166
5.6.1 Squeezing pressure versus water content 169
5.6.2 Chemical composition of the bentonite pore water 170

6 Sample investigations at the liner/heater contact 183
6.1 Mineralogy 188
6.1.1 XRD analyses 188
6.1.2 FTIR analyses 189
6.1.3 TG-DSC analyses 193
6.1.4 SEM analysis 198
6.1.5 TEM analysis 203
6.2 Fe(II)-Fe_{total} in the samples 208
6.3 Physico-chemical properties 209
6.4 Metal-Interface samples analysed after dismantling Heater #1 216
6.4.1 Bentonite sample around sensor SH-SDI-1 219
6.4.2 Bentonite sample around gas pipe GF-SL-03 in Section 29 237

6.4.3 Bentonite sample at contact with the back of Heater #1 and inside the holes of the liner ... 240

7 Discussion of the results ... 247
7.1 Pore water chemistry ... 249
7.1.1 Evolution of the bentonite pore water ... 249
7.1.2 Analysis of the squeezed pore waters: mobile pore water and interlaminar water ... 254
7.1.3 Anion accessible porosity ... 256
7.2 Cation exchange population ... 259
7.3 Bentonite-ground water interactions: transport in compacted bentonite and dissolution/precipitation processes ... 260
7.4 Mineralogical alteration ... 262
7.4.1 Corrosion at bentonite/heater interface ... 262
7.4.2 Bentonite profile affected only by granitic groundwater hydration ... 265
7.4.3 Bentonite/concrete interface ... 265
7.5 Smectite structural stability ... 266
7.5.1 Mg and Fe(II) accumulation at heater interface ... 268
7.5.2 Possible mechanisms for smectite alteration ... 270
7.5.3 Fibrous Mg-phyllosilicates in the bentonite profile affected only by granitic groundwater hydration ... 275
7.5.4 Bentonite/shotcrete interface ... 276
7.6 Physico-chemical properties: CEC, layer charge, zeta-potential, surface area and water adsorption ... 277
7.7 Redox state in the FEBEX in-situ test ... 280
7.8 Microbiology ... 283

8 Summary and conclusions ... 285

9 References ... 299

Acknowledgements ... 313

App. A Samples taken during dismantling of the Heater #1 ... A-1

App. B SEM photomicrographs ... B-1
B1 Bentonite Sections 36, 47, 53 and 59 ... B-1
B2 Bentonite samples at contact with the liner/heater and protrusions (Fig. 174) ... B-81

App. C Analytical results ... C-1

App. D Saturation indices of aqueous extracts ... D-1

App. E TEM photomicrographs ... E-1

App. F Analysis of the samples at direct contact with the liner/Heater #2 ... F-1

List of Tables

Tab. 1: Main characteristics of the FEBEX bentonite 5

Tab. 2: Concrete characteristics used for the two plugs constructed in the FEBEX in-situ test (Huertas et al. 2006) 6

Tab. 3: Temperatures in different sections along x-coordinate (after Martínez et al. 2016) 11

Tab. 4: Bentonite samples obtained for THC (or THG) studies after dismantling of Heater #2 25

Tab. 5: Mineral content (in weight %) of the bentonites samples obtained from XRD 57

Tab. 6: Characteristics of the smectite clay minerals 60

Tab. 7: Positions and assignments of the vibrational bands of dioctahedral smectites 65

Tab. 8: Structural formula of the FEBEX Reference sample based on $O_{10}(OH)_2$ according to Moore & Reynolds (1989) (first row) or maintaining the $\Sigma_{oct} = 2.0$ (second row) 87

Tab. 9: Structural formula of the reference and retrieved samples based on $O_{10}(OH)_2$ according to Moore & Reynolds (1989) and maintaining the $\Sigma_{oct} = 2.0$ 88

Tab. 10: Structural formula of non-montmorillonite clay particles detected in the retrieved samples 89

Tab. 11: Major mineral phases and accessory minerals observed by SEM in bentonite blocks from one radius (Ring 1: granite contact, Ring 2: second block, and Ring 3: third block, i.e. at the heater contact) 102

Tab. 12: Chemical composition of the main oxides in the total fraction (in wt.-%) after dismantling of Heater #2 (for location of the samples see Fig. 30 to Fig. 33) 112

Tab. 13: Chemical composition of the solid phase for different samples of Section 7 taken after dismantling of Heater #1 (see location in Fig. A-1 and Fig. A-4 in Appendix A) 114

Tab. 14: Chemical composition of the solid phase for different samples of Section 12 taken after dismantling of Heater #1 (see location in Fig. A-1 and Fig. A-5 in Appendix A) 115

Tab. 15: Chemical composition of the solid phase for different samples of Section 19 taken after dismantling of Heater #1 (see location in Fig. A-1 and Fig. A-6 in Appendix A) 116

Tab. 16: Structural formula based on $O_{10}(OH)_2$ according to Köster (1977) by using the measure layer charge 118

Tab. 17: Total carbon and sulphur content (in wt.-%) 119

Tab. 18: Free aluminium, silica and iron oxides from different bentonite samples (in wt.-%) 122

Tab. 19: Basal spacings and mean layer charge (MLC) for alkyl chains nC = 12 and nC = 18 126

Tab. 20: Main characteristics of the colloids generated in DW from different block samples from Section 47 as a function of distance to Heater #2 and pH (see location of samples in Fig. 31) 139

Tab. 21: Parameters deduced from the BET and *t*-plot treatment on the adsorption of N_2 at 77 K from samples obtained after dismantling of Heater #2 146

Tab. 22: Parameters deduced from the BET and *t*-plot treatment on the adsorption of N_2 at 77 K from samples obtained after dismantling of Heater #1 146

Tab. 23: Pore size families calculated from the BJH method (desorption branch) for mesopores from samples obtained after dismantling Heater #2 151

Tab. 24: Main parameters calculated from the BJH method for mesopores from samples obtained after dismantling Heater #2 152

Tab. 25: Main parameters calculated from the BJH method for mesopores from samples obtained after dismantling Heater #1 152

Tab. 26: Characteristics of the squeezing tests performed after dismantling Heater #2 in 2015 (see sample location in Fig. 17 to Fig. 20) 168

Tab. 27: Characteristics of the squeezing tests performed after dismantling Heater #1 in 2002 (see sample location in Fig. A-1 from Appendix A) 168

Tab. 28: Chemical composition of the pore water collected from Section 36 at contact with the shotcrete plug after dismantling Heater #2: BB-36-1, BB-36-2 and BB-36-3 bentonite blocks as a function of distance to the gallery axis 173

Tab. 29: Chemical composition of pore water collected from heated Section 47 at different pressures: BB-47-7, BB-47-8 and BB-47-9 bentonite blocks as a function of distance to the gallery axis 174

Tab. 30: Chemical composition of pore water collected from the non-heated Section 59 at different pressures: BB-59-1, BB-59-2, BB-59-3, BB-59-4 and BB-59-5 bentonite blocks as a function of distance to the gallery axis 175

Tab. 31: Chemical composition of pore water obtained by squeezing from samples taken during dismantling of Heater #1 in 2002 176

Tab. 32: Calculated parameters and saturation indices of pore waters from the FEBEX Reference bentonite and from the bentonite sampling section S36 during dismantling of Heater #2 in 2015 177

Tab. 33: Calculated parameters and saturation indices of pore waters from the bentonite sampling Section S47 during dismantling of Heater #2 in 2015 178

Tab. 34: Calculated parameters and saturation indices of pore waters from the bentonite sampling Section S59 during dismantling of Heater #2 in 2015 179

Tab. 35: Calculated parameters and saturation indices of pore waters from the bentonite sampling Sections S7, S12 and S19 (Dismantling Heater #1 in 2002). 180

Tab. 36: Neoformed mineral phases observed in the samples at direct contact with the liner/Heater #2 by means of XRD, FTIR and TG-DSC 190

Tab. 37: Major mineral phases and accessory minerals observed by SEM in samples in contact with the liner and in the protrusions (in cursive: present in the reference sample) 198

Tab. 38: Structural formula of clay mineral particles detected in the samples at contact with the liner/heater and in the protrusions 203

Tab. 39: Total Fe, Fe(II) and Fe(III) in the bentonite samples in contact with the liner at Sections S47 and S53 and in protrusion samples 209

Tab. 40: Parameters deduced from the BET and *t*-plot treatment on the adsorption of N_2 at 77 K from samples obtained after dismantling Heater #2 211

Tab. 41: CEC values in samples at contact with the liner/Heater #2 211

Tab. 42: Cation exchange occupancies in samples at contact with the liner/ Heater #2 (in meq/100g) 212

Tab. 43: Soluble salts from aqueous extracts at 1:4 solid to liquid ratio from the samples at contact with the liner/Heater #2 (in mg/L) 213

Tab. 44: Composition (in wt.-%) of the SHSDI-1 displacement sensor (Madina 2003) 219

Tab. 45: Microbial study of the bentonite samples surrounding the SHSDI-1 displacement sensor, in counting ufc/g (Madina 2003) 219

Tab. 46: Chemical composition of the solid phase (total fraction) 221

Tab. 47: Soluble salts from aqueous extracts at 1:4 solid to liquid ratio (in mg/L) 222

Tab. 48: Cation exchange population in meq/100g extracted with a $CsNO_3$ solution at 1:8 solid to liquid ratio (~ 5 grams of wet sample in 40 mL of deionized water) 222

Tab. 49: Parameters deduced from the BET and t-plot treatment on the adsorption of N_2 at 77 K from samples obtained after dismantling of Heater #1 223

Tab. 50: Anion-accessible porosity fraction (Cl porosity/Water loss porosity) derived from chloride data of squeezed samples and leaching tests 258

Tab. 51: Structural characteristics detected in samples in contact with the liner/Heater #2 and in the protrusion samples taken after dismantling Heater #2 in 2015 273

Tab. A-1: Bentonite samples analysed in thermo-hydro-geochemical tests A-3

Tab. C-1: Total surface area in the bentonite samples (in m^2/g) C-3

Tab. C-2: Total surface area in the bentonite samples (in m^2/g). Continuation C-4

Tab. C-3: CEC from bentonite as a function of the distance from the gallery axis C-5

Tab. C-4: Cation exchange population from bentonite blocks samples (by duplicate: A, B) C-8

Tab. C-5: Chemical composition of the trace elements in the total fraction (in ppm) C-13

Tab. C-6: Chemical composition of the trace elements in the total fraction (in ppm). Continuation C-14

Tab. C-7: Chemical composition of the major oxides in the < 2 µm fraction of a Ba-homoionized sample (in wt.-%) C-15

Tab. C-8: Chemical composition of the trace elements in the < 2 µm fraction of a Ba-homoionized sample (in ppm). Continuation C-16

Tab. C-9: Chemical composition of the trace elements in the < 2 µm fraction of a Ba-homoionized sample (in ppm). Continuation C-17

Tab. C-10: Aqueous leaching tests at 1:4 solid to liquid ratio (in mg/L) C-18

Tab. C-11: Aqueous leaching tests at 1:4 solid to liquid ratio (in mg/L). Continuation C-19

Tab. C-12: Aqueous leaching tests at 1:4 solid to liquid ratio (in mg/L). Continuation C-20

Tab. C-13: Aqueous leaching tests at 1:4 solid to liquid ratio (in mg/L). Continuation C-21

Tab. C-14: Aqueous leaching tests at 1:4 solid to liquid ratio (in mg/L). Continuation C-22

Tab. C-15: Aqueous leaching tests at 1:4 solid to liquid ratio (in mg/L). Continuation C-23

Tab. C-16: Aqueous leaching tests at 1:4 solid to liquid ratio (in mg/L). Continuation C-24

Tab. C-17: Aqueous leaching tests at 1:4 solid to liquid ratio (in mg/L). Continuation C-25

Tab. C-18: Aqueous leaching tests at 1:4 solid to liquid ratio (in meq/L). Continuation C-26

Tab. C-19: Aqueous leaching tests at 1:4 solid to liquid ratio (in mg/L). Continuation C-27

Tab. C-20: Water adsorption isotherms from retrieved samples at heated sections after dismantling of Heater #2 and comparison with FEBEX Reference sample C-28

Tab. C-21: Water adsorption isotherms from retrieved samples at non-heated sections after dismantling of Heater #2. Comparison with the Reference sample C-30

Tab. D-1: Saturation indices from aqueous extracts calculated with the PhreeqC program D-3

List of Figures

Fig. 1: Overall layout of FEBEX in-situ test (left) and mock-up test (right). After Fuentes-Cantillana et al. (1998) 1

Fig. 2: a) Tunnel layout of the Grimsel Test Site (GTS); b) Scheme of the FEBEX in-situ test during the First Operational Phase (1996 – 2002) (after Huertas et al. 2006) 3

Fig. 3: General layout of the FEBEX in-situ test: FEBEX I configuration during the First Operational Phase 1996 – 2002 (Huertas et al. 2006) 4

Fig. 4: Location of the sub-parallel and radial boreholes drilled for the instrumentation of the surrounding rock mass (from J. Farias, ENRESA, pers. com.) 4

Fig. 5: Sampling layout during the dismantling of Heater #1 (AITEMIN 2002) 7

Fig. 6: Status of the FEBEX in-situ test after the partial dismantling: FEBEX II configuration in the Second Operational Phase 2002 – 2015 (Huertas et al. 2006) 8

Fig. 7: Status of the FEBEX in-situ test after the partial dismantling: FEBEX II configuration in the Second Operational Phase 2002 – 2015 (Huertas et al. 2006) 8

Fig. 8: 3-D view of the FEBEX repository with Heater # 2 situated horizontally in the centre of three rings of saturated bentonite buffer (from Nagra) 10

Fig. 9: Sampling layout during dismantling of Heater #2 (from Garcia-Siñeriz et al. 2016) 10

Fig. 10: Water content distribution in a vertical longitudinal section: a) data from dismantling of Heater #1 (Daucausse & Lloret 2003, b) data from dismantling of Heater #2 (Villar et al. 2016) 11

Fig. 11: Dry density distribution in a vertical longitudinal section: a) data from dismantling Heater #1 (Daucausse & Lloret 2003, b) data from dismantling Heater #2 (Villar et al. 2016) 12

Fig. 12: Degree of saturation distribution in a vertical longitudinal section: a) data from dismantling Heater #1 (Daucausse & Lloret 2003, b) data from dismantling Heater #2 (Villar et al. 2016) 12

Fig. 13: In-situ test configuration and location of the gas/water (GRS) and pore water pipes (CIEMAT) during the First and Second Operational Phases. (GRS: green-coloured pipes; CIEMAT: violet-coloured pipes) 13

Fig. 14: Geometry of the bentonite blocks installed in the FEBEX in-situ test (ENRESA 2000) 19

Fig. 15: Location of the bentonite sections selected for THC studies during the dismantling of Heater #1 (2002) and Heater #2 (2015) 20

Fig. 16: Schematic figure of the FEBEX in-situ test divided in dismantling sections: location of the dismantling bentonite sections around Heater #2 selected for THC studies 21

Fig. 17: Bentonite Section 36 (Slice 74): a) Installation photo: shotcrete pumping just before the bentonite Section 36 and, b) Bentonite samples taken during dismantling for THC studies (see García-Siñeriz et al. 2016) 22

Fig. 18: Bentonite Section 47 (Slice 44): a) Installation photo and b) Bentonite samples taken during dismantling for THC studies (see García-Siñeriz et al. 2016) 22

Fig. 19: Bentonite Section 53 (Slice 28): a) Installation photo and b) Bentonite samples taken during dismantling for THC studies (see García-Siñeriz et al. 2016) 23

Fig. 20: Bentonite Section 59 (Slice 8): bentonite samples taken during dismantling for THC studies (see García-Siñeriz et al. 2016) 23

Fig. 21: Bentonite protrusions inside the liner at contact with Heater #2 (see Kober & Van Meir 2017) 24

Fig. 22: Methodology for THC analysis after dismantling of Heater #2 31

Fig. 23: Appearance of the bentonite material and subsampling for THM and THC analyses 32

Fig. 24: Appearance of the bentonite block material and subsampling for THC analyses: a) S1 and S2 for soluble salts (S1: towards granite interface; S2: towards heater interface), CEC and exchangeable cations, b) mineralogy and geochemistry, and c) pore water chemistry 32

Fig. 25: Detail of subsampling for soluble salts, exchangeable cations and CEC determinations (1 or S1: towards granite interface; 2 or S2: towards heater interface) 33

Fig. 26: a) Detail of subsampling for minerology/geochemistry and pore water chemistry studies; b) Preservation of the squeezing sample until analysis 33

Fig. 27: Preparation of the samples for mineralogical and geochemical analysis: disaggregation, homogenisation, air drying, grinding and sieving (< 250 μm) 33

Fig. 28: Squeezed water extraction apparatus used at CIEMAT 43

Fig. 29: Detail of a bentonite sample (BB-59-3) before and after the squeezing test 44

Fig. 30: Bentonite sampling Section 36: Block samples (BB-36-xx) for THC analyses 48

Fig. 31: Bentonite sampling Section 47: Block samples (BB-47-xx) and bentonite-liner samples (BM-S-47-x) for THC analyses 48

Fig. 32: Bentonite sampling Section 53: Block samples (BB-53-xx) and bentonite-liner samples (BM-S-53-x) for THC analyses 49

Fig. 33: Bentonite sampling Section 59: Block samples (BB-59-xx) for THC analyses 49

Fig. 34: Detail of the block samples from Section 36 for THC analyses (Sq: squeezing; 1 or S1: towards granite interface; 2 or S2: towards heater interface) 50

Fig. 35: Detail of the block samples from Section 47 (heated) for THC analyses. (Sq: squeezing; Miner: mineralogy; 1 or S1: granite interface; 2 or S2: towards heater interface) 50

Fig. 36: Detail of the block samples from Section 53 (heated) for THC analyses. (Sq: squeezing; Miner: mineralogy; 1 or S1: granite interface; 2 or S2: towards heater interface)..... 51

Fig. 37: Detail of the block samples from Section 59 (non-heated) for THC analyses. (Sq: squeezing; Miner: mineralogy; 1 or S1: granite interface; 2 or S2: towards heater interface)..... 51

Fig. 38: Gel of smectite generated around the gas pipe FP3 (sample called Pipe 3), which was observed from bentonite Slice 70 (Section 37, Instrumented Section Q) to the end of the tube (Section 52)..... 52

Fig. 39: Water content and dry density of the bentonite block samples from dismantling of Heater #2 analysed at different sections for THC studies. Initial data: 14.4 % w.c. and 1.60 g/cm^3 dry density (after emplacement)..... 53

Fig. 40: Water content and dry density of the bentonite block samples from dismantling of Heater #1 analysed at different sections for THC studies. Initial data: 14.4 % w.c. and 1.60 g/cm^3 dry density (after emplacement)..... 53

Fig. 41: Comparison of water content values from bentonite block samples obtained after dismantling of Heater #1 and Heater #2 analysed at different sections for THC studies. Initial data: 14.4 % w.c. and 1.60 g/cm^3 dry density (after emplacement)..... 54

Fig. 42: Comparison of dry density values from bentonite block samples obtained after dismantling of Heater #1 and Heater #2 analysed at different sections for THC studies. Initial data: 14.4 % w.c. and 1.60 g/cm^3 dry density (after emplacement)..... 54

Fig. 43: XRD patterns of randomly oriented bulk bentonite samples from Section 36 (for location of the samples see Fig. 30 and Fig. 34)..... 55

Fig. 44: XRD patterns of randomly oriented bulk bentonite samples from Section 47 (for location of the samples see Fig. 31)..... 56

Fig. 45: XRD patterns of randomly oriented bulk bentonite samples from Section 53 (for location of the samples see Fig. 32)..... 56

Fig. 46: XRD patterns of randomly oriented bulk bentonite samples from Section 59 (for location of the samples see Fig. 33)..... 57

Fig. 47: XRD patterns of normal oriented aggregate samples from non-heated sections: Section 36 and Section 59 (square root y-scale); and heated sections: Section 47 and Section 53 (normal y-scale) 58

Fig. 48: XRD patterns of oriented aggregate samples after ethylene glycol treatment from non-heated sections: S36 and S59; and heated sections: S47 and S53 (square root y-scale) 59

Fig. 49: XRD patterns of oriented aggregate samples after heating treatment at 550 °C from non-heated sections: S36 and S59; and heated sections: S47 and S53 59

Fig. 50: XRD patterns of randomly oriented bulk bentonite samples from Section 7 (concrete contact) taken after dismantling Heater #1 61

Fig. 51: XRD patterns of randomly oriented bulk bentonite samples from Section 12 (non-heated section) taken after dismantling Heater #1 61

Fig. 52: XRD patterns of randomly oriented bulk bentonite samples from Section 19 (heated section) taken after dismantling Heater #1..... 62

Fig. 53: XRD patterns of oriented aggregate samples (normal, after ethylene glycol treatment and after heating treatment at 550 °C) from Section S12 and Section S19 63

Fig. 54: FTIR spectra of bulk samples from Section 36 in contact with the shotcrete (non-heated during the second operational phase of the FEBEX Project)..... 66

Fig. 55: FTIR spectra of bulk samples from heated Section 47. 66

Fig. 56: FTIR spectra of bulk samples from heated Section 53 67

Fig. 57: FTIR spectra of bulk samples from non-heated Section 59..... 67

Fig. 58: FTIR spectra of < 2 µm fraction samples from Section 36 (shotcrete contact)..... 68

Fig. 59: FTIR spectra of < 2 µm fraction samples from heated Section 47 68

Fig. 60: FTIR spectra of < 2 µm fraction samples from heated Section 53 69

Fig. 61: FTIR spectra of < 2 µm fraction samples from non-heated Section 59 (BB-59-1, BB-59-2, BB-59-3, BB-59-4 and BB-59-5) 69

Fig. 62: FTIR spectra of some powdered samples from the black halo in block BB-36-1 (for sample location, see Fig. 30, Fig. 34) 70

Fig. 63: FTIR spectra of some powdered samples from bentonite blocks in Section 47 (for sample location, see Fig. 31) 70

Fig. 64: FTIR spectra of some powdered samples from Section 53 (for sample location, see Fig. 32)..... 71

Fig. 65: FTIR spectra of some powdered samples from bentonite block BB-59-1 (for sample location, see Fig. 33 and Fig. 37) 71

Fig. 66: FTIR spectra of some powdered samples from bentonite block BB-59-2 1 (for sample location, see Fig. 33 and Fig. 37) 72

Fig. 67: FTIR spectra of some powdered samples from bentonite block BB-59-3 1 (for sample location, see Fig. 33 and Fig. 37) 72

Fig. 68: FTIR spectra of some powdered samples from bentonite block BB-59-4 1 (for sample location, see Fig. 33 and Fig. 37) 73

Fig. 69: FTIR spectra of some powdered samples from bentonite block BB-59-5 1 (for sample location, see Fig. 33 and Fig. 37) 73

Fig. 70: TG-DSC curves from bulk sample BB-36-4 (external bentonite ring)..... 75

Fig. 71: TG-DSC curves from bulk sample BB-36-5 (middle bentonite ring) 75

Fig. 72: TG-DSC curves from bulk sample BB-36-6 (inner bentonite ring) 76

Fig. 73: Comparison of DSC curves of bulk samples from Section 36 (in contact with the concrete plug) and the Reference FEBEX bentonite 76
Fig. 74: TG-DSC curves from bulk sample BB-47-7 (external bentonite ring)..... 77
Fig. 75: TG-DSC curves from bulk sample BB-47-8 (middle bentonite ring) 77
Fig. 76: TG-DSC curves from bulk sample BB-47-9 (internal bentonite ring) 78
Fig. 77: Comparison of DSC curves of bulk samples from Section 47 (heated section) and the Reference FEBEX bentonite..... 78
Fig. 78: TG-DSC curves from the bulk sample BB-53-7 (external bentonite ring)..... 79
Fig. 79: TG-DSC curves from bulk sample BB-53-8 (middle bentonite ring) 79
Fig. 80: TG-DSC curves from bulk sample BB-53-9 (internal bentonite ring) 80
Fig. 81: Comparison of DSC curves of bulk samples from Section 53 (heated section) and the Reference FEBEX bentonite..... 80
Fig. 82: TG-DSC curves from the < 2 μm sample BB-47-9 (internal bentonite ring) 81
Fig. 83: TG-DSC curves from the < 2 μm sample BB-53-9 (internal bentonite ring) 81
Fig. 84: Comparison of the TG-DSC curves from the < 2 μm fraction from the internal bentonite ring (BB-47-9 and BB-53-9) with the reference sample..... 82
Fig. 85: TG-DSC curves from bulk sample BB-59-1 82
Fig. 86: TG-DSC curves from bulk sample BB-59-2 83
Fig. 87: TG-DSC curves from bulk sample BB-59-3 83
Fig. 88: TG-DSC curves from bulk sample BB-59-4 84
Fig. 89: TG-DSC curves from bulk sample BB-59-5 84
Fig. 90: Comparison of DSC curves of bulk samples from Section 59 (non-heated section) and the reference FEBEX bentonite..... 85
Fig. 91: TEM images from < 2 μm clayey suspensions of the FEBEX Reference bentonite 90
Fig. 92: TEM images of < 2 μm montmorillonite clay particles obtained from clay suspensions from samples of different bentonite blocks: a) BB-36-1, b) BB-47-7, c) BB-53-3, d) BB-59-3..... 90
Fig. 93: TEM images of non-smectite particles from < 2 μm clayey suspensions: a) bentonite block BB-36-2: kaolinite type particle; b) bentonite block BB-36-3 red: nontronite type particle and/or iron colloids; c) bentonite block BB-47-9: illite particle; d) bentonite block BB-59-3: illite type particle 91
Fig. 94: TEM images from < 2 μm clayey suspensions of the bentonite block BB-59-5: a) silica colloids (a and c); smectite particle (b); b) smectite particle (a); silica colloids (b)..... 91

Fig. 95: Layer charge, % of tetrahedral charge and % of octahedral charge as a function of distance to the gallery axis determined by TEM analyses (Structural formula based on $O_{10}(OH)_2$ and maintaining the $\Sigma_{oct} = 2.0$) 92

Fig. 96: Magnesium at octahedral sites, at interlayer charge and total as a function of distance to the gallery axis determined by TEM analyses (Structural formula based on $O_{10}(OH)_2$ and maintaining the $\Sigma_{oct} = 2.0$) 93

Fig. 97: TEM analysis: Octahedral Mg-Al-Fe ternary diagram for the FEBEX bentonite samples after dismantling Heater #2 94

Fig. 98: Solid solution in the muscovite (Mu)- celadonite (Ce)-Pyrophyllite system (Hower & Mowatt 1966) 95

Fig. 99: TEM analysis: Solid solution in the muscovite (Mu)- celadonite (Ce)-Pyrophyllite system for the FEBEX bentonite samples after dismantling Heater #2 95

Fig. 100: Solid solution projection in the M^+-4Si-R^{2+} system (Meunier 2005): a) chemical composition of illite/smectite mixed-layers; b) chemical composition domain of beidellite (tetrahedral charge) and montmorillonite (octahedral charge) 96

Fig. 101: TEM analysis: Solid solution projection in the M^+-4Si-R^{2+} system for the reference and retrieved samples from the dismantling of Heater #2 97

Fig. 102: Solid solution projection in the M^+-4Si-3R^{2+} system: a) representation of a series of trioctahedral smectites and saponite/chlorite mixed layers, and b) representation of the compositional range of the theoretical solid solution of tetrahedral smectites limited by saponites (tetrahedral charge) and by stevensite-hectorite series (Meunier 2005) 98

Fig. 103: Solid solution projection in the MR^{3+}-2R^{3+}-3R^{2+} system representing the compositional range of the theoretical solid solution of tetrahedral smectites (Velde 1985) 98

Fig. 104: TEM analysis: Solid solution projection in the M^+-4Si-3R^{2+} system for the reference and retrieved samples from the dismantling of Heater #2 99

Fig. 105: TEM analysis: Solid solution projection in the MR^{3+}- 2R^{3+}-3R^{2+} system for the reference and retrieved samples from the dismantling of Heater #2 99

Fig. 106: Chemical projection system from dioctehedral to trioctahedral 2:1 clay minerals enabling substitutions of $2R^{3+} +$ $\Rightarrow 3R^{2+}$. All Fe content was taken as Fe(III), except for the chlorite sample that was taken as Fe(II); : vacancy, unit Structural formula calculated on the Si_4O_{10} basis for 2:1 minerals, Wiewiora 1990) 100

Fig. 107: SEM photomicrographs of samples from Section 36 in contact with the shotcrete 105

Fig. 108: SEM photomicrographs of samples from Section 47 and 53 in contact with Heater #2 106

Fig. 109: SEM photomicrographs of samples from Section 59 (hydrated section) 107

Fig. 110: SEM analysis: Octahedral Mg-Al-Fe ternary diagram for the FEBEX bentonite samples after dismantling Heater #2 109

Fig. 111: SEM analysis octahedral Al-Fe-total Mg (octahedral+interlayer) ternary diagram for the FEBEX bentonite samples after dismantling Heater #2..... 109

Fig. 112: Solid solution in the muscovite (Mu)- celadonite (Ce)-Pyrophyllite (Py) system for the FEBEX bentonite samples after dismantling Heater #2..... 110

Fig. 113: Solid solution projection in the M+-4Si-R2+ system for the reference and retrieved samples from the dismantling of Heater #2 110

Fig. 114: SEM analysis: Solid solution projection in the M^{+} - 4Si - $3R^{2+}$ system for the reference and retrieved samples from the dismantling of Heater #2..... 111

Fig. 115: SEM analysis: Solid solution projection in the MR^{3+}- $2R^{3+}$-$3R^{2+}$ system for the reference and retrieved samples from the dismantling of Heater #2..... 111

In red: ideal clay minerals 111

Fig. 116: Main oxides in the bulk bentonite samples: SiO_2, Al_2O_3, Fe_2O_3 and MgO 113

Fig. 117: Main oxides in the bulk bentonite samples: Fe_2O_3, MgO, CaO, Na_2O and K_2O 113

Fig. 118: Main oxides in the bulk bentonite samples: TiO_2, P_2O_5 and SO_3 113

Fig. 119: Trace elements in the bulk bentonite samples from Sections S36, S47, S53 and S59 114

Fig. 120: Sulphur and carbon analysed in samples from Sections S33, S47, S53 and S59 120

Fig. 121: Total carbon as a function of distance to the gallery axis..... 120

Fig. 122: Free Fe_2O_3 as a function of distance to the gallery axis 121

Fig. 123: Free Al_2O_3 as a function of distance to the gallery axis (values of reference sample are below detection limits) 121

Fig. 124: Free silica as a function of distance to the gallery axis 122

Fig. 125: Mean layer charge vs. (001) basal reflexion for alkyl chains nC = 12 and nC = 18 in samples from different bentonite sections 125

Fig. 126: Total cation exchange capacity as a function of distance from the tunnel axis: two samples per block (S1 and S2) along three radii from Sections S36, S47, S53 and S59 127

Fig. 127: Total cation exchange capacity as a function of distance from the tunnel axis (data from one average sample from each block along three radii, i.e., mineralogy subsample, see Fig. 26)..... 128

Fig. 128: Relationship between CEC calculated from Alkylammonium Layer Charge determinations and by Cu-trien complex 128

Fig. 129: Sodium occupancy at exchange sites as a function of distance to the gallery axis from samples taken during Dismantling of Heater #2 in 2015 130

Fig. 130: Calcium occupancy at exchange sites as a function of distance to the gallery axis from samples taken during dismantling of Heater #2 in 2015 131

Fig. 131: Magnesium occupancy at exchange sites as a function of distance to the gallery axis from samples taken during dismantling of Heater #2 131

Fig. 132: Potassium occupancy at exchange sites as a function of distance to the gallery axis from samples taken during dismantling of Heater #2 132

Fig. 133: Copper occupancy at exchange sites as a function of distance to the gallery axis from samples taken during dismantling of Heater #2 in 2015 132

Fig. 134: Cation occupancy at interlayer sites from Sections S36, S59, S47 and S53 at different radii taken during dismantling of Heater #2 133

Fig. 135: Cation occupancy at interlayer sites from Sections S7, S12, S19 and S28 taken during the dismantling of Heater #1 in 2002 as a function of distance to the gallery axis (values normalised with respect to CEC = 102 meq/100g)..... 134

Fig. 136: Cation exchange occupancies from Section 19 (dismantling of Heater #1 in 2002) as a function of distance to the gallery axis (values normalised with respect to CEC = 102 meq/100g)..... 135

Fig. 137: Sum of exchangeable cations in Sections S7, S12, S19 and S28 as a function of distance to the gallery axis from samples taken during dismantling of Heater #1 in 2002 135

Fig. 138: Relationship between CEC and: a) Σ exchangeable cations or b) (Σ exchangeable cations-CEC), in samples from dismantling of Heater #2..... 136

Fig. 139: Comparison of methods for extraction of cation exchange occupancies in 2002 (open points) and 2015 (closed points): a) Exchangeable cations obtained with 0.5 M $CsNO_3$ solutions buffered (2015) or not at pH 8.2 (2002), b) sum of exchangeable cations in 0.5 M $CsNO_3$ suspensions buffered (2015) or not at pH 8.2 (2002) 137

Fig. 140: Average particle size for clayey suspensions as a function of pH and distance to the gallery axis in the heated Section 47 and comparison with the Reference sample..... 140

Fig. 141: Light scattering events (count number) for clayey suspensions as a function of pH and distance to the gallery axis in heated Section 47 and comparison with the Reference FEBEX sample..... 141

Fig. 142: Electrophoretic mobility for different bentonite suspensions from Section 47 as a function of pH and distance to the gallery axis 141

Fig. 143: Zeta potential (ξ potential) for different bentonite suspensions from Section 47 as a function of pH and distance to the gallery axis 142

Fig. 144: Zeta potential, mobility and exchangeable Na and Ca for different bentonite suspensions from Section 47 as a function of distance to the gallery axis 142

Fig. 145: Adsorption-desorption isotherms of N_2 gas at 77 K from samples after dismantling of Heater #2 and comparison with the FEBEX Reference sample (see location of samples in Fig. 17, Fig. 18, Fig. 19, Fig. 20 and Fig. 21)144

Fig. 146: Adsorption-desorption isotherms of N_2 gas at 77 K from samples after dismantling of Heater #1 and comparison with the FEBEX Reference sample (see location of samples in Fig. A-1 from Appendix A) 144

Fig. 147: Number of N_2 adsorbed layers as a function of P/P_o according to the de Boer-(1965, 1966) method (*t*-plot treatment on adsorption branch)..... 145

Fig. 148: BET surface area from samples obtained after dismantling of Heater #1 and Heater #2 (data compared to the FEBEX Reference sample)..... 145

Fig. 149: *t*-plot according to Harkins-Jura method for the samples after dismantling Heater #2 149

Fig. 150: *t*-plot according to Harkins-Jura method for the samples after dismantling Heater #1 149

Fig. 151: Pores size distribution (PSD) calculated from the BJH method (adsorption branch) for mesopores from samples obtained after dismantling Heater #2 150

Fig. 152: Total surface area in bentonite samples from the heated sections: Section 47 and Section 53 153

Fig. 153: Total surface area in bentonite samples from Section 36 (shotcrete contact) and Section 59 (non-heated section) 153

Fig. 154: Total surface area in bentonite samples from Sections S36, S47, S53 and S59 as a function of distance to the gallery axis 154

Fig. 155: Water adsorption isotherms for samples from Section 36 and comparison to the reference FEBEX sample 155

Fig. 156: Water adsorption isotherms for samples from Section 47 and comparison to the reference FEBEX sample 155

Fig. 157: Water adsorption isotherms for samples from Section 53 and comparison to the reference FEBEX sample 156

Fig. 158: Water adsorption isotherms for samples from Section 59 and comparison to the reference FEBEX sample. The (001) reflexions correspond to the reference FEBEX sample 156

Fig. 159: Chloride, sodium and potassium content (1:4 aqueous leaching tests) from samples at different sections in three radii after dismantling Heater #2 in 2015 159

Fig. 160: Sulphate, calcium and magnesium content (1:4 aqueous leaching tests) from samples at different sections in three radii after dismantling Heater #2 in 2015 160

Fig. 161: Alkalinity (as bicarbonate), pH and fluoride content (1:4 aqueous leaching tests) from samples at different sections in three radii from the dismantling Heater #2 in 2015 161

Fig. 162: Thiosulfate, acetate and formate content (1:4 aqueous leaching tests) from samples at different sections in three radii after dismantling Heater #2 in 2015 162

Fig. 163: Na versus Cl and Mg versus Cl relationships in aqueous extracts 163

Fig. 164: Comparison of chloride content data after dismantling Heater #1 and Heater #2 164

Fig. 165: Ca versus sulphate and Ca versus HCO_3^- relationships in aqueous extracts 164

Fig. 166: Ion content (in mmol/100g, 1:4 aqueous leaching) at different sections in three radii after dismantling Heater #1 in 2002 165

Fig. 167: Cation content (in mmol/100g, 1:4 aqueous leaching) at different sections in three radii after dismantling Heater #1 in 2002 166

Fig. 168: Preparation of a bentonite sample for a squeezing test after dismantling of Heater #2 167
Fig. 169: Compacted bentonite BB-47-7 in a squeezing test after dismantling of Heater #2: a) prior to the squeezing test, and b) after squeezing test 167
Fig. 170: Extraction of pore water by squeezing under anoxic conditions 167
Fig. 171: Squeezing pressure required for collecting pore water as a function of the water content and dry density of the samples analysed 169
Fig. 172: Ionic strength and water activity of the squeezed waters from bentonite samples taken after dismantling Heater #2 170
Fig. 173: Chloride and sodium in the squeezed pore water samples obtained after dismantling Heater #2 in 2015 as a function of distance to the gallery axis..... 171
Fig. 174: Sulphate, calcium and magnesium in the squeezed pore water samples obtained after dismantling Heater #2 in 2015 as a function of distance to the gallery axis..... 171
Fig. 175: Calcium, magnesium and alkalinity in the squeezed pore water samples obtained after dismantling Heater #2 in 2015 as a function of distance to the gallery axis..... 172
Fig. 176: TOC, acetate and formate in squeezed pore waters obtained after dismantling Heater #2 in 2015..... 181
Fig. 177: Saturation indices of gypsum and calcite in pore waters from squeezed samples obtained after dismantling Heater #2 in 2015..... 181
Fig. 178: Schematic figure of the FEBEX in-situ test divided in dismantling sections: location of the dismantling bentonite sections around Heater #2 selected for THC studies 183
Fig. 179: Bentonite sample BM-S-47-1 taken from liner contact at bentonite sampling Section S47 (bentonite slice 44)..... 183
Fig. 180: Bentonite sample BM-S-47-2 taken from liner contact at bentonite sampling Section S47 (bentonite slice 44)..... 184
Fig. 181: Bentonite samples taken from liner contact at bentonite sampling Section S53 (bentonite slice 28) 184
Fig. 182: Bentonite samples taken from the internal part of the liner at contact with the heater (bentonite slice 59/57, bentonite sampling Section S42-S43)..... 185
Fig. 183: Bentonite samples (protrusions) taken from the internal part of the liner at contact with the heater (bentonite slice 59/57, bentonite sampling Section S42-S43) 185
Fig. 184: Bentonite protrusions through the liner holes towards the heater. Samples taken from the internal part of the liner at contact with the heater (bentonite slice 59/57, bentonite sampling Sections S42-S43)..... 186
Fig. 185: Protrusion taken from inside the liner (around Sampling Section S43/Slice 57) on 11/06/2015 186
Fig. 186: Green bentonite (CL) at direct contact with the frontal part of the heater (Slice 60)..... 187

Fig. 187: XRD patterns of bulk samples from BMS and protrusion samples located at contact with the liner/Heater #2: a) Fe-oxy/hydroxides from magnetic samples, b) brucite, c) chlorite at the frontal part of the Heater #2, and d) ethylene-glycol solvated oriented aggregates 189

Fig. 188: FTIR spectra (OH-stretching and OH-bending regions) from samples taken above (BMS) and inside the liner (protrusions) at contact with Heater #2. 192

Fig. 189: Comparison of DSC curves from the bulk bentonite samples (total fraction): at direct contact with the liner (BMS-47-3) and protrusions through the liner holes towards the heater 195

Fig. 190: TG-DSC curves from the magnetic powder of sample BMS-47-2 at direct contact with the liner: ferrihydrite 195

Fig. 191: Comparison of DSC curves from samples BMS-47-xx and BMS-53-xx (< 2 μm fraction) at direct contact with the liner 196

Fig. 192: TG-DSC curves from the GB-42 bentonite protrusion sample through the liner holes towards the heater 196

Fig. 193: TG-DSC curves from bentonite at direct contact with the frontal surface of Heater #2: Black ball particle (BB): chlorite 197

Fig. 194: SEM photomicrographs of Fe-oxy/hydroxides in different protrusion samples: a) WB-42, d) BSH-42 Black spot: Fe-oxides with Cl 200

Fig. 195: SEM photomicrographs of Fe-carbonates in different samples: a) BSH-42 Black spot inside heater and, b) RNW42 200

Fig. 196: SEM photomicrographs from carbonates in different samples: a) GB-42 inside heater black: Ca-carbonate; b) RNW42 with Dolomite Ca-sulphates 200

Fig. 197: SEM photomicrographs from different samples: a) RV-42: pyrite (1), smectite (2), Ca-sulphate (3); b) GB-42 inside heater black: Ca-sulphates in different samples 201

Fig. 198: SEM photomicrographs of silica from different samples: a) GB-42 inside heater black, b) BSH-42 Black spot inside heater 201

Fig. 199: SEM photomicrographs of clay minerals in different samples: a) smectite: BMS-47-2, b) Nontronite/(Fe-rich illite) type: S43 FR Red particles, c) chlorites (1), Fe-carbonates (2), BSH-42 Black spot inside heater, d) and e) chlorites: Black particles adhered to bentonite (BP), f) chlorites: Black ball (BB) 202

Fig. 200: TEM images from < 2 μm clayey suspensions: smectite particles from the FEBEX reference bentonite 204

Fig. 201: TEM images from < 2 μm clayey suspensions: smectite particles from the sample of bentonite block BMS-47-2 204

Fig. 202: TEM images from < 2 μm clayey suspensions: smectite particles from the sample of bentonite block BMS-53-2 205

Fig. 203: TEM images from < 2 μm clayey suspensions: smectite particles from the sample Black spot inside heater (Protrusion BSH-42) 205

Fig. 204: TEM images from < 2 μm clayey suspensions: smectite particles from the sample Green particles (Protrusion RV-42) 206

Fig. 205: TEM images from < 2 μm clayey suspensions: smectite particles from the sample Red bentonite inside the liner (Protrusion BBIL-42) 206

Fig. 206: TEM images from < 2 μm clayey suspensions: Nontronite particles from the Red bentonite inside the liner (Protrusion BBIL-42) sample 207

Fig. 207: TEM images from < 2 μm clayey suspensions: Chlorites detected in the Black particle (BB) sample 207

Fig. 208: a) Solid solution projection in the MR^{3+}-$2R^{3+}$-$3R^{2+}$ system of the retrieved samples, b) magnesium at octahedral sites as a function of distance to the gallery determined by TEM analysis 208

Fig. 209: Anion concentration in aqueous extracts at 1:4 solid to liquid ratio from samples retrieved after dismantling Heater #2 including BMS and Protrusion samples 214

Fig. 210: Cation concentration in aqueous extracts at 1:4 solid to liquid ratio from samples retrieved after dismantling of Heater #2 including BMS and Protrusion samples 215

Fig. 211: Bentonite corroded sample at contact with sensor SH-SDI-01 in Section 17 216

Fig. 212: Photographs from the internal part of the liner just after extraction of Heater #1 (Section 17) 217

Fig. 213: Bentonite corroded sample at contact with cables and surrounding the ceramic gas pipe GF-SL-06 in Section 29 218

Fig. 214: Bentonite block sample in contact with the back part of Heater #1: a) Samples taken from the back part of Heater #1, b) and c) Bentonite block BS-31-26 and location, c) and d) core sample BS31-22 and location 218

Fig. 215: XRD patterns of randomly oriented bulk samples surrounding SH-SDI-1 sensor: dark-greenish bentonite, greenish-blackish bentonite and reddish bentonite. 223

Fig. 216: Oriented aggregates (AO, EG, 550 °C) from samples: a) dark-greenish bentonite surrounding SH-SDI-1 sensor; b) reddish bentonite surrounding SH-SDI-1 sensor 223

Fig. 217: FTIR spectra of bulk samples surrounding SH-SDI-1 sensor 224

Fig. 218: TG-DSC curves from the bulk sample SHSDI-01/A 224

Fig. 219: TG-DSC curves from the bulk sample SHSDI-01/B 225

Fig. 220: XPS spectrum of the greenish bentonite sample surrounding the SH-SDI-sensor 225

Fig. 221: Convolution of oxygen and iron peaks form the XPS spectrum for the greenish bentonite sample surrounding the SH-SDI-sensor indicating the presence of oxy-hydroxides of iron (FeOOH) 226

Fig. 222: Convolution of Si, Al, Mg and Na peaks from the XPS spectrum for the greenish bentonite sample surrounding the SH-SDI-sensor indicating the presence of silicates (smectite) 227

Fig. 223: Convolution of Ca and C peaks from the XPS spectrum for the greenish bentonite sample surrounding the SH-SDI-sensor indicating the presence of calcite and organic matter 228

Fig. 224: XPS spectrum of the reddish bentonite sample surrounding the SH-SDI-sensor 228

Fig. 225: Convolution of oxygen and iron peaks from the XPS spectrum for the reddish bentonite sample surrounding the SH-SDI-sensor, indicating the presence of silicates (smectite), oxy-hydroxides (FeOOH) and hematite (Fe_2O_3) 229

Fig. 226: Convolution of Ca and C from the XPS spectrum for the reddish bentonite sample surrounding the SH-SDI-sensor, indicating calcite and organic matter 230

Fig. 227: Convolution of Si, Al, and Na peaks from the XPS spectrum for the reddish bentonite sample surrounding the SH-SDI-sensor, indicating the presence of phyllosilicates (smectite) 231

Fig. 228: SEM photomicrographs of the SHSDI-01 greenish sample: a) Cl, Na, S, Ca and smectite; b) EDX of a), c) Ca-carbonate, d) smectite, e) mineral with Si, Al, and high amount of Mg and Fe, with Ca and K, f) EDX of e) 232

Fig. 229: SEM photomicrographs of the SHSDI-01 greenish-black particles: a) SCr, CrO, b) green-rush, Fe, Cl, C, Cr, c) ClCu and Cr.; d) smectite, e) Fe-oxides, f) Fe-oxides 233

Fig. 230: SEM photomicrographs of the SHSDI-01 greenish-black particles: a) Fe-oxides, b) bacteria, Cr, Fe, c) Ti-oxides, Fe-oxides, microorganisms, d) S, Cr, Ca-carbonates, e) Cr, S, f) Cr, S 234

Fig. 231: SEM photomicrographs of the SHSDI-01 greenish-black particles: a) S, Fe, Cr, Pb, b) EDX of a), c) SCr, d) C, Fe, Cr, S 235

Fig. 232: SEM photomicrographs of the SHSDI-01 reddish particles: a) C, Fe, b) barite 235

Fig. 233: SEM photomicrographs of the SHSDI-01 reddish sample: a) bacteria, b) Fe carbonates, c) Fe-Carbonates, S, and Ca, d) Fe-rich smectite 236

Fig. 234: XRD patterns of randomly oriented bulk samples surrounding the ceramic pipes at Section 29 237

Fig. 235: Oriented aggregates (AO: green colour, EG: blue colour, 550 °C: red colour) from the sample surrounding the ceramic pipes at Section 29 237

Fig. 236: FTIR spectra of S29 samples surrounding the ceramic pipes 238

Fig. 237: SEM photomicrographs of the S29 sample surrounding the ceramic pipes: a) and b) silica, c) smectite, d) K-feldspars 238

Fig. 238: SEM photomicrographs of the S29 sample surrounding the ceramic pipes: a) red sample: Fe-oxides and Fe-carbonates; b) greenish-reddish sample: green-rush: Cl, Fe, K; c) C, Na, K, Cl; c) microorganisms and Fe, e) and f) bacteria and smectite 239

Fig. 239: SEM photomicrographs of sample S29 surrounding the ceramic pipes (red sample): a) microorganisms, b) Fe and Ca carbonates, c,d) Fe-oxides, Ca, S 240
Fig. 240: XRD pattern of randomly oriented bulk sample BS-31-26 241
Fig. 241: XRD patterns of randomly oriented bulk sample: liner holes upper part (internal) 241
Fig. 242: Oriented aggregates (AO, EG, 550 °C) from sample BS-31-26 242
Fig. 243: Oriented aggregates (AO, EG, 550 °C) from the sample taken from a liner hole (upper part) located at the internal halfway of the liner around Heater #1 242
Fig. 244: FTIR spectra of the BS-31-26 sample (total fraction) 242
Fig. 245: SEM photomicrographs of the BS-31-26 Sub 2 black particles: Fe and Ca carbonates 243
Fig. 246: TG-DSC curves from the sample BS-31-26 Sub 3 (black-brownish zone) taken from the back part of Heater #1 243
Fig. 247: TG-DSC curves from a black sample taken from a liner hole (bottom part) located at the internal halfway of the liner around Heater #1 244
Fig. 248: TG-DSC curves from a sample taken from a liner hole (upper part) located at the internal halfway of the liner and from the upper part around Heater #1 244
Fig. 249: TG-DSC curves from a black powdered sample taken from a liner hole (bottom part) located at the external halfway of the liner around Heater #1 245
Fig. 250: TG-DSC curves from the samples taken after dismantling Heater #1 close to the Liner/Heater interface and to the displacement sensor SHSDI-01 245
Fig. 251: Water-bentonite interaction processes and possible buffer alterations (after Takase 2004) 248
Fig. 252: Comparison of ion concentrations in the squeezed samples after dismantling Heater #1 in 2002 and Heater #2 in 2015 251
Fig. 253: Comparison of electrical conductivity, ionic strength and saturation index of gypsum in the squeezed samples obtained after dismantling Heater #1 and Heater #2 252
Fig. 254: Comparison of basal spacing before and after squeezing test in the sample BB-47-8. 255
Fig. 255: Anion-accessible porosity fraction in the samples as a function of dry density 257
Fig. 256: CEC, BET external surface area, total surface area and particle size for different bentonite suspensions from Section 47 as a function of distance to the gallery axis 279
Fig. 257: Particle size, BET external surface area and exchangeable Na and Ca for different bentonite suspensions from Section 47 as a function of distance to the gallery axis 279
Fig. 258: Zeta potential and layer charge (MLC) for different bentonite suspensions from Section 47 as a function of distance to the gallery axis 279

Fig. 259: Redox potential values obtained from water samples from the GRS and CIEMAT pipes located around Heater #2. Vertical bars: theoretical redox potential at pH = 7 for different reactions 282

Fig. 260: Concentration of O_2, CH_4, CO_2 and H_2 in the different GRS pipes obtained during the first (1996 – 2002) and second (2002 – 2015) FEBEX operational phases in vol.-% of gas and in mmol/L of gas dissolved in pore water (25 °C, 1 atm.). From Fernández (2017) 282

Fig. A-1: Bentonite Sampling Sections from the FEBEX in-situ test analysed for THC studies after dismantling of Heater #1 in 2002 and Heater #2 in 2015 ..... A-3

Fig. A-2: General layout of the FEBEX in-situ test (instrumented sections and radial boreholes) and geological map from the FEBEX drift A-5

Fig. A-3: Subsampling of the bentonite block for THM and THC analyses A-6

Fig. A-4: Bentonite Sampling Section 7: before dismantling, after dismantling and samples taken for analyses A-7

Fig. A-5: Bentonite Sampling Section 12 before dismantling, after dismantling and samples taken for analyses A-8

Fig. A-6: Bentonite Sampling Section 19 ..... A-9

Fig. A-7: Bentonite Sampling Section 28 ..... A-10

Fig. A-8: Bentonite Sampling Section 31 ..... A-11

Fig. A-9: Core sample obtained at contact with the back part of the heater A-12

Fig. A-10: Bentonite block sample obtained at contact with the back part of the heater A-13

Fig. A-11: Bentonite sample obtained at contact with the corroded displacement sensor SH-SDI- A-14

Fig. A-12: Bentonite sample obtained at contact with the corroded anchors from the gas pipes GF-SL-03 and GP-SM1-01 ..... A-15

Fig. A-13: Bentonite blocks from Sampling Section 7 (at concrete contact): BB7-4, BB7-5 and BB7-6 ..... A-16

Fig. A-14: Bentonite blocks from Sampling Section 12 (non-heated section) A-16

Fig. A-15: Bentonite blocks from Sampling Section 19 (heated section) A-17

Fig. A-16: Bentonite blocks from Sampling Section 28 (heated section): BB28-1, BB-28-2 and BB-28-3 ..... A-17

Fig. A-17: Squeezed water extraction apparatus used at CIEMAT for the pore water from bentonite samples taken during the dismantling of Heater #1 in 2002 ..... A-20

Fig. B-1: SEM photomicrographs in BB-36-1 sample: clay minerals B-1

Fig. B-2: SEM photomicrographs in BB-36-1 sample: a) barite with Sr (1), b) barite B-5

Fig. B-3: SEM photomicrographs in BB-36-1 sample: a) Fe-oxides, b) Fe-Cr oxides, c) Fe-oxides, d) Fe-oxides, e) Fe-Cr, Ni, Cu-oxides, f) Ti-Fe oxides with C B-6

Fig. B-4: SEM photomicrographs in BB-36-1 sample: a) plagioclases (2,3), b) K-feldspar, c) plagioclase, d) plagioclases B-7

Fig. B-5: SEM photomicrographs in BB-36-1 sample: a) apatite (1) and plagioclases (2), b) monazite B-7

Fig. B-6: SEM photomicrographs in BB-36-1 sample: a) and b) zircon B-8

Fig. B-7: SEM photomicrographs in BB-36-1 sample: a) portlandite $Ca(OH)_2$, b) Silica (1) B-8

Fig. B-8: SEM photomicrographs in BB-36-1 sample: a) organic matter (OM), b) carbon and nitrogen (1), monazite (2) B-8

Fig. B-9: SEM photomicrographs in BB-36-1 sample: a) Ca-carbonates (1,2), b) Ca(Mg)-carbonates; c) Fe-carbonate; d) Fe-carbonate..... B-9

Fig. B-10: SEM photomicrographs in BB-36-2 sample: clay minerals B-10

Fig. B-11: SEM photomicrographs in BB-36-2 sample: a) Ca-carbonates, b) Ca-carbonates (2), organic matter (1); c) Ca-carbonates (1), d) dolomite (1) B-13

Fig. B-12: SEM photomicrographs in BB-36-2 sample: a) Fe-carbonates, d) Fe-carbonates and OM B-13

Fig. B-13: SEM photomicrographs in BB-36-2 sample: a) Ca-sulfates (1), barite (2), b) Ca-sulfates (1), Ca-carbonate (2), clay minerals (3), c) Ca-sulfates (ettringite), d) barite..... B-14

Fig. B-14: SEM photomicrographs in BB-36-2 sample: a) plagioclases, b) plagioclases (2), apatite (1); c) K-feldspar (2), ilmenite (1), d) K-feldspars B-15

Fig. B-15: SEM photomicrographs in BB-36-2 sample: a) organic matter (OM), b) silica B-15

Fig. B-16: SEM photomicrographs in BB-36-2 sample: a) Fe-oxides, b) Zircon..... B-16

Fig. B-17: SEM photomicrographs in BB-36-5 sample: a) and b) microorganisms..... B-16

Fig. B-18: SEM photomicrographs in BB-36-5 sample: a) apatite; b) apatite (1), plagioclases (2) B-16

Fig. B-19: SEM photomicrographs in BB-36-5 sample: a) Ca-carbonates (1), Ca-sulfates (2), b) Ca-Mg carbonate (1), c) Ca-carbonates, d) Ca-carbonate (1), plagioclases (2), K-feldspar (3) B-17

Fig. B-20: SEM photomicrographs in BB-36-5 sample: a) Fe-carbonate (1), muscovite (2), plagioclase (3), Silica (4); b) Fe-carbonate (1)..... B-17

Fig. B-21: SEM photomicrographs in BB-36-5 sample: a) Fe-oxides (1), b) Magnesite B-18

Fig. B-22: SEM photomicrographs in BB-36-5 sample: a) plagioclases; b) plagioclases (1), clay minerals (2)..... B-18

Fig. B-23: SEM photomicrographs in BB-36-5 sample: a) Ca-sulfates (1), ilmenite (2); b) barite (2), biotite (1)..... B-18

Fig. B-24: SEM photomicrographs in BB-36-5 sample: a) Fe-oxides with C, b) Fe-oxides (1), Fe-oxides with C, saponite? (3) B-19

Fig. B-25: SEM photomicrographs in BB-36-5 sample: a) silica (1), silica+Ca,S (2), clay minerals (3), b) silica (1), plagioclases (2) B-19

Fig. B-26: SEM photomicrographs in BB-36-5 sample: clay minerals B-20

Fig. B-27: SEM photomicrographs: a) BB-47-4 sample: Ca-sulfates (1), b) BB-47-7: Ca-sulfates (1), zircon (2) B-22

Fig. B-28: SEM photomicrographs in BB-47-7 sample: a): Fe-oxides (1), smectite (2), b) Fe-oxides B-22

Fig. B-29: SEM photomicrographs in BB-47-7 sample: a) and b) silica B-23

Fig. B-30: SEM photomicrographs: a) BB-47-4 sample: apatite, b) BB-47-7 sample: apatite, c) BB-47-7 sample: zircon, d) BB-47-7 sample: zircon B-23

Fig. B-31: SEM photomicrographs: a) BB-47-4 sample: zeolites? (1), plagioclases (1), feldspars (3), b) BB-47-7 sample: plagioclase, c) BB-47-7: plagioclase (1), smectite(2), Fe, Ti (3), d) BB-47-7: biotite (1), plagioclase (2) B-24

Fig. B-32: SEM photomicrographs: BB-47-7 sample: a) K-feldspar; b) barite (1), plagioclase (2) B-24

Fig. B-33: SEM photomicrographs: a) BB-47-4 sample: ilmenite (1), apatite (2), b) BB-47-7 sample: ilmenite (1) B-25

Fig. B-34: SEM photomicrographs in BB-47-7 sample: a) Fe-carbonate, b) Fe-carbonate (1), smectite(2), plagioclase (3), Fe,S (4) B-25

Fig. B-35: SEM photomicrographs in BB-47-7 sample: a) S, Fe (2), b) S, Fe (1), c) smectite (1), S, Fe (2) B-26

Fig. B-36: SEM photomicrographs in BB-47-4 sample: a) microorganisms and plagioclase, b) microorganisms, c) biotite (1), plagioclase (2), microorganisms, d) microorganims B-27

Fig. B-37: SEM photomicrographs in BB-47-7 sample: a) organic matter (OM), C, b) organic matter, c) Ti, Mn, Fe (1), C (OM) (2) B-28

Fig. B-38: SEM photomicrographs in BB-47-7 sample: a) and b) Ca-carbonates B-28

Fig. B-39: SEM photomicrographs in BB-47-4 sample: clay minerals B-29

Fig. B-40: SEM photomicrographs in BB-47-7 sample: clay minerals B-30

Fig. B-41: SEM photomicrographs in BB-47-2 sample: clay minerals B-31

Fig. B-42: SEM photomicrographs in BB-47-5 sample: clay minerals B-32

Fig. B-43: SEM photomicrographs in BB-47-8 sample: clay minerals B-33

Fig. B-44: SEM photomicrographs in BB-47-8 sample: a): Ba-sulfates (1), smectite (2), b) barite B-34

Fig. B-45: SEM photomicrographs in BB-47-5 sample: a) and b) silica B-34

Fig. B-46: SEM photomicrographs: a) BB-47-2: Ca-sulfate (1), b) BB-47-2: Ca-sulfates B-35

Fig. B-47: SEM photomicrographs: a) BB-47-5 sample: a) Ca-sulfates (1), b) Ca-sulfates (2), smectite (1,3), c) Ca-sulfates (1), plagioclases (2), d) Ca-sulfates, e) Ca-sulfates (2), plagioclase (1), K-Fd (3) smectite (4), f) BB-47-8 sample: halloysite? (1), smectite (2), Ca-sulfate (3), C, orthoclase-Na (4) B-36

Fig. B-48: SEM photomicrographs in BB-47-5 sample: Ca-carbonates, P and Ce B-37

Fig. B-49: SEM photomicrographs in BB-47-2 sample: a): Sr (Ba)-sulfates (1), b) Ba (Sr)-sulfate, c) BB-47-2 sample: Ba (Sr)-sulfate B-37

Fig. B-50: SEM photomicrographs in BB-47-8 sample: a) Fe-Ti, V, M, C, b) BB-47-2 sample: Cu, Sn, C B-38

Fig. B-51: SEM photomicrographs in BB-47-8 sample: S, Fe (1), smectite (2)..... B-38

Fig. B-52: SEM photomicrographs: a) BB-47-5 sample: apatite (1), Fe-oxide (2), plagioclase (3), Ti-Fe-Mn (4), b) BB-47-8 sample: apatite (1), c) BB-47-2 sample: Fe-oxides, d) BB-47-2: Fe-oxides, e) BB-47-2 sample: Fe-Cr-oxides, f) BB-47-2: apatite B-39

Fig. B-53: SEM photomicrographs: a) BB-47-2 sample: biotite, b) BB-47-2 sample: biotite? (1), smectite (2) B-40

Fig. B-54: SEM photomicrographs: a) B-47-5 sample: organic matter (OM): C, b) BB-47-2: organic matter (OM), c) BB-47-2: organic matter (1) Ca-carbonate (2), Fe-carbonate (3), plagioclase (4) B-40

Fig. B-55: SEM photomicrographs: a) BB-47-8 sample: plagioclases, b) BB-47-8 sample: orthoclase-Na, c) BB-47-2 sample: plagioclases, d) BB-47-2 sample: K-feldspar..... B-41

Fig. B-56: SEM photomicrographs: a) BB-47-8 sample: Ca-carbonates (1), b) BB-47-2: Ca-carbonates, c) BB-47-2: Ca-carbonates B-42

Fig. B-57: SEM photomicrographs: a) BB-47-6 sample: Ca-sulfates, b) BB-47-9 sample: Ba-sulfates..... B-43

Fig. B-58: SEM photomicrographs: a) BB-47-6 sample: S, Fe, b) BB-47-9 sample: S, Fe, Hg, c) b) BB-47-9 sample: S, Ni, Fe, Hg, d) BB-47-9 sample: S, Hg, Zn, Cu, Fe, e) BB-47-9 sample: S, Hg, Fe, Cu, Mn (1), S, Mn, Cu, Hg (2), smectite (3) B-44

Fig. B-59: SEM photomicrographs: BB-47-9 sample: Fe-carbonate..... B-45

Fig. B-60: SEM photomicrographs: a) BB-47-6 sample: Ti-Fe(Mn) (1), Zircon (2), monazite (3), b) Fe-oxides, c) BB-47-9 sample: Fe-oxides, d) BB-47-9 sample: Ti, Fe (Mn): ilmenite (1), plagioclase (2)..... B-45

Fig. B-61: SEM photomicrographs of clay minerals in samples BB-47-6 and BB-47-9 ..... B-46

Fig. B-62: SEM photomicrographs: a) BB-47-6 sample: apatite (1); b) BB-47-6 sample: monazite (2), smectite (1); c) BB-47-9 sample: apatite (1), d) BB-47-9 sample: biotite B-48

Fig. B-63: SEM photomicrographs: a) BB-47-9 sample: organic matter (OM) B-48

Fig. B-64: SEM photomicrographs: a) BB-47-9 sample: silica B-49

Fig. B-65: SEM photomicrographs in BB-53-3 sample: monazite..... B-50

Fig. B-66: SEM photomicrographs in BB-53-3 sample: a) Ti, Mn, Fe (1), Apatite (2), K-Felspar (3), b) EDX of (1) B-50
Fig. B-67: SEM photomicrographs in BB-53-3 sample: a) OM with Cl and N, b) EDX of (1) B-50
Fig. B-68: SEM photomicrographs in BB-53-3 sample: organic matter (1) B-51
Fig. B-69: SEM photomicrographs in BB-53-3 sample: a) silica; b) ilmenite (1) and Ca-Na-plagioclases B-51
Fig. B-70: SEM photomicrographs in BB-53-3 sample: Ca-sulfates B-51
Fig. B-71: SEM photomicrographs in BB-53-3 sample: Fe-carbonates B-52
Fig. B-72: SEM photomicrographs in BB-53-3 sample: clay minerals B-53
Fig. B-73: SEM photomicrographs in BB-53-9 sample: Fe(Ti)-oxides (1); Organic matter (2), b) EDX of (1) B-54
Fig. B-74: SEM photomicrographs in BB-53-9 sample: a) zircon (1); smectite (2); b) EDX of (1) B-54
Fig. B-75: SEM photomicrographs in BB-53-9 sample: a) ilmenite (1); silica (2); b) EDX of (1) ..... B- B-54
Fig. B-76: SEM photomicrographs in BB-53-9 sample: Ca-sulfates B-55
Fig. B-77: SEM photomicrographs in BB-53-9 sample: a) Fe-Hg-sulphides (1), smectite (2), b) EDX of (1) B-55
Fig. B-78: SEM photomicrographs in BB-53-9 sample: a) Fe-oxides (1), illite (2), b) enlargements of (1) Fe-oxides in a) B-55
Fig. B-79: SEM photomicrographs in BB-53-9 sample: a) Na,Ca-plagioclases, b) Zircon B-56
Fig. B-80: SEM photomicrographs in BB-53-9 sample: a) Zn-carbonate, b) barite (1) B-56
Fig. B-81: SEM photomicrographs in BB-53-9 sample: clay minerals B-57
Fig. B-82: SEM photomicrographs in BB-59-1 sample: microorganisms B-59
Fig. B-83: SEM photomicrographs in BB-59-1 sample: Ca-carbonates (1) B-59
Fig. B-84: SEM photomicrographs: iron oxides in BB-59-1 sample B-59
Fig. B-85: SEM photomicrographs: apatite in BB-59-1 sample B-60
Fig. B-86: SEM photomicrographs in sample BB-59-1: a) monazite, and b) biotite (1) B-60
Fig. B-87: SEM photomicrographs in BB-59-1 sample: K-feldspars (1), plagioclase (2) B-60
Fig. B-88: SEM photomicrographs: smectite clay minerals in sample BB-59-1 ..... B-61
Fig. B-89: SEM photomicrographs in sample BB-59-6: a) Fe-oxides, b) Fe-oxides, apatite and C B-62
Fig. B-90: SEM photomicrographs in sample BB-59-6: a) Fe-oxide (1), smectite (2), b) EDX of (1) B-62

Fig. B-91: SEM photomicrographs in sample BB-59-6: a) Barite (1), albite (2), microorganisms (3), b) microorganisms on smectite B-62

Fig. B-92: SEM photomicrographs in sample BB-59-6: a) Cu, Zn-carbonates, b) EDX of a) B-63

Fig. B-93: SEM photomicrographs in sample BB-59-6: a) OM (1), W, Ca-oxide (2), Ca-carbonate (3), b) microorganisms, c) S, Pb (1), OM (3), silica (4), d) Zircon (1), OM (2), smectite (3), e) Organic matter (1), smectite (2), f) EDX of (1) in e), g) carbon, h) carbon and Fe B-64

Fig. B-94: SEM photomicrographs in sample BB-59-6: a) ilmenite (1) K-feldspar (2), b) EDX of (1) B-65

Fig. B-95: SEM photomicrographs in sample BB-59-6: a) W, Ca-oxide (1), smectite (2), b) EDX of (1) B-65

Fig. B-96: SEM photomicrographs from sample BB-59-6: Fe-carbonates B-65

Fig. B-97: SEM photomicrographs in sample BB-59-6: a) biotite (1), K-Fd (2), S (3), b) EDX of (3) B-66

Fig. B-98: SEM photomicrographs: smectite clay minerals in sample BB-59-6 ..... B-67

Fig. B-99: SEM photomicrographs: smectite clay minerals in sample BB-59-2 ..... B-68

Fig. B-100: SEM photomicrographs in sample BB-59-2: a) microorganisms, b) OM (C) and S B-70

Fig. B-101: SEM photomicrographs from sample BB-59-2: a) barite, b) gypsum (2), illite(1) B-70

Fig. B-102: SEM photomicrographs from sample BB-59-2: a) plagioclases, b) biotite B-70

Fig. B-103: SEM photomicrographs from sample BB-59-2: Fe-carbonates B-71

Fig. B-104: SEM photomicrographs from sample BB-59-2: Ca-carbonates B-71

Fig. B-105: SEM photomicrographs from sample BB-59-2: a) zircon (1), Ti-Mn-Fe-oxides (2), Ti-Fe-Mn oxides (3), apatite (4); and b) Zn-oxides B-71

Fig. B-106: SEM photomicrographs from sample BB-59-2: a) 1: apatites, b) silica B-72

Fig. B-107: SEM photomicrographs: smectite clay minerals in sample BB-59-3 ..... B-73

Fig. B-108: SEM photomicrographs from sample BB-59-3: a) Ca-carbonates, b) dolomite, c) Fe-carbonates, d) Fe-carbonate and Fe-Ti-oxides B-75

Fig. B-109: SEM photomicrographs from sample BB-59-3: a) and b) barite B-75

Fig. B-110: SEM photomicrographs from sample BB-59-3: a) apatite, b) silica B-76

Fig. B-111: SEM photomicrographs from sample BB-59-3: a) 1: C and N, 2: clay minerals, b) EDAX analysis from 1) B-76

Fig. B-112: SEM photomicrographs from sample BB-59-3: a) and b) plagioclases B-76

Fig. B-113: SEM photomicrographs from sample BB-59-3: a) 1: Fe-oxides, 3, b) Mn-Ba-oxides, c) 1: Fe-oxides, 2: Mn-Ba-Mn oxides, d) 1: Ti, Fe-Mn oxides, 2: plagioclases, 3: biotite B-77

Fig. B-114: SEM photomicrographs in BB-59-4 sample: carbon (dark zone) B-77

Fig. B-115: SEM photomicrographs in BB-59-4 sample: a) Fe-carbonates, b) EDX of a) B-78

Fig. B-116: SEM photomicrographs: a) and b) iron oxides in BB-59-4 sample..... B-78

Fig. B-117: SEM photomicrographs in BB-59-4 sample: a) silica, b) ilmenite..... B-78

Fig. B-118: SEM photomicrographs in BB-59-4 sample: plagioclases..... B-79

Fig. B-119: SEM photomicrographs: smectite clay minerals in sample BB-59-4..... B-80

Fig. B-120: SEM photomicrographs from sample BMS-47-1: a) and b) organic matter with Cl..... B-81

Fig. B-121: SEM photomicrographs from sample BMS-47-1: a) Ca-sulfates (1), smectite (2), b) Ca-carbonates..... B-81

Fig. B-122: SEM photomicrographs from sample BMS-47-1: a) K-feldspar (Na), b) EDX of a)..... B-82

Fig. B-123: SEM photomicrographs from sample BMS-47-1: a) Xenotime (1), smectite (2), b) EDX of (1)..... B-82

Fig. B-124: SEM photomicrographs from sample BMS-47-1: clay minerals..... B-83

Fig. B-125: SEM photomicrographs from sample BMS-47-2: a) Ca-sulfates with carbon (1), smectite (2), b) Ca-sulfates..... B-85

Fig. B-126: SEM photomicrographs from sample BMS-47-2: a) and b) organic matter..... B-85

Fig. B-127: SEM photomicrographs from sample BMS-47-2: a) apatite (1) and Na-plagioclase, b) ilmenite (Fe, Ti)..... B-86

Fig. B-128: SEM photomicrographs from sample BMS-47-2: a) Fe-oxide (1), b) EDX from 1)..... B-86

Fig. B-129: SEM photomicrographs from sample BMS-47-2: clay minerals..... B-87

Fig. B-130: SEM photomicrographs from sample BBIL-42: a) Barite-celestine (1), smectite (2), b) Barite-celestine (1), Ca-sulfates (2)..... B-89

Fig. B-131: SEM photomicrographs from sample BBIL-42: a) Ca,Na-plagioclase (1), Fe-oxides (2), smectite (4), b) enlargement of a): Fe-oxides (3)..... B-89

Fig. B-129: SEM photomicrographs from sample BMS-47-2: clay minerals..... B-90

Fig. B-133: SEM photomicrographs from sample WB-42: a) and b) Ca-sulfates..... B-92

Fig. B-134: SEM photomicrographs from sample WB-42: a) Barite-celestine and Ca-carbonates, b) EDX from a)..... B-92

Fig. B-135: SEM photomicrographs from sample WB-42: OM with Cl and Ca..... B-92

Fig. B-136: SEM photomicrographs from sample WB-42: a) and b) Fe-oxides, c) Fe-Ti-Mn-oxides, d) Fe-Ti-Mn-oxides (1), Hg (Mo,Po) (2), Ca-sulfate (3), smectite (4)..... B-93

Fig. B-137: SEM photomicrographs from sample WB-42: a) cristobalite, b) Ca-carbonates (1), Ca,Na-plagioclases (2)..... B-93

Fig. B-138: SEM photomicrographs from sample WB-42: clay minerals..... B-94

Fig. B-139: SEM photomicrographs from sample BSH-42 Black spot inside heater: a) organic matter with N (1), smectite, b) organic matter with N (see EDX)..... B-95

Fig. B-140: SEM photomicrographs from sample BSH-42 Black spot inside heater: a) organic matter with Cl, b) silica B-95

Fig. B-141: SEM photomicrographs from sample BSH-42 Black spot inside heater: Fe-oxides B-96

Fig. B-142: SEM photomicrographs from sample BSH-42 Black spot inside heater: a) Fe-carbonates and Fe-oxides, b) Enlargement of a): Fe-carbonate (1), Fe-oxides (2) B-96

Fig. B-143: SEM photomicrographs from sample BSH-42 Black spot inside heater: a) Fe-carbonates, b) Fe-carbonates (1), Fe-oxides with Cl (2), Fe-carbonates (3), c) Fe-oxides with Cl (1), Fe-carbonates (2), d) Fe-carbonates B-97

Fig. B-144: SEM photomicrographs from sample BSH-42 Black spot inside heater: a) chlorites (1), Fe-oxides (2), b) and c) chlorites (1), d) chlorite (1), smectite (2) B-98

Fig. B-145: SEM photomicrographs from sample BSH-42 Black spot inside heater: clay minerals B-99

Fig. B-146: SEM photomicrographs from sample GB-42 inside heater black: a) organic matter with Cl,K, b) EDX from 1) B-102

Fig. B-147: SEM photomicrographs from sample GB-42 inside heater black: Fe-oxide with Cl B-102

Fig. B-148: SEM photomicrographs from sample GB-42 inside heater black: a) Ca-carbonates, b) silica (1) and (2) B-102

Fig. B-149: SEM photomicrographs from sample GB-42 inside heater black: a) Ca-sulfates with C, b) EDX from a) B-103

Fig. B-150: SEM photomicrographs from sample GB-42 inside heater black: a) Fe-oxide with some C, b) EDX from a) B-103

Fig. B-151: SEM photomicrographs from sample GB-42 inside heater black: a) Barite-celestine (1), smectite (2), Ca-sulfates (3), b) Barite-celestine from a) B-103

Fig. B-152: SEM photomicrographs from sample GB-42 Black spot inside heater: clay minerals B-104

Fig. B-153: SEM photomicrographs from sample RNW42: a) Organic matter, OM, (1), b) OM (1) with Cl B-106

Fig. B-154: SEM photomicrographs from sample RNW42: a) Fe-carbonates (1), b) enlargement of 1) B-106

Fig. B-155: SEM photomicrographs from sample RNW42: a) zircon (1), Na-Ca-plagioclases, Ca-sulfates (3), b) Ca-sulfates B-106

Fig. B-156: SEM photomicrographs from sample RNW42: a) Dolomite (1), Ca-sulfates (2), b) enlargement of a) B-107

Fig. B-157: SEM photomicrographs from sample RNW42: a) Ca-carbonate (1), Ca-sulfate (2), b) Monazite (1), smectite (2) B-107

Fig. B-158: SEM photomicrographs from sample RNW42: a) Ca-sulfate, b) Smectite (1), Ca-sulfate (2), Fe,Ti-oxides (3) B-107

Fig. B-159: SEM photomicrographs from sample RNW42: Ca-carbonate and Mn (1), dolomite (2), Ca-sulfate (3) B-108

Fig. B-160: SEM photomicrographs from sample RNW42: clay minerals B-109

Fig. B-161: SEM photomicrographs from sample RNW-42 grey particles: a) Ca-sulfates, b) Barite(Sr) (1), Plagioclase (2), Gypsum (3) B-111

Fig. B-162: SEM photomicrographs from sample RNW-42 grey particles: barite-celestine B-111

Fig. B-163: SEM photomicrographs from sample RNW-42 grey particles: apatite B-111

Fig. B-164: SEM photomicrographs from sample RNW-42 grey particles: B-Fe-carbonate with Cu and Cl (1), Fe-carbonate with Cr and Cl (2), OM with Cl (3) with Cl, b) EDX from (2) B-112

Fig. B-165: SEM photomicrographs from sample RNW-42 grey particles: clay minerals B-113

Fig. B-166: SEM photomicrographs from sample RV-42: pyrite (1), smectite (2), gypsum (3) B-115

Fig. B-167: SEM photomicrographs from sample RV-42: a) and b) Ca-sulfates B-115

Fig. B-168: SEM photomicrographs from sample RV-42: a) Barite-celestine, b) Barite (1), gypsum (2) B-115

Fig. B-169: SEM photomicrographs from sample RV-42: a) Barite-celestine (1), Ca-carbonate (2) and Hg (points), b) zircon B-116

Fig. B-170: SEM photomicrographs from sample RV-42: clay minerals B-117

Fig. B-171: SEM photomicrographs from sample PS-43: a) Ca-Na plagioclase, b) apatite B-120

Fig. B-172: SEM photomicrographs from sample PS-43: Pb-sulfide B-120

Fig. B-173: SEM photomicrographs from sample PS-43: a) and b) dolomite (1) B-120

Fig. B-174: SEM photomicrographs from sample PS-43: a) Fe-carbonates, b) EDX from a), c) Fe-carbonates (1), Fe-oxide (1), d) Fe-carbonate (2) B-121

Fig. B-175: SEM photomicrographs from sample PS-43: a) organic matter (OM) with N and Cl (1), silica (2), b) EDX from (1) B-121

Fig. B-176: SEM photomicrographs from sample PS-43: a) Hornblende? (1), OM (2) with N, smectite (3), b) EDX from (2) B-122

Fig. B-177: SEM photomicrographs from sample PS-43: a) Fe,Ti-oxides (1), b) EDX from (1) B-122

Fig. B-178: SEM photomicrographs from sample PS-43: a) Fe-oxide (1), Fe-carbonates (2), apatite (3), Hg (4), smectite (5), b) Fe-oxides and Hg particles B-122

Fig. B-179: SEM photomicrographs from sample PS-43: a) and b) Hg particles B-123

Fig. B-180: SEM photomicrographs from sample PS-43: a) Ca-sulfate (1), smectite (2), b) EDX from (1) B-123

Fig. B-181: SEM photomicrographs from sample PS-43: a) Ca-carbonate (1), OM (2), b) barite B-123

Fig. B-182: SEM photomicrographs from sample PS-43: clay minerals B-124

Fig. B-183: SEM photomicrographs from sample PS-43 Red particles: a) Fe-oxide (1), smectite (2), b) Fe-oxides B-127

Fig. B-184: SEM photomicrographs from sample PS-43 Red particles: a) organic matter (with Cl), b) Fe-carbonate (CO_2: 13.67 wt.-%, SiO_2: 0.33 wt.-%, FeO: 86.0 wt.-%) (1), organic matter (with Cl) (2) B-127

Fig. B-185: SEM photomicrographs from sample PS-43 Red particles: a) smectite (1), silica (2), b) Hg particles B-127

Fig. B-186: SEM photomicrographs from sample PS-43 Red particles: barite (with Cl)..... B-128

Fig. B-187: SEM photomicrographs from sample PS-43 Red particles: a) and b) Fe-oxides (with Cl)..... B-128

Fig. B-188: SEM photomicrographs from sample PS-43 Red particles: clay minerals..... B-129

Fig. B-189: SEM photomicrographs from sample Black particles adhered to bentonite: a) chlorites, b) chlorites (1), Ca-carbonates (2), smectite (3), c) and d) chlorites B-131

Fig. B-190: SEM photomicrographs from sample Black particles adhered to bentonite: monazite..... B-131

Fig. B-191: SEM photomicrographs from sample Black particles adhered to bentonite: monazite..... B-132

Fig. B-192: SEM photomicrographs from sample Black particles adhered to bentonite: a), b) and c), Ca-carbonates, d) Ca-sulfates (1), Ca-carbonates (2)..... B-132

Fig. B-193: SEM photomicrographs from sample Black particles adhered to bentonite: a) organic matter with Cl, b) EDX from a), c) Fe-oxide (1), organic matter with Cl (2), d) OM..... B-133

Fig. B-194: SEM photomicrographs from sample Black particles adhered to bentonite: barite-celestine..... B-133

Fig. B-195: SEM photomicrographs from sample Black particles adhered to bentonite: a) Fe-Ti-Mn-oxides, b) Ti-Mn-oxides B-134

Fig. B-196: SEM photomicrographs from sample Black particles adhered to bentonite: Fe-carbonates and Fe-oxides B-134

Fig. B-197: SEM photomicrographs from sample Black particles adhered to bentonite: clay minerals..... B-135

Fig. B-198: SEM photomicrographs from sample Black ball particle: clay minerals B-137

Fig. E-1: TEM images from < 2 μm clayey suspensions of the FEBEX Reference bentonite E-3

Fig. E-2: TEM images from < 2 μm clayey suspensions of the bentonite block BB-36-1 .....E-3

Fig. E-3: TEM images from < 2 μm clayey suspensions of the bentonite block BB-36-2: a) smectite particle; b) kaolinite type particle.....E-3

Fig. E-4: TEM images from < 2 μm clayey suspensions of the bentonite block BB-36-3 red: a) nontronite type particle and/or iron colloids (4a), smectite particle (4b); b) smectite particle....E-4

Fig. E-5: TEM images from < 2 μm clayey suspensions of the bentonite block BB-47-7 ....E-4

Fig. E-6: TEM images from < 2 μm clayey suspensions of the bentonite block BB-47-8 ....E-4

Fig. E-7: TEM images from < 2 μm clayey suspensions of the bentonite block BB-47-9: a) smectite particle; b) illite particle E-5

Fig. E-8: TEM images from < 2 μm clayey suspensions of the bentonite block BB-53-3 ....E-5

Fig. E-9: TEM images from < 2 μm clayey suspensions of the bentonite block BB-59-1 ....E-5

Fig. E-10: TEM images from < 2 μm clayey suspensions of the bentonite block BB-59-3: a) smectite particle; b) illite type particle E-6

Fig. E-11: TEM images from < 2 μm clayey suspensions of the bentonite block BB-59-5: a) silica colloids (a and c); smectite particle (b); b) smectite particle (a); silica colloids (b) E-6

Fig. F-1: XRD pattern of bulk samples from BMS and protrusion samples located at contact with the liner/Heater #2 (feldspars are omitted)....F-3

Fig. F-2: XRD pattern white scraped material from the internal part of the liner (AR sample)....F-4

Fig. F-3: XRD patterns of BMS at Section S47 and S53 at direct contact with the liner and protrusion magnetic samples at direct contact with the liner/Heater #2 (feldspars are omitted). F-4

Vertical lines: hkl reflexions of mineral (see color in the legend) F-4

Fig. F-4: XRD pattern of the sample at direct contact with the Heater #2 (Protrusions samples): d(060) basal reflexion of trioctahedral smectites and brucite F-5

Fig. F-5: XRD pattern of the sample at direct contact with the frontal surface of Heater #2: a) black particles adhered to bentonite block (BPB), b) Black ball particle (BB): chlorite and Chl/S ML. Vertical lines: hkl reflexions of mineral (see color in the legend) F-5

Fig. F-6: XRD patterns of oriented aggregates samples (normal, ethylene glycol solvated and heated at 550 °C): BMS samples at Section S47 and S53 at direct contact with the liner: BMS-47-1 to 3 and BMS-53-1 to 3 ....F-6

Fig. F-7: XRD patterns of oriented aggregates samples (normal, ethylene glycol solvated and heated at 550 °C): Protrusion samples at Sections S42-S43 (CL, GB, BBIL, SR43-FR, RV-42)....F-7

Fig. F-8: FTIR spectrum of the bentonite sample BMS-47-1 adhered to liner....F-8

Fig. F-9: FTIR spectrum of the bentonite sample BMS-53-1 adhered to liner....F-8

Fig. F-10: Samples from inside the liner: adhered white powder to liner (WP) and bentonite protrusions F-9

Fig. F-11: FTIR spectrum from a sample at direct contact with the frontal surface of Heater #2: Black ball particle (BB): chlorite F-9

Fig. F-12: TG-DSC curves from the sample BMS-47-1 (total fraction) at direct contact with the liner F-10

Fig. F-13: TG-DSC curves from the sample BMS-47-2 (total fraction) at direct contact with the liner F-10

Fig. F-15: TG-DSC curves from the sample BMS-47-3 (total fraction) at direct contact with the liner F-11

Fig. F-16: Comparison of DSC curves from the samples BMS-47-xx and BMS-53-xx (total fraction) at direct contact with the liner F-11

Fig. F-17: TG-DSC curves from the sample BMS-47-1 (< 2 μm fraction) at direct contact with the liner F-12

Fig. F-18: TG-DSC curves from the sample BMS-47-2 (< 2 μm fraction) at direct contact with the liner F-12

Fig. F-19: TG-DSC curves from the sample BMS-47-3 (< 2 μm fraction) at direct contact with the liner F-13

Fig. F-20: TG-DSC curves from the sample BMS-53-1 (< 2 μm fraction) at direct contact with the liner F-13

Fig. F-21: TG-DSC curves from the sample BMS-53-2 (< 2 μm fraction) at direct contact with the liner F-14

Fig. F-22: TG-DSC curves from the sample BMS-53-3 (< 2 μm fraction) at direct contact with the liner F-14

Fig. F-23: Comparison of DSC curves from the samples BMS-47-xx and BMS-53-xx (< 2 μm fraction) at direct contact with the liner F-15

Fig. F-24: TG-DSC curves from the Green bentonite (CL) at direct contact with the frontal part of the Heater #2 (Slice 60) F-15

Fig. F-25: TG-DSC curves from bentonite protrusions through the liner holes towards the heater. Samples taken from the internal part of the liner at contact with the heater (bentonite slice 59/57, bentonite sampling Sections S42/S43): R-green (RV) F-16

Fig. F-26: TG-DSC curves from bentonite protrusions through the liner holes towards the heater. Samples taken from the internal part of the liner at contact with the heater (bentonite slice 59/57, bentonite sampling Sections S42/S43): R-black&white (RNW42) F-16

Fig. F-27: TG-DSC curves from bentonite protrusions through the liner holes towards the heater. Samples taken from the internal part of the liner at contact with the heater (bentonite slice 59/57, bentonite sampling Sections S42/S43): R-orange particles (RNW42) F-17

Fig. F-28: TG-DSC curves from bentonite protrusions through the liner holes towards the heater. Samples taken from the internal part of the liner at contact with the heater (bentonite slice 59/57, bentonite sampling Sections S42/S43): R-black particles (RNW42) F-17

Fig. F-29: TG-DSC curves from bentonite protrusions through the liner holes towards the heater. Samples taken from the internal part of the liner at contact with the heater (bentonite slice 59/57, bentonite sampling Sections S42/S43): R-black&white interface particles (RNW42) F-18

Fig. F-30: TG-DSC curves from bentonite protrusions through the liner holes towards the heater. Samples taken from the internal part of the liner at contact with the heater (bentonite slice 59/57, bentonite sampling Sections S42/S43): Black-green (GB) F-18

Fig. F-31: TG-DSC curves from bentonite protrusions through the liner holes towards the heater. Samples taken from the internal part of the liner at contact with the heater (bentonite slice 59/57, bentonite sampling Sections S42/S43): inside heater black (GB-42) total fraction F-19

Fig. F-32: TG-DSC curves from bentonite protrusions through the liner holes towards the heater. Samples taken from the internal part of the liner at contact with the heater (bentonite slice 59/57, bentonite sampling Sections S42/S43): inside heater black (GB-42) < 2 μm fraction F-19

Fig. F-33: TG-DSC curves from bentonite protrusions through the liner holes towards the heater. Samples taken from the internal part of the liner at contact with the heater (bentonite slice 57, bentonite sampling Section S43): inside heater red (PS-43) total fraction F-20

Fig. F-34: TG-DSC curves from bentonite protrusions through the liner holes towards the heater. Samples taken from the internal part of the liner at contact with the heater (bentonite slice 57, bentonite sampling Section S43): inside heater red (PS-43) < 2 μm fraction F-20

Fig. F-35: TG-DSC curves from bentonite protrusions through the liner holes towards the heater. Samples taken from the internal part of the liner at contact with the heater (bentonite slice 59, bentonite sampling Section S42): liner holes red (BBIL-42) total fraction F-21

Fig. F-36: TG-DSC curves from bentonite protrusions through the liner holes towards the heater. Samples taken from the internal part of the liner at contact with the heater (bentonite slice 59, bentonite sampling Section S42): liner holes red (BBIL-42) < 2 μm fraction F-21

Fig. F-37: TG-DSC curves from < 2 μm bentonite sample at direct contact with Gas Pipe 3 ..... F-22

Fig. F-38: TG-DSC curves from < 2 μm bentonite sample at direct contact with Gas Pipe 3 ..... F-22

Fig. F-39: Comparison of DSC curves from the < 2 μm bentonite samples from protrusions through the liner holes towards the heater and around Gas Pipe 3 ..... F-23

1 Introduction

1.1 The FEBEX Project

FEBEX (Full-scale Engineered Barrier EXperiment in Crystalline Host Rock) was a research and demonstration project initiated by ENRESA (Spain) in 1994.

The aim of the project was to study the behaviour of near-field components in a repository for high-level radioactive waste in granite formations. The main objectives of the project can be grouped in two areas:

- Demonstration of the feasibility of constructing the engineered barrier system in a horizontal configuration according to the Spanish concept for deep geological storage (AGP), and analysis of the technical problems to be solved for this type of disposal method
- Better understanding of the thermo-hydro-mechanical (THM) and thermo-hydro-chemical or geochemical (THC or THG) processes in the near field, and development and validation of the modelling tools required for interpretation and prediction of the evolution of such processes

The project consisted of two large-scale tests (Fig. 1) – in-situ and mock-up (the latter is managed by CIEMAT in Spain) –, a series of laboratory tests, and THM and THG modelling tasks (ENRESA 2000).

The full-scale heating in-situ test was performed at the Grimsel underground laboratory in Switzerland, also known as Grimsel Test Site (GTS). A complete description of the FEBEX project objectives and test program can be found in Fuentes-Cantillana et al. (1998): "FEBEX Full-scale Engineered Barriers EXperiment in Crystalline Host Rock. Pre-operational stage summary report".

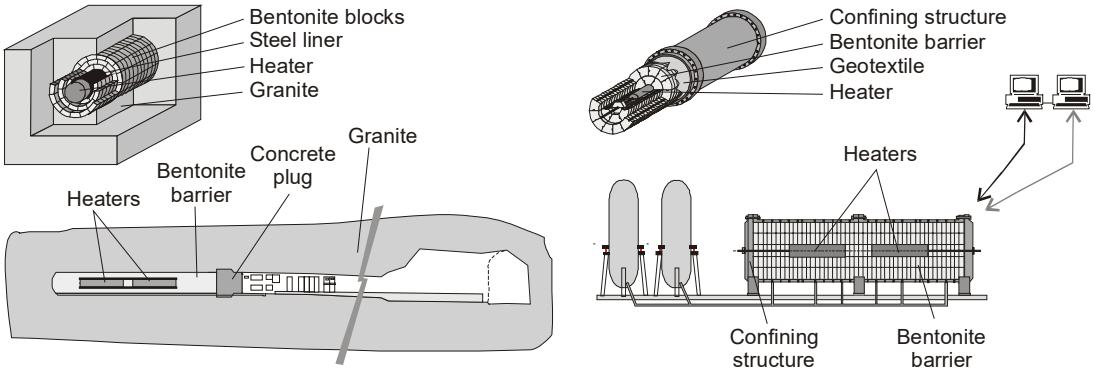

Fig. 1: Overall layout of FEBEX in-situ test (left) and mock-up test (right). After Fuentes-Cantillana et al. (1998)

The project started in 1994, and has been supported by the European Commission through consecutive contracts, identified as FEBEX I (contract n° FI4W-CT-95-0006) for the period January 1996 to June 1999, and FEBEX II (contract n° FIKW-CT-2000-00016), from September 2000 to December 2004. Afterwards, a research program on near-field processes (NF-PRO) lasted from January 2005 to December 2007. Finally, in January 2008 the in-situ test was transferred from ENRESA to a consortium (FEBEX-e Project) composed by SKB (Sweden), POSIVA

(Finland), CIEMAT (Spain), Nagra (Switzerland) with the more recent addition of KAERI (South Korea), forming the FEBEX Consortium, which supported the project.

The final dismantling of the FEBEX in-situ experiment was carried out in 2015 and new partners, interested in taking part in the planned sampling and analysis operations, were incorporated to the Consortium (now called FEBEX-DP) for that purpose, namely US DOE (USA), Obayashi (Japan), RWM (UK), Andra (France), BGR (Germany) and SURAO (Czech Republic).

1.2 Test configuration during FEBEX I

The installation of the FEBEX in-situ test was carried out at the GTS. A horizontal drift with a diameter of 2.28 m was excavated in the Grimsel granodiorite especially for this experiment using a TBM (a tunnel boring machine). Two electrical heaters, of the same size and of a similar weight as the reference canisters, were placed in the axis of the drift (Fig. 2). The gap between the heaters and the rock was backfilled with compacted bentonite blocks, up to a length of 17.40 m, requiring a total 115'716 kg of bentonite (Tab. 1). The backfilled area was sealed with a plain concrete plug placed into a recess excavated in the rock and having a length of 2.70 m and a volume of 17.8 m^3. Fig. 3 shows the dimensions and layout of the test components schematically.

A total of 632 sensors were placed in the system along a number of instrumented sections, both in the bentonite buffer and in the host rock, to monitor relevant parameters such as temperature, humidity, total and pore pressure, displacements, etc. Prior to the bentonite barrier emplacement, nineteen radial boreholes were drilled in 1996 in the test zone from the interior of the drift, for putting the necessary instruments in the surrounding rock mass in place (Fig. 4). The instruments were of many different kinds and their characteristics and positions are fully described in Fuentes-Cantillana and García-Siñeriz (1998): "FEBEX Full-scale Engineered Barriers Experiment in Crystalline Host Rock. Final design and installation of the in-situ test at Grimsel". A Data Acquisition and Control System (DACS) located in the service area of the FEBEX drift collected the data provided by the instruments. This system recorded and stored information from the sensors and also controlled the power applied to the electrical heaters, maintaining a constant temperature at the heaters/bentonite interface. The DACS allowed the experiment to be run in an automated mode, with remote supervision from Madrid. Data stored at the local DACS were periodically downloaded in Madrid and used to build the experimental Master Data Base.

The construction of the concrete plug was completed in October 1996, and the heating operation started on 27 February 1997. A constant temperature of 100 °Cwas maintained at the heaters/bentonite interface, while the bentonite buffer slowly hydrated with water naturally seeping from the granitic rock formation. The total water inflow for the entire test zone (17.3 m) varied from 4.5 to 8.5 mL/min.; the most frequent hydraulic conductivity was 1×10^{-11} m/s; and the hydraulic pressure along a horizontal plane through the axis of the gallery at a distance of 50 m was around 7.2 bar (Huertas et al. 2006). The characteristics of the infiltrating granitic water are: diluted and reducing water (E.C. < 100 µm/cm, Eh -200 mV), a pH close to 9 and a Na-Ca-TIC-F water-type (Huertas et al. 2006, Frick et al. 1992). The main gases dissolved in the groundwater are N_2 (97 %) and Ar (3 %), the content of O_2 and other gases were very low or below detection limits (Hoehn et al. 1990, see Fernández et al. 2018 for other references).

The concrete plug (made of plain concrete without anchors or any reinforcement), was constructed with the only function of supporting the mechanical thrust of the barrier when it was hydrated (swelling pressure up to 5 MPa); i.e., it was not specifically required to seal off hydraulic or gas flow completely. The formulation of the concrete used (Tab. 2) corresponds to a concrete with a relatively low amount of clinker, compensating for this with the addition of silica fume. In addition, the type of cement used, by its composition, releases less heat when hydrated and has a greater resistance to sulphates than the normal Portland cements. 17 m^3 of material was pumped from outside the drift to construct the concrete plug by vibration in three phases (Fuentes-Cantillana & García-Siñeriz 1998). A complete description of the FEBEX in-situ test that includes both the installation of the test and the results gathered after two years of operation is given in Fuentes-Cantillana et al. (2000): "FEBEX Full-Scale Engineered Barriers Experiment for a deep geological repository for high level radioactive waste in crystalline host rock. Final Report".

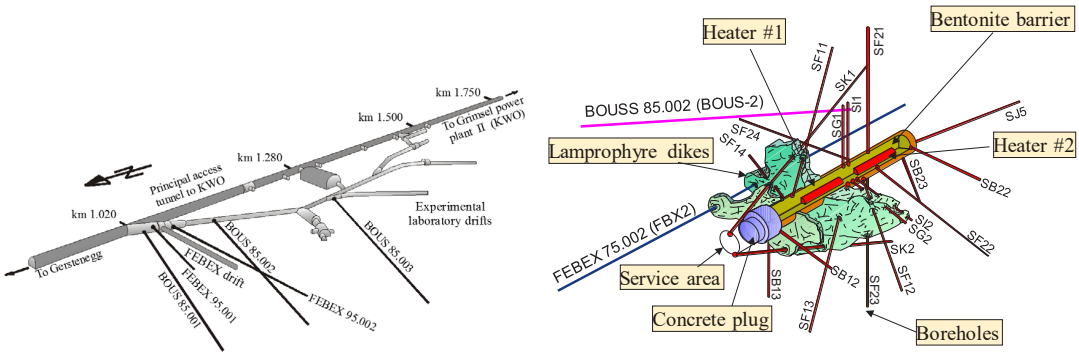

Fig. 2: a) Tunnel layout of the Grimsel Test Site (GTS); b) Scheme of the FEBEX in-situ test during the First Operational Phase (1996 – 2002) (after Huertas et al. 2006)

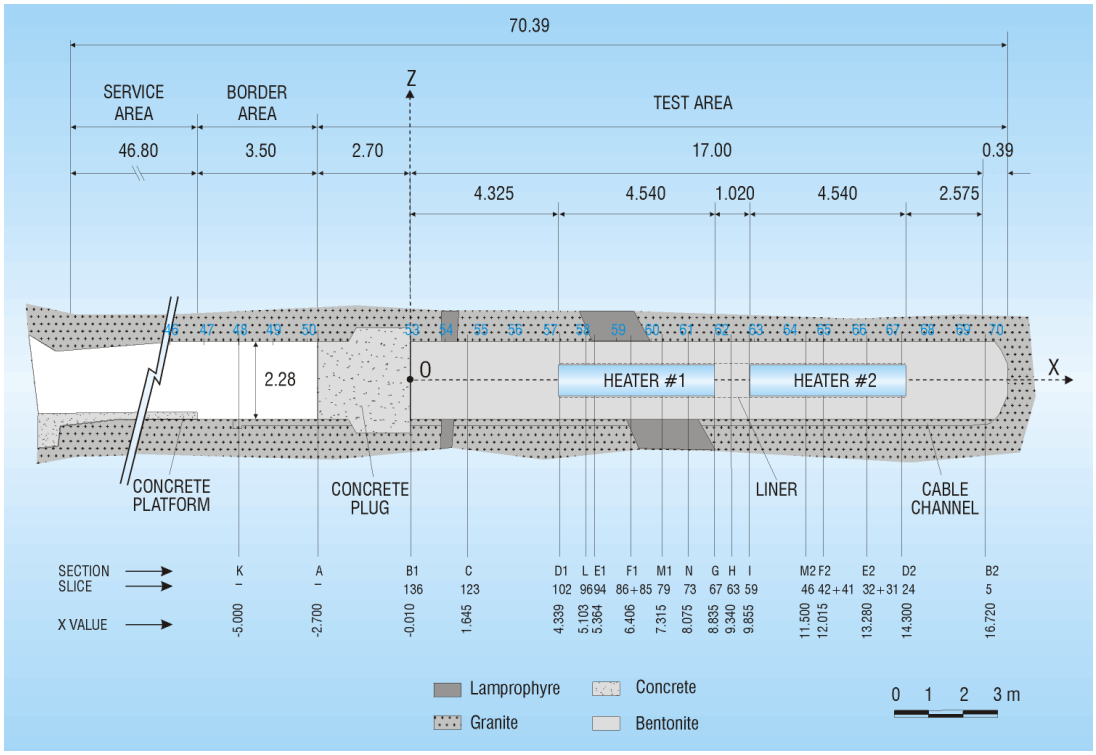

Fig. 3: General layout of the FEBEX in-situ test: FEBEX I configuration during the First Operational Phase 1996 – 2002 (Huertas et al. 2006)

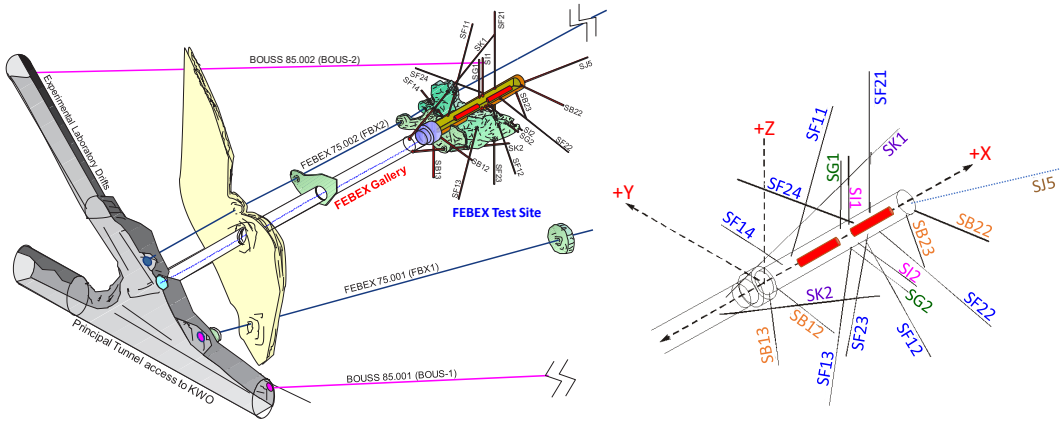

Fig. 4: Location of the sub-parallel and radial boreholes drilled for the instrumentation of the surrounding rock mass (from J. Farias, ENRESA, pers. com.)

Tab. 1: Main characteristics of the FEBEX bentonite

Type of bentonite		Ca-Mg dioctahedral cis-vacant montmorillonite					
Structural formula		$(Si_{3.94}Al_{0.06})^{IV}$ $(Al_{1.35}Fe^{3+}_{0.21}Mg_{0.49}Ti_{0.01})^{VI}$ $O_{10}(OH)_2$ $X_{0.29}$					
S_{BET} *(m²/g)*	59.5	S_{TOT} *(m²/g)*	668 ± 21	*CEC (meq/100g)*	98 ± 2	*ζ-potential (mV)*	-33.4 ± 1.6
Cation Exchange population (meq/100 g)				Na: 28; K: 2.85; Mg: 33.1; Ca: 33.2; Sr: 0.37; Ba: 0.01			
Main minerals (wt.%)		*Accessory minerals (wt.%)*				*Poorly ordered minerals (wt.%)*	
Smectite	92 ± 3	Organic Matter (as CO_2)		0.35 ± 0.05			
Quartz	2 ± 1	Carbonates (calcite, dolomite)		0.60 ± 0.13		SiO_2	0.038 ± 0.005
Plagioclase	2 ± 1	Soluble sulphates (gypsum)		0.14 ± 0.01			
Cristobalite	2 ± 1	Low soluble sulphates (barite, celestite)		0.02 ± 0.00		Al_2O_3	0.035 ± 0.005
K-feldspars	Traces	Sulfides		< d.l.			
Tridymite	Traces	Chlorides (halite)		0.13 ± 0.02		Fe_2O_3	0.105 ± 0.009
Calcite	Traces						

1.3 Dismantling of Heater #1 and test configuration afterwards (FEBEX II)

A partial dismantling of the FEBEX in-situ test was carried out during the summer of 2002, after 5 years of continuous heating (Heater #1 was switched off on 28 February 2002). The operation included the demolition of the concrete plug, the removal of the section of the test corresponding to Heater #1, and the sealing with a new shotcrete plug. A large number of samples from all types of materials were taken for analysis (Fig. 5). A number of instruments were subsequently dismantled, as well as a few new ones were installed. Accordingly, system design was adapted, and the physical layout was changed in order to ease the partial dismantling operation.

The description of the partial dismantling operation is given in Bárcena et al. (2003): "Dismantling of the Heater 1 at the FEBEX in-situ test. Description of operations". The configuration of the test, after completing the partial dismantling operation and construction of the full plug length, is shown in Fig. 6. A more complete report that describes the test and results from the conception up to two years of operation after the partial dismantling is given in Huertas et al. (2006): "FEBEX Full-scale Engineered Barriers Experiment. Updated Final Report 1994 – 2004".

Tab. 2: Concrete characteristics used for the two plugs constructed in the FEBEX in-situ test (Huertas et al. 2006)

1st Concrete plug (1996)**		**2nd Concrete plug (2002 – 2003)*****		
Concrete characteristics (2.7 m length)		**Concrete characteristics** (Gunite type)	**1st plug section** (1 m in 2002)	**2nd plug section** (2 m in 2003)*
Cement CEM I 32, 5 HS (PCO Surfaced)	160 kg/m^3	Cement CEM II A-L 32, 5R	430 kg/m^3	475 kg/m^3
Silica fume (Sikafume HR)	60 kg/m^3	Nanosilica MEYCO MS 660	30 kg/m^3	60 kg/m^3
Fine aggregate (Grimsel granite 4 – 8 mm)	660 kg/m^3	Aggregate 0.8 mm	1'700 kg/m^3	1'700 kg/m^3
Coarse aggregate (Grimsel granite 8 – 16 mm)	430 kg/m^3	Steel fibres (Dramix ZP 306)	50 kg/m^3	--
Sand (quartz 0.1 – 5.6 mm)	800 kg/m^3	Polypropylene fibres	800 kg/m^3	--
Filler (limestone)	170 kg/m^3	Accelerant MEYCO SA 160 E	6 – 8 %	6 – 8 %
Water	155 kg/m^3	Curing compound MEYCO TCC 735	1 %	1 %
Superplasticizer (Sikament-12+)	13 kg/m^3	Superplasticizer Glenium T803	1.5 %	1.5 %
w/c	0.99	w/c	0.40	0.46
Density (g/cm^3) Air content	2.394 0.4 %	Density (g/cm^3)	2.18 ± 0.01	2.24 ± 0.03
Compressive Strength (MPa)	47.1 (28 days)	Compressive Strength (MPa)	32 ± 4	40 ± 8
Hydraulic conductivity (m/s)	< 1 × 10^{-11}	Hydraulic conductivity (m/s)	4.3 × 10^{-11}	9.4 × 10^{-11}

* A layer of approximately 3 – 4 cm of a sprayable polymer product (MASTERSEAL X345) was first applied in Section 34, on top of the existing temporary 1st plug section for the impermeabilisation of shotcrete (as a waterproof membrane) and for improving the water and gas tightness of the test.

** Fuentes-Cantillana et al. (2000)

*** Huertas et al. (2006)

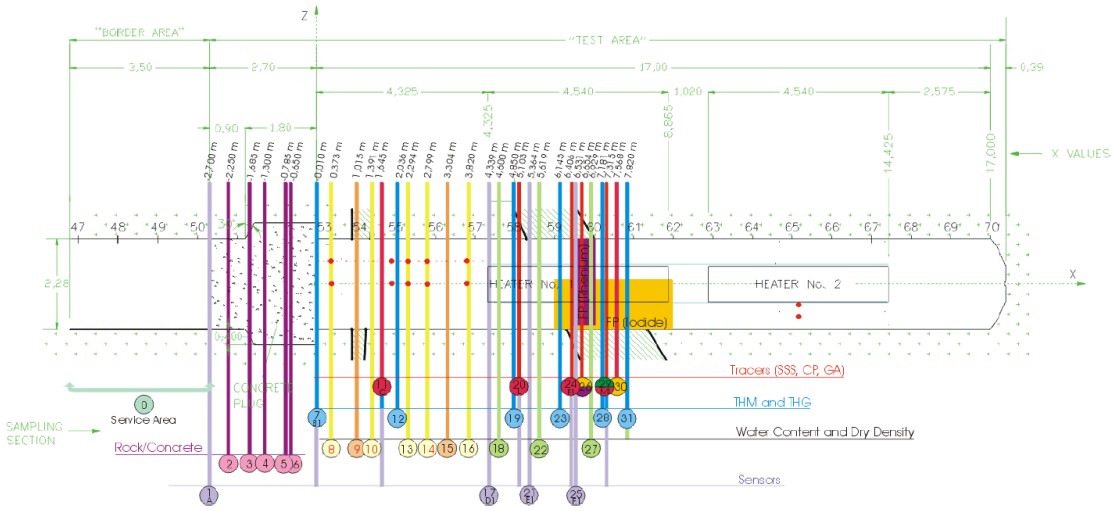

Fig. 5: Sampling layout during the dismantling of Heater #1 (AITEMIN 2002)

The buffer and all components were removed up to a distance of 2 metres from Heater #2 to minimize disturbance of the non-dismantled area. A dummy steel cylinder with a length of 1 m was inserted in the void left by Heater #1 in the centre of the buffer. Some new sensors were installed in that one additional metre of bentonite buffer.

Additional sensors were introduced in boreholes drilled in the buffer parallel to the drift. To simplify this operation, the new concrete plug was constructed in two phases: an initial temporary plug measuring just 1 m in length, built immediately after dismantling, and a second section to complete the plug length to the 3 m planned in the design of the experiment. Unlike FEBEX I, the new plug was a parallel plug, without a recess excavated in the rock, constructed by shotcreting. The characteristics of the concrete used for the new plug were different to that used in the First Operational Phase (Tab. 2), it being a Gunite-type concrete (Bárcena et al. 2003).

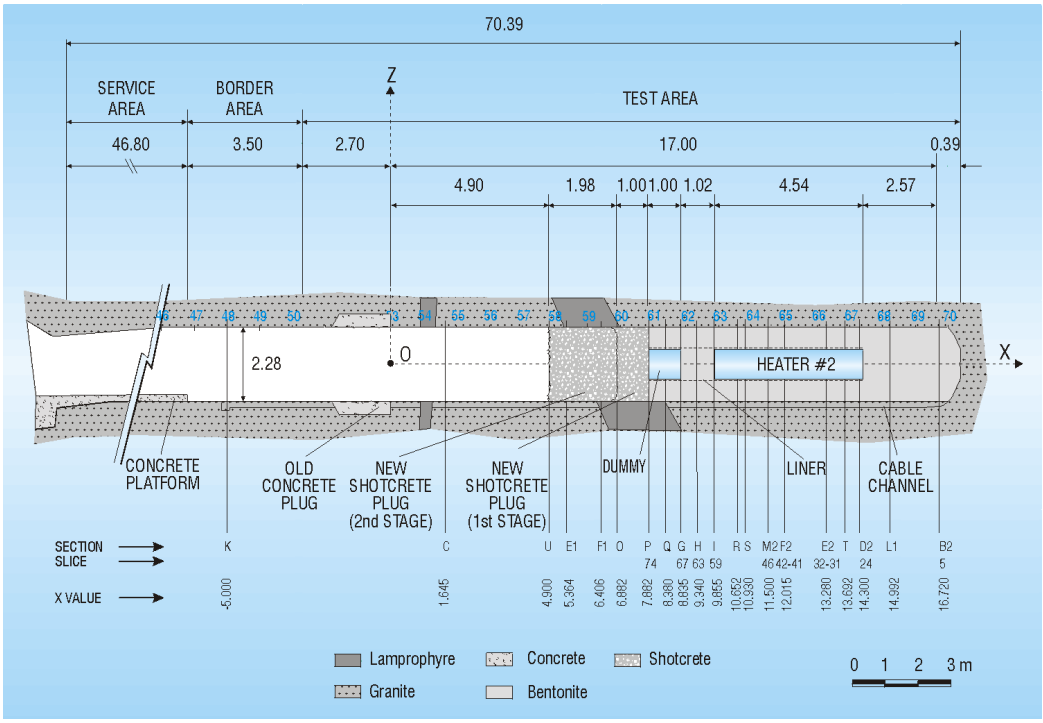

Fig. 6: Status of the FEBEX in-situ test after the partial dismantling: FEBEX II configuration in the Second Operational Phase 2002 – 2015 (Huertas et al. 2006)

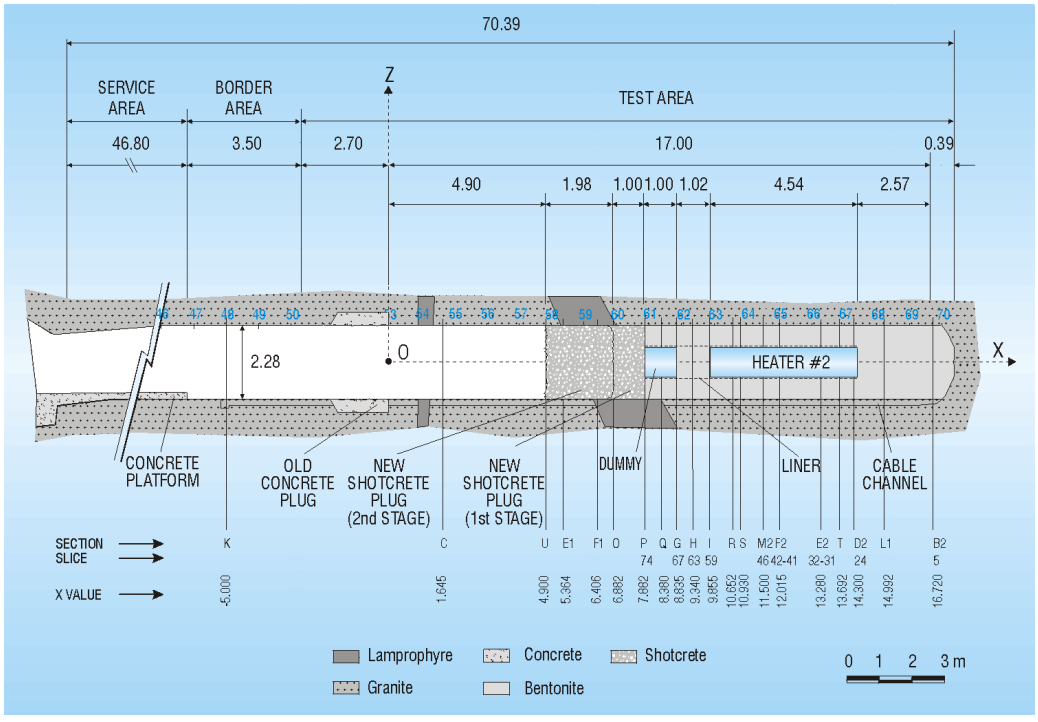

Fig. 7: Status of the FEBEX in-situ test after the partial dismantling: FEBEX II configuration in the Second Operational Phase 2002 – 2015 (Huertas et al. 2006)

1.4 Dismantling Heater #2: concept

Heater #2 was switched off on 24 April 2015. The objective of the second dismantling operation, carried out throughout 2015, was to dismantle all the remaining parts of the in-situ test, including Heater #2 (Fig. 8). This operation included carrying out a complete sampling of the bentonite, rock, relevant interfaces, sensors, metallic components and tracers in order to analyse the barrier condition after 18 years of heating and natural hydration (Fig. 9).

Analytical results will be compared with data obtained from the partial dismantling of Heater #1 (Huertas et al. 2006, Villar et al. 2006); the monitoring data (AITEMIN 2014), as well as with the results derived from modelling efforts (Lanyon & Gaus 2016). The results are expected to increase the current knowledge and confidence for the FEBEX-DP partners in bentonite performance with a focus on thermo-hydro-mechanical (THM) and thermo-hydro-chemical (THC) processes, as well as on corrosion and microbial activity (Bengtsson et al. 2017, Wersin & Kober 2017, Villar et al. 2017, Villar et al. 2017b).

Indeed, the primary objectives of FEBEX-DP were to further the understanding of processes affecting the components of the in-situ test through integration of the dismantling results with earlier monitoring and dismantling data with a focus on:

- Characterisation of the key physical properties (density, water content) of the bentonite and their distribution
- Characterisation of mineralogical interactions at buffer and material interfaces and potential impacts on porosity
- Characterisation of corrosion processes on instruments and coupons under evolving redox conditions and saturation states
- Characterisation of microbiological processes
- Comparison with existing models (blind predictions prior to dismantling Heater #2)

All details about the planned dismantling operation of Heater #2 and sampling program are given in the reference documents: "FEBEX-DP (GTS) Full Dismantling Test Plan" (Bárcena & García-Siñeriz 2015a), "FEBEX-DP (GTS) Full Dismantling Sampling Plan" (Bárcena & García-Siñeriz 2015b) and its update (Rey et al. 2015).

All dismantling operations and sample logs are documented in NAB 16-11: Dismantling of Heater 2 at the FEBEX in-situ test. Description of operations (García-Siñeriz et al. 2016, Kober & Van Meir 2017). The final physical condition of the bentonite along the x-axis of the gallery after dismantling of Heater #1 and #2 (distribution of temperatures, water contents, dry densities and saturation degrees), are shown in Tab. 3, Fig. 10, Fig. 11 and Fig. 12 (Daucausse & Lloret 2003, Martinez et al. 2016, Villar et al. 2016).

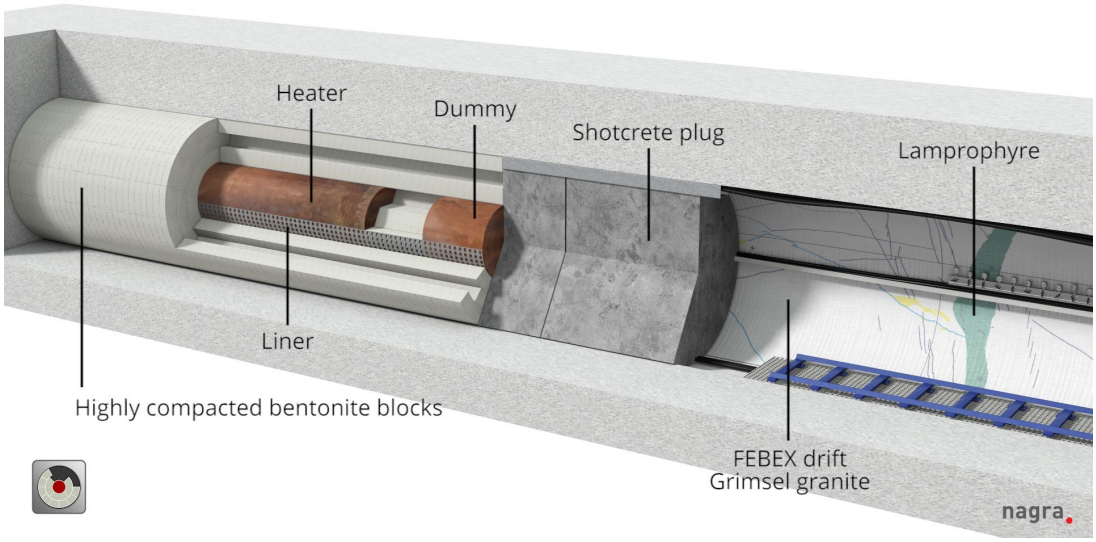

Fig. 8: 3-D view of the FEBEX repository with Heater # 2 situated horizontally in the centre of three rings of saturated bentonite buffer (from Nagra)

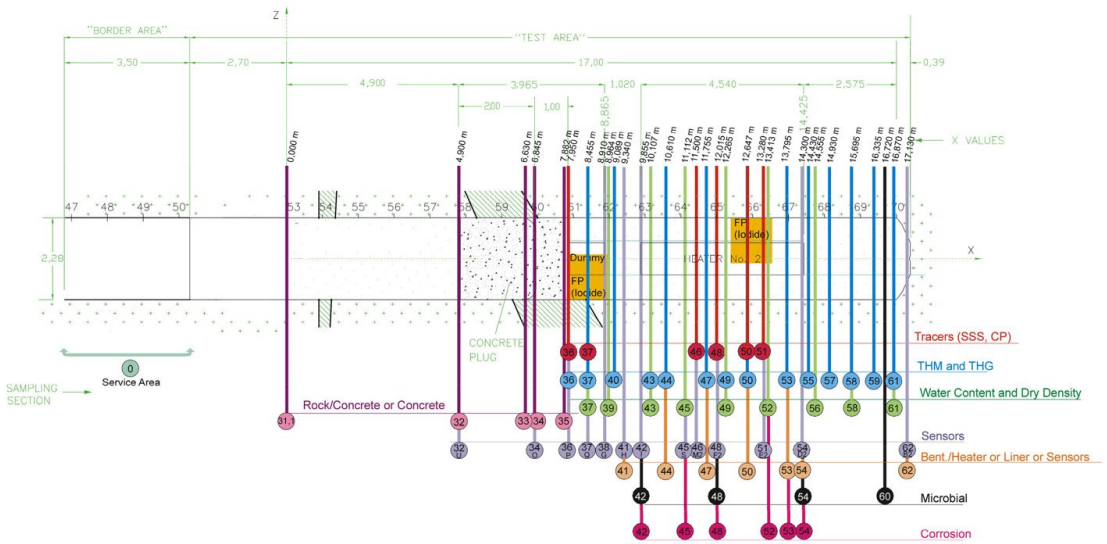

Fig. 9: Sampling layout during dismantling of Heater #2 (from Garcia-Siñeriz et al. 2016)

Tab. 3: Temperatures in different sections along x-coordinate (after Martínez et al. 2016)

Operational Phase	**First Operational Phase: 1996 – 2002**				**Second Operational Phase: 2002 – 2015**					
GTS Gallery	**15 ± 2 °C**				**15 ± 2 °C**					
Bentonite ring	**Section B2** (gallery end)	**Section D1** (Heater #1 front)	**Section G** (Heater #1 rear end)	**Section I** (Heater #2 front)	**Section G** (1 m from Heater #2) *	**Section I** (Heater #2 front)	**Section S** (1 m into Heater #2)	**Section F2** (middle of Heater #2)	**Section D2** (Heater #2 rear end)	**Section B2** (gallery end)
Outer T (°C)	19 – 20	36 – 40	36 – 40	44	30 – 34	37 – 39	--	--	36 – 37	22
Intermediate T (°C)	20	48 – 52	56 – 58	60 – 62	34 – 39	54 – 63	72	75	54 – 56	20 – 22
Inner T (°C)	20	80 – 84	78 – 82	84 – 88	36 – 41	84 – 87	93	94-99	83 – 88	22

* After dismantling Heater #1; Temperature at the Heater #1 surface in Section F1: 95-100 °C; Temperature at Heater #2 surface in Section F2: 96 – 100 °C

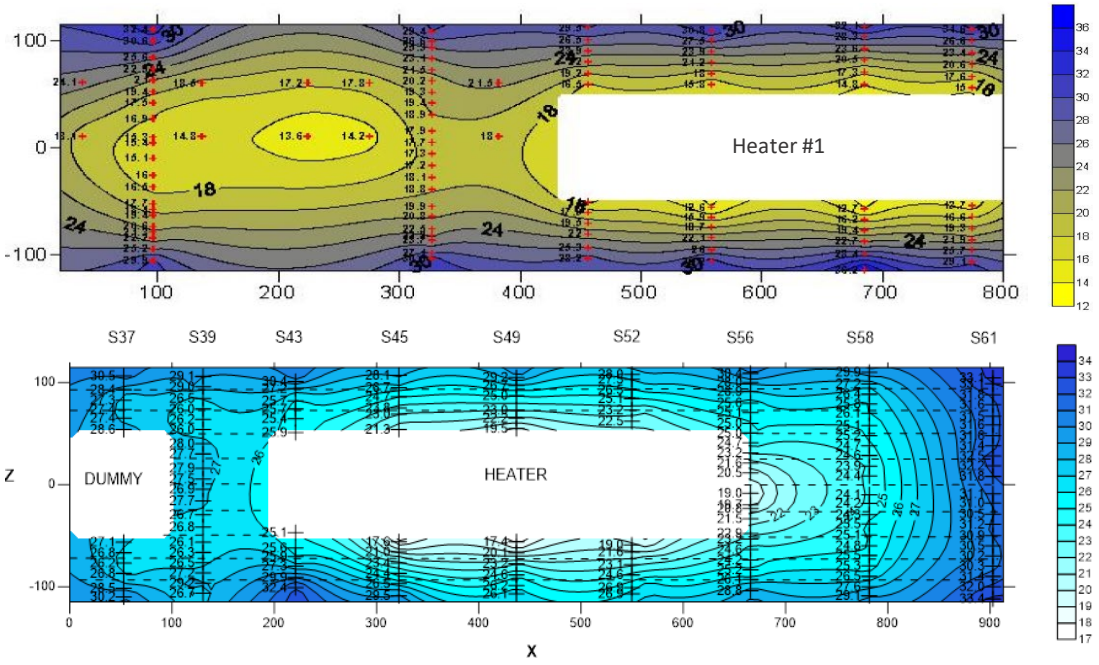

Fig. 10: Water content distribution in a vertical longitudinal section: a) data from dismantling of Heater #1 (Daucausse & Lloret 2003, b) data from dismantling of Heater #2 (Villar et al. 2016)

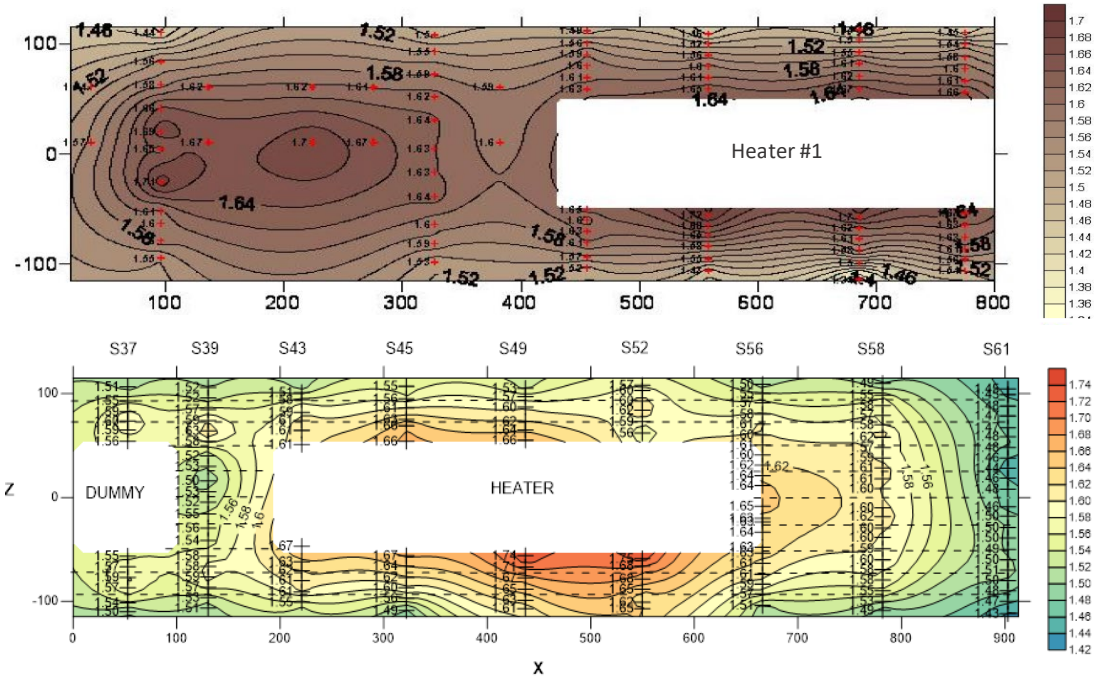

Fig. 11: Dry density distribution in a vertical longitudinal section: a) data from dismantling Heater #1 (Daucausse & Lloret 2003, b) data from dismantling Heater #2 (Villar et al. 2016)

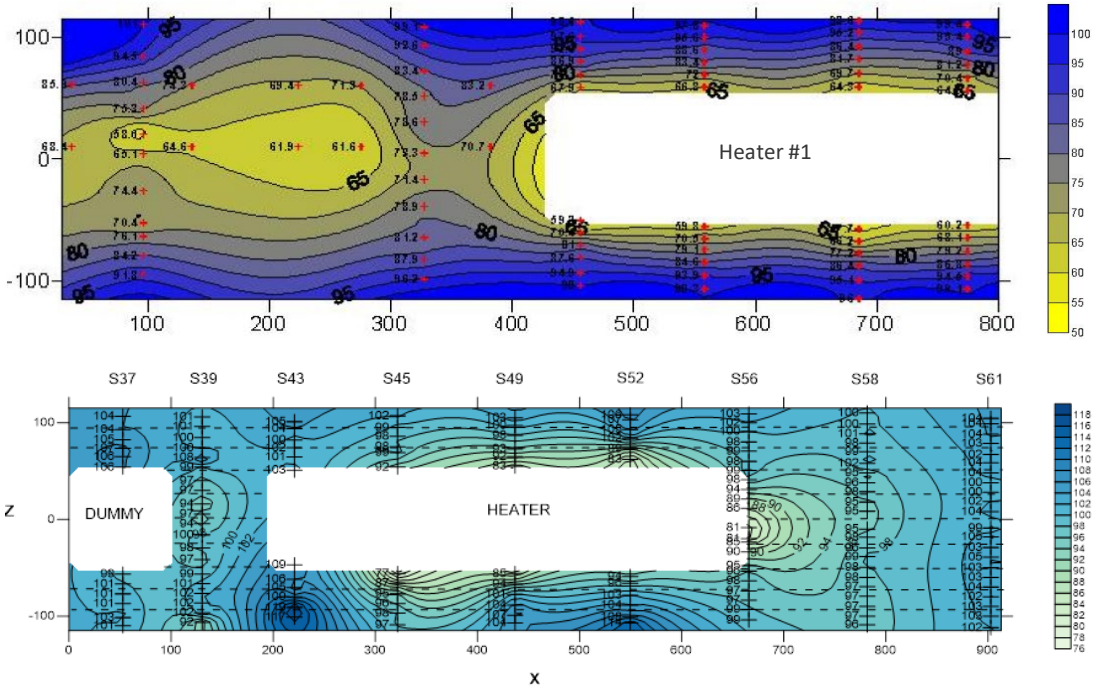

Fig. 12: Degree of saturation distribution in a vertical longitudinal section: a) data from dismantling Heater #1 (Daucausse & Lloret 2003, b) data from dismantling Heater #2 (Villar et al. 2016)

1.5 Gas and water sampling during the FEBEX in-situ test

In the different phases of the FEBEX in-situ test (First Operational Phase: 1996 – 2002, and Second Operation Phase: 2002 – 2015), various pipes were introduced inside the bentonite buffer around Heater #1 and Heater #2 with the aim of knowing the evolution of the gas generation and the chemical composition of the pore water (Fig. 13). Throughout the test operation, different gas/water sampling campaigns were performed from 1996 to 2011, prior and after dismantling of Heater #1 (Jockwer & Wieczorek 2008).

During the FEBEX-DP Project (2013-2016) two additional gas/water sampling campaigns were conducted in order to establish the redox state of the FEBEX in-situ experiment prior to dismantling Heater #2 because the oxido-reduction state inside the buffer controls the chemical reactions affecting metal corrosion and mineral phase alteration and precipitation, as well as the bacterial growth (Giroud 2014). A complete description about the in-situ gas and pore water collected from the FEBEX in-situ test can be found in Fernández (2018).

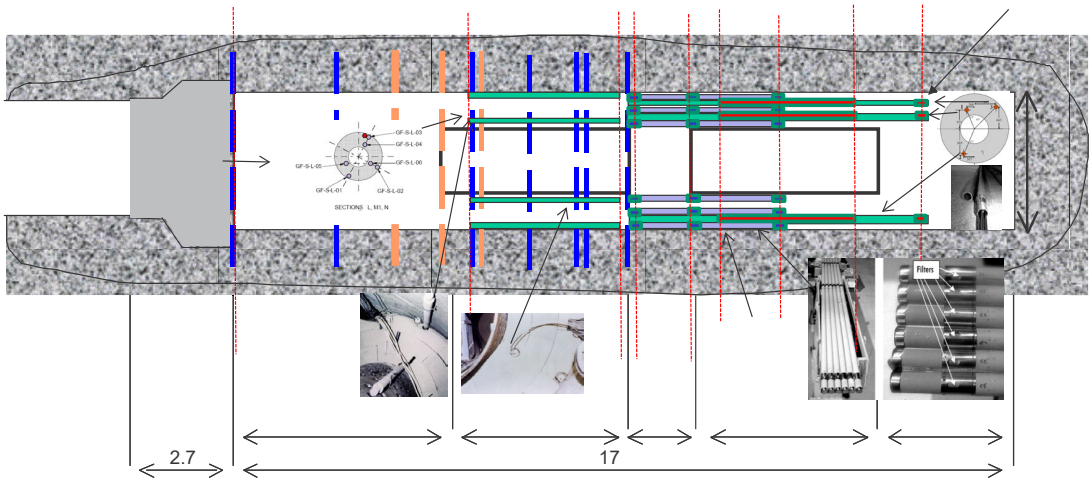

Fig. 13: In-situ test configuration and location of the gas/water (GRS) and pore water pipes (CIEMAT) during the First and Second Operational Phases. (GRS: green-coloured pipes; CIEMAT: violet-coloured pipes)

2 Objectives of the THC studies in the FEBEX in-situ test

Bentonites are one of the more important industrial raw materials, widely used for different technological applications, such as for example catalysis, environmental remediation and engineering. This is because smectite clay minerals, the main component of bentonite, have outstanding physical and chemical properties: large swelling capacity, low permeability and large sorption capacity.

In the context of high-level radioactive waste repositories, bentonites are an essential component of the multi-barrier system securing the long-term safety of the final disposal of nuclear wastes. Unsaturated compacted bentonite is foreseen by several countries as a backfill and sealing material in order to mitigate the transport of radionuclide to biosphere. Therefore, an important issue for performance assessment purposes is to demonstrate the long-term preservation of these properties of bentonite over time under real repository conditions, similar to those present in in-situ large-scale Engineered Barrier System (EBS) experiments, such as the FEBEX in-situ test.

Specific long-term quality requirements for the function of a bentonite buffer material to isolate the canisters from water and retard the migration of radionuclides are (e.g., Ahonen et al. 2008):

1. To ensure favourable mechanical properties: low hydraulic conductivity ($< 10^{-10}$ m/s), high swelling pressure (> 0.1 MPa to ensure homogenization), high dry density after the saturation phase and high thermal conductivity;

2. To maintain a suitable chemical environment for the canister integrity and radionuclide retention over time, buffering possible alteration/deterioration processes:

    - Smectite and their content must remain stable for extensive time periods. Smectite to illite transformation is one of the processes possibly deteriorating isolation properties of bentonite. Parameters affecting this process include: elevated temperature, changes in the layer charge and availability of potassium. Smectite dissolution over time should be considered also.
    - Interaction between bentonite and groundwaters may affect the properties of bentonite by modifying the pore water chemistry, the composition at exchange sites (e.g., Ca-Na), and total cation exchange capacity (CEC). Furthermore, these interactions may induce crystallochemical changes in the smectite structure affecting its stability.
    - Redox processes of iron may affect the smectite lattice and its structural stability. Therefore, amounts and speciation of iron need to be analysed.
    - Sulphur content and redox-speciation of sulphur in bentonite need to be analysed due to its special link to biogeochemical processes, which may affect the mineralogical stability.
    - Carbon content and redox-stages ranging from inorganic (carbonate minerals) and organic compounds need to be evaluated, because carbon is a vital component of biogeochemical processes and a strong buffer of redox processes through the behaviour of saturated reduced hydrocarbons and oxidized non-volatile hydrocarbons.

The FEBEX project provided the opportunity to understand and quantify the geochemical processes taking place in the near-field and to evaluate the long-term behaviour of the compacted FEBEX bentonite after 18 years of experiment of a compacted bentonite. The dismantling of the second part of the FEBEX in-situ test allowed quantifying the modifications of the bentonite, the evolution of the pore water and redox fronts in contact with water, heat, gases, organic components of the sensors, wires, microbes, tracers and metallic components are of great interest.

During 18 years of heating and hydration, physico-chemical, geochemical and mineralogical alterations of the bentonite could have produced a redistribution and neoformation of mineral phases, dissolution processes, changes in total absorption capacity (CEC) and crystallochemical changes in the smectite that could have affected the physico-chemical and mechanical properties of the bentonite. Layer charge and its distribution is coupled with possible chemical changes in:

- The Al/Si ratio in tetrahedral sheets
- Magnesium substitution in octahedral sheets
- Some collapse phenomena in the interlayer region (redistribution of potassium from adjacent crystals)

In addition, parameters as crystal size in the smectite flakes stackings or even silica cements associated to the increase of solubility of silica and migration near the heater could produce physico-chemical changes that can be related to THM measurements.

Therefore, the aims of the THG analyses after dismantling of Heater #2 were:

- Analyse the physico-chemical, mineralogical, chemical and textural changes/alterations occurred in the clay as a consequence of heat and hydration, as well as the redox conditions and microbiological processes occurring in the bentonite buffer after 18 years of experiment
- Analyse the physico-chemical, mineralogical, chemical and textural changes that occurred in the clay as a consequence of the interaction with different interfaces (concrete, granite, metal components)
- Analyse the chemical evolution of the bentonite pore water
- Supply data to validate and check the capacity of the numerical codes (THM and THG) being developed to predict the bentonite behaviour in an engineered barrier
- Supply data for the interpretation of the results obtained from the Corrosion-Microbiology Group: COMIC (Giroud 2014, Bengtsson et al. 2017), as well as, for a global interpretation of the bentonite barrier's behaviour after 18 years of heating and natural hydration.

This report documents the findings of the THC studies performed in bentonite samples obtained during the dismantling of Heater #2 in 2015 after 18 years of experiment. These data were compared with those obtained from samples taken in 2002 during the dismantling of Heater #1 after 5 years of experimental conditions (Villar et al. 2006). In addition, the data were compared with other results obtained from studies about Corrosion and iron-bentonite interactions studies (Wersin & Kober 2017), Microbiology (Bengtsson et al. 2017) and Gas and Water sampling from the pipes installed inside the bentonite barrier (Fernández 2018).

3 Materials

3.1 The bentonite

The bentonite barrier in the FEBEX in-situ test was fabricated by using a Ca-Mg-bentonite material, named FEBEX bentonite (Tab. 1). A complete characterization of the material can be seen in previous works (e.g., Huertas et al. 2006, Fernandez et al. 2004, etc.). This bentonite came from the Cortijo de Archidona deposit, mined by Minas de Gádor, S.A., in the zone of Serrata de Níjar (Province of Almería, Spain). Enresa had an extensive database on this deposit from the many studies prior to FEBEX. About 300 tons of raw material, which had been homogenized and conditioned, were acquired for the fabrication of the blocks for the barriers of the two large-scale tests and for all the laboratory tests. Some properties that characterize this bentonite are the following (Huertas et al. 2006):

- Montmorillonite content: 88 % to 96 %
- Specific weight: 2.67 – 2.75 kg/dm^3
- Swelling pressure for a dry density of 1.60 g/cm^3: 4 MPa to 6 MPa
- Saturated hydraulic conductivity for a dry density of 1.60 g/cm^3: 4.2×10^{-14} – 7.6×10^{-14} m/s

The raw material prepared for the fabrication of the blocks was a granulate of bentonite with less than 5 % of the grains greater than 5 mm, with more than 85 % of the grains less than 74 µm. The clay barrier was formed by blocks, weighing 20 to 25 kg each, of highly-compacted bentonite (Fig. 14). The weighted average values of the dry density and water content of all the blocks were 1.70 g/cm^3 and 14.4 %, respectively. The construction of the barrier needed 5'331 blocks, which corresponds to a mass of 115.7 ton. The in-place barrier had an average dry density, determined during construction, of 1.60 g/cm^3 and a volume, when installed, of construction gaps (separations of variable magnitude) of 5.53 %. The gaps exist: between blocks of the same slice; between slices; between blocks and steel liner; and, systematically, between the clay barrier and the rock, where a gap of increasing width, up to as much as 3 cm, extends from the lower part to the crown (Huertas et al. 2006).

3.2 Sampling during the dismantling of Heater #1

The first dismantling operation of the FEBEX in-situ *test* (Heater #1) began on 2 April 2002, 5 April 2002 and 29 May 2002 with the drilling of cores in the granite, demolition of the concrete plug and bentonite sampling, respectively; and finished on 18 July 2002. Heater # 1 was switched off on 28 February 2002 three months before starting the dismantling operations, since the temperature in the area affected by the dismantling should be reduced to a level compatible with manual work (25 – 30 °C).

During the dismantling of Heater #1, the locations of the bentonite sampling points were fixed to allow a good representation of physico-chemical alterations and hydration distribution. The sampling took place in vertical sections normal to the axis of the tunnel, and in each section several samples were taken along different radii. According to the Sampling Book (AITEMIN 2002), bentonite samples were taken for THG analyses from the following vertical bentonite sampling sections (Fig. 5, Fig. 15):

- Two sections in the heater zone, in order to evaluate the influence of the thermo-hydraulic processes on the bentonite: Section 19 and Section 28

- A section in the zone between the concrete plug and Heater #1 (non-heated section), in order to evaluate the influence of the hydraulic processes on the bentonite: Section 12
- The section in contact with the concrete plug to study the modification of the clay and the pore water in contact with alkaline solutions: Section 7
- Samples of bentonite adhered to the back side of the heater, to the sensors and to the liner, in order to analyse the possible clay alterations occurring due to heating and the formation of possible corrosion products

A complete description of the samples taken and analysed after dismantling of Heater #1 can be found in Appendix A.

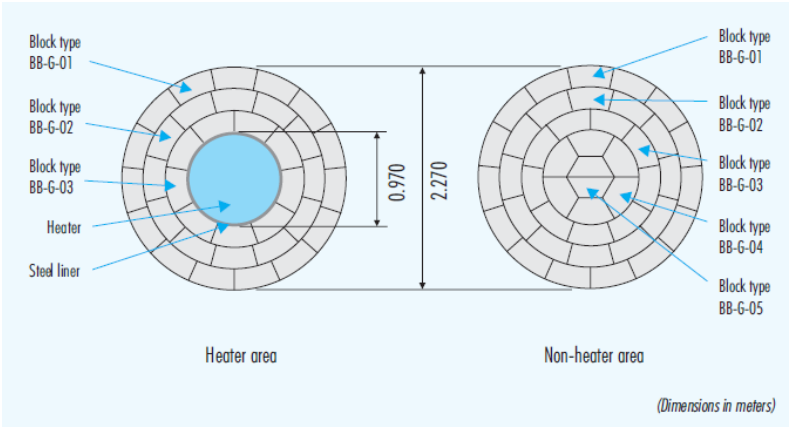

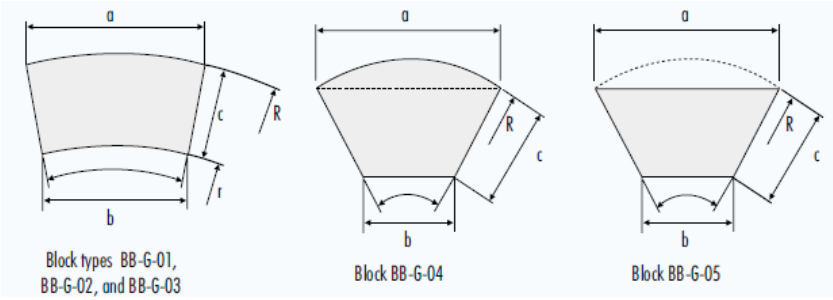

Type	a mm	b mm	c mm	Thicknes mm	R mm	r mm	α
BB-G-01	470.0 $^{2.0}_{5.0}$	380.0 $^{2.0}_{4.0}$	214.0 $^{2.0}_{3.0}$	125.0 $^{2.0}_{2.0}$	1 133	919	24°
BB-G-02	473.0 $^{2.0}_{5.0}$	361.0 $^{2.0}_{4.0}$	214.0 $^{2.0}_{3.0}$	125.0 $^{2.0}_{2.0}$	917	703	30°
BB-G-03	478.0 $^{2.0}_{5.0}$	330.0 $^{2.0}_{3.0}$	214.0 $^{2.0}_{3.0}$	125.0 $^{2.0}_{2.0}$	701	487	40°
BB-G-04	483.0 $^{2.0}_{5.0}$	240.0 $^{2.0}_{3.0}$	240.0 $^{2.0}_{3.0}$	125.0 $^{2.0}_{2.0}$	485	—	60°
BB-G-05	483.0 $^{2.0}_{5.0}$	240.0 $^{2.0}_{3.0}$	240.0 $^{2.0}_{3.0}$	125.0 $^{2.0}_{2.0}$	—	—	60°

	Type of block				
	BB-G-01	BB-G-02	BB-G-03	BB-G-04	BB-G-05
Weight per block (kg)	22.1	21.8	21.3	23.1	18.0
Average water content (%)	14.49	14.07	14.87	13.69	13.07
Average dry density (g/cm³)	1.69	1.69	1.69	1.70	1.70
Number of units fabricated	2 898	2 310	1 614	562	184
Total weight (kg)	64 046	50 358	34 378	12 982	3 312

Fig. 14: Geometry of the bentonite blocks installed in the FEBEX in-situ test (ENRESA 2000)

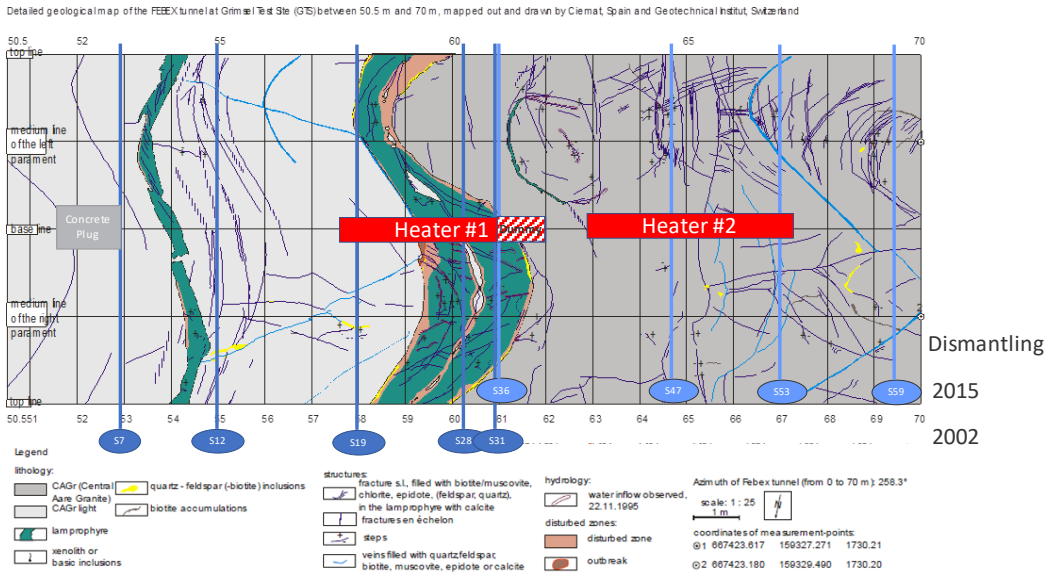

Fig. 15: Location of the bentonite sections selected for THC studies during the dismantling of Heater #1 (2002) and Heater #2 (2015)

The geological map of the gallery along the testing area (m. 20.5 to 70.0) is indicated (after Pardillo et al. 1997).

3.3 Sampling during the dismantling of Heater #2

The second dismantling operation of the FEBEX in-situ *test* (Heater #2) began on 17 February 2015 with the drilling of cores in the concrete plug followed by bentonite dismantling and sampling on 8 May 2015, the whole dismantling operation finished on 5 August 2015. During this period, different bentonite samples were obtained for performing different thermo-hydro-mechanical (THM) and chemical (THC) studies. Heater #2 was switched off on 24 April 2015, 14 days before starting the bentonite dismantling operations.

During dismantling of Heater #2 an exhaustive post-mortem bentonite sampling and analysis program was performed. Bentonite blocks were sampled at different vertical sections along three radii for performing a complete thermo-hydro-mechanical (Villar et al. 2017b) and thermo-hydro-geochemical (THG or THC) characterization (Fig. 15, Fig. 16).

The bentonite sampling sections and other samples taken for the thermo-hydro-chemical (THC) analyses were:

- Bentonite section located at contact with the shotcrete plug: Section 36 (Fig. 17)
- Bentonite sections located around Heater #2: Section 47 and Section 53 (Fig. 18, Fig. 19)
- Bentonite section located at the back of the gallery (non-heated section): Section 59 (Fig. 20)
- Bentonite samples located at the liner contact (external part): BMS-47-x and BMS-53-xx samples, being x = 1, 2, 3 (Fig. 18, Fig. 19); at the frontal part of Heater #2 and protrusions found inside the liner holes (internal part of the liner) around Sections S42 and S43 (Fig. 21). This type of samples were the closest bentonite samples to the contact of Heater #2.

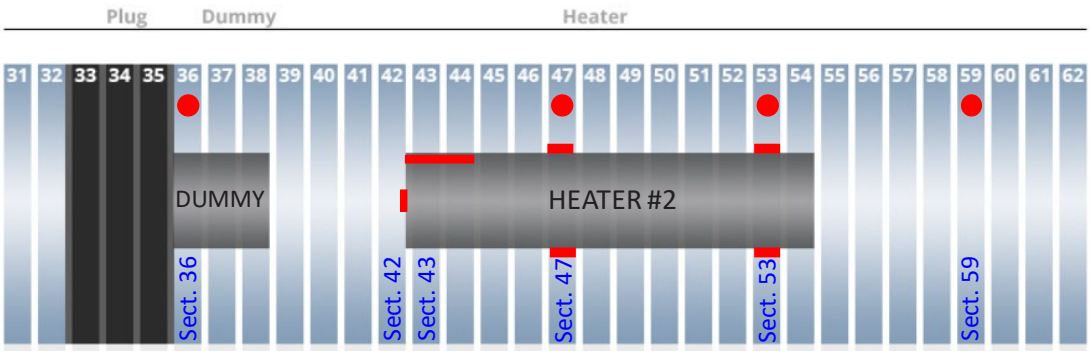

Fig. 16: Schematic figure of the FEBEX in-situ test divided in dismantling sections: location of the dismantling bentonite sections around Heater #2 selected for THC studies

The samples were taken with the intent of getting a good representation of the physical, chemical and mineralogical alterations and water content distribution. The sampling took place according to the AITEMIN's Dismantling Plan (Bárcena & García-Siñeriz 2015a) in vertical sections normal to the axis of the tunnel, and in each section several samples were taken along different radii. A further description on how the samples were taken can be seen in the different FEBEX-DP Sampling Logs (Abós & Martínez 2015: AN 15-578), and in the dismantling daily and extra reports (Kober & Van Meir 2017).

A summary of the bentonite samples used for THC analyses is shown in Tab. 4. These samples were obtained mainly with the use of an electric percussion hammer with a flat-end bit tool attached. Apart from bentonite blocks material, other types of samples were collected at different sections, such as concrete samples from the plug, bentonite-granite interface samples and samples in contact with both the liner and heater. For collecting these samples other methods were used: by hand, with a sharp knife or by using a standard drilling machine having the desired inner diameter barrel (70 – 100 mm in diameter and 10 to 280 cm in length). The dimension of the bentonite blocks installed in the FEBEX in-situ test are shown in Fig. 14.

The samples were wrapped in plastic film inside the FEBEX gallery after their extraction and then transported out of the gallery where a final preservation process inside double vacuum-sealed aluminium-foil bags was performed. A second durable plastic bag and protection against mechanical actions was used to ensure the integrity of the material.

An appropriate labelling was used to identify each sample by its material, shape and location. Except for the sensors removed, which maintained their original labelling as sample code, each sample collected was identified by a code of the type: T-Y-NN-ZZ, where:

- T is the code of material: B (bentonite), C (concrete), R (rock), M (metal), or a combination of two: CR (Interface Concrete-Rock), BC (Interface Bentonite-Concrete), BG (Interface Bentonite-Granite), BM (Interface Bentonite-Metal).
- Y is the sample shape: H (heater), L (liner), B (block), C (bentonite core), T (rock core), S (any other shape including cores, except for rock).
- NN is the sampling section number (S0 to S34).
- ZZ is the consecutive sample number for same-type samples in each section.

Following the same terminology used during the installation of the experiment and during the first dismantling, the term bentonite "Slice" refers to the vertical slices of bentonite blocks as they

were installed (see Fig. 3): from Slice 1, at the back of the gallery, to Slice 136, at the front of the barrier in contact with the first concrete plug, the last one installed. The term bentonite "Section" refers to the vertical bentonite sampling section in which samples were taken during dismantling. They were numbered from the entrance of the gallery towards the back. Sampling Sections S1 to S30 were sampled in 2002 (Fig. 5), and sampling Sections S31 to S61 (Fig. 9) were sampled in 2015. A bentonite sampling section could include two or three slices. On the other hand, different sensors were introduced inside the bentonite in some sections, which are also referred to as bentonite "Instrumented Sections".

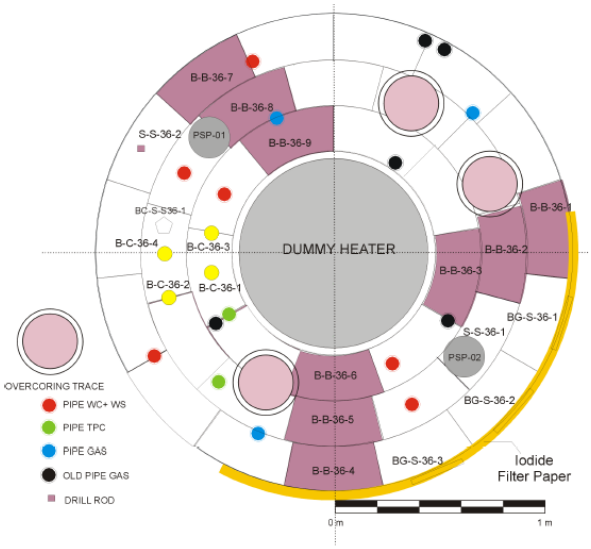

Fig. 17: Bentonite Section 36 (Slice 74): a) Installation photo: shotcrete pumping just before the bentonite Section 36 and, b) Bentonite samples taken during dismantling for THC studies (see García-Siñeriz et al. 2016)

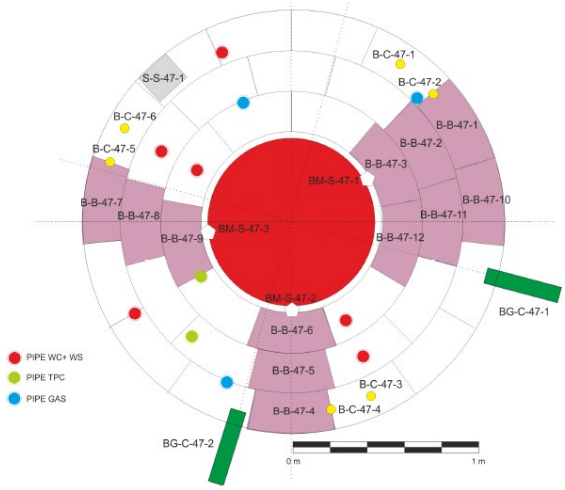

Fig. 18: Bentonite Section 47 (Slice 44): a) Installation photo and b) Bentonite samples taken during dismantling for THC studies (see García-Siñeriz et al. 2016)

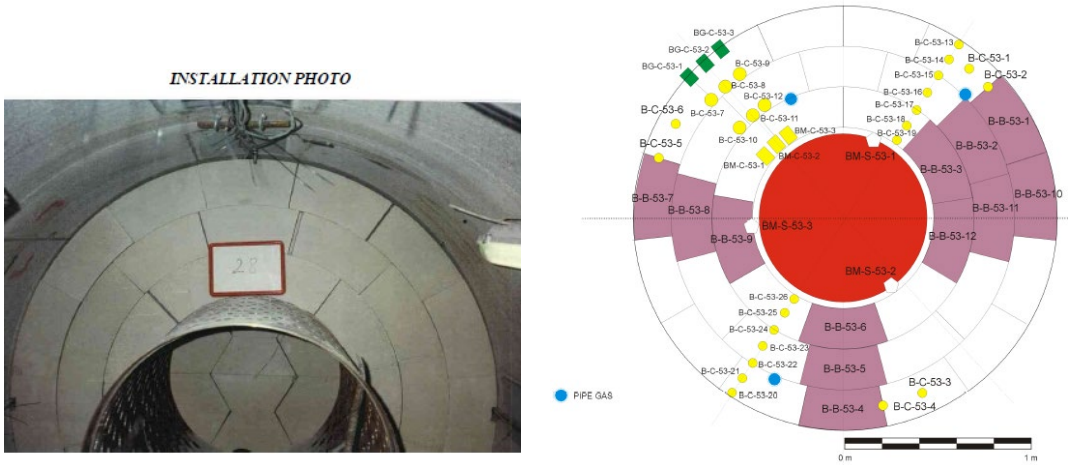

Fig. 19: Bentonite Section 53 (Slice 28): a) Installation photo and b) Bentonite samples taken during dismantling for THC studies (see García-Siñeriz et al. 2016)

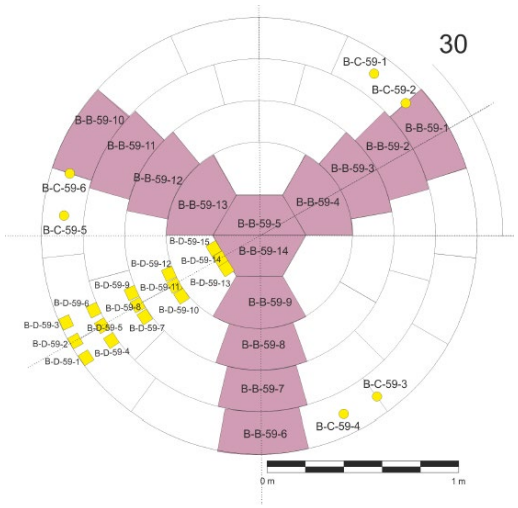

Fig. 20: Bentonite Section 59 (Slice 8): bentonite samples taken during dismantling for THC studies (see García-Siñeriz et al. 2016)

Fig. 21: Bentonite protrusions inside the liner at contact with Heater #2 (see Kober & Van Meir 2017)

Tab. 4: Bentonite samples obtained for THC (or THG) studies after dismantling of Heater #2

Samples*	Section	Instrumented section	Bentonite Slice	Type of sample	Coordinates	On site dimensions	Date	Air exposure	T (°C)	R. H. (%)	Comments
BB-36-1	36	P	74	Bentonite block	$X_{as\ built}$: 7.882, X_{actual}: 7.900; Y: --; Z = --	Δx = 13.5; Δy = 27.5; Δx = 50	8/5/2012	30'	--	--	Bentonite at a heated section. Taken with a pneumatic hammer
BB-36-2	36	P	74	Bentonite block	$X_{as\ built}$: 7.882, X_{actual}: 7.900; Y: --; Z = --	Δx = 13.0; Δy = 22; Δx = 46	8/5/2012	--	--	--	Bentonite at a heated section. Taken with a hammer/saw
BB-36-3	36	P	74	Bentonite block	$X_{as\ built}$: 7.882, X_{actual}: 7.900; Y: --; Z = --	Δx = 13.5; Δy = 22; Δx = 48	8/5/2012	25'	--	--	Bentonite at a heated section. Taken with a hammer/saw. Hole in contact with steel tubing
BB-36-4	36	P	74	Bentonite block	$X_{as\ built}$: 7.882, X_{actual}: 7.900; Y: --; Z = --	Δx = 16; Δy = 70; Δx = 28	8/5/2012	60'	--	--	Bentonite at a heated section. Taken with a hammer/saw: broken in several pieces
BB-36-5	36	P	74	Bentonite block	$X_{as\ built}$: 7.882, X_{actual}: 7.900; Y: --; Z = --	Δx = --; Δy = --; Δx = --	8/5/2012	--	--	--	Bentonite at a heated section. Taken with a hammer/saw: broken in several pieces
BB-36-6	36	P	74	Bentonite block	$X_{as\ built}$: 7.882, X_{actual}: 7.900; Y: --; Z = --	Δx = 17; Δy = 46; Δx = 26	8/5/2012	30'	--	--	Bentonite at a heated section. Taken with a hammer/saw: very damage
BS-46-A3 to A10	46	--	--	Bentonite Bulky (protrusions)	--	--	9/6/2015	--	--	--	Material and protrusions taken from inside the liner at direct contact with Heater #2
BB-47-1	47	--	44	Bentonite block	$X_{as\ built}$: 11.755, X_{actual}: 11.735; Y: -860; Z = 600	Δx = --; Δy = --; Δx = 12.5	26/6/2015	10'	13.9	98	Bentonite at a heated section. Taken with hammer/saw: broken in three parts

Tab. 4: Cont.

Samples*	**Section**	**Instrumented section**	**Bentonite Slice**	**Type of sample**	**Coordinates**	**On site dimensions**	**Date**	**Air exposure**	**T** (°C)	**R. H.** (%)	**Comments**
BB-47-2	47	--	44	Bentonite block	$X_{as\ built}$: 11.755, X_{actual}: 11.735; Y: -670; Z = 450	Δx = --; Δy = --; Δx = 12.5	26/6/2015	10'	13.9	98	Bentonite at a heated section. Taken with hammer/saw: broken in several parts
BB-47-3	47	--	44	Bentonite block	$X_{as\ built}$: 11.755, X_{actual}: 11.735; Y: -520; Z = 300	Δx = --; Δy = --; Δx = 12.6	30/6/2015	15'	--	--	Bentonite at a heated section. Taken with hammer/saw: broken in several parts
BB-47-4	47	--	44	Bentonite block	$X_{as\ built}$: 11.755, X_{actual}: 11.735; Y: --; Z = --	Δx = --; Δy = --; Δx = --	30/6/2015	5'	--	--	Bentonite at a heated section. Taken with hammer/saw: Nearly intact
BB-47-5	47	--	44	Bentonite block	$X_{as\ built}$: 11.755, X_{actual}: 11.735; Y: --; Z = --	Δx = --; Δy = --; Δx = --	30/6/2015	5'	--	--	Bentonite at a heated section. Taken with hammer/saw
BB-47-6	47	--	44	Bentonite block	$X_{as\ built}$: 11.755, X_{actual}: 11.735; Y: --; Z = --	Δx = --; Δy = --; Δx = --	30/6/2015	5'	--	--	Bentonite at a heated section. Taken with hammer/saw: very fragmented
BB-47-7	47	--	44	Bentonite block	$X_{as\ built}$: 11.755, X_{actual}: 11.735; Y: --; Z = --	Δx = --; Δy = --; Δx = --	29/6/2015	5'	--	--	Bentonite at a heated section. Taken with hammer/saw: very fragmented
BB-47-8	47	--	44	Bentonite block	$X_{as\ built}$: 11.755, X_{actual}: 11.735; Y: --; Z = --	Δx = --; Δy = --; Δx = --	29/6/2015	5'	--	--	Bentonite at a heated section. Taken with hammer/saw
BB-47-9	47	--	44	Bentonite block	$X_{as\ built}$: 11.755, X_{actual}: 11.735; Y: --; Z = --	Δx = --; Δy = --; Δx = --	29/6/2015	5'	--	--	Bentonite at a heated section. Taken with hammer/saw: Two pieces

Tab. 4: Cont.

Samples*	Section	Instrumented section	Bentonite Slice	Type of sample	Coordinates	On site dimensions	Date	Air exposure	T (°C)	R. H. (%)	Comments
BM-S-47-1	47	--	44	Bentonite bulky	$X_{as\ built}$: 11.755, X_{actual}: 11.735; Y: --; Z = --	Δx = --; Δy = --; Δx = --	26/6/2015	10'	--	--	Bentonite at contact with the liner-heater. Taken with hammer/saw
BM-S-47-2	47	--	44	Bentonite bulky	$X_{as\ built}$: 11.755, X_{actual}: 11.735; Y: --; Z = --	Δx = --; Δy = --; Δx = --	30/6/2015	10'	--	--	Powder at contact with the liner-heater. Taken with hammer/saw
BM-S-47-3	47	--	44	Bentonite bulky	$X_{as\ built}$: 11.755, X_{actual}: 11.735; Y: --; Z = --	Δx = --; Δy = --; Δx = --	29/6/2015	10'	--	--	Powder at contact with the liner-heater. Taken with hammer/saw
BB-53-1	53	--	28	Bentonite block	$X_{as\ built}$: 13.795, X_{actual}: 13.768; Y: --; Z = --	Δx = --; Δy = --; Δx = --	15/7/2015	--	--	--	Bentonite at a heated section. Taken with hammer/saw
BB-53-2	53	--	28	Bentonite block	$X_{as\ built}$: 13.795, X_{actual}: 13.768; Y: --; Z = --	Δx = --; Δy = --; Δx = --	15/7/2015	--	--	--	Bentonite at a heated section. Taken with hammer/saw
BB-53-3	53	--	28	Bentonite block	$X_{as\ built}$: 13.795, X_{actual}: 13.768; Y: --; Z = --	Δx = --; Δy = --; Δx = --	15/7/2015	--	--	--	Bentonite at a heated section. Taken with hammer/saw
BB-53-4	53	--	28	Bentonite block	$X_{as\ built}$: 13.795, X_{actual}: 13.768; Y: --; Z = --	Δx = --; Δy = --; Δx = --	15/7/2015	--	--	--	Bentonite at a heated section. Taken with hammer/saw
BB-53-5	53	--	28	Bentonite block	$X_{as\ built}$: 13.795, X_{actual}: 13.768; Y: --; Z = --	Δx = --; Δy = --; Δx = --	15/7/2015	--	--	--	Bentonite at a heated section. Taken with hammer/saw
BB-53-6	53	--	28	Bentonite block	$X_{as\ built}$: 13.795, X_{actual}: 13.768; Y: --; Z = --	Δx = --; Δy = --; Δx = --	15/7/2015	--	--	--	Bentonite at a heated section. Taken with hammer/saw

Tab. 4: Cont.

Samples*	Section	Instrumented section	Bentonite Slice	Type of sample	Coordinates	On site dimensions	Date	Air exposure	T (°C)	R. H. (%)	Comments
BB-53-7	53	--	28	Bentonite block	$X_{as\ built}$: 13.795, X_{actual}: 13.768; Y: --; Z = --	Δx = --; Δy = --; Δx = --	15/7/2015	--	--	--	Bentonite at a heated section. Taken with hammer/saw
BB-53-8	53	--	28	Bentonite block	$X_{as\ built}$: 13.795, X_{actual}: 13.768; Y: --; Z = --	Δx = --; Δy = --; Δx = --	15/7/2015	--	--	--	Bentonite at a heated section. Taken with hammer/saw
BB-53-9	53	--	28	Bentonite block	$X_{as\ built}$: 13.795, X_{actual}: 13.768; Y: --; Z = --	Δx = --; Δy = --; Δx = --	15/7/2015	--	--	--	Bentonite at a heated section. Taken with hammer/saw
BM-S-53-1	53	--	28	Bentonite bulky	$X_{as\ built}$: 13.795, X_{actual}: 13.768; Y: --; Z = --	Δx = --; Δy = --; Δx = --	15/7/2015	--	--	--	Powder at contact with the liner-heater. Taken with hammer/saw
BM-S-53-2	53	--	28	Bentonite bulky	$X_{as\ built}$: 13.795, X_{actual}: 13.768; Y: --; Z = --	Δx = --; Δy = --; Δx = --	15/7/2015	--	--	--	Powder at contact with the liner-heater. Taken with hammer/saw
BM-S-53-3	53	--	28	Bentonite bulky	$X_{as\ built}$: 13.795, X_{actual}: 13.768; Y: --; Z = --	Δx = --; Δy = --; Δx = --	15/7/2015	--	--	--	Powder at contact with the liner-heater. Taken with hammer/saw
BB-59-1	59	--	8	Bentonite block	$X_{as\ built}$: 16.338, X_{actual}: 16.375; Y: --; Z = --	Δx = 13.0; Δy = --; Δx = --	28/7/2015	15'	--	--	Bentonite at a non-heated section. Taken with hammer/saw
BB-59-2	59	--	8	Bentonite block	$X_{as\ built}$: 16.338, X_{actual}: 16.375; Y: --; Z = --	Δx = 13.1; Δy = --; Δx = --	28/7/2015	--	--	--	Bentonite at a non-heated section. Taken with hammer/saw: two fragments
BB-59-3	59	--	8	Bentonite block	$X_{as\ built}$: 16.338, X_{actual}: 16.375; Y: --; Z = --	Δx = 13.0; Δy = --; Δx = --	28/7/2015	15'	--	--	Bentonite at a non-heated section. Taken with hammer/saw

Tab. 4: Cont.

Samples*	**Section**	**Instrumented section**	**Bentonite Slice**	**Type of sample**	**Coordinates**	**On site dimensions**	**Date**	**Air exposure**	**T** (°C)	**R. H.** (%)	**Comments**
BB-59-4	59	--	8	Bentonite block	$X_{as\ built}$: 16.338, X_{actual}: 16.375; Y: --; Z = --	Δx = 13.1; Δy = --; Δx = --	28/7/2015	5'	--	--	Bentonite at a non-heated section. Taken with hammer/saw
BB-59-5	59	--	8	Bentonite block	$X_{as\ built}$: 16.338, X_{actual}: 16.375; Y: --; Z = --	Δx = 13.0; Δy = --; Δx = --	28/7/2015	10'	--	--	Bentonite at a non-heated section. Taken with hammer/saw
BB-59-6	59	--	8	Bentonite block	$X_{as\ built}$: 16.338, X_{actual}: 16.375; Y: --; Z = --	Δx = 13.1; Δy = --; Δx = --	29/7/2015	10'	--	--	Bentonite at a non-heated section. Taken with hammer/saw
BB-59-7	59	--	8	Bentonite block	$X_{as\ built}$: 16.338, X_{actual}: 16.375; Y: --; Z = --	Δx = 13.5; Δy = --; Δx = --	29/7/2015	--	--	--	Bentonite at a non-heated section. Taken with hammer/saw: 5 fragments
BB-59-8	59	--	8	Bentonite block	$X_{as\ built}$: 16.338, X_{actual}: 16.375; Y: --; Z = --	Δx = 13.0; Δy = --; Δx = --	29/7/2015	15'	--	--	Bentonite at a non-heated section. Taken with hammer/saw. Oxidation by extensometer
BB-59-9	59	--	8	Bentonite block	$X_{as\ built}$: 16.338, X_{actual}: 16.375; Y: --; Z = --	Δx = 13.0--; Δy = --; Δx = --	29/7/2015	15'	--	--	Bentonite at a non-heated section. Taken with hammer/saw. Oxidation by extensometer
BB-59-10	59	--	8	Bentonite block	$X_{as\ built}$: 16.338, X_{actual}: 16.375; Y: --; Z = --	Δx = 13.6--; Δy = --; Δx = --	29/7/2015	15'	--	--	Bentonite at a non-heated section. Taken with hammer/saw
BB-59-11	59	--	8	Bentonite block	$X_{as\ built}$: 16.338, X_{actual}: 16.375; Y: --; Z = --	Δx = 13.2--; Δy = --; Δx = --	29/7/2015	15'	--	--	Bentonite at a non-heated section. Taken with hammer/saw

Tab. 4: Cont.

Samples*	**Section**	**Instrumented section**	**Bentonite Slice**	**Type of sample**	**Coordinates**	**On site dimensions**	**Date**	**Air exposure**	**T** (°C)	**R. H.** (%)	**Comments**
BB-59-12	59	--	8	Bentonite block	$X_{as\ built}$: 16.338, X_{actual}: 16.375; Y: --; Z = --	Δx = 13.2--; Δy = --; Δx = --	29/7/2015	15'	--	--	Bentonite at a non-heated section. Taken with hammer/saw
BB-59-13	59	--	8	Bentonite block	$X_{as\ built}$: 16.338, X_{actual}: 16.375; Y: --; Z = --	Δx = 13.2--; Δy = --; Δx = --	29/7/2015	15'	--	--	Bentonite at a non-heated section. Taken with hammer/saw: 2 fragments
BB-59-14	59	--	8	Bentonite block	$X_{as\ built}$: 16.338, X_{actual}: 16.375; Y: --; Z = --	Δx = 13.0; Δy = --; Δx = --	29/7/2015	15'	--	--	Bentonite at a non-heated section. Taken with hammer/saw

* Sample code: BB → bentonite block; BMS → bentonite-metal contact any shape; BS: bentonite bulky material any shape

4 Methodology

Laboratory tests analysed blocks and other type of bentonite material in order to determine the physical, physico-chemical, mineralogical and geochemical characteristics of the buffer at the end of the test. The following parameters were considered for the assessment of the bentonite properties after it underwent heating and/or hydration for a period of over 18 years (Fig. 22):

- Physical properties: water content and dry density
- Mineralogical alteration
- Geochemical alteration
- Clay texture
- Total surface area and external specific surface
- Water adsorption measurements
- Cation exchange capacity
- Cation exchange population
- Soluble salts
- Pore water chemistry extracted by squeezing

The methodology used for the THC analysis from samples obtained during the dismantling of Heater #1 in 2002 was quite different and can be found in the Appendix A.

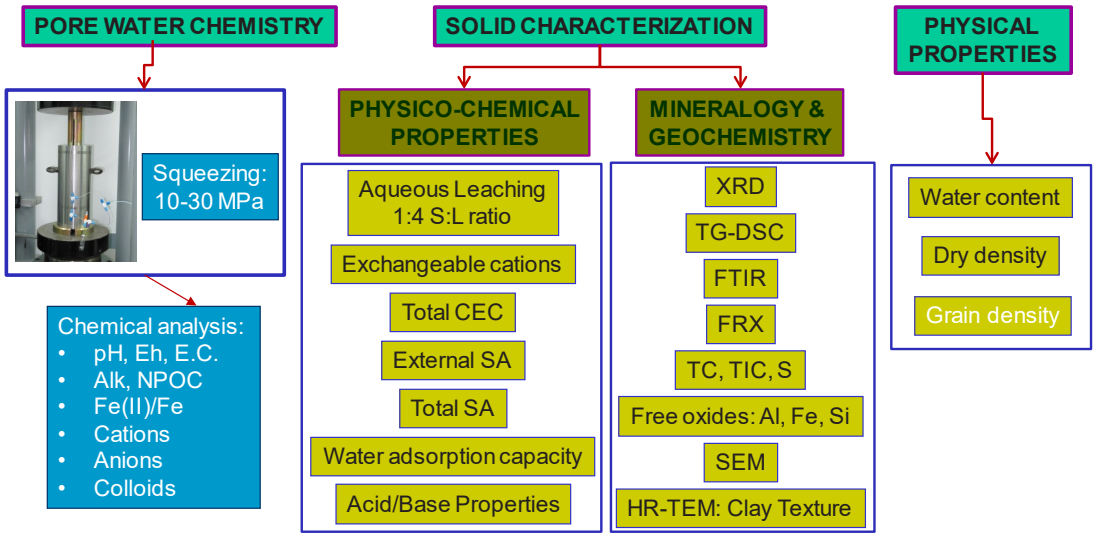

Fig. 22: Methodology for THC analysis after dismantling of Heater #2

4.1 Sub-sampling at the laboratory

Once the samples arrived from the Grimsel Test Site, and prior to their analysis, the samples were stored in a humidity chamber at 15 °C and then at laboratory conditions at a temperature between 18 and 22 °C, except those which were stored in a refrigerator.

Each bentonite block was half-sectioned along the vertical axis, in order to obtain material for geochemical and hydro-mechanical tests (Fig. 23). The geochemical half was sliced in three parts for analysing (Fig. 24): 1) soluble salts, exchangeable cations and CEC, 2) mineralogy and geochemistry, and 3) pore water chemistry. For the first analysis (soluble salts distribution and exchangeable cations), the bentonite was further sliced in two parts following the block c-axis, referenced in the direction from the granite contact as S1 and S2 (Fig. 24, Fig. 25), giving a total of six samples per radii; except in Section 59 (non-heated section), where 10 samples were analysed per radii. In the case of mineralogy/geochemistry, a total of 3 samples were analysed per radii.

The samples for pore water characterization were again preserved inside vacuum-packed Al-foil bags until performing the squeezing tests (Fig. 26). The whole piece for geochemistry and mineralogy was disaggregated, homogenised and air dried prior to analysis (Fig. 27).

Fig. 23: Appearance of the bentonite material and subsampling for THM and THC analyses

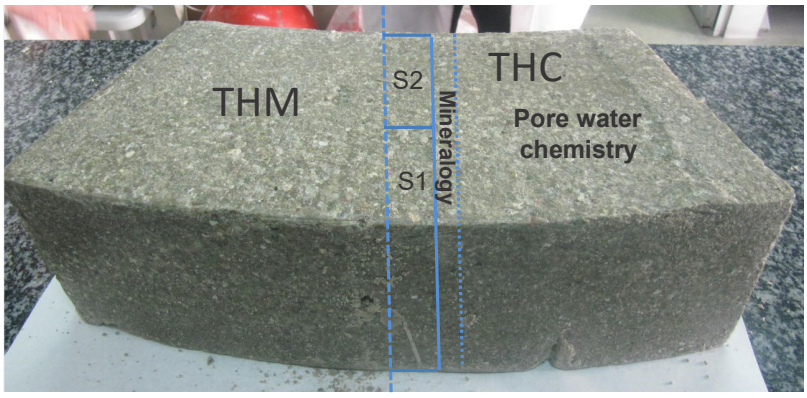

Fig. 24: Appearance of the bentonite block material and subsampling for THC analyses: a) S1 and S2 for soluble salts (S1: towards granite interface; S2: towards heater interface), CEC and exchangeable cations, b) mineralogy and geochemistry, and c) pore water chemistry

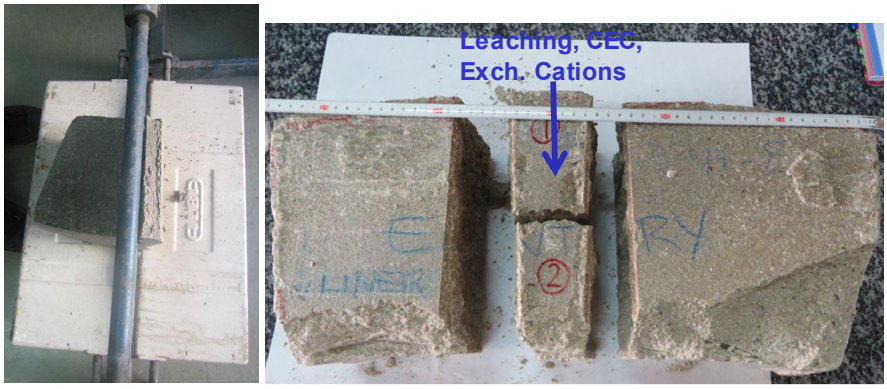

Fig. 25: Detail of subsampling for soluble salts, exchangeable cations and CEC determinations (1 or S1: towards granite interface; 2 or S2: towards heater interface)

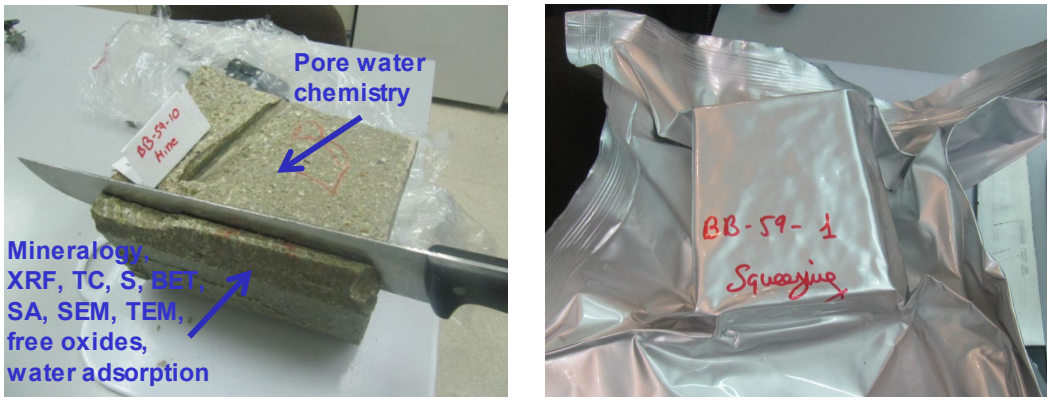

Fig. 26: a) Detail of subsampling for minerology/geochemistry and pore water chemistry studies; b) Preservation of the squeezing sample until analysis

Fig. 27: Preparation of the samples for mineralogical and geochemical analysis: disaggregation, homogenisation, air drying, grinding and sieving (< 250 µm)

4.2 Physical properties

The gravimetric water content (w.c), is defined as the ratio between the weight of water and the weight of dry solid expressed as a percentage. The weight of water was determined as the difference between the weight of the sample and its weight after oven drying at 110 °C for 48 hours (weight of solid).

Dry density, ρ_d, is defined as the ratio between the weight of the dry sample and the volume occupied by it prior to drying. The volume of the specimens was determined by immersing them in a recipient containing mercury and by weighing the mercury displaced, as established in UNE Standard 7045 "Determination of soil porosity".

The specific gravity of the solid particles, γ_s, commonly referred to as grain density (g/cm^3), is defined as the relation between the weight of the solid and the volume occupied by it. Specific gravity (dimensionless) has been determined by pycnometry using water, according to the UNE Standard 103-302: "Determination of the relative density of soil particles". In this method, the weight of the water displaced by a known mass of oven-dried and degassed soil is determined.

Different relationships were used to obtain the following parameters:

The *wet gravimetric water content*, WC_{wet}, was obtained by using the equation:

$$WC_{wet} = \frac{WC_{dry}}{(1 + WC_{dry})}, \quad WC_{dry}(\%) = \frac{M_w}{M_{dry}} \times 100$$

where, WC_{dry} is the gravimetric water content on a dry mass basis of the rock; M_w is the mass of water in the rock, and M_{dry} is the mass of solid dried at 110 °C for 24 hours.

The physical porosity or total porosity was calculated by means of the relationship:

$$n = 1 - \frac{\rho_{dry}}{\gamma_s},$$

where, ρ_{dry} is the dry density, and γ_s is the grain density.

The volumetric moisture content or water-loss porosity, θ, which is the ratio of water-filled pore space to total volume (V_{wat}/V_{tot}); and the saturation degree, S_r, which is the ratio of water-filled to total volume (V_{wat}/V_{pores}), were calculated from the equations:

$$\theta = \frac{WC_{wet} \cdot \gamma_s}{WC_{wet} \cdot \gamma_s + (1 - WC_{wet}) \cdot \rho_w} \text{ or } \theta = WC_{dry} \times \rho_{dry} \text{ or } \theta = WC_{wet} \times \frac{\rho_{bulk}}{\rho_w}$$

$$\theta = \frac{\rho_{wet} \times \rho_{dry}}{\rho_w}, \quad S_r = \frac{\theta}{n}$$

where, *n* is the total or physical porosity, which is the ratio of the pore volume to the total volume (V_{pores}/V_{tot}); ρ_w is the density of the pore water, and ρ_{wet} is the bulk wet density.

The water content at saturation was obtained according to:

$$wc_{sat}(\%) = \frac{\rho_w}{\rho_d} - \frac{\rho_w}{\gamma_s},$$

where, ρ_w is the density of the pore water (assumed to be 1.0 g/cm^3), γ_s is the specific gravity of the solid sample, and ρ_d is the dry density.

4.3 Mineralogical analysis: XRD, SEM, TEM, FTIR and thermal analysis

X-Ray diffraction (XRD) patterns were obtained from random powders and oriented aggregates in order to identify the mineralogical species in the samples. The bulk sample powders were obtained by grinding the samples in a RETSCH RM 100 mortar grinder with an agate pestle to a size of less than 63 µm after drying them at ambient temperature. The powders were analysed with a Philips X'Pert –PRO MPD diffractometer, using an anticathode Cu-K_α at 45 kV and 40 mA, equipped with a fixed divergence slit (0.1245° size), Scientific X'celerator detector. The samples were investigated from 2° to 70° 2θ with a step size 0.017° 2θ , and a scan rate of 50 s per step for the powder samples. The XRD database used for mineral identification has been the Power Diffraction File from the International Center for Diffraction Data (ICDD).

The modified Jackson (2005) treatment was used to separate the clay minerals from the rock matrix (Moore & Reynolds 1989). The fine fraction of less than 2 µm was obtained by suspension and sedimentation in deionised water. In case of necessity and depending on the sample, the clay suspension was successively treated with a 0.5 M sodium acetate (NaOAc) buffer at pH 5 in order to remove carbonates; with a H_2O_2 (30 %)/NaOAc mixture (pH 5) to eliminate organic matter; and with a citrate-bicarbonate-dithionite (CBD) solution to remove Fe and Mn oxy/hydroxides. Each of the preceding treatments was followed by careful washing with deionised water and a mixture solution of ethanol/water at 1:1 ratio.

The final clay suspension was ultrasonically dispersed using 1 g in 5 mL of deionized water. Oriented mounts were prepared by suction of this dispersed suspension through 3 mm thick ceramic tiles by applying a vacuum. These clay films (air dried, ethylene glycol solvated and 550 °C heated) were X-Rayed from 2 to 35° 2θ using a Bruker D8 Advance diffractometer with an anticathode Cu-K_α at 40 kV and 30 mA, equipped with a fixed divergence slit (0.15° size). The samples were investigated with a step size of 0.02° 2θ , and a scan rate of 2 s per step.

Fourier Transform Infrared (FTIR) spectroscopy is complementary to X-Ray diffraction and other methods. Fourier transform IR spectra were obtained in the middle-IR region (4'000 – 400 cm^{-1}) with a Nicolet 6700 with a DTGS KBr detector (resolution 4 cm^{-1}, 32 scans) on KBr-pressed discs in transmission technique in an atmosphere continuously purged from water and atmospheric CO_2. Two milligrams of powdered air-dried sample were dispersed in 200 mg of KBr and pressed to a clear disc. The pressed samples were analysed at room temperature and then after heating in an oven overnight at 110 °C. The spectra were examined in the OH stretching region (3'400 – 3'800 cm^{-1}) and the region below 1'200 cm^{-1}, where intense Si-O absorptions and OH bending bands are present (Kloprogge 2005, Madejová & Komadel 2001, Van der Marel & Beutelspacher 1976).

Thermal Analysis (TG/DSC) of the bulk sample was performed in a Setaram Setsys Evolution 16 equipment at a heating rate of 10 °C/min and under a dynamic argon atmosphere (20 mL/min) at temperatures between 20 °C and 1'100 °C (Mackenzie 1957).

Scanning electron microscopy (SEM). A ZEISS EVO LS 15 SEM microscope coupled to a X LINK LZ_5 energy dispersive X-Ray energy spectrometer (XEDS), which allows for the qualitative analysis of light elements from boron, were used to define the microstructural morphology of clay minerals, possible alteration products and accessory minerals. Most of the clay samples were dried at 40 – 60 °C in an oven overnight, and then subjected to a gold metallization by applying 5×10^{-2} Torr vacuum and a gold coating of 300 to 400 Å thickness, using a BALZERS SCD 004 sputter coater for the scanning electron microscopy analysis. The calculation of the structural formula for smectites from the chemical composition analysed by XEDS was based on the assumption of tetrahedral occupation by 4.0 cations ($^{IV}Si+^{VI}Al$) and complete oxygen/hydroxyl framework of $O_{10}(OH)_2$, resulting in 22 negative anionic charges per half unit cell (p.h.u.c.) according to Newman (1987).

Transmission Electron Microscopy (HRTEM). A JEOL JEM 3000F microscope working at 300 kV accelerating voltage, 0.17 nm of resolution, and coupled to an OXFORD INCA energy dispersive X-Ray energy spectrometer (XEDS), allowed a qualitative analysis. Clay particles (< 2 μm fraction) were fully dispersed in isobutanol by shaking and ultrasonic treatment. A tiny drop of the clay suspension was pipetted and deposited on holey carbon formvar coated copper TEM grids.

4.4 Geochemical analysis of the bentonite samples

4.4.1 Chemical analysis by X-Ray fluorescence

The chemical composition of the rock samples was determined by X-Ray fluorescence.

Major elements in the total fraction

The major elements (SiO_2, Al_2O_3, Fe_2O_3, MnO, MgO, CaO, Na_2O, K_2O, TiO_2, P_2O_5 and SO_3 in %) were analysed by X-Ray fluorescence (XRF) in natural powdered samples, which were ground at a grain size of < 250 μm. The XRF analyses were performed with an Axios spectrometer from Panalytical equipped with a rhodium X-Ray tube (stimulation power: 1 kW). The dissolution or decomposition of the sample into a homogeneous glass was obtained by fusion, which consisted of heating a mixture of sample and flux ($Li_2B_4O_7$) at high temperatures (800 to 1'000 °C) so that the flux melts and the sample dissolves. The end product after cooling is a one-phase glass.

Powdered samples (0.8 g of oven-dried samples at 105 °C) were homogeneously mixed with 7.2 g of lithium tetraborate in the proportion of 34 – 66 %. The whole material was melted stepwise in a platinum crucible at a smelting apparatus. After this procedure, the melt was transferred into a platinum jacket and cooled. The loss on ignition (LOI) was determined separately by oven-drying the dried sample at 1'025 °C for 3 hours in duplicate.

Analysis of trace elements in the total fraction

The trace elements (Cl, Sc, V, Cr, Co, Ni, Cu, Zn, Ga, Ge, As, Se, Br, Rb, Sr, Y, Zr, Nb, Mo, Ag, Cd, Sn, Sb, Te, I, Cs, Ba, La, Ce, Nd, Sm, Yb, Hf, Ta, W, Tl, Pb, Bi, Th and U in ppm) of the solid samples were determined in powdered and < 63 µm ground samples. The XRF analyses were performed on an Axios spectrometer from Panalytical equipped with a rhodium X-Ray tube (stimulation power: 1 KW) using melted pellets. For obtaining pressed pellets, 12 g of the dried samples were mixed with wax, which acts as a binding agent. The material was pelletized at a pressure of 150 kN for 1 minute for obtaining a cylindrical pellets 40 mm diameter and a thickness which depends on the density of the sample. The dissolution or decomposition of the sample into a homogeneous glass was obtained by fusion, which consisted of heating at high temperatures (800 to 1'000 °C) so that the sample dissolves.

Analysis of major and trace elements in the < 2 µm fraction

The major (SiO_2, Al_2O_3, Fe_2O_3, MnO, MgO, CaO, Na_2O, K_2O,TiO_2, P_2O_5 y SO_3 in %) and trace elements (Cl, Sc, V, Cr, Co, Ni, Cu, Zn, Ga, Ge, As, Se, Br, Rb, Sr, Y, Zr, Nb, Mo, Ag, Cd, Sb, Te, I, Ba, La, Nd, Sm, Dy, Er, Yb, Hf, Ta, W, Hg, Tl, Pb, Bi, Th and U in ppm) of the samples in the < 2 µm fraction saturated in barium were measured by XRF in an AXIOS spectrometer from Panalytical equipped with a rhodium X-Ray tube (stimulation power: 1 KW) using melted pellets. The powdered and homogeneously ground sample (> 0.2 g) was prepared as pressed pellets onto boric acid. 0.1 g of sample were mixed with wax as binding agent. The mixed sample was pressed at 200 kN onto boric acid (40 mm thickness) for 1 min. by using the sandwich method for obtaining cylindrical pellets 10 mm diameter and a thickness which depends on the density of the sample. The dissolution or decomposition of the sample into a homogeneous glass was obtained by fusion.

The calculation of the structural formula of smectites from the chemical composition analysed by XRF was based on the assumption of tetrahedral occupation by 4.0 cations ($^{IV}Si+^{VI}Al$) and complete oxygen/hydroxyl framework of $O_{10}(OH)_2$, resulting in 22 negative anionic charges per half unit cell (phuc) according to Newman (1987).

4.4.2 Poorly crystalline and free silica, aluminium and iron

The extractable and free silica and aluminium were determined by using a Na_2CO_3 0.5 M dissolution (pH 10.5) according to the alkali dissolution method (Follet et al. 1965, Wilson 1987). 0.5 grams of sample were mixed with 50 mL of Na_2CO_3 0.5 M solution and allowed to react by end-over-end shaking for 24 hours at ambient temperature. Afterwards, the suspension was centrifuged at a constant rotation speed of 15'500 rpm for 30 min. The supernatant solution was filtered through 0.45 µm, and the concentration of silica and aluminium was analysed by ICP.

The Citrate-Bicarbonate-Dithionite (CBD) method was used for determining extractable iron oxides following Jackson's procedure (Jackson 2005).

4.4.3 Fe(II)-Fe_{total} in the samples at contact with the liner and heater

In order to determine the amount of Fe(III) and Fe(II) in the retrieved bentonite samples, a modification of the method described in Tarafder & Thakur (2012) was used. Fe(III) and Fe(II) were leached from the samples according to the procedure and analysed by 1,10-phenantroline monohydrate spectrophotometric method.

To a finely ground sample of 0.1-0.2 g, 1 g of NH_4HF_2 and 10 mL of 1:1 H_2SO_4 were added to a 40 mL high-density polyethylene (HDPE) tubes. The tubes were closed with caps and heated to 90 °C for 60 minutes in a shaking water bath. After this extraction process, the tubes were allowed to cool to room temperature. The contents were transferred to a 50 – 100 mL volumetric flasks and filled to complete volume with MilliQ water.

For the spectrophotometric determination of Fe(II), a 1 – 5 mL aliquot (duplicate) was taken in a 50 mL volumetric flask; 5 mL of 6 M sodium acetate and 1 mL of 1 % 1,10-phenanthroline monohydrate were added, mixed well and filled to full volume with MilliQ water. After 15 minutes, the absorbance at 510 nm was measured against a blank of reagents.

For the spectrophotometric determination of total-Fe, another aliquot (duplicate) was taken in a separate 50 mL volumetric flask and 2 mL of 10 % hydroxylammonium chloride were added to it. This was mixed well and was allowed to stand 20 min. Then, 5 mL of 6 M sodium acetate and 1 mL of 1 % 1.10 phenanthroline were added, mixed well and filled to full volume with MilliQ water. After 15 minutes, the absorbance at 510 nm was measured against a blank of reagents.

The iron contents were determined in the samples from a calibration curve prepared from iron standard solutions. The estimation of ferric iron was made by subtracting the ferrous iron content from the total iron content.

4.4.4 Total carbon, total inorganic carbon and total sulphur

Total carbon, total sulphur and total inorganic carbon were determined on 0.2 g of powdered solid samples obtained from a representative and homogeneous sample. The powders were obtained by grinding the air-dried samples in a RETSCH RM 100 mortar grinder with an agate pestle to a size of less than 250 µm. Total carbon (TC) and Total Sulphur content were determined on the solid sample by means of a LECO CS-244 analyser by combustion. The total inorganic carbon (TIC) content was obtained with a TOC-V_{CSH} analyser (SHIMADZU, Shimadzu Scientific Instruments, Kyoto, Japan) equipped with an SSM-5000A module. The presence of organic carbon was evaluated by the difference between TC and TIC.

4.5 Physico-chemical characterization

4.5.1 Layer charge

The layer charge (LC) was determined by following the alkylammonium ion expansion method described in Olis et al. (1990). The method uses an empirically relationship between d(001)-XRD basal spacings of one alkylammonium derivative (n_c = 12 or 18) and the mean layer charge calculated from the conventional n-alkylammonium ion-exchange technique (Lagaly 1994). Simple linear regression models describing the relationships for both monolayer-bilayer and bilayer-pseudotrimolecular layer transitions were used to estimate the mean total layer charge (ξ_M) of an expanding clay mineral.

4.5.2 Cation exchange capacity

Total CEC was measured with 0.01 M copper triethylenetetramine (Cu-Trien or $[Cu(trien)]^{2+}$ solution according to Ammann et al. (2005).

200 mg of clayey sample were weighed in 60 mL centrifuge tubes. 25 mL of deionized water were added, and the suspension was dispersed by ultrasonic treatment for 5 min. Then, 10 mL of 0.01 M $[Cu(trien)]^{2+}$ were added and allowed to react by end-over-end shaking for 1 hour. After this procedure, a complete exchange of the $[Cu(trien)]^{2+}$ complex with the exchangeable cations is guaranteed. Afterwards, the suspensions were centrifuged at a constant rotation speed of 15'500 rpm for 20 min. 3 mL of the clear blue solution (filtered through 0.45 µm pore size syringe filter) were filled into 1 cm optical glass cuvettes and the absorbance of the solution was measured at 578 nm wavelength by using a Merck spectrophotometer. The analyses were performed in duplicate. The standard deviation of the measurement is ± 2 meq/100g.

4.5.3 Cation exchange population

The determination of the cation exchange population was performed by using Cs as index cation (Sawhney 1970). Caesium acts as a high selective cation to displace all exchangeable cations from the clay minerals if its concentration is sufficiently high. Solid samples were equilibrated inside a JACOMEX glove box (< 1 ppm O_2) at 1:4 solid to liquid ratio (0.25 kg/L) with 0.5 M $CsNO_3$ at pH 8.2. After phase separation by centrifugation (outside the glove box), the supernatant solutions were filtered through 0.45 µm pore size syringe filter (inside the anoxic glove box), and the concentration of the major cations was analysed. Sodium and calcium results were corrected from their content as soluble salts.

4.5.4 Zeta potential and size of colloid clay particles

A Zetasizer NanoS Malvern instrument was used for determining: a) the surface charge of colloid particles through measurements of the particle mobility and calculation of ζ-potential by means of laser Doppler electrophoresis technique, and b) the colloid particle size by means of the Photon Correlation Spectroscopy (PCS) technique (Missana et al. 2018a).

Homogenised samples from three bentonite blocks at Section 47 (heated section), as a function of the distance from the gallery axis, were used for obtaining smectite colloid (< 1 µm) suspensions after centrifugation at 3000 rpm (700 g) for 10 min. Particle size and ζ potential were measured at a very low ionic strength (I), E.C. ~ 25 µS/cm, guaranteeing colloid stability and avoiding aggregation due to I. Determinations were done at the sample pH and as a function of pH (acid and basic) by adding 0.1 M HCl or NaOH.

Particle size was evaluated as average hydrodynamic diameter (d_h), measured by Photon Correlation Spectroscopy (PCS). PCS is a technique to measure particle hydrodynamic diameter based on the diffused light coming from the interaction of a laser source with suspended particles. PCS uses the basis of particle Brownian motion to obtain the particle dimensions (Hunter 2001). The instrument includes a He-Ne laser source of λ = 633 nm intensity and 15 mW energy. The beam of light is attenuated (in order not to overload the detector) before it interacts with the particles in the disposable plastic cuvette. Detection of photons is carried out at 173° using a photomultiplier, from which the electronical signal is sent to the correlator to transform it into a digital signal. The hydrodynamic diameter is obtained as an average of 15 measurements consisting of three runs of 20 s.

The apparatus allows measuring particle diameters from 0.3 nm to 10 μm in samples with a particle concentration from 1 to 1000 ppm. PCS instruments provide an indicator of the polydispersity degree of the sample. The polydispersity is a parameter which ranges from 0 to 1, where values close to 0 are related to homogeneous systems, with similar particle sizes (monodisperse), while values close to 1 are related to heterogeneous particle sizes (polydisperse). The errors of the size measurements are obtained by the standard deviation of at least five measurements

Zeta potential (ξ potential) was experimentally measured by laser Doppler electrophoresis. According to the Gouy-Chapman theory of the electrical double layer, the relationship between the surface charge density, σ, and the surface potential, ψ, is given (for a symmetric electrolyte) by:

$$\sigma = \sqrt{8n\varepsilon kT}\sinh\left(\frac{ze\psi}{2kT}\right)$$

where, *n* is the bulk concentration of ions of valence z, ε the permittivity, k the Boltzmann constant, T the temperature and e the electron charge.

The zeta potential represents the potential produced by the double layer near the electrolyte/particle interface at the location of the "slipping plane", which limits the layer of fluid adhered to the particle moving with it. Thus, the zeta potential is not exactly equal to the surface potential generated by the surface charge of the particles, but it is often the only possible mean to characterize surface charge at least in terms of sign and magnitude (Delgado et al. 2007).

The ξ potential can be estimated by electrophoresis techniques, measuring the velocity and direction of charged particles under a given electric field, i.e. evaluating their electrophoretic mobility, UE. The electrophoretic mobility is the velocity of the particles divided by the magnitude of the electric field ($m^2/V \cdot s$).

When an electric field is applied to a colloid suspension, charged particles within a fluid move to the electrode oppositely charged with a certain velocity. An opposite force exists against particle motion due to the viscosity of the fluid. When these two opposite forces are equilibrated, particles move with an equilibrium velocity, the electrophoretic mobility (*UE*). In the technique, a laser beam is directed at the sample and by measuring the intensity fluctuations, the movement of the particles can be determined, showing high fluctuation rate when the electrophoretic mobility is high. Knowing the electrophoretic mobility and the properties of the suspension, the ξ potential of the particles can be determined by using the Henry equation:

$$U_E = \frac{2\varepsilon\xi(ka)}{3\eta}$$

where, U_E is the electrophoretic mobility, ε the dielectric constant, ξ the zeta potential, η the viscosity and *f(ka)* is the Henry's function, that has different values from 1 to 1.5. When the salt concentration in the system is higher than 1×10^{-3} M and particle hydrodynamic diameter is higher than 200 nm, the Smoluchowski approximation is commonly used, with *f(ka)* = 1.5; while in low dielectric constant media (non-aqueous environments) the Huckel approximation is used, *f(ka)* = 1.0.

For Zeta potential measurements, a He-Ne laser source (λ = 633 nm) of 4 mW interacts with the sample inside a disposable plastic cuvette U-shaped with electrodes on the top. In this case,

backscattered intensities are detected (at 17°). The error in the measurements is the standard deviation of at least five individual runs.

4.5.5 BET and external surface area

Classical nitrogen adsorption/desorption isotherms were obtained on a discontinuous volumetric sorptometer, Micromeritics ASAP 2020 V3.02 H. Approximately 0.5 – 3 g of total sample was ground in an agate mortar. The samples were dried at 90 °C during at least 24 h before the tests. Prior to the nitrogen adsorption, the samples were out-gassed by heating at 90 °C for 18 hours using a mixture of helium and nitrogen under a residual vacuum between 500 and 6 – 10 μmm Hg. The tests were performed at the boiling point of liquid nitrogen (77 K) considering a molecular cross section area of 0.162 nm for the nitrogen molecule. External surface areas were calculated using the standard N_2-BET method, using a series of data points over the P/P_0 range of 0.02 to 0.25 on the nitrogen adsorption isotherm (Gregg & Sing 1982). The determination was accomplished on two or three aliquots of each subsample, the values being the average of these. The presence of micropores in the sample was assessed using the t-plot method (de Boer et al. 1966). Pore volume distribution as a function of pore size in the mesopore and low macropore size range was attained using the BJH method by reducing isotherm data (adsorption or desorption) between about 0.05 P/Po and saturation (Barrett et al. 1951).

4.5.6 Total surface area

In contrast to nitrogen, which is only adsorbed at the external surface of the stacks of the layers, water molecules can be adsorbed on the whole surface, including both the internal (interlayer) and external surfaces of the clay minerals. The total amount of adsorbed water of a clayey sample with its specific mineralogical composition is in equilibrium with a given relative humidity, the amount of adsorbed water at the interlayers being dependent on the type of adsorbed cations.

In order to obtain the *Total specific surface area (SA)*, *w*ater vapour gravimetric adsorption measurements were performed by Keeling's hygroscopic method (Keeling 1961, Keeling et al. 1980) by storing the samples at a constant 75 % relative humidity atmosphere in a chamber over-saturated in a NaCl solution for 1 month. Prior to the tests the samples were dried at 110 °C for 24 hours. The weight of the samples changes as the adsorbed amount of water was measured and related to the total surface area, SA.

4.5.7 Water adsorption isotherms

The method used to determine the water vapour adsorption isotherms corresponds to the simple diffusion static method in desiccators. As water vapour is not an ideal gas, its adsorption cannot be studied by classical volumetric techniques. It is necessary to measure the adsorbed quantities directly by using gravimetric methods (Villiéras et al. 1997).

In the simple diffusion or static method, the sample is placed in a desiccator which contains a solution of known concentration and at constant temperature. Vapour is transported to the sample by simple diffusion. In this method the time required for reaching equilibrium between the soil and the solution is long (at least 1 month). The diffusion rate of moisture that forms a saturated salt solution is exponential, with a quick approach to the near equilibrium values, but a very gradual final approach to the actual end point. The diffusion rate is governed by the difference in water vapour pressure of the solution and the vapour; and by the attraction of the salt for water. With some salts, reaching complete equilibrium requires days.

The relative humidity or water activity of the reference system can be controlled by varying the chemical potential of different types of aqueous solutions. Both non-volatile solutes (salt solutions) and volatile solutes (acid solutions) can be used; their affinity for water regulates the water vapour pressure in the atmosphere surrounding a material.

In this work, water vapour adsorption isotherms were measured at 295 K (~ 21 ± 1 °C) by gravimetry in quasi-equilibrium mode using desiccators and an analytical balance. Prior to adsorption, bentonite samples, crushed to < 0.1 mm were heated at 110 °C for 48 h. Under these conditions, the bentonite was completely dehydrated (the measured interlayer space of the montmorillonite equated 9.8 Å) without reaching dehydroxylation. Afterwards, 1 – 2 g of the dried bentonite were placed in crucibles in desiccators at ~ 21 °C and 10^{-3} mmHg vacuum in a water vapour atmosphere controlled by means of saturated saline solutions of different chemical compounds (CRC Handbook 1994). During adsorption, the desiccators were placed in a room in which the temperature was ~ 21 ± 1 °C. Once the equilibrium was reached (after ~ 2 months), the samples were weighed (± 0.0001 g) to determine the quantities of adsorbed water (mg H_2O/g of dry clay).

4.5.8 Soluble salts by aqueous leaching

The soluble salts have been analysed in aqueous extract solutions. The subsamples were air-dried and crushed, and placed in contact with deionised and degassed water at 1:4 solid to liquid ratio, shaken end-over-end and allowed to react for one day under anoxic conditions inside an anoxic glove box with oxygen content below 1 ppm. After phase separation by centrifugation (30 minutes at 15'500 rpm), the supernatant solutions were filtered through a 0.45 μm pore-size syringe filter (inside the anoxic glove box) and analysed. The chemical analysis of the water samples was performed with the methods described in Section 4.7.

4.6 Pore water chemistry

The pore water of the bentonite samples was obtained by squeezing at high pressures (Fernández et al. 2003, Fernández 2004, Fernández et al. 2014). Squeezing is analogous to the natural process of consolidation, caused by the deposition of material during geological time, but at a greatly accelerated rate. The squeezing process involves the expulsion of interstitial fluid from the saturated clayey material being compressed (Entwisle & Reeder 1993). In squeezing experiments, the volume of water extracted depends on the water content of the solid sample, the solid properties (e.g. dry density, the relative contents of easily-squeezed clays and of stiffer materials like quartz and calcite), and the experimental conditions, such as, the pressure applied, the squeezing duration and size of the squeezing cell (Fernández et al. 2003).

At CIEMAT the squeezing rig is similar to that developed by Peters et al. (1992) and Entwisle & Reeder (1993). The squeezer has been designed to allow a one-dimensional compression of the sample by means of an automatic hydraulic ram operating downwards, the squeezed water being expelled from the top and bottom of the cell into a vacuum vial (Fig. 28). The compaction chamber is made of type AISI 329 stainless steel (due to its high tensile strength and resistance to corrosion) with an internal diameter of 70 mm. Two compaction chambers were designed. One of them is 250 mm high with 20 mm wall thickness and allows pressures up to 100 MPa. The other one is 500 mm high with 45 mm wall thickness, allowing pressures up to 200 MPa.

The filtration system allows the extraction of interstitial water by drainage at the top and at the bottom of the sample. This system comprises a 0.5 μm stainless steel AISI 316L porous disk (Cr 17.36 %, Ni 11.4 %, Mo 2.15 %, Si 0.94 %, Mn 0.17 %, C 0.027 %, S 0.011 %, P 0.022 %, Fe

66.92 %) in contact with the sample. The liquid is collected through stainless steel tubes ($^{1}/_{16}$ inch) in a vacuum vial sealed by a septum. The whole system remains under ambient conditions (room temperature of about 22 – 25 °C). However, a sampling circuit was designed for collecting the water at anoxic conditions (Fig. 28). At the beginning of the test, the squeezing cell and all the sampling tubing and vials were closed to ambient conditions. Then, several cycles of Ar-flusing and vacuum installation were performed, preserving the system under anoxic conditions.

The bentonite samples for squeezing were prepared using a knife to remove the outer part in order to discard possible contaminated material. The sample was cut in a cylindrical shape, weighed and placed into the cell body (Fig. 29). A small stress of 1 to 5 MPa was initially applied to remove most of the atmospheric gas from the cell and allow the sample to bed in. After applying two additional Ar-flushing and vacuum cycles to the sampling circuit, the stress was progressively increased up to the selected pressure, rather than in a single step. This avoids over-consolidation or collapse of the clay-pore system. When the maximum of squeezed water was obtained for a given pressure, the vial was removed, keeping the sample away from any contact with the atmosphere. The water sample collected was weighed and immediately analysed. The bentonite mass was also weighed, and the final water content and dry density was determined. During the squeezing test, the evolution of the pressure, axial strain and changes in the length of the sample due to consolidation were recorded over time by using a data acquisition system. The chemical analysis of the water samples was performed with the methods described in Section 4.7.

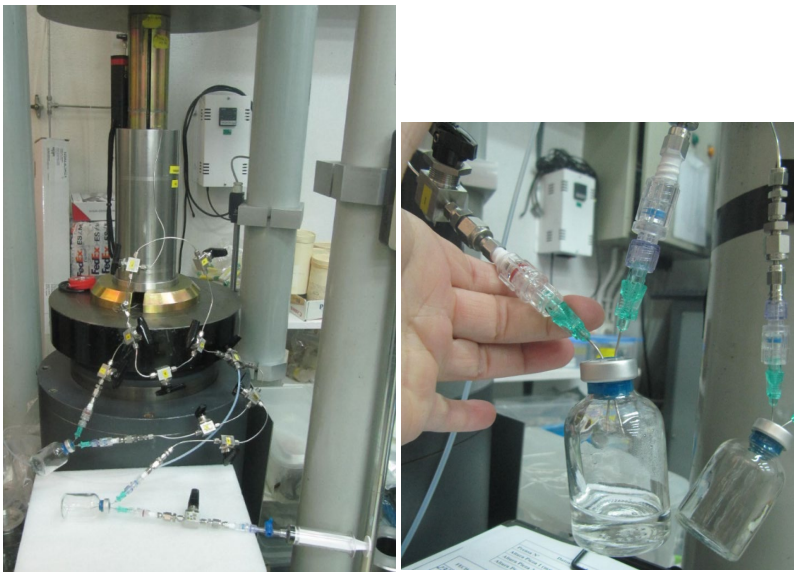

Fig. 28: Squeezed water extraction apparatus used at CIEMAT

Fig. 29: Detail of a bentonite sample (BB-59-3) before and after the squeezing test

4.7 Water chemical analyses

The water samples were filtered through 0.45 μm syringe filters, except those for pH and E.C measurements.

The *pH* was measured by means of an ORION 720A pH-meter equipped with a Metrohm 6.0224.100 combined pH micro-electrode. Merck pH buffer solutions of pH 4.00 and 7.00 were used for pH-meter calibration.

Electrical Conductivity measurements (EC) were performed by means of an ORION 115 conductimeter. The conductivity cell was checked/calibrated with a standard solution of 1413 μS/cm or 12.6 mS/cm (NaCl). The measurements were automatically adjusted to a temperature of 25 °C.

The *redox potential* (Eh) was measured by means of a combined platinum-ring electrode (Metrohm, ref. 6.0451.100) with a built-in Ag/AgCl reference electrode. The standardisation was carried out by using a redox buffer, $Fe(CN)_6^{4-}/Fe(CN)_6^{3-}$ (10^{-3} M), at +250 ± 5 mV vs the Ag-AgCl 3 M KCl electrode.

The total *alkalinity* of the water samples was determined with a specific Dynamic Equivalence point Titration (DET) method for analysing samples of 1 – 2 mL. The instrumentation consists of a Metrohm 888 Titroprocessor equipped with a 5 mL burette and a 6.0224.100 Metrohm combined pH micro-electrode.

The *major and trace cations as well as silica* were analysed by Inductively Coupled Plasma Optical Emission Spectrometry (ICP-OES) in a Varian 735ES spectrometer. Sodium and potassium were determined by atomic absorption spectrometry in an Agilent AA 240 FS spectrometer, and *ultratrace elements* were determined by ICP-MS (Finningan Mat SOLA).

A*nions* were analysed by ion chromatography (Dionex ICS-2000).

An ORION 901 microprocessor ion-analyser, equipped with ion selective electrodes, has been employed for F^- *and* I^- *determination.*

Fe(II)/Fe(III) ratio was determined by UV-Vis spectrophotometry with the ferrozine method after acidification of the samples to pH< 1 with HCl.

The NPOC (non-purgeable organic carbon) which refers to organic carbon present in a non-volatile form was analysed with a TOC-V_{CSH} analyser (SHIMADZU, Shimadzu Scientific Instruments, Kyoto, Japan). Samples were acidified with HCl 2M acid and sparged with synthetic compressed air (99.999 % purity) to remove inorganic carbon. The samples were then injected into a heated reaction chamber at 720 °C packed with a platinum catalyst. The CO_2 formed was transported to the detector in a carrier gas stream and measured directly by a non-dispersive infra-red (NDIR) gas analysis system. The amount of CO_2 is directly proportional to the TOC content in the sample.

5 Results

In this section the results obtained from the bentonite samples collected after the dismantling of Heater #2 in 2015 are described and compared with THG results obtained from samples collected during the dismantling of Heater #1 in 2002. It should be taken into account that the methodologies for obtaining some data have been improved since 2002 and, therefore, some comparisons cannot be made.

For example, it should be taken into account that in the 2015 dismantling of Heater #2, the samples were air-dried prior to any THC analysis; the mean water content value of all samples analysed was 14.8 ± 1.6 %. In the analysis of the samples taken during the dismantling of Heater #1 in 2002, the samples were analysed at the sampled saturation, i.e., without any previous drying (air-drying or oven-drying). The differences in value determination after the 2002 and 2015 dismantling are described in the corresponding section. Reference values for the FEBEX bentonite were also determined with the new procedures and are reported as such.

5.1 Visual aspects

The selected sections for THC analyses were: a) a section located at the contact with concrete (Section 36), b) two sections located at the heater contact (Section 49 and Section 53), and c) a section located at the end of the gallery, not affected by heat (Section 59). Visual aspects of the selected bentonite blocks from these sections are shown in Fig. 30 to 33. The photographs were taken by AITEMIN during the dismantling operation in 2015 after 18 years of experiment. The bentonite blocks and other samples analysed are also displayed.

At CIEMAT laboratories the bentonite blocks were visually examined and subsampled for different studies (mineralogy, CEC, pore water chemistry, etc.) as shown in Fig. 34 to 37 (see Section 4.1). The most altered bentonite blocks were found at Section 36, which showed signs of corrosion with material coloured red, green and black in some parts. This is clearly observed in block BB-36-1 in the part in contact with the granite, where cellulose filter papers were located impregnated with tracers. Furthermore, all the blocks from Section 36 in contact with the dummy showed signs of corrosion. Some black zones, possibly sulphide minerals, were found inside bentonite block BB-36-3 indicating the possible presence of SRB (Sulphate Reducing Bacteria). The blocks from Sections 47, 53 and 59 did not show signs of alteration. Only differences in water content values were observed, especially in blocks in contact with the heater, which were drier. Furthermore, a fine bentonite like a clayey gel was found around the gas pipe FP3 along the whole pipe (Fig. 38).

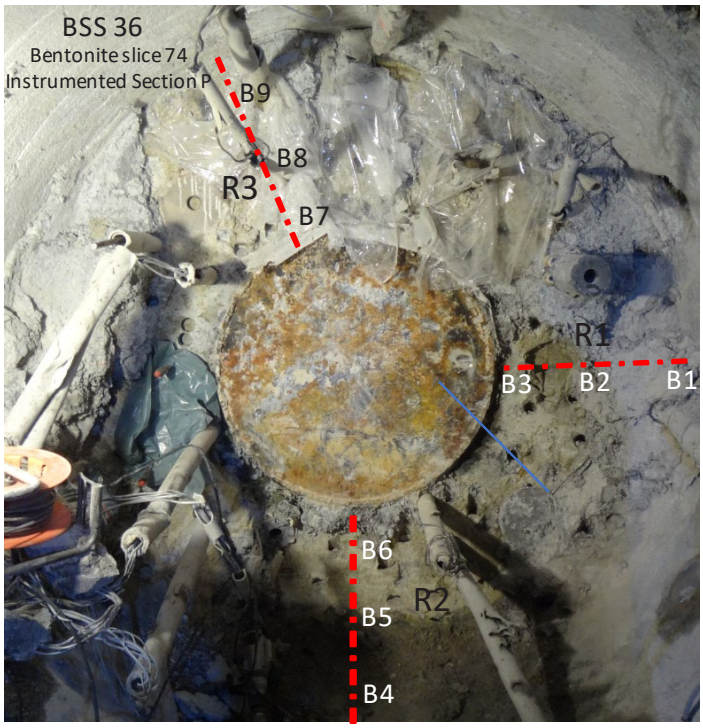

Fig. 30: Bentonite sampling Section 36: Block samples (BB-36-xx) for THC analyses

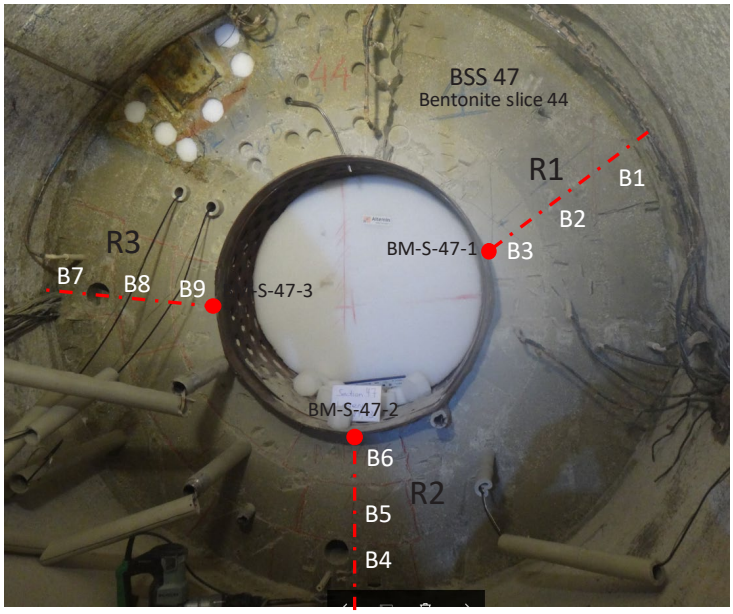

Fig. 31: Bentonite sampling Section 47: Block samples (BB-47-xx) and bentonite-liner samples (BM-S-47-x) for THC analyses

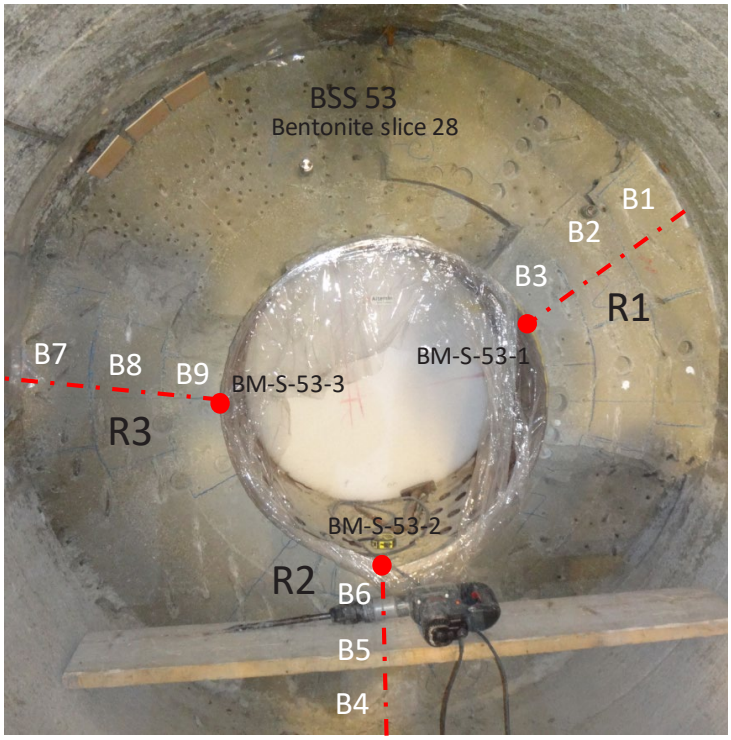

Fig. 32: Bentonite sampling Section 53: Block samples (BB-53-xx) and bentonite-liner samples (BM-S-53-x) for THC analyses

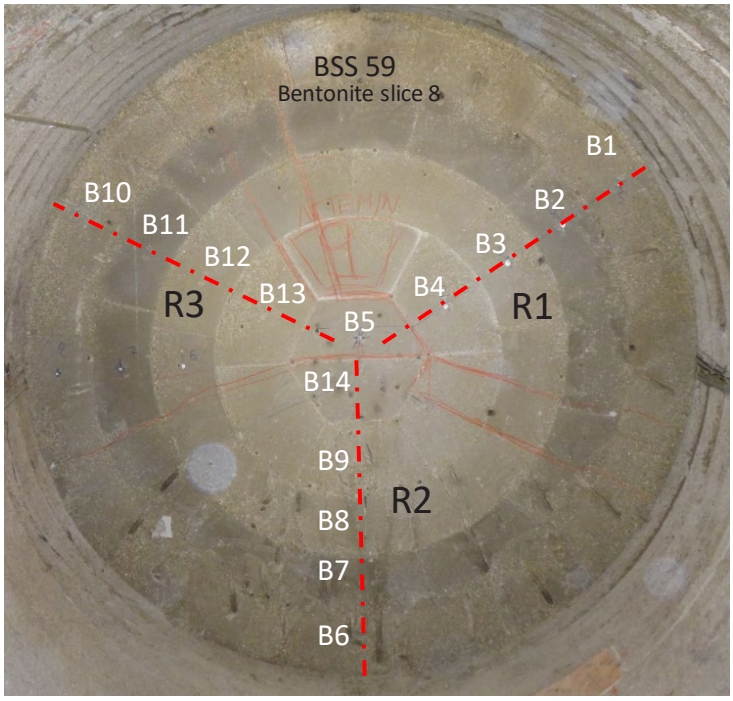

Fig. 33: Bentonite sampling Section 59: Block samples (BB-59-xx) for THC analyses

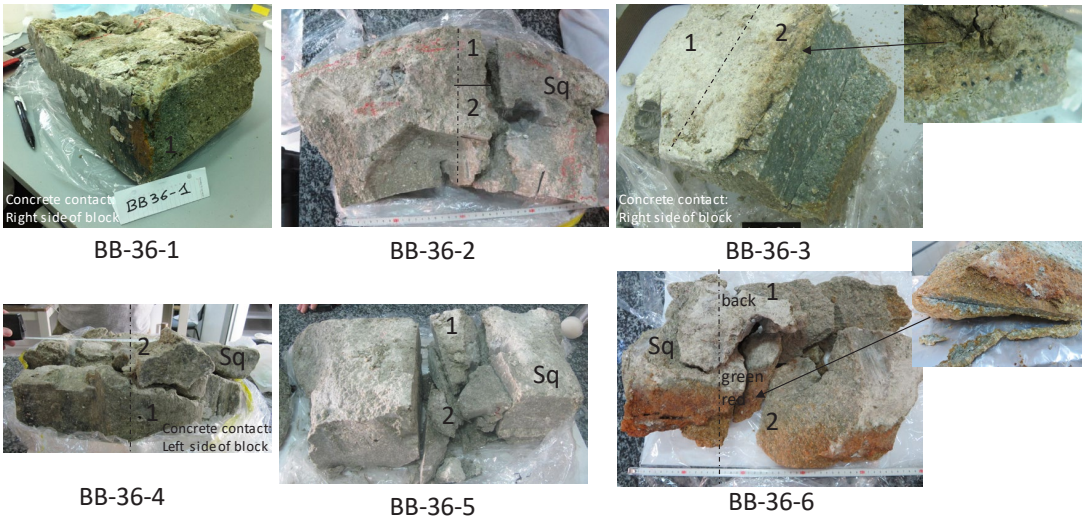

Fig. 34: Detail of the block samples from Section 36 for THC analyses (Sq: squeezing; 1 or S1: towards granite interface; 2 or S2: towards heater interface)

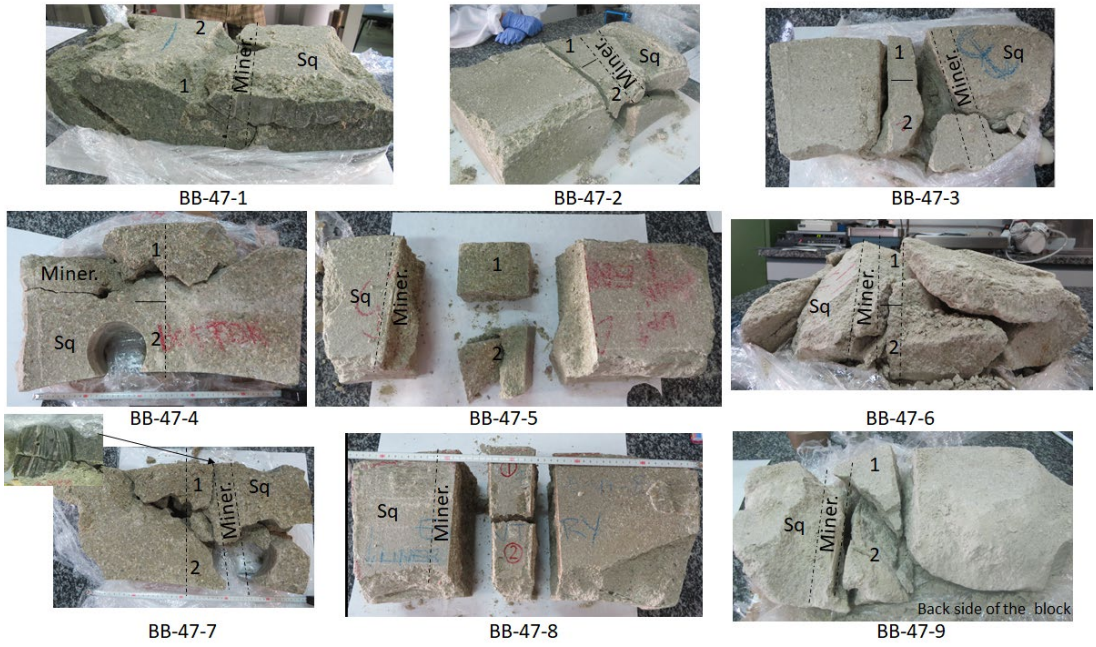

Fig. 35: Detail of the block samples from Section 47 (heated) for THC analyses. (Sq: squeezing; Miner: mineralogy; 1 or S1: granite interface; 2 or S2: towards heater interface)

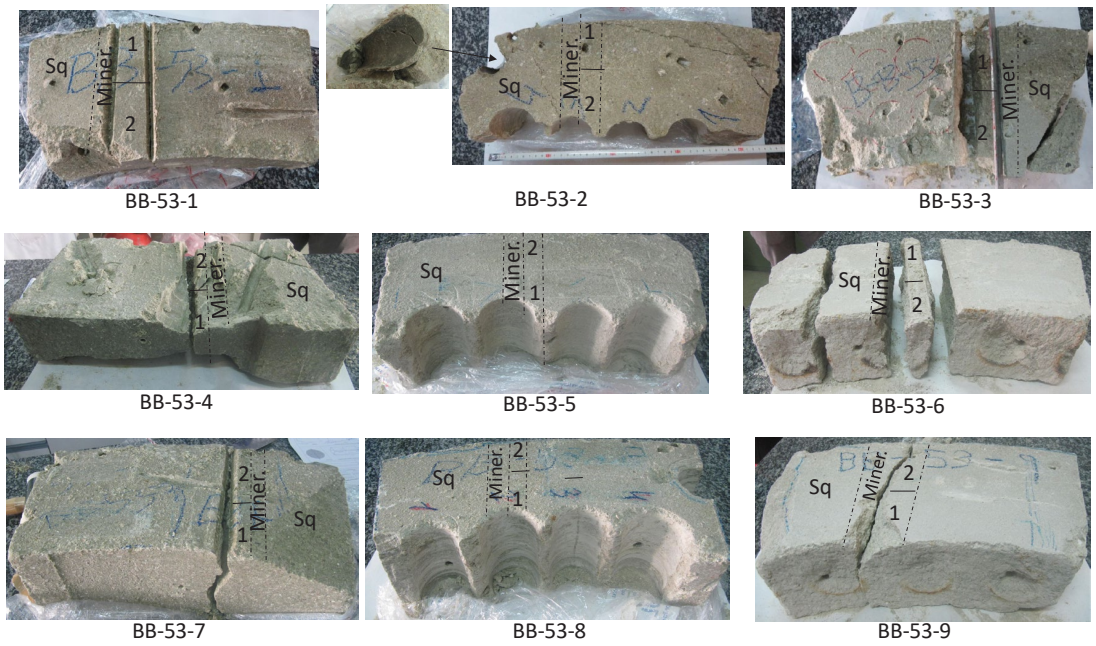

Fig. 36: Detail of the block samples from Section 53 (heated) for THC analyses. (Sq: squeezing; Miner: mineralogy; 1 or S1: granite interface; 2 or S2: towards heater interface)

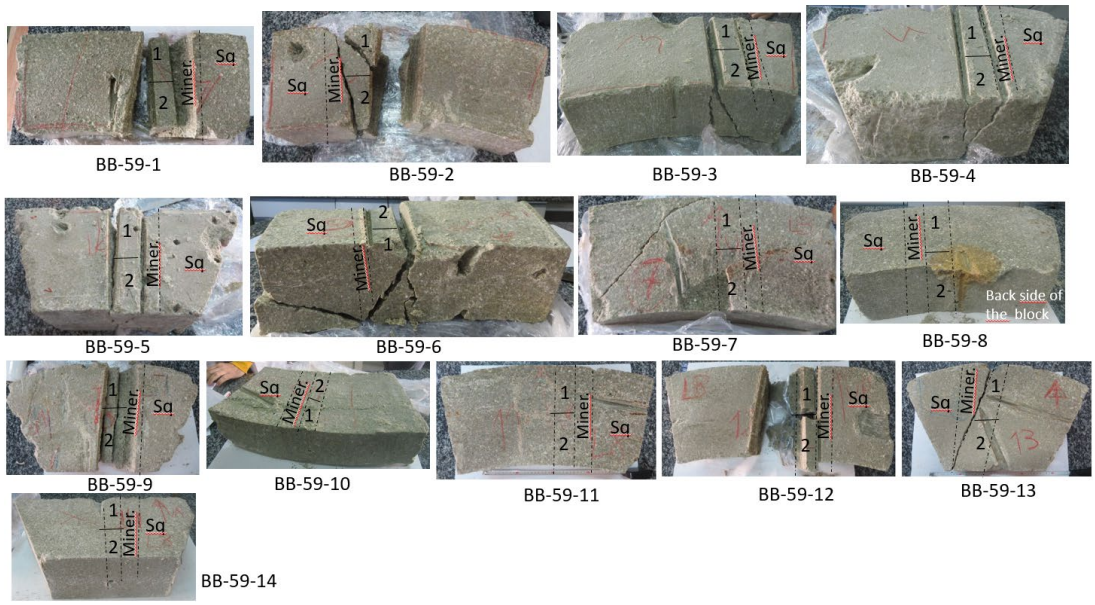

Fig. 37: Detail of the block samples from Section 59 (non-heated) for THC analyses. (Sq: squeezing; Miner: mineralogy; 1 or S1: granite interface; 2 or S2: towards heater interface)

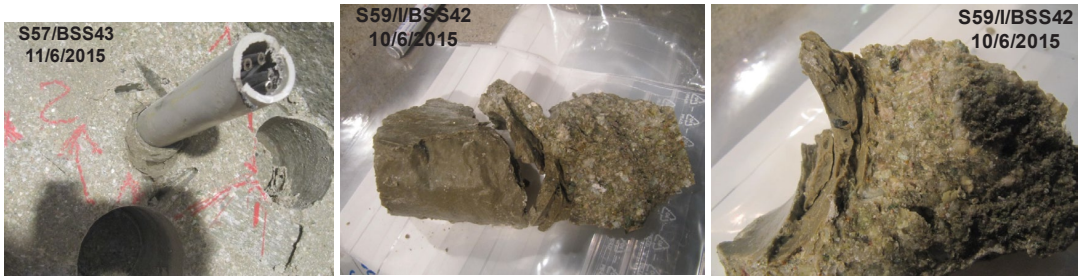

Fig. 38: Gel of smectite generated around the gas pipe FP3 (sample called Pipe 3), which was observed from bentonite Slice 70 (Section 37, Instrumented Section Q) to the end of the tube (Section 52)

The formation of this gel was not observed in the other pipes FP1 and FP2.

5.2 Water content and dry density

The water content and dry density values of the bentonite block samples analysed are shown in Fig. 39. In the non-heated sections, the water content and dry density values ranged from 32.3 to 26.4 % and from 1.43 to 1.56 g/cm^3, respectively; whereas in the heated sections the values ranged from 30.8 to 21.7 % and from 1.51 to 1.65 g/cm^3, respectively. Within of a radial axis from the bentonite barrier, the highest values in water content were observed in the block samples in contact with the granite, where the continuous groundwater flow towards the bentonite barrier was about 7 – 12 L/day (Huertas et al. 2006). The contrary occurs for the dry density values, the lower values being found at the granite contact. Profiles of water content and dry density decreasing and increasing, respectively, towards the inner part of the bentonite were observed, in those sections affected by the heating process as observed from the comparison of data from heated (Section 47 and Section 53) and non-heated (Section 36 and Section 59) sections (see more details in Villar et al. 2016, 2017).

Taking into account the initial water content and dry density of the bentonite blocks, 14 % and 1.70 g/cm^3 (or 1.60 g/cm^3 after emplacement) respectively; the bentonite was fully saturated in all zones of the barrier after 18 years of experiment (average value of 97 %); except in the blocks located close to the heater contact, where the saturation degree was around 85 % (Villar et al. 2016). This picture is quite different from the samples obtained after dismantling of Heater #1 (Fig. 40), where no differences in water content were noticed between the heated (Section 19 and 28) and non-heated sections (Section 12), except the non-heated Section 7 in contact with the concrete plug (Fig. 41, Fig. 42). In 1996 the concrete was pumped with a high water content (ENRESA 2000) modifying the initial conditions of the bentonite in Section 7, as seen in Fig. 41. Indeed, the inner bentonite block (BB-7-6), which contained a total pressure sensor, had a higher water content than the block located at the granite interface (BB-7-4). After dismantling Heater #1, the average degree of saturation in the whole barrier was of 83 % (ranging from 71 to 87 %), and close to 100 % (ranging from 89 to 97 %) in the block samples close to the granite contact (Huertas et al. 2006, Villar et al. 2006).

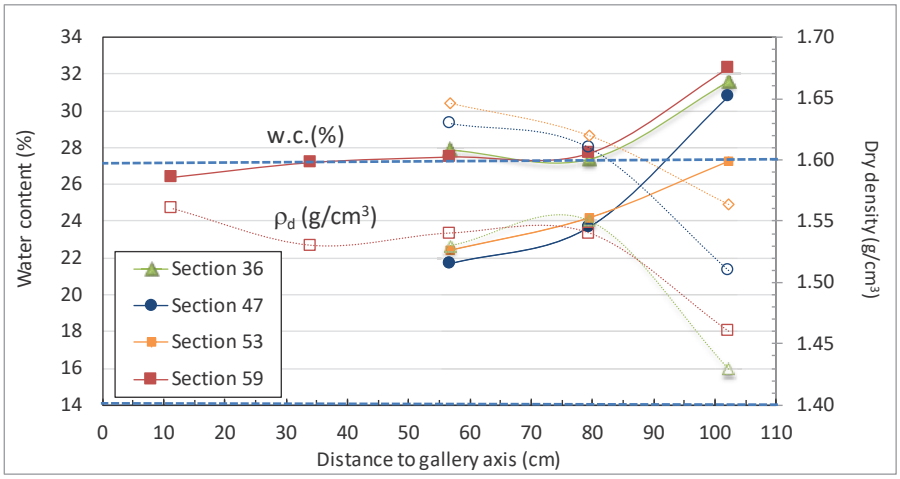

Fig. 39: Water content and dry density of the bentonite block samples from dismantling of Heater #2 analysed at different sections for THC studies. Initial data: 14.4 % w.c. and 1.60 g/cm^3 dry density (after emplacement)

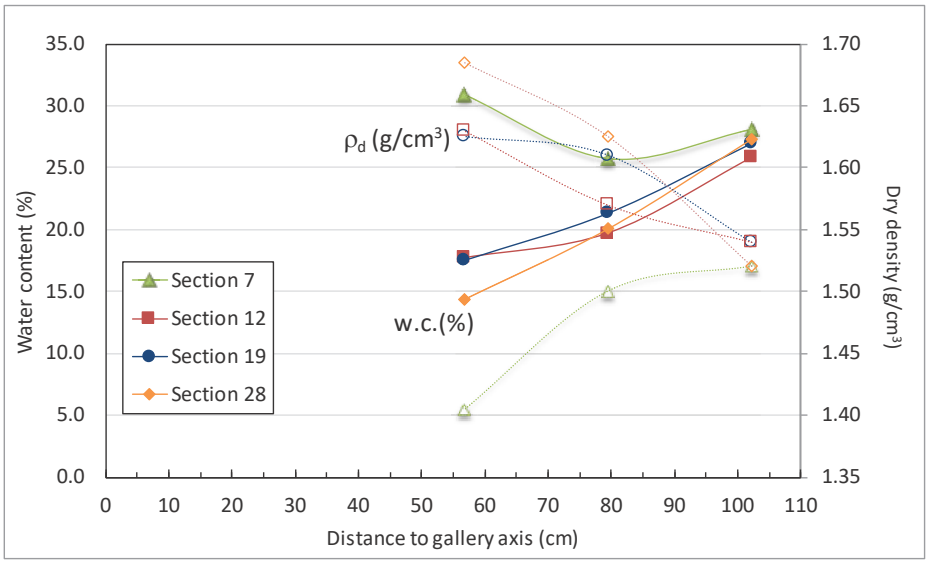

Fig. 40: Water content and dry density of the bentonite block samples from dismantling of Heater #1 analysed at different sections for THC studies. Initial data: 14.4 % w.c. and 1.60 g/cm^3 dry density (after emplacement)

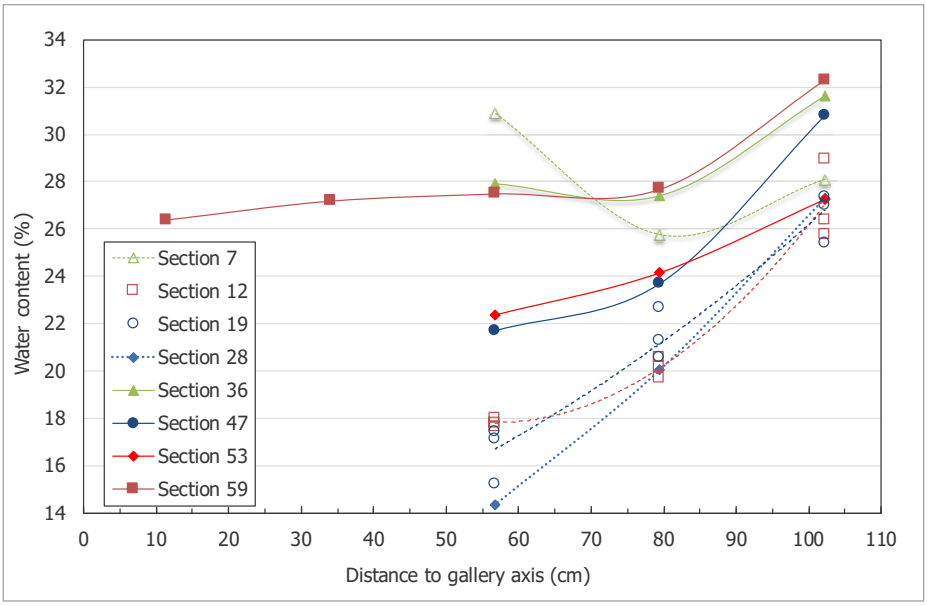

Fig. 41: Comparison of water content values from bentonite block samples obtained after dismantling of Heater #1 and Heater #2 analysed at different sections for THC studies. Initial data: 14.4 % w.c. and 1.60 g/cm^3 dry density (after emplacement)

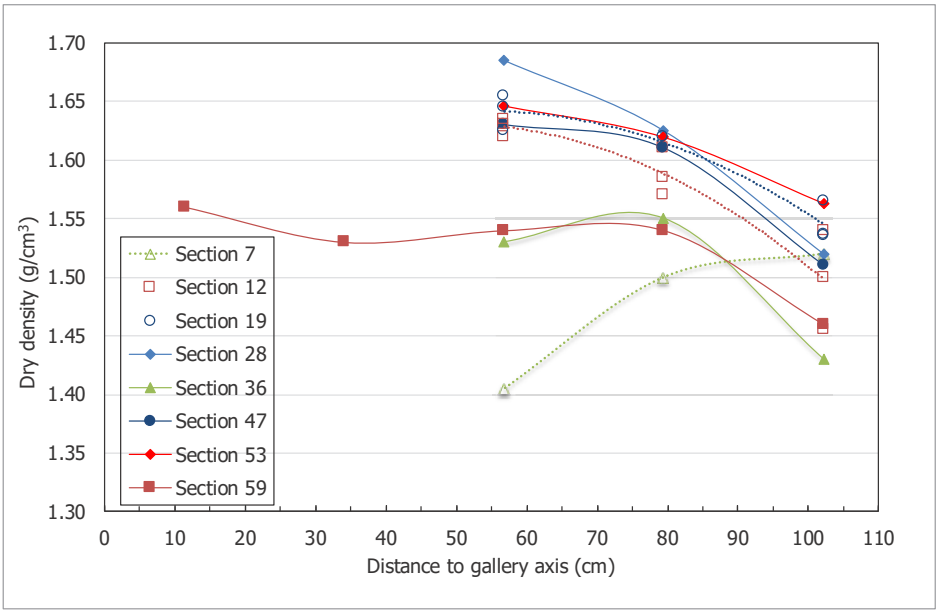

Fig. 42: Comparison of dry density values from bentonite block samples obtained after dismantling of Heater #1 and Heater #2 analysed at different sections for THC studies. Initial data: 14.4 % w.c. and 1.60 g/cm^3 dry density (after emplacement)

5.3 Mineralogical analyses

5.3.1 X-Ray diffraction

5.3.1.1 Total fraction from retrieved samples after dismantling of Heater #2

XRD analyses were carried out to identify and quantify the mineralogical composition on the bulk material. The X-Ray diffraction patterns of random powders of the bulk material from bentonite Sections 36, 47 and 59 are shown in Tab. 5, Fig. 43, Fig. 44 and Fig. 46.

No significant differences were found between the initial FEBEX bentonite and the treated samples from the FEBEX in-situ test. The treated bentonite samples contained smectite (87 – 95 %wt.) as the major mineral phase. The major non-phyllosilicates were quartz (1 – 5 wt.-%), cristobalite (Tz-3 wt.-%.), feldspars (1 – 5 wt.-%) and calcite (Tz-2 wt.-%). Dolomite was only detected by XRD in samples BB-53-4, BB-53-5 and BB-59-4. Iron sulphides were detected as traces in the sample BB-53-5 (SFe) and in BB-36-3 back (as pyrrhotite).

In the XRD-profiles the strongest (001) reflection of smectite is indicated. The peak located at 15.2 Å is indicative of a two-layer hydrate Ca-Mg montmorillonite. The position of the (060) reflections and their broadness in all treated samples were similar to the reference sample indicating no major changes in composition of the smectite clay mineral. Furthermore, no indication of newly formed trioctahedral mineral, appearing at 60 – 61° 2θ was found. Therefore, XRD data provided no evidence of any structural change in the montmorillonite.

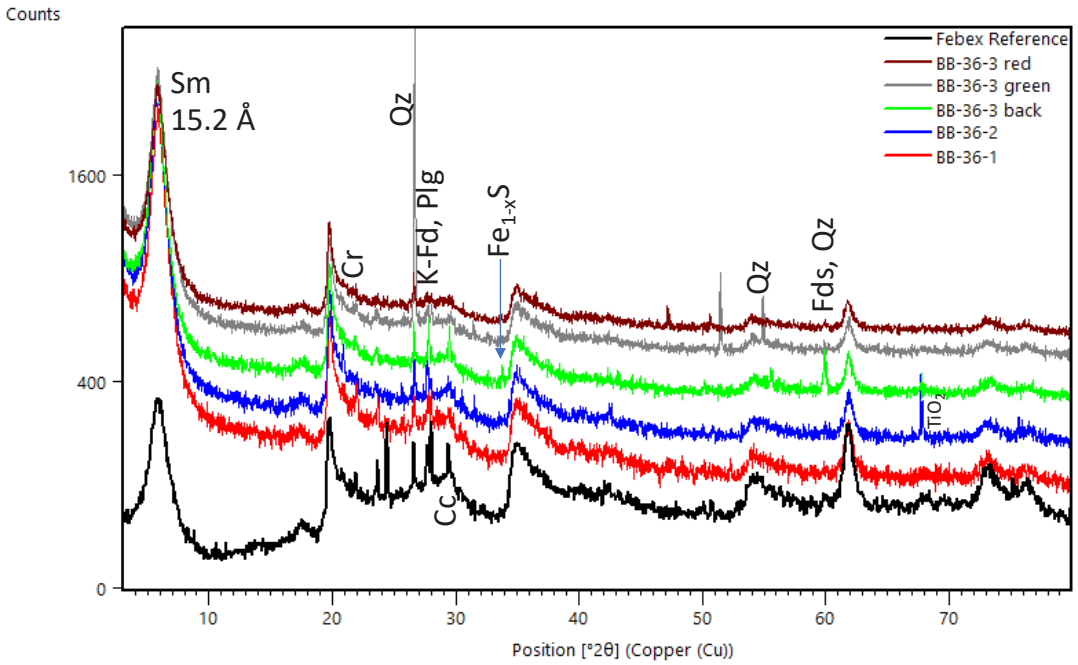

Fig. 43: XRD patterns of randomly oriented bulk bentonite samples from Section 36 (for location of the samples see Fig. 30 and Fig. 34)

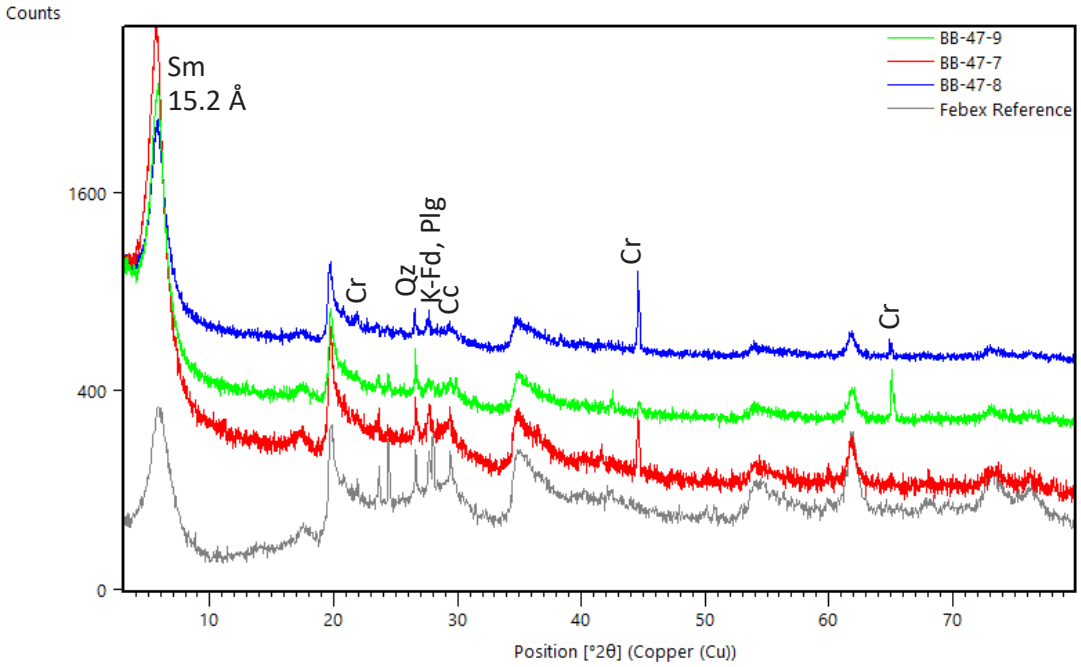

Fig. 44: XRD patterns of randomly oriented bulk bentonite samples from Section 47 (for location of the samples see Fig. 31)

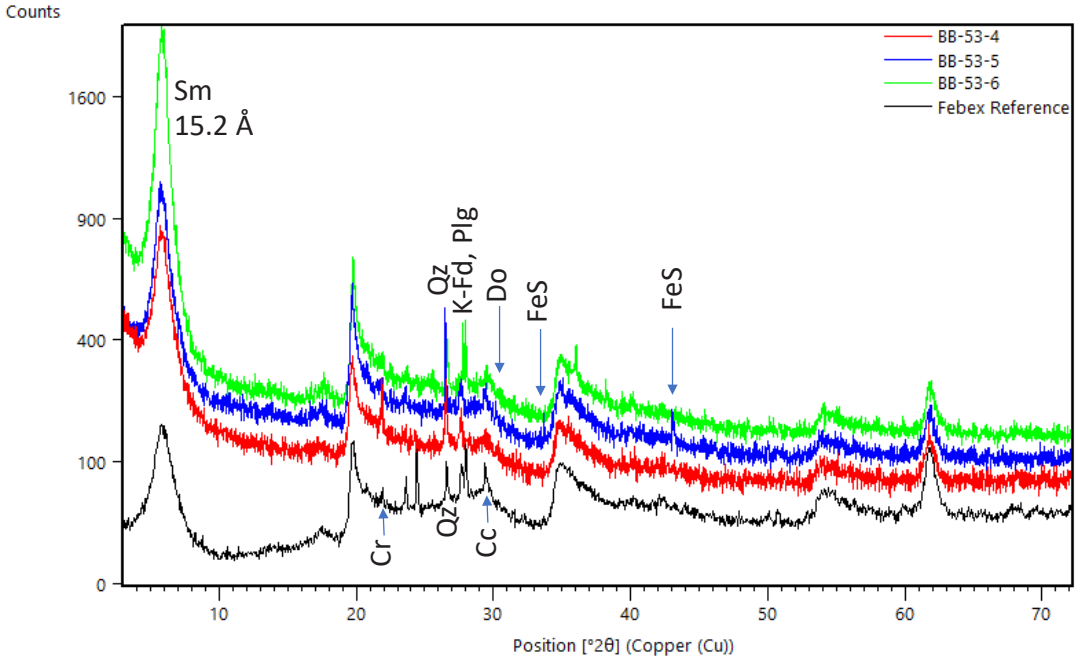

Fig. 45: XRD patterns of randomly oriented bulk bentonite samples from Section 53 (for location of the samples see Fig. 32)

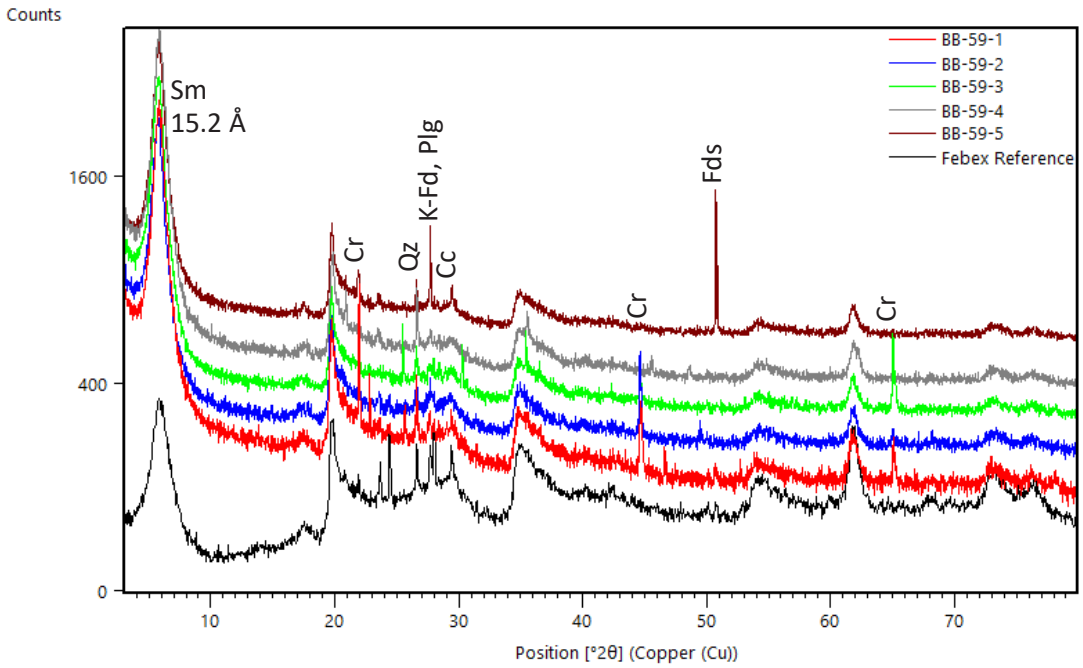

Fig. 46: XRD patterns of randomly oriented bulk bentonite samples from Section 59 (for location of the samples see Fig. 33)

Tab. 5: Mineral content (in weight %) of the bentonites samples obtained from XRD

Samples	Total phyllosilicates	Quartz	Cristobalite	K-Feldspar	Plagioclase	Calcite	Dol.	SFe_{1-x}
FEBEX reference	91	2	Tz	2	2	2	--	--
BB-36-1	93	1	1	2	1	2	--	--
BB-36-2	90	3	3	2	1	1	--	--
BB-36-3 back	94	1	3	1	--	1	--	Tz(*)
BB-36-3 green	87	5	3	3	1	1	--	--
BB-36-3 red	96	1	1	1	Tz	1	--	--
BB-47-7	90	2	3	2	1	2	--	--
BB-47-8	94	2	2	1	Tz	1	--	--
BB-47-9	90	3	2	2	1	2	--	--
BB-53-4	93	1	3	1	1	1	Tz	--
BB-53-5	93	1	2	1	1	1	Tz	Tz
BB-53-6	94	1	2	2	1	Tz	--	--
BB-59-1	91	1	2	4	1	1	--	--
BB-59-2	94	2	1	3	Tz	Tz	--	--
BB-59-3	93	1	1	3	1	1	--	--
BB-59-4	91	1	1	1	1	1	Tz	--
BB-59-5	95	1	1	2	1	Tz	--	--

* Pyrrhotite

5.3.1.2 Oriented clay mineral aggregates from retrieved samples after dismantling of Heater #2

Oriented clay mineral aggregates were prepared from the < 2 µm fraction. The expansion behaviour was tested by solvating the clay with ethylene glycol (EG). Illite/smectite mixed-layers (I/S MLs) were identified according to the method of Moore & Reynols (1989) on these EG patterns. The XRD patterns of the oriented mounts for the different treatments (AO, EG and 550 °C) are shown in Fig. 47, Fig. 48 and Fig. 49.

No significant differences were found between the reference FEBEX bentonite and samples collected after dismantling (Fig. 49). The smectite phases were made up of a R0 illite/smectite mixed layer with about 5 – 23 % of illite layers (Tab. 6). The main basal spacing (001) at around 14.6 Å in the AO XRD patterns for all samples indicated no changes in the Ca-Mg character of the smectite particles, and the (001) reflexion at around 17.0 Å in the EG XRD patterns for all samples indicated complete expansion of the interlayer sites. The crystal thickness of the smectite clay minerals was determined by the Williamson-Hall method (Williamson & Hall 1953), which ranged between 76.5 and 103.1 Å (Tab. 6), the number of TOT layers in the quasicrystals being of 5 – 6 (Tab. 6). This agrees with previous analyses of the reference FEBEX bentonite (Fernández et al. 2004, Huertas et al. 2006). The XRD data from the clay fraction provided no evidence of a structural change of the montmorillonite. Both the expansion behaviour (c-axis, d(001) value, the periodic diffraction pattern of the basal reflections, and the a and b cell dimensions of the clay minerals in the treated samples are typical of dioctahedral montmorillonites and are similar to the reference material.

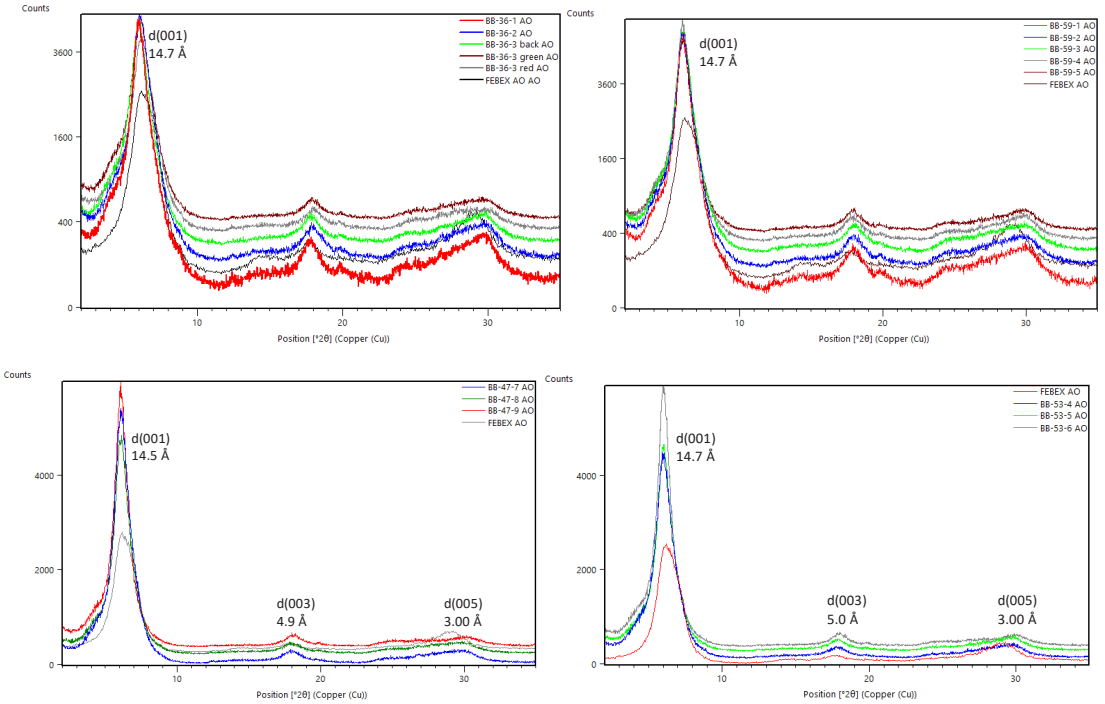

Fig. 47: XRD patterns of normal oriented aggregate samples from non-heated sections: Section 36 and Section 59 (square root y-scale); and heated sections: Section 47 and Section 53 (normal y-scale)

For location of the samples see Fig. 30, Fig. 31, Fig. 32, and Fig. 33.

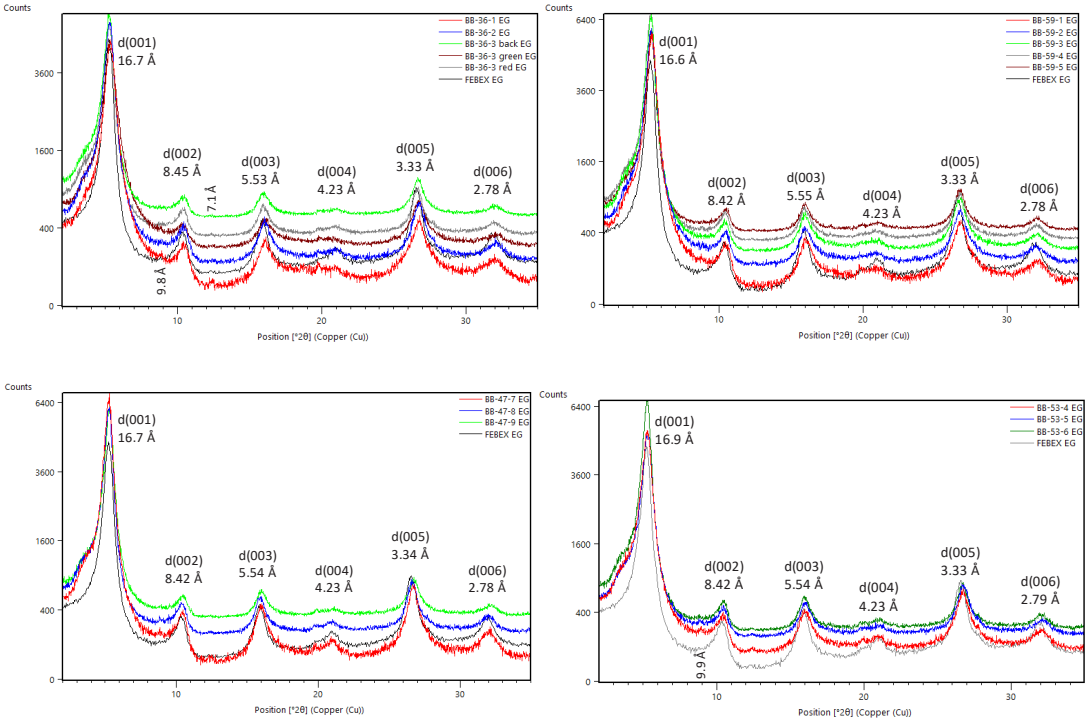

Fig. 48: XRD patterns of oriented aggregate samples after ethylene glycol treatment from non-heated sections: S36 and S59; and heated sections: S47 and S53 (square root y-scale)

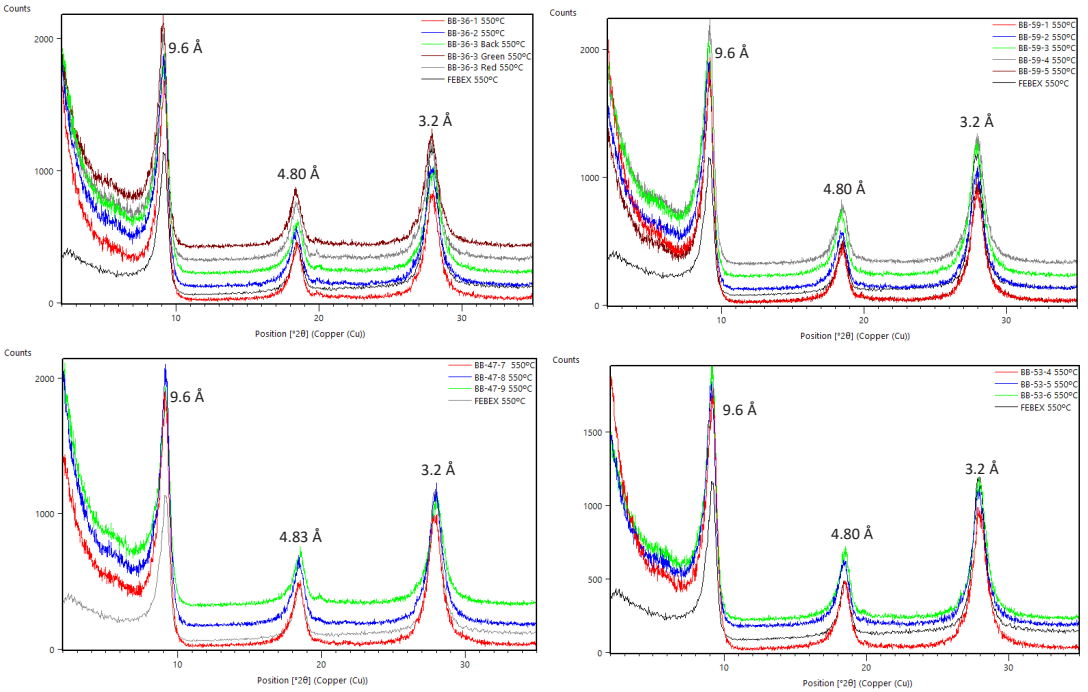

Fig. 49: XRD patterns of oriented aggregate samples after heating treatment at 550 °C from non-heated sections: S36 and S59; and heated sections: S47 and S53

Tab. 6: Characteristics of the smectite clay minerals

Samples	wt.-% total phyllosilicates in total fraction	R0 I/S interstratified	% illite layers	Crystallite thickness (Å)	N° of TOT layers per quasicrystal	Unit cell parameters*		
						a (Å)	**b** (Å)	**c** (Å)
FEBEX initial	92 ± 4	100	8	98.7	6	5.157	9.006	15.557
BB-36-1	93	100	13	94.0	6	5.182	9.000	15.229
BB-36-2	90	100	9	85.9	5	5.167	9.000	15.464
BB-36-3 back	94	100	6	103.1	6	5.190	9.007	15.350
BB-36-3 green	87	100	17	99.9	6	5.187	9.005	15.249
BB-36-3 red	96	100	9	80.2	5	5.190	9.016	15.310
BB-47-7	90	100	13	80.8	5	5.165	9.006	15.068
BB-47-8	94	100	5	84.1	5	5.182	9.007	15.634
BB-47-9	90	100	5	95.4	6	5.152	8.991	15.371
BB-53-4	93	100	9	77.4	5	5.188	9.005	14.595
BB-53-5	93	100	9	90.8	5	5.188	9.015	15.272
BB-53-6	94	100	6	82.0	5	5.198	9.012	15.006
BB-59-1	91	100	10	81.2	5	5.188	9.009	15.327
BB-59-2	94	100	13	84.5	5	5.158	9.001	15.561
BB-59-3	93	100	23	88.6	5	5.160	9.010	15.629
BB-59-4	91	100	9	76.5	5	5.167	9.003	15.342
BB-59-5	95	100	8	88.1	5	5.162	9.024	14.996

* Theoretical: a = 5.196 Å and b = 9.0 Å

5.3.1.3 X-Ray diffraction from retrieved samples after dismantling of Heater #1

XRD analyses were carried out to identify the mineralogical composition on the bulk and < 2 μm fraction of samples obtained after dismantling Heater #1. The X-Ray diffraction patterns of random powders of the bulk material from bentonite Sections S7, S12 and S19 are shown in Fig. 50, Fig. 51 and Fig. 52. In all these figures, the XRD patterns of the untreated or reference FEBEX bentonite is shown for comparison. No significant differences were found between the treated samples and the untreated ones: the predominant mineral was a smectite with (001) basal reflection at around 15 Å (which indicates a predominance of two-layer hydrate Ca-Mg cations at exchange sites).

X-Ray diffraction patterns from the bulk material also indicated the presence of minor quantities of quartz, plagioclase, K-feldspars, calcite, dolomite and cristobalite. Dolomite was detected in most of the retrieved samples. Illite/muscovite, as a separated phase, was found in samples from Section 7 (BB7-4, BB7-5) and Section 12 (BB12-11, BB12-12), although illite was not detected when analysing the < 2 μm fraction. Other types of accessory minerals were found in the bentonite samples at contact with the concrete plug where an increase of calcite was detected as well as the presence of gypsum, aragonite, magnesite and portlandite (Fig. 52). The position of the (060) reflexions and their broadness in all treated samples were similar to the reference sample, indicating no major changes in composition of the smectite clay mineral. Furthermore, no indication of a newly formed trioctahedral mineral, that should appear at 60 – 61° 2θ was found. Therefore, XRD data provided no evidence of any structural change in the montmorillonite. This

was confirmed by analysing the X-Ray diffraction patterns of oriented aggregates (Fig. 53), where only smectite was found as clay mineral.

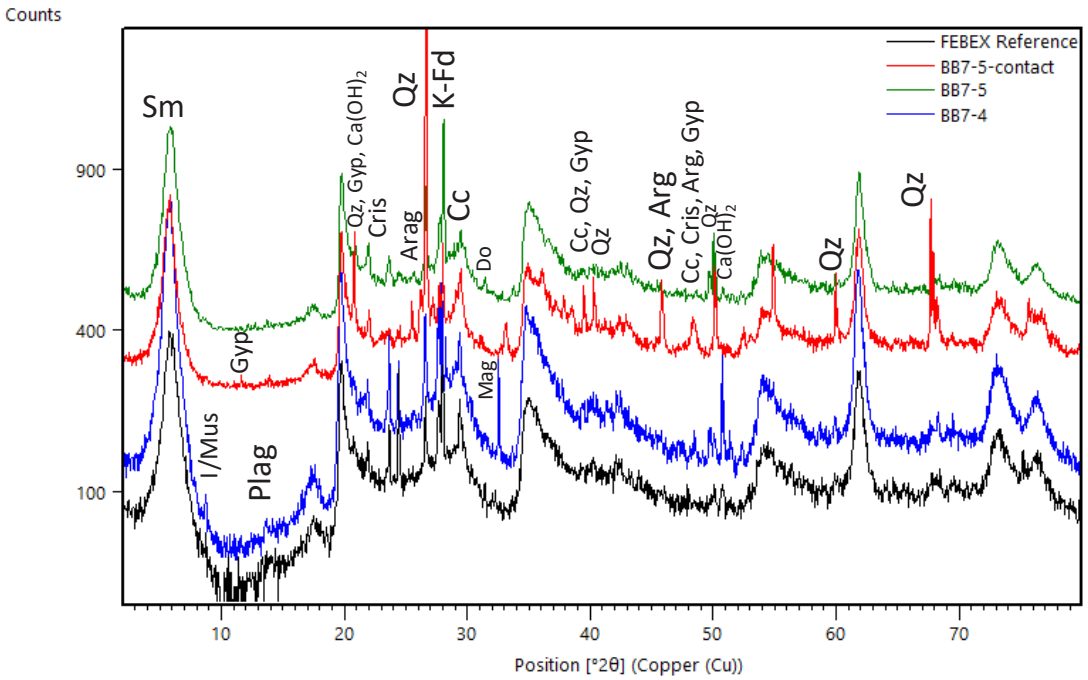

Fig. 50: XRD patterns of randomly oriented bulk bentonite samples from Section 7 (concrete contact) taken after dismantling Heater #1

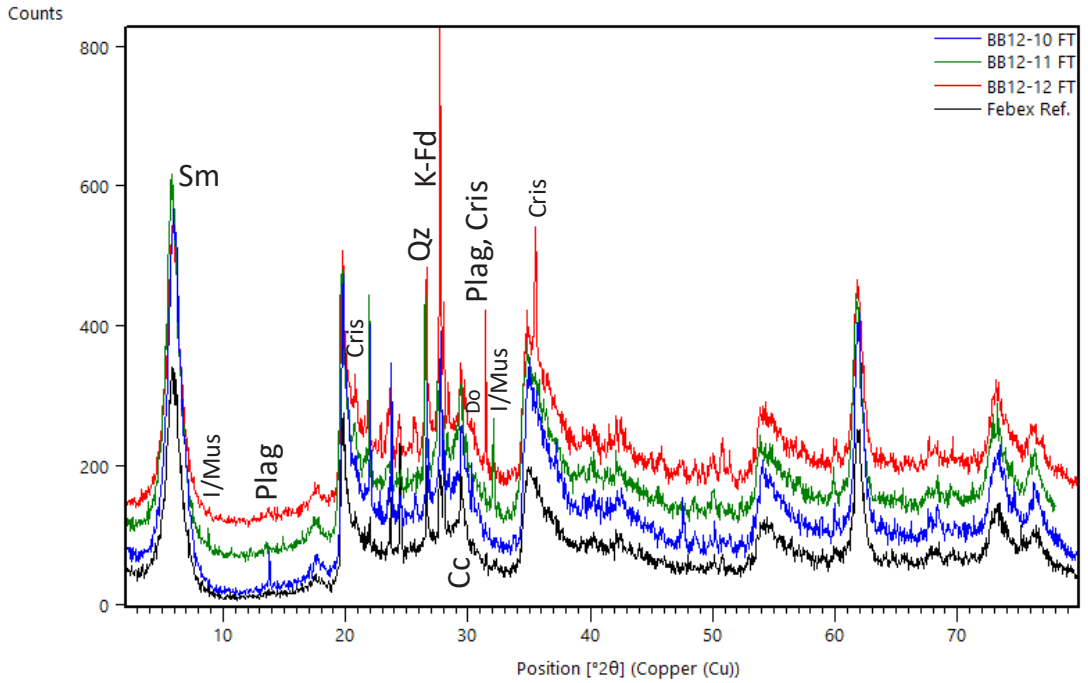

Fig. 51: XRD patterns of randomly oriented bulk bentonite samples from Section 12 (non-heated section) taken after dismantling Heater #1

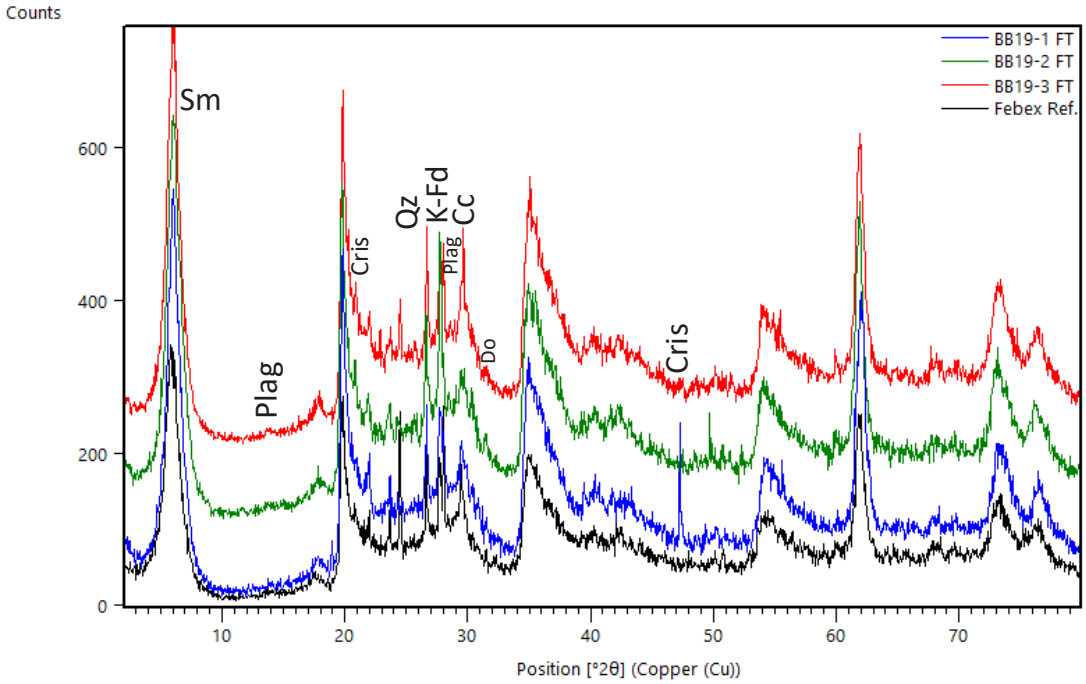

Fig. 52: XRD patterns of randomly oriented bulk bentonite samples from Section 19 (heated section) taken after dismantling Heater #1

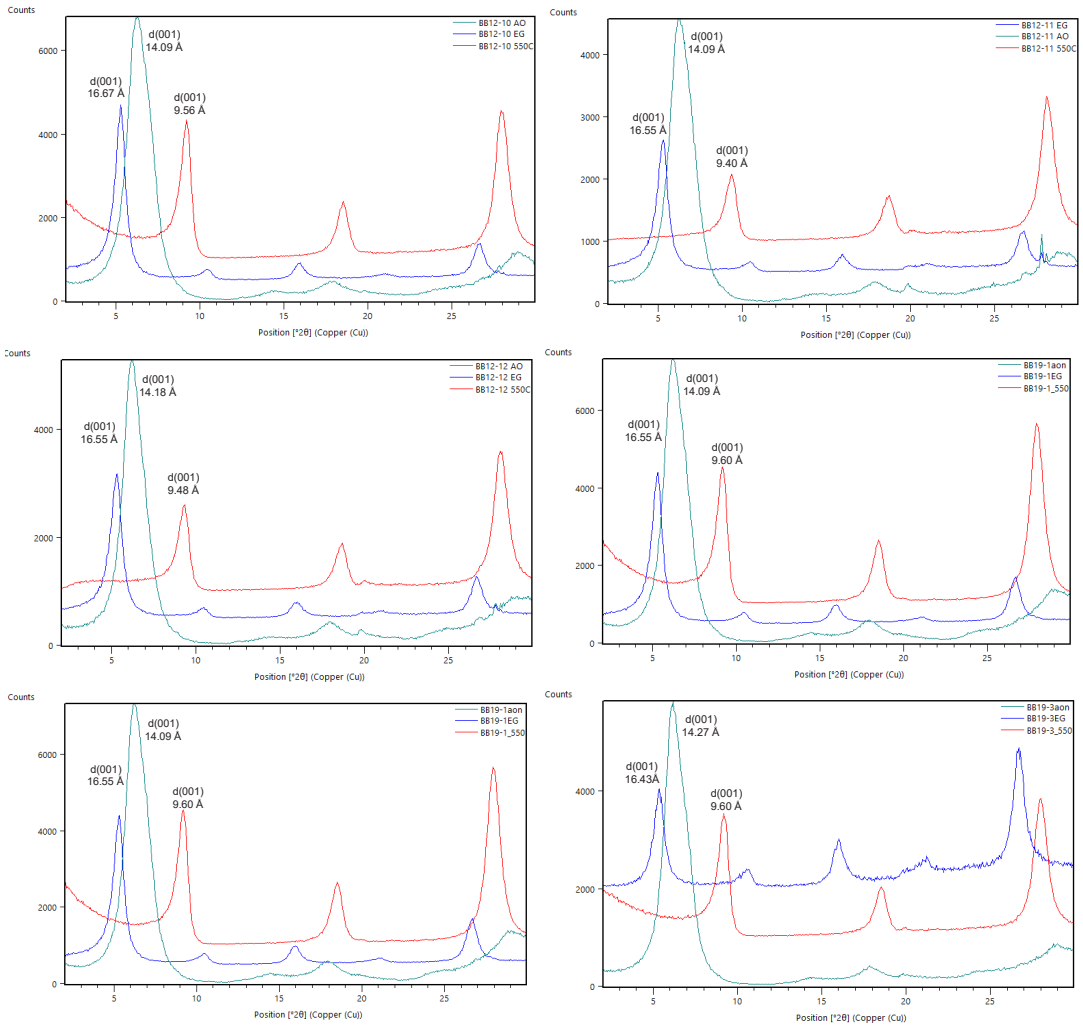

Fig. 53: XRD patterns of oriented aggregate samples (normal, after ethylene glycol treatment and after heating treatment at 550 °C) from Section S12 and Section S19

5.3.2 FTIR analyses

The bentonite samples were also analysed by FTIR for acquiring information on possible changes in the smectite structure, chemical composition and surface properties due to chemical modifications; as well as to investigate mineral neoformations.

The spectra from the bulk samples of different sections (Fig. 54 to Fig. 57) contain the main typical dioctahedral smectite bands, as well as quartz (Tab. 7). The spectra show a band at 3'627 cm^{-1} which corresponds to the typical OH stretching region of structural hydroxyl groups for dioctahedral smectites with Al-rich octahedral sheets. These are inner hydroxyl groups lying between the tetrahedral and octahedral sheets. The broad band near 3'426 cm^{-1} is due to stretching H-O-H vibrations of adsorbed water, while the band at 1'642 cm^{-1} corresponds to the OH deformation or bending adsorption of water. If the Si-O absorptions and OH bending bands in the 1'300 – 400 cm^{-1} range are examined, only one broad, complex Si-O stretching vibration band at around 1'030 cm^{-1} is seen, which is typical of a dioctahedral montmorillonite. The occupancy of

the octahedral sheet strongly influences the position of the OH bending bands, which arise from vibrations of the inner and surface OH groups. In these samples, the presence of a peak at 915 cm^{-1} (δAlAlOH) and at 840 cm^{-1} (δAlMgOH), indicates a partial substitution of octahedral Al by Mg, typical of dioctahedral smectites. The adsorption band at 622 cm^{-1} can be attributed to a R-O-Si vibration (R = Al, Fe, Mg) and indicates a perpendicular vibration of the octahedral cations and their connection to the tetrahedral sheet. The bands at 520 cm^{-1} and 466 cm^{-1} correspond to Si-O-Al vibration of aluminium in the tetrahedral sheet and Si-O-Si bending vibrations, respectively. The weak band at 798 cm^{-1} is caused by the Si-O stretching of quartz.

When the < 2 μm fraction is analysed (Fig. 58 to Fig. 61), similar bands as described above were observed. Therefore, no alteration in the smectite structure occurred during 18 years of experiment.

Although no alterations were observed in the bulk samples, some mineralogical changes were detected in some point samples visually observed and taken from the blocks with a sharp spatula (see Fig. 62 to Fig. 69). These alterations were found: a) in the BB-36-1 block from the concrete interface at the contact with granite, belonging to a corroded part (Fig. 34); b) in some samples from Section 47 (heated section): BB-47-7 block at the contact with the granite interface and BB-47-9 at the contact with the liner/heater, c) in some samples from Section 53 (heated section), and d) in all samples from the radius R1 of Section 59 (non-heated section).

The mineralogical alterations occurring in bentonite block BB-36-1 were related to a corrosion process, probably microbiologically induced. One surface of this block, at the contact with granite, was covered with a cellulose filter paper impregnated with a tracer. The studied sample corresponded to the black halo with red-greenish bentonite material. According to FTIR analyses, this sample contains aragonite, calcite, maghemite, smectite and some other clay mineral due to the new band close to 3'700 cm^{-1}, which may be related to Mg_3OH vibrations in trioctahedral smectites or to kaolinite (Fig. 62).

In the samples from Section 47, bentonite block BB-47-7 at contact with the granite shows bands belonging to calcite, and two new bands close to 3'700 cm^{-1} and to 582 cm^{-1}, probably related to $Mg_3(OH)$ vibrations and feldspars, respectively. In the black sample at contact with the heater/liner, bands corresponding to quartz and maghemite were found in the spectrum (Fig. 63).

In the samples from Section 53 (Fig. 64), calcite was found both precipitated in the zone at contact with the GRS pipes, as well as in a sample from bentonite block BB-53-5 (middle bentonite ring). Anhydrite and silica (cristobalite) were found at contact with the liner/heater (samples BB-53-6 and BB-53-9), as well as a band close to 3'700 cm^{-1}. This band at around 3'700 cm^{-1} may be attributed to Mg_3OH vibrations in dehydrated saponites containing interlayer Na or K (Farmer 1974), chlorite/smectite mixed-layers (Van del Marel & Beutelspacher 1976, Bergaya et al. 1985) or also to outer AlAlOH vibrations in kaolinite (Madejová 2003).

More interesting alterations were found in Section 59 (non-heated section), where bands from palygorskite (BB-59-1), kaolinite (BB-59-2), sepiolite and kaolinite (BB-59-3) were detected (Fig. 65 to Fig. 69). Furthermore, new bands at around 3'695 cm^{-1} and 3'560 cm^{-1}, corresponding to $Mg_3(OH)$ and $MgFe^{3+}OH$ vibrations, respectively, were found in block BB-59-4. Modifications in the shape of the AlAlOH-band seem to indicate also Illite/Smectite Mixed Layer (ML). Other minerals such as quartz, cristobalite, feldspars, calcite and dolomite were also detected in the samples.

Tab. 7: Positions and assignments of the vibrational bands of dioctahedral smectites

Wavenumber (cm^{-1})	**Assignment**[*]
3'800 – 3'500	OH stretching of inner structural hydroxyl groups (influenced by nature of the coordinated octahedral cations): • AlAlOH (dioctahedral): 3'623 cm^{-1} • Mg_3OH (trioctahedral): 3'680 cm^{-1} • FeFeOH: 3'567 cm^{-1}
3'426	OH stretching of adsorbed water
3'240	OH stretching of adsorbed water
3'150 – 3'170	Fe-oxyhydroxide
1'634	OH bending of adsorbed water
1'430 (872, 712)	ν_3^g-CO_3 asymmetric stretching of calcite (ν_2: out of plane bending, ν_4: planar bending): calcite
1'115	Si-O stretching vibration (out-of-plane)
1'030 – 1'020	Si-O stretching vibration (in-plane): • Dioctahedral: 1'030 cm^{-1} • Trioctahedral: 1'020 cm^{-1}
915	AlAlOH bending
885	AlFeOH bending
850	AlMgOH bending
820	FeFeOH bending (nontronite: 817, 676 cm^{-1})
795	MgMgOH bending
765	FeMgOH bending
792 790/800 798 & 780 doublet 794	Si-O stretching of silica Amorphous silica (opal, volcanic glass, etc.) Quartz Cristobalite
655 – 660	Mg_3OH bending (saponite)
624	R-O-Si with R = Al, Mg, Fe
626 792, 624 790	Coupled Al-O and Si-O (out-of-plane) Si-O of cristobalite Si-O of tridymite
520	Si-O-Al bending (Al tetrahedral cation)
465	Si-O-Si bending vibration
426	Si-O bending vibration
825, 750	Illite
740, 790, 890, 1'150	Fe oxyhydroxide
Complex bands 400 – 900	Feldspars

(*) Madejová & Komadel (2001, 2005), Farmer (1974)

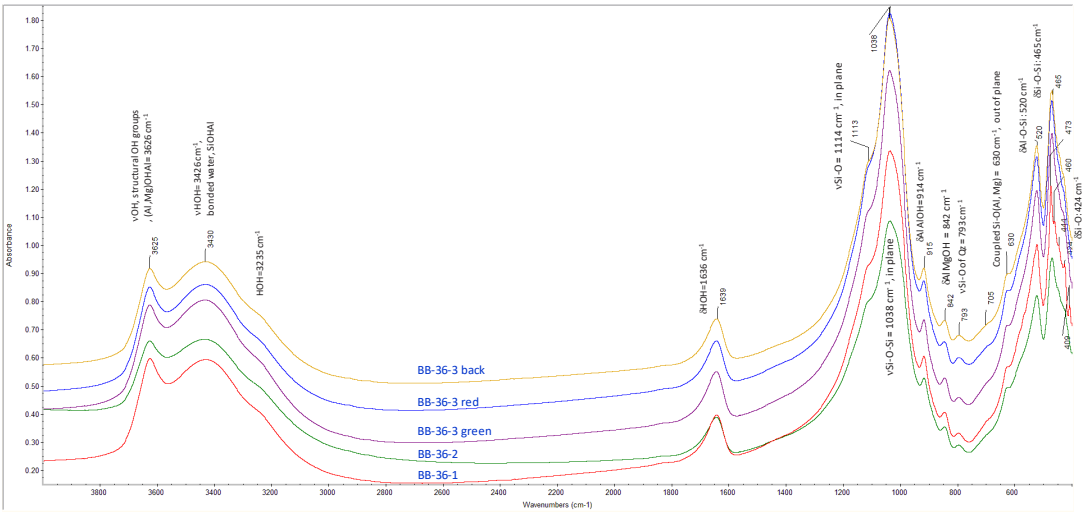

Fig. 54: FTIR spectra of bulk samples from Section 36 in contact with the shotcrete (non-heated during the second operational phase of the FEBEX Project)

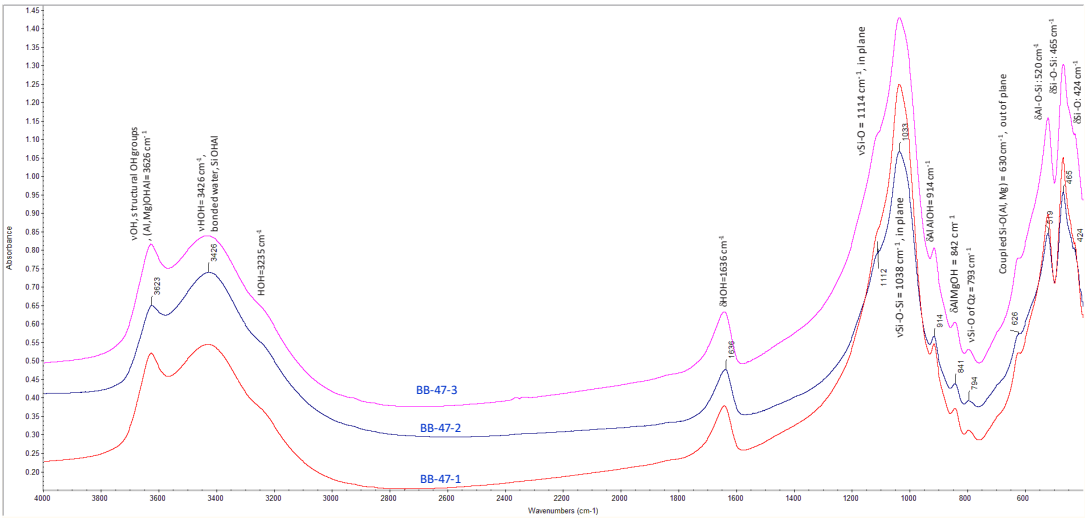

Fig. 55: FTIR spectra of bulk samples from heated Section 47.

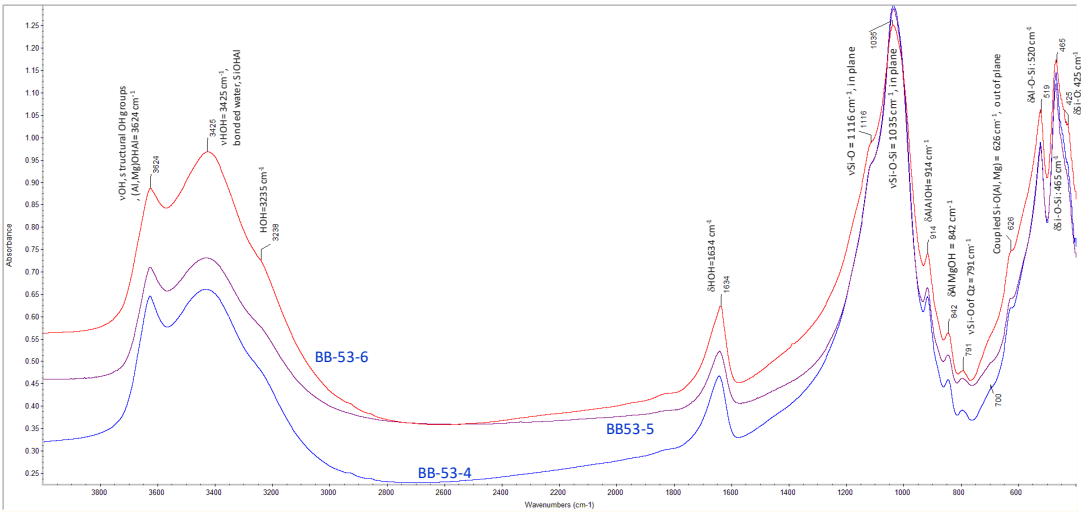

Fig. 56: FTIR spectra of bulk samples from heated Section 53

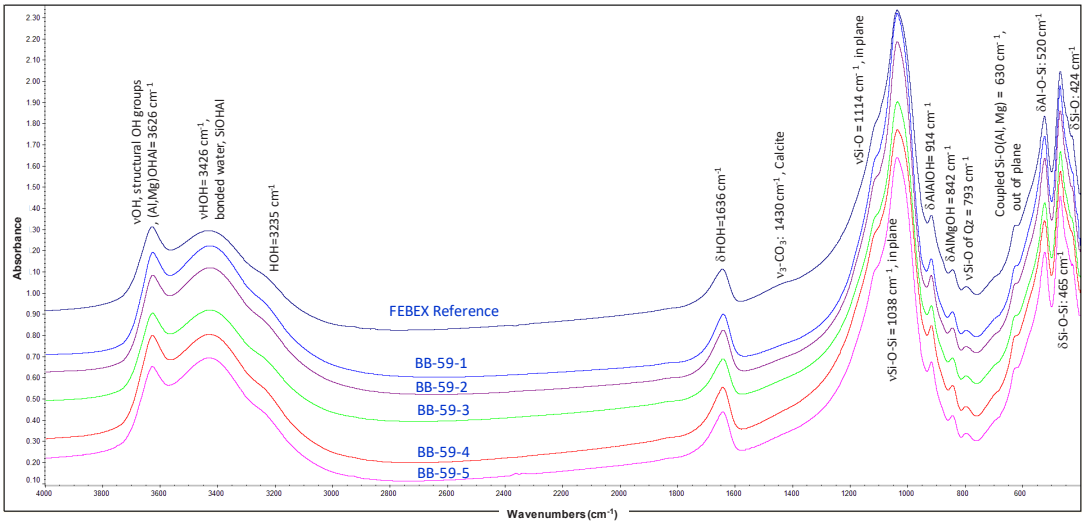

Fig. 57: FTIR spectra of bulk samples from non-heated Section 59

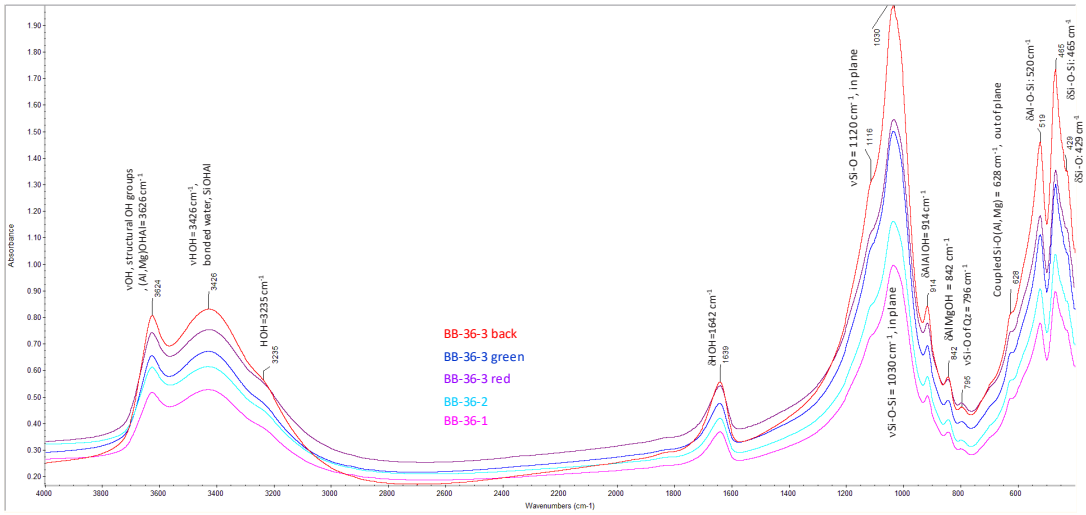

Fig. 58: FTIR spectra of < 2 µm fraction samples from Section 36 (shotcrete contact)

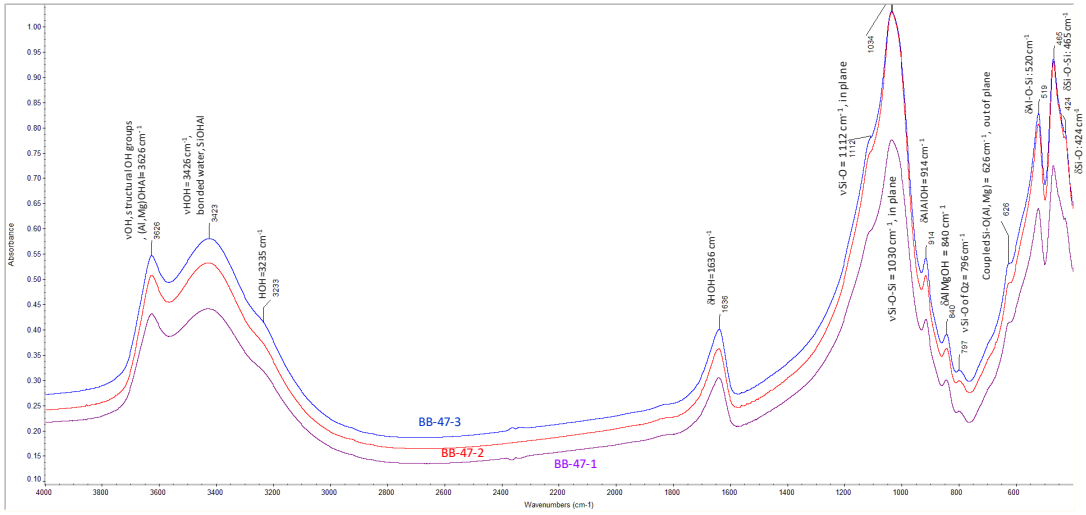

Fig. 59: FTIR spectra of < 2 µm fraction samples from heated Section 47

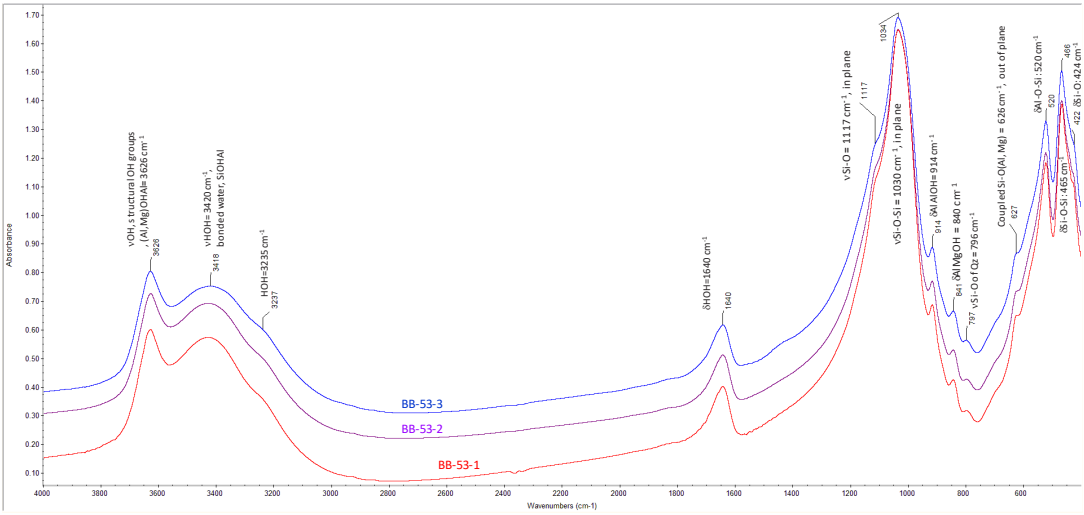

Fig. 60: FTIR spectra of < 2 µm fraction samples from heated Section 53

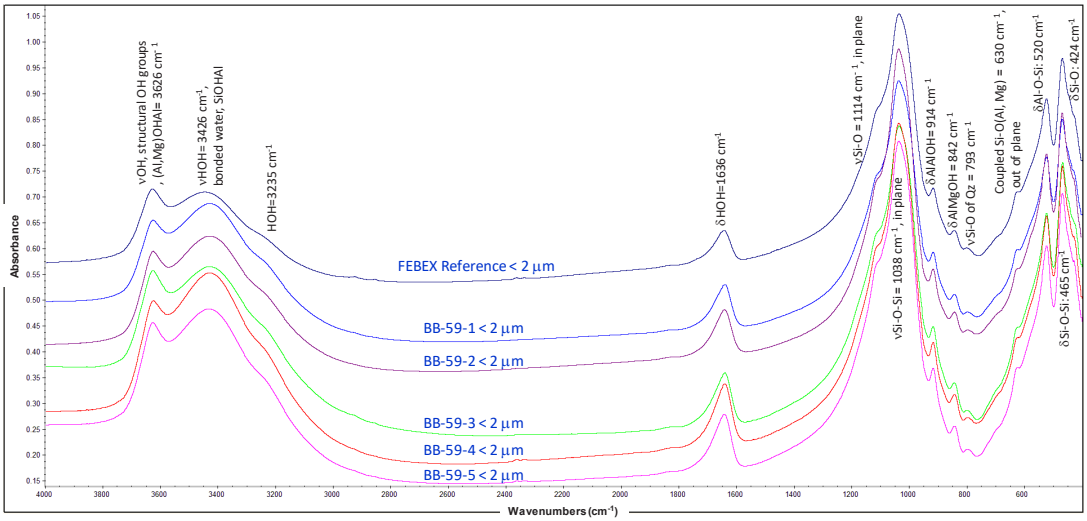

Fig. 61: FTIR spectra of < 2 µm fraction samples from non-heated Section 59 (BB-59-1, BB-59-2, BB-59-3, BB-59-4 and BB-59-5)

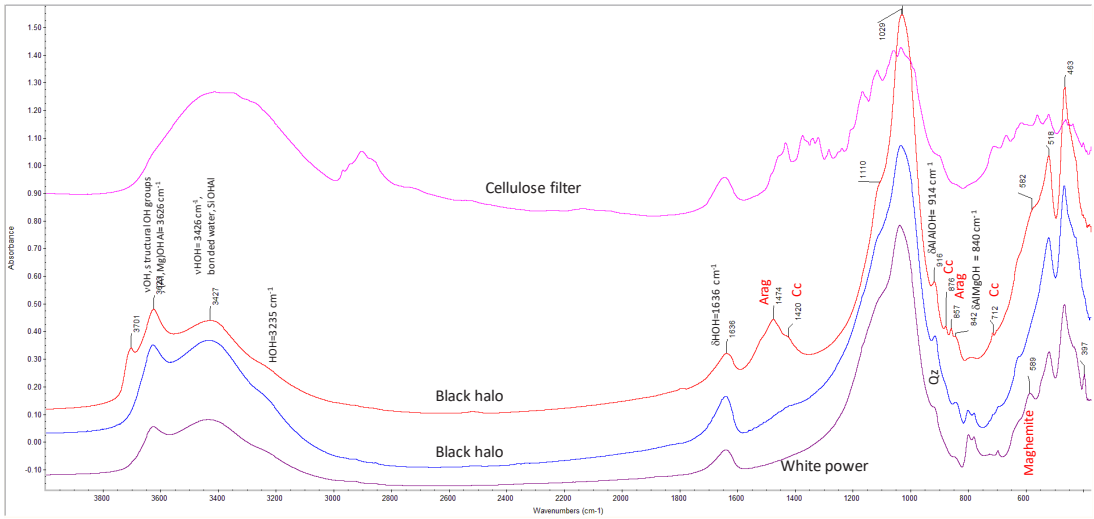

Fig. 62: FTIR spectra of some powdered samples from the black halo in block BB-36-1 (for sample location, see Fig. 30, Fig. 34)

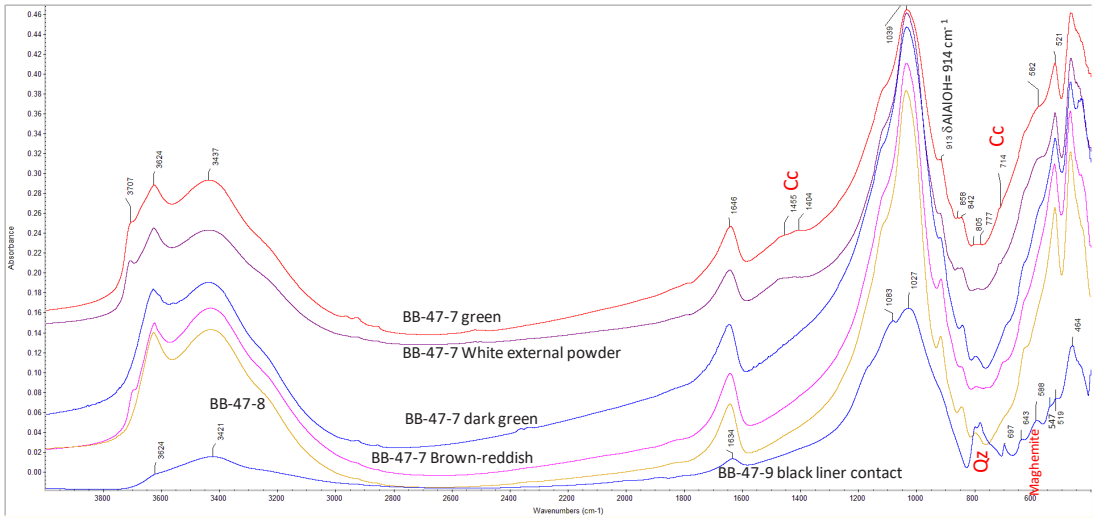

Fig. 63: FTIR spectra of some powdered samples from bentonite blocks in Section 47 (for sample location, see Fig. 31)

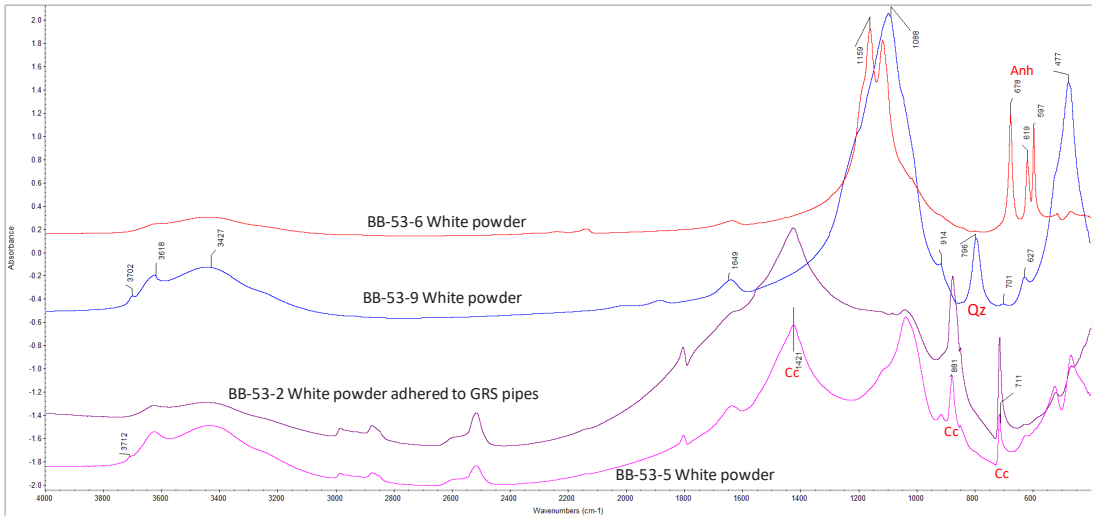

Fig. 64: FTIR spectra of some powdered samples from Section 53 (for sample location, see Fig. 32)

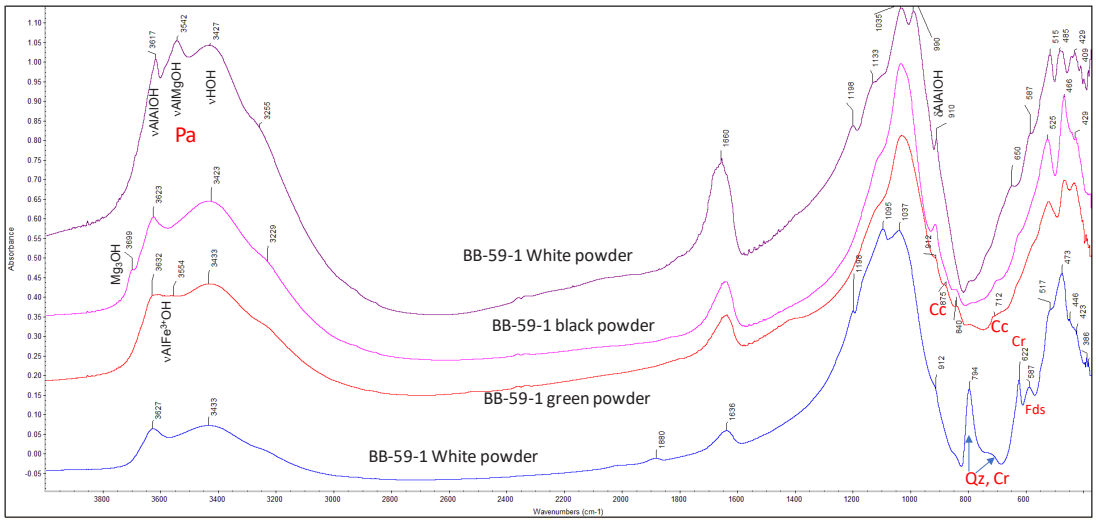

Fig. 65: FTIR spectra of some powdered samples from bentonite block BB-59-1 (for sample location, see Fig. 33 and Fig. 37)

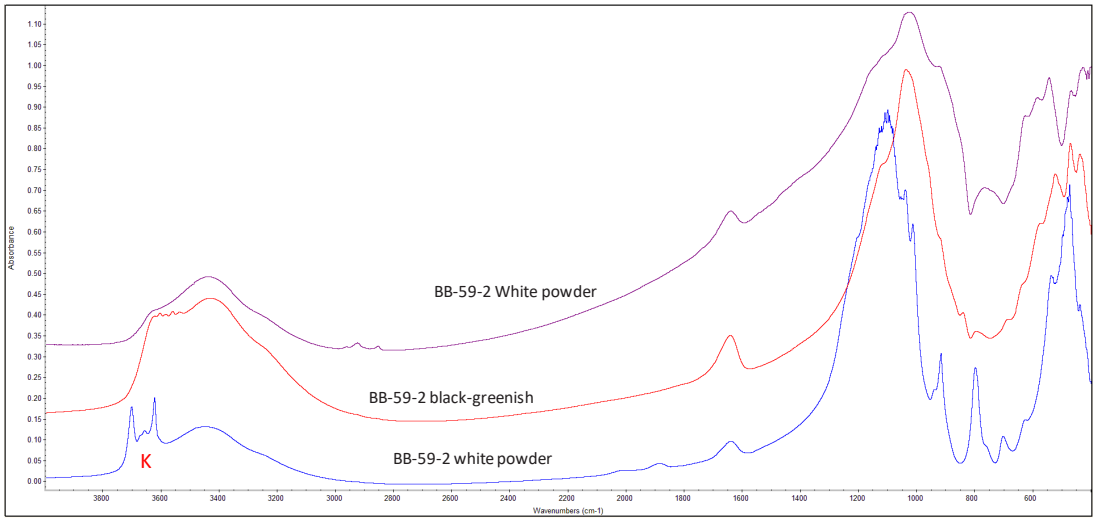

Fig. 66: FTIR spectra of some powdered samples from bentonite block BB-59-2 1 (for sample location, see Fig. 33 and Fig. 37)

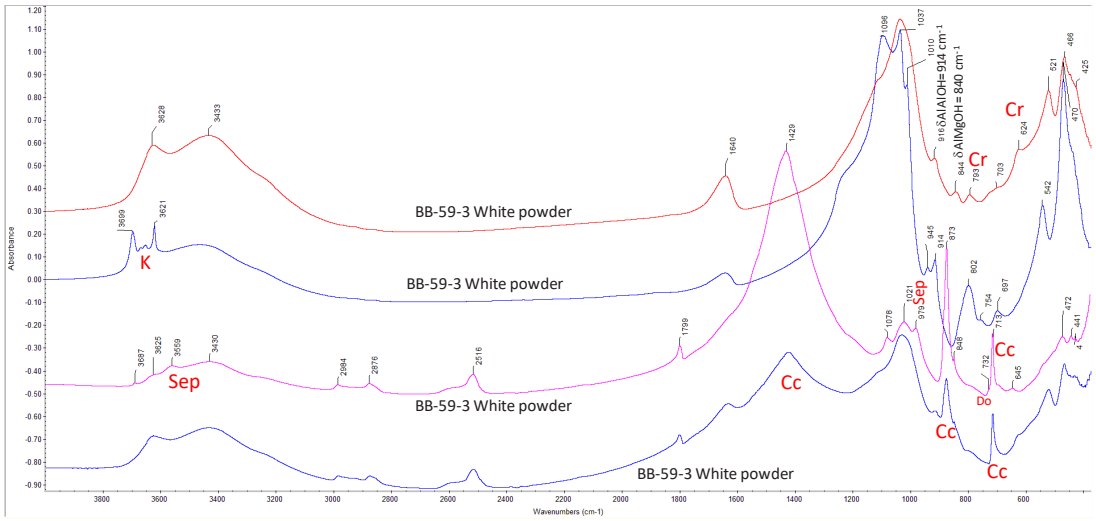

Fig. 67: FTIR spectra of some powdered samples from bentonite block BB-59-3 1 (for sample location, see Fig. 33 and Fig. 37)

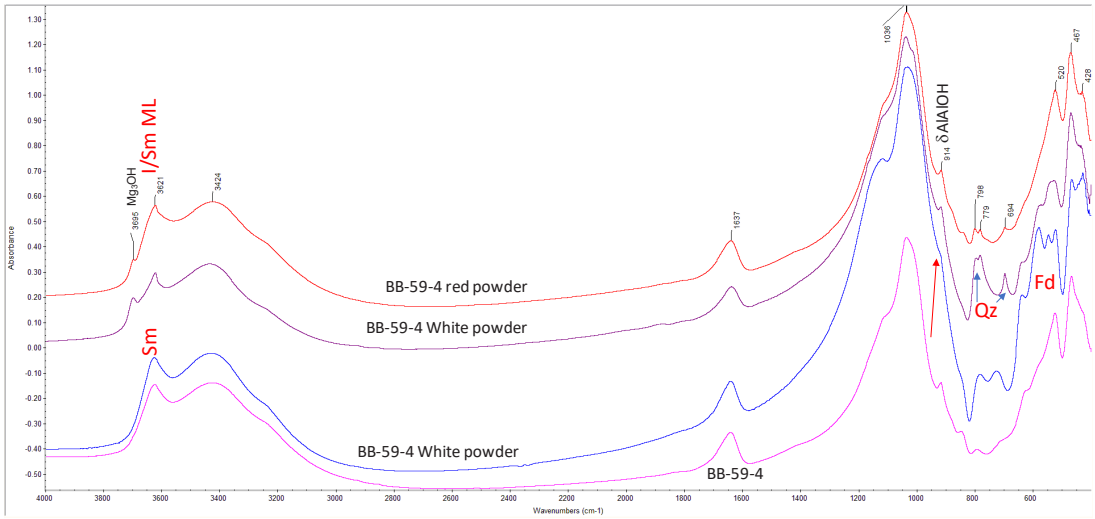

Fig. 68: FTIR spectra of some powdered samples from bentonite block BB-59-4 1 (for sample location, see Fig. 33 and Fig. 37)

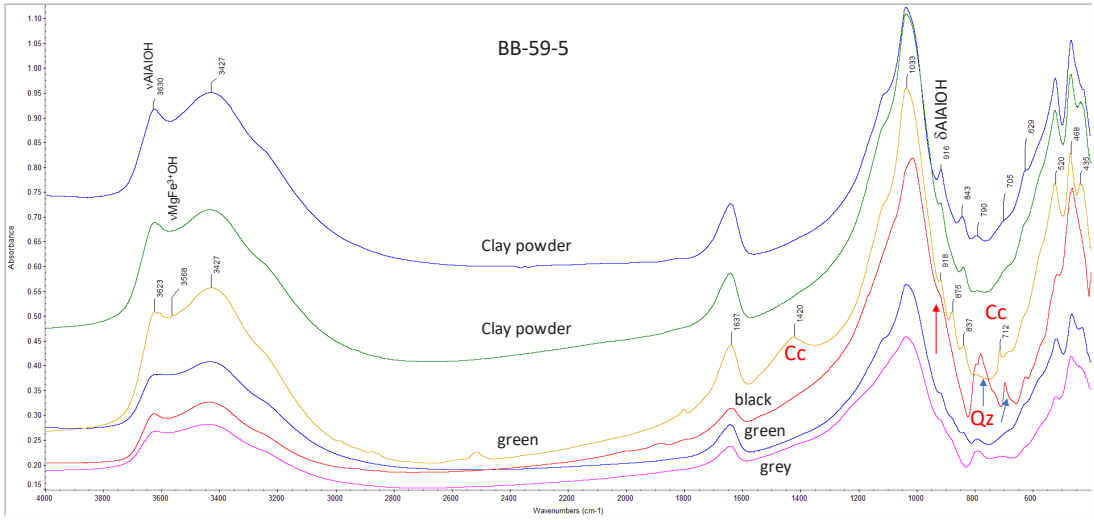

Fig. 69: FTIR spectra of some powdered samples from bentonite block BB-59-5 1 (for sample location, see Fig. 33 and Fig. 37)

5.3.3 Thermal analyses

Thermal analyses associated with calorimetric measurements were performed in samples from heated Section 47 and Section 53 (S47 and S53); and samples from the non-heated Section 36 (at the shotcrete plug contact) and Section 59 (S36 and S59). The data were compared with the FEBEX Reference sample.

Both initial and treated samples showed typical TG-DSC curves of dioctahedral smectites with most of the OH- groups at cis-vacant positions (Fig. 70 to Fig. 90). The dehydration peak is typical of smectites with divalent cations at interlayer sites (peak at 136 °C and a shoulder at 200 °C). The temperature of these dehydration peaks increased in the treated samples indicating a higher concentration of divalent cations at interlayer sites with respect to the reference sample in all sections (Fig. 73, Fig. 77, Fig. 81 and Fig. 90). The temperature of the decomposition peak is between 865 and 870 °C increasing slightly in the treated samples towards the internal part of the barrier. It is interesting to note the exothermic peak between 900 and 1'100 °C, corresponding to the solid phase structural decomposition and crystallization (phase transition), whose shape changes to a higher exothermic peak in the samples close to the heater, decreasing the temperature from 1'010 °C (reference sample) to 998 and 994 °C in samples BB-47-9 and BB-53-9, respectively (Fig. 76, Fig. 80). No accessory minerals were observed in the TG-DSC analyses.

The dehydroxylation behaviour of smectites varies with their origin and is related to the distribution of the cation and vacancies in the octahedral sheet and their cis- and trans-vacant configuration (Mackenzie 1957). The comparison of the DSC curves (Fig. 73, Fig. 77, Fig. 81 and Fig. 90) indicates no significant modifications in the structure of the smectite, except in samples BB-47-9 and BB-53-9 located close to the heater. These samples have an abnormal double dehydroxylation peak (598 – 610 and 652 °C), whereas the other samples from the same radius and the FEBEX reference material contain only a dehydroxylation peak located at around 650 °C. This new peak, at 598 °C in samples BB-47-9 (Fig. 77), and at 610 °C in BB-53-9 (Fig. 81) indicates the presence of either Illite/smectite mixed layers (I/S MLs), another type of clay mineral mixed layer (Chl/S ML), or a mixing of smectites with high-iron and aluminous varieties, since the presence of iron at octahedral sites induces a decrease of the dehydroxylation peak towards 450 – 520 °C, as occurs in nontronites. Al^{3+} substitutions at tetrahedral sheets (e.g., as in beidellites) also decrease the dehydroxylation peak. Thus, the presence of either a combination of clay mineral layers with both cis- (peak at 650 °C) and trans-vacant (peak 598 – 610 °C) configurations, or the combination of clay minerals with mainly octahedral substitutions (peak at 650 °C) and mainly tetrahedral substitutions (peak 598 – 610 °C) is also a possibility. These peaks were also observed in the BMS and protrusion samples located at the liner/heater interface (see further data and discussion in Sections 6.1.3 and 7.5.1).

Furthermore, due to the variation in shape and magnitude of the high temperature endothermic-exothermic peak between 850 and 1'000 °C, a modification of the composition in the structure of the smectite is inferred. The magnitude of the exothermic peak is intensive in the case of a smectite with high Mg content, and decreases or is absent in the case of high Al or Fe content. In this case, the sharp peak indicates a higher Mg content at octahedral sheets in samples in contact with the heater (e.g., Fig. 77, Fig. 81). A very slight almost insignificant mass change is observed during the development of the endothermic peak at around 850 °C in samples BB-47-9 and BB-53-9 in contact with the heater, so the presence of trioctahedral clay minerals (Chl/S MLs) cannot be completely discarded. The endothermic-exothermic peak between 850 and 1'000 °C is clearly stressed when the < 2 μm fraction is observed (Fig. 84), but the abnormal double dehydroxylation peak is not clearly detected, probably due to the low content of the mixed-layer clay mineral components or their existence at higher particle sizes.

Regarding the samples from the non-heated sections during the second operational phase of the FEBEX-DP Project, Section 36 and Section 59 (Fig. 73 and Fig. 90), no significant differences were observed with respect to the reference sample, except an increase of divalent cations at interlayer sites. The TG-DSC curves correspond to dioctahedral smectites with most of the OH^- groups at cis-vacant positions with no evidence of any accessory mineral.

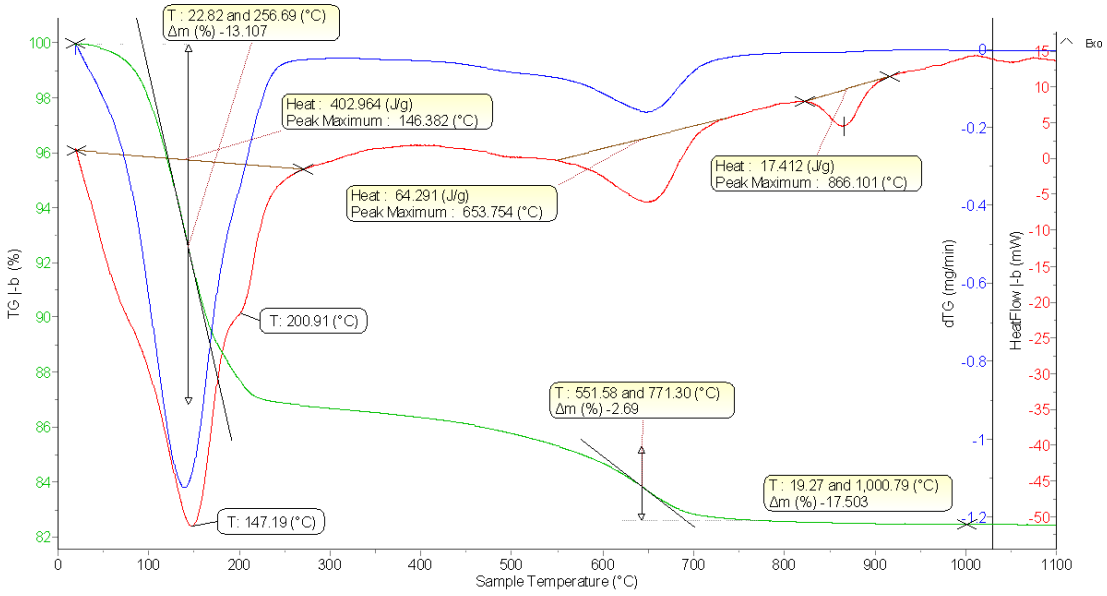

Fig. 70: TG-DSC curves from bulk sample BB-36-4 (external bentonite ring)

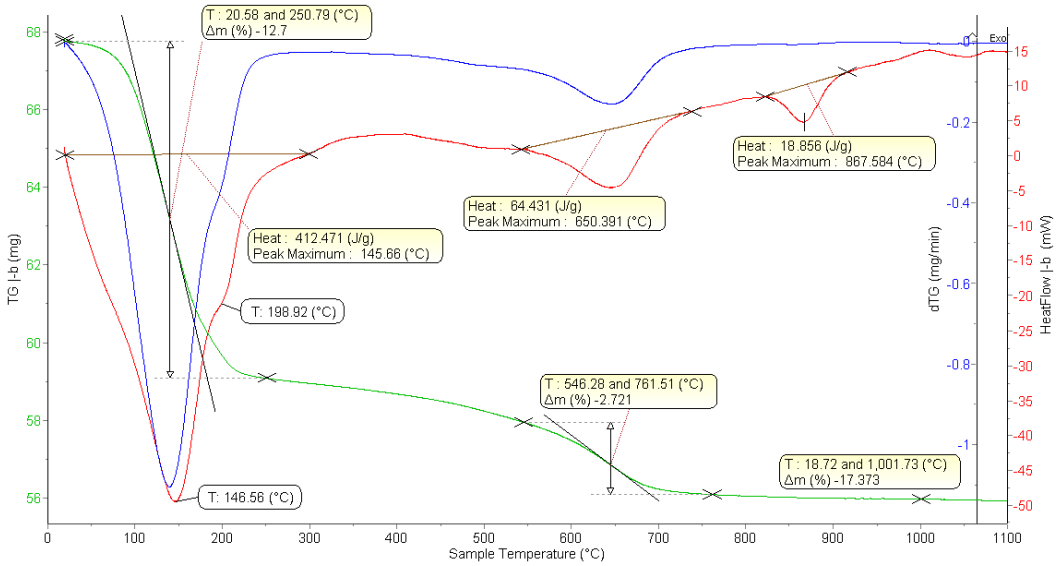

Fig. 71: TG-DSC curves from bulk sample BB-36-5 (middle bentonite ring)

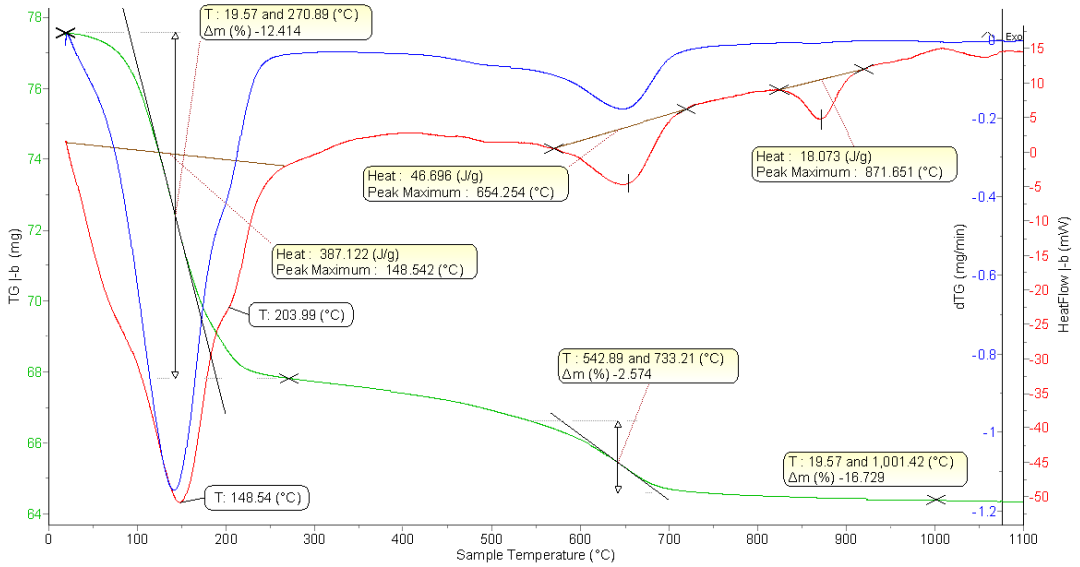

Fig. 72: TG-DSC curves from bulk sample BB-36-6 (inner bentonite ring)

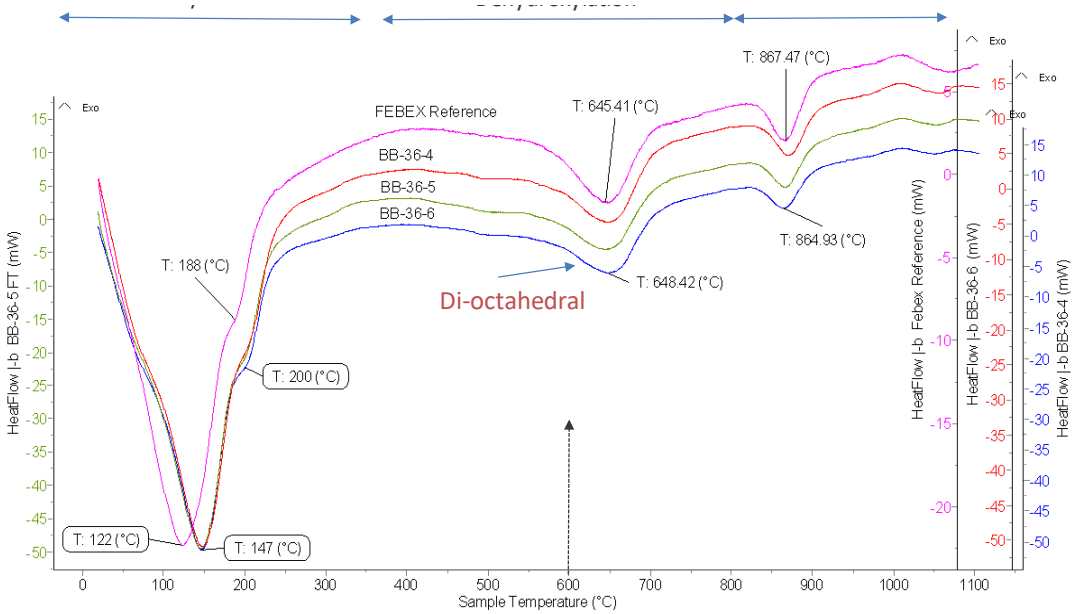

Fig. 73: Comparison of DSC curves of bulk samples from Section 36 (in contact with the concrete plug) and the Reference FEBEX bentonite

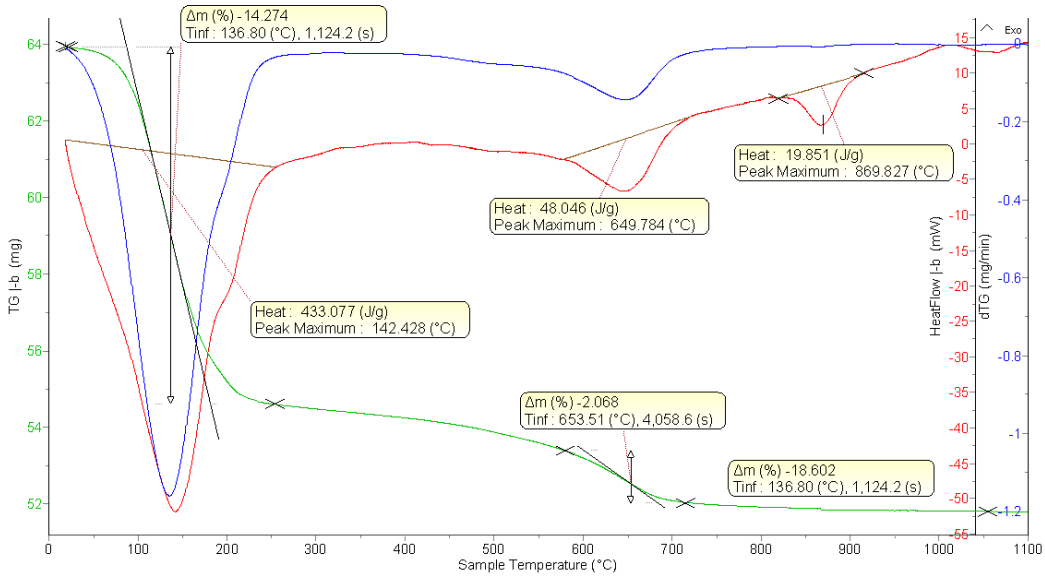

Fig. 74: TG-DSC curves from bulk sample BB-47-7 (external bentonite ring)

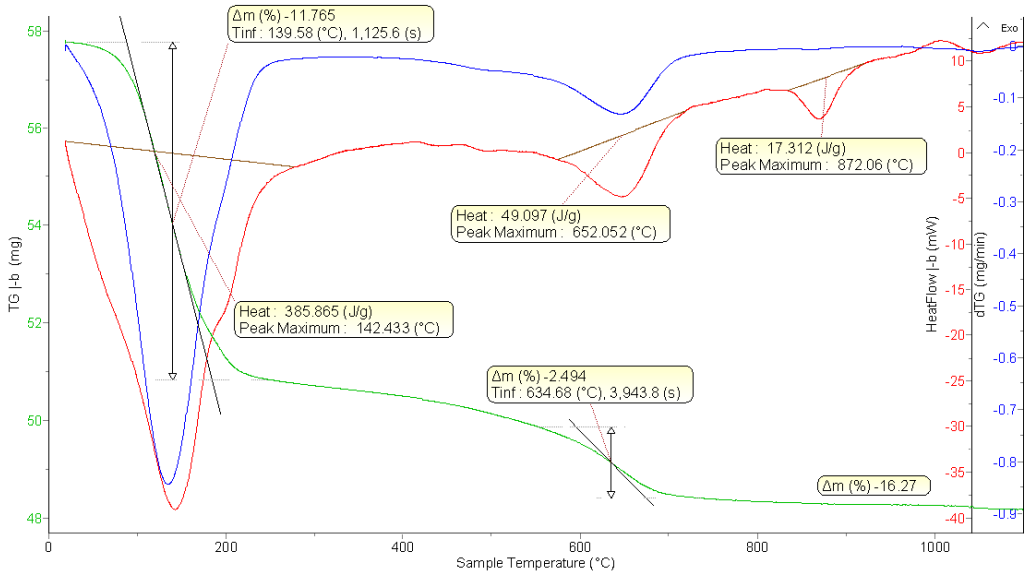

Fig. 75: TG-DSC curves from bulk sample BB-47-8 (middle bentonite ring)

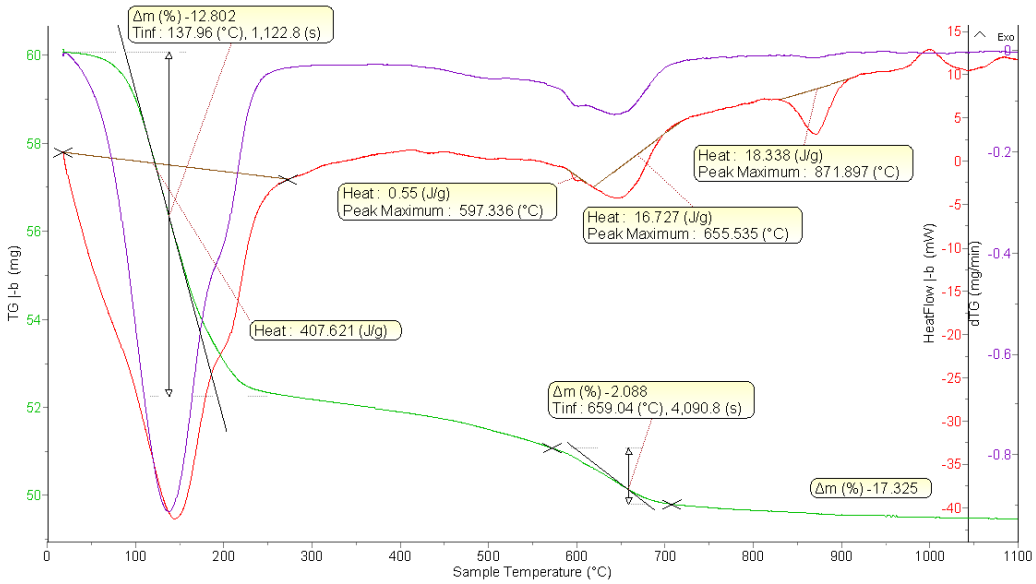

Fig. 76: TG-DSC curves from bulk sample BB-47-9 (internal bentonite ring)

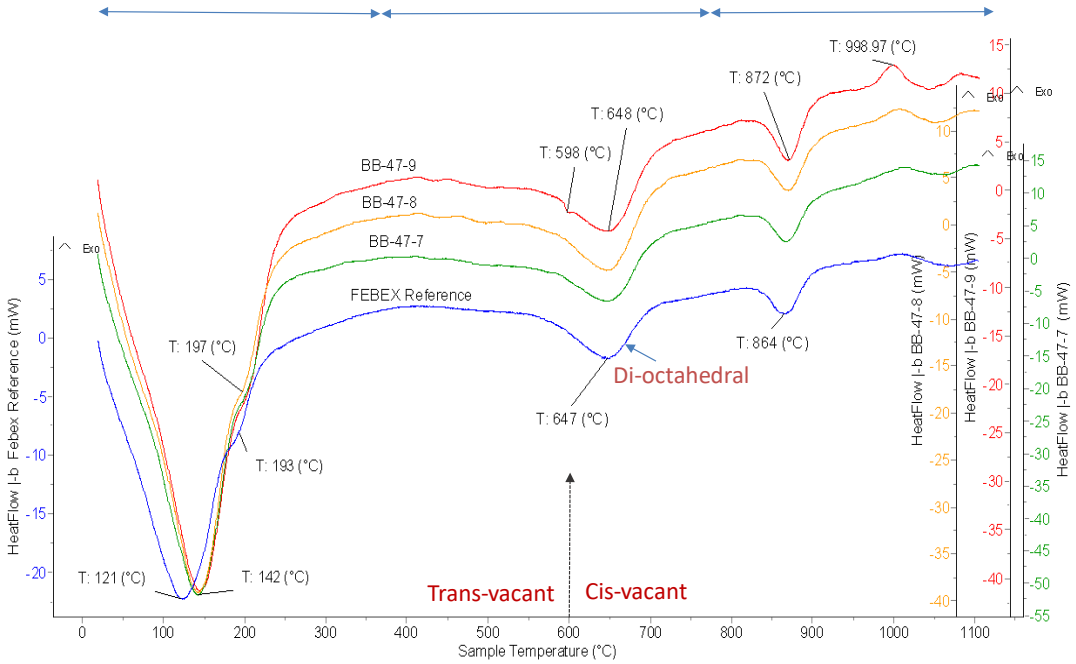

Fig. 77: Comparison of DSC curves of bulk samples from Section 47 (heated section) and the Reference FEBEX bentonite

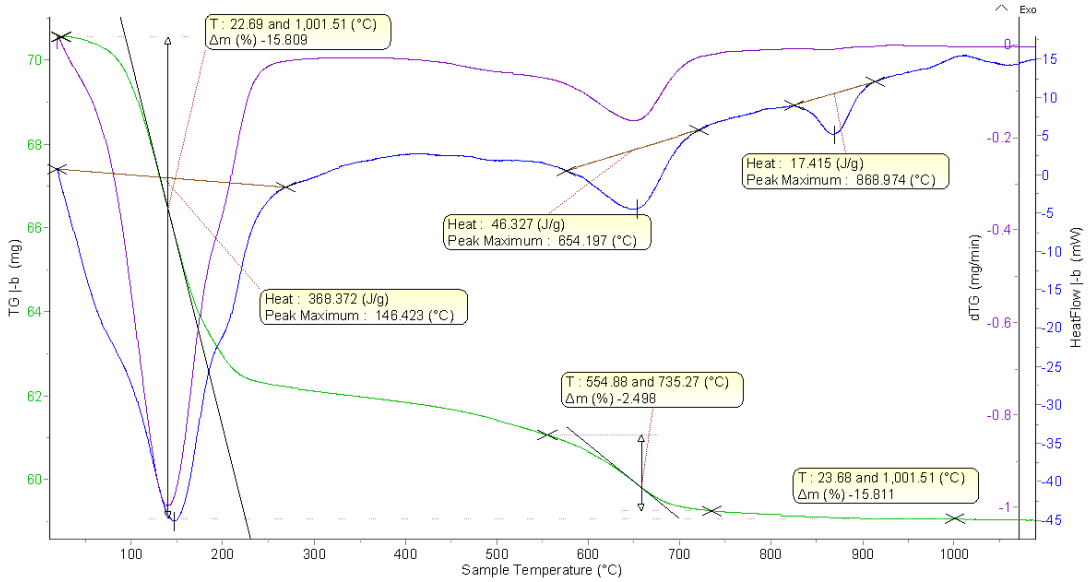

Fig. 78: TG-DSC curves from the bulk sample BB-53-7 (external bentonite ring)

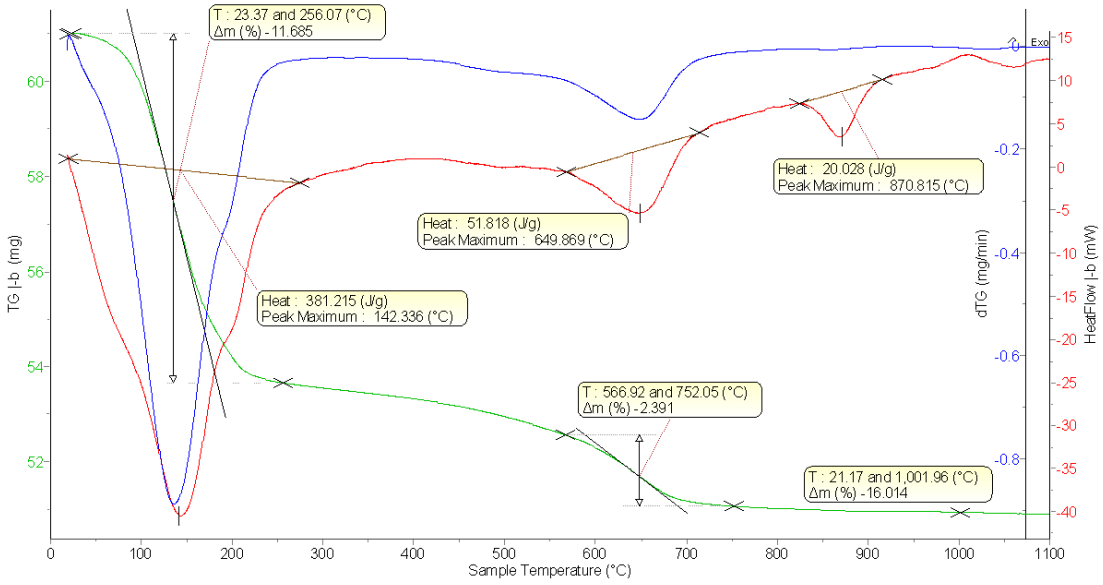

Fig. 79: TG-DSC curves from bulk sample BB-53-8 (middle bentonite ring)

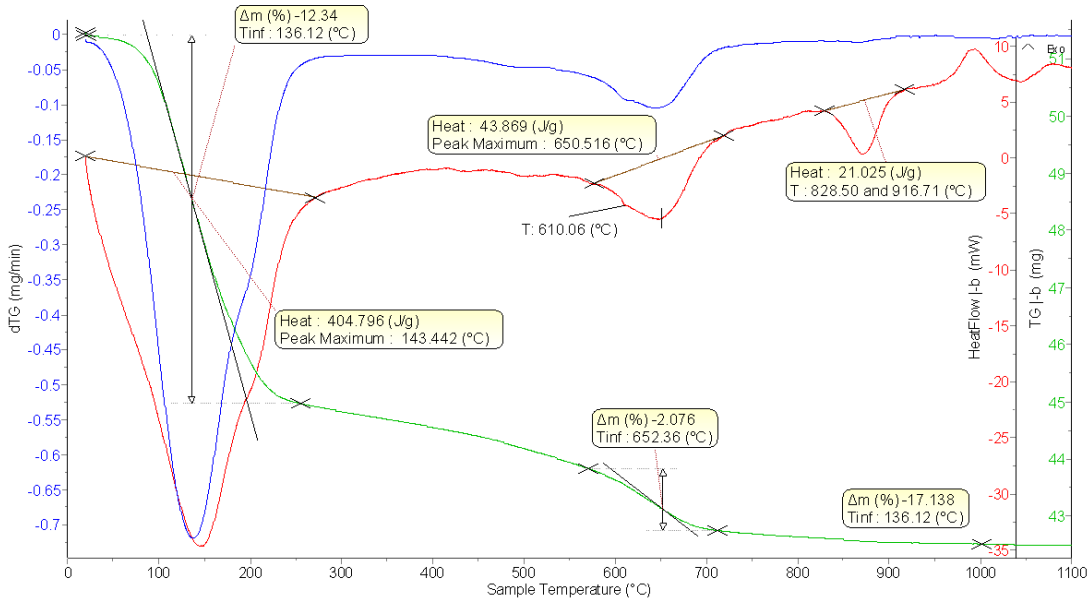

Fig. 80: TG-DSC curves from bulk sample BB-53-9 (internal bentonite ring)

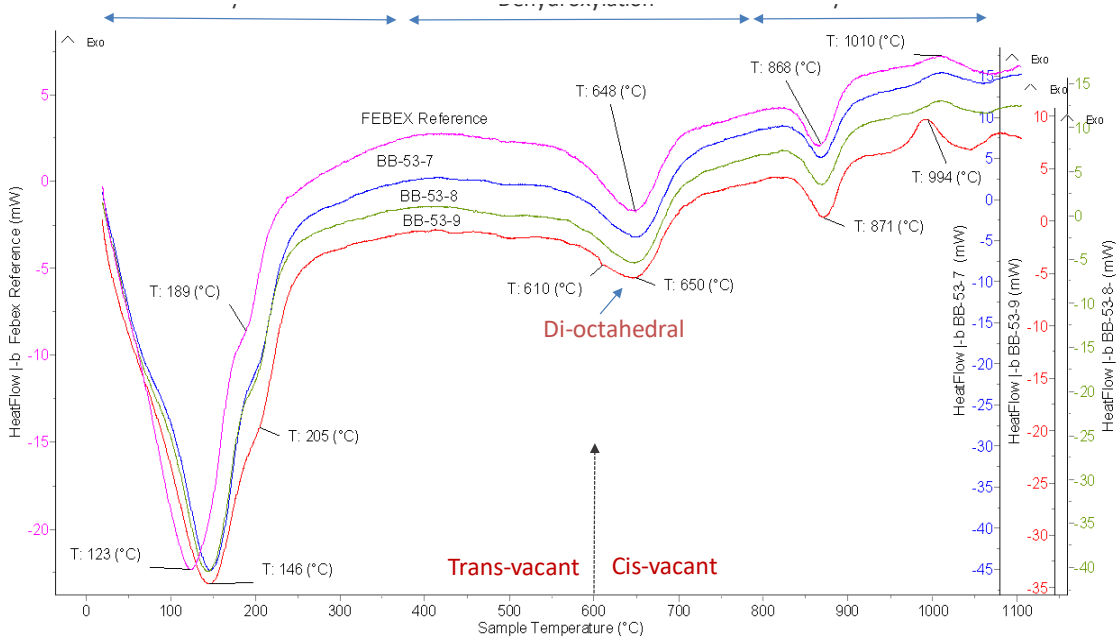

Fig. 81: Comparison of DSC curves of bulk samples from Section 53 (heated section) and the Reference FEBEX bentonite

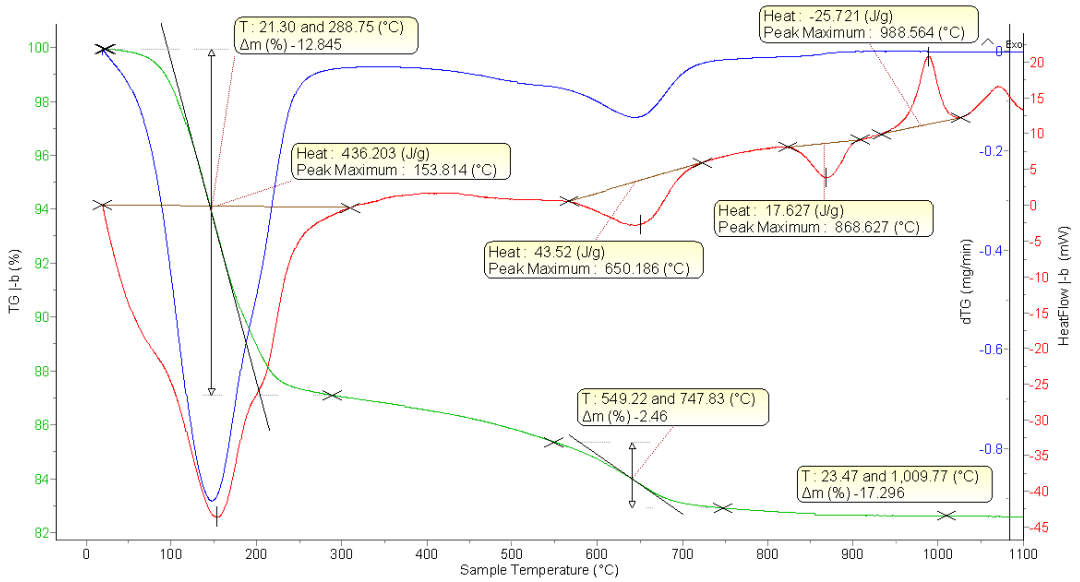

Fig. 82: TG-DSC curves from the < 2 µm sample BB-47-9 (internal bentonite ring)

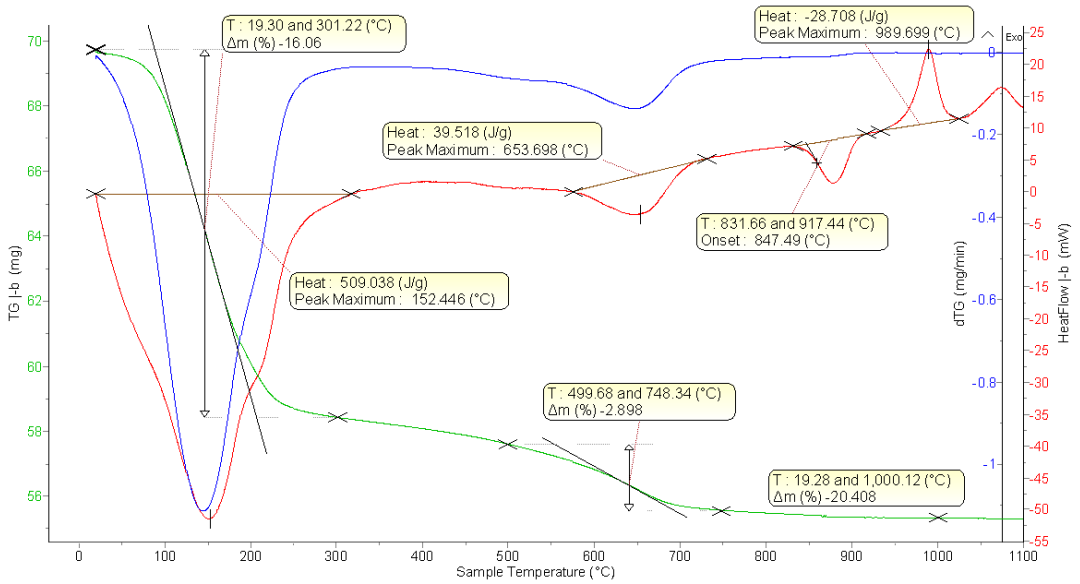

Fig. 83: TG-DSC curves from the < 2 µm sample BB-53-9 (internal bentonite ring)

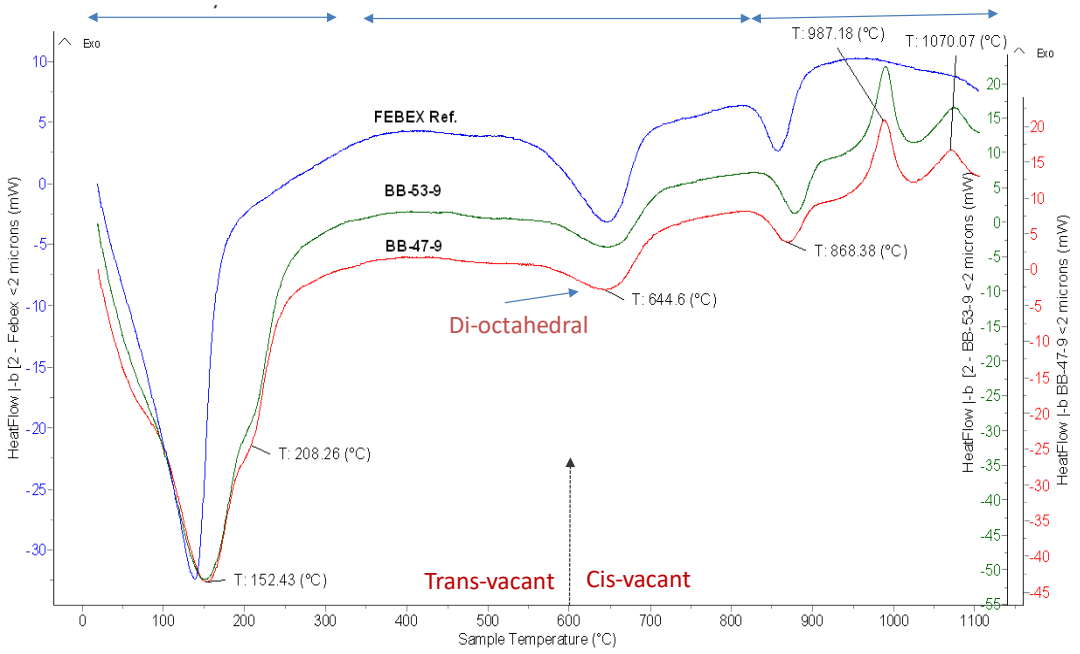

Fig. 84: Comparison of the TG-DSC curves from the < 2 µm fraction from the internal bentonite ring (BB-47-9 and BB-53-9) with the reference sample

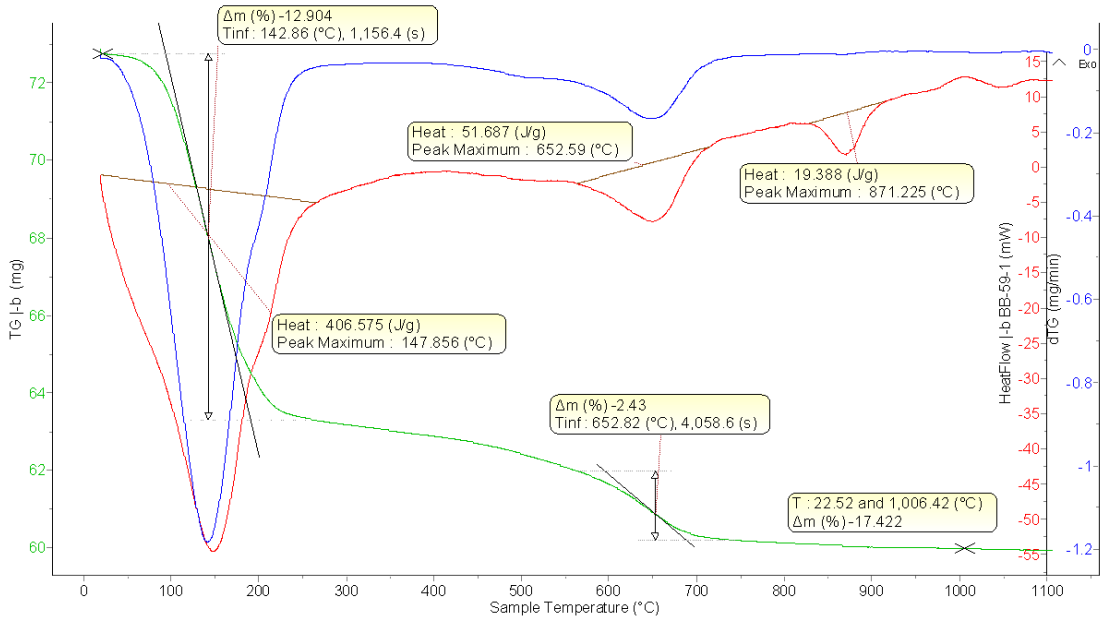

Fig. 85: TG-DSC curves from bulk sample BB-59-1

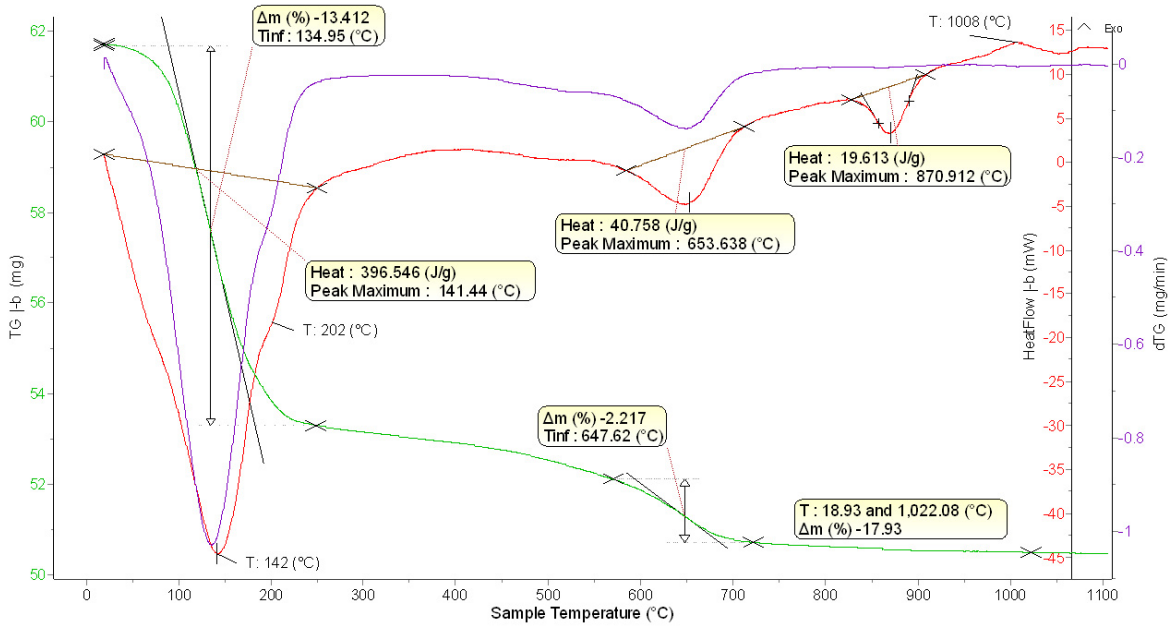

Fig. 86: TG-DSC curves from bulk sample BB-59-2

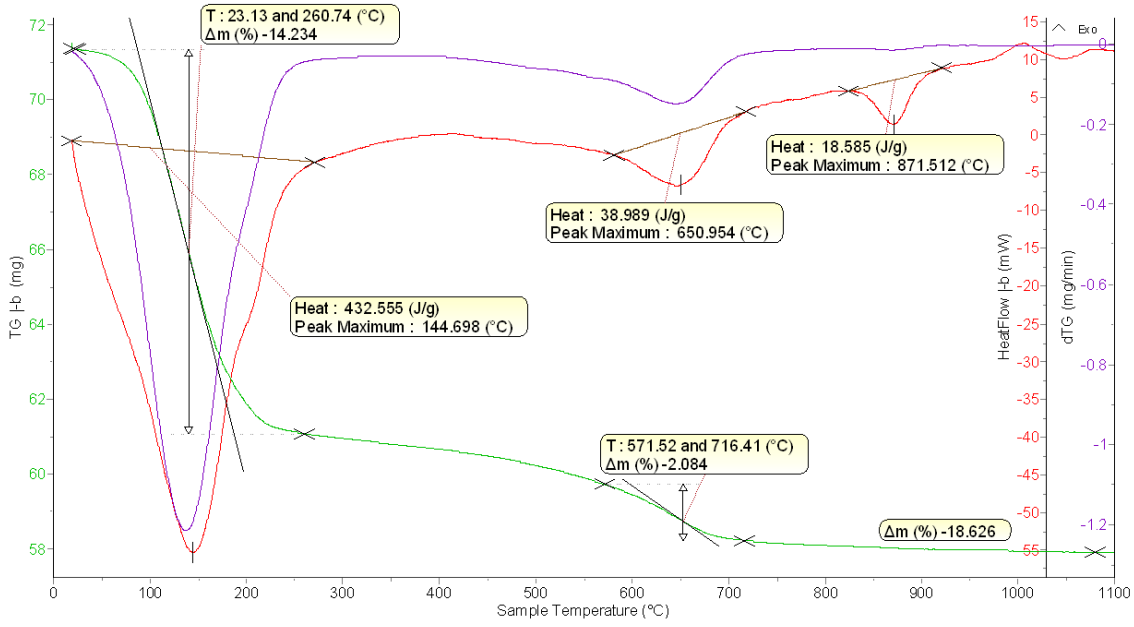

Fig. 87: TG-DSC curves from bulk sample BB-59-3

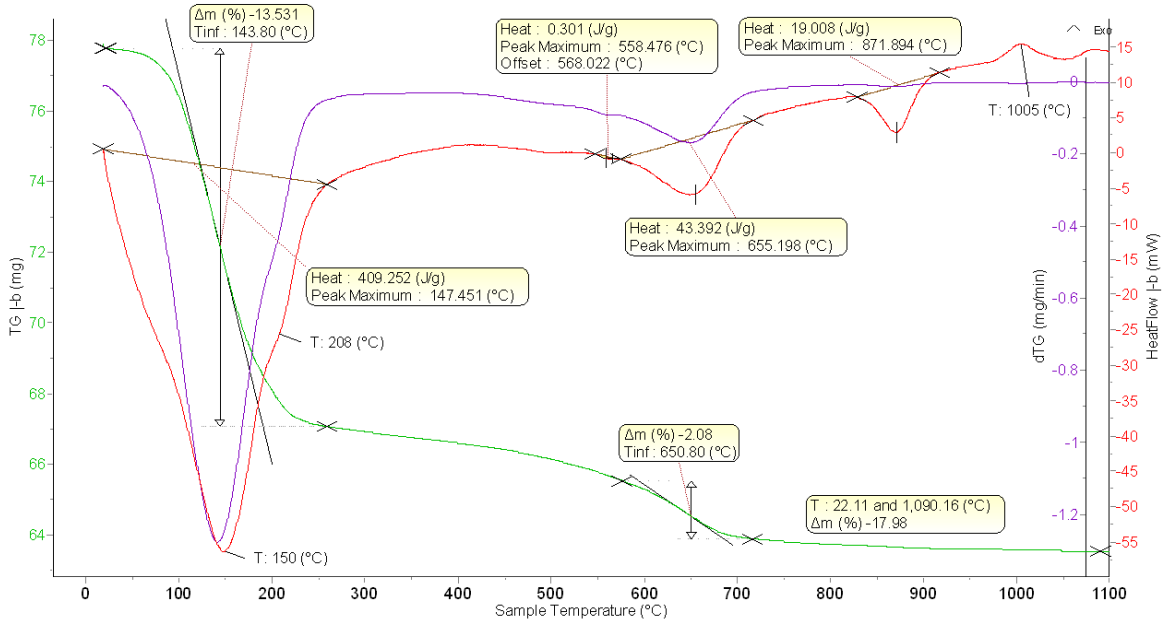

Fig. 88: TG-DSC curves from bulk sample BB-59-4

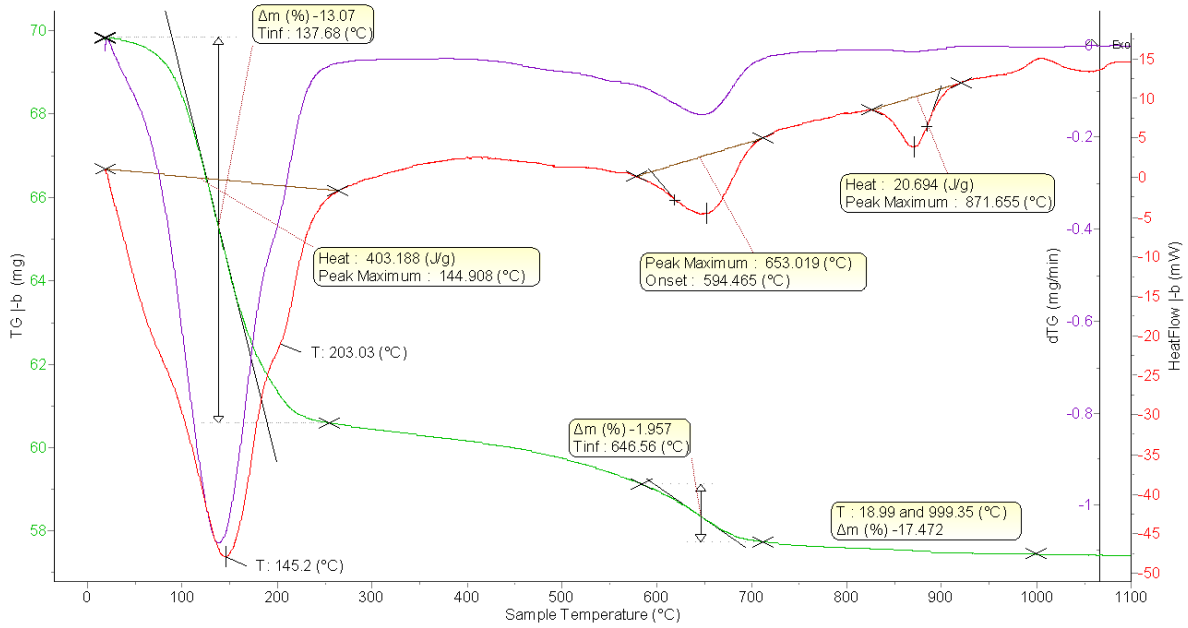

Fig. 89: TG-DSC curves from bulk sample BB-59-5

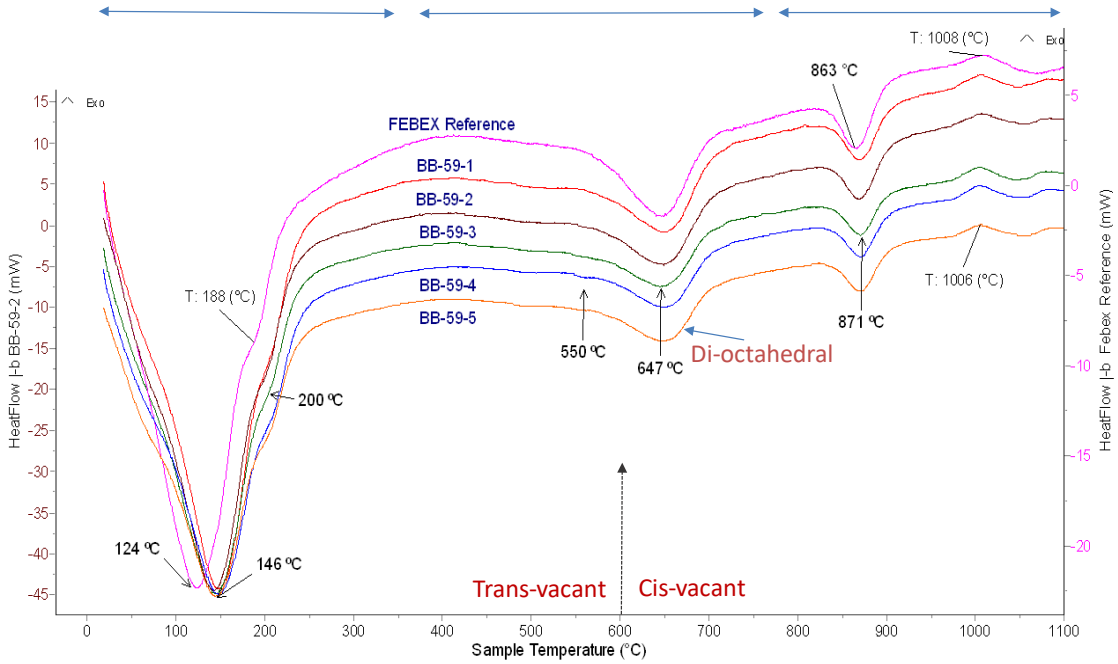

Fig. 90: Comparison of DSC curves of bulk samples from Section 59 (non-heated section) and the reference FEBEX bentonite

5.3.4 TEM analyses

Transmission electron microscopy was used for examining the morphology of the platy clay particles and/or clay aggregates and the crystal chemistry of the clay minerals. EDS-analyses were performed on clay particles for determining the Structural formula, and to observe the thickness of the structural units perpendicular to the plates (c-axis and/or a- or b-axis).

The EDS analyses were obtained from more than five determinations per sample. Based on these, Structural formula of the clay particles were calculated (Moore & Reynolds 1989). The procedure is based on a formula unit with 11 oxygens (4 cations from tetrahedral sheet and 2 from the octahedral sheet) for dioctahedral smectites and illites; 14 for chlorites […$O_{10}(OH)_2$-1H_2O]; and 7 for kaolinites […$O_5(OH)_4$-1H_2O]. Cations were assigned to the tetrahedral sheets first. If there are less than 4 Si cations per formula unit, Al was taken to fill the tetrahedral sites. The remainder of the Al cations were assigned to the octahedral sheets together with Fe, Mg, Mn and Ti. Ca, Na and K were assigned to the interlayer sites. Mg was assigned to interlayer sites depending on the sum of octahedral cations: 2 for dioctahedral clays and 3 for trioctahedral clay minerals) and the total layer charge of the structure: between 0.2 to 0.6 for smectites; 0.6 to 0.9 for vermiculites; and 0.6 to 1 (or 2) for illites (or brittle micas). EDS does not differentiate between the oxidation states of iron, so all iron was considered as Fe^{3+}, except for chlorites where all Fe was considered as Fe^{2+}. It is possible that part of iron is Fe^{2+} that substitutes for Al^{3+} in the octahedral sheets. Furthermore, it should be possible that Fe^{3+} substitutes for Si^{4+} in the tetrahedral sheets. Both substitutions would contribute to the negative charge. It is also possible that Fe^{3+} and/or Fe^{2+} could occupy interlayer sites. For comparison, the structural formula was obtained both according to Moore & Reynolds (1989), i.e., with all magnesium at octahedral sites; or by fixing the sum of octahedral ions to 2.0; i.e., allowing some amount of magnesium at interlayer sites. However, the latter option was considered for crystallochemistry studies. If all magnesium is taken at octahedral sites, the limit of 2.09 per $O_{10}(OH)_2$ indicates a departure from the dioctahedral mineral structure. The layer charge of 0.66 (smectite of high charge, HC) per $O_{10}(OH)_2$ is the upper limit of expandable phases (de la Calle & Suquet 1988)

TEM analyses were performed on the FEBEX Reference sample and all other retrieved samples as a function of the distance to the gallery axis at different sections: Section 36 (shotcrete contact), Section 47, Section 53 (heated sections) and Section 59 (non-heated section). Furthermore, samples in contact with the liner/heater and protrusions were also analysed (see Section 6.1.5). The aim was to analyse possible alterations in the smectite microstructure. TEM images for the Reference and retrieved samples are shown in Fig. 91 and from Fig. 92 to Fig. 94, respectively (see also Appendix E).

The Structural formula calculated for smectite clay particles are shown in Tab. 8 and Tab. 9. The Structural formula calculated for other types of clay minerals found are shown in Tab. 10. The most significant changes observed are related to changes in the cation composition at tetrahedral sheets (increasing Al^{3+}), slight increase in magnesium at octahedral sheets, and increases in the interlayer charge above 0.6 eq/h.u.c., which is the limit for typical smectites. Other types of clay minerals were found, corresponding to nontronite, illite and Fe-rich chlorite clay minerals (Tab. 10 and Tab. 38 in Section 6.1.5). Illites and chlorites were also observed by SEM analyses (see Appendix B).

It is interesting to note the variation of the layer charge and the percentage of tetrahedral charge in the samples close to the liner/Heater #2 and in the protrusions (Fig. 95), where it increases with respect to the reference sample. The same was observed for total magnesium (octahedral and interlayer magnesium, Fig. 96). With respect to iron at octahedral sheets, it increased in the protrusion samples as well as in the red corroded sample BB-36-3 (Fig. 97), where nontronite and Fe-rich chlorites were found.

Tab. 8: Structural formula of the FEBEX Reference sample based on $O_{10}(OH)_2$ according to Moore & Reynolds (1989) (first row) or maintaining the $\Sigma_{oct} = 2.0$ (second row)

Sample	Structural formula	Layer charge (eq/ h.u.c.)	Σ_{tet}	Σ_{oct}	τ charge (%)	O. charge (%)	Weight (g/mol) p.f.u.
FEBEX Ref.*	$(Si_{3.95}Al_{0.05})^{IV}$ $(Al_{1.36}Fe^{3+}_{0.21}Mg_{0.49}Ti^{4+}_{0.01})^{VI}$ $O_{10}(OH)_2$ $(Ca_{0.08}$ $Na_{0.10}K_{0.06})_{0.24}$	0.33	4.0	2.07	14	86	749.96
	$(Si_{3.95}Al_{0.05})^{IV}$ $(Al_{1.36}Fe^{3+}_{0.21}Mg_{0.42}Ti^{4+}_{0.01})^{VI}$ $O_{10}(OH)_2$ $(Ca_{0.08}Mg_{0.07}Na_{0.10}K_{0.06})_{0.31}$	0.46	4.0	2.00	10	90	749.96
FEBEX Ref.**	$(Si_{3.96}Al_{0.04})^{IV}$ $(Al_{1.49}Fe^{3+}_{0.13}Mg_{0.47})^{VI}$ $O_{10}(OH)_2$ $(Na_{0.20}K_{0.04})_{0.23}$	0.23	4.0	2.10	19	81	742.12
	$(Si_{3.96}Al_{0.04})^{IV}$ $(Al_{1.49}Fe^{3+}_{0.13}Mg_{0.38})^{VI}$ $O_{10}(OH)_2$ $(Mg_{0.10}Na_{0.20}K_{0.03})_{0.32}$	0.42	4.0	2.00	10	90	742.12
	$(Si_{3.94}Al_{0.06})^{IV}$ $(Al_{1.43}Fe^{3+}_{0.12}Mg_{0.56}Ti^{4+}_{0.01})^{VI}$ $O_{10}(OH)_2$ $(Ca_{0.01}Na_{0.25}K_{0.01})_{0.28}$	0.29	4.0	2.11	22	78	744.11
	$(Si_{3.94}Al_{0.06})^{IV}$ $(Al_{1.43}Fe^{3+}_{0.12}Mg_{0.45}Ti^{4+}_{0.01})^{VI}$ $O_{10}(OH)_2$ $(Ca_{0.01}Mg_{0.11}Na_{0.25}K_{0.01})_{0.39}$	0.51	4.0	2.00	12	88	744.11
	$(Si_{3.95}Al_{0.05})^{IV}$ $(Al_{1.48}Fe^{3+}_{0.10}Mg_{0.46}Mn^{2+}_{0.01})^{VI}$ $O_{10}(OH)_2$ $(Ca_{0.03}$ $Na_{0.31}K_{0.02})_{0.36}$	0.39	4.0	2.04	13	87	744.76
	$(Si_{3.95}Al_{0.05})^{IV}$ $(Al_{1.48}Fe^{3+}_{0.10}Mg_{0.42}Mn^{2+}_{0.01})^{VI}$ $O_{10}(OH)_2$ $(Ca_{0.03}Mg_{0.04}Na_{0.31}K_{0.02})_{0.40}$	0.48	4.0	2.00	11	89	744.76
	$(Si_{3.89}Al_{0.11})^{IV}$ $(Al_{1.47}Fe^{3+}_{0.12}Mg_{0.46}Ti^{4+}_{0.01})^{VI}$ $O_{10}(OH)_2$ $(Ca_{0.02}Na_{0.30}K_{0.03})_{0.35}$	0.37	4.0	2.07	31	69	746.31
	$(Si_{3.89}Al_{0.11})^{IV}$ $(Al_{1.47}Fe^{3+}_{0.12}Mg_{0.40}Ti^{4+}_{0.01})^{VI}$ $O_{10}(OH)_2$ $(Ca_{0.02}Mg_{0.07}Na_{0.30}K_{0.03})_{0.42}$	0.50	4.0	2.00	23	77	746.31
	$(Si_{3.93}Al_{0.07})^{IV}$ $(Al_{1.29}Fe^{3+}_{0.29}Mg_{0.48}Ti^{4+}_{0.01}$ $Mn^{2+}_{0.01})^{VI}$ $O_{10}(OH)_2$ $(Ca_{0.02}$ $Na_{0.14}K_{0.16})_{0.31}$	0.33	4.0	2.08	22	78	759.44
	$(Si_{3.93}Al_{0.07})^{IV}$ $(Al_{1.29}Fe^{3+}_{0.29}Mg_{0.41}Ti^{4+}_{0.01}$ $Mn^{2+}_{0.01})^{VI}$ $O_{10}(OH)_2$ $(Ca_{0.02}Mg_{0.08}Na_{0.14}K_{0.16})_{0.39}$	0.48	4.0	2.00	15	85	759.44
	$(Si_{3.93}Al_{0.07})^{IV}$ $(Al_{1.43}Fe^{3+}_{0.15}Mg_{0.49}Ti^{4+}_{0.01})^{VI}$ $O_{10}(OH)_2$ $(Ca_{0.02}Na_{0.24}K_{0.05})_{0.30}$	0.32	4.0	2.08	21	79	747.29
	$(Si_{3.93}Al_{0.07})^{IV}$ $(Al_{1.43}Fe^{3+}_{0.15}Mg_{0.41}Ti^{4+}_{0.01})^{VI}$ $O_{10}(OH)_2$ $(Ca_{0.02}Mg_{0.08}Na_{0.24}K_{0.05})_{0.38}$	0.48	4.0	2.00	14	86	747.29

* Calculated from chemical analysis by XRF on the < 2 µm (see Section 5.4.2)
** Calculated from TEM-EDX analysis (Average from 5 analyses)

Tab. 9: Structural formula of the reference and retrieved samples based on $O_{10}(OH)_2$ according to Moore & Reynolds (1989) and maintaining the $\Sigma_{oct} = 2.0$

Data in parentheses are referred to Structural formula without magnesium at interlayer sites.

Sample	**Structural formula**	**Layer charge** (eq/ h.u.c.)	**Σ_{tet}**	**Σ_{oct}**	**τ charge** (%)	**O. charge** (%)	**Weight** (g/mol) p.f.u.
FEBEX Ref. (5)*	$(Si_{3.93}Al_{0.07})^{IV}$ $(Al_{1.43}Fe^{3+}_{0.15}Mg_{0.41}Ti^{4+}_{0.01})^{VI}$ $O_{10}(OH)_2$ $(Ca_{0.02}Mg_{0.08}Na_{0.24}K_{0.05})_{0.38}$	0.48 (0.32)	4.0	2.00 (2.08)	14 (21)	86 (79)	747.29
BB-47-7 (6)*	$(Si_{3.89}Al_{0.11})^{IV}$ $(Al_{1.43}Fe^{3+}_{0.14}Mg_{0.42}Ti^{4+}_{0.01})^{VI}$ $O_{10}(OH)_2$ $(Ca_{0.10}Mg_{0.14}Na_{0.02}K_{0.04})_{0.30}$	0.54 (0.26)	4.0	2.00 (2.14)	21 (43)	79 (57)	745.26
BB-47-8 (5)*	$(Si_{3.94}Al_{0.06})^{IV}$ $(Al_{1.42}Fe^{3+}_{0.14}Mg_{0.44}Ti^{4+}_{0.01})^{VI}$ $O_{10}(OH)_2$ $(Ca_{0.09}Mg_{0.11}Na_{0.06}K_{0.03})_{0.30}$	0.50 (0.28)	4.0	2.00 (2.11)	13 (22)	87 (78)	744.58
BB-47-9 (12)*	$(Si_{3.81}Al_{0.19})^{IV}$ $(Al_{1.33}Fe^{3+}_{0.13}Mg_{0.49}Ti^{4+}_{0.03}$ $Mn^{2+}_{0.02})^{VI}$ $O_{10}(OH)_2$ $(Ca_{0.16}Mg_{0.06}Na_{0.20}K_{0.04})_{0.46}$	0.68 (0.57)	4.0	2.00 (2.06)	29 (34)	71 (66)	755.95
BB-47-9 bis (5)*	$(Si_{3.89}Al_{0.11})^{IV}$ $(Al_{1.36}Fe^{3+}_{0.15}Mg_{0.48})^{VI}$ $O_{10}(OH)_2$ $(Ca_{0.18}Mg_{0.08}Na_{0.01}K_{0.06})_{0.33}$	0.59 (0.44)	4.0	2.00 (2.08)	19 (25)	81 (75)	750.26
BB-53-3 (8)*	$(Si_{3.76}Al_{0.24})^{IV}$ $(Al_{1.56}Fe^{3+}_{0.07}Mg_{0.35}Ti^{4+}_{0.01}$ $Mn^{2+}_{0.01})^{VI}$ $O_{10}(OH)_2$ $(Ca_{0.07}Mg_{0.21}Na_{0.01}K_{0.03})_{0.32}$	0.60	4.0	2.00	40	60	741.65
BB-36-1 (6)*	$(Si_{3.93}Al_{0.07})^{IV}$ $(Al_{1.45}Fe^{3+}_{0.11}Mg_{0.42}Ti^{4+}_{0.01}$ $Mn^{2+}_{0.01})^{VI}$ $O_{10}(OH)_2$ $(Ca_{0.08}Mg_{0.09}Na_{0.03}K_{0.13})_{0.32}$	0.49 (0.31)	4.0	2.00 (2.09)	14 (21)	86 (79)	747.21
BB-36-2 (5)*	$(Si_{3.91}Al_{0.09})^{IV}$ $(Al_{1.45}Fe^{3+}_{0.14}Mg_{0.40}Mn^{2+}_{0.01})^{VI}$ $O_{10}(OH)_2$ $(Ca_{0.09}Mg_{0.11}Na_{0.03}K_{0.05})_{0.29}$	0.49 (0.27)	4.0	2.00 (2.11)	19 (34)	81 (66)	745.09
BB-36-3 red (4)*	$(Si_{3.88}Al_{0.12})^{IV}$ $(Al_{1.40}Fe^{3+}_{0.19}Mg_{0.40}Ti^{4+}_{0.01}$ $Mn^{2+}_{0.01})^{VI}$ $O_{10}(OH)_2$ $(Ca_{0.06}Mg_{0.14}Na_{0.05}K_{0.06})_{0.32}$	0.52 (0.24)	4.0	2.00 (2.14)	23 (51)	77 (49)	748.75
BB-59-1 (7)*	$(Si_{3.91}Al_{0.09})^{IV}$ $(Al_{1.43}Fe^{3+}_{0.11}Mg_{0.46})^{VI}$ $O_{10}(OH)_2$ $(Ca_{0.09}Mg_{0.14}Na_{0.04}K_{0.04})_{0.32}$	0.55 (0.27)	4.0	2.00 (2.14)	17 (35)	83 (65)	744.00
BB-59-3 (7)*	$(Si_{3.85}Al_{0.15})^{IV}$ $(Al_{1.43}Fe^{3+}_{0.13}Mg_{0.43}Mn^{2+}_{0.01})^{VI}$ $O_{10}(OH)_2$ $(Ca_{0.09}Mg_{0.15}Na_{0.06}K_{0.04})_{0.34}$	0.58 (0.29)	4.0	2.00 (2.15)	26 (53)	74 (47)	746.71
BB-59-5 (8)*	$(Si_{3.86}Al_{0.14})^{IV}$ $(Al_{1.46}Fe^{3+}_{0.14}Mg_{0.39}Ti^{4+}_{0.01}$ $Mn^{2+}_{0.01})^{VI}$ $O_{10}(OH)_2$ $(Ca_{0.07}Mg_{0.16}Na_{0.02}K_{0.06})_{0.31}$	0.53 (0.22)	4.0	2.00 (2.16)	27 (65)	73 (35)	745.63

* In parentheses: number of point analyses performed by TEM for calculating the average value

Tab. 10: Structural formula of non-montmorillonite clay particles detected in the retrieved samples

Sample	**Structural formula**	**Layer charge** (eq/ h.u.c.)	Σ_{tet}	Σ_{oct}	**τ charge** (%)	**O. charge** (%)	**Weight** (g/mol) p.f.u.
BB-47-9 *Illite type or high K content*	$(Si_{3.91}Al_{0.09})^{IV}$ $(Al_{1.42}Fe^{3+}_{0.17}Mg_{0.29\ \ 0.10})^{VI}$ $O_{10}(OH)_2$ $(Ca_{0.06}K_{0.58})_{0.63}$	0.69	4.0	1.90	13	87	773.44
BB-36-2 *Kaolinite type*	$(Si_{2.00}Al_{0.00})^{IV}$ $(Al_{1.81}Mg_{0.15}Mn^{2+}_{0.03})^{VI}$ $O_5(OH)_2$ $(Ca_{0.05}Mg_{0.04})_{0.09}$	0.19	4.0	2.00	0	100	615.30
BB-36-3 red *Nontronite type*	$(Si_{3.32}Al_{0.68})^{IV}$ $(Al_{0.88}Fe^{3+}_{1.01}Mg_{0.09}Mn^{2+}_{0.02})^{VI}$ $O_{10}(OH)_2$ $(Ca_{0.08}Mg_{0.26}Na_{0.08}K_{0.03})_{0.44}$	0.78	4.0	2.00	87	13	803.12
BB-59-3 Beidellite/*Illite type*	$(Si_{3.13}Al_{0.87})^{IV}$ $(Al_{1.87}Fe^{3+}_{0.09}Mg_{0.03}Mn^{2+}_{0.01})^{VI}$ $O_{10}(OH)_2$ $(Mg_{0.20}K_{0.49})_{0.70}$	0.91	4.0	2.00	96	4	772.88

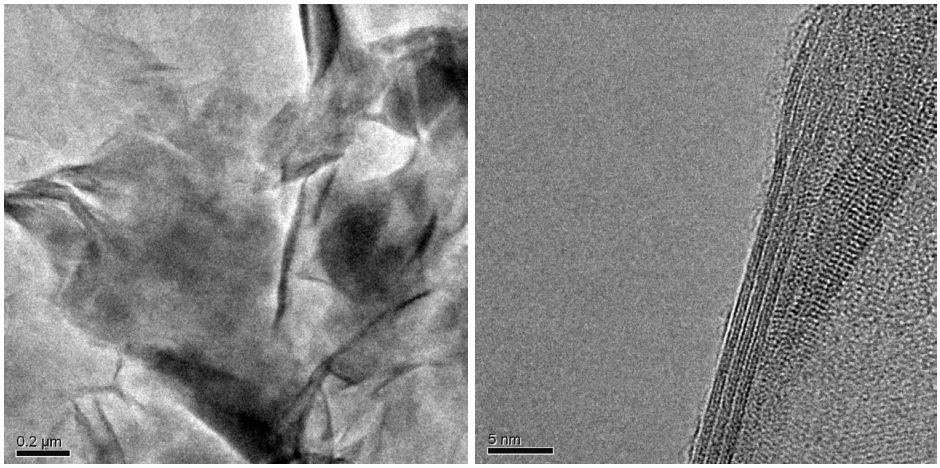

Fig. 91: TEM images from < 2 µm clayey suspensions of the FEBEX Reference bentonite

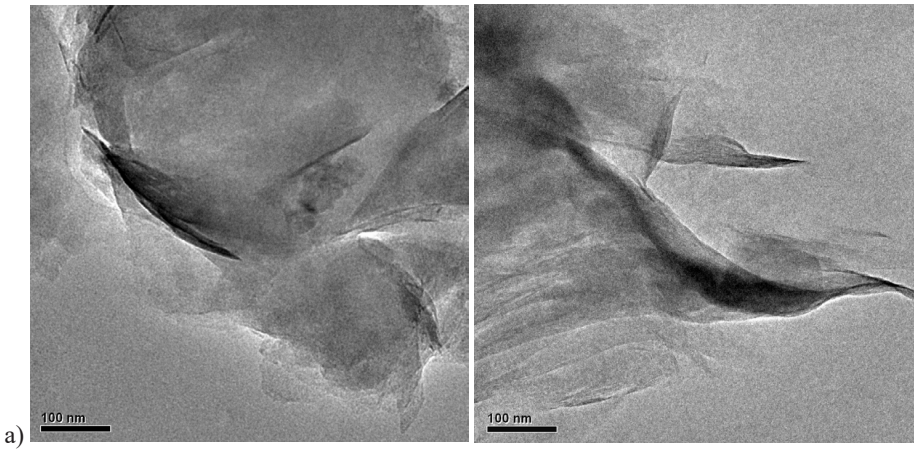

a) b)

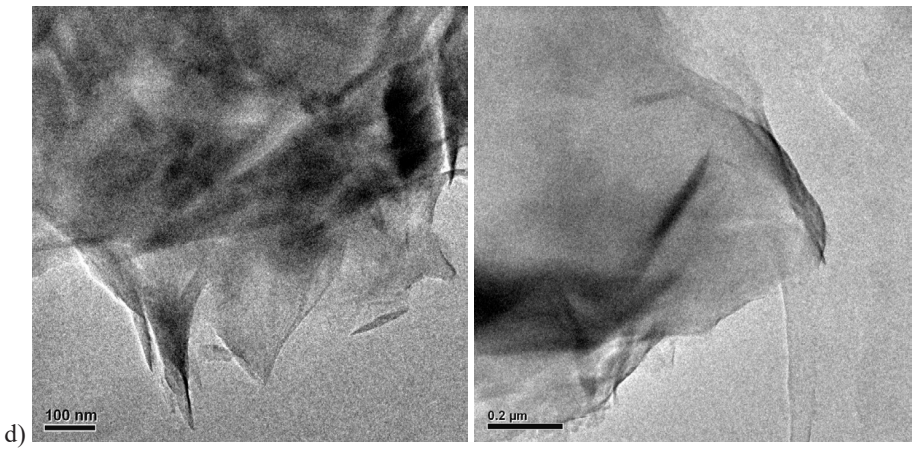

d) e)

Fig. 92: TEM images of < 2 µm montmorillonite clay particles obtained from clay suspensions from samples of different bentonite blocks: a) BB-36-1, b) BB-47-7, c) BB-53-3, d) BB-59-3

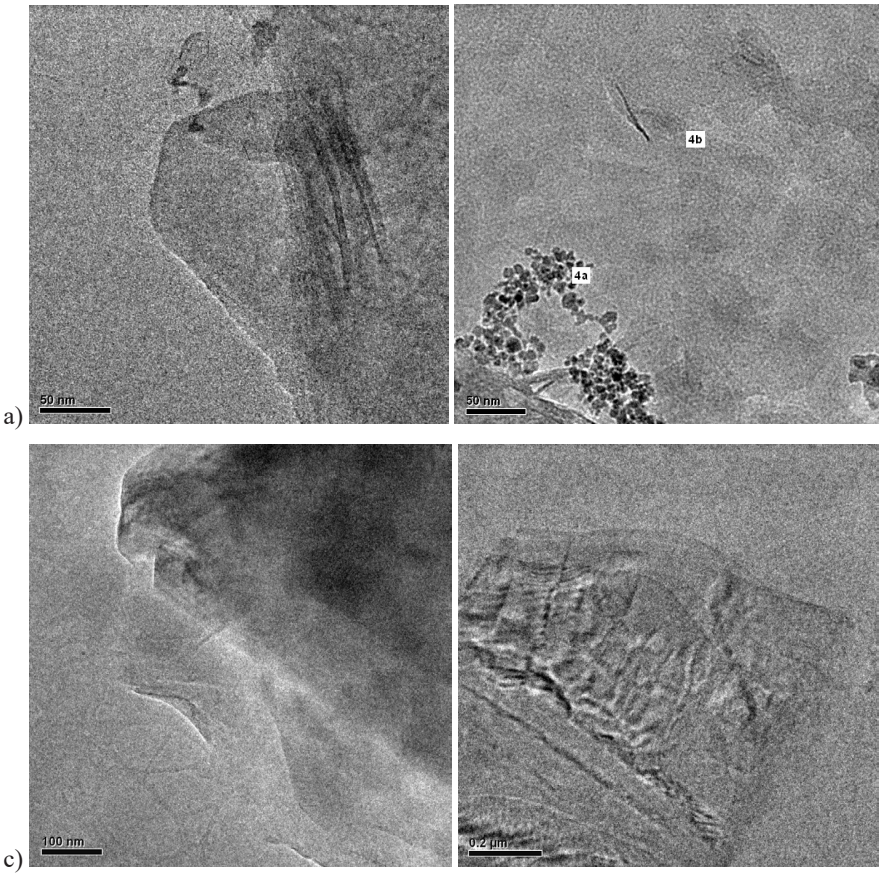

Fig. 93: TEM images of non-smectite particles from < 2 µm clayey suspensions: a) bentonite block BB-36-2: kaolinite type particle; b) bentonite block BB-36-3 red: nontronite type particle and/or iron colloids; c) bentonite block BB-47-9: illite particle; d) bentonite block BB-59-3: illite type particle

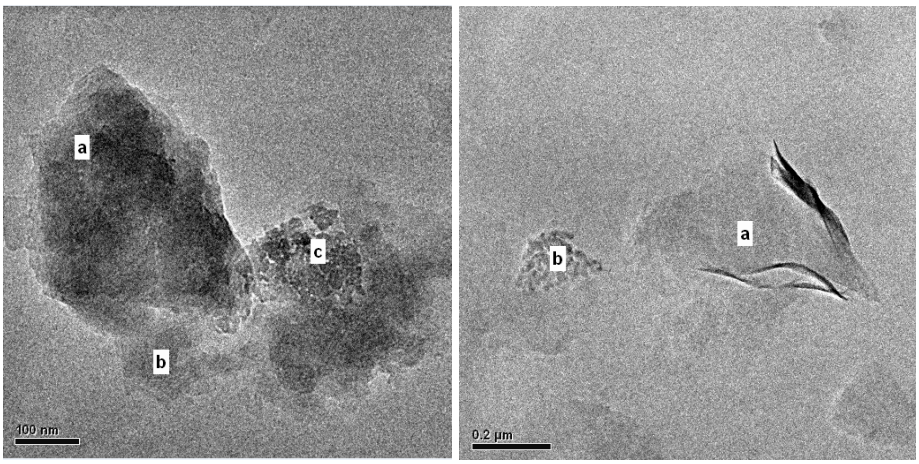

Fig. 94: TEM images from < 2 µm clayey suspensions of the bentonite block BB-59-5: a) silica colloids (a and c); smectite particle (b); b) smectite particle (a); silica colloids (b)

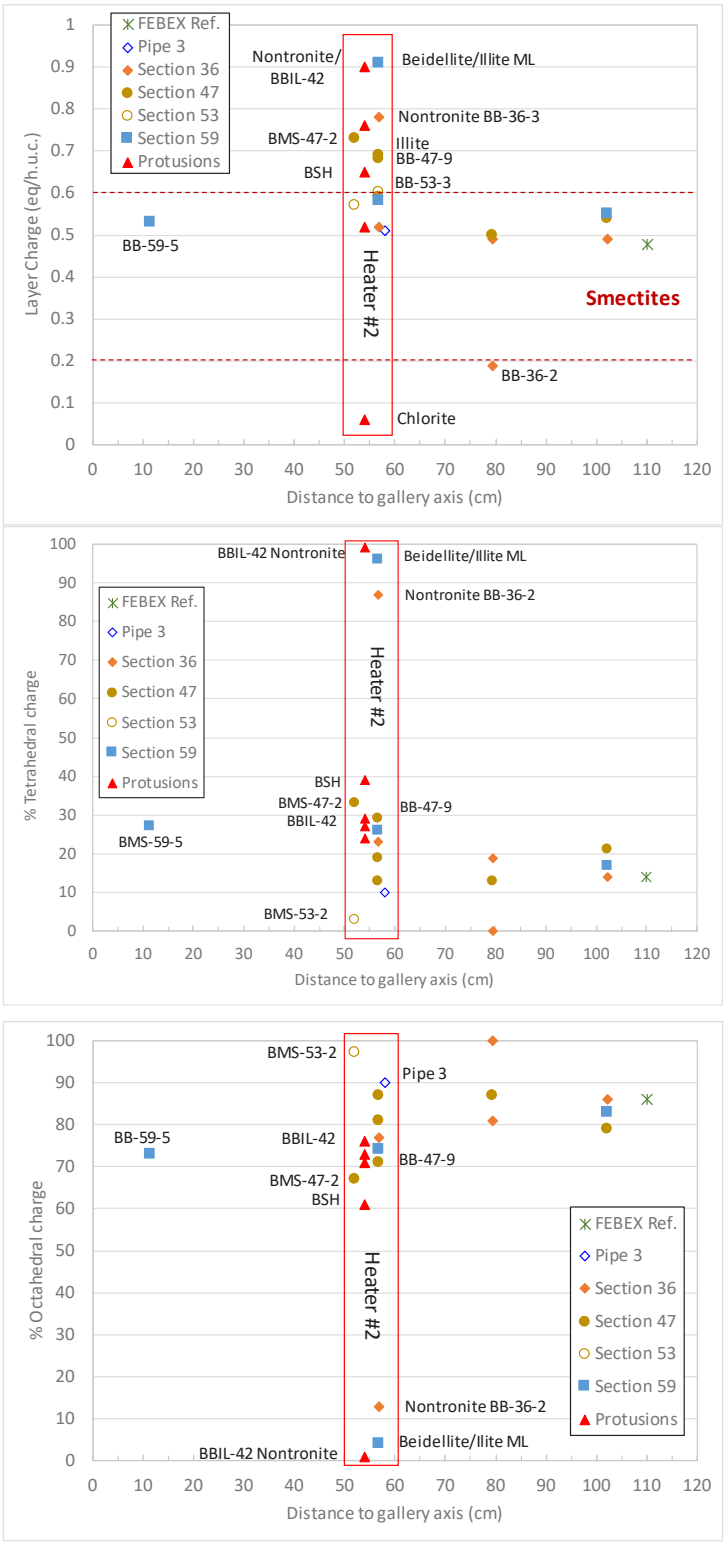

Fig. 95: Layer charge, % of tetrahedral charge and % of octahedral charge as a function of distance to the gallery axis determined by TEM analyses (Structural formula based on $O_{10}(OH)_2$ and maintaining the $\Sigma_{oct} = 2.0$)

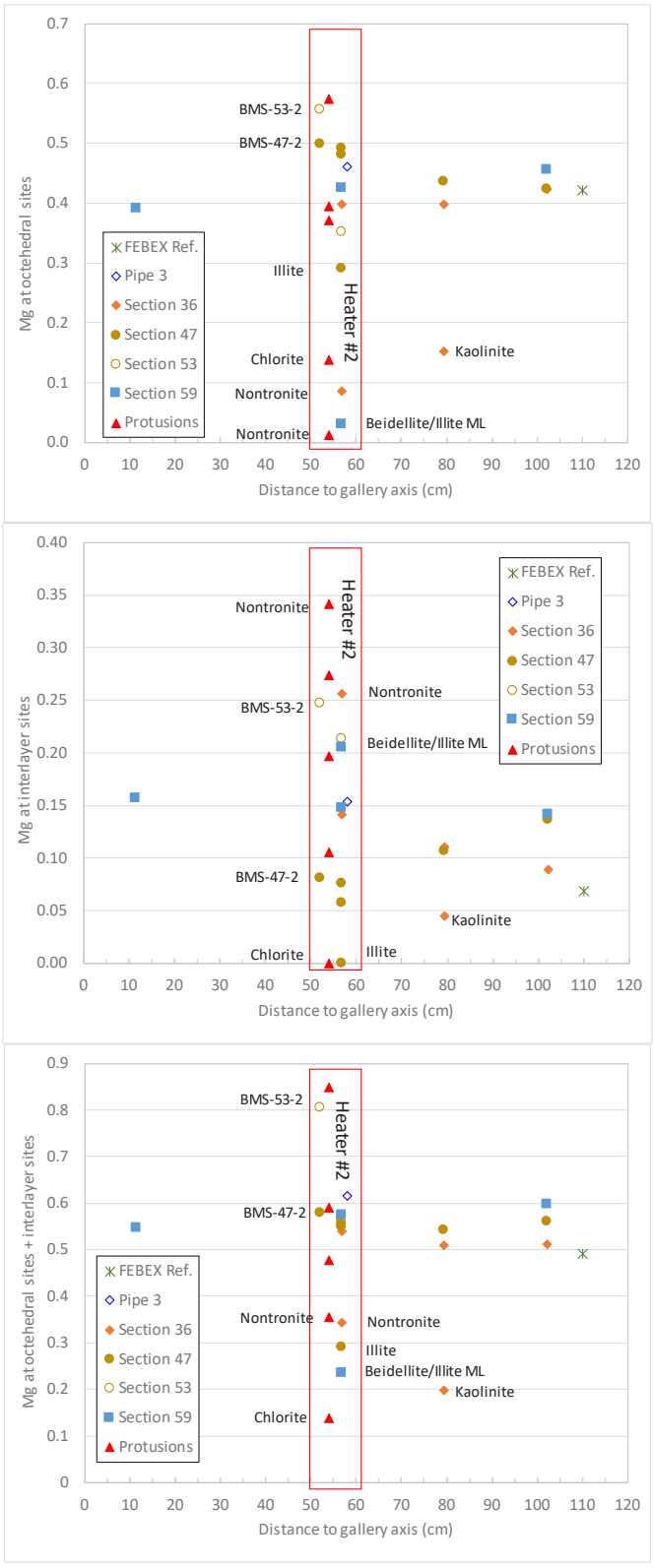

Fig. 96: Magnesium at octahedral sites, at interlayer charge and total as a function of distance to the gallery axis determined by TEM analyses (Structural formula based on $O_{10}(OH)_2$ and maintaining the $\Sigma_{oct} = 2.0$)

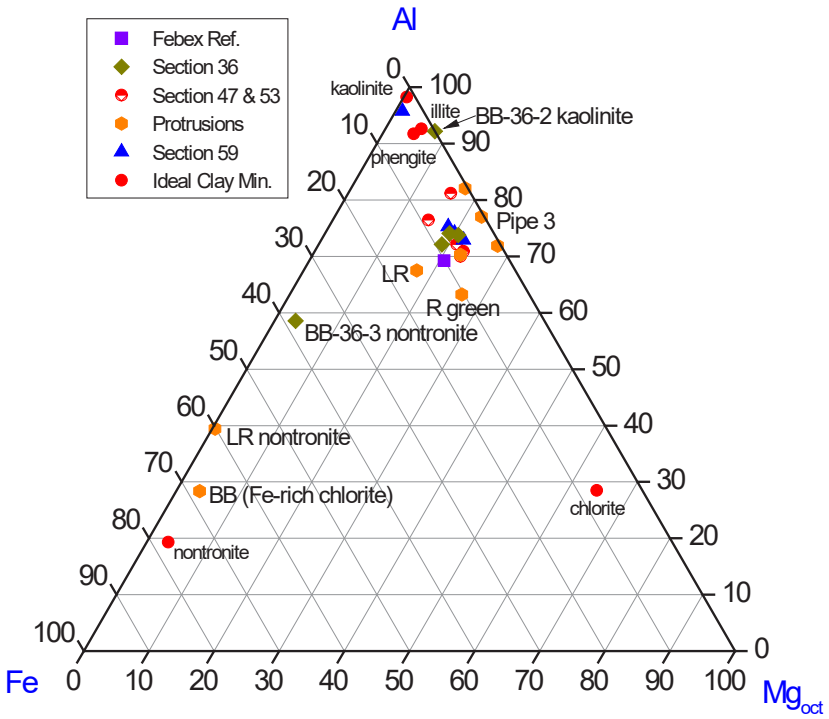

Fig. 97: TEM analysis: Octahedral Mg-Al-Fe ternary diagram for the FEBEX bentonite samples after dismantling Heater #2

In red: ideal clay minerals

Different ternary diagrams representing different systems were also analysed to identify a possible alteration in the structure of the smectite clay mineral particles. It should be taken into account that the structural formula used was that in which $\Sigma_{oct} = 2.0$ (Mg being at both octahedral and interlayer sites), which is the ideal case for dioctahedral smectite clay minerals (montmorillonite). In most of the samples analysed, when Σ_{oct} was not fixed to 2.0, Σ_{oct} ranged between 2.0 and 2.16, which indicates the main dioctahedral character of the samples and that this assumption can be considered properly. Mixtures of di- and tri- smectite clay minerals would tend to have a higher Σ_{oct} (at least between 2.5 and 3.0). More problematic is the Fe speciation for the determination of the di- and tri-character of the smectite. All Fe content was taken as Fe^{3+}, which cannnot be correct in samples close to Heater #2 or where corrosion processes are involved in the system. However, the presence of Fe^{2+} would increase the layer charge even more than what was calculated.

The system Mu-Py-Ce (Hower & Mowatt 1966)

The formation of I/S mixed-layer clay minerals through illitization of a smectitic clay has been described in a lot of works; the proportion of illite to smectite layers in the I/S ML and their layer ordering progressively increasing with increasing temperature and the amount of potassium in pore water (Meunier & Velde, 1989).

We have used the projection in the muscovite-celadonite-pyrophyllite system (Fig. 98) in order to determine the possible presence of interstratified illite/smectite. The interlayer charge of micas is between 0.95 and 1, whether it is of tetrahedral origin like in muscovite ($Si_3AlO_{10}Al_2(OH)_2K$) or of octahedral origin like in celadonite ($Si_4O_{10}AlFe^{2+}(OH)_2K$). Illites have an interlayer charge

between 0.75 and 0.95. When the charge is low (≤ 0.75), the solid solution becomes seemingly continuous but the crystallochemical properties of these minerals are those of illite/smectite mixed layers (Meunier 2005).

The ternary diagram representing the system Mu-Py-Ce for the retrieved FEBEX bentonite samples and the reference is shown in Fig. 99. Most of the samples typically belong to montmorillonites. However, some changes are observed as a function of distance to Heater #2. Samples close to Heater #2 (BB-53-3, BB-47-9), in contact with the liner (BMS-47-2) and protrusions increase the layer charge and enter in the stability of illite/smectite mixed-layers.

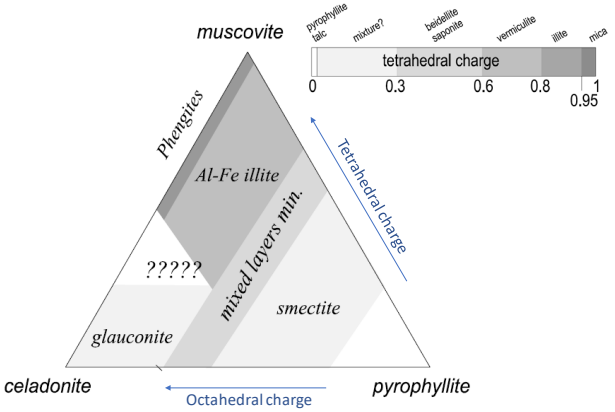

Fig. 98: Solid solution in the muscovite (Mu)- celadonite (Ce)-Pyrophyllite system (Hower & Mowatt 1966)

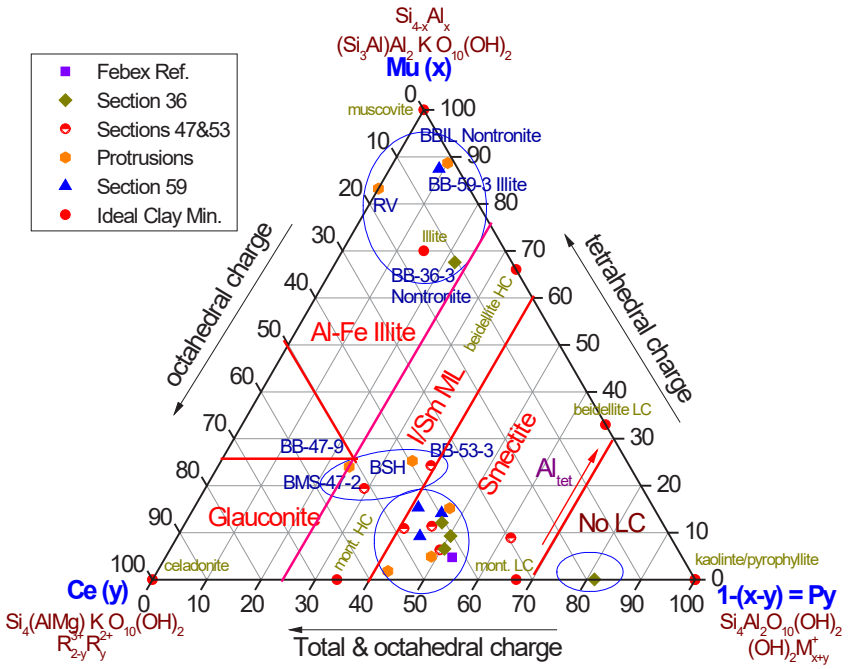

Fig. 99: TEM analysis: Solid solution in the muscovite (Mu)- celadonite (Ce)-Pyrophyllite system for the FEBEX bentonite samples after dismantling Heater #2

The system M^+-4Si-R^{2+} system (Velde 1985)

The system M^+-4Si-R^{2+} is used to characterize: a) the chemical composition of discrete illites, smectites and I/S mixed-layer minerals; i.e., changes in composition of I/S ML, and b) the beidellite-montmorillonite-nontronite domain (Fig. 100). The M+ indicates the layer charge of ideal mica, the 4Si pole represents the maximum Si content of the tetrahedral sheet and the R2+ pole represents the number of divalent cations in the octahedral position.

The typical charge of smectites varies between 0.3 and 0.6 per Si4O10, and a complete solid solution exists between smectites with octahedral charge (montmorillonites) and smectites with tetrahedral charge (beidellites). An increase of layer charge between 0.60 and 0.75 may indicate the existence of illite/smectite mixed layers of different chemical composition.

The ternary diagram representing the system M^+-4Si-R^{2+} for the reference and retrieved samples after dismantling of Heater #2 is shown in Fig. 101. In this diagram, four type of samples are observed. Most of the samples correspond to typical montmorillonites of medium charge as the reference sample, which increase the charge towards Heater #2. Illites and nontronites are represented at the left side of the diagram and chlorites at the bottom-right side of the diagram. Most of these other type of clay minerals belongs to samples at the liner contact and protrusion samples.

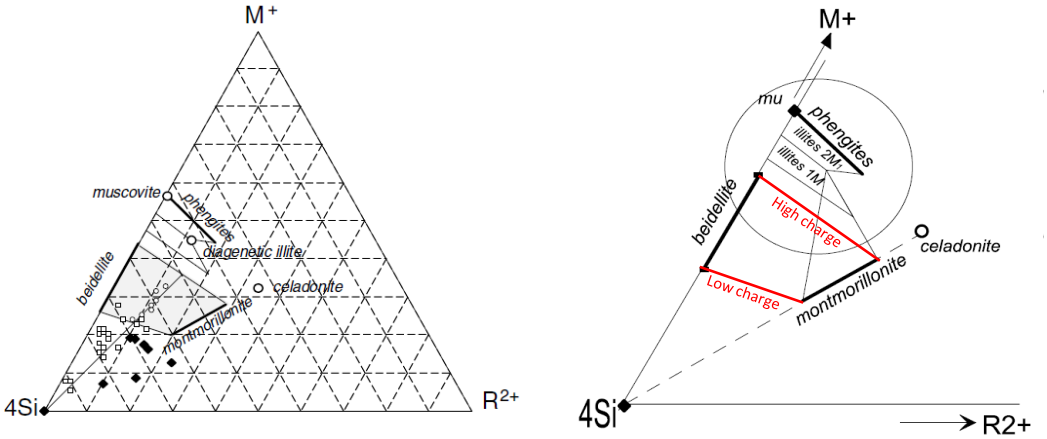

Fig. 100: Solid solution projection in the M^+-4Si-R^{2+} system (Meunier 2005): a) chemical composition of illite/smectite mixed-layers; b) chemical composition domain of beidellite (tetrahedral charge) and montmorillonite (octahedral charge)

The systems M^{+}-4Si-$3R^{2+}$ and MR^{3+}-$2R^{3+}$-$3R^{2+}$ (Velde 1985)

The systems M^{+} (or MR^{3+})-4Si-$3R^{2+}$ and MR^{3+}-$2R^{3+}$-$3R^{2+}$ were used to characterize di- and tri-octahedral smectites and/or trioctahedral smectites/chlorite mixed layers (Fig. 102 and Fig. 103). In both types of systems, the retrieved FEBEX bentonite samples indicate four groups of clay minerals (Fig. 104 and Fig. 105): typical smectites increasing the charge towards the heater contact (i.e. illite/smectite ML), illites and nontronites, a kaolinite and a chlorite. Most of the bentonite block samples correspond to typical montmorillonites. Towards the heater contact, an increase of the layer charge and the proportion of tetrahedral substitution was detected. Trioctahedral structures were not observed, except in the sample at the frontal part of Heater #2 where chlorite was found (Fig. 106). In any case, it must be taken into account that total iron content was considered as Fe(III), except for the chlorite sample in which Fe content was mainly Fe(II) as will be shown in Section 6.2.

According to the results and in spite of modifications in the structural formula with respect to the reference sample, an illitization process cannot be pointed out because of the low amount of potassium in the system; i.e., taken into account the potassium content in the structural formula and potassium content variations in the composition of cations at interlayer sites and in the pore water (see below). The observed structural modifications are related to changes in the cation composition at tetrahedral sheets (Si^{4+} being substituted by Al^{3+}) and an increase in the layer charge due to variations in the magnesium and iron content at octahedral sheets, especially in samples in contact with the liner/Heater #2 and in the protrusions samples.

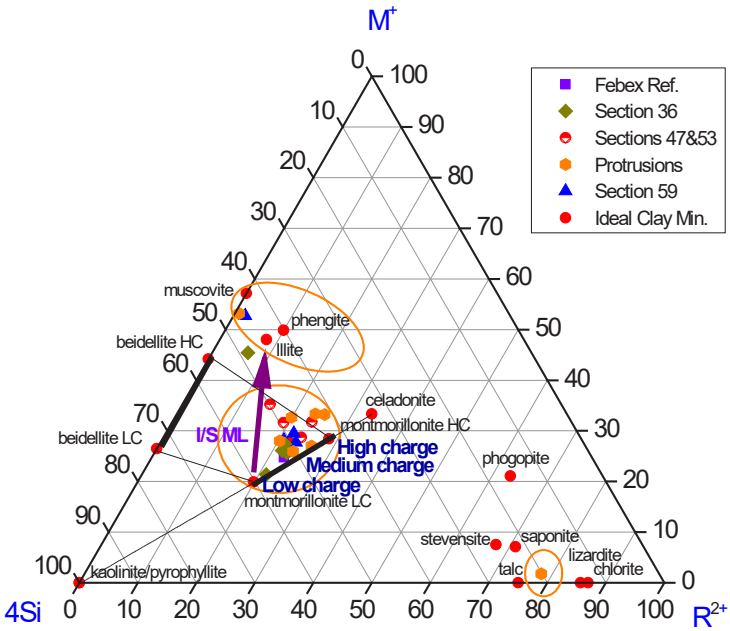

Fig. 101: TEM analysis: Solid solution projection in the M^{+}-4Si-R^{2+} system for the reference and retrieved samples from the dismantling of Heater #2

In red: ideal clay minerals

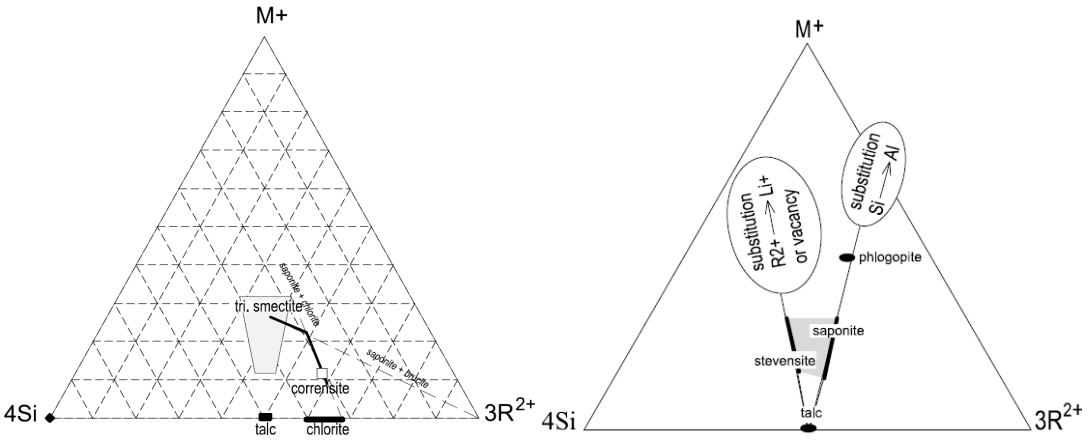

Fig. 102: Solid solution projection in the M^{+}-4Si-$3R^{2+}$ system: a) representation of a series of trioctahedral smectites and saponite/chlorite mixed layers, and b) representation of the compositional range of the theoretical solid solution of tetrahedral smectites limited by saponites (tetrahedral charge) and by stevensite-hectorite series (Meunier 2005)

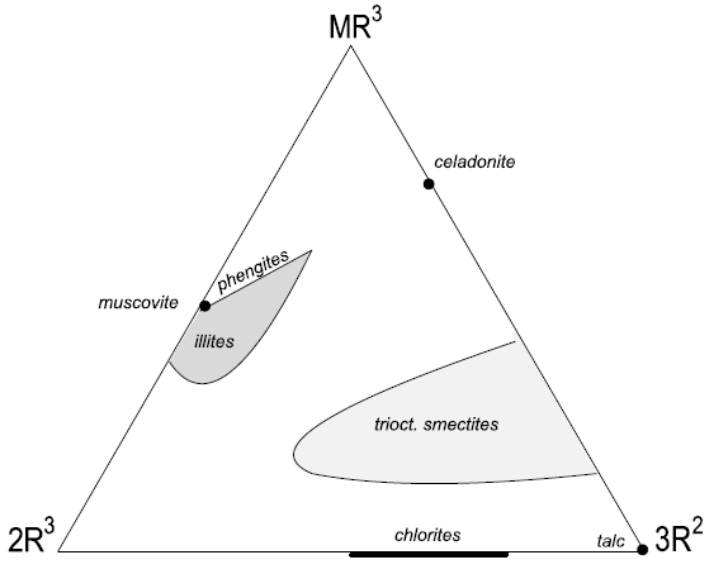

Fig. 103: Solid solution projection in the MR^{3+}-$2R^{3+}$-$3R^{2+}$ system representing the compositional range of the theoretical solid solution of tetrahedral smectites (Velde 1985)

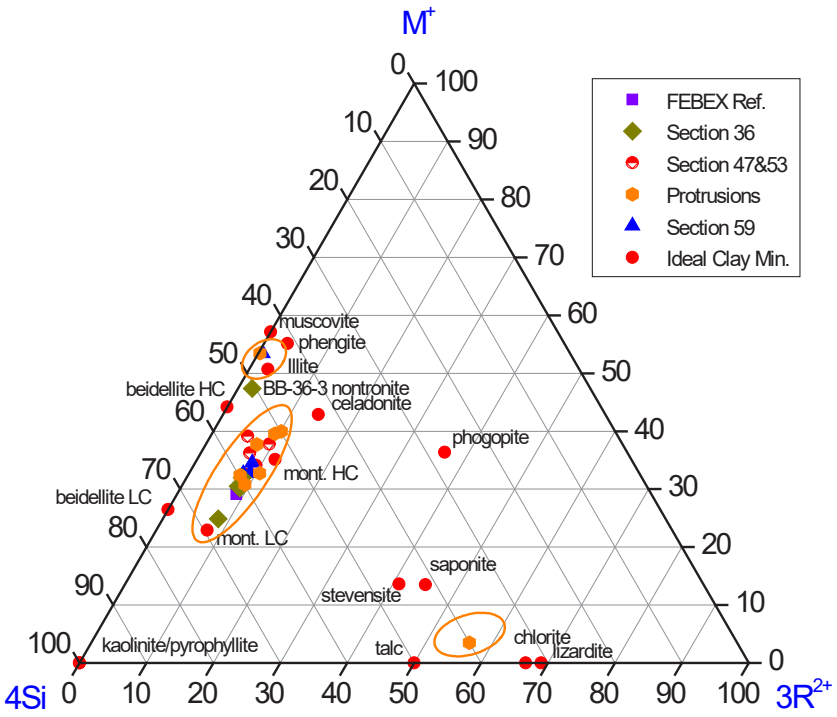

Fig. 104: TEM analysis: Solid solution projection in the M^{+}-4Si-$3R^{2+}$ system for the reference and retrieved samples from the dismantling of Heater #2

In red: ideal clay minerals

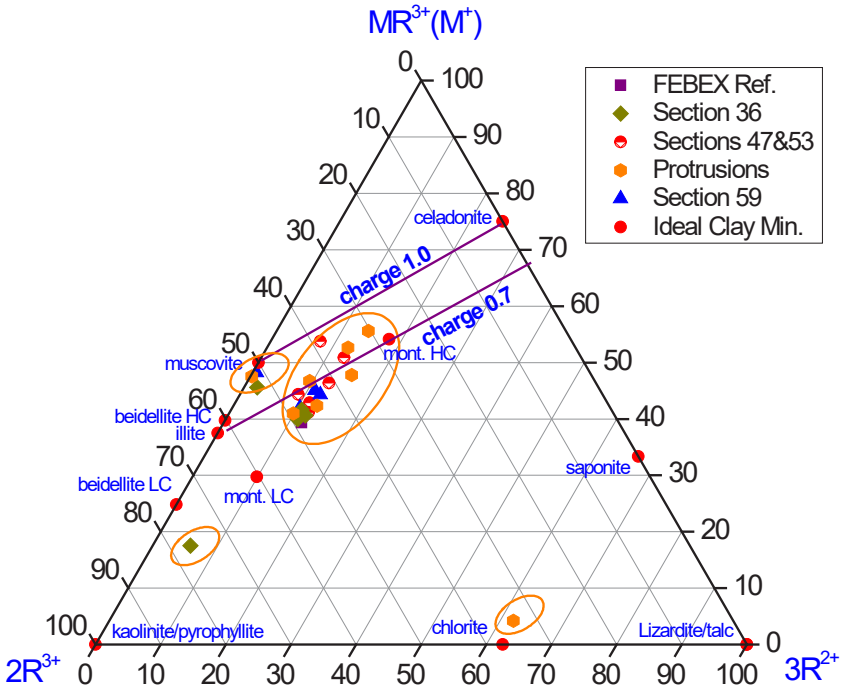

Fig. 105: TEM analysis: Solid solution projection in the MR^{3+}- $2R^{3+}$-$3R^{2+}$ system for the reference and retrieved samples from the dismantling of Heater #2

In red: ideal clay minerals

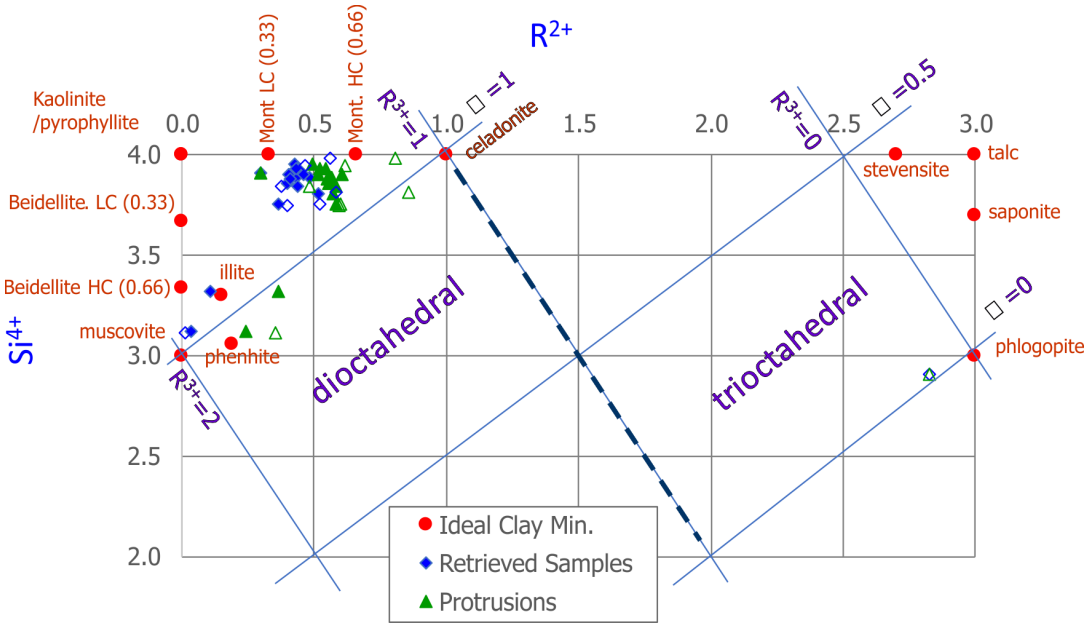

Fig. 106: Chemical projection system from dioctehedral to trioctahedral 2:1 clay minerals enabling substitutions of $2R^{3+} + \square \Rightarrow 3R^{2+}$. All Fe content was taken as Fe(III), except for the chlorite sample that was taken as Fe(II); $\square$: vacancy, unit Structural formula calculated on the Si_4O_{10} basis for 2:1 minerals, Wiewiora 1990)

Closed points: structural formula determined by maintaining the sum of octahedral cations at 2. open symbols: structural formula not fixing the octahedral cations to 2.0 (i.e., no Mg at interlayers)

SEM analyses

Different samples were analysed by scanning electron microscopy (SEM) with the aim of analysing the main and accessory minerals in the bentonite, as well as the microstructure and crystallochemistry of the clay minerals:

- Section 36
  - ✓ Bentonite Ring 1 (close to the granite interface): BB-36-1
  - ✓ Bentonite Ring 2: BB-36-2, BB-36-5
  - ✓ Bentonite Ring 3: BB-36-6
- Section 47
  - ✓ Bentonite Ring 1 (close to the granite interface): BB-47-4, BB-47-7
  - ✓ Bentonite Ring 2: BB-47-2, BB-47-5, BB-47-8
  - ✓ Bentonite Ring 3 (close to the heater interface): BB-47-6, BB-47-9
- Section 53
  - ✓ Bentonite Ring 3 (close to the heater interface): BB-53-3, BB-53-9

- Section 59
  - ✓ Bentonite Ring 1 (close to the granite interface): BB-59-1, BB-59-6
  - ✓ Bentonite Ring 2: BB-59-2
  - ✓ Bentonite Ring 3: BB-59-3
  - ✓ Bentonite Ring 4: BB-59-4
  - ✓ Bentonite Ring 5: BB-59-14

The results are summarised in Tab. 11. The SEM photomicrographs as well the crystallochemical formula of the clay minerals analysed for the different samples are shown in Appendix B. The major mineral phases are smectite, quartz and feldspars. In general, the accessory minerals found are: carbonates, sulphates, zircon, monazite, biotite, muscovite, ilmenite and apatite, which are also found in the FEBEX bentonite reference sample. In other retrieved samples, and as a function of the location in the bentonite barrier, other mineral phases were detected:

- In Section 36 at the shotcrete contact (Fig. 107): dolomite, magnesite, Fe-carbonates, Fe-oxides, Fe-Cr-Ni-Zn-Cu oxides, organic matter (C), N, portlandite, ettringite. Regarding clay minerals, increases of K and Mg in the structure were found, as well as changes in the Al/Si ratio at tetrahedral sheets.
- In the heated Section 47 (Fig. 108): Fe-carbonates, Fe-, Cu-, Zn-sulphides, Fe-oxides, OM
- In the heated Section 53 (Fig. 108): Fe(Ti,Mn)-oxides, OM, NaCl, Ca-sulphates
- In the non-heated Section 59 (Fig. 109): Dolomite, barite, Fe-carbonates, sulphates, sulphur, Fe-oxides, OM

Tab. 11: Major mineral phases and accessory minerals observed by SEM in bentonite blocks from one radius (Ring 1: granite contact, Ring 2: second block, and Ring 3: third block, i.e. at the heater contact)

H: Hydrated; H&H: Hydrated and Heated

Mineral phases	**Section 36 at shotcrete contact** (H)			**Section 47 and Section 53** (H&H)			**Section 59** (H)
	Ring 1	**Ring 2**	**Ring 3**	**Ring 1**	**Ring 2**	**Ring 3**	**Along R1 radius**
$Ca(OH)_2$	BB-36-1	--	--	--	--	--	--
Ca-carbonates	BB-36-1	BB-36-2 BB-36-5	--	BB-47-4	BB-47-2 BB-47-5 BB-47-8	--	BB-59-1/BB-59-6 BB-59-2 BB-59-14
Dolomite	BB-36-1	BB-36-2 BB-36-5	--	--	--	--	BB-59-3
Magnesite		BB-36-5	--	--	--	--	--
Fe-carbonates	BB-36-1	BB-36-2 BB-36-5	--	BB-47-7	BB-47-2	BB-47-9 BB-53-3	BB-59-6 BB-59-2 BB-59-3 BB-59-4
Cu,Zn-carbonates	--	--	--	--	--	BB-53-9	BB-59-6
Ca-sulphates		BB-36-2 BB-36-5	BB-36-6	BB-47-7	BB-47-2 BB-47-5 BB-47-8	BB-47-6 BB-53-3 BB-53-9	BB-59-2 BB-59-14
Ba(Sr)-sulphates	BB-36-1	BB-36-2 BB-36-5	BB-36-6	BB-47-7	BB-47-2 BB-47-5 BB-47-8	BB-47-9 BB-53-9	BB-59-6 BB-59-2 BB-59-3 BB-59-14
Sr(Ba)-sulphates	--	--	--	--	BB-47-2	--	--
Fe-sulphides	--	--	BB-36-6	BB-47-7	BB-47-8	BB-47-6 BB-47-9	--
ZnS or PbS	--	--	--	--	BB-47-8		BB-59-6
Fe, Cu-S	--	--	--	--	--	BB-47-9 BB-53-9	--
S	--	--	--	--	--	--	BB-59-6
Fe-oxides	BB-36-1	BB-36-2 BB-36-5	BB-36-6	BB-47-7	BB-47-2 BB-47-5	BB-47-6 BB-47-9 BB-53-3 BB-53-9	BB-59-1/BB-59-6 BB-59-2 BB-59-3 BB-59-4 BB-59-14
Fe-Cr-oxides	BB-36-1	--	--	--	BB-47-2	--	--
Zn-Cu-Sn-Ni-Oxides	BB-36-1	--	--	--	BB-47-2	--	BB-59-2
Mn,Ba-oxides	--	--	--	--	--	--	BB-59-3 BB-59-14

Tab. 11: Cont.

Mineral phases	**Section 36 at shotcrete contact** (H)			**Section 47 and Section 53** (H&H)			**Section 59** (H)
	Ring 1	**Ring 2**	**Ring 3**	**Ring 1**	**Ring 2**	**Ring 3**	**Along R1 radius**
Ilmenite	BB-36-1	BB-36-2 BB-36-5	BB-36-6	BB-47-4 BB-47-7	BB-47-2 BB-47-5 BB-47-8	BB-47-6 BB-47-9 BB-53-3 BB-53-9	BB-59-1/BB-59-6 BB-59-2 BB-59-3 BB-59-4
Zircon	BB-36-1	BB-36-2 BB-36-5		BB-47-7	BB-47-2	BB-47-6 BB-47-9 BB-53-9	BB-59-6 BB-59-2
Monazite	BB-36-1	BB-36-2 BB-36-5	BB-36-6	BB-47-7	BB-47-2	BB-47-6 BB-53-3	BB-59-1 BB-59-2 BB-59-4
Silica	BB-36-1	BB-36-2 BB-36-5		BB-47-7	BB-47-5	BB-47-9 BB-53-3 BB-53-9	BB-59-1/BB-59-6 BB-59-3 BB-59-4 BB-59-14
Plagioclases	BB-36-1	BB-36-2 BB-36-5	BB-36-6	BB-47-4 BB-47-7	BB-47-2 BB-47-5 BB-47-8	BB-47-9 BB-53-3	BB-59-1/BB-59-6 BB-59-2 BB-59-3 BB-59-4 BB-59-14
K-feldspars	BB-36-1	BB-36-2 BB-36-5	BB-36-6	BB-47-7	BB-47-2 BB-47-8	BB-53-3	BB-59-1/BB-59-6 BB-59-2 BB-59-14
Biotite	BB-36-1	BB-36-2 BB-36-5	BB-36-6	BB-47-7	BB-47-2	BB-47-6 BB-47-9	BB-59-1/BB-59-6 BB-59-2 BB-59-3 BB-59-4
Muscovite	BB-36-1	BB-36-5	--	--	--	--	--
Apatite	BB-36-1	BB-36-2 BB-36-5	BB-36-6	BB-47-4	BB-47-2 BB-47-5 BB-47-8	BB-47-6 BB-47-9 BB-53-3	BB-59-1/BB-59-6 BB-59-2 BB-59-3 BB-59-4 BB-59-14
Organic matter (OM)	BB-36-1	BB-36-2 BB-36-5	BB-36-6	BB-47-7	BB-47-2 BB-47-5	BB-47-9 BB-53-3 BB-53-9	BB-59-1/BB-59-6 BB-59-2 BB-59-4
Microorganisms	--	BB-36-5	BB-36-6	BB-47-4 BB-47-7	--	--	BB-59-1/BB-59-6 BB-59-2
C, N	BB-36-1	--	--	--	--	--	BB-59-3
Zeolites	--	BB-36-2 BB-36-5	--	BB-47-4? BB-47-7?	--	--	--

Tab. 11: Cont.

Mineral phases	**Section 36 at shotcrete contact** (H)			**Section 47 and Section 53** (H&H)			**Section 59** (H)
	Ring 1	**Ring 2**	**Ring 3**	**Ring 1**	**Ring 2**	**Ring 3**	**Along R1 radius**
Smectite	BB-36-1	BB-36-2 BB-36-5	BB-36-6	BB-47-4 BB-47-7	BB-47-2 BB-47-5 BB-47-8	BB-47-6 BB-47-9 BB-53-3 BB-53-9	BB-59-1/BB-59-6 BB-59-2 BB-59-3 BB-59-4 BB-59-14
Other clay minerals	BB-36-1	BB-36-2	BB-36-6	--	--	BB-53-9	--

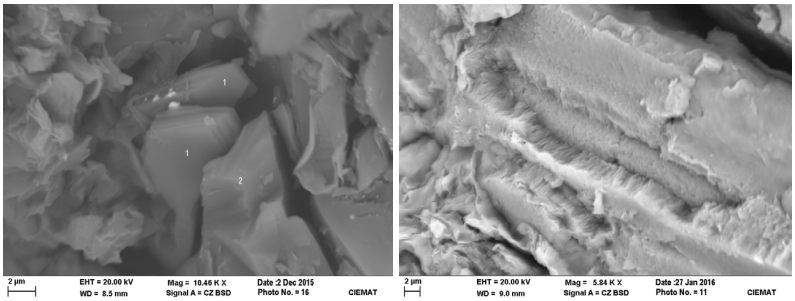

BB-36-1 (black halo): chlorites (1) BB-36-1 (shotcrete contact): Mg-rich smectite

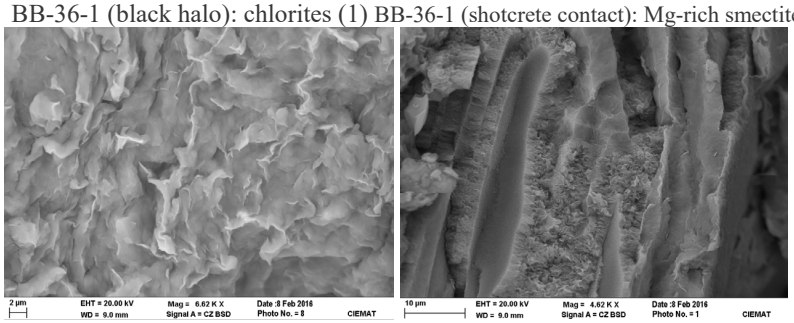

BB-36-2: FEBEX montmorillonite BB-36-2: FEBEX montmorillonite

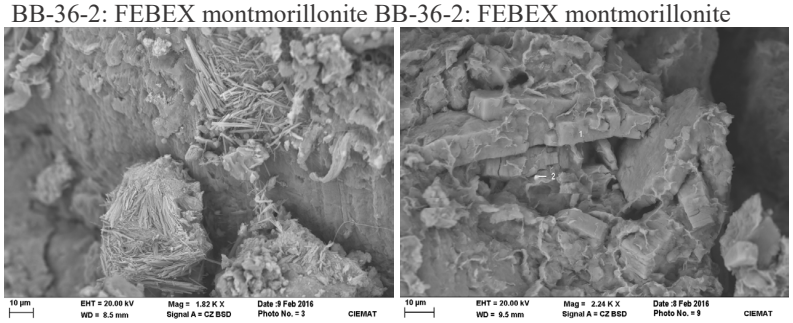

BB-36-2: Ettringite BB-36-2: Ca-sulphates

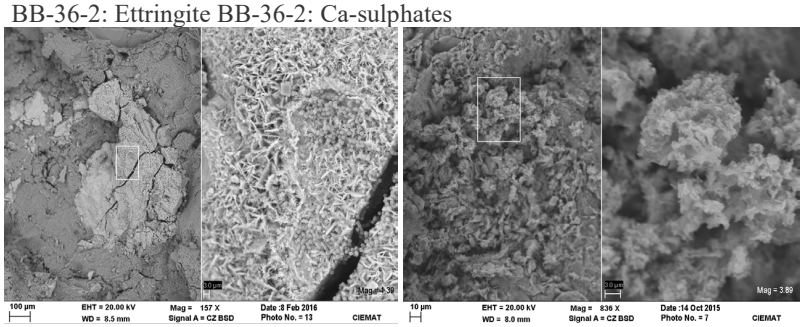

BB-36-2: Fe-carbonates BB-36-5: Magnesite

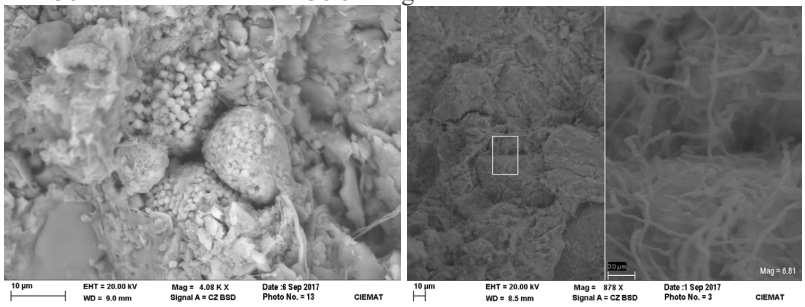

BB-36-6: Fe-sulphides and Fe-oxides BB-36-6: microorganisms

Fig. 107: SEM photomicrographs of samples from Section 36 in contact with the shotcrete

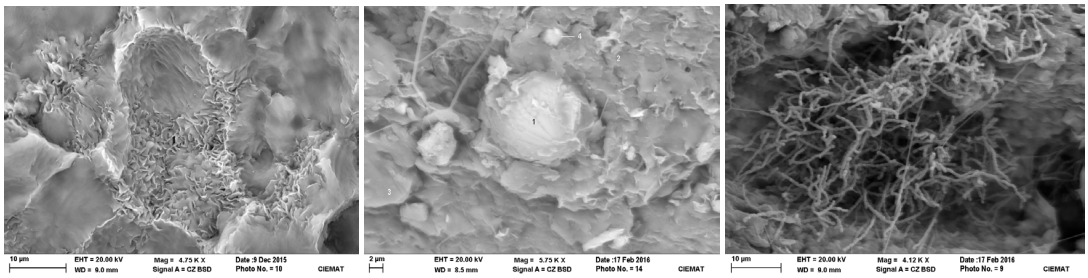

BB-47-7: Montmorillonite BB-47-7**:** Fe-carbonate (1), Fe,S (4) BB-47-4: microorganisms

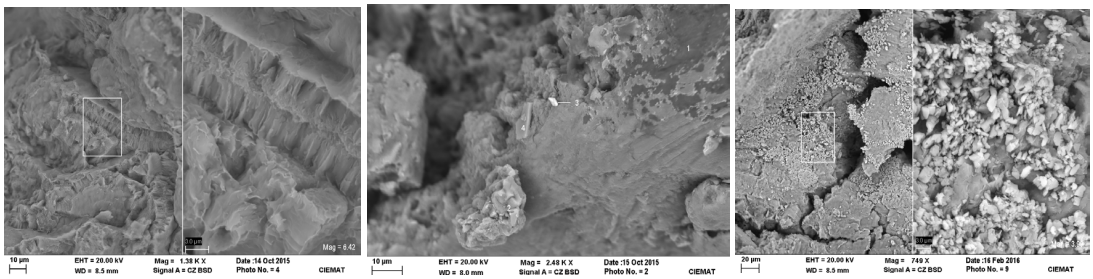

BB-47-2: Montmorillonite BB-47-2: OM (1), Ca-(2),Fe-(3)-CO_3, Plag (4) BB-47-5: Ca-sulphates

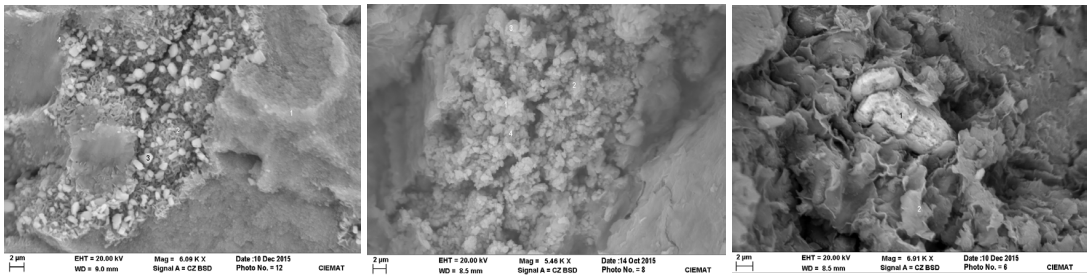

BB-47-8: Ca-sulphates BB-47-8: Ca-carbonates BB-47-8: S, Fe-sulphides (1)

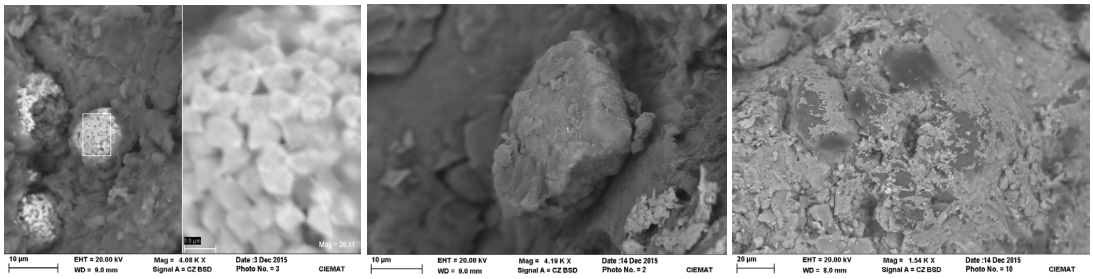

BB-47-6: Fe, S BB-47-9: Fe-carbonate (1) BB-47-9: organic matter

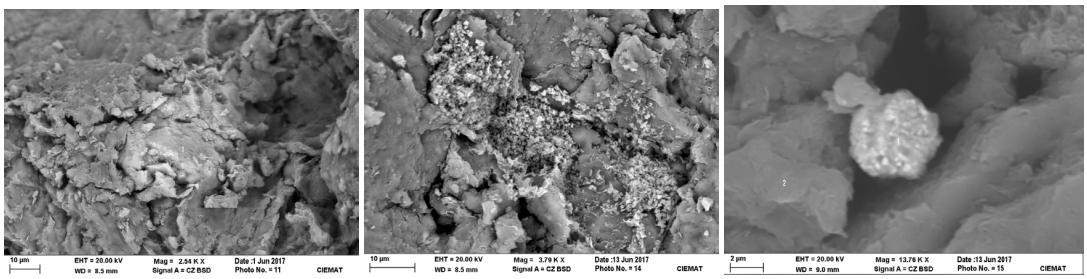

BB-53-3: Fe-carbonate BB-53-9: Ca-sulphates BB-53-9: Fe, S

Fig. 108: SEM photomicrographs of samples from Section 47 and 53 in contact with Heater #2

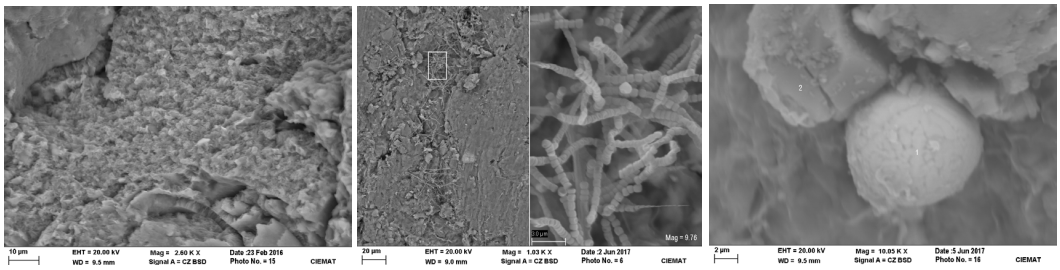

BB-59-1: Montmorillonite BB-59-6: microorganisms BB-59-6: Fe-carbonate

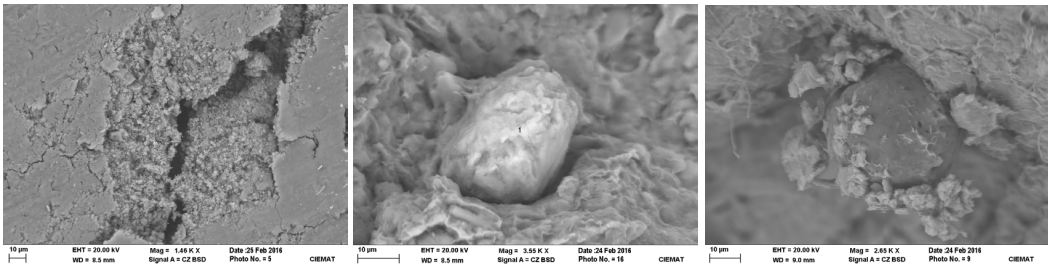

BB-59-2: Ca-carbonates BB-59-2: Fe-carbonates BB-59-2: OM (C) and S

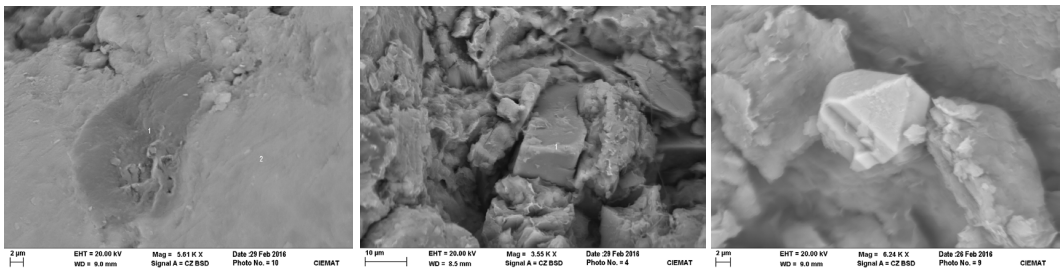

BB-59-3: C,N (1), smectite (2) BB-59-3: dolomite (1) BB-59-3: Fe-carbonate, Fe-oxides

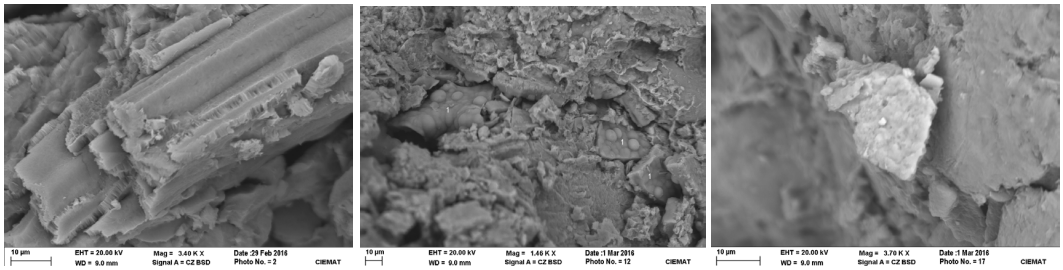

BB-59-4: Smectite BB-59-4: Silica BB-59-4: Fe-carbonate

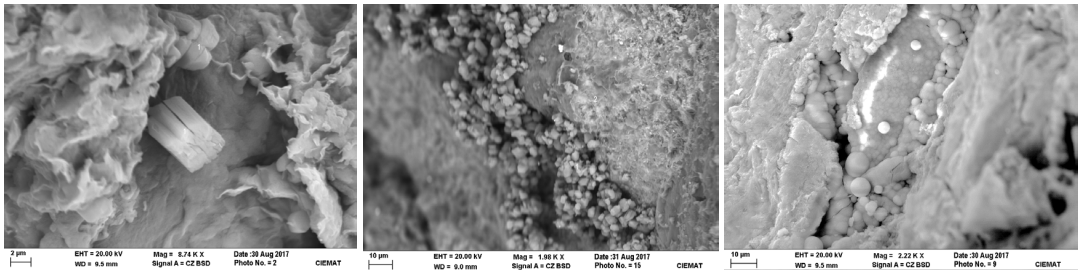

BB-59-14: Ca-sulphates (1) BB-59-14: Ca-sulphates (1), Fe-oxides (2) BB-59-14: silica

Fig. 109: SEM photomicrographs of samples from Section 59 (hydrated section)

Based on the semi-quantitative EDX atomic composition, the Structural formula for the clay minerals were calculated only to compare the relative ratios between elements in each clay mineral particle found by SEM (see Appendix B). These may help to identify possible alteration in the structure of the smectite clay mineral. Therefore, different ternary diagrams representing different systems were also analysed (Fig. 110 to Fig. 115), as it was done with the TEM analyses.

The ternary diagram Mg-Al-Fe was used to follow the possible changes of cations at octahedral sheets (Fig. 110 and Fig. 111). In order to determine the formation of I/S mixed-layer clay minerals or interstratified, the projection in the muscovite-celadonite-pyrophyllite system (Hower & Mowatt, 1966) was used. The system M^{+}-4Si-R^{2+} was used to characterize: a) the chemical composition of discrete illites, smectites and I/S mixed-layer minerals; and b) the beidellite-montmorillonite-nontronite domain. The systems M^{+} (or MR^{3+})-4Si-$3R^{2+}$ and MR^{3+}-$2R^{3+}$-$3R^{2+}$ were used to characterize di- and trioctahedral smectites and/or trioctahedral smectites/chlorite mixed layers (Fig. 114 and Fig. 115).

In the case of the SEM analyses, more samples and more chemical analyses of different clay particles were performed than by TEM, but similar patterns were found. Most of the clay mineral particles are in the same stability field of the smectite clay mineral as the reference sample, a montmorillonite (dioctahedral smectite). However, some particles deviate from the reference crystallochemical structure, especially the corroded samples from Section 36 (bentonite/shotcrete interface) and the samples close to the Heater #2 contact. The most significant changes observed in the smectite clay particles are related to changes in the cation composition at tetrahedral sheets, increase in magnesium and iron content at octahedral sheets (Fig. 110), and an interlayer charge above 0.6 eq/h.u.c., which is the limit for typical smectites (Fig. 112, Fig. 113). Other types of clay minerals were found corresponding to illite, nontronite and Fe-rich chlorite clay minerals.

According to Fig. 114 and Fig. 115 (see also Discussion Section), most of the bentonite block samples correspond to typical montmorillonites of medium charge as the reference sample, but there is an increase of layer charge towards Heater #2, as it is observed from the analyses of samples at the liner contact (BMS) and of protrusion samples. Towards the heater contact, an increase of the layer charge and the proportion of tetrahedral substitution was detected. Some of these samples are in the stability field of montmorillonites with a high layer charge (HC), increasing also the tetrahedral charge. Other samples belong to illite/smectite MLs, illites and chlorites. No trioctahedral structures were observed, except in the sample found at the frontal part of Heater #2 where chlorite was found (see Appendix B.2). In any case, it must be taken into account that speciation of Fe in Fe(II) and Fe(III) could not be performed, so the total iron content was considered as Fe(III), except for the chlorite sample in which Fe content was taken as Fe(II). Fe^{2+} instead of Fe^{3+} would increase the layer charge of the clay mineral.

As in the TEM analyses, the potassium content in the smectite mineral particles is very low so an illitization process can be ruled out. Only an increase of the layer charge and variations in the location of the charge were observed, due to Al substitutions at tetrahedral sheets and Mg and Fe substitutions at octahedral sheets, especially in samples close to the liner/Heater #2 contact and in the altered samples from Section 36 (shotcrete contact).

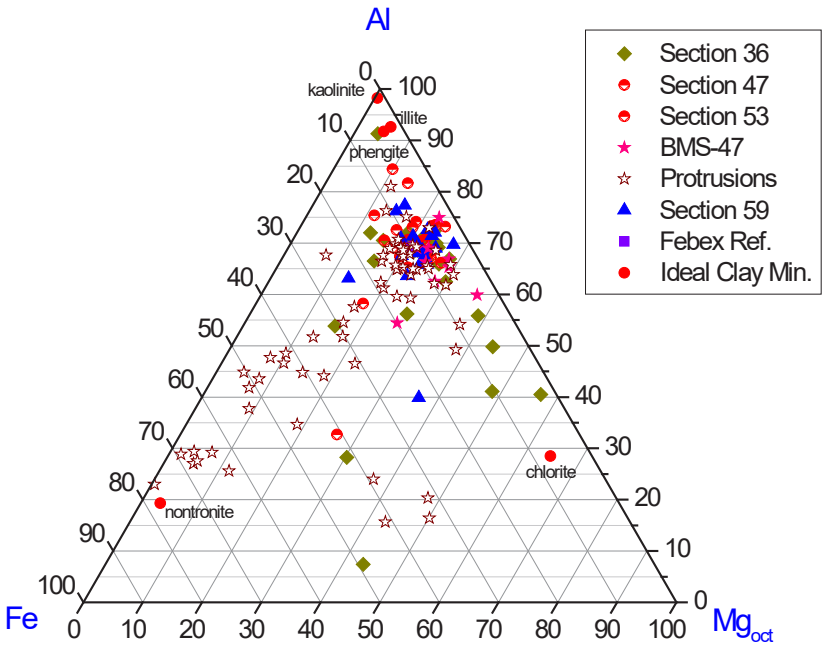

Fig. 110: SEM analysis: Octahedral Mg-Al-Fe ternary diagram for the FEBEX bentonite samples after dismantling Heater #2

In red: ideal clay minerals

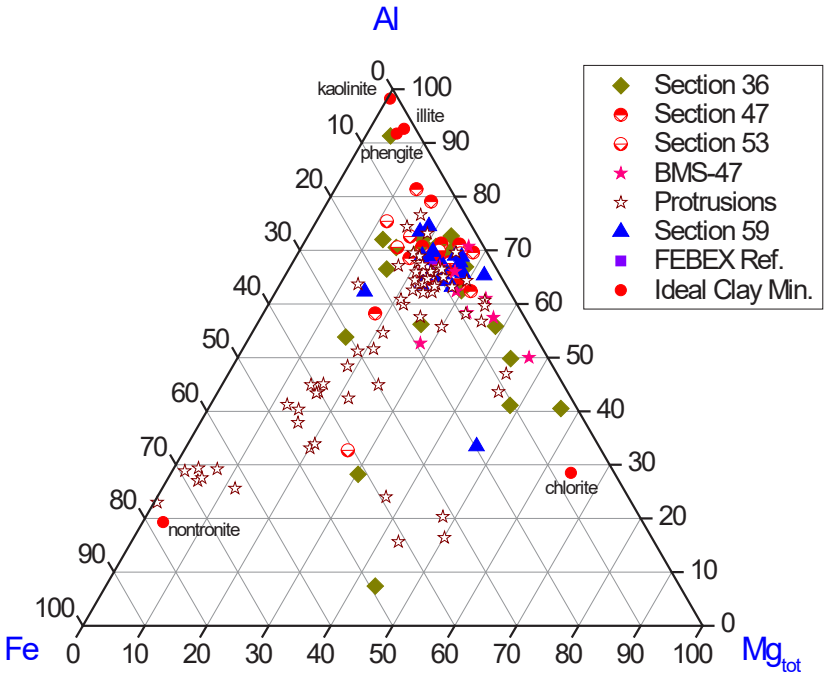

Fig. 111: SEM analysis octahedral Al-Fe-total Mg (octahedral+interlayer) ternary diagram for the FEBEX bentonite samples after dismantling Heater #2

In red: ideal clay minerals

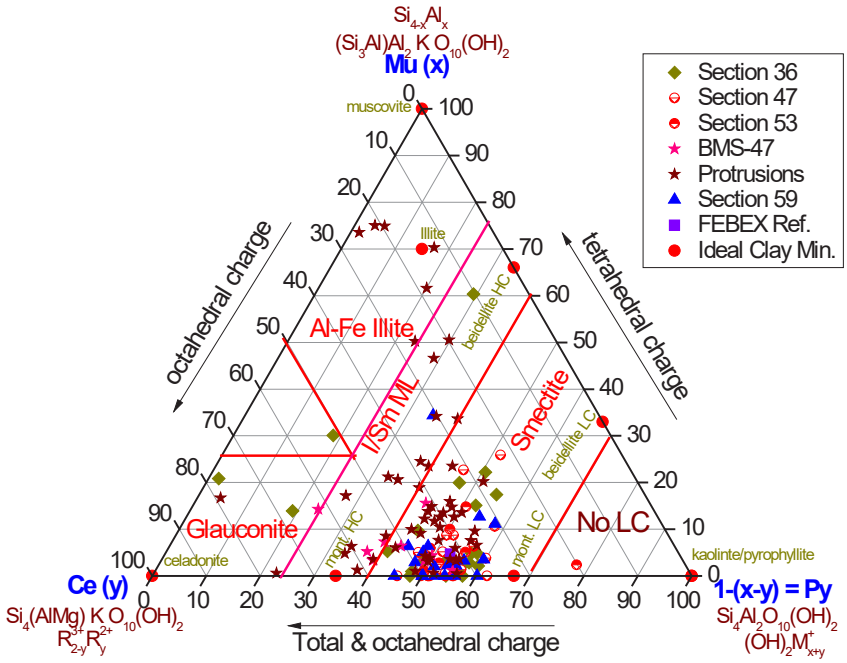

Fig. 112: Solid solution in the muscovite (Mu)- celadonite (Ce)-Pyrophyllite (Py) system for the FEBEX bentonite samples after dismantling Heater #2

Relative ionic compounds of clay particles obtained by SEM analysis

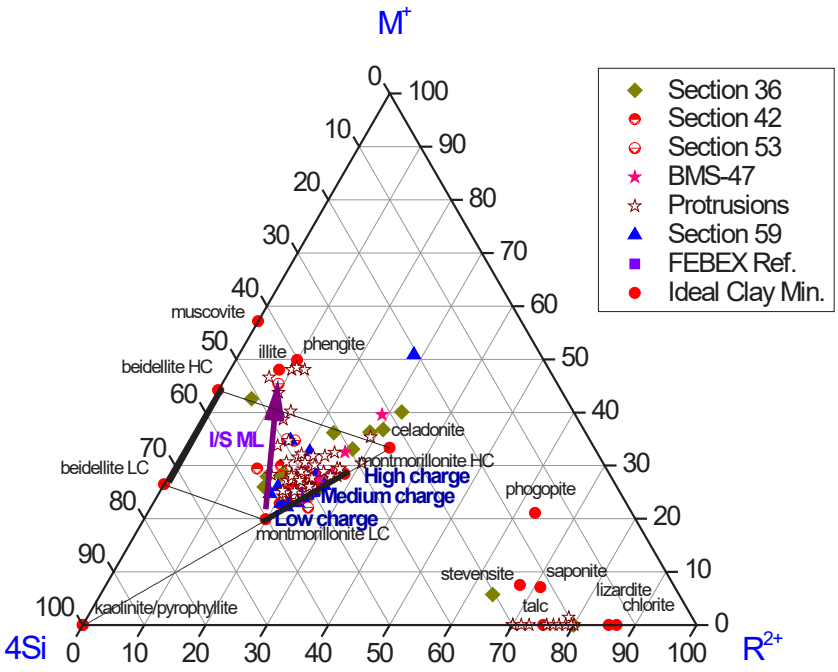

Fig. 113: Solid solution projection in the M+-4Si-R2+ system for the reference and retrieved samples from the dismantling of Heater #2

Relative ionic compounds of clay particles obtained by SEM analysis

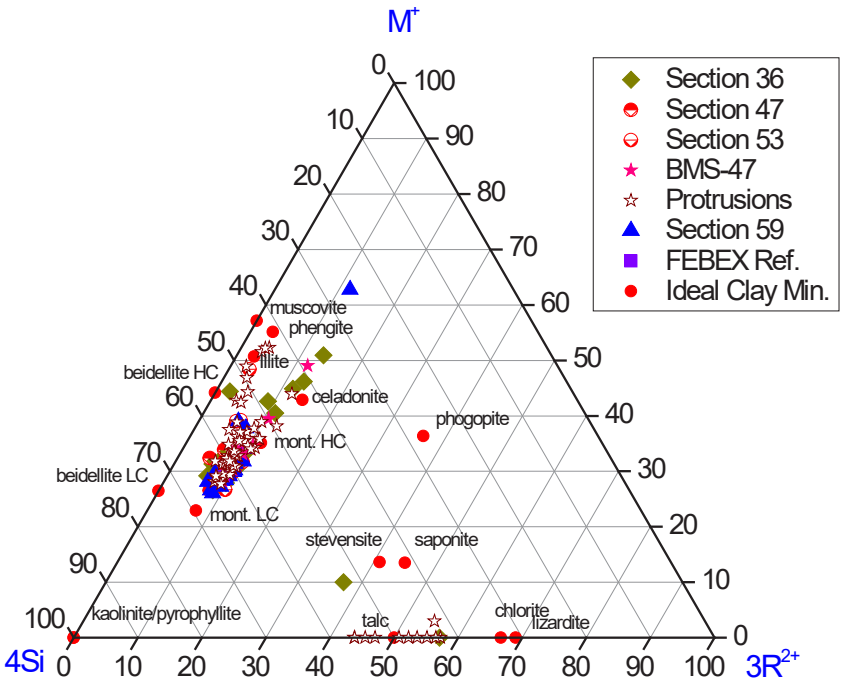

Fig. 114: SEM analysis: Solid solution projection in the M^+ - 4Si - $3R^{2+}$ system for the reference and retrieved samples from the dismantling of Heater #2

In red: ideal clay minerals

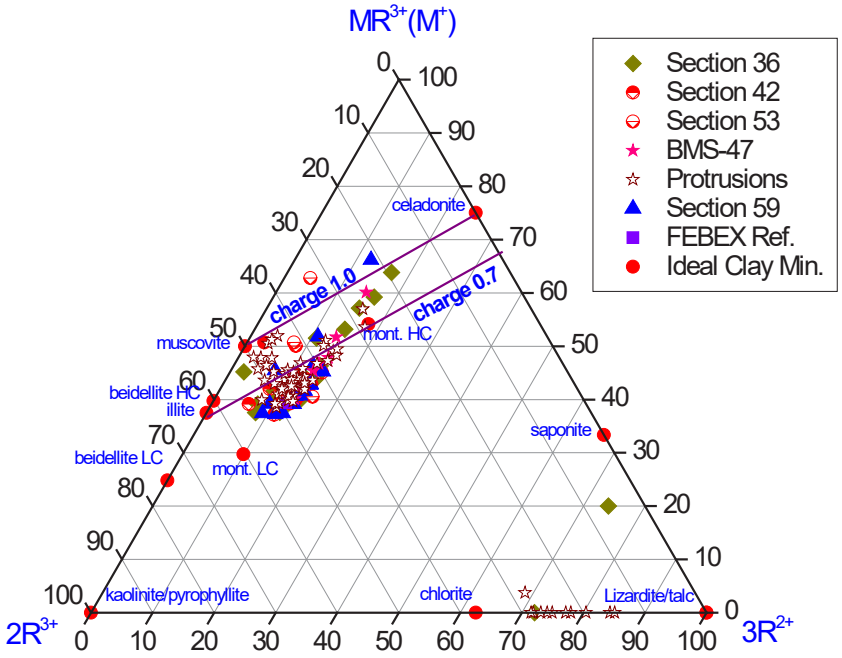

Fig. 115: SEM analysis: Solid solution projection in the MR^{3+}- $2R^{3+}$-$3R^{2+}$ system for the reference and retrieved samples from the dismantling of Heater #2

In red: ideal clay minerals

5.4 Geochemical analysis of the bentonite samples

5.4.1 Composition of the bentonite by X-Ray fluorescence

The bulk material was analysed by XRF. The chemical analyses of the main oxides for different bentonite samples are given in Tab. 12; for trace element concentrations please see Tab. C.5. and Tab. C.6 in Appendix C. As can be seen in Fig. 116, Fig. 117 and Fig. 118, no significant variations were observed in the oxides' content, except in the CaO content (Fig. 117), which seems to increase in bentonite blocks close to the granitic interface. In the case of trace elements (Tab. C.5. and Tab. C.6 from Appendix C), the variations were not noticeable either (Fig. 119). Cu and Cr used for checking the formation of corrosion products slightly increased with respect to the reference sample; and F^- increased in all samples, indicating the infiltration of the granitic groundwater from the surrounding formation, which contains fluoride (Frick et al. 1992). Similar results were observed in samples taken after dismantling Heater #1 (Tab. 13, Tab. 14 and Tab. 15), where, again, no significant differences were detected.

Tab. 12: Chemical composition of the main oxides in the total fraction (in wt.-%) after dismantling of Heater #2 (for location of the samples see Fig. 30 to Fig. 33)

Samples	SiO_2	Al_2O_3	Fe_2O_3	MnO	MgO	CaO	Na_2O	K_2O	TiO_2	P_2O_5	SO_3	LOI	Total
FEBEX Reference*	57.89	17.95	3.12	0.04	4.21	1.83	1.31	1.04	0.23	0.03	0.04	13.8	101.49
FEBEX Reference**	55.46	17.28	3.09	0.03	4.37	1.75	1.16	0.99	0.15	0.03	0.04	16.82	101.17
BB-36-1	57.09	17.79	3.35	0.04	4.32	2.11	1.31	1.11	0.20	0.04	< 0.27	10.48	98.14
BB-36-2	57.37	17.81	3.36	0.04	4.40	2.11	1.22	1.13	0.19	0.04	< 0.34	10.01	98.02
BB-36-3/1 back	58.91	18.25	3.39	0.04	4.72	1.79	1.15	1.08	0.19	0.04	< 0.30	10.14	100.00
BB-36-3/2 green	58.21	18.05	3.70	0.04	4.56	1.59	1.13	1.16	0.18	0.04	< 0.27	10.93	99.85
BB-36-3/2 red	57.36	17.82	3.96	0.03	4.46	1.51	1.11	1.16	0.17	0.04	< 0.26	10.69	98.58
BB-36-4	59.17	18.42	3.44	0.04	4.45	2.45	1.29	1.12	0.19	0.04	< 0.25	10.09	100.95
BB-36-5	58.17	18.02	3.44	0.04	4.41	2.23	1.20	1.19	0.18	0.04	< 0.30	10.34	99.56
BB-36-6	58.68	18.16	3.33	0.04	4.49	1.98	1.15	1.24	0.19	0.04	< 0.30	9.93	99.53
BB-47-7	58.05	18.12	3.41	0.04	4.65	1.88	1.25	1.06	0.19	0.04	< 0.25	10.47	99.41
BB-47-8	59.26	18.49	3.45	0.04	4.74	1.98	1.28	1.07	0.19	0.04	< 0.38	10.51	101.43
BB-47-9	56.12	17.51	3.28	0.04	4.79	1.84	0.97	1.03	0.17	0.04	< 0.30	12.48	98.57
BB-53-4	55.40	17.2	3.22	0.04	4.39	1.88	1.25	1.05	0.21	0.04	n.d.	15.26	100.00
BB-53-5	55.08	16.98	3.23	0.04	4.07	1.94	1.16	1.06	0.25	0.04	n.d.	14.57	98.54
BB-53-6	55.13	16.95	3.15	n.d.	4.33	1.83	1.05	0.99	0.22	0.04	n.d.	14.82	98.68
BB-59-1	58.21	17.64	3.04	0.04	4.09	2.47	1.42	1.35	0.17	0.04	< 0.29	10.31	99.07
BB-59-2	58.38	18.19	3.39	0.04	4.65	2.02	1.26	1.09	0.19	0.04	< 0.31	10.57	100.15
BB-59-3	57.11	17.71	3.28	0.04	4.58	1.82	1.18	1.00	0.18	0.04	< 0.30	11.30	98.54
BB-59-4	57.20	17.65	3.22	0.04	4.61	1.78	1.14	0.98	0.18	0.04	< 0.28	10.94	98.06
BB-59-5	58.38	18.07	3.31	0.04	4.66	1.83	1.19	1.04	0.18	0.04	< 0.30	10.25	99.28

* Reference sample determined by chemical analysis after dissolution of the samples (Fernández 2004, see Appendix C)
** Reference sample determined by XRF

Fig. 116: Main oxides in the bulk bentonite samples: SiO_2, Al_2O_3, Fe_2O_3 and MgO

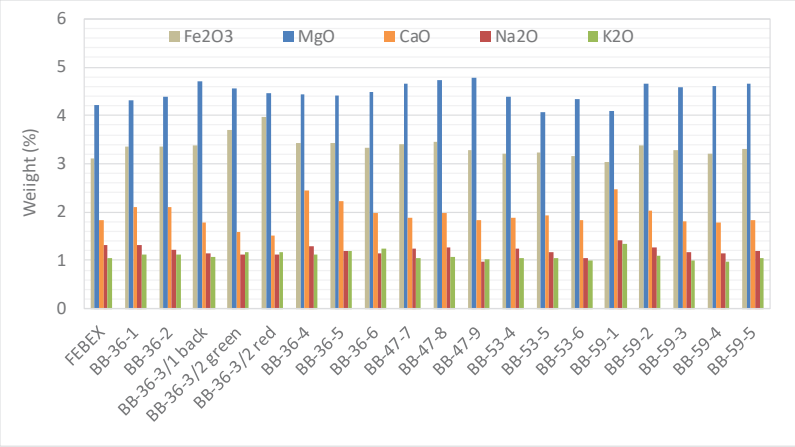

Fig. 117: Main oxides in the bulk bentonite samples: Fe_2O_3, MgO, CaO, Na_2O and K_2O

Fig. 118: Main oxides in the bulk bentonite samples: TiO_2, P_2O_5 and SO_3

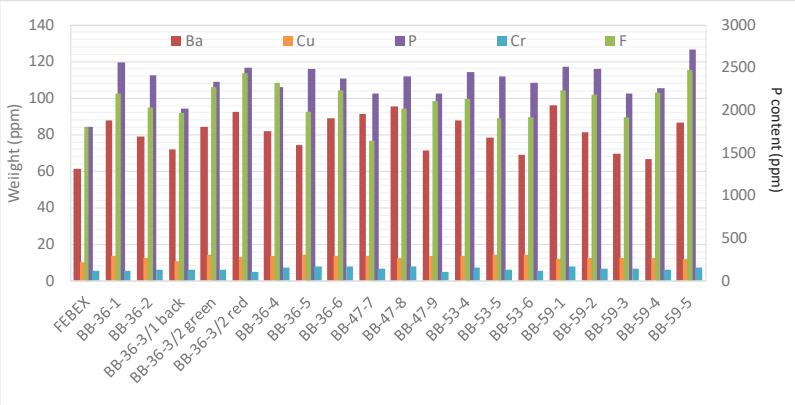

Fig. 119: Trace elements in the bulk bentonite samples from Sections S36, S47, S53 and S59

Tab. 13: Chemical composition of the solid phase for different samples of Section 7 taken after dismantling of Heater #1 (see location in Fig. A-1 and Fig. A-4 in Appendix A)

Oxides and elements*	**BB-7-4**	**BB-7-5**	**FEBEX Reference**
SiO_2 (%)	58.3	58.2	57.89 ± 1.55
Al_2O_3 (%)	16.9	17.3	17.95 ± 0.71
FeO (%)	0.12	0.14	0.25 ± 0.10
Fe_2O_3 (%)	2.4	2.3	2.84 ± 0.12
MgO (%)	3.7	3.8	4.21 ± 0.21
MnO (%)	--	--	0.04 ± 0.00
CaO (%)	1.5	1.5	1.83 ± 0.10
Na_2O (%)	1.4	1.4	1.31 ± 0.09
K_2O (%)	1.2	1.0	1.04 ± 0.05
TiO_2(%)	0.16	0.14	0.23 ± 0.01
P_2O_5 (%)	0.06	0.06	0.03 ± 0.01
H_2O (130 °C) (%)	13.4	13.0	--
H_2O (220 °C) (%)	14.6	13.8	14.1 ± 0.7
LOI (30-950 °C) (%)	19.7	19.8	19.5 ± 1.8
CO_2 Total (%)	0.48	0.70	0.61 ± 0.05
CO_2 organic (%)	0.26	0.51	0.35 ± 0.05
CO_2 inorganic (%)	0.22	0.18	0.26 ± 0.06
SO_3 Total (%)	0.15	0.20	0.26 ± 0.12
F^- (%)	0.16	0.15	0.18 ± 0.01
Ba (ppm)	116	78	164 ± 25
Sr (ppm)	145	138	220 ± 23

* Determined by chemical analysis after solid dissolution (see Appendix A)

Tab. 14: Chemical composition of the solid phase for different samples of Section 12 taken after dismantling of Heater #1 (see location in Fig. A-1 and Fig. A-5 in Appendix A)

Oxides* (%)					**Element*** (ppm)				
Samples	BB12-10	BB12-11	BB12-12	FEBEX Ref.		BB12-10	BB12-11	BB12-12	FEBEX
SiO_2	59.4	59.3	58.7	57.89 ± 1.55	Ba	86	95	115	164 ± 25
Al_2O_3	17.38	17.38	18.31	17.95 ± 0.71	Sr	165	155	123	220 ± 23
FeO	0.08	0.10	0.08	0.25 ± 0.10	Ce	43	48	50	74 ± 6
Fe_2O_3	3.30	3.32	3.29	2.84 ± 0.12	Co	9.2	9.7	9.4	9 ± 3
MgO	3.5	3.6	3.4	4.21 ± 0.21	Cr	9.2	8.7	14	8 ± 2
MnO	0.04	0.04	0.05	0.04 ± 0.00	Cu	12	13	11	25 ± 9
CaO	0.9	0.92	1.1	1.83 ± 0.10	La	19	22	23	40 ± 3
Na_2O	1.2	1.2	1.4	1.31 ± 0.09	Mo	< 5	< 5	< 5	--
K_2O	1.0	1.0	1.1	1.04 ± 0.05	Ni	16	17	15	20 ± 3
TiO_2	0.22	0.24	0.24	0.23 ± 0.01	Sn	< 10	< 10	< 10	--
P_2O_5	0.06	0.07	0.06	0.03 ± 0.01	V	9.9	11	10	16 ± 2
H_2O (130 °C)	11.70	11.70	11.30	--	W	< 25	< 25	< 25	
H_2O (220 °C)	13.08	12.69	12.69	14.1 ± 0.7	Y	13	13	14	25 ± 3
LOI (30 – 950 °C)	19.00	18.60	18.40	19.5 ± 1.8	Zn	50	49	45	65 ± 4
CO_2 Total	0.51	0.51	0.59	0.61 ± 0.05	Cs	5.9	6	6.9	--
CO_2 organic	0.22	0.22	0.37	0.35 ± 0.05	Eu	--	--	--	--
CO_2 inorganic	0.29	0.29	0.22	0.26 ± 0.06	Se	< 0.1	< 0.1	< 0.1	--
SO_3 Total	0.10	0.10	0.10	0.26 ± 0.12	Li	51.0	50.0	47.0	--
F^- (%)	0.17	0.16	0.17	0.18 ± 0.01					

* Determined by chemical analysis after solid dissolution (see Appendix A)

Tab. 15: Chemical composition of the solid phase for different samples of Section 19 taken after dismantling of Heater #1 (see location in Fig. A-1 and Fig. A-6 in Appendix A)

Oxides* (%)					**Element*** (ppm)				
Samples	BB19-1	BB19-2	BB19-3	FEBEX Ref.	Samp.	BB19-1	BB19-2	BB19-3	FEBEX
SiO_2	58.69	59.16	58.89	57.89 ± 1.55	Ba	138	177	221	164 ± 25
Al_2O_3	17.47	16.68	16.52	17.95 ± 0.71	Sr	154	163	160	220 ± 23
FeO	0.08	0.08	0.06	0.25 ± 0.10	Ce	58	55	50	74 ± 6
Fe_2O_3	3.08	2.95	2.98	2.84 ± 0.12	Co	11	11	10	9 ± 3
MgO	3.6	3.4	3.4	4.21 ± 0.21	Cr	6.9	7.2	5.6	8 ± 2
MnO	0.03	0.03	0.03	0.04 ± 0.00	Cu	12	12	12	25 ± 9
CaO	1.0	1.1	1.0	1.83 ± 0.10	La	21	17	16	40 ± 3
Na_2O	1.3	1.3	1.3	1.31 ± 0.09	Mo	< 5	< 5	< 5	
K_2O	1.1	1.1	0.99	1.04 ± 0.05	Ni	16	16	9.3	20 ± 3
TiO_2	0.24	0.24	0.23	0.23 ± 0.01	Sn	< 10	< 10	< 10	
P_2O_5	0.06	0.06	0.06	0.03 ± 0.01	V	10	11	9.4	16 ± 2
H_2O (130 °C)	8.2	10.6	11.7	--	W	< 25	< 25	< 25	--
H_2O (220 °C)	9.2	11.92	13.08	14.1 ± 0.7	Y	13	11	10	25 ± 3
LOI (30-950 °C)	14.4	16.8	18	19.5 ± 1.8	Zn	49	49	47	65 ± 4
CO_2 Total	0.48	0.55	0.48	0.61 ± 0.05	Cs	6	6.1	5.5	--
CO_2 organic	0.22	0.26	0.26	0.35 ± 0.05	Eu	2	2.2	1.7	--
CO_2 inorganic	0.26	0.29	0.22	0.26 ± 0.06	Se	< 0.1	< 0.1	< 0.1	--
SO_3 Total	0.05	0.07	0.05	0.26 ± 0.12	Li	< 2	< 2	< 2	--
F^-	0.22	0.18	0.18	0.18 ± 0.01					

* Determined by chemical analysis after solid dissolution (see Appendix A)

5.4.2 Analysis of the < 2 µm fraction by XRF

The smectite mineral formula were calculated from XRF data obtained from the < 2 µm fraction after homoionization with Ba^{2+} ions (Tab. C.7 from Appendix C). The stoichiometric elemental composition of the smectites was calculated based on the assumption of 22 negative charges per formula unit, but the measured layer charge, determined in Section 5.5.1, was involved in the calculation of the structural formula as recommended by Köster (1977). For each bulk sample (< 2 µm fraction), both the layer charge and the chemical analysis by XRF were determined and both results were used for calculating the structural formula. In this method, 22 cationic charges are distributed into tetrahedral, octahedral and interlayer positions while considering the measured layer charge. Because the layer charge, determined by the alkylammonium method, was fixed, the Σ_{oct} is close to 2.0. This method is different to that used from the TEM and SEM analyses, where the layer charge was not fixed.

The results are shown in Tab. 16 from samples in Sections S36 (at shotcrete contact), S47 and S53 (heated) and S59 (non-heated). A comparison with the reference raw FEBEX bentonite sample is also given, and no significant differences were observed among the reference and

retrieved samples. All smectites showed substantial substitution in the octahedral sheet (85 – 95 %), whereas the substitution in the tetrahedral sheet was much lower (between 5 to 15 %). In the octahedral sheet, Mg mainly substituted for Al, the amount of Fe being low. All the smectites from unaltered and retrieved samples displayed an octahedral filling below 2.05 mol/phuc indicating the dioctahedral character. Furthermore, because the laminar charge is < 0.42 and the percentage of tetrahedral charge is < 15 %, the smectites can be classified as Wyoming type smectites (Emmerich et al. 2001).

5.4.3 Total carbon and total sulphur

The total carbon (C_T) and total sulphur (S_T) contents were determined by a LECO CS-244 elemental analyser; whereas total inorganic carbon (TIC) was determined with a TOC-V_{CSH} analyser. The values obtained from samples analysed after dismantling are shown in Tab. 17 and compared to the initial values of the raw FEBEX bentonite in Fig. 120.

Sulphur was always below the detection limit (< 0.1 wt.-%), as in the reference FEBEX sample; except in sample BB-47-8 (0.13 wt.-%). Regarding the total carbon (Fig. 121), although some variations were observed with respect to the initial FEBEX bentonite, these variations (above the reference value) are not highly significant (all values below 0.18 wt.-%), except in sample BB-36-5 (0.23 wt.-%). The organic carbon, determined as C_T-TIC, was always below the detection limit, so total carbon, C_T, can be considered as TIC (total inorganic carbon). Accumulations in inorganic carbon may be attributed to carbonates precipitation. The C_T amount expressed as calcite is always lower than 2 wt.-%, as observed by XRD analysis (ranging between Tz and 2 wt.-%).

Tab. 16: Structural formula based on $O_{10}(OH)_2$ according to Köster (1977) by using the measure layer charge

Sample	Structural formula	Layer charge (eq/h.u.c.)	Σ_{tet}	Σ_{oct}	τ charge (%)	O. charge (%)	Weight p.f.u. (g/mol)	CEC cal. (meq/100g)
FEBEX Ref.	$(Si_{3.94}Al_{0.06})^{IV}$ $(Al_{1.35}Fe^{3+}_{0.21}Mg_{0.49}Ti_{0.01})^{VI}$ $O_{10}(OH)_2$ $X_{0.29}$	0.38	4.0	2.05	15	85	752.66(*)	100.3
BB-36-1	$(Si_{3.96}Al_{0.04})^{IV}$ $(Al_{1.35}Fe^{3+}_{0.19}Mg_{0.48}Ti_{0.02})^{VI}$ $O_{10}(OH)_2$ $X_{0.20}$	0.37	4.0	2.05	11	89	780.64	94.8
BB-36-2	$(Si_{3.96}Al_{0.04})^{IV}$ $(Al_{1.34}Fe^{3+}_{0.20}Mg_{0.48}Ti_{0.02})^{VI}$ $O_{10}(OH)_2$ $X_{0.20}$	0.37	4.0	2.05	10	90	781.12	94.8
BB-36-3 back	$(Si_{3.97}Al_{0.03})^{IV}$ $(Al_{1.36}Fe^{3+}_{0.18}Mg_{0.48}Ti_{0.01})^{VI}$ $O_{10}(OH)_2$ $X_{0.20}$	0.37	4.0	2.04	9	91	779.92	94.8
BB-36-3 green	$(Si_{3.98}Al_{0.02})^{IV}$ $(Al_{1.36}Fe^{3+}_{0.18}Mg_{0.48}Ti_{0.01})^{VI}$ $O_{10}(OH)_2$ $X_{0.20}$	0.37	4.0	2.04	6	94	779.90	95.6
BB-36-3 red	$(Si_{3.96}Al_{0.04})^{IV}$ $(Al_{1.33}Fe^{3+}_{0.23}Mg_{0.47}Ti_{0.01})^{VI}$ $O_{10}(OH)_2$ $X_{0.20}$	0.37	4.0	2.04	12	88	782.28	94.0
BB-47-7	$(Si_{3.96}Al_{0.04})^{IV}$ $(Al_{1.35}Fe^{3+}_{0.20}Mg_{0.48}Ti_{0.02})^{VI}$ $O_{10}(OH)_2$ $X_{0.21}$	0.37	4.0	2.04	10	90	781.01	95.7
BB-47-8	$(Si_{3.96}Al_{0.04})^{IV}$ $(Al_{1.35}Fe^{3+}_{0.20}Mg_{0.48}Ti_{0.02})^{VI}$ $O_{10}(OH)_2$ $X_{0.20}$	0.37	4.0	2.05	11	89	781.18	95.4
BB-47-9	$(Si_{3.95}Al_{0.05})^{IV}$ $(Al_{1.35}Fe^{3+}_{0.19}Mg_{0.50}Ti_{0.01})^{VI}$ $O_{10}(OH)_2$ $X_{0.20}$	0.37	4.0	2.05	13	87	781.32	95.2
BB-53-4	$(Si_{3.96}Al_{0.04})^{IV}$ $(Al_{1.35}Fe^{3+}_{0.19}Mg_{0.49}Ti_{0.01})^{VI}$ $O_{10}(OH)_2$ $X_{0.21}$	0.38	4.0	2.05	11	89	781.64	96.6
BB-53-5	$(Si_{3.96}Al_{0.04})^{IV}$ $(Al_{1.35}Fe^{3+}_{0.19}Mg_{0.49}Ti_{0.01})^{VI}$ $O_{10}(OH)_2$ $X_{0.20}$	0.37	4.0	2.05	11	89	781.03	95.9
BB-53-6	$(Si_{3.97}Al_{0.03})^{IV}$ $(Al_{1.35}Fe^{3+}_{0.20}Mg_{0.48}Ti_{0.01})^{VI}$ $O_{10}(OH)_2$ $X_{0.20}$	0.37	4.0	2.04	9	91	781.20	95.1
BB-59-1	$(Si_{3.95}Al_{0.05})^{IV}$ $(Al_{1.35}Fe^{3+}_{0.19}Mg_{0.49}Ti_{0.01})^{VI}$ $O_{10}(OH)_2$ $X_{0.21}$	0.37	4.0	2.05	13	87	781.88	96.9
BB-59-2	$(Si_{3.96}Al_{0.04})^{IV}$ $(Al_{1.34}Fe^{3+}_{0.20}Mg_{0.48}Ti_{0.01})^{VI}$ $O_{10}(OH)_2$ $X_{0.20}$	0.37	4.0	2.05	10	90	781.29	95.4
BB-59-3	$(Si_{3.96}Al_{0.04})^{IV}$ $(Al_{1.35}Fe^{3+}_{0.20}Mg_{0.48}Ti_{0.01})^{VI}$ $O_{10}(OH)_2$ $X_{0.20}$	0.38	4.0	2.04	12	88	782.00	96.5
BB-59-4	$(Si_{3.96}Al_{0.04})^{IV}$ $(Al_{1.34}Fe^{3+}_{0.22}Mg_{0.47}Ti_{0.02})^{VI}$ $O_{10}(OH)_2$ $X_{0.20}$	0.37	4.0	2.04	11	89	782.33	95.6
BB-59-5	$(Si_{3.98}Al_{0.02})^{IV}$ $(Al_{1.37}Fe^{3+}_{0.17}Mg_{0.48}Ti_{0.01})^{VI}$ $O_{10}(OH)_2$ $X_{0.20}$	0.37	4.0	2.04	5	95	779.05	94.9

* Non-homoionised in barium

Tab. 17: Total carbon and sulphur content (in wt.-%)

Samples	S_T	C_T	C_T as $CaCO_3$	Sample	S_T	C_T	C_T as $CaCO_3$
FEBEX Ref.	< 0.1	0.12	1.0	BB-59-1	< 0.1	0.17	1.4
BB-47-1	< 0.1	0.12	1.1	BB-59-2	< 0.1	0.13	1.1
BB-47-2	< 0.1	0.13	0.9	BB-59-3	< 0.1	0.12	1.0
BB-47-3	< 0.1	0.11	1.2	BB-59-4	< 0.1	0.11	0.9
BB-47-4	< 0.1	0.14	0.9	BB-59-5	< 0.1	0.12	1.0
BB-47-5	< 0.1	0.11	0.9	BB-59-6	< 0.1	0.14	1.2
BB-47-6	< 0.1	0.11	1.3	BB-59-7	< 0.1	0.18	1.5
BB-47-7	< 0.1	0.15	1.0	BB-59-8	< 0.1	0.16	1.3
BB-47-8	0.13	0.12	0.8	BB-59-9	< 0.1	0.15	1.3
BB-47-9	< 0.1	0.10	1.3	BB-59-10	< 0.1	0.13	1.1
BB-53-1	< 0.1	0.15	1.3	BB-59-11	< 0.1	0.15	1.3
BB-53-2	< 0.1	0.16	0.8	BB-59-12	< 0.1	0.18	1.5
BB-53-3	< 0.1	0.10	1.2	BB-59-13	< 0.1	0.11	0.9
BB-53-4	< 0.1	0.14	1.2	BB-59-14	< 0.1	0.15	1.3
BB-53-5	< 0.1	0.14	0.9	BB-36-1	< 0.1	0.15	1.0
BB-53-6	< 0.1	0.11	1.3	BB-36-2	< 0.1	0.15	1.3
BB-53-7	< 0.1	0.16	1.2	BB-36-3	< 0.1	0.16	1.3
BB-53-8	< 0.1	0.14	1.0	BB-36-3	< 0.1	0.16	1.3
BB-53-9	< 0.1	0.12	1.0	BB-36-4	< 0.1	0.16	1.3
				BB-36-5	< 0.1	0.23	1.9
				BB-36-6	< 0.1	0.16	1.3

Detection limits: S_T < 0.10 %; C_T < 0.10 %
TOC = C_T-TIC

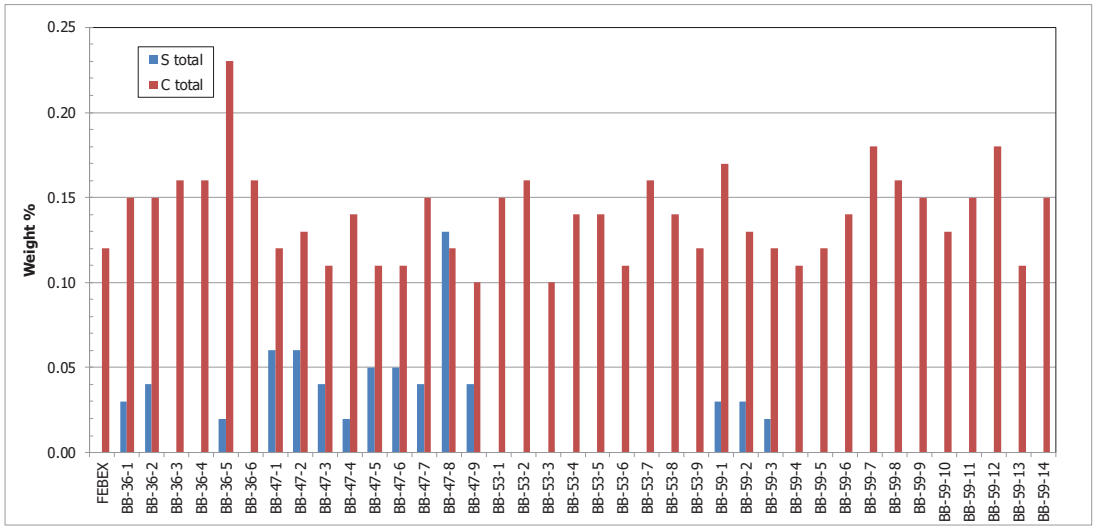

Fig. 120: Sulphur and carbon analysed in samples from Sections S33, S47, S53 and S59

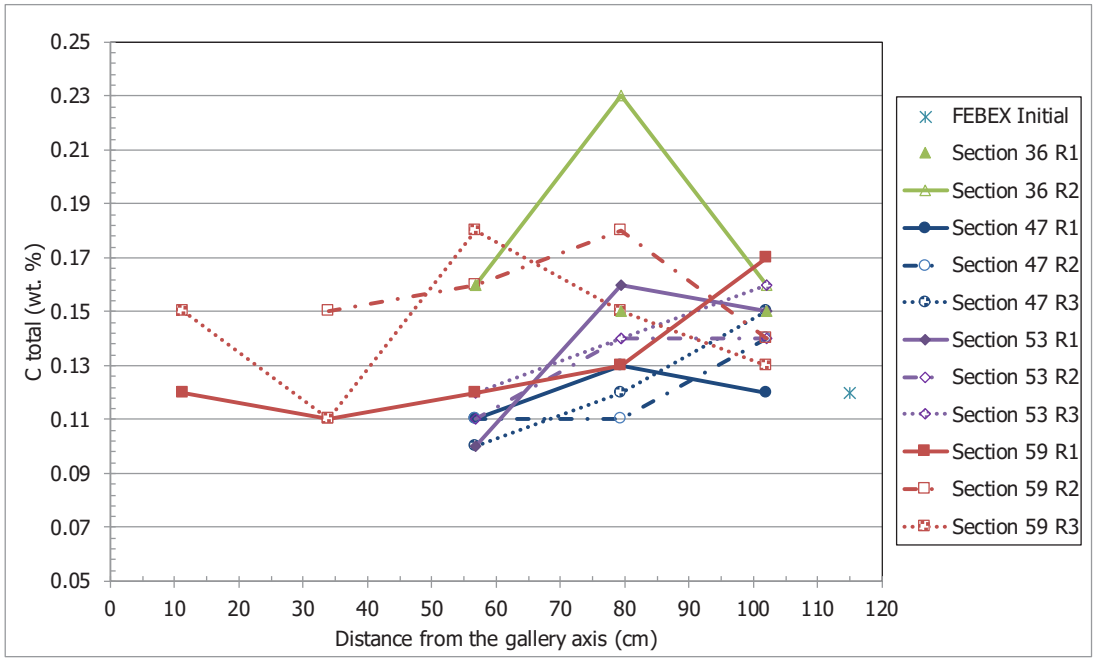

Fig. 121: Total carbon as a function of distance to the gallery axis

5.4.4 Poorly crystalline and free silica, aluminium and iron

The free silica, aluminium and iron contents were determined in different samples from bentonite blocks at Sections S36, S47, S53 and S59 with the aim of investigating the possible silicate dissolution, and/or the presence of iron phases. The results are shown in Tab. 18. No significant differences were found in most of the samples among the untreated FEBEX bentonite sample and the samples analysed after 18 years of experimental conditions. Exceptions are free iron contents (Fig. 122) in the bentonite blocks in contact with the dummy heater in the Section 36 (BB-36-3), and free Al_2O_3 (Fig. 123) in some samples from Section 36 (e.g., samples BB-36-1, BB-36-2 and BB-36-4), and samples from one radius in Sections S59 and S47. The variations in free silica content were insignificant, within the experimental error, and even below the reference value in some samples (Fig. 124).

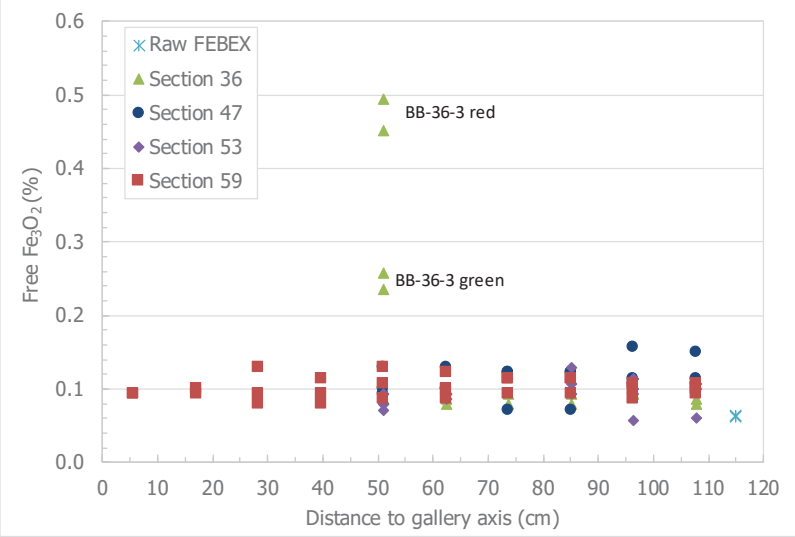

Fig. 122: Free Fe_2O_3 as a function of distance to the gallery axis

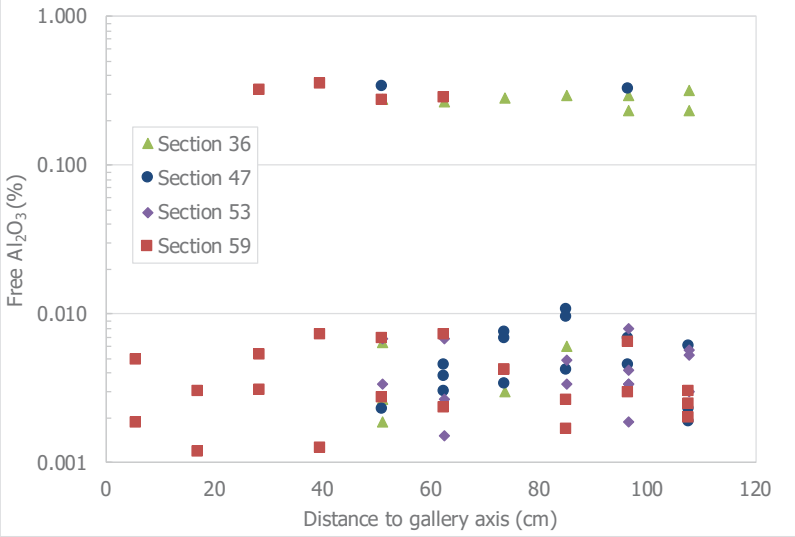

Fig. 123: Free Al_2O_3 as a function of distance to the gallery axis (values of reference sample are below detection limits)

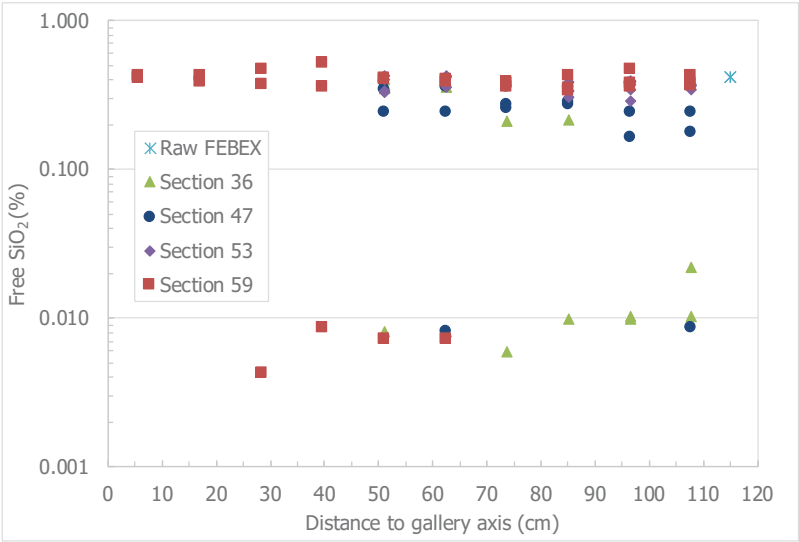

Fig. 124: Free silica as a function of distance to the gallery axis

Tab. 18: Free aluminium, silica and iron oxides from different bentonite samples (in wt.-%)

Samples	**Al_2O_3**	**SiO_2**	**Fe_2O_3**	**Samples**	**Al_2O_3**	**SiO_2**	**Fe_2O_3**
FEBEX Ref.	< 0.001	0.415	0.064	BB53-3/S2	0.003	0.402	0.079
FEBEX Ref.	< 0.001	0.419	0.062	BB53-4/S1	0.003	0.368	0.100
BB36-1/S1	0.317	0.022	0.086	BB53-4/S2	0.008	0.368	0.100
BB36-1/S2	0.291	0.010	0.093	BB53-5/S1	0.003	0.338	0.107
BB36-2/S1	0.295	0.010	0.093	BB53-5/S2	< 0.001	0.389	0.100
BB36-2/S2	0.280	0.006	0.093	BB53-6/S1	0.002	0.415	0.093
BB36-3/back S1	< 0.001	0.355	0.086	BB53-6/S2	0.007	0.424	0.093
BB36-3/back S2	< 0.001	0.402	0.086	BB53-7/S1	0.006	0.342	0.060
BB36-3/red S1	< 0.001	0.372	0.450	BB53-7/S2	0.003	0.342	0.058
BB36-3/red S2	0.006	0.368	0.493	BB53-8/S1	< 0.001	0.304	0.093
BB36-3/green S1	0.003	0.355	0.257	BB53-8/S2	0.002	0.287	0.093
BB36-3/green S2	0.002	0.351	0.236	BB53-9/back 1	0.003	0.359	0.086
BB36-4/S1	0.231	0.010	0.079	BB53-9/back 1	< 0.001	0.329	0.093
BB36-4/S2	0.231	0.010	0.093	BB53-9/heater 1	< 0.001	0.334	0.079
BB36-5/S1	0.006	0.214	0.079	BB53-9/heater 2	< 0.001	0.329	0.071
BB36-5/S2	0.003	0.201	0.079	BB59-1/S1	0.003	0.381	0.107
BB36-6/S1	0.265	0.008	0.079	BB59-1/S2	< 0.001	0.359	0.107
BB36-6/S2	0.276	0.008	0.086	BB59-2/S1	< 0.001	0.347	0.114
BB47-1/S1	0.006	0.175	0.150	BB59-2/S2	< 0.001	0.359	0.114

Tab. 18: Cont.

Samples	Al_2O_3	SiO_2	Fe_2O_3	Samples	Al_2O_3	SiO_2	Fe_2O_3
BB47-1/S2	0.007	0.163	0.157	BB59-3/S1	0.007	0.398	0.100
BB47-2/S1	0.009	0.282	0.071	BB59-3/S2	0.007	0.411	0.107
BB47-2/S2	0.008	0.270	0.071	BB59-4/S1	0.001	0.359	0.093
BB47-3/S1	0.004	0.244	0.129	BB59-4/S2	0.003	0.372	0.093
BB47-3/S2	0.002	0.240	0.129	BB59-5/S1	0.001	0.389	0.093
BB47-4/S1	0.002	0.009	0.114	BB59-5/S2	0.002	0.406	0.093
BB47-4/S2	0.325	0.377	0.114	BB59-6/S1	0.002	0.428	0.100
BB47-5/S1	0.004	0.355	0.122	BB59-6/S2	0.006	0.471	0.100
BB47-5/S2	0.007	0.355	0.122	BB59-7/S1	0.003	0.428	0.114
BB47-6/S1	0.005	0.008	0.100	BB59-7/S2	0.004	0.389	0.114
BB47-6/S2	0.336	0.385	0.093	BB59-8/S1	0.002	0.389	0.122
BB47-7/S1	0.002	0.240	0.107	BB59-8/S2	0.003	0.402	0.129
BB47-7/S2	0.005	0.244	0.107	BB59-9/S1	0.007	0.513	0.114
BB47-8/S1	0.011	0.274	0.122	BB59-9/S2	0.005	0.471	0.129
BB47-8/S2	0.003	0.257	0.122	BB59-10/S1	0.002	0.364	0.093
BB47-9/S1	0.003	0.359	0.100	BB59-10/S2	0.003	0.377	0.086
BB47-9/S2	< 0.001	0.342	0.100	BB59-11/S1	0.002	0.338	0.093
BB53-1/S1	0.005	0.364	0.107	BB59-11/S2	0.004	0.381	0.093
BB53-1/S2	0.004	0.389	0.114	BB59-12/S1	0.283	0.007	0.086
BB53-2/S1	0.005	0.389	0.129	BB59-12/S2	0.272	0.007	0.086
BB53-2/S2	0.003	0.394	0.114	BB59-13/S1	0.348	0.009	0.079
BB53-3/S1	0.007	0.424	0.093	BB59-13/S2	0.317	0.004	0.079
				BB59-14/S1	0.003	0.428	0.100
				BB59-14/S2	0.005	0.428	0.093

5.5 Physico-chemical characterization

5.5.1 Layer charge

Layer charge is the charge deficit, derived from ionic substitutions in the mineral structure which is balanced by the exchangeable cations in smectites. Layer charge is a key parameter because it strongly affects key smectite properties, such as swelling, cation exchange capacity and ion exchange. Because smectites are often compositionally and structurally heterogeneous, the layer charge may be heterogenous, both in terms of charge location (tetrahedral versus octahedral) and charge magnitude (i.e., individual smectite 2:1 layers may differ in charge, with the total layer charge being an average of these different charges). According to Christidis & Eberl (2003), low charge smectites have layer charges < -0.425 p.h.f.u. and high charge smectites have layer charges > -0.470 p.h.f.u.

In order to estimate the mean layer charge of the smectite particles in the FEBEX in-situ test samples, an empirical method was used based on the relationship between XRD basal spacings and the mean layer charge (Olis et al. 1990). This method is a simplification of the conventional n-alkylammonium ion-exchange technique, where monolayer-bilayer and bilayer-pseudo-trimolecular layer transitions can be discriminated. Here, the d-spacings from two particular long-chain alkylammonium expansions (nC = 12 and nC = 18; nC being the number of carbon atoms in the alkyl chain), were related to mean layer charge. However, according to Olis et al. (1990), nC = 12 is preferred over nC = 18 due to certain difficulties encountered with nC = 18 exchange, including some steric hindrance in expanding the interlayer separation, and the requirement to very careful wash the samples. It should be noted that this method gives a mean layer charge of all clay mineral particles from the bulk analysed samples and can differ from the results obtained on individual clay mineral particle as determined in TEM or SEM analyses.

For expansions from monolayer (14 to 18 Å) to bilayer (18 to 21 Å) transitions, the regression equations used for determining the mean layer charge were:

$$\text{nC} = 12 \; d(001) \; = \; 5.52 + 32.98 \times MLC$$

$$\text{nC} = 18 \; d(001) \; = \; 8.21 + 34.22 \times MLC$$

The results obtained from different samples from Sections S36, S47, S53 and S59 are shown in Fig. 125 and Tab. 19. MLC (ξ) values of 0.37 ± 0.01 eq/h.f.u. and 0.38 ± 0.01 eq/h.f.u. were found for the alkylammonium nC = 12 and nC = 18, respectively, in the analysed samples. No significant differences in the MLC were found with respect the initial FEBEX bentonite sample, which has a mean ξ = 0.38 ± 0.02 eq/h.f.u. Bimodal smectite particles with ξ values below 0.425 phfc and higher than 0.47 phfc were not found; i.e. the material is very homogeneous concerning the layer charge ξ. Therefore, the smectite particles prior and after the FEBEX in-situ test can be classified as low-medium charge smectites, which are dominated by expansible 17.6 Å layers. The location of the charge is mainly at octahedral layers as shown in Section 5.4.2.

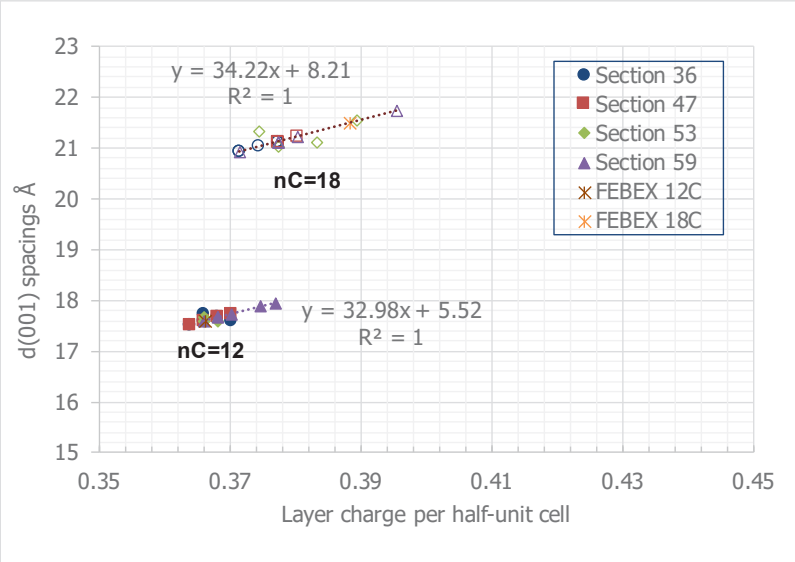

Fig. 125: Mean layer charge vs. (001) basal reflexion for alkyl chains nC = 12 and nC = 18 in samples from different bentonite sections

Tab. 19: Basal spacings and mean layer charge (MLC) for alkyl chains nC = 12 and nC = 18

Sample	**alkyl chains nC = 12**		**alkyl chains nC = 18**	
	d(001)	**MLC (ξ)**	**d(001)**	**MLC (ξ)**
FEBEX Ref.	17.6000	0.37	21.5000	0.39
BB-36-1	17.5892	0.37	21.0213	0.37
BB-36-2	17.5195	0.36	21.1219	0.38
BB-36-3 green	17.5892	0.37	21.1219	0.38
BB-36-3 green	17.7304	0.37	21.1219	0.38
BB-36-3 red	17.5195	0.36	20.9217	0.37
BB-36-3 back	17.6596	0.37	20.9217	0.37
BB-47-7	17.7304	0.37	21.1219	0.38
BB-47-8	17.6596	0.37	21.1219	0.38
BB-47-9	17.5195	0.36	21.1219	0.38
BB-47-9	17.5892	0.37	21.2234	0.38
BB-53-4	17.5892	0.37	21.5338	0.39
BB-53-8	17.5892	0.37	21.3258	0.38
BB-53-6	17.5892	0.37	21.1219	0.38
BB-53-6	17.6596	0.37	21.0213	0.37
BB-59-1	17.9516	0.38	21.1219	0.38
BB-59-1	17.5892	0.37	21.7459	0.40
BB-59-2	17.6596	0.37	21.1219	0.38
BB-59-3	17.8739	0.37	21.2234	0.38
BB-59-4	17.7304	0.37	21.1219	0.38
BB-59-5	17.6596	0.37	20.9217	0.37

5.5.2 Cation exchange capacity

One of the most important parameters for characterising the bentonite adsorption behaviour is the cation exchange capacity (CEC). This parameter is equivalent to the total negative surface charge of a clay mineral and reflects the degree of reactivity of the bentonite; CEC is related to the capacity of adsorption and retention of ions and to the swelling capacity of bentonites.

The CEC was determined by using a complex of Cu(II). The results obtained from the reference and samples obtained during dismantling of Heater #2 are shown in Fig. 126 and Tab. C.3 in Appendix C. The CEC ranges from 88 to 100 meq/100g for all sections (Fig. 127). In general, these values are similar or slightly lower than the reference FEBEX bentonite. The differences are probably due to small smectite content heterogeneities rather than variations in the CEC. A slight, although unclear, decrease in CEC is observed in samples close to Heater #2, which is more evident in the BMS and protrusion samples located at the liner/Heater #2 interface (see Section 6).

Theoretical CEC derived both from Alkylammonium layer charge, ξ (Section 5.5.1), and molar mass from the Structural formula (Tab. 16) were similar to CEC values obtained from the Cu-trien complex method (Fig. 128). The data follow a linear relationship, but CEC values derived from layer charge determination are higher than those derived from Cu-trien complex. This is probably due to the percentage of smectite particles in the samples, 100 % in the Alkylammonium layer charge determinations (analyses on the < 2 µm fraction), and 86 – 94 % in the Cu-trien complex determinations (analyses on the total fraction).

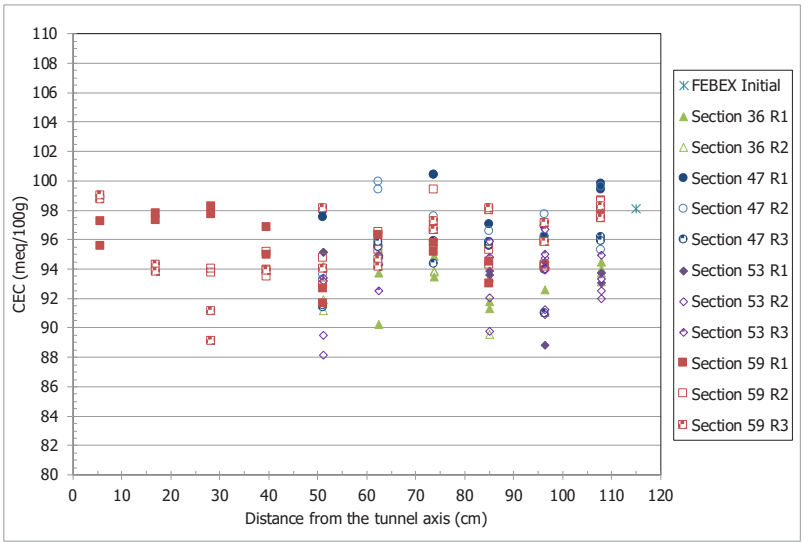

Fig. 126: Total cation exchange capacity as a function of distance from the tunnel axis: two samples per block (S1 and S2) along three radii from Sections S36, S47, S53 and S59

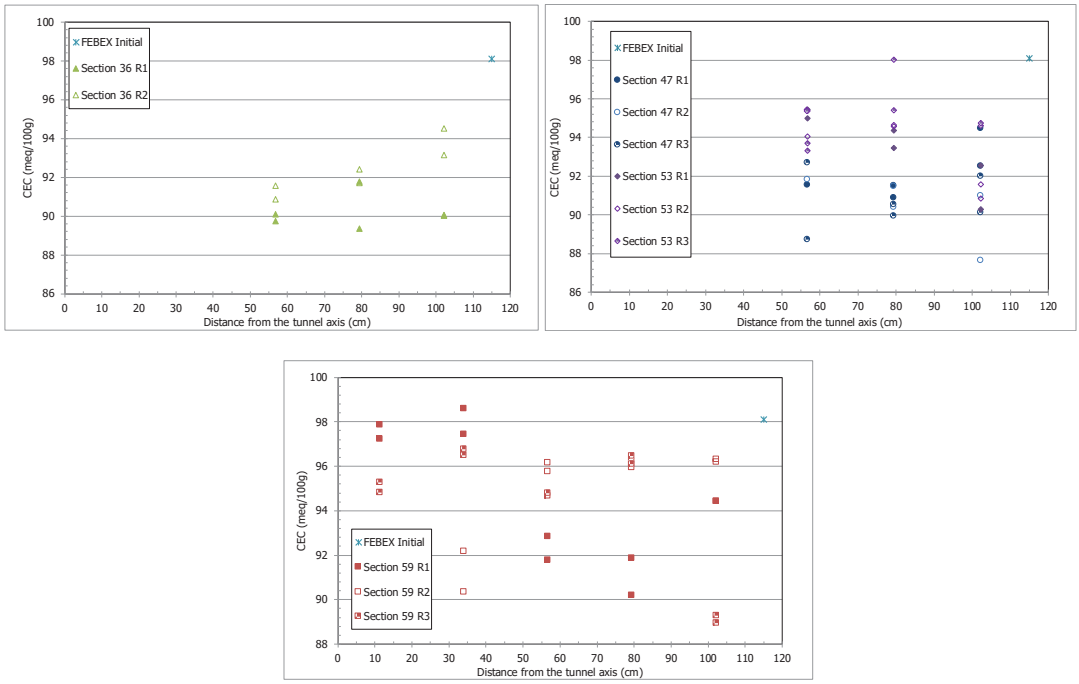

Fig. 127: Total cation exchange capacity as a function of distance from the tunnel axis (data from one average sample from each block along three radii, i.e., mineralogy subsample, see Fig. 26)

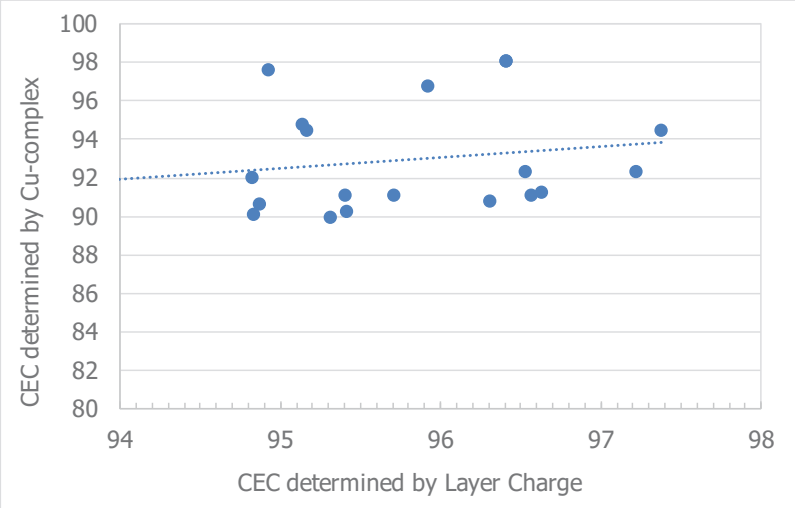

Fig. 128: Relationship between CEC calculated from Alkylammonium Layer Charge determinations and by Cu-trien complex

5.5.3 Cation exchange population

The nature of interlayer cations is also an important issue because the cation composition at exchange sites affects not only the exchange properties but also the plasticity, the swelling capacity and the rheological behaviour.

The cation occupancy at interlayers was determined in samples from three radii of the buffer at Sections S36, S47, S53 and S59. The results are shown in Tab. C.4 in Appendix C. According to the data, there were several changes in the composition of the exchangeable cations as a consequence of both the heating and hydration processes.

In most samples, except in Section 59, Na occupancy increased close to the interface with granite and decreased towards the inner part of the barrier. However, this decrease is very sharp in the heated sections in contact with Heater #2. In Section 59, the values were below the reference value at the granitic contact, decreasing towards the internal part of the barrier (Fig. 129).

Ca occupancy behaviour is different in heated and non-heated sections. In non-heated sections exchangeable calcium was higher at the contact with granite and decreased until reference values at the centre of the barrier. The higher values were found in Section 36 in contact with the shotcrete plug. In heated sections, values were higher than reference values and increased towards the internal part of the barrier at the heater contact (Fig. 130). Therefore, there was an increase of calcium at exchange positions as a consequence of the heating and hydration processes. However, the calcium concentration profiles as a function of distance from the gallery axis were not similar in Section 47 and 53, the changes being higher in Section 47. This Section 47 was located at the central part of Heater #2 and, therefore, the temperatures were higher than in Section 53, which was located at the back part of the heater.

Mg occupancy was depleted in Section 36 in all samples, this decrease being strongest towards the granitic interface and less evident in contact with the dummy canister in some bentonite radii. In Section 59, Mg was always above the reference value and correlated with the Na decrease. In the heated Sections S47 and S53, Mg slightly decreases from the granitic interface towards the internal part and increases in close contact with Heater #2 (Fig. 131).

K occupancy increased in all samples with respect to the reference sample, with a more significant increase in Section 36 towards the dummy interface (Fig. 132). Copper was found at interlayer sites in some samples at very low concentrations, especially in Section 36 (Fig. 133).

All results indicate that the FEBEX bentonite became more of a calcium type in Section 36, with a decreased Na and Mg content. This behaviour was more accentuated in the blocks with higher water content where Na and Mg values decreased towards the reference value towards the internal part of the barrier. In Section 59, the FEBEX bentonite became more of a magnesium type, especially in the internal part of the barrier, through a decreasing sodium content, although, at the granitic interface Ca also increased. In the case of the heated sections, Ca increased, whereas Mg decreased and Na kept similar or slightly higher values. At the contact with the heater, on the other hand, Ca and Mg increased and Na decreased with respect to reference values (Fig. 134).

Data were compared to results obtained from samples taken during the dismantling of Heater #1, which are given in Fig. 135 and Fig. 136. However, it should be taken into account that the methodology for the CEC determination in samples from the dismantling of Heater #1 was different than that followed after dismantling Heater #2, because in 2002 the 0.5 M $CsNO_3$ extracting solution was not buffered to pH 8.2. This buffering avoids the dissolution of carbonates and sulphates, which affects the cation concentration, increasing the Ca content at exchange sites, replacing mainly Na. This is observed in Fig. 137 where, as a result of carbonate dissolution, the sum of the cation exchange population is much higher than total CEC. For this reason, and in terms of comparison, cation exchange values were normalized with respect to a total CEC of 102

meq/100g in 2002. In samples from the dismantling of Heater #2 in 2015, the methodology for extracting the exchangeable cations was improved by buffering the pH to 8.2. As a consequence, the relationships between CEC and the sum of exchangeable cations follows a linear relationship, the differences between both variables being between 0 and 15 meq/100 g in absolute value (Fig. 138). A comparison of methodologies used in 2002 and 2015 is given in Fig. 142 with the samples of Section 7. A clear increase of calcium at exchange sites (Fig. 142a), and the increase of the sum of cations (Fig. 142b) when the extracting solution was not buffered to pH 8.2 can be seel. However, the tendencies observed in the evolution of the cation concentrations are the same, independently of buffering the pH of the extracting $CsNO_3$ solution.

The results obtained in 2002 indicate that in Section 7 located at the concrete contact, Mg is depleted along the whole bentonite buffer (this depletion is more visible at the granitic contact), whereas Ca, Na and K increased. In the other sections the tendencies are not so clear but always an increase of Ca and a slight increase of K are observed, except in the heated Section S19 where in two radii an increase of Mg and a depletion of Na are observed close to the heater contact.

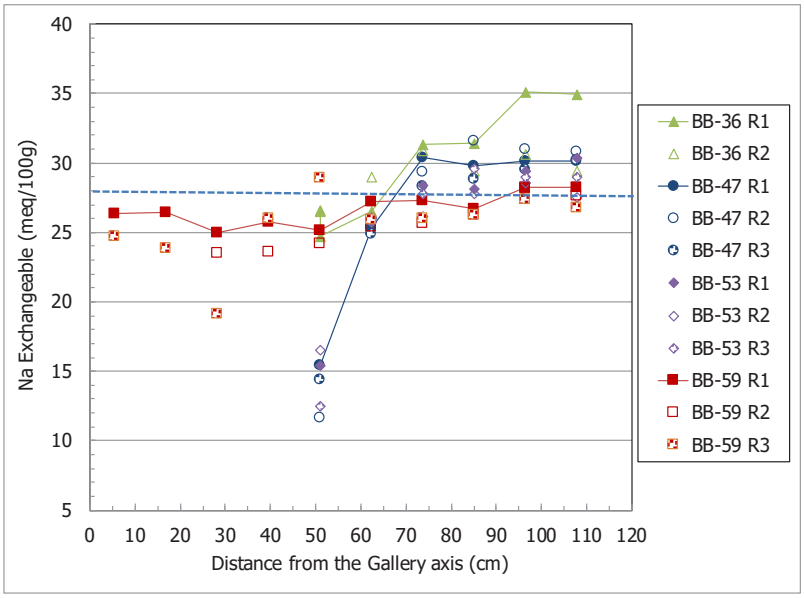

Fig. 129: Sodium occupancy at exchange sites as a function of distance to the gallery axis from samples taken during Dismantling of Heater #2 in 2015

Dotted line: reference value

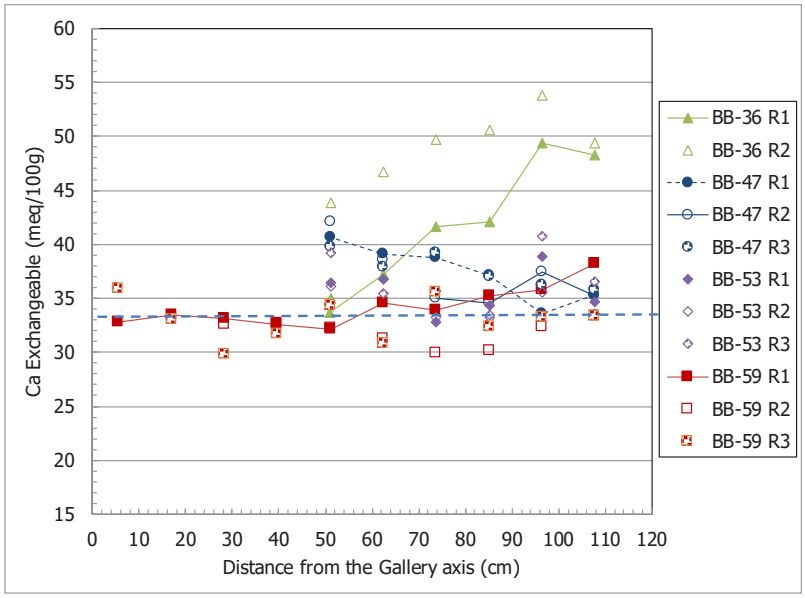

Fig. 130: Calcium occupancy at exchange sites as a function of distance to the gallery axis from samples taken during dismantling of Heater #2 in 2015

Dotted line: reference value

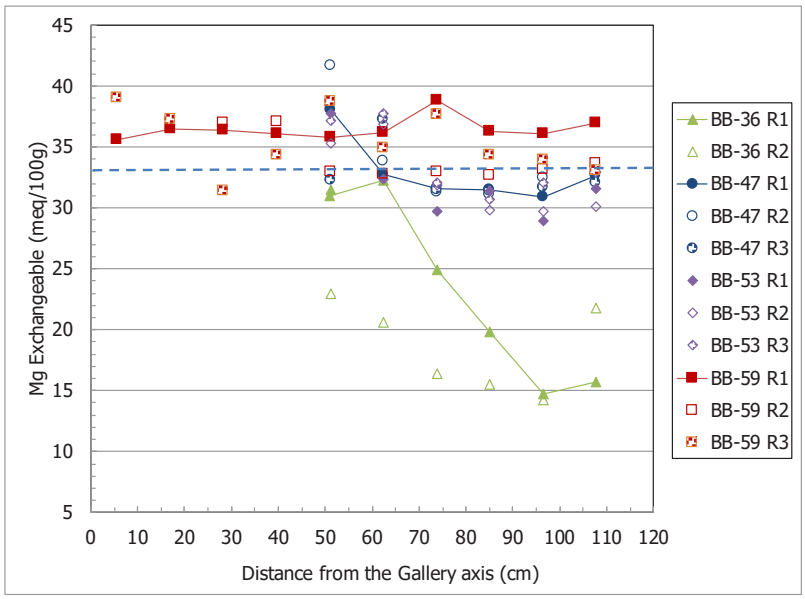

Fig. 131: Magnesium occupancy at exchange sites as a function of distance to the gallery axis from samples taken during dismantling of Heater #2

Dotted line: reference value

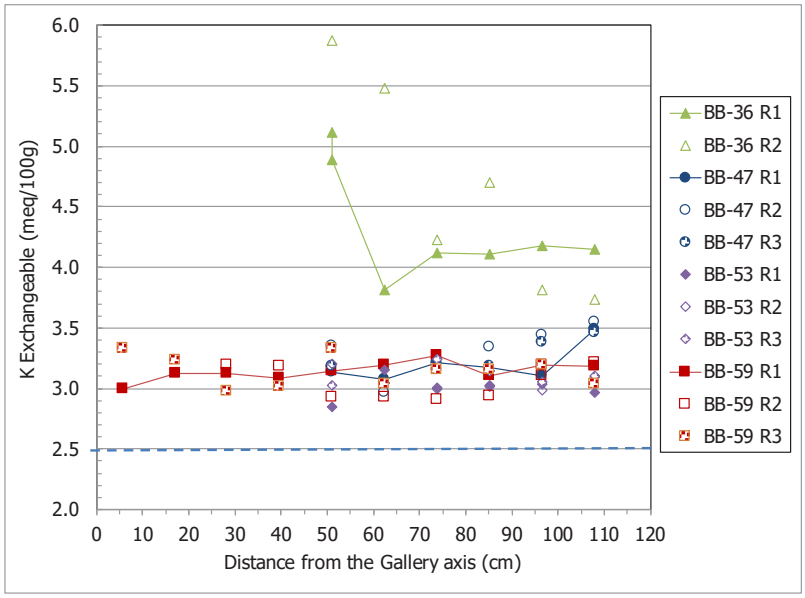

Fig. 132: Potassium occupancy at exchange sites as a function of distance to the gallery axis from samples taken during dismantling of Heater #2

Dotted line: reference value

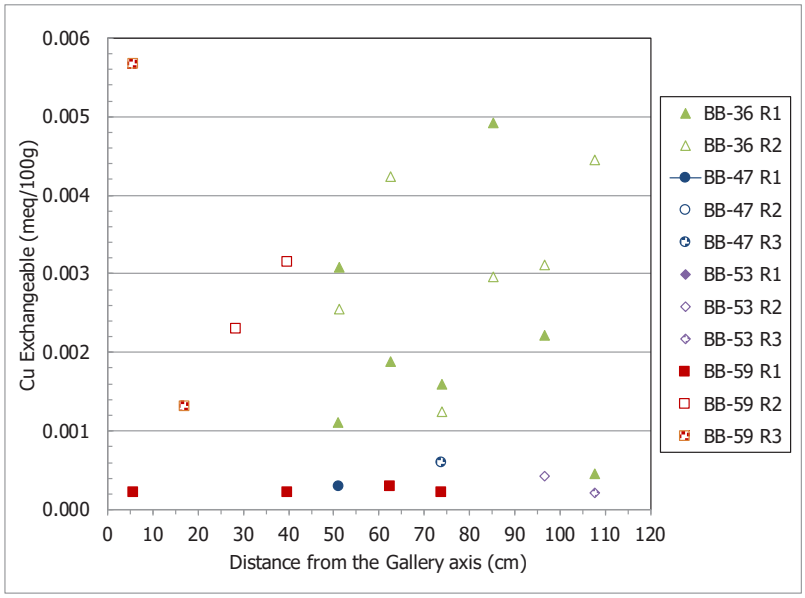

Fig. 133: Copper occupancy at exchange sites as a function of distance to the gallery axis from samples taken during dismantling of Heater #2 in 2015

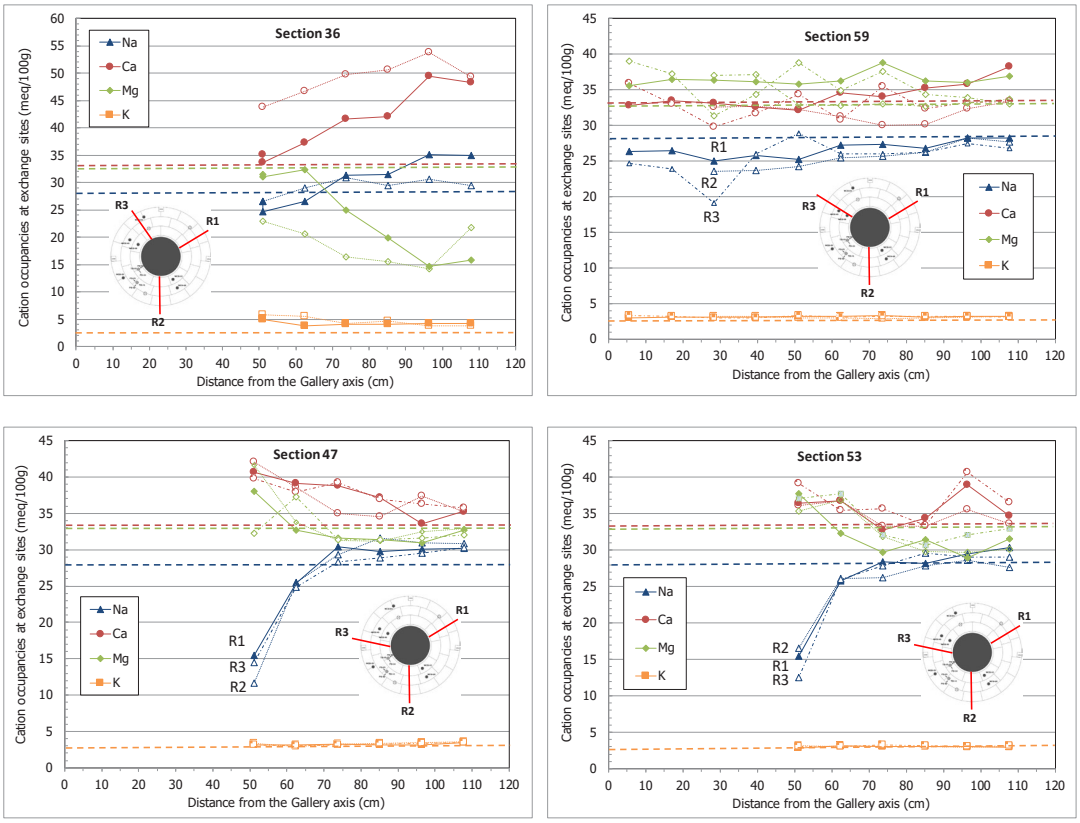

Fig. 134: Cation occupancy at interlayer sites from Sections S36, S59, S47 and S53 at different radii taken during dismantling of Heater #2

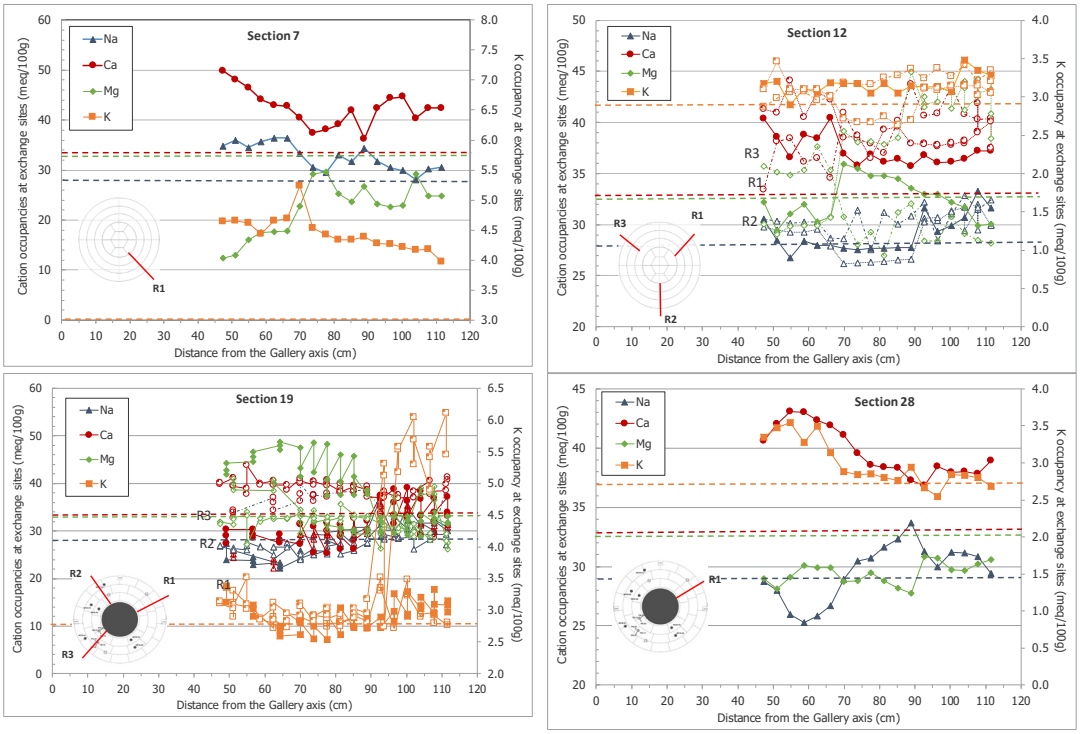

Fig. 135: Cation occupancy at interlayer sites from Sections S7, S12, S19 and S28 taken during the dismantling of Heater #1 in 2002 as a function of distance to the gallery axis (values normalised with respect to CEC = 102 meq/100g)

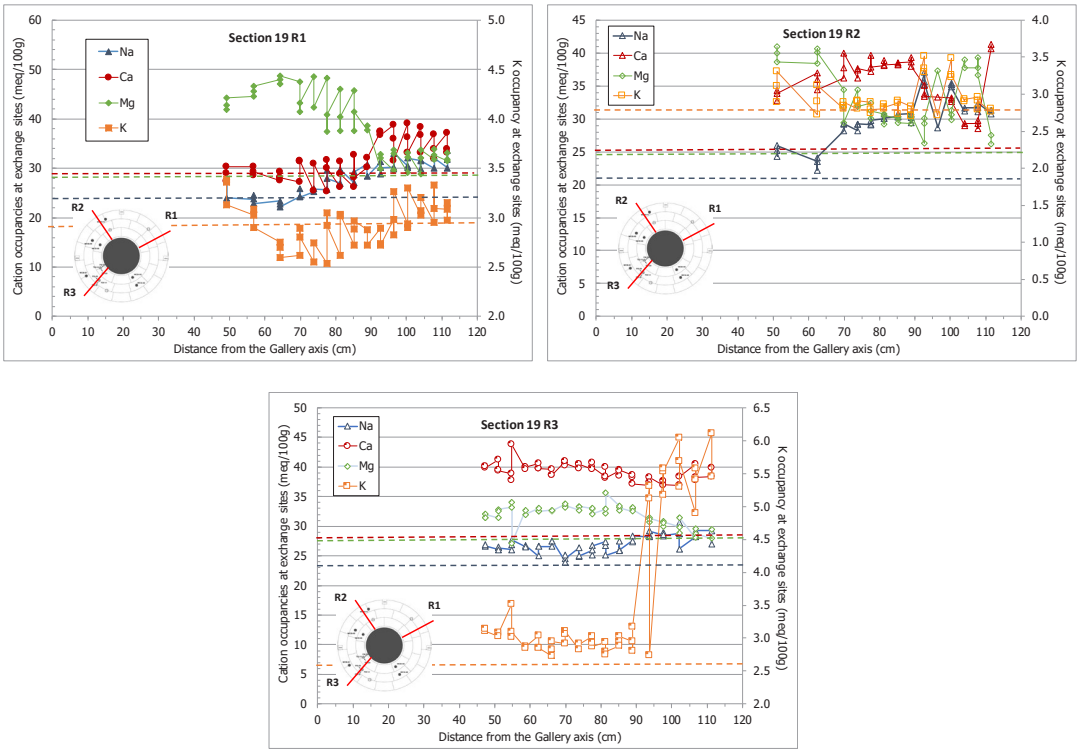

Fig. 136: Cation exchange occupancies from Section 19 (dismantling of Heater #1 in 2002) as a function of distance to the gallery axis (values normalised with respect to CEC = 102 meq/100g)

Dashed lines: reference values

Fig. 137: Sum of exchangeable cations in Sections S7, S12, S19 and S28 as a function of distance to the gallery axis from samples taken during dismantling of Heater #1 in 2002

Dashed lines: reference values

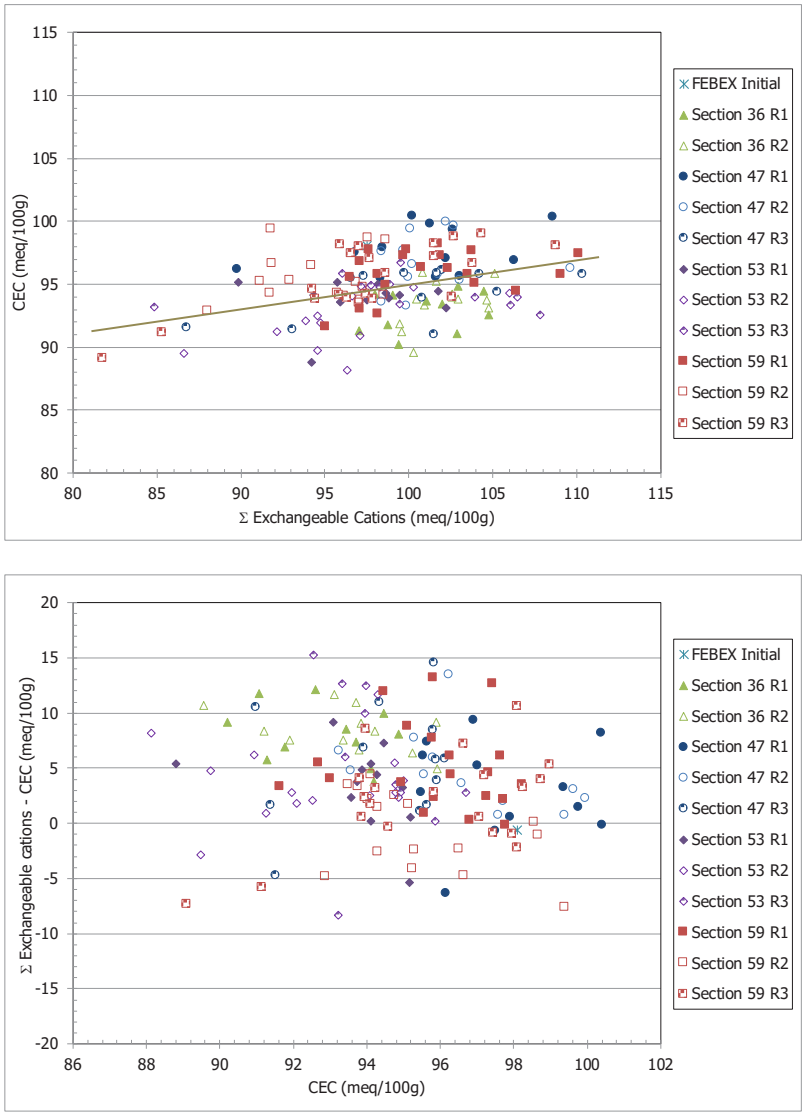

Fig. 138: Relationship between CEC and: a) Σ exchangeable cations or b) (Σ exchangeable cations-CEC), in samples from dismantling of Heater #2

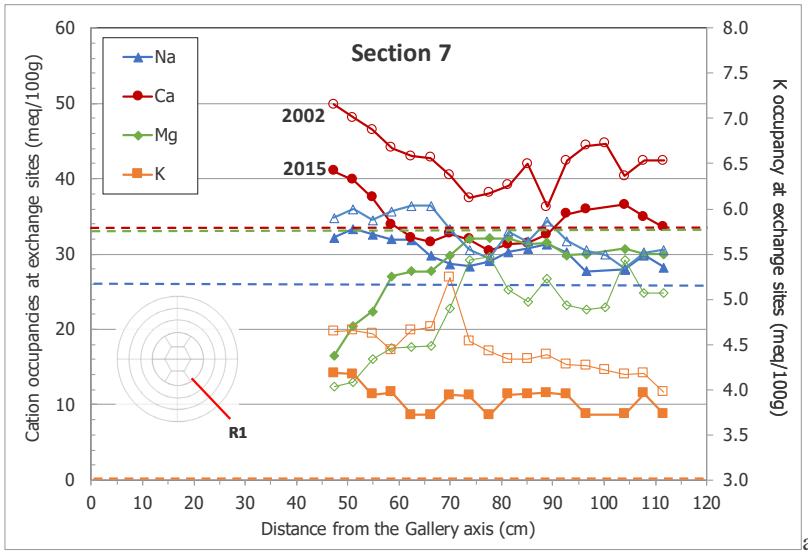

a)

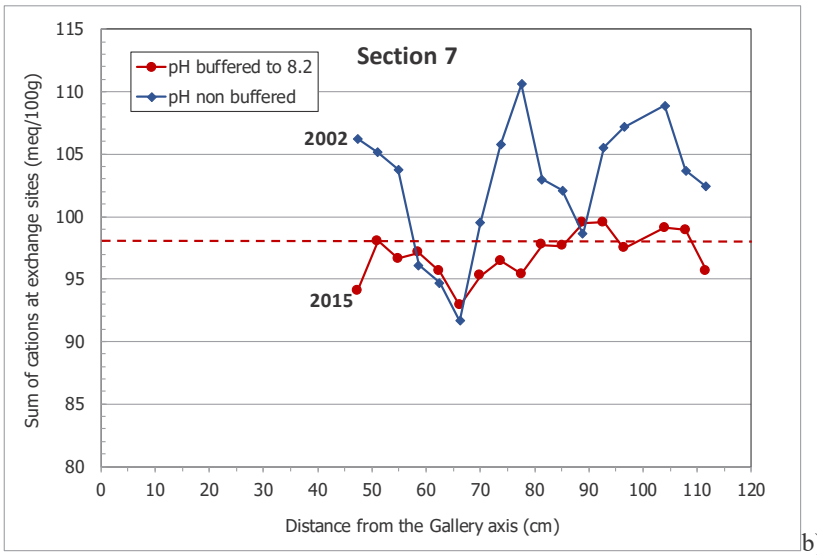

b)

Fig. 139: Comparison of methods for extraction of cation exchange occupancies in 2002 (open points) and 2015 (closed points): a) Exchangeable cations obtained with 0.5 M $CsNO_3$ solutions buffered (2015) or not at pH 8.2 (2002), b) sum of exchangeable cations in 0.5 M $CsNO_3$ suspensions buffered (2015) or not at pH 8.2 (2002)

5.5.4 Zeta potential and size of colloid clay particles

The mean size and ξ potential of colloids from the heated bentonite Section 47 were analysed. The mean size of the colloids generated from samples is summarised in Tab. 20 as a function of distance from the gallery axis. The size measured by photon correlation spectroscopy (PCS) is the hydrodynamic size, which includes the molecules of water adhered to the particles while they are moving.

The particle size ranged from 246 to 707 nm (Fig. 142); for samples from bentonite blocks BB-47-7 and BB-47-8 the values remained constant (~ 300 nm) at all pHs. For sample BB-47-9 close to contact with Heater #2 the values increased at pHs between 4 to 8.5. The increase of size indicates an aggregation of clay particles in the BB-47-9 sample at those pH values, which are in the range of those found in the analysed pore waters (see Section 5.6). The light scattering events (or counts number) obtained from the clay suspensions are shown Fig. 141, which change as a function of distance to the gallery axis. They decrease towards the Heater #2 contact, indicating a lower particle concentration, in agreement with the increase of the particle size.

The determination of colloid charge was done by means of electrophoretic mobility measurements. Decreases and increases in mobility will be referred to absolute values. The mobility is related to the zeta potential via the Henry equation (see Section 4.5.4). Zeta (ξ) potential is an intrinsic property of a mineral particle in a liquid. It determines the strength of the diffuse double layer (DDL) repulsive forces between particles and identifies the stability of a colloidal system (Çelik 2004). In general, zeta potential values of smectites are dominated more by their layer charge than the variable charge.

Fig. 142 shows the mobility of colloids in the suspensions from heated Section 47 as a function of pH and distance to Heater #2. The mobility of the suspensions ranged from approximately -84 to -3.86 $(\mu m \cdot s^{-1})/(V \cdot cm^{-1})$, in agreement with the mobility of 2:1 clay minerals, which is always negative according to their negative permanent charge. The small variation in charge observed as a function of the pH is due to the low amphoteric charge present on the edge surface groups. This variable charge represents a small fraction (5 – 10 %) of the total charge, so the mobility of these smectite suspensions is mainly dominated by their layer charge at exchange sites more than variable charge at silanol and aluminol edge sites. This mobility decreases with distance to the gallery axis, the lowest values being found in the sample close to Heater #2 (BB-47-9). Zeta potential is negative for the whole pH region (Fig. 143), and basically independent of pH (values between -24 to -45 mV), due to the dominant role of constant negative charge of faces, which makes the contribution of edges in the electrokinetics of smectite particles negligible.

The data related to colloid size and the mobility of colloids in suspension can be linked to the main physico-chemical properties of the clay minerals, such as the main exchangeable cation, the layer charge (CEC) and BET surface area (see Discussion Section). The colloid properties (size and mobility) of the clays are also affected by the electrolyte concentration. The aggregation of clay particles can occur due to the increase of ionic strength because the electrostatic repulsion between particles diminishes, which mainly leads to face to face, FF, interactions. An increase of the pore water salinity was observed at the Heater #2 contact, which can explain the increase of the clay particles' size in sample BB-47-9 as well. Changes in pH may also lead to particle aggregation (edge to face, EF, or edge to edge, EE, interactions) as the small amphoteric charge present in the edges of clay particles may interact with the negatively charged layers. These aggregates form large structures (honeycomb –like), which tend to flocculate rapidly. Specific adsorption of cations, provoking changes in surface potential, can be also a cause of aggregation.

Tab. 20: Main characteristics of the colloids generated in DW from different block samples from Section 47 as a function of distance to Heater #2 and pH (see location of samples in Fig. 31)

Sample	**pH**	**E. Mobility** (µm·cm/V·s)	**ξ Potential** (mV)	**Counts or Light scattering events**	**Size** (nm)
Ref. FEBEX	8.8	-2.18 ± 0.06	-33.4 ± 1.6	--	349 ± 1
Initial BB-47-7	7.23	-3.0	-38.6	307.2	260.7
BB-47-7 (pH 2)	2.14	-2.54 ± 0.26	-35.1 ± 3.6	221.9	339.5
BB-47-7 (pH 4)	4.02	-2.49 ± 0.02	-34.4 ± 0.25	257.1	458.5
BB-47-7 (pH 6)	6.32	-3.15 ± 0.03	-43.6 ± 0.5	309.8	245.9
BB-47-7 (pH 7)	7.14	-2.87 ± 0.06	-39.6 ± 0.87	326.7	249.6
BB-47-7 (pH 8)	8.07	-3.08 ± 0.04	-39.4 ± 0.51	256.9	263.9
BB-47-7 (pH 10)	9.61	-3.09 ± 0.06	-39.4 ± 0.81	300.7	254.1
BB-47-7 (pH 12)	11.45	-3.15 ± 0.17	-40.2 ± 2.27	191.9	389.5
Initial BB-47-8	7.44	-2.96	-37.8	189.2	268.5
BB-47-8 (pH 2)	2.23	-2.30 ± 0.14	-29.5 ± 1.85	121.3	> d.l.
BB-47-8 (pH 4)	4.08	-2.40 ± 0.08	-31.0 ± 1.06	163.1	312.1
BB-47-8 (pH 6)	6.44	-2.70 ± 0.04	-35.3 ± 0.60	172.5	334.1
BB-47-8 (pH 7)	7.24	-3.00 ± 0.04	-38.3 ± 0.53	188.4	294.7
BB-47-8 (pH 8)	7.57	-2.90 ± 0.05	-37.1 ± 0.65	175	290.3
BB-47-8 (pH 10)	9.65	-3.09 ± 0.06	-39.5 ± 0.87	172.6	295.3
BB-47-8 (pH 12)	11.43	-3.30 ± 0.01	-42.2 ± 0.15	91.8	285.2
Initial BB-47-9	7.44	-2.06	-26.3	87.6	452.5
BB-47-9 (pH 2)	2.26	-1.84 ± 0.05	-23.6 ± 0.70	63.2	> d.l.
BB-47-9 (pH 4)	3.97	-1.94 ± 0.01	-24.8 ± 0.20	84.6	460
BB-47-9 (pH 6)	5.87	-2.08 ± 0.02	-26.6 ± 0.25	91.1	609.4
BB-47-9 (pH 7)	7.14	-2.43 ± 0.02	-31.0 ± 0.21	88	558.5
BB-47-9 (pH 8)	8.19	-2.24 ± 0.01	-28.6 ± 0.11	93.8	707.8
BB-47-9 (pH 10)	9.8	-2.68 ± 0.03	-34.2 ± 0.36	69.3	325.1
BB-47-9 (pH 12)	11.58	-3.56 ± 0.31	-45.5 ± 4.00	191	332.2

The colloid size and mobility, and hence zeta potential, are very sensitive to the valence of the ion adsorbed onto interlayer sites. This fact is well known (Bar-on & Shainberg 1970). The size of the particles is expected to depend on the Na and Ca content in the exchange complex. Fig. 257 shows the variation of particle size as a function of Na and Ca percentage at exchange sites. The largest colloid size (> 500 nm) corresponds to the sample close to the Heater #2 contact (BB-47-9), where there is an increase of exchangeable Ca. Thus, the increase of Ca as exchangeable

cation clearly favours the formation of large particles when sodium decreases at values below ~ 20 % (Missana et al. 2018a,b). Values of exchangeable sodium higher than ~ 25 % are enough to provide clay particles similar to the Reference value. The large size of the particles close to the heater contact is in agreement with the lower BET values measured. Larger particles imply lower BET surface area values (see Fig. 256 in the Discussion Section). The mobility and zeta potential decrease when exchangeable Ca increases and exchangeable Na decreases close to the Heater #2 contact (Fig. 144). At the contact with the heater, the samples show less mobility than the other ones, but when the exchange complex has about 25 % of Na, the electrophoretic mobility is similar to those of Na-clays, as observed in Fig. 144.

On the other hand, although CEC seems to decrease towards the heater contact, this is not well observed in the CEC values obtained with the macroscopic determination method, except for the BMS and protrusion samples located in close contact with Heater #2. Nevertheless, the zeta potential, a parameter related to the layer charge, clearly decreases (in absolute values) as a function of distance to the Heater #2 contact (Fig. 256 and Fig. 258), which indicates a real decrease of layer charge in the samples close to Heater #2.

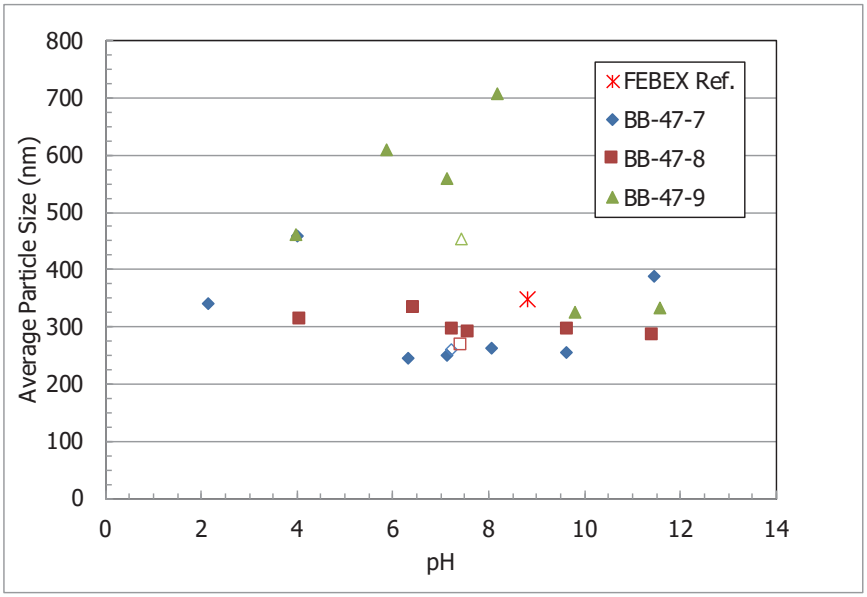

Fig. 140: Average particle size for clayey suspensions as a function of pH and distance to the gallery axis in the heated Section 47 and comparison with the Reference sample

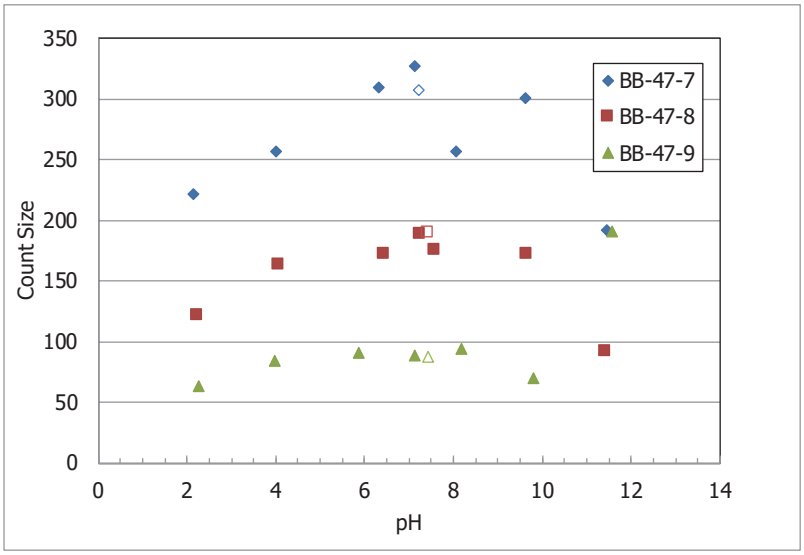

Fig. 141: Light scattering events (count number) for clayey suspensions as a function of pH and distance to the gallery axis in heated Section 47 and comparison with the Reference FEBEX sample

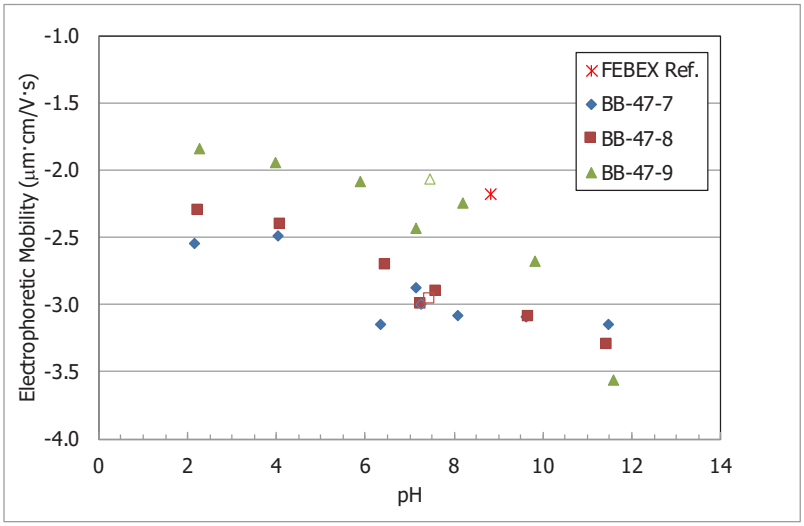

Fig. 142: Electrophoretic mobility for different bentonite suspensions from Section 47 as a function of pH and distance to the gallery axis

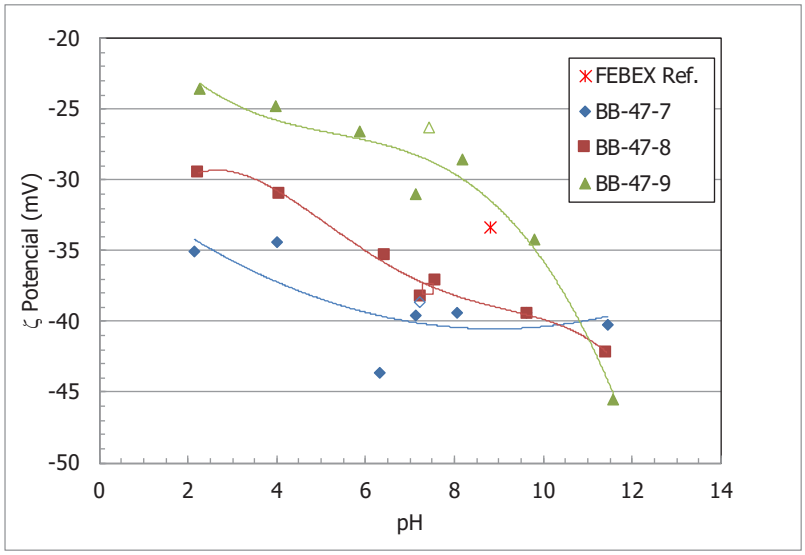

Fig. 143: Zeta potential (ξ potential) for different bentonite suspensions from Section 47 as a function of pH and distance to the gallery axis

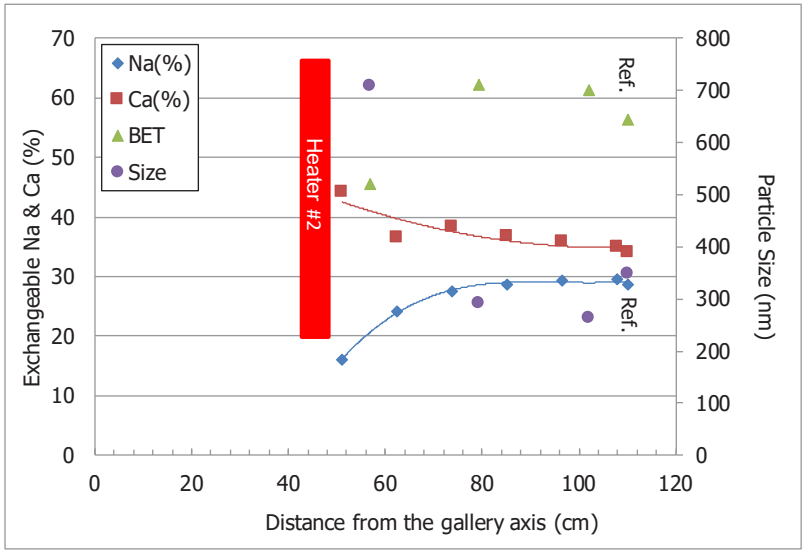

Fig. 144: Zeta potential, mobility and exchangeable Na and Ca for different bentonite suspensions from Section 47 as a function of distance to the gallery axis

Data are compared with the Reference values (Ref. at 110 cm).

5.5.5 External surface area

The dry state of the bentonite can be further characterized by nitrogen adsorption-desorption isotherms. In the adsorption of non-polar molecules such as N_2, the layered structure remains closed, and the external surface area of the stacks of layers, corresponding to both the external faces and the edges of the montmorillonite particles, is obtained. N_2 adsorption-desorption isotherms were obtained at 77 K (liquid nitrogen temperature) on a discontinuous volumetric sorptometer Micromeritics ASAP 2020, where pore size distribution can be analysed between 1.5 and 300 nm.

Fig. 145 and Fig. 146 display the nitrogen adsorption-desorption isotherms obtained for an untreated FEBEX bentonite sample (reference) and other retrieved samples from the dismantling of Heater #2 and Heater #1, expressed as gas volume. From the dismantling of Heater #2 in 2015, the treated samples belong to the non-heated Section 36, the heated Section 47, a sample at the contact with the liner (BMS-47-2) and a bentonite protrusion (RN-42) sample. From the dismantling of Heater #1 in 2002 the samples belong to: bentonite blocks BB12 (non-heated section) and BB19 (heated section), two samples adhered to the back side of the heater (BS31-26 and BS31-22) and a block in contact with a corroded instrument at Section 17 (BSH-SDI01).

All adsorption isotherms have the characteristic feature of the type IV isotherm (albeit without a plateau at high P/P_0) with a very important hysteresis loop due to capillary condensation in macro- and mesopores formed between different montmorillonite particles or quasicrystals. The curves exhibit a H3 hysteresis loop in desorption characterizing the presence of slit-shaped pores (Greeg & Sing 1982). Hysteresis closure at $P/P_0 \sim 0.4$ indicates the presence of small mesopores. The rounded knee at low P/P_0 values indicates the approximate location of monolayer formation (Fig. 147). After the knee region ($P/P_0 \sim 0.1$), micropores cease to contribute to the adsorption process. The presence of a low slope region in the middle of the isotherm indicates the adsorption of up to five multilayers (Fig. 147) on external surfaces, including meso- and macropores, and before the onset of capillary condensation (> 0.98). The N_2 adsorption-desorption curves of the samples close to both Heater #1 and Heater #2 show a large difference with respect to the other ones; the total volume of gas adsorbed for the samples in contact with the heater is lower than for the other samples.

BET-external surface areas were calculated according to the standard N_2-BET method, using a series of data points over the P/P_0 range of 0.02 to 0.20 of the nitrogen adsorption isotherms (Brunauer et al. 1938, Gregg & Sing 1982), with P/P_0 the relative N_2 pressure and P_0 the saturation pressure). Tab. 21 and Tab. 22 show the relevant parameters deduced form the BET and *t*-plot treatments for the retrieved samples after dismantling of Heater #2 in 2015 and Heater #1 in 2002, respectively. It is interesting to note that the BET surface area decreased as a function of the Heater #2 contact. This was observed for samples taken from both dismantling operations (Fig. 148) in 2002 (Heater #1) and in 2005 (Heater #2). Regarding the non-heated Sections S36 and S59, all samples have values similar to the reference value after 18 years of experiment (Fig. 148).

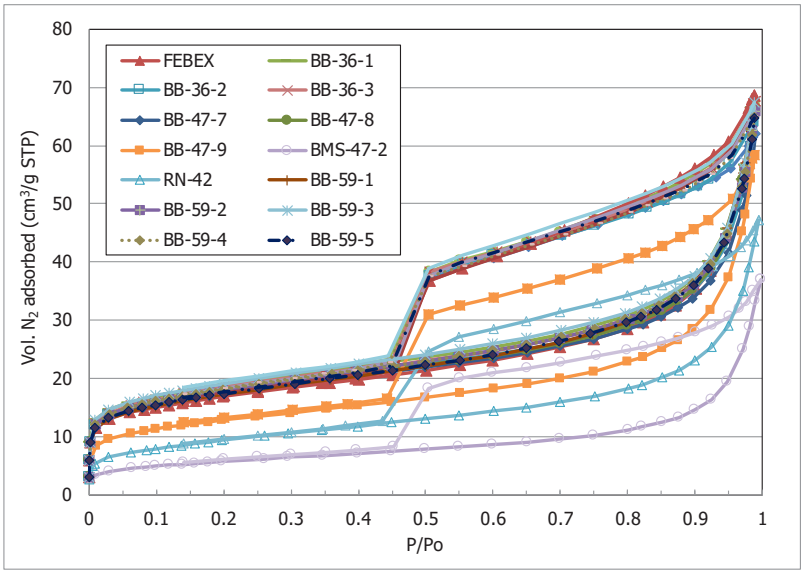

Fig. 145: Adsorption-desorption isotherms of N_2 gas at 77 K from samples after dismantling of Heater #2 and comparison with the FEBEX Reference sample (see location of samples in Fig. 17, Fig. 18, Fig. 19, Fig. 20 and Fig. 21)

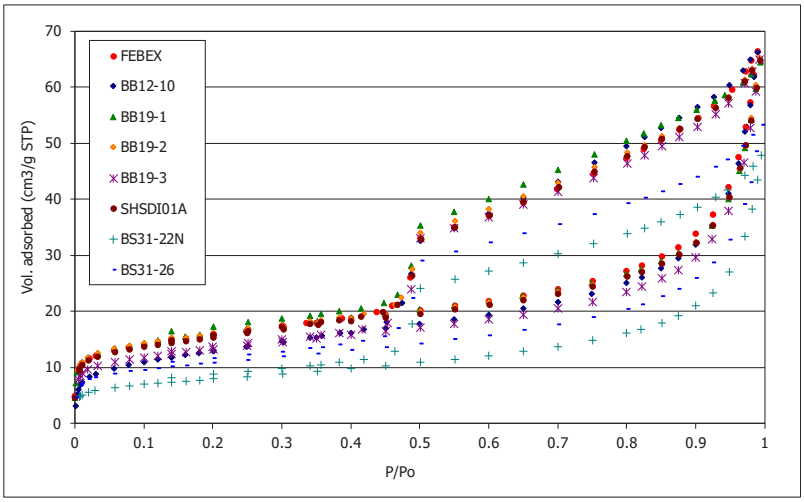

Fig. 146: Adsorption-desorption isotherms of N_2 gas at 77 K from samples after dismantling of Heater #1 and comparison with the FEBEX Reference sample (see location of samples in Fig. A-1 from Appendix A)

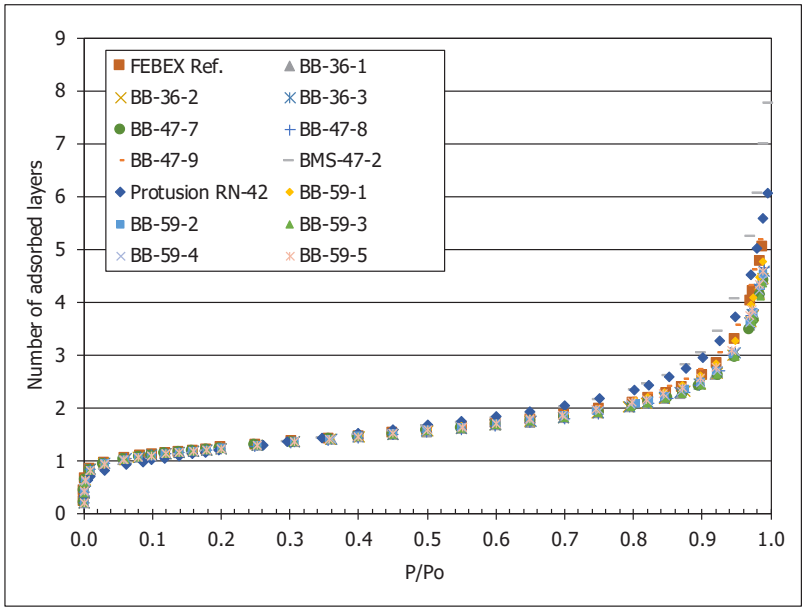

Fig. 147: Number of N_2 adsorbed layers as a function of P/P_o according to the de Boer-(1965, 1966) method (*t*-plot treatment on adsorption branch)

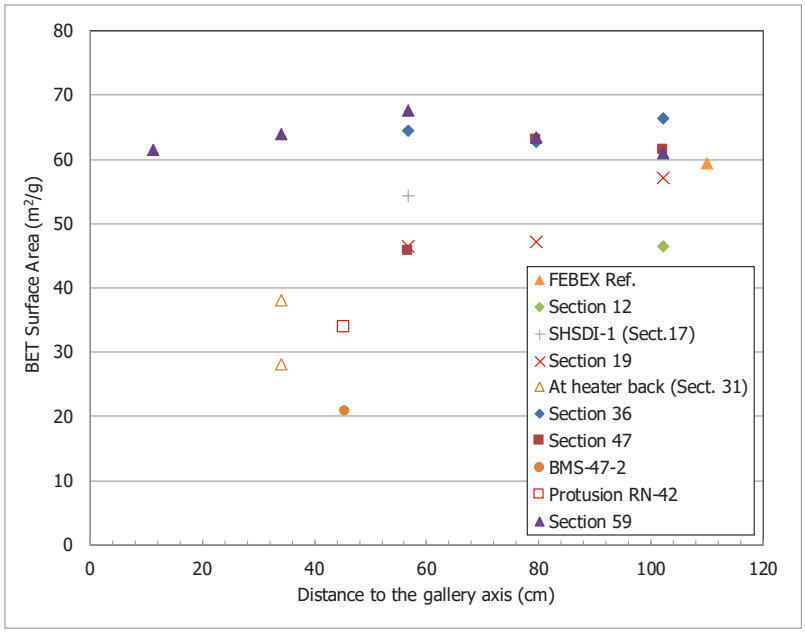

Fig. 148: BET surface area from samples obtained after dismantling of Heater #1 and Heater #2 (data compared to the FEBEX Reference sample)

Tab. 21: Parameters deduced from the BET and *t*-plot treatment on the adsorption of N_2 at 77 K from samples obtained after dismantling of Heater #2

Parameter	C_{BET}	V_m (cm^3/g)	S_{BET} (m^2/g)	St_{or} (m^2/g)	V_{tot} (cm^3/g)	S_{micro} (m^2/g)	V_{micr} (cm^3/g)	$S_{ext\ micro}$ (m^2/g)	$S_{ext\ meso}$ (m^2/g)	V_{meso} (cm^3/g)
FEBEX Ref.	1934	2.11×10^{-2} (l)	59.45	62.88	1.01×10^{-1}	20.20	8.92×10^{-3} (l)	39.25	28.42	1.48×10^{-2} (l)
BB-36-1	2016	2.35×10^{-2} (l)	66.40	69.89	9.80×10^{-2}	23.66	1.04×10^{-2} (l)	42.75	28.61	1.81×10^{-2} (l)
BB-36-2	1218	2.22×10^{-2} (l)	62.78	63.12	9.24×10^{-2}	20.90	9.20×10^{-3} (l)	41.88	27.06	1.73×10^{-2} (l)
BB-36-3	1710	2.28×10^{-2} (l)	64.48	65.90	9.68×10^{-2}	21.93	9.68×10^{-3} (l)	42.55	28.08	1.75×10^{-2} (l)
BB-47-7	618	2.18×10^{-2} (l)	61.54	64.09	7.98×10^{-2}	21.53	8.29×10^{-3} (l)	42.55	25.75	1.74×10^{-2} (l)
BB-47-8	1109	2.23×10^{-2} (l)	63.07	65.96	9.67×10^{-2}	25.90	9.97×10^{-3} (l)	40.06	26.89	1.71×10^{-2} (l)
BB-47-9	369	1.62×10^{-2} (l)	45.71	47.56	7.45×10^{-2}	14.38	5.39×10^{-3} (l)	33.18	23.77	1.05×10^{-2} (l)
BMS-47-2	120	7.37×10^{-3} (l)	20.80	20.57	4.47×10^{-2}	2.79	1.00×10^{-3} (l)	18.01	13.11	3.63×10^{-3} (l)
Protrusion RN-42	102	1.21×10^{-2} (l)	34.02	33.27	6.05×10^{-2}	3.04	9.04×10^{-4} (l)	30.98	20.48	6.97×10^{-3} (l)
BB-59-1	549	2.16×10^{-2} (l)	61.02	61.27	$9.67 \times \cdot 10^{-2}$	18.97	8.26×10^{-3} (l)	42.05	29.72	1.51×10^{-2} (l)
BB-59-2	1495	2.25×10^{-2} (l)	63.47	64.11	9.69×10^{-2}	19.34	8.58×10^{-3} (l)	44.13	28.54	1.71×10^{-2} (l)
BB-59-3	992	2.39×10^{-2} (l)	67.54	67.08	9.83×10^{-2}	22.86	1.00×10^{-2} (l)	44.68	29.11	1.86×10^{-2} (l)
BB-59-4	761	2.26×10^{-2} (l)	63.98	64.37	9.57×10^{-2}	20.47	8.96×10^{-3} (l)	43.51	29.31	1.67×10^{-2} (l)
BB-59-5	633	2.18×10^{-2} (l)	61.56	61.87	9.45×10^{-2}	19.04	8.32×10^{-3} (l)	42.52	29.65	1.53×10^{-2} (l)

V_m: Monolayer capacity derived from the BET treatment; expressed as (l):liquid; S_{BET}: BET Surface area
St_{or}: Total surface area derived from the slope of the straight line passing through the origin of the *t*-plot
V_{micr}: Liquid microporous volume derived from the ordinate at the origin in the second straight line of the *t*-plot
$S_{ext\ micro}$: Surface area derived from the slope of the second straight line of the *t*-plot
V_{tot}: Total pore volume, derived from the amount of nitrogen adsorbed at p/p_o of 0.98
$S_{ext\ meso}$: Surface area derived from the slope of the third straight line of the *t*-plot
V_{meso}: Liquid microporous volume derived from the ordinate at the origin in the third straight line of the *t*-plot
S_{micro}: $= S_{BET} - S_{ext\ micro}$: Surface area of the micropores

Tab. 22: Parameters deduced from the BET and *t*-plot treatment on the adsorption of N_2 at 77 K from samples obtained after dismantling of Heater #1

Parameter	C_{BET}	V_m (cm^3/g)	S_{BET} (m^2/g)	St_{or} (m^2/g)	V_{tot} (cm^3/g)	S_{micro} (m^2/g)	V_{micr} (cm^3/g)	$S_{ext\ micro}$ (m^2/g)	$S_{ext\ meso}$ (m^2/g)	V_{meso} (cm^3/g)
FEBEX Ref.	1934	2.11×10^{-2} (l)	59.45	62.88	1.01×10^{-1}	20.20	8.92×10^{-3} (l)	39.25	28.42	1.48×10^{-2} (l)
BB12-10	117	1.65×10^{-2} (l)	46.53	45.64	9.56×10^{-2}	7.81	2.83×10^{-3} (l)	38.72	29.45	8.3×10^{-3} (l)
BSHSDI	402	1.92×10^{-2} (l)	54.34	54.34	9.25×10^{-2}	17.4	7.56×10^{-3} (l)	36.94	26.26	1.32×10^{-2} (l)
BB19-1	765	2.02×10^{-2} (l)	57.12	60.93	9.23×10^{-2}	18.23	3.29×10^{-3} (l)	38.89	25.73	1.47×10^{-2} (l)
BB19-2	464	1.67×10^{-2} (l)	47.08	65.48	9.16×10^{-2}	15.46	6.65×10^{-3} (l)	31.62	26.16	9.21×10^{-3} (l)
BB19-3	774	2.00×10^{-2} (l)	46.53	64.02	9.32×10^{-2}	7.98	7.82×10^{-3} (l)	38.55	25.11	1.48×10^{-2} (l)
BS31-26	382	1.35×10^{-2} (l)	38.16	38.16	7.49×10^{-2}	8.26	3.76×10^{-3} (l)	29.90	25.32	5.45×10^{-3} (l)
BS31-22N	310	$9.97v10^{-2}$ (l)	28.17	28.17	7.10×10^{-2}	5.88	2.56×10^{-3} (l)	22.29	23.39	7.70×10^{-4} (l)

V_m: Monolayer capacity derived from the BET treatment; expressed as (l):liquid; S_{BET}: BET Surface area
St_{or}: Total surface area derived from the slope of the straight line passing through the origin of the *t*-plot
V_{micr}: Liquid microporous volume derived from the ordinate at the origin in the second straight line of the *t*-plot
$S_{ext\ micro}$: Surface area derived from the slope of the second straight line of the *t*-plot
V_{tot}: Total pore volume, derived from the amount of nitrogen adsorbed at p/p_o of 0.98
$S_{ext\ meso}$: Surface area derived from the slope of the third straight line of the *t*-plot
V_{meso}: Liquid microporous volume derived from the ordinate at the origin in the third straight line of the *t*-plot
S_{micro}: $= S_{BET} - S_{ext\ micro}$: Surface area of the micropores

Microporosity analysis

The microporosity analysis was performed by the *t*-plot method (de Boer et al. 1965, 1966), the adsorbed layer thickness was calculated by means of the Harkins-Jura method (Harkins & Jura 1944). In the Harkins and Jura method, the adsorbed amount of gas at a given relative pressure P/P_0 is related to the statistical thickness t of the adsorbed film by means of the equation:

$$t(\text{Å}) = \left[\frac{13.99}{0.034 - \log_{10}\left(P/P_o\right)} \right]^{1/2}$$

In the de Boer method, the thickness t is calculated from the adsorbed gas volume, V_{ads} (typically expressed as cubic centimetre gas at STP per mass of dry solid), and the monolayer volume, V_m, obtained by means of the BET method,

$$t(\text{Å}) = 3.54\left(\frac{V_{ads}}{V_m}\right).$$

Note that the volume of adsorbed gas V_{ads} (or the monolayer capacity V_m) can also be expressed as volume of pores, V_p, in mL of liquid per mass of dry solid, by multiplicating with 1.548×10^{-3} mL/cm^3 STP for N_2. The statistical number of adsorbed layers n_l on the surface is obtained by dividing t by the molecular thickness of the adsorbed gas. In the case of nitrogen, we have

$$n_l = \frac{t}{3.54\ \text{Å}}.$$

The adsorption isotherms were replotted following the procedure of de Boer et al. (1965) in the form V_a versus t, where the t is the mean thickness of the adsorbed layer calculated according to the Harkins & Jura (1944) method. This method has been used for analysing the microporosity and the micro-, meso- and total external surface areas (Tab. 21 and Tab. 22). The original slope of the t plot indicates a total specific surface area from 66.4 to 20.8 m^2/g after dismantling of Heater #2 (Fig. 149) with decreasing values towards the heater contact. This was also observed for retrieved samples from dismantling of Heater #1 (Fig. 150), where values changed from 59.45 m^2/g (Reference) to 28.2 m^2/g (a sample located in contact with the back part of the Heater #1). The reduction of micropores in the treated samples as a function of distance to the heater is significant; this can be observed by the decrease of the BET surface area from micropores, whose values changed from 20.2 m^2/g (Reference) to 2.8 m^2/g. The samples are around 40 % microporous (plus some interlayer pores that are not seen by N_2) and 60 % meso- and macroporous; with very different values for the protrusion sample where these vary from 9 % microporous to 91 % meso- and macroporous. No significant changes with respect to the Reference FEBEX bentonite were observed for the non-heated Sections S36 and S59 (Fig. 149).

Mesoporosity analysis

Pore structure analysis can be performed by mercury intrusion porosimetry (MIP), nitrogen adsorption and water adsorption. These methods consider surface tension, capillary forces and pressure. Pores are classified according to size into three categories (IUPAC, 1997): micropores (pore diameter < 20 Å), mesopores (pore diameter 20 – 500 Å) and macropores (pore diameter > 500 Å). Whereas low-pressure Hg-porosimetry determines macropores and mesopores in the pore diameter range between 360 μm and 3 nm; the detection range of nitrogen adsorption isotherms is for pore diameter between 3000 Å and 15 Å. The smallest pores can be only analysed by water absorption tests.

The pore volume distribution as a function of pore size (pore size distribution PSD) in the mesopore (pore radius 10 – 250 Å) and low macropore (radius > 250 Å) size range, as well as the volume of mesopores were inferred by the Barrett-Joyner-Halenda (BJH) method. This method is based on a model for the adsorbent as a collection of cylindrical pores and on isotherm data (adsorption or desorption) between about 0.35 and 0.99 P/P_0 (Barrett et al. 1951). In this method, pore sizes are derived from the Kelvin equation and a relation for the statistical thickness of an adsorbed surface layer. The theory accounts for capillary condensation in the pores using the classical Kelvin equation, which in turn assumes a hemispherical liquid-vapour meniscus and a well-defined surface tension. According to Kelvin's equation, it is possible to calculate the minimum pore radius where capillary condensation starts by means of the relative pressure in the low limit of the hysteresis loop:

$$\ln\frac{P}{P_o} = \frac{-2\gamma V_{mol}}{RT}\frac{\cos\varphi}{r_k} \quad 250\text{ Å} < r_k < 10\text{ Å (cylindrical pores)}$$

where, γ is the gas surface tension at the boiling point (N_2: 8.85 mN/m at 77 K), V_{mol} is the molar volume of the liquid adsorbed (N_2: 34.68 mL/mol), R is the gas constant (8.3143 J/mol·K), T represents the nitrogen boiling point (77 K), P/P_o is the relative pressure, φ is the contact angle, and r_k is the Kelvin pore radius in which the capillary condensation starts at a relative pressure of P/P_o. Thus, the Kelvin radius and diameters are given by the following equations:

$$r_k = \frac{-2\gamma V_{mol}}{RT\ln\left(P/P_o\right)} \text{ and } D_k = 2r_k.$$

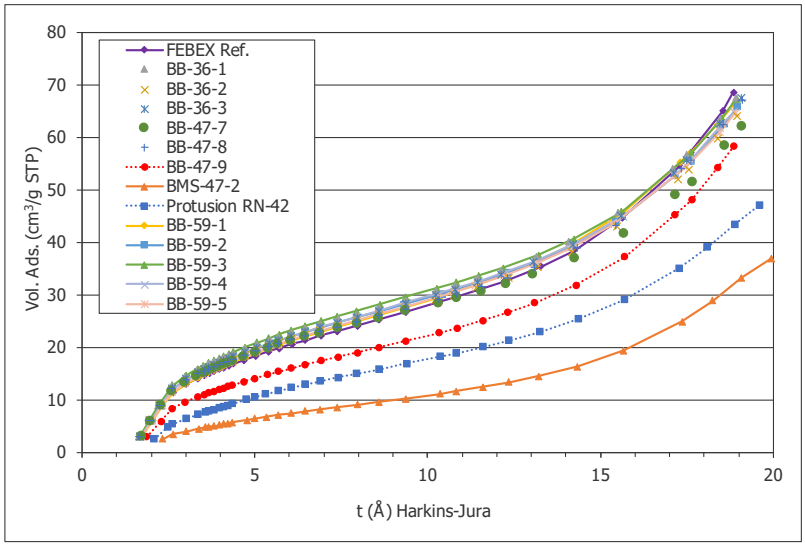

Fig. 149: *t*-plot according to Harkins-Jura method for the samples after dismantling Heater #2

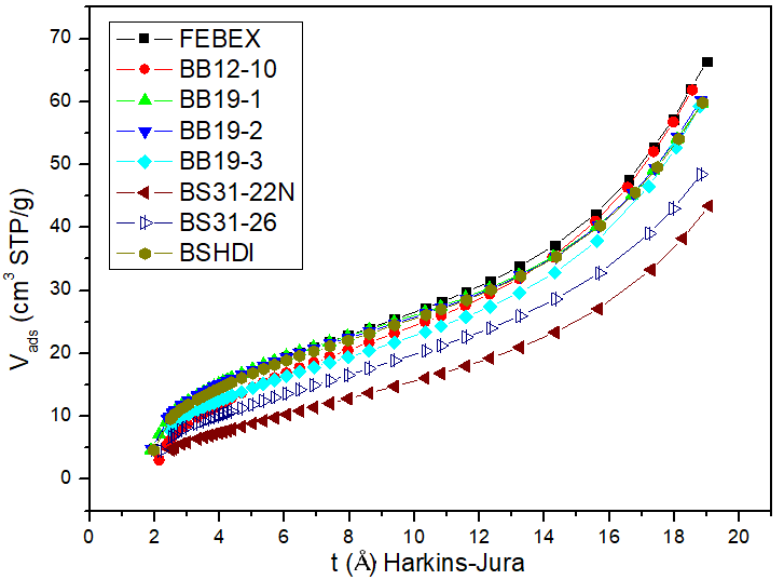

Fig. 150: *t*-plot according to Harkins-Jura method for the samples after dismantling Heater #1

For N_2, the equations are:

$$r_k(\text{nm}) = \frac{0.41604}{\log(P_o/P)} \text{ and } D_k(\text{nm}) = \frac{0.83208}{\log(P_o/P)}.$$

The BJH theory incorporates thinning of the adsorbed layer. A pore loses its condensed liquid adsorbate, known as the core of the pore, at a particular relative pressure related to the core radius by the Kelvin equation. After the core has evaporated, a layer of adsorbate remains on the wall of the pore. The thickness of this layer is calculated for a particular relative pressure from the thickness equation. This layer becomes thinner with successive decreases in pressure, so that the measured quantity of gas desorbed in a step is composed of a quantity equivalent to the liquid cores evaporated in that step plus the quantity desorbed from the pore walls of pores whose cores have been evaporated in that and previous steps. Condensation occurs in pores that already have some multilayers on the walls. Therefore, the pore size is calculated from the Kelvin equation and the selected statistical thickness (*t*-curve) equation through the use of a reference isotherm:

$$r_p = r_k + t$$

where, r_p is the actual radius of the pore, r_k is the Kelvin radius of the pore and t is the thickness of the adsorbed film. To determine the PSD (Pore Size Distribution) in the mesopore range with the BJH approach, the thickness of the adsorbed layer at a relative pressure was calculated using the Frenkel-Halsey-Hill method and the Halsey formulation with a Faas correction:

$$t(\text{Å}) = 3.54\left[\frac{-5}{\ln(P/P_o)}\right]^{1/3}.$$

The mesopores size distribution was analysed by the BJH method (Fig. 151). Three pore size families are observed in the mesopore range (Tab. 23), a first centred at around a pored diameter of 494 Å (21 %), a second at 77 Å (25 %), and a third family at 36 Å (54 %).

The main parameters calculated are shown in Tab. 24 and Tab. 25 for the samples retrieved after dismantling of Heater #2 and Heater #1, respectively. In the case of mesopores, no significant differences were observed. Nevertheless, the main differences are detected in samples close to both heaters where pore size values decreased, indicating an increase of macroporosity.

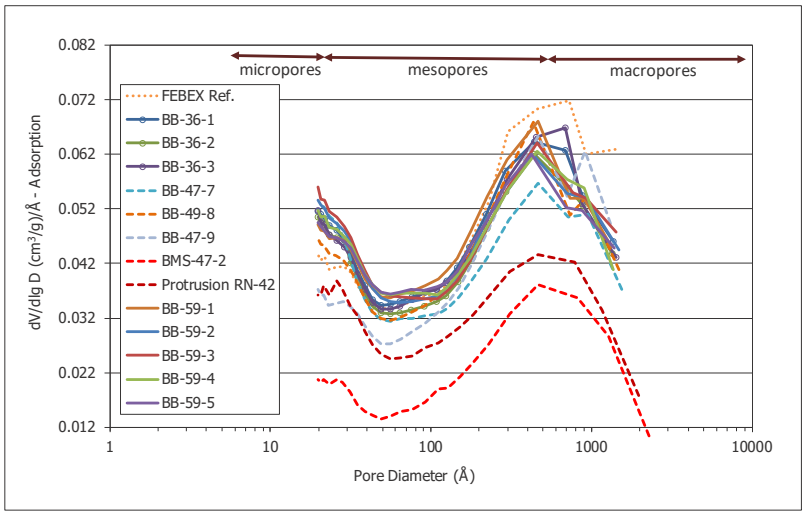

Fig. 151: Pores size distribution (PSD) calculated from the BJH method (adsorption branch) for mesopores from samples obtained after dismantling Heater #2

Tab. 23: Pore size families calculated from the BJH method (desorption branch) for mesopores from samples obtained after dismantling Heater #2

Samples	**Large Radius > 100 Å**		**Radius medium r: 100 – 25 Å**		**Radius small r: < 25 Å**	
	%	**Mode (Å)**	**%**	**Mode (Å)**	**%**	**Mode (Å)**
FEBEX	20.2	241.4	28.1	45.02	51.8	18.2
BB-36-1	19.1	252.8	27.1	46.21	53.8	19.3
BB-36-2	18.8	248.5	24.2	27.47	57.1	19.0
BB-36-3	21.0	244.3	24.6	46.01	54.4	18.9
BB-47-7	15.9	254.6	26.1	37.85	58.0	18.6
BB-47-8	20.8	233.4	23.6	37.34	55.6	18.3
BB-47-9	23.8	268.0	24.8	36.55	51.4	17.6
BMS-47-2	26.1	232.8	22.2	35.16	51.7	16.4
Protrusion RN-42	20.5	819.6	25.4	35.89	54.1	16.8
BB-59-1	20.0	255.7	27.0	45.96	53.0	18.9
BB-59-2	18.1	272.1	26.9	46.03	55.0	19.1
BB-59-3	18.7	265.8	25.8	27.73	55.5	19.1
BB-59-4	18.9	249.8	25.3	27.89	55.8	19.0
BB-59-5	18.0	268.3	25.0	45.93	57.0	18.6

Tab. 24: Main parameters calculated from the BJH method for mesopores from samples obtained after dismantling Heater #2

Parameters	Desorption branch			Adsorption Branch		
	Cumulative pore volume (cm^3/g)	Pore surface area (m^2/g)	Average pore diameter (Å)	Cumulative pore volume (cm^3/g)	Pore surface area (m^2/g)	Average pore diameter (Å)
FEBEX	1.0910×10^{-1}	77.0312	56.653	9.7181×10^{-2}	36.824	105.56
BB36-1	1.0814×10^{-1}	73.9850	58.468	9.3499×10^{-2}	39.337	95.024
BB36-2	1.0254×10^{-1}	73.8033	55.575	8.9037×10^{-2}	37.846	94.106
BB36-3	1.0829×10^{-1}	75.1244	57.660	9.4215×10^{-2}	38.573	97.699
BB47-7	9.9317×10^{-2}	74.1987	53.541	8.6433×10^{-2}	37.606	91.935
BB47-8	1.0729×10^{-1}	77.4513	55.410	9.3412×10^{-2}	36.780	101.589
BB47-9	9.2383×10^{-2}	65.685	56.259	8.5035×10^{-2}	31.412	108.284
BMS-47-2	5.6444×10^{-2}	42.7187	54.161	5.7842×10^{-2}	17.434	129.505
Protrusion RN-42	$7.4184v10^{-2}$	52.4010	56.629	7.2102×10^{-2}	29.369	98.203
BB-59-1	1.0628×10^{-1}	73.5258	57.819	9.4757×10^{-2}	39.619	95.668
BB-59-2	1.0537×10^{-1}	74.3738	56.673	9.2498×10^{-2}	40.004	92.488
BB-59-3	1.0828×10^{-1}	76.5565	56.578	9.3534×10^{-2}	40.7803	91.745
BB-59-4	1.0405×10^{-1}	73.6889	56.482	9.0821×10^{-2}	39.7070	91.491
BB-59-5	1.0346×10^{-1}	75.7461	54.635	9.1478×10^{-2}	39.3162	93.069

Tab. 25: Main parameters calculated from the BJH method for mesopores from samples obtained after dismantling Heater #1

Parameters	Desorption branch			Adsorption Branch		
	Cumulative pore volume (cm^3/g)	Pore surface area (m^2/g)	Average pore diameter (Å)	Cumulative pore volume (cm^3/g)	Pore surface area (m^2/g)	Average pore diameter (Å)
FEBEX	1.09×10^{-1}	77.0	56.7	9.7×10^{-2}	36.8	105.6
BB12-10	1.04×10^{-1}	75.3	55.2	1.0×10^{-1}	39.2	102.9
SHSDI01A	1.03×10^{-1}	69.3	59.2	9.2×10^{-2}	34.4	107.3
BB19-1	1.03×10^{-1}	73.6	55.6	9.0×10^{-2}	34.1	106.2
BB19-2	1.03×10^{-1}	71.1	58.3	$9.2v10^{-2}$	33.4	109.9
BB19-3	6.20×10^{-2}	43.5	56.8	5.7×10^{-2}	18.7	121.9
BS31-26	8.4×10^{-2}	61.5	54.6	7.8×10^{-2}	27.5	114.2
BS31-22N	$7.5v10^{-2}$	54.1	55.5	$7.2v10^{-2}$	22.8	126.8

5.5.6 Total surface area

The total surface area is an important parameter related to the water absorption and swelling capacity of bentonites. It determines the amount of water needed for hydrating all the clay particles. The lower the particle size, the higher the total surface area.

Data for total surface area were obtained from the initial sample and those obtained after the FEBEX in-situ test. The results obtained are shown in Tab. C.1 and Tab. C.2 in Appendix C, which list samples from bentonite Sections S47 and S53 (heated) and Sections S36 and S59 (non-heated). The mean SA for the initial FEBEX bentonite is 655 m^2/g. After the FEBEX in-situ test, the mean SA for the samples in Section 36, Section 59, Section 47 and Section 53 was 574, 579, 586 and 609 m^2/g, respectively (Fig. 152 and Fig. 153). Therefore, a slight decrease in total SA is observed with respect to the initial FEBEX bentonite (Fig. 154). However, the mean values are in the typical range expected for smectite clay minerals.

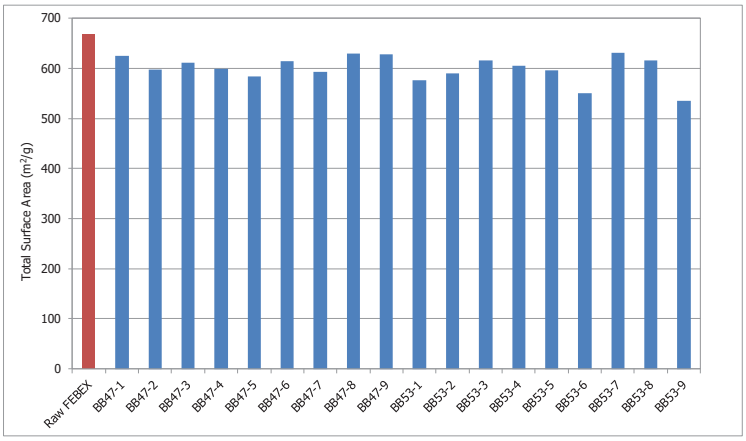

Fig. 152: Total surface area in bentonite samples from the heated sections: Section 47 and Section 53

Data are compared to the reference sample.

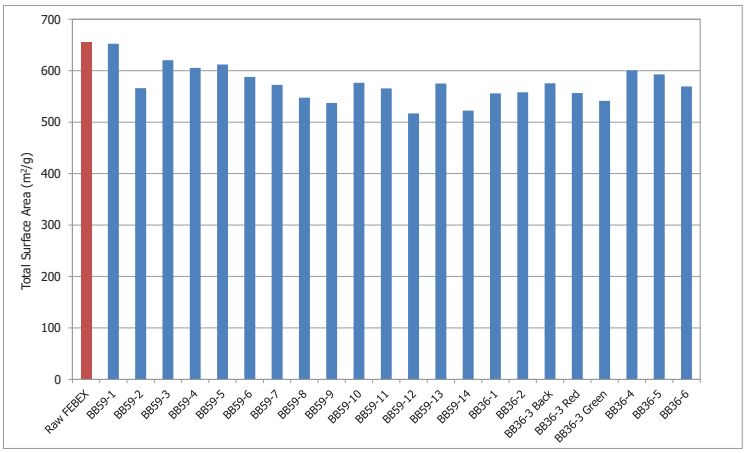

Fig. 153: Total surface area in bentonite samples from Section 36 (shotcrete contact) and Section 59 (non-heated section)

Data are compared to the reference sample.

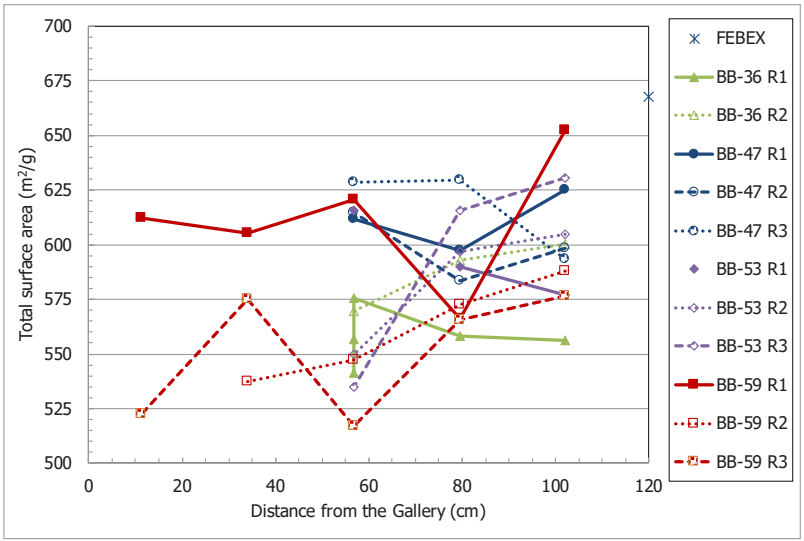

Fig. 154: Total surface area in bentonite samples from Sections S36, S47, S53 and S59 as a function of distance to the gallery axis

5.5.7 Water adsorption isotherms

The swelling capacity of the smectites is due to their property of adsorbing water in the interlayer space (intra-crystalline swelling). The 001 reflexion increases due to the hydration of smectite and the formation of successive monomolecular layers of water.

The water uptake behaviour of bentonite samples obtained after dismantling of the FEBEX in-situ test was analysed by water adsorption isotherms, where powdered samples, previously dried at 110 °C, were submitted to various relative humidity (RH) atmospheres. The results are shown in Fig. 155 to Fig. 158 for samples from different heated and non-heated sections. The data were compared with the reference FEBEX bentonite sample.

No significant differences were found between the treated samples and the reference FEBEX material. Water was adsorbed by successive steps. Four different states during the water filling of the interlayer space can be distinguished from an analysis of changes in slope and the correlation with the basal spacings (Fernández & Rivas 2005b): a) interlayer collapse (d_{001} = 9.8 Å; aw: 0 – 0.05), b) one layer hydrate (d_{001} = 12.0 Å; aw: 0 – 0.1), c) two-layer hydrate (d_{001} = 15.2 Å, aw: 0 – 0.97), and c) three-layer hydrate (d_{001} = 18.8 Å, aw: 0.97 – 0.99). Next, capillary condensation in intra-aggregates or inter-aggregates starts occurring.

According to the water vapour adsorption isotherms, retrieved samples preserved their swelling capacity and interlayers may expand up to the point of developing a three-layer hydrate state.

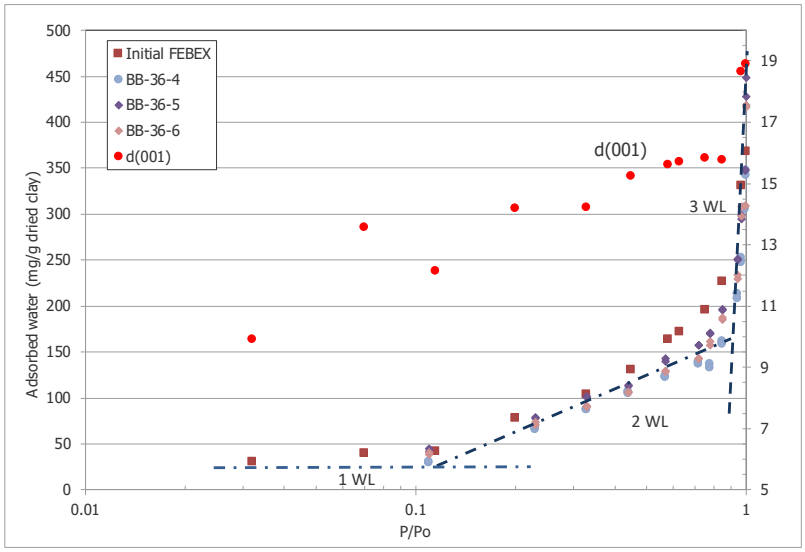

Fig. 155: Water adsorption isotherms for samples from Section 36 and comparison to the reference FEBEX sample

The (001) reflexions correspond to the reference FEBEX sample. Sample BB-36-4 is close to the granite interface; Sample BB-36-6 is close to the heater.

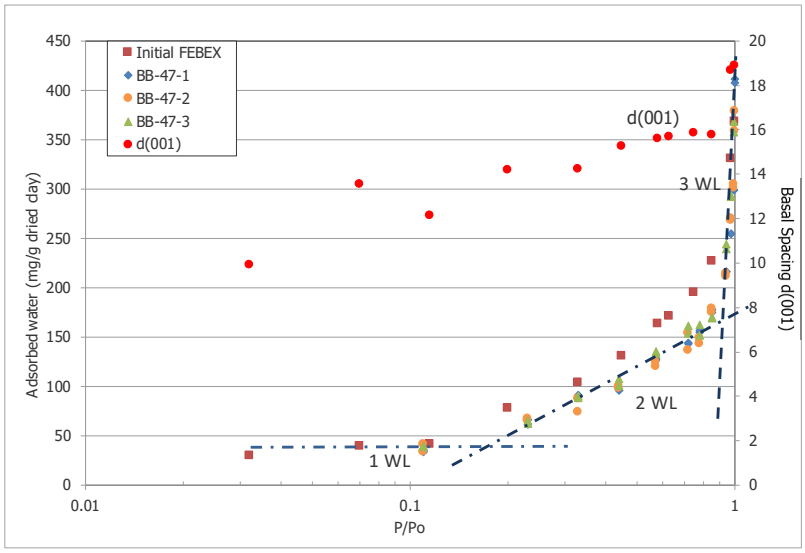

Fig. 156: Water adsorption isotherms for samples from Section 47 and comparison to the reference FEBEX sample

The (001) reflexions correspond to the reference FEBEX sample. Sample BB-47-1 is close to the granite interface; Sample BB-47-3 is close to the heater.

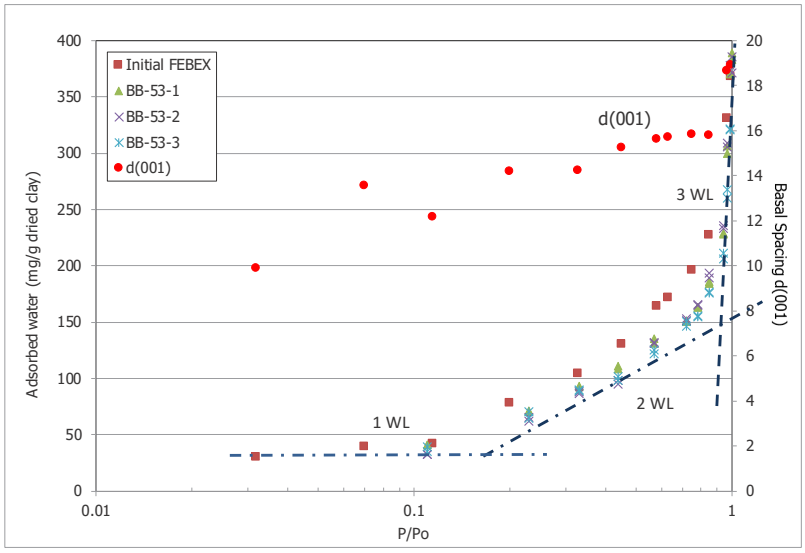

Fig. 157: Water adsorption isotherms for samples from Section 53 and comparison to the reference FEBEX sample

The (001) reflexions correspond to the reference FEBEX sample. Sample BB-53-1 is close to the granite interface; Sample BB-53-3 is close to the heater.

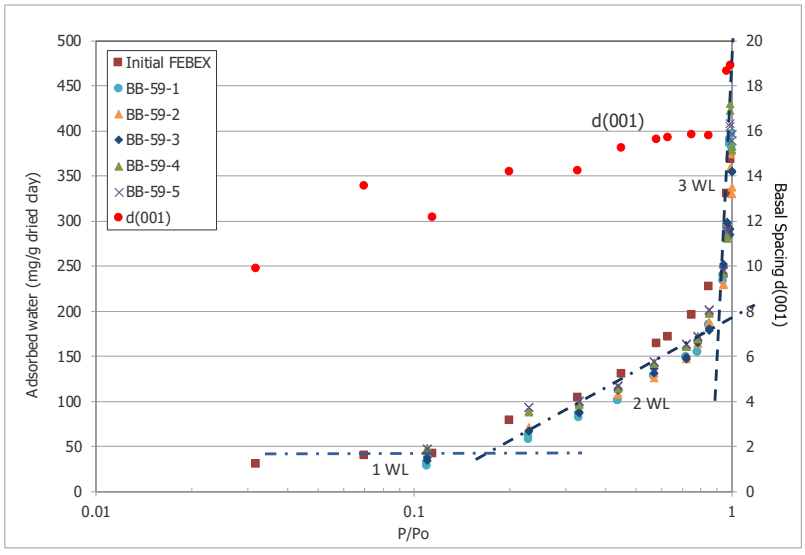

Fig. 158: Water adsorption isotherms for samples from Section 59 and comparison to the reference FEBEX sample. The (001) reflexions correspond to the reference FEBEX sample

Sample BB-59-1 is close to the granite interface; Sample BB-36-5 is at the inner part of the bentonite barrier.

5.5.8 Soluble salts by aqueous leaching

Ion inventories and ion distributions along the bentonite barrier were obtained by aqueous leaching tests. It should be taken into account that only Cl^-, F^-, and Br^- can be considered as conservative ions during the leaching tests, whereas the rest of anions and cations are controlled by mineral dissolution/precipitation processes and ion exchange reactions. Therefore, extraction conditions were selected to suppress mineral oxidation, by working in an oxygen-free atmosphere, and to avoid large modifications of cation concentration at exchange sites by carbonates dissolution, which affect the cation distribution in the aqueous extract solution. The time needed to attain calcite equilibrium in the FEBEX bentonite is more than six days, which affects the exchange composition to a large extent (Fernández 2004).

The ion concentration in aqueous tests offers information about the pore water composition inside the barrier, but back-calculation of pore water concentrations is only possible for non-reactive compounds (Cl^-, F^-, Br^-) taking into account the anion-accessible porosity (see Section 5.6 for references). This value is quite difficult to obtain, and in bentonites it is usually calculated from diffusion tests.

The soluble salts obtained from samples taken during dismantling of Heater #2 of the FEBEX in-situ test are shown in Fig. 159 to Fig. 165 and in Tab. C.10 to Tab. C.19 in Appendix C. In all figures the data were compared to the reference data. These data can be compared with results obtained from samples taken during the dismantling of Heater #1 in 2002, which are shown in Fig. 166 and Fig. 167.

The main ions are sodium and chloride, and these control the pore water chemistry of the system. These ions are clearly leached in zones close to the granitic formation and increase towards the internal part of the barrier. The ions behave differently in the different sections: in the heated zones, sodium and chloride concentrations seem to be concentrated at the heater contact, whereas in Section 59 (non-heated section), the concentration is distributed towards the inner bentonite blocks, due to the advective movement of groundwater towards the internal part of the barrier, saturating the bentonite (Fig. 159). In Section 36, the solution never has the initial ion concentration, so a large leaching process seems to have taken place at that section.

Chloride and sodium follow a linear relationship (Fig. 163), nevertheless the sodium concentration is always higher than chloride concentration. This indicates that sodium increased in solution due to ion-exchange reactions provoked by dissolution of carbonates and/or sulphates. The Na and Cl distribution is not homogeneous in all sections. At the Heater #2 interface, the Na:Cl ratio seems controlled by an equilibrium with halite as water evaporates due to the heating process. The saturation process of the bentonite and the advection-diffusion process of ions inside the bentonite is clearly observed over time. In 2015, the salinity (represented mainly by Cl^- content) was concentrated close to Heater #2, whereas in 2002 salinity was concentrated in the second ring of bentonite blocks (Fig. 164). In addition, when the heated and non-heated sections are compared, the ion transport seems dependent on the heating process, because chloride depletion is higher close to the granite contact in the heated Sections S47 and S53 than in the non-heated Section S59. Thus, water suction towards the inner part of the bentonite due to the heat, enhances the transport of solutes (Fig. 159, Fig. 164) and, in turn, the difference in solute concentration between the granite and the heater generates a solute concentration gradient with a corresponding water diffusion. Ion concentration is then controlled by dissolution/precipitation processes and exchange reactions.

Potassium increases in all sections with respect to the reference value, being especially concentrated close to Heater #2 in the heated sections, as is true for the rest of the cations: Ca, Mg and Na (Fig. 159, Fig. 160). Ca and Mg behaviour is different as a function of the location of the bentonite section. In Section 59, Ca and Mg contents are lower than the reference value close

to the contact with granite and then increase towards the internal part of the barrier. In Section 36 both cations are always depleted with respect to the reference value in all samples, i.e., along the whole section. In the heated Sections S47 and S53, Ca and Mg are depleted, except at the heater contact where Ca and Mg increase above the reference values. The decrease of Ca and the increase of Mg at the contact with granite may indicate dissolution of carbonates due to bentonite/ groundwater interactions and exchange reactions at interlayer sites (the incoming groundwaters are sodic-calcic-TIC-fluoride water-type, Huertas et al. 2006). A linear relationship between Cl and Mg in the solution is noted, as well as an increase of Mg with respect to the reference value both in all samples from the non-heated Section 59; and in those close to the heater in Sections S47 and S53. This may imply the formation of positively charged Mg-Cl ion pairs (positively charged species) which may enter the interlayers.

Regarding sulphate (Fig. 160), it is depleted at the granite contact and increases towards the inner part of the barrier; the maximum concentration is centred at the end of the second block of the barrier (74 cm from the gallery) or at the beginning of the third bentonite block (62 cm from the gallery), depending on the radius of each section. It seems that sulphate moves with groundwater towards the inner part of the barrier but at a lower rate than chloride. This was also observed in the samples from the dismantling of Heater #1 (Fig. 166), and is probably due to mineral dissolution/precipitation processes.

Alkalinity values are also affected by dissolution/precipitation processes of carbonates and the carbonate/bicarbonate concentration of the incoming groundwater. However, the distribution profiles indicate a different behaviour between the heated and non-heated sections (Fig. 161). In the heated sections (S47 and S53), the bicarbonate content is higher than the reference values in samples close to the granite interface and decreases below reference values towards the heater contact, correlated to the calcium content (Fig. 165). However, in non-heated sections (S36 and S59), bicarbonate increases at contact with the granite interface but maintains values similar to the reference values in the inner parts of the barrier. This indicates that heat affects carbonates, which would tend to be dissolved towards the granite contact and precipitated at the heater contact. Indeed, calcite solubility is controlled by temperature, decreasing with temperature. pH values are alkaline ranging from 8.0 to 9.2, with a trend to decrease towards the inner part of the bentonite. The higher pH values correspond to Section 36 at contact with the shotcrete. The alkalinity behaviour from Section 7 (dismantling of Heater #1) and Section 36 (dismantling Heater #2) seems to be different; the bicarbonate content being higher in Section 7 than in Section 36. This indicates a higher interaction of bentonite with the first plug constructed. The two plugs were made with different compositions (see Tab. 2). However, a depletion of Cl, Na and Mg in these sections at both dismantling operations is observed, indicating some diffusion process from bentonite towards the concrete interface, as indicated by the formation of Friedel's salts in the shotcrete up to 5 cm and the precipitation of Mg-phases in the bentonite (Turrero & Cloet 2018). The increase of cations at the granite interface in some of the samples retrieved from dismantling of Heater #1 (Fig. 167) are due to the extraction and analysis of bentonite colloids during the soluble salts extraction, which is observed by the increase of the Al, Mg and Si contents in the suspensions.

Other anions, such as fluoride and thiosulphate are also detected in the aqueous extracts. Fluoride is higher than the FEBEX reference values at contact with the granite interface and comes from the granitic groundwater. It decreases below this value in the inner part of the barrier, except in Section 36 (Fig. 161). In the heated sections, the decrease of F^- at the heater contact becomes quite pronounced. The presence of thiosulphate may be related to the reduction of sulphates or to the oxidation of sulphide minerals from the samples (Fig. 162).

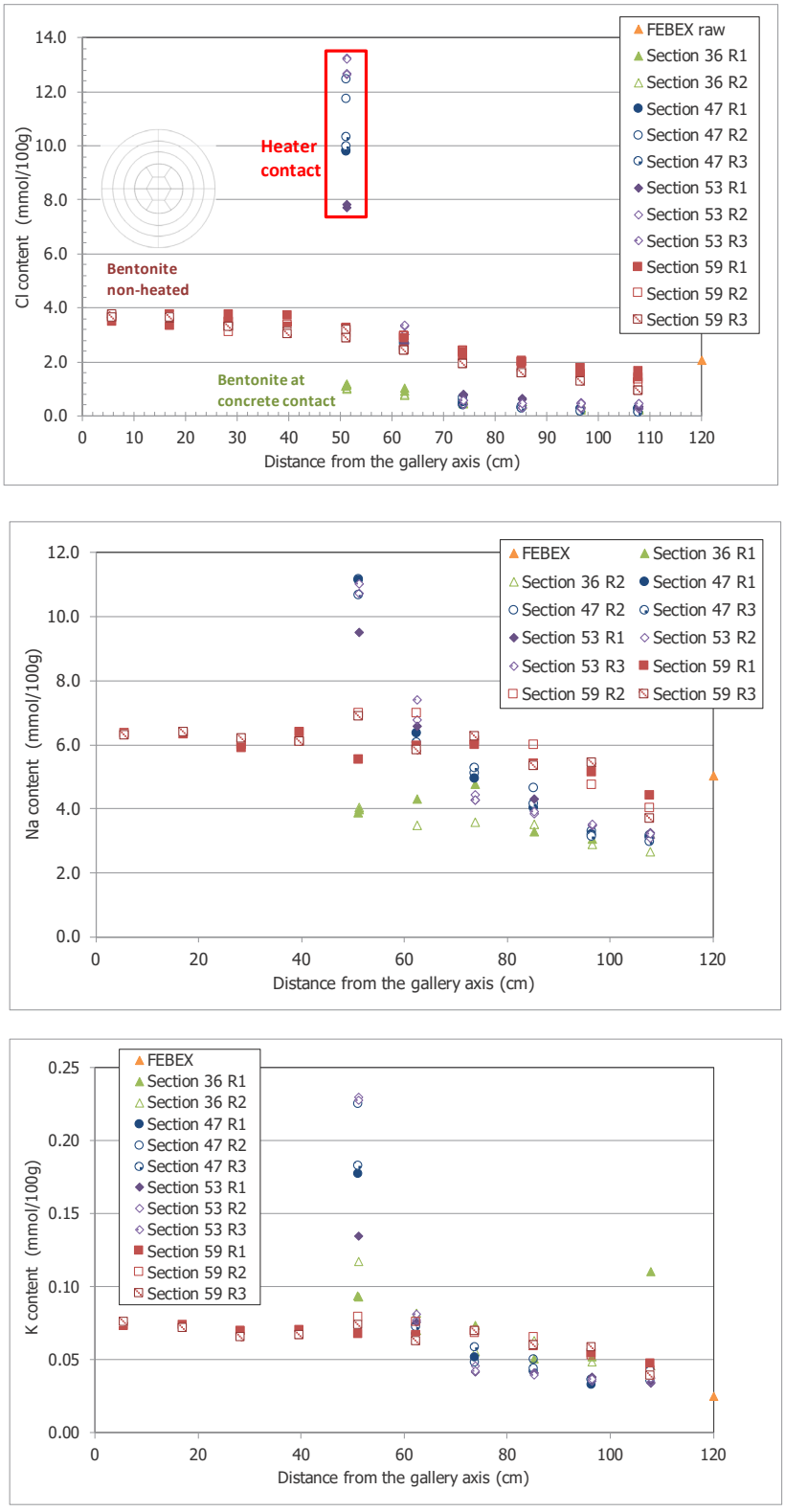

Fig. 159: Chloride, sodium and potassium content (1:4 aqueous leaching tests) from samples at different sections in three radii after dismantling Heater #2 in 2015

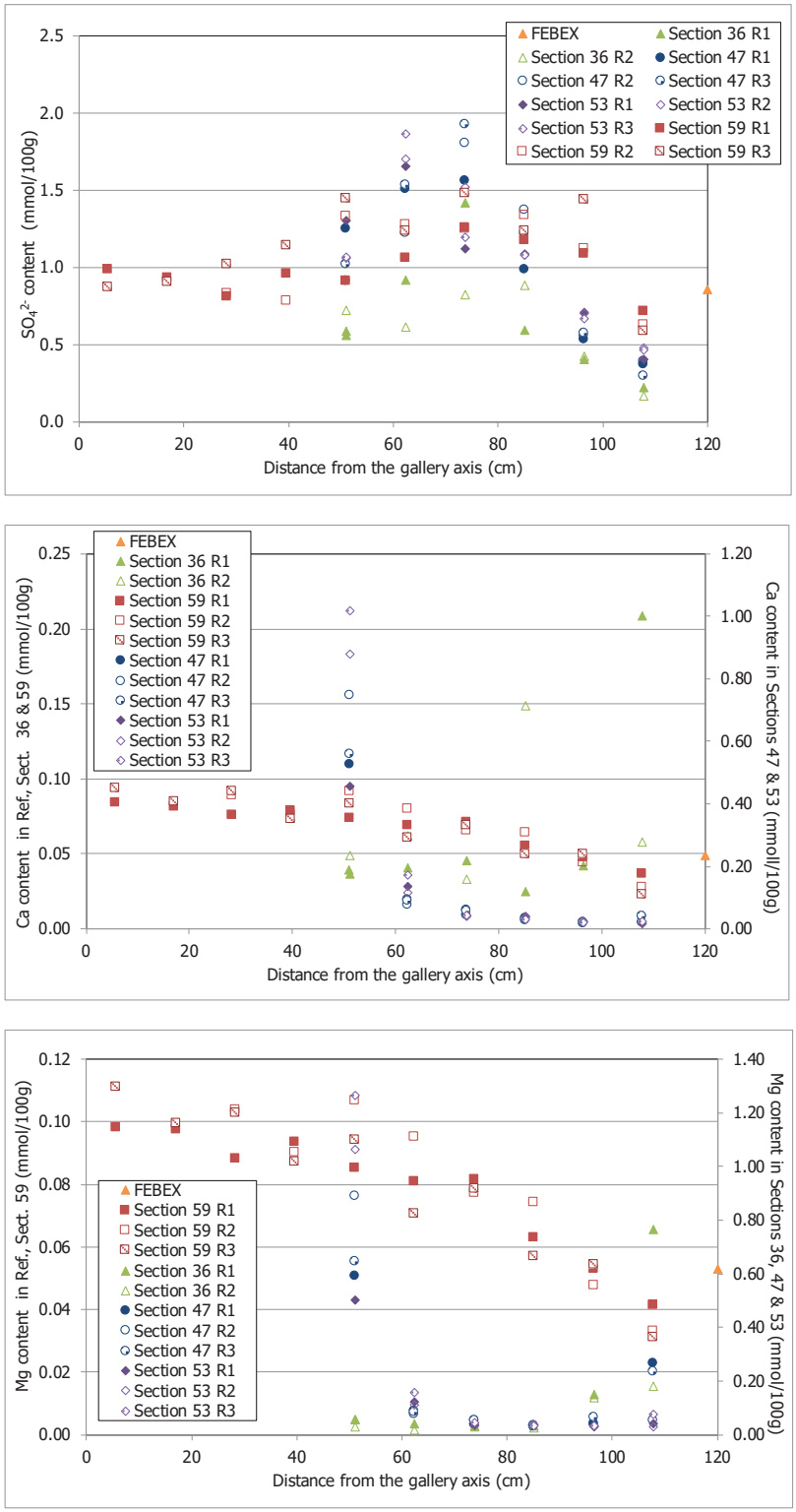

Fig. 160: Sulphate, calcium and magnesium content (1:4 aqueous leaching tests) from samples at different sections in three radii after dismantling Heater #2 in 2015

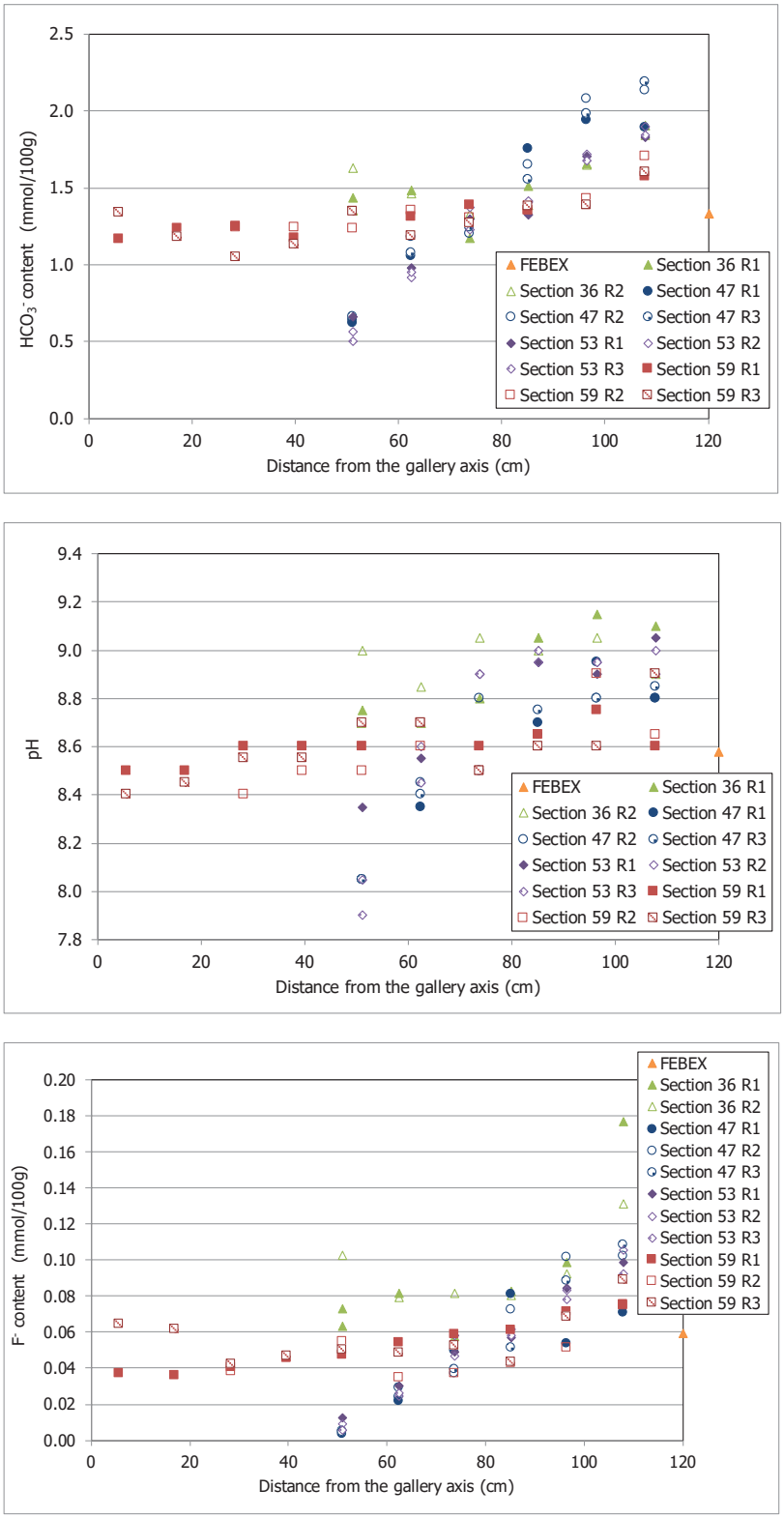

Fig. 161: Alkalinity (as bicarbonate), pH and fluoride content (1:4 aqueous leaching tests) from samples at different sections in three radii from the dismantling Heater #2 in 2015

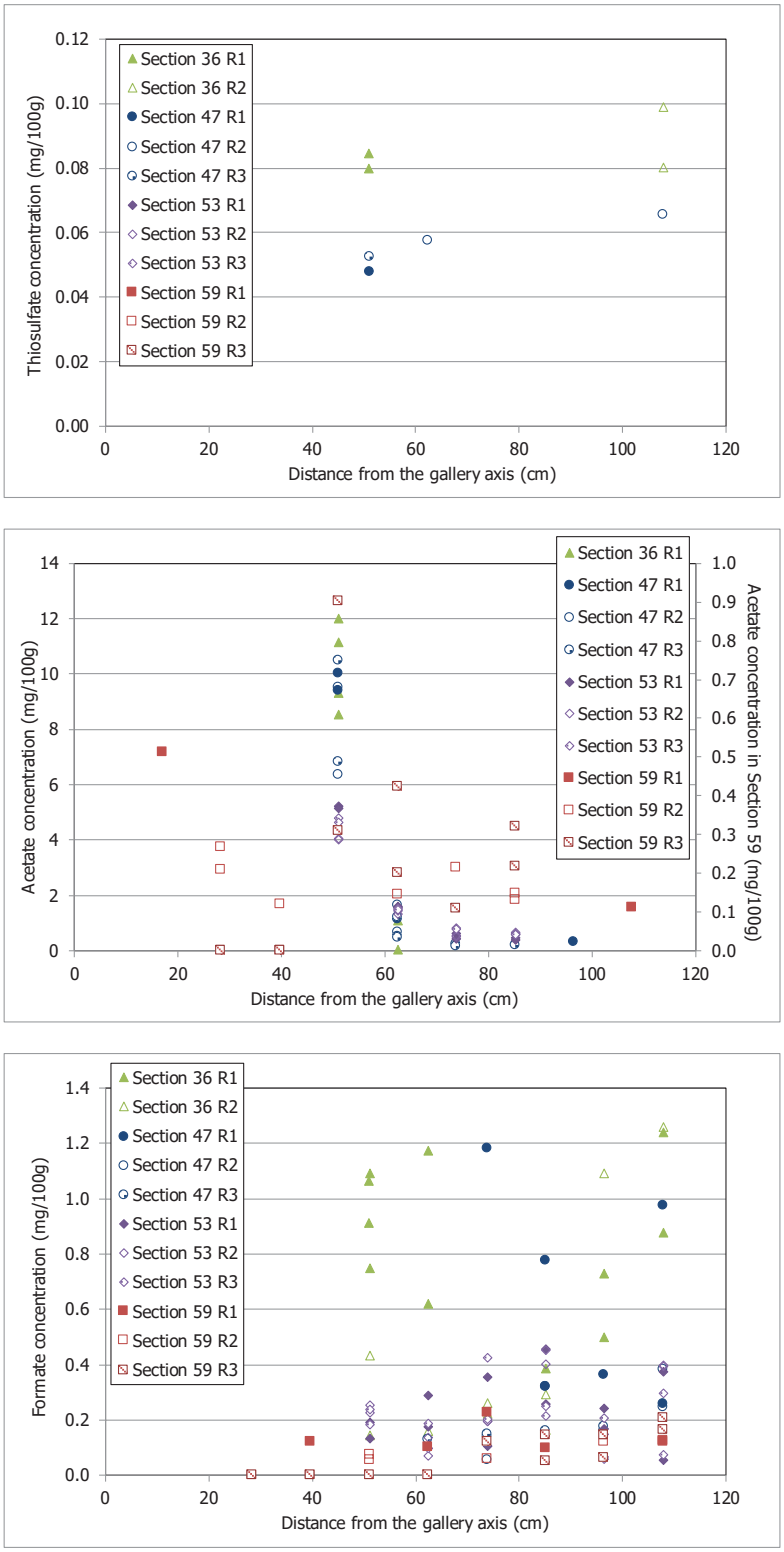

Fig. 162: Thiosulfate, acetate and formate content (1:4 aqueous leaching tests) from samples at different sections in three radii after dismantling Heater #2 in 2015

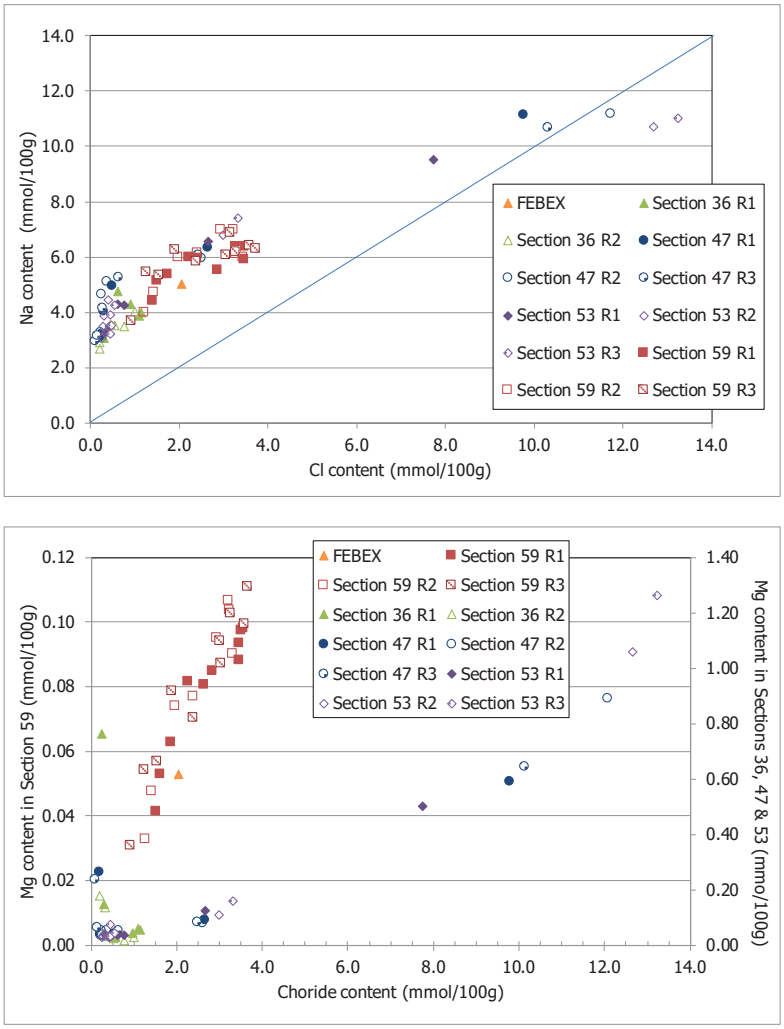

Fig. 163: Na versus Cl and Mg versus Cl relationships in aqueous extracts

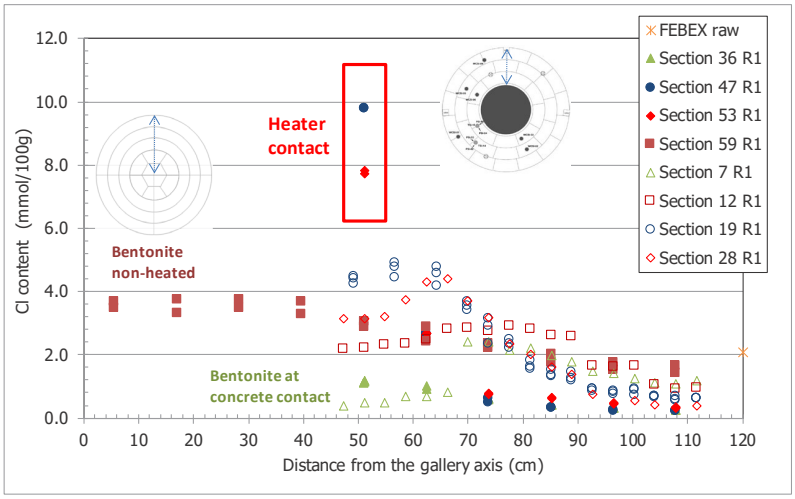

Fig. 164: Comparison of chloride content data after dismantling Heater #1 and Heater #2

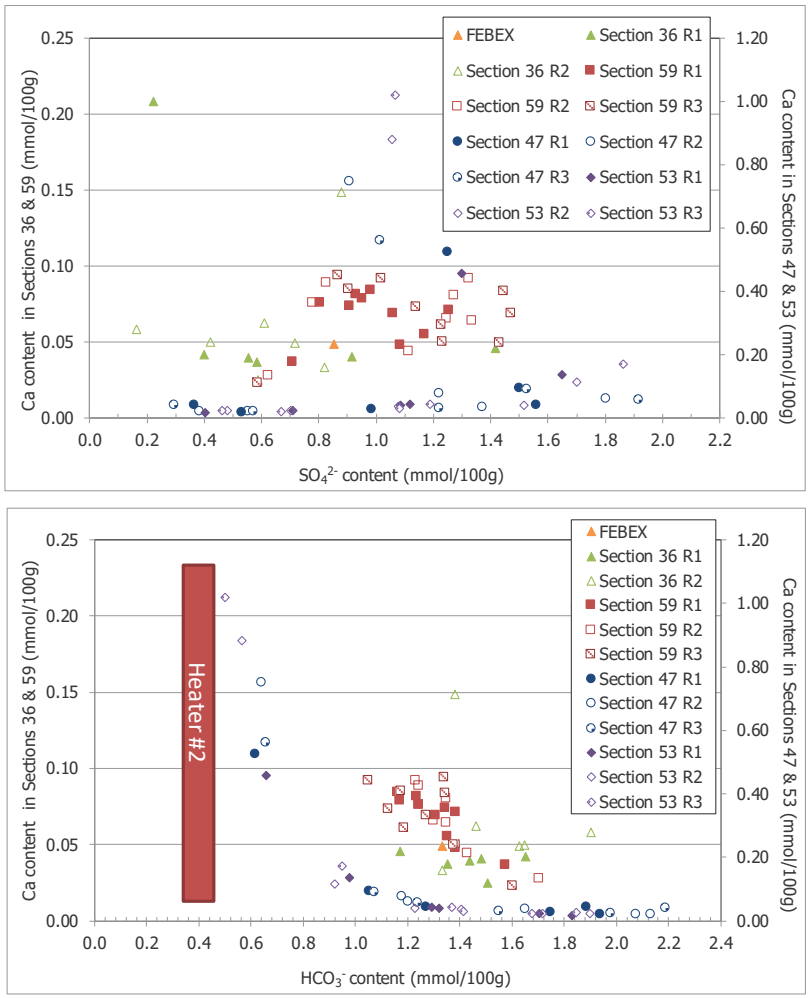

Fig. 165: Ca versus sulphate and Ca versus HCO_3^- relationships in aqueous extracts

Furthermore, volatile fatty acids (VFAs), such as acetate and formate, were found in the aqueous extracts (Fig. 162). Both organic compounds are produced either as fermentation products through the degradation of organic matter under anaerobic conditions or with the corrosion process and subsequent oxidation of hydrocarbons (see Section 7.4.1). These compounds are observed in all sections at different points of the bentonite barrier but the higher contents are observed in Section 36 at contact with the dummy; and in the heated Sections S47 and S53 at contact with Heater #2 where corrosion processes of the C-steel liner and heaters (Heater #1 and Heater #2) took place.

Saturation indices (SI) were calculated with the geochemical code PHREEQC (Version 3.3.9) (Parkhurst & Appelo 2013) and the Thermoddem database (Blanc 2017). Aqueous extracts at the 1:4 solid to liquid ratio are in equilibrium and/or oversaturated with calcite and dolomite in most of the samples; in equilibrium with quartz and chalcedony; and undersaturated with respect to gypsum, celestine, halite and fluorite (see Appendix D). This is in agreement with the correlations observed in Fig. 163 and Fig. 165.

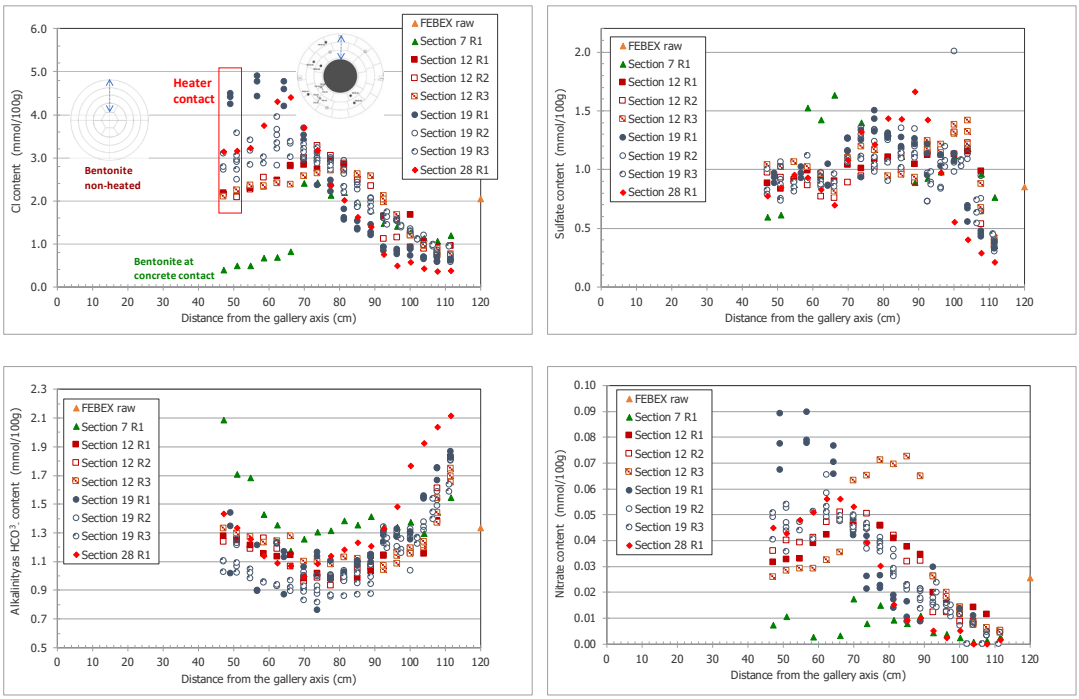

Fig. 166: Ion content (in mmol/100g, 1:4 aqueous leaching) at different sections in three radii after dismantling Heater #1 in 2002

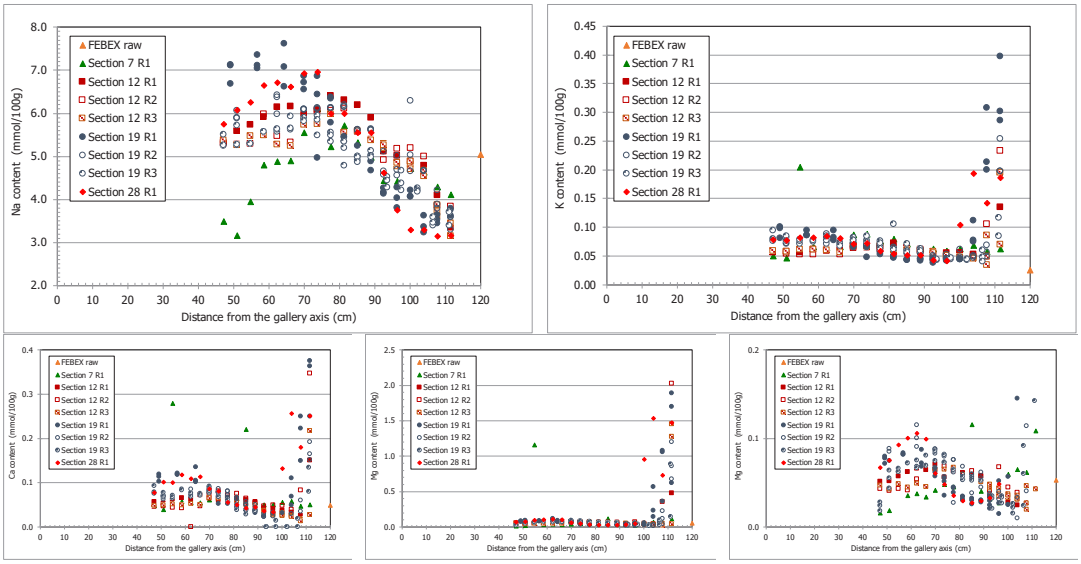

Fig. 167: Cation content (in mmol/100g, 1:4 aqueous leaching) at different sections in three radii after dismantling Heater #1 in 2002

5.6 Pore water chemistry

The pore water chemistry from the compacted bentonite from the FEBEX in-situ test was analysed by the squeezing technique. The samples selected were different block samples located along a radius at three sections: Section 36 (at the concrete interface), Section 47 (at the middle of the heater) and Section 59 (at the end of the gallery, non-affected by heat).

Prior to starting the test, the samples were dry-cut into cylindrical forms (Fig. 168, Fig. 169) to the size and shape needed for the squeezing cell (70 mm diameter); at least the outermost 3 – 4 cm of the block was first removed. All the tests were performed under anoxic conditions preserving the whole extraction system from the atmosphere, after several cycles of Ar flushing and under vacuum conditions (Fig. 170). Prior and after the tests, the samples were weighted, and the length and diameter were measured. Initial and final water content as well as dry density were also determined. The characteristics of each squeezing test performed after dismantling of Heater #2 in 2015 are shown in Tab. 26, whereas those for squeezing test performed after dismantling of Heater #1 in 2002 are shown in Tab. 27. Data for the squeezed pore water from the FEBEX reference are also given (Fernández 2004).

The procedure for pore water extractions by squeezing after dismantling of Heater #2 and after dismantling of Heater #1 in 2002 were quite different. In the 2002 squeezing tests, the samples were trimmed in separate pieces of about 25 – 200 grams using a large knife. Furthermore, the pore waters were collected inside syringes and anoxic conditions where not preserved at all (see Appendix A and Fernández et al. 2014).

Fig. 168: Preparation of a bentonite sample for a squeezing test after dismantling of Heater #2

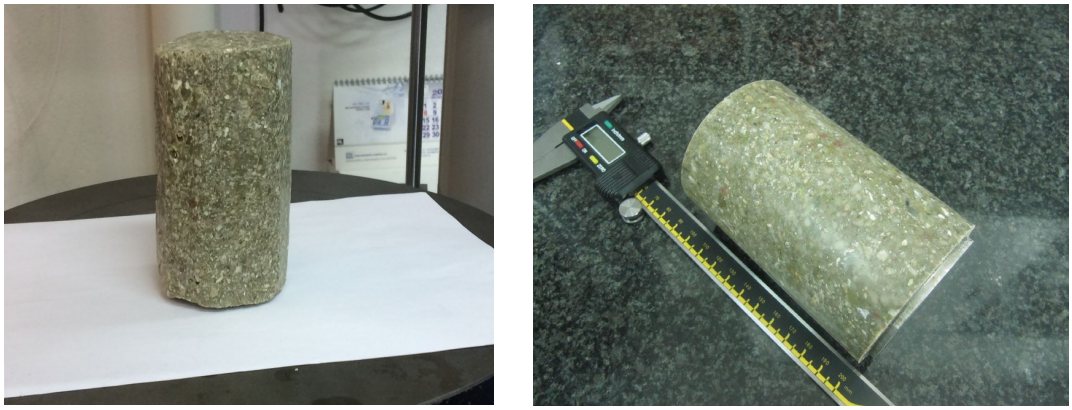

Fig. 169: Compacted bentonite BB-47-7 in a squeezing test after dismantling of Heater #2: a) prior to the squeezing test, and b) after squeezing test

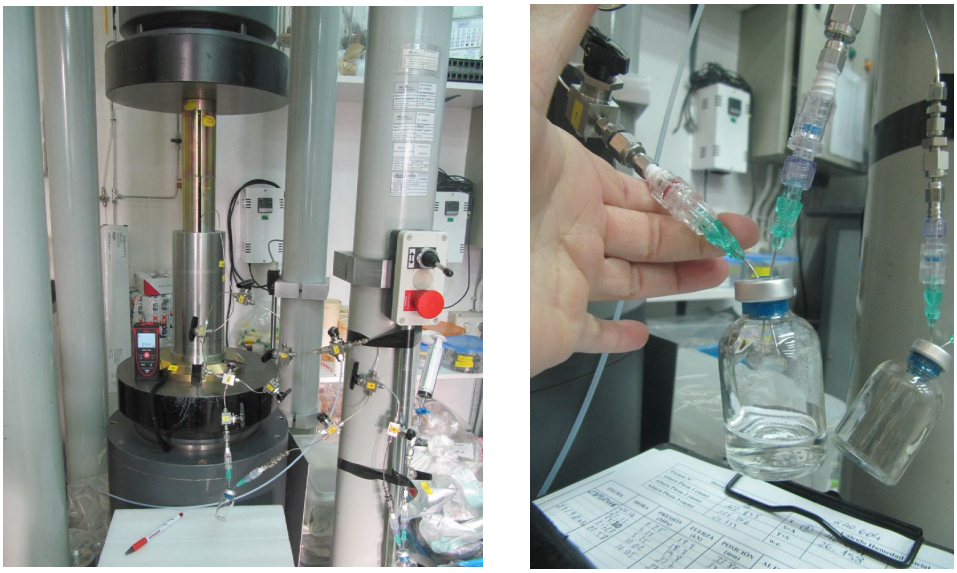

Fig. 170: Extraction of pore water by squeezing under anoxic conditions

Tab. 26: Characteristics of the squeezing tests performed after dismantling Heater #2 in 2015 (see sample location in Fig. 17 to Fig. 20)

Core sample	Initial mass (g)	Initial dry density (g/cm^3)	Initial w.c. (%)	Time elapsed (days)	Squeezing pressure (MPa)	Pore fluid extracted/ mass loss (g)	Final mass (g)	Final dry density (g/cm^3)	Final w.c. (%)	Efficiency[1] (%)	Total efficiency[2] (%)
FEBEX Ref.	350.00	1.53	28.2	50	25	15.9	329.420	1.73	21.4	77.2	26.7
BB-36-1	705.325	1.43	31.6	11	20	11.2/14.8	690.484	1.55	27.5	75.2	8.8
BB-36-2	706.185	1.55	27.4	10	20	5.9/9.4	696.801	1.56	26.6	62.6	6.2
BB-36-3	725.931	1.53	27.9	14	30,50	16.2/22.5	703.433	1.63	24.6	72.0	14.2
BB-47-7	819.096	1.51	30.8	17	20	11.2/15.7	803.389	1.57	26.7	71.2	8.2
BB-47-8	649.687	1.61	23.7	23	30,40	5.5/9.9	639.797	1.68	22.2	55.6	8.0
BB-47-9	797.052	1.63	21.7	10	70,85	3.2/6.2	790.850	1.72	20.5	51.0	4.4
BB-59-1	657.485	1.46	32.3	6	20	7.2/10.6	646.920	1.53	28.8	67.8	6.6
BB-59-2	719.756	1.54	27.7	6	30	6.3/11.6	708.117	1.59	26.7	53.8	7.5
BB-59-3	894.320	1.54	27.5	17	20,40	9/14.5	879.839	1.61	25.3	62.5	7.5
BB-59-4	839.100	1.53	27.2	18	30,50	12.6/16.7	822.411	1.62	24.9	75.4	9.3
BB-59-5	732.787	1.56	26.4	10	40	6.8/12.0	720.776	1.62	25.0	56.5	7.9

[1] Efficiency (%) = (Collected water x 100)/Extracted water
[2] Total Efficiency (%) = (100 x extracted water)/($P_{Initial} - P_{dry}$)

Tab. 27: Characteristics of the squeezing tests performed after dismantling Heater #1 in 2002 (see sample location in Fig. A-1 from Appendix A)

Core sample	Initial mass (g)	Initial dry density (g/cm^3)	Initial w.c. (%)	Time elapsed (days)	Squeezing pressure (MPa)	Pore fluid extracted/ mass loss (g)	Final mass (g)	Final dry density (g/cm^3)	Final w.c. (%)	Efficiency[1] (%)	Total efficiency[2] (%)
FEBEX Ref.*	600.0	1.65	23.5	25	64	2.5/3.8	596.2	1.72	20.4	68	3.3
BB-7-4	620.9	1.52	28.1	15	25	9.8/13.4	607.5	1.64	24.0	73.1	9.8
BB-7-5	601.4	1.50	25.8	25	25	0.5/6.4	595.0	1.64	24.5	7.8	5.2
BB-12-10	687.0	1.54	25.8	28	25	7.5/12.5	674.5	1.65	23.2	60.0	8.9
BB-12-11	598.4	1.57	19.7	53	70	1.8/3.6	594.8	1.77	19.0	50.0	3.7
BB-19-1	649.4	1.54	27.0	19	25	12.0/17.4	632.0	1.62	26.1	69.0	12.6
BB-19-2	641.2	1.61	21.3	18	70	5.3/9.2	632.0	1.65	23.2	57.6	8.2

[1] Efficiency (%) = (Collected water x 100)/Extracted water
[2] Total Efficiency (%) = (100 x extracted water)/(Pinitial – Pdry)
* Fernández (2004)

5.6.1 Squeezing pressure versus water content

To obtain a representative pore water sample of homogeneously distributed electrolytes in the bulk aqueous phase, sampling of different portions of the diffuse layer water should be avoided. The greater the squeezing pressure, the greater the ease with which water bound to clay particle surfaces is expelled (Fernández et al. 2014).

Therefore, the squeezing tests were designed to obtain enough water volume for chemical analysis at the lowest squeezing pressure. Thus, depending on the initial water content and dry density of the compacted samples different pressures were applied. The pressure ranged between 20 and 70 MPa in 2015 samples, and between 25 and 70 MPa in 2002 (Fig. 171). The higher the water content of the sample, the lower the squeezing pressure needed (and vice-versa for dry density).

In 2015, some samples were squeezed at different pressures to analyse the influence of squeezing pressure on the chemical composition of the pore water. In this case, pore waters obtained at each pressure step were collected separately. The amount of water extracted ranged between 6 and 17 mL for a given pressure step, where higher volumes were extracted at higher water content values. The inner bentonite blocks from the dismantling of Heater #1 in 2002 had water contents below 18 %, so these samples could not be squeezed at pressures lower than 70 MPa.

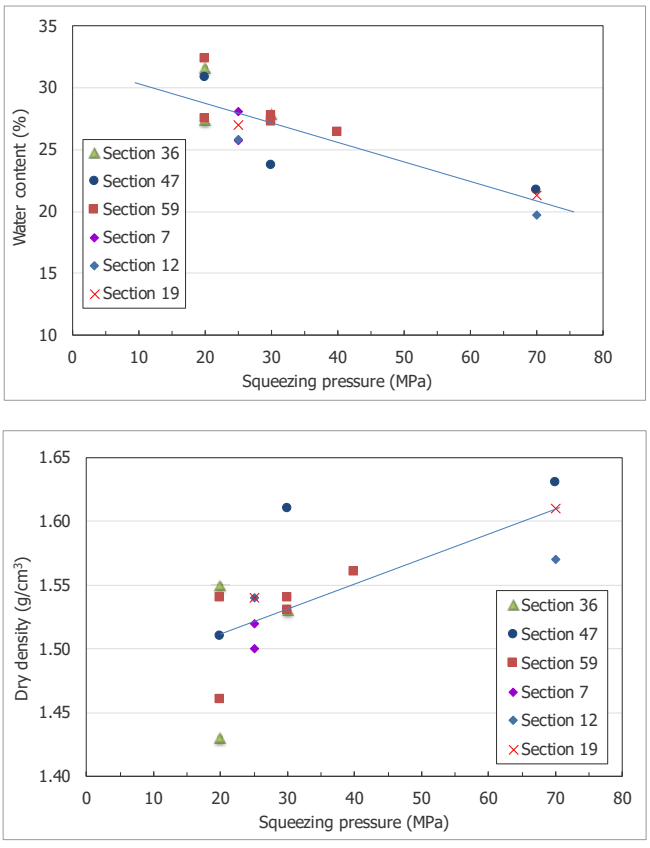

Fig. 171: Squeezing pressure required for collecting pore water as a function of the water content and dry density of the samples analysed

5.6.2 Chemical composition of the bentonite pore water

The pore water chemical composition is shown in Tab. 28, Tab. 29 and Tab. 30 for all the samples collected from bentonite blocks taken after dismantling of Heater #2 in 2015 as a function of squeezing pressure. Those obtained after dismantling Heater #1 are shown in Tab. 31. After dismantling Heater #2, the salinity along the barrier evolved according to the bentonite saturation front as observed by the ionic strength and water activity values; pore waters are more diluted at the granite contact (Fig. 172). Ionic strength changed from 0.044 to 0.13 M in Section 36 (at contact with the shotcrete plug), whereas it increased towards the inner parts of the bentonite in Sections S47 and S59, reaching maximum values of 0.50 M at the central part of the bentonite buffer. The water activities vary from 0.988 to 0.999 in all sections, decreasing when salinity increased.

The chemical composition of all bentonite pore waters is dominated by Cl- and Na, followed by SO42-, Ca and Mg. Nevertheless, Mg is higher than Ca in some samples, especially in Sections S47 and S59 (Fig. 173, Fig. 174) far away from the granite contact. The granitic groundwater (Na-Ca-TIC-F water type) is very diluted and highly alkaline (Tab. 28). During infiltration, the FEBEX bentonite pore water changes in Section 36 from Na-Mg-Cl water type (initial) towards a Na-Cl-SO_4 pore water in all bentonite blocks. In the heated Section 47, it shifts towards a Na-Cl-SO_4 water type (in bentonite block N° 1 close to granite and the inner bentonite block N° 2), and a Na-Mg-Ca-Cl water type (in bentonite block N° 3 close to Heater #2). In the non-heated Section 59, pore water changes to Na-Cl-SO_4 (in bentonite block N° 1 close to granite), Na-Mg-Cl-SO_4 (in bentonite block N° 2) and Na-Mg-Cl water type (in blocks N° 3, 4 and 5). The pH values are neutral/slightly alkaline, ranging values from 6.8 to 7.9. Alkalinity values ranged from 2.06 to 5.42 meq/L in the 2015 samples, whereas in 2002 they ranged from 1.43 to 3.31 meq/L (Fig. 175). The presence of Cu, Mn, and Zn in some samples from Sections S47 and S59, especially at the inner part of the bentonite barrier, should be noted. TOC, acetate, formate and oxalate were also detected in the 2015 samples (Fig. 176). Thiocyanate was detected in Section 59 in bentonite blocks BB-59-1 and BB-59-2 (Tab. 30).

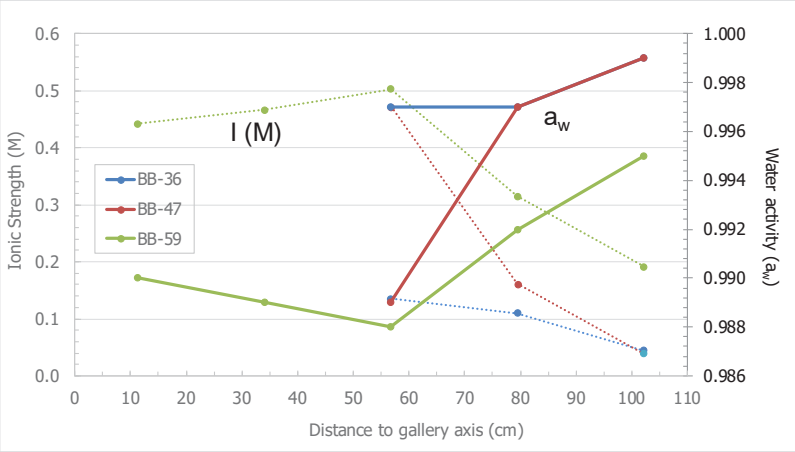

Fig. 172: Ionic strength and water activity of the squeezed waters from bentonite samples taken after dismantling Heater #2

The geochemical code PHREEQC, Version 3.4 (Parkhurst & Appelo 2013) and the Thermoddem database (Blanc, 2017) were used for equilibrium modelling and saturation index calculations (Tab. 32, Tab. 33, Tab. 34, Tab. 35) at 25 °C. The saturation indices indicate that the pore waters from all samples are undersaturated with respect to calcite, gypsum and celestine; and saturated with respect chalcedony and quartz, except for those located in the central part of the buffer, where pore waters are saturated with respect to gypsum in Sections S47 (heated) and S59 (non-heated) (Fig. 177).

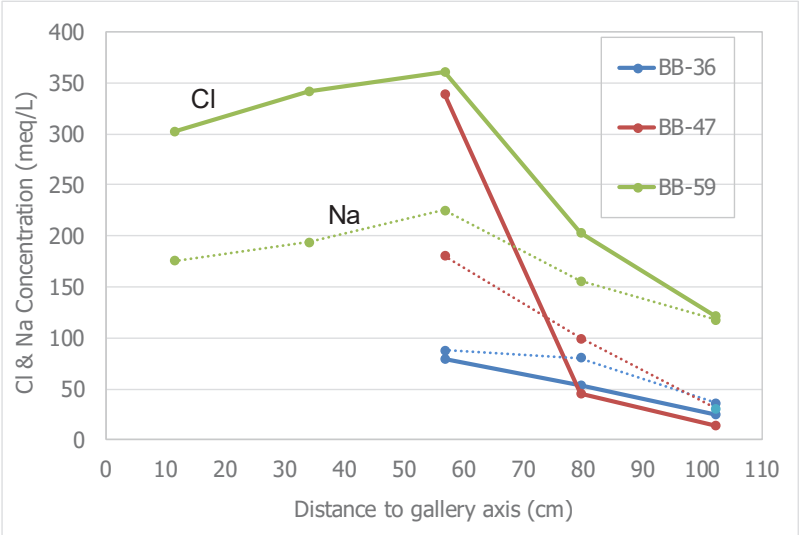

Fig. 173: Chloride and sodium in the squeezed pore water samples obtained after dismantling Heater #2 in 2015 as a function of distance to the gallery axis

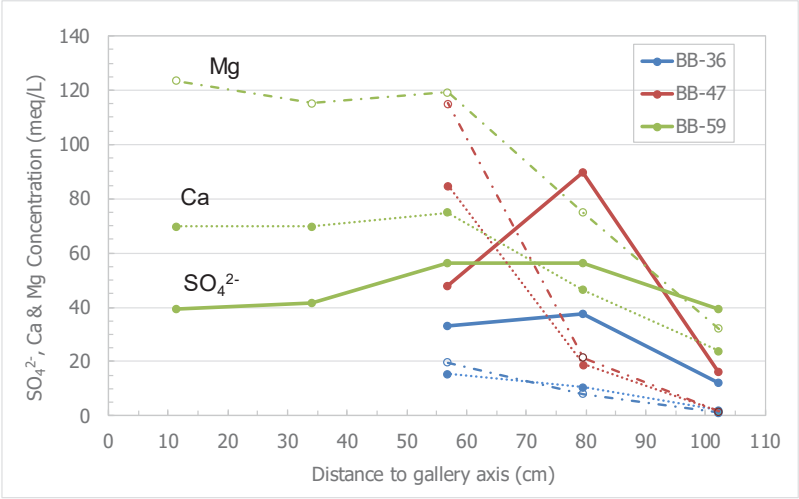

Fig. 174: Sulphate, calcium and magnesium in the squeezed pore water samples obtained after dismantling Heater #2 in 2015 as a function of distance to the gallery axis

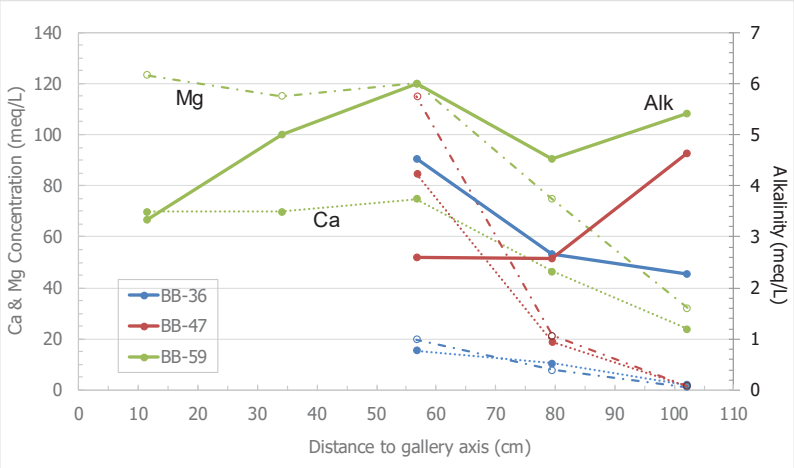

Fig. 175: Calcium, magnesium and alkalinity in the squeezed pore water samples obtained after dismantling Heater #2 in 2015 as a function of distance to the gallery axis

Tab. 28: Chemical composition of the pore water collected from Section 36 at contact with the shotcrete plug after dismantling Heater #2: BB-36-1, BB-36-2 and BB-36-3 bentonite blocks as a function of distance to the gallery axis

Squeezed reference pore waters were obtained over time and are given at different pressures.

Sample			**Grimsel GW***	**FEBEX Ref.**	**FEBEX Ref.**	**BB-36-1**	**BB-36-2**	**BB-36-3**	**BB-36-3**
Distance from gallery axis	d	cm	--	--	--	102.15	79.45	56.75	56.75
Pressure	P	MPa	--	64	25	20	20	30	50
Extracted water	Vol.	g	--	3.8	5	11.2	5.9	7.7	8.5
Sensoric parameter lab									
Colour/Turbidity			--	--	--	No	No	No	No
Physical-chemical parameter lab									
pH value (20 °C) Lab. (Glove box/lab)	pH		9.59	8.0	7.3	7.7	7.7	7.7	7.7
Redox (mV, SHE)	Eh	mV	-382	--	--	--	--	--	--
Alkalinity	Alk.	meq/L	0.42	4.23	2.06	2.28	2.66	4.52	4.01
pCO_2	pCO_2	atm	-5.47	-4.58	-4.09	-4.37	-4.46	-4.15	-4.15
Main ions									
Sodium	Na^+	mg/L	16	3'600	3'200	838	1'840	2'020	1'460
Potassium	K^+	mg/L	0.22	0.7	34	14	31	41	25
Calcium	Ca^{2+}	mg/L	5.6	1'040	649	41	210	310	190
Magnesium	Mg^{2+}	mg/L	0.044	920	591	15	97	240	160
Chloride	Cl^-	mg/L	5.5	8'100	6'600	874	1'900	2'800	2'000
Sulphate	SO_4^{2-}	mg/L	5.5	2'100	2'600	576	1'800	1'600	1'100
Nitrate	NO_3^-	mg/L	--	18	143	1.7	11.3	5.7	0.91
Nitrite	NO_2^-	mg/L	--	< 1	< 1	< 1	< 1	< 1	< 1
Phosphate	PO_4^{3-}	mg/L	--	< 1	< 1	< 1	< 1	< 1	< 1
Bromide	Br^-	mg/L	< 1	14	12	2.4	5.3	7.6	5.3
Fluoride	F^-	mg/L	6.1	n.d.	n.d.	0.38	0.21	0.18	0.17
Thiosulfate	$S_2O_3^{2-}$	mg/L	--	n.d.	n.d.	4.2	< 1	4.8	3.2
Trace compounds									
Aluminium	Al	mg/L	0.012	< 0.5	0.27	< 0.3	< 0.3	< 0.3	< 0.3
Silicon	Si	mg/L	12	n.d.	14	17	17	18	15
Iron	Fe (II/III)	mg/L	--	0.09	0.15	< 0.3	< 0.3	< 0.3	< 0.3
Strontium	Sr	mg/L	--	16	11	0.65	3.2	4.6	2.9
Copper	Cu	mg/L	--	0.5	< d.l.	< 0.3	0.38	0.48	< 0.3
Boron	B	mg/L	--	0.68	1.2	0.83	2.0	1.0	1.0
Manganese	Mn	mg/L	--	< 0.3	0.22	< 0.3	< 0.3	1.4	0.82
Nickel	Ni	mg/L	--	< 0.3	< 0.3	< 0.3	< 0.3	< 0.3	< 0.3
Lead	Pb	mg/L	--	< 0.5	< 0.3	< 0.3	< 0.3	< 0.3	< 0.3
Zinc	Zn	mg/L	--	< 0.5	0.63	< 0.3	< 0.3	< 0.3	< 0.3
Organic parameter									
Total organic carbon	TOC	mg/L	--	n.d.	n.d.	39.9	n.d.	96.7	74.9
Acetate	CH_3-COO^-	mg/L	--	n.d.	n.d.	20	3	32	26
Formate	$HCOO^-$	mg/L	--	n.d.	n.d.	6	1	13	9

* BOMI 87.009 (see Fernández 2018 for references)

Tab. 29: Chemical composition of pore water collected from heated Section 47 at different pressures: BB-47-7, BB-47-8 and BB-47-9 bentonite blocks as a function of distance to the gallery axis

Sample			**BB-47-7**	**BB-47-8**	**BB-47-8**	**BB-47-9**	**BB-47-9**
Distance from the gallery axis	d	cm	102.15	79.45	79.45	56.75	56.75
Pressure	P	MPa	20	30	40	70	85
Extracted water	Vol.	g	11.2	1.5	4.0	0.58	2.58
Sensoric parameter lab							
Colour/Turbidity			No	No	No	No	No
Physical-chemical parameter lab							
pH value (20 °C) Lab. (Glove box/lab)	pH		7.9	7.8	7.6	6.8	7.8
Alkalinity	Alk.	meq/L	4.63	2.58	2.53	< 5	2.59
pCO_2	pCO_2	atm	-4.30	-5.37	-4.35	n.d.	-4.74
Main ions							
Sodium	Na^+	mg/L	710	2'300	1'500	4'161	3'210
Potassium	K^+	mg/L	9.2	24	13	23	23
Calcium	Ca^{2+}	mg/L	32	380	210	1'700	2'000
Magnesium	Mg^{2+}	mg/L	20	260	150	1'400	1'000
Chloride	Cl^-	mg/L	481	1'600	976	12'000	10'700
Sulphate	SO_4^{2-}	mg/L	779	4'300	2'900	2'300	1'400
Nitrate	NO_3^-	mg/L	1.9	15	8.3	124	114
Nitrite	NO_2^-	mg/L	< 1	< 1	< 1	< 1	< 2
Phosphate	PO_4^{3-}	mg/L	< 1	< 1	< 1	< 0.1	< 2
Bromide	Br^-	mg/L	1.1	2.5	0.74	12.7	11.9
Fluoride	F^-	mg/L	< 1	< 1	< 1	< 1	< 2
Thiosulfate	$S_2O_3^{2-}$	mg/L	< 1	< 1	< 1	< 1	< 1
Trace compounds							
Aluminium	Al	mg/L	< 0.1	< 0.3	< 0.3	< 2.9	< 0.3
Silicon	Si	mg/L	23	22	24	15	14
Iron	Fe (II/III)	mg/L	< 0.1	< 0.3	< 0.3	< 2.9	< 0.3
Strontium	Sr	mg/L	0.59	6.7	4.0	29	30
Copper	Cu	mg/L	0.15	1.4	0.3	< 2.9	0.5
Boron	B	mg/L	1.5	1.8	1.3	< 2.9	1.4
Manganese	Mn	mg/L	0.15	0.70	0.3	5.6	4.6
Nickel	Ni	mg/L	0.09	0.41	< 0.3	< 2.9	0.6
Lead	Pb	mg/L	0.18	< 0.3	< 0.3	< 2.9	< 0.3
Zinc	Zn	mg/L	0.08	0.59	< 0.3	< 2.9	< 0.3
Organic parameter							
Total organic carbon	TOC	mg/L	38	n.d.	83	n.d.	n.d.
Acetate	CH_3-COO^-	mg/L	< 0.1	86	45	142	141
Formate	$HCOO^-$	mg/L	0.36	25	12	1.3	13
Oxalate	$(COO)_2^{2-}$	mg/L	n.d.	n.d.	n.d.	17.7	23

Tab. 30: Chemical composition of pore water collected from the non-heated Section 59 at different pressures: BB-59-1, BB-59-2, BB-59-3, BB-59-4 and BB-59-5 bentonite blocks as a function of distance to the gallery axis

Sample			**BB-59-1**	**BB-59-2**	**BB-59-3**	**BB-59-3**	**BB-59-4**	**BB-59-4**	**BB-59-5**
Distance from gallery axis	d	cm	102.15	79.45	56.75	56.75	34.05	34.05	11.35
Pressure	P	MPa	20	30	20	40	30	50	40
Extracted water	Vol.	g	7.2	6.3	2.2	6.9	7.0	5.6	6.8
Sensoric parameter lab									
Colour/Turbidity			No	No	Red colloids	No	No	No	No
Physical-chemical parameter lab									
pH value (20 °C) Lab. (Glove box/lab)	pH		7.9	7.8	7.6	7.8	7.6	7.7	7.8
Alkalinity	Alk.	meq/L	5.42	4.52	*6.0*	6.15	*5.0*	4.80	3.33
pCO_2	pCO_2	atm	-4.35	-4.36	*-4.14*	-4.24	*-4.15*	-4.26	-4.62
Main ions									
Sodium	Na^+	mg/L	2'700	3'575	5'170	3'840	4'450	3'710	4'040
Potassium	K^+	mg/L	25	31	48	31	49	27	34
Calcium	Ca^{2+}	mg/L	480	930	1'500	1'100	1'400	1'200	1'400
Magnesium	Mg^{2+}	mg/L	390	910	1'460	1'100	1'400	1'100	1'500
Chloride	Cl^-	mg/L	4'300	7'200	12'800	8'900	12'100	8'900	10'700
Sulphate	SO_4^{2-}	mg/L	1'900	2'700	2'700	2'000	2'000	1'500	1'900
Nitrate	NO_3^-	mg/L	3.7	63	120	2.0	171	58	118
Nitrite	NO_2^-	mg/L	5.8	22	39	41	34	54	26
Phosphate	PO_4^{3-}	mg/L	< 1	< 1	< 2	< 1	< 2	< 1	< 1
Bromide	Br^-	mg/L	10.6	19	33	20	31	22	24
Fluoride	F^-	mg/L	< 1	< 1	< 1	< 1	< 1	< 1	< 1
Thiosulfate	$S_2O_3^{2-}$	mg/L	< 1	< 1	< 2	< 1	< 2	< 1	< 1
Thiocyanate	SCN^-	mg/L	1.8	3.8	--	--	--	--	2.2
Trace compounds									
Aluminium	Al	mg/L	< 0.3	< 0.3	< 0.6	< 0.3	< 0.2	< 0.3	< 0.3
Silicon	Si	mg/L	20	16.0	18	17	14	18	13
Iron	Fe (II/III)	mg/L	< 0.3	< 0.3	< 0.6	< 0.3	0.43	< 0.3	< 0.3
Strontium	Sr	mg/L	7.2	14	27	19	24	20	20
Copper	Cu	mg/L	0.28	< 0.3	< 0.6	0.38	0.26	< 0.3	0.36
Boron	B	mg/L	1.8	1.5	8.0	1.4	1.1	2.0	1.6
Manganese	Mn	mg/L	0.49	2.3	2.0	1.2	< 0.2	1.5	1.9
Nickel	Ni	mg/L	0.32	< 0.3	11	< 0.3	4.2	1.2	0.32
Lead	Pb	mg/L	< 0.3	< 0.3	< 0.6	< 0.3	< 0.2	< 0.3	< 0.3
Zinc	Zn	mg/L	0.35	≤0.3	≤0.6	< 0.3	0.29	< 0.3	0.46
Organic parameter									
Total organic carbon	TOC	mg C/L	26.3	15.8	n.d.	13	24	14.4	84.8
Acetate	$CH_3\text{-}COO^-$	mg/L	< 1	3.2	< 2	< 1	< 2	< 1	< 1
Formate	$HCOO^-$	mg/L	1.6	937	< 2	< 1	< 2	< 1	1.0

Tab. 31: Chemical composition of pore water obtained by squeezing from samples taken during dismantling of Heater #1 in 2002

Sample			**BB-7-4**	**BB-7-5**	**BB-12-10**	**BB-12-11**	**BB-19-1**	**BB-19-2**
Distance from gallery axis	d	cm	102.15	79.45	102.15	79.45	102.15	79.45
Pressure	P	MPa	25	25	25	70	25	70
Extracted water	Vol.	g	13.4	6.4	12.5	3.6	17.4	9.2
Physical-chemical parameter lab								
pH value (20 °C) Lab. (Glove box/lab)	pH		7.8	7.9	7.6	7.4	7.5	7.7
Alkalinity	Alk.	mmol/L	1.98	3.31	1.43	1.33	2.57	2.64
pCO_2	pCO_2	atm	-4.66	-4.78	-4.55	-4.62	-4.3	-4.36
Main ions								
Sodium	Na^+	mg/L	2'000	4'300	763	5'800	1'200	'
Potassium	K^+	mg/L	31	6.1	12	22	13	13
Calcium	Ca^{2+}	mg/L	350	1100	89	3'200	106	453
Magnesium	Mg^{2+}	mg/L	173	800	52	2'500	67	353
Chloride	Cl^-	mg/L	2'400	8'400	871	18'500	1'500	3'900
Sulphate	SO_4^{2-}	mg/L	2'100	2'900	568	2'600	883	1'800
Nitrate	NO_3^-	mg/L	4.3	81	7.5	388	1.5	38
Bromide	Br^-	mg/L	29.0	6.2	1.6	30.0	2.6	7.4
Trace compounds								
Aluminium	Al	mg/L	< 0.25	0.69	< 0.25	< 5.3	0.65	0.56
Silicon	Si	mg/L	n.d.	n.d.	26.2	n.d.	n.d.	n.d.
Iron	Fe (II/III)	mg/L	< 0.15	0.58	< 0.15	< 3.2	0.25	< 0.3
Strontium	Sr	mg/L	4.3	14	1.4	38	1.7	7.1
Boron	B	mg/L	1.9	4.1	1.4	< 5.3	0.63	< 0.5
Manganese	Mn	mg/L	0.28	0.57	0.25	< 3.2	0.17	0.83

Tab. 32: Calculated parameters and saturation indices of pore waters from the FEBEX Reference bentonite and from the bentonite sampling Section S36 during dismantling of Heater #2 in 2015

Parameters	**FEBEX Ref.**	**FEBEX Ref.**	**BB-36-1**	**BB-36-2**	**BB-36-3**	**BB-36-3**
Sq. pressure (MPa)	***64***	***25***	***20***	***20***	***30***	***50***
a_w	0.992	0.993	0.999	0.997	0.997	0.998
Specific conductance (µS/cm, 25 °C)	24'874	21'043	4'077	9'075	11'102	8'094
I (M)	0.3355	0.2638	$4.398 \cdot 10^{-2}$	$1.095 \cdot 10^{-1}$	$1.348 \cdot 10^{-1}$	$9.517 \cdot 10^{-2}$
Water type	Na-Mg-Cl	Na-Mg-Cl	Na-Cl-SO_4	Na-Cl-SO_4	Na-Cl-SO_4	Na-Cl-SO_4
Saturation index						
Anhydrite	-0.48	-0.49	-1.7	-0.84	-0.79	-1.04
Gypsum	-0.18	-0.19	-1.40	-0.53	-0.49	-0.74
Celestine	-0.26	-0.23	-1.47	-0.62	-0.58	-0.82
Calcite	-0.43	-1.55	-2.03	-1.55	-1.07	-1.23
Dolomite	-0.52	-2.80	-4.16	-3.11	-1.91	-2.20
Strontianite	-1.80	-2.88	-3.38	-3.38	-2.45	-2.60
CO_2 (g)	-4.58	-4.09	-4.37	-4.46	-4.15	-4.15
Chalcedony	--	-0.04	0.01	0.01	0.04	-0.04
Quartz	--	0.38	0.43	0.44	0.47	0.39
Halite	-3.32	-3.45	-4.78	-4.17	-3.97	-4.24
Fluorite	--	--	-2.38	-2.46	-2.52	-2.66

Tab. 33: Calculated parameters and saturation indices of pore waters from the bentonite sampling Section S47 during dismantling of Heater #2 in 2015

Parameters	**BB-47-7**	**BB-47-8**	**BB-47-8**	**BB-47-9**	**BB-47-9**
Sq. pressure (MPa)	***20***	***30***	***40***	***70***	***85***
a_w	0.999	0.997	0.998	0.989	0.991
Specific conductance (µS/cm, 25 °C)	3'323	11'480	7'802	33'574	29'701
I (M)	3.914×10^{-2}	1.614×10^{-1}	1.069×10^{-1}	4.717×10^{-1}	4.124×10^{-1}
Water type	Na-SO_4-Cl	Na-SO_4-Cl	Na-SO_4-Cl	Na-Mg-Ca-Cl	Na-Mg-Ca-Cl
Saturation index					
Anhydrite	-1.69	-0.41	-0.69	-0.34	-0.43
Gypsum	-1.38	-0.11	-0.38	-0.05	-0.14
Celestine	-1.39	-0.13	-0.38	-0.08	-0.22
Calcite	-1.68	-2.13	-1.71	*0.00**	-0.70
Dolomite	-3.25	-4.10	-3.25	--	-1.34
Strontianite	-2.98	-3.44	-2.99	-1.32	-2.08
CO_2 (g)	-4.30	-5.37	-4.35	-5.29	-4.74
Chalcedony	0.13	0.13	0.16	-0.02	-0.03
Quartz	0.56	0.56	0.59	0.41	0.40
Halite	-5.11	-4.18	-4.55	-3.10	-3.25

* Equilibrium with calcite

Tab. 34: Calculated parameters and saturation indices of pore waters from the bentonite sampling Section S59 during dismantling of Heater #2 in 2015

Parameters	**BB-59-1**	**BB-59-2**	**BB-59-3**	**BB-59-3**	**BB-59-4**	**BB-59-4**	**BB-59-5**
Sq. pressure (MPa)	***20***	***30***	***20***	***40***	***30***	***50***	***40***
a_w	0.995	0.992	0.988	0.991	0.989	0.991	0.990
Specific conductance (µS/cm, 25 °C)	15'400	23'409	36'243	26'838	33'810	26'699	3'1089
I (M)	1.911×10^{-1}	3.144×10^{-1}	5.033×10^{-1}	3.646×10^{-1}	4.661×10^{-1}	3.657×10^{-1}	4.419×10^{-1}
Water type	Na-Cl- SO_4	Na-Mg-Cl- SO_4	Na-Mg-Cl	Na-Mg-Cl	Na-Mg-Cl	Na-Mg-Cl	Na-Mg-Cl
Saturation index							
Anhydrite	-0.65	-0.40	-0.34	-0.50	-0.47	-0.59	-0.50
Gypsum	-0.35	-0.11	-0.05	-0.21	-0.18	-0.29	-0.20
Celestine	-0.43	-0.19	-0.05	-0.23	-0.21	-0.33	-0.31
Calcite	-0.70	-0.67	-0.66	-0.47	-0.69	-0.64	-0.75
Dolomite	-1.15	-1.00	-0.96	-0.56	-0.99	-0.94	-1.09
Strontianite	-2.08	-2.05	-1.96	-1.78	-2.01	-1.97	-2.15
CO_2 (g)	-4.35	-4.36	-4.14	-4.24	-4.15	-4.26	-4.62
Chalcedony	0.09	0.02	0.09	0.05	-0.02	0.07	-0.06
Quartz	0.52	0.44	0.52	0.48	0.41	0.50	0.37
Halite	-3.68	-3.37	-2.98	-3.25	-3.06	-3.27	-3.16

Tab. 35: Calculated parameters and saturation indices of pore waters from the bentonite sampling Sections S7, S12 and S19 (Dismantling Heater #1 in 2002)

Parameters	**BB-7-4**	**BB-7-5**	**BB-12-10**	**BB-12-11**	**BB-19-1**	**BB-19-2**
Sq. Pressure (mpa)	25	25	25	70	25	70
a_w	0.997	0.991	0.999	0.983	0.998	0.996
Specific Conductance (µs/cm, 25 °C)	10'677	26'514	4'050	49'096	6'306	13'926
I (M)	0.1325	0.3502	0.0459	0.7736	0.0708	0.1718
Water type	Na-Cl- SO_4	Na-Mg-Cl	Na-Cl- SO_4	Na-Mg-Ca-Cl	Na-Cl- SO_4	Na-Cl- SO_4
Saturation index						
Anhydrite	-0.63	-0.32	-1.41	-0.19	-1.27	-0.66
Gypsum	-0.32	-0.02	-1.11	0.10	-0.97	-0.36
Celestine	-0.50	-0.18	-1.18	-0.08	-1.03	-0.43
Calcite	-1.35	-0.83	-2.06	-1.21	-1.83	-1.13
Dolomite	-2.69	-1.43	-4.03	-2.13	-3.53	-2.02
Strontianite	-2.82	-2.28	-3.42	-2.70	-3.18	-2.49
CO_2 (g)	-4.66	-4.78	-4.55	-4.62	-4.13	-4.36
Chalcedony	--	--	0.19	--	--	--
Quartz	--	--	0.62	--	--	--

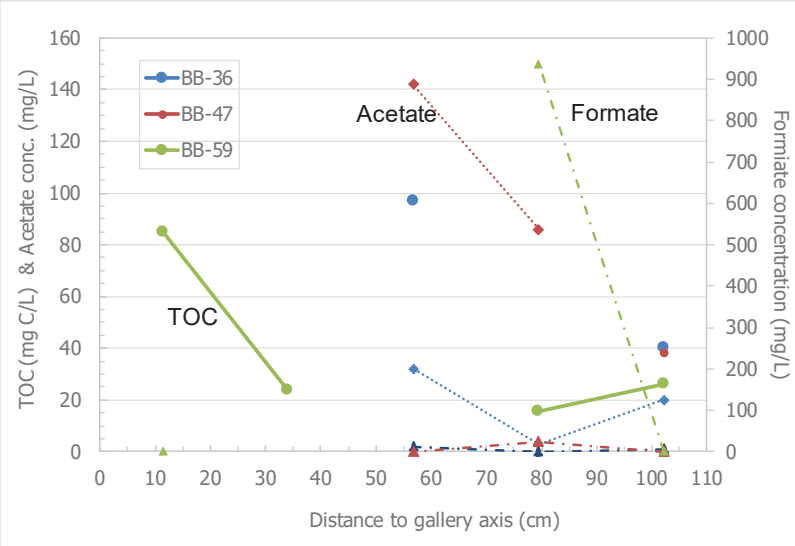

Fig. 176: TOC, acetate and formate in squeezed pore waters obtained after dismantling Heater #2 in 2015

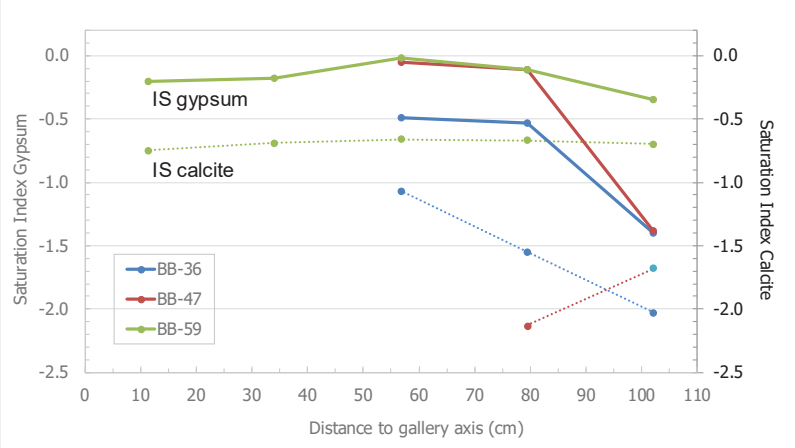

Fig. 177: Saturation indices of gypsum and calcite in pore waters from squeezed samples obtained after dismantling Heater #2 in 2015

6 Sample investigations at the liner/heater contact

Two types of samples were studied at the liner/Heater #2 contact (Fig. 179):

- Bentonite samples located at the liner contact (external part of the liner) in Section 47 (BM-S-47-1, BM-S-47-2 and BM-S-47-3 samples) and Section 53 (BM-S-53-1, BM-S-53-2 and BM-S-53-3 samples)
- Bentonite protrusions found inside the liner holes (internal part of the liner) around Section 42 and Section 43. Both types of samples were the closest bentonite samples to the Heater #2 contact

The BMS samples were taken from the contact with the liner at different positions (Fig. 178, Fig. 179 to Fig. 181) by AITEMIN at Sections S47 and S53. The bentonite protrusion samples were taken *on site* (10 – 11 June 2015) inside the liner after removing the heater on 4 June 2015 (Fig. 182 to Fig. 186). All samples were preserved *on site* in Al-foil vacuum-sealed bags. The samples analysed correspond to those given in Tab. 4 (BMS-xx and BS-46-A3 to BS-46-A10), but for lab working activities intuitive labels were used, which are defined in Fig. 179 to Fig. 186.

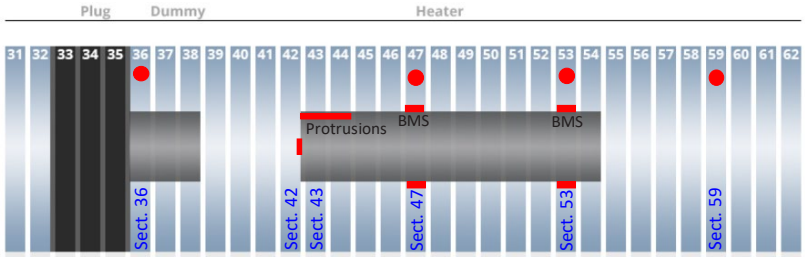

Fig. 178: Schematic figure of the FEBEX in-situ test divided in dismantling sections: location of the dismantling bentonite sections around Heater #2 selected for THC studies

Fig. 179: Bentonite sample BM-S-47-1 taken from liner contact at bentonite sampling Section S47 (bentonite slice 44)

Photographs shows the subsampling for analysis.

Fig. 180: Bentonite sample BM-S-47-2 taken from liner contact at bentonite sampling Section S47 (bentonite slice 44)

Photographs shows the subsampling for analysis.

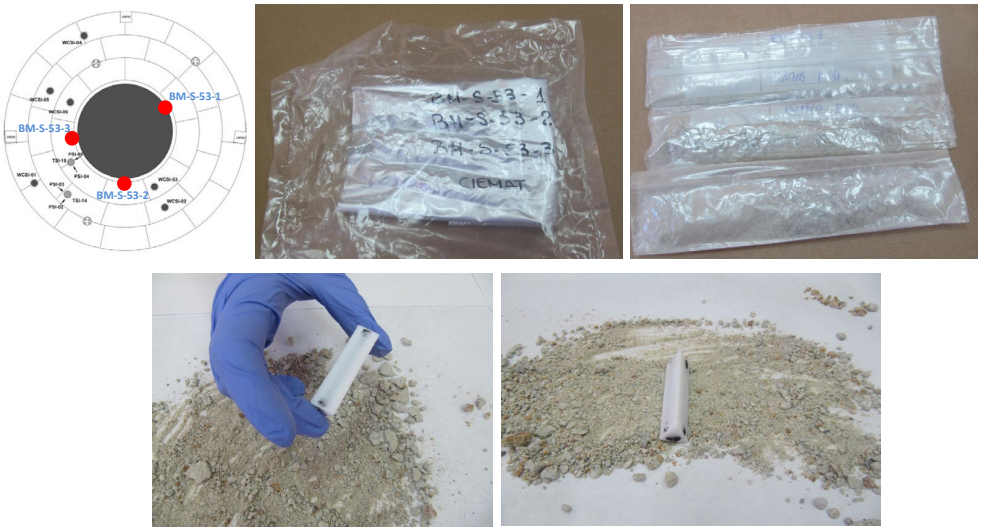

BM-S-53-1 BM-S-53-3

Fig. 181: Bentonite samples taken from liner contact at bentonite sampling Section S53 (bentonite slice 28)

Photographs show the subsampling for analysis: bentonite and separated magnetic material.

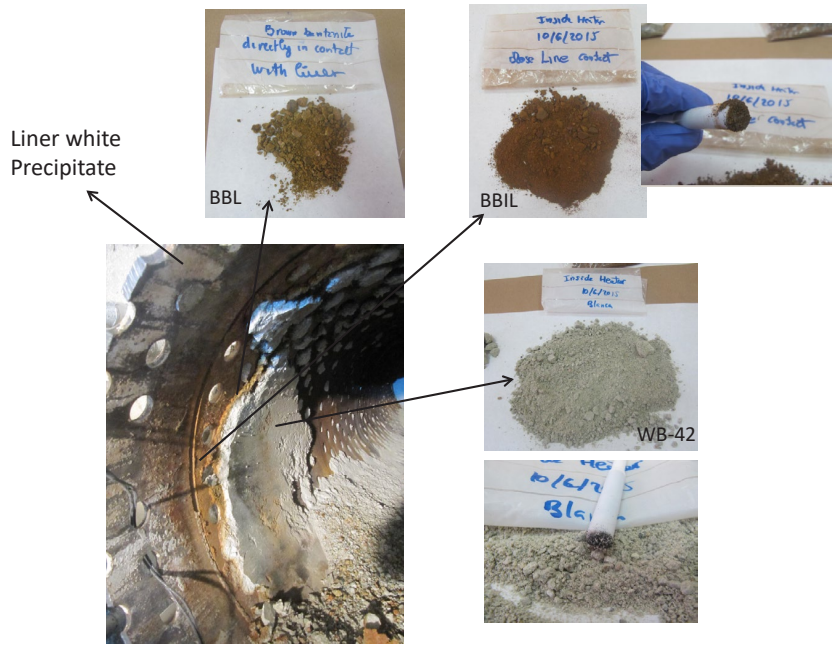

Fig. 182: Bentonite samples taken from the internal part of the liner at contact with the heater (bentonite slice 59/57, bentonite sampling Section S42-S43)

Photographs show the subsampling for analysis: a) white precipitate at contact with the liner, b) brownish bentonite at direct contact with the liner (BBL), c) brownish-red bentonite inside the liner (BBIL), d) bentonite white material inside the liner (WB), which contains magnetic material.

Fig. 183: Bentonite samples (protrusions) taken from the internal part of the liner at contact with the heater (bentonite slice 59/57, bentonite sampling Section S42-S43)

Photographs show the subsampling for analysis: a) black spots (BSH) and b) black-greenish material (GB).

Fig. 184: Bentonite protrusions through the liner holes towards the heater. Samples taken from the internal part of the liner at contact with the heater (bentonite slice 59/57, bentonite sampling Sections S42-S43)

Photographs show the subsampling for analysis: S43 black, S43 red, S43 green, RV-42: R-green, and RNW-42: R-black-white (which contains magnetic material).

Fig. 185: Protrusion taken from inside the liner (around Sampling Section S43/Slice 57) on 11/06/2015

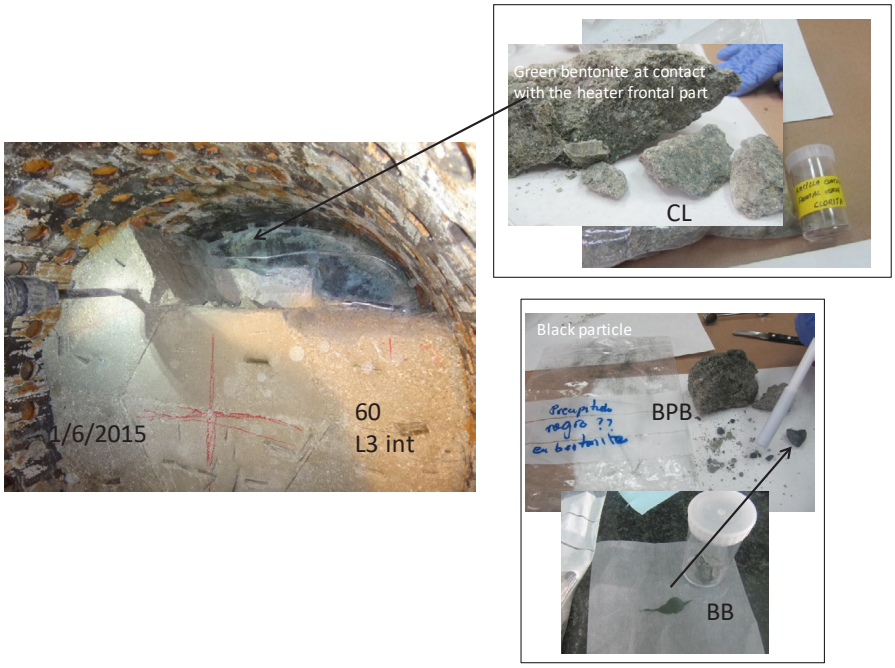

Fig. 186: Green bentonite (CL) at direct contact with the frontal part of the heater (Slice 60)

Black particles (BPB) adhered to bentonite mass and a black ball (BB) (green colour powder after grinding) were also sampled, with no signal of magnetic properties.

6.1 Mineralogy

The mineralogy of the samples was analysed by XRD, FTIR, TG-DSC, SEM and TEM. Results are described below.

6.1.1 XRD analyses

BMS and protrusion samples were analysed by XRD. Apart from the main minerals of the reference sample (Mg-Ca smectite, quartz, cristobalite, feldspars and calcite), neoformed minerals were found both in the BMS (above the liner) and protrusion (inside liner holes) samples (Tab. 36). Aragonite was found in the white powder adhered to the internal part of the liner (WP), at direct contact with Heater #2 (Fig. 182), as well as in protrusion samples. Apart from calcite, dolomite, siderite and magnesite were also detected by XRD. Iron corrosion products were found:

a) ferromagnetic minerals: magnetite, titanomagnetite and hematite (ferrihydrite was only detected by TG-DSC)

b) weak ferromagnetic minerals: goethite (Fig. 187a and Appendix F)

S-phases were also detected as FeS, mackinawite, and pyrrhotite. Other mineral phases were celestine, anatase and rutile. Brucite was detected in the protrusion samples with a black-greenish colour (RV-42 and BSH) (Fig. 187b and Appendix F).

With respect to clay minerals, Ca-Mg-montmorillonite was the main clay mineral phase, but changes in the d(060) reflexion were observed in some samples indicating a modification of the clay mineral structure. Apart from the d(060) reflexion at 1.49 Å of dioctahedral smectites, a peak at 1.53 – 1.52 Å (Fig. 187d) appears in some samples (RV-42 green), indicating the presence of clay minerals of trioctahedral character (Fernández et al. 2018b, submitted). Saponite seems to appear in some samples analysed: BMS-47-2; GB-42 green-black and CL green bentonite, and it was also detected in the E5 and E6 samples analysed by BGR (Wersin & Kober 2017, Kaufhold et al. submitted). The formation of trioctahedral domains in bentonites containing dioctahedral smectites at the very contact to a heater surface was described in other large scale experiments (Kaufhold et al. 2013, Svensson et al. 2011, Svensson 2015).

On the other hand, chlorite seems to appear in some samples analysed by CIEMAT (BMS-47-2; GB-42 green-black and CL green bentonite), but especially in the samples taken at the frontal part of Heater #2: the black scraping powder obtained from a block (Fig. 186, BPB) and a separated piece (Fig. 186, BB). As shown below, chlorite was also detected by SEM and FTIR.

However, when analysing the < 2 μm fraction, a fully expansible Ca-Mg-montmorillonite is the main phase (Fig. 187d and Appendix F), being a R0 S/I mixed layer. In the retrieved samples the calculated percentage of illite layers of the smectitic phase is ~ 10 ± 1 %, which is similar to that found in the reference bentonite (8 % of illite layers in the R0 I/S ML). No other mineral phases, such as illite, I/S ML or chlorite were identified in the oriented aggregates performed with the < 2 μm fraction.

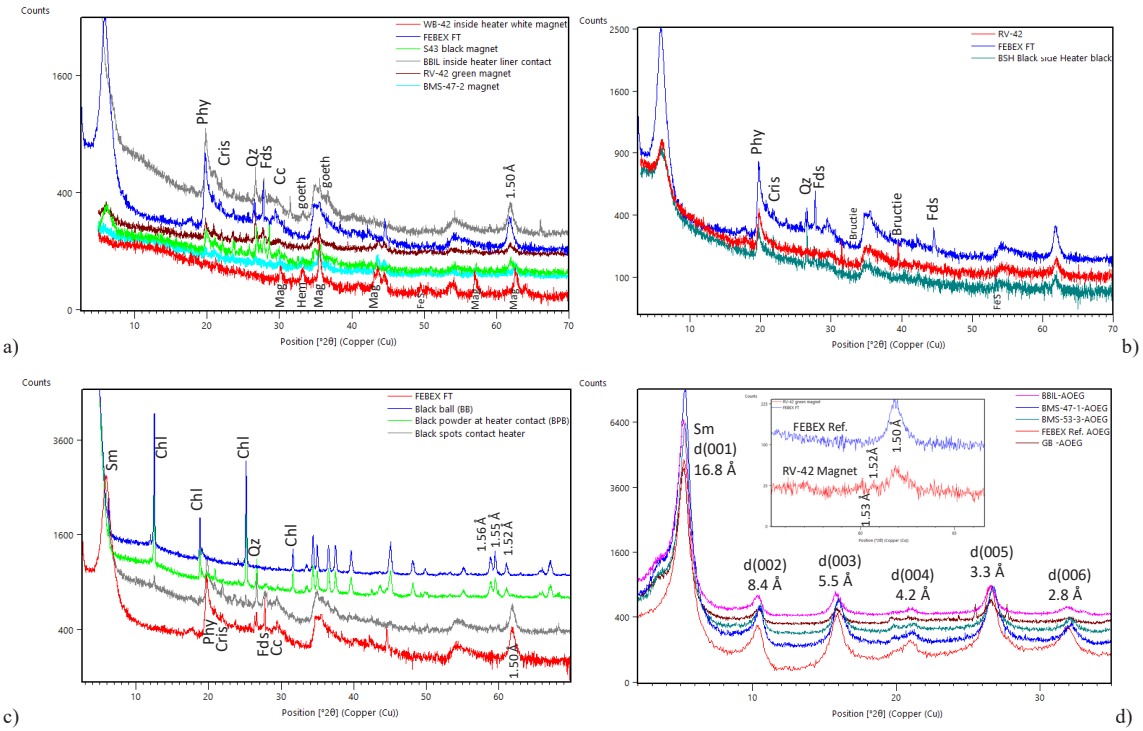

Fig. 187: XRD patterns of bulk samples from BMS and protrusion samples located at contact with the liner/Heater #2: a) Fe-oxy/hydroxides from magnetic samples, b) brucite, c) chlorite at the frontal part of the Heater #2, and d) ethylene-glycol solvated oriented aggregates

6.1.2 FTIR analyses

In general, the spectra from the bulk samples contain the main typical dioctahedral smectite bands, as well as quartz (Fig. 188). The spectra show a band at 3'627 cm^{-1} which corresponds to the typical OH stretching region of structural hydroxyl groups for dioctahedral smectites with Al-rich octahedral sheets. These are inner hydroxyl groups lying between the tetrahedral and octahedral sheets. The broad band near 3'426 cm^{-1} is due to stretching H-O-H vibrations of adsorbed water, while the band at 1'642 cm^{-1} corresponds to the OH deformation or bending of water. If the Si-O absorptions and OH bending bands in the 1'300 – 400 cm^{-1} range are examined, only one broad, complex Si-O stretching vibration band at around 1'030 cm^{-1} is seen, which is typical of a dioctahedral montmorillonite. The occupancy of the octahedral sheet strongly influences the position of the OH bending bands, which arise from vibrations of the inner and surface OH groups. In these samples, the presence of a band at 914 cm^{-1} (δAlAlOH) and at 840 cm^{-1} (δAlMgOH), indicates a partial substitution of octahedral Al by Mg, typical of dioctahedral smectites. The absorption band at 622 cm^{-1} can be attributed to a R-O-Si vibration (R = Al, Fe, Mg) and indicates a perpendicular vibration of the octahedral cations and their connection to the tetrahedral sheet. The bands at 520 cm^{-1} and 466 cm^{-1} correspond to Si-O-Al vibration of aluminium in the tetrahedral sheet and Si-O-Si bending vibrations, respectively. The weak band at 798 cm^{-1} is caused by the Si-O stretching of quartz.

Hematite and goethite were observed also by FTIR in the BMS (BMS-47-1, BMS-53-1) samples at direct contact with the liner (Tab. 36). Aragonite, calcite and quartz were the main minerals from the white powder (WP) adhered to the liner surface (Fig. 182). In most of the samples

analysed, no changes were found, except in the GB and RV-42 green samples (Fig. 183, Fig. 184) where possible modifications in the smectite clay mineral structure were found; and in the black ball (BB) sample (Fig. 186), where chlorite was identified (Fig. 188). An increment of the δMgFeOH stretching band at 3'563 cm^{-1} as well as a decrease of the δAlAlOH bending band at 914 cm^{-1} were detected in the black (BSH, Fig. 183), black-reddish (BBIL, Fig. 182) and reddish (S43-FR, Fig. 184) material, slightly increasing the δAlFeOH band at 885 cm^{-1} in the BBIL and BSH samples. An increase in the δAlMgOH bending band at 840 cm^{-1} was also observed in the RV-42 black-greenish sample (Fig. 188).

Tab. 36: Neoformed mineral phases observed in the samples at direct contact with the liner/Heater #2 by means of XRD, FTIR and TG-DSC

Type of mineral phases	**Mineral phases**	**Samples**
Fe-oxyhydroxides	Goethite (weak FM)	BMS-42-2 (1 mm, 1 cm), BMS-47-3 black, BBIL-42 magnet, S43 black magnet, RNW42 magnet
	Magnetite (FM)	BMS-42, BMS-47-2 black purple, BMS-47-2 magnet, BMS-47-3 black, RV-42 green magnet, BSH, BBIL-42 magnet, S43 black, WB-42 magnet, RNW42 magnet
	Titanomagnetite	S43 black
	Hematite (AFM)	BMS-47-2 magnet, WB-42, S43 black, GB-42, BMS-47-1[2], BMS-53-1[2]
	Ferrihydrite	BMS-42-2[3]
Carbonates	Aragonite	WP, BSH, RV-42 green magnet
	Dolomite	BMS-47-2 black-purple, BSH, CL
	Magnesite	BSH
	Siderite	BBIL-42 magnet, S43 black magnet
Sulphides	Pyrrhotite	BMS-47-2 green, RV-42 green magnet, S43 black
	Mackinawite	BMS-47-2 black-purple, WB-42
	FeS	S43 black magnet, WB-42
Mg-hydroxides	Brucite	S43 black, RV-42 green, BSH, GB[2]
Chlorites	Clinochlore/chamosite	BMS-47-2 green, BMS-47-2 magnet, GB-42, CL, BB[1,2], BPB
Mg-smectite	Saponite	BMS-42, GB-42, S43 black, BMS-47-2 magnet, BMS-47-1, 2 ,3[3], BMS-53-1,2,3[3], CL, CL[3], RV-42 green[3], RNW42[3], GB-42, GB-42[3]

XRD: Non-numbered samples and denoted with [1,2]FTIR; [3]TG-DSC. FM: ferromagnetic
AFM: Antiferromagnetic

In the black-greenish (GB) material new bands at 3'700 and 705 cm^{-1} were distinguished (Fig. 188), indicating the presence of Mg_3OH vibrations, such as in trioctahedral structures. Farmer (1974) attributed this band close to 3'700 cm-1 to Mg3OH vibrations in dehydrated saponites containing interlayer Na or K, whereas Van der Marel & Beutelspacher (1976) and Bergaya et al. (1985) attribute this to chlorite/smectite mixed-layers; Pelayo et al. (2018) to smectite with intermediate composition between beidellite and Fe-rich saponite; and Madejová (2003) to outer AlAlOH vibrations in kaolinite. However, kaolinite can be excluded since it has not been identified by XRD. This new band at 3'698 cm-1 was also observed in the BM-S-54-5B1 studied by BGR, with a high MgO content (Wersin & Kober 2017). In this sample, slight changes were also observed in the oxide deformation range (400 – 600 cm-1) of the spectrum, where both additional humps (570 and 440 cm-1) can be explained by a larger brucite content, because the pure brucite also reveals bands at these positions and kaolinite was not observed in XRD analyses. Brucite and saponite were identified by XRD and TG-DSC analyses in the BMS and protrusion samples (Tab. 36).

In the case of the BB sample, a Fe-rich chlorite containing aluminium was detected (Fig. 188). This chlorite shows bands at 3'547 and 3'409 cm-1, which are associated with the OH-stretching vibrations of the interlayer hydroxide sheet (clear evidence for O-H stretches in the interlayer sheet and molecular H_2O). The exact position of this doublet (at 3'565 and 3'434 cm^{-1} theoretically) varies with composition, shifting to lower frequency with increasing Al and Fe content. The band at 3'547 cm^{-1} indicates high substitution of Mg by Fe at octahedral sheets (MgFeOH vibration). The band at 3'650 cm^{-1} is related to OH-stretching vibrations of the inner hydroxyl groups at octahedral sheets, close to the unsubstituted brucite position (Mg_3OH ~ 3'698 cm^{-1}). The shift of the stretching Mg_3OH vibrations towards lower frequencies (~ 3'650 cm^{-1}), as well as the non-marked splitting of the principal Si-O band at 998 cm^{-1}, reflect some Al-for-Si substitution in the tetrahedral sheet in the 2:1 layer. The bands around 667 cm^{-1} comprise OH deformation components from the 2:1 layer and the hydroxide sheet. This band is strongly dependent on the composition of the interlayer octahedral sheet and is split into two components (664 and 637 cm^{-1}) when Fe content increases (Russell 1987). The bending vibration of Mg-O-H groups are observed at 664 cm^{-1}, but those for the Al-O-H groups are also observed at 750 cm^{-1}. With increasing substitution of Mg by Al, chlorites become more dioctahedral; on the contrary, with increasing Mg, chlorites become more trioctahedral. However, the 3'547 and 3'409 cm^{-1} doublets suggest that the hydroxide sheets have also a trioctahedral character. In any case, the strong band at 750 cm^{-1} may also indicate the presence of illite (2:1 layer).

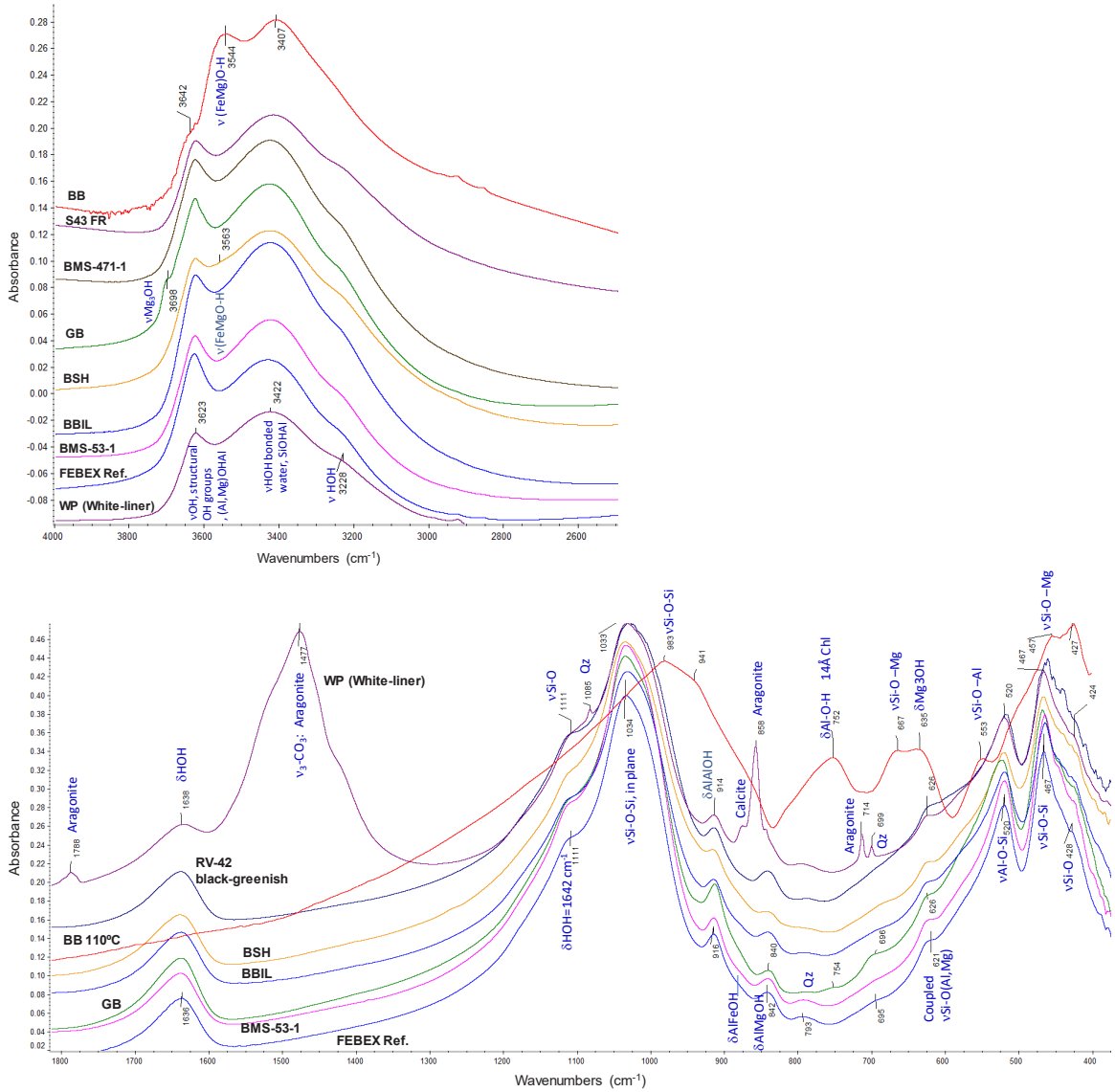

Fig. 188: FTIR spectra (OH-stretching and OH-bending regions) from samples taken above (BMS) and inside the liner (protrusions) at contact with Heater #2

6.1.3 TG-DSC analyses

Significant differences were found in the TG-DSC curves of the analysed samples, which indicate the presence of corrosion by-products and a structural modification of the smectite clay mineral in the samples at close contact with Heater #2 (Fig. 189 and Appendix F). These changes were observed both in the BMS material, taken from direct contact with the liner, and in the protrusions samples, taken from inside the liner holes. Ferrihydrite was identified from the magnetic material of the BMS-47-2 sample (Fig. 190). Other Fe-oxyhydroxides were detected in the BBIL-42 and RV-42 green samples.

When the DSC curves are compared (Fig. 189), GB and RV-42 green protrusion samples show a new peak around 492 °C. This peak is assigned to brucite, $Mg(OH)_3$, corroborating the $Mg(OH)_3$ vibrations observed by FTIR analyses. This was also confirmed in the BMS-54 samples analysed by BGR, where a new peak appeared at about 530 °C in the water curve, which was assigned to brucite (Kaufhold et al., submitted; Wersin & Kober, 2017).

Furthermore, apart from the main dehydroxylation peak at around 650 °C (typical of dioctahedral smectites), two new peaks between 520 and 550 °C and between 592 and 622 °C appear in the total fraction (Fig. 189). The peak between 520 and 550 °C is only observed in the < 2 μm fraction (Fig. 191). These peaks are observed both in the BMS and in the protrusion samples. The presence of these additional and/or abnormal dehydroxylation peaks indicates the presence of other types of clay minerals in addition to the cis-vacant dioctahedral smectite clay particles characteristic of the FEBEX reference sample. The seven possibilities that explain these peaks are (e.g., MacKenzie 1957):

1. The presence of illite/smectite mixed layers (I/S ML), because illite has a trans-vacant configuration
2. The presence of another type of clay mineral mixed layer, such as Chl/S ML
3. A mixing of smectite particles with high-iron and aluminous varieties, since the presence of iron at octahedral sites induces a decrease of the dehydroxylation peak towards 450 – 520 °C, as occurs in nontronites (the main smectite types exhibit different dehydroxylation temperatures: 450 – 520 °C for dioctahedral Fe-smectites (trans-vacant); 670 – 730 °C for dioctahedral Al-smectites (cis-vacant) and 770 – 860 °C for trioctahedral Mg-smectites, octahedral cations determining the dehydroxylation temperature)
4. A change of the smectite structure, with an increase of octahedral OH groups at trans-vacant positions (and hence more tetrahedral charge), instead of being mostly at cis-vacant positions as occurs in the FEBEX reference sample
5. A change in the smectite structure with the presence of two types of smectite particles: those with mainly tetrahedral substitutions (beidellitic type) and those with mainly octahedral substitution (montmorillonite type)
6. Crystal structure changes as result of Fe(III) reduction in order to accommodate the larger size of Fe(II) and increased negative charge, which generate partial dehydroxylation and loss of structural OH groups (Stucki & Roth 1977) or finally
7. Structural transformations of the cv 2:1 layers, which were dehydroxylated due to heating or another process, such as Fe(III) reduction

This process involves not only the loss of hydroxyls but also the migration of Al cations into vacant sites in a portion of the sample. Thus, after rehydroxylation (e.g., cooling in water vapour) a cis-vacant montmorillonite transforms to a mixture of two montmorillonites one having trans-vacant and the other cis-vacant 2:1 layers (Drits et al. 1995, Emmerich et al. 1999).

The retrieved samples show, in turn, a variation in the temperature of the decomposition/ recrystallization peak. The associated endothermic peak located around 867 °C in the reference sample shifts to lower temperatures (down to 845 °C). Indeed, there is a modification in the shape and magnitude of the high temperature endothermic-exothermic peak between 850 and 1'000 °C. The exothermic peak also shifts from 1'010 °C in the reference sample to a higher exothermic peak at a lower temperature around 985 °C (Fig. 189). This is well observed when the < 2 μm fraction is analysed (Fig. 191). In this fraction the peak between 592 and 622 °C is not detected (maybe because of the low content, being overlapped within the range of the peak at 650 °C, or the particle size), but the additional dehydroxylation peak around 550 °C is well distinguished and associated with a modification in the high temperature endothermic-exothermic decomposition peak between 850 and 1'000 °C (Fig. 191 and Fig. 192). Therefore, a possible modification of the composition in the structure of the smectite is also inferred from these peaks. The magnitude of the exothermic peak is intensive in the case of a smectite with high Mg content and decreases or disappears in the case of high Al or Fe content, i.e., this peak increases in height when Mg increases, and decreases in temperature when Mg increases. In this case, the sharp exothermic peak indicates a higher Mg content at octahedral sheets in the samples at contact with the heater, as observed from the < 2 μm fraction in the BMS samples in Section 47 and Section 53 (Fig. 191) and in the GB protrusion sample (Fig. 192). The presence of the sharp exothermic-endothermic peak is observed in all BMS samples but not in all the protrusion samples. This depends on the type of sample, it is missing, for example, in the protrusion samples with an apparent lower degree of alteration (RNW-42 black&white) or having a reddish colour (BBIL-42, S-43 FR red); but is found in the GB and RV-42 black-greenish samples. The latter samples have a higher Fe(II) content (see below).

More interesting is that in the samples with abnormal behaviour, i.e., having two dehydroxylation peaks around 550 °C and 650 °C, a slight mass change is observed in the dTG curves at 835 – 850 °C (Fig. 191 and Fig. 192). This is mandatory and restricted to trioctahedral smectites. Therefore, a modification of the smectite clay mineral structure from the reference dioctahedral to a trioctahedral character is inferred in the samples in close contact with Heater #2. From possible trioctahedral clay minerals, only saponite shows a dehydroxylation peak around 850 – 900 °C with a mass change in this peak. Chlorites or Chl/S MLs do not show mass changes at this temperature. Therefore, different types of clay mineral particles are in these samples:

1. The double dehydroxylation peaks at 550 °C and 650 °C indicate the presence of two types of smectite particles, those with tetrahedral substitutions (550 °C) and those with octahedral substitutions (650 °C), supported by the crystallochemistry of the clay particles analysed by TEM and SEM (see below), discarding the increase of octahedral OH groups at trans-vacant positions or the increase of iron at octahedral sites.
2. The mass change in the dTG curves at 835 – 850 °C indicates the presence of trioctahedral smectite (saponite).
3. The peak around 620 °C may be indicative of the presence of interstratified smectite particles (e.g., I/S MLs, Chl/S MLs, ...).

Finally, as observed by XRD, FTIR, TEM and SEM, chlorite was identified by TG-DSC in the black ball (BB) sample, located at the frontal part of Heater #2 (Fig. 186), showing a dehydroxylation peak at 589 °C and an exothermic peak at 948 °C with no mass variation at this temperature (Fig. 193).

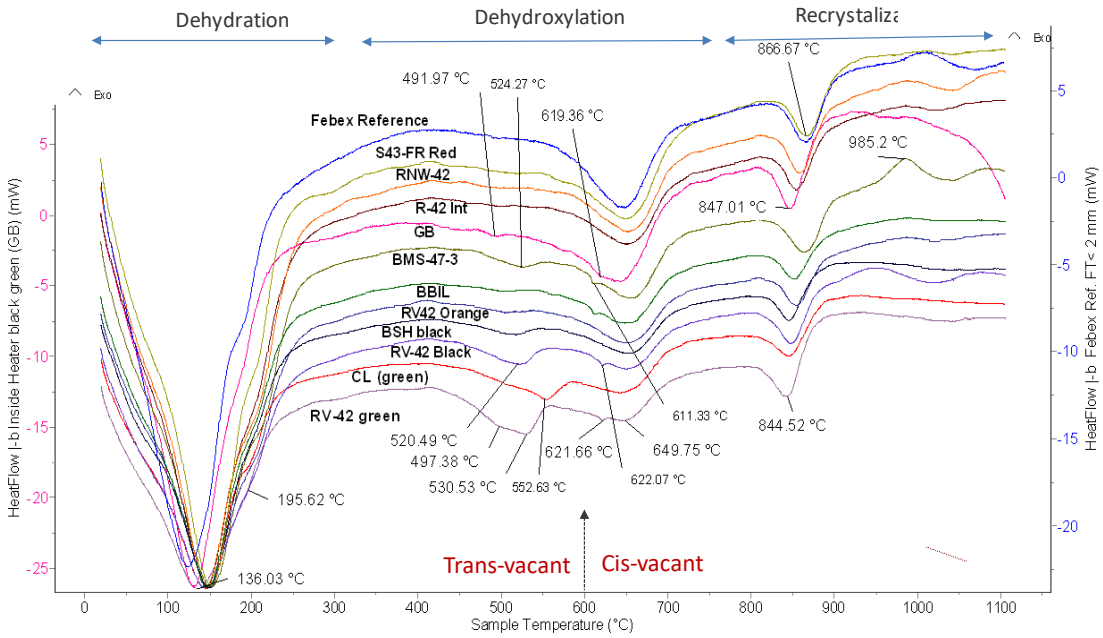

Fig. 189: Comparison of DSC curves from the bulk bentonite samples (total fraction): at direct contact with the liner (BMS-47-3) and protrusions through the liner holes towards the heater

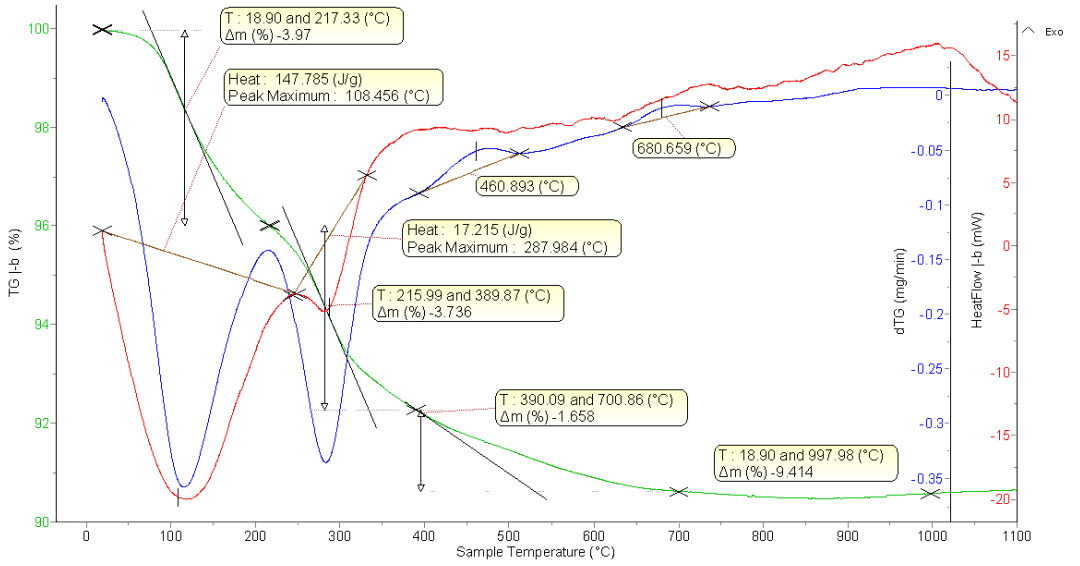

Fig. 190: TG-DSC curves from the magnetic powder of sample BMS-47-2 at direct contact with the liner: ferrihydrite

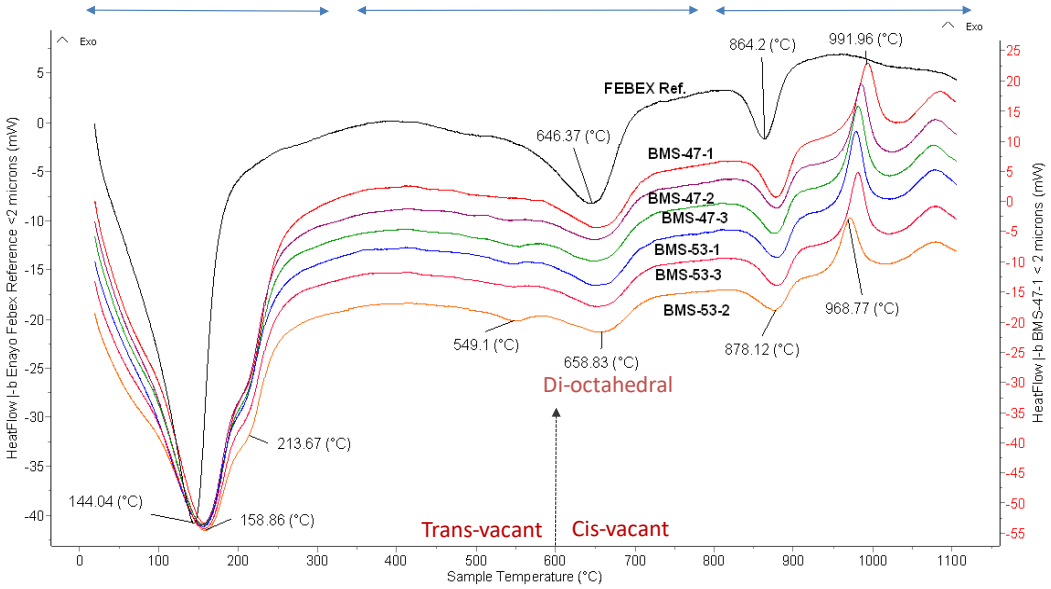

Fig. 191: Comparison of DSC curves from samples BMS-47-xx and BMS-53-xx (< 2 µm fraction) at direct contact with the liner

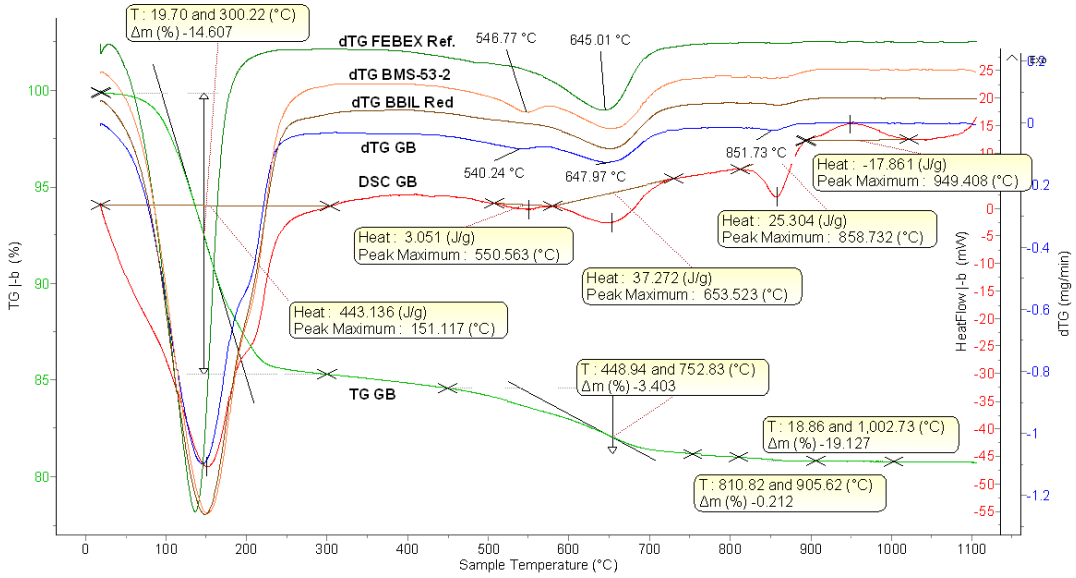

Fig. 192: TG-DSC curves from the GB-42 bentonite protrusion sample through the liner holes towards the heater

dTG curve is compared with dTG curves from other < 2 µm fraction samples: FEBEX reference, BBIL red (protrusion) and BMS-53-2 (above the liner).

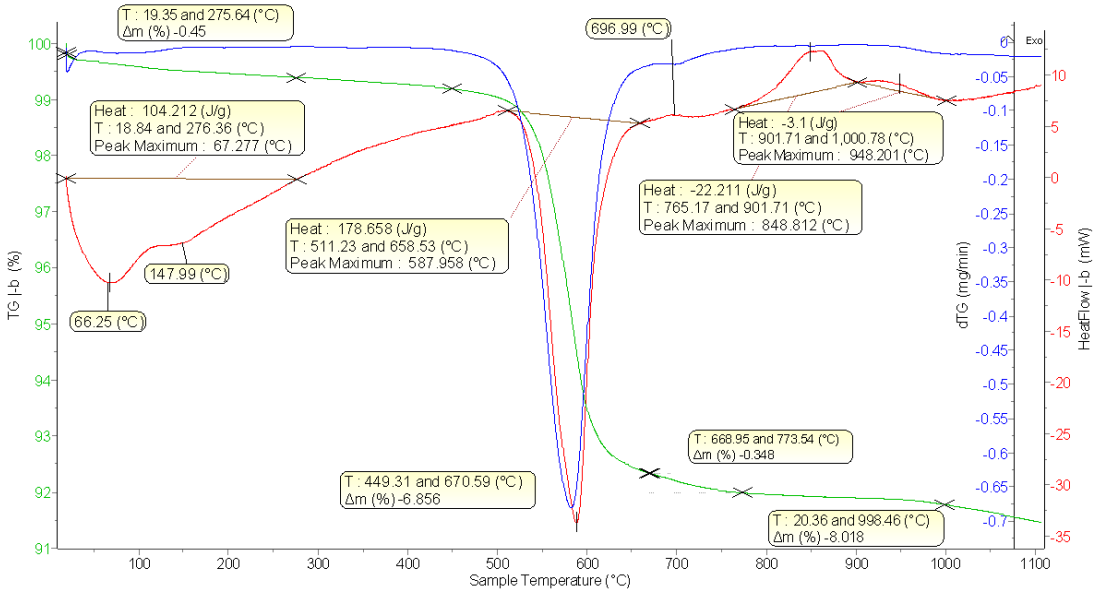

Fig. 193: TG-DSC curves from bentonite at direct contact with the frontal surface of Heater #2: Black ball particle (BB): chlorite

6.1.4 SEM analysis

Scanning electron microscopy (SEM) aimed at analysing the main and accessory minerals in different bentonite samples, as well as identifying the microstructure and crystallochemistry of the clay minerals:

- Samples in contact with the liner at Section 47: BMS- 47-1, BMS-47-2 (Fig. 179 and Fig. 180)
- Samples from the internal part of the liner at direct contact with Heater #2:
  - ✓ BBIL-42: Brownish-red bentonite inside the liner (Fig. 182)
  - ✓ WB-42: White Bentonite from the internal part of the liner: (Fig. 182)
- Protrusions taken from the liner holes:
  - ✓ Protrusion BSH-42: black spot inside heater (Fig. 183)
  - ✓ Protrusion GB-42: inside Heater, black (Fig. 183)
  - ✓ Protrusion RNW42: black and white particles (Fig. 184)
  - ✓ Protrusion RNW-42: grey particles (Fig. 184)
  - ✓ Protrusion RV-42: green particles (Fig. 184)
  - ✓ Protrusion PS-43 (Fig. 185)
  - ✓ Protrusion PS-43: red particles (Fig. 185)
- Samples at direct contact with the frontal surface of Heater #2:
  - ✓ Black particles adhered to bentonite: BPB (Fig. 186)
  - ✓ Black ball particle: BB (Fig. 186)

The SEM photomicrographs as well the crystallochemical formula of the clay minerals analysed from the different samples are shown in Appendix B2. The results are summarised in Tab. 37.

Tab. 37: Major mineral phases and accessory minerals observed by SEM in samples in contact with the liner and in the protrusions (in cursive: present in the reference sample)

Mineral phases	**Section 47 and Section 54**	**Protrusions**
Ca-carbonates	BMS-47-1	WB-42; PS-43; RNW42; RV-42 GB-42; BPB
Dolomite		PS-57; RNW42
Fe-carbonates		BBIL-42; PS-43; PS-43 Red; RNW42; BSH-42; GB-42
Ca-sulphates	BMS-47-2	BBIL-42; WB-42; PS-57; RNW42 RV-42; GB-42
Ba(Sr)-sulphates	BMS-47-1 BMS-47-2	BBIL-42; WB-42; PS-43; PS-43 Red; RV-42; GB-42
Fe-sulphides		RV-42

Tab. 37: Cont.

Mineral phases	**Section 47 and Section 54**	**Protrusions**
PbS		PS-43
Fe-oxides	BMS-47-2	BBIL-42; WB-42; PS-43 PS-43 Red; BSH-42; GB-42; BPB
Fe-Ti-Mn-oxides	BMS-47-2	WB-42; PS-57; PS-43 Red; RNW42; BPB
Ilmenite	BMS-47-1	BBIL-42; RNW42; RV-42
Hg particles		WB-42; PS-43; PS-57 Red; RV-42
Zircon		RNW42; RV-42; BSH-42
Xenotime	BMS-47-1	
Monazite		RNW42; GB-42; BPB
Apatite	BMS-47-2	PS-43; BSH-42; GB-42
Silica	BMS-47-1 BMS-47-2	WB-42; PS-43; PS-43 Red RNW42; RV-42; GB-42; BPB
Plagioclases	BMS-47-1 BMS-47-2	BBIL-42; WB-42; PS-43 PS-43 Red; RNW42; RV-42 BSH-42;GB-42; BPB
K-feldspars	BMS-47-1	RNW42; BSH-42; GB-42; BPB
Biotite	BMS-47-1 BMS-47-2	BSH-42
Organic matter (OM)	BMS-47-1 BMS-47-2	WB-42; PS-43; PS-43 Red RNW42; BSH-42; GB-42; BPB
C, N		PS-43
Cl	BMS-47-1 BMS-47-2	BBIL-42; WB-42; PS-43; PS-43 Red; RNW42; BSH-42; GB-42
Smectite	BMS-47-2	PS-43; RNW42; RV-42 BBIL-42; BSH-42; GB-42; BPB
Brucite or Mg-rich clay mineral	BMS-54-5B-1	
Nontronite/Fe-rich type with ↑K		S43FR red particles
Chlorites		BSH-42; BPB; BB
Kaolinite		GB-42

The major mineral phases are smectite, quartz and feldspars. In general, the accessory minerals of the FEBEX bentonite are: carbonates, sulphates, zircon, monazite, biotite, muscovite, ilmenite and apatite, which were also found in the retrieved samples. However, other accessory minerals were identified, which correspond to iron-bentonite interactions at the liner/Heater #2 contact, i.e., corrosion byproducts, such as: Fe-oxy/hydroxides, sometimes impregnated with Cl (Fig. 194), Fe-carbonates (Fig. 195), calcite and dolomite (Fig. 196), pyrite and sulphates (Ca- and Ba-Sr-sulphates) (Fig. 197), silica (Fig. 198) and organic matter with nitrogen. Furthermore,

apart from smectite, other types of clay minerals were found, such as nontronite/Fe-rich illite and chlorites (Fig. 199).

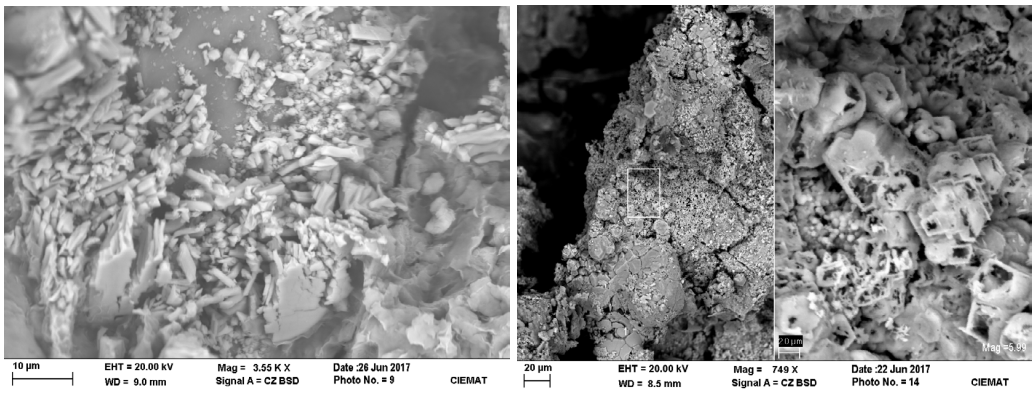

Fig. 194: SEM photomicrographs of Fe-oxy/hydroxides in different protrusion samples: a) WB-42, d) BSH-42 Black spot: Fe-oxides with Cl

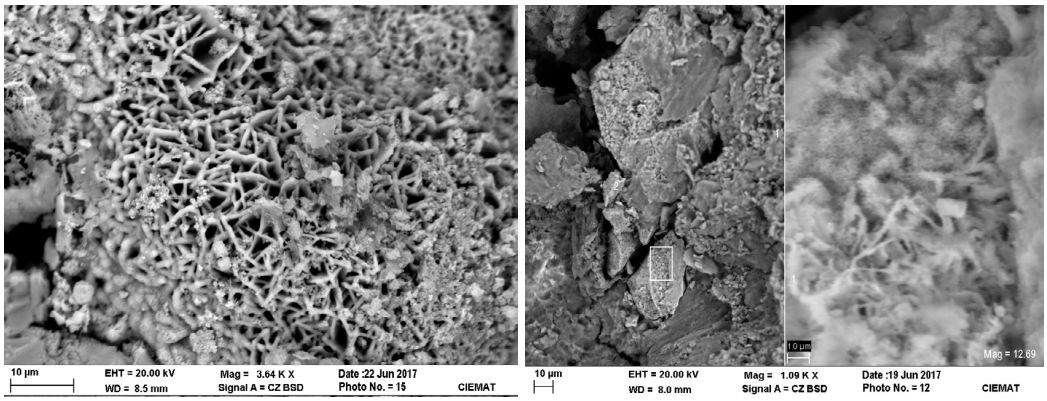

Fig. 195: SEM photomicrographs of Fe-carbonates in different samples: a) BSH-42 Black spot inside heater and, b) RNW42

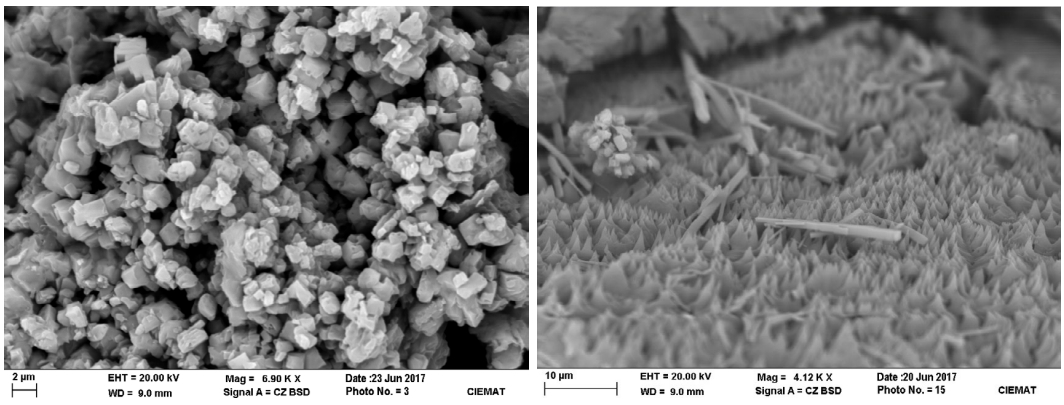

Fig. 196: SEM photomicrographs from carbonates in different samples: a) GB-42 inside heater black: Ca-carbonate; b) RNW42 with Dolomite Ca-sulphates

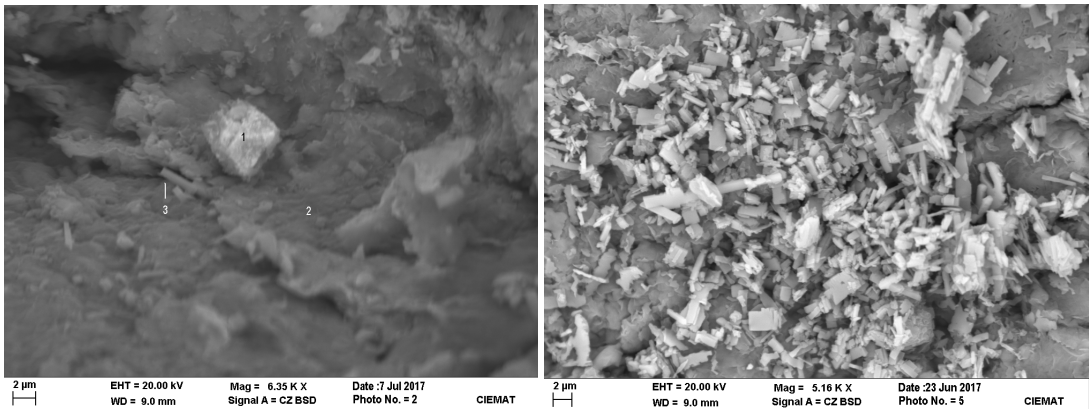

Fig. 197: SEM photomicrographs from different samples: a) RV-42: pyrite (1), smectite (2), Ca-sulphate (3); b) GB-42 inside heater black: Ca-sulphates in different samples

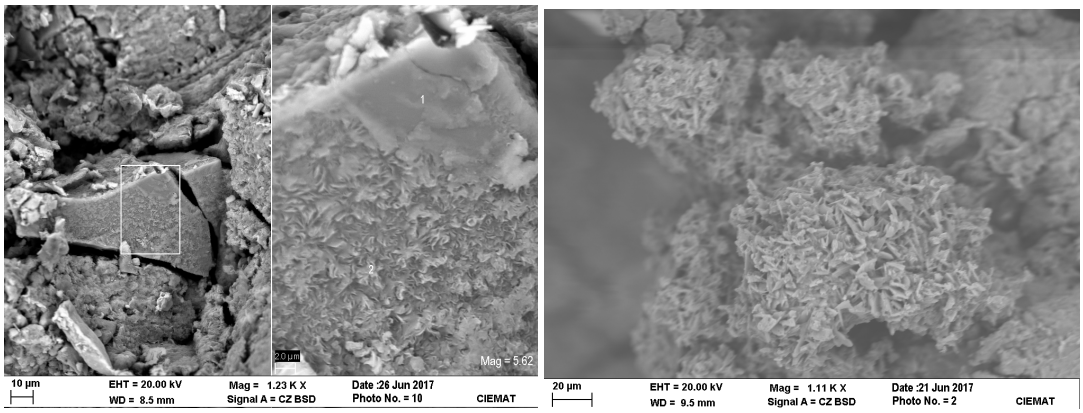

Fig. 198: SEM photomicrographs of silica from different samples: a) GB-42 inside heater black, b) BSH-42 Black spot inside heater

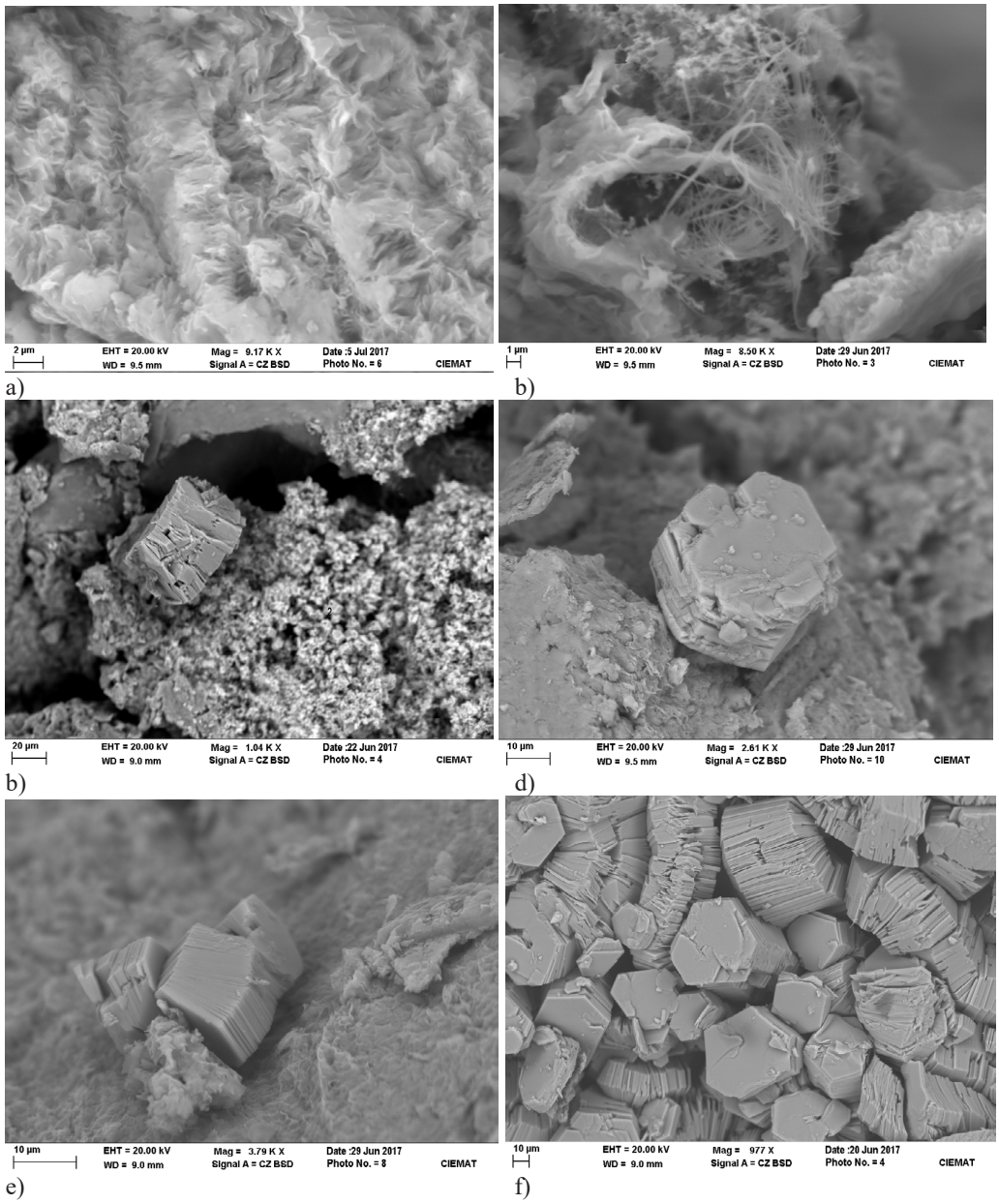

Fig. 199: SEM photomicrographs of clay minerals in different samples: a) smectite: BMS-47-2, b) Nontronite/(Fe-rich illite) type: S43 FR Red particles, c) chlorites (1), Fe-carbonates (2), BSH-42 Black spot inside heater, d) and e) chlorites: Black particles adhered to bentonite (BP), f) chlorites: Black ball (BB)

6.1.5 TEM analysis

Transmission electron microscopy examined the morphology of the platy clay particles and/or clay aggregates and the crystal chemistry of the clay minerals. EDS-analyses on clay particles determined the Structural formula and measured the thickness of the structural units perpendicular to the plates (c-axis and/or a- or b-axis). The EDS analyses were obtained from more than five determinations per sample. Based on these, Structural formula of the clay particles were calculated as shown in Tab. 38 (Moore & Reynolds 1989). See Section 5.3.4 for further information.

Tab. 38: Structural formula of clay mineral particles detected in the samples at contact with the liner/heater and in the protrusions

Sample	Structural formula	Layer charge (eq/h.u.c.)	Σ_{tet}	Σ_{oct}	τ charge (%)	O. charge (%)	Weight p.f.u. (g/mol)
FEBEX Ref. [5]*	$(Si_{3.93}Al_{0.07})^{IV}$ $(Al_{1.43}Fe^{3+}_{0.15}Mg_{0.49}Ti^{4+}_{0.01})^{VI}$ $O_{10}(OH)_2$ $(Ca_{0.02}Na_{0.24}K_{0.05})_{0.30}$	0.32	4.0	*2.08*	21	79	747.29
	$(Si_{3.93}Al_{0.07})^{IV}$ $(Al_{1.43}Fe^{3+}_{0.15}Mg_{0.41}Ti^{4+}_{0.01})^{VI}$ $O_{10}(OH)_2$ $(Ca_{0.02}Mg_{0.08}Na_{0.24}K_{0.05})_{0.38}$	0.48	4.0	*2.00*	14	86	747.29
BMS-47-2 [13] *montmorillonite*	$(Si_{3.76}Al_{0.24})^{IV}$ $(Al_{1.30}Fe^{3+}_{0.15}Mg_{0.50}$ $Ti^{4+}_{0.03}$ $Mn^{2+}_{0.02})^{VI}$ $O_{10}(OH)_2$ $(Ca_{0.17}Mg_{0.08}Na_{0.17}K_{0.06})_{0.48}$	0.73 (0.57)	4.0	2.00 (2.08)	33 (42)	67 (58)	758.70
BMS-53-2 [5] *montmorillonite*	$(Si_{3.98}Al_{0.02})^{IV}$ $(Al_{1.43}Fe^{3+}_{0.01}Mg_{0.56})^{VI}$ $O_{10}(OH)_2$ $(Ca_{0.02}Mg_{0.25}$ $Na_{0.02}K_{0.02})_{0.31}$	0.57 (0.08)	4.0	2.00 (2.25)	3 (22)	97 (78)	734.40
RV-42 Green [7] *montmorillonite*	$(Si_{3.82}Al_{0.18})^{IV}$ $(Al_{1.19}Fe^{3+}_{0.22}Mg_{0.57}Ti^{4+}_{0.01})^{VI}$ $O_{10}(OH)_2$ $(Ca_{0.08}Mg_{0.27}K_{0.06})_{0.41}$	0.76 (0.22)	4.0	2.00 (2.27)	24 (85)	76 (15)	754.82
Liner Red (BBIL-42) [6] *montmorillonite*	$(Si_{3.85}Al_{0.15})^{IV}$ $(Al_{1.29}Fe^{3+}_{0.32}Mg_{0.37}Ti^{4+}_{0.01})^{VI}$ $O_{10}(OH)_2$ $(Ca_{0.13}Na_{0.01}Mg_{0.11}K_{0.03})_{0.28}$	0.52 (0.31)	4.0	2.00 (2.11)	29 (49)	71 (51)	756.31
Heater Black (BSH) [5] *montmorillonite*	$(Si_{3.75}Al_{0.25})^{IV}$ $(Al_{1.60}Fe^{3+}_{0.01}Mg_{0.39})^{VI}$ $O_{10}(OH)_2$ $(Ca_{0.03}$ $Mg_{0.20}Na_{0.15}K_{0.05})_{0.42}$	0.65	4.0	2.00	39	61	741.18
Liner Red (BBIL-42) *Nontronite*	$(Si_{3.11}Al_{0.89})^{IV}$ $(Al_{0.25}Fe^{3+}_{1.74}Mg_{0.01})^{VI}$ $O_{10}(OH)_2$ $(Ca_{0.10}Mg_{0.34}K_{0.02})_{0.46}$	0.90	4.0	2.00	99	1	844.98
P. Black (BB) [7] *Chlorite Fe-rich***	$(Si_{2.91}Al_{1.09})^{IV}$ $(Fe^{2+}_{2.61}Mg_{0.14}Mn^{2+}_{0.08\ \ 0.17})^{VI}$ $O_{10}(OH)_2$ $(Ca_{0.02}Na_{0.01}K_{0.01})_{0.04}$ $[Al_{1.37}Mg_{1.63}(OH)_6]$	0.06	4.0	3.00	--	--	n.d.
P. Black (BB) [7] *Chlorite Fe-rich***	$(Si_{2.95}Al_{1.05})^{IV}$ $(Fe^{3+}_{0.38}Fe^{2+}_{1.90}Mg_{0.22}Mn^{2+}_{0.08\ \ 0.42})^{VI}$ $O_{10}(OH)_2$ $(Ca_{0.02}Na_{0.01}K_{0.01})_{0.04}$ $[Al_{1.43}Mg_{1.57}(OH)_6]$	0.06	4.0	3.00	--	--	n.d.

* In square brackets: number of point analyses performed for calculating the average structural formula. Smectite structural formula calculated by fixing the sum of octahedral cations at 2.0, except in the first row (FEBEX ref.). The data given in parentheses are those calculated without fixing the sum of octahedral cations at 2.0

** Total Fe as Fe(II)

*** Previous structural formula but considering the % of Fe(II) and Fe(III) determined in Section 6.2: Fe(II) = 92.7 %; Fe(III) = 7.3 %

TEM analyses were performed on the FEBEX reference sample and samples in contact with the liner/heater and protrusions. The aim was to analyse possible alterations in the smectite microstructure. TEM images for the retrieved samples are shown in Fig. 200 to Fig. 207. The Structural formula calculated for the clay minerals found are shown in Tab. 38. Most of the clay mineral particles were montmorillonite type smectites, as in the reference FEBEX bentonite. This agrees with further bentonite analyses performed on samples taken from different sections throughout the bentonite barrier. However, some significant variations were observed in some clay particles, which were related to changes in the cation composition at tetrahedral sheets (increasing the tetrahedral charge), a slight increase in magnesium at octahedral sheets, and increases in the layer charge above 0.6 eq/h.u.c., which is the limit for typical smectites (Fig. 208).

With respect to iron content at octahedral sheets, taken as Fe(III), it increases in the protrusion samples, where, apart from montmorillonite particles, other types of clay minerals were found (Tab. 38): nontronite (dioctahedral smectite with mainly tetrahedral substitutions), Fe-rich chlorites (tri(-di)octahedral chlorite), and illite in a sample from the bentonite block BB-47-9 close to liner contact (see Section 5.3.4).

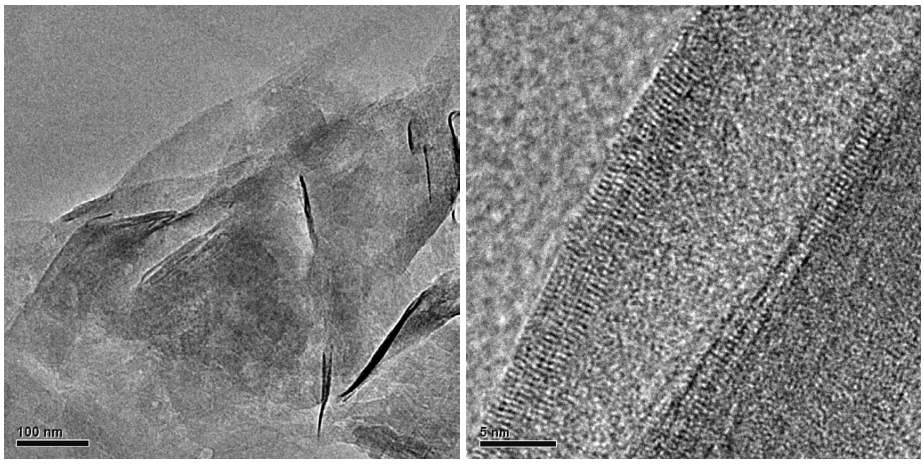

Fig. 200: TEM images from < 2 μm clayey suspensions: smectite particles from the FEBEX reference bentonite

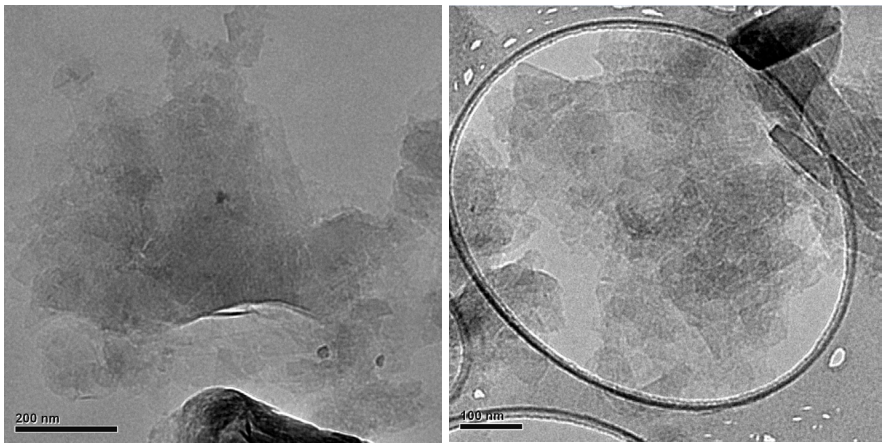

Fig. 201: TEM images from < 2 μm clayey suspensions: smectite particles from the sample of bentonite block BMS-47-2

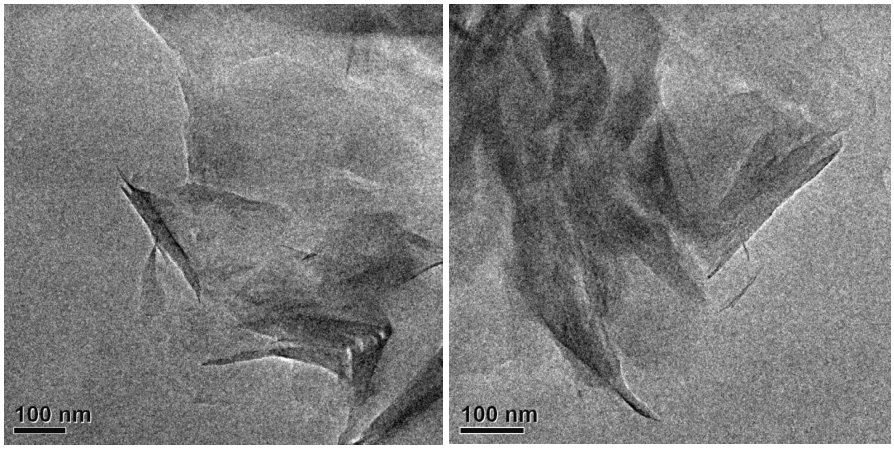

Fig. 202: TEM images from < 2 µm clayey suspensions: smectite particles from the sample of bentonite block BMS-53-2

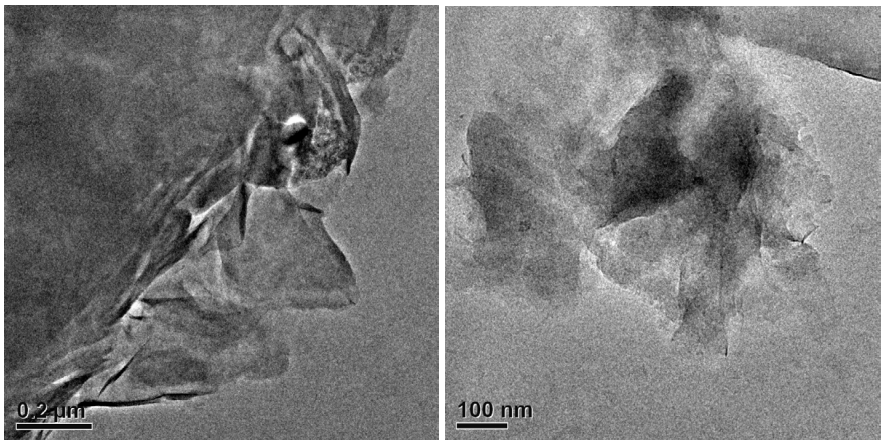

Fig. 203: TEM images from < 2 µm clayey suspensions: smectite particles from the sample Black spot inside heater (Protrusion BSH-42)

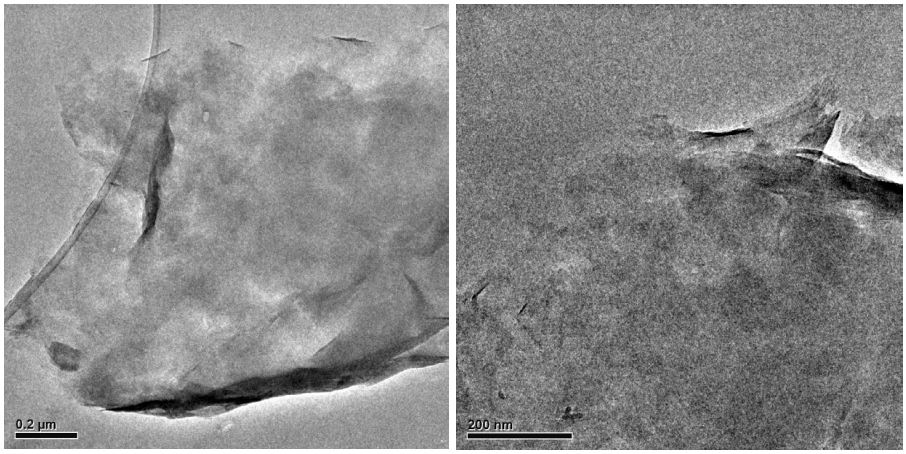

Fig. 204: TEM images from < 2 µm clayey suspensions: smectite particles from the sample Green particles (Protrusion RV-42)

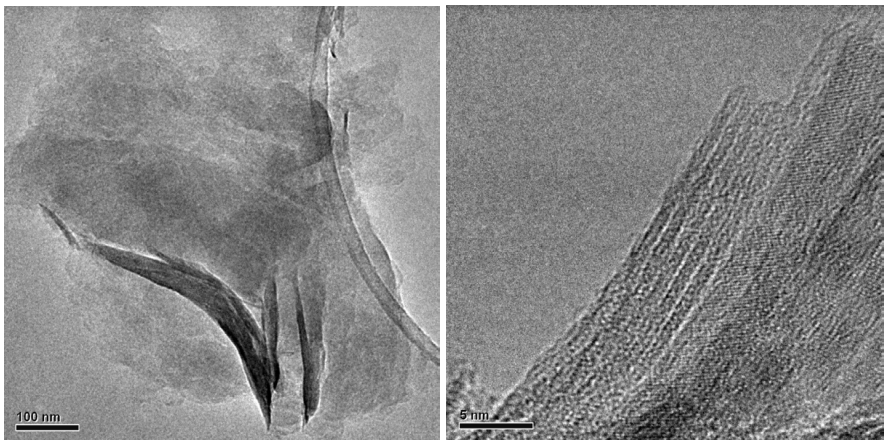

Fig. 205: TEM images from < 2 µm clayey suspensions: smectite particles from the sample Red bentonite inside the liner (Protrusion BBIL-42)

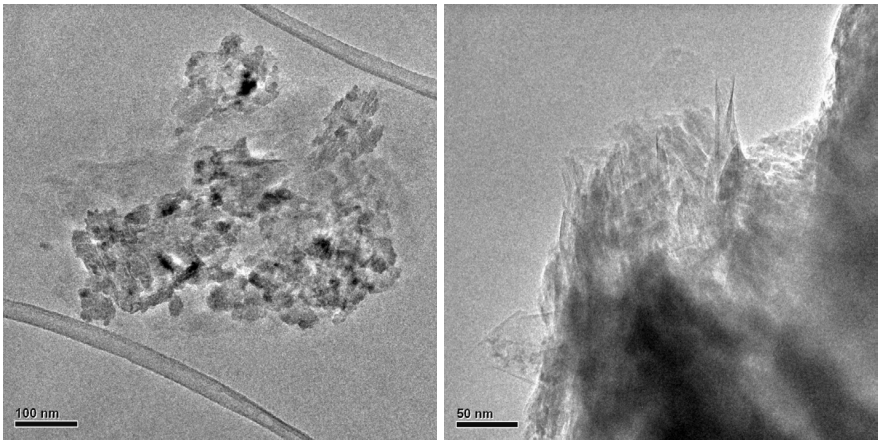

Fig. 206: TEM images from < 2 µm clayey suspensions: Nontronite particles from the Red bentonite inside the liner (Protrusion BBIL-42) sample

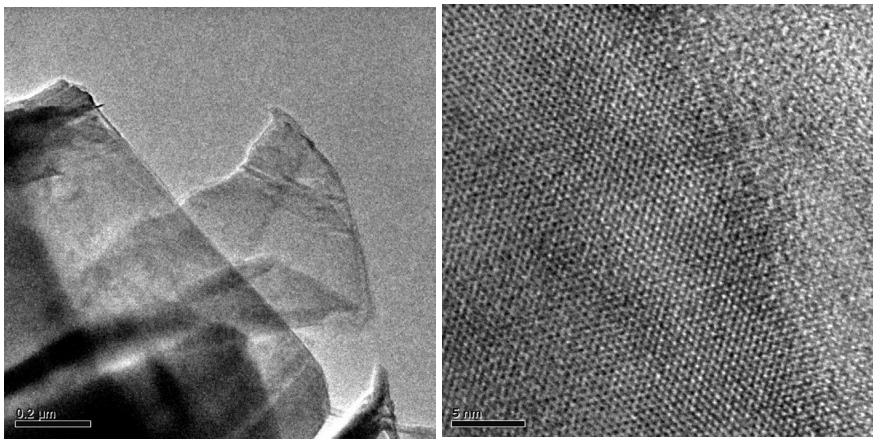

Fig. 207: TEM images from < 2 µm clayey suspensions: Chlorites detected in the Black particle (BB) sample

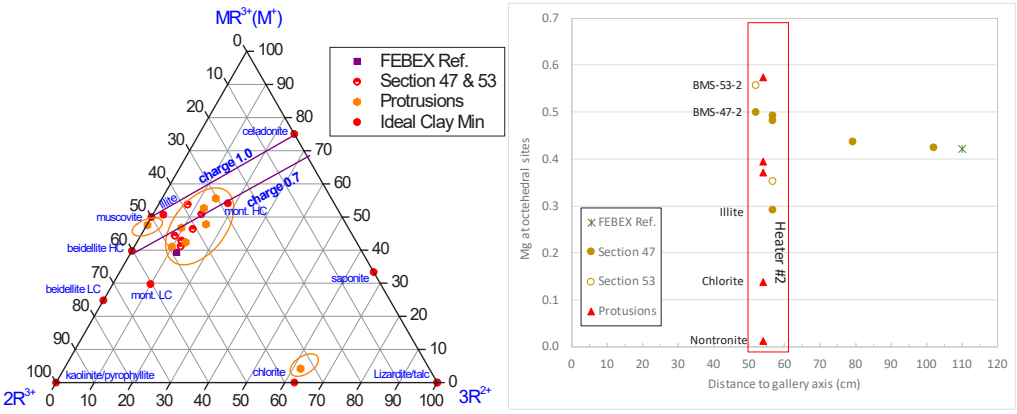

Fig. 208: a) Solid solution projection in the MR^{3+}-$2R^{3+}$-$3R^{2+}$ system of the retrieved samples, b) magnesium at octahedral sites as a function of distance to the gallery determined by TEM analysis

6.2 Fe(II)-Fe_{total} in the samples

Determining the presence of Fe(II) in the bentonite samples is of interest for knowing which redox processes occur inside the bentonite buffer. The results are shown in Tab. 39 and are compared to the values obtained from the FEBEX reference sample. An increase in total iron is observed in the protrusion samples with respect to the reference value and the retrieved BMS samples. Fe(III) is the main iron species in the samples, indicating a high degree of oxidation, but some amount of Fe(II) is observed, ranging from 0 to 2 % in the BMS samples and from 3 to 18 % in the protrusion samples, whereas it is 7 % in the FEBEX reference. Thus, higher values of Fe(II) than in the reference sample are observed mainly in the protrusion samples: CL, RV-42, RN-42, BSH-42, GB-42 and S43-FV, with values ranging from 0.31 to 0.64 wt.-%. Fe(II) may be from the clay mineral structure and from magnetite. However, it should be taken into account that the magnetized particles were discarded from the samples before analysis, so this Fe(II) is supposed to be mainly from the smectite structure. However, the increase of Fe(III) in the samples, from 2.5 wt.-% (CL) to 5.30 wt.-% (BBIL or S43-FV) with respect to the reference sample (2.15 wt.-%) may indicate also the presence of non-magnetic iron oxy-hydroxides, as goethite is observed in XRD and FTIR analyses, or an increase of Fe(III) in the clay particles. It is interesting to note the lower amount of Fe(II) in the BMS samples (from above the liner), which are practically oxidized, with respect to the protrusion samples (from inside the liner). The Fe speciation in the BB sample (chlorite) is 93 % as Fe(II) and only 7 % as Fe(III).

Tab. 39: Total Fe, Fe(II) and Fe(III) in the bentonite samples in contact with the liner at Sections S47 and S53 and in protrusion samples

Sample	**w.t. % Fe_{total} average**	**w.t. % Fe(II) average**	**w.t. % Fe(III) average**	**Sample**	**w.t. % Fe_{total} average**	**w.t. % Fe (II) average**	**w.t. % Fe(III) average**
FEBEX Ref.	2.30	0.15 (7 %)	2.15	CL	3.05	0.54 (18 %)	2.51
BM-S-47-1 white	1.84	0.04 (2 %)	1.80	RV-42	3.65	0.48 (13 %)	3.17
BM-S-47-1 red	2.00	0.05 (2 %)	1.95	RN-42	4.68	0.31 (7 %)	4.38
BM-S-47-2 white	1.77	0.03 (1 %)	1.74	RI-42	2.12	0.08 (4 %)	2.04
BM-S-47-2 red	2.17	< 0.02 (0 %)	2.17	RNW-42	3.07	0.06 (2 %)	3.01
BM-S-47-3 white	1.84	0.06 (3 %)	1.78	RO-42	1.60	0.09 (6 %)	1.51
BM-S-47-3 red	2.35	< 0.02 (0 %)	2.35	BSH-42	3.09	0.27 (9 %)	2.82
BM-S-53-1	2.15	0.04 (2 %)	2.11	BBIL-42	5.43	0.13 (2 %)	5.30
BM-S-53-2	2.58	0.03 (1 %)	2.55	BBL-42	5.03	0.11 (2 %)	4.92
BM-S-53-3	2.21	0.01 (0.4 %)	2.19	WB-42	1.87	0.06 (3 %)	1.81
				GB-42	3.91	0.64 (16 %)	3.27
				S43-FV	5.63	0.34 (6 %)	5.29
				BB	24.5	22.7 (92.7 %)	1.80

6.3 Physico-chemical properties

Different physicochemical properties were analysed both in the BMS and protrusion samples: external surface area (Tab. 40), total CEC (Tab. 41), cation exchange occupancies (Tab. 42) and soluble salts (Tab. 43). The results were compared with data from the reference FEBEX bentonite and with a smectite gel (see Fig. 36, bentonite block BB-53-3) found around the GRS pipe FP-3 (Fernández 2018).

A clear decrease of the BET surface area is observed in the samples (from 60 to 21 m^2/g), representing a value 54 % lower than the reference as average. This decrease was not only observed in the BMS samples (at external contact of the liner) and protrusion samples (in close contact with Heater #2), but also in the inner bentonite block of the Section 47 (BB-47-9, see Section 5.5.5).

CEC values seem to decrease in the bentonite samples close to the Heater #2 contact (from 98 meq/100 g in reference value to 86 meq/100 g in sample BMS-53-2), representing a 12 % decrease compared to the reference value. This trend of decreasing BET and CEC values was also observed in the rest of samples analysed close to Heater #2 (see Section 5.5.2 and 5.5.5).

Most significant is the change in the cation exchange occupation at interlayer sites (Tab. 42). A clear decrease of sodium and an increase of magnesium and calcium at exchange sites is observed in the BMS and protrusion samples with respect to the reference FEBEX sample, potassium slightly increases from 2.9 meq/100g (reference) to a maximum value of 3.4 meq/100g. However, the magnesium at interlayer sites maybe overestimated, as detected by the difference in the CEC values and the sum of exchangeable cations. This is due to the high salinity of the samples close to the liner/Heater #2 contact (see below). In the determination of exchangeable cations, sodium and calcium concentrations were corrected from the soluble salts present in the solid phase, but this was not the case for magnesium.

A sharp increase in salinity and in the Cl, Na, Mg, Ca and K contents, as well as a decrease of bicarbonates is observed from 1:4 aqueous leaching tests (Tab. 43) in the rest of the samples compared to the reference sample (Fig. 209, Fig. 210). This indicates that the hydration front saturating the bentonite barrier from the surrounding granite reached the inner part of the barrier. Consequently, the salts are transported with water by an advection-diffusion process. This can be observed looking at data from the granite to the Heater #2 contact in samples from Section 47 and Section 53 along the whole bentonite barrier (Fig. 209). The decrease of bicarbonates in samples at Heater #2 contact indicates the precipitation of Ca-carbonates, as observed in the mineralogy of some samples. A sharp increase of sulphate was observed in the protrusion sample BSH. At this bentonite-Heater #2 interface the temperature was higher than ~ 95 °C (Tab. 3); consequently, anhydrite is close to saturation (SI = -0.14) at this temperature. Anhydrite would be precipitated instead of gypsum at in-situ conditions, which is confirmed by the Ca-sulphates detected by SEM in the protrusion samples RV-42 and GB-42 (Fig. 197). The high amount of chlorides, sodium and magnesium imply a high salinity close to the heater, where due to the low water content (< 18 %) and heat, the precipitation of halite and other Mg-Cl salts in some zones is possible. Furthermore, at these high concentrations the presence of Mg-Cl ion parings, which can occupy the interlayer sites, is possible. More interesting is the presence of volatile fatty acids, VFAs, or carboxylic acids, such as acetate, formate and oxalate in the aqueous extracts (Tab. S5 from SI), which are related to a corrosion process and the subsequent degradation/oxidation of organic matter (hydrocarbons, see below). Thiosulfate ($S_2O_3^{2-}$) was found in the protrusions samples BBIL and BHS. An increase of silica from 12 mg/L to 56 mg/L was detected in sample S43 FR red.

Tab. 40: Parameters deduced from the BET and *t*-plot treatment on the adsorption of N_2 at 77 K from samples obtained after dismantling Heater #2

Parameter	**C_{BET}**	**V_m** (cm^3/g)	**S_{BET}** (m^2/g)	**St_{or}** (m^2/g)	**V_{tot}** (cm^3/g)	**S_{micro}** (m^2/g)	**V_{micr}** (cm^3/g)	**$S_{ext\ micro}$** (m^2/g)	**$S_{ext\ meso}$** (m^2/g)	**V_{meso}** (cm^3/g)
FEBEX Ref.	1934	2.11×10^{-2} (l)	59.45	62.88	1.01×10^{-1}	20.20	8.92×10^{-3} (l)	39.25	28.42	1.48×10^{-2} (l)
BMS-47-2	120	7.37×10^{-3} (l)	20.80	20.57	4.47×10^{-2}	2.79	1.00×10^{-3} (l)	18.01	13.11	3.63×10^{-3} (l)
Protrusion RN-42	102	1.21×10^{-2}(l)	34.02	33.27	6.05×10^{-2}	3.04	9.04×10^{-4} (l)	30.98	20.48	6.97×10^{-3} (l)

V_m: Monolayer capacity derived from the BET treatment; expressed as (l): liquid; S_{BET}: BET Surface area
St_{or}: Total surface area derived from the slope of the straight line passing through the origin of the *t*-plot
V_{micr}: Liquid microporous volume derived from the ordinate at the origin in the second straight line of the *t*-plot
$S_{ext\ micro}$: Surface area derived from the slope of the second straight line of the *t*-plot
V_{tot}: Total pore volume, derived from the amount of nitrogen adsorbed at p/p_o of 0.98
$S_{ext\ meso}$: Surface area derived from the slope of the third straight line of the *t*-plot
V_{meso}: Liquid microporous volume derived from the ordinate at the origin in the third straight line of the *t*-plot
S_{micro}: $= S_{BET} - S_{ext\ micro}$: Surface area of the micropores

Tab. 41: CEC values in samples at contact with the liner/Heater #2

Sample	**CEC** (meq/100 g)
FEBEX Reference	98.1 ± 2.0
BMS-47-1	90.6 ± 0.6
BMS-47-2	92.8 ± 0.9
BMS-47-3	92.7 ± 0.9
BMS-53-1	92.4 ± 1.1
BMS-53-2	86.3 ± 2.3
BMS-53-3	93.2 ± 0.5
Inside heater red (BBIL)	95.3 ± 1.8
Inside Heater black (BSH)	95.3 ± 2.1
Liner Holes red (S43 FR)	91.2 ± 0.1
Pipe 3 Section 42-43 (gel like)	93.2 ± 0.4

Tab. 42: Cation exchange occupancies in samples at contact with the liner/Heater #2 (in meq/100g)

Sample	Na	K	Mg	Ca	Sr	Ba	Cu	Σ cations
FEBEX Ref.	28.0	2.85	33.1	33.2	0.37	0.01	--	97.5
BM-S-47-1	5.94	2.86	50.13	43.93	0.30	0.005	0.002	103.16
BM-S-47-2	2.14	3.19	51.94	46.31	0.32	0.005	0.001	103.92
BM-S-47-3	1.62	3.44	53.55	45.47	0.31	0.005	0.002	104.41
BM-S-53-1	--	3.18	44.62	50.26	0.29	0.006	0.006	98.37
BM-S-53-2	--	3.14	51.44	34.33	0.31	0.007	0.001	89.22
BM-S-53-3	--	3.18	59.48	45.74	0.30	0.005	0.002	108.71
Inside heater black (bsh)	15.36	2.72	60.05	29.20	0.26	0.004	0.004	107.60
Inside Heater red (BBIL)	9.80	2.66	37.48	42.86	0.31	0.006	0.001	93.11
liner holes red (s43 fr)	23.35	2.55	39.11	37.82	0.33	0.002	0.001	103.16
Pipe 3 sect 42-43	28.79	2.93	33.96	32.86	0.32	0.006	0.004	98.88

Tab. 43: Soluble salts from aqueous extracts at 1:4 solid to liquid ratio from the samples at contact with the liner/Heater #2 (in mg/L)

Sample	**BMS-47-1**	**BMS-47-2**	**BMS-47-3**	**BMS-53-1**	**BMS-53-2**	**BMS-53-3**	**Inside heater red** (bbil)	**liner holes red** (s43 fr)	**Inside heater black** (bsh)	**Pipe 3 sect 42-43**
Water content (%)	12.8	136	12.2	13.0	11.7	12.9	13.9	13.2	14.1	14.7
Total Weight (g)	10.0002	10.0004	10.0003	10.0004	10.0006	10.0005	10.0007	10.0008	10.0005	10.0005
pH	8.2	8.2	8.4	7.9	8.4	8.1	8.0	7.0	8.2	9.0
F^-	0.12	< 1	< 1	< 1	< 1	< 1	< 1	1.2	< 1	2.1
Br^-	2.6	3.1	2.9	3.6	3.1	3.8	5.2	0.64	4.5	0.23
Cl^-	1'100	'1400	1'300	1'700	1'600	1'700	'2000	292	1'800	113
NO_3^-	15	22	13	38	34	37	0.61	0.3	0.36	0.48
SO_4^{2-}	124	155	175	170	156	167	196	81	1100	230
HCO_3^-	74.42	78.08	84.18	51.24	78.69	49.41	132.98	< 12	122	168.97
Al^{3+}	< 0.03	< 0.03	< 0.03	< 0.03	< 0.03	< 0.03	< 0.03	14	< 0.03	0.2
Ca^{2+}	100	150	120	170	100	200	130	4.2	240	60
Mg^{2+}	70	110	90	150	80	180	80	5.5	120	46
Na^+	525	575	525	550	600	575	1025	240	1150	520
K^+	21	33	30	35	38	35	23	4.5	30	11
Sr^{2+}	1.5	2.4	2.3	3	2.8	3.3	2.3	0.07	3.1	1
Fe	< 0.03	< 0.03	< 0.03	< 0.03	< 0.03	< 0.03	< 0.03	4.2	< 0.03	0.06
Ba	0.26	0.05	0.05	0.08	0.09	0.12	0.08	< 0.03	0.04	< 0.03
B	0.93	1	1.05	1.1	1.13		1.2	0.3	2.2	0.67
Mn	0.1	1.19	0.14	0.38	0.28	1.14	0.24	< 0.03	0.12	0.11
Si	11	15	11	12	12	15	9.7	56	10	12
Ti	< 0.07	< 0.03	< 0.03	< 0.03	< 0.03	< 0.03	< 0.03	0.06	< 0.03	< 0.03
V	< 0.03	< 0.03	< 0.03	< 0.03	< 0.03	< 0.03	< 0.03	< 0.03	< 0.03	< 0.03
Zn	< 0.03	< 0.03	< 0.03	< 0.03	< 0.03	< 0.03	< 0.03	< 0.03	< 0.03	< 0.03
$S_2O_3^{2-}$	< 1	< 1	< 1	< 1	< 1	< 1	0.97	< 1	0.54	< 1
Acetate	18.3	20.3	22.9	14.2	13.8	15.8	24.1	7.1	84	< 1
Formate	0.55	0.85	0.81	1.1	1.3	2.1	3.6	< 1	< 1	< 1
Oxalate	5.1	6.2	5.3	5.4	5.4	5.5	5.4	4.4	3.8	1.7

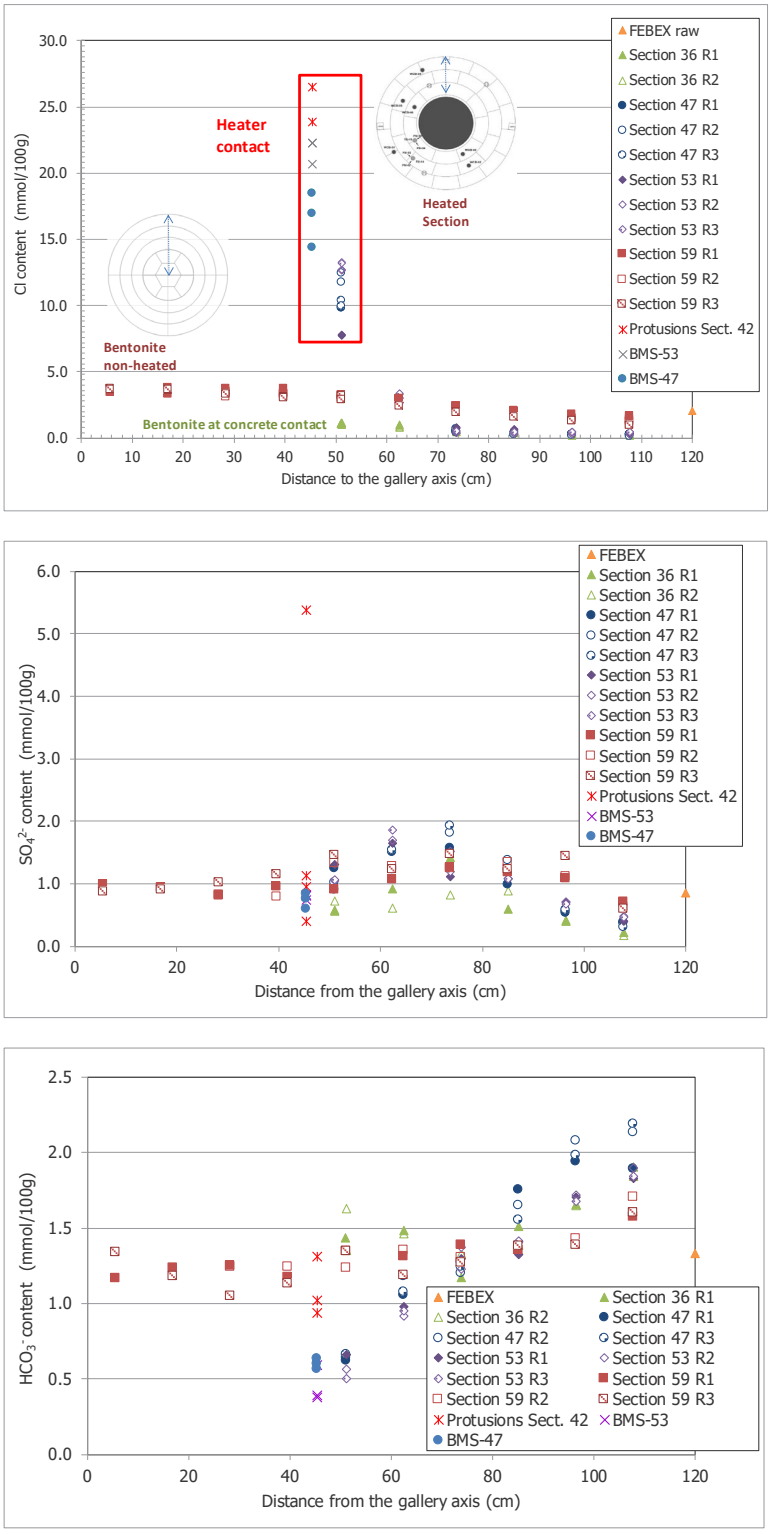

Fig. 209: Anion concentration in aqueous extracts at 1:4 solid to liquid ratio from samples retrieved after dismantling Heater #2 including BMS and Protrusion samples

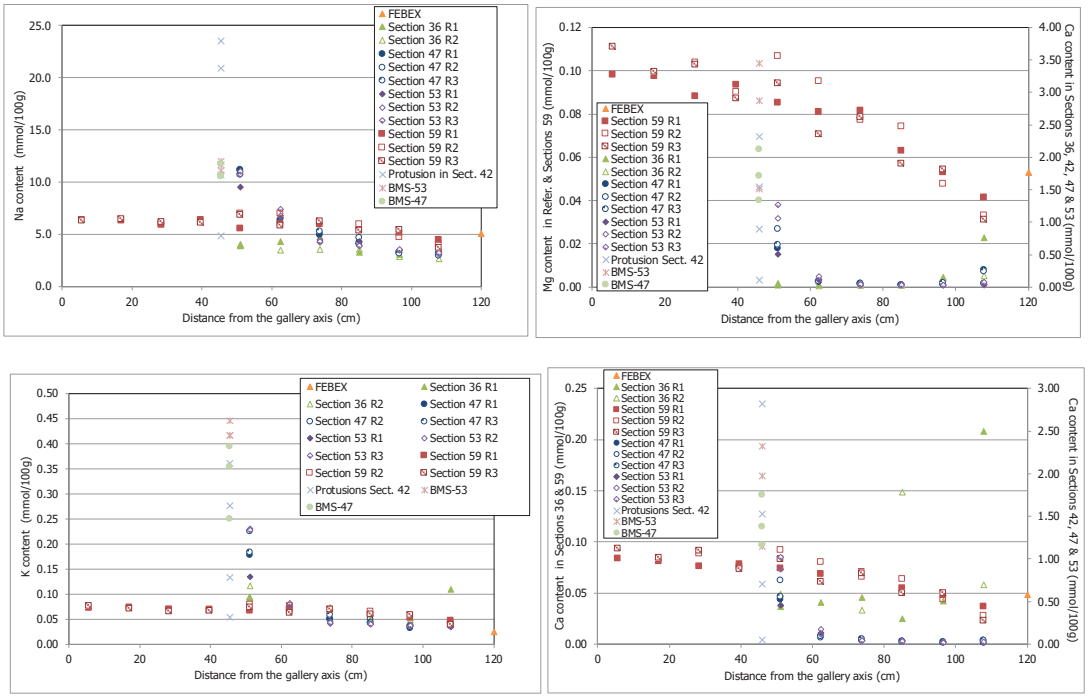

Fig. 210: Cation concentration in aqueous extracts at 1:4 solid to liquid ratio from samples retrieved after dismantling of Heater #2 including BMS and Protrusion samples

6.4 Metal-Interface samples analysed after dismantling Heater #1

After dismantling Heater #1 in 2002, three types of bentonite samples were analysed at (see Appendix A for sample location):

- Corroded bentonite surrounding the displacement sensor SH-SDI-01 from Section 17 (Fig. 211). This sensor was analysed by INASMET (Madina 2003, Madina & Azkárate 2004).
- Bentonite inside the holes of the liner. No large protrusions where found after dismantling Heater #1, although the bentonite had pushed through the liner holes (Fig. 212). Therefore, powdered samples could be taken by scraping from the inner part of the liner holes.
- Corroded bentonite around the gas pipe GF-SL-06 (Fig. 213, see Fernández 2018)
- Bentonite at contact with the back part of Heater #1 (Fig. 214)

Fig. 211: Bentonite corroded sample at contact with sensor SH-SDI-01 in Section 17

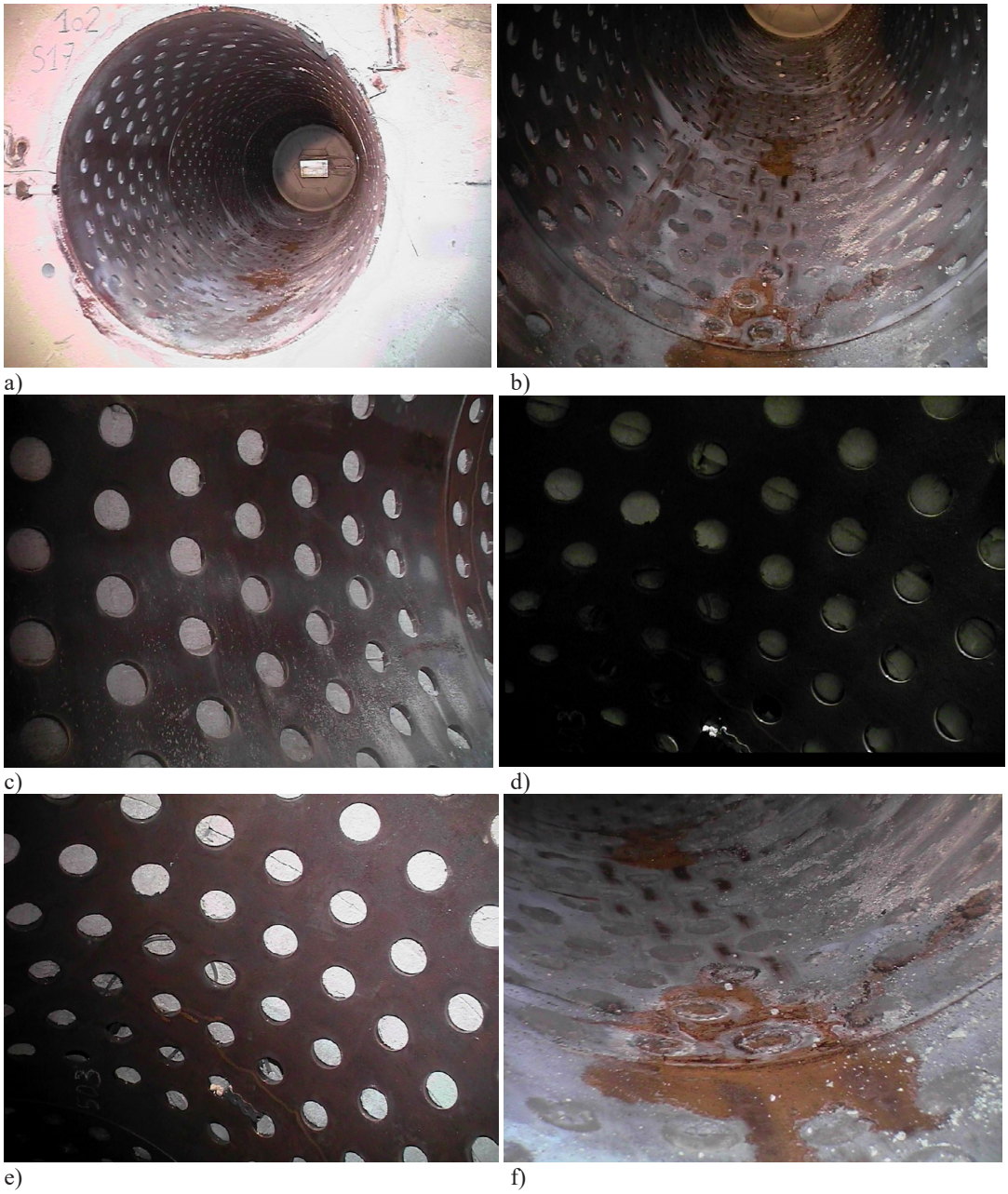

Fig. 212: Photographs from the internal part of the liner just after extraction of Heater #1 (Section 17)

Photos taken on 19 and 21 June 2002: a) and b) general view, c) left side of the liner, d) right side of the liner, e) upper part of the liner, f) bottom part

Fig. 213: Bentonite corroded sample at contact with cables and surrounding the ceramic gas pipe GF-SL-06 in Section 29

Fig. 214: Bentonite block sample in contact with the back part of Heater #1: a) Samples taken from the back part of Heater #1, b) and c) Bentonite block BS-31-26 and location, c) and d) core sample BS31-22 and location

6.4.1 Bentonite sample around sensor SH-SDI-1

The extensometer sensor SH-SDI-1, located in Section 17 (Instrumented Section D1, bentonite slice 102) and used to monitor the possible displacement of the heater, was made of stainless steel (SS) AISI 316 L with the composition shown in Tab. 44. At this section, 13 temperature sensors were also introduced for bentonite temperature monitoring, which were externally covered by a case made of Ni-alloyed 304 or 316L SS. Internally the thermocouple wires were separated from each other by a magnesia (MgO) filling used as insulating material.

According to INASMET (Madina 2003, Madina & Azkárate, 2004), the SH-SD1-1 sensor suffered localized pitting corrosion under bentonite deposits and subsequent release of corrosion products, there is also stress corrosion through cracking in the anchors close to granite. The corrosion products were of dark greenish colour, and close to the liner the generated corrosion products were of a brownish-black colour. The components of the anchors (304 or 302 SS plate, screw, bolts, nuts) of the sensor close to the granite were also corroded, showing greenish corrosion products, except those made of carbon steel (screws) which were of a brownish-reddish and/or reddish colour. In the analysis of the bentonite samples, INASMET found different types of microorganisms associated with the corrosion of these sensors (Tab. 45). The presence of sulphate-reducing bacteria indicated that the localized pitting corrosion was microbially induced at this zone, which has a high water content (> 22 %). As a consequence of the metabolic activity of the SRB, sulphides were generated, a highly corroding agent and responsible for the corrosion observed in these sensors. Calcite also precipitated as a consequence of microbial activity. The cracking of the anchors seems to be due to the presence of chlorides in the bentonite pore water and/or the presence of SRB.

Tab. 44: Composition (in wt.-%) of the SHSDI-1 displacement sensor (Madina 2003)

C	Si	Mn	P	S	Cr	Ni	Mo	Fe
0.024	0.44	1.6	0.028	0.005	17.1	12.3	2.0	68.5

Tab. 45: Microbial study of the bentonite samples surrounding the SHSDI-1 displacement sensor, in counting ufc/g (Madina 2003)

Microbial group	**Aerobic bacteria**	**Anaerobic bacteria**	**Sulphate reducing bacteria** (srb)	**Ferro-oxidants**	**Sulfo-oxidants**
Bentonite surrounding the sensor (greenish colour)	2 × 102 (all fungi type)	0	1.08 × 102	0	0
Bentonite surrounding the sensor close to the liner (reddish colour)	4.23 × 103 (all fungi type)	0	3.77 × 102	0	0

At CIEMAT two bentonite samples surrounding the SHSDI-1 sensor were studied: one them of dark-greenish colour and the another one of reddish colour (closer to the liner). The chemical composition of the bentonite samples analysed (Tab. 46) showed an increase in labile Fe, P, Cr, Mo, Ni and Sn. Higher contents of Cr, Mo, Ni and Sn were found in the greenish bentonite than in the reddish bentonite. The water content of the samples was 25 % (Tab. 47).

The mineralogy of the samples was analysed by XRD, FTIR, TG-DSC, XPS and SEM. Goethite, calcite, quartz, feldspars and pyrrhotite were detected by XRD (Fig. 215, Fig. 216). Hematite was only observed in the reddish sample, which contained also siderite (see FTIR in Fig. 217). No significant modifications were observed in the clay fraction and in the exchangeable cation composition (Tab. 48). However, BET surface area slightly decreased (Tab. 49) with respect to the reference value.

The dark-greenish and reddish samples were analysed by XPS (Fig. 220 to Fig. 226). The samples contained Fe-oxides, carbonates, organic matter and smectite. The magnesium content in the smectite was much higher in the greenish sample than in the reddish sample. The analysis of the carbon peak indicated the presence of both inorganic and organic carbon. The peak around 289 – 291 eV revealed the presence of carbonates (calcite) in both samples. The peaks at around 286 – 287 eV indicated the presence of alcohols and ethers (C-O) in both samples. A peak at 288 – 289 eV: carboxyls (C = O), was only found in the greenish sample, whereas a peak at 283 eV: carbides (C = C) was only present in the reddish sample. Regarding the Fe peak and its speciation (Fe^{2+} and Fe^{3+}), the peak at 712 eV indicated the presence of FeOOH, which was seen in both samples. Only in the reddish sample, and additional peak at 711 eV was observed, which indicates the presence of hematite. According to the shape of the Fe $2p_{3/2}$ peak, iron seems to be only as Fe(III). Fe(II) was not found in the samples.

Tab. 46: Chemical composition of the solid phase (total fraction)

Oxides (%)					**Element** (ppm)				
Samples	BS-31-26	SH-SDI-01-A (green)	SH-SDI-01-B (red)	FEBEX Ref.	Samp.	BS-31-26	SH-SDI-01-A (green)	SH-SDI-01-B (red)	FEBEX Ref.
SiO_2	59.97	59.01	60.15	57.89 ± 1.55	Ba	253	152	98	164 ± 25
labile Al_2O_3	0.09	0.07	0.07	0.03 ± 0.02	Be	< 5	< 5	< 5	--
Al_2O_3	16.65	12.23	12.13	17.95 ± 0.71	Ce	58	51	56	74 ± 6
FeO	0.07	0.09	0.11	0.25 ± 0.10	Co	10	14	10	9 ± 3
labile Fe_2O_3	0.06	0.15	0.06	0.01 ± 0.01	Cr	5.5	3550	6.5	8 ± 2
Fe_2O_3	2.83	2.25	2.12	2.84 ± 0.12	Cu	12	25	12	25 ± 9
MgO	3.5	3.4	3.4	4.21 ± 0.21	La	27	21	21	40 ± 3
MnO	< 0.03	< 0.03	0.03	0.04 ± 0.00	Mo	< 5	400	< 5	--
CaO	0.96	0.79	0.94	1.83 ± 0.10	Ni	15	218	20	20 ± 3
Na_2O	1.3	1.3	1.2	1.31 ± 0.09	Sn	< 10	201	< 10	--
K_2O	1.1	0.99	0.99	1.04 ± 0.05	Sr	164	136	152	220 ± 23
TiO_2	0.22	0.23	0.23	0.23 ± 0.01	V	10	16	10	16 ± 2
P_2O_5	0.06	0.07	0.06	0.03 ± 0.01	W	< 25	< 25	< 25	--
H_2O (130 °C)	9.1	10.1	11.4	6.58 ± 2.52	Y	15	11	11	25 ± 3
H_2O (220 °C)	10.5	11.3	12.69	14.1 ± 0.7	Zn	50	51	50	65 ± 4
LOI (30 – 950 °C)	15.5	16.7	17.7	19.5 ± 1.8	Cs	6.3	5.8	6.1	--
CO_2 Total	0.44	0.2567	0.5133	0.61 ± 0.05	Eu	2.1	1.9	2	--
CO_2 organic	0.22	0.2200	0.2567	0.35 ± 0.05	Se	< 0.1	< 0.1	< 0.1	--
CO_2 inorganic	0.22	0.0367	0.2567	0.26 ± 0.06	Li	< 2	< 2	< 2	54 ± 3
SO_2 Total	0.04	0.08	0.04	0.21 ± 0.10					
H_20^+ (130 – 950 °C)	5.9	6.3	5.7	--					
H_20^+ (220 – 950 °C)	4.5	5.1	4.5	4.31 ± 0.41					
SUM	97.05	97.06	99.06	101					

Tab. 47: Soluble salts from aqueous extracts at 1:4 solid to liquid ratio (in mg/L)

Parameters	**BS31-22/1**	**BS31-22/2**	**BS31-22/3**	**BS31-22/4**	**BS31-22/5**	**BS31-26/2**	**SH-SDI-01 A**	**SH-SDI-01 B**
w.c. (%)	14.0	14.6	14.3	14.5	13.9	13.9	24.6	25.7
Clay mass (g)	10.0004	10.0007	10.0008	10.0007	10.0007	10.0018	10.1599	9.9866
pH	8.4	8.4	8.4	8.4	8.6	8.4	8.1	8.2
Br	< 1	< 1	< 1	< 1	< 1	< 1	< 1	< 1
Cl^-	201	188	180	175	166	166	88	76
NO_3^-	4.3	4.2	4.2	4.2	4.3	3.6	< 1	< 1
SO_4^{2-}	154	298	144	152	161	154	166	88
$HCO_3^{-(*)}$	165	145	155	159	154	183	138	159
Al^{3+}	< 0.05	< 0.05	0.1	< 0.05	< 0.05	0.14	3.2	0.51
Ca^{2+}	3.8	6.7	3.2	4.6	3.4	3.4	2.3	< 1
Mg^{2+}	2.4	4.1	2.2	1.7	2.6	2.1	2.6	< 0.4
Na^+	255	295	240	235	235	235	175	140
K^+	5.8	7.5	5.2	5.2	5.2	5.4	4.2	2.4
Sr^{2+}	0.07	0.12	0.06	0.06	0.07	0.07	0.07	< 0.05
Fe	0.03	0.19	0.05	< 0.03	< 0.03	0.05	1.8	0.15

* Alkalinity as HCO_3^-

Tab. 48: Cation exchange population in meq/100g extracted with a $CsNO_3$ solution at 1:8 solid to liquid ratio (~ 5 grams of wet sample in 40 mL of deionized water)

Sample	**w.c.** (%)	**Clay mass** (g)	**S:L ratio**	**Na**	**K**	**Mg**	**Ca**	**Sr**	**Ba**	**CEC**
			Kg/L	meq/100g	meq/100g	meq/100g	meq/100g	meq/100g	meq/100g	meq/100g
BS31-22/1	14.0	5.0005	0.2128	28.53	3.37	31.70	36.28	0.333	0.0066	100.2
BS31-23/2	14.6	5.0004	0.2114	28.71	3.27	32.88	38.75	0.346	0.0069	104.0
BS31-22/3	14.3	5.0003	0.2121	28.83	3.26	29.47	38.84	0.334	0.0067	100.7
BS31-22/4	14.5	5.0002	0.2117	28.87	3.14	32.64	36.52	0.345	0.0068	101.5
BS31-22/5	13.9	5.0003	0.2129	28.85	3.12	30.91	38.50	0.332	0.0065	101.7
BS31-26/2	13.9	5.0004	0.2129	28.83	3.36	32.45	36.30	0.354	0.0059	101.3
SH-SDI-01 A	24.6	5.2591	0.2006	31.24	2.93	32.39	48.18	0.296	0.0102	115.1
SH-SDI-01 B	25.7	5.0931	0.1926	32.77	3.05	31.19	48.42	0.332	0.0091	115.8

Tab. 49: Parameters deduced from the BET and t-plot treatment on the adsorption of N_2 at 77 K from samples obtained after dismantling of Heater #1

Parameter	C_{BET}	V_m (cm^3/g)	S_{BET} (m^2/g)	St_{or} (m^2/g)	V_{tot} (cm^3/g)	S_{micro} (m^2/g)	V_{micr} (cm^3/g)	$S_{ext\ micro}$ (m^2/g)	$S_{ext\ meso}$ (m^2/g)	V_{meso} (cm^3/g)
FEBEX Ref.	1934	2.11×10^{-2} (l)	59.45	62.88	1.01×10^{-1}	20.20	8.92×10^{-3} (l)	39.25	28.42	1.48×10^{-2} (l)
BSHSDI	402	1.92×10^{-2} (l)	54.34	54.34	9.25×10^{-2}	17.4	7.56×10^{-3} (l)	36.94	26.26	1.32×10^{-2} (l)
BS31-26	382	1.35×10^{-2} (l)	38.16	38.16	7.49×10^{-2}	8.26	3.76×10^{-3} (l)	29.90	25.32	5.45×10^{-3} (l)
BS31-22N	310	9.97×10^{-2} (l)	28.17	28.17	7.10×10^{-2}	5.88	2.56×10^{-3} (l)	22.29	23.39	7.70×10^{-4} (l)

V_m: Monolayer capacity derived from the BET treatment; expressed as (l):liquid; S_{BET}: BET Surface area
St_{or}: Total surface area derived from the slope of the straight line passing through the origin of the *t*-plot
V_{micr}: Liquid microporous volume derived from the ordinate at the origin in the second straight line of the *t*-plot
$S_{ext\ micro}$: Surface area derived from the slope of the second straight line of the *t*-plot
V_{tot}: Total pore volume, derived from the amount of nitrogen adsorbed at p/p_o of 0.98
$S_{ext\ meso}$: Surface area derived from the slope of the third straight line of the *t*-plot
V_{meso}: Liquid microporous volume derived from the ordinate at the origin in the third straight line of the *t*-plot
S_{micro}: = $S_{BET} - S_{ext\ micro}$: Surface area of the micropores

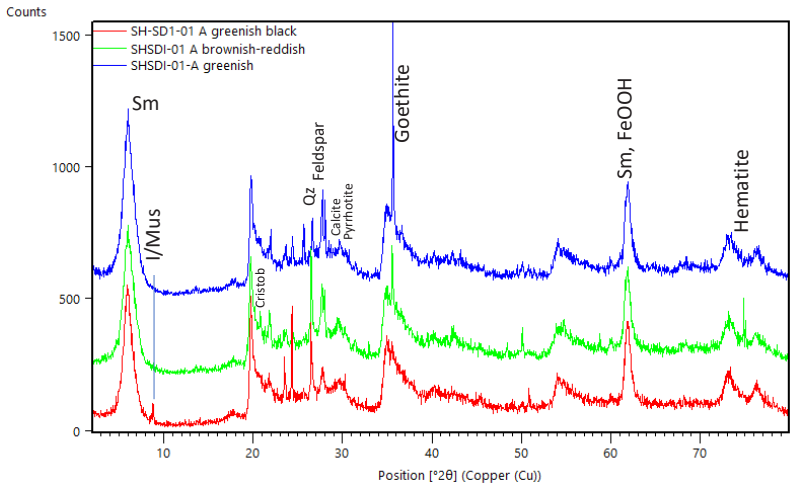

Fig. 215: XRD patterns of randomly oriented bulk samples surrounding SH-SDI-1 sensor: dark-greenish bentonite, greenish-blackish bentonite and reddish bentonite.

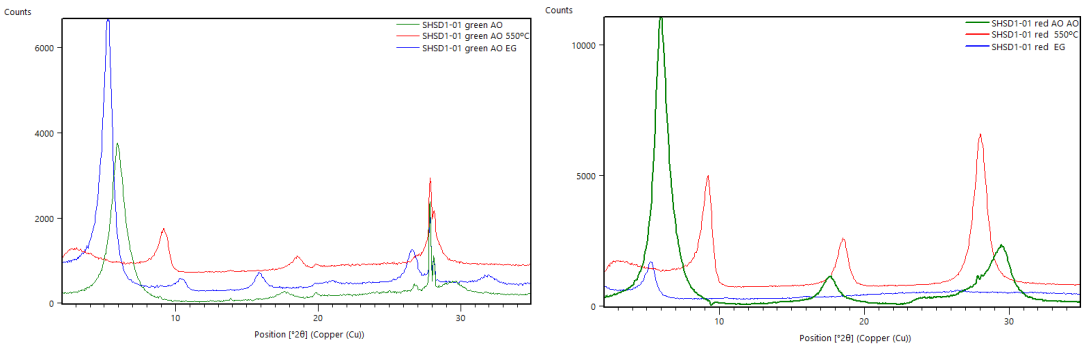

Fig. 216: Oriented aggregates (AO, EG, 550 °C) from samples: a) dark-greenish bentonite surrounding SH-SDI-1 sensor; b) reddish bentonite surrounding SH-SDI-1 sensor.

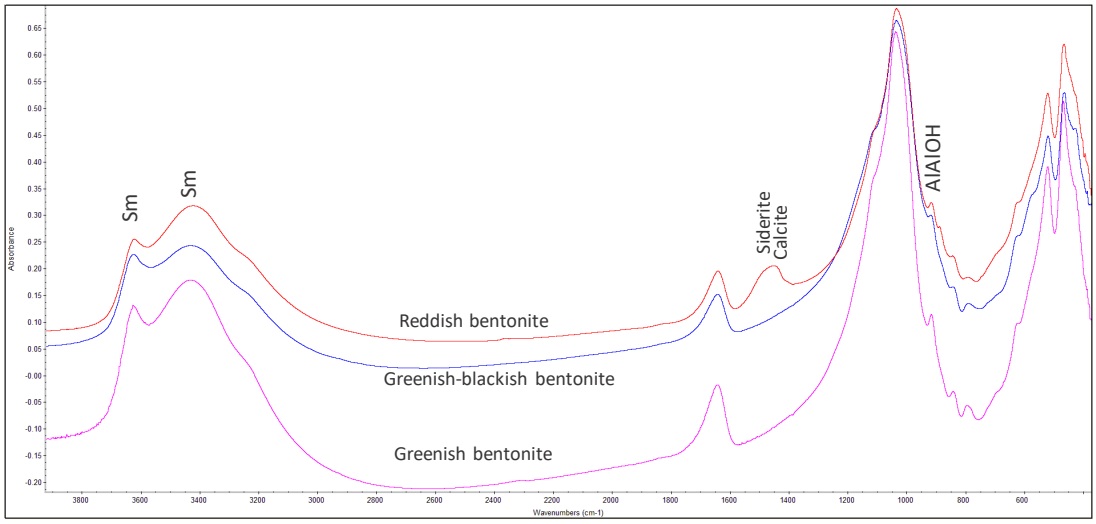

Fig. 217: FTIR spectra of bulk samples surrounding SH-SDI-1 sensor

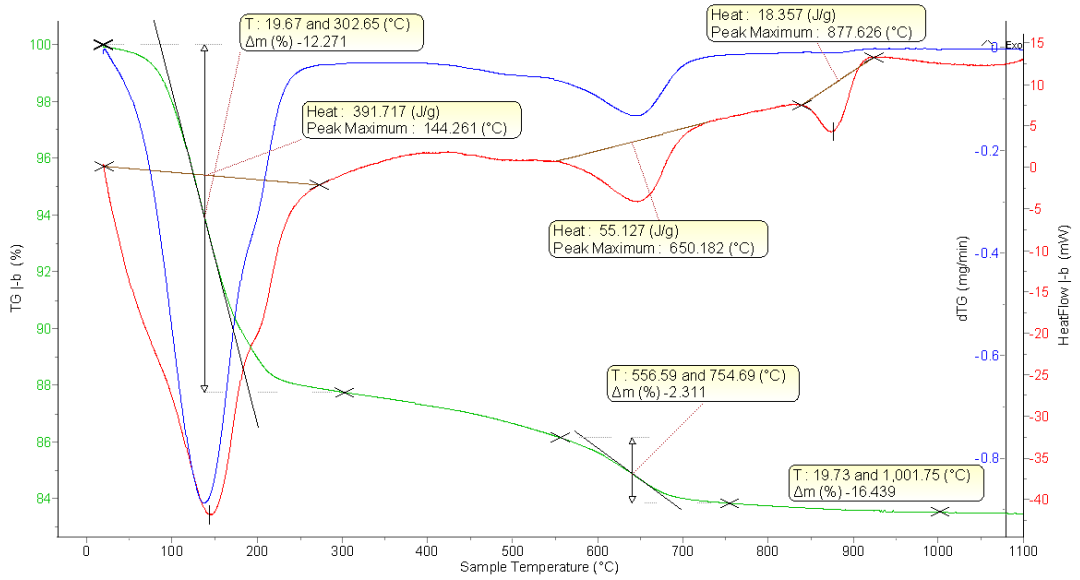

Fig. 218: TG-DSC curves from the bulk sample SHSDI-01/A

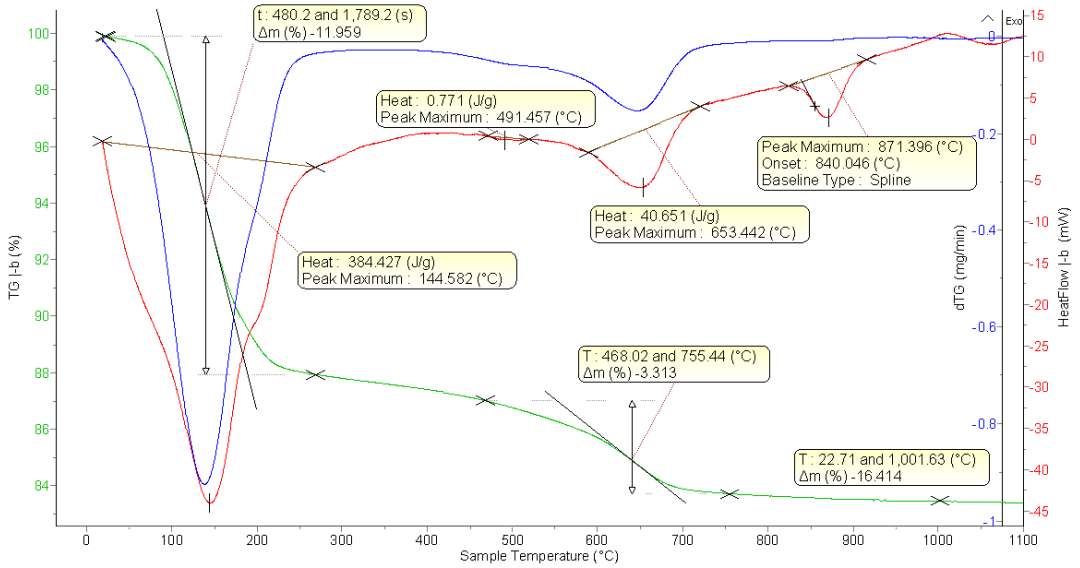

Fig. 219: TG-DSC curves from the bulk sample SHSDI-01/B

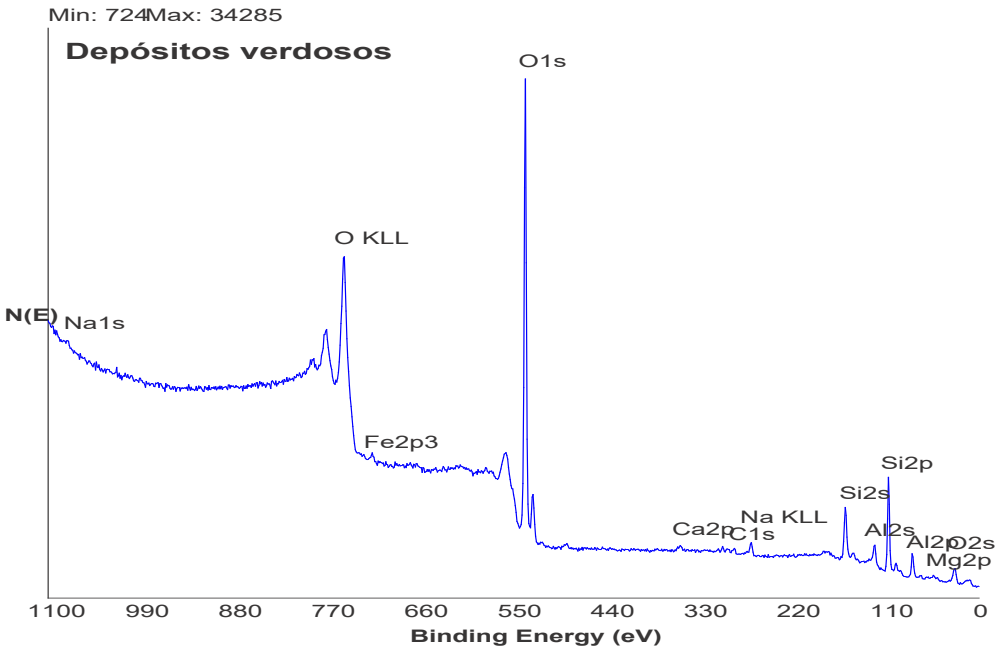

Na (0.4%) – Fe (0.4%) – O (63.7%) – Ca (0.4%) – C (1.8%) – Si (22.3%) – Al (9.3%) – Mg (1.6%)

Fig. 220: XPS spectrum of the greenish bentonite sample surrounding the SH-SDI-sensor

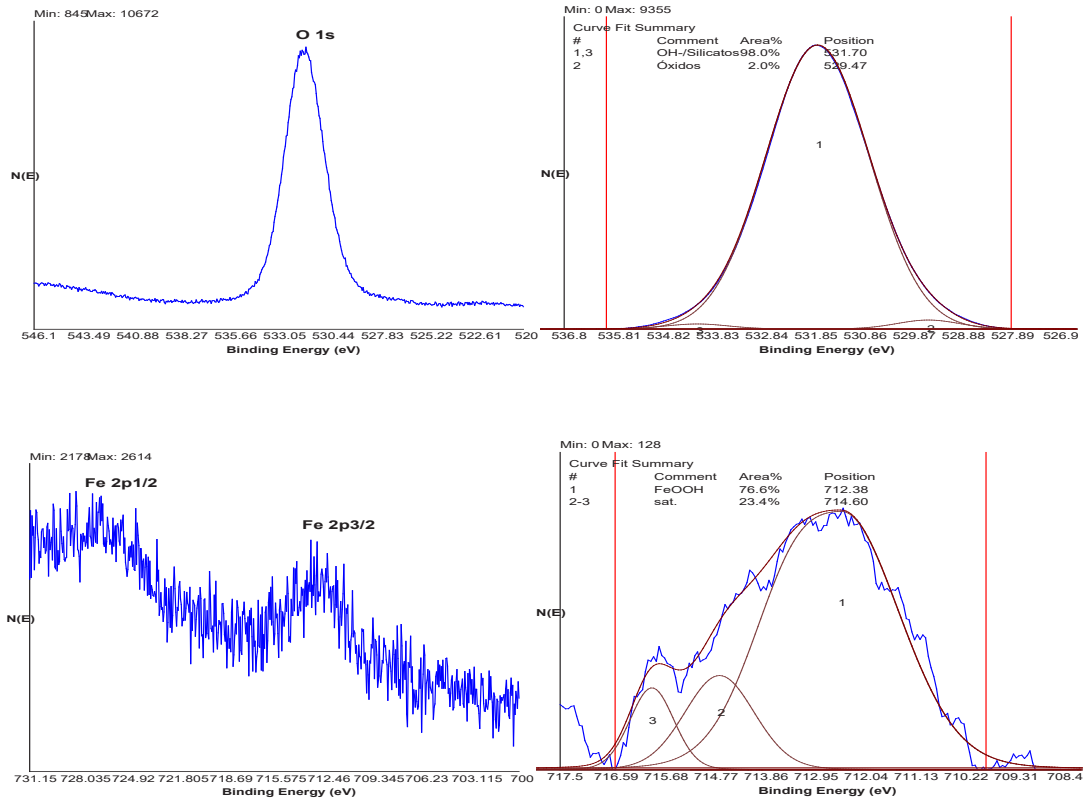

Fig. 221: Convolution of oxygen and iron peaks form the XPS spectrum for the greenish bentonite sample surrounding the SH-SDI-sensor indicating the presence of oxy-hydroxides of iron (FeOOH)

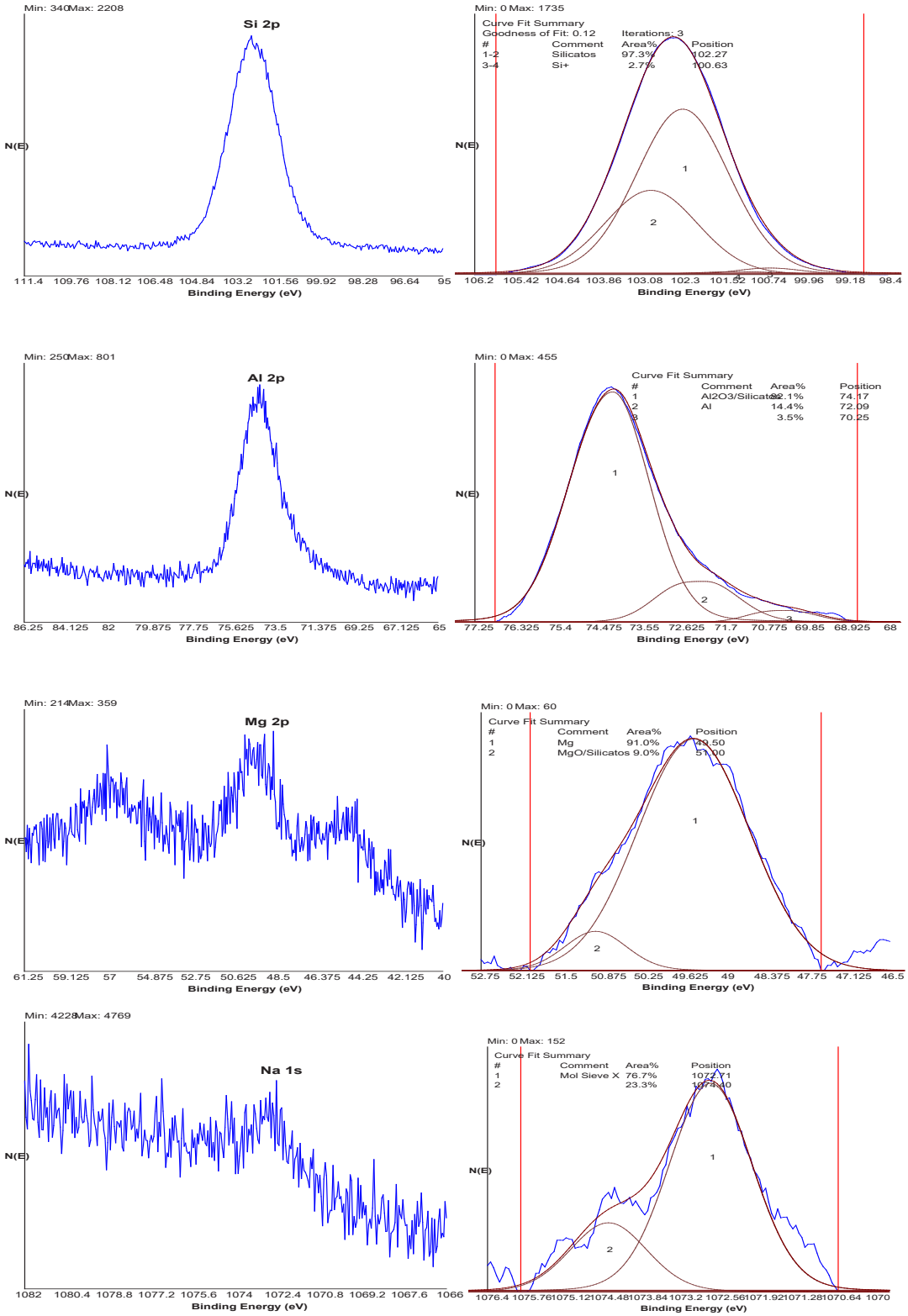

Fig. 222: Convolution of Si, Al, Mg and Na peaks from the XPS spectrum for the greenish bentonite sample surrounding the SH-SDI-sensor indicating the presence of silicates (smectite)

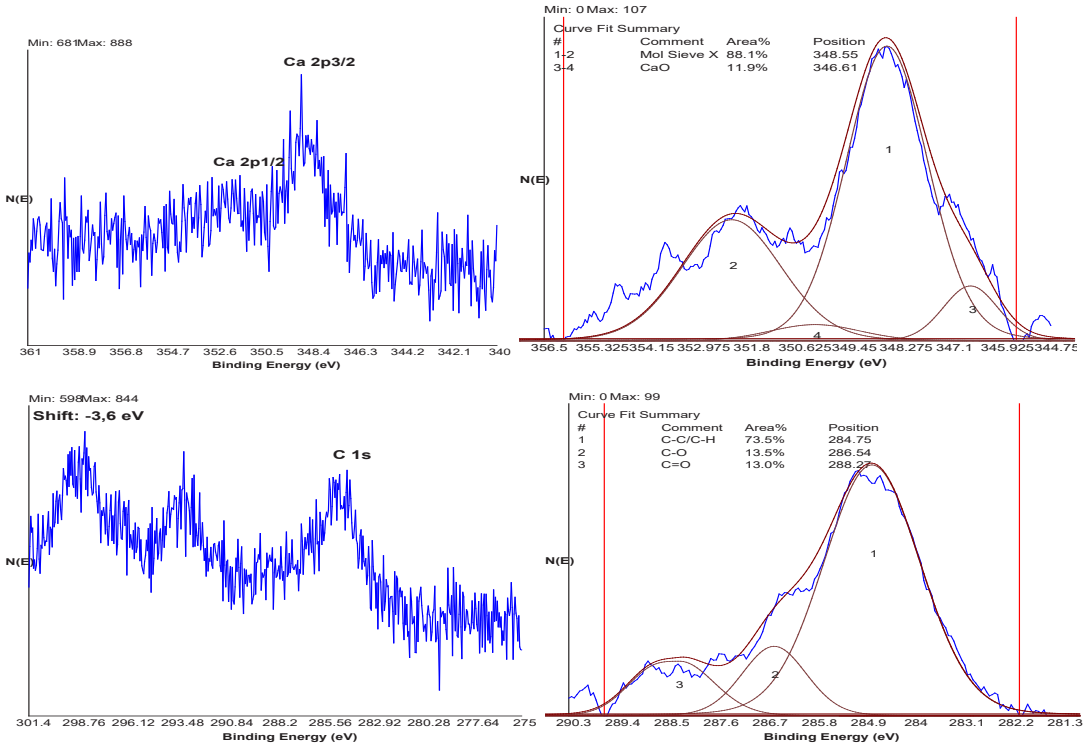

Fig. 223: Convolution of Ca and C peaks from the XPS spectrum for the greenish bentonite sample surrounding the SH-SDI-sensor indicating the presence of calcite and organic matter

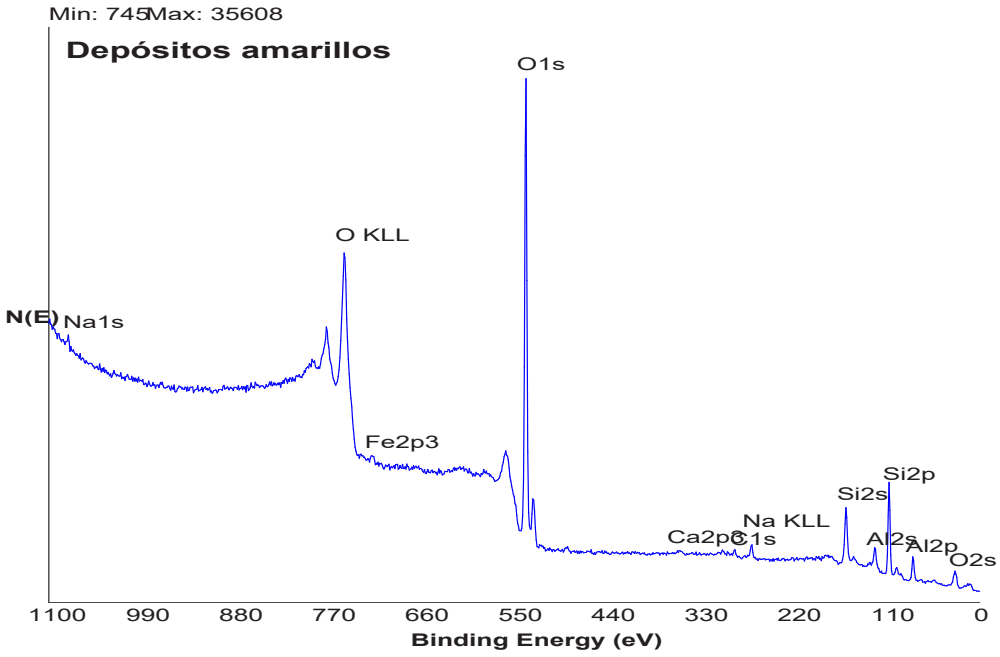

Na (0.5%) – Fe (0.7%) – O (71.5%) – Ca (0.5%) – C (1.6%) – Si (24.8%) – Al (0.4%)

Fig. 224: XPS spectrum of the reddish bentonite sample surrounding the SH-SDI-sensor

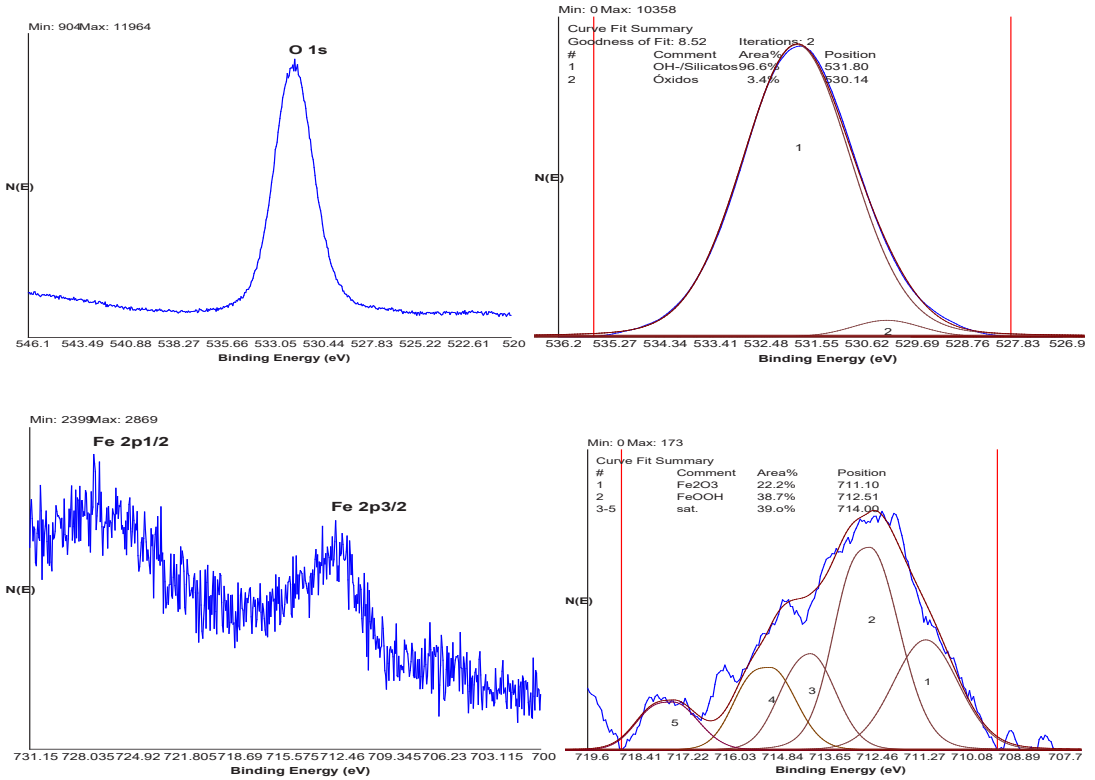

Fig. 225: Convolution of oxygen and iron peaks from the XPS spectrum for the reddish bentonite sample surrounding the SH-SDI-sensor, indicating the presence of silicates (smectite), oxy-hydroxides (FeOOH) and hematite (Fe_2O_3)

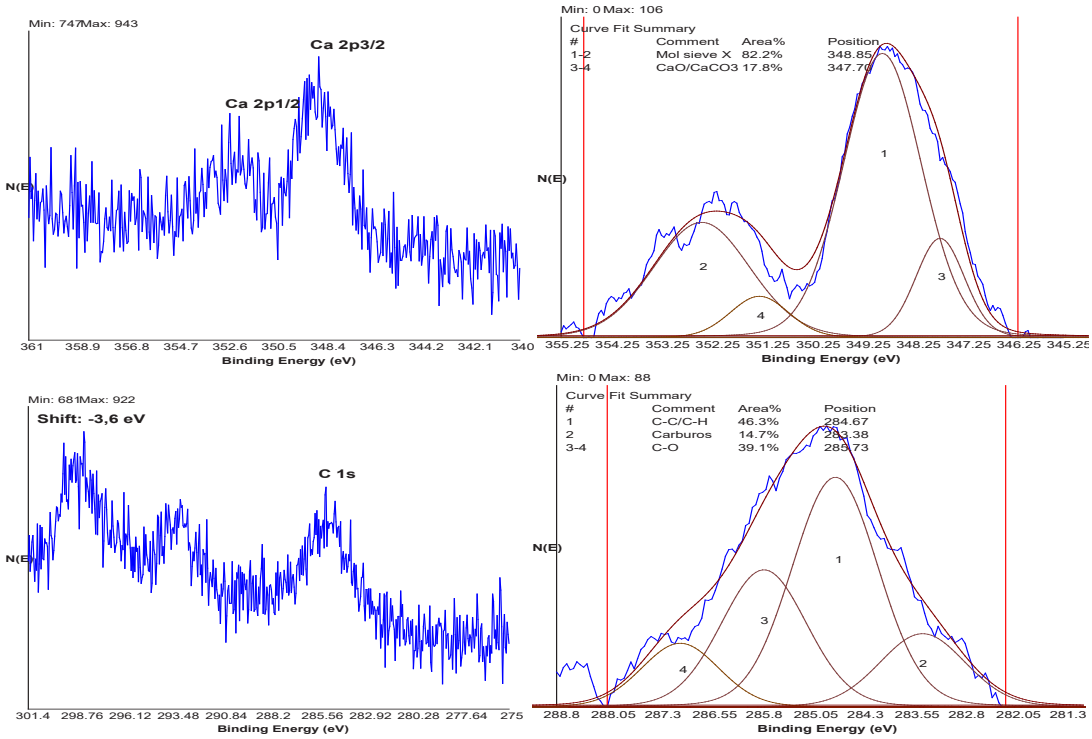

Fig. 226: Convolution of Ca and C from the XPS spectrum for the reddish bentonite sample surrounding the SH-SDI-sensor, indicating calcite and organic matter

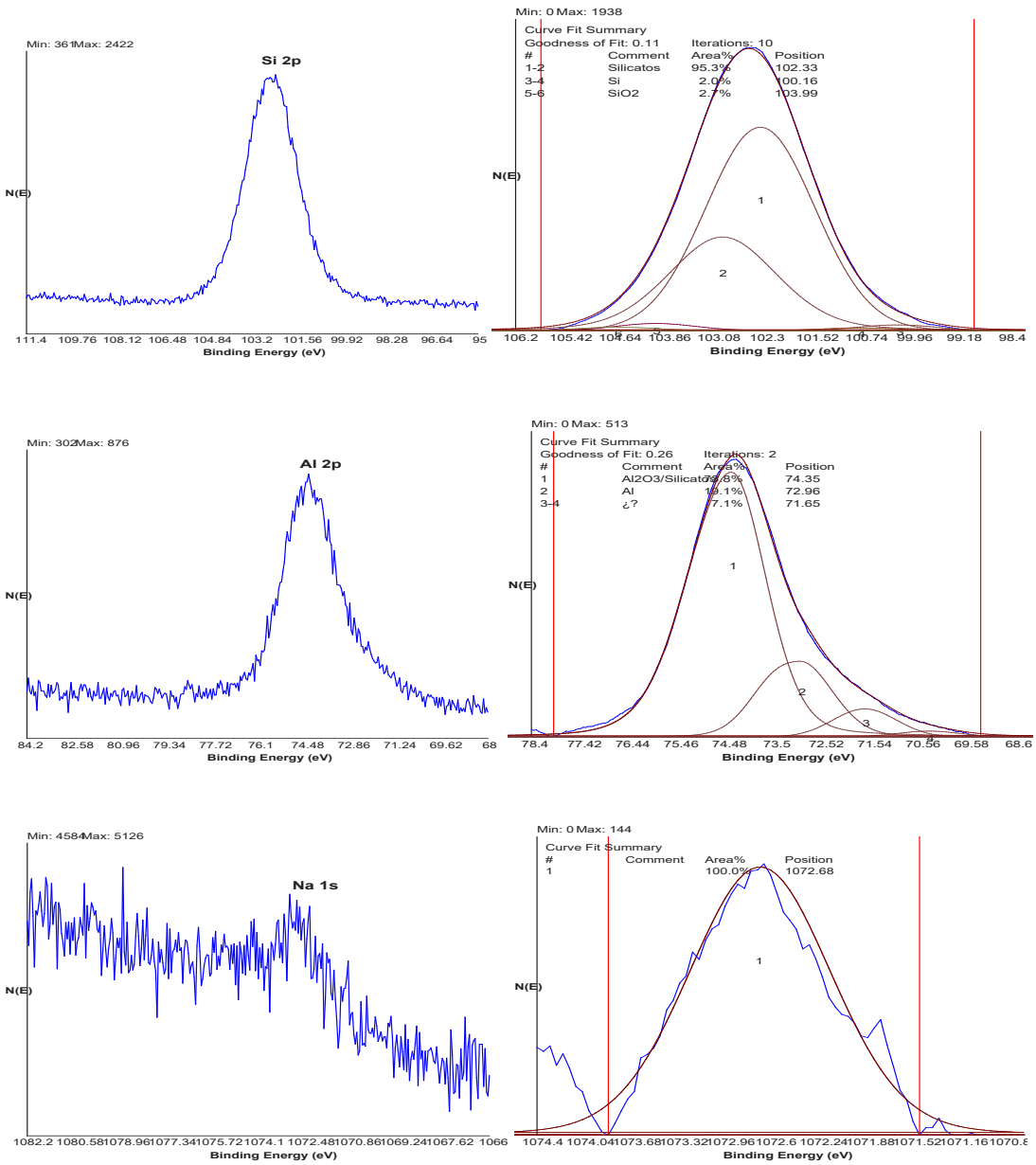

Fig. 227: Convolution of Si, Al, and Na peaks from the XPS spectrum for the reddish bentonite sample surrounding the SH-SDI-sensor, indicating the presence of phyllosilicates (smectite)

The dark-greenish and reddish parts of the bentonite were also analysed by SEM. In the greenish samples, apart from Fe-oxides, Cr and S were detected (greenish black particles). Green-rush with Cl, Na, K and Fe apperared in the samples as well as microorganisms and Ca-carbonates (Fig. 228 to Fig. 230). The presence of S in the corrosion products and microorganisms indicate corrosion induced by SRB. In the reddish samples Fe-oxides, Ca- and Fe-carbonates and Fe-rich smectite were found (Fig. 232, d).

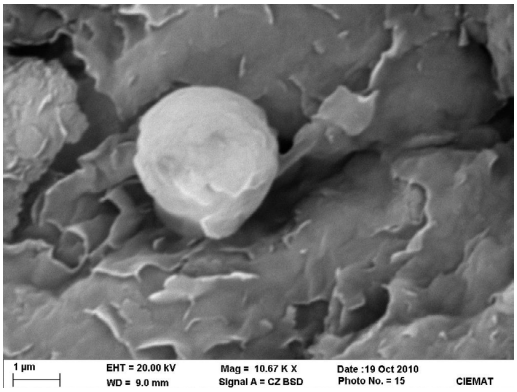

a)

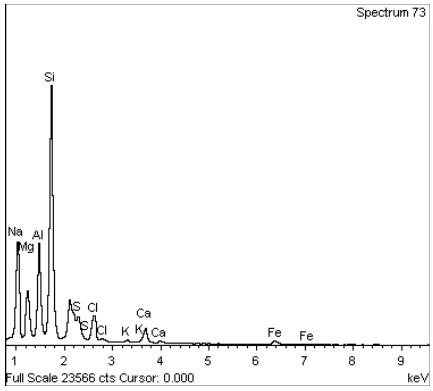

b)

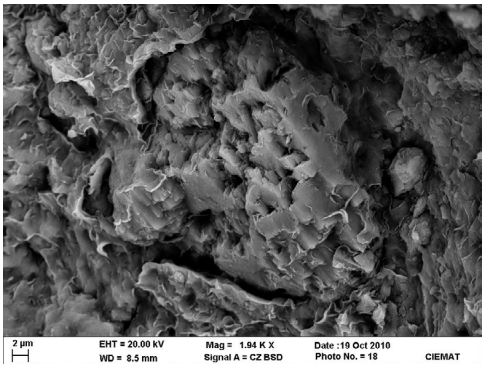

c)

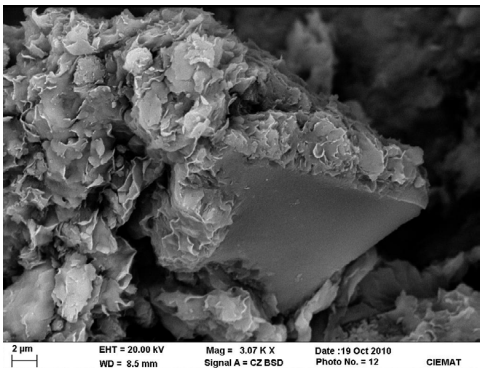

d)

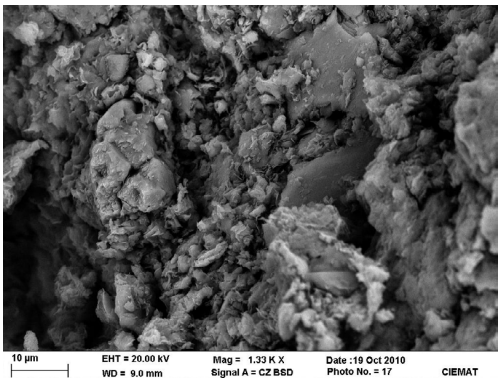

e)

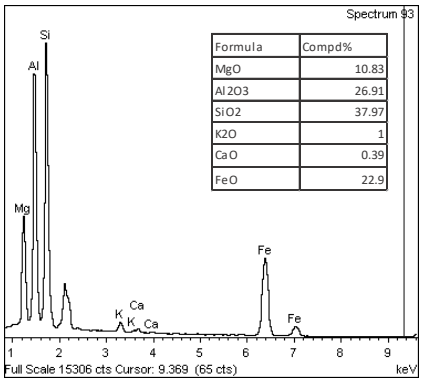

f)

Fig. 228: SEM photomicrographs of the SHSDI-01 greenish sample: a) Cl, Na, S, Ca and smectite; b) EDX of a), c) Ca-carbonate, d) smectite, e) mineral with Si, Al, and high amount of Mg and Fe, with Ca and K, f) EDX of e)

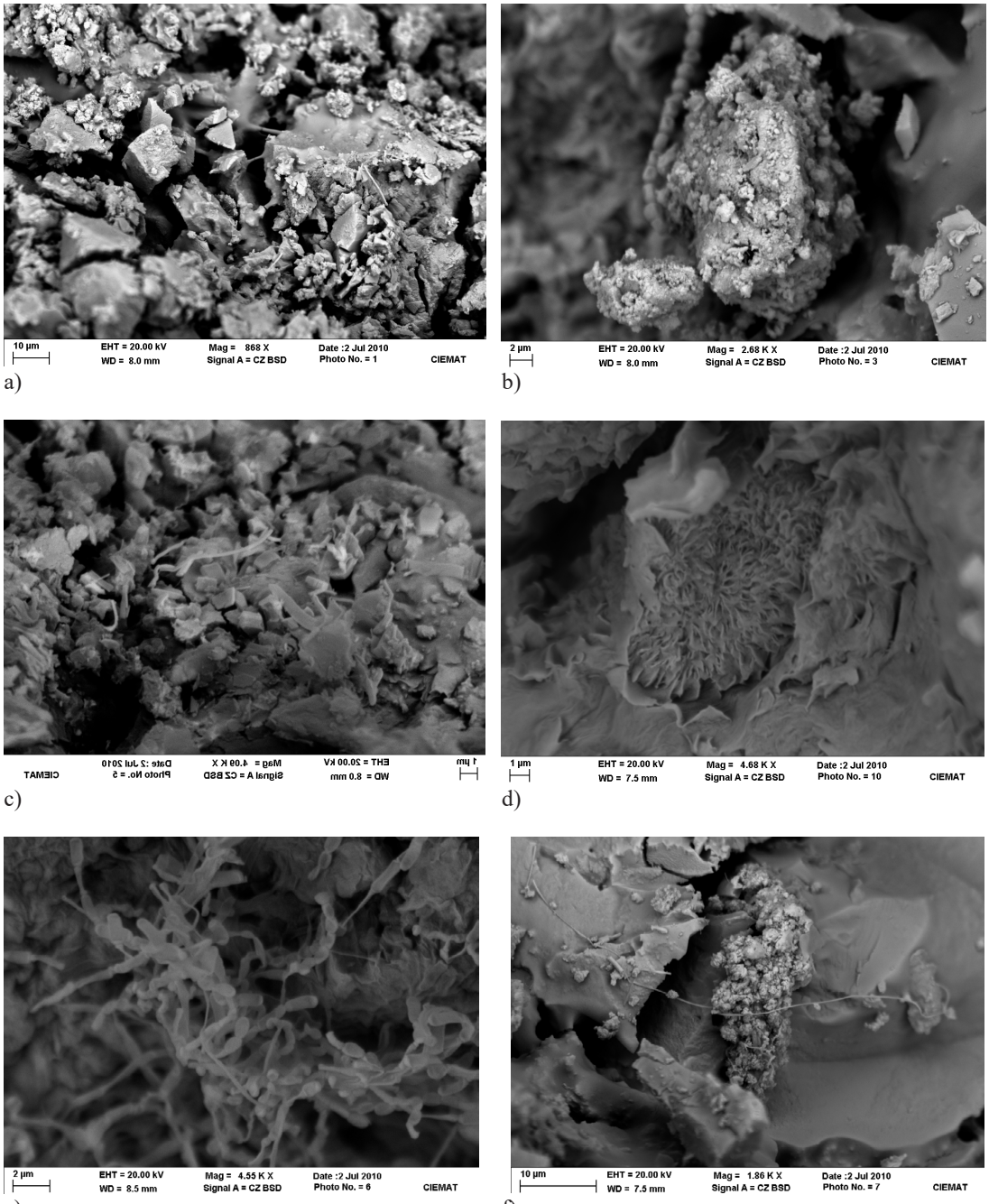

Fig. 229: SEM photomicrographs of the SHSDI-01 greenish-black particles: a) SCr, CrO, b) green-rush, Fe, Cl, C, Cr, c) ClCu and Cr.; d) smectite, e) Fe-oxides, f) Fe-oxides

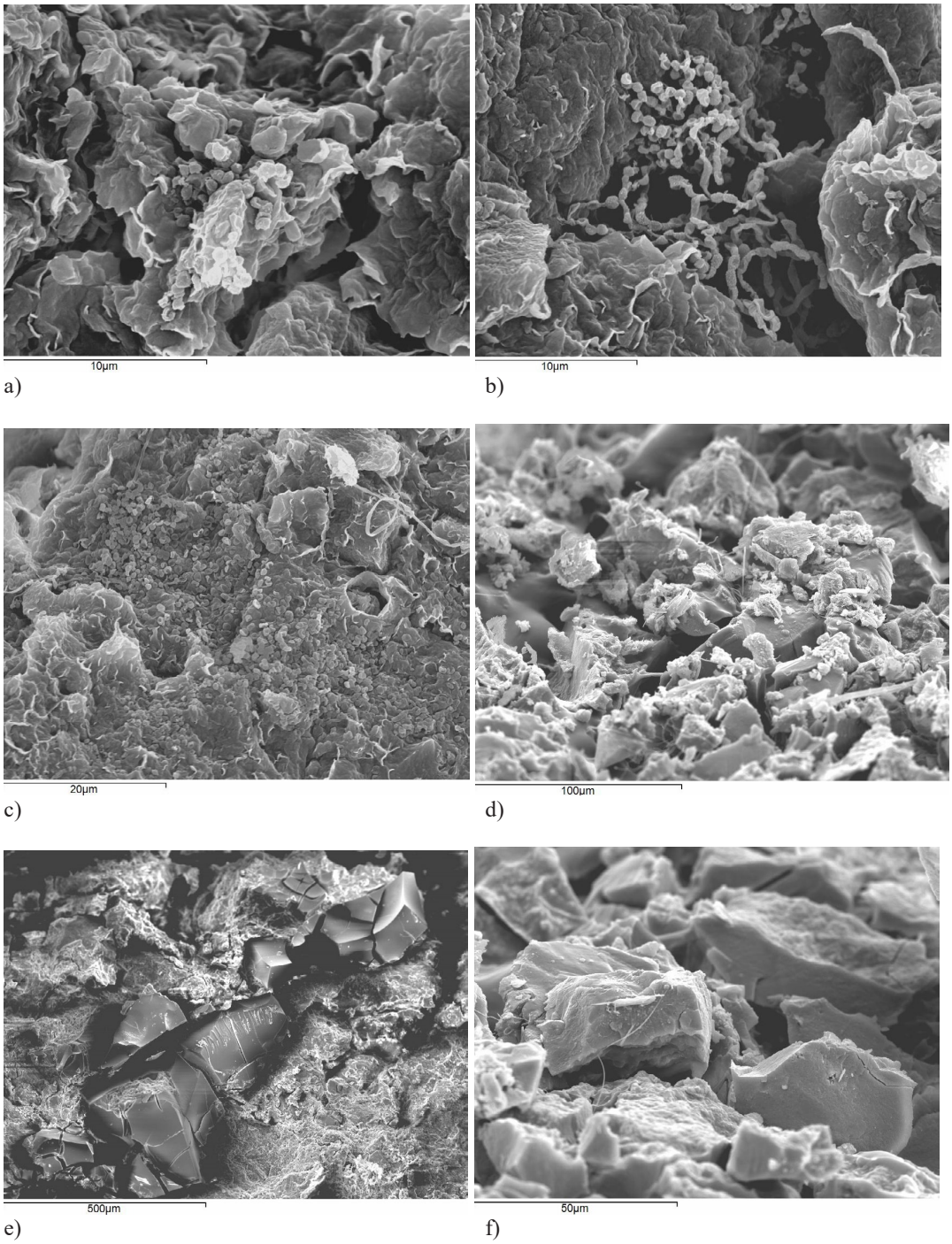

Fig. 230: SEM photomicrographs of the SHSDI-01 greenish-black particles: a) Fe-oxides, b) bacteria, Cr, Fe, c) Ti-oxides, Fe-oxides, microorganisms, d) S, Cr, Ca-carbonates, e) Cr, S, f) Cr, S

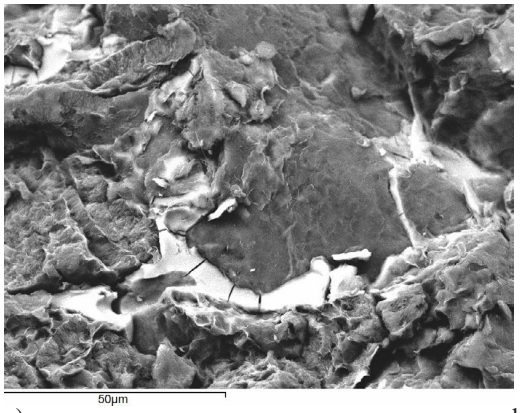

a)

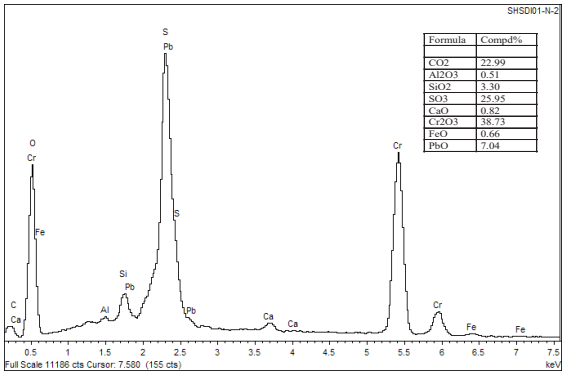

b)

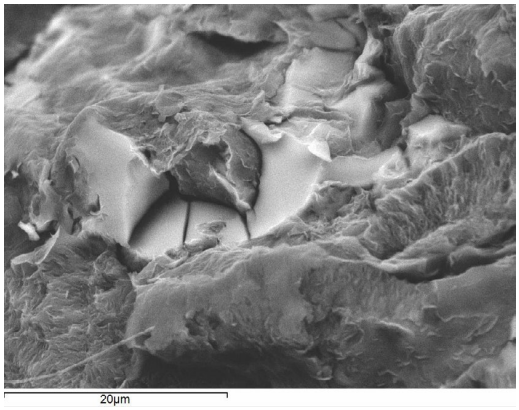

c)

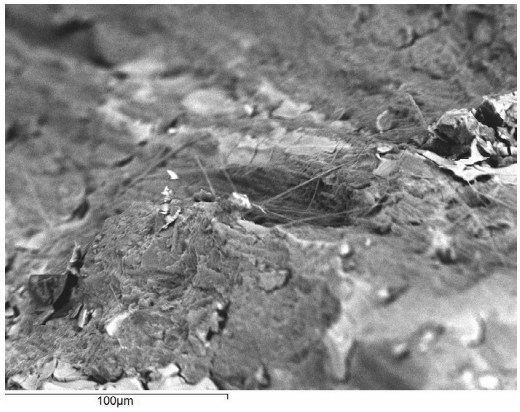

d)

Fig. 231: SEM photomicrographs of the SHSDI-01 greenish-black particles: a) S, Fe, Cr, Pb, b) EDX of a), c) SCr, d) C, Fe, Cr, S

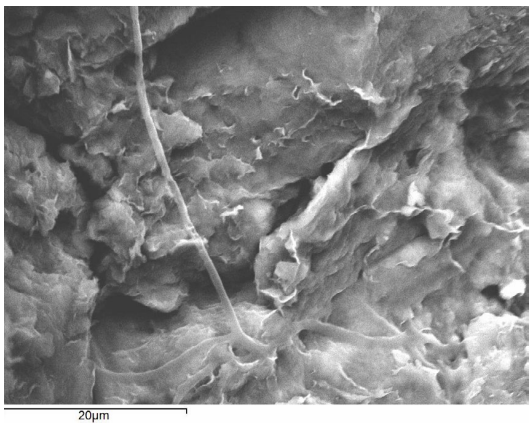

a)

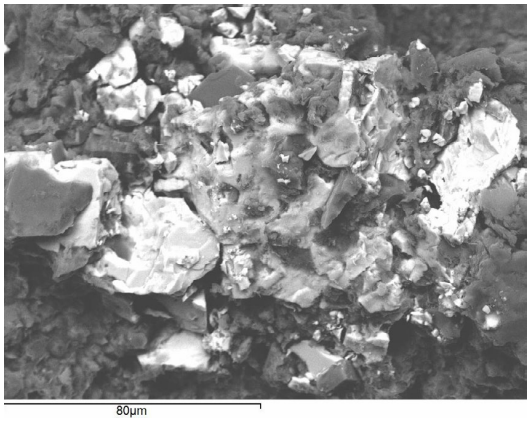

b)

Fig. 232: SEM photomicrographs of the SHSDI-01 reddish particles: a) C, Fe, b) barite

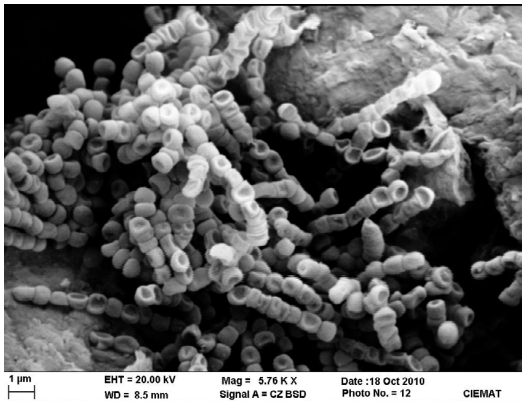

a)

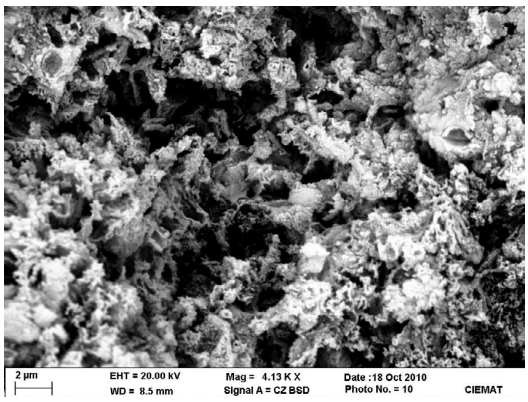

b)

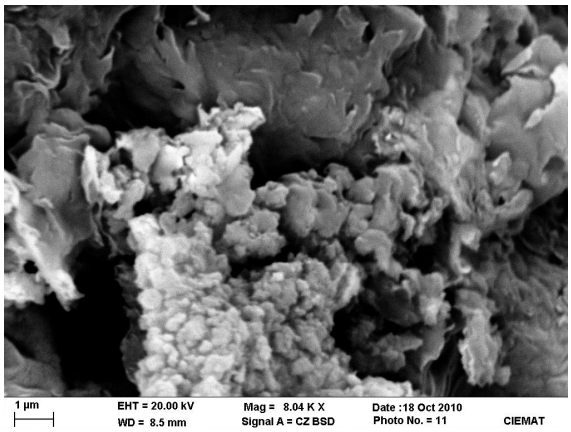

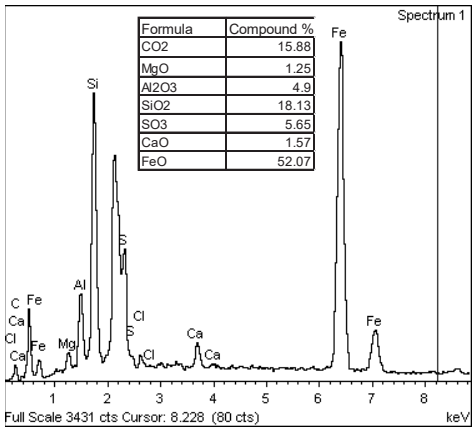

c)

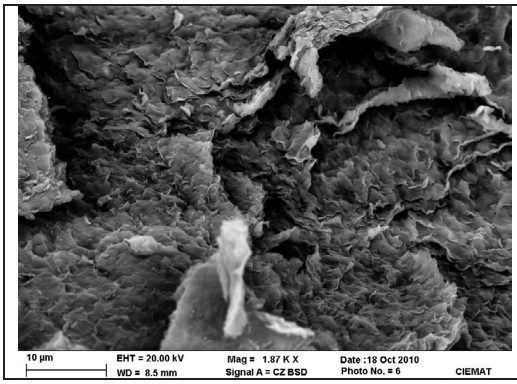

$(Si_{3.72}Al_{0.28})^{IV}(Al_{0.75}Mg_{0.33}Fe^{3+}_{0.92})^{VI}$
$(Ca_{0.12}\ Mg_{0.10}Na_{0.09}K_{0.09})_{0.39}\ O_{10}(OH)_2$
$\Sigma_{tet.} = 4.0$; $\Sigma_{oct.} = 2.0$
τ charge = -0.28; O. charge = -0.33
Total charge = -0.60 (τ % = 46; o % = 54)
F.W. (g/mol) = 796.65
(No Mg at interlayer: $\Sigma_{oct} = 2.10$; Total charge: -0.41, τ % = 67; o % = 33)

d)

Fig. 233: SEM photomicrographs of the SHSDI-01 reddish sample: a) bacteria, b) Fe carbonates, c) Fe-Carbonates, S, and Ca, d) Fe-rich smectite

6.4.2 Bentonite sample around gas pipe GF-SL-03 in Section 29

The bentonite sample surrounding the ceramic gas pipe GF-SL-03 at Section 29 was analysed by XRD (Fig. 234 and Fig. 235), FTIR (Fig. 236) and SEM (Fig. 237 to Fig. 239).

This sample contained smectite, zeolite, quartz, cristobalite, feldspars, iron sulphides (pyrrhotite and mackinawite), calcite, dolomite, siderite, goethite, hematite, magnesite, Cl-green-rush and microorganisms. Although a new peak at 7.1 Å was observed in the XRD patterns of total fraction, no modifications were observed in the XRD patterns of the clay mineral fraction (Fig. 235), so this peak was associated to a zeolite.

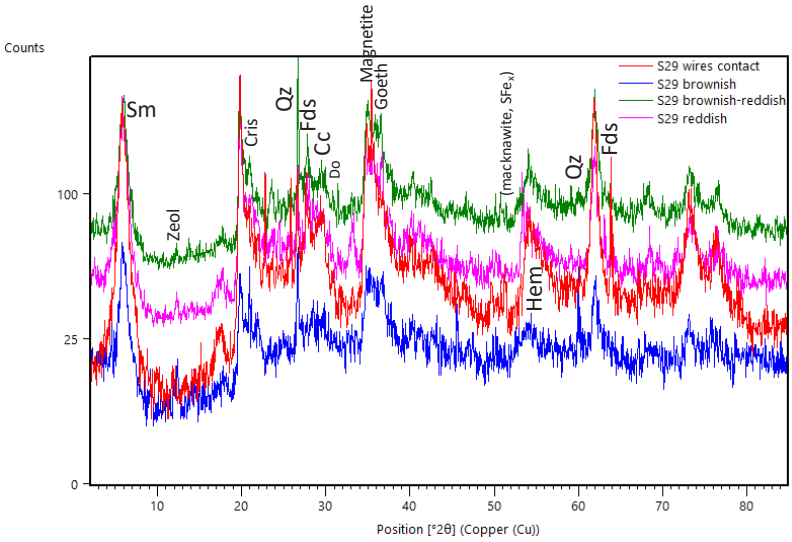

Fig. 234: XRD patterns of randomly oriented bulk samples surrounding the ceramic pipes at Section 29

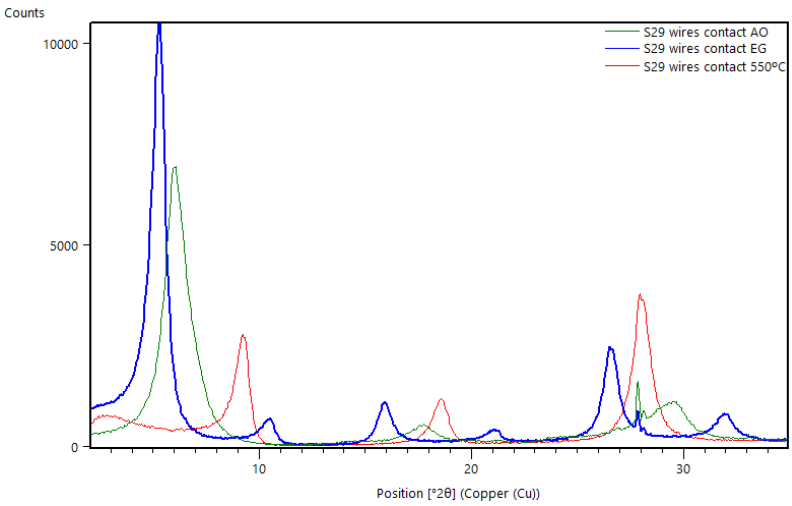

Fig. 235: Oriented aggregates (AO: green colour, EG: blue colour, 550 °C: red colour) from the sample surrounding the ceramic pipes at Section 29

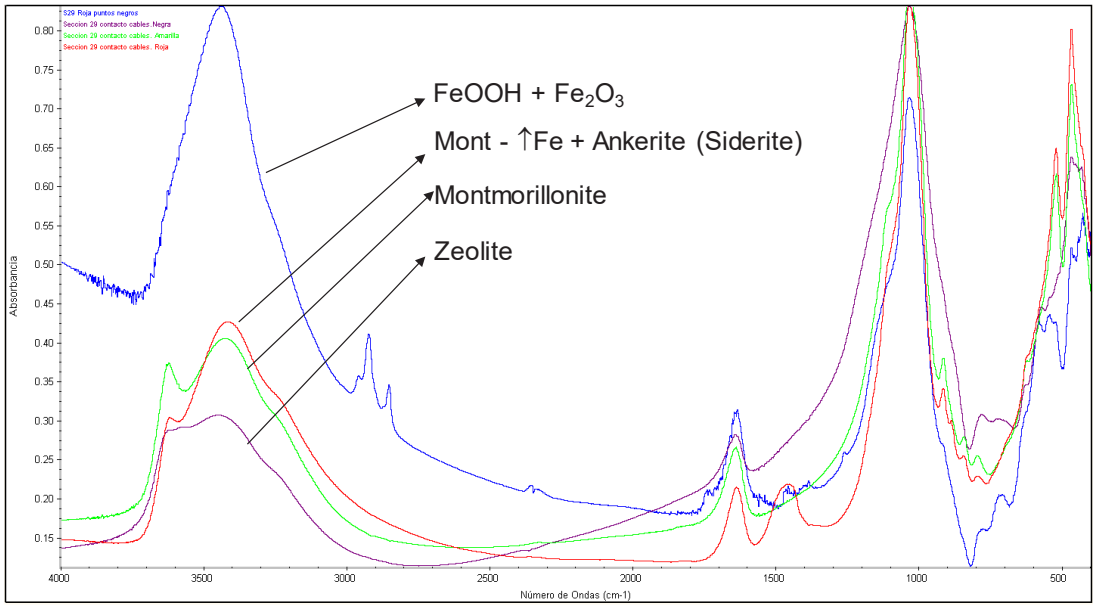

Fig. 236: FTIR spectra of S29 samples surrounding the ceramic pipes

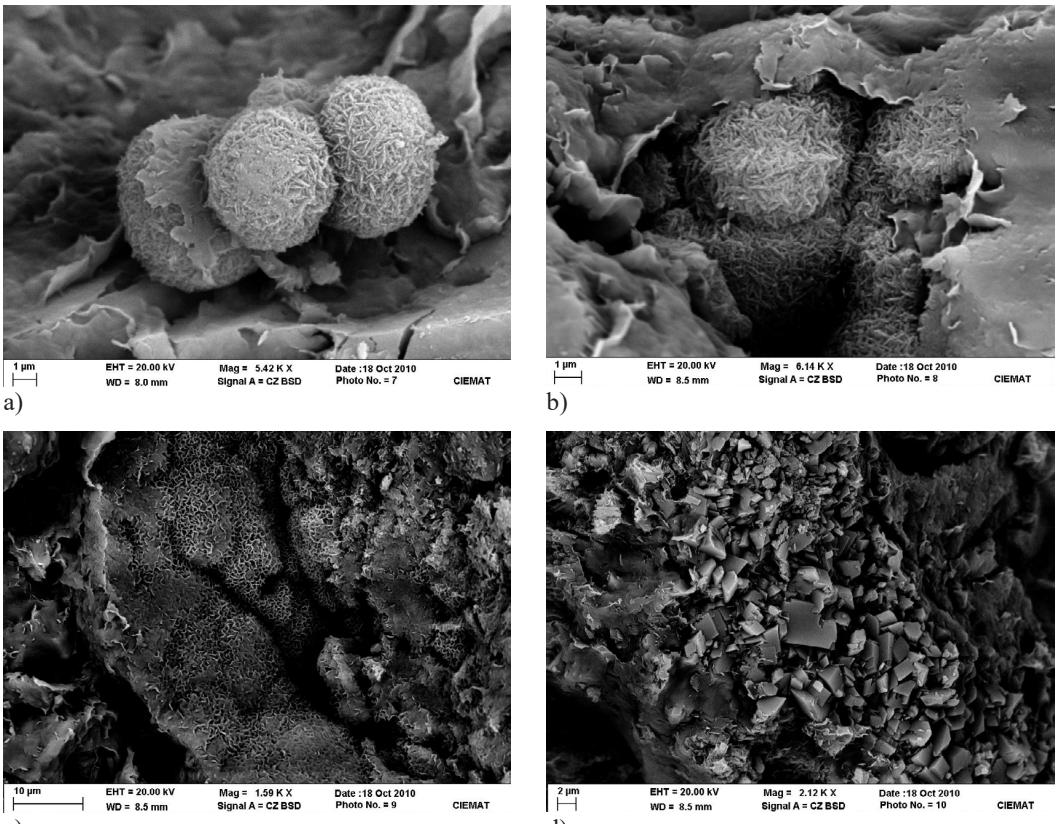

Fig. 237: SEM photomicrographs of the S29 sample surrounding the ceramic pipes: a) and b) silica, c) smectite, d) K-feldspars

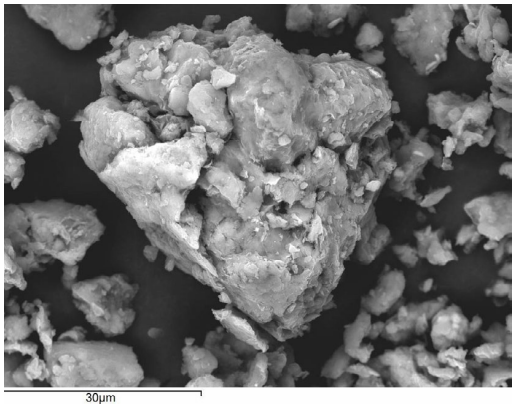

a)

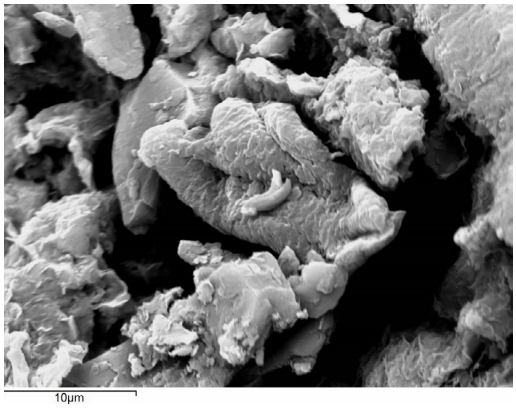

b)

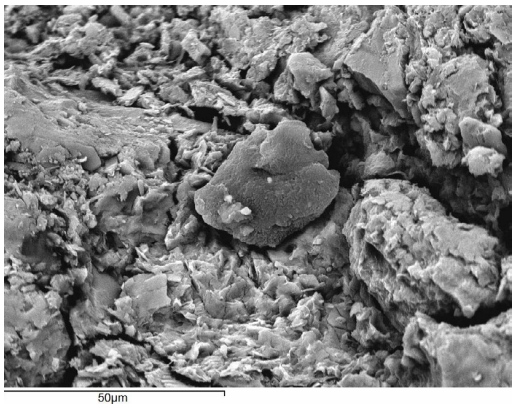

c)

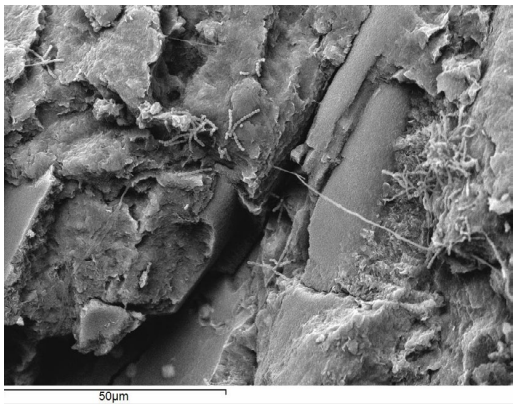

d)

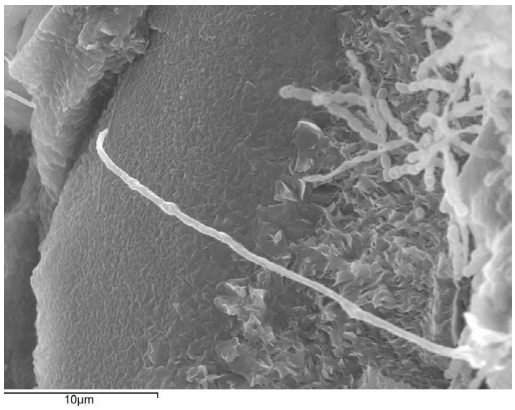

e)

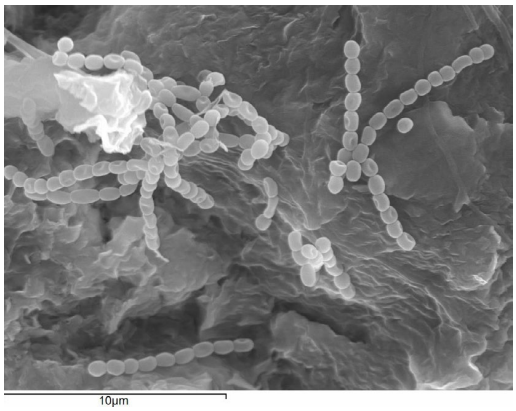

f)

Fig. 238: SEM photomicrographs of the S29 sample surrounding the ceramic pipes: a) red sample: Fe-oxides and Fe-carbonates; b) greenish-reddish sample: green-rush: Cl, Fe, K; c) C, Na, K, Cl; c) microorganisms and Fe, e) and f) bacteria and smectite

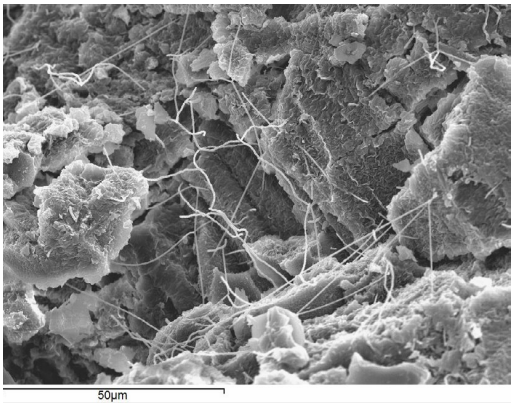

a)

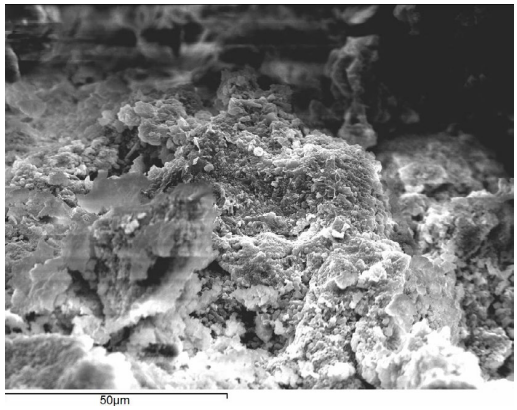

b)

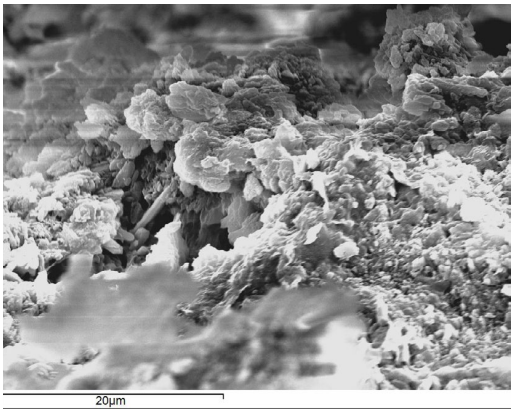

c)

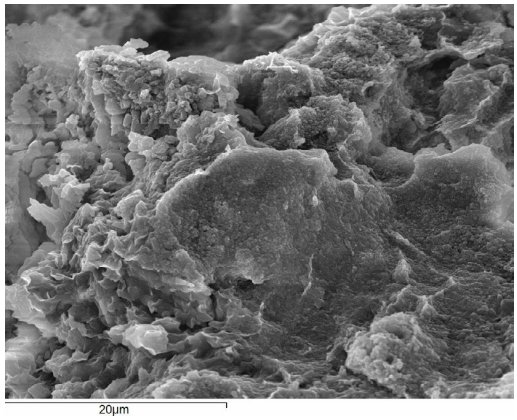

d)

Fig. 239: SEM photomicrographs of sample S29 surrounding the ceramic pipes (red sample): a) microorganisms, b) Fe and Ca carbonates, c,d) Fe-oxides, Ca, S

6.4.3 Bentonite sample at contact with the back of Heater #1 and inside the holes of the liner

The bentonite block sample BS-31-26 at direct contact with Heater #1 as well as different bentonite samples from inside the liner holes were analysed by XRD (Fig. 240 to Fig. 243), FTIR (Fig. 244), SEM (Fig. 245) and TG-DSC (Fig. 246 to Fig. 250).

The BS-31-26 sample contained smectite, quartz, cristobalite, feldspars, iron sulphides (pyrrhotite), calcite, siderite, magnetite and hematite. No smectite modifications were observed according to the FTIR spectra (Fig. 244) and XRD patterns of the clay mineral fraction (Fig. 242). No significant modifications were observed in the chemical analysis (Tab. 46, Tab. 47) and exchangeable cation composition (Tab. 48). However, BET surface area decreased (Tab. 49) with respect to the reference value.

In the case of the samples taken inside the holes of the liner, no modifications were observed either. Only a new peak at 528 °C was detected by TG-DSC (Fig. 250), indicating a change of the structural composition of the smectite as in the case of the samples in contact with Heater #2 and

the protrusions (see Section 6.1.3); this may be due to the presence of cis-trans vacant structures, an increase of Fe(II) at octahedral sheets inducing the location of OH^- groups at trans-vacant positions, or an increase of Al^{3+} substitutions at tetrahedral sheets.

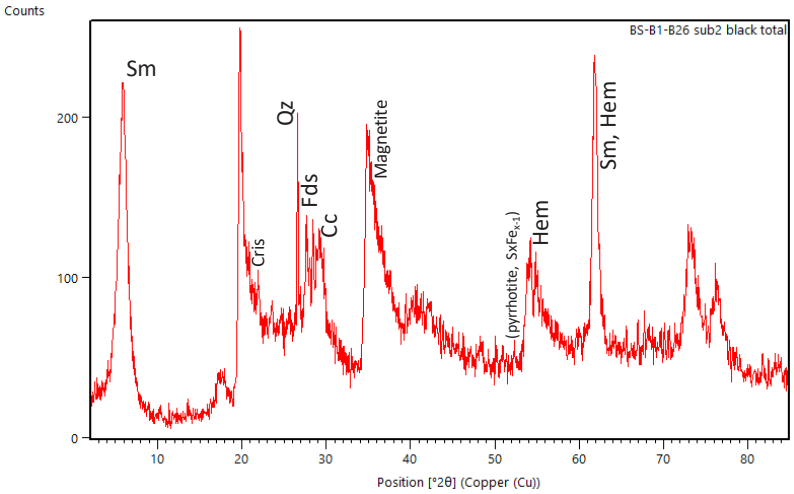

Fig. 240: XRD pattern of randomly oriented bulk sample BS-31-26

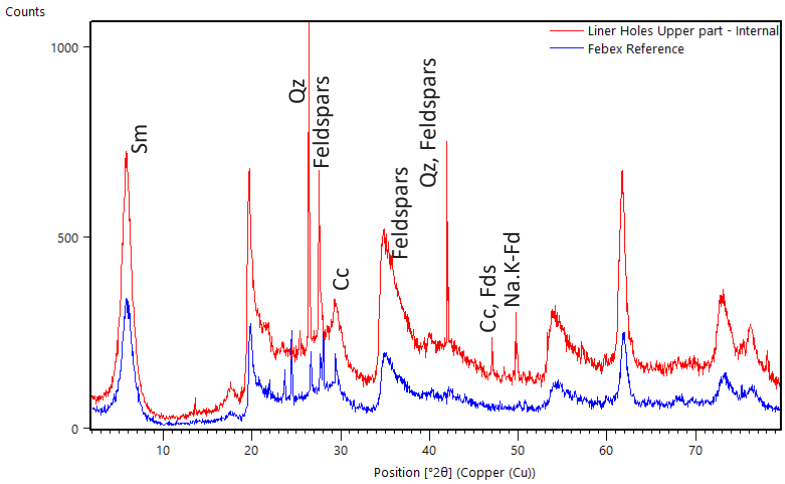

Fig. 241: XRD patterns of randomly oriented bulk sample: liner holes upper part (internal)

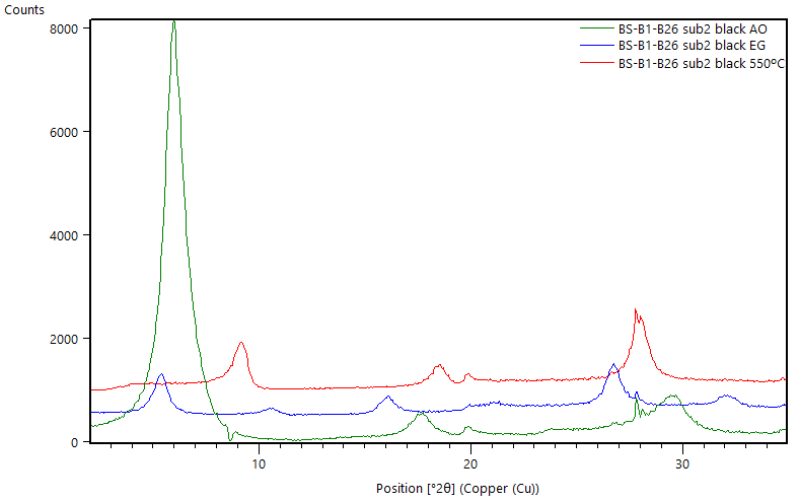

Fig. 242: Oriented aggregates (AO, EG, 550 °C) from sample BS-31-26

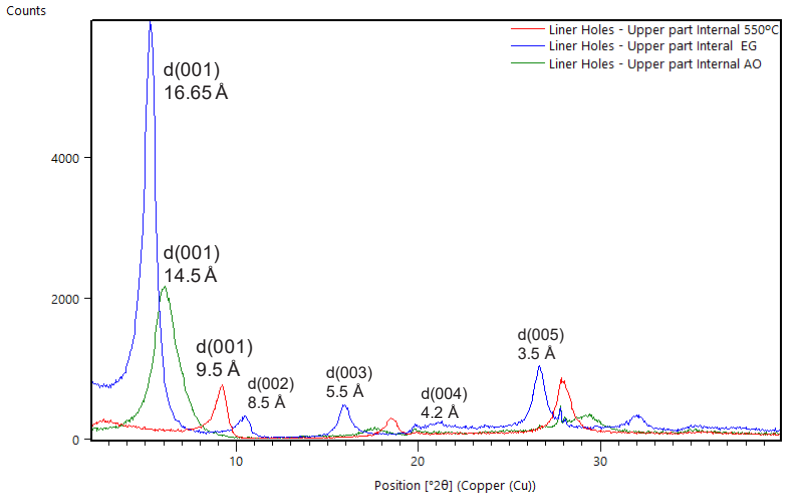

Fig. 243: Oriented aggregates (AO, EG, 550 °C) from the sample taken from a liner hole (upper part) located at the internal halfway of the liner around Heater #1

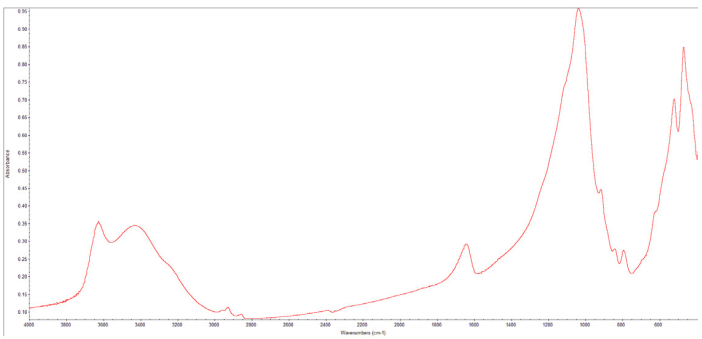

Fig. 244: FTIR spectra of the BS-31-26 sample (total fraction)

Fig. 245: SEM photomicrographs of the BS-31-26 Sub 2 black particles: Fe and Ca carbonates

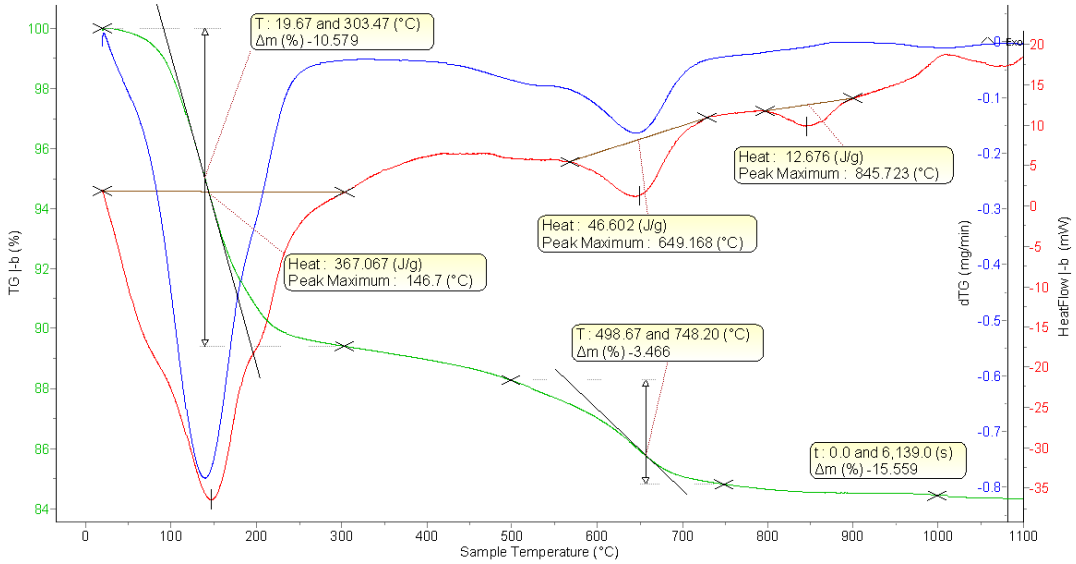

Fig. 246: TG-DSC curves from the sample BS-31-26 Sub 3 (black-brownish zone) taken from the back part of Heater #1

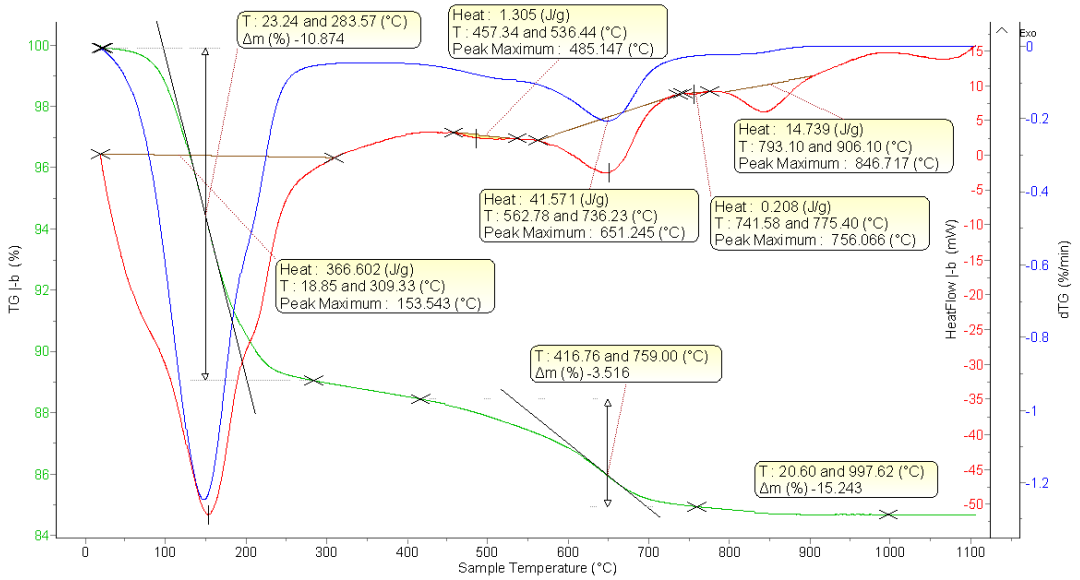

Fig. 247: TG-DSC curves from a black sample taken from a liner hole (bottom part) located at the internal halfway of the liner around Heater #1

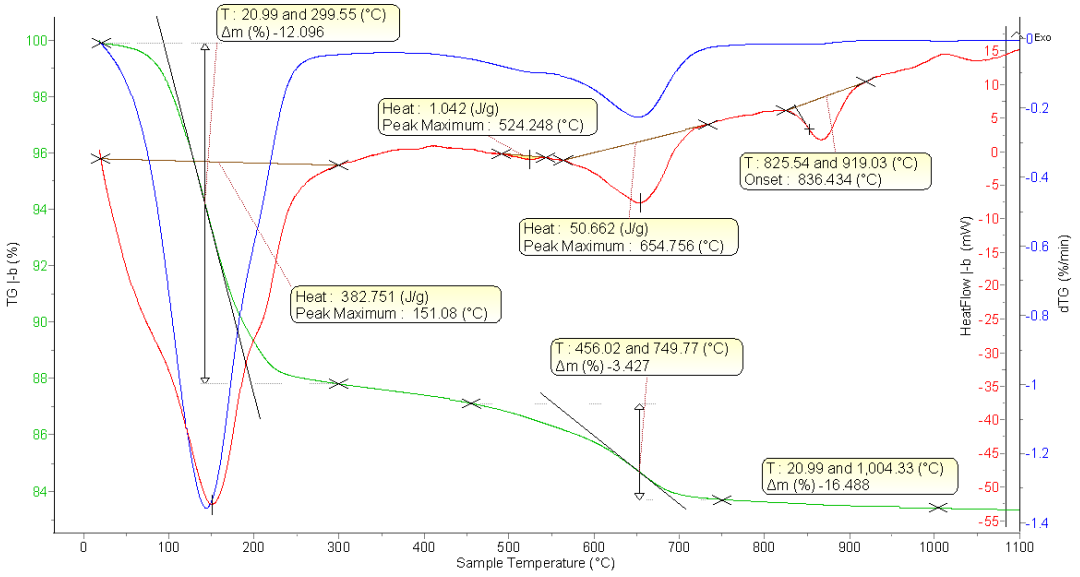

Fig. 248: TG-DSC curves from a sample taken from a liner hole (upper part) located at the internal halfway of the liner and from the upper part around Heater #1

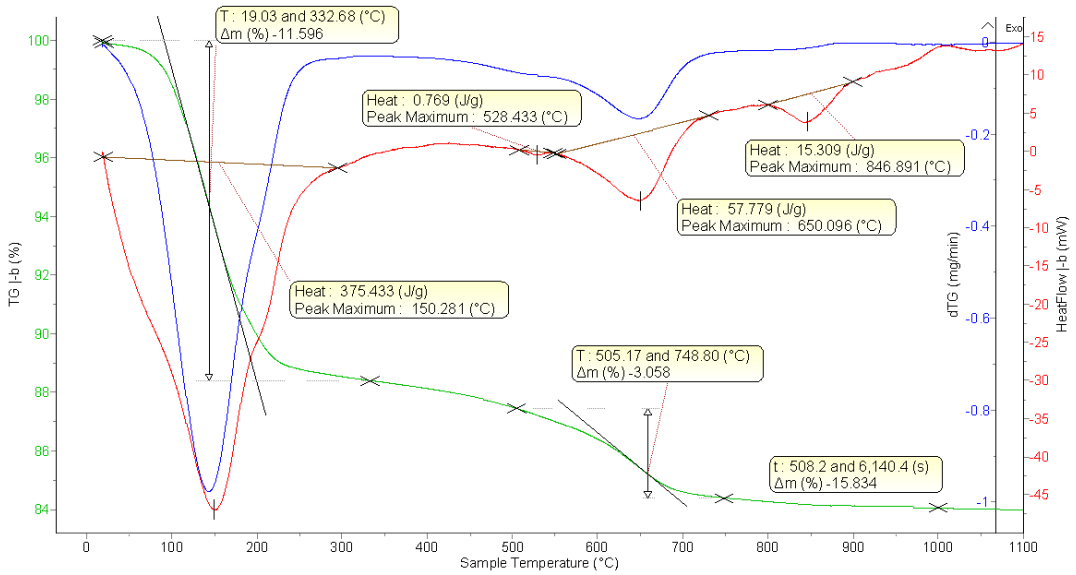

Fig. 249: TG-DSC curves from a black powdered sample taken from a liner hole (bottom part) located at the external halfway of the liner around Heater #1

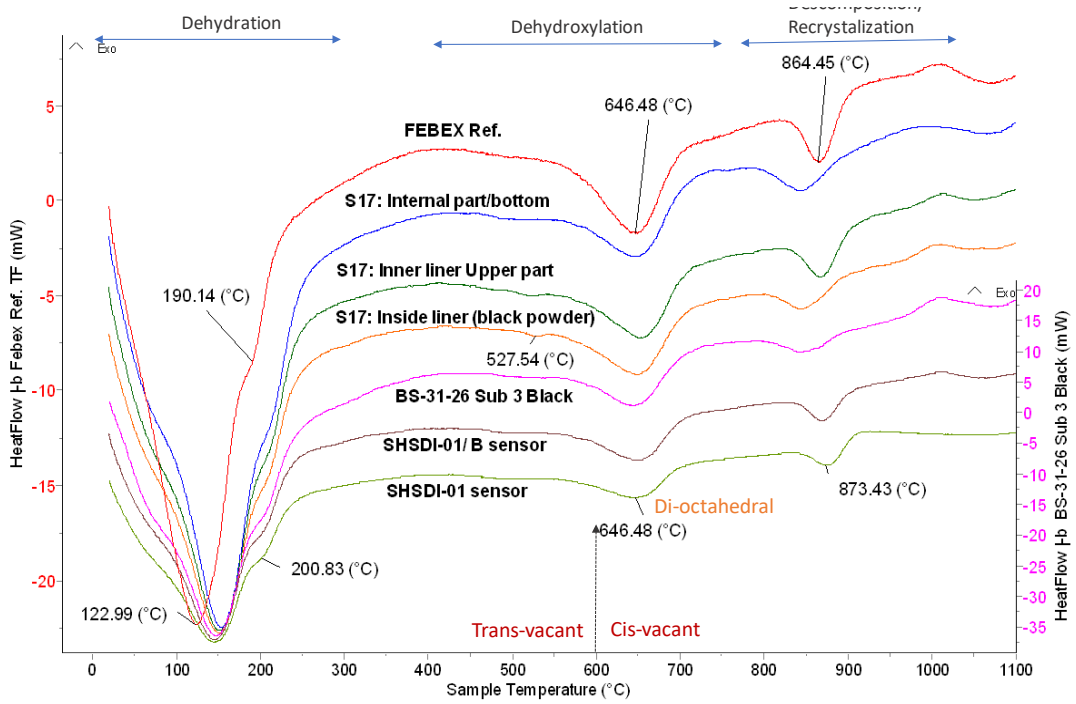

Fig. 250: TG-DSC curves from the samples taken after dismantling Heater #1 close to the Liner/Heater interface and to the displacement sensor SHSDI-01

7 Discussion of the results

Bentonites are an essential component of the multi-barrier system securing the long-term safety of the final nuclear waste disposal site. The efficiency of such an engineered clay barrier relies on its physical and chemical confinement properties: low permeability, low diffusivity, high retention, and swelling capacity. Therefore, an important issue for performance assessment purposes is to have confidence and demonstrate the long-term preservation of these properties over periods of i.e., hundreds of thousands of years under real repository conditions.

The scientific approach taken in the FEBEX experiment to tackle the problem of predicting the long-term clay barrier behaviour is analysing the results from experiments conducted in underground research laboratories (URL) at real scale and in real conditions (Tournassat et al. 2015). Most of the bentonite barrier experiments described in literature have been carried out at laboratory conditions (e.g., Fernández et al. 2010, and references therein), and there are only a few large experiments, as for example the LOT and the ABM in-situ experiments (Karnland et al. 2009, Svensson et al. 2011). The FEBEX in-situ test project provided the opportunity to understand and quantify the processes taking place in the near-field and to evaluate the behaviour and interactions of the compacted bentonite barrier at real conditions of a HLW repository system because:

a) It is a real-scale experiment performed at similar boundary conditions of the near field.

b) It is the longest real-scale in-situ experiment up to date.

From the geochemical point of view, specific long-term requirements for the sealing bentonite is to maintain a suitable chemical environment for the canister integrity and radionuclide retention over time, buffering possible alteration/deterioration processes of the bentonite.

The dismantling of the second part of the FEBEX in-situ test allowed quantifying the bentonite modifications due to changes in the initial physico-chemical conditions and different types of perturbations:

c) Interaction with granitic groundwater (saturation phase)

d) Desaturation phase due to heating

e) Perturbations linked to the interactions between the bentonite and the allochthonous engineered solid materials (concrete, iron, steel, organics, etc.)

f) Interactions with different gases produced and consumed and in the system (CO2, H2, CH4, etc.), due to mineral dissolution/precipitation, microbiological reactions and corrosion processes

The impact of the different perturbations can be described in terms of:

1. Modifications in the pore water chemistry and redox conditions, possibly affecting the smectite structural stability and speciation of dissolved ions
2. Mineralogical alteration: dissolution and redistribution of primary mineral phases and precipitation/neoformation of secondary minerals
3. Clay mineral stability and alteration of the clay mineral properties (especially cation exchange capacity, cation exchange population, crystallochemical structure, layer charge and swelling ability)
4. Modification of transport properties through modifications in porosity, permeability and tortuosity due to cementation processes

Depending on the overall conditions all types of alteration/perturbation processes may result in changed physical, hydraulic and mechanical properties of the bentonite system (Fig. 251).

The processes in the near field are complex, especially in the early, non-isothermal and unsaturated period, when thermal and hydraulic gradients affect the properties of the bentonite barrier and its performance. Therefore, a comprehensive THC analysis of the blocks and another type of FEBEX bentonite material was performed for a physico-chemical assessment, i.e., to identify different reactions that the bentonite may undergo, which could alter its engineering and chemical performance.

This section discusses the possible modifications of the FEBEX bentonite as a consequence of the 18-year-long experiment that changed the initial conditions and subjected it to different types of perturbations (dismantling Heater #2 in 2015). These results are compared to those obtained after 5 years (dismantling Heater #1 in 2002).

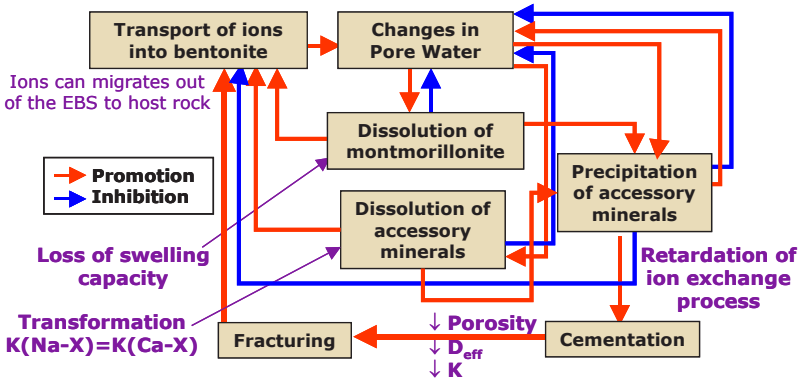

Fig. 251: Water-bentonite interaction processes and possible buffer alterations (after Takase 2004)

Eighteen years of heating and hydration could have changed the physico-chemical, geochemical, mechanical and mineralogical properties of the bentonite and may have led to a redistribution and neoformation of mineral phases, dissolution processes, changes in total adsorption capacity (CEC) and crystallochemical changes in the smectite. Variations in layer charge and its distribution were analysed because these parameters are coupled with possible chemical changes in:

a) The Al/Si ratio in tetrahedral sheets

b) Magnesium substitution in octahedral sheets

c) Some collapse phenomena in the interlayer region (redistribution of potassium from adjacent crystals)

In addition, parameters as crystal size in the smectite flakes stackings or even silica cements associated to the increase of solubility of silica and migration near the heater were evaluated because they could produce physico-chemical changes affecting mechanical properties (swelling, permeability, etc).

Some specific reactions already observed in laboratory and large experiments over time were detected in the FEBEX in-situ experiment as well: dissolution/precipitation, cation exchange,

metal corrosion, gas production, hydrocarbons oxidation, and Mg accumulation at the heater interface. However, some results were obtained exclusively from this FEBEX in-situ experiment, which is the longest real-scale in-situ experiment performed until now.

7.1 Pore water chemistry

The chemical state of the buffer is defined by the bentonite composition (clay minerals and accessory minerals) and the pore water composition. Consequently, the chemical stability of the bentonite, measured by the alkalinity and redox buffering capacity, will be firstly controlled by the bentonite-water interactions and the resulting pore water chemistry (pH, redox potential, ionic strength, ionic composition, speciation and complexation).

Therefore, knowledge of the pore water chemistry in the clay barrier is essential for performance assessment since it may influence processes involved in the release and transport of radionuclides, such as corrosion of canisters, sorption on mineral surfaces, solubility of radionuclides, etc. Therefore, a thorough analysis of the pore water composition in bentonites is a pre-requisite for understanding sorption and diffusion processes, assessing the influence of long-term groundwater-bentonite interactions, predicting radionuclide solubilities, defining the bentonite stability, and developing data bases for repository performance assessment studies (Fernández et al. 2018a submitted). For example, the concentration, sorption and mobility (by surface diffusion as the major transport mechanism) of many trace elements and radionuclides depends on the ionic strength of the pore water, the redox conditions and pH of the pore water.

In the FEBEX in-situ test, the pore water composition was obtained by squeezing (see Section 5.6). The squeezing tests were performed at the lowest squeezing pressure that allowed obtaining sufficient volume for pore water analysis, thereby trying to avoid the sampling of different portions of the diffuse layer water and interlayer water (Fernández et al. 2014). Depending on the initial water content and dry density of the compacted samples, the squeezing pressures ranged between 20 and 70 MPa in 2015 (dismantling Heater #2), and between 25 and 70 MPa in 2002 (dismantling Heater #1). A higher water content of the sample allowed a lower squeezing pressure.

7.1.1 Evolution of the bentonite pore water

The comparison of pore waters obtained by squeezing after dismantling Heater #1 and Heater #2; i.e., after 5 and 18 years of experiment, respectively, is shown in Fig. 252. It is must be kept in mind that this bentonite originated from the hydrothermal alteration of volcanic material and it was under sea conditions during some periods of time. Therefore, the initial pore water composition before the FEBEX in-situ *test* is Na-Mg-Cl-(SO_4) type (I ~ 0.3M), reflecting its marine origin (Fernández 2004), the infiltrating granitic groundwater, on the other hand, is a diluted and reduced water (EC < 100 µS/cm, Eh ~ -200 mV, pH~ 9) of sodic-calcic-TIC-fluoride water-type (Huertas et al. 2006). During the evolution of the FEBEX in-situ test, the composition of all pore waters was dominated by Cl- and Na, followed by SO42-, Ca and Mg (Fig. 252), with ionic strengths increasing towards the inner part of the barrier, from 0.04 M to 0.50 M in Sections S47 and S59 during the dismantling of Heater #2 in 2015, the pH was neutral to very slightly alkaline (6.8 to 7.9); and from 0.07 to 0.77 M in Sections S19 and S12 after dismantling of Heater #1 (Fig. 253).

The saturation indices indicate that pore waters from all samples were undersaturated with respect to calcite, gypsum and celestine; and saturated with respect to chalcedony and quartz, except for those located in the central part of the buffer, where the pore waters were saturated with respect

to gypsum (Fig. 253) in Sections S47 (heated) and S59 (non-heated). This is a consequence of the saturation evolution of the bentonite and the subsequent ion advective process, increasing the electrical conductivity and the ionic strength of the pore water as a function of time, as observed from samples analysed after the dismantling of Heater #1 and Heater #2, i.e., after 5 years and 18 years, respectively (Fig. 252, Fig. 253). However, precipitated Ca-carbonates and Ca-sulphates were widely observed in all sections of the bentonite buffer by SEM analyses, indicating localized saturated conditions with respect to these mineral phases, especially at the bentonite-heater interface due to the heating and evaporation processes of the pore water (Fig. 196, Fig. 197). Anhydrite was found by FTIR in the sample in contact with Heater #2 in sample BB-53-6 (Fig. 64).

The evolution of the pore water chemistry as a function of distance to the gallery axis and time indicated an advective transport of ions. This transport evolved following different profiles as a function of the conservative or non-conservative behaviour of the dissolved ions.

Chloride, sodium and magnesium, although the latter to a lower degree, seem to control the ion content in pore water. An advective-diffusive transport of ions towards the inner part of the barrier was observed in Sections S47 and S59 from the dismantling of Heater #2, and in Sections S12 and S19 from the dismantling of Heater #1 in 2002. The conservative chlorides, present in the bentonite pore water, were transported with water (advective transport), followed by sodium. Their content in the bentonite depended on the water gradient in the bentonite (suction water potential) rather than the hydraulic pressure of the granitic rock (0.72 MPa). Therefore, the maximum content of chlorides was observed at the second bentonite ring after 5 years of experiment (dismantling of Heater #1), whereas the maximum Cl content was observed at the contact of Heater #2 after 18 years of experiment (Fig. 252). Thus, the initial pore water is more diluted at the contact with granite than the initial reference pore water. In Section 36 the chloride content is much lower than the reference sample in all bentonite blocks, indicating a higher dilution and/or lixiviation of the pore water at this interface with time.

The difference in chloride content distribution along the buffer indicates the influence of the heating process on the chloride transport as well as the possible precipitation or neoformation of chloride salts at the heater interface. Heat seems to enhance the ion transport because different chloride profiles were found in the heated (Section 47) and non-heated section (Section 59). In Section 47 chloride content in the external bentonite blocks was lower than that of the reference sample, but higher than in Section 59. The precipitation of salts at the Heater #2 contact in Section 47 was observed when the chloride distribution in aqueous extracts (Fig. 159, Fig. 164) and squeezed pore waters (Fig. 252) were compared. Cl content in aqueous leaching tests was higher at the Heater #2 contact in Section 47 than in Section 59, contrary to what occurred in squeezed waters. Also, a time dependence in the chloride transport was observed when data from aqueous leaching and squeezing tests after dismantling of Heater #1 (5 years) and the dismantling of Heater #2 (18 years) were compared (Fig. 252, Fig. 164).

Bromide showed a trend similar to chloride; it is transported with the water front controlled by the suction water potential of the bentonite. The Cl/Br mass ratios were in the range of about 808 – 2'130, thus above the seawater ratio (154 – 1'463), with increasing values in Sections S47 and S59 towards the inner part of the barrier, and almost constant in Section 36.

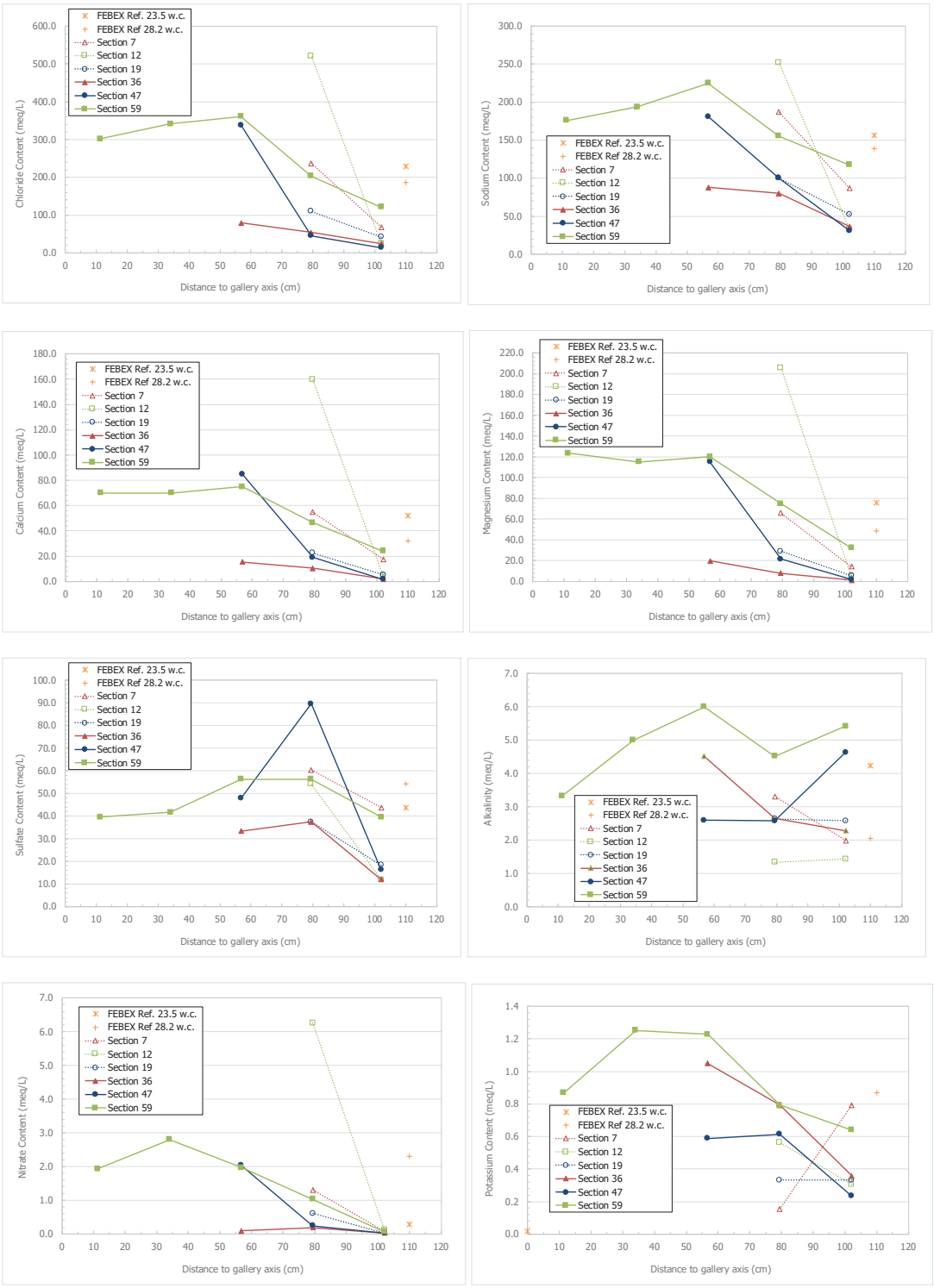

Fig. 252: Comparison of ion concentrations in the squeezed samples after dismantling Heater #1 in 2002 and Heater #2 in 2015

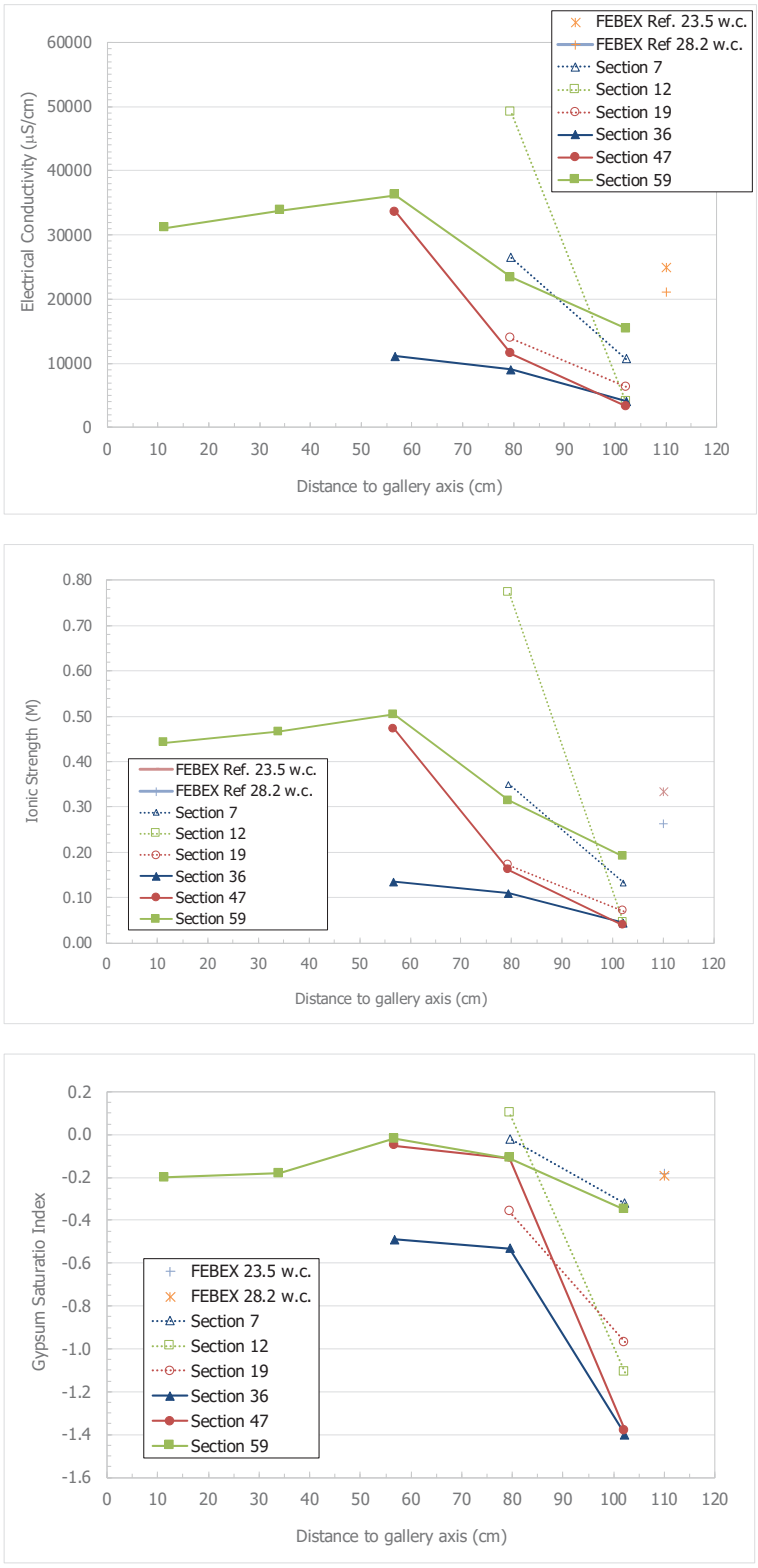

Fig. 253: Comparison of electrical conductivity, ionic strength and saturation index of gypsum in the squeezed samples obtained after dismantling Heater #1 and Heater #2

F-, comes mainly from the infiltrating groundwater (Frick et al. 1992), it was transported through the bentonite, but its movement was slower than chloride due to its interaction with the smectite particles (F- may replace hydroxyl groups in the clay structure), and probably by its ionic size. Whereas the infiltration of F- in the bentonite barrier was detected up to the middle bentonite ring in aqueous extract solutions (Fig. 161), it was detected in all leaching solutions and squeezed pore waters from Section 36 (close to shotcrete plug). This is due to the slightly higher degree of saturation and lixiviation of these samples at the bentonite/shotcrete interface.

Other non-conservative ions such as carbonates and sulphates were transported but at a slower rate because they were involved in time-dependent dissolution/precipitation processes in bentonite. Gypsum is close to saturation in the inner part of the barrier in Sections S59 and S47. However, at the Heater #2 interface in Section 47, anhydrite should control the sulphate equilibrium due to the temperature (88 – 99 °C) at the heater contact (Tab. 3). Indeed, anhydrite was detected by FTIR in sample BB-53-6 at the contact with Heater #2 (Fig. 64). Alkalinity values were higher than those from the reference sample in the non-heated sections (S59 and S36) in both the inner and external parts of the bentonite, indicating the dissolution of carbonates and the infiltration of granitic groundwater. In Section 47, alkalinity is higher at the external part (granite interface), but remained constant in the inner sections, probably due to carbonate precipitation at the bentonite/heater interface, as observed in Tab. 37 and Fig. 196 (Fernández et al. 2018b submitted). However, according to the saturation indices, carbonate dissolution at the granite contact and precipitation at the heater interface is deduced from aqueous leaching data but is not confirmed in results from the squeezed pore waters; these are always undersaturated with respect to carbonates, which indicates possible CO_2-degassing.

Cations also moved with the water front, but their transport was controlled by dissolution/ precipitation processes of carbonates and sulphates and exchange reactions at interlayer sites, as observed by aqueous leaching tests and the mineral saturation indices. Although Na is the main cation in pore waters and Ca the second one; it is interesting to note the increase of magnesium with respect to calcium in the pore waters from the inner part of the bentonite barrier (i.e., at the contact with Heater #2 in Sections S47 and S53; and the inner bentonite rings in Section 59).

Sodium and chloride contents follow a linear relationship, but sodium concentration is always lower than chloride in the non-heated Section 59. The opposite occurs in Section 36 (shotcrete contact) and close to the granite interface in Section 47, where higher lixiviation and dissolution processes were involved and, hence, cation exchange reactions, increasing calcium at interlayer sites and sodium in the pore water. This was also observed from samples taken after dismantling of Heater #1. Indeed, lower concentrations of Cl, SO_4, Ca and Mg were found in all blocks from Section 36 located at shotcrete contact with respect to the other heated and non-heated sections (S47 and S59). It should be taken into account that Section 36 was a heated section surrounding Heater #1 prior to the first dismantling and afterwards it was the section where the bentonite barrier was sealed with shotcrete.

Calcium and magnesium concentration increased in the inner part of the heated and non-heated Sections S47 and S59, respectively, whereas it is depleted for these cations at the granite interface and in all bentonite blocks from Section 36 (shotcrete contact) with respect to the reference values. However, an increase of magnesium with respect to calcium was observed in the inner parts of both Sections S47 (at the Heater #2 contact) and S59 (non-heated), indicating an accumulation of magnesium in the pore water. Due to the increase of chlorides at the heater contact, MgCl+ ion pairs, a positively charged species, may enter the interlayer sites, although absorption of bivalent cations is favoured.

Potassium increased towards the inner parts of the bentonite, being higher than the reference sample only in the non-heated Section 59. However, the values were lower than 1.25 meq/L (Fig. 252), taking into account samples from dismantling of Heater #1 and Heater #2, which is a low value for a possible illitization process of the smectite. Silica data were also lower than 0.44 meq/L, and in equilibrium with quartz/chalcedony; silica does not increase towards the heater contact, which indicates that dissolution of smectite can be ruled out. pH values were neutral to slightly alkaline in all sections, even close to the bentonite/shotcrete interface, indicating the high buffering potential of the FEBEX bentonite, and affirming the preservation of chemical conditions that avoid smectite alteration over time.

It is interesting to see the depletion of Cl, Na and Mg observed in Sections S7 and S36 in contact with the concrete and shotcrete plugs, respectively, from both dismantling operations. This seems to indicate a diffusion process towards the concrete interface, which is also observed from the aqueous leaching tests results and the decrease in exchangeable Mg content. Indeed, the formation of Friedel's salts in the shotcrete up to 5 cm and the precipitation of Mg-phases in the bentonite were observed at the bentonite/shotcrete interface (Alonso et al. 2017, Turrero & Cloet 2018).

Electrical conductivity, ionic strength and gypsum/anhydrite saturation indices of samples taken during the dismantling of Heater #1 and Heater #2 are shown in Fig. 253. Both show similar trends in the water saturation evolution of the bentonite barrier and, show consequently, the ion transport from samples taken during both dismantling operations, as controlled by time, cation exchange and dissolution/precipitation reactions.

Although, organic matter (TOC) and volatile fatty acids (VFAs), such as acetate, formate and oxalate, were found in samples from different sections sampled in 2015 (S36, S47 and S59), it is interesting to note that oxalate was only observed in the sample close to the Heater #2 interface (sample BB-47-9), together with a high amount of acetate (Tab. 29). At this interface, the factors of temperature and possibly hydrogen, available due to corrosion processes, may result in the reduction of CO_2 to produce acetate, then formate and then oxalate. On the other hand, acetate and formate are also produced as fermentation products through the degradation of organic matter under anaerobic conditions. Nevertheless, the implication of microorganisms in different reactions at the Heater #2/bentonite interface could not be confirmed (Bengtsson et al. 2017). More plausible is the idea that oxic corrosion and hydrolysis of carbon-containing steel material (liner, Heater #2, etc.), led to the generation of H_2, CO_2 and hydrocarbons (alkanes, alkenes and carboxylic acids), and is as such the possible main process for the presence of acetate, formate and oxalate in pore water close to the heater interface (see below and Fernández 2018).

7.1.2 Analysis of the squeezed pore waters: mobile pore water and interlaminar water

It is known that pore water extraction by squeezing could alter the pore water's composition if the exerted pressure is higher than a threshold pressure value (Fernández et al. 2014 and references therein). In bentonites this is due to anion exclusion effects, but mainly because a mixture of interlayer water and mobile external pore water is extracted (e.g., Järvinen et al. 2016).

Different squeezing pressures were used for obtaining the pore water from the bentonite samples (see Section 7.1.1), ranging from 20 to 70 MPa depending on the water content. Only 20 – 25 MPa was needed for samples with an initial water content higher than 27 % (Tab. 26, Tab. 27). However, the dry density of the samples also affected the required pressure for pore water extraction, as observed in sample BB-47-8. Samples with water contents below 22 % needed pressures of about 70 MPa. After dismantling Heater #1, samples from the inner parts of the bentonite could not be squeezed because the water content was lower than 18 % and squeezing pressures higher than 100 MPa were needed.

In this work, the required squeezing pressure was the minimum pressure necessary for obtaining and analysing the pore water. However, it was observed that an increase of the squeezing pressure affected the major ions, decreasing concentrations. Indeed, a reduction in the chloride content was detected when the pressure was increased in some samples (Tab. 28, Tab. 29, Tab. 30). At higher pressures, Cl and Na were presumably affected by dilution due to both ion filtration and extraction of some interlayer water. Pressure-driven carbonate mineral dissolution can be neglected when dilution by ion filtration and mixing with interlayer water are considered as the main processes involved and low pressures are used.

In order to analyse the influence of the possible extraction of interlayer water during squeezing, some studies about the changes of the 001 smectite basal reflexion before and after squeezing were performed (Fig. 254). Preliminary analyses indicated that only a partial extraction of interlayer water during squeezing occurred if the minimum pressure is exerted. For example, in sample BB-47-8 (middle block from a heated section) before squeezing, the bentonite contains a mixture of two populations of water-hydrated montmorillonite clay minerals: 77 % two-layers hydrated (001 reflexion at 15.4 Å) and 22 % both three- and two-layers hydrated (001 reflexion at 16.4 Å) after 18 years of experiment. After squeezing, only water at interlayer sites was produced, with 69 % two-layers hydrated (15.4 Å) and 31 % three-layers hydrated (~ 17.1 Å) clay minerals. Indeed, it is known that the amount of water at interlayer sites changes as a function of dry density (Fernandez & Rivas 2005b; Muurinen 1994), and squeezing implies a reduction of volume (dry density) of a saturated sample due to the expulsion of water (macropore water). In any case, this issue should be further investigated.

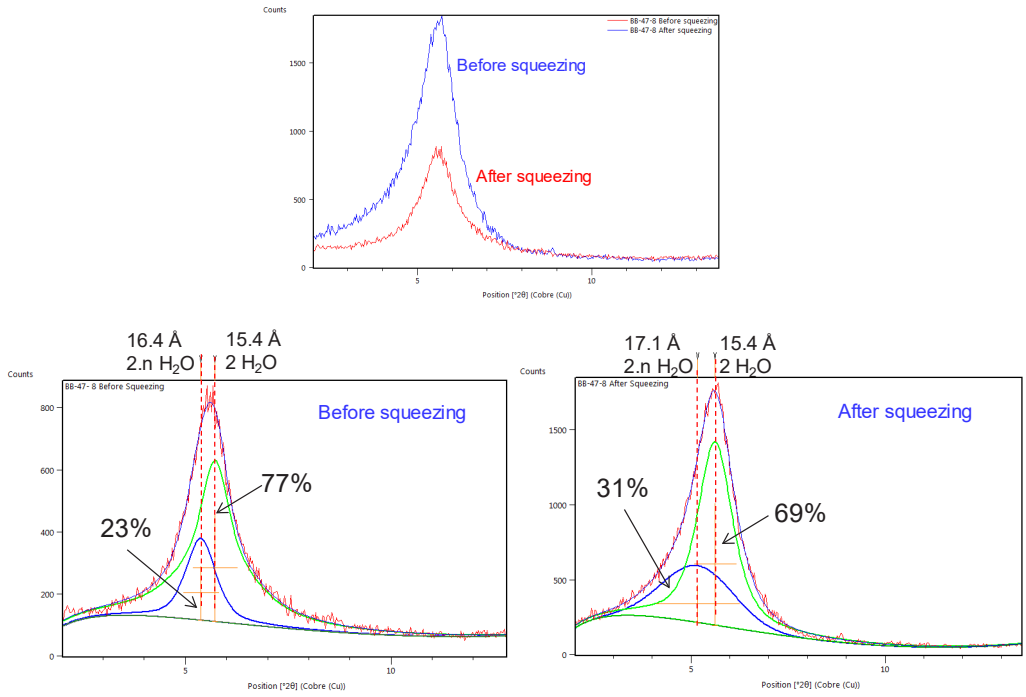

Fig. 254: Comparison of basal spacing before and after squeezing test in the sample BB-47-8.

7.1.3 Anion accessible porosity

An important issue in a clayey media is to determine the respective volume accessible to cations and anions, i.e, the amount of water actually available for chemical reactions or solute transport. This amount is usually referred to as anion-accessible porosity (Pusch et al. 1999), geochemical porosity (Pearson 1999) or external porosity (Muurinen 1994, Fernández et al. 2004). This parameter is necessary for any model of pore water composition evolution, and it is intimately related to the nature of porosity and the behaviour of fluids in close proximity to the charged clay surfaces.

Therefore, in all the investigations related to pore water chemistry in clayey systems, questions about microstructure and porosity of water-saturated clay systems, the distribution of different types of waters and the fraction of pore space that is accessible to anions remain open to debate (e.g., Savage et al. 2011, Tournassat & Appelo 2011, Birgersson & Karnland 2009, Järvinen et al. 2016, Muurinen et al. 2013, 2007, Fernández & Rivas 2005a,b).

Most of the currently available conceptual models for pore water behaviour in clays describe the clay-water system as a function of different types of porosity (double porosity models), whereas only some of them use a single porosity system (single porosity model).

In the double porosity models, the total porosity in a compacted clay is subdivided in interlamellar/interlayer porosity, which contains interlayer water; and external porosity, which includes different types of water (e.g., Pearson 1999, Bradbury & Baeyens 1998):

a) water from electrical double layers on the surfaces of the clay particles (double layer water, DDL)

b) free water (chloride porosity or anion accessible porosity), which consists of water as interconnected thin films on the outside of clay stacks and also as films surrounding other minerals (e.g. quartz)

Therefore, Cl porosity is much lower than the total physical porosity, and each porosity type varies with compaction density in bentonite, with free/chloride porosity being significantly less than the total porosity as compaction density increases (Muurinen 1994, Fernández & Rivas 2005b, Kozaki et al. 2005, Glaus et al. 2007). In a single porosity model (Birgersson & Karnland 2009) the pore water composition in the total pore space is controlled by ion equilibria within the interlamellar pore space involving two basic processes: Donnan equilibrium and cation exchange.

In this work, a double porosity model was chosen. The anion-accessible porosity only includes the free water; while the total physical porosity includes both the external (free water) and internal water (DDL + interlayer water). Thus, a reduction factor has to be applied to the total porosity value to estimate the pore water concentration for an anion.

Anion accessible porosity or Cl-accessible porosity (εcl), values were calculated based on the chloride concentrations obtained both from squeezing (Cl_{pw},) and leaching tests (Cl content of the rock, Cl_{rock}), according to the following relationship:

$$Cl_{pw}\left(\frac{\text{mol Cl}}{\text{L pore water}}\right)=\frac{Cl_{rock}\left(\frac{\text{mol Cl}}{\text{kg bulk}}\right)\cdot\rho_{bulk,dry}\left(\frac{\text{kg bulk}}{\text{L bulk rock}}\right)}{\varepsilon_{Cl}\left(\frac{\text{L Cl bearing pore water}}{\text{L bulk rock}}\right)}$$

By knowing the anion-accessible porosity fraction, the anion concentration in pore water can be inferred from its concentration in the aqueous leaching solution at a specific S:L ratio, by assuming that all anions leached in the aqueous extracts originate from pore water. The results are shown in Tab. 50 and Fig. 255. The average value for FEBEX reference samples and samples obtained after dismantling of Heater #2 was about 0.43 and for all samples (reference, dismantling of Heater #2 and dismantling of Heater #1) around 0.48. These values are in agreement with those obtained in clayrock samples (Pearson et al. 2003), although they are much higher than those obtained from bentonite diffusion tests for similar dry densities, these being between 0.04 and 0.03 (Gutiérrez et al. 2001).

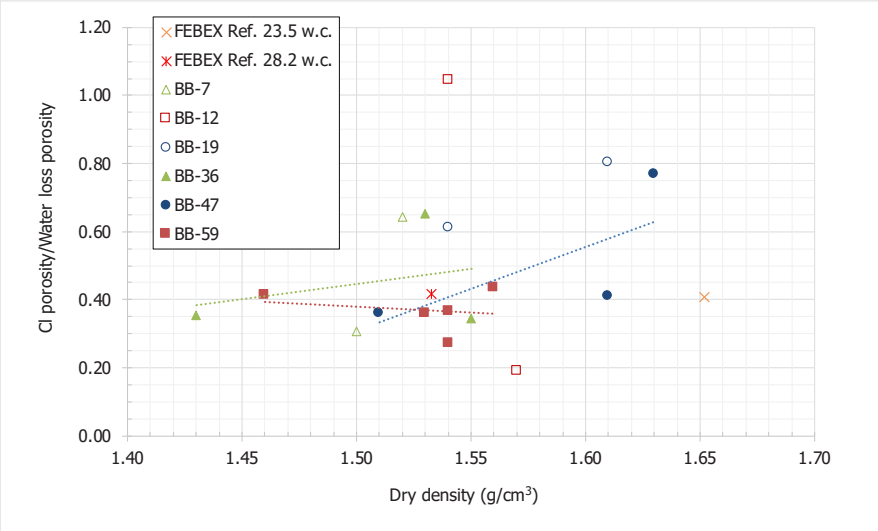

Fig. 255: Anion-accessible porosity fraction in the samples as a function of dry density

Tab. 50: Anion-accessible porosity fraction (Cl porosity/Water loss porosity) derived from chloride data of squeezed samples and leaching tests

Sample	**Sq. Pressure** (MPa)	**Bulk dry density** (g/cm^3)	**Grain density** (g/cm^3)	**Water content by heating** (% dry weight)	**Total (physical) porosity (densities)** (% vol.)	**Degree of satur-ation** (%)	**Water content at saturation** (% dry weight)	**Cl (leaching)** (mol/kg rock)	**Pore water Cl (borehole or squeezed sample) mol/L** (H_2O)	**Cl porosity** (% vol.)	**Cl porosity/ water loss porosity**
FEBEX Ref.	64	1.65	2.70	23.5	38.8	100	23.5	2.19×10^{-2}	2.28×10^{-1}	15.8	0.41
FEBEX Ref.	25	1.53	2.70	28.2	43.2	100	28.2	2.19×10^{-2}	1.86×10^{-1}	18.0	0.42
BB-7-4	25	1.52	2.70	28.1	43.7	98	28.8	1.25×10^{-2}	6.76×10^{-2}	28.1	0.64
BB-7-5	25	1.5	2.70	25.8	44.4	87	29.6	2.15×10^{-2}	2.37×10^{-1}	13.6	0.31
BB-12-10	25	1.54	2.70	25.8	43.0	92	27.9	7.16×10^{-3}	2.45×10^{-2}	44.9	1.05
BB-12-11	70	1.57	2.70	19.7	41.9	74	26.7	2.64×10^{-2}	5.21×10^{-1}	8.0	0.19
BB-19-1	25	1.54	2.70	27	43.0	97	27.9	7.22×10^{-3}	4.23×10^{-2}	26.3	0.61
BB-19-2	70	1.61	2.70	21.3	40.4	85	25.1	2.21×10^{-2}	1.10×10^{-1}	32.5	0.80
BB-36-1	20	1.43	2.70	31.6	47.0	96	32.9	2.86×10^{-3}	2.46×10^{-2}	16.6	0.35
BB-36-2	20	1.55	2.70	27.4	42.6	100	27.5	5.05×10^{-3}	5.35×10^{-2}	14.6	0.34
BB-36-3	30	1.53	2.70	27.9	43.3	99	28.3	1.04×10^{-2}	5.63×10^{-2}	28.2	0.65
BB-47-7	20	1.51	2.70	30.8	44.1	106	29.2	1.43×10^{-3}	1.35×10^{-2}	15.9	0.36
BB-47-8	30	1.61	2.70	23.7	40.4	95	25.1	4.64×10^{-3}	4.51×10^{-2}	16.6	0.41
BB-47-9	70	1.63	2.70	21.7	39.6	89	24.3	$6.32 \cdot 10^{-2}$	3.38×10^{-1}	30.5	0.77
BB-59-1	20	1.46	2.70	32.3	45.9	103	31.5	1.58×10^{-2}	1.21×10^{-1}	19.1	0.41
BB-59-2	30	1.54	2.70	27.7	43.0	99	27.9	2.08×10^{-2}	2.03×10^{-1}	15.8	0.37
BB-59-3	20	1.54	2.70	27.5	43.0	99	27.9	2.75×10^{-2}	3.61×10^{-1}	11.8	0.27
BB-59-4	30	1.53	2.70	27.2	43.3	96	28.3	3.48×10^{-2}	3.41×10^{-1}	15.6	0.36
BB-59-5	40	1.56	2.70	26.4	42.2	98	27.1	3.54×10^{-2}	3.01×10^{-1}	18.3	0.43

7.2 Cation exchange population

The nature of cations at interlayer sites are of primary importance because it is involved in the bentonite-pore water equilibrium, but also affects the balance of charge deficit at interlayer sites and plays a role in the macroscopic properties of the bentonite such as plasticity, swelling capacity and the rheological behaviour. Furthermore, the cation composition at interlayers acts as a powerful buffer to all the perturbing reactions in the bentonite barrier system, where equilibrium is reached very fast. Thus, the naturally present cation population (type and number of exchangeable cations) is always equilibrated with the surrounding pore water.

Apart from dissolution/precipitation processes, cation exchange reactions were observed in various laboratory and large scale tests (e.g. Fernández & Villar 2010, Kaufhold et al. 2017). Although experimental studies pointed to the importance of the exchange reactions in the mineral-pore water equilibrium, the experiments were always time-limited. The FEBEX in-situ test offered valuable results on the behaviour and modification of the cation exchange composition at real scale after an experimental period of 18 years.

The THC results indicated that the most significant changes observed in the FEBEX in-situ test after 5 and 18 years of experiment concerned the cation concentration at interlayer sites throughout the bentonite barrier and at the different interfaces (see Section 5.5.3).

At the bentonite-concrete contact (Section 36), a significant loss of magnesium at interlayer sites is observed, with increasing sodium, potassium and calcium concentrations, probably as a result of highly alkaline pore water diffusion from the shotcrete towards the bentonite. This process was also observed in samples taken after dismantling Heater #1, i.e., after 5 years of experiment (Section 7), especially at the granite contact. The accumulation of Mg in the pore water seems to be involved in the precipitation of Mg-silicates in various forms: brucite, trioctahedral smectite, chlorites, etc., as observed in this in-situ test (see also Fernández et al. 2017, Turrero & Cloet 2018), and in other laboratory tests (Fernández et al. 2013). It is interesting to note that this Mg loss at interlayer sites was observed also in the bulk mass of the bentonite blocks belonging to Section 36, meaning that more than a few mm of bentonite were affected by shotcrete-bentonite interactions. However, neoformed Mg-silicates were not detected in the samples from Section 36, except for chlorite (Fig. 107), Mg-rich montmorillonite (Fig. 107), and brucite by the FTIR band at 3'701 cm^{-1} (Fig. 62) in block BB-36-1 favoured possibly by higher alkaline pH conditions at the bentonite/shotcrete interface. In any case, this sample was also possibly affected by microbial activity indicated by the black halo in the analysed sample at contact with the granite interface, and a cellulose filter impregnated with a tracer, where Fe-sulphides were also found (Fig. 107).

In the non-heated sections, the cation exchange composition remained stable although a slight increase of magnesium with respect to calcium, and a slight decrease of sodium, were observed with respect to the reference sample, except at the granite interface where calcium was higher than magnesium. This pattern is similar to that observed after 5 years of experiment (dismantling Heater #1 in 2002), with exception of the inner blocks where the water saturation was not reached, where calcium remained higher than magnesium, and sodium was depleted.

At the bentonite/heater interface, cation exchange reactions may be enhanced by temperature and by dissolution/precipitation processes during the saturation of the bentonite barrier. In the FEBEX in-situ experiment the temperature was 100 °C but relatively little water was available (w.c. ≤ 18 % close to Heater #2 contact, full saturation not achieved). Nevertheless, modifications in the cation exchange population were observed. Exchangeable Mg and Ca increased towards Heater #2, while Na decreased, as observed both from the cation exchange composition and from

XRF analyses of the total solid phase (Fernández et al. 2018b submitted). Potassium slightly increased or remained constant at the Heater #2 contact from 2.9 meq/100g (reference) to a maximum 3.4 – 4.0 meq/100g. Mg was transported towards the heater together with other soluble ions, which at the same time explains the Mg accumulation near Heater #2. The possible presence of $MgCl^+$ ion pairings, which may enter the interlayer sites, may explain the higher mobility and higher amount of Mg than calcium at exchange sites, Ca being involved, in turn, in the precipitation of Ca-carbonates and Ca-sulphates at the heater contact, as observed in the mineralogy of some samples (Fig. 196, Fig. 197), and in the decrease of alkalinity values from aqueous extracts.

However, it should be taken into account that the determined Ca content at exchange sites was corrected from contents in soluble salts, which was not performed for Mg. Therefore, Mg content at interlayers may be overestimated because of its association with sulphates, carbonates (dolomite) and $MgCl_2$ soluble salts. The decrease of Na at exchange sites, on the other hand, is clear. Its initial value was 33 % in the reference bentonite and decreased to a 9 % at the Heater #2 interface. Exchangeable Na decreased from interlayer sites, but the sink of sodium could not be identified yet, probably because of the low amount and the respective detection limits of both XRF and XRD. However, high concentrations of sodium and magnesium were detected in pore water from bentonite blocks taken from the inner part of the bentonite barrier, closest to the Heater #2 contact. Therefore, the presence of NaCl and $MgCl_2$ salts due to evaporation at the heater interface needs to be taken into account. In addition, volatile organics acids were detected in pore water samples close to the heater and some association with sodium cations cannot be ruled out; e.g., as sodium oxalate and/or sodium acetate.

The amount of potassium at interlayer sites, which increased in all sections with respect to the reference sample, needs to be highlighted. This is especially true at the concrete contact, but at much lower quantities than the rest of cations, the maximum content is around 5 meq/100g. Thus, the option of an illitization of bentonite may be discarded because of the low increase of potassium concentration both at interlayers sites and in pore water.

7.3 Bentonite-ground water interactions: transport in compacted bentonite and dissolution/precipitation processes

The initial compacted bentonite had a water content of 14 % and a dry density of 1.60 g/cm^3 at the time of emplacement, it evolved towards full saturation during the 18 years of the experiment, except in blocks located at the heater contact, where the saturation degree was around 85 % (see Villar et al. 2016). During the infiltration of the surrounding granitic groundwater and the saturation process of the bentonite, the more soluble salts of the bentonite dissolved in pore water, and together with ions from the infiltrating granitic groundwater, were transported through the porous compacted bentonite by an advective (-diffusive) transport towards the inner part of the bentonite barrier.

This transport evolved following different profiles as a function of the conservative or non-conservative behaviour of the dissolved ions, modifying the pore water chemistry, the composition of the cations at exchange sites and the mineral equilibria of minerals, especially the more soluble accessory minerals, as shown in Section 7.1.1 and Section 7.2.

According to the evolution of the ion content in aqueous extracts (Section 5.5.8) and in the squeezed pore waters (Section 5.6), this transport had the following characteristics (Fig. 252, Fig. 164):

1. It depended on the evolution of water saturation of the bentonite.
2. It was time-dependent (Fig. 252, Fig. 164).
3. It depended on the ion involved in the system: conservative or non-conservative.
4. It depended on the heat flux or heat gradient.
5. Although almost full saturation is achieved, a homogenised distribution of ions was not observed, even in the non-heated areas.

Dissolution and precipitation processes were mostly restricted to partly soluble minerals, such as carbonates and sulphates, and depended on the pore water chemistry evolution through the bentonite barrier (see Section 7.1.1), except at the different interfaces (shotcrete/bentonite, metal/bentonite), where other type of mineral phases were found (see next Section 7.4).

Chlorides, present in the bentonite pore water, were transported with water (advective transport) and their content in the bentonite depended on the water gradient/suction of the bentonite rather than on the hydraulic pressure of the granitic rock (0.72 MPa). The pore water composition extracted by squeezing from bentonite blocks changed from Na-SO_4-Cl water-type and I ~ 0.04 M at the granitic interface to Na-Mg-Ca-Cl water-type and I ~ 0.41 M at the heater contact (being the reference Na-Mg-Cl-SO_4 water-type with I ~ 0.3 M). The maximum content of chlorides after 18 years of experiment was observed at 57 cm from the gallery axis; i.e., in the middle of the bentonite barrier in Section 59; or at the contact of Heater #2 (Sections S47 and S53), possibly precipitated due to heat (Fig. 209). After 5 years of experiment, the maximum amount of chlorides was observed at 79.5 cm from gallery axis, i.e., in the second bentonite ring.

Other non-conservative ions such as carbonates and sulphates were transported at a slower rate because they were involved in dissolution/precipitation processes in the bentonite. Precipitated Ca-carbonates and Ca-sulphates (probably as anhydrite due to the temperature at liner/Heater #2 contact: > 93 °C), were widely observed in all sections of the bentonite buffer by SEM (Section 5.3.5), but particularly at the liner/Heater #2 interface (Fig. 196, Fig. 197). Anhydrite was detected by FTIR in samples BB-53-6 and BB-53-9, and the pore waters are saturated with respect to these mineral phases. These mineral dissolution/precipitation processes modified the cation concentration at interlayer sites (Section 7.2).

Increase of silica may be due to either dissolution of clay minerals; or to the effect of heating that provokes the dissolution of SiO_2 with the subsequent re-precipitation in cooler areas and a possible cementation of pores. Increase of quartz and/or silica were observed by XRD (Fig. 187) and SEM (Fig. 198) in some samples, especially at the Heater #2 contact, such as in protrusion samples RV-42 green and BSH black; whereas dissolution of cristobalite and feldspars, were not detected. However, an increase of dissolved silica was detected in the aqueous extracts in the protrusion sample SR43 FV red, as indicated in Section 6.3. Dissolution of cristobalite (and zeolites) was found in the ABM experiment (Kaufhold et al. 2013), but it seems that this does not occur in the FEBEX in-situ test.

7.4 Mineralogical alteration

The reference FEBEX bentonite contains around 90 wt.-% of smectite clay minerals. Quartz (2 wt.-%), cristobalite (2 wt.-%), feldspars (3 wt.-%), and calcite (1 wt.-%), are the rest of the main minerals. The accessory minerals are in a proportion around 1 wt.-%: organic matter, chlorides and sulphates; and around 1 % for micas, chlorite, silicates, augite, hypersthene, hornblende, oxides (ilmenite, rutile, magnetite and Fe-oxides) and phosphates (apatite, xenotime and monazite) (Fernández 2004).

In the samples taken after dismantling Heater #1 in 2002 and Heater #2 in 2015, some neoformed mineral phases were detected mainly by XRD (Section 5.3.1) and SEM (Tab. 11, Tab. 37 and Appendix B) as described in the next sections.

7.4.1 Corrosion at bentonite/heater interface

In real repository conditions, after a transient period, the system is supposed to be water saturated, anoxic and slightly reducing. Under these conditions, it is expected that anoxic corrosion of canisters takes place.

In the FEBEX in-situ test, only 85 – 92 % of water saturation was achieved at the Heater #2 contact after running the experiment during 18 years. Furthermore, real anoxic conditions with dissolved O_2 values below 1×10^{-3} mmol/L were never reached, the minimum measured O_2 contents accounted for $\sim 2 \times 10^{-2}$ mmol/L after 1.5 years of switching on the heaters; i.e. the system was not gas-tight, and there was an inflow of O_2 during the experiment over time (Fernández 2018). A corrosion layer on the surface of the liner/Heater #2 was detected with maximum thicknesses of 180 – 350 μm (Wersin & Kober 2017). In addition, during dismantling, the bentonite close to the liner/Heater #2 contact presented different colours: pale-yellowish (reference), brown-reddish, green and black, which implies different redox stages, the latter two being representative of anoxic/anaerobic conditions with presence of Fe(II). Therefore, although most of the corrosion products resulted from oxic corrosion, localized or partially reduced conditions were achieved in the bentonite barrier.

Metal corrosion was observed by an increase of the Fe-content in bentonite samples taken from the first mm from the liner/Heater #2 contact, with values increasing from 3.1 wt.-% to 6 – 19 % wt.-%, and the presence of corrosion products (newly formed Fe-phases) observed in some samples. A range of Fe-oxyhydroxides were detected, the most prominent being goethite, hematite and magnetite (Tab. 36, Fig. 194).

The redox evolution in the bentonite buffer could be described on the corrosion products detected, because metal corrosion is one of the main processes affecting the redox state (Duro et al. 2014). However, the gas and water evolution also allow describing the redox system inside the barrier (Fernández 2018). The initial stages of the FEBEX in-situ test occurred at oxic conditions due to the residual air in the unsaturated bentonite material, and the gaps between bentonite blocks and the liner/Heater #2. The corrosion of the C-steel Heater #2 and other metals produced oxygen depletion and, as a consequence, the precipitation of Fe(III) oxides and hydroxides, such as ferrihydrite ($Fe(OH)_3$(s)), goethite (FeOOH (s)), and hematite (Fe_2O_3 (s)), which were observed by different techniques (XRD, FTIR and TG-DSC). Thermodynamically, hematite is the stable Fe(III) oxide, followed by goethite and ferrihydrite or hydrous ferric oxides. However, goethite and ferrihydrite have faster formation kinetics than hematite in presence of oxygen and can prevail as metastable solid phases for long periods of time.

After oxygen consumption, metals corrode in the absence of oxygen, under anoxic conditions. Since Fe(s) is thermodynamically unstable in water, in absence of any other oxidant, metals

corrode through water reduction, with subsequent hydrogen generation and the formation of ferrous hydroxide, which evolves towards the formation of magnetite, in the so-called Schikorr reaction (e.g. Wersin et al. 2007). Magnetite is the reduced iron oxide corrosion product detected in the samples close to the liner/Heater #2 contact, hydrogen is also detected and monitored over the 18 years of the FEBEX in-situ test (Fernández 2018).

However, the presence of hydrogen, methane and other reduced saturated hydrocarbons when oxygen was present at the beginning of the test and during the entire test period, because the set-up was not gas-tight, indicated another possible reaction. This reaction is related with to corrosion and hydrolysis of carbon-containing steels and metal carbides, liner and heater through a similar Fischer-Tropsch (FT) synthesis reaction using iron as catalyst, yielding a mixture of H_2, CO, CO_2, alkanes, alkenes and oxygenated organic compounds (Wieland & Hummel 2015, Cataldo 2003). This reaction was corroborated by the detection of these compounds over the test period, and because the cross plots of $\delta^{13}C$-CH_4 versus $\delta^{13}C$-CO_2 indicated methane formation via methyl type reduction, rather than by CO_2 reduction (Fernández 2018).

The presence of reduced saturated hydrocarbons and oxidized carboxylic acids implies reversible states of redox-dependent metastable equilibria regulated by hydration and oxidation; i.e. controlled by hydrogen and oxygen fugacities. Thermodynamically, both reduced and oxidized hydrocarbons are in partial equilibrium with bi-/carbonates under highly reduced oxidation states, below those of ion-oxide assemblage and even at the verge of water stability (Wieland & Hummel 2015). Therefore, oxygen, mineral assemblages and water play an integral role in regulating the redox state and activities of all species involved, by acting as oxidizing agents (terminal electron acceptors, TEAs) and a sink for generated H_2 through redox-dependent processes, such as: a) sulphate reduction to H_2S and pyrite b) reduction of Fe-oxides (e.g., hematite and goethite) to magnetite and siderite, c) pyrite to siderite, and d) reduction of Fe(III)-bearing phyllosilicates to saponite and/or chlorite, for example.

Because the stability of aqueous low molecular weight of n-alkanes and other hydrocarbons is highly sensitive to the redox state (Seewald 2001a,b; Shock 1988), they were degraded by oxidation depending on the redox buffer in the system. The continuous oxygen inflow acted as a self-feedback of oxic C-steel corrosion producing iron (III) oxides and hydrocarbons, the last ones being in turn oxidized, and generating reducing conditions and oxygen consumption. H_2 generated in the process was consumed in further biotic and abiotic reactions (Fernández 2018). This is consistent with the instability of Fe-oxyhydroxides relative to siderite, as well as the reduction of sulphates from pore water to sulphides. Indeed, apart from Fe-oxyhydroxides, other types of corrosion products, such as siderite (Fig. 195) and sulphides (Fig. 197), were detected by XRD and SEM analyses (Tab. 36, Tab. 37). These point to localized reducing conditions in bentonite pore waters at the liner/Heater #2-bentonite interface with non-negligible concentrations of sulphides and carbonates (> 1 mol/L), that precipitate the dissolved Fe^{2+} generated during corrosion and iron alteration. A decrease of the alkalinity of the pore waters was observed as a function of the Heater #2 contact both in aqueous leaching tests (Tab. 43) and squeezed pore waters (Tab. 29), indicating carbonate precipitation. Furthermore, the hematite (and goethite) generated during oxic corrosion was partially reduced by the organic compounds producing magnetite and dissolved Fe(II) ions, which may have diffused away. This is probably the reason for the red corroded bentonite surrounded by green halos, which was observed in the bentonite samples taken during dismantling operations, as well as the presence of both hematite (and/or goethite) and magnetite iron mineral phases; i.e., Fe(III) and Fe(II) mineral phases.

The oxygenated organic species found in the aqueous extracts and squeezed pore waters is an indicator of n-alkane oxidation by oxidizing agents and/or water. Carboxylic acids, such as acetate, formate and oxalate were dissolved in the pore water acting as a sink of O_2 and H_2

(Tab. 29, Tab. 43). The rate of hydrocarbon oxidation is controlled by oxygen fugacities at temperatures higher than 88 °C and by microbial activity at lower temperatures (Shock 1988). In absence of reduced saturated hydrocarbons produced by the FT synthesis, the presence of both siderite and iron(II) sulphides should indicate highly reducing conditions or the presence of sulphate reducing bacteria (SRB), that would reduce sulphates from the pore water to sulphides, as the FEBEX bentonite does not contain sulphides (Fernández et al. 2004). However, the effective abiotic or thermo-chemical reduction of sulphates is only observed at high temperatures (> 200 – 250 °C), the reaction is too slow at low temperatures unless it is catalysed by sulphate-reducing bacteria (SRB), which have an optimum growth at 80 – 95 °C (e.g., Libert et al. 2011). At 90 °C, the extrapolated half-life of sulphate reduction is ~ 210'000 years (Truche et al. 2009). Although, some SRB could be cultivated in some bentonite blocks at different sections from the FEBEX in-situ test, the presence of microorganisms at temperatures higher than 70 °C and close to the Heater #2 contact has not been proved (Bengtsson et al. 2017).

Due to the high chloride contents in pore water at the Heater #2 contact (Fig. 209), the precipitation of GR-Cl-green rusts and other chloride salts was expected, and were detected by SEM (Tab. 37). Cl-bearing Fe(III) oxyhydroxide (akageneite) was detected in other samples analysed (Wersin & Kober 2017). In turn, the high salinity of the pore water close to the Heater #2 interface favours corrosion processes. The corrosion products detected may imply an increase of volume and, hence, an increase of stress.

The presence of siderite, sulphides and magnetite indicate that reduced Fe(II) was at least partly preserved at the end of the test. This was corroborated by the Fe(III)/Fe(II) contents in the bentonite samples. Although most of the Fe was Fe(III), the Fe(II) content of samples close to the Heater #2 (protrusion samples) increased from 7 w.t. % to 9 – 18 w.t. % (Tab. 39), which is probably reflected by the greenish colour observed in some of the samples. From the results, the extent of line/Heater #2 corrosion was limited in time due to possible passivation and because the hydrocarbon oxidation rate decreased over time due to the increase of hydrogen and consumption of oxygen (Fernández 2018). Dissolved Fe(II) was consumed in different precipitation reactions (siderite, sulphides, etc.), preventing the diffusion of Fe(II) through the outer parts of the bentonite barrier. Indeed, the corrosion processes close to liner/Heater #2 were quite localized affecting the bentonite in the highest altered zone to a maximum thickness of 200 mm, as observed by the blueish-greenish colour at the frontal part of Heater #2. The estimated depths of corrosion of the liner/Heater #2 and bentonite enriched in iron were 109 – 191 μm and between 0 to 30 mm, respectively (Wersin & Kober 2017).

After dismantling Heater #1 in 2002 (after 5 years of experiment), the corrosion processes were of a minor level. It was a uniform corrosion type, affecting 20 μm of the Heater #1 surface and between 130 – 200 μm of the liner surface (Madina & Azkárate 2004, Madina 2003). The bentonite in contact with Heater #1 was practically non-affected by iron enrichment, except for a zone located at the bottom part of Heater #1 (Fig. 212). In addition, no large protrusions where found after dismantling Heater #1, although the bentonite had pushed through the liner holes (Fig. 212).

The BS-31-26 bentonite sample taken at close contact with the back part of Heater #1 showed a black-brownish colour (Fig. 214). Iron sulphides (pyrrhotite), calcite, siderite, magnetite and hematite were detected in this sample. In the case of the samples taken inside the holes of the liner, no modifications were observed in the analyses, except in the smectite signals as discussed in Section 7.5.1.

XPS analyses of bentonite around the corroded SH-SDI-1 fisurometer corroborated the presence of both inorganic and organic carbon inside the bentonite as a consequence of corrosion of

C-containing steels. Oxidized hydrocarbons, such as alcohols and ethers (C-O), were found in dark-greenish and reddish samples, and carboxyls (C = O) in the greenish sample. Carbides (C = C) were found in the reddish sample (see Section 6.4.1), which supports the dissolution of carbides present in the C-steels during the corrosion process through a similar Fisher-Tropsch synthesis, generating reduced saturated hydrocarbons (alkanes, alkenes, ...), and oxidized non-volatile hydrocarbons (carboxylic acids, alcohols, aldehydes).

7.4.2 Bentonite profile affected only by granitic groundwater hydration

In the non-heated Section 59, i.e., only subjected to hydration, no significant neoformed minerals were detected. Ca-carbonates, dolomite, Fe-carbonates, Fe oxy-hydroxides, Ca-sulphates and Ba(Sr)-sulphates were observed in different samples in one radius along the bentonite barrier (Tab. 11). Only some neoformed clay mineral phases precipitated in small pores, mainly Mg-phyllosilicates (palygorskite and sepiolite), Mg_3OH vibrations, such as in trioctahedral structures (brucite, saponite, ...), and kaolinite were found in some specific points by FTIR, as discussed in Section 7.5.3. The high Mg content in pore waters and the high pH of the infiltrating granitic groundwater (pH 9 and Eh -200 mV) favoured the neoformation of magnesian clay minerals, but the driving force for those mineral clay transformations should be better analysed.

In the bentonite samples taken from Section 12 (non-heated section) after dismantling Heater #1 in 2002, no neoformed mineral phases were observed by XRD analyses (other techniques were not used).

7.4.3 Bentonite/concrete interface

The different composition of the concrete plugs used in both operational phases, i.e., before (concrete type) and after (shotcrete type) the dismantling of Heater #1 in 2002 (Tab. 2) should be kept in mind. This could influence the neoformed mineral phases detected after both dismantling operations in 2002 and 2015, respectively. Concrete materials in contact with groundwater are progressively degraded, especially when the pH is lower than 12. A complete decomposition of the calcium silicate hydrate (CSH) compounds occurs at pH < 9. Factors increasing concrete degradation are: a) lixiviation, b) CO_2 attack, and c) chemical attack by sulphate, chloride and magnesium (Taylor 1997).

The concrete pore water solution is highly alkaline, so when it interacts with bentonite pore water and/or granite groundwater, a leaching process starts by removing alkalis (Na+ and K+), followed by portlandite dissolution and subsequently by the leaching of calcium from CSH silicates (e.g. Soler & Mäder 2007). During the degradation process, chemical reactions of dissolution/ precipitation and a transport of mass by diffusion from the concrete occurs (Taylor 1997, Alonso et al. 2017).

After dismantling Heater #1 (5 years experimental period), gypsum, aragonite, dolomite, magnesite and portlandite (Ca(OH)2), were detected from bentonite blocks at the concrete/ bentonite interface in Section 7.

After dismantling Heater #2 (18 years experimental period), portlandite, ettringite, calcite, dolomite magnesite, aragonite, Ca-sulphates, Fe-oxides, Fe-carbonates and zeolites were detected from bentonite blocks at the shotcrete/bentonite interface in Section 36.

The presence of portlandite implies a pH higher than 12.5. At lower pH values portlandite dissolves reacting with sulphate ions from the pore water to form gypsum, which reacts with Al

(probably from smectite dissolution at alkaline interface) to form ettringite. The presence of portlandite and ettringite indicated a transport of calcium and highly alkaline pH solutions from the concrete towards the bentonite. This was corroborated by the decrease in Section 7 and Section 36 of Mg at smectite interlayer sites, because Ca and Na from concrete pore water displaced Mg, which was involved in two types of reactions: a) Mg diffusion into the concrete or b) neoformation of Mg-mineral phases (brucite, trioctahedral Mg-clay minerals) or M-S-H phases in the bentonite (Alonso et al. 2017, Fernández et al. 2017). The diffusion of calcium from concrete towards bentonite also implies the precipitation of carbonates as calcite, aragonite, dolomite and magnesite, after reaction with the bicarbonates from bentonite pore water and granite groundwater.

The diffusion of chlorides (5 cm) and sulphates (a few mm) from bentonite to concrete, was observed both by the decrease of Cl and sulphate from the bentonite pore water in Section 7 and Section 36 (see aqueous extracts (Fig. 159, Fig. 160) and squeezed pore waters (Fig. 252)); as well as by the precipitation of Friedel's salts and ettringite (after dissolution of portlandite) in the concrete (Alonso et al. 2017).

Both a decrease of Mg at interlayer sites, and a decrease of chlorides and sulphates from the bentonite pore water were detected in the whole mass of the bentonite blocks from Section 7 and Section 36 (12.5 cm depth per bentonite block). Therefore, the influence of the concrete/shotcrete degradation implies more than 35 – 40 mm of the bentonite barrier, as reported in Fernandez et al. (2017), or 2 cm in Turrero & Cloet (2018). However, Mg-silicates, ettringite and portlandite were not detected in the bulk mass, but only in some mm of the shotcrete/bentonite interface (see Section 7.5.4). This implies that the high alkaline concrete(shotcrete) pore water front (rich in Ca, K and Na ions) advanced a few tens of cm inside the bentonite, but the bentonite buffered the high alkaline pH, avoiding smectite alteration (e.g., Mg-smectite and zeolites are neoformed at pH > 9.5). Other mineral dissolution-precipitation and cation exchange reactions (scale analysed being < 12.5 cm from the shotcrete contact) did take place. Savage (2014) estimated the diffusion of the concrete pH plume alteration front to about 20 cm.

It is interesting to note that the Mg depletion at interlayer sites (increasing Ca and Na) was lower in the inner parts of the bentonite buffer (Fig. 130, Fig. 131) than towards the granite interface (the average radius of highest impact was about 40 cm from the gallery axis per bentonite slice radius), where diluted groundwater of a high bicarbonate content was infiltrating, which hydrated and degraded the concrete/shotcrete plug. Therefore, both the saturation degree of bentonite and concrete hydration play a role in the degradation process (apart from the porosity of both types of materials). This was observed at both dismantling operations in 2002 (Section 7) and 2015 (Section 36).

7.5 Smectite structural stability

One of the long-term quality requirements of a functioning bentonite buffer is buffering possible alteration/deterioration processes which affect the smectite's stability for extensive periods of time. Processes which may deteriorate isolation properties of bentonite are (Meunier et al. 1998):

- Smectite dissolution (e.g. Rozalén et al. 2008)
- Smectite to illite transformation (e.g., Ionue et al. 1988)
- Formation of mixed-layer structures: illite/smectite (I/S ML), chlorite/smectite (Chl/S ML), etc.

- Formation of other types of clay minerals: chlorites, serpentines, nontronites, magnesium clay minerals (saponites, palygorskites, sepiolites), etc.

Experimental studies from Eberl (1978) showed that different families of clay minerals can be formed hydrothermally from dioctahedral smectite by making simple changes in hydrothermal run conditions, including changes in the initial interlayer and solution chemistry. Dioctahedral smectite will react under the proper hydrothermal conditions to yield one of four structural trends: the mica, chlorite, pyrophyllite or kaolinite trend. The trend that evolves depends on the temperature, time, interlayer cation and salt concentration in the run solution. Generally:

- All the alkali and alkaline earth interlayer cations yield the mica trend:

  Smectite → Mica/Smectite → Mica

  Low-charge montmorillonite + K+ (mica) → high-charge montmorillonite + illite + quartz

- Montmorillonite will follow the chlorite trend if the run solution contains Mg^{2+}:

  Low-charge montmorillonite + quartz-saturated solution → high-charge beidellitic smectite + Mg-trioctahedral smectite (saponite) + quartz-oversaturated solution

  Low-charge montmorillonite + Na-Ca-solutions → vermiculite + Mg-rich smectite + quartz

  High-charge beidellite + saponite + K+ → ordered I-S (Al-rich illite) + chlorite + quartz (via illite-beidellite mixed layers and corrensite)

  Montmorillonite → Chlorite/Smectite → Chlorite

  High-charge montmorillonite layers → illite + chlorite + quartz

- The pyrophyllite and kaolinite trends are produced from Ca-montmorillonite if the run solution contains $A1^{3+}$:

  Montmorillonite → high charge smectite + kaolinite (or pyrophyllite) + quartz

The general direction in a reaction series is towards the development of a collapsed structure with increasing run time and temperature (Eberl 1978). For the mica and chlorite trends, the formation of this structure probably results from the development of a highly negative charge on the 2:1 layers which leads either to a dehydration of the interlayer cation to form a mica-like interlayer, or to a loss of protons from the hydrated interlayer cation to form a hydroxide interlayer. Al^{3+} must enter into the hydroxide interlayer as well to produce the net positive charge necessary for electrical neutrality. The negative charge on the 2:1 layers arises most likely from the substitution of Al^{3+} for Si^{4+} in the tetrahedral sheets, with charge balance achieved by an increase in interlayer cations. Al^{3+} and the interlayer cations for this reaction come from the breakdown of some of the montmorillonite, a reaction which also leads to the formation of quartz and kaolinite (or pyrophyllite).

If montmorillonite is the sole source of Al on the water/smectite reaction, the excess Mg and Si released by a dioctahedral smectite reaction is either incorporated in secondary Al-poor phases or remains in the aqueous phase. Indeed, experimental alteration of montmorillonite indicates that these components concentrate in by-products of the reaction as quartz, unidentified non-crystalline (Al, Mg) (OH) phases and chlorite (Howard & Roy 1985, Whitney & Northrop 1988). Mg-smectites are the most likely Mg-phyllosilicates to be formed in the 100 – 200 °C thermal range and may be considered as a precursor in the overall reaction of chloritization which occurs at higher temperature (Ionue & Utada 1991). High Al concentration in the bulk systems decreases

the reaction rates, since Al is well known to be an inhibitor of dissolution of aluminosilicates (Oelkers et al. 1994).

The bentonite samples from the FEBEX in-situ test analysed after the first dismantling of Heater #1 (5 years of experiment) and the dismantling of Heater #2 (18 years of experiment) indicate that the bulk mass of bentonite (homogenised samples from a block) maintained its smectite content over time. This was confirmed by XRD, FTIR, TG-DSC, TEM and SEM analyses. The smectite phases were made up of a R0 illite/smectite mixed-layer with about 5 – 23 % of illite layers (the reference FEBEX sample being a R0 I/S ML with 7 – 15 % of illite layers, Fernández 2004). FTIR spectra from the retrieved bulk samples reveal than the smectite phases corresponded to dioctahedral smectites, Al-rich at octahedral sheets. Furthermore, TG-DCS curves indicate that this dioctahedral smectite has most of the OH-groups at cis-vacant positions with divalent cations at interlayer sites. Moreover, the smectite, with contents higher than 87 – 90 wt.-%, maintained its main physicochemical properties unaltered: CEC (~ 98 m^2/g), layer charge (~ 0.37 eq/hfu), zeta-potential (-35 mV), total (~ 590 m^2/g) and external (~ 59.5 m^2/g) surface area and water adsorption capacity.

However, analyses from some bentonite blocks in Section 36, point analyses from bentonite blocks in Section 59 (neoformed mineral phases in small pores), and samples analysed at close contact with Heater #2 (BMS and protrusion samples) reveal some type of smectite alteration.

7.5.1 Mg and Fe(II) accumulation at heater interface

In samples analysed at close contact with the liner/Heater #2, an increase in Fe(II) and Mg contents is detected. It is known that the thermodynamics and kinetics of possible alteration processes of bentonite depend on different factors (fluid composition, temperature, pH, and initial smectite composition).

In most laboratory (Fernandez & Villar 2010) and large-scale (Karnland et al. 2007, 2009) tests, Mg accumulation is found at the metal/bentonite interface. The high amount of magnesium may be indicative of: a) the dissolution of dioctahedral smectite clay mineral particles with the corresponding structural changes, b) a decrease of Mg at interlayer sites and/or c) Mg-enriched pore waters originating from groundwater inflow through the clay barrier towards the heater interface over time (or mixtures of those). In the present study, the largest increase of MgO (about 6 mass %) was found at the contact with Heater #2, which is correlated with an increase of Mg content both at exchange sites and in pore water (Fig. 209, Fig. 210). In addition, formation of trioctahedral clay minerals or domains was also identified, as observed in other large scale tests (Kaufhold et al. 2013, Kaufhold et al. 2017, Svensson 2015). In contrast, the presence of a Mg-mineral (brucite), a Fe-rich chlorite, and a modification in the dehydroxylation temperature of clay mineral particles is exclusive of the FEBEX in-situ test.

Smectites can be transformed into other minerals as soon as the chemical composition allows precipitating a more stable phase. The addition of K, as an example, leads to the formation of illite, which is much more stable than diocthaedral smectites. This conversion will, consequently, go on as long as K is present and as long as the conditions are suitable for smectite destabilisation (high T and/or high pH). The addition of Mg to the system will lead to formation of trioctahedral minerals and/or domains which are slightly more stable than dioctahedral smectites.

A pH perturbation may be responsible for the presence of a transformed clay mineral layer showing systematic dissolution of primary clay minerals (S, I/S ML and/or even illite). If the smectite structure becomes unstable, it begins to dissolve and secondary mineral phases, such as amorphous silica, pyrite, siderite, illite, etc. are neoformed, depending on the specific

experimental conditions (e.g., Bourdelle et al. 2014, Savage 2014, Kumpulainen et al. 2010, Wersin et al. 2007 and references herein). Zeolites were found in the ABM experiment (Kaufhold et al. 2017) but not in the FEBEX in-situ test; indicating pH values < 11, probably due to carbonate buffering. Possible smectite dissolution also buffers the pH. At pH > 10 smectite becomes more soluble along with increased SiO_2 solubility. Possible smectite dissolution would decrease the pH, and dissolved silica would precipitate at the ends of smectite stacks in lower pH environments, collapsing pores.

In the case of an influx of iron, the system evolves with the precipitation of either non-swelling silicates: Fe-serpentine, berthierine or Fe-silicates (e.g., Lantenois et al. 2005, Jodin-Caumon et al. 2012, Perronnet et al. 2008, Kaufhold et al. 2015) or iron-rich smectite: Fe-montmorillonite or nontronite (e.g., Guillaume et al. 2004, Charpentier et al. 2006, Wilson et al. 2006a,b). Fe-bearing chlorite or trioctahedral saponite are described as neoformed phases at higher temperatures (> 150 °C) (Wersin & Mettler 2006, Wersin et al. 2007).

The thermodynamic modelling of Wilson et al. (2006a,b), analysed the Fe-rich phyllosilicate mineral stability at the canister–backfill interface. It suggests that according to the logarithmic activity diagrams (for the system Al_2O_3–FeO–Fe_2O_3–MgO–Na_2O–SiO_2–H_2O), and if pore waters were supersaturated with respect to magnetite, Fe(II)-rich saponite would be the most likely montmorillonite alteration product when fO_2(g) values are significantly lower than the magnetite–hematite equilibrium. But if fO_2(g) exceeds the magnetite–hematite equilibrium, and solutions are saturated with respect to magnetite, berthierine would be more stable than smectite minerals, evolving towards chlorite as a long-term alteration product (Savage et al. 2010). Berthierine was absent in the FEBEX in-situ test, but Fe(II)-rich chlorite was found.

The presence of Fe-rich chlorite is expected at temperatures higher than 150 °C (Wersin et al. 2007). However, chlorite was detected both in protrusion samples and in the samples taken at the frontal part of the Heater #2, where temperatures were lower than 100 °C. From the TEM analyses (Tab. 38), the chlorite detected at the frontal part of the Heater #2 can be classified as a chamosite (Fe-rich chlorite); the total Fe(II) content is equal to 93 % (Section 6.2). As described above, because the reduced saturated hydrocarbons generated during C-steel heater corrosion were oxidized by oxygen and other oxidizing agents, Fe(III)-bearing FEBEX smectite could be reduced producing a Fe(II)-rich clay mineral. The final products found were chlorite and saponite, which were observed in different zones, probably depending on local conditions, such as lower temperatures and/or higher depletions in fO_2(g). It is interesting to note that trioctahedral smectites were only identified in the vicinity of the corroding iron in other large experiments, while it was absent when the heaters were made of copper (Svensson 2015).

The modelling results of Marty et al. (2010) describe the transformation of the initial MX-80 montmorillonite due to chemical perturbation induced by the corrosion of steel overpacks: Fe^{2+} solutions, low redox potential and high pH values. Montmorillonite is transformed by a partial illitization, saponification and vermiculitization. Part of the released Fe^{2+} ions are incorporated into precipitated chlorite and saponite, whereas formation of magnetite, greenalite, chrysotile, laumontite, chabazite and phillipsite are also identified in these numerical simulations. Zeolites and serpentines were not found in the FEBEX in-situ test, except zeolites in close contact with the shotcrete interface.

7.5.2 Possible mechanisms for smectite alteration

Giving a definition of bentonite alteration and its extent is complex because a large number of mineralogical alteration fronts and possible pathways may exist. In the context of high-level nuclear waste repositories, the most important mechanisms are related to the transformation of montmorillonite to non-expandable or less-expandable clay minerals. The transformation of smectite to illite (illitization) or dioctahedral vermiculite, dV (vermiculitization) (and/or to beidellite and then to illite) through the formation of mixed layered structures, MLM (disordered or ordered, expansible or non-expansible diV/S ML or I/S ML), has been the main research focus for years (e.g., Mosser-Ruck et al. 2010). Indeed, controversy exists over whether montmorillonite transformation forms a continuous solid solution or mixed layers (Meunier 2005).

Most of the different reaction mechanisms for smectite alteration described in literature are related to an illitization process (e.g., Meunier et al. 2000):

a) Solid-State Transformation (SST), where the tetrahedral sheets of some montmorillonite layers are modified by the replacement of Si by Al, increasing the total layer charge because a tetrahedral charge is added to the original octahedral one, and producing high-charge/low-charge (bi-substituted) layers similar to vermiculite ones (diV/S ML). Note that the formation of illite layers from high-charge vermiculite will not occur unless the charge is compensated by available K^+ (> 200 mg/L) (Eberl & Hower 1976, Eberl 1978).

b) Dissolution and Crystallization (DC) without or with Ostwald ripening, where quartz precipitates as some montmorillonite layers are dissolved. The chemical balance of this reaction implies that the Mg and Si released is either incorporated in secondary Al-poor phases or remains in the aqueous phase. The crystallization of an Mg-rich component is supposed to precipitate in the interlayer or as a separate phyllosilicate phase (brucite-like sheets: (Al, Mg) (OH)-phases, or Mg-rich trioctahedral smectite (Beaufort et al. 2001):

   - Low-charge montmorillonite (10 mont. units) + Na-Ca solutions → vermiculite (high-charge, octa- and tetrahedrally substituted, only partly expandable) + Mg-rich smectite (3 saponite units) + quartz
   - Low-charge montmorillonite + Qz -saturated solution → high-charge beidellitic smectite (tetrahedral substitution) + Mg-trioctahedral smectite + quartz-oversaturated solution

Beidellite (or vermiculite) and saponite, may be transformed into an Al, Fe-rich illite and Mg-Fe-rich chlorite via illite-beidellite mixed layers and corrensite; Mg-phyllosilicates are considered a precursor of chlorite (chloritization) at higher temperatures (Ionue & Utada 1991).

The smectite alteration mechanisms depend on temperature and other variables, the stability of smectites is constrained not only by temperature and pH but also by the ionic strength of the solution and its chemical composition (e.g, Zysset & Schindler 1996, Herbert et al. 2004). However, the equilibrium of clay minerals is a question still open to debate (Blanc et al. 2013).

Karnland et al. (2007) found that montmorillonite dissolution in contact with high pH fluids generally is congruent leading to an increased Al/Si ratio, an increase in tetrahedral charge and the formation of beidellite. Depending on the availability of K^+, high-charge smectite would be further converted to illite (e.g., Bauer & Velde 1999). In the FEBEX in-situ test, no increase in potassium content is observed neither in the solid phase (XRF and exchangeable cations) nor in the pore water solutions, so a further illitization process is not expected or will be insignificant.

The presence of two newly-formed Mg phases in the FEBEX in-situ test, brucite and saponite, is important when analysing the reactions taking place. In a dissolution-precipitation transformation, quartz precipitates as some montmorillonite layers are dissolved. The chemical balance of this reaction also implies the crystallization of a Mg-rich component that was supposed to precipitate in the interlayer (Howard & Roy 1985), or as a separate phyllosilicate phase (Meunier et al. 1998). Brucite was unambiguously proven by different labs by different methods (XRD, FTIR, TG-DTA-DSC), which proves that a solid-state reaction is not the only reason for Mg accumulation. Dissolution/crystallization reactions are involved in montmorillonite transformation, apart from the advective-diffusion process of soluble salts towards Heater #2 during saturation of the bentonite barrier.

However, both dissolution/precipitation and solid-state transformations seem to be involved in the FEBEX in-situ test. The solid-state transformation may be inferred by the TEM-EDX-studies, which allows to distinguish reaction paths from low-charge (LC) montmorillonite particles to high-charge (HC) beidellite or illite, as well as I/S-ML and diV/S ML in the sense of Środon et al. (1992) and Nguyen-Thanh et al. (2010). The diV/S ML are characterised by a K- charge-deficiency with vermiculite layer charge ranging from high charges (HC) of 0.9 eq/h.u.c. to low charges (LC) of 0.65 eq/h.u.c. The trends of the possible reactions involved were determined by using graphical projections in the MR^{3+}-$2R^{3+}$-$3R^{2+}$ system (Sections 5.3.4 and 6.1.5). In Fig. 208 it is observed that most of the samples belongs to the stability field of a low-medium layer charge montmorillonite, as the reference FEBEX bentonite, but in samples close to the liner/Heater #2 contact the layer charge increased, as well as increasing the tetrahedral charge and the octahedral magnesium content. Although some uncertainties arise when Structural formula are calculated (because Mg content may be both at octahedral and interlayer sites, and because the speciation of Fe as Fe(III) and Fe(II) is unknown); these changes were also observed, but to a lower degree, when the Σ_{oct} cations is not fixed at 2.0 and Fe is considered as Fe(II) in the chemical formula calculation (see Tab. 38). In this work, cation homoionization pre-treatments of the samples were not performed in order to avoid alteration of possible neorformed clay minerals.

The most discussed smectite solid-state alteration mechanism is the development of high charge expandable layers replacing the low-charge layers of the starting montmorillonite. The formation of high-charge layers is linked to an increase in the tetrahedral charge, the altered samples having a mixed montmorillonite-vermiculite/beidellite composition. The development of a highly negative charge on the 2:1 layers leads either to a dehydration of the interlayer cation, or to a loss of protons from the hydrated interlayer cation to form a hydroxide interlayer. Al^{3+} must move into tetrahedral sheets to produce the net positive charge necessary for electrical neutrality, balanced by an increase in interlayer cations (Eberl 1978, Beaufort et al. 2001). Total layer charge increases because a tetrahedral charge is added to the original octahedral, when Si is replaced by Al (Meunier et al. 2000). This is in agreement with the TG-DSC signals, which indicate the presence of an additional dehydroxylation peak at a lower temperature, which may point to smectite particles with tetrahedral charge substitutions apart from the original ones with octahedral charge substitutions (Fig. 191, Fig. 192), as noted in Section 6.1.3. The dehydration of interlayer cations is hindered due to the presence of divalent cations (especially Ca) with a high hydration energy. Thus, this solid-state transformation produces high-charge/low-charge bi-substituted layers similar to vermiculite ones, due to the high content of magnesium at the liner/Heater #2 contact.

However, the oxidation state of Fe in the octahedral sheets affects the layer charge, and the reduction of structural Fe(III) to Fe(II) implies an increase of this parameter. The crystal structure must change in order to accommodate the larger size of Fe(II) and the increased negative charge. Some of the Fe atoms migrate from cis- to trans-sites in the reduced state. This migration is necessarily accompanied by a dehydroxylation reaction due to the protonation of OH groups initially coordinated to Fe. Hadi et al. (2013) also observed the dehydroxylation of the structure

during Fe(III) to Fe(II) reduction. Such a structural modification would result in the formation of small trioctahedral Fe(II) clusters or domains of separated clusters of vacancies or defect cavities (Manceau et al. 2000, Komadel et al. 2006). Here, it should be taken into account that saponite is a tetrahedrally-charged trioctahedral smectite, with the redox state of Fe equal to Fe(II); most chlorites contain Fe(II).

Because FEBEX bentonite is a cv dioctahedral montmorillonite, the presence of two dehydroxylation peaks in the TG-DSC signals, may indicate a solid-state transformation as well. Trans-vacant (tv) and cis-vacant (cv) polymorphs of smectites may be distinguished by studying different cation substitutions in octahedral and tetrahedral sheets and in the interlayer. In a trans-vacant structure of 2:1 dioctahedral smectites, all cations occupy only the M2 (cis) octahedral sites, which implies that within the vacant M1 (trans) site two hydroxyl groups are opposite to each other (hence trans-vacant). In the cis-vacant structure, the cations occupy two non-equivalent octahedral sites M1 and M2 with the hydroxyl groups in a cis (M2) position (Tsipursky & Drits 1984). The cis-vacant configuration dehydroxylates at a higher temperature compared to the trans-vacant configuration. The cv/tv proportion in the interstratifications can be determined by X-Ray diffraction and thermal analysis. Al-rich smectites are cis-vacant, whereas those of high charge and greater tetrahedral charge with Al(IV) in all tetrahedral sheets are trans-vacant; the trans-vacant form is more stable than the cis-vacant form. On the other hand, for samples with very high Mg^{2+} and Fe^{2+} contents in octahedral sheets, the trans-vacant configuration is more stable than the cis-vacant (McCarty & Reynolds 1995).

In addition, the tv and cv configurations cannot be together in the same octahedral sheet, but they may occur in different layers, forming an interstratified mineral (Sáinz-Díaz et al. 2001, Manceau et al. 2000). Thus, tv and cv forms can be considered as polymorphs of these dioctahedral phyllosilicates. Different authors have shown that octahedral cation arrangements are not random at all. Al^{3+} and Fe^{3+} cations tend to segregate from each other (AlAl-OH and $AlFe^{3+}$-OH prefer cis-vacant positions and FeFe-OH trans-vacant positions); whereas Mg^{2+} and Fe^{2+} ($AlFe^{2+}$-, AlMg-, and MgMg-pairs) tend to be dispersed, forming spatial clusters (Marchel & Stanjek 2012, Cuadros et al. 1999, Sainz-Díaz et al. 2001).

The cation substitutions at octahedral sites were analysed by TEM, TG-DSC and FTIR analyses. In Tab. 51, the Al(IV), Mg+Fe/Al(VI) Fe/Al(VI) and Fe(II) composition ratios are described for the analysed samples. The samples showing a cis-vacant configuration (Tab. 51), according to Muller et al. (2000), are the FEBEX reference sample and BBIL samples with a high Fe content at octahedral sites (shown by the νMgFe-OH bending band). The high amount of iron should lead to an increase in the trans-vacant positions. However, only one dehydroxylation peak is observed which corresponds to cis-vacant positions. This is probably because the Fe(II) content is lower than 6 wt.-% and Fe(III) fills cis sites (Tsipursky & Drits 1984). In other protrusion samples (e.g., BMS-47-2, BMS-53-2, RV-42, BSH), the total magnesium and total Fe(II) content are higher than in the other altered and reddish samples, and show two dehydroxylation peaks and, hence, a cis-trans-vacant configuration. In addition, brucite and saponite were detected in these samples, which were not observed in the BBIL samples; brucite is found only when Fe(II) content was above 12 wt.-%. Therefore, rearrangements in crystal lattice structure due to Mg^{2+} and Fe^{2+} migration at trans octahedral sites replacing Al have produced order-disorder phenomena. This means the existence of cis-trans interstratifications of the structure forming Fe(II) and/or Mg^{2+} trioctahedral domains or clusters separated by dioctahedral domains. Depending on the conditions and the Mg^{2+} and Fe^{2+}content, these domains may be completely segregated forming different phyllosilicate phases: brucite-like sheets, Mg-rich trioctahedral smectite, nontronite or chlorite, similar to a dissolution/precipitation process.

Kaufhold et al. (2016) investigated the possibility of a solid-state transformation of dioctahedral smectites to trioctahedral smectites by Mg addition to octahedral vacancies demonstrating that Mg can occupy octahedral sites, but to a lower extent than monovalent ions (Li^+) and it can only reach the vacancy when it is really dry (120 °C). Therefore, the implication of Fe(II) in the smectite destabilization and this solid-state transformation should be further analysed. Mechanisms for structural Fe(II) or Fe reduction in smectites are based on: a) the migration of Fe^{2+} from interlayer sites to octahedral sheets (Lantenois et al. 2005), or b) due to several reaction steps: an increase of the layer charge density, a smectite destabilization forming a Si-Al-Fe gel, and Fe^{2+} diffusion in that gel inducing the formation of 7 or 14 Å Fe-rich silicates (Perronnet et al. 2008). However, these results are not unequivocal because the inevitable short-term nature of lab experiments introduces issues of metastability and kinetics (Savage et al. 2010).

Tab. 51: Structural characteristics detected in samples in contact with the liner/Heater #2 and in the protrusion samples taken after dismantling Heater #2 in 2015

Sample	**FEBEX Ref.**	**BB-47-9**	**BMS-47-2** *mont.*	**BMS-53-2** *mont.*	**RV-42 Green** *mont.*	**Liner red (BBIL-42)** *mont.*	**Liner red (BBIL-42)** *Nontronite*	**Heater black (BSH)** *mont.*	**P. black (BB)** *Fe-rich chlorite*
Al(VI)-Fe(VI)(*)	Al-cis-vacant	**Cis-trans vacant**	**Cis-trans vacant**	**Cis-trans vacant**	**Cis-trans vacant**	Al,Fe-cis-vacant	Al,Fe-cis-vacant	**Cis-trans vacant**	--
Si/Al(IV)	83	20 – 36	16	220	21	25	4	15	3
Mg_{tot}+Fe/Al (VI)	0.49	0.31 – 0.48	0.48	0.56	0.78	**0.56**	**1.83**	0.32	2.52
Mg_{tot}/Al (VI)	0.35	0.19 – **0.38**	**0.38**	**0.55**	**0.62**	0.33	0.31	0.32	0.13
Fe/Al(VI)	0.15	0.10	0.10	0.01	0.16	0.22	1.52	0.01	2.40
Dehydroxylation temp	648 °C	598 °C 648 °C	536 °C 658 °C	550 °C 660 °C	528 °C 650 °C	652 °C	652 °C	547 °C 648 °C	588 °C
Saponite	--	?	√	√	√	--	--	√	--
Brucite	--	--	--	--	√	--	--	√	--
νMgFe-OH	--	--	--	--	--	√	√	√	√
% Fe(II)	0.15 (7 %)	n.d.	0.03 (1 %)	0.03 (1 %)	**0.48 (13%)**	0.11 (2 %)	0.13 (2 %)	**0.27 (9 %)**	22.7 (92.7 %)

* Smectites may be classified into three types based on their octahedral Al3+ and Fe3+ contents derived from thermal analysis (Muller et al. 2000): a) trans-vacant: those smectites with Al3+(VI) < 1.4 and Fe3+(VI) > 0.3 per [O10(OH)2]; b) cis-vacant: smectites with Al3+(VI) > 1.4 and Fe3+(VI) < 0.3 per [O10(OH)2], and c) smectites trans-vacant mostly and predominantly ferroan: Al3+ (VI) > 1.4 per [O10(OH)2] and Fe3+(VI) > 0.3 per [O10(OH)2]

The oxidation of native iron to Fe^{3+}, enhanced by temperature, is recognized as the main driving force for smectite dissolution, since the reducing potential of oxidation of iron raises pH to become alkaline and increases dissolution of Si from clay particles. As described by Lantenois et al. (2005) metal Fe is probably the proton acceptor triggering smectite deprotonation during its oxidation process. Both the oxidation of metal Fe and the deprotonation of smectite are strongly favoured by the accessibility of metal Fe to smectite interlayers (Charlet & Tournassat 2005). In turn, deprotonation increases the layer charge deficit in the smectite octahedral sheets considerably, enhancing their reactivity. Thus, deprotonation may be the driving force for the oxidation of metal ions, and for the initiation of smectite destabilization. However, as discussed above, another process is also involved in the case of the FEBEX in-situ test. Because oxygen is

present, the oxidation of hydrocarbons generated by the C-steel corrosion and carbide hydrolysis (see gas evolution during the FEBEX in-situ test, Fernández 2018) could provoke Fe(III) reduction of iron oxyhydroxides and smectite. Consequently, smectite deprotonation increases the layer charge which is compensated by the migration of Al^{3+} into tetrahedral sheets, as supported by the cis-trans interstratification in the clay mineral structure. This is achieved by an increase in divalent interlayer cations depleting Na^{+}, and finally by the migration of Fe^{2+} and Mg^{2+} to octahedral sites. In addition, dissolved Fe^{2+} cations in pore water probably migrate in the interlayers to compensate for the increased layer charge, favouring the Fe^{2+}-for-Na^{+} cation exchange. It is likely that Fe^{2+} cations migrate either into the di-trigonal cavities of smectite tetrahedral sheets or into the smectite octahedral sheets, the latter is favoured due to the absence of protons inside the di-trigonal cavity and absence of electrostatic repulsion (Lantenois et al. 2005). This migration is similar to that of Li^{+} cations involved in the Hofmann-Klemen test under dry conditions (Hofmann & Klemen 1950, Greene-Kelly 1952). Reduced and adsorbed Fe^{2+} would create structural sites, which would favour adsorption of Mg^{2+} because of its almost equal ionic radius, and the filling of structural vacancies after cationic valence changes. All these mechanisms are not really proved experimentally but should be considered in further studies.

According to the results from Tab. 51, most of the samples with a high amount of Mg^{2+} and Fe(II) at octahedral sites show a cis-trans vacant configuration indicating the formation of interstratified minerals, possibly due to the segregation and clustering of octahedral sheets containing Mg^{2+} and Fe^{2+} cations. The entry of Mg^{2+} to octahedral sites could be enhanced by Fe(III) reduction and the deprotonation of smectite. Only if the amount of Al(VI) is lower than Mg(VI), cis-trans vacant interstratified minerals are formed because in other cases (higher AlAlOH and $AlFe^{3+}OH$ interactions), cis-vacant positions are preserved. The samples with a higher cis-trans interstratifications and the presence of brucite (RV-42 and BSH, Fig. 189) are correlated with a higher Fe^{2+} content, which favours also tv structures and an order/disorder process. This is because the coexistence of cis- and trans-occupied sites within the same octahedral sheet is unfavourable from a crystal chemical point of view: it violates the principle of local charge balance, consequently, cis and trans sites belong to different layers (Manceau et al. 2000). However, the presence of saponite is not always correlated with a high corrosion degree and a high Fe content, but only with a high Mg content and cis-trans vacant dehydroxylation peaks, as observed in the BMS samples. In Section 54 (sample BMS-54-xx) the highest MgO increase was observed along with the presence of saponite and brucite, but an iron increase was not detected. Thus, either oxic corrosion at the heater/liner acted as a kind of sacrificial anode, or structural Fe(III)-bearing smectite reduction was induced by another mechanism, such as the oxidation of saturated reduced hydrocarbons generated during C-steel corrosion. The reduced Fe(II) migrated from cis to trans sites and further migration of Mg^{2+} to octahedral sites was accompanied by an increase in the negative layer charge and subsequent elimination of structural hydroxyls to maintain constant layer charge, depending of the Fe(II) content (Stucki & Roth 1977). Therefore, it seems that corrosion is not related with the trioctrahedralisation process but with a Fe(III) structural reduction and Mg content. Due to temperature, high Mg content and Fe(III) reduction, rearrangements in crystal lattice seem to have produced cis-trans interstratifications. It also separated Mg^{2+} trioctahedral domains, which appeared completely segregated, as occurs in a dissolution/ precipitation process. This can then form Mg-rich trioctahedral smectite and/or brucite depending on the amount of structural Fe(II). The more Fe(II) is present the higher the segregation, spatial clustering and the presence of dispersed brucite-like sheets. However, further studies should be performed to confirm such processes.

7.5.3 Fibrous Mg-phyllosilicates in the bentonite profile affected only by granitic groundwater hydration

In the non-heated Section 59 (bentonite only subjected to hydration), the bulk samples retrieved after dismantling Heater #2 did not show smectite alteration, as seen from results obtained by different techniques (DRX, TEM, FTIR, SEM and TEM). The bentonite maintained its main physicochemical properties unaltered: CEC, layer charge, water adsorption capacity and surface area (total+external).

However, in the whole radius analysed from Section 59, (bentonite blocks BB-59-1, BB-59-2, BB-59-3, BB-59-4 and BB-59-5), minor neoformed minerals were detected in very small pores, which FTIR analyses determined to be palygorskite, sepiolite, kaolinite and I/S mixed-layers. Furthermore, new bands corresponding to Mg3OH vibrations (such as in trioctahedral structures (brucite, saponite, ...), or to outer AlAlOH vibrations in kaolinite; and νMgFeOH vibrations were also observed (Fig. 65 to Fig. 69).

In order to explain this local neoformation, the high ionic strength of the pore waters (Fig. 253) from Section 59, up to 0.5 M, should be kept in mind. The high amount of Mg (Fig. 252) and the classification of pore water as Na-Mg-Cl is also of interest. In the rest of the sections, pore waters were Na-Cl water-type with ionic strengths from 0.04 to 0.47 M for heated Section 47, and from 0.04 to 0.14 M in Section 36 at the shotcrete interface. Furthermore, a slight increase of Mg was observed in the structure (especially at interlayer sites) of some smectite particles by TEM analyses, as well as a slight increase in layer charge and in Al content at tetrahedral sheets (Tab. 9, Fig. 95, Fig. 96). A slight increase of Mg at interlayer sites in this section was also detected in the exchangeable cation determination with respect to the other ones (see Section 7.2).

Authigenesis of Mg-clays in highly reactive hydrogeochemical conditions may be induced by hydrolysis that may produce alkaline, silica-rich fluids; which in turn, interact with Al-clay minerals. Mg-clays may form by (Pozo & Galán 2015):

a) Direct precipitation (neoformation) from solutions containing dissolved ionic species (colloidal silica in a Mg-rich environment), or

b) By transformation of aluminous precursors (transformation by dissolution-precipitation or by addition)

Although the precise mechanism of Si and Mg uptake to neoformed minerals is still not well understood, the formation of a type of Mg-clays is controlled by several physico-chemical parameters including pH (alkalinity), P_{CO2}, salinity (Na+), and Mg/Si ratio (Jones & Galán 1988). Palygorskite is formed in moderate saline conditions at pH < 8.5 with presence of Al. Sepiolite is formed in intermediate saline conditions, high alkalinity (low P_{CO2}), high Si/Mg ratio, and absence of Al at a pH between 8 and 9.5. Mg-smectite is formed in high saline conditions at pH > 9.8 (Pozo & Galán 2015).

Different clay mineral associations were detected as a precipitate in very small point pores as a function of distance to the gallery axis by FTIR analyses (Fig. 64 to Fig. 69). At the bentonite/granite interface (102.15 cm from the gallery axis), palygorskite, Mg_3OH and νMgFeOH vibrations were observed. Kaolinite, sepiolite, quartz and calcite were detected at 70 cm from the gallery axis. I/S MLs, a peak at 3'698 cm^{-1} belonging to a Mg_3OH vibration (characteristic of trioctahedral structures: brucite, saponite, …; or to outer AlAlOH vibrations in kaolinite); and quartz were detected at 34 cm. Increases of νMgFeOH vibrations, calcite and quartz were observed at 11 cm from the gallery axis. Therefore, groundwater inflow and bentonite/groundwater interactions induced variable changes in the chemical conditions of the

pore water (pH, Si/Mg ratio and salinity) over time, leading to increases in the Mg/Ca ratio followed by mainly calcite precipitation and localised Mg-clay precipitation.

The infiltrating granitic groundwater is a diluted and reduced water (EC < 100 µS/cm, Eh ~ -200 mV, pH ~ 9) of sodic-calcic-TIC-fluoride type (Huertas et al. 2006, Garralón et al. 2017). It is expected that hydrolysis reactions in the bentonite were produced closer to the granitic interface because of the lower dry density of the bentonite compared to the rest of the bentonite barrier (Section 5.2). The alkaline and silica-Al-rich fluids then could, after interaction with bentonite (smectite hydrolysis and calcite dissolution), lead to a direct precipitation of palygorskite in some pores (Fig. 65). In inner sections, depending on pH as well as Al and Si contents in the pore water, kaolinite and sepiolite could precipitate, as well as carbonates and quartz (Fig. 66, Fig. 67). Close to the bentonite buffer centre (34 – 11 cm from the gallery axis), the highest salinity and Mg content in pore water are observed (Fig. 173 to Fig. 175, Tab. 30), which could favour the interlayer Mg^{2+} uptake and Ca^{2+} release, followed by the incorporation of magnesium (Mg addition) and silica in the structure forming Mg-silicate interstratification (clustering) and/or Mg-rich interlayers (brucitic layers) in the pre-existing 2:1 Al-phyllosilicate. This would explain the detection of Mg_3OH (Fig. 68) and νMgFeOH (Fig. 69) vibrations along with quartz (Fig. 94).

Indeed, cation substitutions in the tetrahedral and octahedral layers result in a negative charge and produce an order–disorder phenomena in the crystal structure of phyllosilicates. Layers can be stacked with different sequences, and the geometrical similarity of these layers' silicate structure facilitates the formation (and precipitation) of structures containing different kinds of layers and different ordered and disordered sequences of layers.

On the other hand, a possible replacement of the original Al-rich dioctahedral smectite by a newly formed Mg-rich phase in a dissolution/precipitation process may explain the I/S MLs, Mg_3OH vibrations and quartz detected (Fig. 68, Fig. 94).

The I/S MLs may be due to heterogeneities within the swelling layers as well, because the high-charge layers (beidellitic nature) alternate regularly with the low-charge ones (Whitney & Northrop 1988). The illite layers would be interstratified with both high- and low-charge dioctahedral smectites in a three-component mixed layer forming illite-smectite-vermiculite mixed layers (I-S-V MLs).

In any case, these neoformations were insignificant, almost imperceptible, and detected in small pores, the rest of smectite mass maintained unaltered.

7.5.4 Bentonite/shotcrete interface

In Section 36, the bentonite analysed was affected by the concrete pore water interactions and by the corrosion processes of the dummy canister introduced after dismantling Heater #1.

The chemical analyses of the clay mineral particles indicated most of the smectite clay particles maintained its crystallochemical composition and structure (Tab. 9, Fig. 96, Fig. 97, Fig. 98, Fig. 112). The potassium content in the smectite mineral particles was very low ruling out an illitization process. Only some clay mineral particles showed an increase of Mg and layer charge, as well as variations in the charge location, due to Al substitutions at tetrahedral sheets and Mg and Fe substitutions at octahedral sheets.

In the bentonite with a rich iron content due to corrosion of the liner/dummy canister, some nontronite clay mineral particles were detected (Block BB-36-3, Tab. 10, Fig. 93, Fig. 97).

At the shotcrete/bentonite interface (mm scale), chlorites (BB-36-2, BB-36-6 by SEM: Appendix B), kaolinite (BB-36-3, Tab. 10, Fig. 93, Fig. 96, Fig. 105, Appendix E), zeolites (BB-36-2, BB-36-5 by SEM) and Mg-rich montmorillonite were detected by TEM (Fig. 96) and SEM (Fig. 110, BB-36-5: Appendix B) analyses. These clay minerals were neoformed due to alteration of the FEBEX smectite through the diffusion of the high alkaline pore solution from the shotcrete towards the bentonite, where Mg from interlayer sites is lost from the FEBEX bentonite (see Section 7.4.3).

Furthermore, the bentonite block BB-36-1, located at the bentonite/granite interface, was in part affected by the corrosion of a screw that was probably microbiologically induced (see Section 7.8). In the altered bentonite, showing a reddish-black halo, chlorite (by SEM: Fig. 107), Mg-rich montmorillonite (by SEM: Fig. 107), Fe-rich and K-rich clay mineral particles (by SEM: Appendix B) were found; as well as a peak at ~ 3'700 cm^{-1} belonging to either Mg_3OH vibrations (characteristic of trioctahedral structures: brucite, saponite, …), or to outer AlAlOH vibrations in kaolinite (Fig. 62).

7.6 Physico-chemical properties: CEC, layer charge, zeta-potential, surface area and water adsorption

The physico-chemical properties of the bentonite: CEC, layer charge, zeta-potential, surface area (total and external) and water adsorption are important parameters reflecting the reactivity of the clay minerals and affecting the adsorption and retention of ions and the swelling capacity of the bentonite.

None of the physicochemical parameters analysed changed during the evolution of the FEBEX in-situ test. Only a slight decrease of CEC, increases in layer charge, a slight decrease in the water adsorption capacity and a decrease of the BET surface area were detected in samples at the Heater #2 contact. A decrease of the BET surface area was also observed in samples in close contact with Heater #1 (5 years of experiment). Determinations of total CEC, layer charge and water adsorption capacity were not performed in 2002.

The total cation exchange capacity and BET surface area decreased only in samples in close contact with the liner/Heater #2 by around 11 – 35 % and 43 – 65 %, respectively, compared to the reference value of the FEBEX bentonite. This was observed in the samples at close contact with the Heater #2 (BMS and protrusion samples), as well as in the bulk mass of the blocks from the third bentonite ring (BB-47-9, BB-53-9). This may be related to a lower content of smectite in the bentonite samples or to a modification of the smectite's crystal structure at this interface. The variation in smectite and total phyllosilicates content in most of samples is similar to the reference FEBEX bentonite value. Thus, other explanations need to be given.

The decrease in BET and total CEC seem to be related to the structure of the smectite clay mineral particles as shown by the variation of the zeta potential, the size of the smectite particles and the cation composition at exchange sites (Fig. 256, Fig. 257 and Fig. 258). The zeta potential increased (absolute value) towards the heater contact, increasing the particle size.

A decrease in the CEC may be also caused by:

a) The collapse of clay particles, particularly of highly charged smectites (Kaufhold & Dohrmann 2010)

b) The collapse of clay particles caused by large ionic strength, which generally reduces the swelling pressure (e.g. Karnland et al. 2007, Herbert et al. 2004)

c) Extensive drying process due to increased Ca/Mg fixation and/or K fixation at interlayer sites (Kaufhold & Dohrmann 2010b)

d) The formation of Al-Mg-hydroxide complexes in the smectite interlayer (Howard & Roy 1985)

e) The formation of trioctahedral clusters of reduced Fe^{2+} (Hadi et al. 2013)

f) Interlamellar collapse due to an dehydroxylation process produced because the Fe(II) migration from cis-sites to trans-sites when structural Fe(III) is reduced to Fe(II) (Stucki & Roth 1977)

As shown by the results all these factors: increase of layer charge, high salinity, presence of Fe(II) and drying, are involved in the bentonite-liner/Heater #2 interface, which may influence the decrease of water adsorption behaviour of the bentonite samples from the heated Sections S47 and S53 (Fig. 156, Fig. 157) with respect to the non-heated sections (Sections S36 and S59) and the reference sample.

On the other hand, Missana et al. (2018a,b) analysed the size of clay colloids as a function of the exchangeable cation and layer charge location. They showed that the presence of more than 80 % divalent cations at exchange sites favours the formation of very large particles, but also that an increase in tetrahedral charge produces an increase in clay colloid size, independently of the main interlayer cation. In the case of the FEBEX retrieved samples at contact with the liner/Heater #2, sodium at exchange sites was almost absent (around 7 %), increasing the divalent cations around 93 %. This would imply an increase of particle size and, hence, of the external surface area. Furthermore, TEM and TG-DSC analyses showed an increase of tetrahedral charge in these BMS and protrusion samples.

The colloid properties (size and mobility) of the clay minerals are also affected by the electrolyte concentration. The aggregation of clay particles can occur due to an increase of ionic strength as a result of the diminution of the electrostatic repulsion between particles, which mainly leads to face to face, FF, interactions. An increase of the pore water salinity was observed at the heater contact, which may explain an increase of clay particles' size close to the Heater #2 contact and, as consequence, a decrease of the external surface area. Also changes in pH (< 6) may lead to particle aggregation (edge to face, EF, or edge to edge, EE, interactions) as the small amphoteric charge present in the edges of clay particles might interact with the negatively charged layers. These aggregates form large structures which rapidly tend to flocculate. Changes in pH occur are during the corrosion of the C-steel heater and liner. Furthermore, the aggregation/cementation of particles due to silica dissolution because of heating and/or smectite alteration should not be discarded.

Nevertheless, other authors associated the reduction of surface area with growth of larger and more compact aggregates as a consequence of smectite dissolution and recrystallization of I/S and/or trioctahedral clay minerals (saponite and/or Chl/S mixed layers; Whitney & Velde 1993). Indeed, Fe(II) content increased in samples in contact with the liner/Heater #2, especially the protrusion samples (Section 7.5.1), which may imply a destabilization of the smectite structure and, consequently, a modification of the bentonite properties (Neaman et al. 2003, Stucki 1988, Shen et al. 1992). Although the decrease of the external surface area was detected in other samples close to Heater #2 and taken during the dismantling after 18 years of experiment (see Villar et al. 2017) as well as in samples close to Heater #1 after 5 years of experiment (see Section 5.5.5), the variations of CEC and external surface area are restricted to samples in very close contact with the liner/heater (BMS, protrusions and the third bentonite ring); the rest of the analysed bentonite samples from the FEBEX in-situ tests preserved their physico-chemical properties.

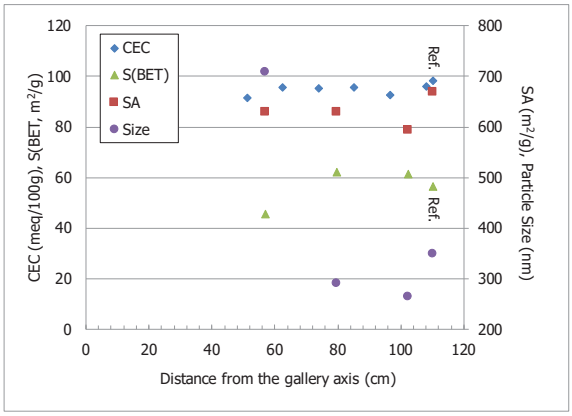

Fig. 256: CEC, BET external surface area, total surface area and particle size for different bentonite suspensions from Section 47 as a function of distance to the gallery axis

Data are compared to Reference values (Reference sample at 110 cm).

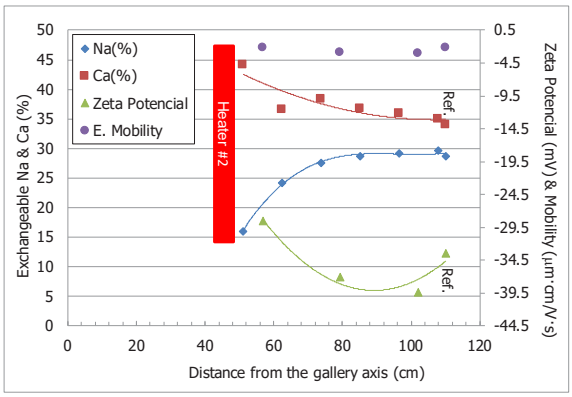

Fig. 257: Particle size, BET external surface area and exchangeable Na and Ca for different bentonite suspensions from Section 47 as a function of distance to the gallery axis

Data are compared to Reference values (Reference sample at 110 cm).

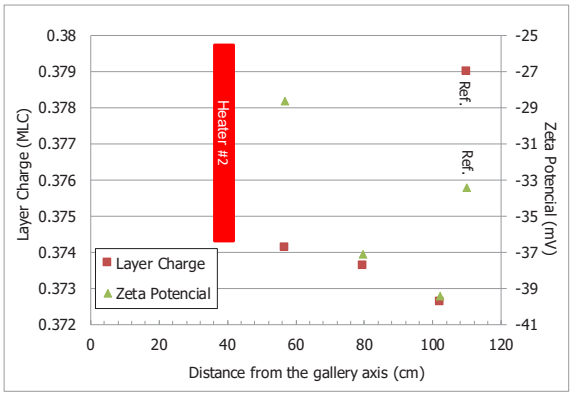

Fig. 258: Zeta potential and layer charge (MLC) for different bentonite suspensions from Section 47 as a function of distance to the gallery axis

Data are compared to Reference values (Reference sample at 110 cm).

7.7 Redox state in the FEBEX in-situ test

The redox conditions in the bentonite buffer are an important issue for safety assessment purposes of a HLW repository (Giroud 2014), because they strongly affect the pore water chemistry and the mobility and sorption of many, highly relevant, radionuclides. The different processes that *a priori* can have a large influence in the short and long-term redox evolution of the repository are:

a) Oxygen consumption

b) C-steels and other metal corrosion

c) Organic matter degradation, and d) microbial activity

A redox system may involve gases (O_2, N_2, H_2, CH_4 , CO_2, ...), dissolved components (NO_3^-, NH_4^+, CH_2O (TOC), Fe^{2+}, Mn^{2+}, SO_4^{2-}, HS^-, H^+, ...), as well as solids (FeOOH, MnO_2, $FeCO_3$, $MnCO_3$, ...) and components (Fe^{2+}, Mn^{2+}, NH_4^+, ...) associated with the solids by ion exchange (Christensen et al. 2000). The most important species that undergo redox reactions are carbon, iron, sulphur and nitrogen.

Determination of redox conditions in a system is still no simple task and different approaches can be performed (Christensen et al. 2000):

a) Measuring the redox potential from a pore water sample

b) Analysing the dissolved components in pore water

c) Analysing gases (e.g., hydrogen and methane concentrations)

d) Measuring volatile fatty acids (VFAs) concentrations in pore water

e) Characterising reducing mineral phases, and f) characterising microbial populations

The redox state inside the bentonite barrier from the FEBEX in-situ test was analysed by means of Eh (Fig. 259) and gas composition analysis (Fig. 260) over time from gas and water samples collected from pipes inserted inside the bentonite (see Fernández 2018). These measurements indicated that after 1.5 – 2 years, oxygen in the barrier was depleted to levels of a post-oxic period. Anoxic levels with oxygen concentrations less than 10^{-6} M were never reached, because the bentonite barrier was not gas-tight. However, according to the redox measurements and the presence of hydrogen, methane and other reduced saturated hydrocarbons, anoxic conditions were established, at least in some zones of the bentonite barrier. Therefore, alternate oxic and anoxic episodes could occur during the experiment as a consequence of the non-tight gas conditions (see Fernández 2018).

The description of the redox evolution in the bentonite buffer may be based also on the by-products detected. Apart from gas and pore water samples, some reducing mineral phases were detected in the retrieved samples obtained after dismantling Heater #1 and Heater #2 and may help to elucidate the redox conditions in the FEBEX in-situ test.

Fe-carbonates (see Tab. 11, Tab. 37 and Appendix B) were detected in most of the bentonite blocks from Section 36: bentonite ring 1 and 2 at the shotcrete/bentonite interface (Fig. 107), Section 47: bentonite ring 1, 2 and 3 from a heated section and Section 53: bentonite ring 3 (Fig. 108), as well as in protrusions located in contact with the heater (Fig. 195), and in the non-heated Section 59 (Fig. 109). The presence of Fe-carbonates in these Sections S36, S47 and S53 indicates the presence of Fe(II) circulating inside the bentonite pore water.

Sulphides were also detected in Section 36 (Fig. 107), Section 47 in bentonite rings 1, 2 and 3 (Fig. 108), and in the BMS and protrusion samples, as mackinawite, pyrrhotite and FeS (Fig. 197),

most of them with a framboidal texture indicating the absence of oxygen, sulphate reduction and possible biological intervention, because the reference FEBEX bentonite does not contain sulphides (Tab. 1, Fernández 2004).

During the dismantling of the Heater #1 in 2002, the presence of sulphate reducing bacteria around sensor SH-SDI-1 (see Section 6.4.1), and of sulphides and Fe-carbonates indicated that the bentonite buffer reached reducing conditions. Sulphides were also detected at the back part of Heater #1. However, the presence of goethite and hematite indicated processes of aerobic corrosion.

The presence of magnetite, saponite and chlorite at the Heater #2 contact are also indicative of the presence of Fe(II) and of anoxic conditions. The presence of Fe(III) oxides (hematite, ferrihydrite and goethite) were probably formed during the initial aerobic phase of the experiment and afterwards under oxic corrosion conditions (Wersin & Kober 2017).

VFA concentrations (acetate, formate and oxalate) were detected in pore water from all bentonite sections analysed (see Section 5.6.2 and Section 7.1.1), reflecting ongoing redox processes. VFAs are intermediate products produced under anaerobic conditions as H2 is, increasing its concentration when electron acceptors are depleted; or are connected to a shift in the predominant redox process from sulphate reduction to methanogenesis (Christensen et al. 2000). However, the high pool of acetate and oxalate in pore water from bentonite block BB-47-9 in close contact with Heater #2 (Tab. 29), points also to the generation of hydrocarbons due to the corrosion of the C-steel liner/heater.

From all mineral and species involved, it seems that the degradation of hydrocarbons (reduced saturated hydrocarbons and oxidized non-volatile hydrocarbons) generated during the oxic C-steel corrosion processes and carbides hydrolysis in the FEBEX in-situ test regulated the redox state in the bentonite buffer through reversible states of redox-dependent metastable equilibrium regulated by hydrogen and oxygen fugacities. This is because the redox stability of both reduced and oxidized hydrocarbons is below that of iron-oxide. Oxygen, corrosion, mineral assemblages and water played an integral role in regulating the redox state and activities of all species involved, by acting as oxidizing agents (terminal electron acceptors, TEAs) and a sink for generated H_2 through biotic and abiotic redox-dependent processes (see Section 7.4.1).

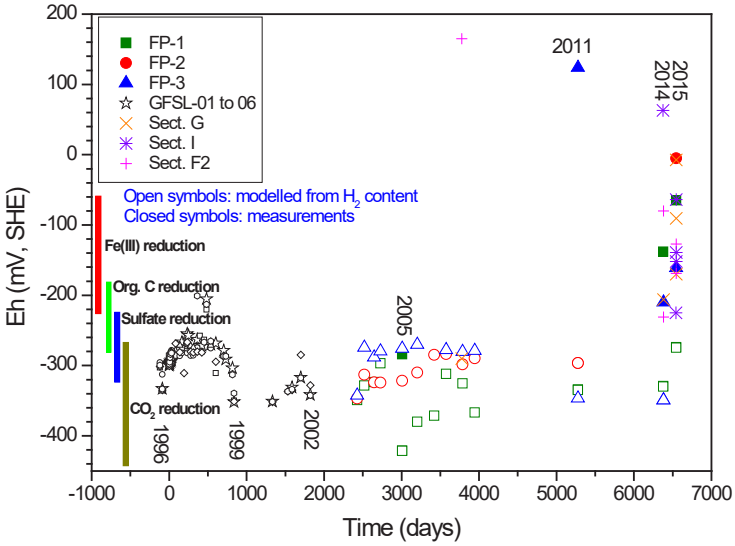

Fig. 259: Redox potential values obtained from water samples from the GRS and CIEMAT pipes located around Heater #2. Vertical bars: theoretical redox potential at pH = 7 for different reactions

Open symbols: redox values modelled from the H_2 content. From Fernández (2017)

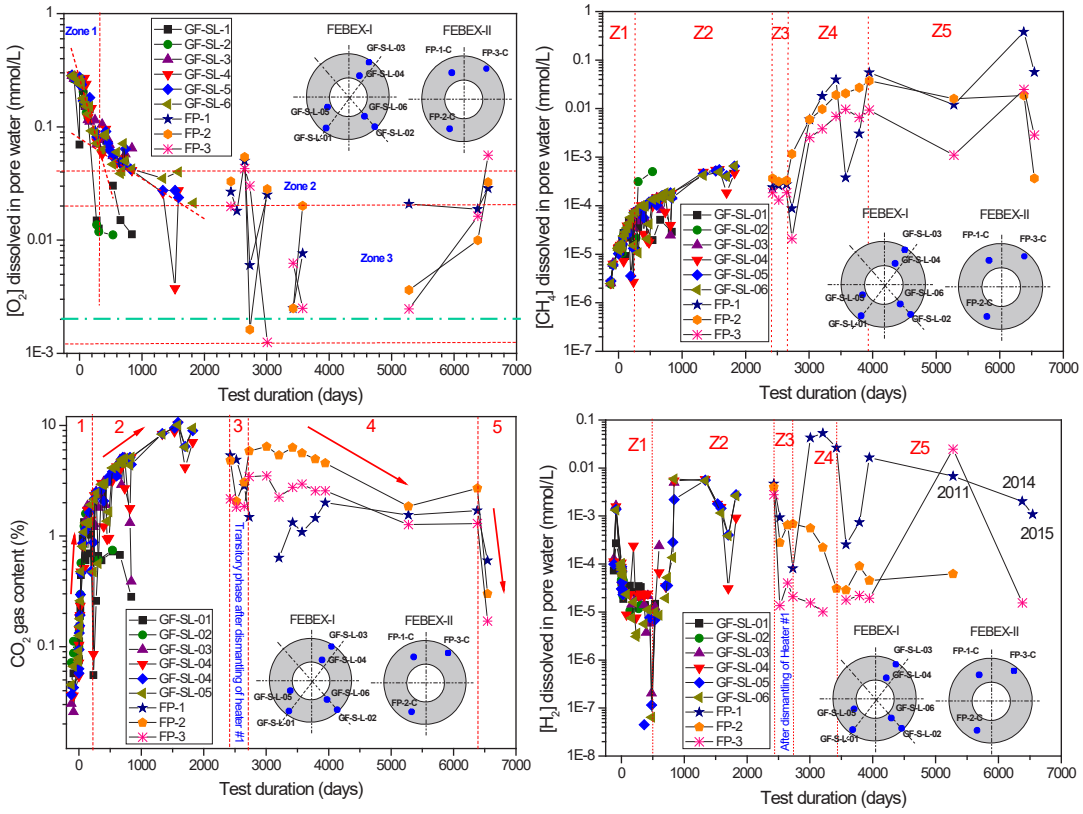

Fig. 260: Concentration of O_2, CH_4, CO_2 and H_2 in the different GRS pipes obtained during the first (1996 – 2002) and second (2002 – 2015) FEBEX operational phases in vol.-% of gas and in mmol/L of gas dissolved in pore water (25 °C, 1 atm.). From Fernández (2017)

7.8 Microbiology

Although this study was not focussed on microbiology (see dedicated microbiology study in Bengtsson et al. 2017), and no special precautions, microbiologically speaking, were taken during the sampling of the solid phase; different organic species were detected both in pore water (acetate, formate and oxalate), and in the solid phase, which could act as a carbon source and energy source, though redox reactions, for microbial activity.

Microbes and organic matter were detected by SEM dispersed in the whole bentonite mass, both in non-heated sections (S36 and S59) and heated sections (S47 and S53) (Fig. 107, Fig. 108, Fig. 109 and Appendix B), as well as both at the contact with granite and Heater #2. However, the aspect of the organic matter was different as a function of water availability and temperature (see Section 5.3.5 and 6.1.4). Microbes were seen in wet areas (e.g. Fig. 107: BB-36-6, Fig. 108: BB-47-7, Fig. 109: BB-59-6) and organic matter (Fig. 108: BB-47-9) with N (Tab. 11, Tab. 37, Appendix B) in the hottest areas. This is in agreement with the microbial studies performed on the FEBEX in-situ test, where aerobic and anaerobic bacteria (SRB, NRB, IRB) were found in non-heated sections (S60 and S62), but the presence of microorganisms at temperatures higher than 70 °C and close to the Heater #2 contact could not be proved (Bengtsson et al. 2017). The organic carbon found associated with N is probably due to oxidized non-volatile hydrocarbons produced after corrosion processes of C-steels and carbides hydrolysis with the subsequent oxidation of reduced saturated hydrocarbons.

The presence of Fe-sulphides of framboidal texture was observed in different samples from Sections S36, S47, S53 and S59, as discussed in Section 7.7. However, the presence of sulphate reducing bacteria (SRB) was only confirmed by microbiological analyses in some bentonite blocks from the dismantling of Heater #2 and located in different non-heated sections (Bengtsson et al. 2017). Therefore, most of Fe-sulphides is probably related to the abiotic processes of hydrocarbon oxidation as described in the previous sections.

In any case, at low temperatures, microbially induced sulphate reduction processes have occurred. Analyses of different stable isotopes' pairs carried out on the gas/water samples from the GRS pipes located in low temperatures zones of the bentonite pointed to microbially induced isotope fractionation (Fernández 2018). Microbes generally prefer to interact metabolically with the lighter stable isotope of an element. A sulphur fractionation ε (SO_4^{2-}-H_2S) of 19.4‰ was found in the FP-3 pipe, located close to the granite interface (low temperatures). When $\delta^{34}S$-SO_4^{2-} and $\delta^{34}S$-H_2S values were compared with those obtained from Grimsel groundwaters, the isotope signals pointed to microbial sulphate reduction, enriching $\delta^{34}S$-SO_4^{2-} values and depleting $\delta^{34}S$-H_2S values. Because abiotic reduction of sulphates is very low at low temperatures (< 250 °C), SRB should have induced this reaction. FP-3 was close to the displacement sensor SH-SD-2 and, according to Madina (2016), the corrosion morphology of this sensor resembled that of MIC, although SRB bacteria could not be cultivated from the bentonite (Bengtsson et al. 2017). However, after dismantling Heater #1, SRB were found around this type of sensor, sensor SH-SDI-1, located at the heated Section S17 (Madina & Azkárate 2004).

Furthermore, $\delta^{15}N$–N_2 variations were observed in all the gas pipes. Nitrogen dissolved in granitic groundwater was introduced in the bentonite barrier during its hydration process. The $\delta^{15}N$–N_2 enrichments observed in all pipes are related to microbial mediated processes in the conversions of N_2 to NH_4^+, because most of nitrogen isotopic variations result from biological processes. The Micans Laboratory found nitrate reducing bacteria (NRB) in Sections 42 and 54 near a displacement sensor, which was close to the FP-3 pipe. The BGR laboratory also found anaerobic bacteria in Section 52 close to pipe FP-3 (Bengtsson et al. 2017).

In sample BB-36-1 from Section 36, a clear influence of microbial activity was observed in one zone where a screw was corroded (Fig. 34). The affected zone was in contact with the granite interface and a cellulose filter (source of carbon for microbial growth), impregnated with a tracer. A reddish-black halo was visually detected, indicating corrosion probably microbially induced by SRB bacteria. Fe-oxyhydroxides, Fe-carbonates and carbon with N were detected by SEM in this sample (see Appendix B). From FTIR analyses (Fig. 62), aragonite, calcite, magnetite (maghemite), and a new band corresponding to Mg_3OH vibrations, such as in trioctahedral structures (brucite, saponite, ...) and/or kaolinite were also detected in this sample, as well as chlorite and Mg-rich smectite. Framboidal Fe-sulphides, Fe-oxides, organic matter and microorganisms were also found in other samples from Section 36 (Tab. 11, Fig. 107).

8 Summary and conclusions

An important issue for performance assessment purposes is to have confidence in and demonstrate the long-term preservation of the bentonite properties (low permeability, low diffusivity, high retention, and swelling capacity) over long periods of time, i.e., hundreds of thousands of years under real repository conditions.

The scientific approach used here for predicting the long-term clay barrier behaviour, is by analysing the results from experiments conducted at real scale and at real conditions. Most of bentonite barrier experiments have been carried out at laboratory conditions and there are only a few large laboratory experiments (Mock-up tests: FEBEX (Martín et al. 2006, Ophelie (Van Humbeeck et al. 2009); and in-situ experiments: LOT, ABM (Karnland et al. 2007, 2009, Svensson et al. 2011)). The FEBEX in-situ test project provided the opportunity to understand and quantify the processes taking place in the near-field and to evaluate the behaviour and interactions of the compacted bentonite barrier at real conditions of a HLW repository system because: a) it is a real-scale experiment performed at similar boundary conditions of the near field, and b) it is the longest real-scale in-situ experiment up to date.

From a geochemical point of view, specific long-term requirements for the function of a bentonite to isolate the canisters from water and slow down the migration of radionuclides, is to maintain a suitable chemical environment for the canister integrity and radionuclide retention over time and buffering possible alteration/deterioration processes of the bentonite.

The dismantling of the second part of the FEBEX in-situ test allowed quantifying the bentonite modifications due to changes in the initial physico-chemical conditions and different types of perturbations: a) interaction with granitic groundwater (saturation phase), b) desaturation phase due to heating; c) perturbations linked to the interactions between the bentonite and the allochthonous engineered solid materials (concrete, iron, steel, organics, etc.), and d) interactions with different gases produced and consumed in the system (CO_2, H_2, CH_4, etc.) due to mineral dissolution/precipitation, microbiological reactions and corrosion processes.

During 18 years of heating and hydration different alterations of the bentonite could have produced a redistribution and neoformation of mineral phases, dissolution processes, changes in total adsorption capacity (CEC) and crystallochemical changes in the smectite that could have affected the physico-chemical and mechanical properties of the bentonite.

Therefore, a comprehensive analysis of the blocks and another type of bentonite material was performed in order to determine the physical, physico-chemical, mineralogical and geochemical characteristics of the buffer at the end of the FEBEX in-situ test. The following parameters were considered in the assessment of the bentonite properties, i.e., identifying different reactions that the bentonite had undergone which could alter its engineering and chemical performance:

- Physical properties: water content and dry density
- Mineralogical alteration
- Clay texture
- Geochemical alteration
- Layer charge
- Cation exchange capacity
- Cation exchange population

- Total surface area and external specific surface
- Water adsorption measurements
- Soluble salts
- Pore water chemistry extracted by squeezing

The impact of the different perturbations can be described in terms of:

1. Modifications in the pore water chemistry and redox conditions, which may affect the smectite structural stability and speciation of dissolved ions
2. Mineralogical alteration: dissolution and redistribution of primary mineral phases and precipitation/neoformation of secondary minerals
3. Clay mineral stability and alteration of the clay mineral properties (especially cation exchange capacity, cation exchange population, crystallochemical structure, layer charge and swelling ability)
4. Modification of transport properties through modifications in porosity, permeability and tortuosity due to cementation processes

Some specific reactions observed in laboratory and large experiments over time were also detected in the FEBEX in-situ experiment. These reactions are: dissolution/precipitation, cation exchange, metal corrosion, gas production, hydrocarbons oxidation, and Mg accumulation at the heater interface. However, specific results were obtained from this FEBEX in-situ experiment, which is the longest real scale in-situ experiment up to date performed during a period of 18 years. Furthermore, the results were compared as a function of time, because data could be obtained from two dismantling operations performed in 2002 and 2015, i.e., after 5 years (Heater #1) and 18 years (Heater #2) of running the experiment.

Evolution of Pore water chemistry

The chemical state of the buffer is defined by the bentonite composition (clay minerals and accessory minerals) and the pore water composition. Consequently, the chemical stability of the bentonite, this is the alkalinity and redox buffering capacity, will be firstly controlled by the bentonite-water interactions and the resulting pore water chemistry (pH, redox potential, ionic strength, ionic composition, speciation and complexation).

In the FEBEX in-situ test the pore water composition was obtained by squeezing, with a pre-requirement of obtaining enough water volume for chemical analysis at the lowest squeezing pressure, thereby trying to avoid sampling different portions of the diffuse layer water and interlayer water. Depending on the initial water content and dry density of the compacted samples, the squeezing pressures ranged between 20 and 70 MPa in 2015 (dismantling Heater #2), and between 25 and 70 MPa in 2002 (dismantling Heater #1). The higher the water content of the sample, the lower the required squeezing pressure (and vice versa for dry density). 20 – 25 MPa was needed for obtaining pore water from samples with an initial water content higher than 27 %, whereas 70 MPa was required at initial water contents below 22 %.

The evolution of the pore water chemistry as a function of distance to the gallery axis and time indicated an advection (-diffusion) transport of ions. This transport followed different profiles as a function of the conservative or non-conservative behaviour of the dissolved ions.

The initial pore water composition before the FEBEX in-situ *test* was Na-Mg-Cl-SO_4 water type with I ~ 0.3 M, reflecting its marine origin (Fernández 2004), whereas the infiltrating granitic groundwater was a diluted and reduced water (EC < 100 µS/cm, Eh~ -200 mV, pH ~ 9) of sodic-calcic-TIC-fluoride type (Huertas et al. 2006, Frick et al. 1992). During the evolution of the FEBEX in-situ test, the composition of all pore waters was dominated by Cl^- and Na, followed by SO_4^{2-}, Ca and Mg, with ionic strengths increasing towards the inner part of the barrier, from 0.04 M to 0.50 M in Sections S47 (heated section) and S59 (non-heated) sampled during the dismantling of Heater #2 in 2015; pH values were neutral to very slightly alkaline (6.8 to 7.9). In Sections S19 (heated) and S12 (non-heated), sampled during the dismantling of Heater #1, ionic strength varied from 0.07 to 0.77 M. The pore water composition extracted by squeezing from bentonite blocks changed from Na-SO_4-Cl water-type and I ~ 0.04 M at the granitic interface to Na-Mg-Ca-Cl water-type and I~ 0.41 M at the Heater #2 contact.

Chloride, sodium and magnesium, although the latter at a lower degree, controlled the ion content in the pore water. The conservative chlorides, present in the bentonite pore water, were transported with water (advective transport), followed by sodium. The sodium and chloride content in the bentonite depended on the water gradient in the bentonite (suction water potential) rather than the hydraulic pressure of the granitic rock (0.72 MPa). The maximum content of chloride after 18 years of experiment was observed at 57 cm from the gallery axis; i.e., in the middle of the bentonite barrier in Section 59; or at the contact of Heater #2 (Sections S47 and S53), where it possibly precipitated due to heat. The difference in the chloride content distribution along the buffer indicated an influence of heat and time on the chloride transport, as well as the precipitation of chloride salts at the heater interface. A dependence on time in the chloride transport was also observed when data from aqueous leaching and squeezing tests after dismantling Heater #1 (5 years) and dismantling Heater #2 were compared.

Other non-conservative ions such as carbonates and sulphates were transported but at a slower rate, because they were involved in dissolution/precipitation processes in the bentonite. Gypsum is close to saturation in the inner part of the barrier in Sections S59 and S47. However, anhydrite controls the sulphate equilibrium due to the temperature (88 – 99 °C) at the heater contact, as detected by FTIR in some samples. Alkalinity values were higher than those from the reference sample in the non-heated sections (S59 and S36) both in the inner and external parts of the bentonite, indicating the dissolution of carbonates and the inflow of the sodic-calcic-TIC-fluoride granitic groundwater. In heated Section 47, alkalinity is higher in the external part (granite interface), but remained constant in inner sections, probably due to carbonates' precipitation at the Heater/bentonite interface.

Bromide showed a trend similar to chloride. Fluoride, coming mainly from the infiltrating groundwater was transported through the bentonite but its movement was slower than chloride; it is detected up to the middle bentonite ring in aqueous extract solutions, except in Section 36, where it is detected in all the squeezed pore waters due to a higher degree of lixiviation at the bentonite/shotcrete interface.

Cations moved also with the water front, but their transport was controlled by dissolution/ precipitation processes of carbonates and sulphates and exchange reactions at interlayer sites, as observed by aqueous leaching tests and the mineral saturation indices. Sodium and chloride contents follow a linear relationship. Calcium and magnesium concentration increased in the inner part of the heated and non-heated Sections S47 and S59, respectively, but is depleted at the granite interface and in all bentonite blocks from Section 36 (shotcrete contact) with respect to the reference values. However, an increase of magnesium with respect to calcium is observed in the inner parts of both Sections S47 (at Heater #2 contact) and S59 (non-heated), indicating an accumulation of magnesium in pore water.

Potassium increased towards the inner parts of the bentonite and is higher than the reference sample only in the non-heated Section 59. However, the values were lower than 1.25 meq/L, in samples from both dismantling of Heater #1 and Heater #2, which is too low a value for a possible illitization process of smectite. Silica data were also lower than 0.44 meq/L, and in equilibrium with quartz/chalcedony; silica does not increase towards the heater contact, which indicates that dissolution of smectite can be ruled out. pH values were neutral to slightly alkaline in all sections, even close to the bentonite/shotcrete interface, indicating the high buffering potential of the FEBEX bentonite and confirming that chemical conditions for avoiding smectite alteration were preserved over time.

Although organic matter (TOC) and volatile fatty acids (VFAs), such as acetate, formate and oxalate, are found in samples from different sections sampled in 2015 (S36, S47 and S59), it is interesting to note that oxalate is only observed in the sample closer to the Heater #2 interface (BB-47-9 sample), together with a high amount of acetate. Oxic corrosion and hydrolysis of carbon-containing steels (liner, Heater #2, etc.), leading to the generation of H_2, CO_2 and hydrocarbons (alkanes, alkenes and carboxylic acids), is possibly the main process for explaining the presence of acetate, formate and oxalate in the pore water close to the heater interface.

Summarising, during the infiltration of the granitic groundwater and the saturation process of the bentonite, the more soluble salts of the bentonite dissolved in the pore water. Together with these, ions from the infiltrating granitic groundwater, were transported through the porous compacted bentonite by an advective (-diffusive) transport towards the inner part of the bentonite barrier. This transport followed different profiles as a function of the conservative or non-conservative behaviour of the dissolved ions, thereby modifying the pore water chemistry, the composition of the cations at exchange sites and the mineral equilibria of minerals, especially the more soluble accessory minerals. The transport had following characteristics:

1. It depended on the water saturation evolution of the bentonite.
2. It was time-dependent.
3. It depended on the ion involved in the system: conservative or non-conservative.
4. It depended on the heat flux or heat gradient.
5. Although almost full saturation is achieved, a homogenised distribution of ions was not observed, even in non-heated areas.

Anion-accessible porosity data were obtained based on squeezing and aqueous leaching data. The anion-accessible porosity only includes the free water; while the total physical porosity includes both the external (free water) and internal water (DDL + interlayer water). By knowing the anion-accessible porosity fraction, the anion concentration in pore water can be inferred from its concentration in the aqueous leaching solution at a specific S:L ratio, by assuming that all anions leached in the aqueous extracts originate from pore water. The average value for FEBEX reference samples and samples obtained after dismantling Heater #2 was about 0.43 and for all samples (reference, dismantling of Heater #2 and dismantling of Heater #1) around 0.48. These values are in agreement with those obtained in clay rock samples (Pearson et al. 2003), although they are higher than those obtained from bentonite diffusion tests for similar dry densities (García-Gutiérrez et al. 2004).

Modification in the cation population at interlayer sites

The nature of cations at interlayer sites are of primary importance because they are involved in the bentonite-pore water equilibrium, but they also affect the charge deficit balance at interlayer sites as well as the macroscopic properties of bentonite such as plasticity, swelling capacity and the rheological behaviour. Furthermore, the cation composition at interlayers acts as a powerful buffer to all the perturbing reactions in the bentonite barrier system reacting with a rapid equilibrium. Thus, the naturally present cation population (type and number of exchangeable cations) is always equilibrated with the surrounding pore water.

Although experimental studies point the importance of the exchange reactions in the mineral-pore water equilibrium, the experiments were always limited in time. The FEBEX in-situ test offers valuable results of the behaviour and modification of the cation exchange composition at real scale after 5 and 18 years of running the experiment. Indeed, the most significant changes observed in the FEBEX in-situ test were the cation concentration at interlayer sites throughout the bentonite barrier and the different interfaces.

At the bentonite-concrete contact (Section 36), a relevant process was detected, which is the significant loss of magnesium at interlayer sites, increasing calcium and sodium. This process was also observed in the samples taken after dismantling of Heater #1, i.e., after 5 years of experiment (Section 7), especially at the contact with granite. This process was evident in the whole bentonite radius after 18 years of experiment, affecting at least 6.25 mm from the shotcrete contact.

In the non-heated sections, the cation exchange composition remained stable although a slight increase of magnesium and a slight decrease of sodium was observed with respect to the reference sample, except at the granitic interface where calcium was higher than magnesium. This pattern was similar to that observed after 5 years of experiment, with exception of the inner blocks where water saturation was not reached yet: calcium was higher than magnesium, and sodium was depleted.

In the bentonite/heater interface, exchangeable Ca (and Mg) increased towards the Heater #2 interface while Na decreased.

The amount of potassium at interlayer sites increased in all sections with respect to the reference sample, especially at the contact with concrete, but at a much lower quantities than the other cations; the maximum content found is 5 meq/100g. In general, low potassium contents were found both at interlayers sites and in pore water.

After 18 years of running the experiment the bentonite maintained its Ca-Mg character, with an increase of the Ca content, except in the non-heated section where Mg is slightly higher than calcium at interlayer sites.

Mineralogical alteration

The reference FEBEX bentonite contains around 90 wt.-% of smectite clay minerals. Quartz (2 wt.-%), cristobalite (2 wt.-%), feldspars (3 wt.-%), and calcite (1 wt.-%), make up the rest of the main minerals. The accessory minerals are in a proportion around 1 wt.-%: organic matter, chlorides and sulphates; and around 1 % for micas, chlorite, silicates, augite, hypersthene, hornblende, oxides (ilmenite, rutile, magnetite and Fe-oxides) and phosphates (apatite, xenotime and monazite) (Fernández 2004).

In the retrieved samples taken after dismantling Heater #1 in 2002 and Heater #2 in 2015, some neoformed mineral phases were detected.

Bentonite/heater interface

Corrosion processes were detected at the bentonite/heater interface. However, they were quite localized and affected the bentonite to a maximum thickness of 200 mm in the highest altered zone, as observed by the blueish-greenish colour at the frontal part of Heater #2. The estimated corrosion depths of the liner and Heater #2 were 109 – 191 μm, with bentonite being enriched in iron between 0 to 30 mm (Wersin & Kober 2017).

In the analysed samples, metal corrosion was represented by an increase of the Fe-content in bentonite samples taken from the first mm of the liner/Heater #2 contact, and the presence of corrosion products (newly formed Fe-phases).

The main iron oxyhydroxides found were goethite, hematite and magnetite. Therefore, corrosion was produced initially under oxidizing conditions. In absence of oxygen, metals corrode under anoxic conditions, with subsequent hydrogen generation and the formation of magnetite. However, the presence of hydrogen, methane and other reduced saturated hydrocarbons when oxygen was still present in the beginning of the test and detected over time, indicates another possible reaction for the presence of magnetite. This reaction is related to the corrosion and hydrolysis of carbon-containing steels and metal carbides of the liner and heater through a similar Fischer-Tropsch (FT) synthesis reaction using iron as catalyst, yielding a mixture of H_2, CO, CO_2, alkanes, alkenes and oxygenated organic compounds. This reaction was corroborated by the monitoring of these compounds over the 18 years of experiment, and because the cross plots of $\delta^{13}C$-CH_4 versus $\delta^{13}C$-CO_2 indicated methane formation via methyl-type reduction, rather than by CO_2 reduction (Fernández 2018). Because thermodynamically, both reduced and oxidized hydrocarbons are in partial equilibrium with bi-/carbonates under highly reduced oxidation states, i.e. below those of ion-oxide assemblage and even at the verge stability of water, we can state that oxygen, mineral assemblages and water played an integral role in regulating the redox state and activities of all species involved. They acted as oxidizing agents (terminal electron acceptors, TEAs) and a sink for generated H_2 through redox-dependent processes such as: a) sulphate reduction to H_2S and pyrite, b) reduction of Fe-oxides (e.g., hematite and goethite) to magnetite and siderite, c) pyrite to siderite, and d) reduction of Fe(III)-bearing phyllosilicates (Fe(III)-montmorillonite) to Fe(II)-saponite or chlorite.

The continuous inflow of oxygen (see chapter 7.4.1 and Wersin & Kober, 2017) acted as a self-feedback of oxic C-steel corrosion producing iron (III) oxides and hydrocarbons. As hydrocarbons were then oxidized, they generated reducing conditions and oxygen consumption. H_2 generated in the process was further consumed in both biotic and abiotic reactions. This is consistent with the instability of Fe-oxyhydroxides relative to siderite, as well as the reduction of sulphates from pore water to sulphides. Furthermore, the hematite (and goethite), generated during oxic corrosion, was partially reduced by the organic compounds thereby producing magnetite and dissolved Fe(II) ions, which may have diffused away. This is probably the reason for the red corroded bentonite surrounded by green halos observed in the bentonite samples taken during dismantling operations, as well as the presence of both hematite (and/or goethite) and magnetite iron mineral phases; i.e., Fe(III) and Fe(II) mineral phases.

After dismantling Heater #1 in 2002, the corrosion processes affected 20 μm of the Heater #1 surface and between 130 – 200 μm of the liner surface (Madina & Azkárate 2004, Madina 2003). The bentonite at contact with the Heater #1 was practically unaffected by iron enrichment, except

for a zone located at the bottom part of Heater #1. In addition, no large protrusions where found after dismantling Heater #1, although the bentonite had pushed through the liner holes. In close contact with the back part of Heater #1, iron sulphides (pyrrhotite), calcite, siderite, magnetite and hematite were detected.

XPS analyses of bentonite around the corroded SH-SDI-1 fisurometer dismantled in 2002 corroborated the presence of both inorganic and organic carbon inside the bentonite as a consequence of corrosion of C-containing steels. Oxidized hydrocarbons, such as alcohols and ethers (C-O) were found in dark-greenish and reddish samples, and carboxyls (C = O) in the greenish sample. Carbides (C = C) were found in the reddish sample, a fact that supports the possible dissolution of the carbides present in the C-steels during the corrosion process, which generates reduced saturated hydrocarbons and oxidized non-volatile hydrocarbons.

Because of the high salinity of the pore water close to the Heater #2 interface, chlorides were precipitated as GR-Cl-green rusts and other chloride salts. Cl-bearing Fe(III) oxyhydroxide (akageneite) was detected in other samples (Wersin & Kober 2017).

Bentonite profile affected only by granitic groundwater hydration

In the non-heated Section 59 and Section 12 from both dismantling operations in 2015 and 2002, respectively, which were only subjected to hydration, no significant neoformed minerals were detected. However, in 2015, point precipitates inside very small pores were found corresponding to neoformed clay mineral phases (see below).

Bentonite/concrete interface

The concrete pore water solution is highly alkaline, so when it interacts with bentonite porewater and/or granitic groundwater a leaching process starts by removing alkalis (Na^+ and K^+), followed by portlandite dissolution and subsequent leaching of calcium from CSH silicates, chemical reactions of dissolution/precipitation and a diffusive mass transport from the concrete (e.g. Soler & Mäder 2007, Turrero & Cloet 2018).

After dismantling Heater #1, gypsum, aragonite, dolomite, magnesite and portlandite ($Ca(OH)_2$), were detected in bentonite blocks at the concrete/bentonite interface in Section 7. After dismantling Heater #2, portlandite, ettringite, calcite, dolomite magnesite, aragonite, Ca-sulphates, Fe-oxides, Fe-carbonates and zeolites were detected in bentonite blocks at the shotcrete/bentonite interface in Section 36.

The presence of portlandite implies a pH higher than 12.5. At lower pH values portlandite dissolves reacting with sulphate ions from the pore water to form gypsum, which reacts with Al (probably from smectite dissolution at the alkaline interface) to form ettringite. The presence of portlandite and ettringite indicates a transport of calcium and highly alkaline pH solutions from the concrete towards the bentonite. This was corroborated by the decrease in Section 7 and Section 36 of Mg at smectite interlayer sites, because Ca and Na from concrete pore water displace Mg from interlayers. The diffusion of calcium from concrete towards bentonite also implies the precipitation of carbonates as calcite, aragonite, dolomite and magnesite, after reaction with the bicarbonates from bentonite pore water and granitic groundwater.

The diffusion of chlorides and sulphates from bentonite to concrete was observed both by the decrease of Cl and sulphate from the bentonite pore water in Section 7 and Section 36 and from squeezed pore waters. Cl diffused up to 5 cm and sulphate a few millimeters into the concrete

according to Alonso et al. (2017). The precipitation of Friedel's salts and ettringite (after dissolution of portlandite), in the concrete (Alonso et al. 2017) is further proof of this diffusion process.

The decrease of Mg at interlayer sites, and the decrease of chlorides and sulphates from the pore water were detected in the whole mass of the bentonite blocks from Section 7 and Section 36 (12.5 cm depth per bentonite block). Therefore, the high alkaline concrete(shotcrete) pore water front (rich in Ca, K and Na ions) advanced inside the bentonite a few tens of centimeters. However, the bentonite buffered the high alkaline pH, thus avoiding smectite alteration (e.g. Mg-smectite and zeolites are neoformed at pH > 9.5), but not other mineral dissolution-precipitation and cation exchange reactions (scale analysed being < 12.5 cm from the shotcrete contact). Savage (2014) gives an estimation of the concrete pH plume diffusive alteration front of about 20 cm.

Smectite structural stability

The analysis of the bentonite samples from the FEBEX in-situ test after both dismantling operations indicates that the bulk mass of bentonite (homogenised samples from a block) maintained its smectite content over time. This was confirmed by XRD, FTIR, TG-DSC, TEM and SEM analyses.

XRD data provide no evidence of any structural change in the montmorillonite. XRD analyses of random powders of the bulk material indicate no significant differences between the reference FEBEX bentonite and the treated samples from the FEBEX in-situ test. The treated bentonite samples contained smectite (87 – 95 %wt.) as the major mineral phase. The peak located at 15.2 Å is indicative of a two-layer hydrate Ca-Mg montmorillonite. The position of the d(060) peak and other peaks 60 – 61° 2θ indicate no major changes in composition of the smectite clay mineral and the formation of newly trioctahedral minerals can be discarded.

The XRD data from the clay mineral fraction provide no evidence of a structural change of the montmorillonite. Both the expansion behaviour (c-axis, d(001)), the periodic diffraction pattern of the basal reflections, and the a and b cell dimensions of the clay minerals in the treated samples are typical of dioctehedral montmorillonites and are similar to the reference material. The main basal reflexion d(001) at around 14.6 Å in the AO XRD patterns for all samples indicated no changes in the Ca-Mg character of the smectite particles, and the d(001) reflexion at around 17.0 Å in the EG XRD patterns for all samples indicate complete expansion of the interlayer sites. The smectite phases were made up of a R0 illite/smectite mixed-layer with about 5 – 23 % of illite layers (the reference FEBEX sample being a R0 I/S ML with 7 – 15 % of illite layers, Fernández 2004).

FTIR spectra from the retrieved bulk samples reveal that the smectite phases correspond to dioctahedral smectites, Al-rich at octahedral sheets. Furthermore, TG-DCS curves indicate that this dioctahedral smectite has most of the OH-groups at cis-vacant positions with divalent cations at interlayer sites.

From these global results, the smectite maintained its main physicochemical properties unaltered: CEC, layer charge, water adsorption capacity and total surface area. However, analyses from some bentonite blocks in Section 36, from neoformed phases in small pores in Section 59, and from the samples in close contact with Heater #2 (BMS and protrusion samples), reveal some type of smectite alteration.

Mg and Fe(II) accumulation at the heater interface

In analysed samples in close contact with liner/Heater #2, an increase in Fe(II) and Mg contents is detected. Fe-content in bentonite samples taken from the first mm from the liner/Heater #2 contact, has increasing values from 3.1 wt.-% to 6 – 19 % wt.-%, and although most of the Fe was Fe(III), the Fe(II) content of samples close to Heater #2 (protrusions) increases from 7 wt.-% to 9 – 18 wt.-%. The largest increase of MgO of about 6 mass % (Fernández et al. 2018b submitted) is found at the contact with Heater #2 from the FEBEX in-situ test, which is correlated with an increase of Mg content at exchange sites and in pore water. Apart from the formation of trioctahedral clay minerals or domains, observed in other mock-up and large scale tests; the presence of a further Mg-mineral (brucite), a Fe-rich chlorite, and a modification in the dehydroxylation temperature of clay mineral particles (cis-trans vacant double dehydroxylation peak) are also identified, which is an exclusive FEBEX in-situ test result.

The driving force for the smectite structural changes seems to be the oxidation and hydrolysis of carbon-containing steels, which affect the redox in the bentonite buffer due to the generation of hydrocarbons (alkanes, alkenes and carboxylic acids), which were oxidized due to non-gastight conditions. Consequently, it seems that Fe(III)-bearing montmorillonite is reduced to saponite and chlorite depending on the fugacity of oxygen.

Therefore, the mechanism for the structural clay mineral alteration seems to be the Fe(III) structural reduction, rather than the C-steel heater/liner corrosion process itself. Because Fe^{2+} cations are more stable in trans-sites than in cis-sites at octahedral sheets, rearrangements in crystal lattice seem to have formed cis-trans interstratifications favouring the migration of Mg present in high concentrations in pore water and interlayer octahedral sites. Because the coexistence of cis- and trans-occupied sites within the same octahedral sheet is unfavourable, separated Mg^{2+} trioctahedral domains are formed, which are completely segregated into Mg-rich trioctahedral smectite and/or brucite depending on the amount of Mg and structural Fe(II). It seems that with a higher Fe(II) content more segregation, spatial clustering and presence of dispersed brucite-like sheets, apart from saponite, are observed.

The migration of Fe^{2+} and Mg^{2+} to octahedral sites is accompanied by an increase in the negative layer charge and, possibly with the elimination of structural hydroxyls to maintain a constant layer. Deprotonation of the smectite is compensated by the migration of Al^{3+} into tetrahedral sheets, and an increase of divalent interlayer cations for Na^{+}. For this reason and because Fe^{2+} instead of Fe^{3+} is present, high-charge interstratified clay minerals with a cis-trans vacant double configuration were observed in the samples. Thus, both a solid-state transformation, producing high-charge/low charge (bi-substituted) layers similar to vermiculite ones; as well as dissolution-precipitation transformation, with the crystallization of a trioctahedral Mg-smectite (saponite), brucite and chlorite, is possible, depending, probably, on $f(O_2)$ and temperature. However, further studies should be performed to confirm such processes. Because an increase in potassium content is not observed, neither in the solid phase and pore water solutions, a further transformation of the high-charge smectite to illite (illitization) is not expected nor would it be insignificant.

These mineral transformations and Fe(III) reduction induced changes in some of the physico-chemical properties of the bentonite decrease the total cation exchange capacity and BET surface area. However, these mineralogical and physico-chemical changes are restricted to the bentonite in close contact to liner/Heater #2. The rest of bentonite from the FEBEX in-situ test maintained its performance as an engineered barrier.

Fibrous Mg-phyllosilicates in bentonite affected only by granitic groundwater hydration

In the non-heated Sections S59 and S12 after dismantling of both Heater #2 and Heater #1, the bulk samples analysed did not show smectite alteration, as results obtained by different techniques (DRX, TEM, FTIR, SEM and TEM) show. The bentonite maintained its main physico-chemical properties unaltered: CEC, layer charge, water adsorption capacity and surface area (total and external).

However, in the whole radius analysed from Section 59, minor neoformed magnesian clay minerals are detected in very small pores by FTIR analyses. The formation of a type of Mg-clays is controlled by several physico-chemical parameters including pH (alkalinity), PCO_2, salinity (Na^+), and Mg/Si ratio (Jones & Galán 1988).

Different clay mineral associations are detected as a precipitate in very small pores as a function of distance to the gallery axis by FTIR analyses. At contact with the granite interface (102.15 cm from the gallery axis), palygorskite and Mg_3OH and νMgFeOH vibrations are observed. Kaolinite, sepiolite, quartz and calcite are detected at 70 cm. I/S MLs, a peak at 3'698 cm^{-1} belonging to a Mg_3OH vibrations (characteristic of trioctahedral structures: brucite, saponite, ...; or to outer AlAlOH vibrations in kaolinite); and quartz are detected at 34 cm. Increase of νMgFeOH vibrations, calcite and quartz are observed at 11 cm from the gallery axis. Therefore, groundwater inflow and bentonite/groundwater interactions induce variable changes in the chemical conditions of the pore water (pH, Si/Mg ratio and salinity) over time, leading to an increase of the Mg/Ca ratio followed by mainly calcite precipitation and Mg-clays precipitation.

These neoformations seem to be related to the the pore water chemistry evolution along the bentonite barrier and to hydrolysis reactions in the bentonite. Alkaline and silica-Al-rich fluids after interaction with bentonite (smectite hydrolysis and calcite dissolution) could lead to a direct precipitation of Mg clays in some pores. This is because the high ionic strength of pore waters from Section 59 (up to 0.5 M) as well as the high amount of Mg; the pore water is a Na-Mg-Cl water-type. In the other sections, pore waters were Na-Cl type with ionic strengths from 0.04 to 0.47 M in the heated Section 47, and from 0.04 to 0.14 M in Section 36 at the shotcrete interface. Furthermore, a slight increase of Mg was observed in the structure (especially at interlayer sites) of some smectite particles by TEM analyses, as well as a slight increase in layer charge and in the Al content at tetrahedral sheets. The increase of Mg at interlayer sites was corroborated by the exchangeable cation determination.

In any case, these neoformations were insignificant, almost imperceptible, and detected in small pores. The rest of the smectite mass remained unaltered.

Bentonite/concrete interface

In Section 36, the analysed bentonite is affected by the concrete pore water interactions and by the corrosion processes of the dummy canister introduced after dismantling Heater #1.

The chemical analyses of the clay mineral particles indicate that most of the smectite clay particles maintained their crystallochemical composition and structure. The potassium content in the smectite mineral particles was very low ruling out an illitization process.

Only some clay mineral particles show an increase of Mg and layer charge, as well as variations in the location of the charge, due to Al substitutions in tetrahedral sheets and Mg and Fe substitutions in octahedral sheets:

- In bentonite with a rich iron content due to corrosion of the liner/dummy canister, some nontronite clay mineral particle is detected.
- At the shotcrete/bentonite interface (mm scale), chlorites, kaolinite, zeolites and Mg-rich montmorillonite are detected by TEM and SEM. These clay minerals were neoformed due to alteration of the FEBEX smectite as a consequence of the diffusion of the high alkaline pore solution from the shotcrete towards the bentonite; Mg source then stems from interlayer sites in the FEBEX bentonite.
- A block located at the bentonite/granite interface was in part affected by the corrosion of a screw probably microbiologically induced, seen in a reddish-black halo on the bentonite. Chlorite, Mg-rich montmorillonite, Fe-rich and K-rich clay mineral particles are found; as well as, a peak at ~ 3'700 cm^{-1} belonging to either Mg_3OH vibrations (characteristic of trioctahedral structures: brucite, saponite, ...), or to outer AlAlOH vibrations in kaolinite.

Physico-chemical properties

The physico-chemical properties of the bentonite: CEC, layer charge, zeta-potential, total and external surface area, and water adsorption are important parameters reflecting the reactivity of the clay minerals and affecting the adsorption and retention of ions and the swelling capacity of the bentonite.

All physico-chemical parameters analysed did not change significantly during the evolution of the FEBEX in-situ test. Although the values were slightly lower than the reference sample, it can be said the physico-chemical properties were preserved over time: CEC (~ 95 ± 2 meq/100 g), layer charge (~ 0.37 eq/hfu), zeta-potential (-35 mV), total (~ 590 m^2/g) and external (~ 64 m^2/g) surface area and water adsorption capacity. The most significant variations observed are restricted to the samples in very close contact with the liner/heater interface.

A slight decrease of CEC (11 – 35 %), an increase in layer charge, a slight decrease in the water adsorption capacity and a decrease of the BET surface area (43 – 65 %), are detected in samples at the Heater #2 contact (protrusions, BMS and blocks from the third bentonite ring). A decrease of the BET surface area is also observed in samples in close contact to Heater #1 (5 years of experiment).

Because the variation in smectite and total phyllosilicates content in most of the samples maintain similar values to the reference FEBEX bentonite value, the decrease of these parameters seem to be related with the structure of the smectite clay mineral particles, as shown by the variation of the zeta potential, the size of the smectite particles and the cation composition at exchange sites. The zeta potential increased (absolute value) towards the heater contact, increasing the particle size. These variations could be related to changes in redox state of the bentonite; i.e., structural Fe(III) reduction due to hydrocarbon oxidation. Indeed, the Fe(II) contents in the samples in contact with the liner/Heater #2, and especially in the protrusion samples, increase, possibly implying a destabilization of the smectite structure and, consequently, a modification of the bentonite properties.

Redox state

The redox conditions in the bentonite buffer are an important issue for safety assessment purposes a HLW repository (Giroud 2014), because they strongly affect the pore water chemistry and the mobility and sorption of many highly relevant radionuclides. The different processes that *a priori* can have a larger influence in the short and long-term redox evolution of the repository are:

a) oxygen consumption

b) metal corrosion

c) organic matter degradation

d) microbial activity

The redox conditions in the squeezed pore waters were not evaluated, but the redox state inside the bentonite barrier from the FEBEX in-situ test was analysed by monitoring Eh and gas composition over time from gas and water samples collected from pipes inserted inside the bentonite (see Fernández 2018). These measurements indicated that after 1.5 – 2 years, oxygen was depleted in the barrier to levels of a post-oxic period. Anoxic levels with oxygen concentrations less than 10^{-6} M were never reached, because the bentonite barrier was not gas-tight. The redox measurements and the presence of methane and hydrogen indicate anoxic conditions, at least in some zones of the bentonite barrier, so alternate oxic and anoxic episodes along the experiment were present, again, because the experiment were not gas-tight.

Furthermore, the description of the redox conditions in the FEBEX in-situ test can be based on the by-products and/or reducing mineral phases detected in the retrieved samples obtained after dismantling Heater #1 and Heater #2:

- Fe-carbonates are detected in most of the samples from different bentonite blocks from Sections S36 (concrete contact), S47, S53 (heated sections), and S59 (non-heated section), as well as in protrusions located in contact with the heater. The presence of Fe-carbonates in these Sections S36, S47 and S53 indicates that Fe(II) circulates in the bentonite pore water.
- The presence of magnetite, saponite and chlorite at the Heater #2 contact are also indicative of anoxic conditions. Fe(III) oxides (hematite, ferrihydrite and goethite) were probably formed during the initial aerobic phase of the experiment and afterwards under oxic corrosion conditions (Wersin & Kober 2017).
- Sulphides are also detected in Section 36, Section 47 and in the BMS and protrusion samples, as mackinawite, pyrrhotite and FeS, most of them with a framboidal texture indicating abiotic sulphate reduction, although possible biological intervention cannot be discarded in zones close to the granite contact and under low temperatures.
- Finally, VFA concentrations (acetate, formate and oxalate) are detected in the pore water from all bentonite sections analysed, reflecting ongoing redox processes. The high pool of acetate and oxalate in the pore water from bentonite block BB-47-9 in close contact with Heater #2, points also to the generation of hydrocarbons due to C-steel liner/heater corrosion.

From all mineral and species involved, it seems that the degradation of hydrocarbons (reduced saturated hydrocarbons and oxidized non-volatile hydrocarbons) generated during the oxic C-steel corrosion processes and carbides hydrolysis in the FEBEX in-situ test regulated the redox state in the bentonite buffer through reversible states of redox-dependent metastable equilibria regulated by hydrogen and oxygen fugacities.

Microbiology

Although this study was not focussed on microbiology, microbes and organic matter are detected by SEM dispersed in the whole bentonite mass both in non-heated sections (S36 and S59) and heated sections (S47 and S53), as well as in contact with the granite and Heater #2. However, the aspect of the organic matter was different as a function of the water availability and temperature, with microbes in the wet areas and organic matter with N in the hottest areas.

Although it should be taken into account that Grimsel granitic groundwaters contain dissolved nitrogen, the organic carbon found associated with N is probably due to oxidized non-volatile hydrocarbons produced after corrosion processes of C-steels and carbides hydrolysis with the subsequent oxidation of reduced saturated hydrocarbons generated due to non-gastight conditions.

Most of Fe-sulphides found in the bentonite are probably related with the abiotic processes of hydrocarbon oxidation. However, at low temperatures microbially-induced sulphate reduction processes have occurred as detected by analysing different stable isotope pairs carried out on the gas/water samples (Fernández 2018). Although SRB bacteria could not be cultivated from the bentonite after dismantling Heater #2, SRB were found around a type of sensor, sensor SH-SDI-1, located at the heated Section S17 (Madina & Azkárate 2004, Bengtsson et al. 2017).

Furthermore, $\delta^{15}N–N_2$ enrichments observed in all gas pipes seem to be related to microbially-mediated processes in the conversions of N_2 to NH_4^+, because most of nitrogen isotopic variations result from biological processes. This is in agreement with results from Micans Laboratory, which found nitrate reducing bacteria (NRB) in Sections 42 and 54 near a displacement sensor, which was close to the FP-3 gas pipe. BGR laboratory also found anaerobic bacteria in Section 52 close to gas pipe FP-3 (Bengtsson et al. 2017).

Finally, the global data analysed from samples obtained after the dismantling operations of the Heater #1 in 2002 and Heater #2 in 2015, indicate that no significant structural changes in the smectite are produced, the whole bentonite barrier preserves its main physico-chemical properties unaltered (CEC, layer charge, water adsorption capacity, and total and external surface area). The alterations observed are restricted to localized zones, mainly at the bentonite/concrete (< 6.5 – 12.5 cm) and bentonite/heater (< 5 – 10 cm) interfaces.

9 References

Abós, H., Martínez, V. (AITEMIN) (2015): Sample Log Book 34 to 62 FEBEX-DP. AN 15-578 September 2015.

Ahonen, L., Korkeakoski, P., Tiljander, M., Kivikoski, H. & Laaksonen, R. (2008): Quality assurance of the bentonite material. Posiva WR 2008-33. Posiva Oy, Olkiluoto, Finland.

AITEMIN (2002): Sampling plan for dismantling of Section 1 of in-situ test. Sampling book. Procedure 70-AIT-G-6-27.

AITEMIN (2014): Sensors Data Report, In-situ Experiment. Report N°: 8 – Full Report, June 2014.

Alonso, M.C., García Calvo, J.L., Cuevas, J., Turrero, M.J., Fernández, R., Torres, E. & Ruiz, A.I. (2017): Interaction processes at the concrete-bentonite interface after 13 years of FEBEX-plug operation. Part I: concrete alteration. Physics and Chemistry of the Earth 99, pp. 38–48.

Ammann, L., Bergaya, F. & Lagaly, G. (2005): Determination of the cation exchange capacity of clays with copper complexes revisited. Clay Minerals 40, 441-453.

Bárcena, I. & García-Siñeriz, J.L. (2015a): FEBEX-DP (GTS) Full Dismantling Sampling Plan. Nagra Arbeitsbericht NAB 15-14.

Bárcena, I. & García-Siñeriz, J.L. (2015b): FEBEX-DP (GTS) Full Dismantling Test Plan. Nagra Arbeitsbericht NAB 15-15.

Bárcena, I., Fuentes-Cantillana, J.L. & García-Siñeriz, J.L. (2003): Dismantling of the Heater 1 at the FEBEX in-situ test. Description of operations. Enresa Technical Report 9/2003.

Bar-On, P. & Shainberg, I. (1970): Electrophoretic mobility of montmorillonite particles saturated with Na/Ca ions, Journal of Colloids and interface science, Vol. 33. pp. 471–472.

Barrett, E.P., Joyner, L.G. & Hallenda, P.P. (1951): The determination of pore volume and area distributions in porous substances. I. Computation from nitrogen isotherms. J. Amer. Chem. Soc., 76, pp. 373–380.

Bauer, A. & Velde, B. (1999)_ Smectite transformation in high molar KOH solutions. Clays Minerals 34, pp. 259–273.

Beaufort, D., Berger, G., Lacharpagne, J.C. & Meunier, A. (2001): An experimental alteration of montmorillonite to a di + trioctahedral smectite assemblage at 100 and 200 °C. Clay Minerals 36, pp. 211–225.

Bengtsson, A., Blom, A., Taborowski, T., Schippers, A., Edlund, J. & Pedersen, K. (2017): FEBEX-DP: Microbiological Report. Nagra Arbeitsbericht NAB 16-15.

Bergaya, F., Brigatti, M.F. & Fripiat, J.J. (1985)_ Contribution of infrared spectroscopy to the study of corrensite. Clays and Clay Minerals, 33, pp. 458–462.

Birgersson, M. & Karnland, O. (2009): Ion equilibrium between montmorillonite interlayer space and an external solution. Geochimica et Cosmochimica Acta 73, pp. 1908–1923.

Blanc, P. (2017): Thermoddem: update for the 2017 version. Report BRGM/RP-66811-FR, 20 pp.

Blanc, P., Vieillard, P., Gailhanou, H. & Gaboreau, S. (2013): Thermodynamics of clay minerals. In: F. Bergaya and G. Lagaly (eds.): Handbook of Clay Science, Section 6, pp. 173–210.

Bourdelle, F., Truche, L., Pignatelli, I., MosserRuck, R., Lorgeoux, C., Roszypal, C. & Michau, N. (2014): Iron-clay interactions under hydrothermal conditions: impact of iron specific surface area on reaction pathway revealed by mineralogy and a continuous monitoring of pH, solution and gas compositions. Chem. Geol. 381, pp. 194–205.

Bradbury, M.H. & Baeyens, B. (1998): A physicochemical characterisation and geochemical modelling approach for determining porewater chemistries in argillaceous rocks. Geochim. Cosmochim. Acta 62, pp. 783–795.

Brunauer, S., Emmett, P.H. & Teller, E. (1938): Adsorption of gases in multimolecular layers. J. Am. Chem. Soc. 62, pp. 1723–1732.

Cataldo, F. (2003): Organic matter formed from hydrolysis of metal carbides of the iron peak of cosmic elemental abundance. International Journal of Astrobiology 2, pp. 51–63.

Çelik, M.S. (2004): Electrokinetic behaviour of clay surfaces. In: Clay Surfaces. Fundamentals and Applications. Wypych, F., Satyanarayana (Ed.). Interface Science and Technology. Vol. 1. Elsevier Ltd., pp. 57–89.

Charlet, L. & Tournassat, C. (2005): Fe(II)-Na(I)-Ca(II) cation exchange on montmorillonite in chloride medium: evidence for preferential clay adsorption of ions pairs in marine environment chemical modelling and XRD profile modelling study. Aquatic Geochemistry 11, pp. 115–137.

Charpentier, D., Devineau, K., Mosser-Ruck, R., Cathelineau, M. & Villiéras, F. (2006): Bentonite-iron interactions under alkaline condition: an experimental approach. Applied Clay Sciences, 32, 1–13.

Christensen, T.H., Bjerg, P.L., Banwart, S.A., Jakobsen, R., Heron, G. & Albrechtsen, H.-J. (2000): Characterization of redox conditions in groundwater contaminant plumes. Journal of Contaminant Hydrology, 45, pp. 165–241.

Christidis, G.E. & Eberl, D.D. (2003): Determination of layer charge characteristics of smectites, Clays and Clay Minerals, 51, pp. 644–655.

CRC Handbook of chemistry and physics. (1994): Ed. Lide David R. CRC Press, Inc.

Cuadros, J., Sáinz-Diaz, C., Ramírez, R. & Hernández-Laguna, A. (1999): Analysis of Fe segregation in the octahedral sheet of bentonitic illite-smectite by means of FT-IR, 27Al MAS NMR and reverse Monte Carlo simulations. American Journal of Science, 299, pp. 289–308.

Daucausse, D. & Lloret, A. (2003): Results of "in-situ" measurements of water content and dry density. FEBEX report 70-UPC-L-5-012. 85 pp. Barcelona.

de Boer, J.H., Linsen, B.G. & Osinga, Th.J. (1965): Studies on pore systems in catalysts. VI. The universal t-curve. J. Catalysis 4, pp. 643–648.

de Boer, J.H., Lippens, B.C., Linesen, B.G., Brokhoff, J.C.P., Van der Heuvel, A. & Osinga., J. (1966): The t-curve of multimolecular N_2 adsorption. J. Colloid Interface Sci., 21, pp. 405–414.

de la Calle, C. & Suquet, H. (1988): Vermiculite. In: Bailey, S.W., Ed.. Hydrous phyllosilicates (exclusive of micas). Mineralogical Society of America. Reviews in Mineralogy, 19, pp. 455–496.

Delgado, A.V., González-Caballero, F., Hunter, R.J., Koopal, L.K. & Lyklema, J. (2007): Measurement and interpretation of electrokinetic phenomena. Journal of Colloid and Interface Science 309, pp. 194–224.

Drits, V.A., Besson, G. & Muller, F. (1995): An improved model for structural transformations of heat-treated aluminous dioctahedral 2:1 layer silicates. Clays and Clay Minerals 43, pp. 718–731.

Duro, L., Domènech, C., Grivé, M., Roman-Ross, G., Bruno, J. & Källström, K. (2014): Assessment of the evolution of the redox conditions in a low and intermediate level nuclear waste repository. Applied Geochemistry 49, pp. 192–205.

Eberl, D. (1978): Reaction Series for dioctahedral smectites. Clay and Clay Minerals, Vol. 26, pp. 327–340.

Eberl, D.D. & Hower, J. (1976): Kinetics of illite formation. Bull. Geol. Soc. Amer. 87, pp. 1326–1330.

Emmerich, K., Madsen, F. & Kahr, G. (1999): Dehydroxylation behaviour of heat-treated and steam-treated homoionic cis-vacant montmorillonites. Clays and Clay Minerals 47, pp. 591–604.

Emmerich, K., Plötze, M. & Kahr, G. (2001): Reversible collapse and Mg2+ release of de- and rehydroxylated homoionic cis-vacant montmorillonites. Applied Clay Science 19, pp. 143–154.

ENRESA (2000): FEBEX Project. Full-scale engineered barriers experiment for a deep geological repository for high level radioactive waste in crystalline host rock. Final Report. Technical Publication ENRESA 1/2000, 354 pp. Madrid.

Entwisle, D.C. & Reeder, S. (1993): New apparatus for pore fluid extraction from mudrocks for geochemical analysis. In: Geochemistry of Clay-Pore Fluid Interactions. The Mineralogical Society Series. Chapman and Hall, pp. 365–388.

Farmer, V.C. (1974): The infrared spectra of minerals. Mineralogical Society Monograph 4, 539 pp. Mineralogical Society, London.

Fernández A.M. & Villar, M.V. (2010): Geochemical behaviour of a bentonite barrier: results up to 8 years of thermo-hydraulic treatment in the laboratory. Applied Geochemistry 25, pp. 809–824.

Fernández A.M. (2004): Caracterización y modelización del agua intersticial en materiales arcillosos: Estudio de la bentonita de Cortijo de Archidona. Ph. D. Thesis. CIEMAT, Madrid, 505 pp.

Fernández, A.M. & Rivas, P. (2005a): Pore water chemistry of saturated Febex bentonite compacted at different densities. In: Alonso, E.E., Ledesma, A. (Eds.), Advances in understanding Engineered Clay Barriers. A.A. Balkema Publishers, Leiden, pp. 505–514.

Fernández, A.M. & Rivas, P. (2005b): Analysis and distribution of waters in the compacted Febex bentonite: pore water chemistry and adsorbed water properties. In: Alonso, E.E., Ledesma, A. (Eds.), Advances in understanding Engineered Clay Barriers. A.A. Balkema Publishers, Leiden, pp. 257–275.

Fernández, A. M., Sánchez-Ledesma, D.M., Tournassat, C., Melón, A., Gaucher, E. C., Astudillo, J. & Vinsot, A. (2014): Applying the Squeezing Technique to Highly Consolidated Clayrocks for Pore Water Characterisation: Lessons Learned from Experiments at the Mont Terri Rock Laboratory. Applied Geochemistry 49, pp. 2–21.

Fernández, A.M. (2018): Gas and water sampling in different pipes from the FEBEX in-situ test at the Grimsel Test Site. Nagra Arbeitsbericht NAB 16-13.

Fernández, A.M., Baeyens, B., Bradbury, M. & Rivas, P. (2004): Analysis of the pore water chemical composition of a Spanish compacted bentonite used in an engineered barrier. Physics and Chemistry of the Earth 29, pp. 105–118.

Fernández, A.M., Jockwer, N. & Martín P.L. (2007): Evolution of the Chemical Parameters in the FEBEX in-situ experiment. NF-PRO Project (Contract Number: FI6W-CT-2003-02389). Deliverable D2.2.10, 32 pp.

Fernández, A.M., Kaufhold, S., Sánchez-Ledesma, D.M., Rey, J.J., Melón, A., Robredo, L.M., Fernández, S., Labajo, M.A. & Clavero, M.A. (2018b, submitted): Evolution of the THC conditions in the FEBEX in-situ test after 18 years of experiment: interactions of bentonite with the C-steel Heater #2. Applied Geochemistry.

Fernández, A.M., Rey, J.J., Sánchez-Ledesma, D.M. & Clavero, M.A. (2018a, submitted): Evolution of the thermo-hydro-chemical (THC) conditions in the FEBEX in-situ test after 18 years of experiment: study of the pore water chemistry. Applied Geochemistry.

Fernández, A.Mª., Bath, A., Waber, H.N. & Oyama, T. (2003): Annex 2: water sampling by squeezing drillcores. In: Pearson, F.J., Arcos, D., Bath, A., Boisson, J.Y., Fernández, A.Mª., Gäbler, H.-E., Gaucher, E., Gautschi, A., Griffault, L., Hernán, P. & Waber, H.N., (Eds.). Geochemistry of Water in the Opalinus Clay Formation at the Mont Terri Rock Laboratory. FOWG No. 5, pp. 171–199.

Fernández, R., Torres, E., Ruiz, A.I., Cuevas, J., Alonso, M.C., García Calvo, J.L., Rodríguez, E. & Turrero, M.J. (2017): Interaction processes at the concrete-bentonite interface after 13 years of FEBEX-plug operation. Part II: Bentonite contact. Physics and Chemistry of the Earth 99, pp. 49–63.

Follett, E.A.C., Mchardy, W.J., Mitchell, B.D. & Smith, B.F.L. (1965): Chemical dissolution techniques in the study of soil clays: Parts I and II. Clay Minerals 6, pp. 23–34.

Frick, U., Alexander, W.R., Baeyens, B., Bossart, P., Brandbury, M.H., Bühler, Ch., Eilenberg, J., Fierz, Th., Heer, W., Hoehn, E., McKinley, I.G. & Smith, P.A. (1992): The radionuclide migration experiment – Overview of investigations 1985 – 1990. Nagra Technical Report NTB 91-04.

Fuentes-Cantillana, J.L. & García-Siñeriz, J.L. (1998): FEBEX Full-scale Engineered Barriers Experiment in Crystalline Host Rock. Final Design and installation of the "in-situ" Test at Grimsel". Enresa Technical Report 12/98.

Fuentes-Cantillana, J.L., García-Siñeriz, J.L., Franco, J.J., Obis, J., Pérez, A., Jullien, F., Alberdi, J., Barcala, J.M., Campos, R., Cuevas, J., Fernández, A.M., Gamero, E., García, M., Gómez, P., Hernández, A., Illera, A., Martín, P.L., Melón, A.M., Missana, T., Ortuno, F., Pardillo, J., Rivas, P., Turrero, M.J., Villar, M.V., Mingarro, M., Pelayo, M., Caballero, E., Cuadros, J., Huertas, F., Huertas, F.J., Jiménez de Cisneros, C., Linares, J., Bazargan-Sabet, B., Ghoreychi, M., Jockwer, N., Wieczorek, K., Kickmaier, W., Marschall, P., Martínez, M.A., Carretero, P., Dai, Z., Delgado, J., Juncosa, R., Molinero, J., Ruiz, A., Samper, J., Vázquez, A.; Alonso, E., Carrera, J., Gens, A., García-Molina, A. J., Guimera, J., Guimaraes, L.do N., Lloret, A., Martínez, L., Olivella, S., Pintado, X., Sánchez, M., Elorza, F.J., Borregón, J.L., Canamon, I., Rodriguez Pons-Esparver, R. (UPM), Fariña, P, Farias, J. & Huertas, F. (2000): FEBEX full-scale engineered barriers experiment for a deep geological repository for high level radioactive waste in crystalline host rock Final Report. Enresa, Technical Report 1/2000.

Fuentes-Cantillana, J.L., García-Siñeriz, J.L., Obis, J., Pérez, A. (AITEMIN); Alberdi, J., Barcala, J.M., Campos, R., Cuevas, J., Fernández, A.M., Gamero, E., García, M., Gómez, P., Hernández, A., Illera, A., Martín, P.L., Melón, A.M., Mingarro, M., Ortuño, F., Pardillo, J., Pelayo, M., Rivas, P., Rodriguez, V., Turrero, M.J., Villar, M.V. (CIEMAT), Caballero, E., Jiménez de Cisneros, C., Linares, J. (CSIC-Zaidín), Martínez, M.A. (TECNOS), Samper, J., Delgado, J., Juncosa, R., Molinero (ULC), Alonso, E., Carrera, J., Gens, A., García-Molina, A. J., Guimera, J., Guimaraes, L.do N., Lloret, A., Martínez, L., (UPC-DIT), Elorza, F.J., Borregón, J.L. (UPM), Fariña, P. (DM Iberia, S.A.) & Farias, J. (Geocontrol, S.A.) were the technical editors of this report under the direction of Huertas, F. (Enresa). (1998): FEBEX full-scale engineered barriers experiment in crystalline host rock. Pre-operational Stage. Summary Report. Enresa Technical Report 01/98.

García-Gutiérrez, M., Missana, T., Mingarro, M., Samper, J., Dai, Z. & Molinero, J. (2001): Solute transport properties of compacted Ca-bentonite used in the FEBEX project. Journal of Contaminant Hydrology (Migration '99), Bd. 47, Nr. 2–4, S. 127–137.

García-Gutiérrez, M., Cormenzana, J.L., Missana, T. & Mingarro, M. (2004): Diffusion coefficients and accessible porosity for HTO and 36Cl in compacted FEBEX bentonite. Applied Clay Science, 26: 65–73

García-Siñeriz, J.L., Abós, H., Martínez, V., De la Rosa, C., Mäder, U. & Kober, F. (2016): FEBEX DP: Dismantling of heater 2 at the FEBEX in-situ test. Description of operations. Nagra Arbeitsbericht NAB 16-11.

Garralón, A., Gómez, P., Peña, J., Buil, B., Turrero, M.J., Torres, E. & Sánchez, L. (2017): Hydrogeochemical characterization of the groundwater in the FEBEX gallery. Nagra Arbeitsbericht NAB 16-14.

Giroud, N. (2014): FEBEX – Assessment of redox conditions in Phase 2 before dismantling. Nagra Arbeitsbericht NAB 14-55.

Glaus, M.A., Baeyens, B., Bradbury, M.H., Jakob, A., Van Loon, L.A. & Yaroshchuck, A. (2007): Diffusion of ^{22}Na and ^{85}Sr in Montmorillonite: Evidence of interlayer diffusion being the dominant pathway at high compaction. Environmental Science and Technology 41, pp. 478–485.

Greene-Kelly, R. (1952): A test for montmorillonite. Nature 170, pp. 1130–1131.

Gregg, S. J. & Sing, K.S.W. (1982): Adsorption, Surface area and Porosity. Academic Press. 303 pp.

Guillaume, D., Neaman, A., Cathelineau, M., Mosser-Ruck, R., Peiffert, C., Abdelmoula, M., Dubessy, F., Villiéras, F. & Michau, N. (2004): Experimental study of the transformation of smectite at 80 °C and 300 °C in the presence of Fe oxides. Clay Minerals, 39, 17–34.

Guillaume, D., Neaman, A., Cathelineau, M., Mosser-Ruck, R., Peiffert, C., Abdelmoula, M., Dubessy, F., Villiéras, F. & Michau, N. (2004): Experimental study of the transformation of smectite at 80 °C and 300 °C in the presence of Fe oxides. Clay Minerals, 39, 17–34.

Hadi, J., Tournassat, C., Ignatiadis, I., Greneche, J.M. & Charlet, L. (2013) : Modelling CEC variations versus structural iron reduction levels in dioctahedral smectites. Existing approaches, new data and model refinements. Journal and Colloid and Interface Science 407, pp. 397–409.

Harkins, W.D. & Jura, G. (1944): Vapor Adsorption Method for the Determination of the Area of a Solid without the Assumption of a Molecular Area, and the Areas Occupied by Nitrogen and Other Molecules on the Surface of a Solid. J. Amer. Chem. Soc. 66, pp. 1366–1373.

Herbert, H.J., Kasbohm, J. & Henning, K.H. (2004): Long-term behaviour of the Wyoming bentonite MX-80 in high saline solutions. Applied Clay Science 26, pp. 275–291.

Hoehn, E., Fierz, T.H. & Thorne, P. (1990): Hydrogeological characterization of the migration experimental area at the Grimsel Test Site. Nagra Technical Report 89-15.

Hofmann, U. & Klemen, R. (1950): Verlust der Austauschfähigkeit von Lithiumionen an Bentonit durch Erhitzung. Z. Anorg. Allg. Chemie 262, pp. 95–99.

Howard, J.J. & Roy, D.M. (1985): Development of layer charge and kinetics of experimental smectite alteration. Clays and Clay Mineral 33, pp. 81–88.

Hower, J. & Mowatt, T.C. (1966): The mineralogy of illites and mixed-layer illite/ montmorillonite. Amer. Mineralogist 51, pp. 825–854.

Huertas, F., Fariña, P., Farias, J., García-Siñeriz, J.L., Villar, A.M., Fernández, A.M., Martín, P.L., Elorza, F.J., Gens, A., Sánchez, M., Lloret, A., Samper, J. & Martínez, M.A. (2006): FEBEX Project. Full-scale engineered barriers experiment for a deep geological repository for high level radioactive waste in crystalline host rock. Updated Final Report 1994 – 2004. Technical Publication ENRESA 5-0/2006, 590 pp. Madrid.

Hunter R.J. (2001): Foundations of Colloid Science. Oxford University Press, Oxford, United Kingdom.

Ionue, A. & Utada, M. (1991): Smectite to chlorite transformation in thermally altered volcanoclastic rocks in the Kamikita area, Northern Honshu, Japan. American Mineralogist 76, pp. 628–640.

Ionue, A., Velde, B., Meunier, A. & Touchard, G. (1988) : Mechanism of illite formation during smectite-to-illite conversion in a hydrothermal system. American Mineralogist 73, pp. 1325–1334.

Jackson, M.L. (2005): Soil Chemical Analysis. Advanced course. Revised Second Edition. Parallel Press. University of Wisconsin-Madison Libraries. Madison, Wisconsin, 930 pp.

Järvinen, J., Matusewicz, M. & Itälä, A. (2016): Methodology for studying the composition of non-interlamellar pore water in compacted bentonite Clay Minerals 51, pp. 173–187.

Jockwer, J. & Wieczorek, K. (2008): Investigations on gas generation, release, and migration in the frame of FEBEX. GRS Report 243, 79 pp.

Jodin-Caumon, M. C., Mosser-Ruck, R., Randi, A., Pierron, O., Cathelineau, M., & Michau, N. (2012): Mineralogical evolution of a claystone after reaction with iron under thermal gradient. Clays and Clay Minerals, 60(5), 443–455.

Jones, B.F. & Galán, E. (1988): Sepiolite and palygorskite. In: Hydrous Phyllosilicates (Bailey, S.W., editor). Mineralogical Society of America, Reviews in Mineralogy 19, pp. 631–674.

Karnland, O., Olsson, S., Dueck, A., Birgersson, M., Nilsson, U., Hernan-Haakansson, T. & Rosborg, B. (2009): Long term test of buffer material at the Äspö Hard Rock Laboratory, LOT project. Final report on the A2 test parcel (No. SKB-TR-09-29). Swedish Nuclear Fuel and Waste Management Co..

Karnland, O., Olsson, S., Nilsson, U. & Sellin, P. (2007): Experimentally determined swelling pressures and geochemical interactions of compacted Wyoming bentonite with highly alkaline solutions. Physics and Chemistry of the Earth, Parts A/B/C 32, pp. 275–286.

Kaufhold, S. & Dohrmann, R. (2010): Stability of bentonites in salt solutions: II. Potassium chloride solution. Initial step of illitization?. Applied Clay Science 49 pp. 98–107.

Kaufhold, S. & Dohrmann, R. (2010b): Effect of extensive drying on the cation exchange capacity of bentonites. Clay Minerals 45, pp. 441–448.

Kaufhold, S., Dohrmann, R. & Ufer, K. (2016): Interaction of magnesium cations with dioctahedral smectites under HLRW repository conditions. Clays and Clay Minerals 64, pp. 743–752.

Kaufhold, S., Dohrmann, R., Götze, N. & Svensson, D. (2017): Characterisation of the second parcel of the alternative buffer material (ABM) experiment – I mineralogical reactions. – Clays and Clay Minerals, 65, 27–41.

Kaufhold, S., Dohrmann, R., Sandén, T., Sellin, P. & Svensson, D. (2013): Mineralogical investigations of the alternative buffer material test – I. Alteration of bentonites. – Clay Minerals 48, pp. 199–213.

Kaufhold, S., Dohrmann, R., Ufer, K. & Kober, F. (submitted): Interactions of bentonite with metal and concrete from the FEBEX experiment. Mineralogical and geochemical investigation of selected sampling sites. Clay Minerals.

Kaufhold, S., Hassel, A.W., Sanders, D. & Dohrmann, R. (2015): Corrosion of high-level radioactive waste iron-canisters in contact with bentonite. Journal of Hazardous Materials, 285, 464–473.

Keeling, P.S. (1961): The examination of clays by IL/MA. Trans. Brit. Ceram. Soc. 60, pp. 217–244.

Keeling, P.S., E.C. Kirby & Robertson, R.H.S. (1980): Moisture adsorption and specific surface area. J. Brit. Ceram. Soc. 79, pp. 36–40.

Kloprogge, J.T. (2005): The application of vibrational spectroscopy to clay minerals and layered double hydroxides. CMS Workshop Lectures 13. The Clay Minerals Society. 285 pp.

Kober, F., Van Meir, N. (2017): FEBEX-DP – Dismantling related supplementary documents. Nagra Arbeitsbericht NAB 16-68.

Komadel, P., Madejová, J. & Stucki, J.W. (2006): Structural Fe(III) reduction in smectites Applied Clay Science 34, pp. 88–94.

Köster, H.M. (1977): Die Berechnung kristallchemischer Strukturformeln von 2:1 – Schichtsilikaten unter Berücksichtigung der gemessenen Zwischenschichtladungen und Ka tionenumtauschkapazitäten, sowie die Darstellung der Ladungsverteilung in der Struktur mittels Dreieckskoordinaten. Clay Minerals, 12, pp. 45–54.

Kozaki, T., Fujishima, A., Saito, N., Sato, S. & Ohashi, H. (2005): Effects of dry density and exchangeable cations on the diffusion process of sodium ions in compacted bentonite. Engineering Geology 81, pp. 246–254.

Kumpulainen S., Kiviranta K., Carlsson T., Muurinen A., Svensson D., Sasamoto H., Yui M. & Wersin P. (2010): Long-term alteration of bentonite in the presence of metallic iron. SKB Report R-10-52. Swedish Nuclear Fuel and Waste Management SKB, Stockholm.

Lagaly, G. (1994): Layer charge determination by alkylammonium ions. In: Layer Charge Characteristics of 2:1 Silicate Clay Minerals (A.R. Mermut, editor). Workshop Lectures volume 6, The Clay Minerals Society, Boulder, Colorado, USA., pp. 1–46.

Lantenois, S., Lanson B., Muller, F., Bauer, A., Jullien, M. & Plaçon, A. (2005) : Experimental study of smectite interaction with metal Fe at low temperature: 1. Smectite destabilization. Clays and Clay Minerals 53, pp. 597–612.

Lanyon G.W. & Gaus, I. (2016): Main outcomes and review of the FEBEX In-situ Test (GTS) and Mock-Up after 15 years of operation. Nagra Arbeitsbericht NAB 15-04.

Libert, M., Bildstein, O., Esnault, L., Jullien, M. & Sellier, R. (2011): Molecular hydrogen: an abundant energy source for bacterial activity in nuclear waste repositories. Physics and chemistry of the Earth 36, pp. 1616–1623.

Mackenzie, R.C. (1957): The differential thermal investigation of clays. Mineralogical Society. Clay minerals group. London.

Madejová, J. & Komadel, P. (2001): Baseline studies of the Clay Minerals Society Source Clays: Infrared methods. Clays and Clay Minerals 49, pp. 410–432.

Madejová, J. & Komadel, P. (2005): Information available from infrared spectra of the fine fractions of bentonites. In: The application of vibrational spectroscopy to Clay Minerals and Layered Double Hydroxides. CMS workshop lectures (Kloprogge Eds.), 66–98 pp. The Clay Minerals Society.

Madejová, J. (2003): FTIR techniques in clay mineral studies. Vibrational Spectroscopy 31, pp. 1–10.

Madina, V. & Azkárate, I. (2004): FEBEX Project. Post-mortem analysis: Corrosion Study. Enresa Technical Report 8-2004, 87 pp.

Madina, V. (2003): Estudio de Corrosión de componentes de proyecto FEBEX. Report 36.0045.0, 76 pp.

Madina, V. (2016): Corrosion study of FEBEX-DP components. Nagra Arbeitsbericht NAB 16-54.

Manceau, A., Lanson, B., Drits, V.A., Chateigner, D., Gates, W.P., Wu, J., Huo, D. & Stucki, J.W. (2000): Oxidation-reduction mechanism of iron in dioctahedral smectites: I. Crystal chemistry of oxidized reference nontronites. American Mineralogist 85, pp. 133–152.

Marchel, C. & Stanjek, H. (2012): Cation ordering in cis-and trans-vacant dioctahedral smectites and its implications for growth mechanisms. Clay Minerals 47, pp. 105–115.

Martín, P.L., Barcala, J.M. & Huertas, F. (2006): Large-scale and long-term coupled thermos-hydro-mechanic experiments with bentonite: the FEBEX mock-up test. Journal of Iberian Geology 32, pp. 259–282.

Martínez, V., Abós, H. & García-Siñeriz, J.-L. (2016): FEBEXe: Final Sensor Data Report (FEBEX "in-situ" Experiment). Nagra Arbeitsbericht NAB 16-19.

Marty, N.C.M., Fritz, B., Clement, A. & Michau, N. (2010): Modelling the long-term alteration of the engineered bentonite barrier in an underground radioactive waste repository. Applied Clay Science 47, pp. 82–90.

McCarty, D.K. & Reynolds, R.C. (1995): Rotationally disordered illite-smectite in paleozoic K-bentonites. Clays and Clay Minerals 43, pp. 271–284.

Meunier, A. & Velde, B. (1989): Solid solution in I/S mixed-layer minerals and illite. American Mineralogist, 74, pp. 1106-1112.

Meunier, A. (2005): Clays. Springer, 472 pp.

Meunier, A., Lanson, B. & Beaufort, D. (2000): Vermiculitization of smectite interfaces and illite layer grow has a possible dual model for illite/smectite illitization in diagenetic environments: a synthesis. Clay Mineral 35, pp. 573–586.

Meunier, A., Velde, B. & Griffault, L. (1998): The reactivity of bentonites: a review. An application to clay barrier stability for nuclear waste storage. Clay Minerals 33, pp. 187–196.

Missana, T., Alonso, U., Fernández, A.M. & García-Gutiérrez, M. (2018a): Colloidal properties of different smectite clays: significance for the bentonite barrier erosion and radionuclide transport in radioactive waste repositories. Submitted to Applied Geochemistry.

Missana, T., Alonso, U., Fernández, A.M. & García-Gutiérrez, M. (2018b): Analysis of the stability behaviour of colloids obtained from different smectite clays. Applied Geochemistry 92, pp. 180v187.

Moore, D. & Reynolds, R. (1989): X-Ray diffraction and the identification and analysis of Clay Minerals. Oxford University Press, N.Y., 332 pp.

Mosser-Ruck, R., Cathelineau, M., Guillaume, G., Charpentier, D., Rousset. D., Barres, O. & Michau, N. (2010): Effects of temperature, pH and iron/clay and liquid/clay ratios on experimental conversion of dioctahedral smectite to berthierine, chlorite, vermiculite or saponite. Clays and Clay Minerals 58, pp. 280–291.

Muller, F., Drits, V., Plancon, A. & Robert, J.L. (2000): Structural transformation of 2:1 dioctahedral layer silicates during dehydroxylation-rehydroxylation reactions. Clays and Clay Minerals 48, pp. 572–585.

Muurinen, A. (1994): Diffusion of anions and cations in compacted sodium bentonite. Technical research centre of Finland. VTT publications 168, 75 pp.

Muurinen, A., Carlsson, T. & Root, A. (2013): Bentonite pore distribution based on SAXS, chloride exclusion and NMR studies. Clay Minerals 48, pp. 251–266.

Neaman, A., Gillaume, D., Pelletier, M. & Villieras, F. (2003): The evolution of textural properties of Na/Ca-bentonite following hydrothermal treatment at 80 and 300 °C in the presence of Fe and/or Fe oxides. Clay Minerals 38, pp. 213–223.

Newman, A.C.D. (1987): Chemistry of Clays and Clay Minerals. Mineral Society. Monograph N° 6. Longman Scientific & Technical, 480 pp.

Nguyen-Thanh, L., Kasbohm, J. & Hoang-Minh, T. (2010): How to calculate mineral formula for 2-member dioctahedral mixed layers from EDX-analysis by Transmission Electron Microscopy: Example-Friedland clay. 2010 SEA-CSSJ-CMS. Trilateral Meeting on Clays. Sevilla, Spain, 6 – 11 June. Clay Minerals Society.

Oelkers, E.H., Schott, J. & Devidal, J.L. (1994): The effect of aluminium, pH and chemical affinity on the rates of aluminosilicate dissolution reactions. Geochimica et Cosmochimica Acta 58, pp. 2011–2024.

Olis, A.C., Malla, P.B. & Douglas, L.A. (1990): The rapid estimation of the layer charges of 2:1 expanding clays from a single alkylammonium ion expansion. Clay Minerals 25, pp. 39–50.

Pardillo, J., Campos, R. & Guimerá, J. (1997): Caracterización geológica de la zona de ensayo FEBEX (Grimsel-Suiza). Technical Report CIEMAT-70-IMA-M-2-01.

Parkhurst, D.L. & Appelo, C.A.J. (2013): Description of input and examples for PHREEQC Version 3 – A computer program for speciation, batch-reaction, one-dimensional transport, and inverse geochemical calculations: U.S. Geological Survey Techniques and Methods, book 6, chap. A43, 497 pp.

Pearson, F. J. (1999): What is the porosity of a mudrock?, in: Aplin, A. C., Fleet, A. J., Macquaker, J. H. S. (Eds), Muds and Mudstones: Physical and Fluid Flow Properties. Geological Society, London. Special Publications 158, pp. 9–21.

Pearson, F.J., Arcos, D., Bath, A., Boisson, J. Y., Fernández, A.M., Gäbler, H-E, Gaucher, E., Gautschi, A., Griffault, L., Hernán, P. & Waber, H.N. (2003): Geochemistry of water in the Opalinus Clay Formation at the Mont Terri Rock Laboratory. Swiss Federal Office for Water and Geology Series, N° 5, 319 pp.

Pelayo, M., Marco, J.F., Fernández, A.M., Vergara, L., Melón, A.M. & Pérez del Villar, L. (2018): Infrared and Mössbauer spectroscopy of Fe-rich smectites from Morrón de Mateo bentonite deposit (Spain). Clay Minerals 53, pp. 17–28.

Perronnet, M., Jullien, M., Villieras, F., Raynal, J., Bonnin, D. & Bruno, G. (2008): Evidence of a critical content in Fe(0) on FoCa7 bentonite reactivity at 80 °C. Applied Clay Science, 38, 187202.

Peters, C.A., Yang, Y.C., Higgins, J.D. & Burger, P.A. (1992): A preliminary study of the chemistry of pore water extracted from tuff by one-dimensional compression. Water-Rock Interaction, Kharaka & Maest (eds.), pp. 741–745.

Pozo, M. & Galán, E. (2015): Magnesian Clays. Characterization, Origin and Applications. AIPEA Educational Series N° 2, 380 pp.

Pusch, R., Muurinen, A., Lehikoinen, J., Bors, J. & Eriksen, T. (1999): Microstructural and chemical parameters of bentonite as determinants of waste isolation efficiency. European Commission. Nuclear Science and Technology. Project Report EUR 18950 EN.

Rey, M., Bárcena, I. & García-Siñeriz, J.L. (2015): Full Dismantling Sampling Plan. Rev. 5. AITEMIN May 2015.

Rozalén, M.L., Huertas, F.J., Brady, P.V., Cama, J., García-Palma, S. & Linares, J. (2008): Experimental study of the effect of pH on the kinetics of montmorillonite dissolution at 25 °C. Geochimica et Cosmochimica Acta 72, pp. 4224–4253.

Russell, J.D. (1987): Infrared methods. In: A Handbook of determinative methods in clay mineralogy. Wilson M.J. (Ed.). Blackie, New York, pp. 133–173.

Sainz-Díaz, C.I., Hernández-Laguna, A. & Dove, M.T. (2001): Theoretical modelling of cis-vacant and trans-vacant configurations in the octahedral sheet of illites and smectites. Physics and Chemistry of Minerals 28, pp. 322–331.

Savage, D., Arthur, R., Watson, C., Wilson, J. & Strömberg, B. (2011): Testing geochemical models of bentonite pore water evolution against laboratory experimental data. Physics and Chemistry of the Earth 36, pp. 1817–1829.

Savage, D. (2014): An assessment of the impact of the long term evolution of engineered structures on the safety-relevant functions of the bentonite buffer in an HLW repository. Nagra Technical Report NTB 13-02.

Savage, D., Watson, C., Benbow, S. & Wilson, J. (2010): Modelling iron-bentonite interactions. Applied Clay Science 47, pp. 91–98.

Seewald, J.S. (2001a): Model for the origin of carboxylic acids in basinal brines. Geochimica et Cosmochimica Acta 65, pp. 3779–3789.

Seewald, J.S. (2001b): Aqueous geochemistry of low molecular weight hydrocarbons at elevated temperatures and pressures: Constrains from mineral buffered laboratory experiments. Geochimica et Cosmochimica Acta 65, pp. 1641–1664.

Shen, S., Stucki, J.W. & Boast, C.W. (1992): Effects of structural iron reduction on the hydraulic conductivity of Na-smectite. Clays and Clay Minerals 40, pp. 381–386.

Shock, E.L. (1988): Organic acid metastability in sedimentary basins. Geology 16, pp. 886–890.

Soler, J.M. & Mäder, U.K. (2007): Mineralogical alteration and associated permeability changes induced by a high-pH plume: modelling of a granite core infiltration experiment. Appl. Geochem. 22, pp. 17–29.

Środon, J., Elsass, F., McHardy, W.J. & Morgan, D.J. (1992): Chemistry of illite-smectite inferred from TEM measurements of fundamental particles. Clay Minerals 27, pp. 137–158.

Stucki, J.W. (1988): Structural iron in smectites. In Iron in Soils and Clay Minerals, Stucki, J.W., Goodman, B.A. & Schwertmann, U., eds., Reidel, D., Dordrecht, pp. 625–675.

Stucki, J.W.& Roth, C.B. (1977): Oxidation-reduction mechanism for structural Fe in nontronite. Soil Science Society of America Journal 41, pp. 808–814.

Svensson, D. (2015): The Bentonite Barrier. Swelling Properties, Redox Chemistry and Mineral Evolution. Doctoral dissertation, Faculty of Engineering, Lund University, Sweden.

Svensson, D., Dueck, A., Nilsson, U., Olsson, S., Sandén, T., Lydmark, S., Jägerwal, D., Pedersen, K. & Hansen, S. (2011): Alternative Buffer Material. Status of the ongoing laboratory investigation of reference materials and test package 1, Swedish Nuclear Fuel and Waste Management Company Technical Report, SKB TR-11-06.

Takase, H. (2004): Discussion on PA model development for bentonite barriers affected by chemical interaction with concrete: do we have enough evidence to support bentonite stability? In: International Workshop on Bentonite-Cement Interaction in Repository Environments, Tokyo, Japan, NUMO-TR 04-05, A3-172 – A3-177; Posiva Report 2004-25, 192 pp.

Tarafder, P.K. & Thakur, R. (2012): An optimised 1,10-Phenathroline method for the determination of ferrous and ferric oxides in silicate rocks, soils and minerals. Geostandards and Geoanalytical research 37, pp. 155–168.

Taylor, H.F.W. (1997): Cement Chemistry. 2nd Edition. Thomas Telford Publishing, 459 pp.

Tournassat, C. & Appelo, C.A.J. (2011): Modelling approaches for anion-exclusion in compacted Na-bentonite. Geochim Cosmochim Acta 75, pp. 3698–3710.

Tournassat, C., Steefel, C.I., Bourg, I.C. & Bergaya, F. (2015): Natural and Engineered Clay Barriers. In: Developments in Clay Science Vol. 6. Elsevier, 432 pp.

Truche, L., Berger, G., Destrigneville, C., Guillaume, D., Giffaut, E. & Pages, A. (2009): Experimental reduction of aqueous sulphate by hydrogen under hydrothermal conditions: implication for the nuclear waste storage. Geochimica et Cosmochimica Acta 73, pp. 4824–4835.

Tsipursky, S.I. & Drits, V.A. (1984): The distribution of octahedral cations in the 2:1 layers of dioctahedral smectites studied by oblique-texture electron diffraction. Clay Minerals 19, pp. 177–193.

Turrero, M.J. & Cloet, V. (Eds.) (2018): Synthesis of concrete results. BGR, CIEMAT, CSIC, Nagra, OBAYASHI, SANDIA, UAM, UNIBERN. Nagra Arbeitsbericht NAB 16-18.

Van der Marel, H.W. & Beutelspacher, H. (1976): Atlas of infrared spectroscopy of clay minerals and their mixtures. Elsevier, Amsterdam, 396 pp.

Van Humbeeck, H., Verstricht, J., Li, X.L., De Cannière, P., Bernier, F. & Kursten B. (2009): The Ophelie mock-up. Final Report. EURIDICE Report 09-134, 197 pp.

Velde, B. (1985): Clay minerals: a physico-chemical explanation of their occurrence. Elsevier, 426 pp.

Villar M.V., Iglesias R.J., Abós, H., Martínez, V., de la Rosa, C. & Manchón, M.A. (2016): FEBEX-DP: Onsite Analysis Report. Nagra Arbeitsbericht NAB 16-12.

Villar, M.V. (Ed). (2006): FEBEX Project. Final Report. Post-mortem bentonite analysis. ENRESA Technical Report 05-1/2006, 183 pp.

Villar, M.V., Iglesias, R.J., Abós, H., Martínez, V., de la Rosa, C. & Manchón, M.A. (2017): FEBEX-DP: Post-mortem THM/THC Report. Analysis of Results. Nagra Arbeitsbericht NAB 16-12.

Villar, M.V., Iglesias, R.J., Gutiérrez-Álvarez, C., Carbonell, B., Campos, R., Campos, G., Martín, P.L. & Castro, B. (2017b): FEBEX-DP: Thermo-hydro-mechanical postmortem analysis of bentonite performed at CIEMAT. Nagra Arbeitsbericht NAB 16-24.

Villiéras, F., Michot, L.J., Cases, J.M., Berend, I., Bardot, F., Francois, M., Gérard, G. & Yvon, J. (1997): Static and dynamic studies of the energetic surface heterogeneity of clay minerals. In: Rudzinki, W., Steele, W.A., Zgrablich, G. (Eds.). Equilibria and Dynamics of Gas Adsorption on Heterogenous Solid Surfaces. Studies in Surface Science and Catalysis, Vol. 104, pp. 573–623.

Wersin, P. & Kober, F. (2017): FEBEX-DP. Metal corrosion and Iron-Bentonite Interaction Studies. Nagra Arbeitsbericht NAB 16-16.

Wersin, P. & Mettler, S. (2006): Workshop on Fe-clay interactions in repository environments, a joint initiative by ANDRA, SKB and Nagra, 2006. Nagra Arbeitsbericht NAB 06-15.

Wersin, P., Birgersson, M., Olsson, S., Karnland, O. & Snellman, M. (2007): Impact of corrosion-derived iron on the bentonite buffer within the KBS-3H disposal concept. The Okiluoto site as case study. Posiva Report 2007-11. Finland.

Whitney, G. & Northrop, H.R. (1988): Experimental investigation of the smectite to illite reaction: Dual reaction mechanisms and oxygen isotope systematics. American Mineralogists 73, pp. 77–90.

Whitney, G. & Velde, B. (1993): Changes in particle morphology during illitization: an experimental study. Clays and Clay Mineral 41, pp. 209–218.

Wieland, E. & Hummel, W. (2015): Formation and stability of ^{14}C-cointaining organic compounds in alkaline iron-water systems: preliminary assessment based on a literature survey and thermodynamic modelling. Mineralogical Magazine 79, pp. 1275–1286.

Wiewiora, A. (1990): Crystallochemical classifications of phyllosillicates based on the unified system of projection of chemical composition. I. The mica group. Clay Minerals 25, pp. 77–90.

Williamson, G.K. & Hall, A.H. (1953): X-Ray line broadening from filed aluminium and wólfram. Acta Metall. Mater., Vol. 1, pp. 22–31.

Wilson, J., Cressey, G., Cressey, B., Cuadros, J., Ragnarsdottir, K.V., Savage, D. & Shibata, M. (2006a): The effect of iron on montmorillonite stability (II) Experimental investigation. Geochimica et Cosmochimica Acta 70, pp. 323–336.

Wilson, J., Cressey, G., Cressey, B., Cuadros, J., Ragnarsdottir, K.V., Savage, D. & Shibata, M. (2006b): The effect of iron on montmorillonite stability. (II) Experimental investigations. Geochimica et Cosmochimica Acta 70, pp. 306–322.

Wilson, M.J. (1987): A handbook of determinative methods in Clay Mineralogy. Blackie. 308 pp.

Zysset, M. & Schindler, P.W. (1996): The proton promoted dissolution kinetics of K-montmorillonite. Geochimica et Cosmochimica Acta 60, pp. 921–931.

Acknowledgements

This work has been carried out in the framework of two projects: FEBEX-II: Full-scale Engineered Barriers Experiment in crystalline host rock (UE Contract FIKW-CT-2000-00016) with respect to the dismantling of Heater #1 and the FEBEX-DP Project with respect to the dismantling of Heater #2. Special thanks to colleagues from AITEMIN for performing the dismantling activities and the collection of samples. We acknowledge CITIUS (Sevilla, Spain), UCM (Madrid, Spain) and the Chemical Department from CIEMAT for performing the XRF, XRD, TEM and chemical analyses. Special acknowledgements to Tiziana Missana and Ursula Alonso for their help in the zeta potential measurements and to Xabier Arroyo from the CAI-Geológicas (UCM, Madrid) for his help in the layer charge measurements.

This work has been financed by the FEBEX-DP consortium (FEBEX: NAGRA, SKB, POSIVA, CIEMAT, KAERI and DP partners: ANDRA, BGR, Obayashi, RWM, SURAO; USDOE,) and by the ENRESA-CIEMAT framework agreement.

Appendix A

Samples taken during dismantling of the Heater #1

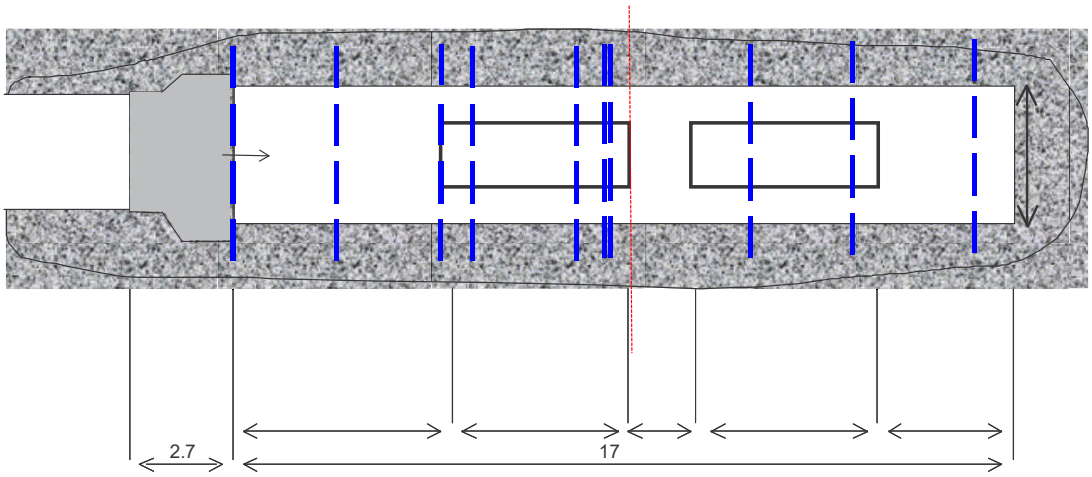

Fig. A-1: Bentonite Sampling Sections from the FEBEX in-situ test analysed for THC studies after dismantling of Heater #1 in 2002 and Heater #2 in 2015

Tab. A-1: Bentonite samples analysed in thermo-hydro-geochemical tests

Sample	Section	Instrumented section	Bentonite slice	Type of sample	Coordinates	Date collection	Site collection
BB7-4	S7	B1	136	Bentonite block	$X_{as\ built}$: -0.010, X_{actual}: 0.000; Y: 0.92; Z = -0.47	24/5/02	Air exposure: 20' T (°C): 14 R.H.(%): 70
BB7-5	S7	B1	136	Bentonite block	$X_{as\ built}$: -0.010, X_{actual}: 0.000; Y: -0.5; Z = 0.61	24/5/02	Air exposure: 30' T (°C): 14 R.H.(%): 70
BB7-6	S7	B1	136	Bentonite block	$X_{as\ built}$: -0.010, X_{actual}: 0.000; Y: 0.54; Z = -0.11	24/5/02	Air exposure: 30' T (°C): 14 R.H.(%): 70
BB12-1	S12	--	120	Bentonite block	$X_{as\ built}$: 2.036, X_{actual}: 1.981; Y: -0.88; Z = 0.4	7/6/02	Air exposure: 5 h T (°C): 16 R.H.(%): 70
BB12-2	S12	--	120	Bentonite block	$X_{as\ built}$: 2.036, X_{actual}: 1.981; Y: -0.7; Z = 0.3	7/6/02	Air exposure: 5 h T (°C): 16 R.H.(%): 70
BB12-3	S12	--	120	Bentonite block	$X_{as\ built}$: 2.036, X_{actual}: 1.981; Y: -0.52; Z = 0.19	7/6/02	Air exposure: 5 h T (°C): 16 R.H.(%): 70
BB12-4	S12	--	120	Bentonite block	$X_{as\ built}$: 2.036, X_{actual}: 1.981; Y: 0.01; Z = -1.02.	7/6/02	Air exposure: 5 h T (°C): 16 R.H.(%): 70
BB12-5	S12	--	120	Bentonite block	$X_{as\ built}$: 2.036, X_{actual}: 1.981; Y: -0.03; Z = 0.80	7/6/02	Air exposure: 6 h T (°C): 16 R.H.(%): 70

Tab. A-1: Cont.

Sample	Section	Instrumented section	Bentonite slice	Type of sample	Coordinates	Date collection	Site collection
BB12-6	S12	--	120	Bentonite block	$X_{as\ built}$: 2.036, X_{actual}: 1.981; Y: 0.05; Z = -0.59	7/6/02	Air exposure: 6 h T (°C): 16 R.H.(%): 70
BB12-10	S12	--	120	Bentonite block	$X_{as\ built}$: 2.036, X_{actual}: 1.981; Y: 0.59; Z = 0.85	7/6/02	Air exposure: 6 h T (°C): 16 R.H.(%): 70
BB12-11	S12	--	120	Bentonite block	$X_{as\ built}$: 2.036, X_{actual}: 1.981; Y: 0.70; Z = 0.41	7/6/02	Air exposure: 6 h T (°C): 16 R.H.(%): 70
BB12-12	S12	--	120	Bentonite block	$X_{as\ built}$: 2.036, X_{actual}: 1.981; Y: 0.50; Z = 0.35	7/6/02	Air exposure: 6 h T (°C): 16 R.H.(%): 70
BH-SD1-01	S17	D1	102	Bentonite close to displacement sensor	X_{actual}: 4.3; Y: -0.4; Z = 1.06	20/7/02	Air exposure: 7 days T (°C): 15 R.H.(%): 88
BB19-1	S19	--	98	Bentonite block	$X_{as\ built}$: 4.850, X_{actual}: 4.819; Y: -0.91; Z = 0.53	24/6/02	Air exposure: -- T (°C): 16 R.H.(%): 95
BB19-2	S19	--	98	Bentonite block	$X_{as\ built}$: 4.850, X_{actual}: 4.819; Y: -0.69; Z = 0.45	24/6/02	Air exposure: -- T (°C): 16 R.H.(%): 95
BB19-3	S19	--	98	Bentonite block	$X_{as\ built}$: 4.850, X_{actual}: 4.819; Y: -0.51; Z = 0.33	24/6/02	Air exposure: 1 h T (°C): 16 R.H.(%): 95
BB19-10	S19	--	98	Bentonite block	$X_{as\ built}$: 4.850, X_{actual}: 4.819; Y: 0.87; Z = 0.52	24/6/02	Air exposure: 1.3 h T (°C): 16 R.H.(%): 95
BB19-11	S19	--	98	Bentonite block	$X_{as\ built}$: 4.850, X_{actual}: 4.819; Y: 0.7; Z = 0.42	24/6/02	Air exposure: 1.3 h T (°C): 16 R.H.(%): 95
BB19-12	S19	--	98	Bentonite block	$X_{as\ built}$: 4.850, X_{actual}: 4.819; Y: 0.49; Z = 0.32	24/6/02	Air exposure: 1.3 h T (°C): 16 R.H.(%): 95
BB19-13	S19	--	98	Bentonite block	$X_{as\ built}$: 4.850, X_{actual}: 4.819; Y: 0.68; Z = -0.64	25/6/02	Air exposure: 2 h T (°C): 16 R.H.(%): 95
BB19-14	S19	--	98	Bentonite block	$X_{as\ built}$: 4.850, X_{actual}: 4.819; Y: 0.60; Z = -0.39	25/6/02	Air exposure: 2 h T (°C): 16 R.H.(%): 95
BB19-15	S19	--	98	Bentonite block	$X_{as\ built}$: 4.850, X_{actual}: 4.819; Y: 0.28; Z = -0.41	25/6/02	Air exposure: 2 h T (°C): 16 R.H.(%): 95
BB28-1	S28	--	80	Bentonite block	$X_{as\ built}$: 7.181, X_{actual}: 6.985; Y: -0.9; Z = 0.52	9/7/02	Air exposure: 1 h T (°C): 18 R.H.(%): 80
BB28-2	S28	--	80	Bentonite block	$X_{as\ built}$: 7.181, X_{actual}: 6.985; Y: -0.71; Z = 0.42	9/7/02	Air exposure: 5.3 h T (°C): 18 R.H.(%): 80

Tab. A-1: Cont.

Sample	Section	Instrumented section	Bentonite slice	Type of sample	Coordinates	Date collection	Site collection
BB28-3	S28	--	80	Bentonite block	$X_{as\ built}$: 7.181, X_{actual}: 6.985; Y: -0.48; Z = 0.34	9/7/02	Air exposure: 1 h T (°C): 18 R.H.(%): 80
BS31-22	S31	(G)	75 (67)	Core sample in contact wit h t he back face of t he heater	$X_{as\ built}$: 7.820, X_{actual}: 8.698; Y: -0.075; Z = -0.715	18/7/02	Air exposure: 2 h T (°C): 18 R.H.(%): 86
BS31-26	S31	(G)	75 (67)	Bentonite block in contact wit h t he back face of t he heater	$X_{as\ built}$: 7.820, X_{actual}: 8.698; Y: 0; Z = 0.17	18/7/02	Air exposure: 10' T (°C): 18 R.H.(%): 86

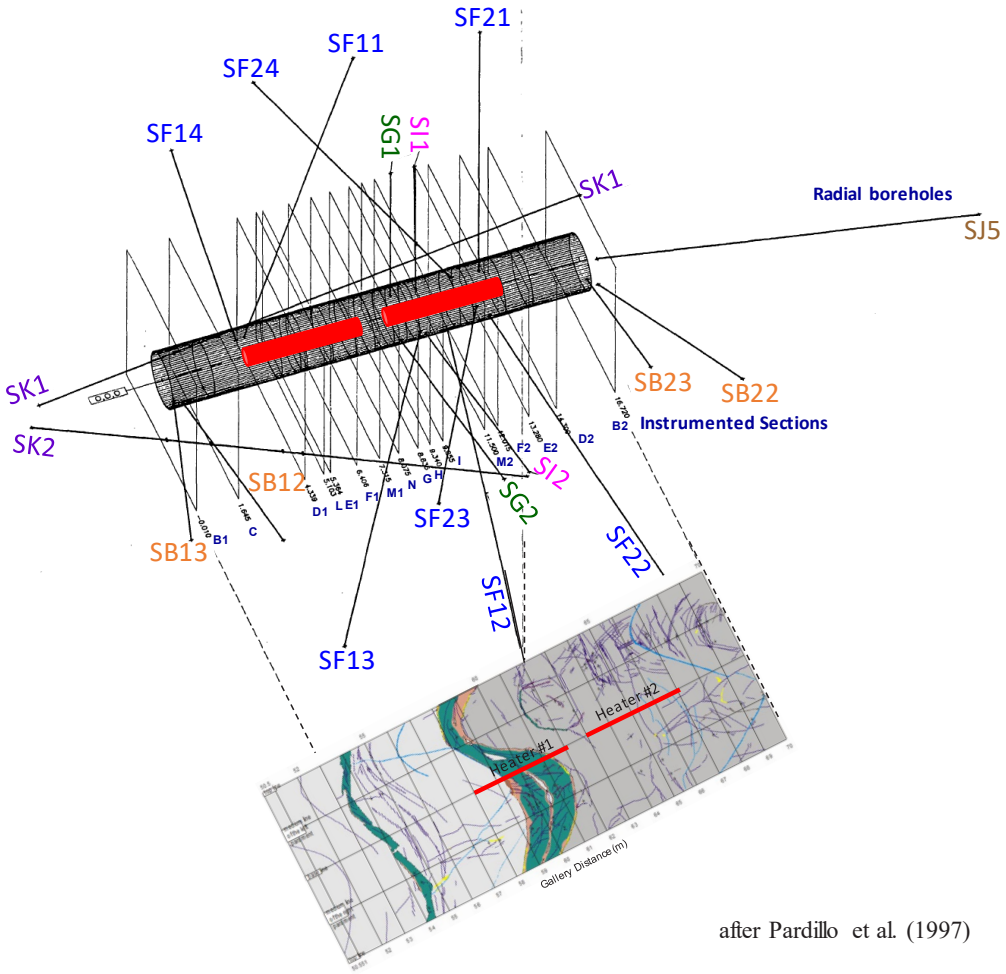

Fig. A-2: General layout of the FEBEX in-situ test (instrumented sections and radial boreholes) and geological map from the FEBEX drift

Subsampling at the laboratory

Once at CIEMAT laboratories, the blocks were half-sectioned along the radius, in order to obtain material for the THG and THM tests. Depending on their subsequent use, or in order to obtain a more detailed sampling, these sections was further sectioned in the sense perpendicular to the radius. The sub-samples obtained in this way was referenced by adding a correlative number to the initial reference of the block. The numbers were given starting by the outer side of the block (Fig. A-3).

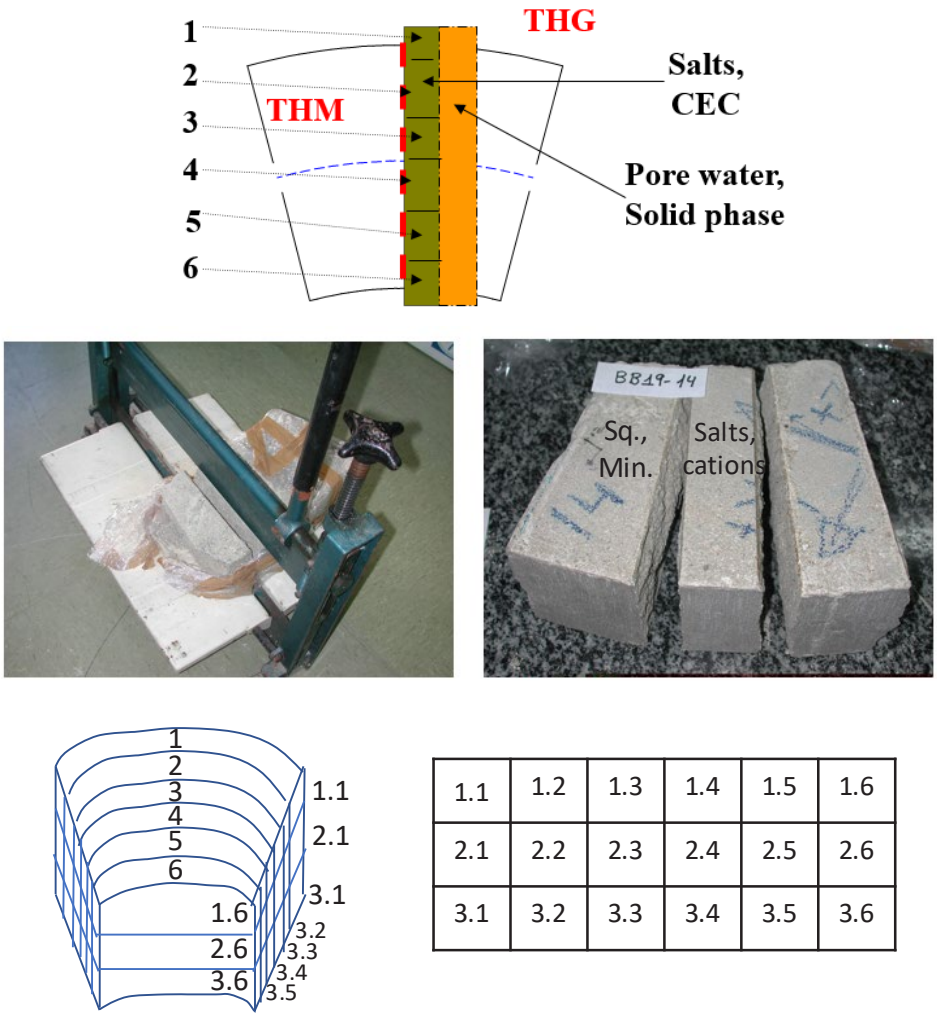

1.1	1.2	1.3	1.4	1.5	1.6
2.1	2.2	2.3	2.4	2.5	2.6
3.1	3.2	3.3	3.4	3.5	3.6

Fig. A-3: Subsampling of the bentonite block for THM and THC analyses

The blocks were cut with a mechanical machine and the THG subsample was sliced in three parts: an internal part (which was used for analysing the soluble salts and exchangeable cations, subsampled in 18 parts: 1.1 to 3.6 as shown), an intermediate part (which was used for squeezing and solid characterization), and an external part (spare sample).

Visual aspect before and after dismantling

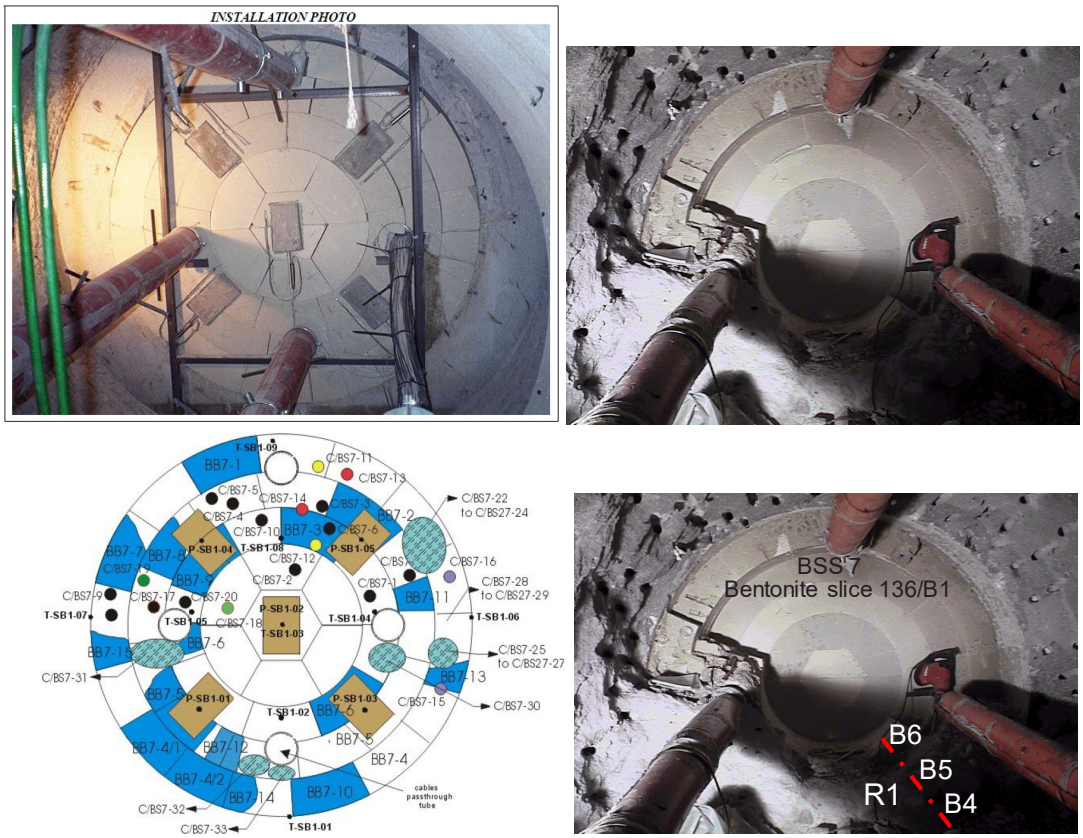

Fig. A-4: Bentonite Sampling Section 7: before dismantling, after dismantling and samples taken for analyses

As built x-coordinate = -0.010 m. Actual x-coordinate = 0.00 m. Instrumented Section B1. Bentonite Slice 136

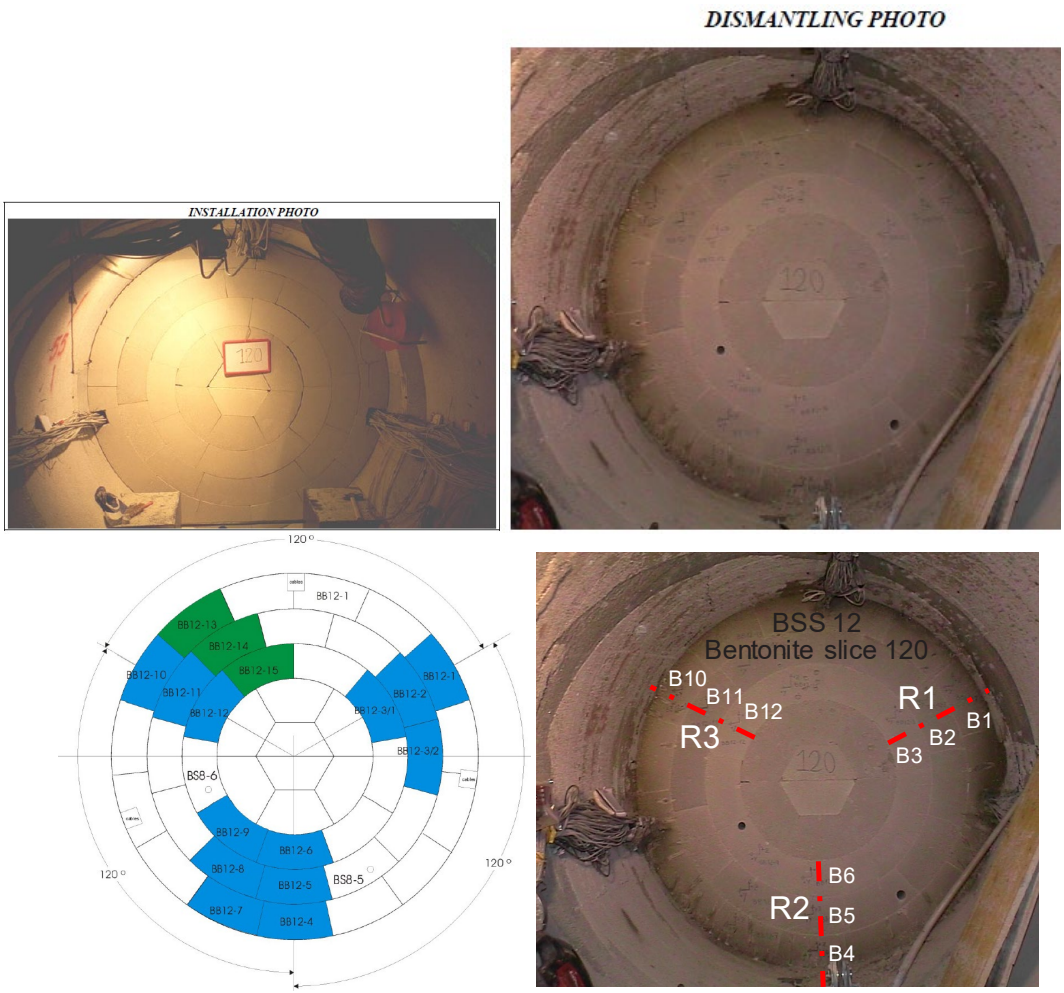

Fig. A-5: Bentonite Sampling Section 12 before dismantling, after dismantling and samples taken for analyses

As built x-coordinate = 2.036 m. Actual x-coordinate = 1.981 m. Bentonite Slice 120

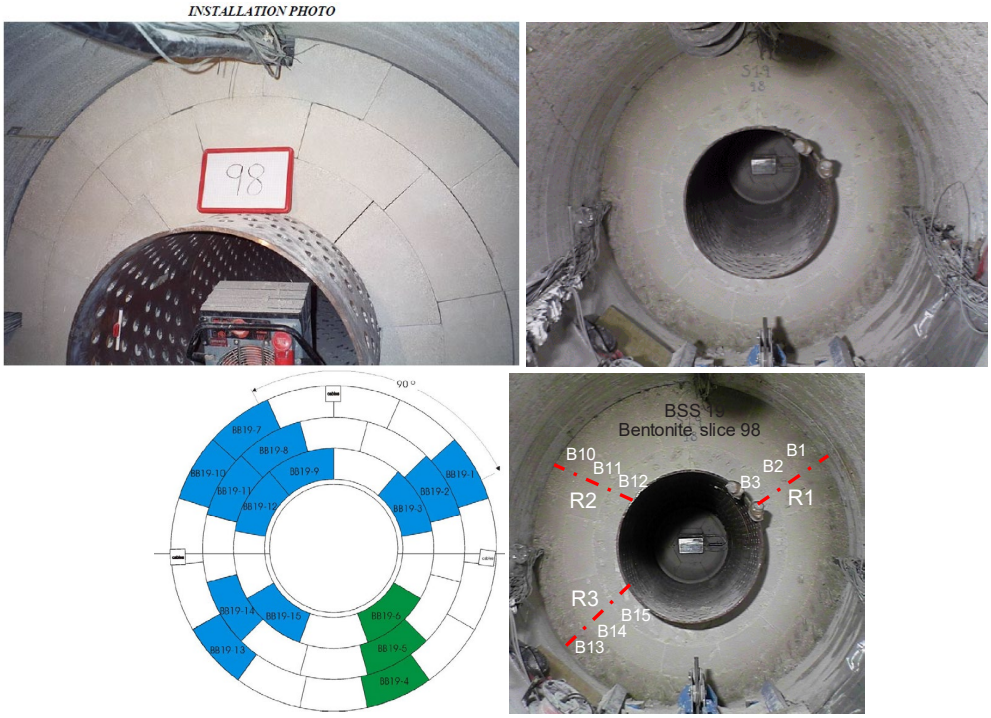

Fig. A-6: Bentonite Sampling Section 19

Bentonite Slice 98. As built x coordinate = 4.850 m. Actual x-coordinate = 4.819 m

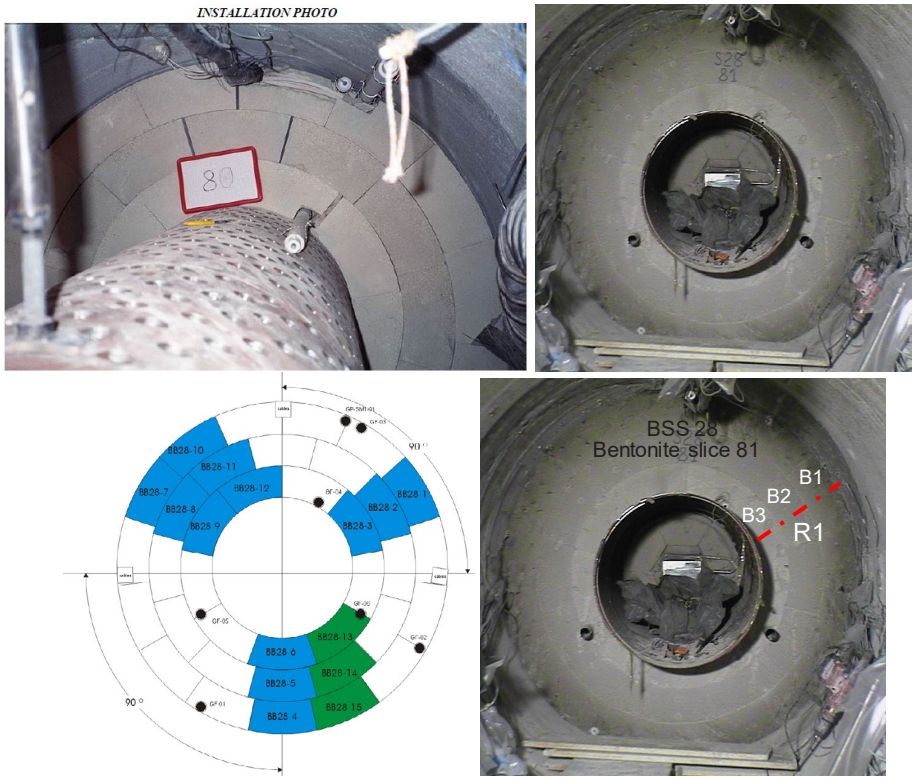

Fig. A-7: Bentonite Sampling Section 28

As built x coordinate = 7.181 m. Actual x-coordinate = 6.985 m. Bentonite Slice 80. It was changed to Slice 81.

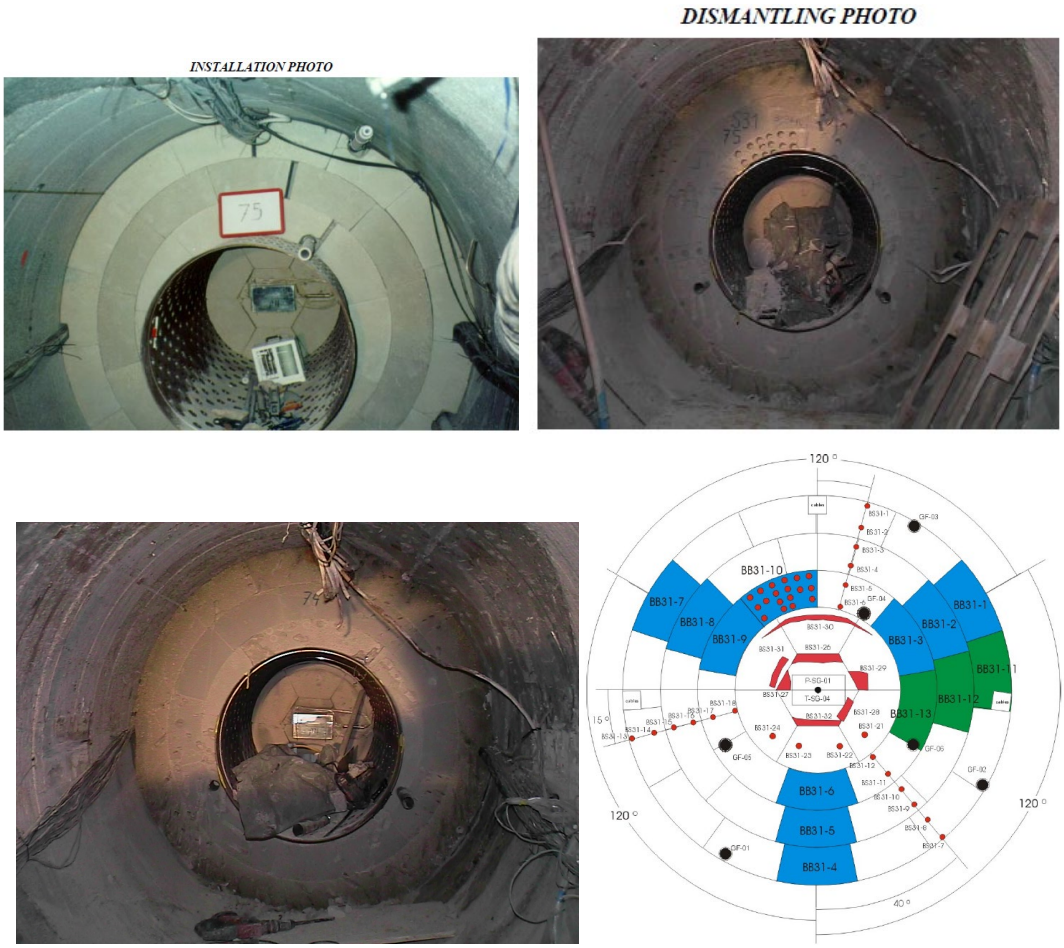

Fig. A-8: Bentonite Sampling Section 31

As built x coordinate = 7.820 m. Actual x-coordinate = 7.748/8.698 m. Bentonite Slice 75

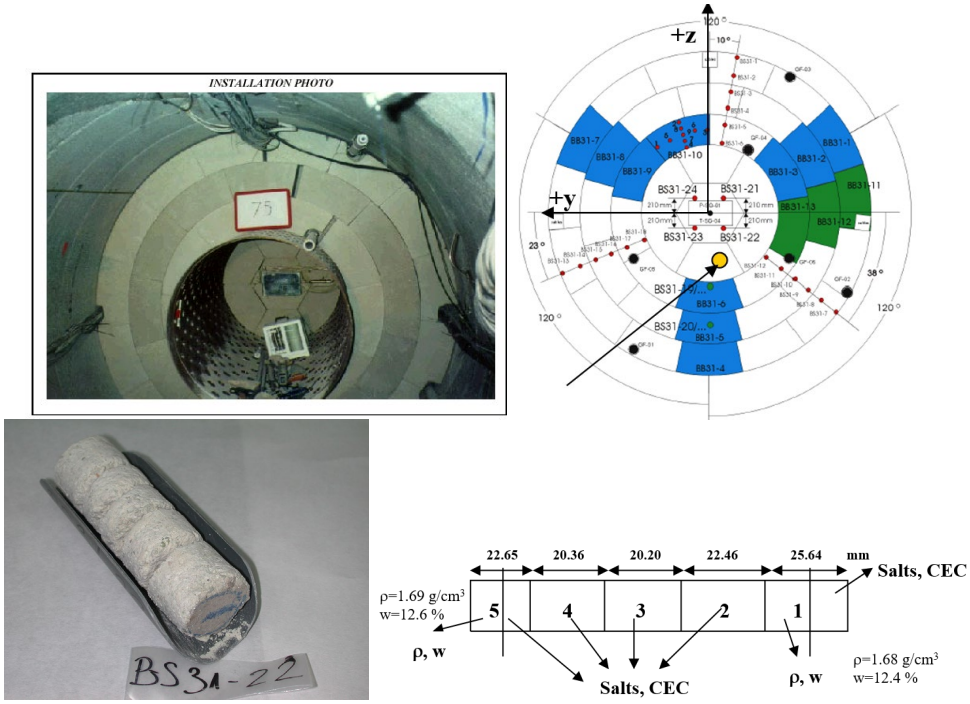

Fig. A-9: Core sample obtained at contact with the back part of the heater
Bentonite Sampling Section 31. Bentonite Slice 67. Actual x-coordinate = 8.698 m

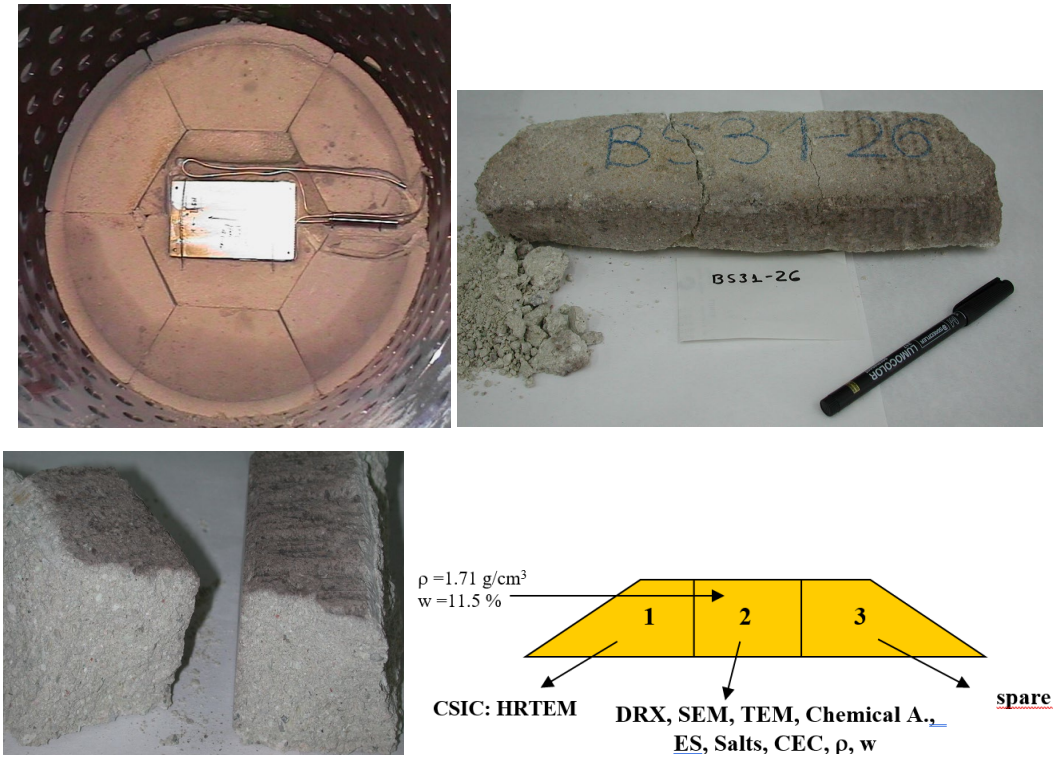

Fig. A-10: Bentonite block sample obtained at contact with the back part of the heater
Bentonite Sampling Section 31. Bentonite Slice 67. x-coordinate = 8.698 m

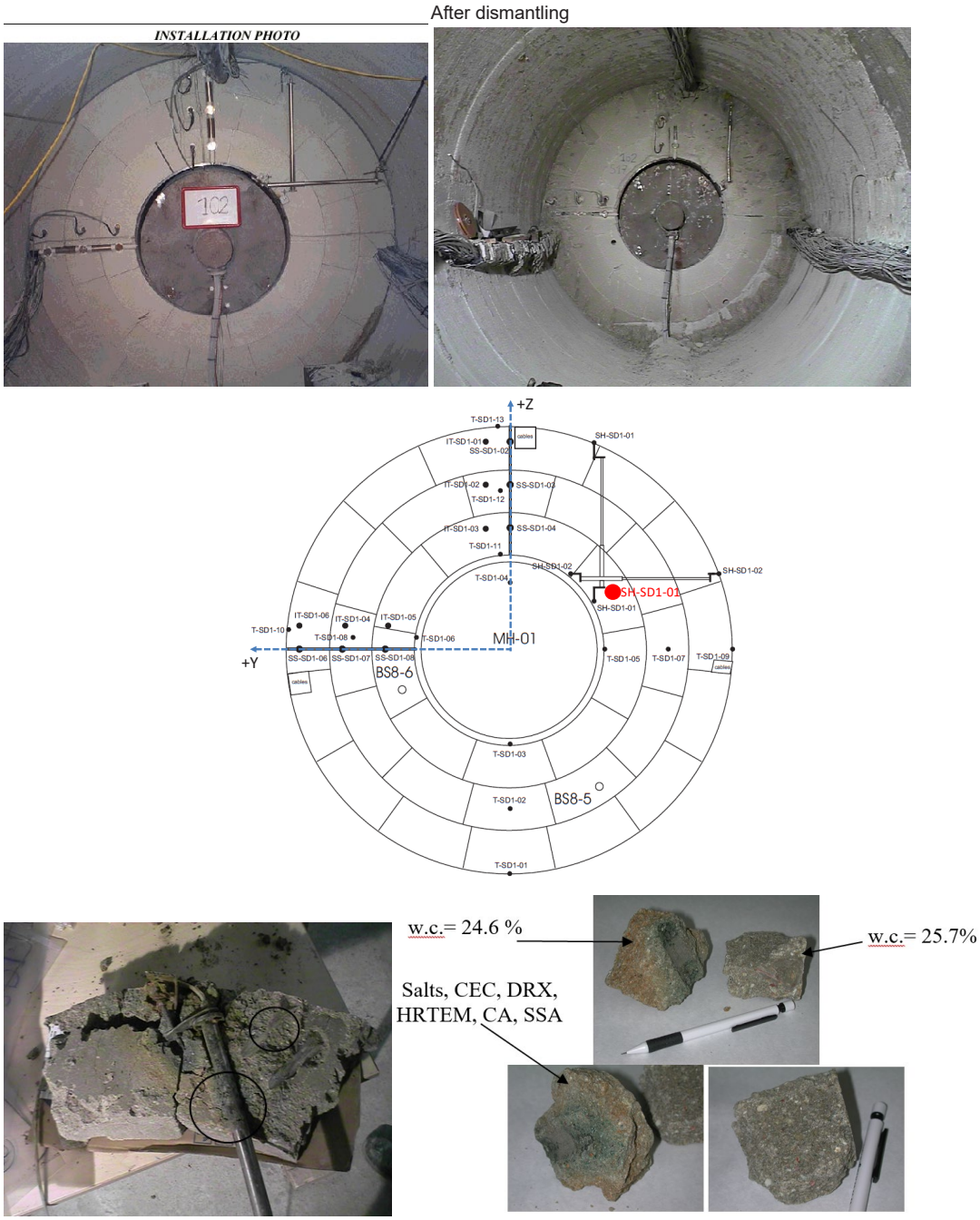

Fig. A-11: Bentonite sample obtained at contact with the corroded displacement sensor SH-SDI-

Bentonite Sampling Section 17. Instrumented section D1. Bentonite Slice 102. x-coordinate = 4.3 m

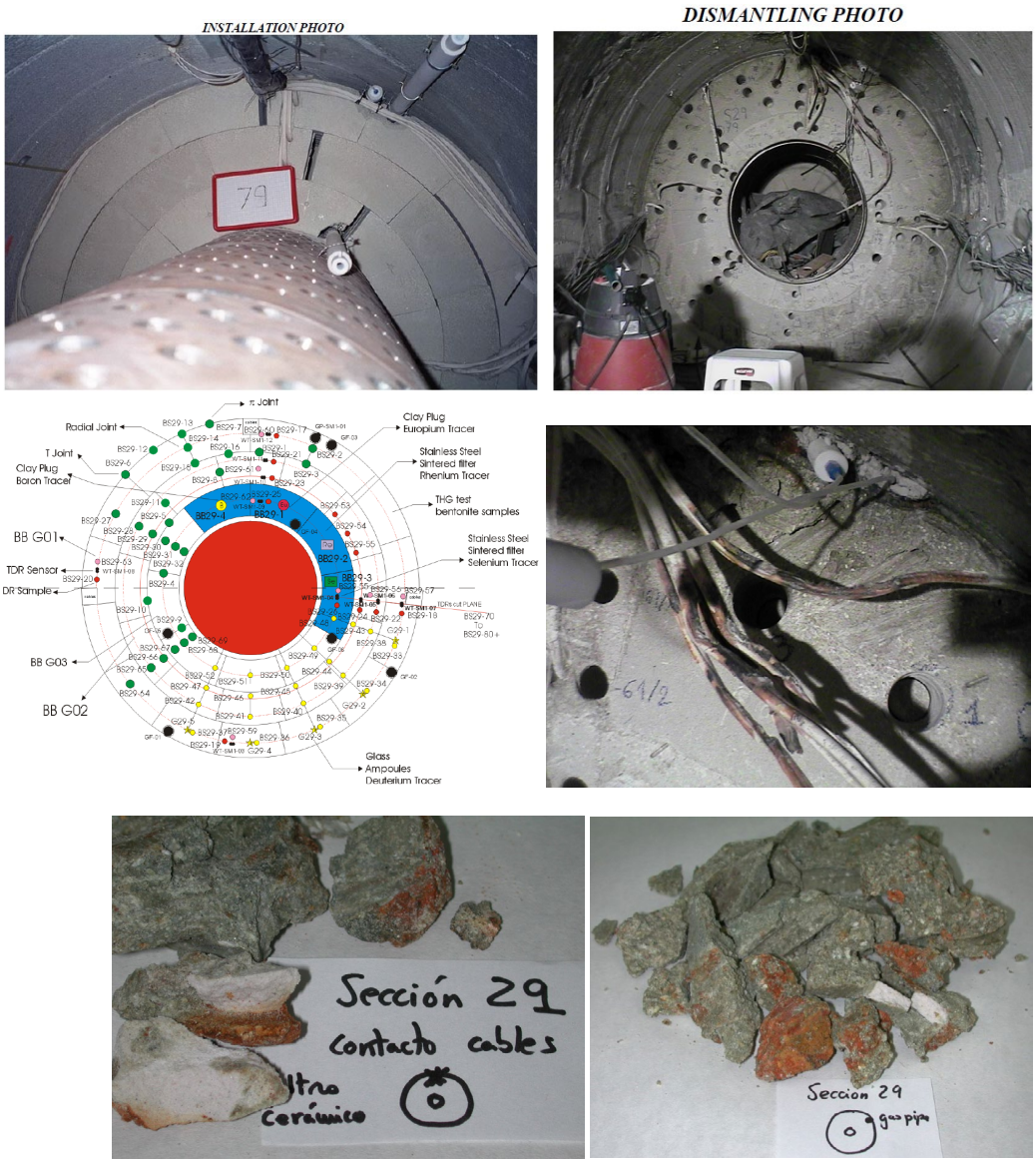

Fig. A-12: Bentonite sample obtained at contact with the corroded anchors from the gas pipes GF-SL-03 and GP-SM1-01

Bentonite Sampling Section 29. Instrumented section M1. Bentonite Slice 72. x-coordinate = 7.315 m, actual x-coordinate = 7.239 m

Visual aspect of the bentonite blocks analysed

Fig. A-13: Bentonite blocks from Sampling Section 7 (at concrete contact): BB7-4, BB7-5 and BB7-6

Fig. A-14: Bentonite blocks from Sampling Section 12 (non-heated section)

Fig. A-15: Bentonite blocks from Sampling Section 19 (heated section)

Fig. A-16: Bentonite blocks from Sampling Section 28 (heated section): BB28-1, BB-28-2 and BB-28-3

Technical procedures

The ***dry density*** of the samples was determined by the mercury displacement method.

The percentage ***water content*** is defined as the ratio between the weight of the water lost after heating the sample to 110 or 150 °C for 24 hours and the weight of the dried clay.

The ***specific weigh or grain density*** of the solid was measured on a powder of oven-dried specimen with a pycnometer.

X-Ray diffraction for mineralogical analysis: diffractometer patterns from samples dried at 60 °C and powdered to a particle size below 60 μm were analysed. From the < 2 μm particle size fraction, obtained by sedimentation, the aggregate oriented diffractometer patterns were obtained on an air dried sample under glass plate (OA), an ethylene glycol solvated (OA + E.G.) and heating at 300° and at 500° C. A Philips PW 1730 diffractometer has been used, with an anticathode of Cu (CuKα), using an acceleration voltage of 35 kV and an current intensity in the filament of 40 mA. The apertures of divergence and reception were 1 and 0.2°, respectively, using a Ni filter. The exploration velocity was of 2°/min for the disoriented powder sample (total analysis of the sample) and 1°/min for the randomly oriented preparations with the < 2μm fraction. On the powder diffractometer a semiquantitative analysis of the present minerals in the sample was carried out (% in mass). The mineral percentage content of the sample was corrected by their corresponding reflectance powder (Schultz, 1964).

The X-Ray diffraction data were also used to determine the distribution of water molecules along the normal to the (a,b) plane of the layer of clay samples under different states of hydration, immediately after the water vapour adsorption tests.

Thermal analysis (TG/DTA/ATD) of the bulk sample have been determined using a Perkin-Elmer 1700 DTA (differential thermal analysis) apparatus at a scan rate of 10 °C/min and under a dynamic air atmosphere (40 cm^3/min) at temperatures between 25 °C and 980 °C.

Scanning electron microscopy (SEM). A ZEISS, DSM 960 SEM microscope coupled to an energy dispersive X-Ray spectrometer (EDS) (LINK, EXL model) was used to identify the accessory and trace minerals.

X-Ray photoelectron spectroscopy (XPS). A Perkin-Elmer PHI 5400 equipped with a excitation source with anode of Al Kα (hν = 1486,6 eV) and 1 mm diameter beam size. The conditions of operation were: 15 kV y 20 mA; analysis chamber pressure of ~ 10-8 Torr; 89 energy steps for general spectra (0-1100 eV) and 35.75 eV for high resolution spectra.

Classical N_2 adsorption/desorption isotherms will be obtained at 77 K (nitrogen liquid temperature) on a discontinuous volumetric sorptometer, Micromeritics ASAP 2010. Before measurement, the samples were outgassed by heating to 90 °C under a residual vacuum of 0.01 Pa. Depending on the porosity, about 0.05 to 0.25 grams of a sample was used. Surface areas will be determined using the standard N_2-BET method. The presence of micropores in the samples will be assessed using the *t*-plot method (de Boer et al. 1966).

The ***soluble salts*** are analysed in aqueous extract solutions. Crushed rock samples were placed in contact with de-ionised and de-gassed water, shaken end-over-end at a solid to liquid ratios of 1:4 and allowed to react for 2 days under atmospheric conditions. After phase separation by centrifuging (30 minutes at 12'500 rpm), the supernatant solutions were analysed.

In order to determine the ***Exchangeable cations***, a $CsNO_3$ solution were used (Sawhney, 1970). Cs act as a high selective cation to displace all exchangeable cations from the montmorillonite if its concentration is sufficiently high. Bentonite samples was equilibrated with 0.5 M $CsNO_3$ at a S:L ratio of 0.25 $kg \cdot L^{-1}$ in a glove box. Samples were shaken end-over-end for 2 days. After phase separation by centrifuging, the supernatant solutions were analysed. Na and Ca contents were corrected from their concentration as soluble salts.

Squeezing technique. Squeezing is analogous to the natural process of consolidation, caused by the deposition of material during geological time, but at a greatly accelerated rate. The squeezing rig at CIEMAT is similar to that developed by Peters et al. (1992) and Entwisle & Reeder (1993). The squeezer has been designed to allow a one-dimensional compression of the sample (Cuevas et al. 1997, Fernández et al. 2000) by means of an automatic hydraulic ram operating downwards with squeezed water expelled into polypropylene syringes at both top and bottom of the cell (Fig. A-17). The compaction chamber is made of type AISI 329 stainless steel (due to high tensile strength and resistance to corrosion) with an internal diameter of 70 mm. Two compaction chambers were designed. One of them is 250 mm high with 20 mm wall thickness and allows pressures up to 100 MPa. The other one is 500 mm high with 45 mm wall and allows pressures up to 200 MPa.

The filtration system allows the extraction of interstitial water by drainage at the top and at the bottom of the sample. This system comprises of a 0.5 μm stainless steel AISI 316L porous disk (Cr 17.36 %, Ni 11.4 %, Mo 2.15 %, Si 0.94 %, Mn 0.17 %, C 0.027 %, S 0.011 %, P 0.022 %, Fe 66.92 %) in contact with the sample. The liquid is collected through polyamide, stainless steel (1/16 inch) or PEEK (1/16 inch) tubes in a septum vial under vacuum. The whole system is under ambient conditions (lab temperature of about 25 °C) and not under anoxic atmosphere, although at the first time of the test the system is flushed with nitrogen gas.

Before squeezing, sub-samples of each sample were taken for different physical determinations. The grain density was measured by the water pycnometer method. The dry density (ρ_d) of the samples was determined by the mercury displacement method. The gravimetric water content is determined by weighting the sample before and after oven-drying at 110 °C for 24 hours.

The samples for squeezing were trimmed in separate pieces using a large knife, fragmented ideally to lumps fitted to the squeezing cell or small pieces of about 25 – 200 grams. The trimming was carried out in plastic bags flushed with N_2. Then the sample was weighed and placed into the body of the cell. A small stress was applied initially to remove most of the air from the cell and allow the sample to bed in. Then the syringe was assembled to collect the squeezed water. The applied stress was increased progressively up to the selected pressure. When the maximum of squeezed water has been obtained, the syringe was removed and covered with Parafilm®, avoiding any sample contact with the atmosphere. The sample collected was weighted, filtered and stored in a refrigerator at 4 °C until it is analysed, in order to prevent any possible alterations. For most samples, Millipore and Pall Gelman Sciences Acrodisc 25, 13 and 4 mm (Osmonics Cameo®), 0.45 μm nylon filters were used, depending on the water volume sampled.

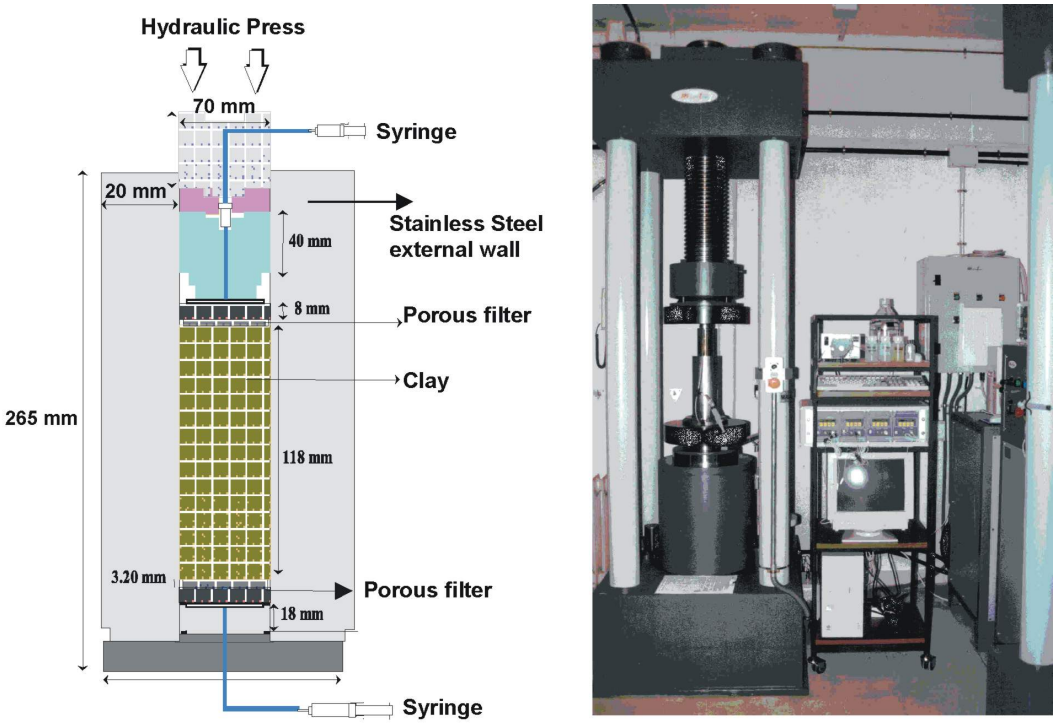

Fig. A-17: Squeezed water extraction apparatus used at CIEMAT for the pore water from bentonite samples taken during the dismantling of Heater #1 in 2002

Solid phase treatment for chemical analysis. For major and trace elements analysis, rock sample is dissolved using a HF – aqua regia mixture. 500 milligrams of sample were transferred to a PTFE closed vessel and 4 mL of concentrated HF and 2 mL of aqua regia were added. The vessel was kept overnight at 90° C and, after cooling, the content was transferred to a PTFE evaporating dish, 2 mL of concentrated $HClO_4$ added, and evaporated until white fumes under IR lamp. Finally, the residue was dissolved using diluted HNO_3 and the solution transferred to a 50 mL volumetric flask and analysed.

Chemical analysis. The total alkalinity of the samples (expressed as mg/L of HCO_3^-) was determined by potentiometric titration using a Metrohm 682 titrator. The major cations were analysed by Inductively Coupled Plasma-Atomic Emission Spectrometry (ICP-AES) in a Perkin-Elmer Elan 5000 spectrometer. Sodium and potassium were determined by flame atomic emission spectrometry, AAS-Flame, in a Perkin Elmer 2280 spectrometer, and trace elements were determined by ICP-MS (Finningan Mat SOLA). Anions were analysed by ion chromatography (Dionex DX-4500i). The silica was determined using a UV-Vis spectrophotometer by means of the silico-molybdic colourimetric method. It was estimated that the maximum analytical errors were ± 10 % for the major ions.

Appendix B

SEM photomicrographs

(Note: The structural formula of the clay minerals was calculated to detect relative variations in the proportion of the ion content among the clay particles analysed.)

B1 Bentonite Sections 36, 47, 53 and 59

Section 36

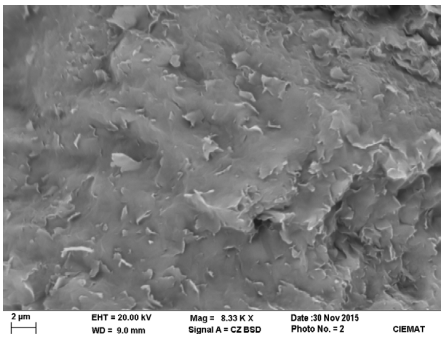

Black halo

$(Si_{3.99}Al_{0.01})^{IV}(Al_{1.47}Mg_{0.44}Fe^{3+}_{0.09})^{VI}(Ca_{0.10}Mg_{0.03}Na_{0.15}K_{0.04})_{0.32}O_{10}(OH)_2$
τ charge = -0.01; O. charge = -0.44
Total charge = -0.45 (τ % = 3; o % = 97); FW (g/mol) = 742.72
(No Mg at interlayer: Σ_{oct} = 2.03; Total charge: -0.38, τ % = 4; o % = 96)

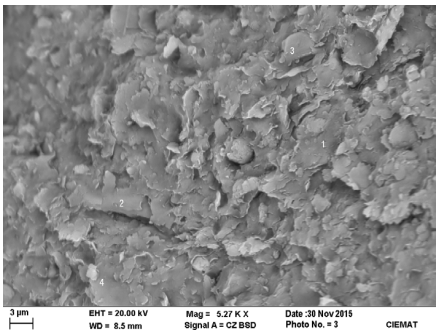

Black halo 1: illite-smectite

$(Si_{3.80}Al_{0.20})^{IV}(Al_{1.26}Mg_{0.33}Fe^{3+}_{0.39}Ti^{4+}_{0.02})^{VI}(Ca_{0.06}Mg_{0.02}Na_{0.07}K_{0.28})_{0.43}O_{10}(OH)_2$
τ charge = -0.20; O. charge = -0.31
Total charge = -0.51 (τ % = 39; o % = 61); FW (g/mol) = 772.90
(No Mg at interlayer: Σ_{oct} = 2.02; Total charge: -0.48, τ % = 41; o % = 59)

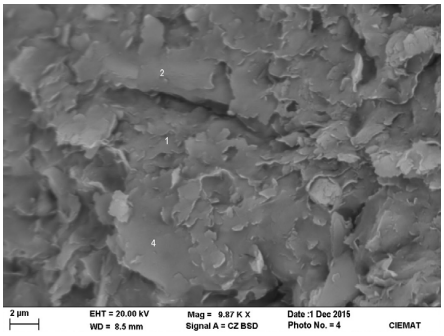

Black halo 1: K-rich smectite

$(Si_{3.83}Al_{0.17})^{IV}(Al_{1.37}Mg_{0.27}Fe^{3+}_{0.34}Ti^{4+}_{0.02\ \ 0.01})^{VI}(Ca_{0.06}Na_{0.09}K_{0.24})_{0.39}O_{10}(OH)_2$
τ charge = -0.17; O. charge = -0.28
Total charge = -0.45 (τ % = 39; o % = 61); FW (g/mol) = 765.91

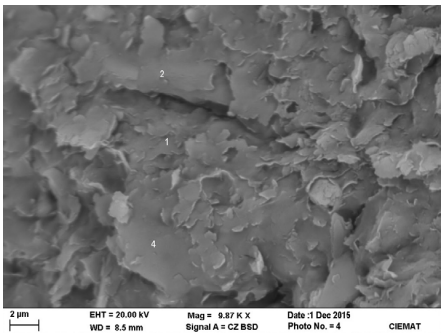

Black halo 2: illite-muscovite;

$(Si_{3.40}Al_{0.60})^{IV}(Al_{1.74}Mg_{0.10}Fe^{3+}_{0.12}Ti^{4+}_{0.03\ \ 0.01})^{VI}(Na_{0.11}K_{0.60})_{0.71}O_{10}(OH)_2$
τ charge = -0.60; O. charge = -0.10
Total charge = -0.71 (τ % = 86; o % = 14); FW (g/mol) = 778.10

Fig. B-1: SEM photomicrographs in BB-36-1 sample: clay minerals

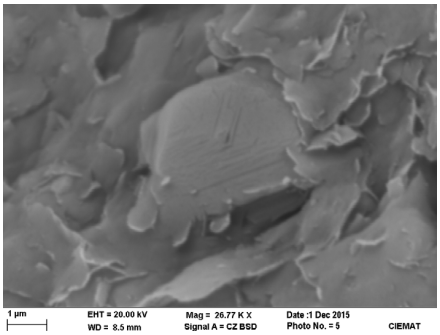

Black halo

$(Si_{3.85}Al_{0.15})^{IV}(Al_{1.35}Mg_{0.34}Fe^{3+}_{0.30}Ti^{4+}_{0.01\ \ 0.01})^{VI}(Ca_{0.07}Na_{0.08}K_{0.28})_{0.43}O_{10}(OH)_2$
τ charge = -0.15; O. charge = -0.35
Total charge = -0.41 (τ % = 70; o % = 30); FW (g/mol) = 767.30

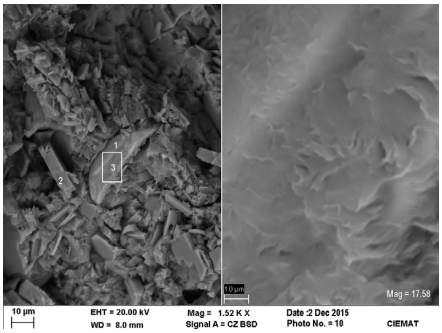

Black halo: green material

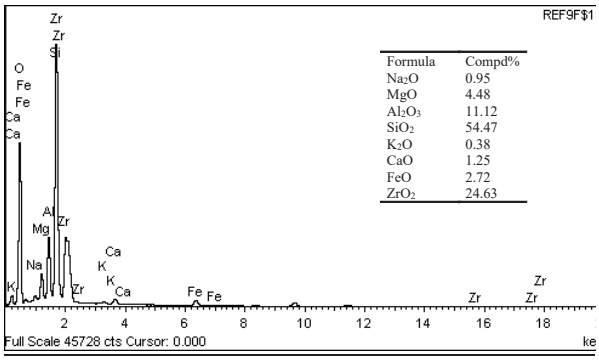

Formula	Compd%
Na_2O	0.95
MgO	4.48
Al_2O_3	11.12
SiO_2	54.47
K_2O	0.38
CaO	1.25
FeO	2.72
ZrO_2	24.63

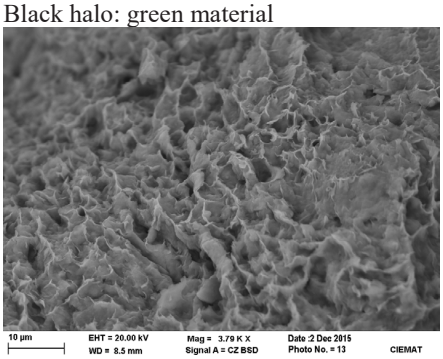

Black halo: green material

$(Si_{3.97}Al_{0.03})^{IV}(Al_{1.40}Mg_{0.48}Fe^{3+}_{0.12})^{VI}(Ca_{0.12}Mg_{0.04}Na_{0.16}K_{0.04})_{0.36}O_{10}(OH)_2$
τ charge = -0.03; O. charge = -0.48
Total charge = -0.51 (τ % = 6; o % = 94); FW (g/mol) = 746.61
(No Mg at interlayer: Σ_{oct} = 2.04; Total charge: -0.44, τ % = 7; o % = 93)

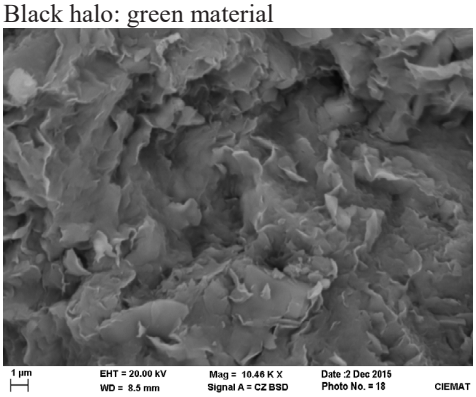

Black halo: green material

$(Si_{3.99}Al_{0.01})^{IV}(Al_{1.34}Mg_{0.51}Fe^{3+}_{0.15})^{VI}(Ca_{0.14}Mg_{0.04}Na_{0.15}K_{0.02})_{0.34}O_{10}(OH)_2$
τ charge = -0.01; O. charge = -0.51
Total charge = -0.52 (τ % = 2; o % = 98); FW (g/mol) = 747.48
(No Mg at interlayer: Σ_{oct} = 2.04; Total charge: -0.45, τ % = 2; o % = 98)

Fig. B-1: Cont.

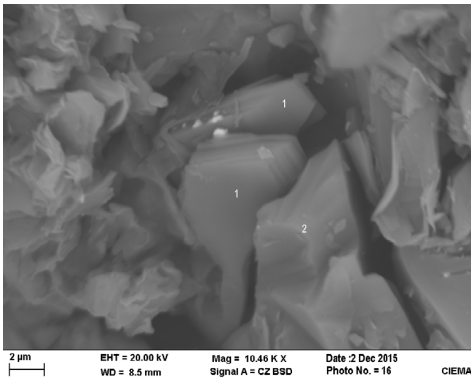

Black halo: green material
1: Chlorites; 2: plagioclases

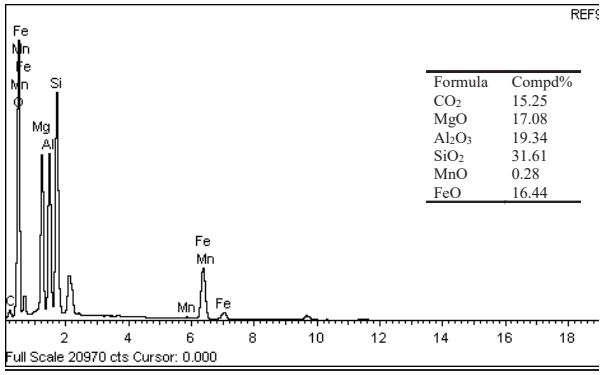

Chlorite:
$(Si_{3.23}Al_{0.77})^{IV}$ $(Fe^{2+}_{1.41}Mg_{1.17}Mn^{2+}_{0.02\ \ 0.40})^{VI}$ $O_{10}(OH)_2$
$[Al_{1.57}Mg_{1.43}](OH)_6]$

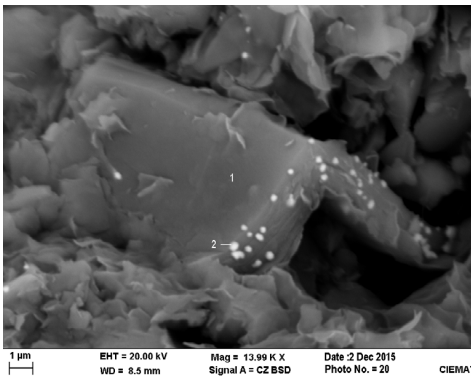

Black halo: green material

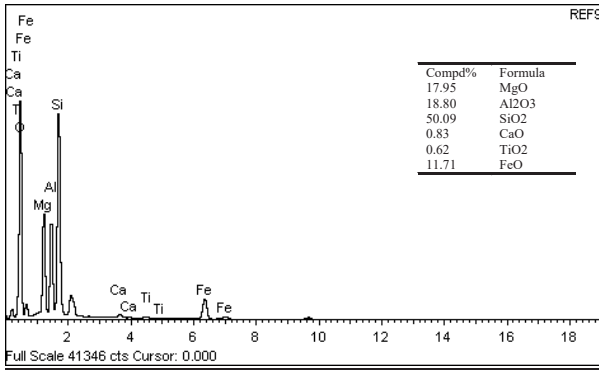

Chlorite?

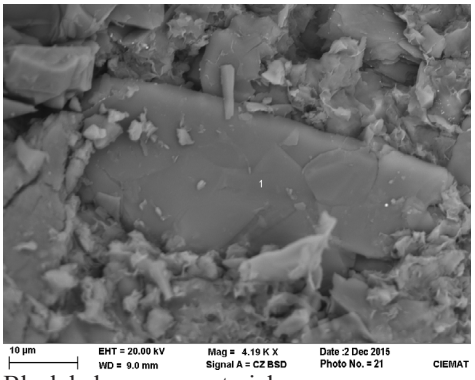

Black halo: green material

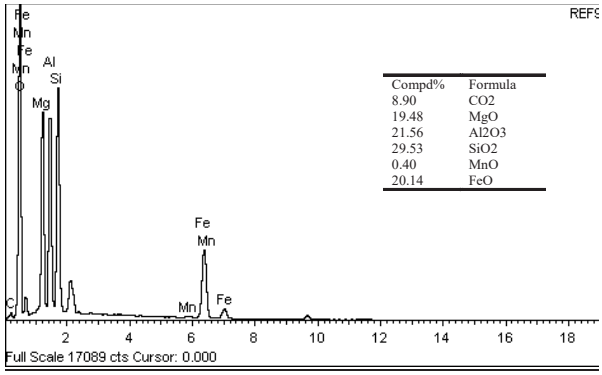

Chlorite:
$(Si_{2.88}Al_{1.12})^{IV}$ $(Fe^{2+}_{1.64}Mg_{1.20}Mn^{2+}_{0.03\ \ 0.12})^{VI}$ $O_{10}(OH)_2$
$[Al_{1.36}Mg_{1.64}](OH)_6]$

Fig. B-1: Cont.

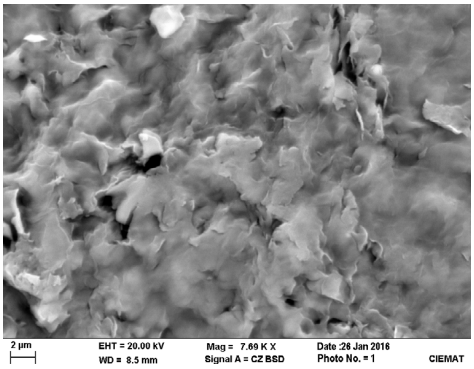

At shotcrete contact

$(Si_{3.74}Al_{0.26})^{IV}(Al_{0.78}Mg_{0.87}Fe^{3+}_{0.27}Ti^{4+}_{0.08})^{VI}(Ca_{0.11}Mg_{0.35}Na_{0.04}K_{0.09})_{0.59}O_{10}(OH)_2$
τ charge = -0.26; O. charge = -0.79
Total charge = -1.05 (τ % = 25; o % = 75); FW (g/mol) = 768.97
(No Mg at interlayer: Σ_{oct} = 2.35; Total charge: -0.36, τ % = 72; o % = 28)

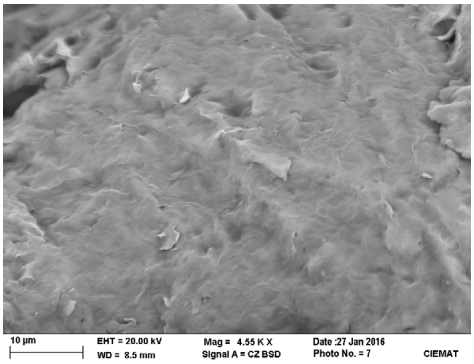

At shotcrete contact

$(Si_{3.86}Al_{0.14})^{IV}(Al_{1.20}Mg_{0.67}Fe^{3+}_{0.13})^{VI}(Ca_{0.09}Mg_{0.25}Na_{0.09}K_{0.03})_{0.47}O_{10}(OH)_2$
τ charge = -0.14; O. charge = -0.67
Total charge = -0.81 (τ % = 17; o % = 83); FW (g/mol) = 750.47
(No Mg at interlayer: Σ_{oct} = 2.25; Total charge: -0.30, τ % = 46; o % = 54)

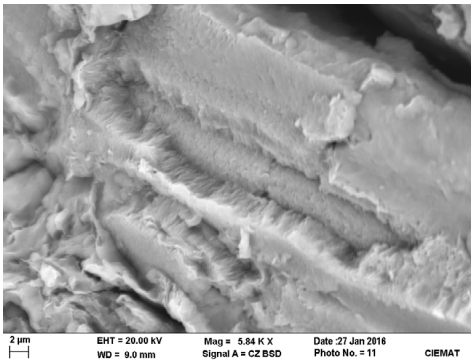

At shotcrete contact

$(Si_{3.73}Al_{0.27})^{IV}(Al_{0.86}Mg_{1.06}Fe^{3+}_{0.07})^{VI}(Ca_{0.09}Mg_{0.53}Na_{0.10})_{0.72}O_{10}(OH)_2$
τ charge = -0.27; O. charge = -1.06
Total charge = -1.34 (τ % = 20; o % = 80); FW (g/mol) = 755.86
(No Mg at interlayer: Σ_{oct} = 2.53; Total charge: -0.27, τ % = 100; o % = 1)

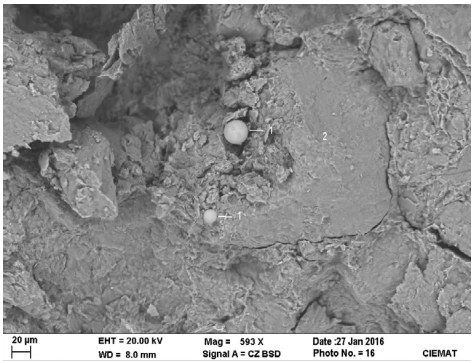

At shotcrete contact. 1: $FeCO_3$; 2: smectite

$(Si_{3.70}Al_{0.30})^{IV}(Al_{1.06}Mg_{0.51}Fe^{3+}_{0.42})^{VI}(Ca_{0.12}Mg_{0.13}Na_{0.08}K_{0.24})_{0.57}O_{10}(OH)_2$
τ charge = -0.30; O. charge = -0.51
Total charge = -0.81 (τ % = 37; o % = 63); FW (g/mol) = 779.80
(No Mg at interlayer: Σ_{oct} = 2.13; Total charge: -0.56, τ % = 54; o % = 46)

Fig. B-1: Cont.

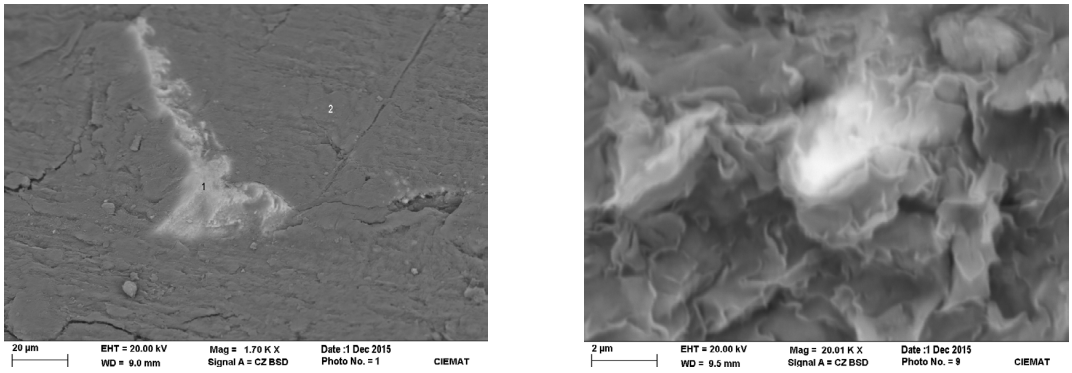

Fig. B-2: SEM photomicrographs in BB-36-1 sample: a) barite with Sr (1), b) barite

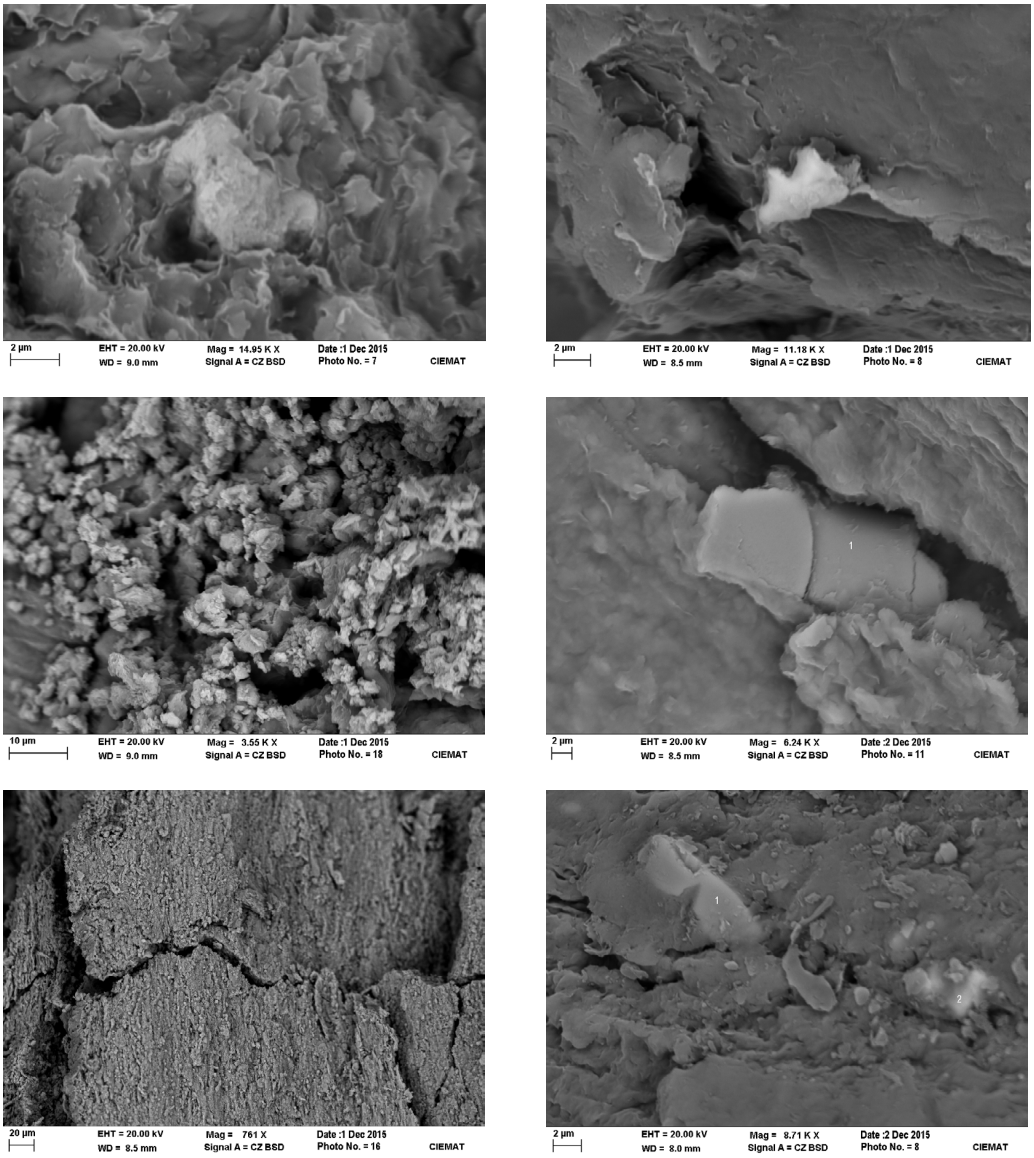

Fig. B-3: SEM photomicrographs in BB-36-1 sample: a) Fe-oxides, b) Fe-Cr oxides, c) Fe-oxides, d) Fe-oxides, e) Fe-Cr, Ni, Cu-oxides, f) Ti-Fe oxides with C

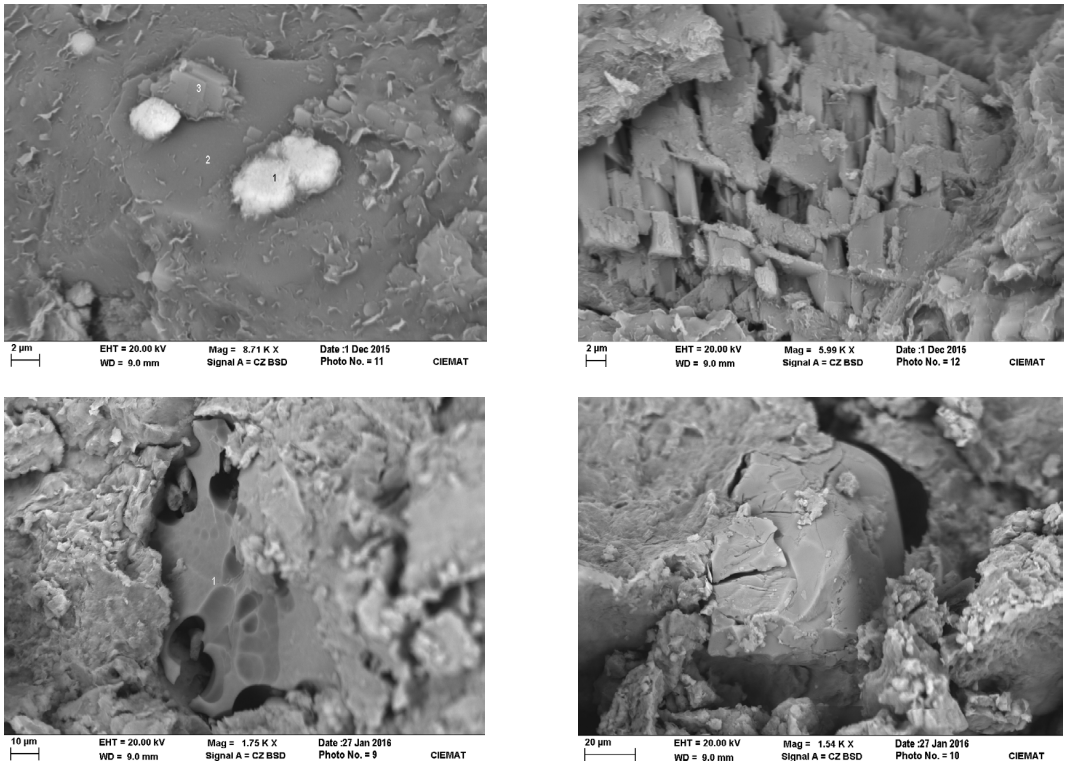

Fig. B-4: SEM photomicrographs in BB-36-1 sample: a) plagioclases (2,3), b) K-feldspar, c) plagioclase, d) plagioclases

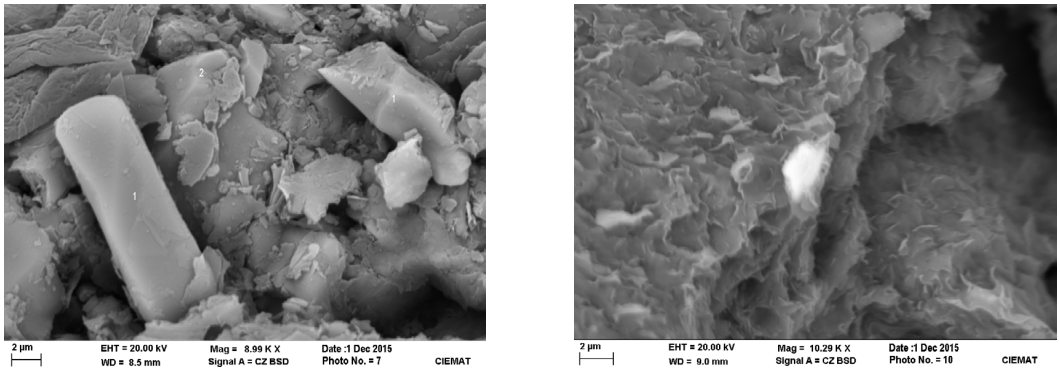

Fig. B-5: SEM photomicrographs in BB-36-1 sample: a) apatite (1) and plagioclases (2), b) monazite

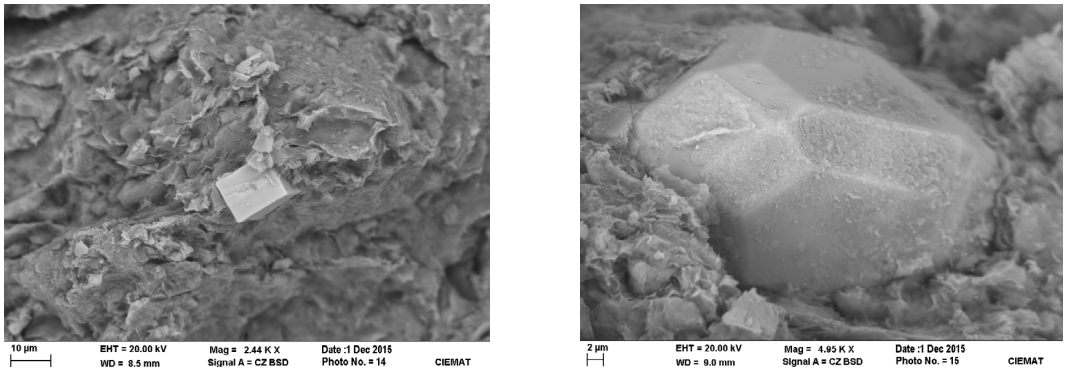

Fig. B-6: SEM photomicrographs in BB-36-1 sample: a) and b) zircon

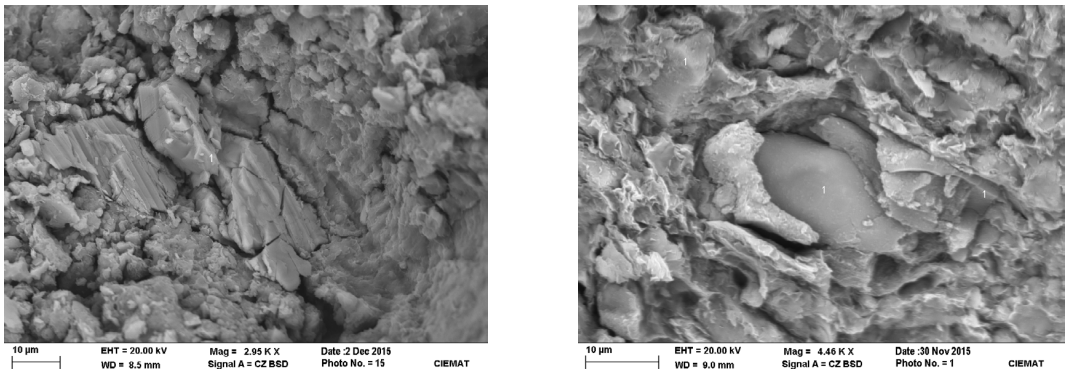

Fig. B-7: SEM photomicrographs in BB-36-1 sample: a) portlandite $Ca(OH)_2$, b) Silica (1)

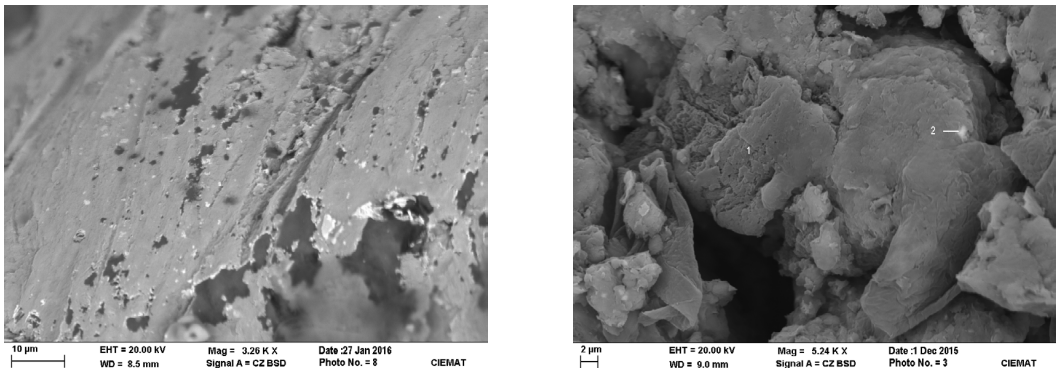

Fig. B-8: SEM photomicrographs in BB-36-1 sample: a) organic matter (OM), b) carbon and nitrogen (1), monazite (2)

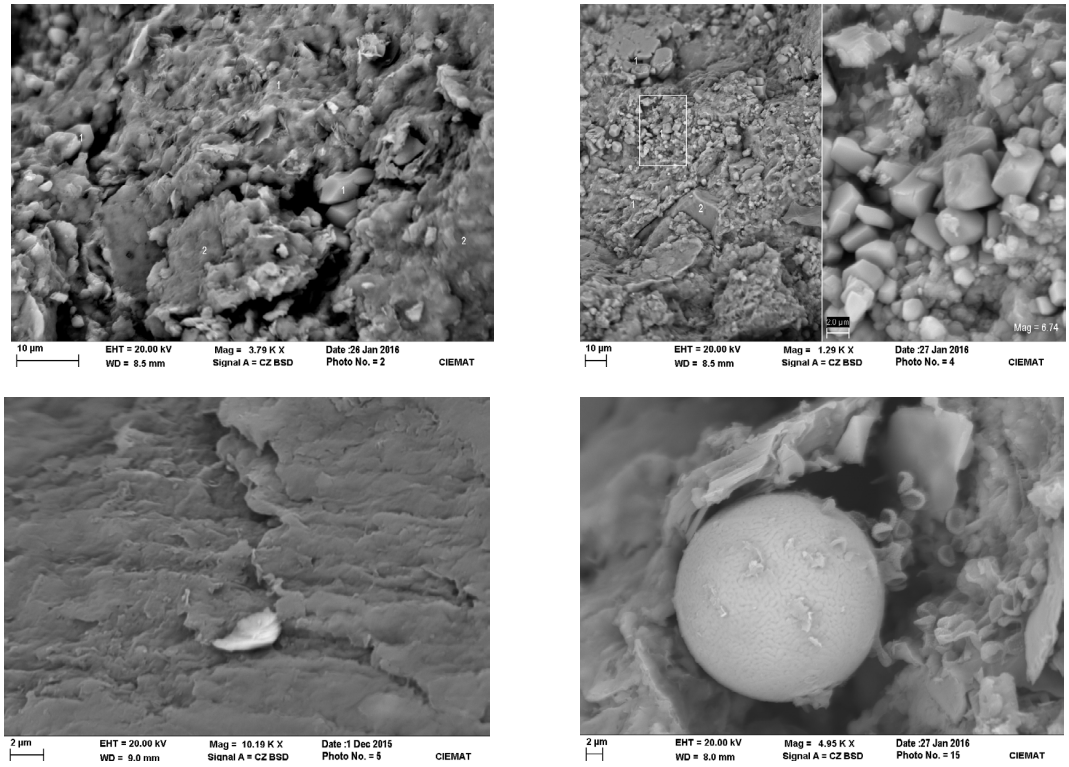

Fig. B-9: SEM photomicrographs in BB-36-1 sample: a) Ca-carbonates (1,2), b) Ca(Mg)-carbonates; c) Fe-carbonate; d) Fe-carbonate.

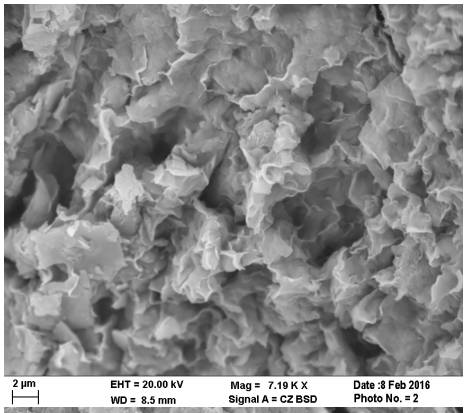

$(Si_{3.96}Al_{0.04})^{IV}(Al_{1.35}Mg_{0.47}Fe^{3+}_{0.18})^{VI}(Ca_{0.14}Mg_{0.04}Na_{0.11}K_{0.06})_{0.34}O_{10}(OH)_2$
τ charge = -0.04; O. charge = -0.47
Total charge = -0.51 (τ % = 8; o % = 92); FW (g/mol) = 750.81
(No Mg at interlayer: Σ_{oct} = 2.04; Total charge: -0.44, τ % = 9; o % = 91)

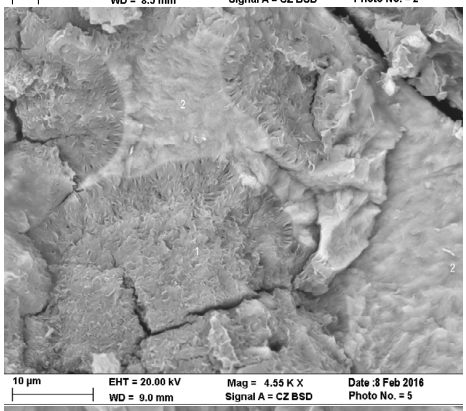

$(Si_{3.78}Al_{0.22})^{IV}(Al_{1.01}Mg_{0.27}Fe^{3+}_{0.70}Ti^{4+}_{0.02})^{VI}(Ca_{0.09}Mg_{0.08}Na_{0.09}K_{0.05})_{0.30}O_{10}(OH)_2$
τ charge = -0.22; O. charge = -0.25
Total charge = -0.47 (τ % = 47; o % = 53); FW (g/mol) = 778.54
(No Mg at interlayer: Σ_{oct} = 2.08; Total charge: -0.31, τ % = 72; o % = 28)

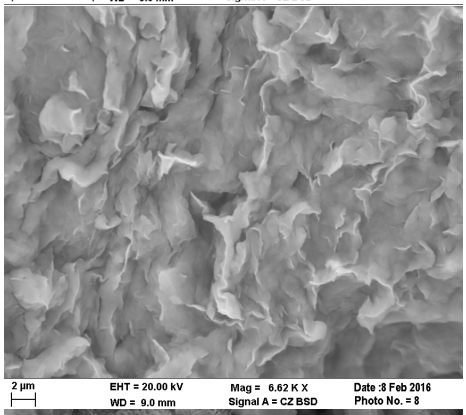

$(Si_{4.00}Al_{0.00})^{IV}(Al_{1.39}Mg_{0.42}Fe^{3+}_{0.15\ \ 0.03})^{VI}(Ca_{0.17}Na_{0.12}K_{0.08})_{0.36}O_{10}(OH)_2$
τ charge = -0.00; O. charge = -0.53
Total charge = -0.53 (τ % = 0; o % = 100); FW (g/mol) = 749.99

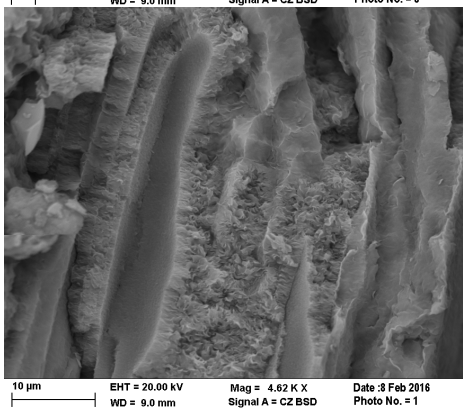

$(Si_{3.98}Al_{0.02})^{IV}(Al_{1.40}Mg_{0.38}Fe^{3+}_{0.21})^{VI}(Ca_{0.15}Mg_{0.01}Na_{0.07}K_{0.02})_{0.25}O_{10}(OH)_2$
τ charge = -0.02; O. charge = -0.39
Total charge = -0.41 (τ % = 5; o % = 95); FW (g/mol) = 748.08
(No Mg at interlayer: Σ_{oct} = 2.01; Total charge: -0.39, τ % = 6; o % = 94)

Fig. B-10: SEM photomicrographs in BB-36-2 sample: clay minerals

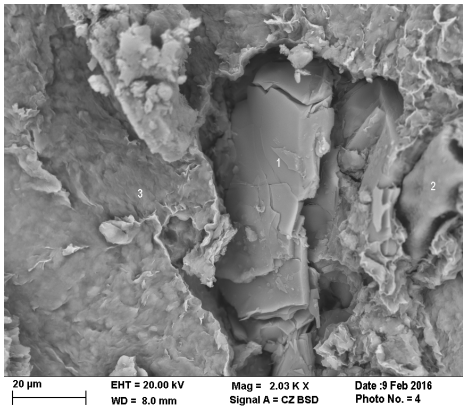

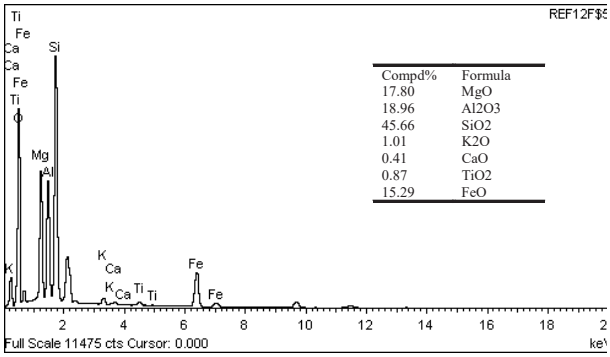

1: Chlorite, 2: SiO_2

Chlorite:
$(Si_{3.84}Al_{0.16})^{IV}$ $(Fe^{2+}_{1.07}Mg_{0.95}Ti^{4+}_{0.06\ \ 0.98})^{VI}$ $(Ca_{0.04}K_{0.11})_{0.15}O_{10}(OH)_2$
$[Al_{1.72}Mg_{1.28}](OH)_6]$

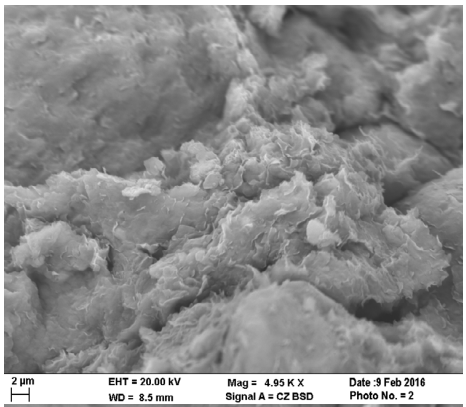

$(Si_{3.90}Al_{0.10})^{IV}(Al_{1.31}Mg_{0.46}Fe^{3+}_{0.11}Ti^{4+}_{0.12})^{VI}(Ca_{0.12}Mg_{0.03}Na_{0.08}K_{0.05})_{0.29}O_{10}(OH)_2$
τ charge = -0.10; O. charge = -0.34
Total charge = -0.44 (τ % = 22; o % = 78); FW (g/mol) = 748.18
(No Mg at interlayer: Σ_{oct} = 2.03; Total charge: -0.37, τ % = 26; o % = 74)

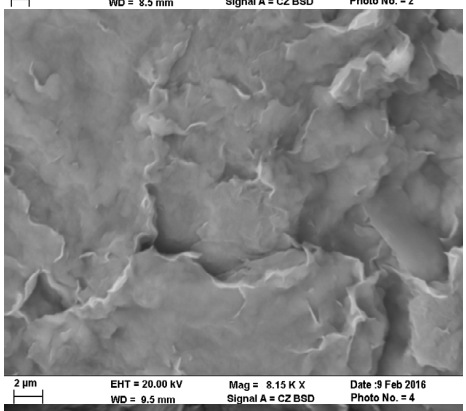

$(Si_{3.97}Al_{0.03})^{IV}(Al_{1.41}Mg_{0.40}Fe^{3+}_{0.19})^{VI}(Ca_{0.12}Mg_{0.03}Na_{0.09}K_{0.04})_{0.28}O_{10}(OH)_2$
τ charge = -0.03 O. charge = -0.40
Total charge = -0.43 (τ % = 7; o % = 93); FW (g/mol) = 747.35
(No Mg at interlayer: Σ_{oct} = 2.03; Total charge: -0.36, τ % = 8; o % = 92)

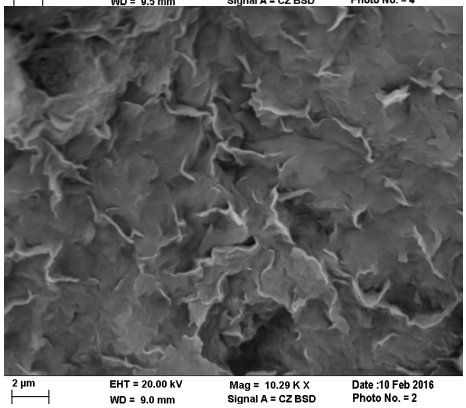

$(Si_{3.98}Al_{0.02})^{IV}(Al_{1.44}Mg_{0.41}Fe^{3+}_{0.14})^{VI}(Ca_{0.10}Mg_{0.05}Na_{0.08}K_{0.05})_{0.29}O_{10}(OH)_2$
τ charge = -0.02 O. charge = -0.41
Total charge = -0.44 (τ % = 5; o % = 95); FW (g/mol) = 744.91
(No Mg at interlayer: Σ_{oct} = 2.05; Total charge: -0.33, τ % = 7; o % = 93)

Fig. B-10: Cont.

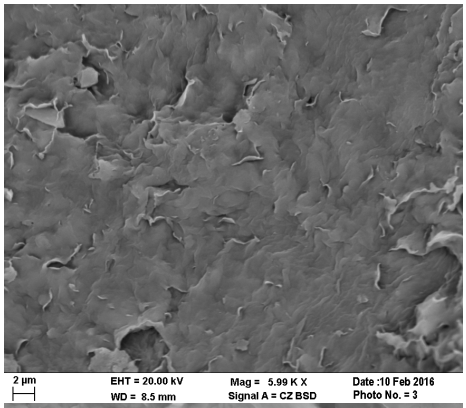

$(Si_{3.95}Al_{0.05})^{IV}(Al_{1.40}Mg_{0.37}Fe^{3+}_{0.23})^{VI}(Ca_{0.10}Mg_{0.02}Na_{0.08}K_{0.09})_{0.29}O_{10}(OH)_2$
τ charge = -0.05 O. charge = -0.37
Total charge = -0.42 (τ % = 12; o % = 88); FW (g/mol) = 751.85
(No Mg at interlayer: Σ_{oct} = 2.02; Total charge: -0.37, τ % = 13; o % = 87)

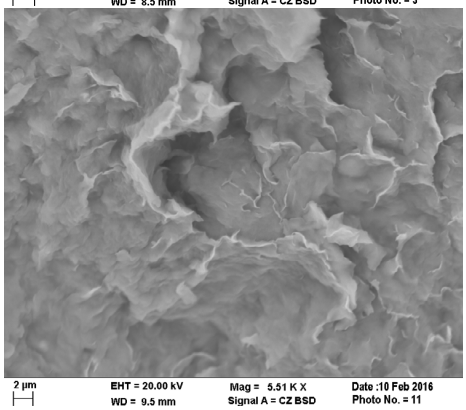

$(Si_{4.00}Al_{0.00})^{IV}(Al_{1.42}Mg_{0.46}Fe^{3+}_{0.12})^{VI}(Ca_{0.10}Mg_{0.06}Na_{0.09}K_{0.04})_{0.29}O_{10}(OH)_2$
τ charge = -0.00 O. charge = -0.46
Total charge = -0.46 (τ % = 0; o % = 100); FW (g/mol) = 743.76
(No Mg at interlayer: Σ_{oct} = 2.05; Total charge: -0.34, τ % = 0; o % = 100)

Fig. B-10: Cont.

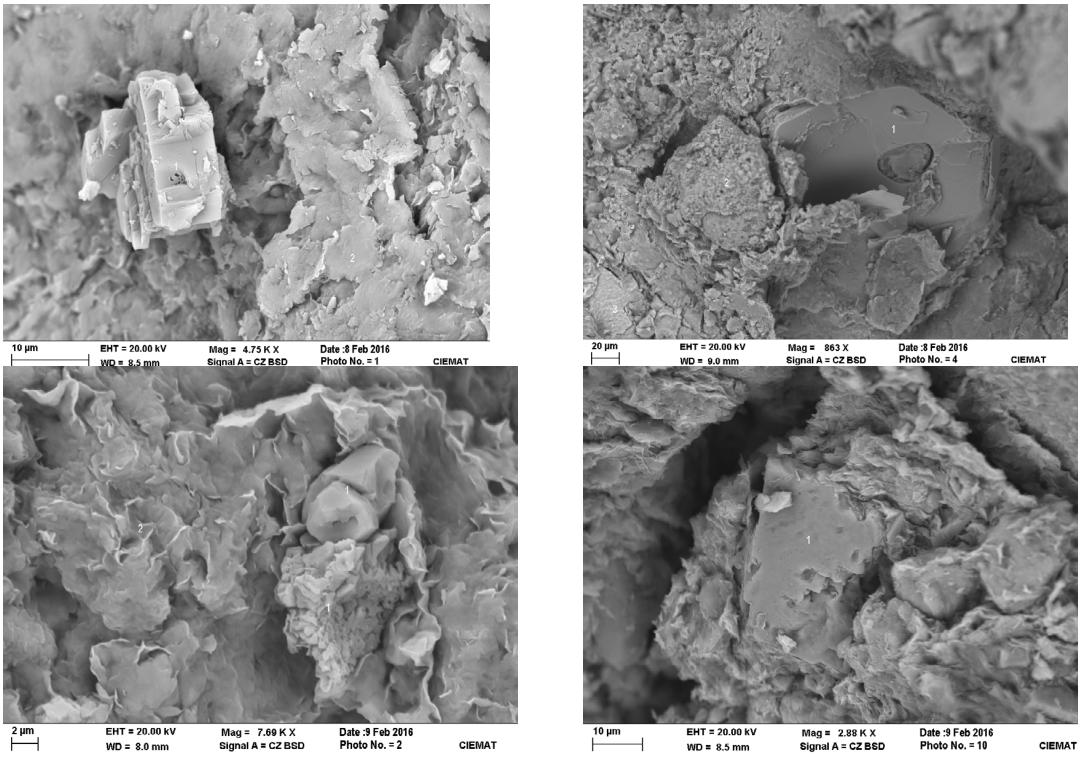

Fig. B-11: SEM photomicrographs in BB-36-2 sample: a) Ca-carbonates, b) Ca-carbonates (2), organic matter (1); c) Ca-carbonates (1), d) dolomite (1)

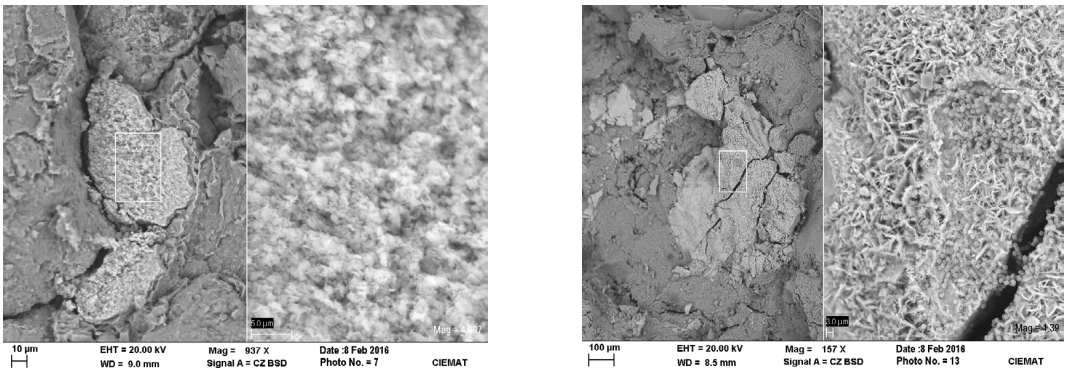

Fig. B-12: SEM photomicrographs in BB-36-2 sample: a) Fe-carbonates, d) Fe-carbonates and OM

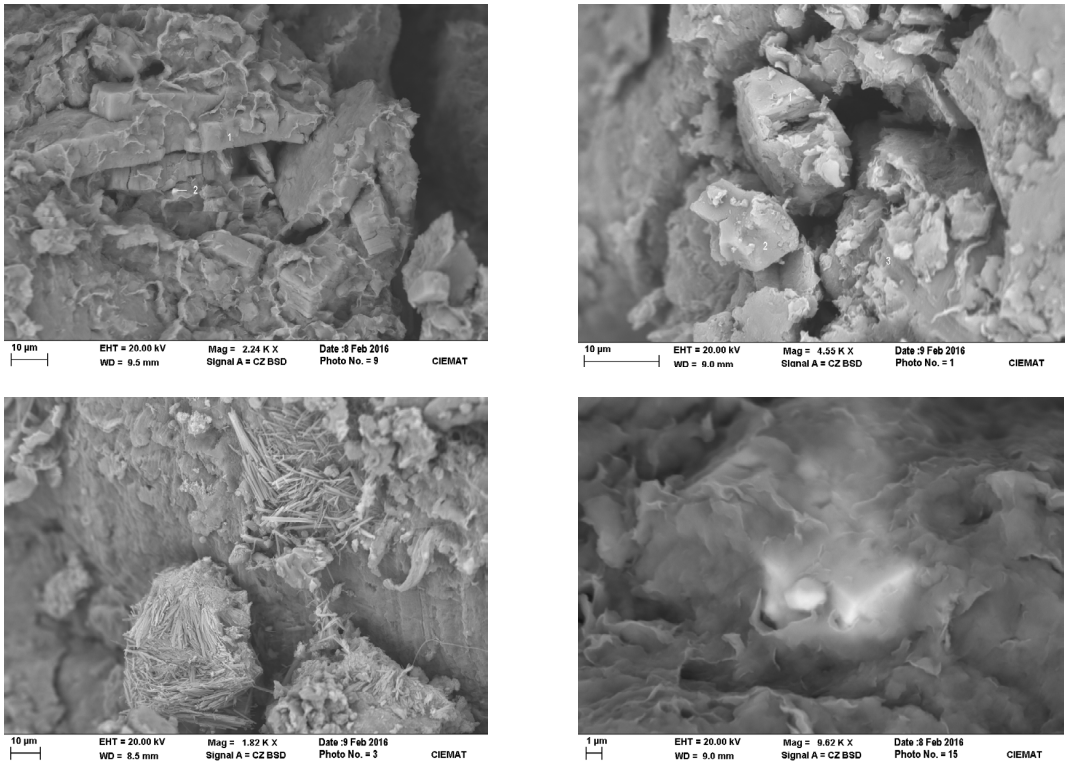

Fig. B-13: SEM photomicrographs in BB-36-2 sample: a) Ca-sulfates (1), barite (2), b) Ca-sulfates (1), Ca-carbonate (2), clay minerals (3), c) Ca-sulfates (ettringite), d) barite

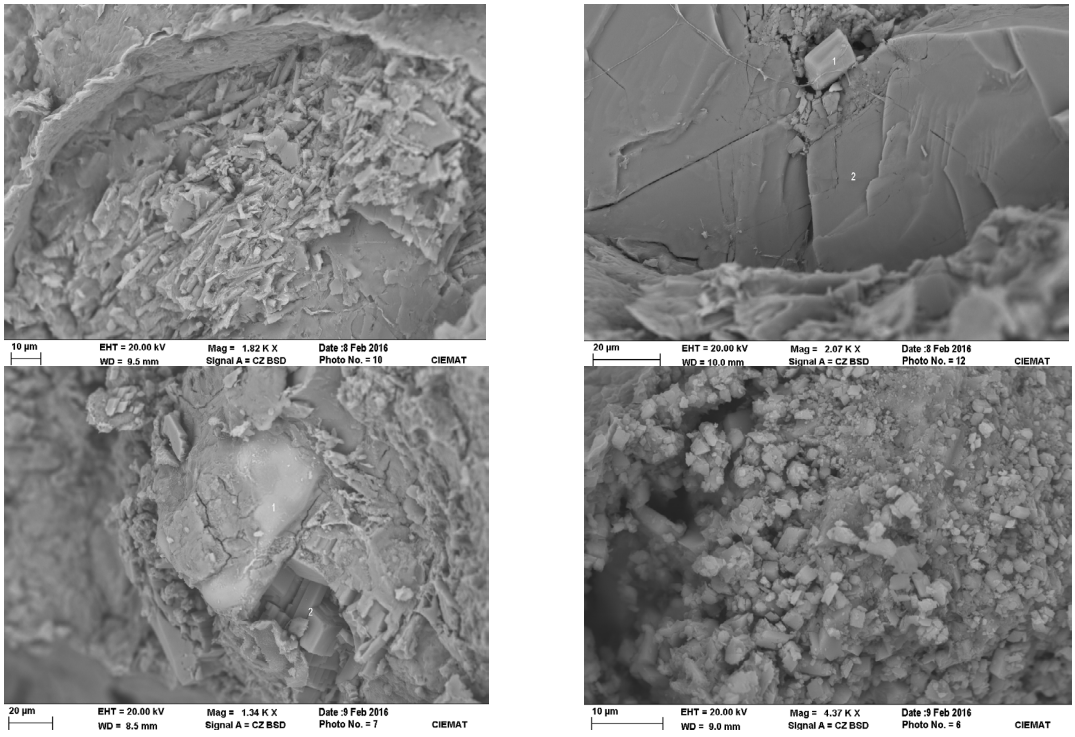

Fig. B-14: SEM photomicrographs in BB-36-2 sample: a) plagioclases, b) plagioclases (2), apatite (1); c) K-feldspar (2), ilmenite (1), d) K-feldspars

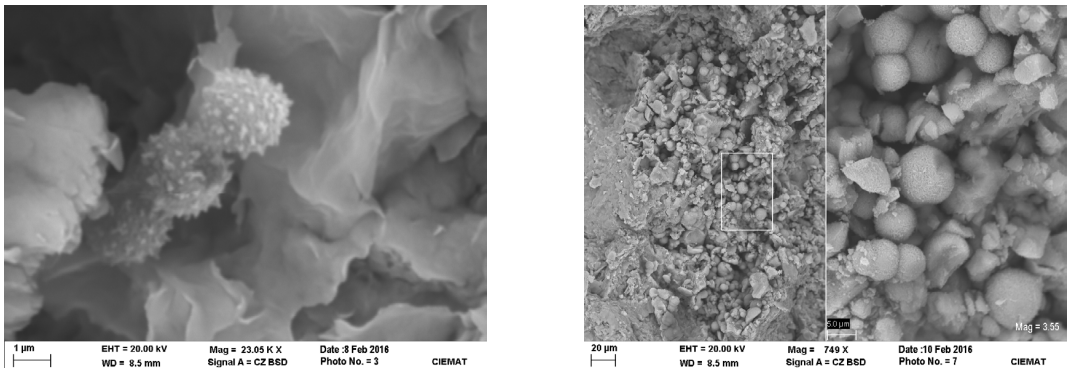

Fig. B-15: SEM photomicrographs in BB-36-2 sample: a) organic matter (OM), b) silica

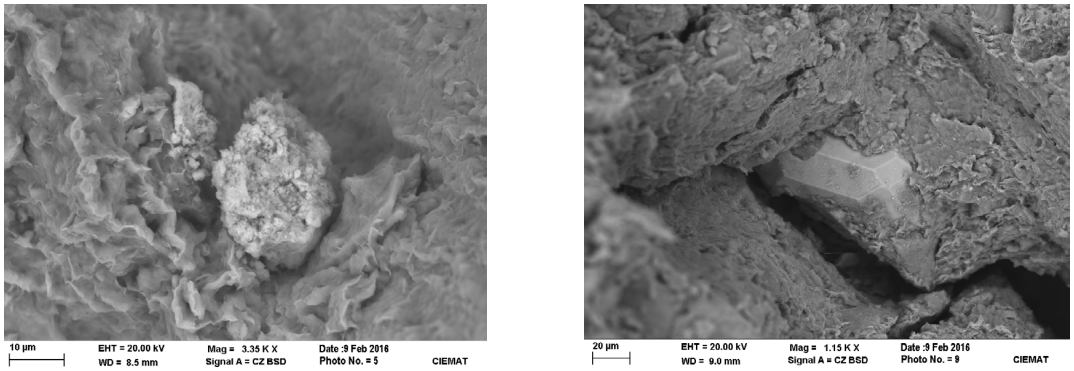

Fig. B-16: SEM photomicrographs in BB-36-2 sample: a) Fe-oxides, b) Zircon

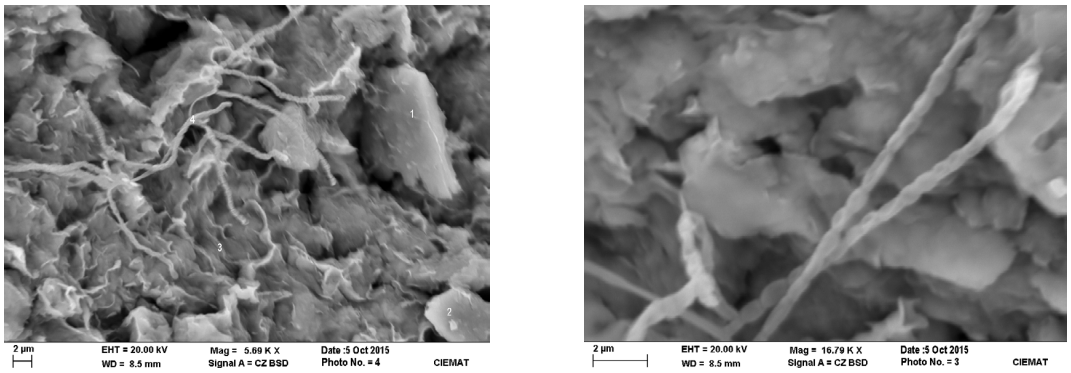

Fig. B-17: SEM photomicrographs in BB-36-5 sample: a) and b) microorganisms

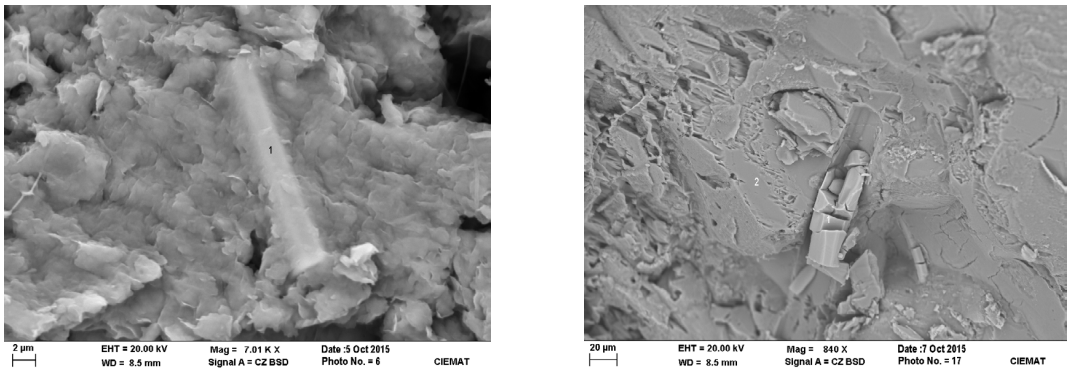

Fig. B-18: SEM photomicrographs in BB-36-5 sample: a) apatite; b) apatite (1), plagioclases (2)

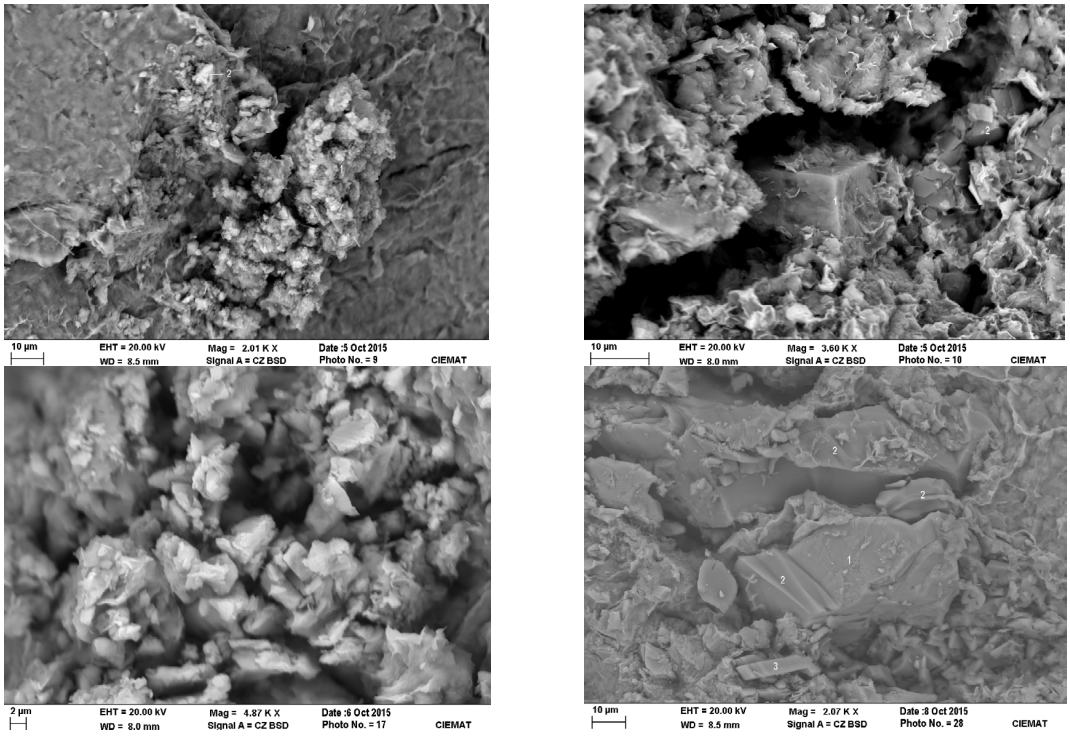

Fig. B-19: SEM photomicrographs in BB-36-5 sample: a) Ca-carbonates (1), Ca-sulfates (2), b) Ca-Mg carbonate (1), c) Ca-carbonates, d) Ca-carbonate (1), plagioclases (2), K-feldspar (3)

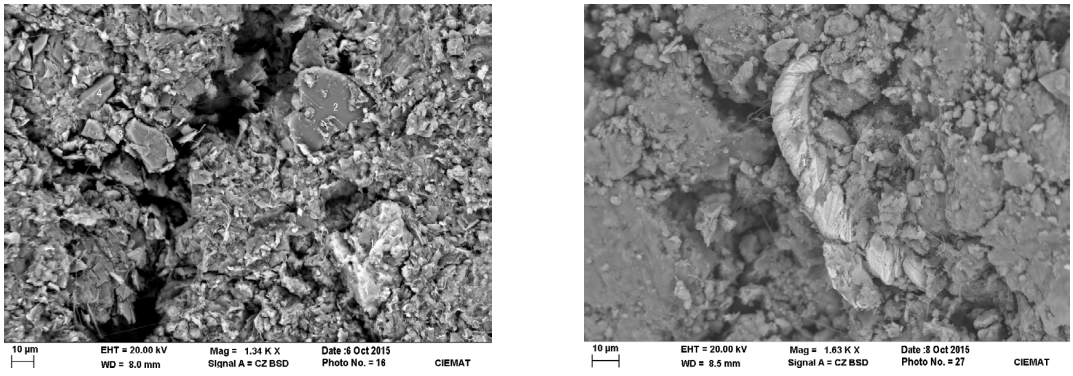

Fig. B-20: SEM photomicrographs in BB-36-5 sample: a) Fe-carbonate (1), muscovite (2), plagioclase (3), Silica (4); b) Fe-carbonate (1)

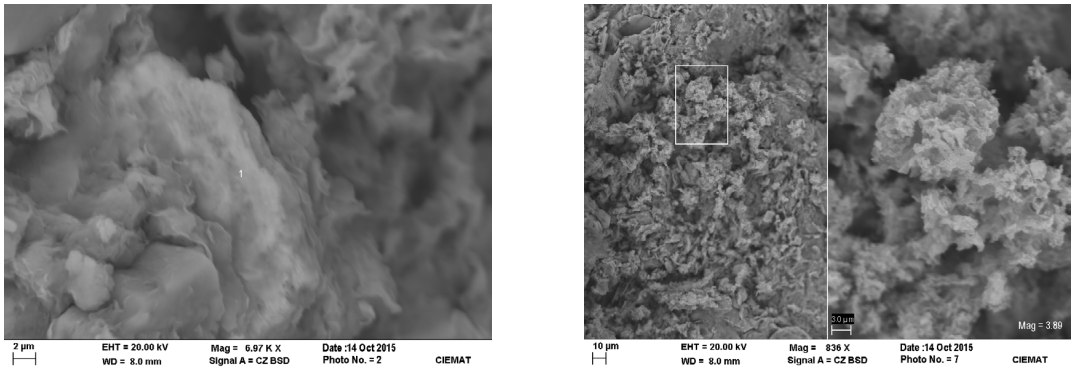

Fig. B-21: SEM photomicrographs in BB-36-5 sample: a) Fe-oxides (1), b) Magnesite

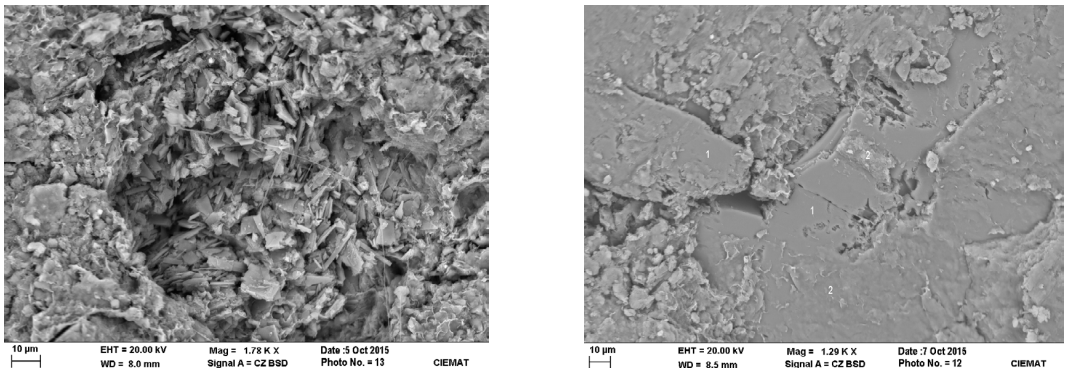

Fig. B-22: SEM photomicrographs in BB-36-5 sample: a) plagioclases; b) plagioclases (1), clay minerals (2)

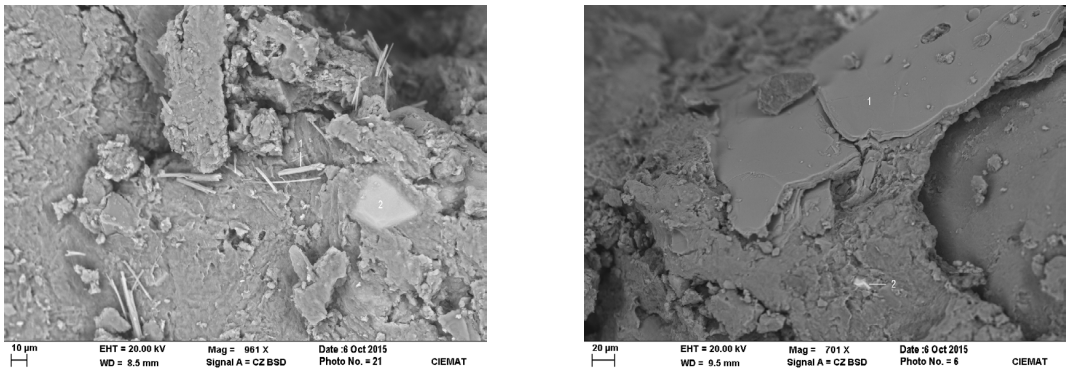

Fig. B-23: SEM photomicrographs in BB-36-5 sample: a) Ca-sulfates (1), ilmenite (2); b) barite (2), biotite (1)

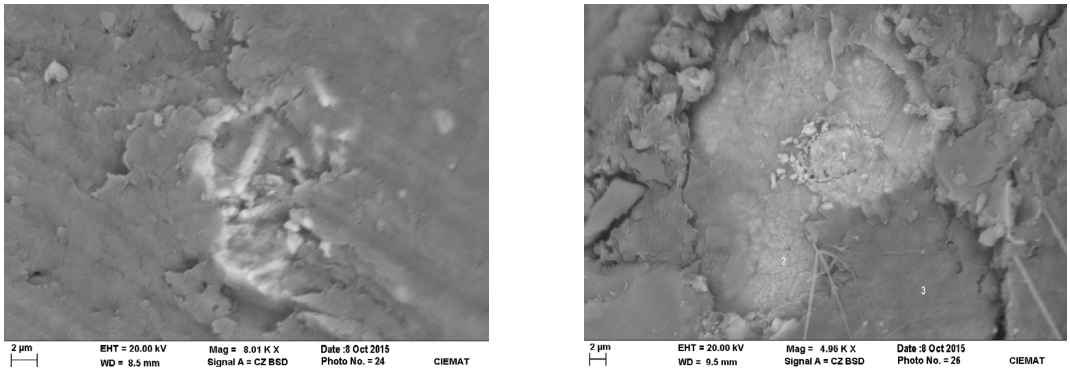

Fig. B-24: SEM photomicrographs in BB-36-5 sample: a) Fe-oxides with C, b) Fe-oxides (1), Fe-oxides with C, saponite? (3)

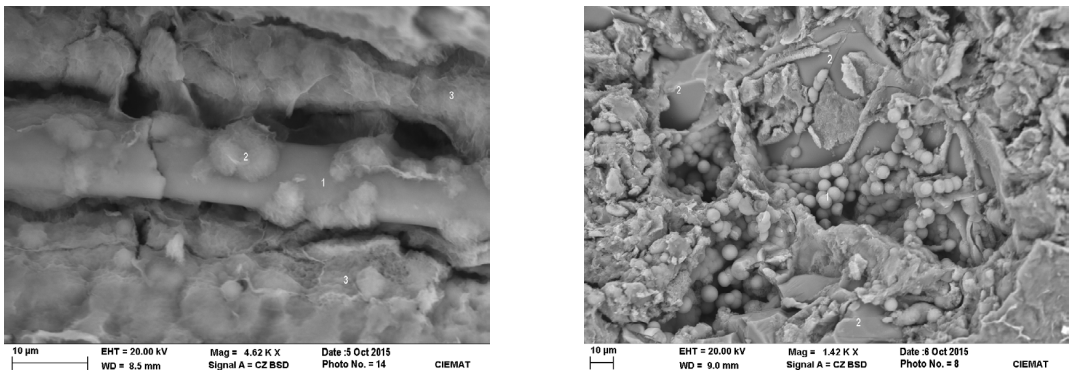

Fig. B-25: SEM photomicrographs in BB-36-5 sample: a) silica (1), silica+Ca,S (2), clay minerals (3), b) silica (1), plagioclases (2)

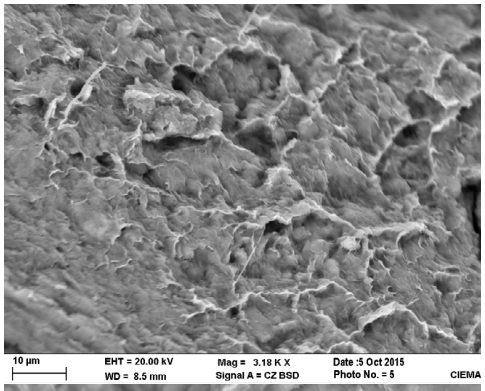

$(Si_{3.95}Al_{0.05})^{IV}(Al_{1.43}Mg_{0.39}Fe^{3+}_{0.19})^{VI}(Ca_{0.16}Na_{0.07}K_{0.04})_{0.27}O_{10}(OH)_2$
τ charge = -0.05; O. charge = -0.39
Total charge = -0.43 (τ % = 11; ο % = 89); FW (g/mol) = 748.69

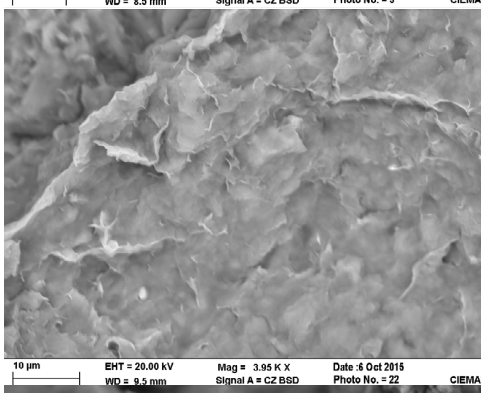

$(Si_{3.99}Al_{0.01})^{IV}(Al_{1.37}Mg_{0.44}Fe^{3+}_{0.19})^{VI}(Ca_{0.13}Mg_{0.01}Na_{0.08}K_{0.08})_{0.31}O_{10}(OH)_2$
τ charge = -0.01; O. charge = -0.44
Total charge = -0.45 (τ % = 3; ο % = 97); FW (g/mol) = 750.45
(No Mg at interlayer: Σ_{oct} = 2.01; Total charge: -0.43, τ % = 3; ο % = 97)

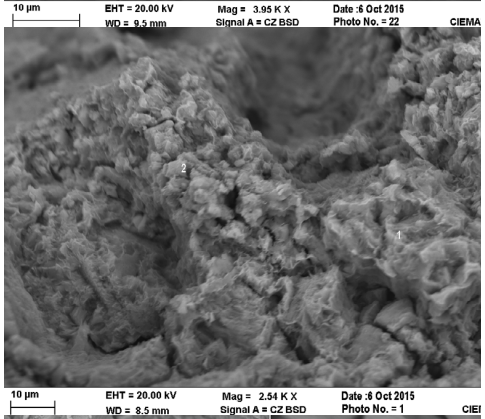

$(Si_{3.97}Al_{0.03})^{IV}(Al_{1.36}Mg_{0.44}Fe^{3+}_{0.21})^{VI}(Ca_{0.13}Na_{0.10}K_{0.10})_{0.34}O_{10}(OH)_2$
τ charge = -0.03; O. charge = -0.44
Total charge = -0.47 (τ % = 7; ο % = 93); FW (g/mol) = 753.60

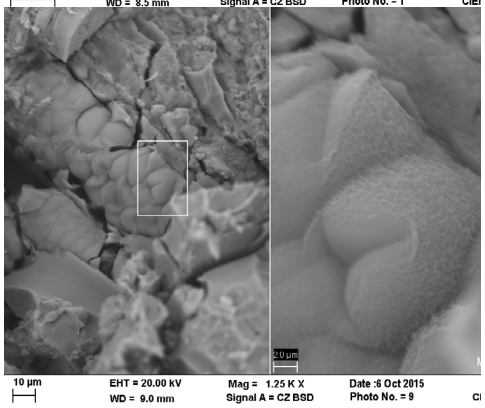

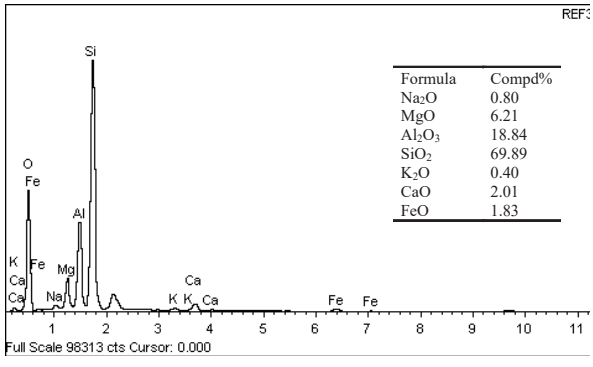

Formula	Compd%
Na_2O	0.80
MgO	6.21
Al_2O_3	18.84
SiO_2	69.89
K_2O	0.40
CaO	2.01
FeO	1.83

Fig. B-26: SEM photomicrographs in BB-36-5 sample: clay minerals

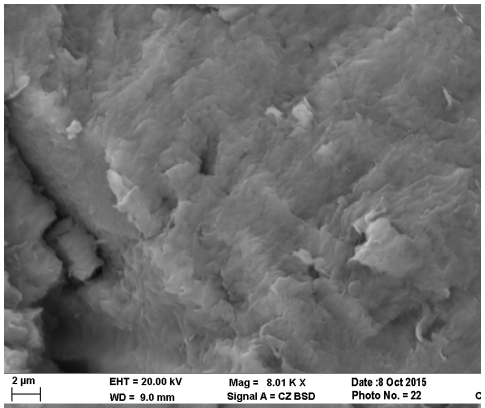

$(Si_{3.79}Al_{0.21})^{IV}(Al_{1.07}Mg_{0.77}Fe^{3+}_{0.16})^{VI}(Ca_{0.09}Mg_{0.36}Na_{0.06}K_{0.13})_{0.53}O_{10}(OH)_2$
τ charge = -0.21; O. charge = -0.77
Total charge = -0.98 (τ % = 21; o % = 79); FW (g/mol) = 753.78
(No Mg at interlayer: Σ_{oct} = 2.36; Total charge: -0.26, τ % = 80; o % = 20)

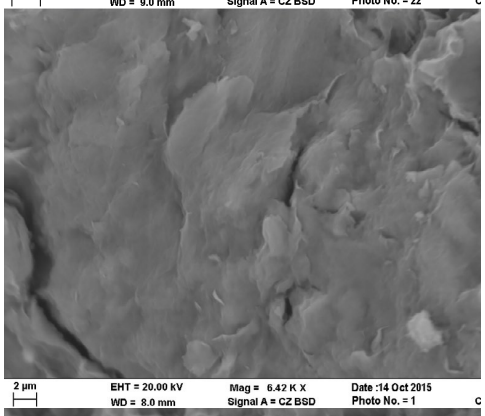

$(Si_{3.95}Al_{0.05})^{IV}(Al_{1.30}Mg_{0.54}Fe^{3+}_{0.17})^{VI}(Ca_{0.11}Mg_{0.11}Na_{0.09}K_{0.07})_{0.37}O_{10}(OH)_2$
τ charge = -0.05; O. charge = -0.54
Total charge = -0.59 (τ % = 9; o % = 91); FW (g/mol) = 750.68
(No Mg at interlayer: Σ_{oct} = 2.11; Total charge: -0.38, τ % = 14; o % = 86)

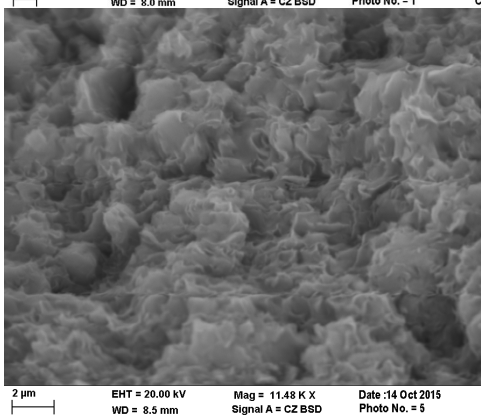

$(Si_{4.00}Al_{0.00})^{IV}(Al_{1.38}Mg_{0.52}Fe^{3+}_{0.10})^{VI}(Ca_{0.14}Mg_{0.06}Na_{0.08}K_{0.04})_{0.32}O_{10}(OH)_2$
τ charge = -0.00; O. charge = -0.52
Total charge = -0.52 (τ % = 0; o % = 100); FW (g/mol) = 744.44
(No Mg at interlayer: Σ_{oct} = 2.06; Total charge: -0.40, τ % = 0; o % = 100)

Fig. B-26: Cont.

Section 47

Samples BB-47-4 and BB-47-7: external bentonite ring (granite contact)

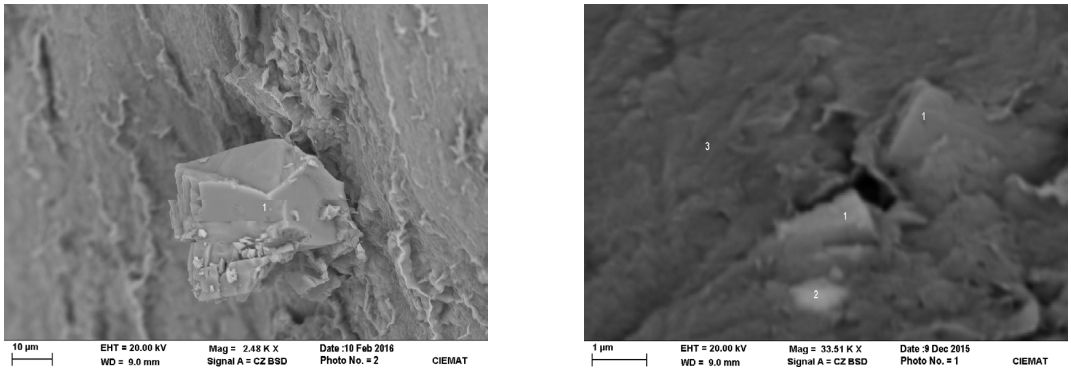

Fig. B-27: SEM photomicrographs: a) BB-47-4 sample: Ca-sulfates (1), b) BB-47-7: Ca-sulfates (1), zircon (2)

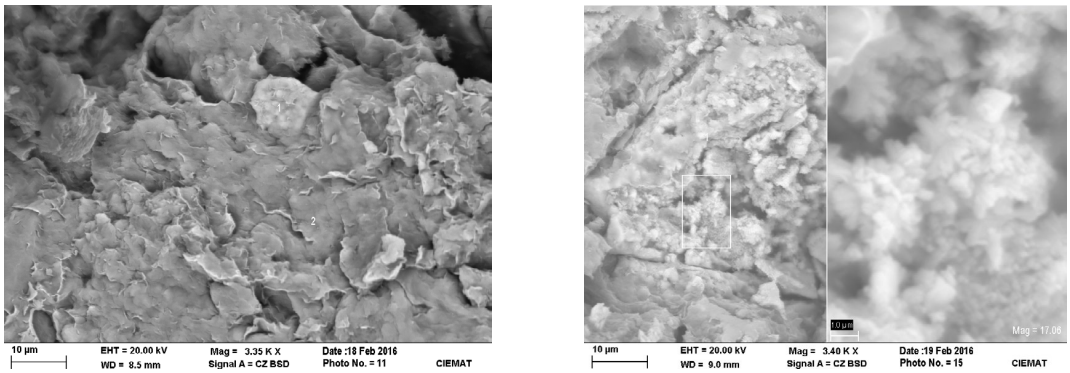

Fig. B-28: SEM photomicrographs in BB-47-7 sample: a): Fe-oxides (1), smectite (2), b) Fe-oxides

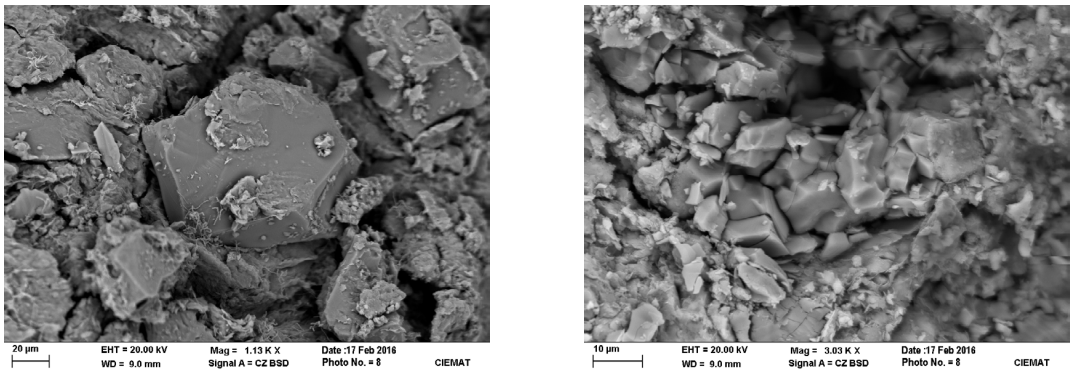

Fig. B-29: SEM photomicrographs in BB-47-7 sample: a) and b) silica

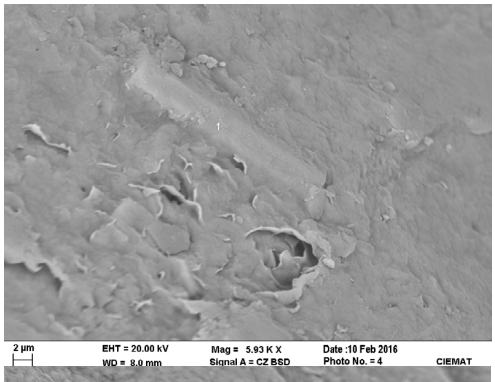

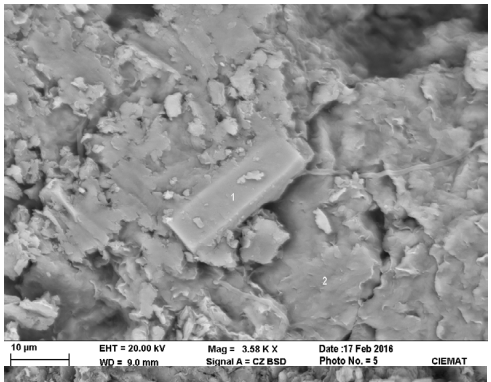

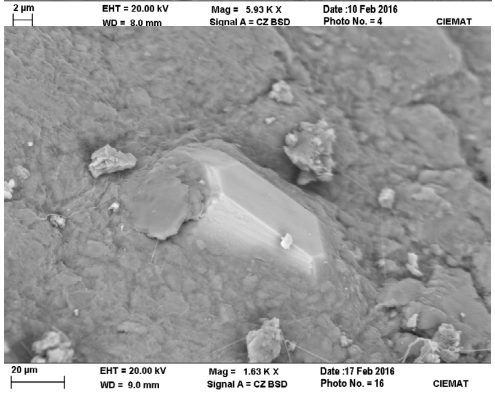

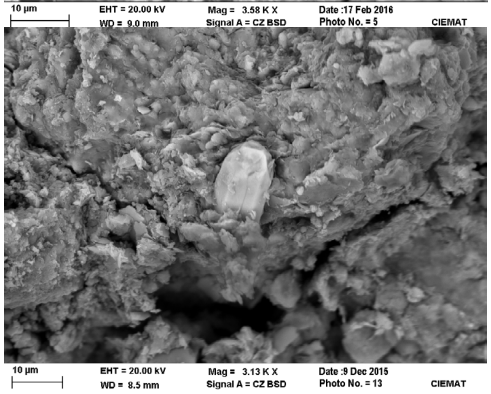

Fig. B-30: SEM photomicrographs: a) BB-47-4 sample: apatite, b) BB-47-7 sample: apatite, c) BB-47-7 sample: zircon, d) BB-47-7 sample: zircon

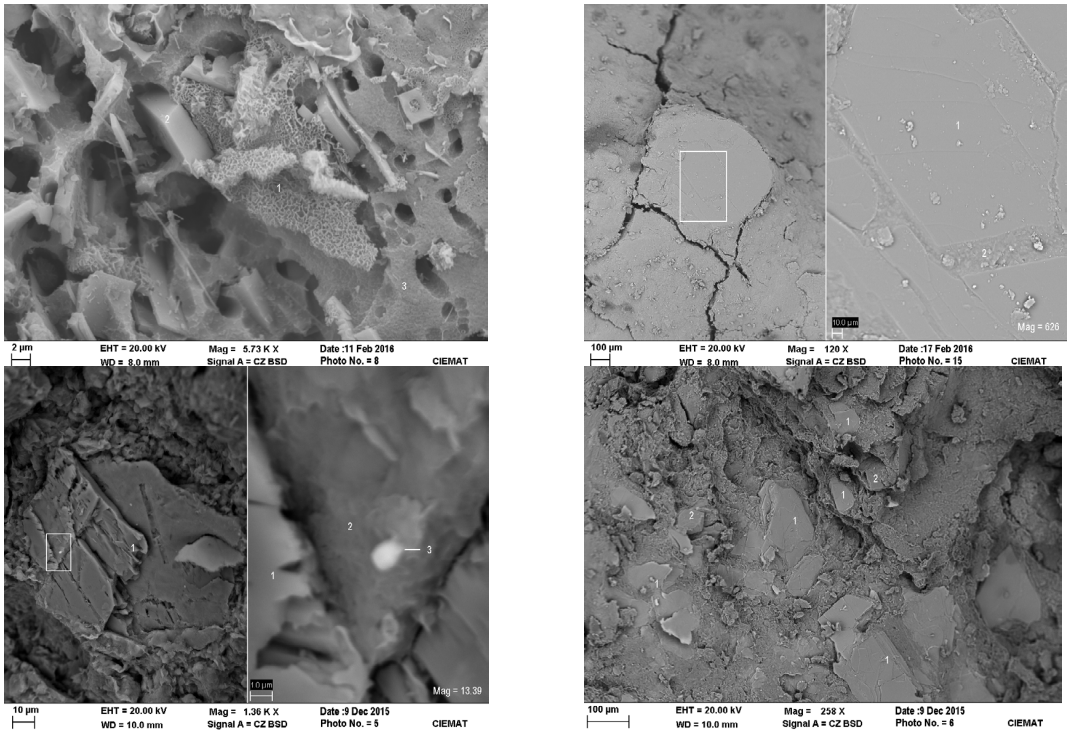

Fig. B-31: SEM photomicrographs: a) BB-47-4 sample: zeolites? (1), plagioclases (1), feldspars (3), b) BB-47-7 sample: plagioclase, c) BB-47-7: plagioclase (1), smectite(2), Fe, Ti (3), d) BB-47-7: biotite (1), plagioclase (2)

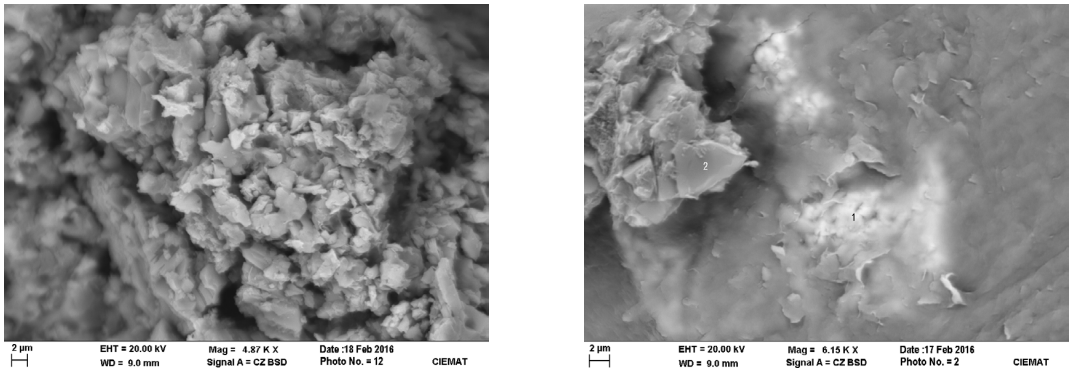

Fig. B-32: SEM photomicrographs: BB-47-7 sample: a) K-feldspar; b) barite (1), plagioclase (2)

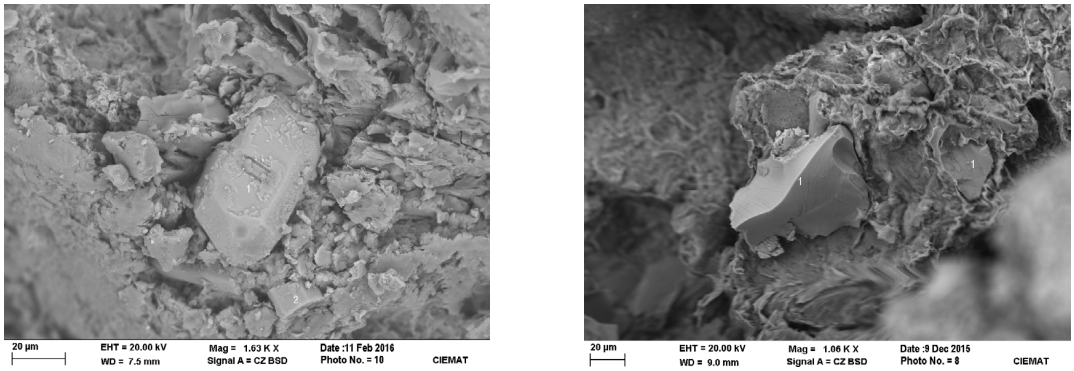

Fig. B-33: SEM photomicrographs: a) BB-47-4 sample: ilmenite (1), apatite (2), b) BB-47-7 sample: ilmenite (1)

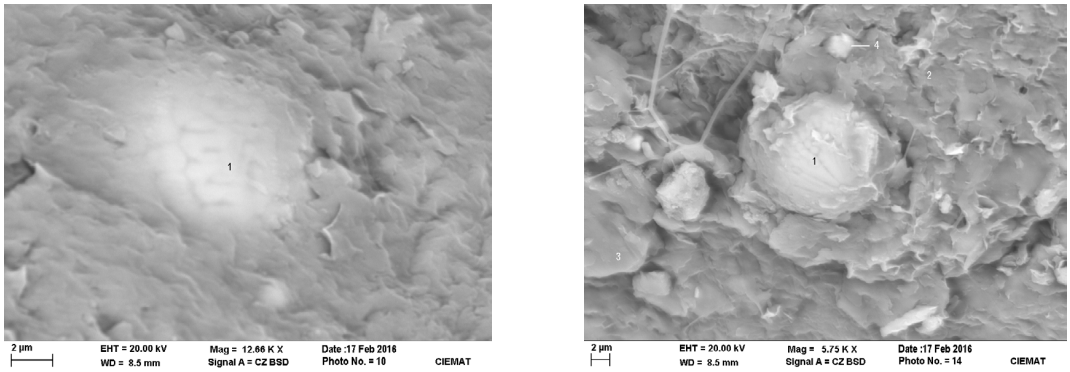

Fig. B-34: SEM photomicrographs in BB-47-7 sample: a) Fe-carbonate, b) Fe-carbonate (1), smectite(2), plagioclase (3), Fe,S (4)

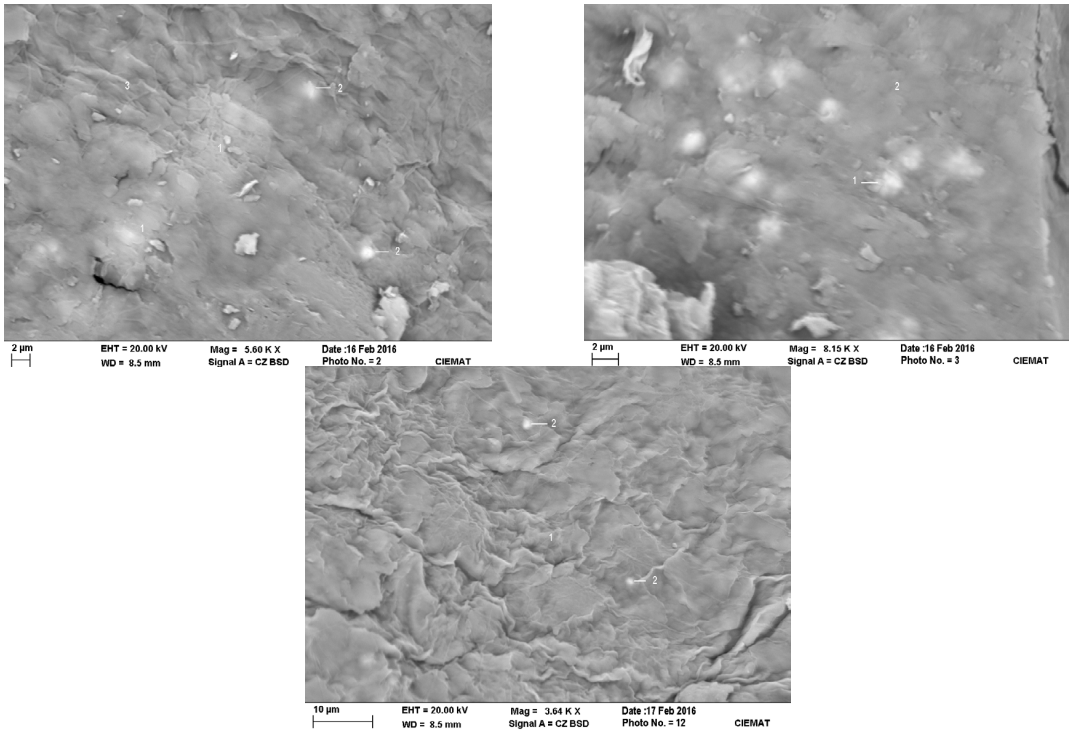

Fig. B-35: SEM photomicrographs in BB-47-7 sample: a) S, Fe (2), b) S, Fe (1), c) smectite (1), S, Fe (2)

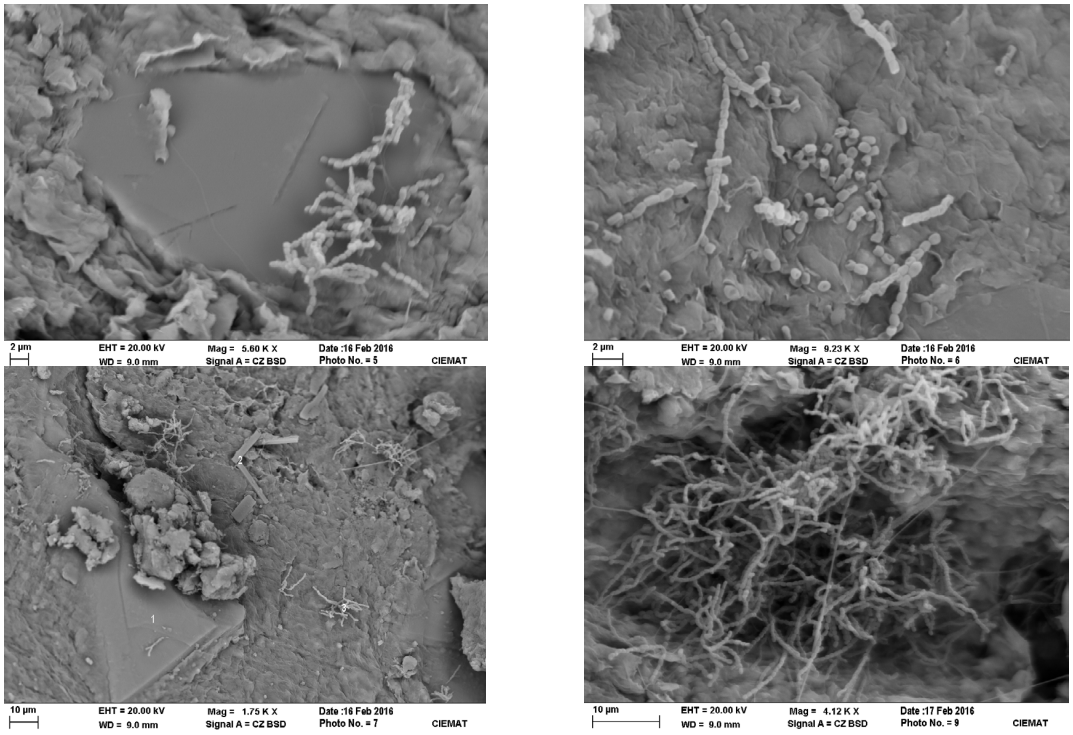

Fig. B-36: SEM photomicrographs in BB-47-4 sample: a) microorganisms and plagioclase, b) microorganisms, c) biotite (1), plagioclase (2), microorganisms, d) microorganims

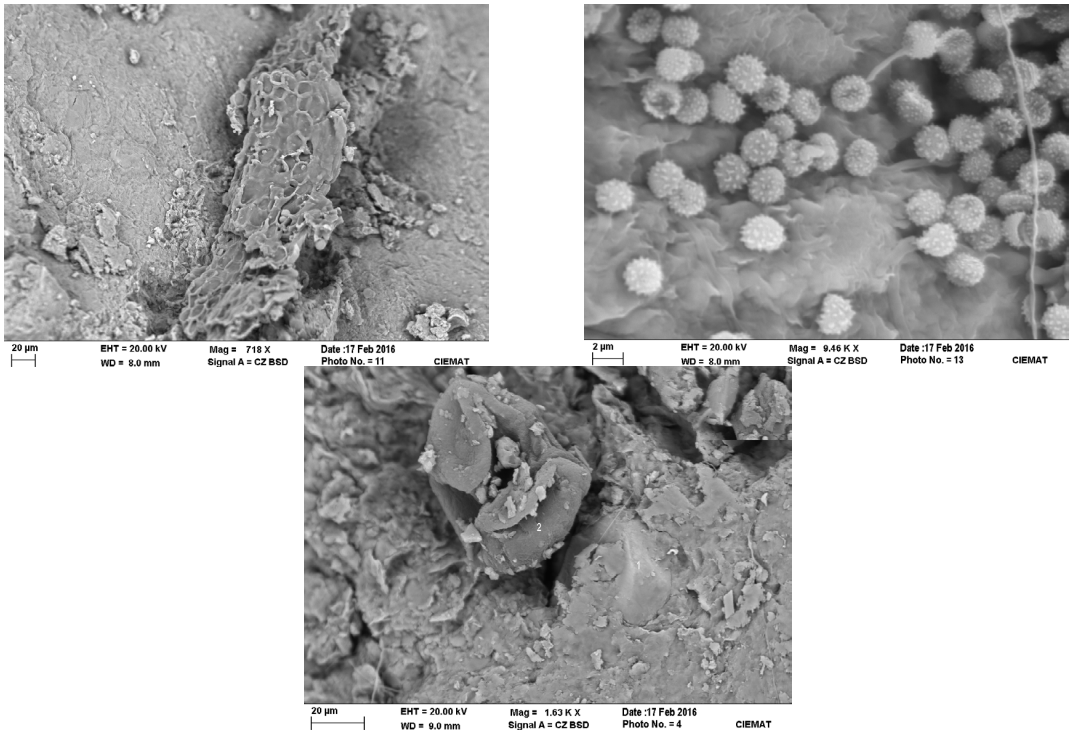

Fig. B-37: SEM photomicrographs in BB-47-7 sample: a) organic matter (OM), C, b) organic matter, c) Ti, Mn, Fe (1), C (OM) (2)

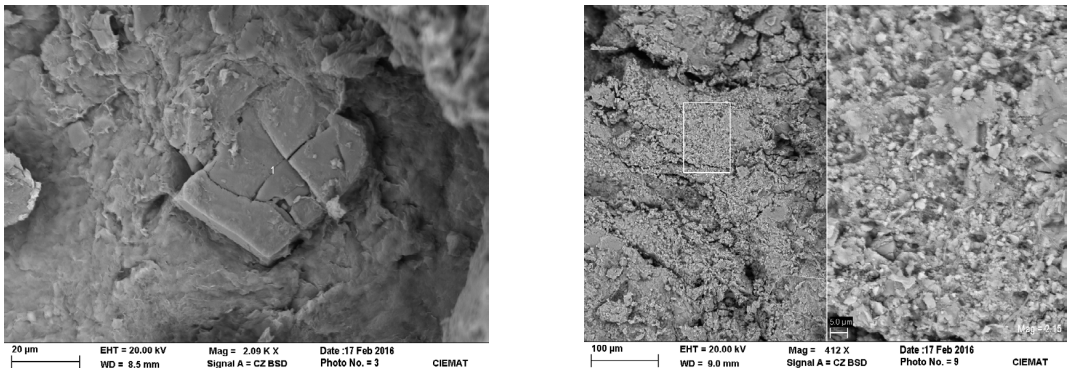

Fig. B-38: SEM photomicrographs in BB-47-7 sample: a) and b) Ca-carbonates

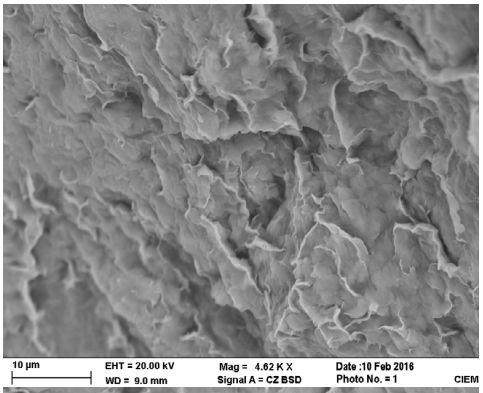

$(Si_{4.00}Al_{0.00})^{IV}(Al_{1.34}Mg_{0.49}Fe^{3+}_{0.17})^{VI}(Ca_{0.07}Mg_{0.07}Na_{0.13}K_{0.07})_{0.34}O_{10}(OH)_2$
τ charge = -0.00; O. charge = -0.49
Total charge = -0.49 (τ % = 0; o % = 100); FW (g/mol) = 748.45
(No Mg at interlayer: Σ_{oct} = 2.07; Total charge: -0.34, τ % = 0; o % = 100)

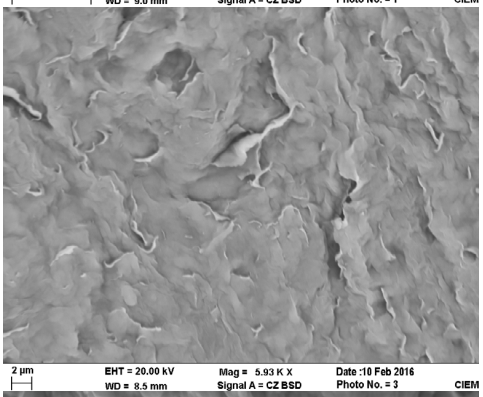

$(Si_{4.00}Al_{0.00})^{IV}(Al_{1.46}Mg_{0.49}Fe^{3+}_{0.05})^{VI}(Ca_{0.08}Mg_{0.10}Na_{0.10}K_{0.01})_{0.30}O_{10}(OH)_2$
τ charge = -0.00; O. charge = -0.49
Total charge = -0.49 (τ % = 0; o % = 100); FW (g/mol) = 738.16
(No Mg at interlayer: Σ_{oct} = 2.10; Total charge: -0.28, τ % = 0; o % = 100)

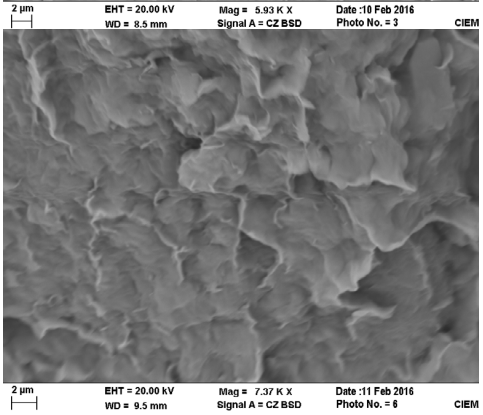

$(Si_{3.99}Al_{0.01})^{IV}(Al_{1.40}Mg_{0.42}Fe^{3+}_{0.18})^{VI}(Ca_{0.10}Mg_{0.07}Na_{0.07}K_{0.10})_{0.27}O_{10}(OH)_2$
τ charge = -0.01; O. charge = -0.42
Total charge = -0.43 (τ % = 3; o % = 97); FW (g/mol) = 745.68
(No Mg at interlayer: Σ_{oct} = 2.07; Total charge: -0.30, τ % = 4; o % = 96)

Fig. B-39: SEM photomicrographs in BB-47-4 sample: clay minerals

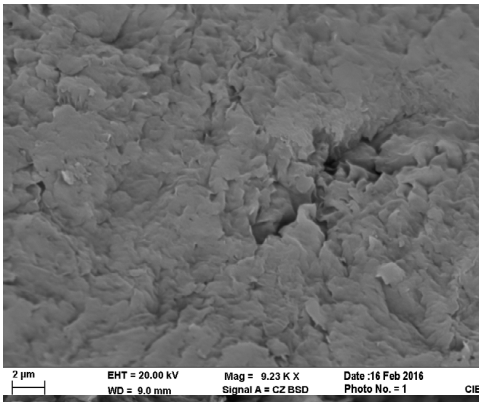

$(Si_{4.00}Al_{0.00})^{IV}(Al_{1.31}Mg_{0.44}Fe^{3+}_{0.25})^{VI}(Ca_{0.11}Mg_{0.06}Na_{0.05}K_{0.06})_{0.28}O_{10}(OH)_2$
τ charge = -0.00; O. charge = -0.44
Total charge = -0.44 (τ % = 0; o % = 100); FW (g/mol) = 751.52
(No Mg at interlayer: Σ_{oct} = 2.06; Total charge: -0.33; τ % = 0; o % = 100)

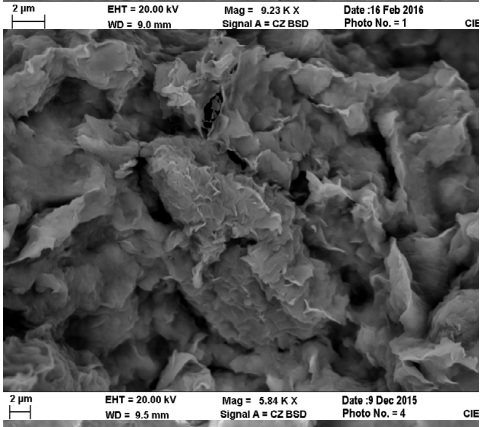

$(Si_{4.00}Al_{0.00})^{IV}(Al_{1.37}Mg_{0.49}Fe^{3+}_{0.14})^{VI}(Ca_{0.10}Mg_{0.09}Na_{0.10}K_{0.02})_{0.30}O_{10}(OH)_2$
τ charge = -0.00; O. charge = -0.49
Total charge = -0.49 (τ % = 0; o % = 100); FW (g/mol) = 744.16
(No Mg at interlayer: Σ_{oct} = 2.09; Total charge: -0.31; τ % = 0; o % = 100)

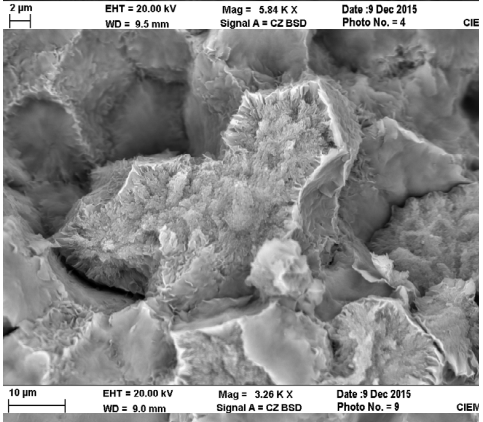

$(Si_{3.74}Al_{0.26})^{IV}(Al_{1.65}Mg_{0.23}Fe^{3+}_{0.13})^{VI}(Ca_{0.11}Mg_{0.08}Na_{0.07}K_{0.02})_{0.29}O_{10}(OH)_2$
τ charge = -0.26; O. charge = -0.23
Total charge = -0.48 (τ % = 53; o % = 47); FW (g/mol) = 744.25
(No Mg at interlayer: Σ_{oct} = 2.08; Total charge: -0.32; τ % = 81; o % = 19)

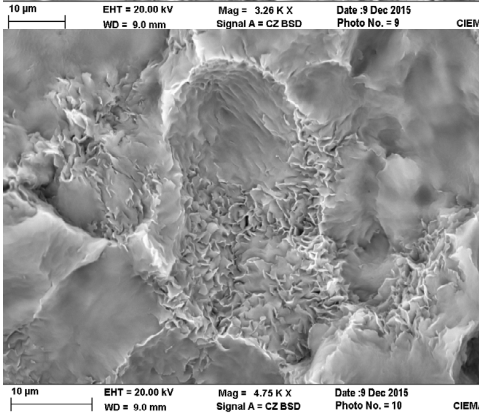

$(Si_{3.91}Al_{0.09})^{IV}(Al_{1.46}Mg_{0.40}Fe^{3+}_{0.14})^{VI}(Ca_{0.09}Mg_{0.09}Na_{0.08}K_{0.05})_{0.31}O_{10}(OH)_2$
τ charge = -0.09; O. charge = -0.40
Total charge = -0.49 (τ % = 18; o % = 82); FW (g/mol) = 745.51
(No Mg at interlayer: Σ_{oct} = 2.09; Total charge: -0.31; τ % = 28; o % = 72)

Fig. B-40: SEM photomicrographs in BB-47-7 sample: clay minerals

Samples BB-47-2, BB-47-5 and BB-47-8: middle bentonite ring

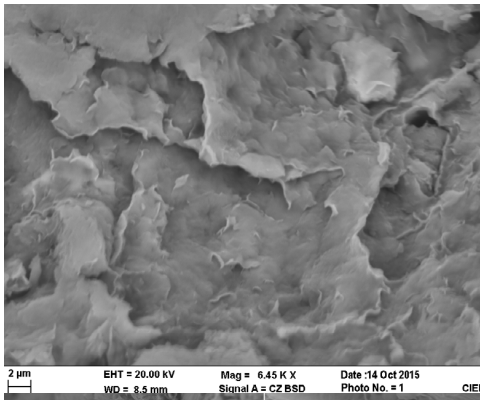

$(Si_{4.00}Al_{0.00})^{IV}(Al_{1.38}Mg_{0.38}Fe^{3+}_{0.19\ \ 0.05})^{VI}(Ca_{0.09}Na_{0.09}K_{0.26})_{0.44}O_{10}(OH)_2$
τ charge = -0.00; O. charge = -0.53
Total charge = -0.53 (τ % = 0; ο % = 100); FW (g/mol) = 758.88

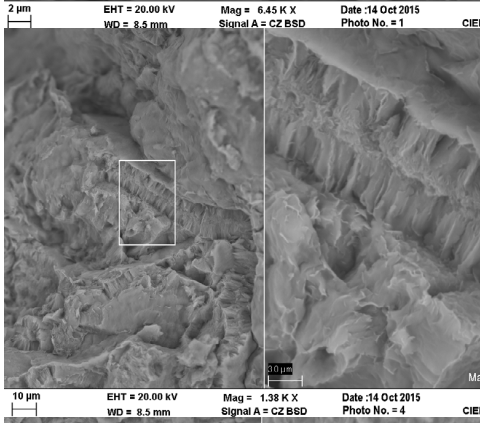

$(Si_{3.99}Al_{0.01})^{IV}(Al_{1.44}Mg_{0.46}Fe^{3+}_{0.10})^{VI}(Ca_{0.09}Mg_{0.09}Na_{0.11})_{0.29}O_{10}(OH)_2$
τ charge = -0.01; O. charge = -0.46
Total charge = -0.47 (τ % = 3; ο % = 97); FW (g/mol) = 740.70
(No Mg at interlayer: Σ_{oct} = 2.09; Total charge: -0.29; τ % = 5;
ο % = 95)

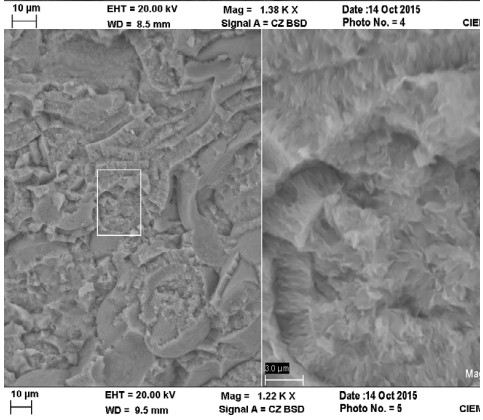

$(Si_{3.99}Al_{0.01})^{IV}(Al_{1.41}Mg_{0.44}Fe^{3+}_{0.15})^{VI}(Ca_{0.10}Mg_{0.08}Na_{0.07}K_{0.01})_{0.27}O_{10}(OH)_2$
τ charge = -0.01; O. charge = -0.45
Total charge = -0.46 (τ % = 3; ο % = 97); FW (g/mol) = 743.26
(No Mg at interlayer: Σ_{oct} = 2.08; Total charge: -0.29; τ % = 4;
ο % = 96)

Fig. B-41: SEM photomicrographs in BB-47-2 sample: clay minerals

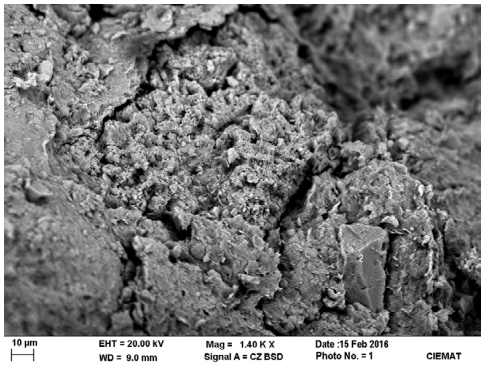

1:Ca-carbonate; 2: smectite; Na-orthoclase

$(Si_{3.98}Al_{0.02})^{IV}(Al_{1.40}Mg_{0.43}Fe^{3+}_{0.17})^{VI}(Ca_{0.11}Mg_{0.04}Na_{0.09}K_{0.05})_{0.29}O_{10}(OH)_2$
τ charge = -0.02; O. charge = -0.43
Total charge = -0.45 (τ % = 4; o % = 96); FW (g/mol) = 747.33
(No Mg at interlayer: Σ_{oct} = 2.04; Total charge: -0.37; τ % = 4; o % = 96)

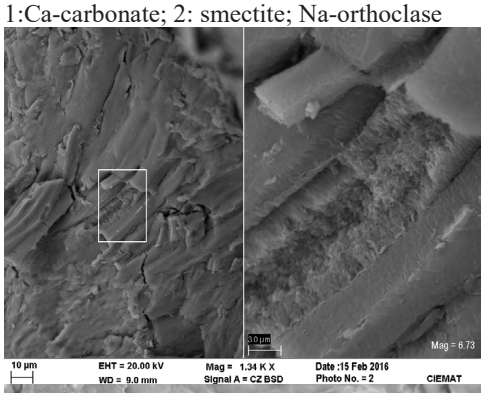

$(Si_{3.96}Al_{0.04})^{IV}(Al_{1.37}Mg_{0.36}Fe^{3+}_{0.27})^{VI}(Ca_{0.14}Mg_{0.02}Na_{0.06}K_{0.04})_{0.25}O_{10}(OH)_2$
τ charge = -0.04; O. charge = -0.36
Total charge = -0.40 (τ % = 9; o % = 91); FW (g/mol) = 751.44
(No Mg at interlayer: Σ_{oct} = 2.02; Total charge: -0.37; τ % = 10; o % = 90)

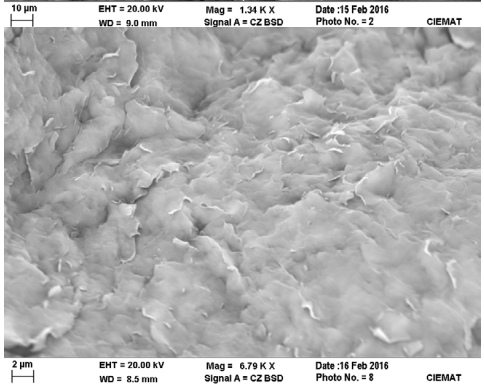

$(Si_{4.00}Al_{0.00})^{IV}(Al_{1.37}Mg_{0.46}Fe^{3+}_{0.18})^{VI}(Ca_{0.10}Mg_{0.01}Na_{0.10}K_{0.14})_{0.35}O_{10}(OH)_2$
τ charge = -0.00; O. charge = -0.46
Total charge = -0.46 (τ % = 0; o % = 100); FW (g/mol) = 752.09
(No Mg at interlayer: Σ_{oct} = 2.01; Total charge: -0.43; τ % = 0; o % = 100)

Fig. B-42: SEM photomicrographs in BB-47-5 sample: clay minerals

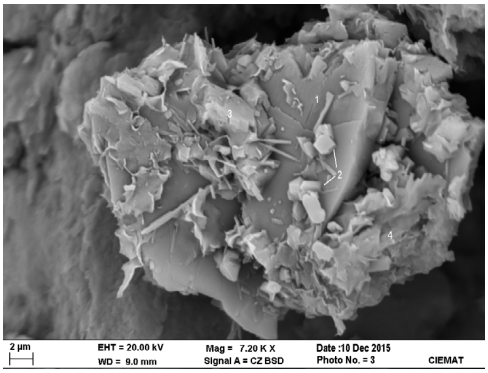

1: Ca-Na-plagioclases; 2: Ca-sulfates; 3: K-feldspars; 4: smectite

$(Si_{3.94}Al_{0.06})^{IV}(Al_{1.13}Mg_{0.37}Fe^{3+}_{0.49\ \ 0.01})^{VI}(Ca_{0.15}Na_{0.12}K_{0.02})_{0.30}O_{10}(OH)_2$
τ charge = -0.06; O. charge = -0.39
Total charge = -0.45 (τ % = 14; o % = 86); FW (g/mol) = 766.08

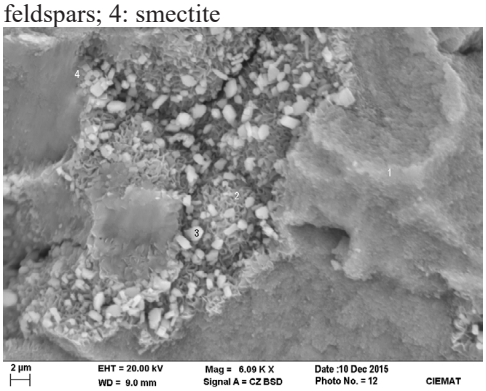

1: halloysite?; 2: smectite; 3: Ca-sulfates

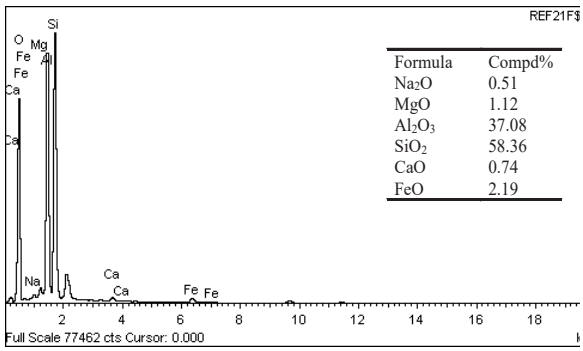

Formula	Compd%
Na_2O	0.51
MgO	1.12
Al_2O_3	37.08
SiO_2	58.36
CaO	0.74
FeO	2.19

1:halloysite?

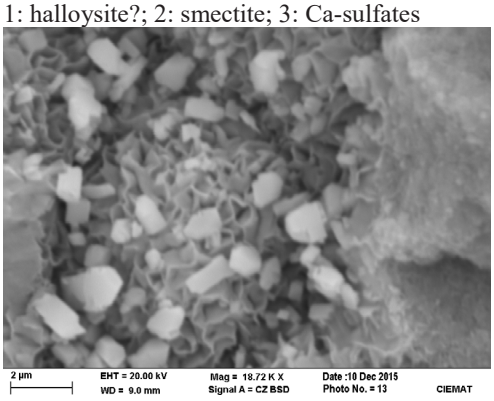

2: smectite (see above)

$(Si_{3.77}Al_{0.23})^{IV}(Al_{1.59}Mg_{0.31}Fe^{3+}_{0.10})^{VI}(Ca_{0.10}Mg_{0.07}Na_{0.10}K_{0.10})_{0.37}O_{10}(OH)_2$
τ charge = -0.23; O. charge = -0.31
Total charge = -0.54 (τ % = 42; o % = 58); FW (g/mol) = 747.69
(No Mg at interlayer: Σ_{oct} = 2.07; Total charge: -0.39; τ % = 58; o % = 42)

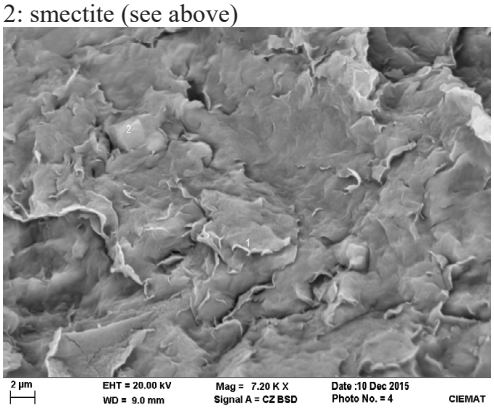

1: Smectite; 2: K-Fd

$(Si_{3.99}Al_{0.01})^{IV}(Al_{1.47}Mg_{0.45}Fe^{3+}_{0.08})^{VI}(Ca_{0.09}Mg_{0.07}Na_{0.12}K_{0.02})_{0.30}O_{10}(OH)_2$
τ charge = -0.01; O. charge = -0.45
Total charge = -0.46 (τ % = 1; o % = 99); FW (g/mol) = 740.30
(No Mg at interlayer: Σ_{oct} = 2.07; Total charge: -0.32; τ % = 2; o % = 98)

Fig. B-43: SEM photomicrographs in BB-47-8 sample: clay minerals

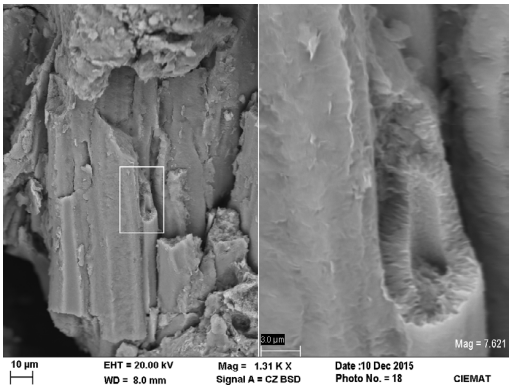

Smectite

Fig. B-43: Cont.

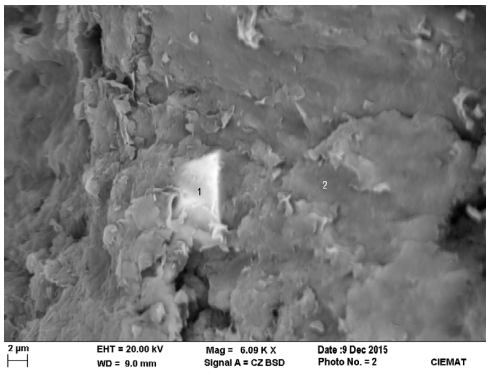

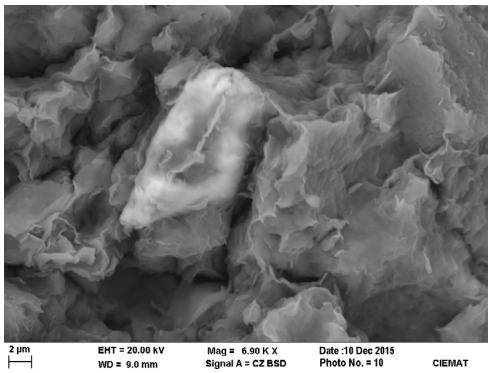

Fig. B-44: SEM photomicrographs in BB-47-8 sample: a): Ba-sulfates (1), smectite (2), b) barite

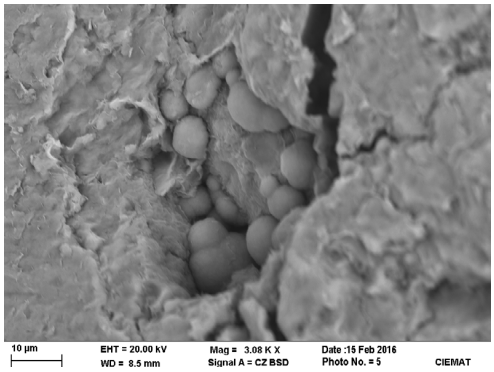

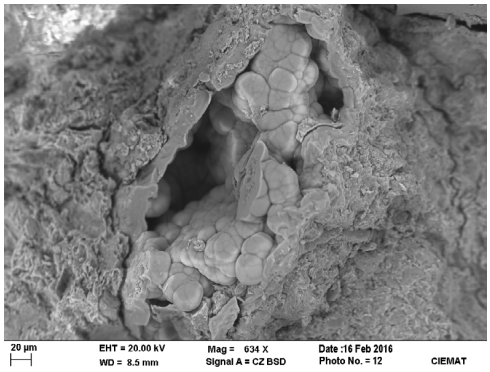

Fig. B-45: SEM photomicrographs in BB-47-5 sample: a) and b) silica

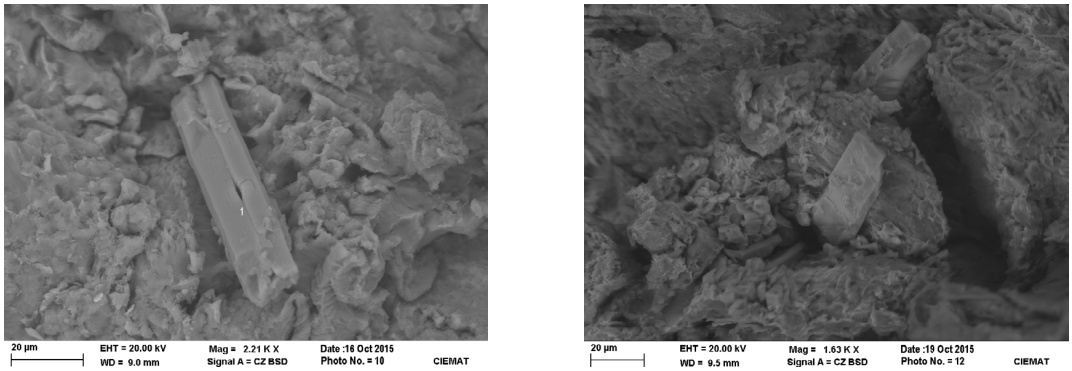

Fig. B-46: SEM photomicrographs: a) BB-47-2: Ca-sulfate (1), b) BB-47-2: Ca-sulfates

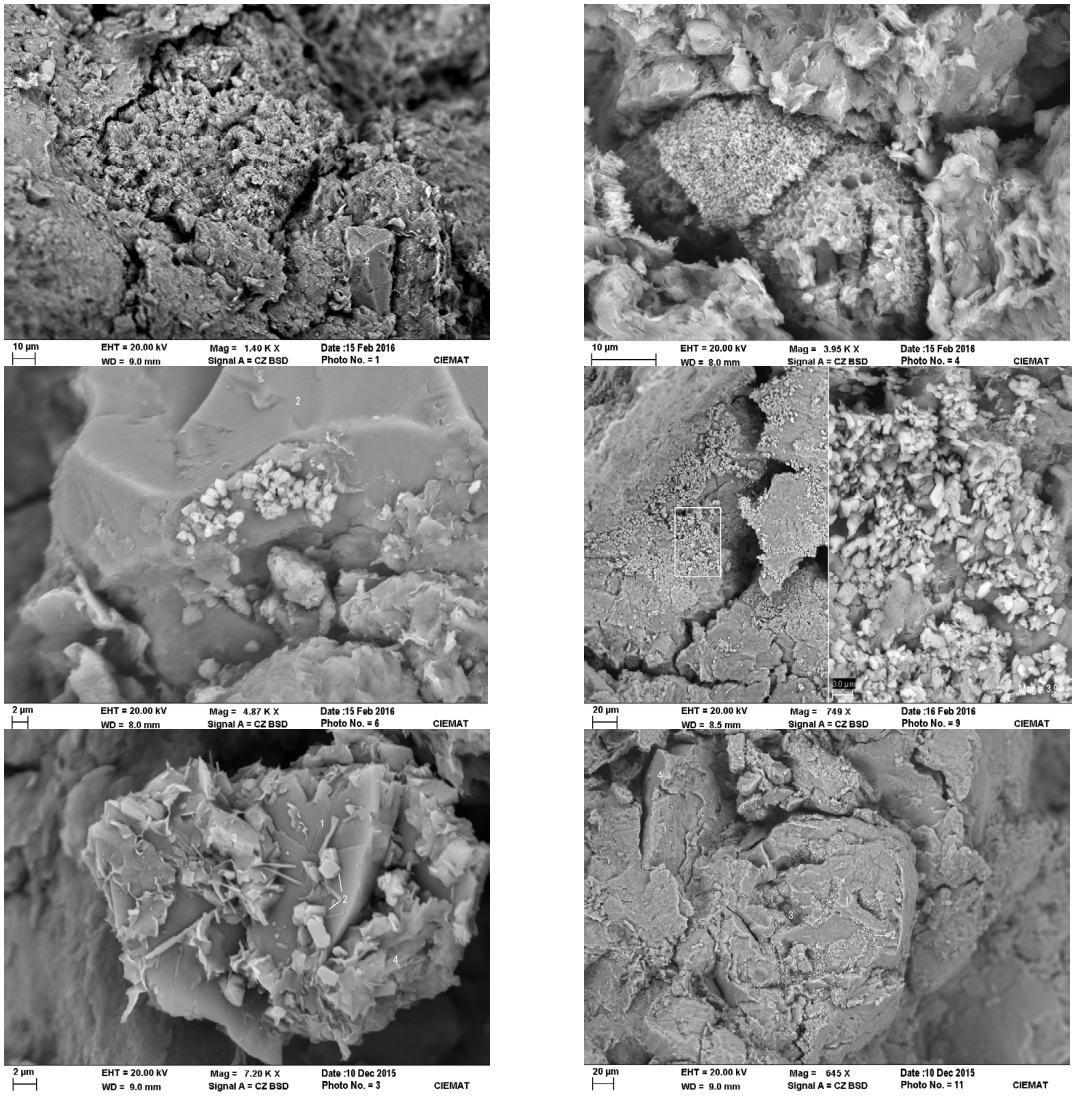

Fig. B-47: SEM photomicrographs: a) BB-47-5 sample: a) Ca-sulfates (1), b) Ca-sulfates (2), smectite (1,3), c) Ca-sulfates (1), plagioclases (2), d) Ca-sulfates, e) Ca-sulfates (2), plagioclase (1), K-Fd (3) smectite (4), f) BB-47-8 sample: halloysite? (1), smectite (2), Ca-sulfate (3), C, orthoclase-Na (4)

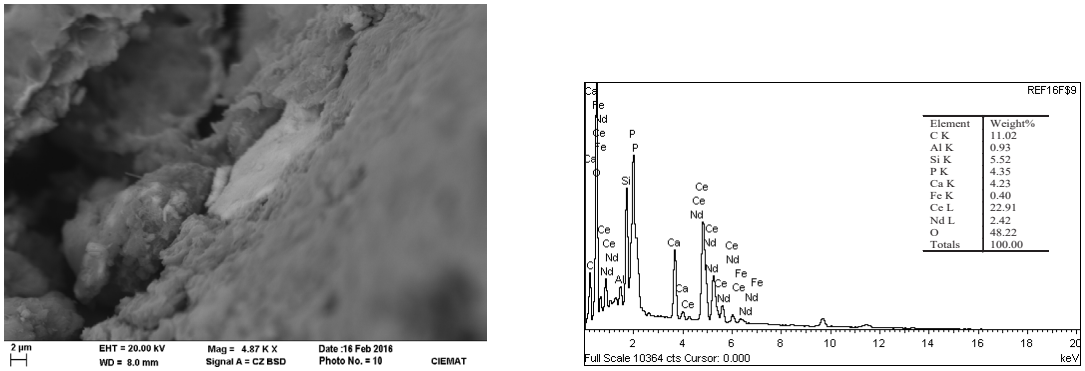

Fig. B-48: SEM photomicrographs in BB-47-5 sample: Ca-carbonates, P and Ce

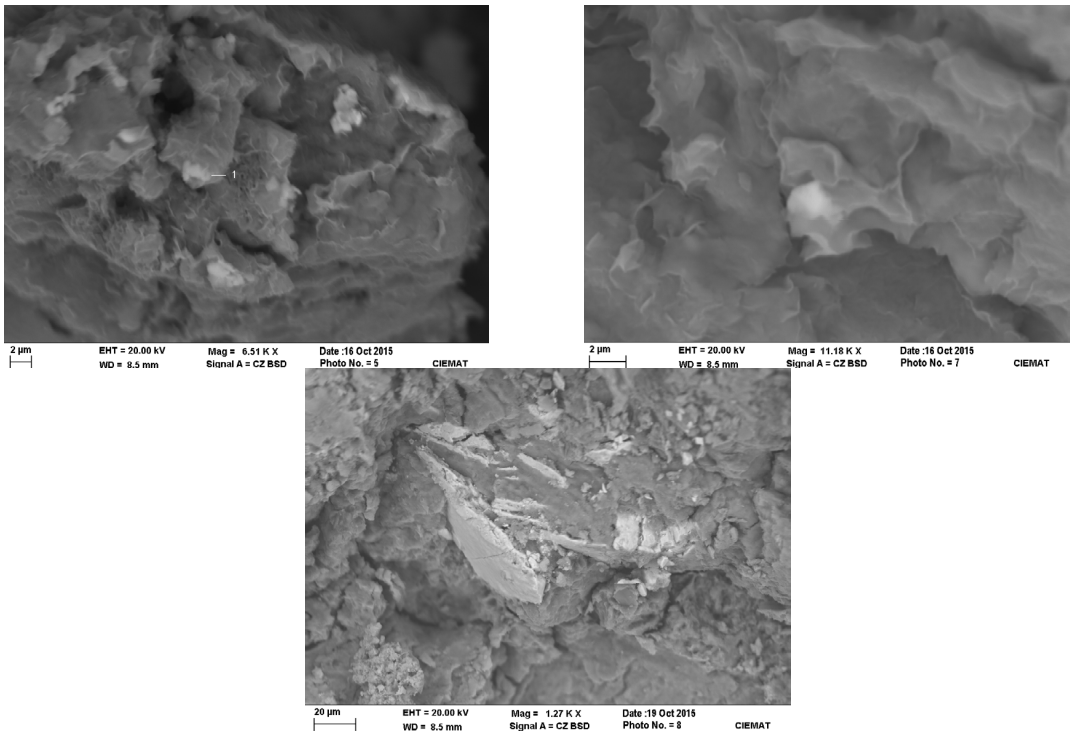

Fig. B-49: SEM photomicrographs in BB-47-2 sample: a): Sr (Ba)-sulfates (1), b) Ba (Sr)-sulfate, c) BB-47-2 sample: Ba (Sr)-sulfate

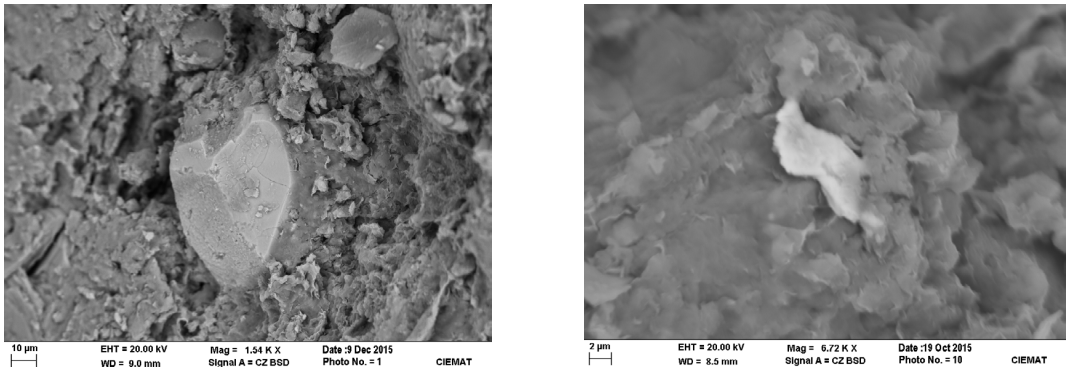

Fig. B-50: SEM photomicrographs in BB-47-8 sample: a) Fe-Ti, V, M, C, b) BB-47-2 sample: Cu, Sn, C

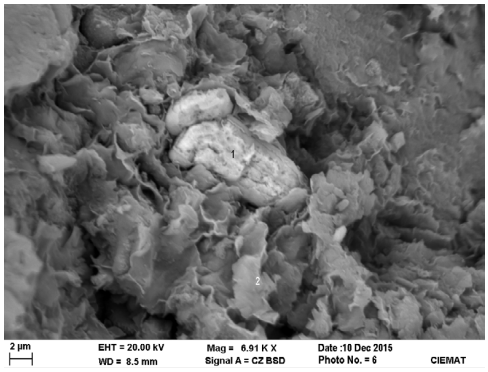

Fig. B-51: SEM photomicrographs in BB-47-8 sample: S, Fe (1), smectite (2)

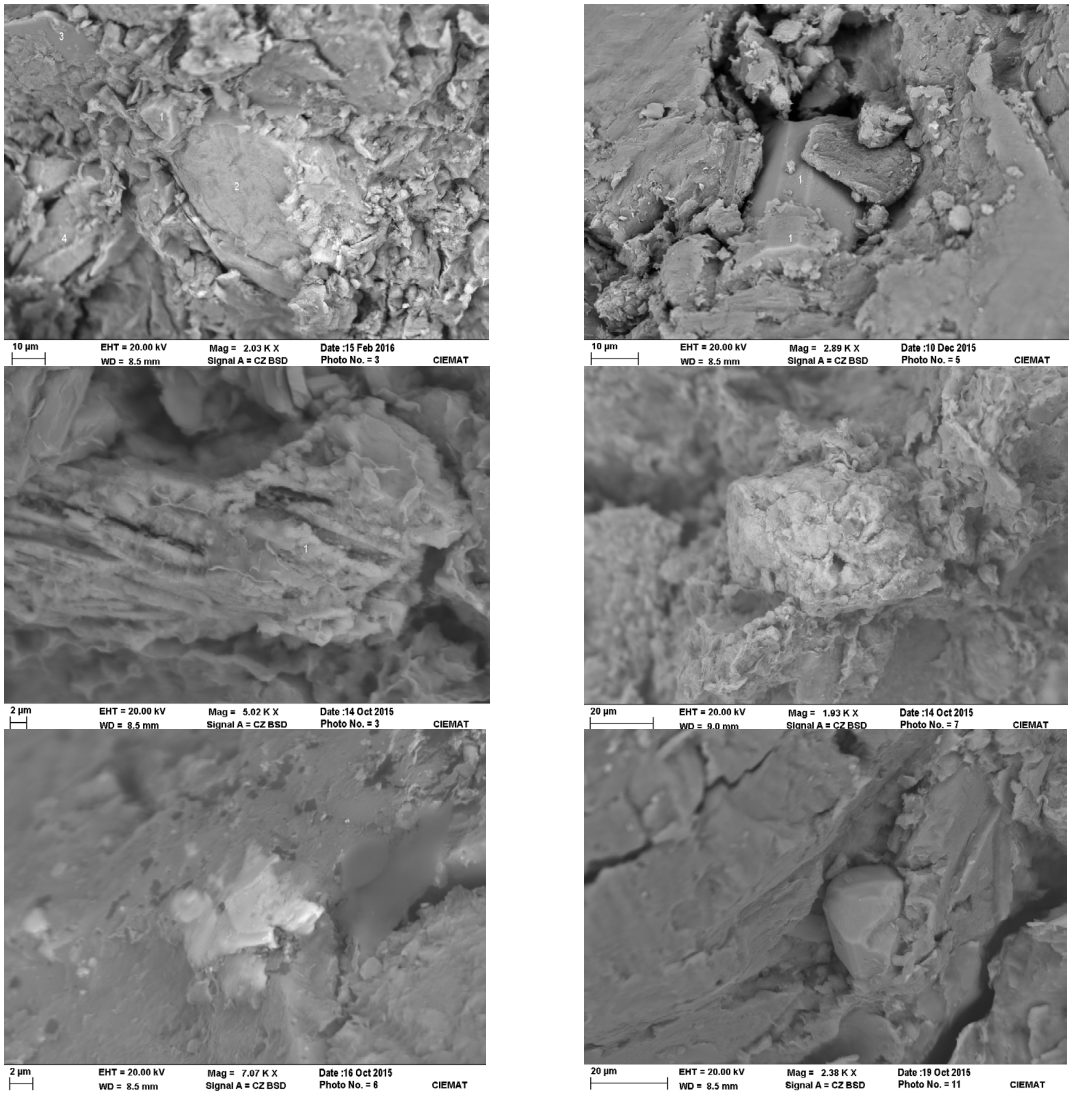

Fig. B-52: SEM photomicrographs: a) BB-47-5 sample: apatite (1), Fe-oxide (2), plagioclase (3), Ti-Fe-Mn (4), b) BB-47-8 sample: apatite (1), c) BB-47-2 sample: Fe-oxides, d) BB-47-2: Fe-oxides, e) BB-47-2 sample: Fe-Cr-oxides, f) BB-47-2: apatite

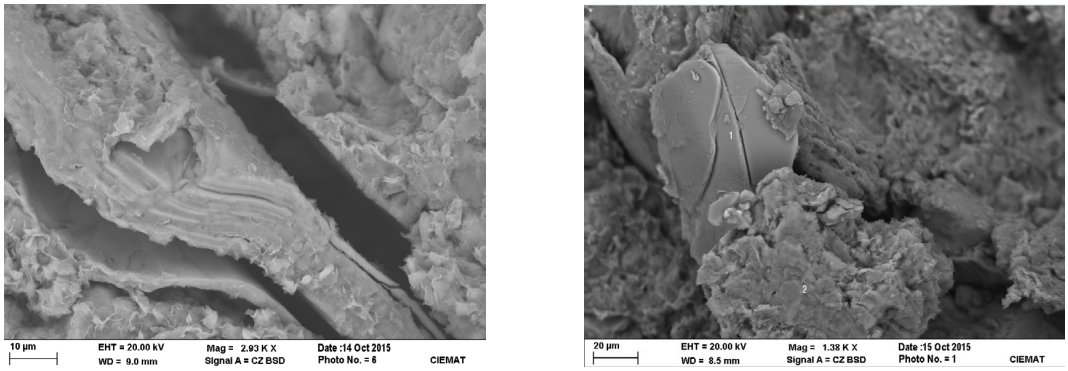

Fig. B-53: SEM photomicrographs: a) BB-47-2 sample: biotite, b) BB-47-2 sample: biotite? (1), smectite (2)

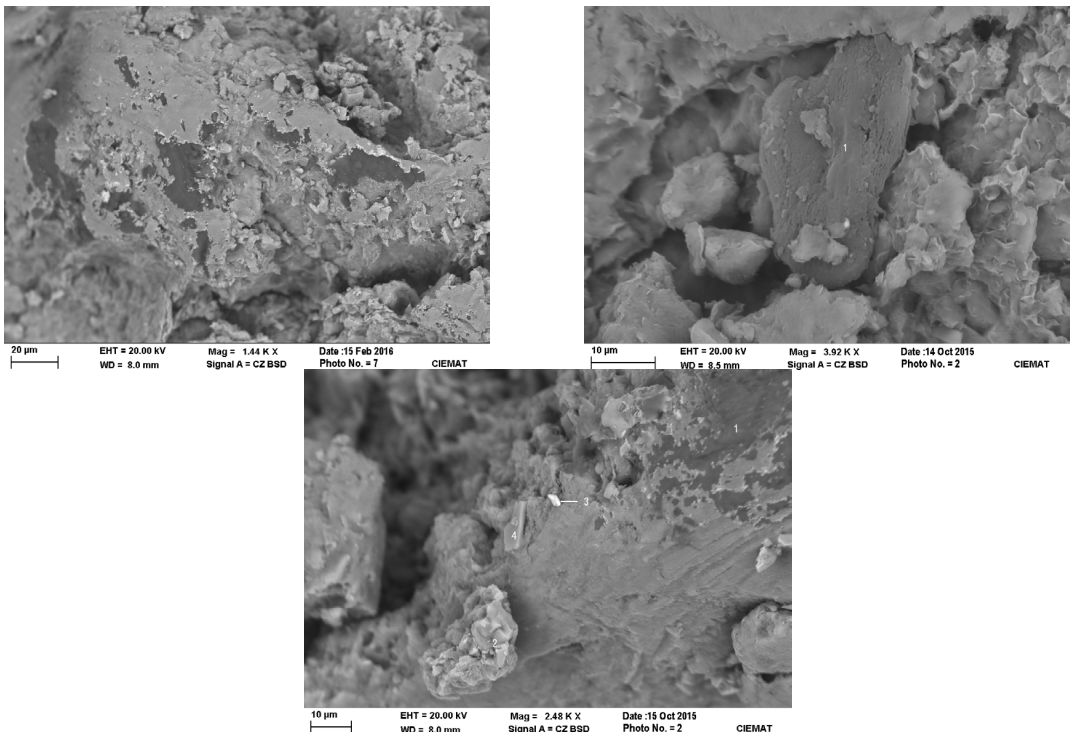

Fig. B-54: SEM photomicrographs: a) B-47-5 sample: organic matter (OM): C, b) BB-47-2: organic matter (OM), c) BB-47-2: organic matter (1) Ca-carbonate (2), Fe-carbonate (3), plagioclase (4)

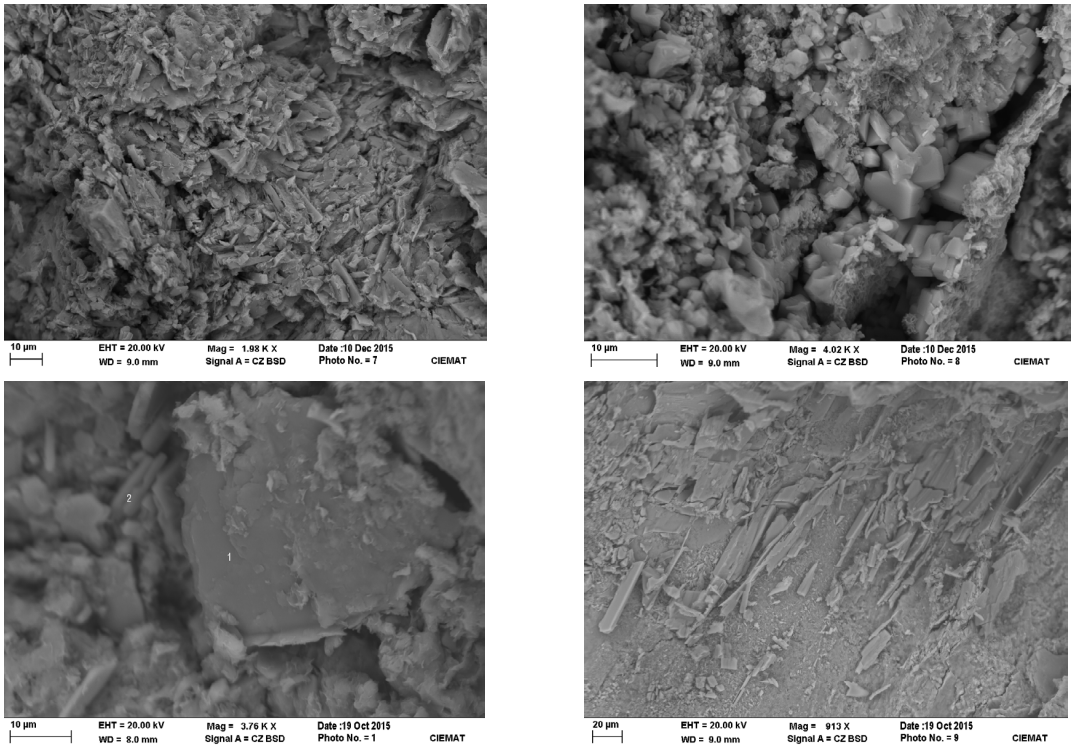

Fig. B-55: SEM photomicrographs: a) BB-47-8 sample: plagioclases, b) BB-47-8 sample: orthoclase-Na, c) BB-47-2 sample: plagioclases, d) BB-47-2 sample: K-feldspar

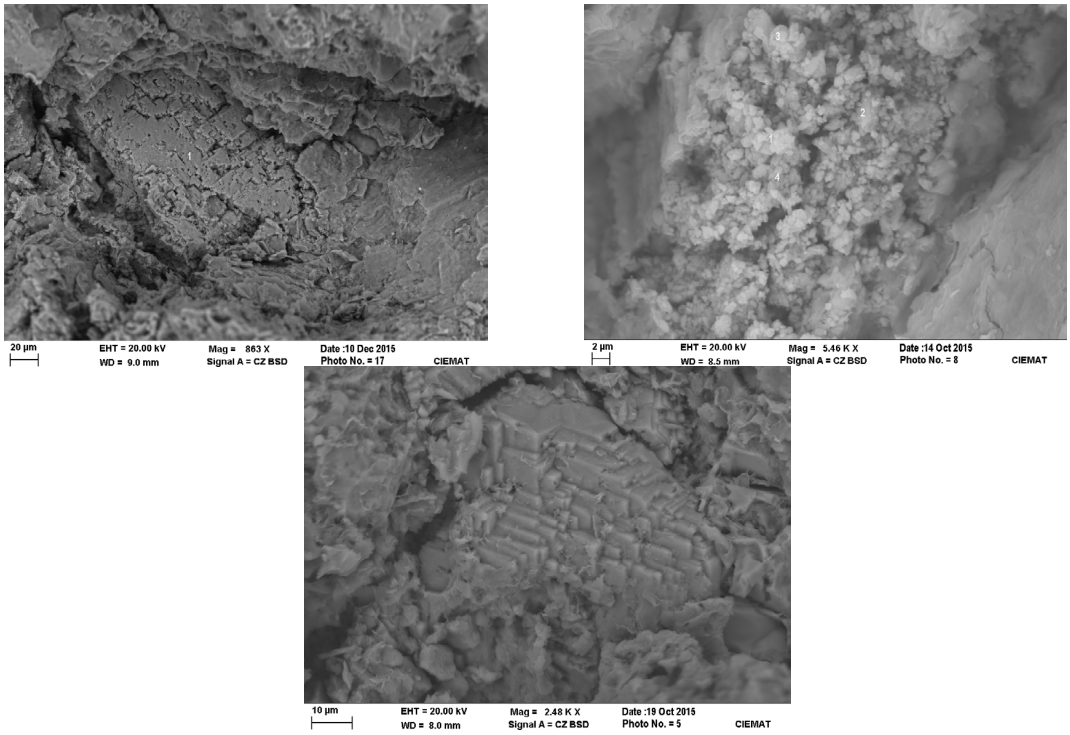

Fig. B-56: SEM photomicrographs: a) BB-47-8 sample: Ca-carbonates (1), b) BB-47-2: Ca-carbonates, c) BB-47-2: Ca-carbonates

Samples BB-47-6 and BB-47-9: internal bentonite ring (heater contact)

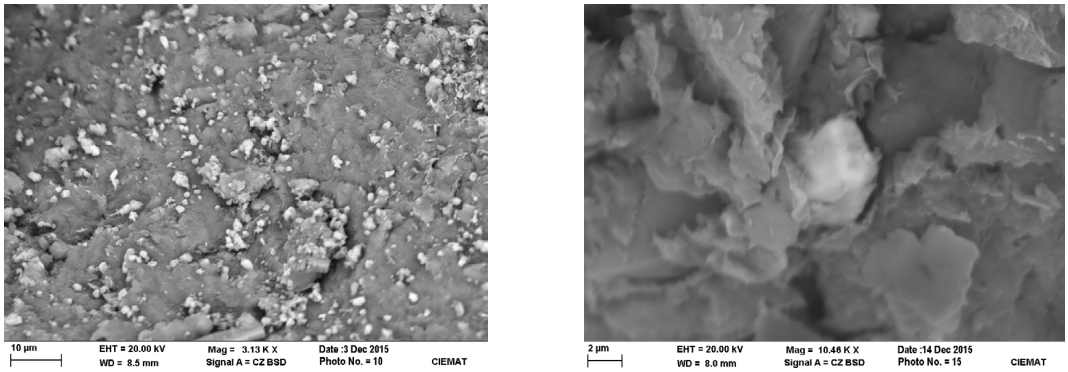

Fig. B-57: SEM photomicrographs: a) BB-47-6 sample: Ca-sulfates, b) BB-47-9 sample: Ba-sulfates

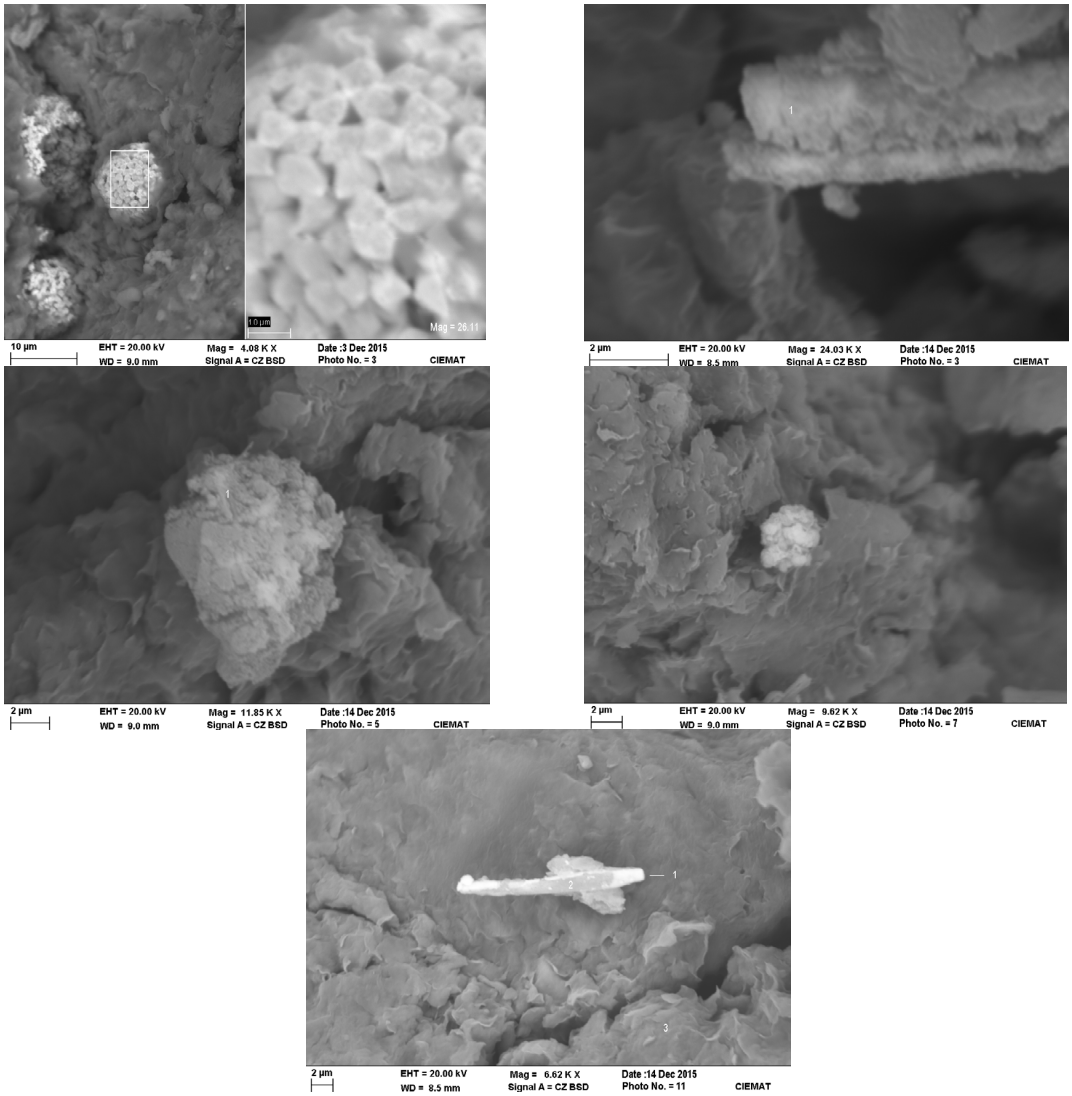

Fig. B-58: SEM photomicrographs: a) BB-47-6 sample: S, Fe, b) BB-47-9 sample: S, Fe, Hg, c) b) BB-47-9 sample: S, Ni, Fe, Hg, d) BB-47-9 sample: S, Hg, Zn, Cu, Fe, e) BB-47-9 sample: S, Hg, Fe, Cu, Mn (1), S, Mn, Cu, Hg (2), smectite (3)

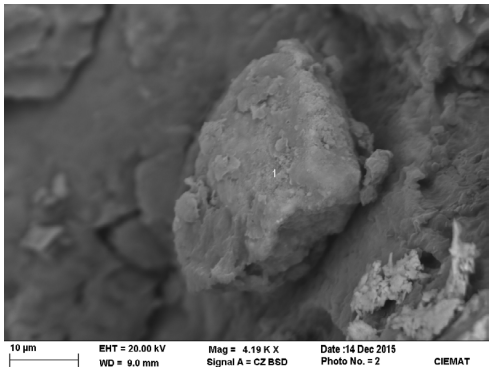

Fig. B-59: SEM photomicrographs: BB-47-9 sample: Fe-carbonate

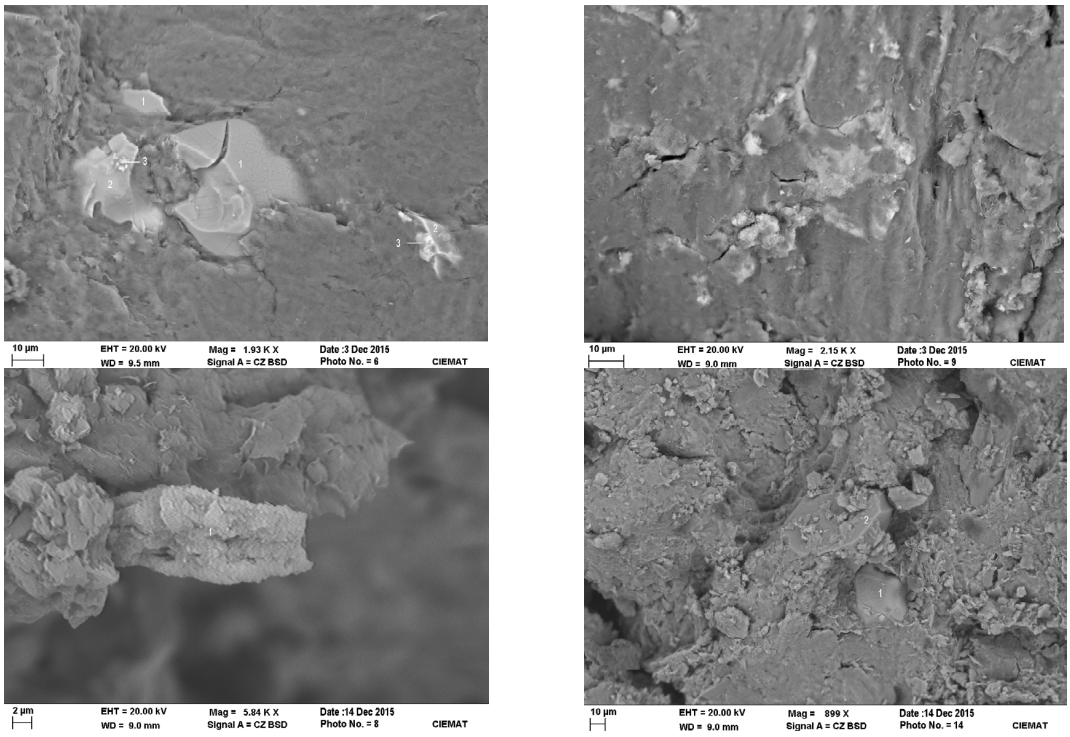

Fig. B-60: SEM photomicrographs: a) BB-47-6 sample: Ti-Fe(Mn) (1), Zircon (2), monazite (3), b) Fe-oxides, c) BB-47-9 sample: Fe-oxides, d) BB-47-9 sample: Ti, Fe (Mn): ilmenite (1), plagioclase (2)

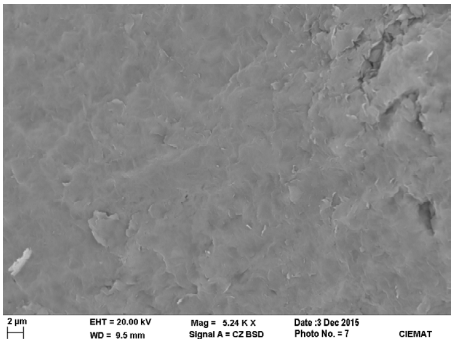

BB-47-6

$(Si_{4.00}Al_{0.00})^{IV}(Al_{1.32}Mg_{0.55}Fe^{3+}_{0.13})^{VI}(Ca_{0.09}Mg_{0.12}Na_{0.10}K_{0.03})_{0.34}O_{10}(OH)_2$
τ charge = -0.00; O. charge = -0.55
Total charge = -0.55 (τ % = 0; o % = 100); FW (g/mol) = 744.99
(No Mg at interlayer: Σ_{oct} = 2.12; Total charge: -0.31; τ % = 0; o % = 100)

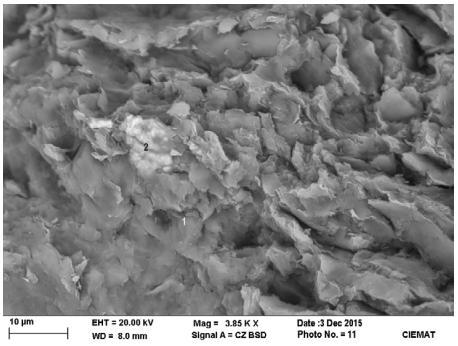

BB-47-6

$(Si_{4.00}Al_{0.00})^{IV}(Al_{1.34}Mg_{0.50}Fe^{3+}_{0.16})^{VI}(Ca_{0.07}Mg_{0.11}Na_{0.10}K_{0.05})_{0.33}O_{10}(OH)_2$
τ charge = -0.00; O. charge = -0.50
Total charge = -0.50 (τ % = 0; o % = 100); FW (g/mol) = 746.04
(No Mg at interlayer: Σ_{oct} = 2.11; Total charge: -0.29; τ % = 0; o % = 100)

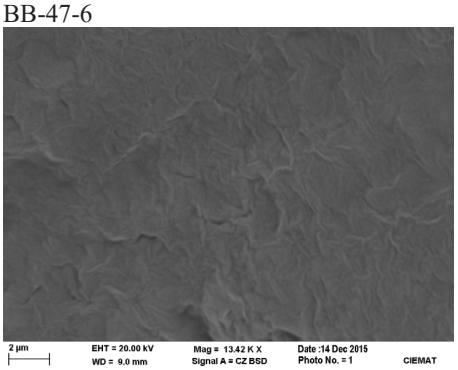

BB-47-9

$(Si_{3.95}Al_{0.05})^{IV}(Al_{1.38}Mg_{0.44}Fe^{3+}_{0.19})^{VI}(Ca_{0.09}Mg_{0.07}Na_{0.12}K_{0.05})_{0.33}O_{10}(OH)_2$
τ charge = -0.05; O. charge = -0.44
Total charge = -0.49 (τ % = 11; o % = 89); FW (g/mol) = 748.66
(No Mg at interlayer: Σ_{oct} = 2.07; Total charge: -0.35; τ % = 15; o % = 85)

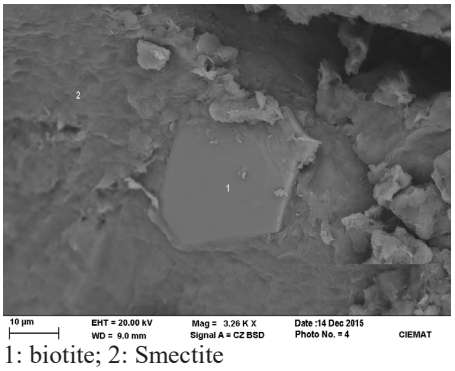

1: biotite; 2: Smectite
BB-47-9

2: Smectite
$(Si_{3.91}Al_{0.09})^{IV}(Al_{1.32}Mg_{0.41}Fe^{3+}_{0.27})^{VI}(Ca_{0.09}Mg_{0.08}Na_{0.09}K_{0.07})_{0.33}O_{10}(OH)_2$
τ charge = -0.09; O. charge = -0.41
Total charge = -0.50 (τ % = 17; o % = 83); FW (g/mol) = 754.73
(No Mg at interlayer: Σ_{oct} = 2.08; Total charge: -0.34; τ % = 25; o % = 75)

Fig. B-61: SEM photomicrographs of clay minerals in samples BB-47-6 and BB-47-9

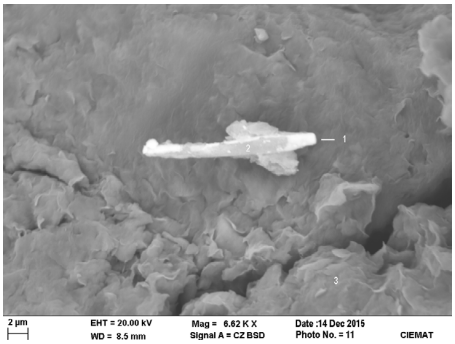

$(Si_{3.95}Al_{0.05})^{IV}(Al_{1.36}Mg_{0.48}Fe^{3+}_{0.16})^{VI}(Ca_{0.09}Mg_{0.09}Na_{0.11}K_{0.05})_{0.34}O_{10}(OH)_2$
τ charge = -0.05; O. charge = -0.48
Total charge = -0.53 (τ % = 9; o % = 91); FW (g/mol) = 747.63
(No Mg at interlayer: Σ_{oct} = 2.09; Total charge: -0.34; τ % = 15; o % = 85)

3. smectite

Fig. B-61: Cont.

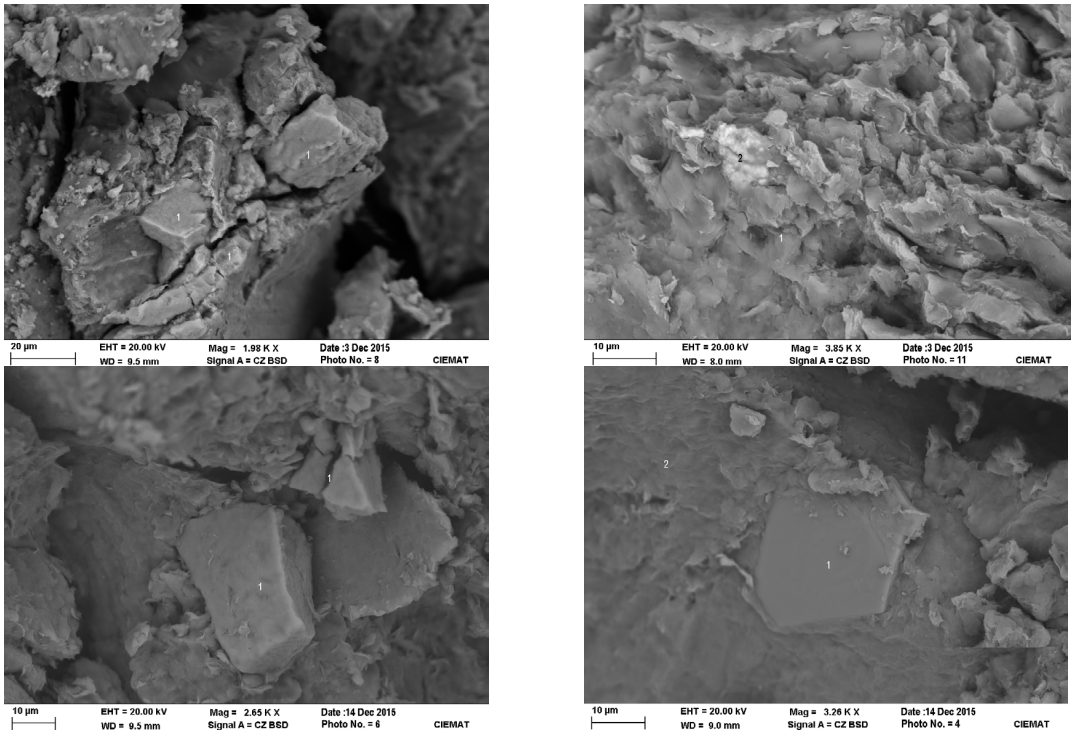

Fig. B-62: SEM photomicrographs: a) BB-47-6 sample: apatite (1); b) BB-47-6 sample: monazite (2), smectite (1); c) BB-47-9 sample: apatite (1), d) BB-47-9 sample: biotite

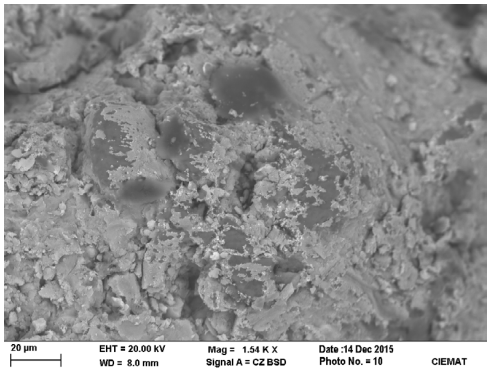

Fig. B-63: SEM photomicrographs: a) BB-47-9 sample: organic matter (OM)

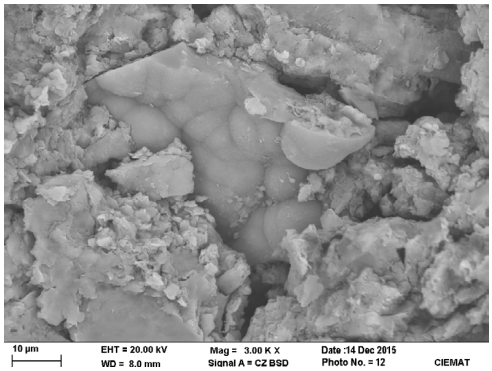

Fig. B-64: SEM photomicrographs: a) BB-47-9 sample: silica

Section 53

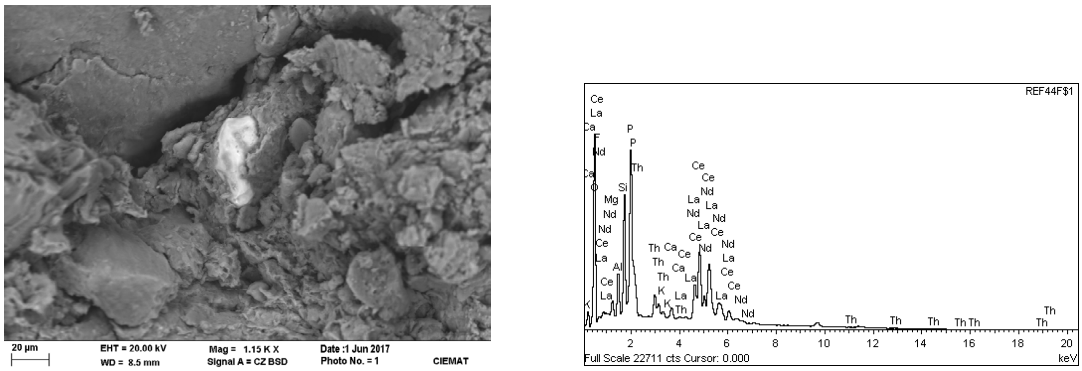

Fig. B-65: SEM photomicrographs in BB-53-3 sample: monazite

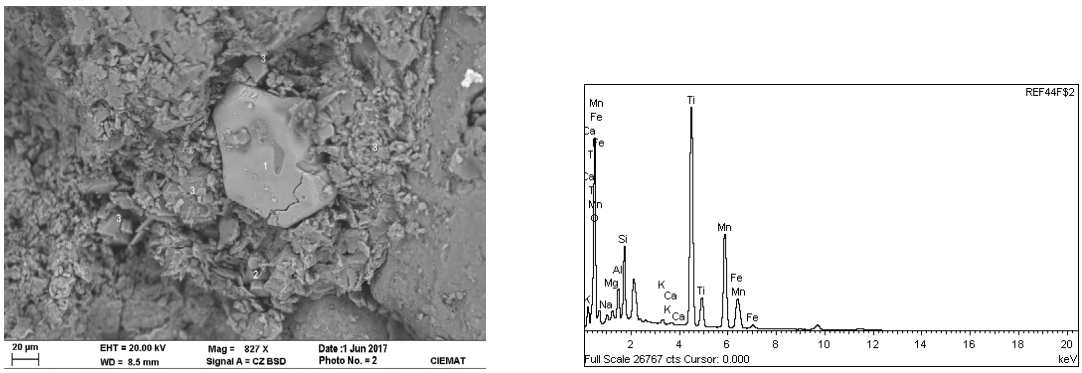

Fig. B-66: SEM photomicrographs in BB-53-3 sample: a) Ti, Mn, Fe (1), Apatite (2), K-Felspar (3), b) EDX of (1)

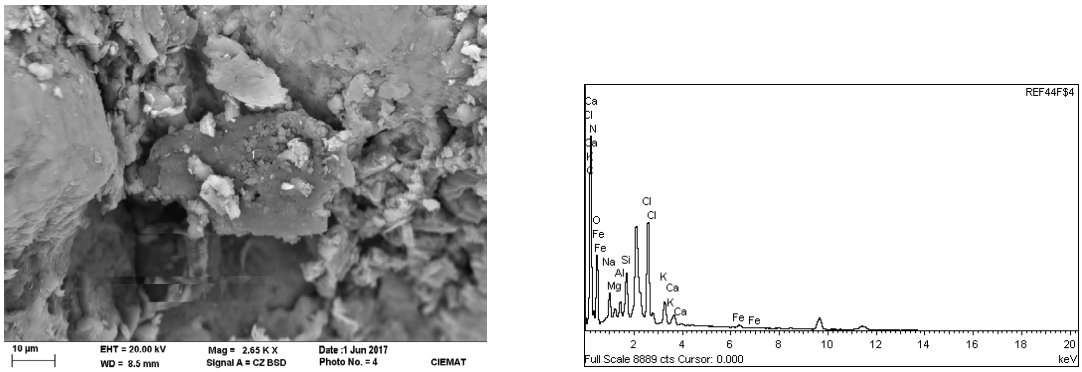

Fig. B-67: SEM photomicrographs in BB-53-3 sample: a) OM with Cl and N, b) EDX of (1)

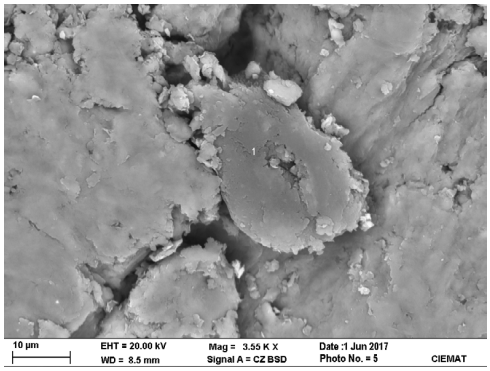

Fig. B-68: SEM photomicrographs in BB-53-3 sample: organic matter (1)

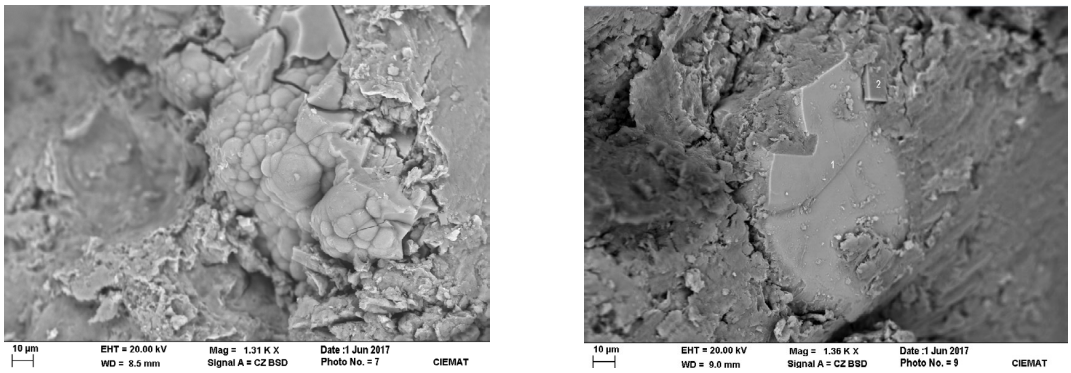

Fig. B-69: SEM photomicrographs in BB-53-3 sample: a) silica; b) ilmenite (1) and Ca-Na-plagioclases

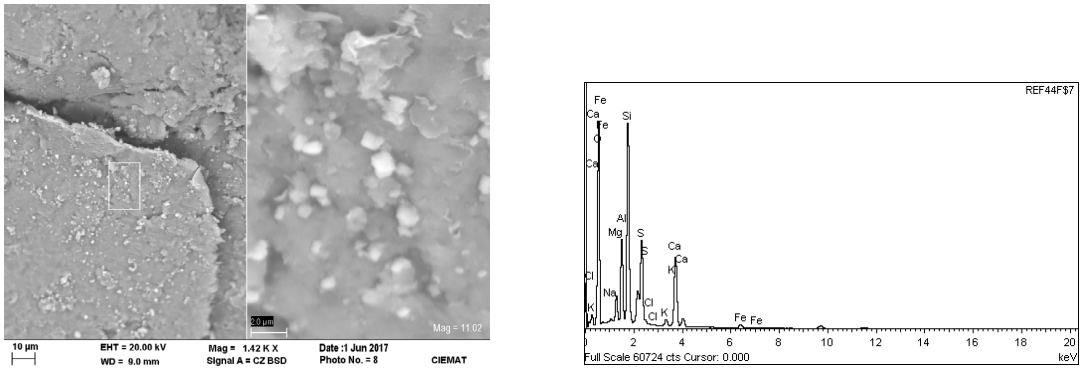

Fig. B-70: SEM photomicrographs in BB-53-3 sample: Ca-sulfates

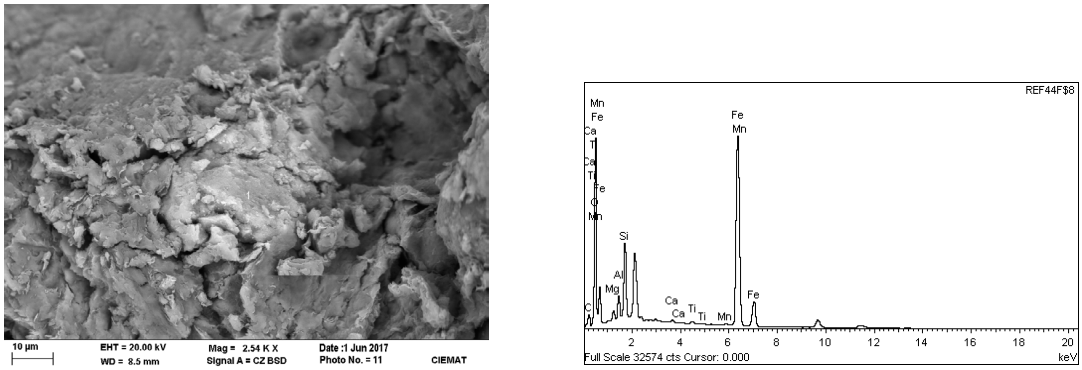

Fig. B-71: SEM photomicrographs in BB-53-3 sample: Fe-carbonates

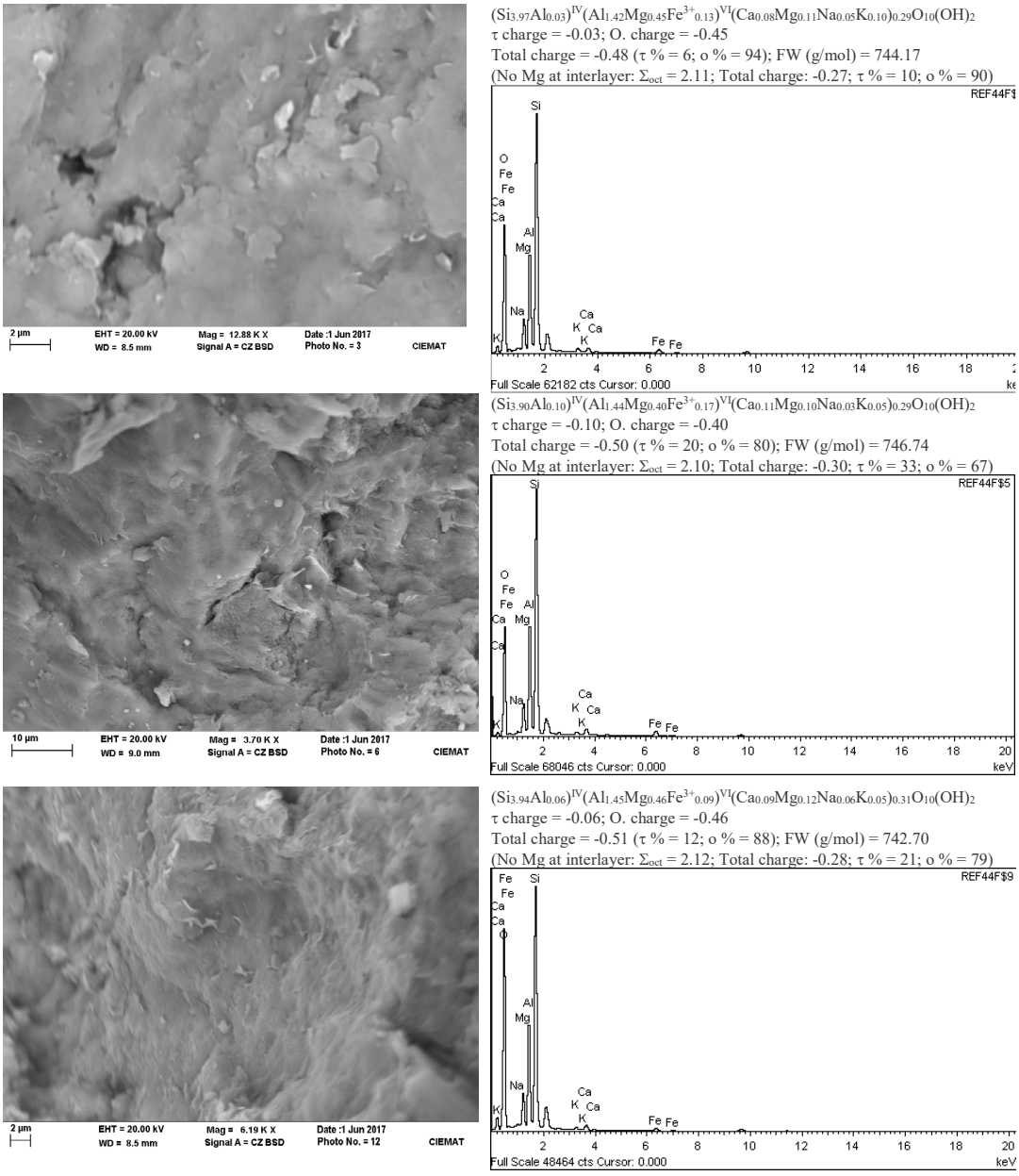

Fig. B-72: SEM photomicrographs in BB-53-3 sample: clay minerals

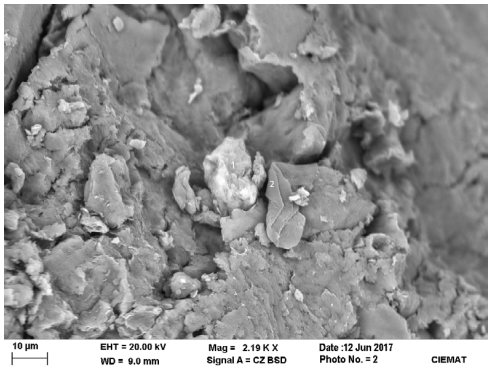

Fig. B-73: SEM photomicrographs in BB-53-9 sample: Fe(Ti)-oxides (1); Organic matter (2), b) EDX of (1)

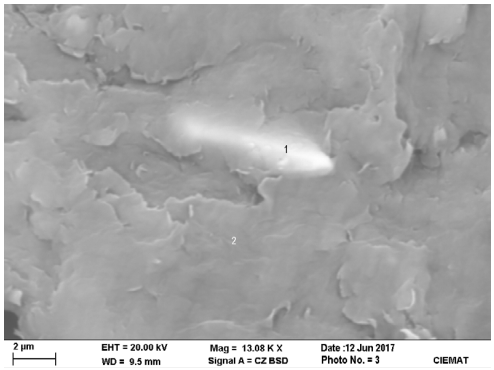

Fig. B-74: SEM photomicrographs in BB-53-9 sample: a) zircon (1); smectite (2), b) EDX of (1)

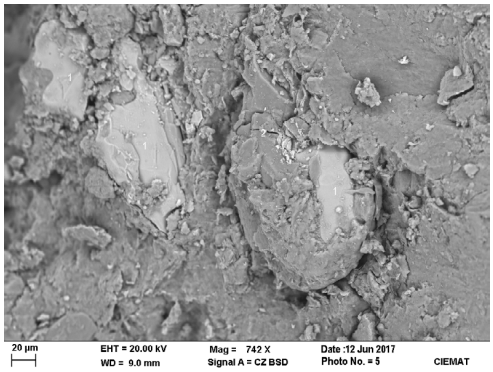

Fig. B-75: SEM photomicrographs in BB-53-9 sample: a) ilmenite (1); silica (2); b) EDX of (1)

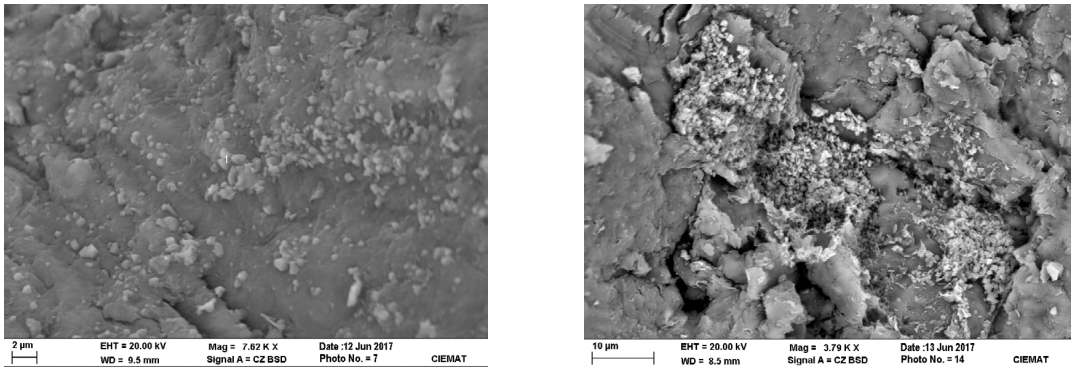

Fig. B-76: SEM photomicrographs in BB-53-9 sample: Ca-sulfates

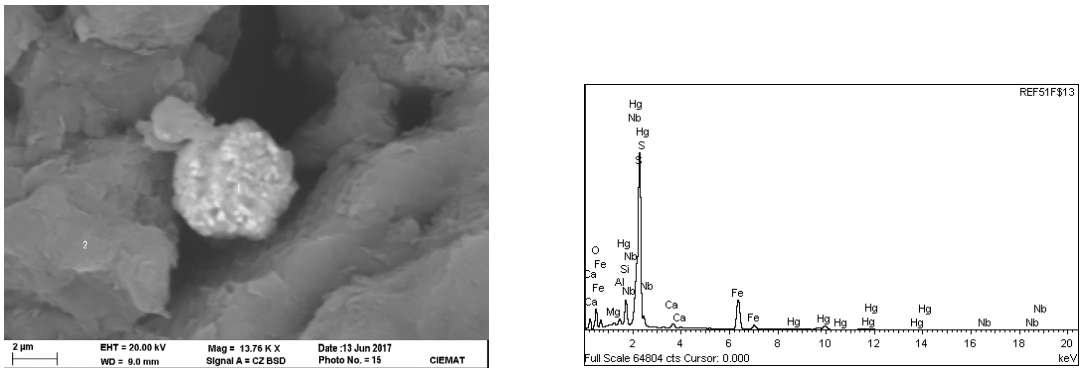

Fig. B-77: SEM photomicrographs in BB-53-9 sample: a) Fe-Hg-sulphides (1), smectite (2), b) EDX of (1)

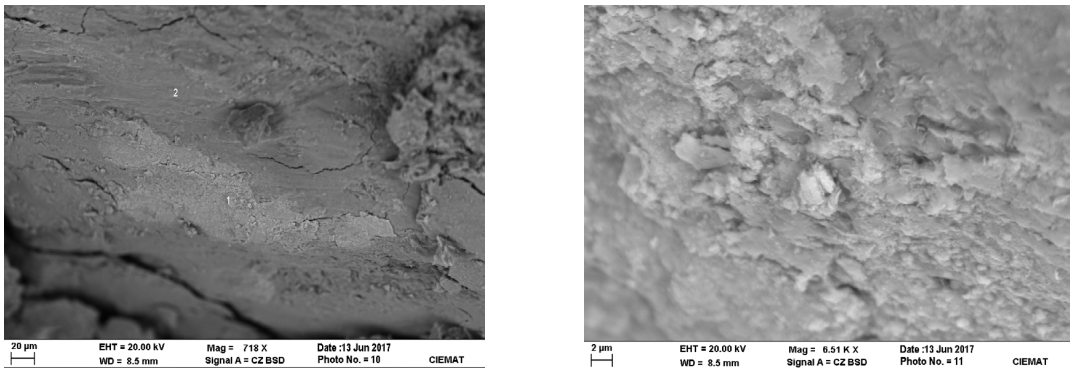

Fig. B-78: SEM photomicrographs in BB-53-9 sample: a) Fe-oxides (1), illite (2), b) enlargements of (1) Fe-oxides in a)

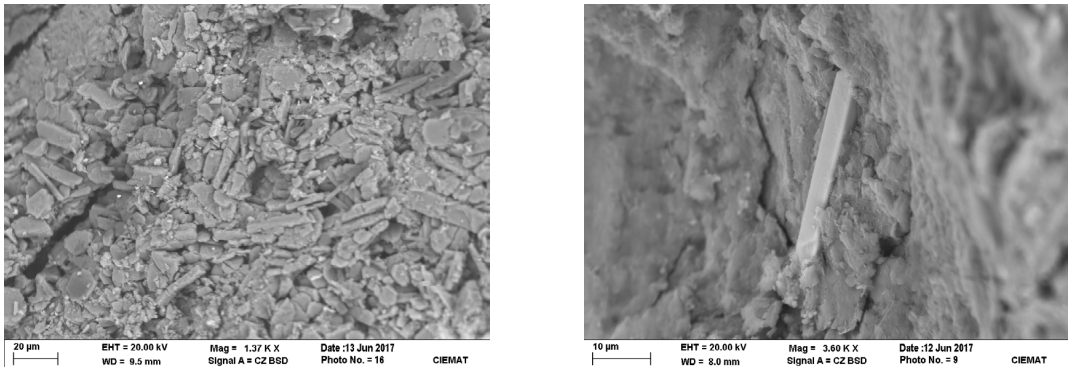

Fig. B-79: SEM photomicrographs in BB-53-9 sample: a) Na,Ca-plagioclases, b) Zircon

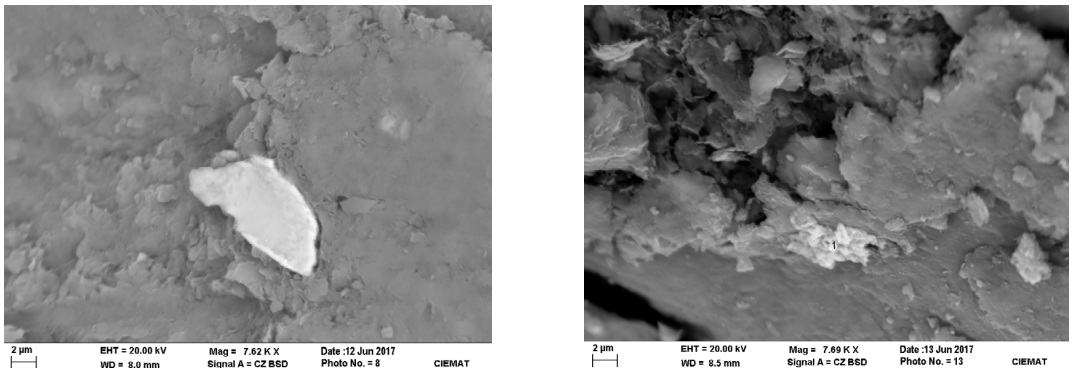

Fig. B-80: SEM photomicrographs in BB-53-9 sample: a) Zn-carbonate, b) barite (1)

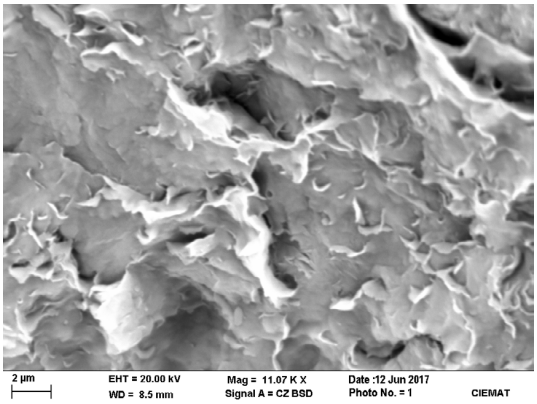

$(Si_{3.99}Al_{0.01})^{IV}(Al_{1.36}Mg_{0.49}Fe^{3+}_{0.15})^{VI}(Ca_{0.09}Mg_{0.10}Na_{0.07}K_{0.05})_{0.31}O_{10}(OH)_2$
τ charge = -0.01; O. charge = -0.49
Total charge = -0.50 (τ % = 1; o % = 99); FW (g/mol) = 746.06
(No Mg at interlayer: Σ_{oct} = 2.10; Total charge: -0.30; τ % = 2; o % = 98)

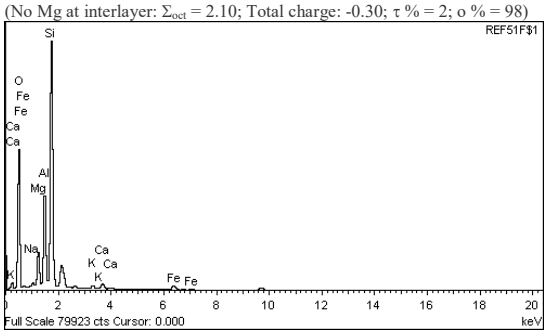

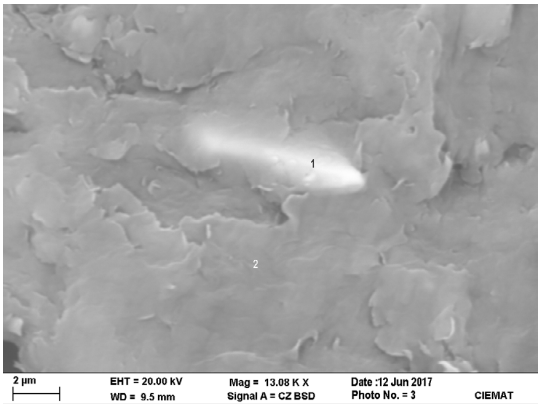

(2) $(Si_{4.00}Al_{0.00})^{IV}(Al_{1.41}Mg_{0.44}Fe^{3+}_{0.15})^{VI}(Ca_{0.09}Mg_{0.09}Na_{0.05}K_{0.05})_{0.27}O_{10}(OH)_2$
τ charge = -0.00; O. charge = -0.44
Total charge = -0.44 (τ % = 0; o % = 100); FW (g/mol) = 743.96
(No Mg at interlayer: Σ_{oct} = 2.09; Total charge: -0.27; τ % = 0; o % = 100)

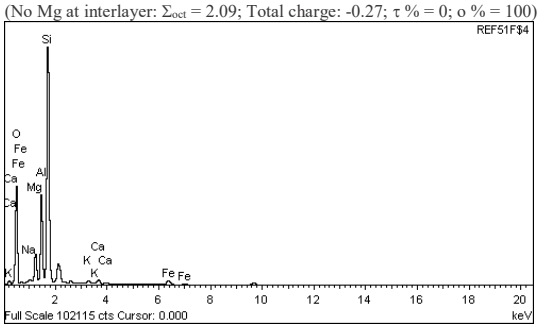

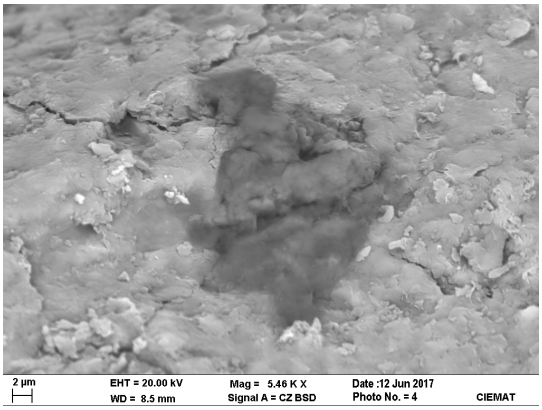

Illite
$(Si_{3.85}Al_{0.15})^{IV}(Al_{1.36}Mg_{0.34}Fe^{3+}_{0.23\ \ 0.07})^{VI}(Ca_{0.06}Na_{0.04}K_{0.54})_{0.64}O_{10}(OH)_2$
τ charge = -0.15; O. charge = -0.55
Total charge = -0.69 (τ % = 21; o % = 79); FW (g/mol) = 776.63
Illite
$(Si_{3.98}Al_{0.02})^{IV}(Al_{1.31}Mg_{0.20}Fe^{3+}_{0.23\ \ 0.26})^{VI}(Na_{0.04}K_{0.95})_{0.99}O_{10}(OH)_2$
τ charge = -0.02; O. charge = -0.97; FW (g/mol) = 795.66
Total charge = -0.99 (τ % = 2; o % = 98)

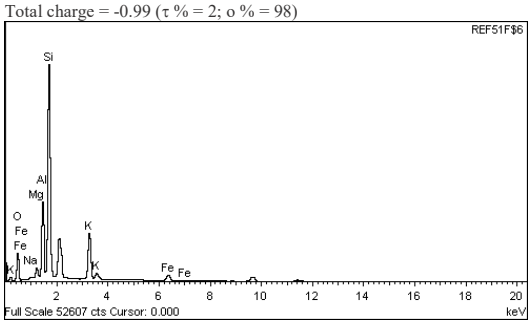

Fig. B-81: SEM photomicrographs in BB-53-9 sample: clay minerals

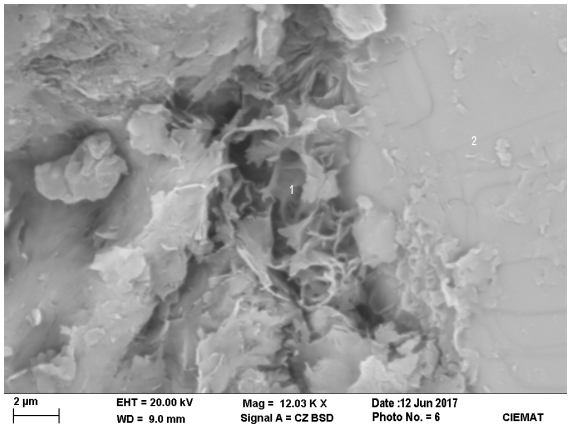

1: Fe-rich smectite; 2: silica

Fe-rich smectite (1):

$(Si_{3.99}Al_{0.01})^{IV}(Al_{0.60}Mg_{0.49}Fe^{3+}_{0.76}Ti^{4+}_{0.14\ \ 0.02})^{VI}(Ca_{0.05}Na_{0.04}K_{0.27})_{0.37}O_{10}(OH)_2$

τ charge = -0.01 O. charge = -0.42

Total charge = -0.42 (τ % = 3 o % = 97); FW (g/mol) = 793.98

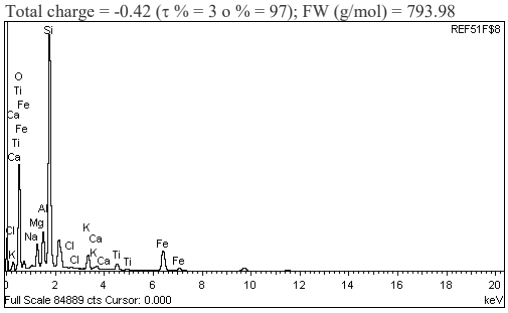

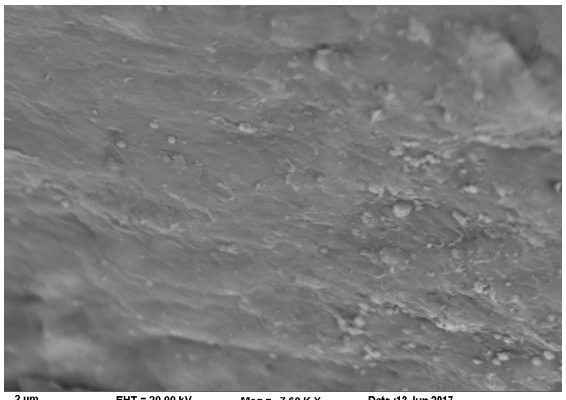

Illite

$(Si_{3.89}Al_{0.11})^{IV}(Al_{1.32}Mg_{0.31}Fe^{3+}_{0.28\ \ 0.09})^{VI}(Na_{0.04}K_{0.65})_{0.69}O_{10}(OH)_2$

τ charge = -0.11; O. charge = -0.58; FW (g/mol) = 782.73

Total charge = -0.69 (τ % = 15; o % = 85)

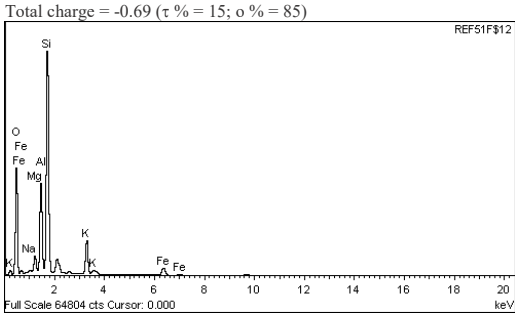

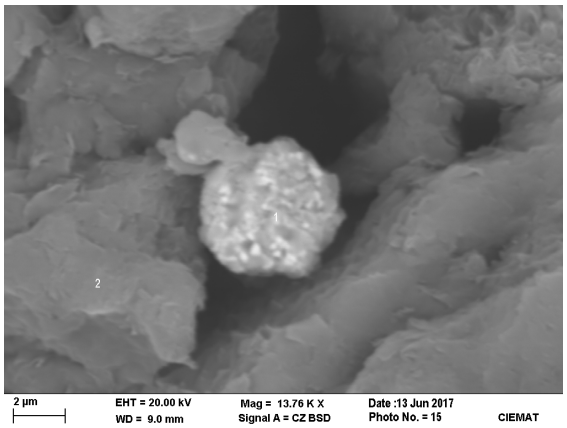

Fe-Sulfides (1), smectite (2)

(2)

$(Si_{3.95}Al_{0.05})^{IV}(Al_{1.37}Mg_{0.39}Fe^{3+}_{0.24})^{VI}(Ca_{0.09}Mg_{0.09}Na_{0.05}K_{0.04})_{0.27}O_{10}(OH)_2$

τ charge = -0.05 O. charge = -0.39

Total charge = -0.45 (τ % = 11 o % = 89); FW (g/mol) = 749.04

(No Mg at interlayer: Σ_{oct} = 2.09; Total charge: -0.26; τ % = 19; o % = 81)

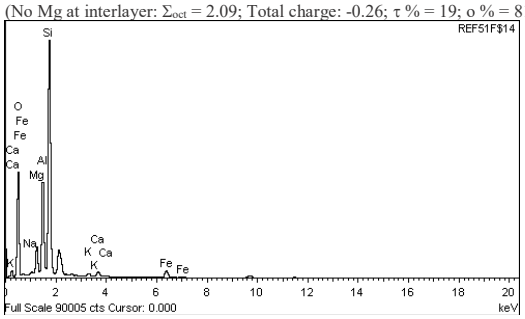

Fig. B-81: Cont.

Section 59

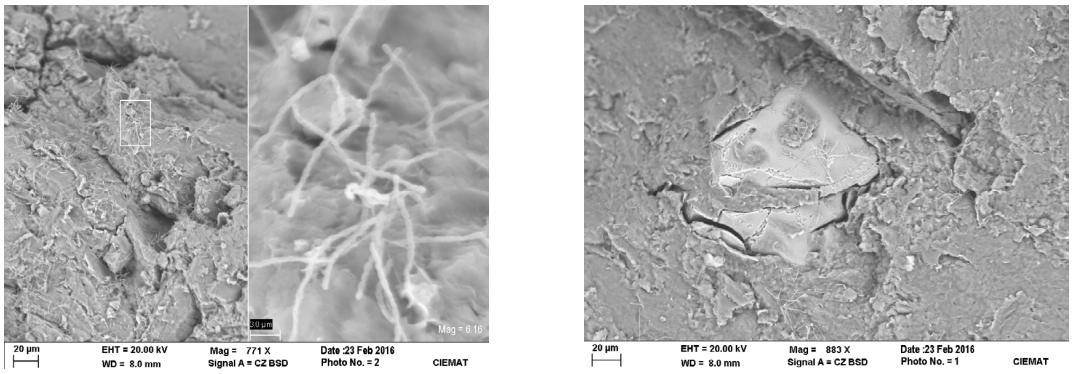

Fig. B-82: SEM photomicrographs in BB-59-1 sample: microorganisms

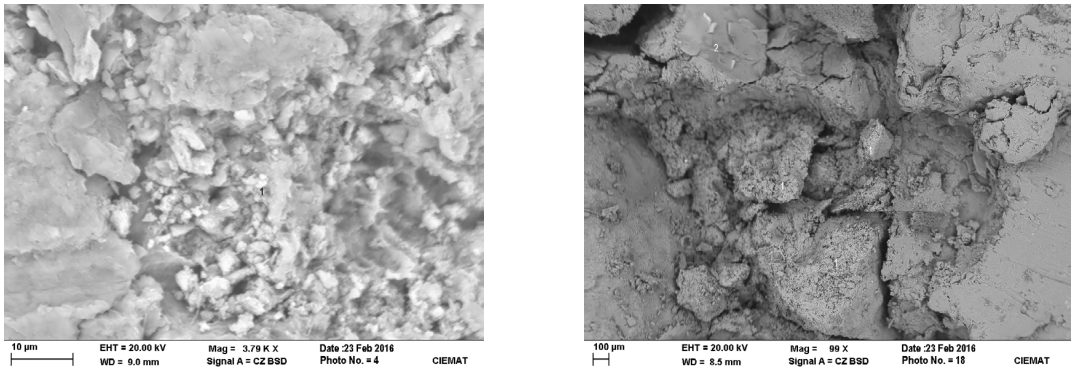

Fig. B-83: SEM photomicrographs in BB-59-1 sample: Ca-carbonates (1)

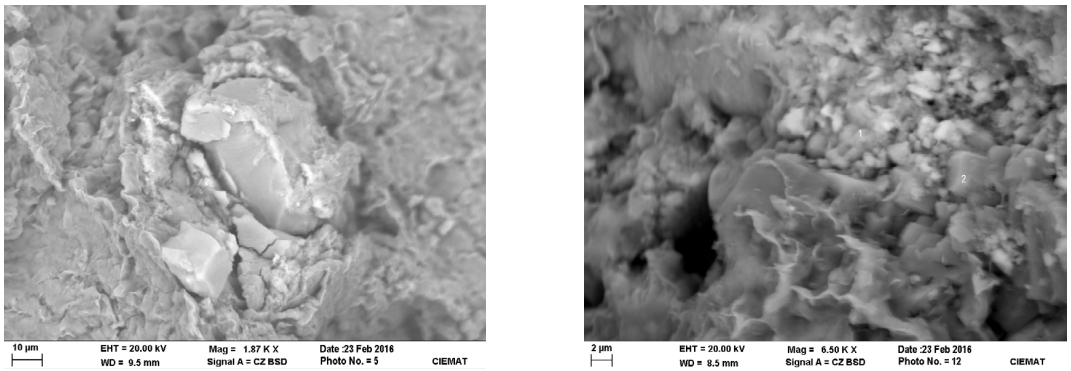

Fig. B-84: SEM photomicrographs: iron oxides in BB-59-1 sample

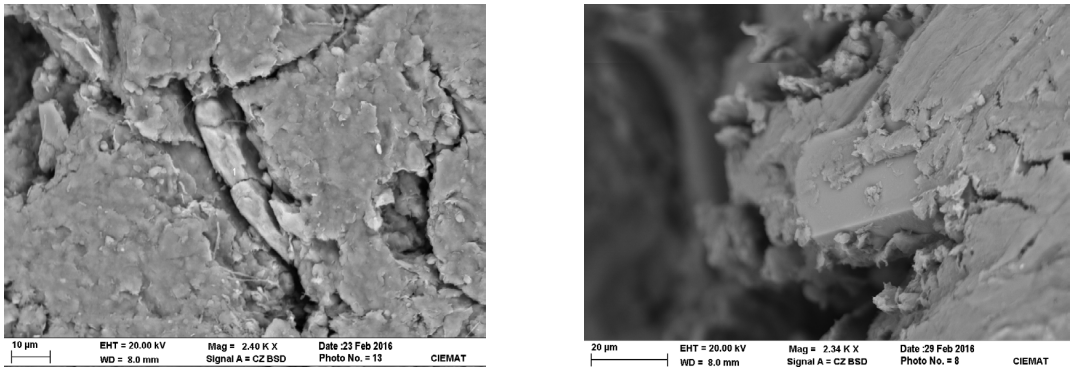

Fig. B-85: SEM photomicrographs: apatite in BB-59-1 sample

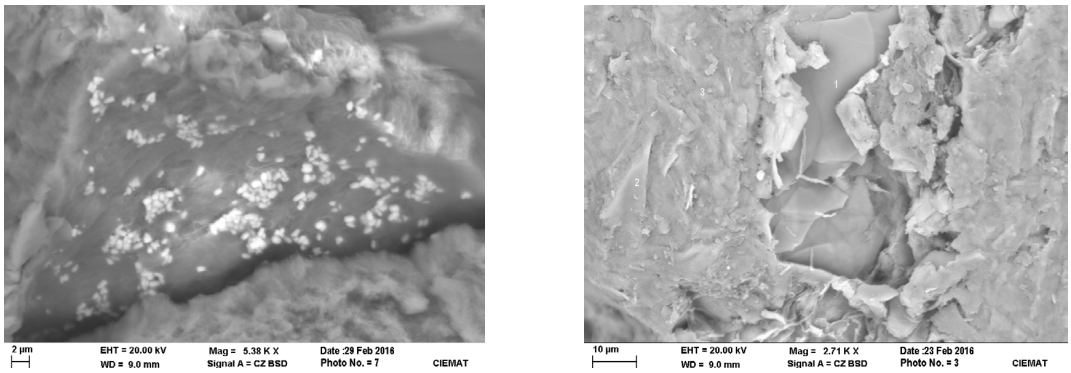

Fig. B-86: SEM photomicrographs in sample BB-59-1: a) monazite, and b) biotite (1)

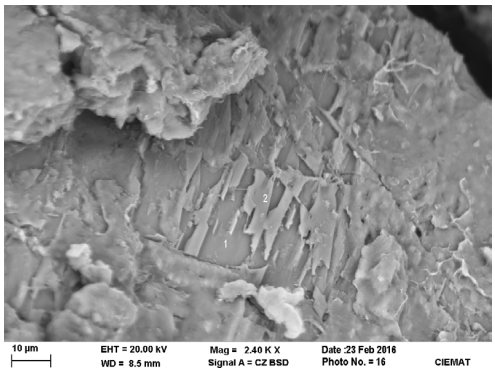

Fig. B-87: SEM photomicrographs in BB-59-1 sample: K-feldspars (1), plagioclase (2)

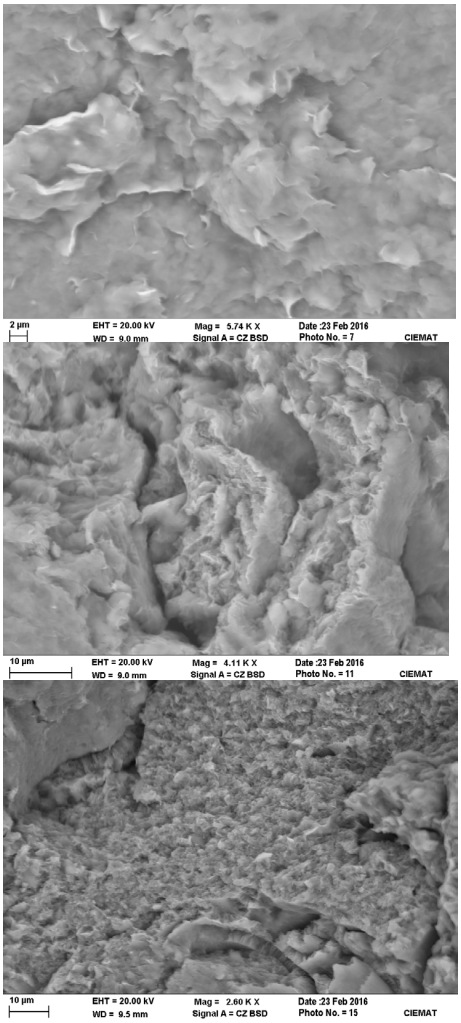

$(Si_{3.98}Al_{0.02})^{IV}(Al_{1.43}Mg_{0.47}Fe^{3+}_{0.09}Ti^{4+}_{0.01})^{VI}(Ca_{0.08}Mg_{0.09}Na_{0.07}K_{0.06})_{0.30}O_{10}(OH)_2$
τ charge = -0.02 O. charge = -0.45
Total charge = -0.48 (τ % = 4 o % = 96); FW (g/mol) = 742.69
(No Mg at interlayer: Σ_{oct} = 2.09; Total charge: -0.29 τ % = 7; o % = 93)

$(Si_{4.00}Al_{0.00})^{IV}(Al_{1.39}Mg_{0.55}Fe^{3+}_{0.06})^{VI}(Ca_{0.09}Mg_{0.13}Na_{0.09}K_{0.02})_{0.33}O_{10}(OH)_2$
τ charge = -0.00 O. charge = -0.55
Total charge = -0.55 (τ % = 0 o % = 100); FW (g/mol) = 740.91
(No Mg at interlayer: Σ_{oct} = 2.13; Total charge: -0.28; τ % = 0; o % = 100)

$(Si_{3.97}Al_{0.03})^{IV}(Al_{1.35}Mg_{0.50}Fe^{3+}_{0.12}Ti_{0.03})^{VI}(Ca_{0.08}Mg_{0.09}Na_{0.09}K_{0.07})_{0.33}O_{10}(OH)_2$
τ charge = -0.03 O. charge = -0.47
Total charge = -0.50 (τ % = 6 o % = 94); FW (g/mol) = 746.56
(No Mg at interlayer: Σ_{oct} = 2.09; Total charge: -0.32; τ % = 9; o % = 91)

Fig. B-88: SEM photomicrographs: smectite clay minerals in sample BB-59-1

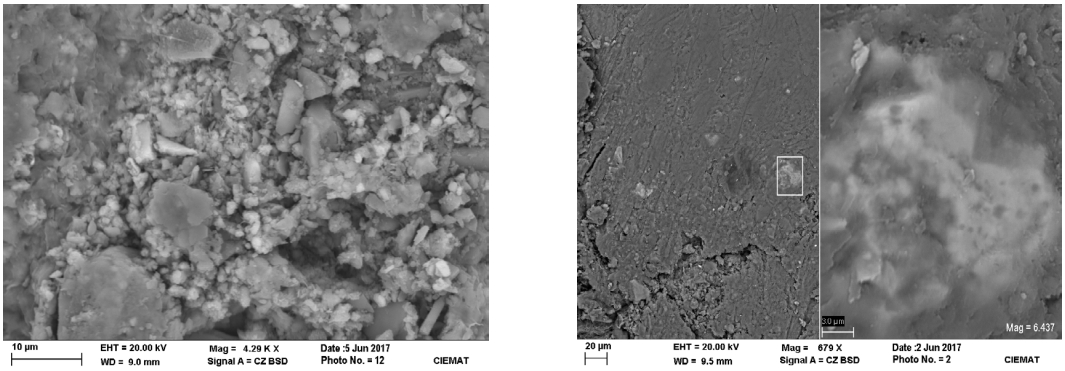

Fig. B-89: SEM photomicrographs in sample BB-59-6: a) Fe-oxides, b) Fe-oxides, apatite and C

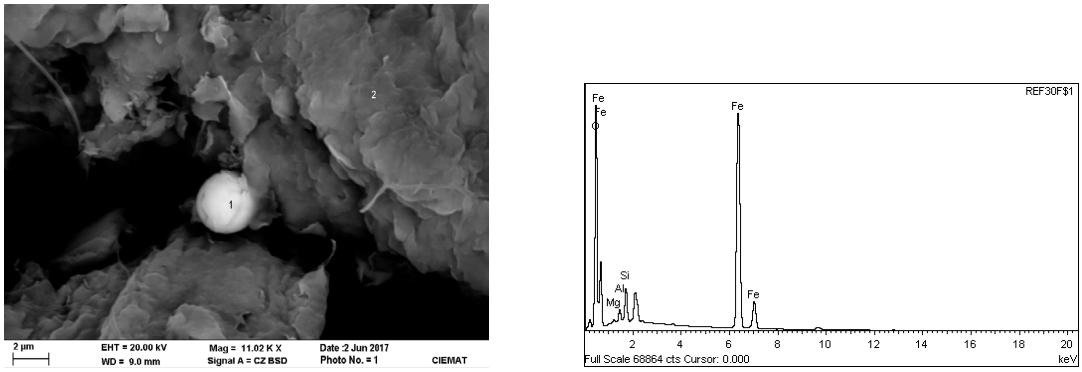

Fig. B-90: SEM photomicrographs in sample BB-59-6: a) Fe-oxide (1), smectite (2), b) EDX of (1)

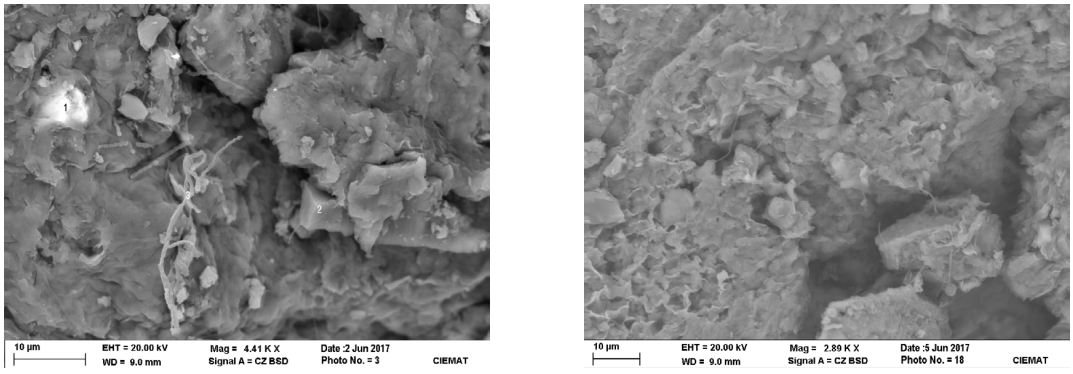

Fig. B-91: SEM photomicrographs in sample BB-59-6: a) Barite (1), albite (2), microorganisms (3), b) microorganisms on smectite

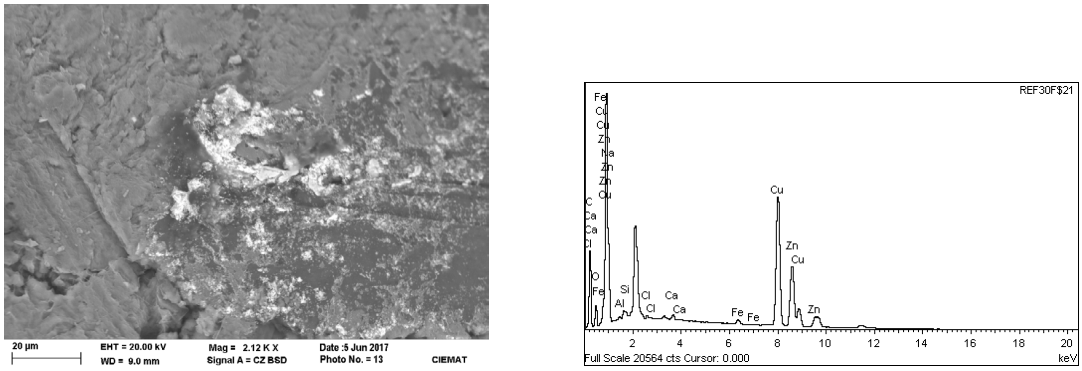

Fig. B-92: SEM photomicrographs in sample BB-59-6: a) Cu, Zn-carbonates, b) EDX of a)

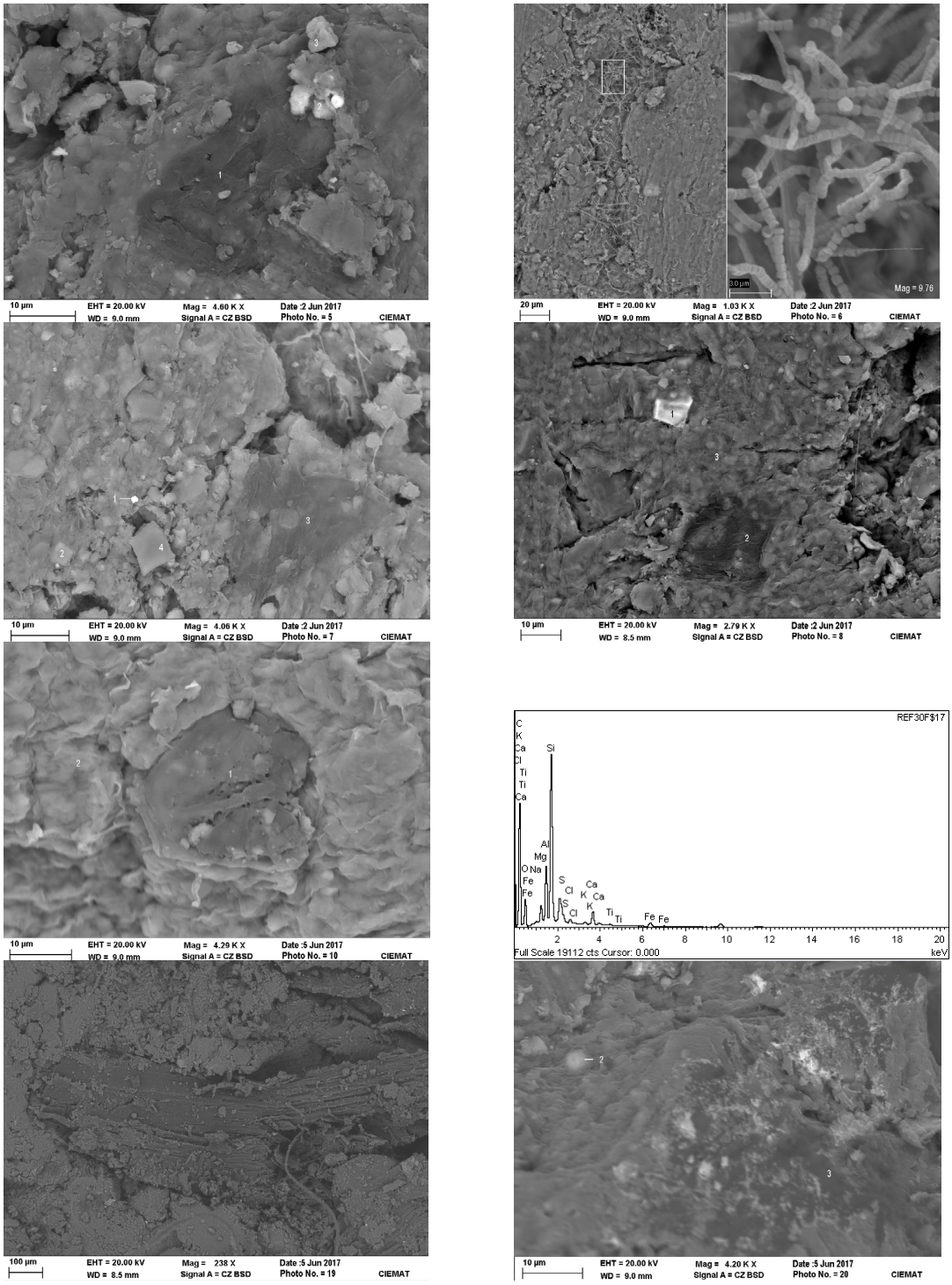

Fig. B-93: SEM photomicrographs in sample BB-59-6: a) OM (1), W, Ca-oxide (2), Ca-carbonate (3), b) microorganisms, c) S, Pb (1), OM (3), silica (4), d) Zircon (1), OM (2), smectite (3), e) Organic matter (1), smectite (2), f) EDX of (1) in e), g) carbon, h) carbon and Fe

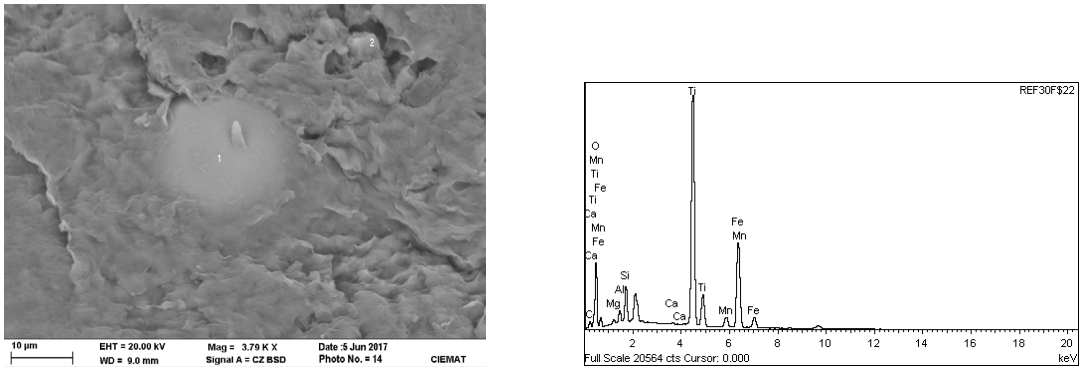

Fig. B-94: SEM photomicrographs in sample BB-59-6: a) ilmenite (1) K-feldspar (2), b) EDX of (1)

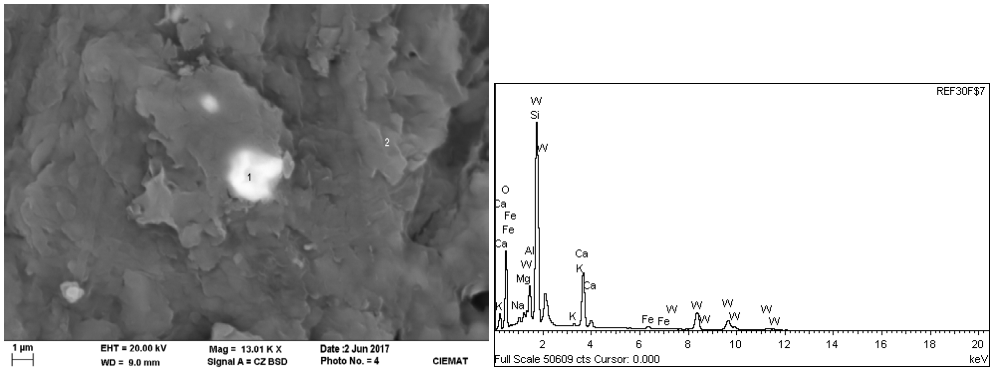

Fig. B-95: SEM photomicrographs in sample BB-59-6: a) W, Ca-oxide (1), smectite (2), b) EDX of (1)

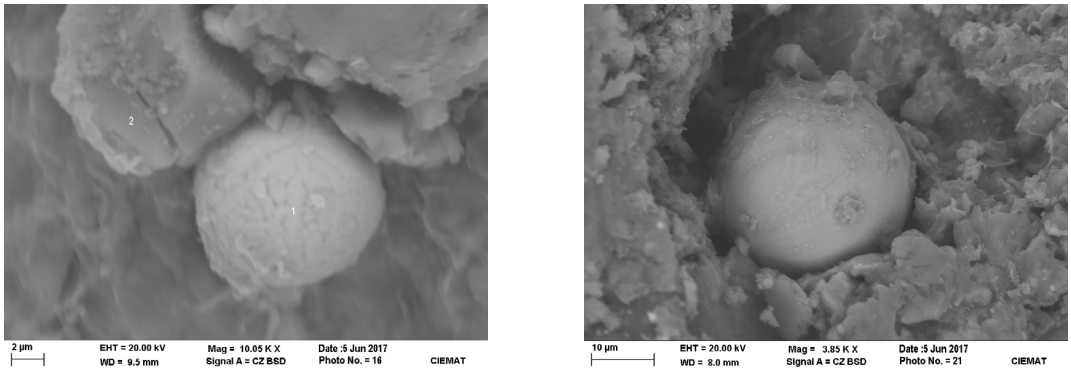

Fig. B-96: SEM photomicrographs from sample BB-59-6: Fe-carbonates

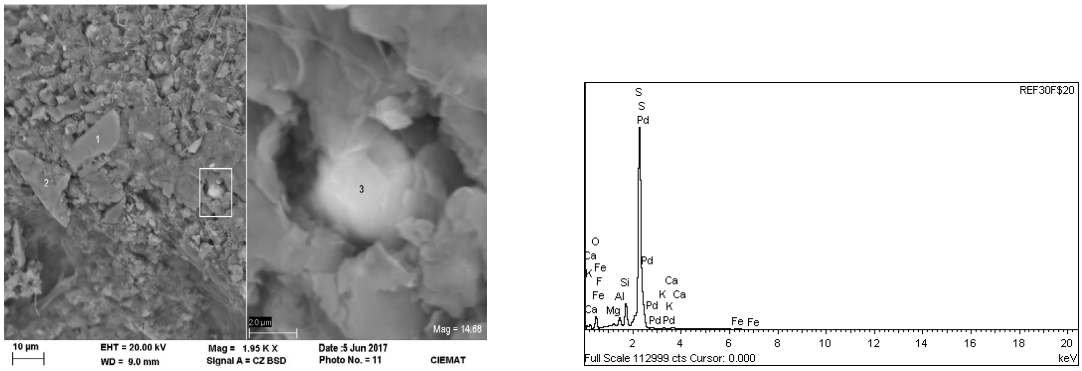

Fig. B-97: SEM photomicrographs in sample BB-59-6: a) biotite (1), K-Fd (2), S (3), b) EDX of (3)

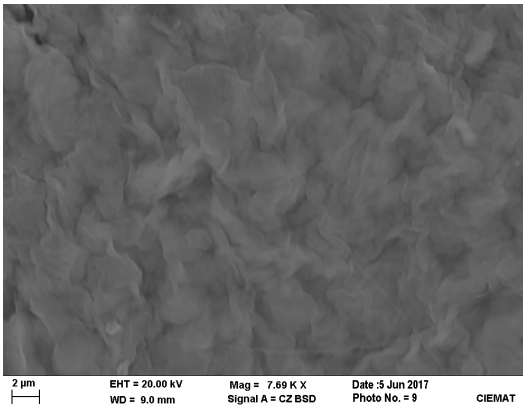

$(Si_{4.00}Al_{0.00})^{IV}(Al_{1.37}Mg_{0.46}Fe^{3+}_{0.17})^{VI}(Ca_{0.10}Mg_{0.05}Na_{0.10}K_{0.06})_{0.31}O_{10}(OH)_2$
τ charge = -0.00 O. charge = -0.46
Total charge = -0.46 (τ % = 0 o % = 100); FW (g/mol) = 747.83
(No Mg at interlayer: Σ_{oct} = 2.05; Total charge: -0.36; τ % = 0; o % = 100)

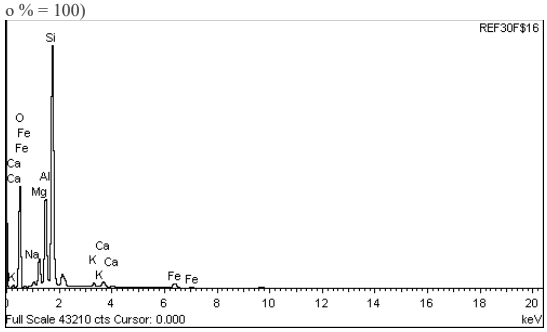

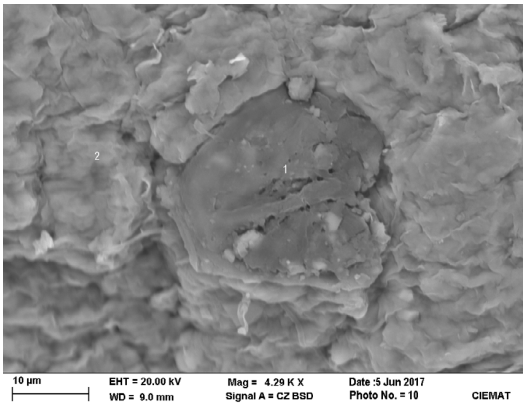

(2) $(Si_{3.94}Al_{0.06})^{IV}(Al_{1.31}Mg_{0.49}Fe^{3+}_{0.18\ \ 0.01})^{VI}(Ca_{0.24}Na_{0.06}K_{0.05})_{0.35}O_{10}(OH)_2$
τ charge = -0.06 O. charge = -0.53
Total charge = -0.59 (τ % = 11o % = 89); FW (g/mol) = 753.45

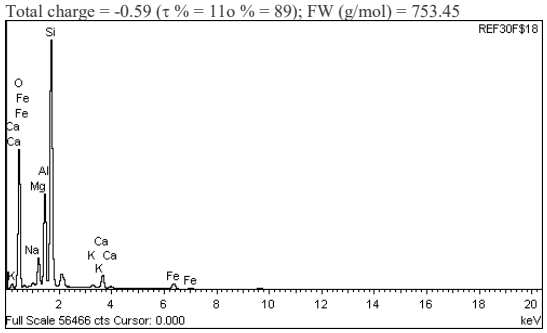

1: organic carbon; 2. Smectite

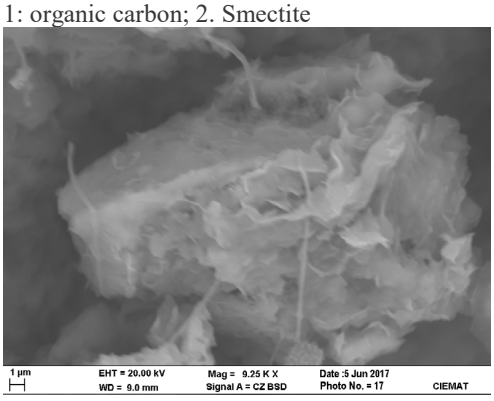

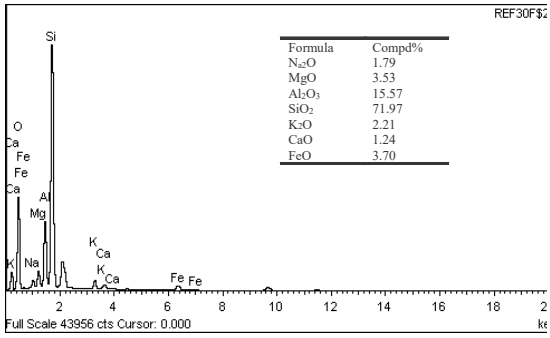

Formula	Compd%
Na_2O	1.79
MgO	3.53
Al_2O_3	15.57
SiO_2	71.97
K_2O	2.21
CaO	1.24
FeO	3.70

Fig. B-98: SEM photomicrographs: smectite clay minerals in sample BB-59-6

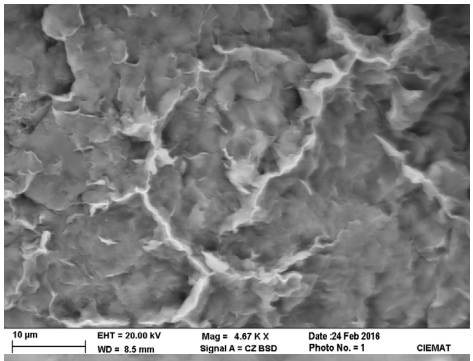

$(Si_{4.00}Al_{0.00})^{IV}(Al_{1.36}Mg_{0.44}Fe^{3+}_{0.20})^{VI}(Ca_{0.14}Na_{0.08}K_{0.07})_{0.29}O_{10}(OH)_2$
τ charge = -0.00 O. charge = -0.43
Total charge = -0.43 (τ % = 0 o % = 100); FW (g/mol) = 750.16

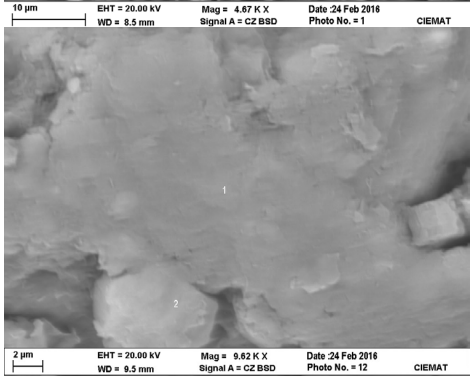

$(Si_{3.66}Al_{0.34})^{IV}(Al_{1.14}Mg_{0.31}Fe^{3+}_{0.56})^{VI}(Ca_{0.07}Mg_{0.03}Na_{0.05}K_{0.40})_{0.55}O_{10}(OH)_2$
τ charge = -0.34 O. charge = -0.31
Total charge = -0.65 (τ % = 53o % = 47); FW (g/mol) = 790.98
(No Mg at interlayer: Σ_{oct} = 2.03; Total charge: -0.59; τ % = 58; o % = 42)

1: illite; 2: Ca-sulfate

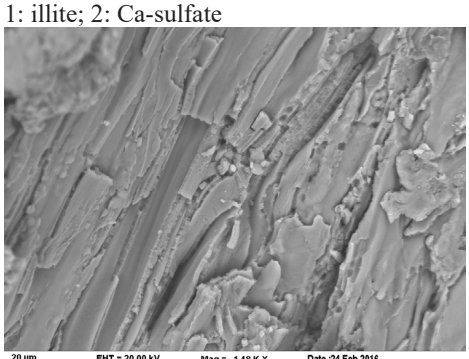

$(Si_{3.96}Al_{0.04})^{IV}(Al_{1.41}Mg_{0.37}Fe^{3+}_{0.22})^{VI}(Ca_{0.11}Mg_{0.06}Na_{0.05}K_{0.03})_{0.24}O_{10}(OH)_2$
τ charge = -0.04 O. charge = -0. 37
Total charge = -0.40 (τ % = 9o % = 91); FW (g/mol) = 747.30
(No Mg at interlayer: Σ_{oct} = 2.06; Total charge: -0.29; τ % = 12; o % = 88)

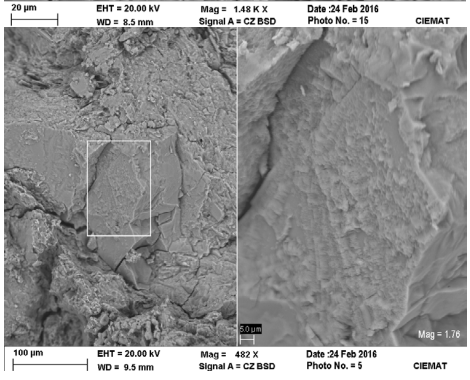

$(Si_{3.98}Al_{0.02})^{IV}(Al_{1.21}Mg_{0.44}Fe^{3+}_{0.26\ \ 0.08})^{VI}(Ca_{0.19}Na_{0.27}K_{0.04})_{0.50}O_{10}(OH)_2$
τ charge = -0.02 O. charge = -0.67
Total charge = -0.69 (τ % = 3 o % = 97); FW (g/mol) = 760.53

Fig. B-99: SEM photomicrographs: smectite clay minerals in sample BB-59-2

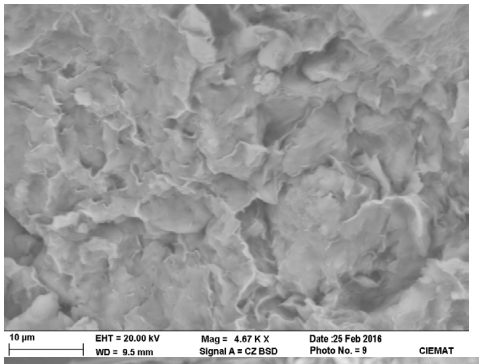

$(Si_{3.95}Al_{0.05})^{IV}(Al_{1.41}Mg_{0.47}Fe^{3+}_{0.11})^{VI}(Ca_{0.07}Mg_{0.11}Na_{0.10}K_{0.06})_{0.34}O_{10}(OH)_2$
τ charge = -0.05 O. charge = -0.47
Total charge = -0.52 (τ % = 10 o % = 90); FW (g/mol) = 744.88
(No Mg at interlayer: Σ_{oct} = 2.11; Total charge: -0.30; τ % = 17; o % = 83)

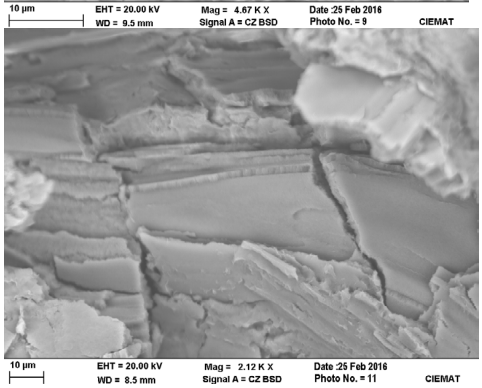

$(Si_{3.98}Al_{0.02})^{IV}(Al_{1.45}Mg_{0.44}Fe^{3+}_{0.11})^{VI}(Ca_{0.09}Mg_{0.11}Na_{0.07})_{0.27}O_{10}(OH)_2$
τ charge = -0.02 O. charge = -0.44
Total charge = -0.46 (τ % = 5 o % = 95); FW (g/mol) = 740.47
(No Mg at interlayer: Σ_{oct} = 2.11; Total charge: -0.25; τ % = 9; o % = 91)

Fig. B-99: Cont.

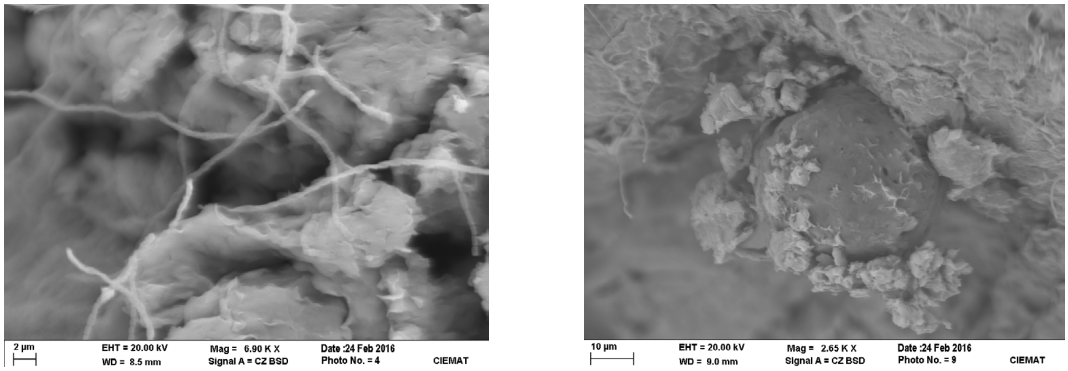

Fig. B-100: SEM photomicrographs in sample BB-59-2: a) microorganisms, b) OM (C) and S

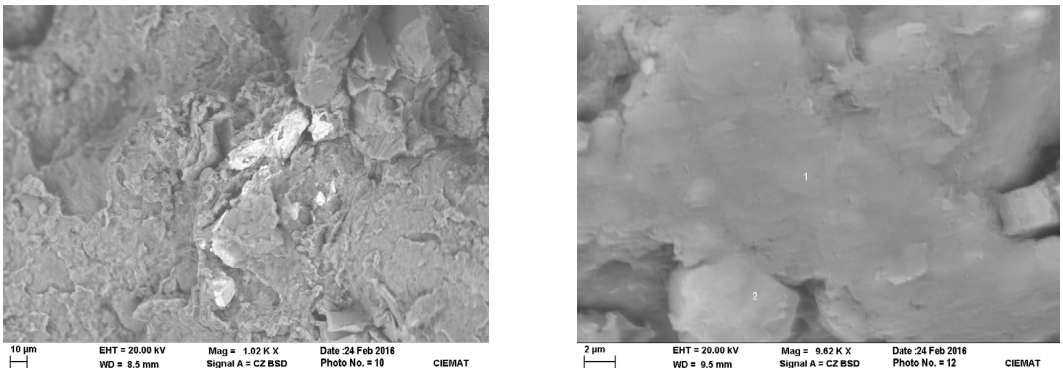

Fig. B-101: SEM photomicrographs from sample BB-59-2: a) barite, b) gypsum (2), illite(1)

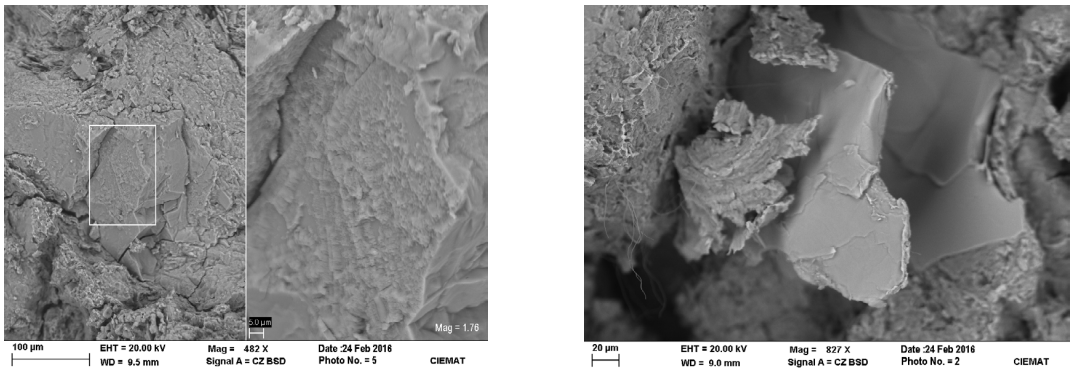

Fig. B-102: SEM photomicrographs from sample BB-59-2: a) plagioclases, b) biotite

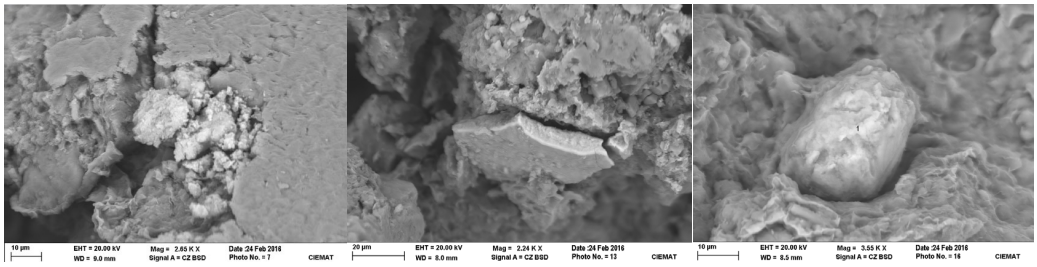

Fig. B-103: SEM photomicrographs from sample BB-59-2: Fe-carbonates

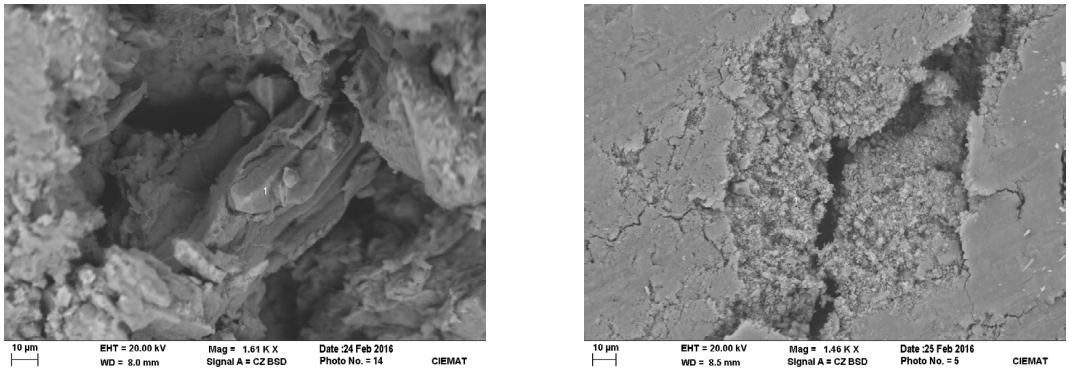

Fig. B-104: SEM photomicrographs from sample BB-59-2: Ca-carbonates

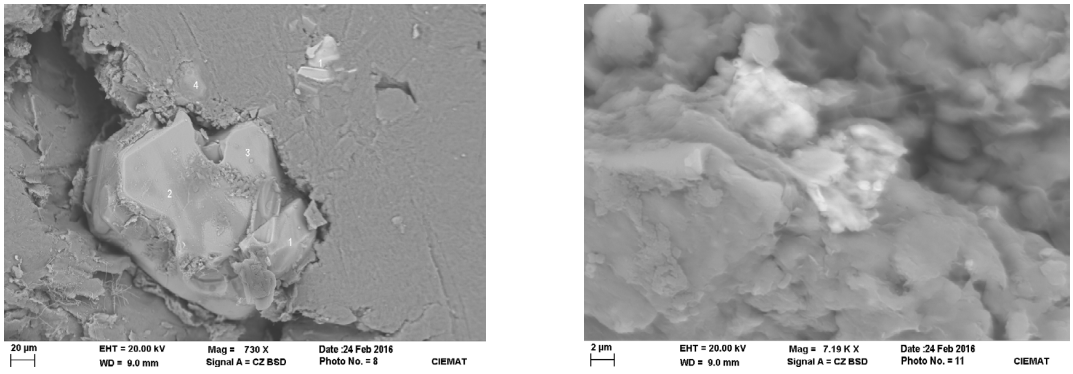

Fig. B-105: SEM photomicrographs from sample BB-59-2: a) zircon (1), Ti-Mn-Fe-oxides (2), Ti-Fe-Mn oxides (3), apatite (4); and b) Zn-oxides

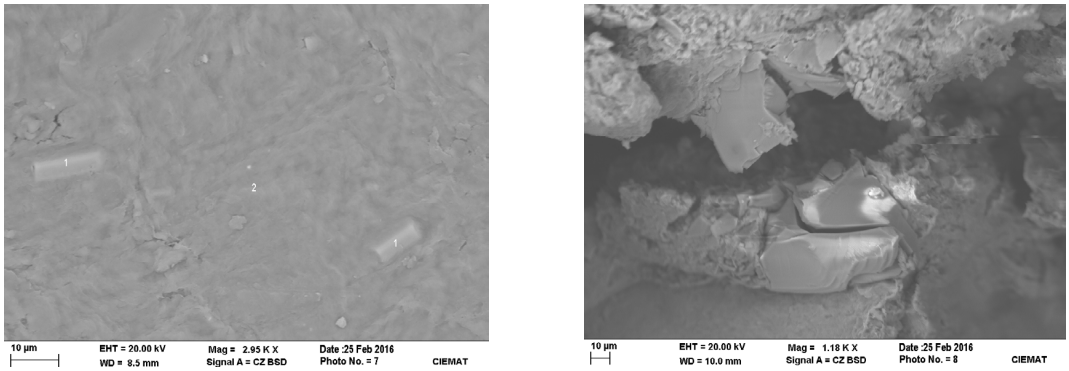

Fig. B-106: SEM photomicrographs from sample BB-59-2: a) 1: apatites, b) silica

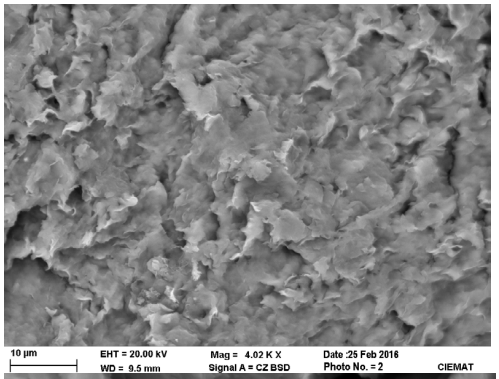

$(Si_{4.00}Al_{0.00})^{IV}(Al_{1.32}Mg_{0.50}Fe^{3+}_{0.18})^{VI}(Ca_{0.09}Mg_{0.08}Na_{0.11}K_{0.05})_{0.33}O_{10}(OH)_2$
τ charge = -0.00 O. charge = -0.50
Total charge = -0.50 (τ % = 0 o % = 100); FW (g/mol) = 748.60
(No Mg at interlayer: Σ_{oct} = 2.08; Total charge: -0.33; τ % = 0; o % = 100)

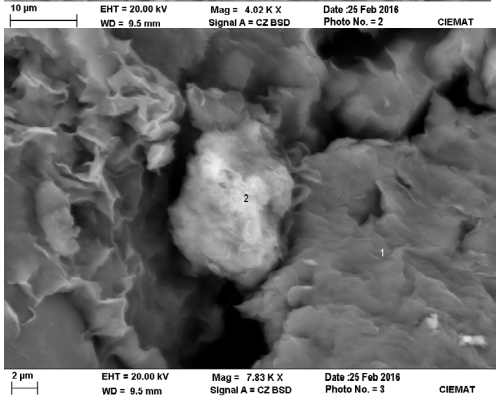

$(Si_{4.00}Al_{0.00})^{IV}(Al_{1.43}Mg_{0.40}Fe^{3+}_{0.18})^{VI}(Ca_{0.09}Mg_{0.04}Na_{0.09}K_{0.04})_{0.26}O_{10}(OH)_2$
τ charge = -0.00 O. charge = -0.40
Total charge = -0.40 (τ % = 0 o % = 100); FW (g/mol) = 745.15
(No Mg at interlayer: Σ_{oct} = 2.04 Total charge: -0.31; τ % = 0; o % = 100)

1: Smectite; 2: Ba-Mn-oxides

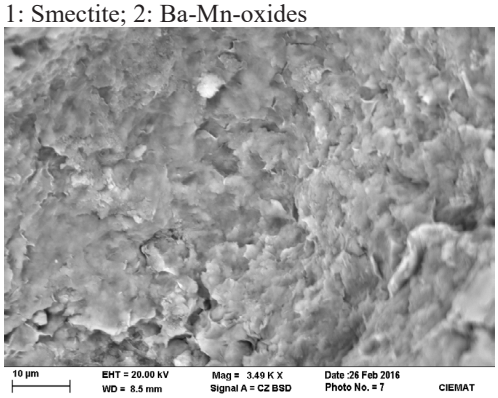

$(Si_{3.98}Al_{0.02})^{IV}(Al_{1.40}Mg_{0.43}Fe^{3+}_{0.18})^{VI}(Ca_{0.06}Mg_{0.01}Na_{0.10}K_{0.02})_{0.37}O_{10}(OH)_2$
τ charge = -0.02 O. charge = -0.43
Total charge = -0.45 (τ % = 5 o % = 95); FW (g/mol) = 754.15
(No Mg at interlayer: Σ_{oct} = 2.01 Total charge: -0.42; τ % = 5; o % = 95)

Fig. B-107: SEM photomicrographs: smectite clay minerals in sample BB-59-3

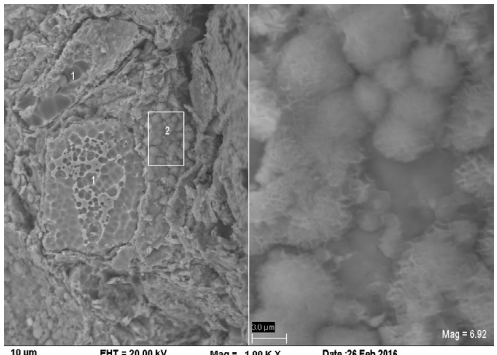

$(Si_{4.00}Al_{0.00})^{IV}(Al_{1.38}Mg_{0.50}Fe^{3+}_{0.12})^{VI}(Ca_{0.06}Mg_{0.10}Na_{0.13}K_{0.06})_{0.24}O_{10}(OH)_2$
τ charge = -0.00 O. charge = -0.50
Total charge = -0.50 (τ % = 0 o % = 100; FW (g/mol) = 744.88
(No Mg at interlayer: Σ_{oct} = 2.10 Total charge: -0.30; τ % = 0; o % = 100)

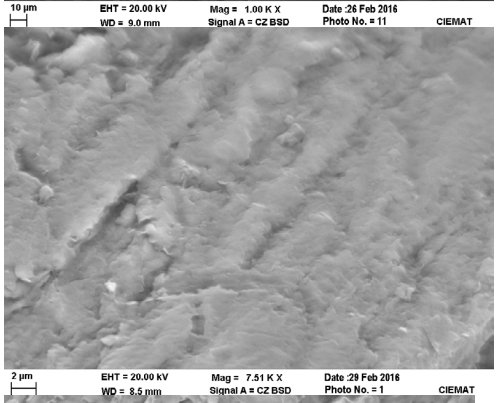

$(Si_{3.89}Al_{0.11})^{IV}(Al_{1.50}Mg_{0.31}Fe^{3+}_{0.19})^{VI}(Ca_{0.08}Mg_{0.08}Na_{0.07}K_{0.03})_{0.26}O_{10}(OH)_2$
τ charge = -0.11 O. charge = -0.31
Total charge = -0.42 (τ % = 26 o % = 74; FW (g/mol) = 745.93
(No Mg at interlayer: Σ_{oct} = 2.08 Total charge: -0.27; τ % = 42; o % = 58)

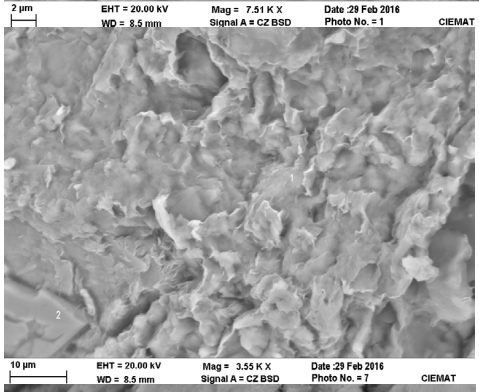

$(Si_{4.00}Al_{0.00})^{IV}(Al_{1.32}Mg_{0.48}Fe^{3+}_{0.21})^{VI}(Ca_{0.08}Mg_{0.05}Na_{0.14}K_{0.07})_{0.35}O_{10}(OH)_2$
τ charge = -0.00 O. charge = -0.48
Total charge = -0.48 (τ % = 0 o % = 100 FW (g/mol) = 751.04
(No Mg at interlayer: Σ_{oct} = 2.05 Total charge: -0.37; τ % = 0; o % = 100)

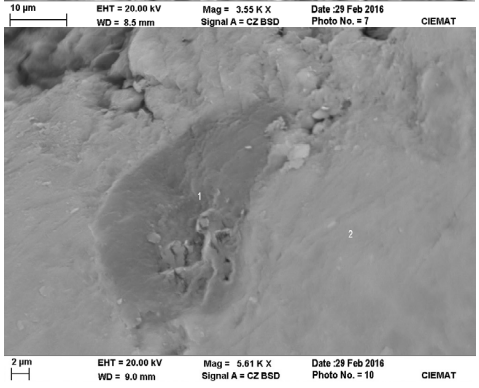

2)
$(Si_{3.87}Al_{0.13})^{IV}(Al_{1.52}Mg_{0.33}Fe^{3+}_{0.15})^{VI}(Ca_{0.09}Mg_{0.08}Na_{0.09}K_{0.03})_{0.28}O_{10}(OH)_2$
τ charge = -0.13 O. charge = -0.33
Total charge = -0.46 (τ % = 28 o % = 72) FW (g/mol) = 744.64
(No Mg at interlayer: Σ_{oct} = 2.08 Total charge: -0.30; τ % = 43; o % = 57)

1: C, N; 2: smectite

Fig. B-107: Cont.

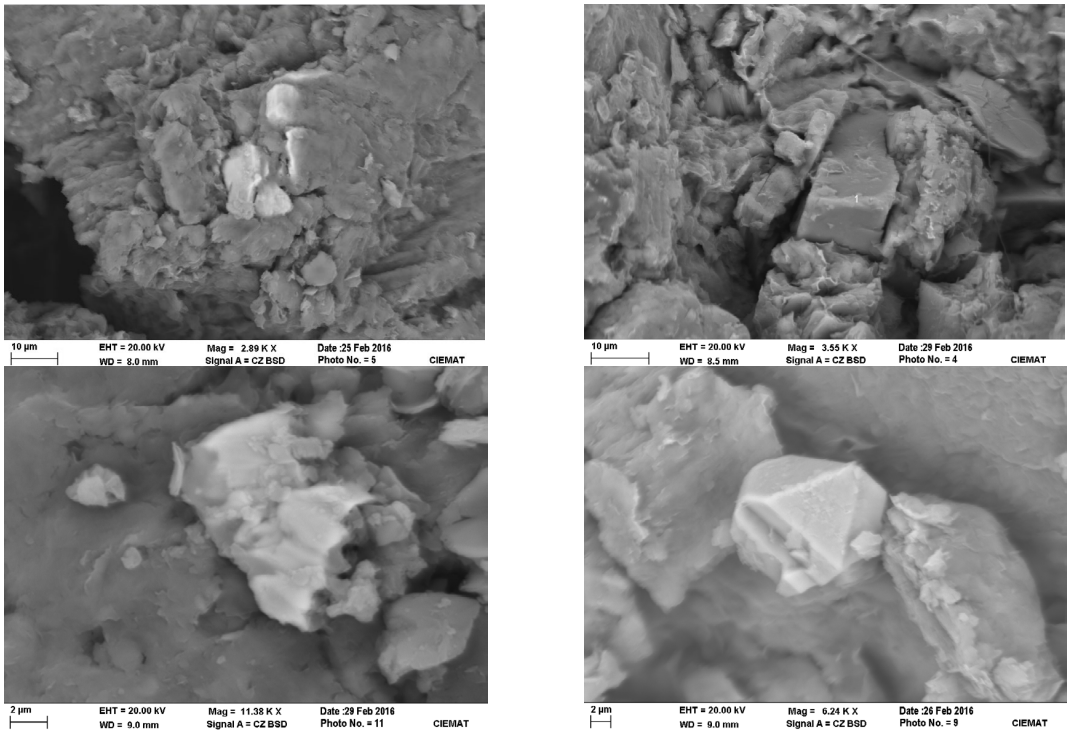

Fig. B-108: SEM photomicrographs from sample BB-59-3: a) Ca-carbonates, b) dolomite, c) Fe-carbonates, d) Fe-carbonate and Fe-Ti-oxides

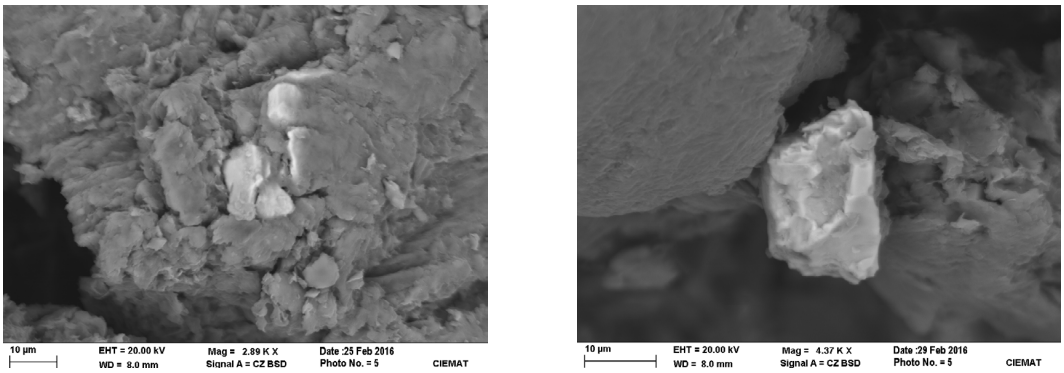

Fig. B-109: SEM photomicrographs from sample BB-59-3: a) and b) barite

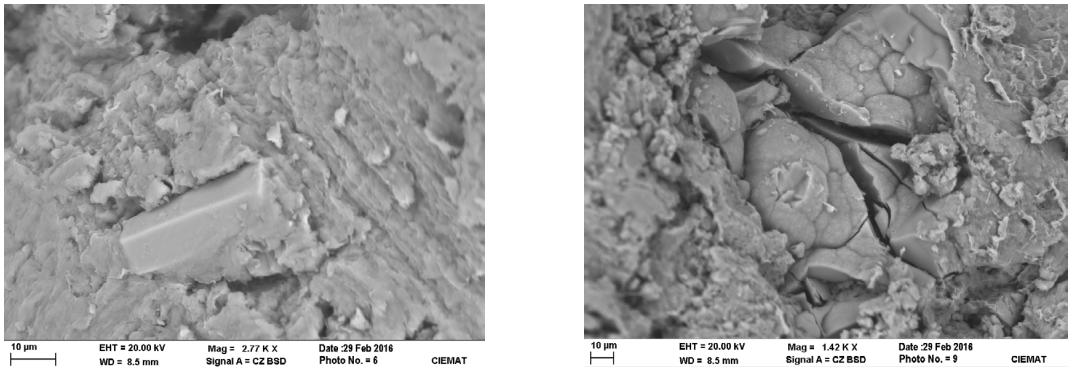

Fig. B-110: SEM photomicrographs from sample BB-59-3: a) apatite, b) silica

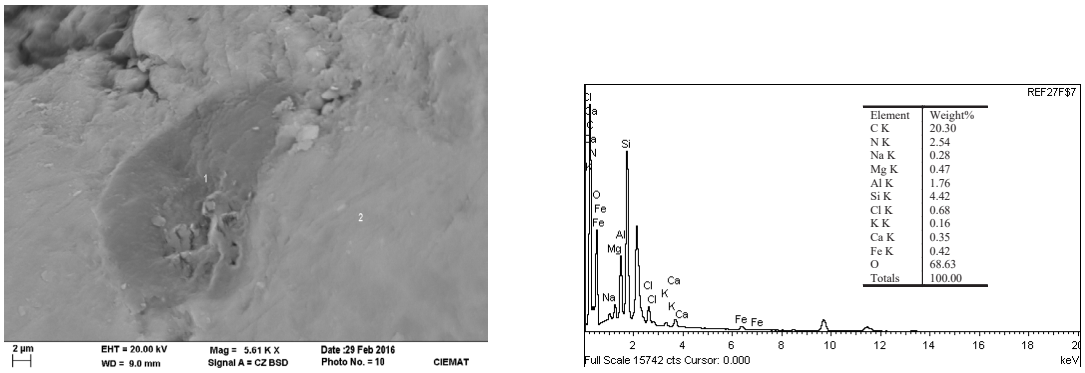

Fig. B-111: SEM photomicrographs from sample BB-59-3: a) 1: C and N, 2: clay minerals, b) EDAX analysis from 1)

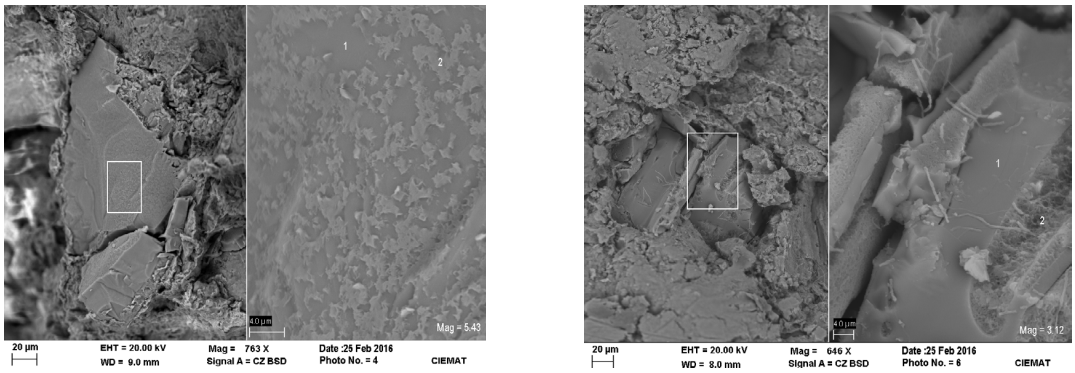

Fig. B-112: SEM photomicrographs from sample BB-59-3: a) and b) plagioclases

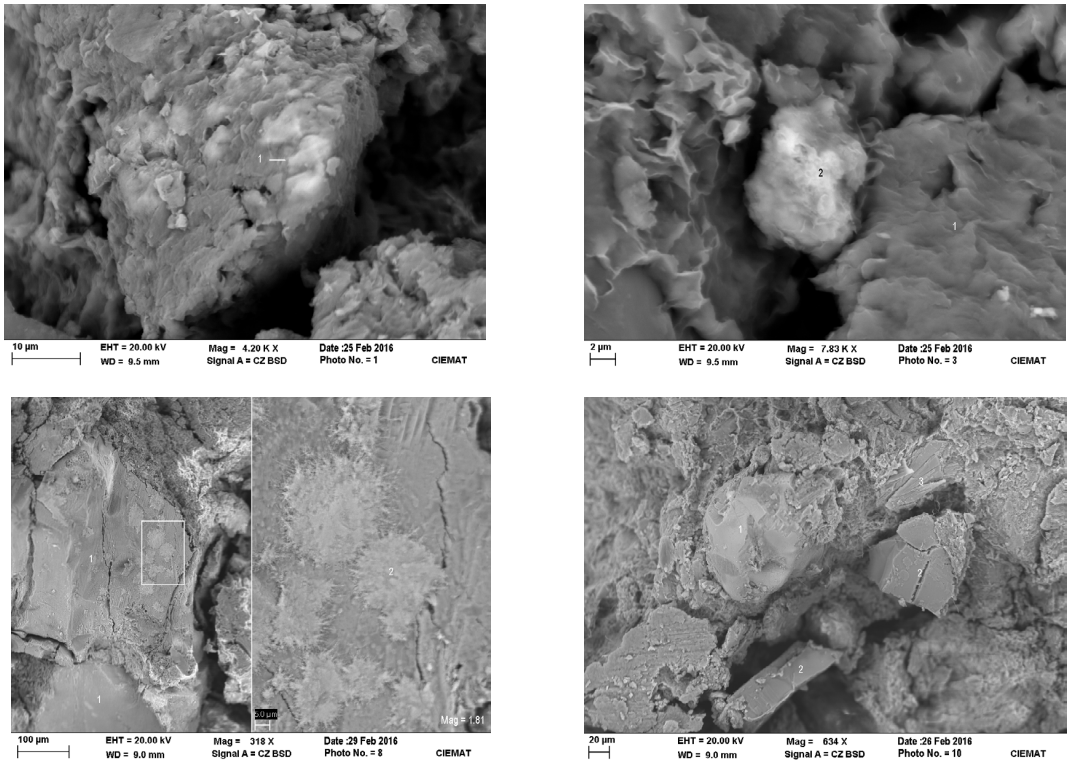

Fig. B-113: SEM photomicrographs from sample BB-59-3: a) 1: Fe-oxides, 3, b) Mn-Ba-oxides, c) 1: Fe-oxides, 2: Mn-Ba-Mn oxides, d) 1: Ti, Fe-Mn oxides, 2: plagioclases, 3: biotite

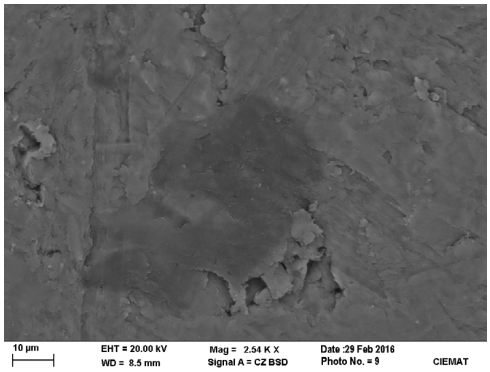

Fig. B-114: SEM photomicrographs in BB-59-4 sample: carbon (dark zone)

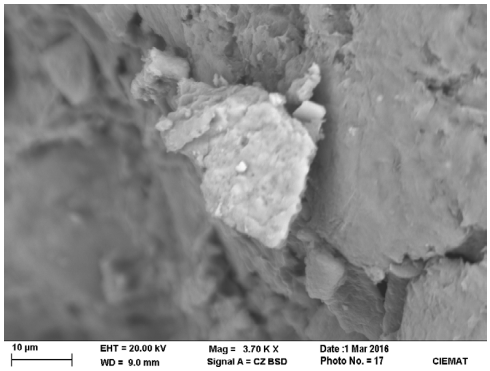

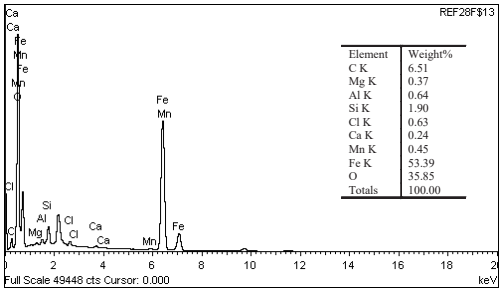

Fig. B-115: SEM photomicrographs in BB-59-4 sample: a) Fe-carbonates, b) EDX of a)

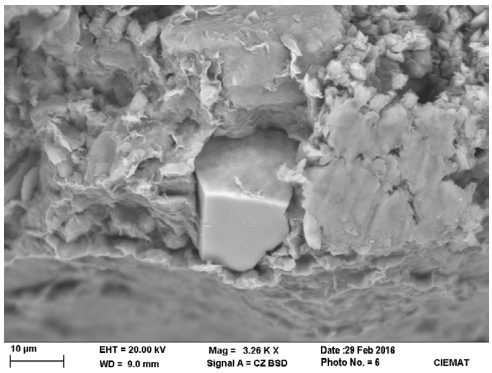

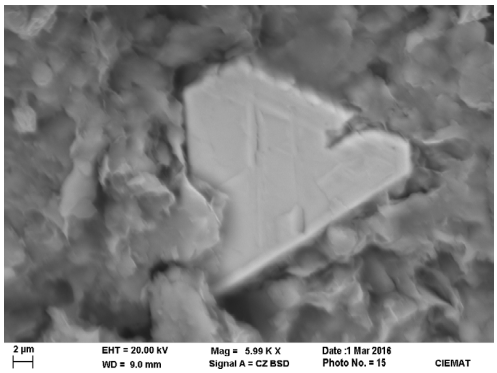

b)

Fig. B-116: SEM photomicrographs: a) and b) iron oxides in BB-59-4 sample

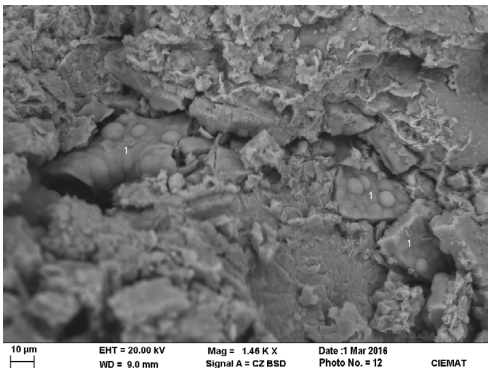

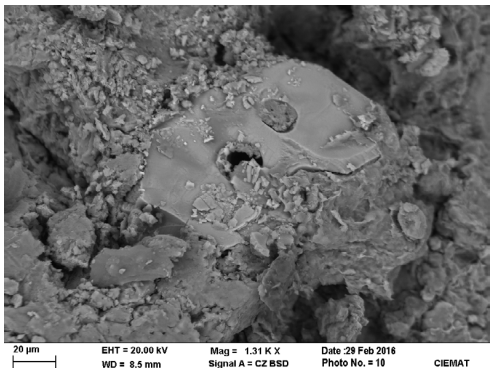

Fig. B-117: SEM photomicrographs in BB-59-4 sample: a) silica, b) ilmenite

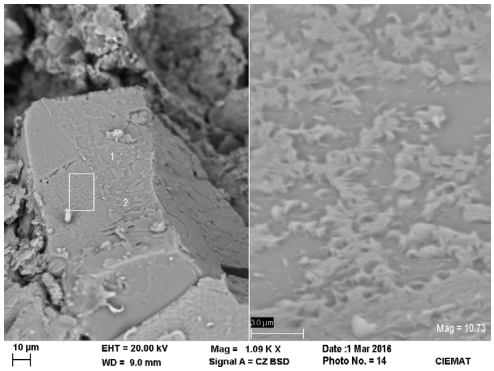

Fig. B-118: SEM photomicrographs in BB-59-4 sample: plagioclases

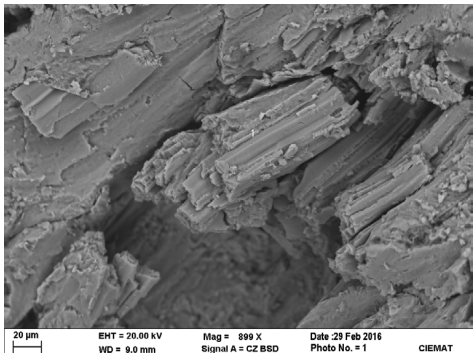

$(Si_{4.00}Al_{0.00})^{IV}(Al_{1.39}Mg_{0.40}Fe^{3+}_{0.21})^{VI}(Ca_{0.13}Mg_{0.02}Na_{0.06}K_{0.03})_{0.24}O_{10}(OH)_2$
τ charge = -0.00 O. charge = -0.40
Total charge = -0.40 (τ % = 0 o % = 100) FW (g/mol) = 747.75
(No Mg at interlayer: Σ_{oct} = 2.02 Total charge: -0.35; τ % = 0; o % = 100)

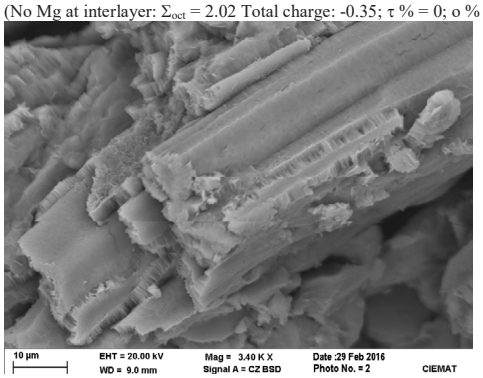

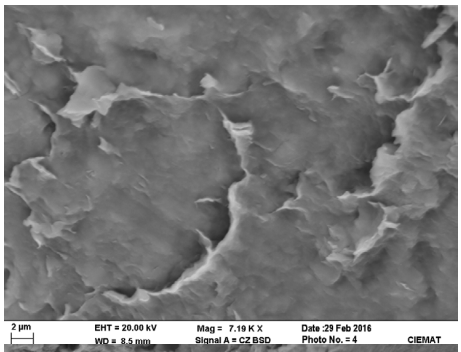

$(Si_{3.97}Al_{0.03})^{IV}(Al_{1.34}Mg_{0.41}Fe^{3+}_{0.26})^{VI}(Ca_{0.07}Mg_{0.07}Na_{0.09}K_{0.08})_{0.30}O_{10}(OH)_2$
τ charge = -0.03 O. charge = -0.41
Total charge = -0.44 (τ % = 7 o % = 93) FW (g/mol) = 752.00
(No Mg at interlayer: Σ_{oct} = 2.07 Total charge: -0.30; τ % = 11; o % = 89)

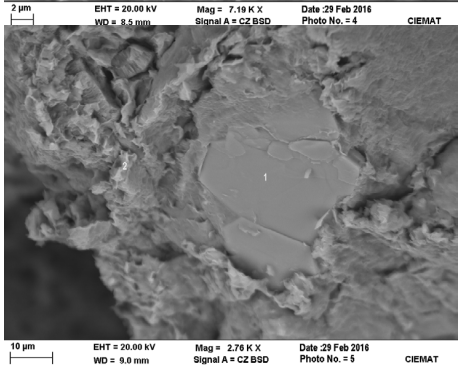

1)biotite
$(Si_{2.97}Al_{1.03})^{IV}(Al_{0.08}Mg_{1.03}Fe^{3+}_{0.66}Ti^{4+}_{0.23})^{VI}(Mg_{0.54}Na_{0.06}K_{0.69})_{1.29}O_{10}(OH)_2$
τ charge = -1.03 O. charge = -0.79
Total charge = -1.83 (τ % = 57 o % = 43) FW (g/mol) = 843.55
2) smectite
$(Si_{3.94}Al_{0.06})^{IV}(Al_{1.33}Mg_{0.46}Fe^{3+}_{0.20}Ti^{4+}_{0.02})^{VI}(Ca_{0.10}Mg_{0.08}Na_{0.08}K_{0.07})_{0.33}O_{10}(OH)_2$
τ charge = -0.06 O. charge = -0.44
Total charge = -0.50 (τ % = 13 o % = 87) FW (g/mol) = 750.86
(No Mg at interlayer: Σ_{oct} = 2.08 Total charge: -0.34; τ % = 18; o % = 82)

Fig. B-119: SEM photomicrographs: smectite clay minerals in sample BB-59-4

B2 Bentonite samples at contact with the liner/heater and protrusions (Fig. 174)

BMS-47-1 (Fig. 175)

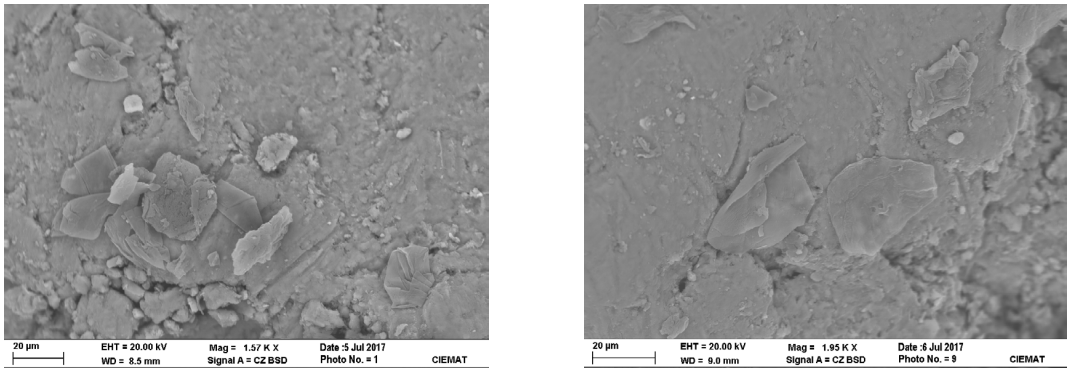

Fig. B-120: SEM photomicrographs from sample BMS-47-1: a) and b) organic matter with Cl

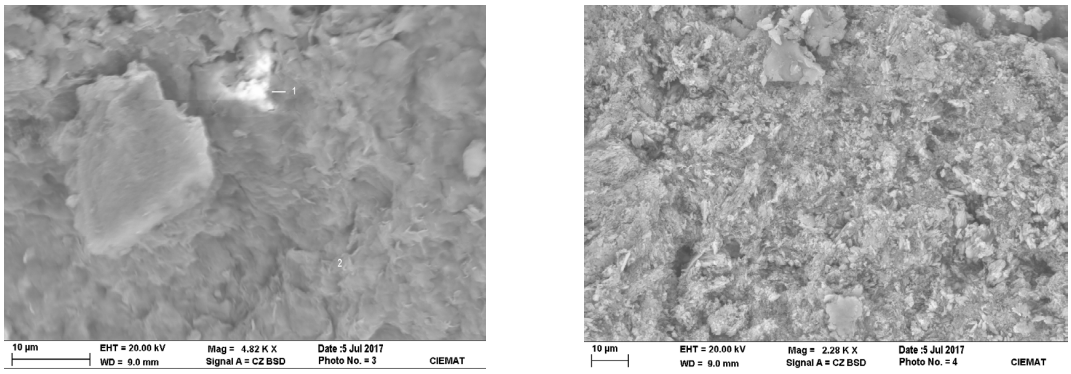

Fig. B-121: SEM photomicrographs from sample BMS-47-1: a) Ca-sulfates (1), smectite (2), b) Ca-carbonates

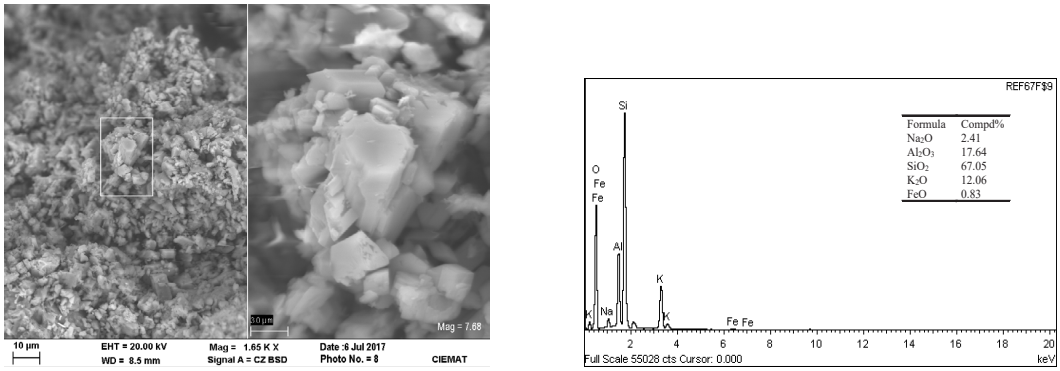

Fig. B-122: SEM photomicrographs from sample BMS-47-1: a) K-feldspar (Na), b) EDX of a)

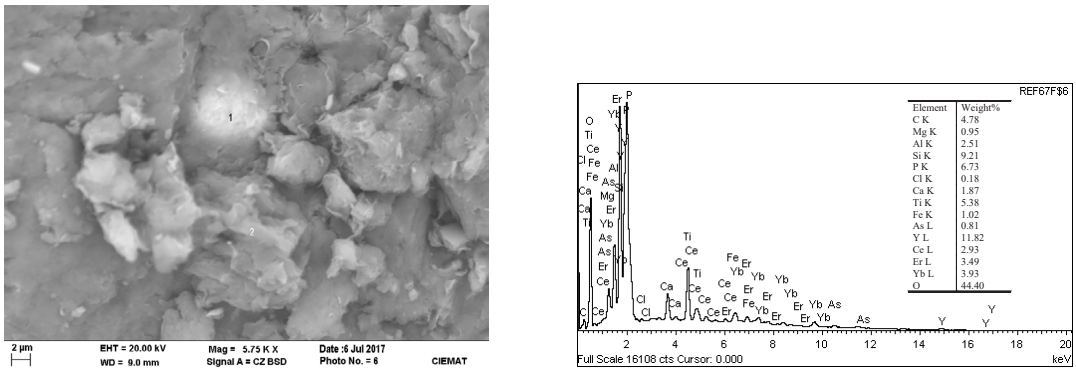

Fig. B-123: SEM photomicrographs from sample BMS-47-1: a) Xenotime (1), smectite (2), b) EDX of (1)

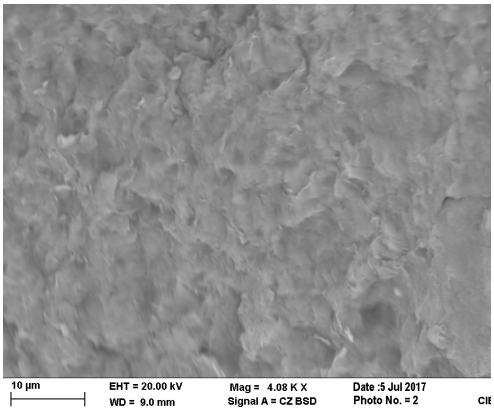

$(Si_{3.94}Al_{0.06})^{IV}$ $(Al_{1.30}Mg_{0.51}Fe^{3+}_{0.19})^{VI}$ $(Ca_{0.08}Mg_{0.13}Na_{0.07}K_{0.07})_{0.36}O_{10}(OH)_2$
τ charge = -0.06; O. charge = -0.51
Total charge = -0.57 (τ % = 11; o % = 89); FW (g/mol) = 750.54
(No Mg at interlayer: Σ_{oct} = 2.13; Total charge: -0.51, τ % = 21; o % = 79)

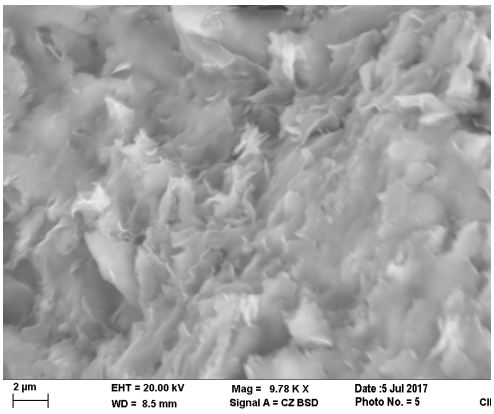

$(Si_{3.84}Al_{0.16})^{IV}$ $(Al_{1.33}Mg_{0.42}Fe^{3+}_{0.26})^{VI}$ $(Ca_{0.07}Mg_{0.05}Na_{0.09}K_{0.23})_{0.44}O_{10}(OH)_2$
τ charge = -0.16; O. charge = -0.42
Total charge = -0.57 (τ % = 27; o % = 73); FW (g/mol) = 763.32
(No Mg at interlayer: Σ_{oct} = 2.05; Total charge: -0.47, τ % = 33; o % = 67)

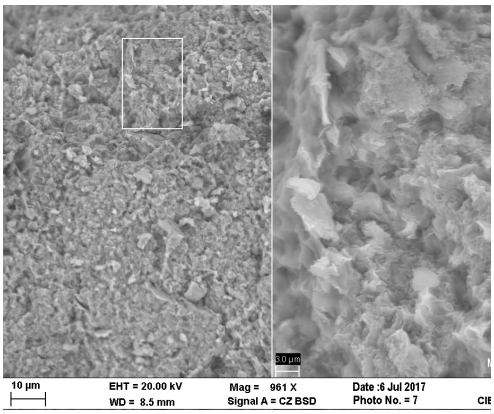

$(Si_{3.96}Al_{0.04})^{IV}$ $(Al_{1.49}Mg_{0.46}Fe^{3+}_{0.05})^{VI}$ $(Ca_{0.09}Mg_{0.12}Na_{0.05}K_{0.02})_{0.29}O_{10}(OH)_2$
τ charge = -0.04; O. charge = -0.46
Total charge = -0.50 (τ % = 9; o % = 91); FW (g/mol) = 738.53
(No Mg at interlayer: Σ_{oct} = 2.12; Total charge: -0.26, τ % = 17; o % = 83)

Fig. B-124: SEM photomicrographs from sample BMS-47-1: clay minerals

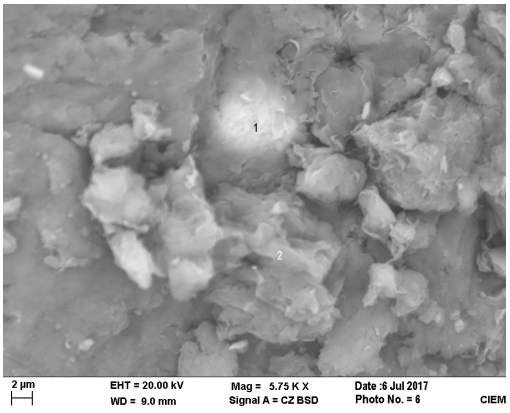

1: xenotine; 2: smectite

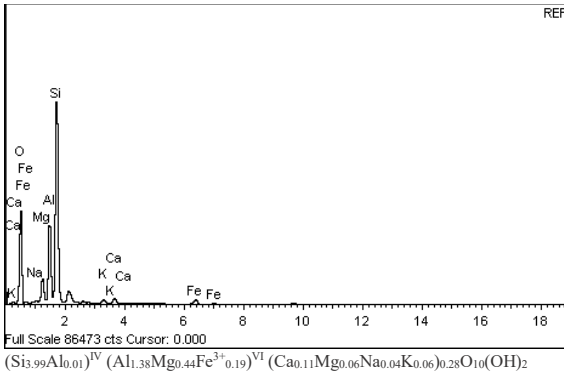

$(Si_{3.99}Al_{0.01})^{IV}$ $(Al_{1.38}Mg_{0.44}Fe^{3+}_{0.19})^{VI}$ $(Ca_{0.11}Mg_{0.06}Na_{0.04}K_{0.06})_{0.28}O_{10}(OH)_2$
τ charge = -0.01; O. charge = -0.44
Total charge = -0.45 (τ % = 3 o % = 97); FW (g/mol) = 747.59
(No Mg at interlayer: Σ_{oct} = 2.06; Total charge: -0.32, τ % = 4; o % = 96)

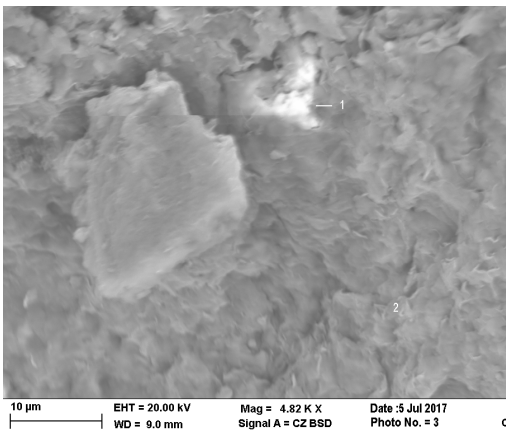

1: Ba-sulfate; 2: smectite

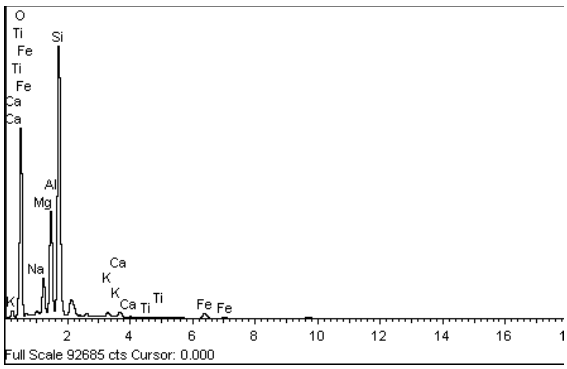

$(Si_{3.97}Al_{0.03})(Al_{1.36}Mg_{0.48}Fe^{3+}_{0.15}Ti^{4+}_{0.01})(Ca_{0.08}Mg_{0.09}Na_{0.08}K_{0.07})_{0.32}O_{10}(OH)_2$
τ charge = -0.03; O. charge = -0.47
Total charge = -0.50 (τ % = 6 o % = 94); FW (g/mol) = 747.28
(No Mg at interlayer: Σ_{oct} = 2.09; Total charge: -0.32, τ % = 10; o % = 90)

Fig. B-124: Cont.

BMS-47-2 (Fig. 176)

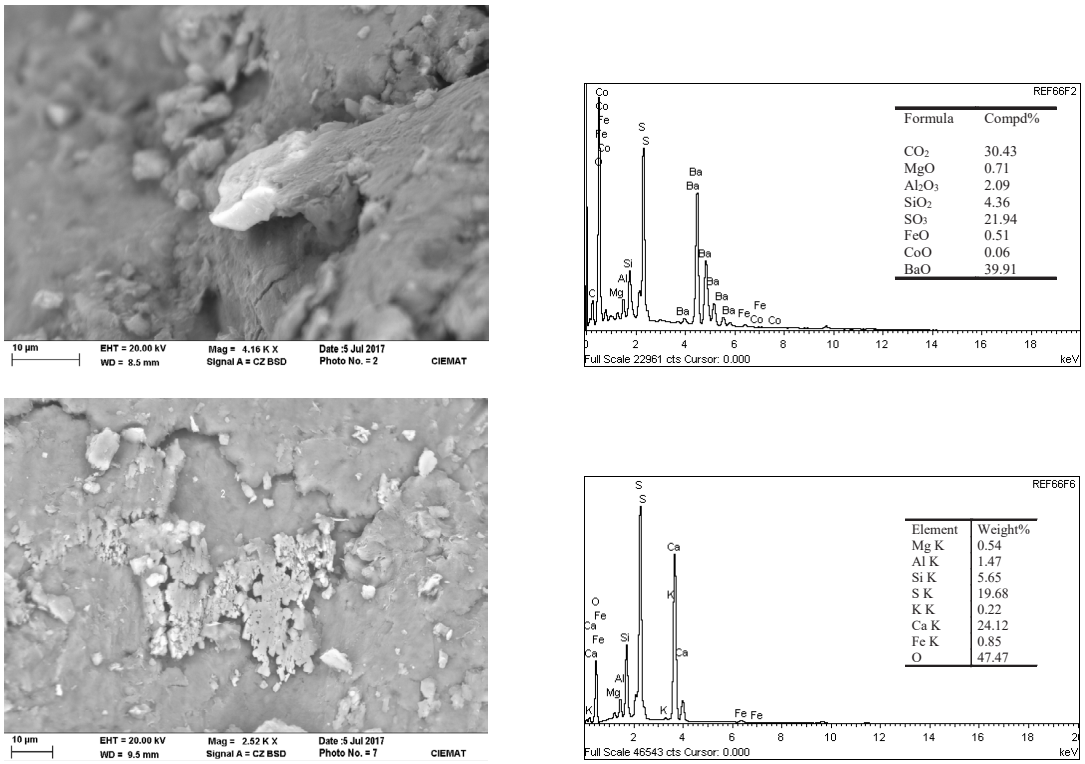

Fig. B-125: SEM photomicrographs from sample BMS-47-2: a) Ca-sulfates with carbon (1), smectite (2), b) Ca-sulfates

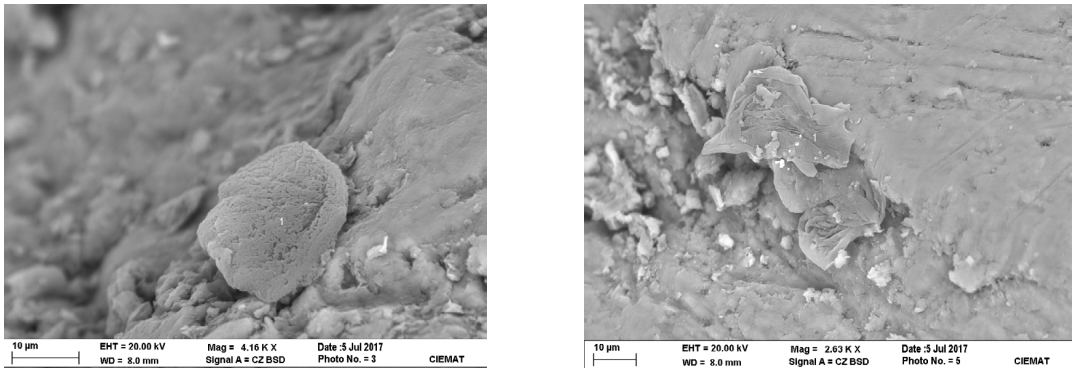

Fig. B-126: SEM photomicrographs from sample BMS-47-2: a) and b) organic matter

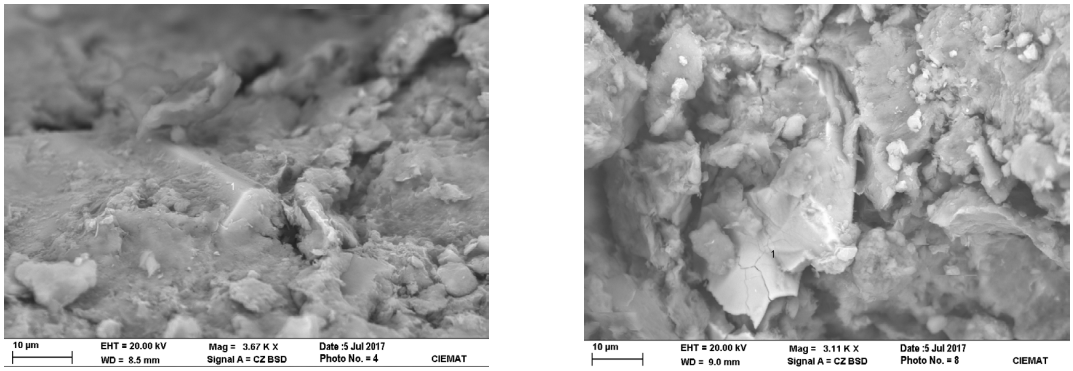

Fig. B-127: SEM photomicrographs from sample BMS-47-2: a) apatite (1) and Na-plagioclase, b) ilmenite (Fe, Ti)

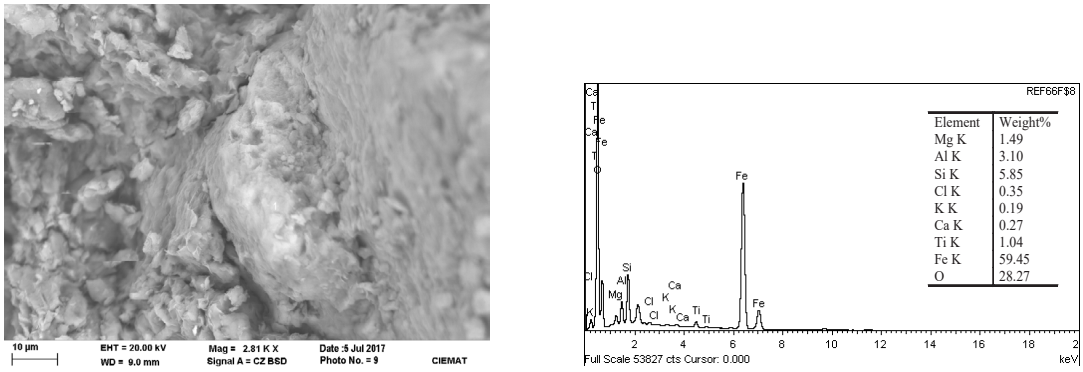

Fig. B-128: SEM photomicrographs from sample BMS-47-2: a) Fe-oxide (1), b) EDX from 1)

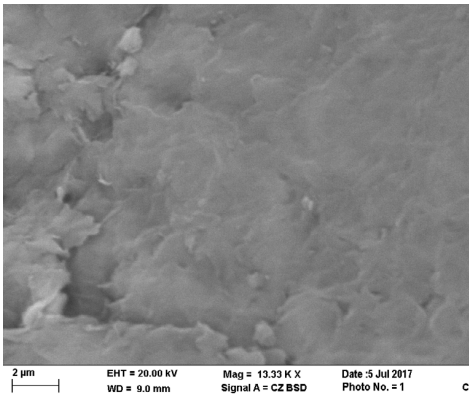

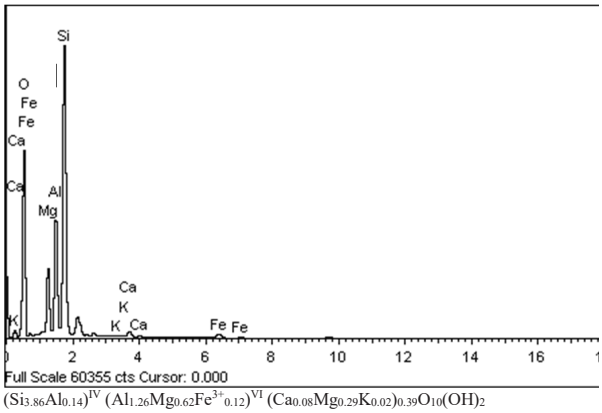

$(Si_{3.86}Al_{0.14})^{IV}$ $(Al_{1.26}Mg_{0.62}Fe^{3+}_{0.12})^{VI}$ $(Ca_{0.08}Mg_{0.29}K_{0.02})_{0.39}O_{10}(OH)_2$
τ charge = -0.14; O. charge = -0.62
Total charge = -0.76 (τ % = 19 o % = 81); FW (g/mol) = 746.06
(No Mg at interlayer: Σ_{oct} = 2.29; Total charge: -0.18, τ % = 19; o % = 81)

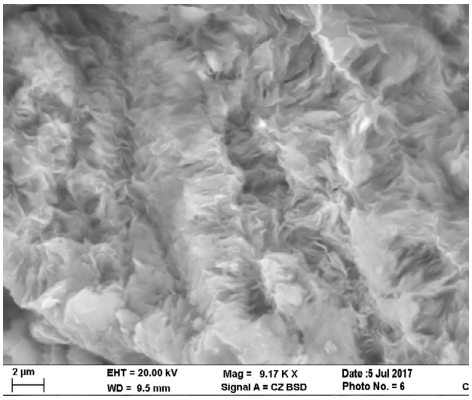

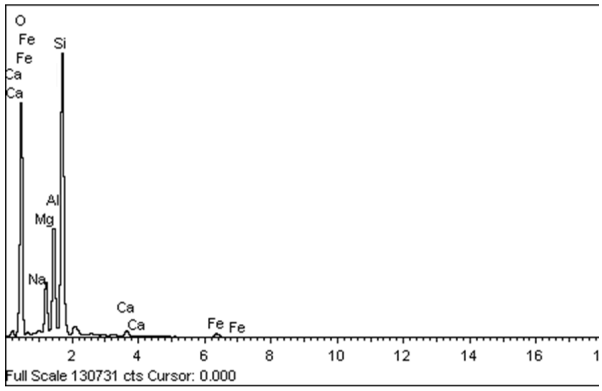

$(Si_{3.97}Al_{0.03})^{IV}$ $(Al_{1.33}Mg_{0.57}Fe^{3+}_{0.10})^{VI}$ $(Ca_{0.08}Mg_{0.20}Na_{0.06})_{0.33}O_{10}(OH)_2$
τ charge = -0.03; O. charge = -0.57
Total charge = -0.61 (τ % = 5 o % = 95); FW (g/mol) = 741.78
(No Mg at interlayer: Σ_{oct} = 2.20; Total charge: -0.22, τ % = 15; o % = 85)

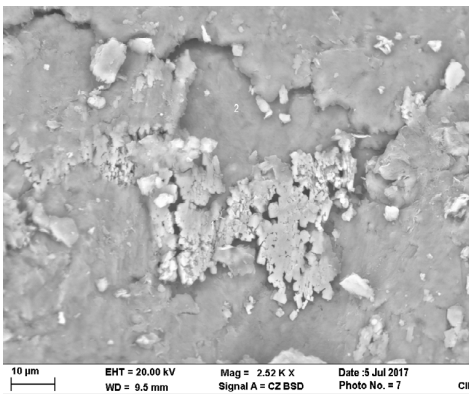

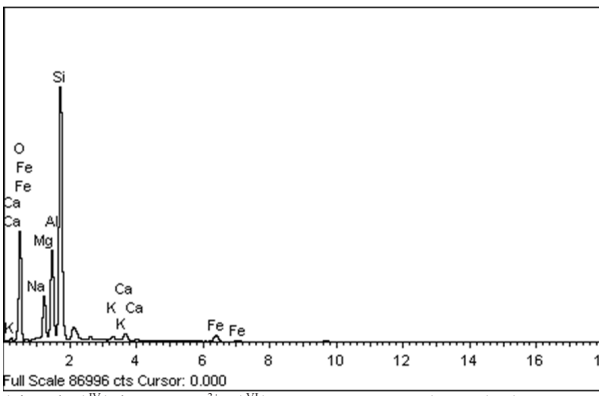

$(Si_{3.95}Al_{0.05})^{IV}(Al_{1.23}Mg_{0.58}Fe^{3+}_{0.19})^{VI}(Ca_{0.12}Mg_{0.15}Na_{0.04}Na_{0.06})_{0.36}O_{10}(OH)_2$
τ charge = -0.05; O. charge = -0.58
Total charge = -0.63 (τ % = 8 o % = 92); FW (g/mol) = 751.72
(No Mg at interlayer: Σ_{oct} = 2.15; Total charge: -0.33, τ % = 16; o % = 84)

Fig. B-129: SEM photomicrographs from sample BMS-47-2: clay minerals

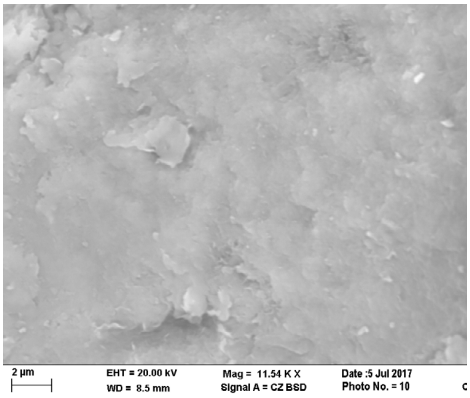

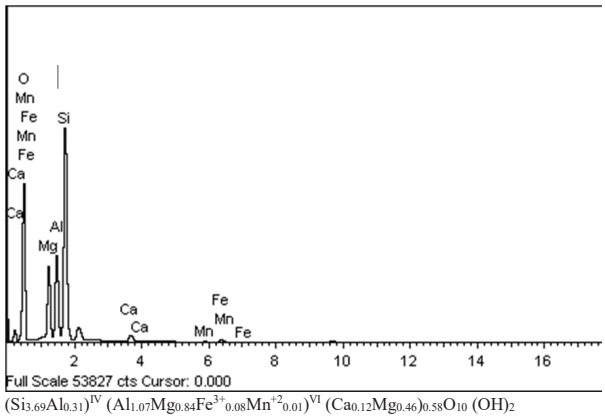

$(Si_{3.69}Al_{0.31})^{IV}$ $(Al_{1.07}Mg_{0.84}Fe^{3+}_{0.08}Mn^{+2}_{0.01})^{VI}$ $(Ca_{0.12}Mg_{0.46})_{0.58}O_{10}$ $(OH)_2$
τ charge = -0.31; O. charge = -0.85
Total charge = -1.16 (τ % = 27 o % = 73); FW (g/mol) = 753.05

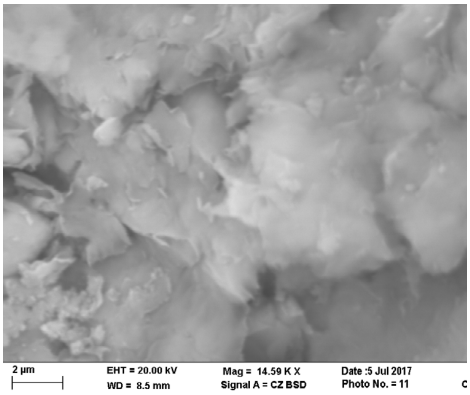

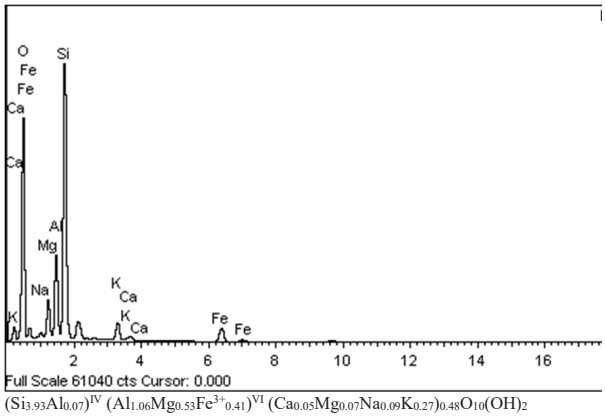

$(Si_{3.93}Al_{0.07})^{IV}$ $(Al_{1.06}Mg_{0.53}Fe^{3+}_{0.41})^{VI}$ $(Ca_{0.05}Mg_{0.07}Na_{0.09}K_{0.27})_{0.48}O_{10}(OH)_2$
τ charge = -0.07; O. charge = -0.53
Total charge = -0.61 (τ % = 12 o % = 88); FW (g/mol) = 774.26
(No Mg at interlayer: Σ_{oct} = 2.07; Total charge: -0.46, τ % = 16; o % = 84)

Fig. B-129: Cont.

BBIL-42: Brownish-red bentonite inside the liner (Fig. 178)

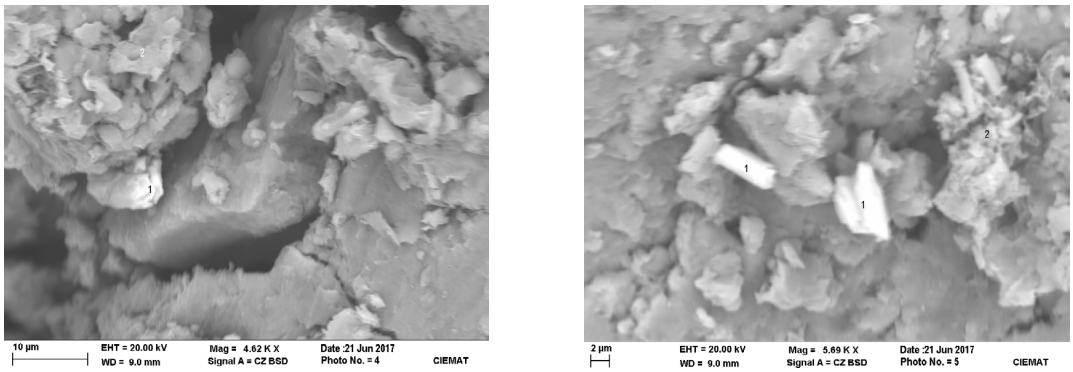

Fig. B-130: SEM photomicrographs from sample BBIL-42: a) Barite-celestine (1), smectite (2), b) Barite-celestine (1), Ca-sulfates (2)

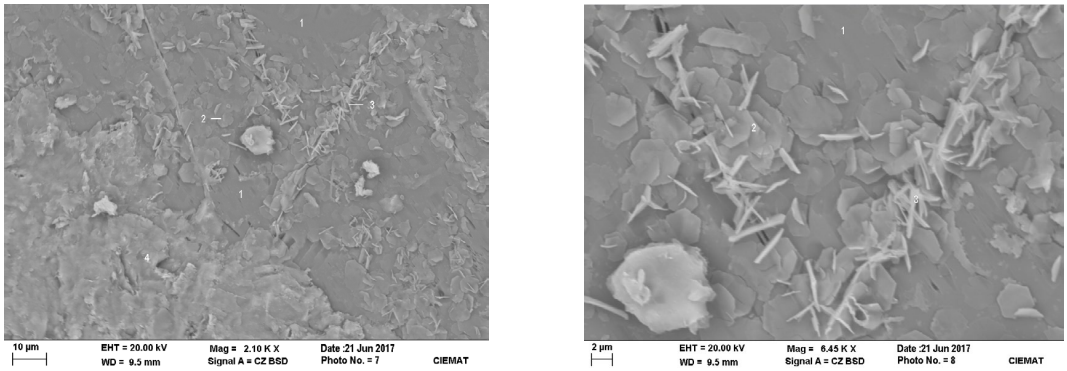

Fig. B-131: SEM photomicrographs from sample BBIL-42: a) Ca,Na-plagioclase (1), Fe-oxides (2), smectite (4), b) enlargement of a): Fe-oxides (3)

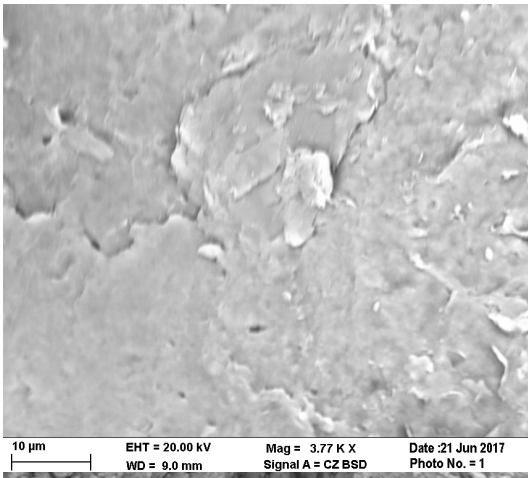

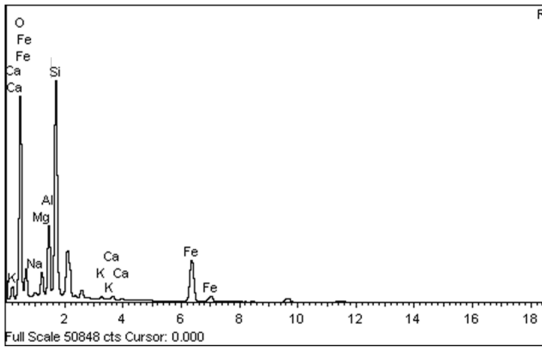

$(Si_{3.38}Al_{0.62})^{IV}(Al_{0.48}Mg_{0.18}Fe^{3+}_{1.34})^{VI}(Ca_{0.06}Mg_{0.27}Na_{0.10}K_{0.03})_{0.47}O_{10}(OH)_2$
τ charge = -0.62; O. charge = -0.18
Total charge = -0.80 (τ % = 77 o % = 23); FW (g/mol) = 820.85

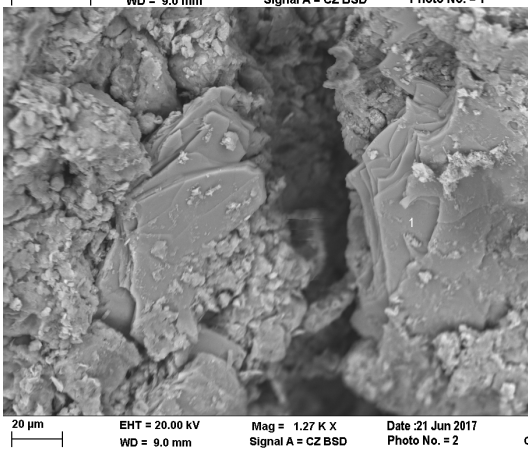

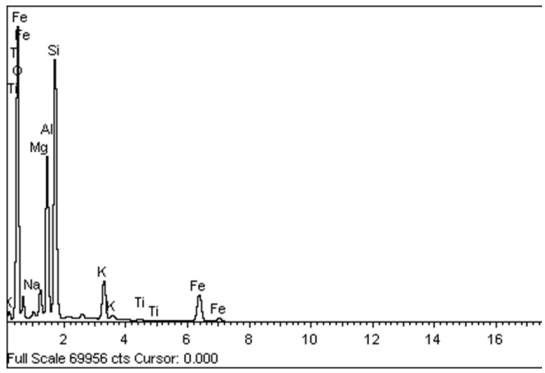

$(Si_{3.25}Al_{0.75})$ $(Al_{1.10}Mg_{0.19}Fe^{3+}_{0.69}Ti^{4+}_{0.01})$ $(Mg_{0.17}Na_{0.10}K_{0.47})_{0.76}O_{10}(OH)_2$
τ charge = -0.75; O. charge = -0.18
Total charge = -0.93 (τ % = 80 o % = 20); FW (g/mol) = 809.52

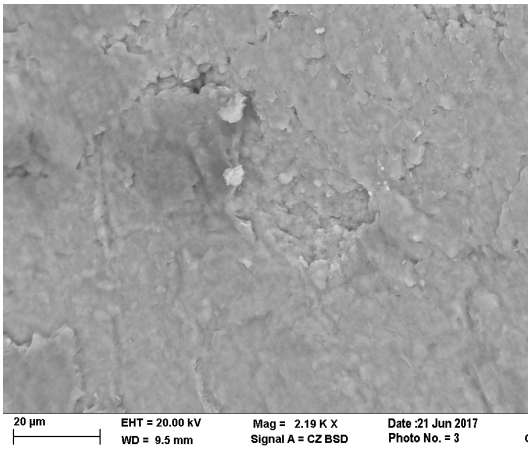

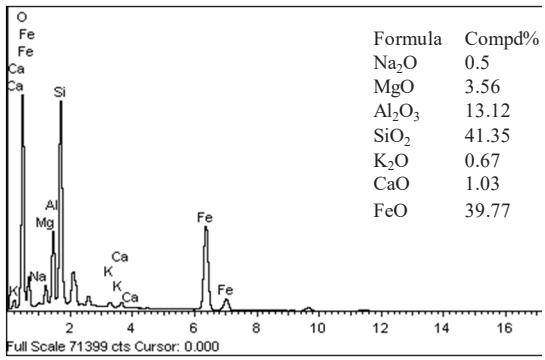

Formula	Compd%
Na_2O	0.5
MgO	3.56
Al_2O_3	13.12
SiO_2	41.35
K_2O	0.67
CaO	1.03
FeO	39.77

Fig. B-129: SEM photomicrographs from sample BMS-47-2: clay minerals

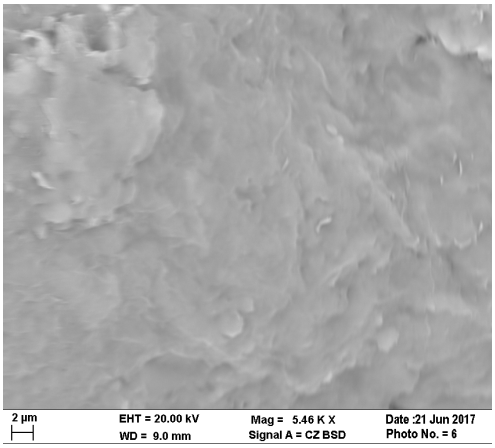

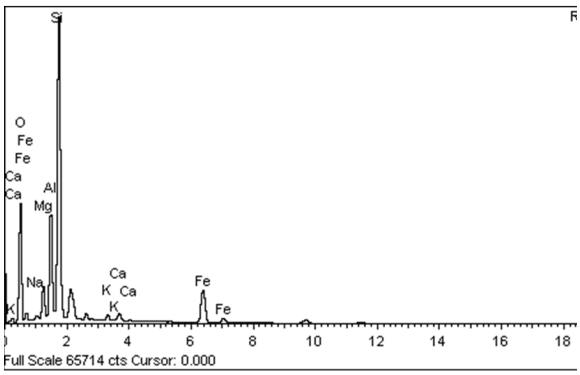

$(Si_{3.66}Al_{0.34})^{IV}(Al_{0.87}Mg_{0.30}Fe^{3+}_{0.83})^{VI}(Ca_{0.09}Mg_{0.16}Na_{0.08}K_{0.07})_{0.39}O_{10}(OH)_2$
τ charge = -0.34; O. charge = -0.30
Total charge = -0.64 (τ % = 53 o % = 47); FW (g/mol) = 789.76

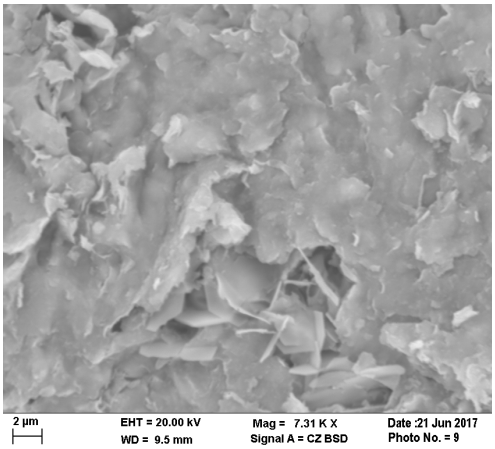

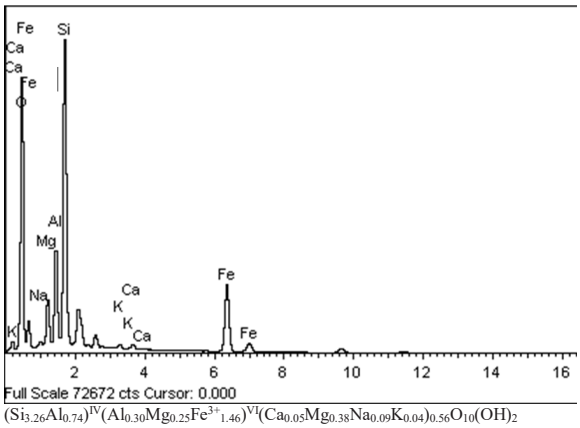

$(Si_{3.26}Al_{0.74})^{IV}(Al_{0.30}Mg_{0.25}Fe^{3+}_{1.46})^{VI}(Ca_{0.05}Mg_{0.38}Na_{0.09}K_{0.04})_{0.56}O_{10}(OH)_2$
τ charge = -0.74; O. charge = -0.25
Total charge = -0.98 (τ % = 75 o % = 25); FW (g/mol) = 831.45

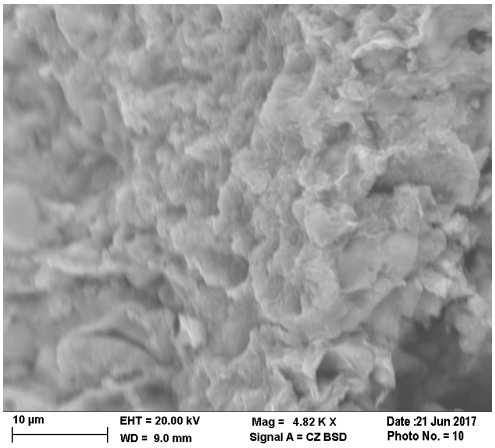

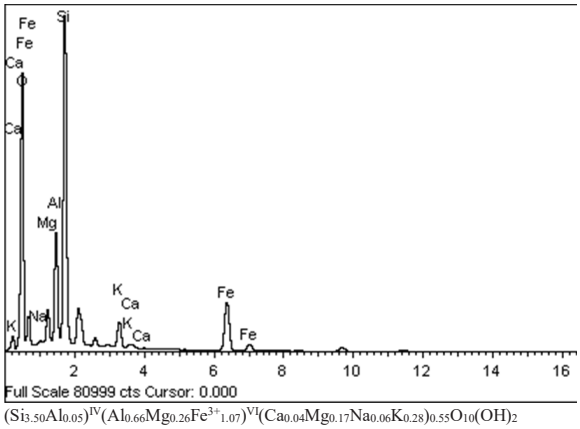

$(Si_{3.50}Al_{0.05})^{IV}(Al_{0.66}Mg_{0.26}Fe^{3+}_{1.07})^{VI}(Ca_{0.04}Mg_{0.17}Na_{0.06}K_{0.28})_{0.55}O_{10}(OH)_2$
τ charge = -0.50; O. charge = -0.26
Total charge = -0.76 (τ % = 66 o % = 34); FW (g/mol) = 816.45

Fig. B-132: Cont.

WB-42: White Bentonite from the internal part of the liner (Fig. 178)

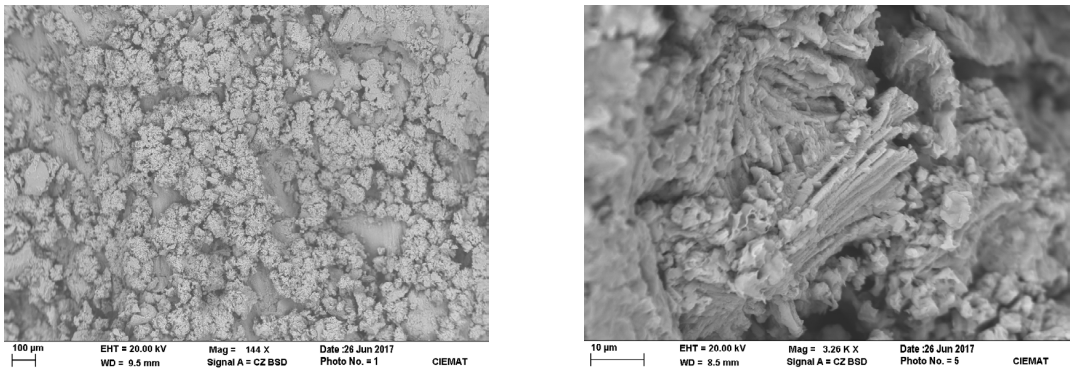

Fig. B-133: SEM photomicrographs from sample WB-42: a) and b) Ca-sulfates

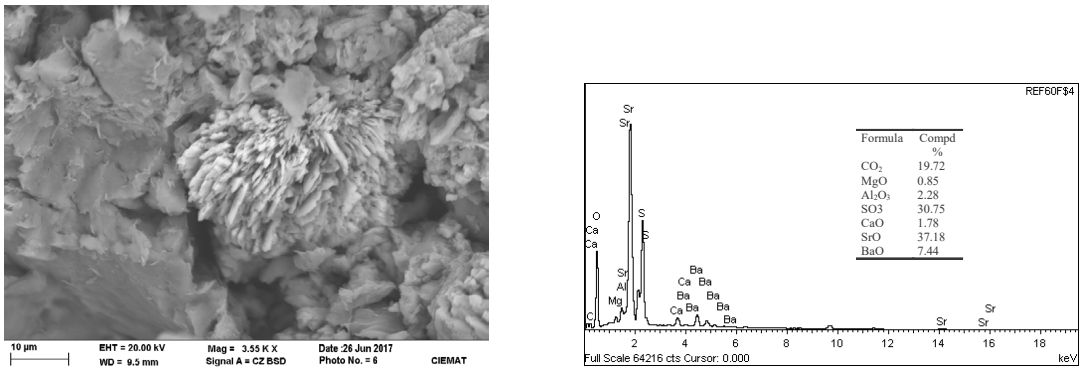

Fig. B-134: SEM photomicrographs from sample WB-42: a) Barite-celestine and Ca-carbonates, b) EDX from a)

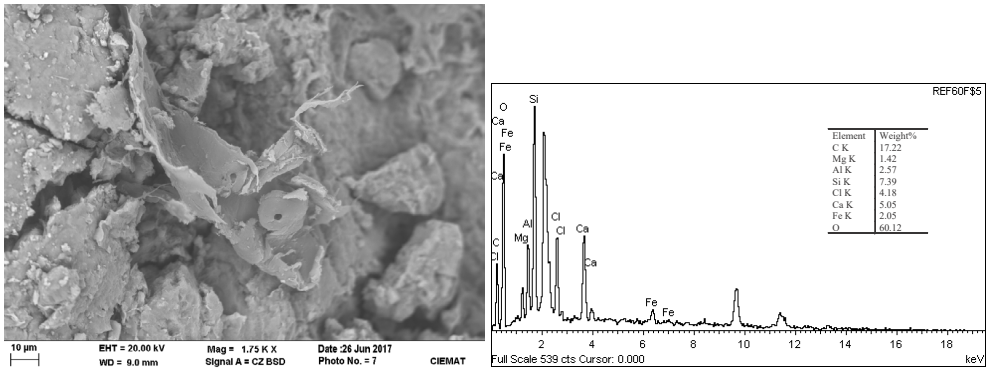

Fig. B-135: SEM photomicrographs from sample WB-42: OM with Cl and Ca

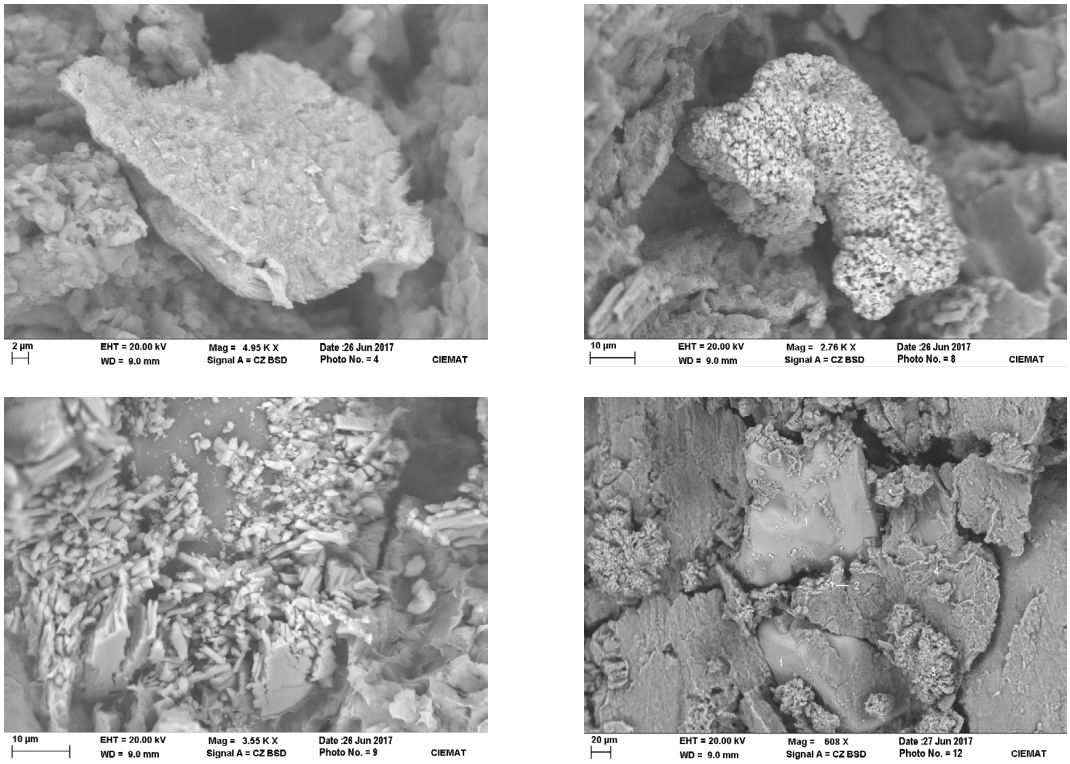

Fig. B-136: SEM photomicrographs from sample WB-42: a) and b) Fe-oxides, c) Fe-Ti-Mn-oxides, d) Fe-Ti-Mn-oxides (1), Hg (Mo,Po) (2), Ca-sulfate (3), smectite (4)

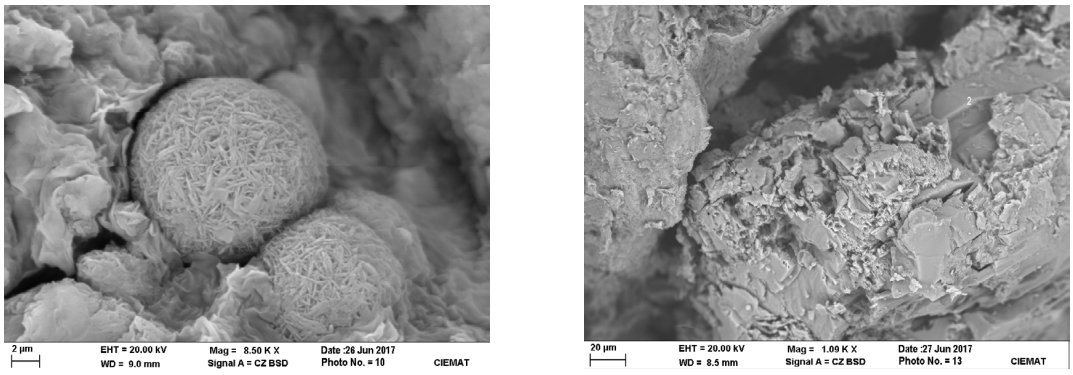

Fig. B-137: SEM photomicrographs from sample WB-42: a) cristobalite, b) Ca-carbonates (1), Ca,Na-plagioclases (2)

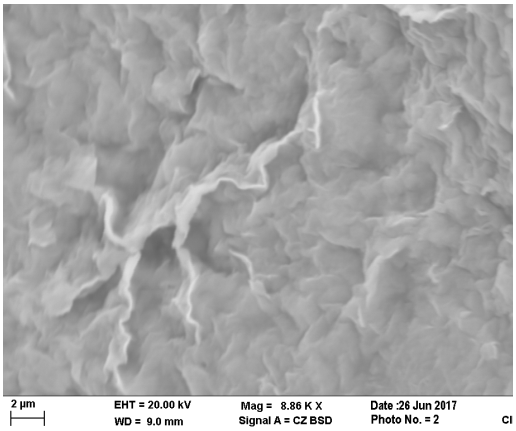

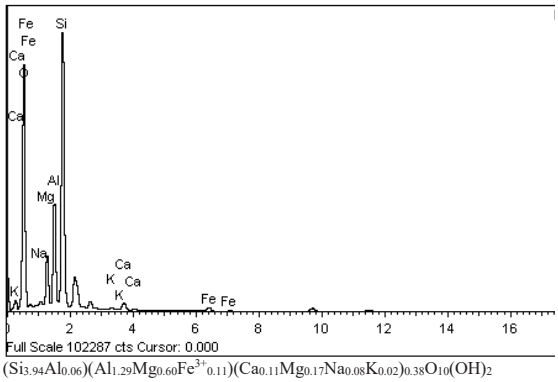

$(Si_{3.94}Al_{0.06})(Al_{1.29}Mg_{0.60}Fe^{3+}_{0.11})(Ca_{0.11}Mg_{0.17}Na_{0.08}K_{0.02})_{0.38}O_{10}(OH)_2$
τ charge = -0.06; O. charge = -0.60
Total charge = -0.66 (τ % = 10 o % = 90); FW (g/mol) = 745.75
(No Mg at interlayer: Σ_{oct} = 2.17; Total charge: -0.31, τ % = 20; o % = 80)

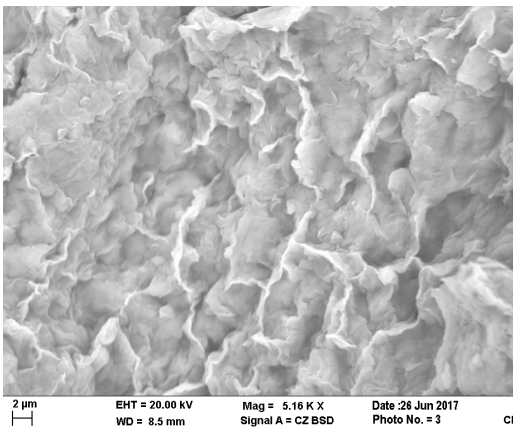

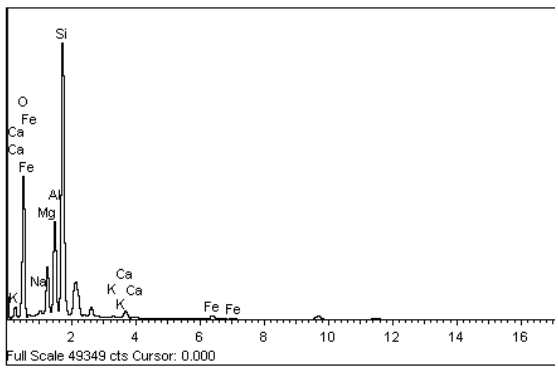

$(Si_{3.99}Al_{0.01})(Al_{1.27}Mg_{0.61}Fe^{3+}_{0.11})(Ca_{0.12}Mg_{0.14}Na_{0.08}K_{0.02})_{0.36}O_{10}(OH)_2$
τ charge = -0.01; O. charge = -0.62
Total charge = -0.63 (τ % = 2 o % = 98); FW (g/mol) = 745.64
(No Mg at interlayer: Σ_{oct} = 2.14; Total charge: -0.34, τ % = 4; o % = 96)

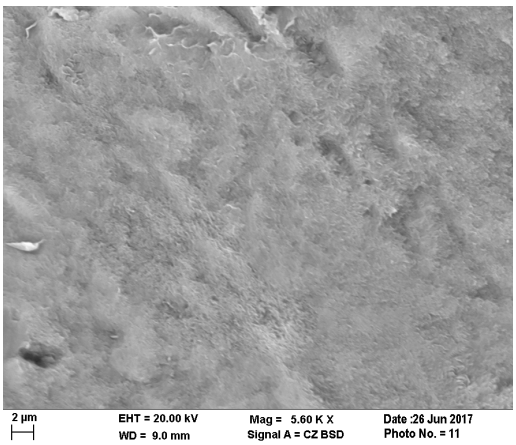

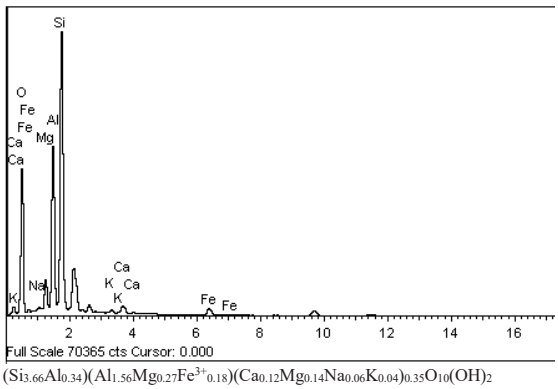

$(Si_{3.66}Al_{0.34})(Al_{1.56}Mg_{0.27}Fe^{3+}_{0.18})(Ca_{0.12}Mg_{0.14}Na_{0.06}K_{0.04})_{0.35}O_{10}(OH)_2$
τ charge = -0.34; O. charge = -0.27
Total charge = -0.60 (τ % = 56 o % = 44); FW (g/mol) = 750.35

Fig. B-138: SEM photomicrographs from sample WB-42: clay minerals

Protrusion BSH-42: black Spot inside heater (Fig. 179)

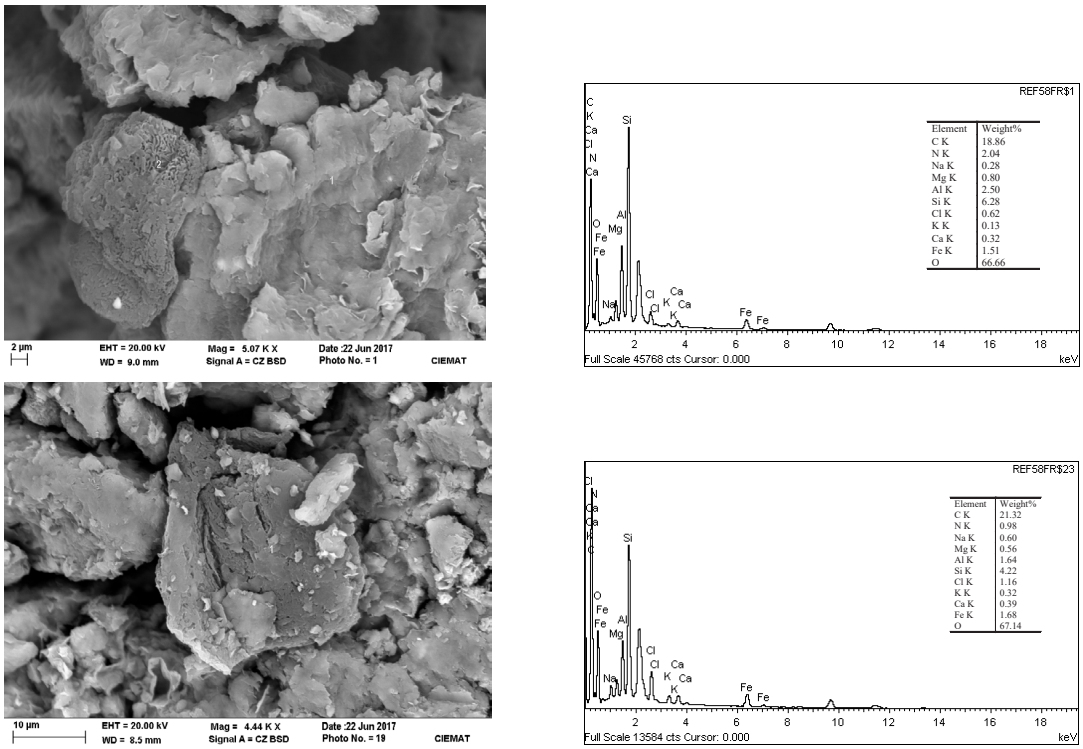

Fig. B-139: SEM photomicrographs from sample BSH-42 Black spot inside heater: a) organic matter with N (1), smectite, b) organic matter with N (see EDX)

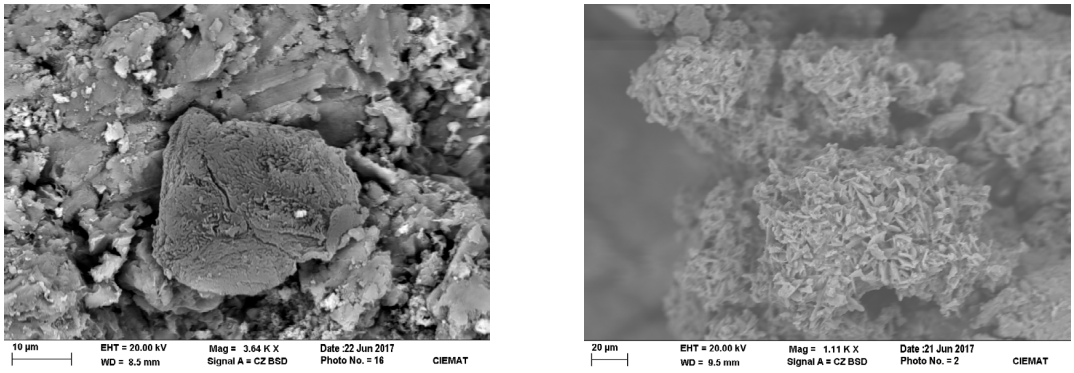

Fig. B-140: SEM photomicrographs from sample BSH-42 Black spot inside heater: a) organic matter with Cl, b) silica

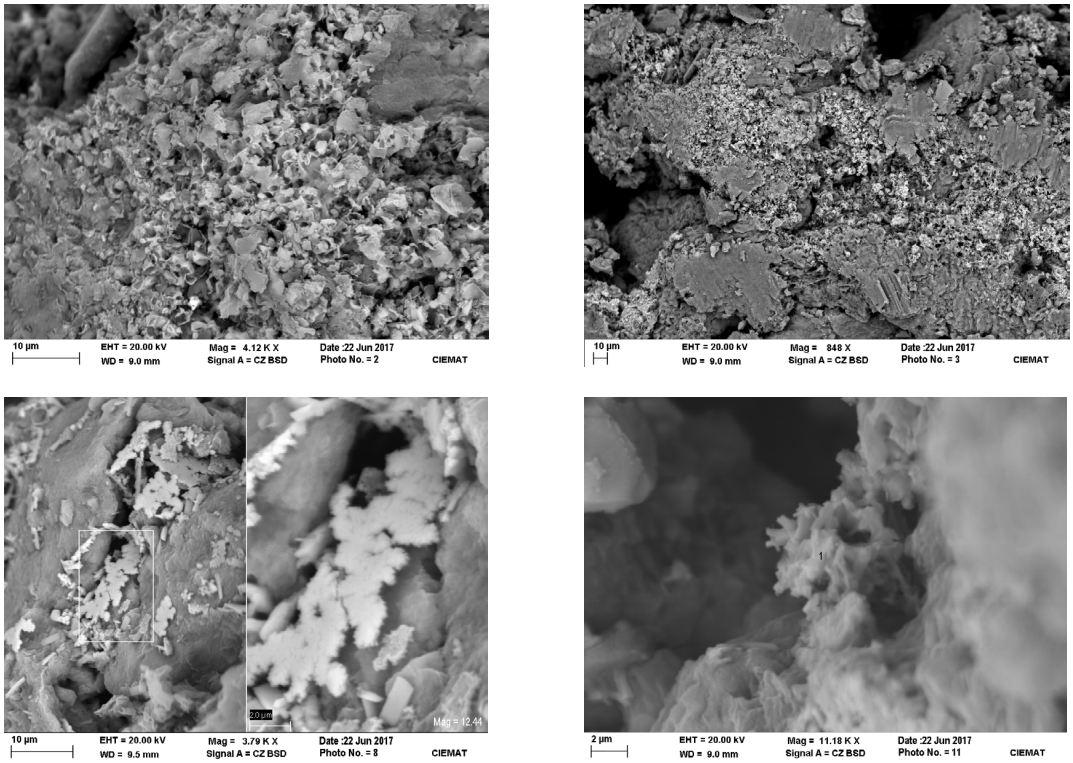

Fig. B-141: SEM photomicrographs from sample BSH-42 Black spot inside heater: Fe-oxides

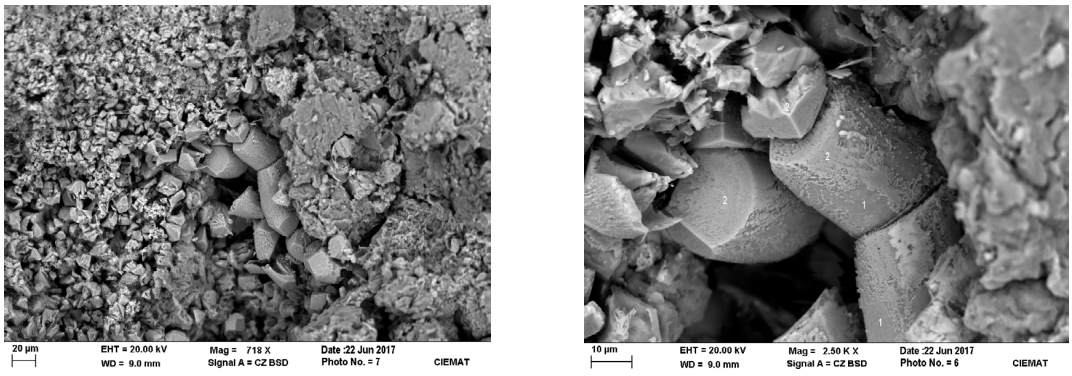

Fig. B-142: SEM photomicrographs from sample BSH-42 Black spot inside heater: a) Fe-carbonates and Fe-oxides, b) Enlargement of a): Fe-carbonate (1), Fe-oxides (2)

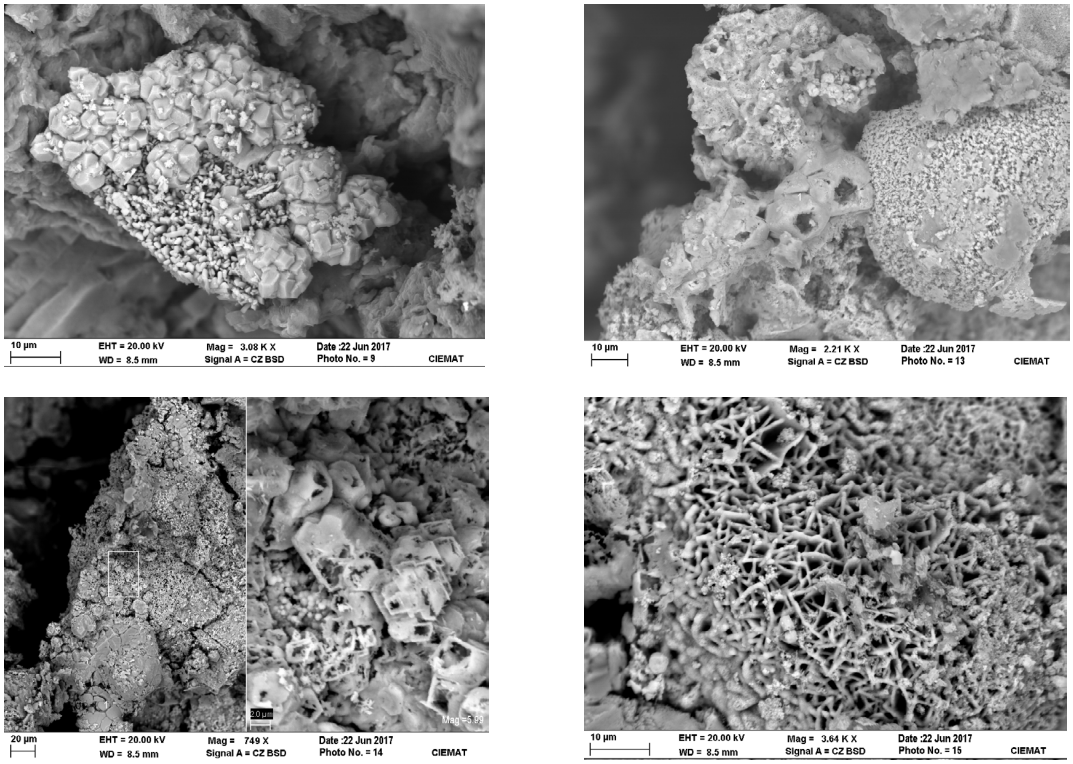

Fig. B-143: SEM photomicrographs from sample BSH-42 Black spot inside heater: a) Fe-carbonates, b) Fe-carbonates (1), Fe-oxides with Cl (2), Fe-carbonates (3), c) Fe-oxides with Cl (1), Fe-carbonates (2), d) Fe-carbonates

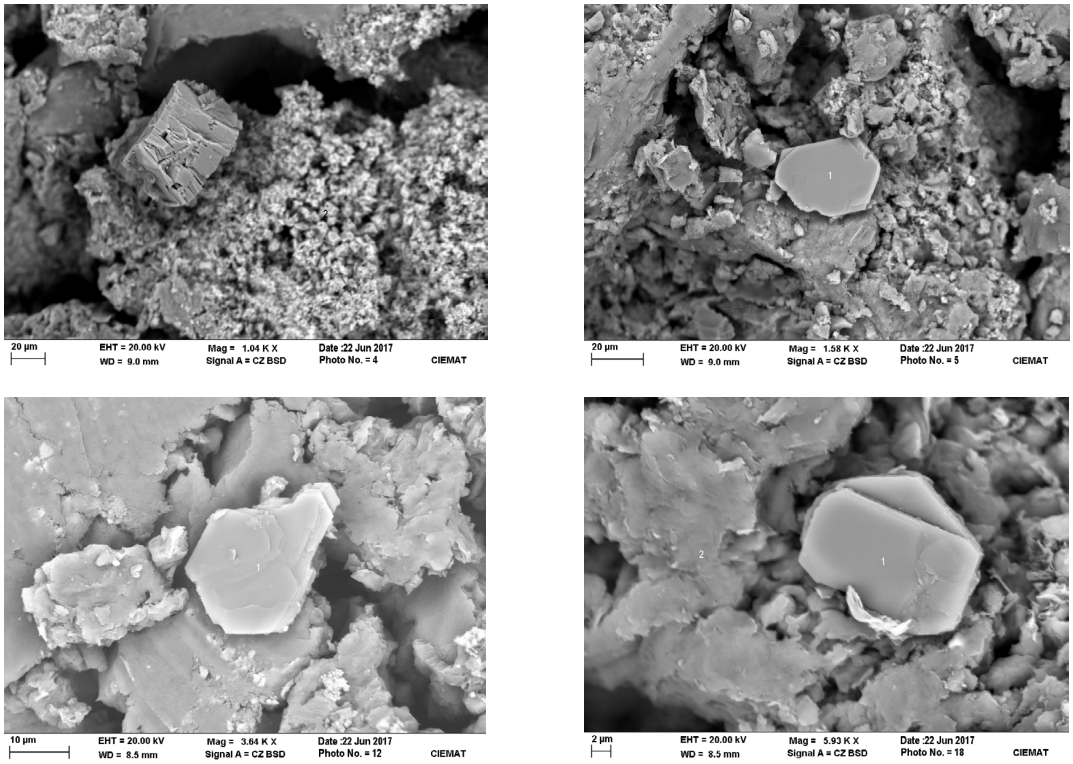

Fig. B-144: SEM photomicrographs from sample BSH-42 Black spot inside heater: a) chlorites (1), Fe-oxides (2), b) and c) chlorites (1), d) chlorite (1), smectite (2)

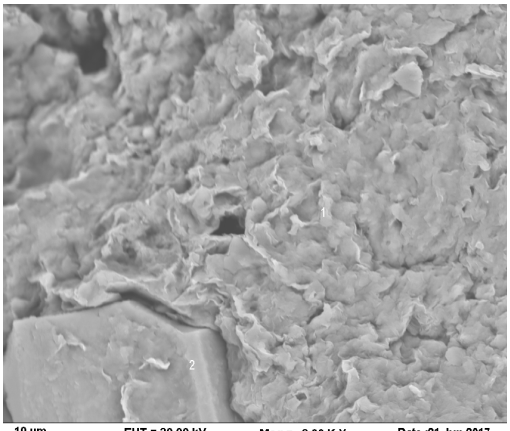

(1) Smectite; (2) apatite

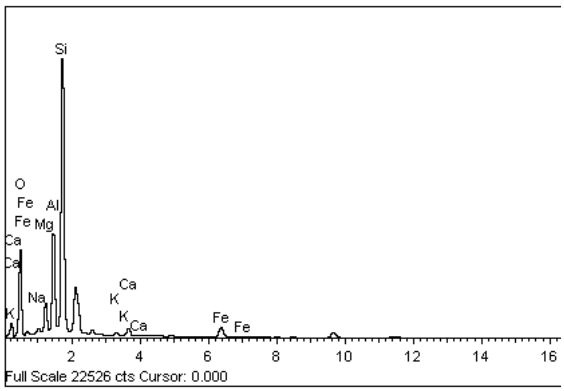

$(Si_{3.97}Al_{0.03})(Al_{1.29}Mg_{0.42}Fe^{3+}_{0.29})(Ca_{0.11}Mg_{0.04}Na_{0.10}K_{0.04})_{0.30}O_{10}(OH)_2$
τ charge = -0.03; O. charge = -0.42
Total charge = -0.45 (τ % = 7 o % = 93); FW (g/mol) = 753.99
(No Mg at interlayer: Σ_{oct} = 2.04; Total charge: -0.36, τ % = 9; o % = 91)

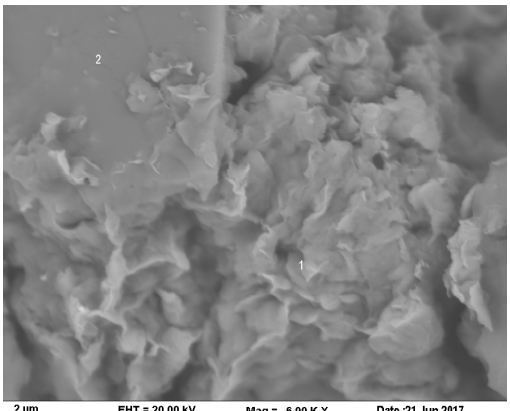

(1) Smectite; (2) plagioclases

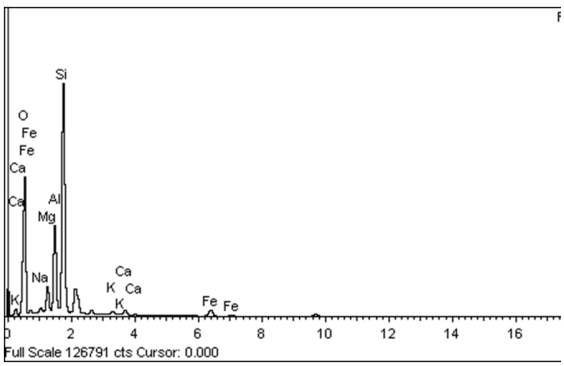

$(Si_{3.96}Al_{0.04})(Al_{1.35}Mg_{0.43}Fe^{3+}_{0.22})(Ca_{0.09}Mg_{0.06}Na_{0.12}K_{0.05})_{0.32}O_{10}(OH)_2$
τ charge = -0.04; O. charge = -0.43
Total charge = -0.47 (τ % = 8 o % = 92); FW (g/mol) = 750.82
(No Mg at interlayer: Σ_{oct} = 2.06; Total charge: -0.35, τ % = 10; o % = 90)

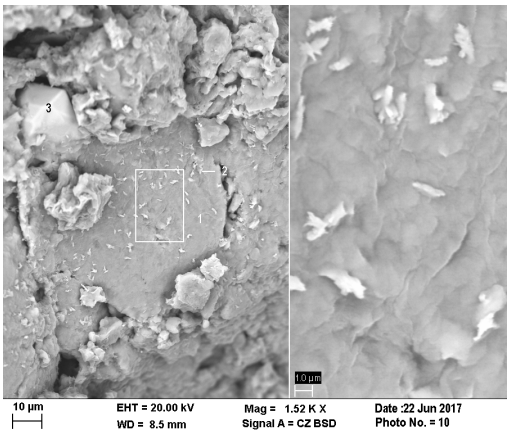

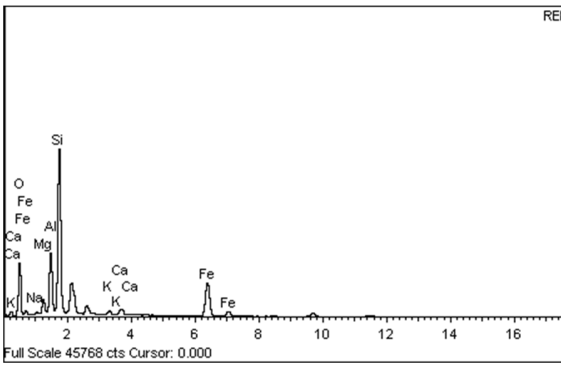

$(Si_{3.30}Al_{0.70})(Al_{0.51}Mg_{0.13}Fe^{3+}_{1.37})(Ca_{0.11}Mg_{0.24}Na_{0.06}K_{0.07})_{0.48}O_{10}(OH)_2$
τ charge = -0.70; O. charge = -0.13
Total charge = -0.83 (τ % = 85 o % = 15); FW (g/mol) = 826.08

Fig. B-145: SEM photomicrographs from sample BSH-42 Black spot inside heater: clay minerals

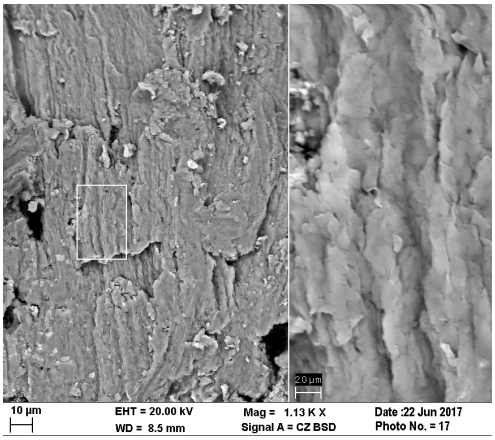

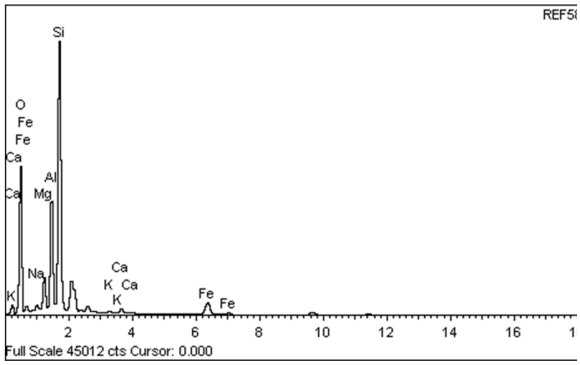

$(Si_{3.84}Al_{0.16})(Al_{1.28}Mg_{0.37}Fe^{3+}_{0.36})(Ca_{0.07}Mg_{0.14}Na_{0.10}K_{0.02})_{0.33}O_{10}(OH)_2$
τ charge = -0.16; O. charge = -0.37
Total charge = -0.53 (τ % = 30 o % = 70); FW (g/mol) = 757.27
(No Mg at interlayer: Σ_{oct} = 2.14; Total charge: -0.26, τ % = 62; o % = 38)

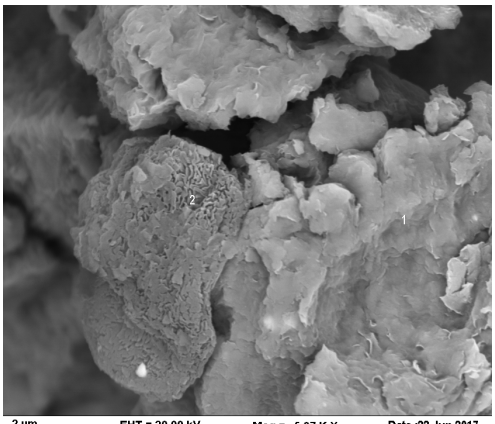

1: clay mineral; 2: carbon: 18.7 w.t. %;
N: 2.04 w.t. %.

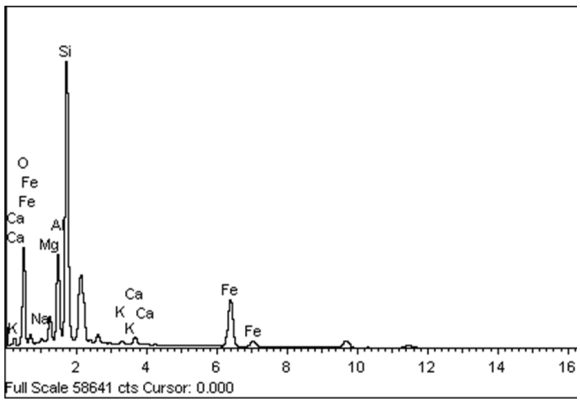

$(Si_{3.93}Al_{0.07})(Al_{1.38}Mg_{0.37}Fe^{3+}_{0.26})(Ca_{0.09}Mg_{0.07}Na_{0.09}K_{0.02})_{0.27}O_{10}(OH)_2$
τ charge = -0.07; O. charge = -0.37
Total charge = -0.43 (τ % = 15 o % = 8); FW (g/mol) = 750.09
(No Mg at interlayer: Σ_{oct} = 2.07; Total charge: -0.30, τ % = 22; o % = 78)

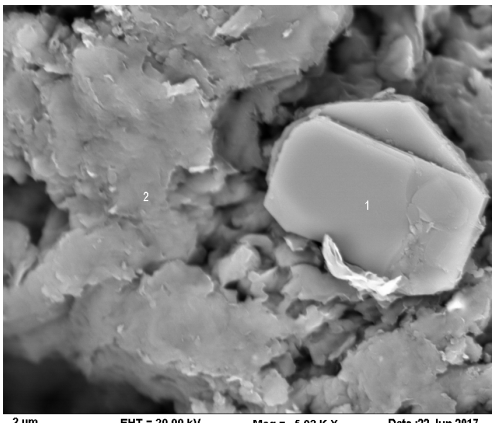

1: chlorite; 2: smectite

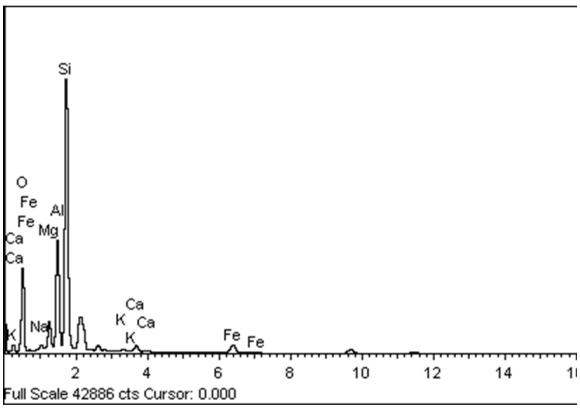

2: $(Si_{3.49}Al_{0.51})(Al_{0.59}Mg_{0.20}Fe^{3+}_{1.22})(Ca_{0.10}Mg_{0.20}Na_{0.07}K_{0.03})_{0.40}O_{10}(OH)_2$
τ charge = -0.50; O. charge = -0.20
Total charge = -0.70 (τ % = 72 o % = 28); FW (g/mol) = 812.30

Fig. B-145: Cont.

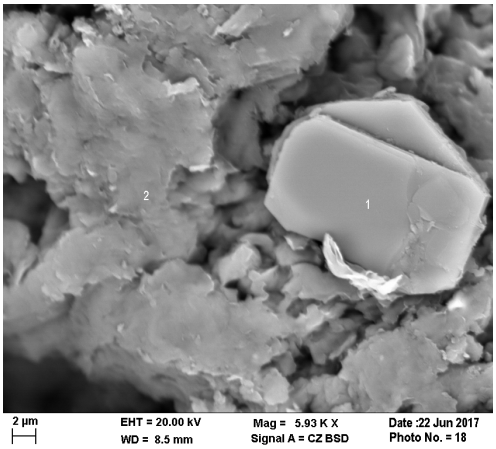

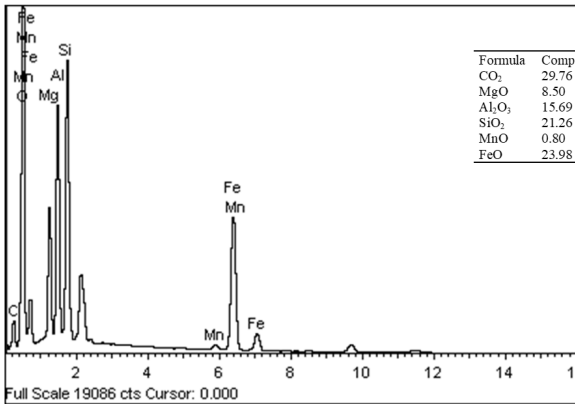

1: chlorite; 2: smectite

Chlorite (1):

$(Si_{2.87}Al_{1.13})^{IV}(Fe^{2+}_{2.71}Mg_{0.08}Mn^{2+}_{0.09\ \ 0.12})^{VI}O_{10}(OH)_2[Al_{1.37}Mg_{1.63}(OH)_6]$

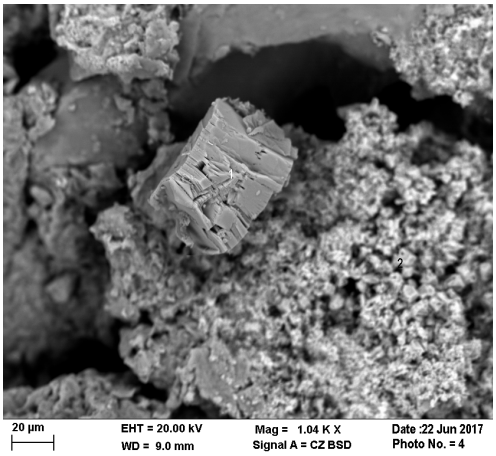

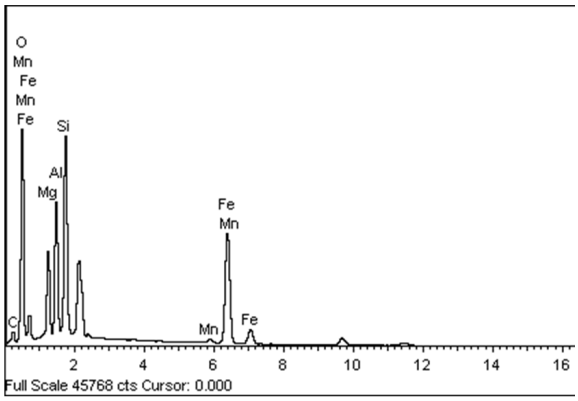

1: chlorite; 2: Fe-oxides and Fe-carbonates

$(Si_{3.61}Al_{0.39})^{IV}(Fe^{2+}_{0.80}Mg_{1.20}Mn^{2+}_{0.11\ \ 0.89})^{VI}O_{10}(OH)_2[Al_{2.18}Mg_{0.82}(OH)_6]$ + 49.1 %wt. $FeCO_3$

Fig. B-145: Cont.

Protrusion GB-42: Inside Heater Black (Fig. 179)

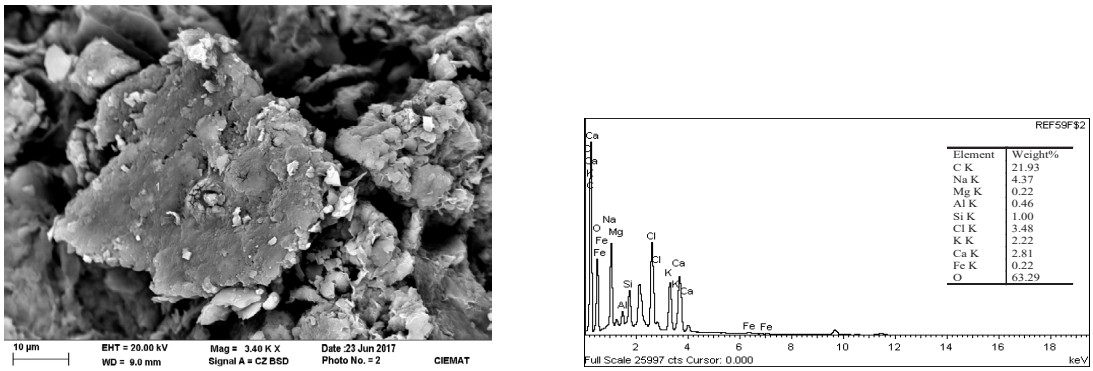

Fig. B-146: SEM photomicrographs from sample GB-42 inside heater black: a) organic matter with Cl,K, b) EDX from 1)

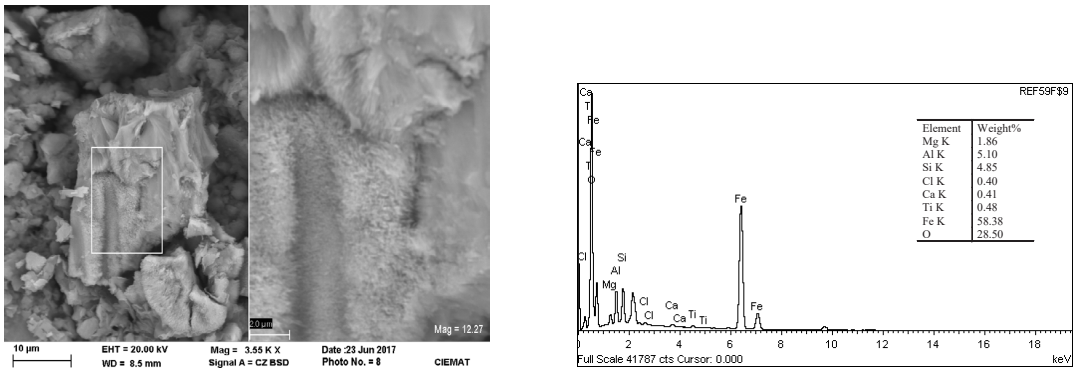

Fig. B-147: SEM photomicrographs from sample GB-42 inside heater black: Fe-oxide with Cl

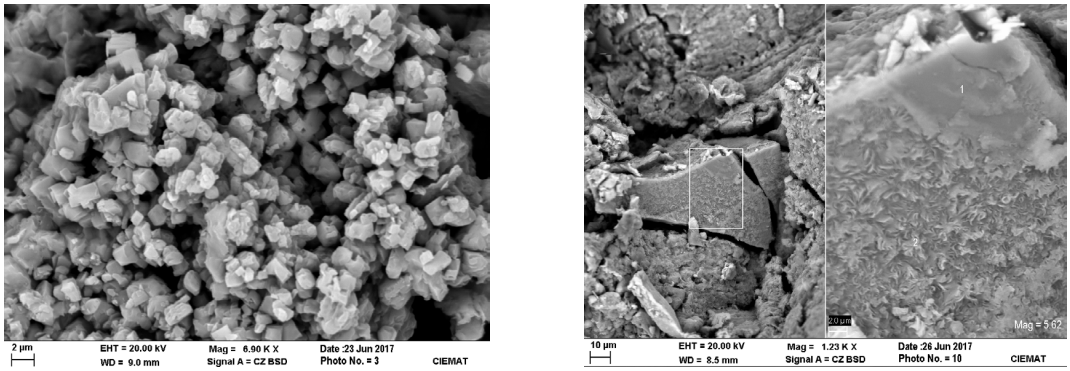

Fig. B-148: SEM photomicrographs from sample GB-42 inside heater black: a) Ca-carbonates, b) silica (1) and (2)

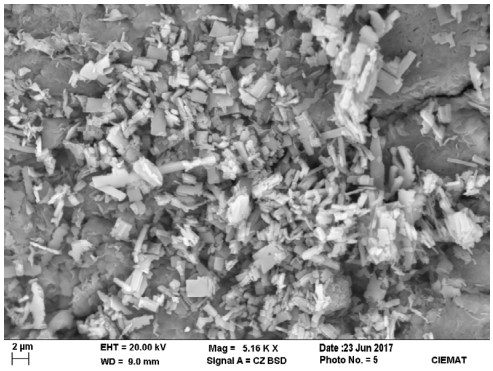

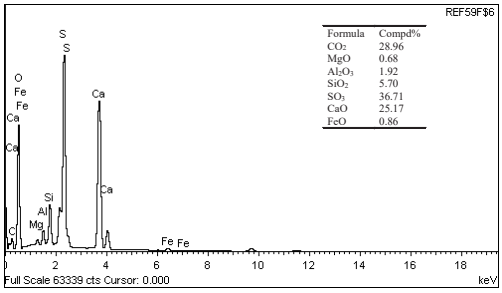

Fig. B-149: SEM photomicrographs from sample GB-42 inside heater black: a) Ca-sulfates with C, b) EDX from a)

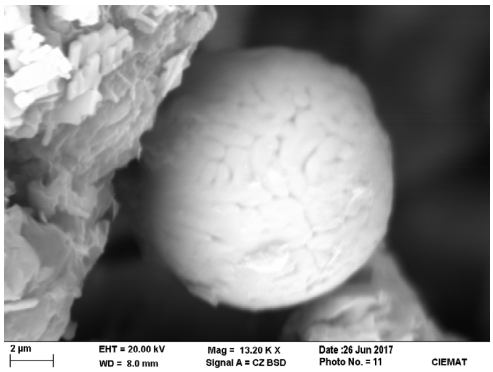

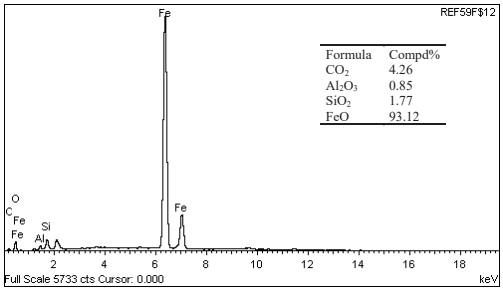

Fig. B-150: SEM photomicrographs from sample GB-42 inside heater black: a) Fe-oxide with some C, b) EDX from a)

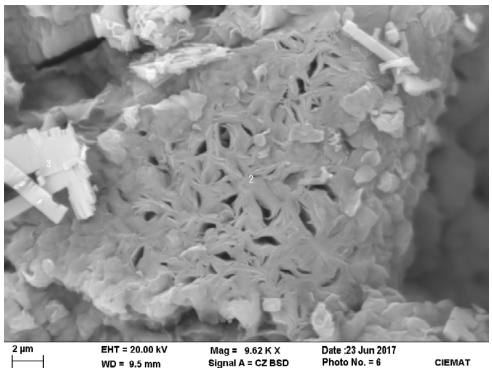

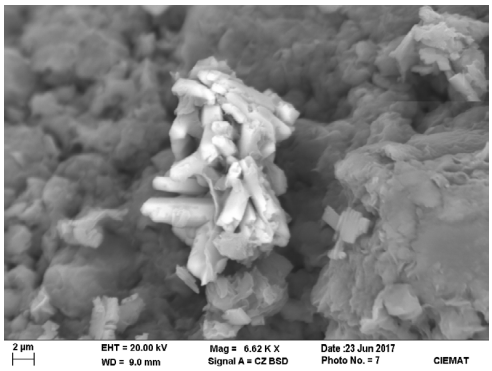

Fig. B-151: SEM photomicrographs from sample GB-42 inside heater black: a) Barite-celestine (1), smectite (2), Ca-sulfates (3), b) Barite-celestine from a)

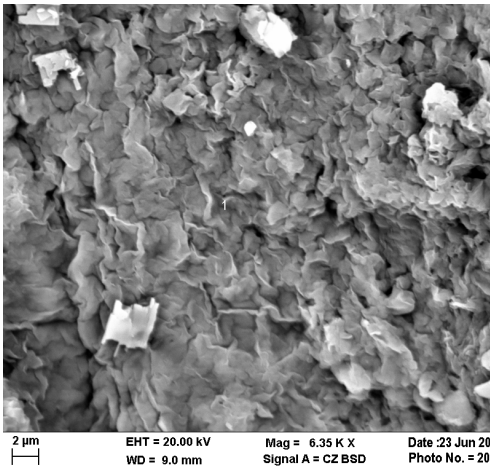

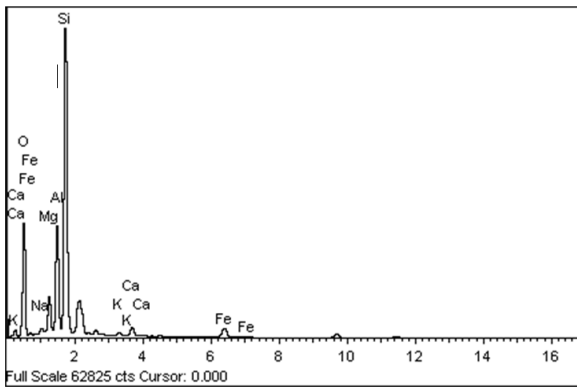

(1) Smectite, (2) Ca-sulfate

$(Si_{3.97}Al_{0.03})^{IV}(Al_{1.26}Mg_{0.47}Fe^{3+}_{0.26})^{VI}(Ca_{0.13}Mg_{0.05}Na_{0.11}K_{0.04})_{0.33}O_{10}(OH)_2$
τ charge = -0.03; O. charge = -0.47
Total charge = -0.50 (τ % = 6 o % = 94); FW (g/mol) = 753.81
(No Mg at interlayer: Σ_{oct} = 2.05; Total charge: -0.40, τ % = 8; o % = 92)

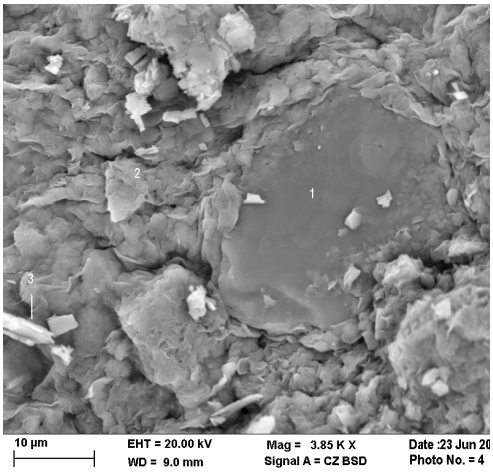

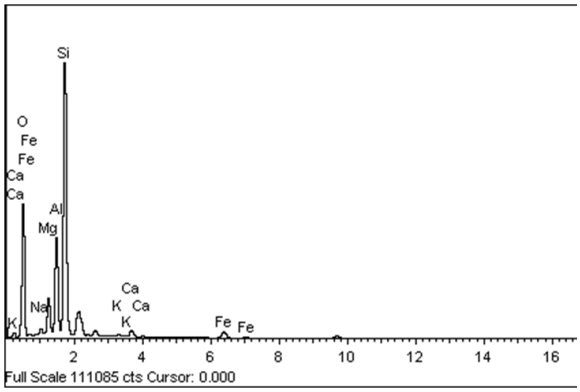

(1) Kaolinite, smectite (2), Ca-sulfate (3)

$(Si_{3.99}Al_{0.01})^{IV}(Al_{1.31}Mg_{0.51}Fe^{3+}_{0.19})^{VI}(Ca_{0.11}Mg_{0.08}Na_{0.13}K_{0.02})_{0.33}O_{10}(OH)_2$
τ charge = -0.01; O. charge = -0.51
Total charge = -0.52 (τ % = 2 o % = 98); FW (g/mol) = 748.43
(No Mg at interlayer: Σ_{oct} = 2.08; Total charge: -0.36, τ % = 3; o % = 97)

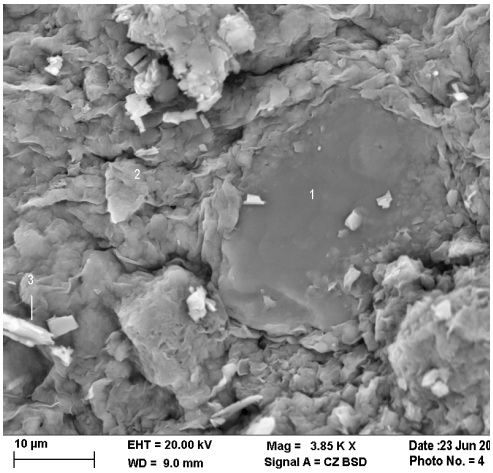

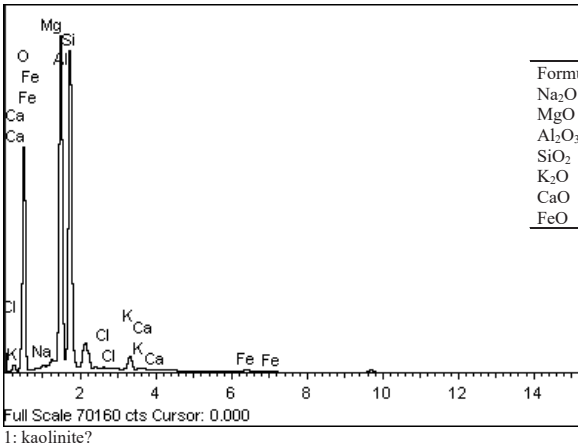

1: kaolinite?

(1) Kaolinite?, smectite (2), Ca-sulfate (3)

Fig. B-152: SEM photomicrographs from sample GB-42 Black spot inside heater: clay minerals

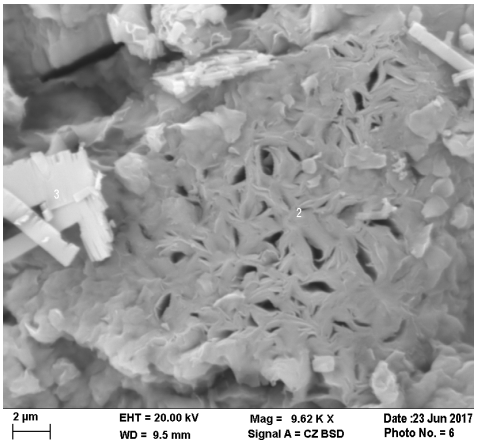

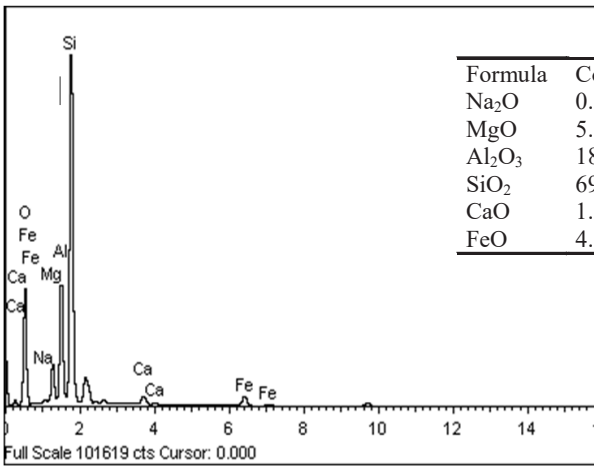

Formula	C
Na_2O	0.
MgO	5.
Al_2O_3	18
SiO_2	69
CaO	1.
FeO	4.

2: smectite

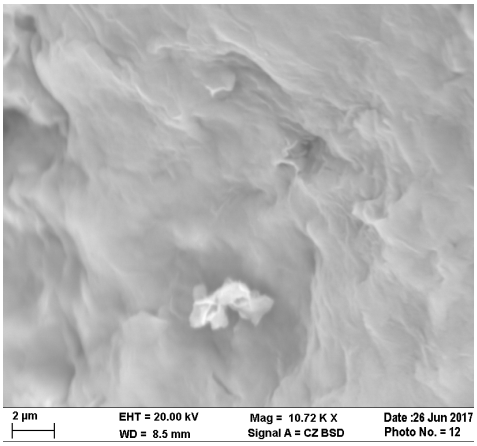

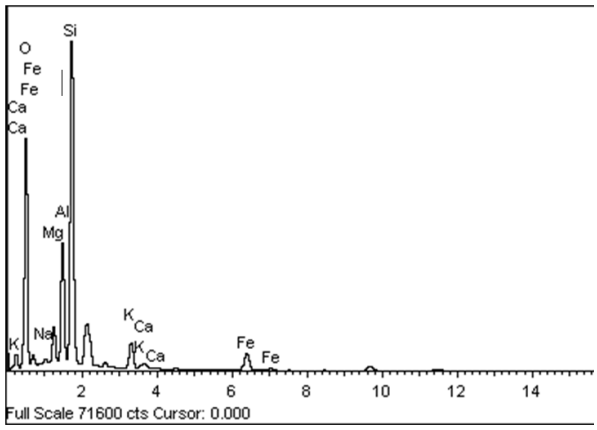

$(Si_{3.79}Al_{0.21})^{IV}(Al_{1.14}Mg_{0.44}Fe^{3+}_{0.41})^{VI}(Ca_{0.06}Mg_{0.05}Na_{0.09}K_{0.33})_{0.53}O_{10}(OH)_2$
τ charge = -0.21; O. charge = -0.44
Total charge = -0.65 (τ % = 32 o % = 68); FW (g/mol) = 778.98
(No Mg at interlayer: Σ_{oct} = 2.05; Total charge: -0.54, τ % = 38; o % = 62)

Fig. B-152: Cont.

Protrusion RNW42: Black and white particles (Fig. 180)

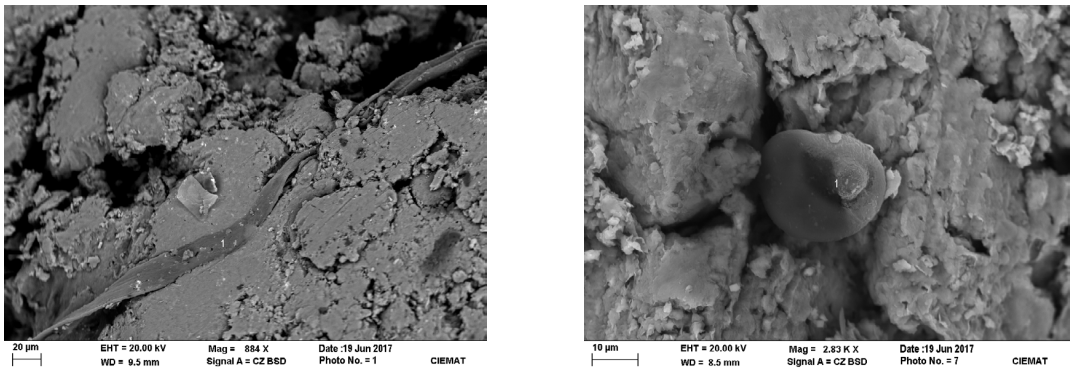

Fig. B-153: SEM photomicrographs from sample RNW42: a) Organic matter, OM, (1), b) OM (1) with Cl

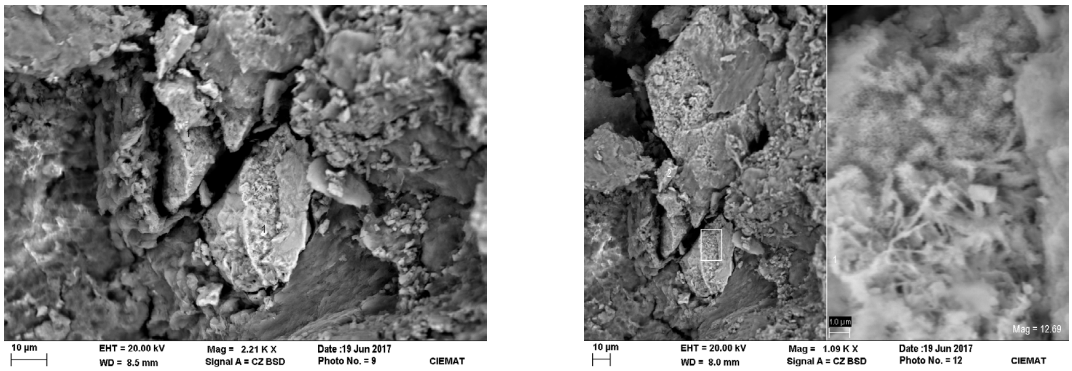

Fig. B-154: SEM photomicrographs from sample RNW42: a) Fe-carbonates (1), b) enlargement of 1)

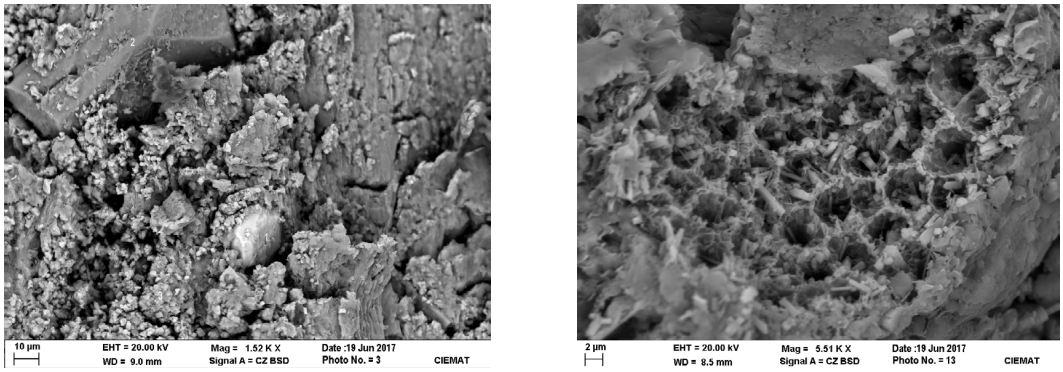

Fig. B-155: SEM photomicrographs from sample RNW42: a) zircon (1), Na-Ca-plagioclases, Ca-sulfates (3), b) Ca-sulfates

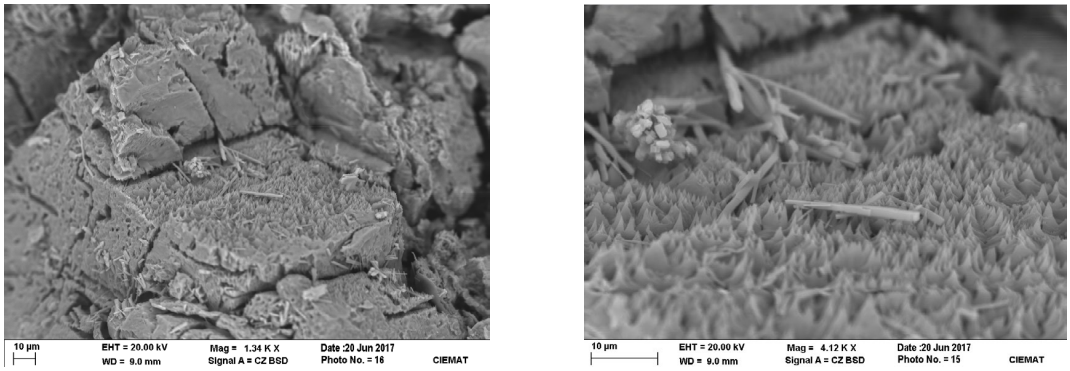

Fig. B-156: SEM photomicrographs from sample RNW42: a) Dolomite (1), Ca-sulfates (2), b) enlargement of a)

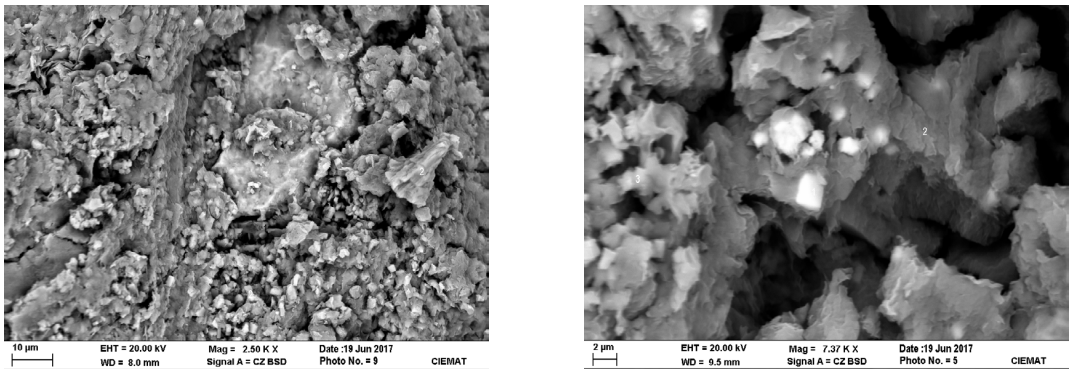

Fig. B-157: SEM photomicrographs from sample RNW42: a) Ca-carbonate (1), Ca-sulfate (2), b) Monazite (1), smectite (2)

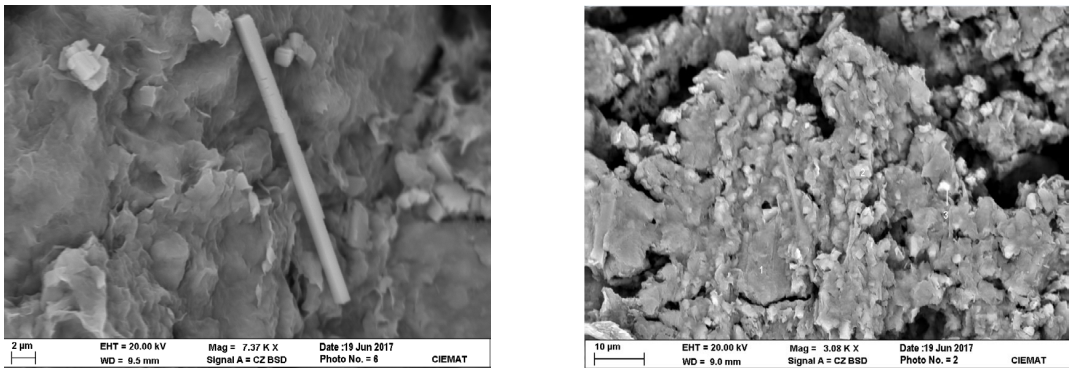

Fig. B-158: SEM photomicrographs from sample RNW42: a) Ca-sulfate, b) Smectite (1), Ca-sulfate (2), Fe,Ti-oxides (3)

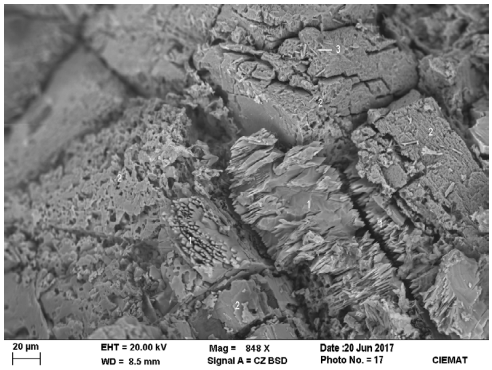

Fig. B-159: SEM photomicrographs from sample RNW42: Ca-carbonate and Mn (1), dolomite (2), Ca-sulfate (3)

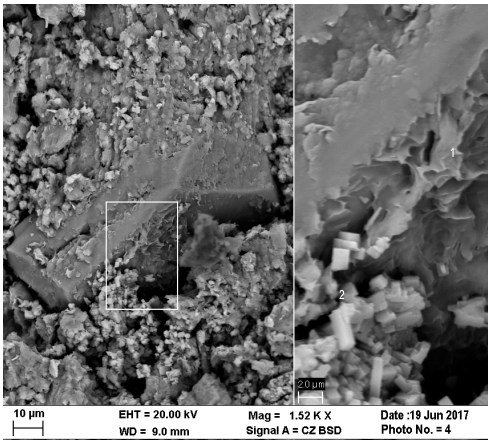

1: clay mineral: 2: Ca-sulfates

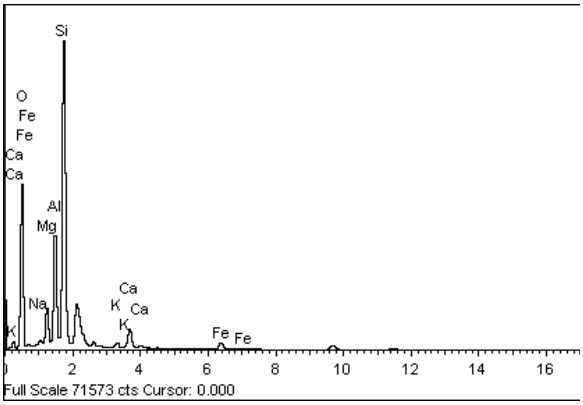

$(Si_{3.94}Al_{0.06})^{IV}(Al_{1.25}Mg_{0.52}Fe^{3+}_{0.19\ \ 0.04})^{VI}(Ca_{0.28}Na_{0.09}K_{0.06})_{0.43}O_{10}(OH)_2$
τ charge = -0.06; O. charge = -0.64
Total charge = -0.70 (τ % = 9 o % = 91); FW (g/mol) = 753.12

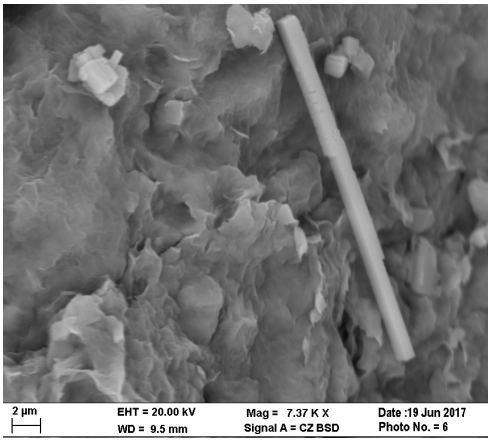

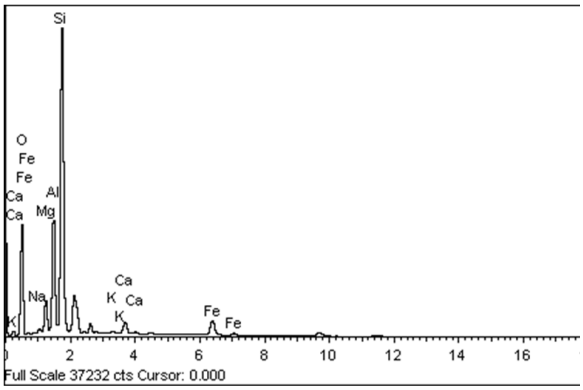

$(Si_{3.87}Al_{0.13})^{IV}(Al_{1.20}Mg_{0.40}Fe^{3+}_{0.04})^{VI}(Ca_{0.16}Mg_{0.05}Na_{0.07}K_{0.03})_{0.31}O_{10}(OH)_2$
τ charge = -0.13; O. charge = -0.40
Total charge = -0.53 (τ % = 24 o % = 76); FW (g/mol) = 762.12
(No Mg at interlayer: Σ_{oct} = 2.05; Total charge: -0.42, τ % = 30; o % = 70)

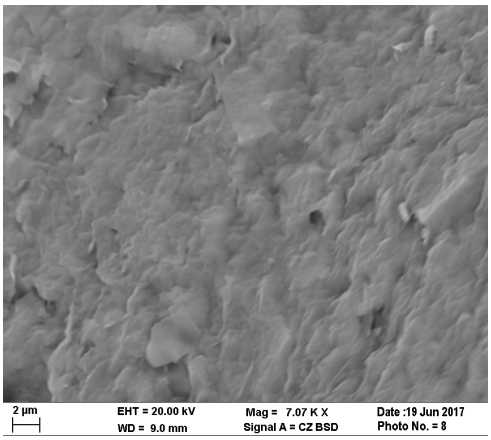

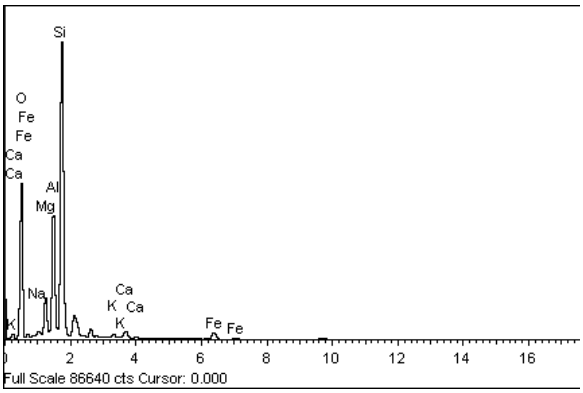

$(Si_{3.92}Al_{0.08})^{IV}(Al_{1.37}Mg_{0.43}Fe^{3+}_{0.20})^{VI}(Ca_{0.10}Mg_{0.09}Na_{0.08}K_{0.04})_{0.31}O_{10}(OH)_2$
τ charge = -0.08; O. charge = -0.43
Total charge = -0.51 (τ % = 15 o % = 85); FW (g/mol) = 749.25
(No Mg at interlayer: Σ_{oct} = 2.09; Total charge: -0.33, τ % = 23; o % = 77)

Fig. B-160: SEM photomicrographs from sample RNW42: clay minerals

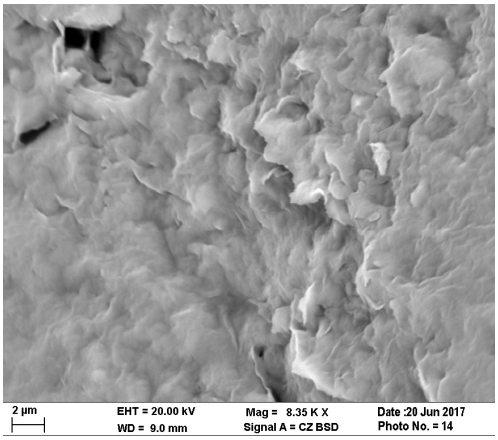

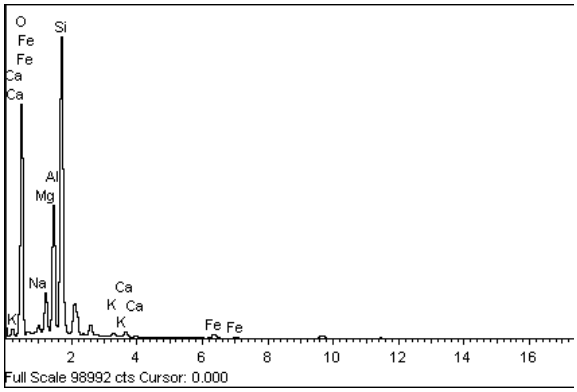

$(Si_{3.91}Al_{0.09})^{IV}(Al_{1.43}Mg_{0.46}Fe^{3+}_{0.11})^{VI}(Ca_{0.08}Mg_{0.10}Na_{0.13}K_{0.05})_{0.36}O_{10}(OH)_2$
τ charge = -0.09; O. charge = -0.46
Total charge = -0.55 (τ % = 17 o % = 83); FW (g/mol) = 745.65
(No Mg at interlayer: Σ_{oct} = 2.10; Total charge: -0.35, τ % = 26; o % = 74)

Fig. B-160: Cont.

Protrusion RNW-42: grey particles (Fig. 180)

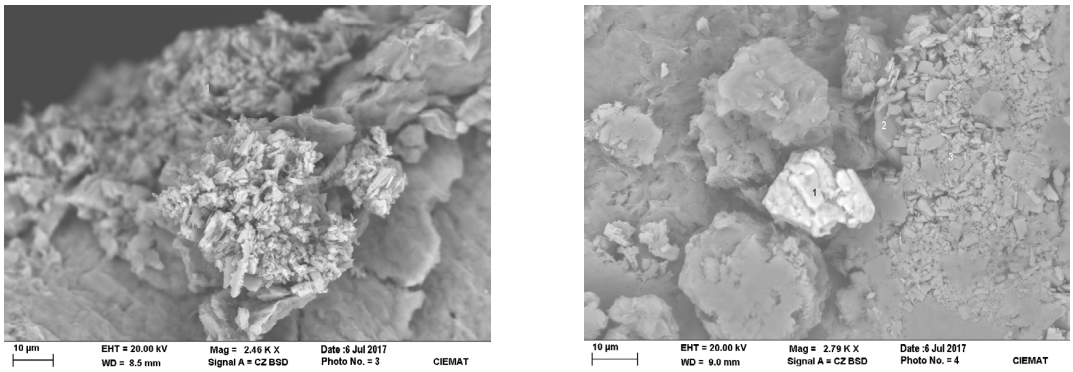

Fig. B-161: SEM photomicrographs from sample RNW-42 grey particles: a) Ca-sulfates, b) Barite(Sr) (1), Plagioclase (2), Gypsum (3)

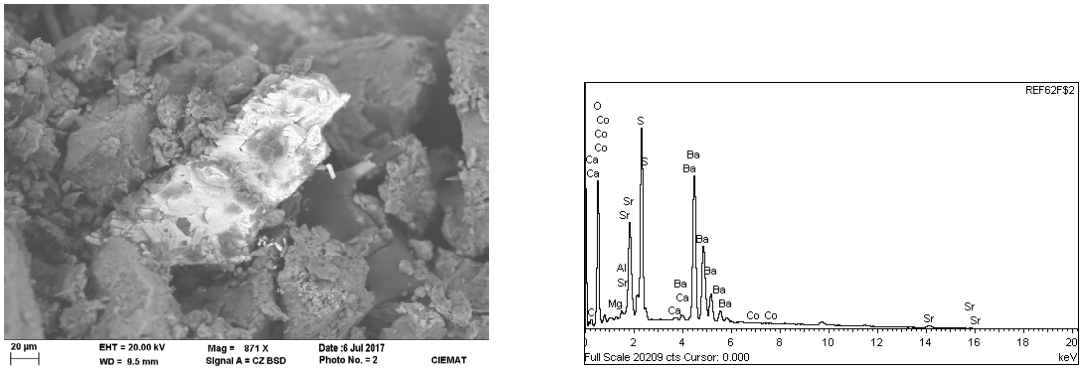

Fig. B-162: SEM photomicrographs from sample RNW-42 grey particles: barite-celestine

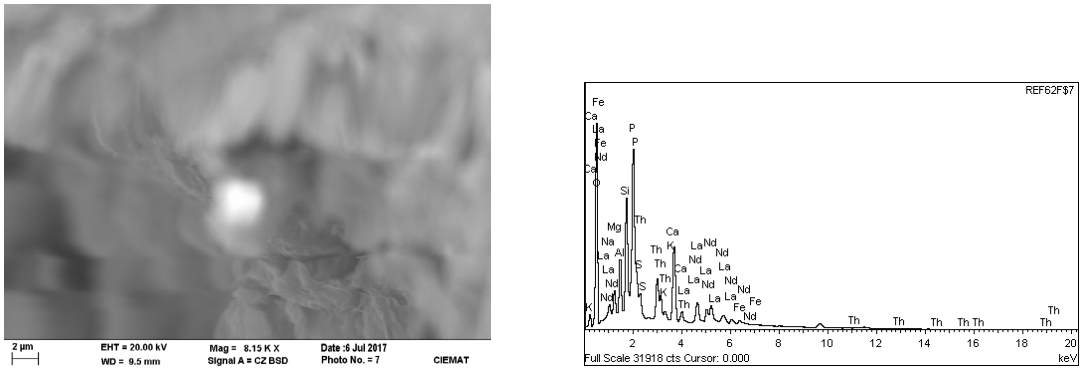

Fig. B-163: SEM photomicrographs from sample RNW-42 grey particles: apatite

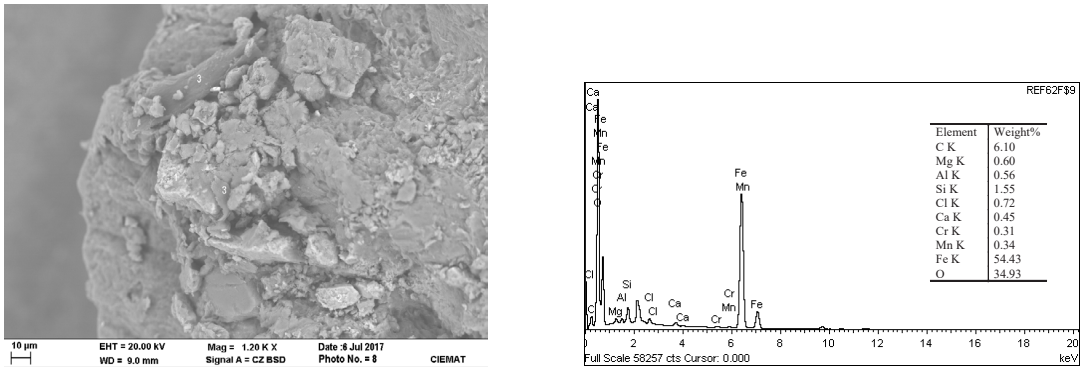

Fig. B-164: SEM photomicrographs from sample RNW-42 grey particles: Fe-carbonate with Cu and Cl (1), Fe-carbonate with Cr and Cl (2), OM with Cl (3) with Cl, b) EDX from (2)

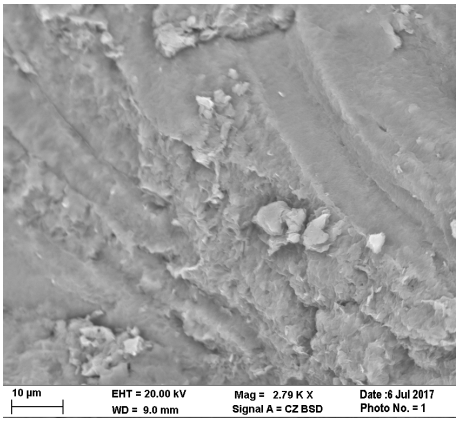

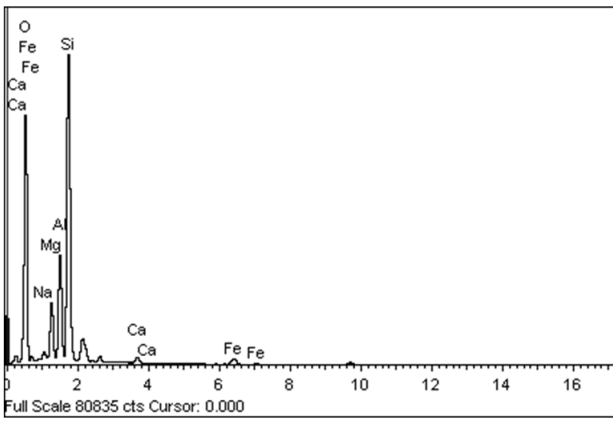

$(Si_{3.95}Al_{0.05})^{IV}(Al_{1.22}Mg_{0.62}Fe^{3+}_{0.16})^{VI}(Ca_{0.08}Mg_{0.18}Na_{0.14})_{0.40}O_{10}(OH)_2$
τ charge = -0.05; O. charge = -0.62
Total charge = -0.67 (τ % = 7 o % = 93); FW (g/mol) = 748.41
(No Mg at interlayer: Σ_{oct} = 2.18; Total charge: -0.30, τ % = 16; o % = 84)

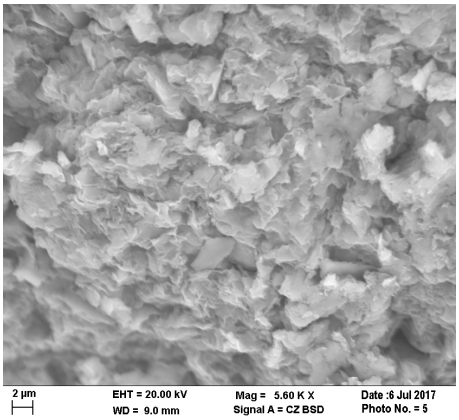

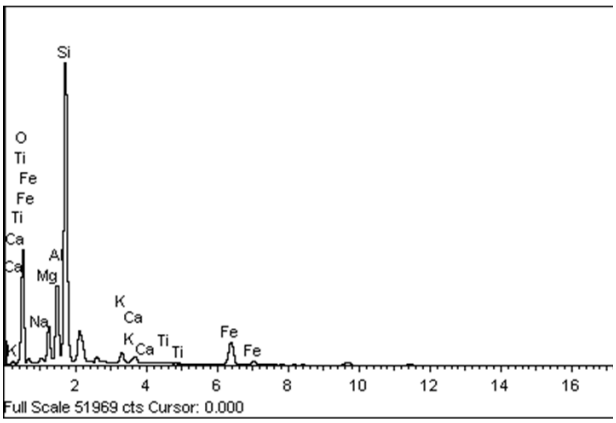

$(Si_{3.90}Al_{0.10})^{IV}(Al_{0.87}Mg_{0.47}Fe^{3+}_{0.64}Ti^{4+}_{0.02})^{VI}(Ca_{0.09}Mg_{0.08}Na_{0.08}K_{0.14})_{0.38}O_{10}(OH)_2$
τ charge = -0.10; O. charge = -0.45
Total charge = -0.55 (τ % = 18 o % = 82); FW (g/mol) = 781.24
(No Mg at interlayer: Σ_{oct} = 2.08; Total charge: -0.40, τ % = 27; o % = 75)

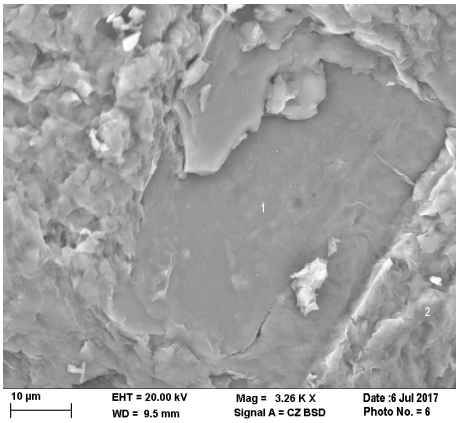

1: I/Sm ML?; 2: smectite

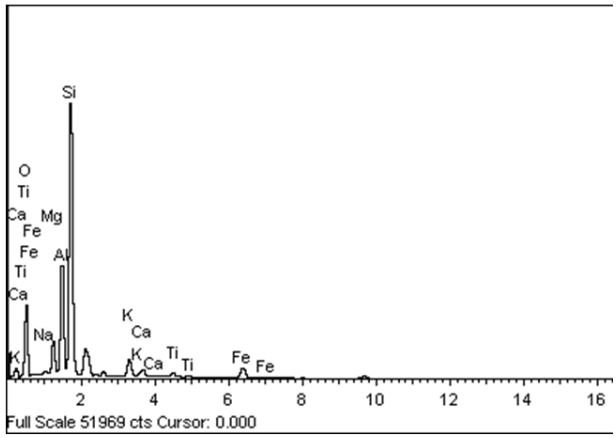

1:$(Si_{3.79}Al_{0.21})^{IV}(Al_{1.19}Mg_{0.46}Fe^{3+}_{0.29}Ti^{4+}_{0.06})^{VI}(Ca_{0.10}Mg_{0.05}Na_{0.06}K_{0.24})_{0.45}O_{10}(OH)_2$
τ charge = -0.21; O. charge = -0.39
Total charge = -0.60 (τ % = 35 o % = 65); FW (g/mol) = 769.28
(No Mg at interlayer: Σ_{oct} = 2.05; Total charge: -0.51, τ % = 42; o % = 58)

Fig. B-165: SEM photomicrographs from sample RNW-42 grey particles: clay minerals

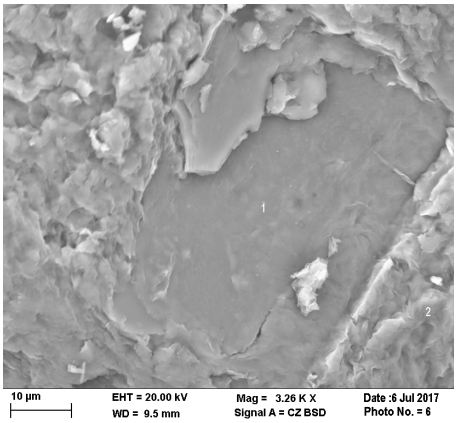

1: illite; 2: smectite

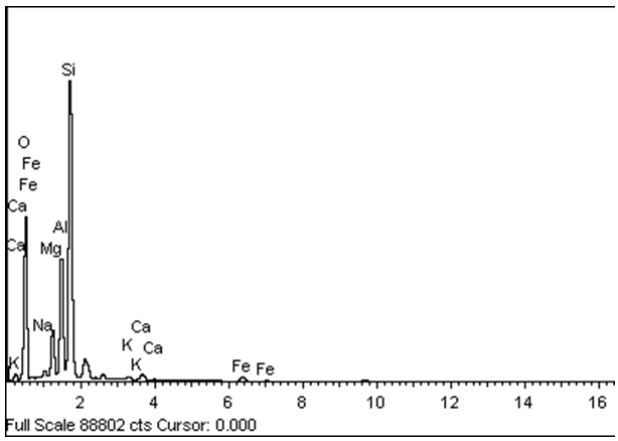

2:$(Si_{3.91}Al_{0.09})^{IV}(Al_{1.34}Mg_{0.52}Fe^{3+}_{0.13})^{VI}(Ca_{0.09}Mg_{0.14}Na_{0.12}K_{0.04})_{0.38}O_{10}(OH)_2$
τ charge = -0.09; O. charge = -0.52
Total charge = -0.61 (τ % = 14 o % = 86); FW (g/mol) = 747.40
(No Mg at interlayer: Σ_{oct} = 2.14; Total charge: -0.33, τ % = 26; o % = 74)

Fig. B-165: Cont.

Protrusion RV-42: green particles (Fig. 180)

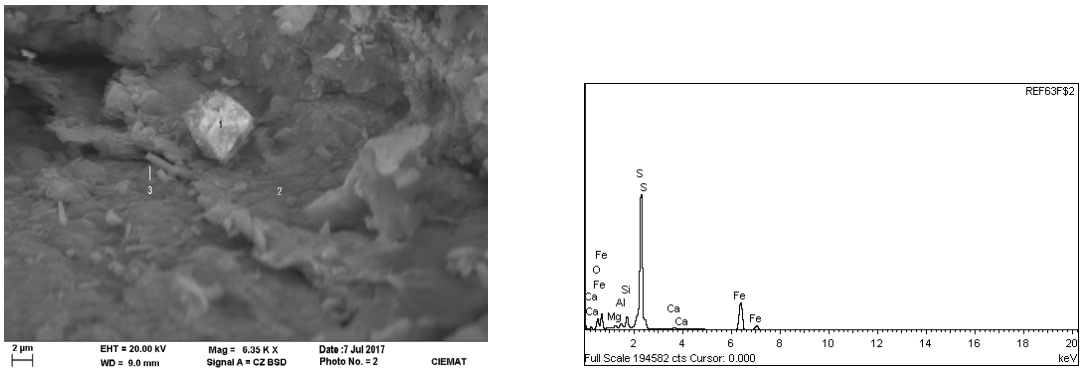

Fig. B-166: SEM photomicrographs from sample RV-42: pyrite (1), smectite (2), gypsum (3)

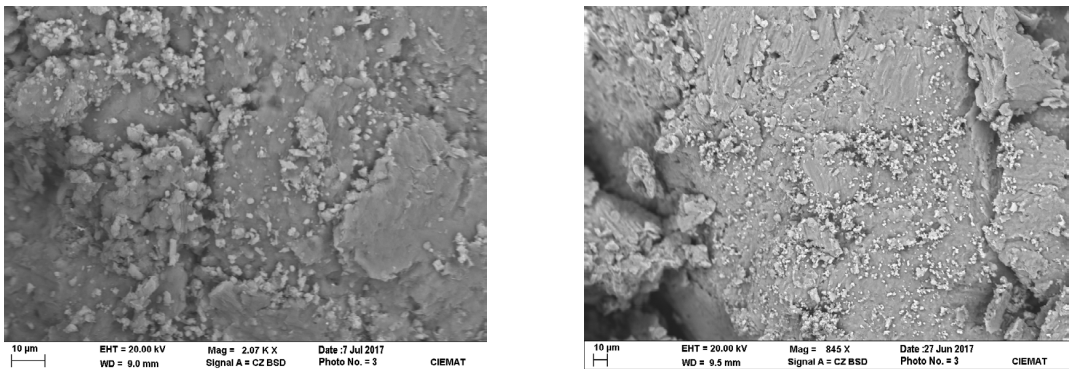

Fig. B-167: SEM photomicrographs from sample RV-42: a) and b) Ca-sulfates

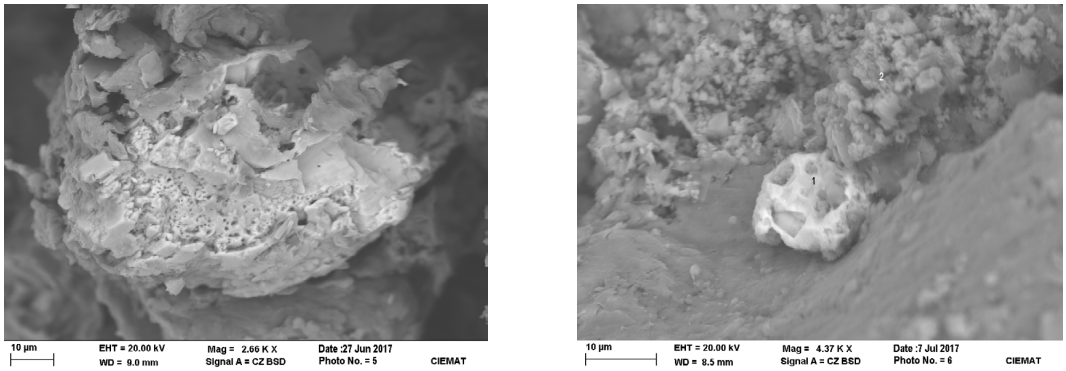

Fig. B-168: SEM photomicrographs from sample RV-42: a) Barite-celestine, b) Barite (1), gypsum (2)

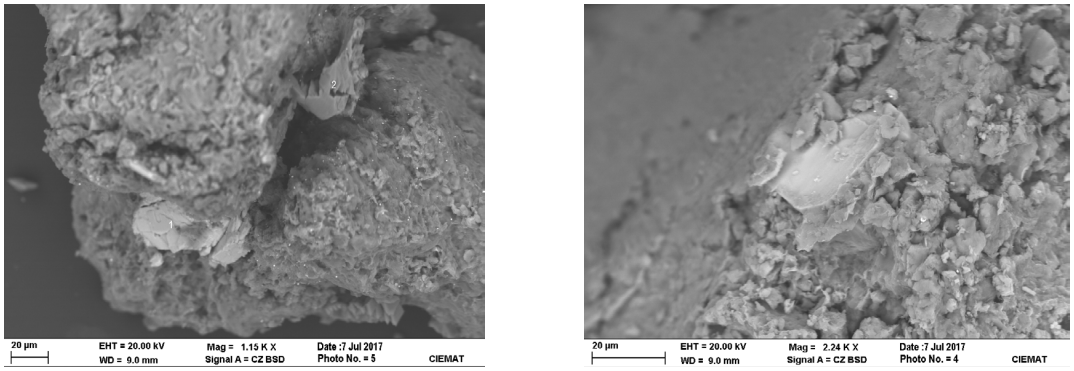

Fig. B-169: SEM photomicrographs from sample RV-42: a) Barite-celestine (1), Ca-carbonate (2) and Hg (points), b) zircon

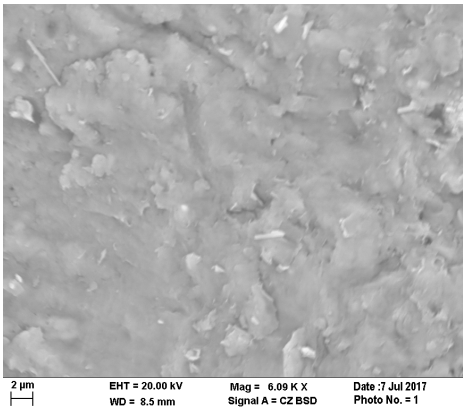

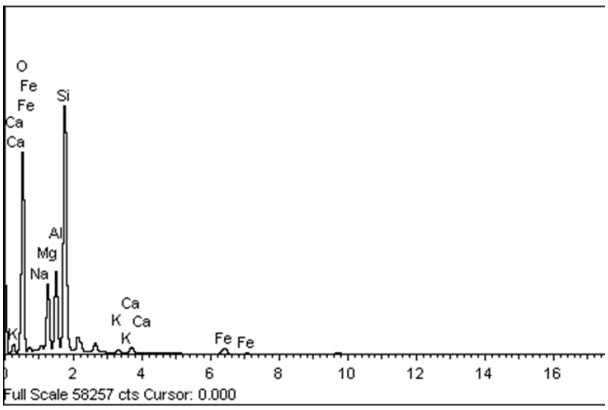

$(Si_{3.83}Al_{0.17})^{IV}(Al_{1.01}Mg_{0.79}Fe^{3+}_{0.21})^{VI}(Ca_{0.09}Mg_{0.33}Na_{0.08}K_{0.04})_{0.54}O_{10}(OH)_2$
τ charge = -0.17; O. charge = -0.79
Total charge = -0.96 (τ % = 17 o % = 73); FW (g/mol) = 757.72
(No Mg at interlayer: Σ_{oct} = 2.33; Total charge: -0.30, τ % = 56; o % = 44)

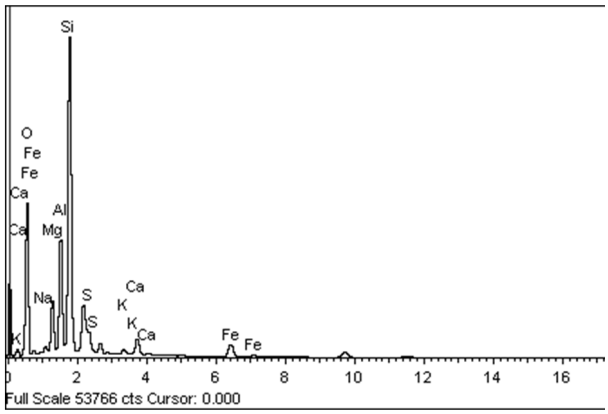

$(Si_{3.83}Al_{0.17})^{IV}(Al_{1.12}Mg_{0.56}Fe^{3+}_{0.33})^{VI}(Ca_{0.14}Mg_{0.14}Na_{0.10}K_{0.06})_{0.45}O_{10}(OH)_2$
τ charge = -0.17; O. charge = -0.56
Total charge = -0.73 (τ % = 24 o % = 76); FW (g/mol) = 764.10
(No Mg at interlayer: Σ_{oct} = 2.14; Total charge: -0.45, τ % = 38; o % = 62)

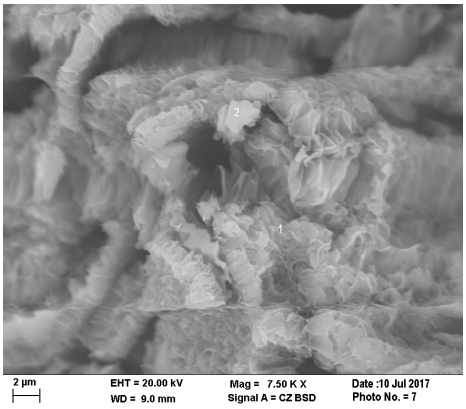

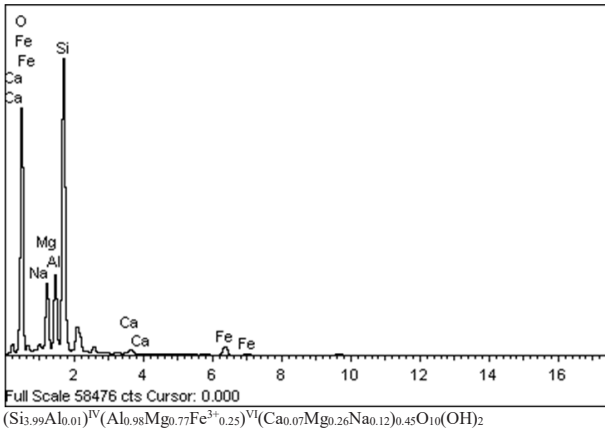

$(Si_{3.99}Al_{0.01})^{IV}(Al_{0.98}Mg_{0.77}Fe^{3+}_{0.25})^{VI}(Ca_{0.07}Mg_{0.26}Na_{0.12})_{0.45}O_{10}(OH)_2$
τ charge = -0.01; O. charge = -0.76
Total charge = -0.77 (τ % = 1 o % = 99); FW (g/mol) = 754.52
(No Mg at interlayer: Σ_{oct} = 2.26; Total charge: -0.25, τ % = 2; o % = 98)

Fig. B-170: SEM photomicrographs from sample RV-42: clay minerals

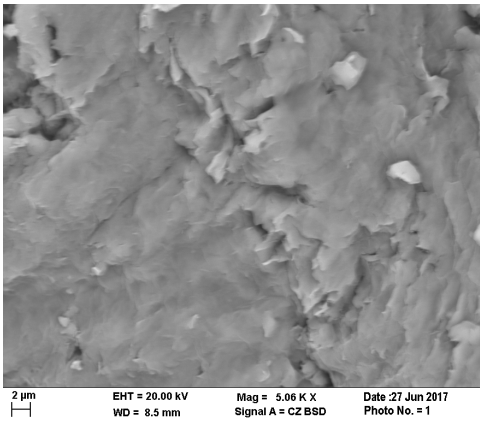

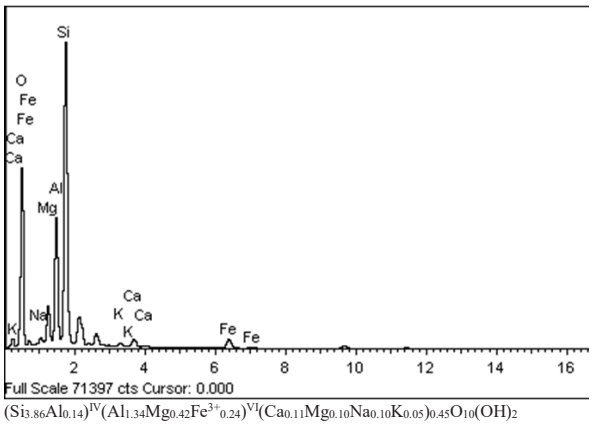

$(Si_{3.86}Al_{0.14})^{IV}(Al_{1.34}Mg_{0.42}Fe^{3+}_{0.24})^{VI}(Ca_{0.11}Mg_{0.10}Na_{0.10}K_{0.05})_{0.45}O_{10}(OH)_2$
τ charge = -0.14; O. charge = -0.42
Total charge = -0.56 (τ % = 25 o % = 75); FW (g/mol) = 753.83
(No Mg at interlayer: Σ_{oct} = 2.10; Total charge: -0.37 τ % = 38; o % = 62)

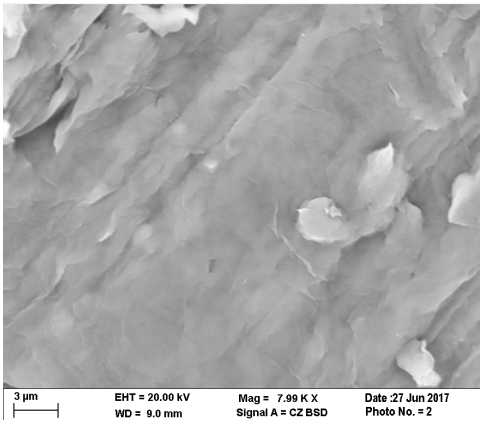

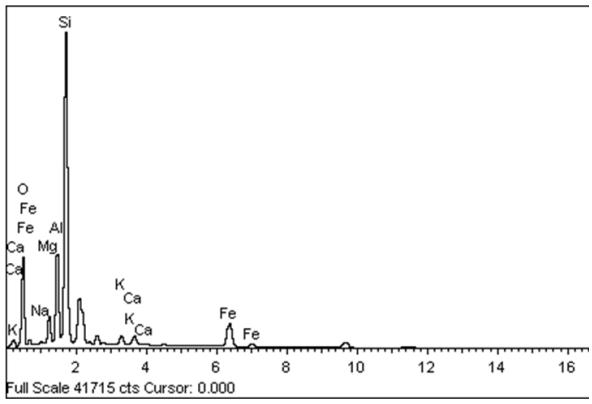

$(Si_{3.92}Al_{0.08})^{IV}(Al_{1.00}Mg_{0.37}Fe^{3+}_{0.63})^{VI}(Ca_{0.12}Mg_{0.02}Na_{0.05}K_{0.11})_{0.31}O_{10}(OH)_2$
τ charge = -0.08; O. charge = -0.37
Total charge = -0.45 (τ % = 17 o % = 83); FW (g/mol) = 776.71
(No Mg at interlayer: Σ_{oct} = 2.02; Total charge: -0.40, τ % = 19; o % = 81)

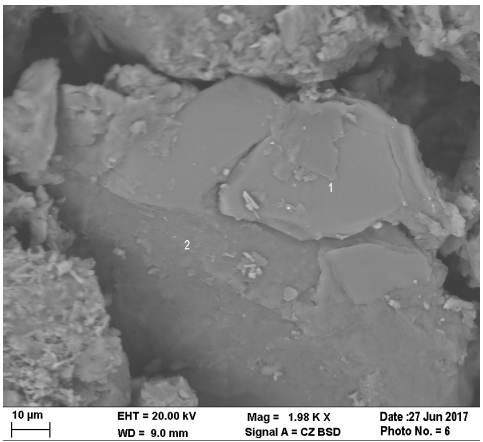

1): biotite type, ML?; 2): smectite

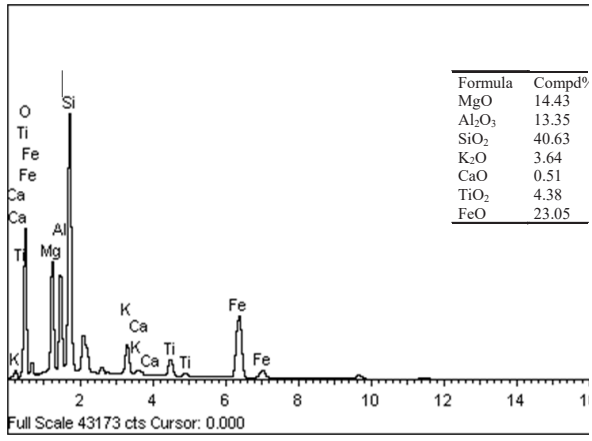

Formula	Compd%
MgO	14.43
Al_2O_3	13.35
SiO_2	40.63
K_2O	3.64
CaO	0.51
TiO_2	4.38
FeO	23.05

EDX from 1).

Fig. B-170: Cont.

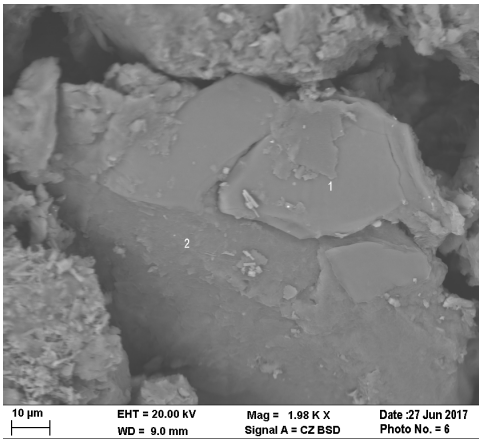

2: smectite

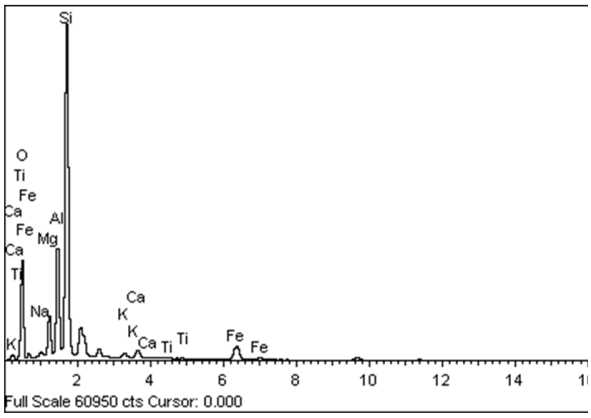

$(Si_{3.96}Al_{0.04})^{IV}(Al_{1.17}Mg_{0.47}Fe^{3+}_{0.35}Ti^{4+}_{0.01})^{VI}(Ca_{0.11}Mg_{0.07}Na_{0.08}K_{0.05})_{0.31}O_{10}(OH)_2$
τ charge = -0.04; O. charge = -0.45
Total charge = -0.49 (τ % = 8 o % = 92); FW (g/mol) = 758.67
(No Mg at interlayer: Σ_{oct} = 2.07; Total charge: -0.35, τ % = 11; o % = 89)

Fig. B-170: Cont.

Protrusion PS-43 (Fig. 181)

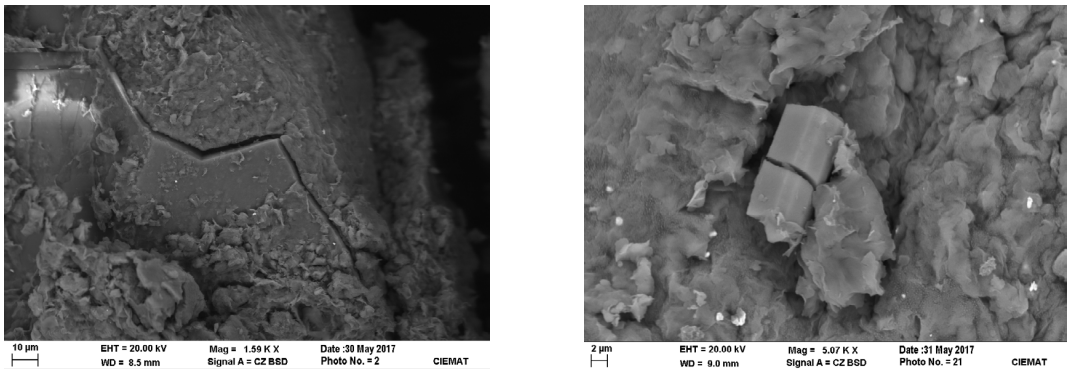

Fig. B-171: SEM photomicrographs from sample PS-43: a) Ca-Na plagioclase, b) apatite

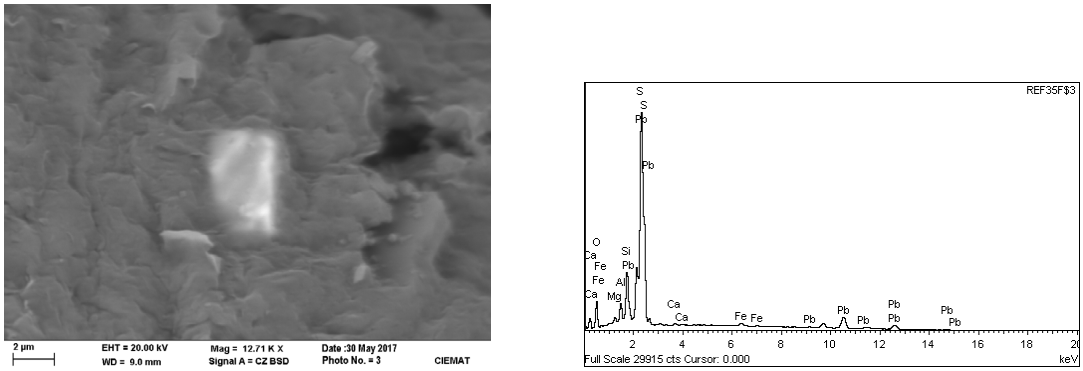

Fig. B-172: SEM photomicrographs from sample PS-43: Pb-sulfide

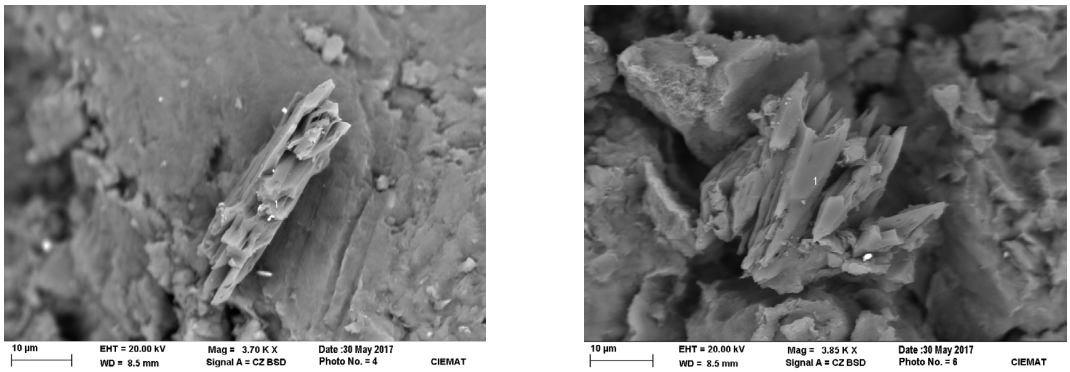

Fig. B-173: SEM photomicrographs from sample PS-43: a) and b) dolomite (1)

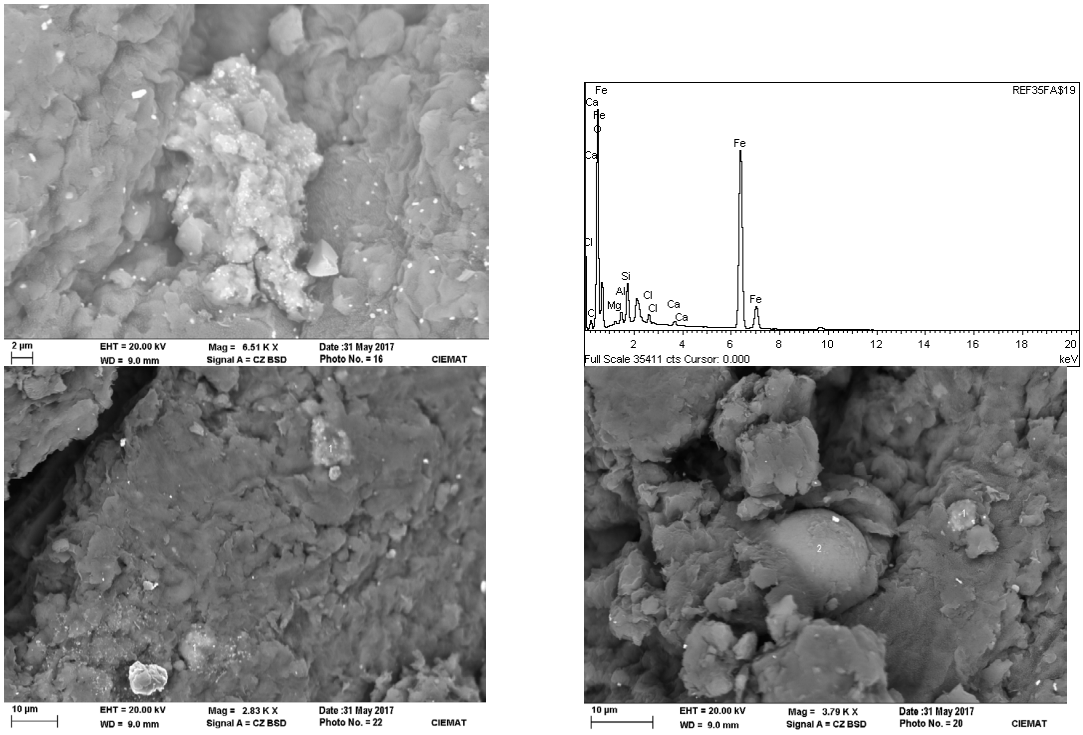

Fig. B-174: SEM photomicrographs from sample PS-43: a) Fe-carbonates, b) EDX from a), c) Fe-carbonates (1), Fe-oxide (1), d) Fe-carbonate (2)

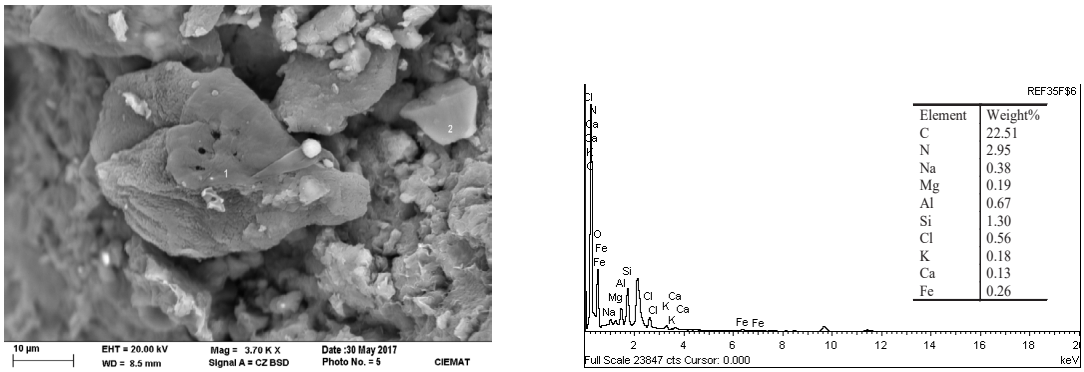

Fig. B-175: SEM photomicrographs from sample PS-43: a) organic matter (OM) with N and Cl (1), silica (2), b) EDX from (1)

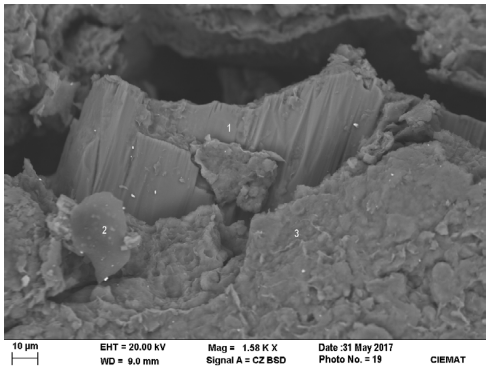

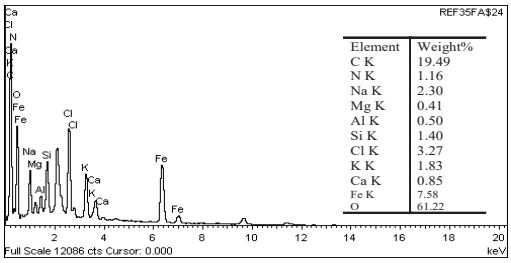

Fig. B-176: SEM photomicrographs from sample PS-43: a) Hornblende? (1), OM (2) with N, smectite (3), b) EDX from (2)

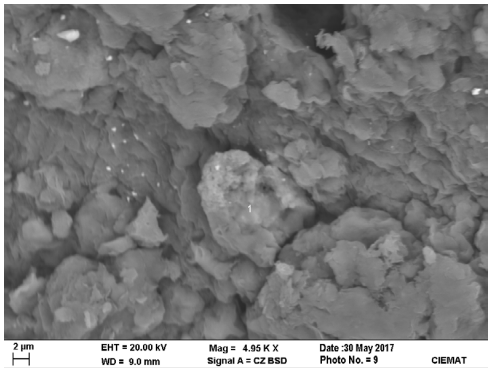

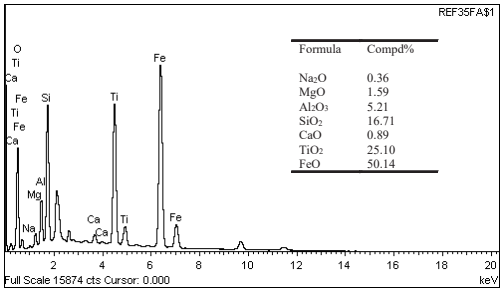

Fig. B-177: SEM photomicrographs from sample PS-43: a) Fe,Ti-oxides (1), b) EDX from (1)

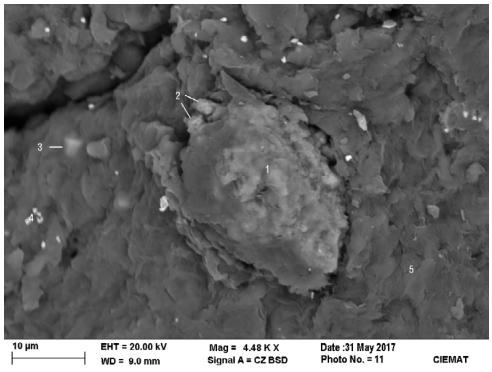

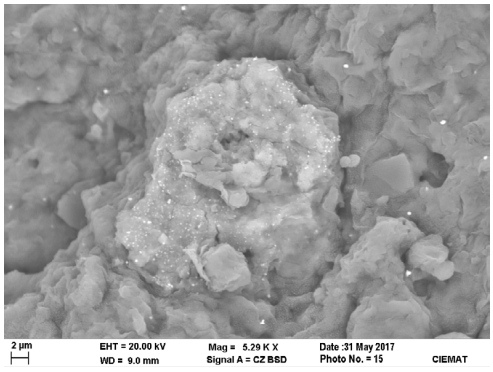

Fig. B-178: SEM photomicrographs from sample PS-43: a) Fe-oxide (1), Fe-carbonates (2), apatite (3), Hg (4), smectite (5), b) Fe-oxides and Hg particles

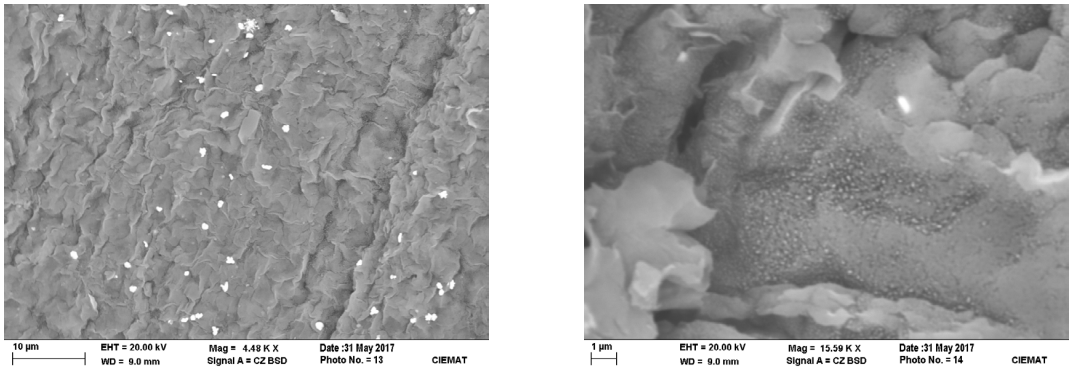

Fig. B-179: SEM photomicrographs from sample PS-43: a) and b) Hg particles

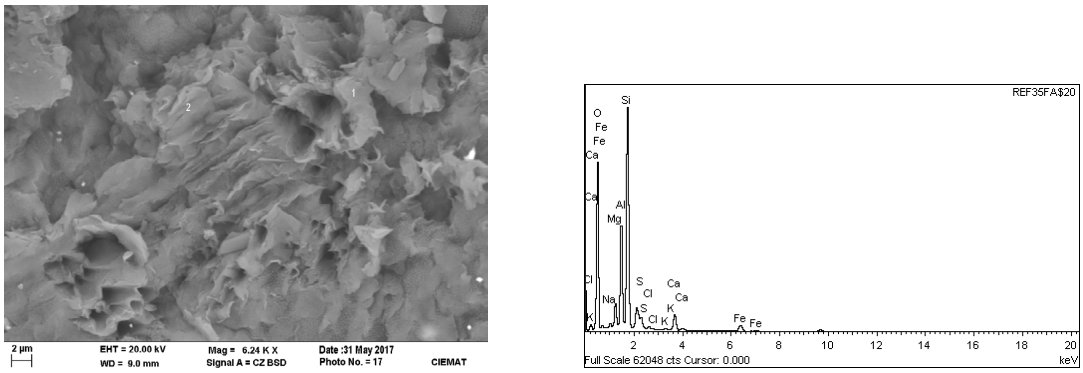

Fig. B-180: SEM photomicrographs from sample PS-43: a) Ca-sulfate (1), smectite (2), b) EDX from (1)

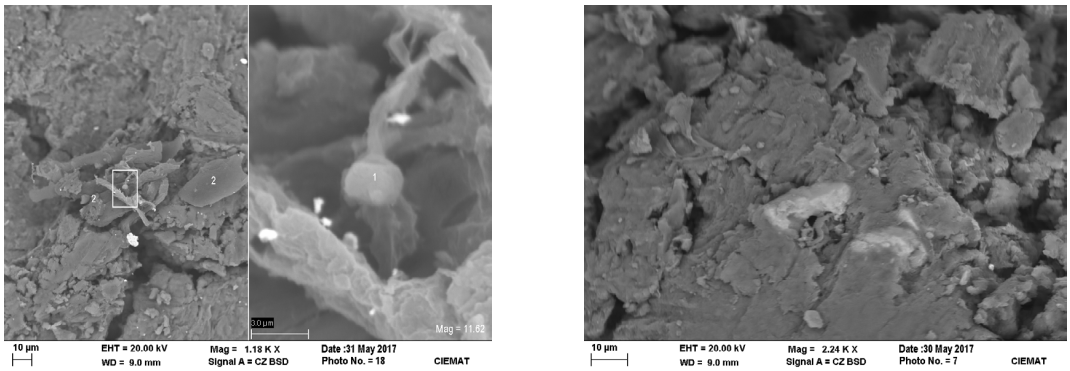

Fig. B-181: SEM photomicrographs from sample PS-43: a) Ca-carbonate (1), OM (2), b) barite

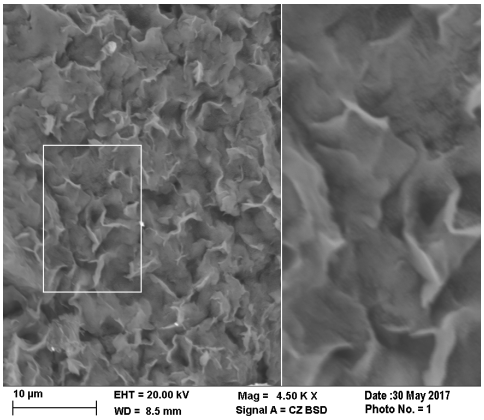

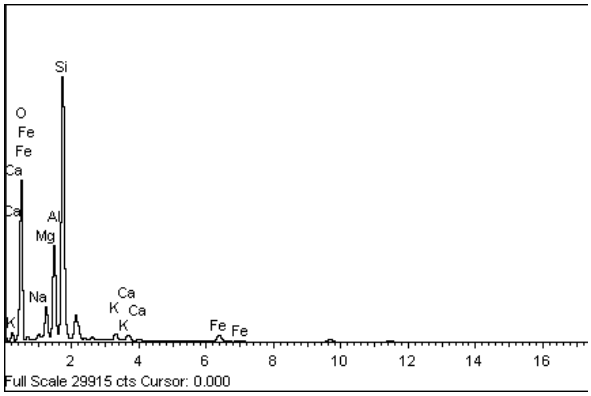

$(Si_{3.99}Al_{0.01})^{IV}(Al_{1.30}Mg_{0.48}Fe^{3+}_{0.23})^{VI}\ (Ca_{0.10}Mg_{0.04}Na_{0.09}K_{0.11})_{0.34}O_{10}(OH)_2$
τ charge = -0.01; O. charge = -0.47
Total charge = -0.48 (τ % = 1; o % = 99); FW (g/mol) = 754.13
(No Mg at interlayer: Σ_{oct} = 2.04; Total charge: -0.40, τ % = 1; o % = 99)

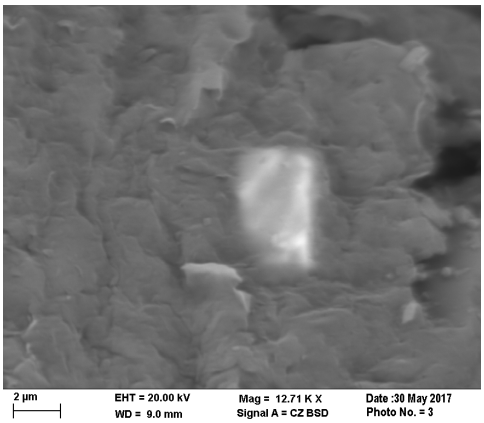

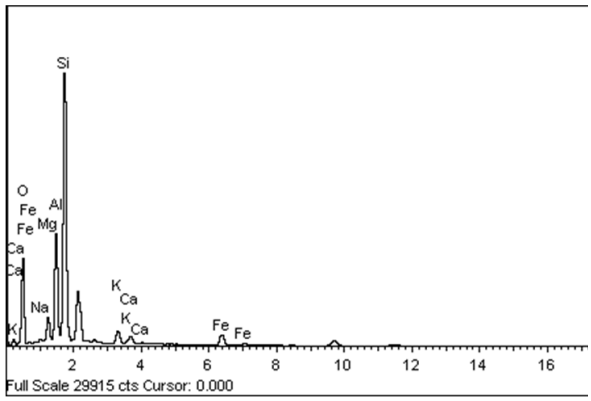

$(Si_{3.86}Al_{0.14})^{IV}(Al_{1.31}Mg_{0.36}Fe^{3+}_{0.33})^{VI}\ (Ca_{0.11}Mg_{0.01}Na_{0.05}K_{0.20})_{0.37}O_{10}(OH)_2$
τ charge = -0.14; O. charge = -0.36
Total charge = -0.49 (τ % = 27; o % = 73); FW (g/mol) = 764.76
(No Mg at interlayer: Σ_{oct} = 2.01; Total charge: -0.46, τ % = 29; o % = 71)

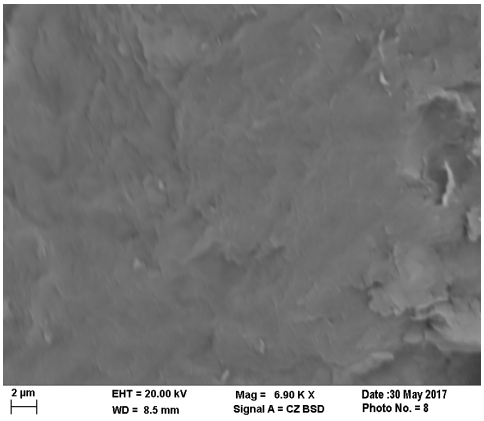

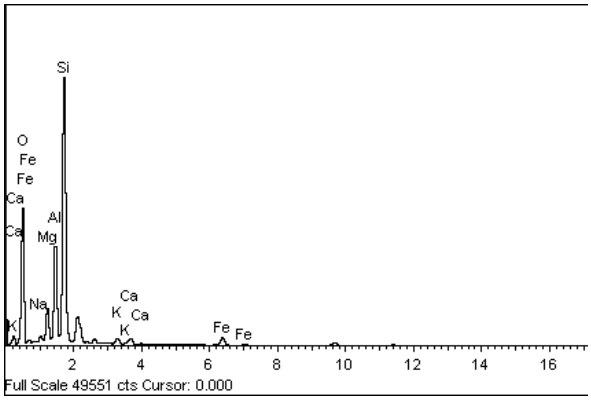

$(Si_{3.96}Al_{0.04})^{IV}(Al_{1.28}Mg_{0.47}Fe^{3+}_{0.24})^{VI}\ (Ca_{0.09}Mg_{0.05}Na_{0.13}K_{0.09})_{0.37}O_{10}(OH)_2$
τ charge = -0.04; O. charge = -0.47
Total charge = -0.52 (τ % = 8; o % = 92); FW (g/mol) = 755.13
(No Mg at interlayer: Σ_{oct} = 2.05; Total charge: -0.41, τ % = 10; o % = 90)

Fig. B-182: SEM photomicrographs from sample PS-43: clay minerals

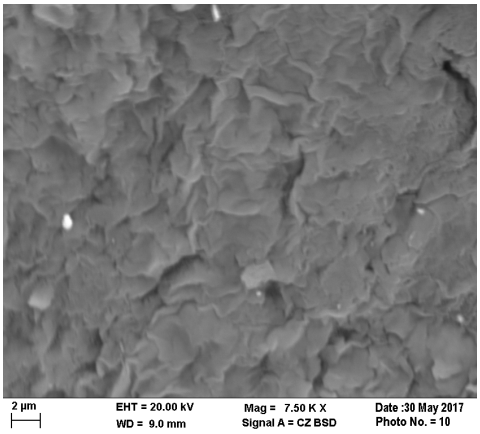

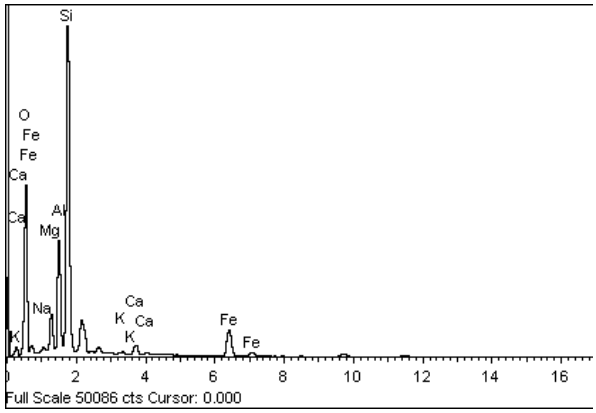

$(Si_{3.77}Al_{0.23})^{IV}(Al_{0.98}Mg_{0.37}Fe^{3+}_{0.65})^{VI}(Ca_{0.12}Mg_{0.13}Na_{0.08}K_{0.02})_{0.35}O_{10}(OH)_2$
τ charge = -0.23; O. charge = -0.37
Total charge = -0.60 (τ % = 39; o % = 61); FW (g/mol) = 776.88
(No Mg at interlayer: Σ_{oct} = 2.13; Total charge: -0.35, τ % = 68; o % = 32)

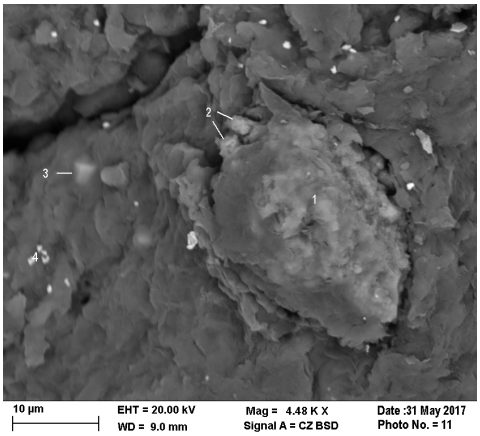

5: smectite

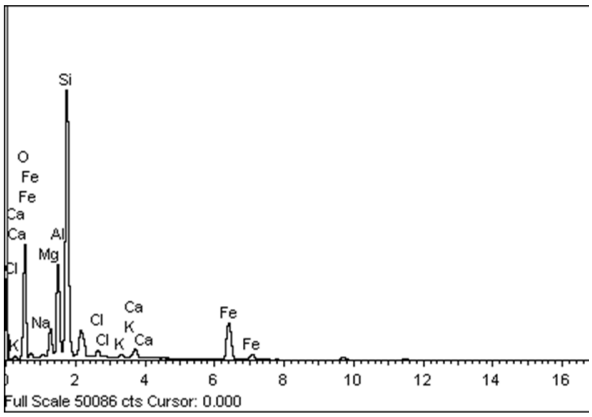

$(Si_{3.53}Al_{0.47})^{IV}(Al_{0.73}Mg_{0.24}Fe^{3+}_{1.03})^{VI}(Ca_{0.12}Mg_{0.19}Na_{0.06}K_{0.04})_{0.40}O_{10}(OH)_2$
τ charge = -0.47; O. charge = -0.24
Total charge = -0.71 (τ % = 66; o % = 34); FW (g/mol) = 801.75

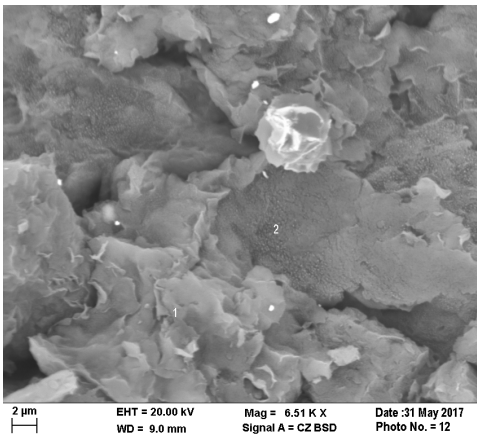

1: smectite

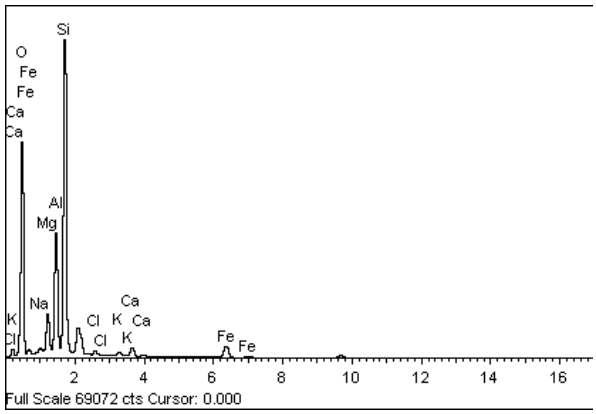

$(Si_{3.88}Al_{0.12})^{IV}(Al_{1.25}Mg_{0.43}Fe^{3+}_{0.31})^{VI}(Ca_{0.12}Mg_{0.10}Na_{0.10}K_{0.04})_{0.35}O_{10}(OH)_2$
τ charge = -0.12; O. charge = -0.43
Total charge = -0.56 (τ % = 22; o % = 78); FW (g/mol) = 757.41
(No Mg at interlayer: Σ_{oct} = 2.10; Total charge: -0.37, τ % = 33; o % = 67)

Fig. B-182: Cont.

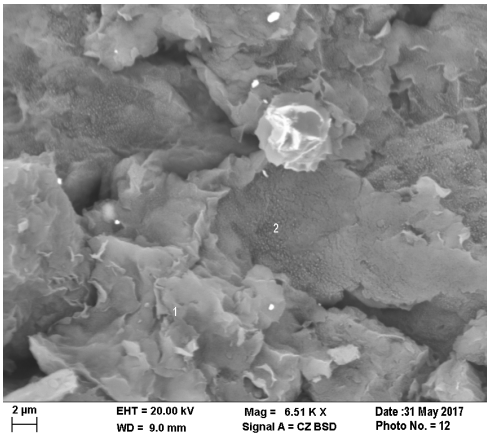

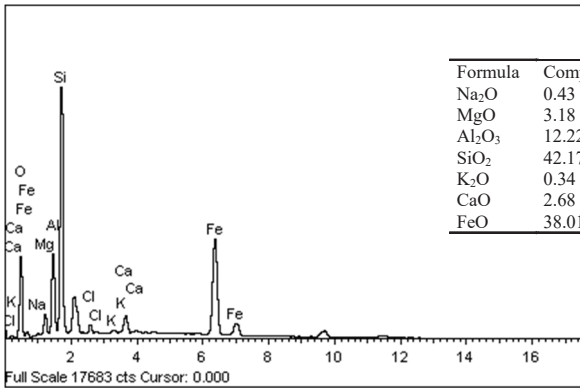

Formula	Com
Na_2O	0.43
MgO	3.18
Al_2O_3	12.2
SiO_2	42.1
K_2O	0.34
CaO	2.68
FeO	38.0

2: smectite

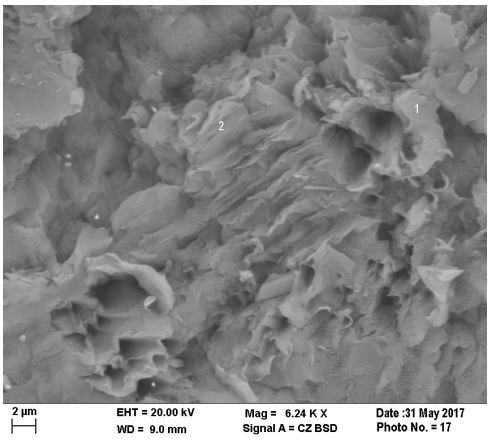

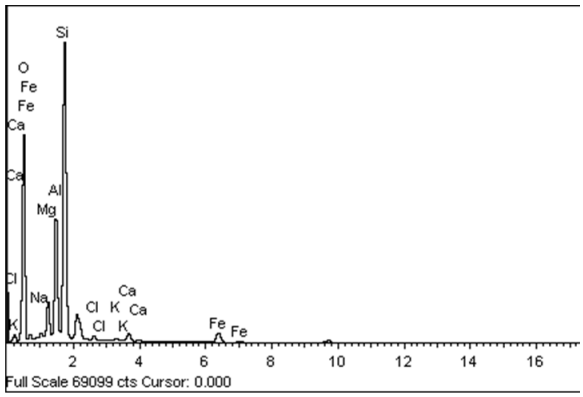

2: smectite

$(Si_{3.88}Al_{0.12})^{IV}(Al_{1.32}Mg_{0.42}Fe^{3+}_{0.27})^{VI}(Ca_{0.10}Mg_{0.10}Na_{0.10}K_{0.03})_{0.33}O_{10}(OH)_2$
τ charge = -0.12; O. charge = -0.42
Total charge = -0.54 (τ % = 22; o % = 78); FW (g/mol) = 753.62
(No Mg at interlayer: Σ_{oct} = 2.10; Total charge: -0.34, τ % = 34 o % = 66)

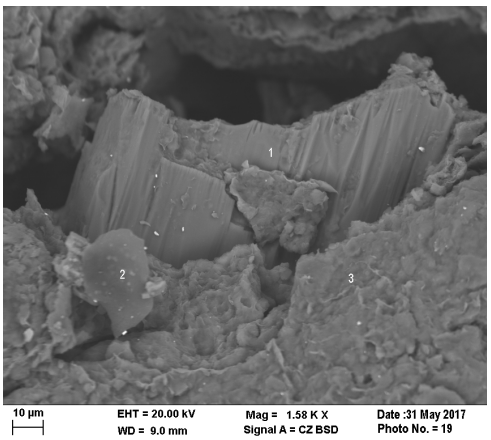

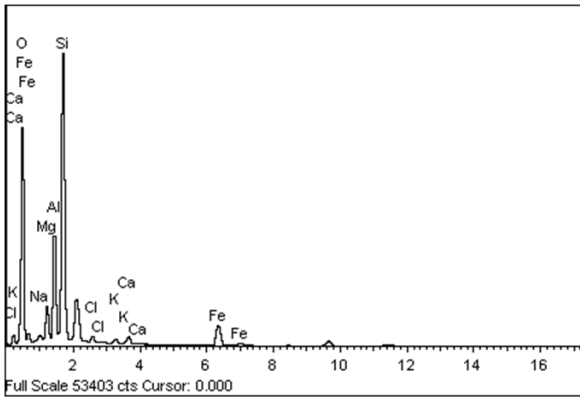

3: smectite

$(Si_{3.75}Al_{0.25})^{IV}(Al_{1.05}Mg_{0.38}Fe^{3+}_{0.57})^{VI}(Ca_{0.10}Mg_{0.12}Na_{0.11}K_{0.06})_{0.40}O_{10}(OH)_2$
τ charge = -0.25; O. charge = -0.38
Total charge = -0.63 (τ % = 39; o % = 61); FW (g/mol) = 775.44
(No Mg at interlayer: Σ_{oct} = 2.12; Total charge: -0.38, τ % = 64; o % = 36)

Fig. B-182: Cont.

Protrusion PS-43: Red particles (Fig. 181)

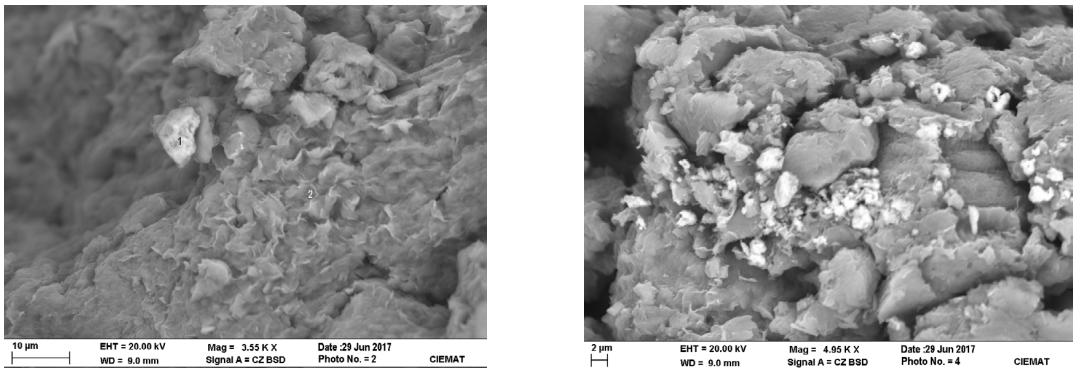

Fig. B-183: SEM photomicrographs from sample PS-43 Red particles: a) Fe-oxide (1), smectite (2), b) Fe-oxides

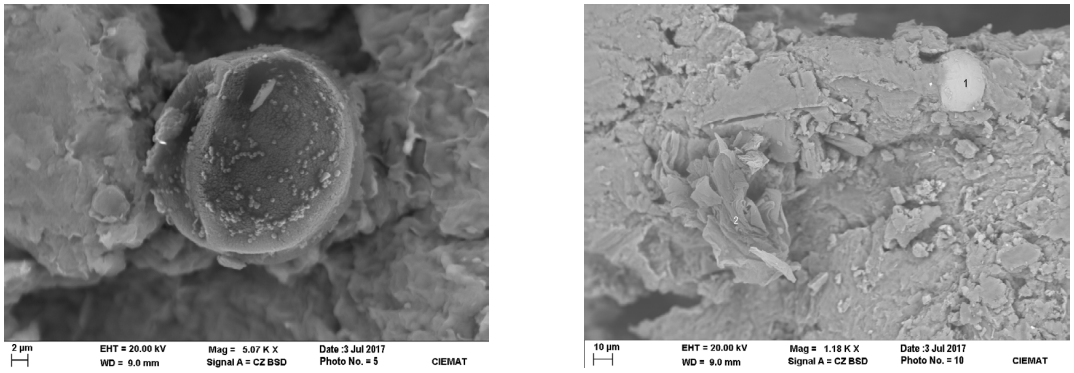

Fig. B-184: SEM photomicrographs from sample PS-43 Red particles: a) organic matter (with Cl), b) Fe-carbonate (CO_2: 13.67 wt.-%, SiO_2: 0.33 wt.-%, FeO: 86.0 wt.-%) (1), organic matter (with Cl) (2)

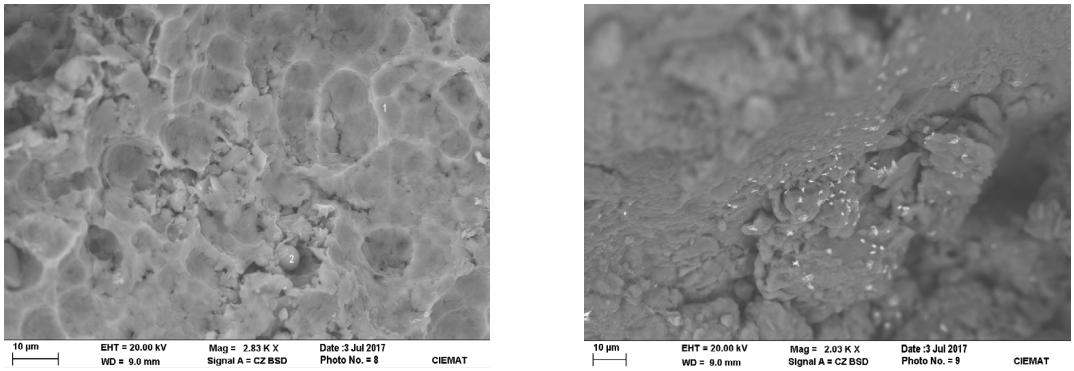

Fig. B-185: SEM photomicrographs from sample PS-43 Red particles: a) smectite (1), silica (2), b) Hg particles

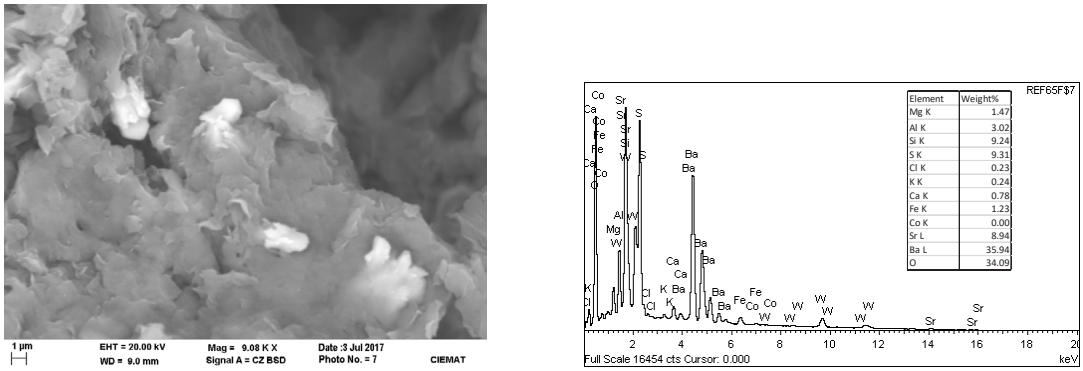

Fig. B-186: SEM photomicrographs from sample PS-43 Red particles: barite (with Cl)

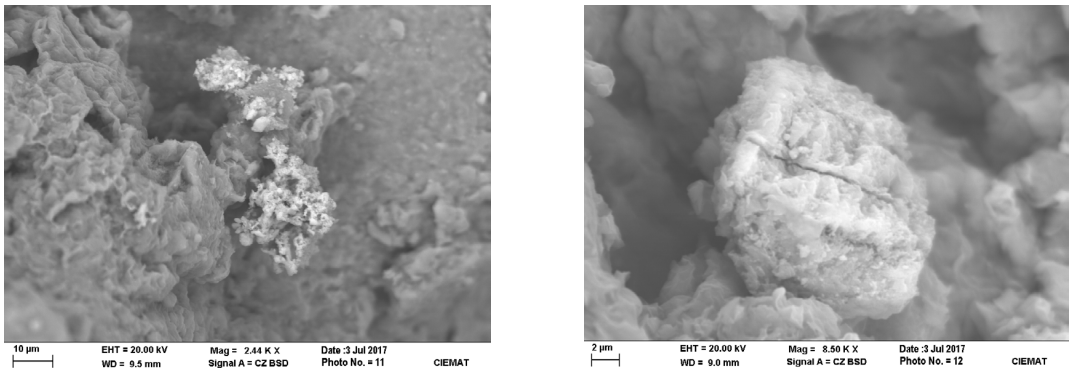

Fig. B-187: SEM photomicrographs from sample PS-43 Red particles: a) and b) Fe-oxides (with Cl)

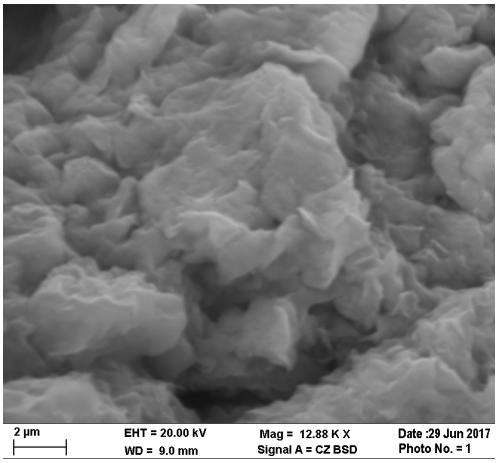

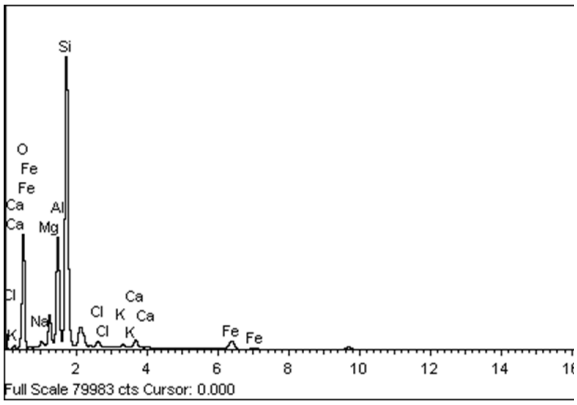

$(Si_{3.96}Al_{0.04})^{IV}(Al_{1.34}Mg_{0.41}Fe^{3+}_{0.25})^{VI}(Ca_{0.11}Mg_{0.04}Na_{0.09}K_{0.04})_{0.29}O_{10}(OH)_2$
τ charge = -0.04; O. charge = -0.41
Total charge = -0.45 (τ % = 8 o % = 92); FW (g/mol) = 751.64
(No Mg at interlayer: Σ_{oct} = 2.04; Total charge: -0.36, τ % = 10; o % = 90)

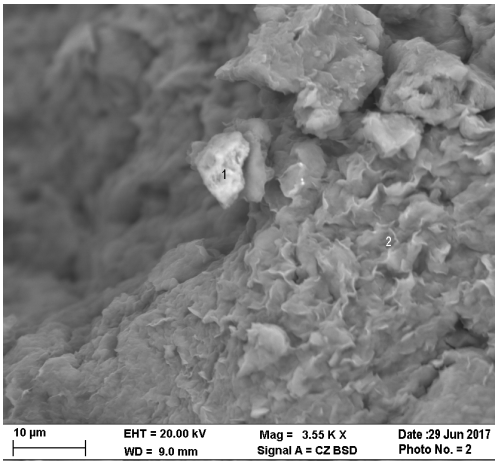

(1): Fe-oxides; (2): smectite

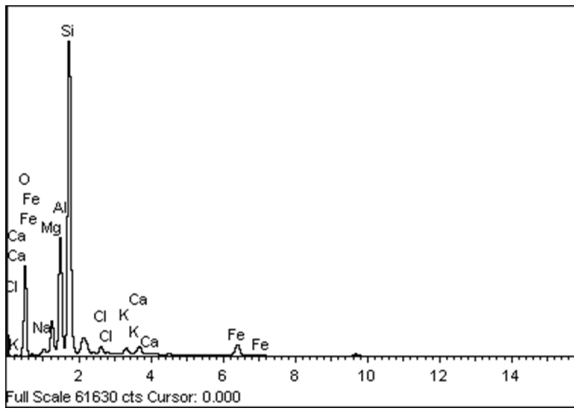

$(Si_{3.94}Al_{0.06})^{IV}(Al_{1.29}Mg_{0.41}Fe^{3+}_{0.30})^{VI}(Ca_{0.11}Mg_{0.04}Na_{0.09}K_{0.08})_{0.32}O_{10}(OH)_2$
τ charge = -0.06; O. charge = -0.41
Total charge = -0.47 (τ % = 13 o % = 87); FW (g/mol) = 756.49
(No Mg at interlayer: Σ_{oct} = 2.04; Total charge: -0.39, τ % = 15; o % = 85)

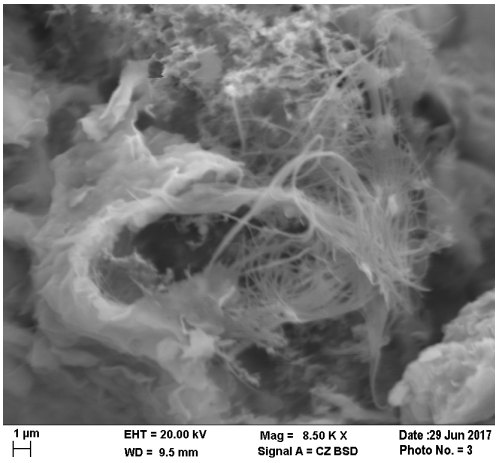

Nontronite type

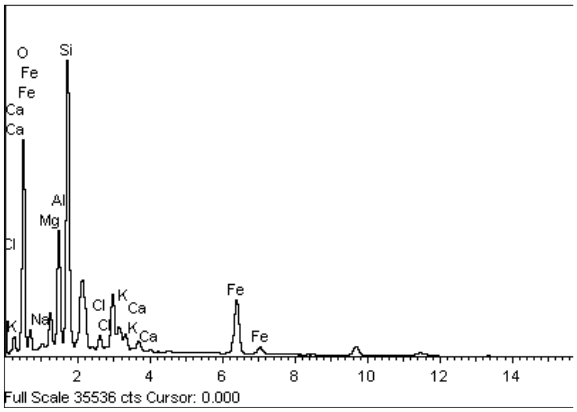

$(Si_{3.25}Al_{0.75})^{IV}(Al_{0.56}Mg_{0.21}Fe^{3+}_{1.23})^{VI}(Ca_{0.12}Mg_{0.27}Na_{0.08}K_{0.10})_{0.57}O_{10}(OH)_2$
τ charge = -0.75; O. charge = -0.21
Total charge = -0.96 (τ % = 78 o % = 22); FW (g/mol) = 823.12

Fig. B-188: SEM photomicrographs from sample PS-43 Red particles: clay minerals

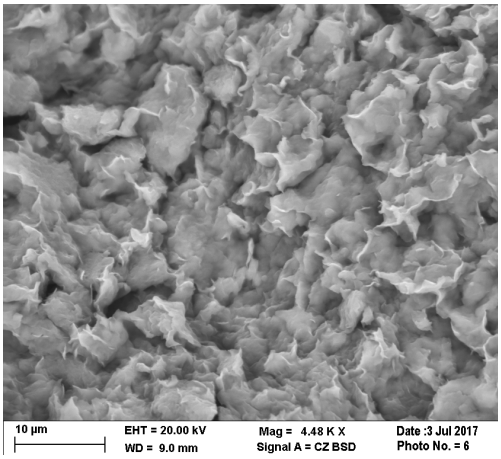

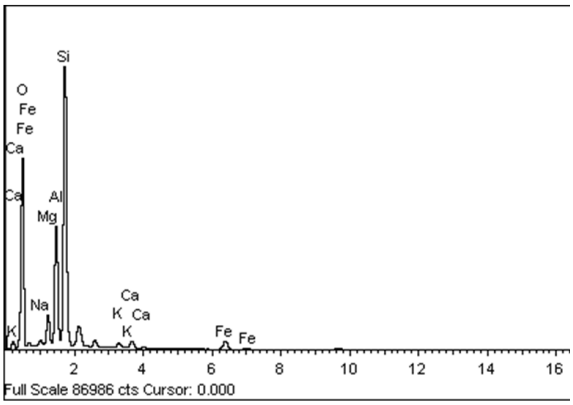

$(Si_{3.87}Al_{0.13})^{IV}(Al_{1.38}Mg_{0.38}Fe^{3+}_{0.25})^{VI}(Ca_{0.11}Mg_{0.06}Na_{0.11}K_{0.07})_{0.34}O_{10}(OH)_2$
τ charge = -0.13; O. charge = -0.38
Total charge = -0.50 (τ % = 25 o % = 75); FW (g/mol) = 754.12
(No Mg at interlayer: Σ_{oct} = 2.06; Total charge: -0.39, τ % = 32; o % = 68)

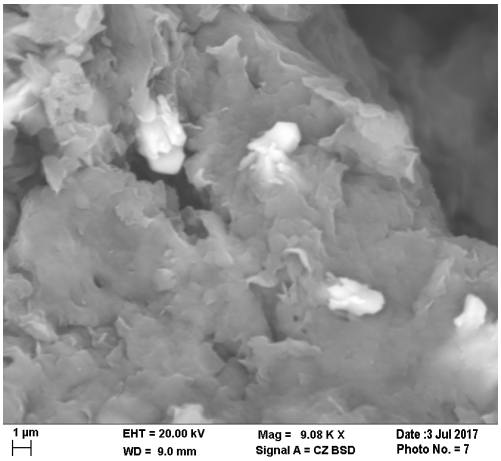

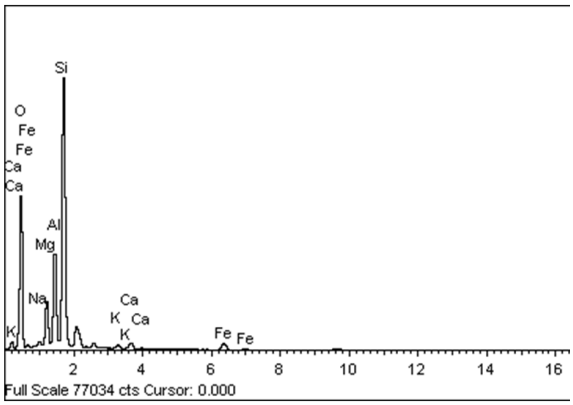

$(Si_{3.96}Al_{0.04})^{IV}(Al_{1.23}Mg_{0.57}Fe^{3+}_{0.20})^{VI}(Ca_{0.09}Mg_{0.14}Na_{0.09}K_{0.05})_{0.38}O_{10}(OH)_2$
τ charge = -0.04; O. charge = -0.57
Total charge = -0.61 (τ % = 6 o % = 94); FW (g/mol) = 751.45
(No Mg at interlayer: Σ_{oct} = 2.14; Total charge: -0.33, τ % = 11; o % = 89)

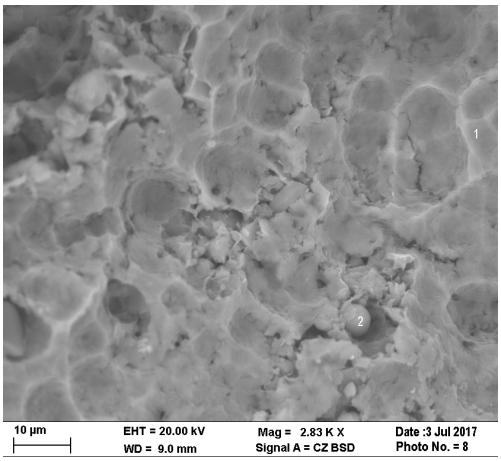

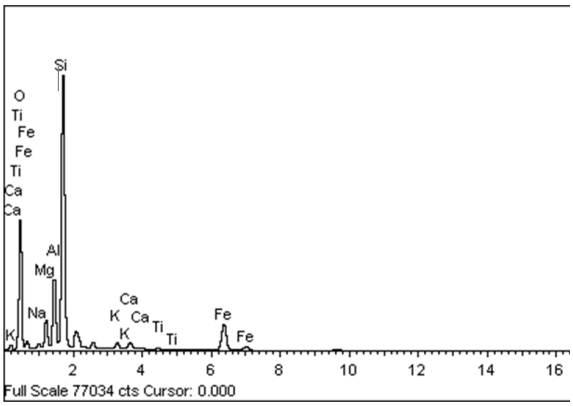

$(Si_{3.86}Al_{0.14})^{IV}(Al_{0.80}Mg_{0.39}Fe^{3+}_{0.79}Ti^{4+}_{0.01})^{VI}(Ca_{0.09}Mg_{0.09}Na_{0.08}K_{0.08})_{0.34}O_{10}(OH)_2$
τ charge = -0.14; O. charge = -0.38
Total charge = -0.52 (τ % = 26 o % = 74); FW (g/mol) = 786.09
(No Mg at interlayer: Σ_{oct} = 2.09; Total charge: -0.35, τ % = 39; o % = 61)

Fig. B-188: Cont.

Black particles adhered to bentonite at contact with Heater #2 surface (BPB, Fig. 182)

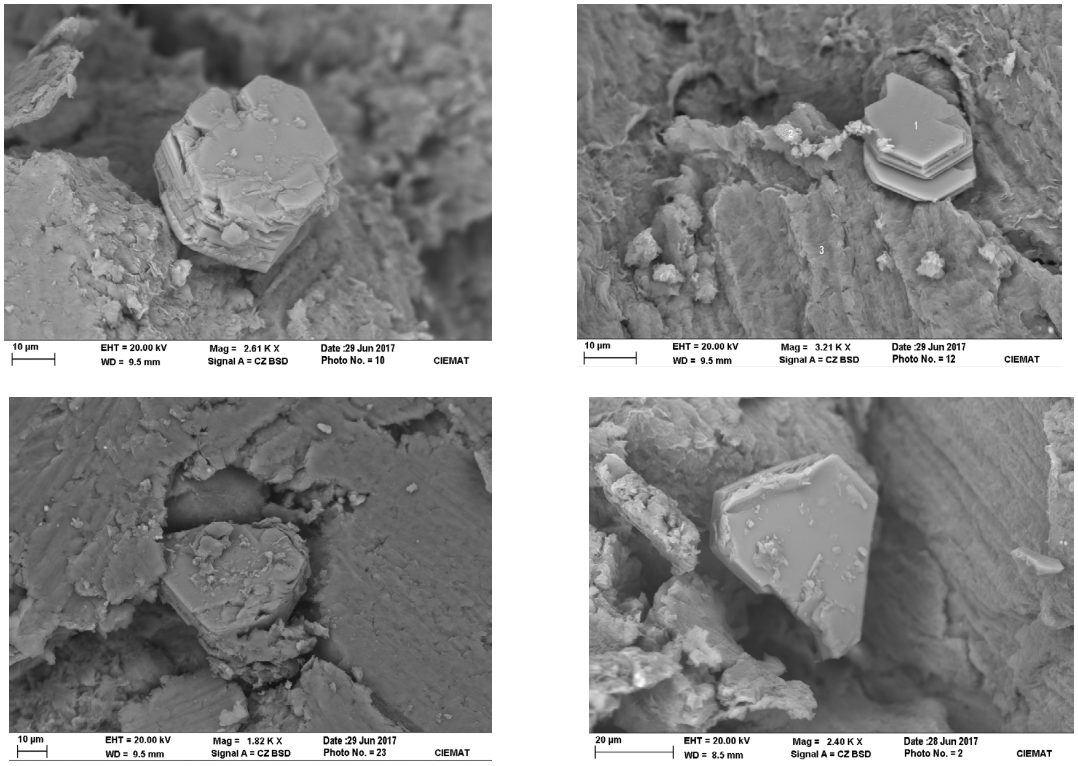

Fig. B-189: SEM photomicrographs from sample Black particles adhered to bentonite: a) chlorites, b) chlorites (1), Ca-carbonates (2), smectite (3), c) and d) chlorites

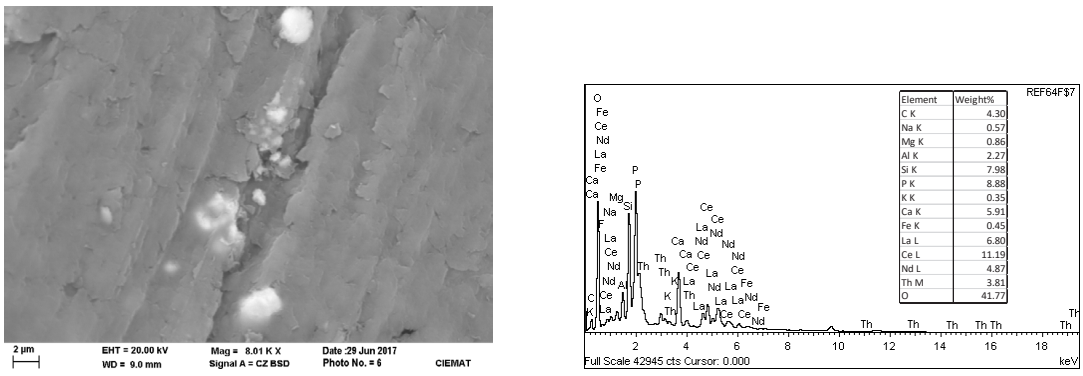

Fig. B-190: SEM photomicrographs from sample Black particles adhered to bentonite: monazite

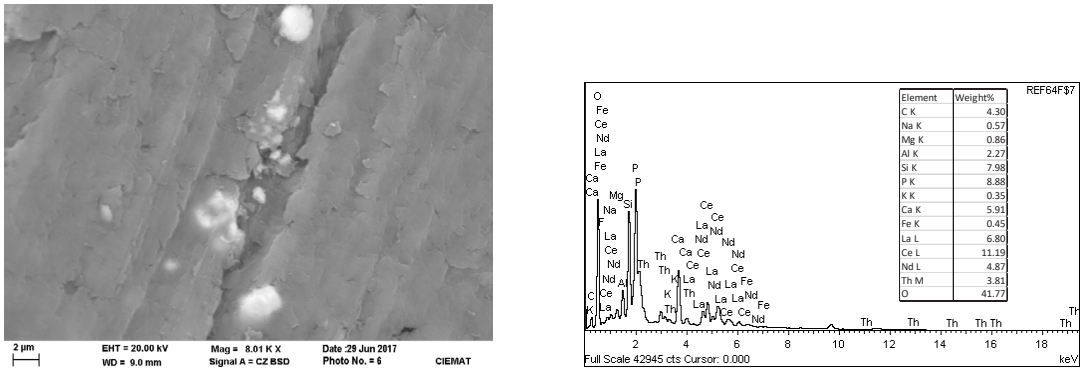

Fig. B-191: SEM photomicrographs from sample Black particles adhered to bentonite: monazite

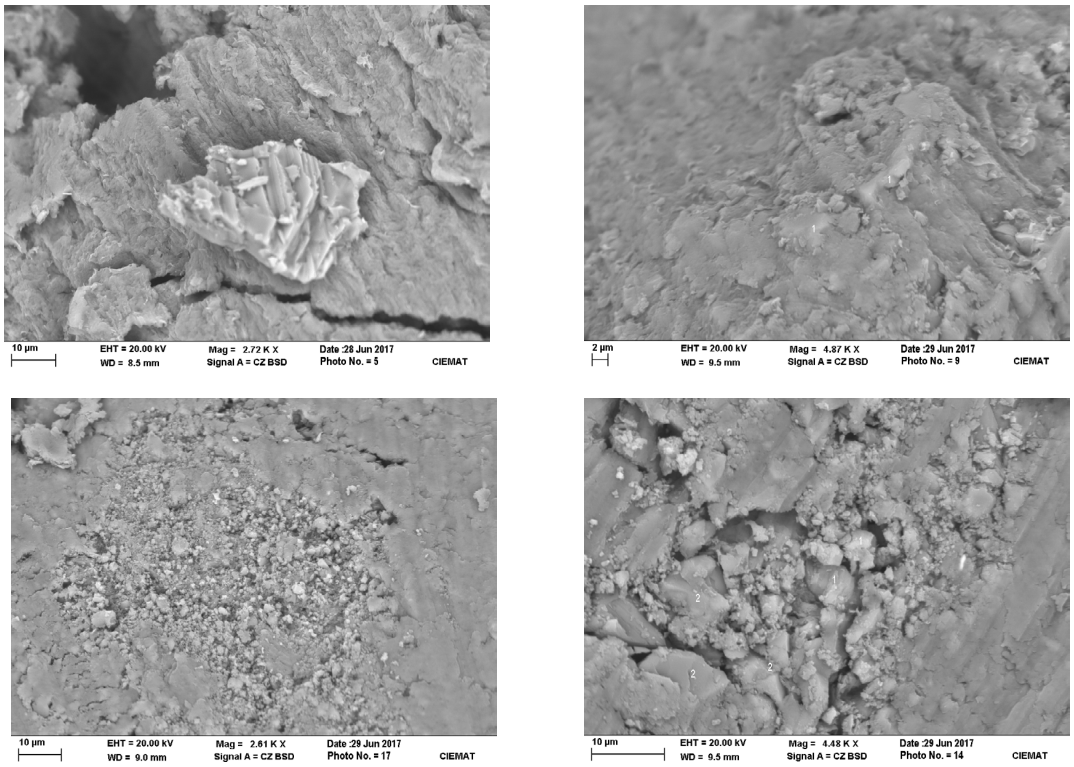

Fig. B-192: SEM photomicrographs from sample Black particles adhered to bentonite: a), b) and c), Ca-carbonates, d) Ca-sulfates (1), Ca-carbonates (2)

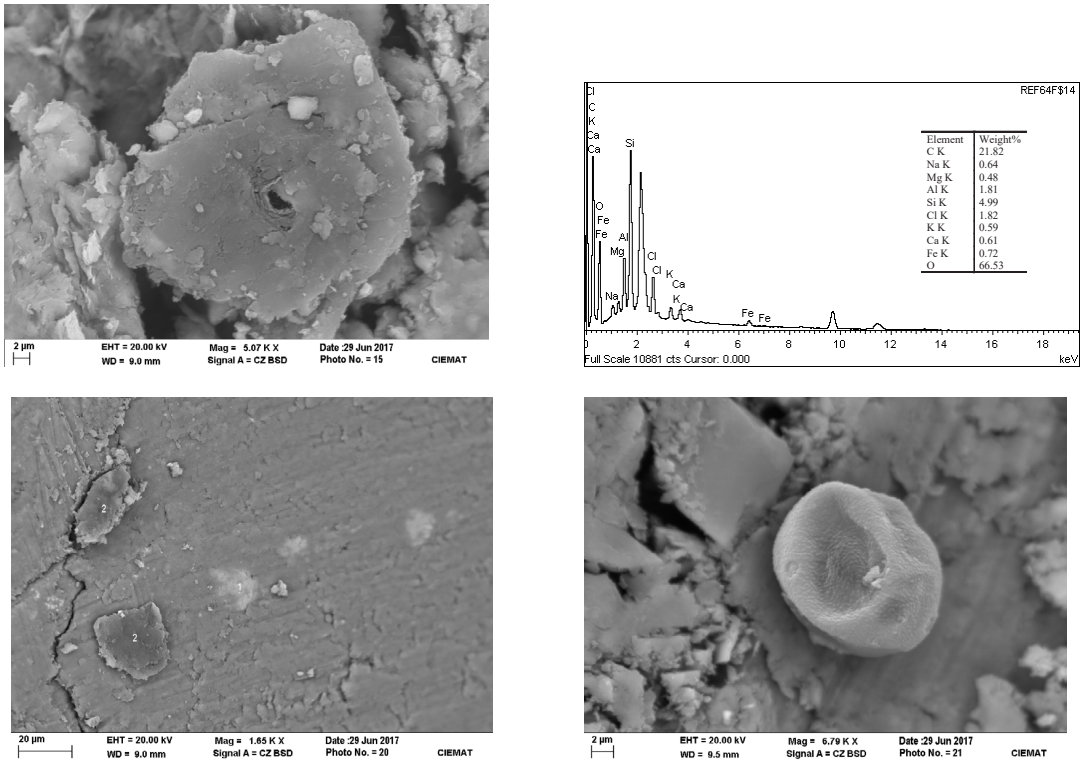

Fig. B-193: SEM photomicrographs from sample Black particles adhered to bentonite: a) organic matter with Cl, b) EDX from a), c) Fe-oxide (1), organic matter with Cl (2), d) OM

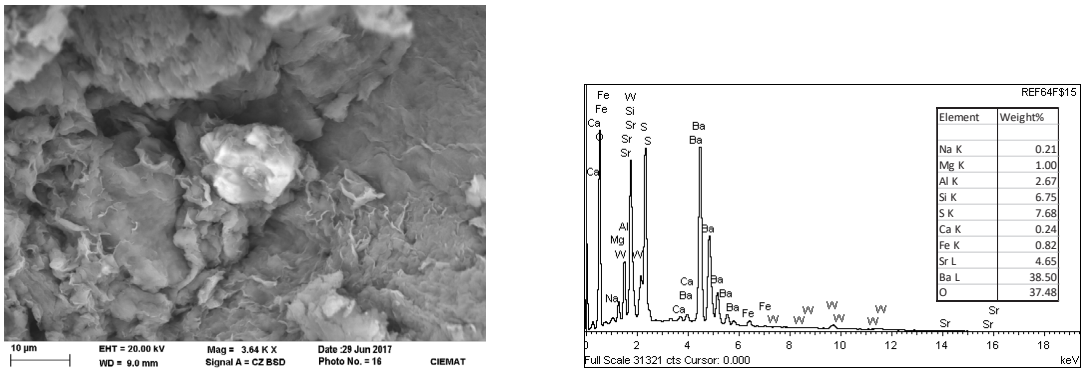

Fig. B-194: SEM photomicrographs from sample Black particles adhered to bentonite: barite-celestine

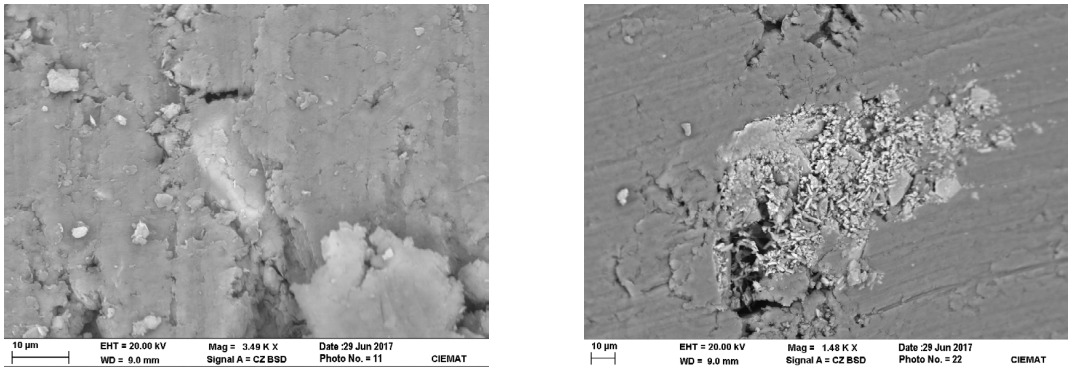

Fig. B-195: SEM photomicrographs from sample Black particles adhered to bentonite: a) Fe-Ti-Mn-oxides, b) Ti-Mn-oxides

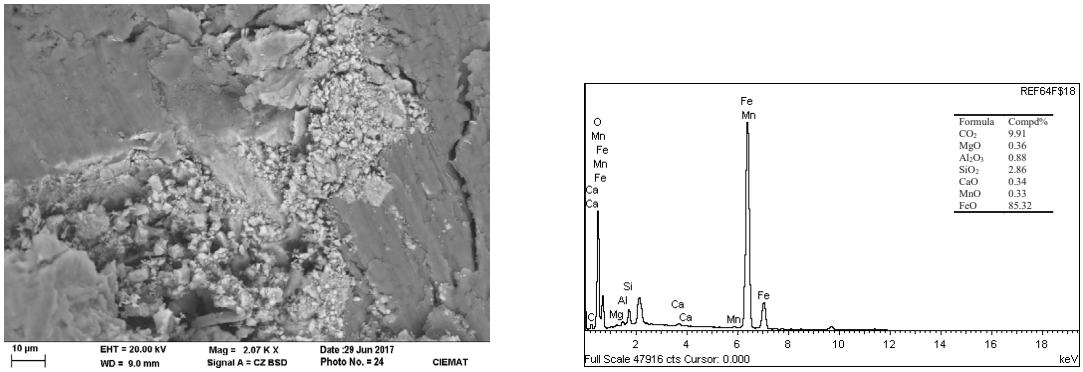

Fig. B-196: SEM photomicrographs from sample Black particles adhered to bentonite: Fe-carbonates and Fe-oxides

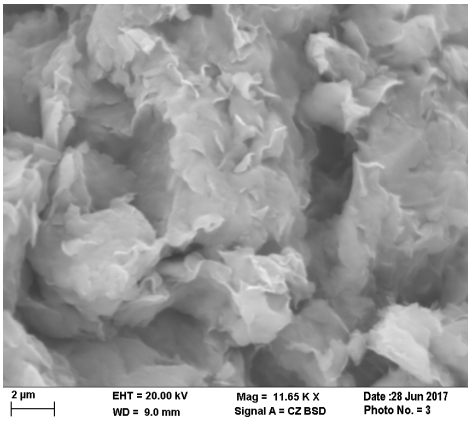

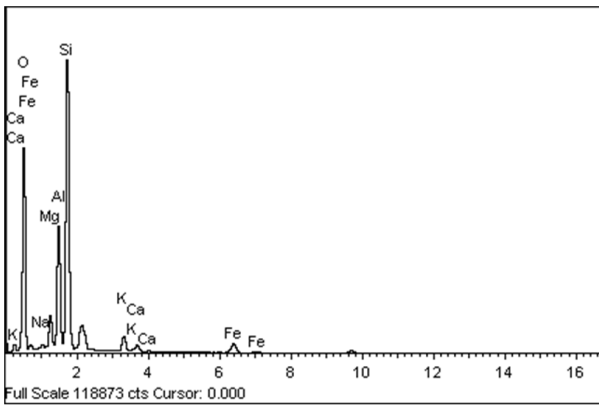

$(Si_{3.85}Al_{0.15})^{IV}(Al_{1.34}Mg_{0.41}Fe^{3+}_{0.26})^{VI}(Ca_{0.09}Mg_{0.06}Na_{0.06}K_{0.20})_{0.41}O_{10}(OH)_2$
τ charge = -0.15; O. charge = -0.41
Total charge = -0.56 (τ % = 27 o % = 73); FW (g/mol) = 761.34
(No Mg at interlayer: Σ_{oct} = 2.06; Total charge: -0.43, τ % = 34; o % = 66)

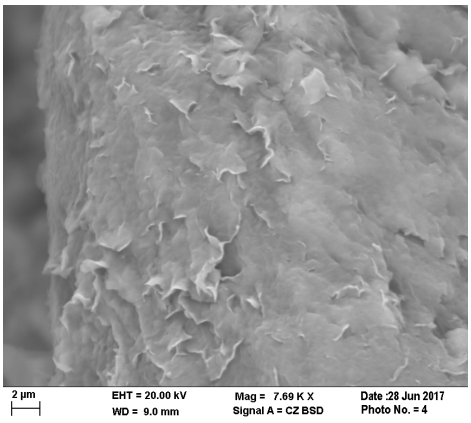

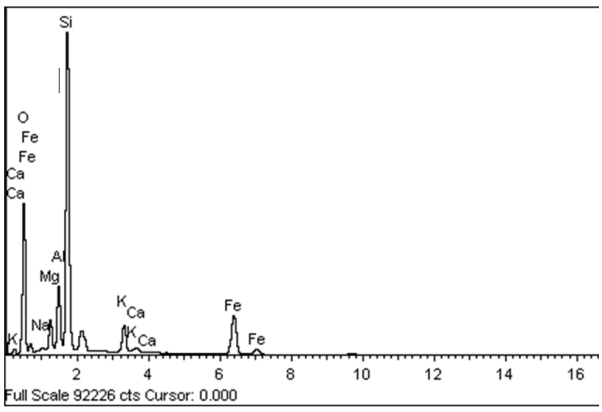

$(Si_{3.81}Al_{0.19})^{IV}(Al_{0.57}Mg_{0.41}Fe^{3+}_{1.02})^{VI}(Ca_{0.06}Mg_{0.05}Na_{0.05}K_{0.34})_{0.49}O_{10}(OH)_2$
τ charge = -0.19; O. charge = -0.41
Total charge = -0.60 (τ % = 31 o % = 69); FW (g/mol) = 812.81
(No Mg at interlayer: Σ_{oct} = 2.05; Total charge: -0.50, τ % = 37; o % = 63)

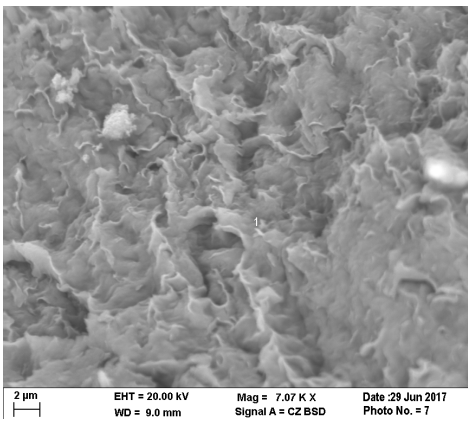

(1) Smectite; (2) monacite

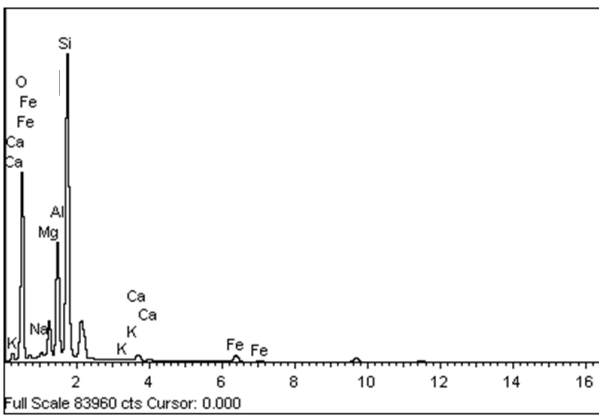

$(Si_{4.00}Al_{0.00})^{IV}(Al_{1.38}Mg_{0.43}Fe^{3+}_{0.18})^{VI}(Ca_{0.09}Mg_{0.08}Na_{0.09}K_{0.01})_{0.27}O_{10}(OH)_2$
τ charge = -0.00; O. charge = -0.44
Total charge = -0.44 (τ % = 1 o % = 99); FW (g/mol) = 744.96
(No Mg at interlayer: Σ_{oct} = 2.08; Total charge: -0.27, τ % = 2; o % = 98)

Fig. B-197: SEM photomicrographs from sample Black particles adhered to bentonite: clay minerals

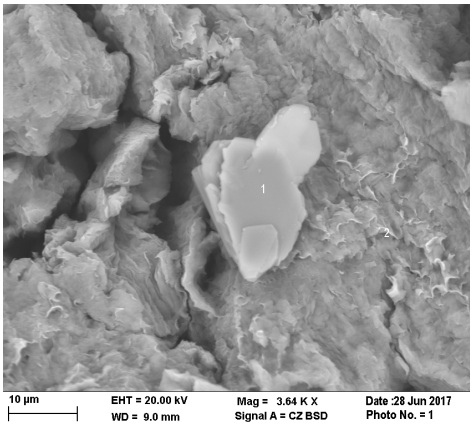

1: Chlorite; 2: smectite

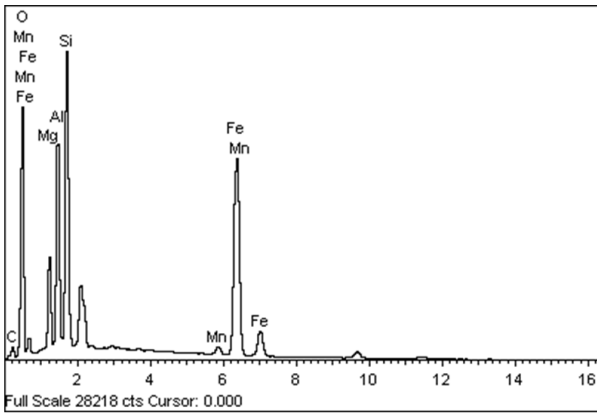

Chlorite (1): $(Si_{3.28}Al_{0.72})^{IV}$ $(Fe^{2+}_{2.39}Mg_{0.02}Mn^{2+}_{0.13\ \ 0.46})^{VI}$ $O_{10}(OH)_2$ $[Al_{1.64}Mg_{1.36}](OH)_6]$ + 28.5 wt.-% $FeCO_3$

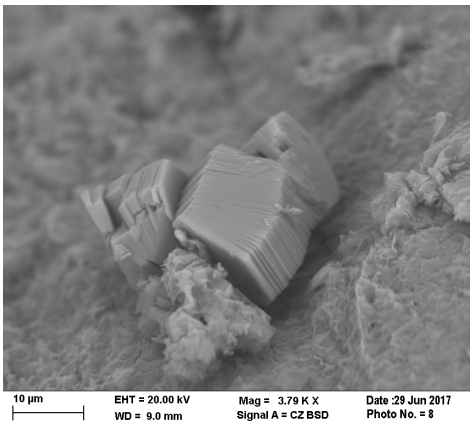

Chlorite

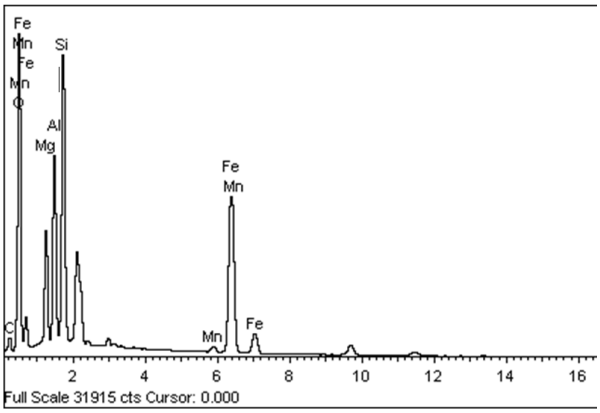

$(Si_{3.63}Al_{0.37})^{IV}$ $(Fe^{2+}_{0.98}Mg_{1.03}Mn^{2+}_{0.11\ \ 0.88})^{VI}$ $O_{10}(OH)_2$ $[Al_{2.13}Mg_{0.87}](OH)_6]$ + 46.7 wt.-% $FeCO_3$

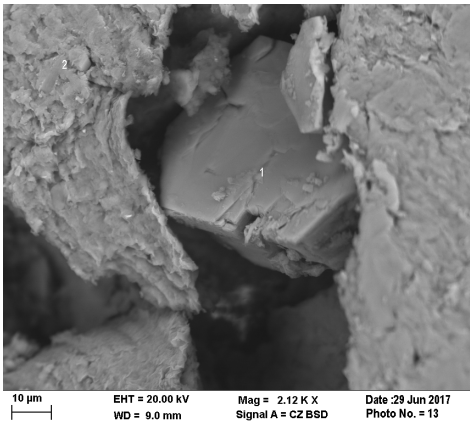

1: Chlorite

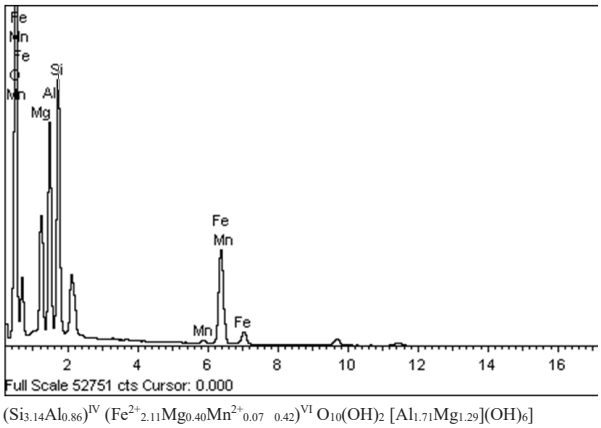

$(Si_{3.14}Al_{0.86})^{IV}$ $(Fe^{2+}_{2.11}Mg_{0.40}Mn^{2+}_{0.07\ \ 0.42})^{VI}$ $O_{10}(OH)_2$ $[Al_{1.71}Mg_{1.29}](OH)_6]$

Fig. B-197: Cont.

Black ball particle at direct contact with the frontal surface of Heater #2 (BB, Fig. 182)

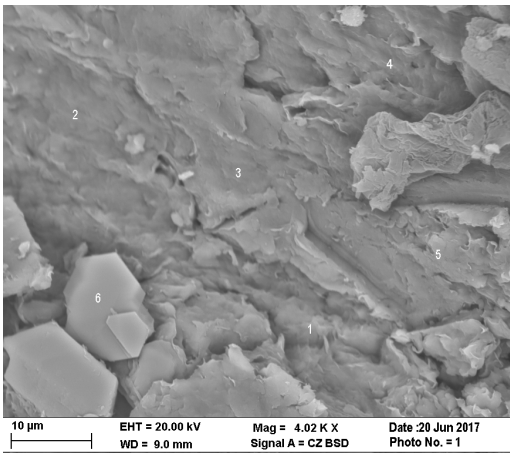

(1) to 5) smectite clay minerals; (6) chlorites

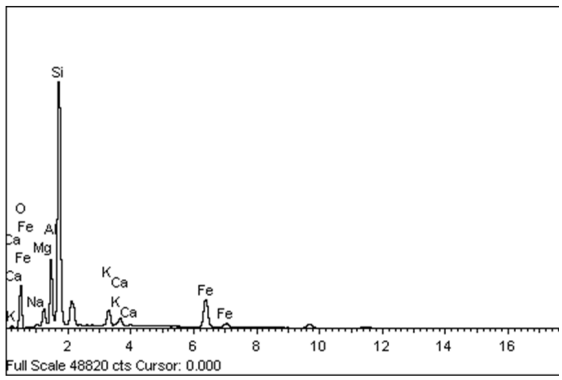

(1):$(Si_{3.77}Al_{0.23})^{IV}(Al_{0.77}Mg_{0.32}Fe^{3+}_{0.91\ \ 0.01})^{VI}(Ca_{0.13}Na_{0.06}K_{0.26})_{0.45}O_{10}(OH)_2$
τ charge = -0.23; O. charge = -0.34
Total charge = -0.57 (τ % = 41 o % = 59); FW (g/mol) = 803.62

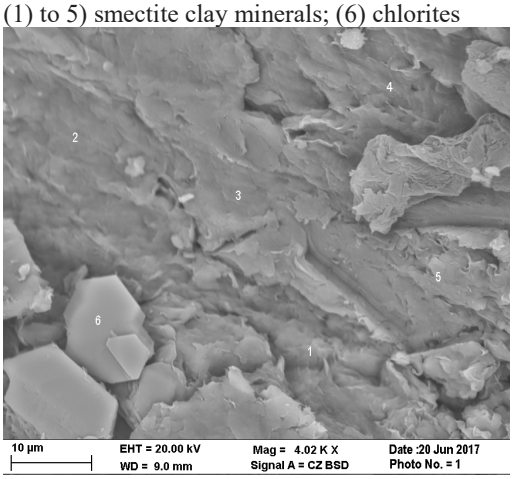

(1) to 5) smectite clay minerals; (6) chlorites

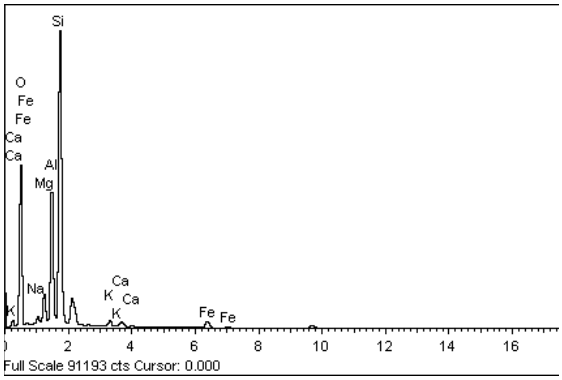

2):$(Si_{3.90}Al_{0.10})(Al_{1.48}Mg_{0.35}Fe^{3+}_{0.17})(Ca_{0.07}Mg_{0.05}Na_{0.13}K_{0.07})_{0.33}O_{10}(OH)_2$
τ charge = -0.10; O. charge = -0.35
Total charge = -0.45 (τ % = 21 o % = 79); FW (g/mol) = 748.15
(No Mg at interlayer: Σ_{oct} = 2.05; Total charge: -0.34, τ % = 28; o % = 72)

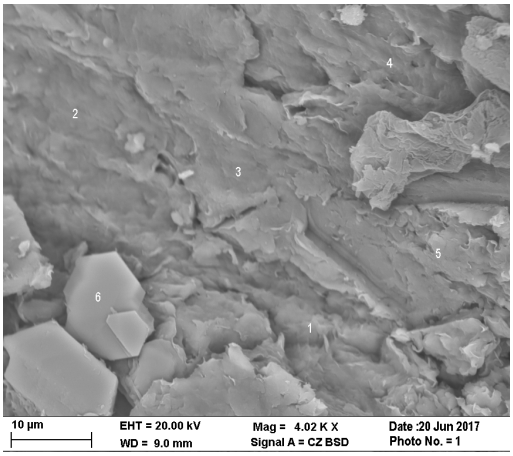

(1) to 5) smectite clay minerals; (6) chlorites

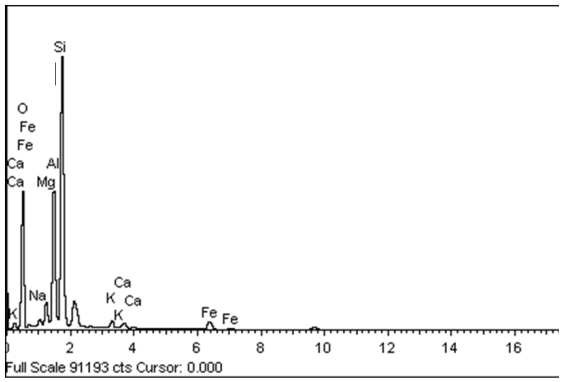

3):$(Si_{3.80}Al_{0.20})(Al_{1.48}Mg_{0.29}Fe^{3+}_{0.24})(Ca_{0.08}Mg_{0.06}Na_{0.12}K_{0.10})_{0.35}O_{10}(OH)_2$
τ charge = -0.20; O. charge = -0.29
Total charge = -0.49 (τ % = 41 o % = 59); FW (g/mol) = 754.67
(No Mg at interlayer: Σ_{oct} = 2.06; Total charge: -0.37, τ % = 54; o % = 46)

Fig. B-198: SEM photomicrographs from sample Black ball particle: clay minerals

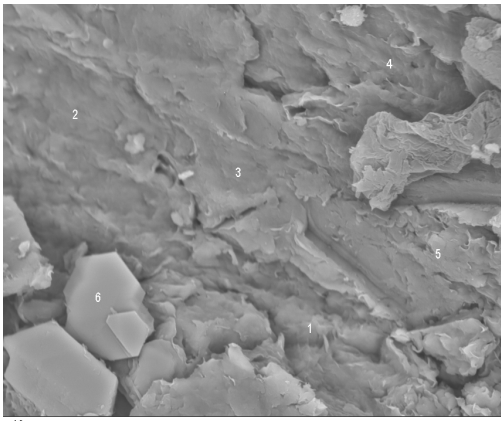

(1) to 5) smectite clay minerals, (6) chlorites

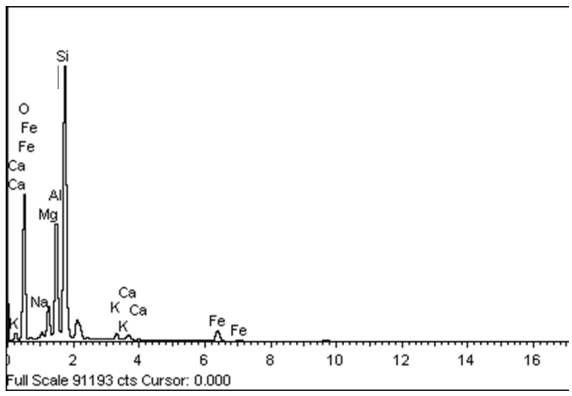

4):$(Si_{3.85}Al_{0.15})(Al_{1.33}Mg_{0.37}Fe^{3+}_{0.30})(Ca_{0.07}Mg_{0.10}Na_{0.10}K_{0.08})_{0.35}O_{10}(OH)_2$
τ charge = -0.15; O. charge = -0.37
Total charge = -0.52 (τ % = 28 o % = 72); FW (g/mol) = 756.94
(No Mg at interlayer: $\Sigma_{oct} = 2.10$; Total charge: -0.32, τ % = 46; o % = 54)

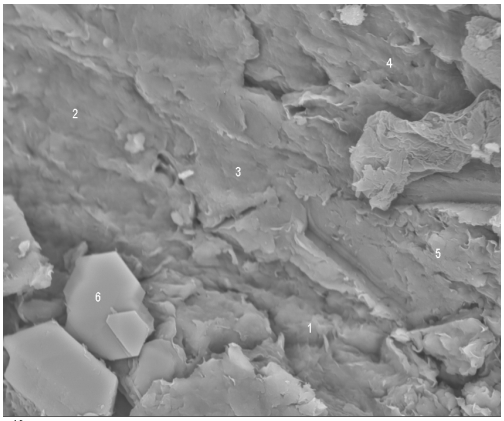

(1) to 5) smectite clay minerals, (6) chlorites

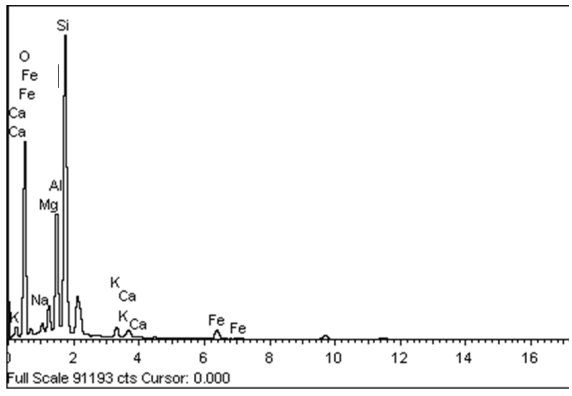

5): $(Si_{3.90}Al_{0.10})^{IV}(Al_{1.34}Mg_{0.39}Fe^{3+}_{0.25\ \ 0.03})^{VI}(Ca_{0.11}Na_{0.22}K_{0.14})_{0.46}O_{10}(OH)_2$
τ charge = -0.10; O. charge = -0.47
Total charge = -0.58 (τ % = 18 o % = 82); FW (g/mol) = 760.64

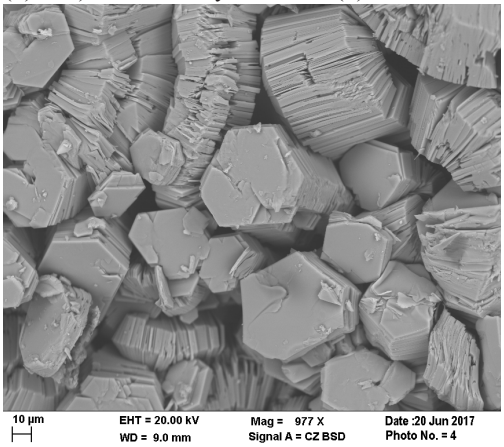

Chlorites

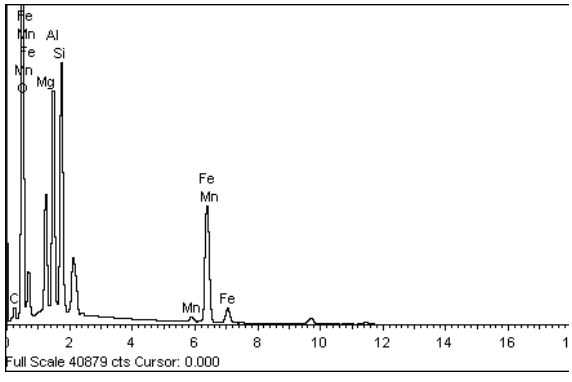

$(Si_{2.87}Al_{1.13})^{IV}$ $(Fe^{2+}_{2.56}Mg_{0.15}Mn^{2+}_{0.09\ \ 0.20})^{VI}$ $O_{10}(OH)_2$ $[Al_{1.47}Mg_{1.53}](OH)_6]$

Fig. B-198: Cont.

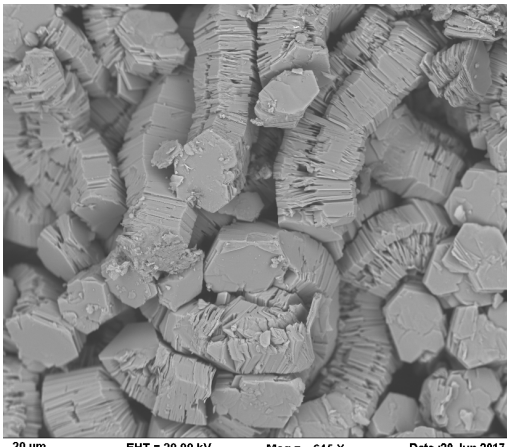

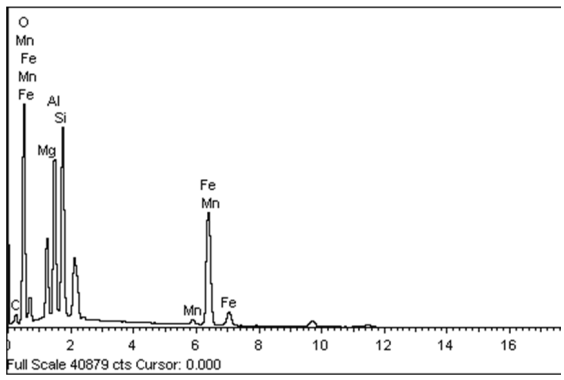

$(Si_{3.34}Al_{0.66})^{IV}$ $(Fe^{2+}_{1.07}Mg_{1.02}Mn^{2+}_{0.14\ \ 0.77})^{VI}$ $O_{10}(OH)_2$ $[Al_{2.21}Mg_{0.79}](OH)_6$ + 44.2 wt.-% $FeCO_3$

Chlorites

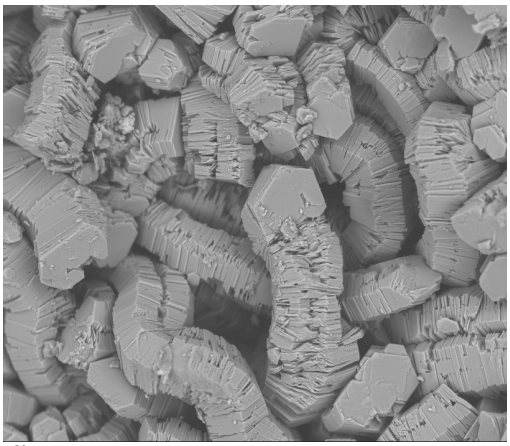

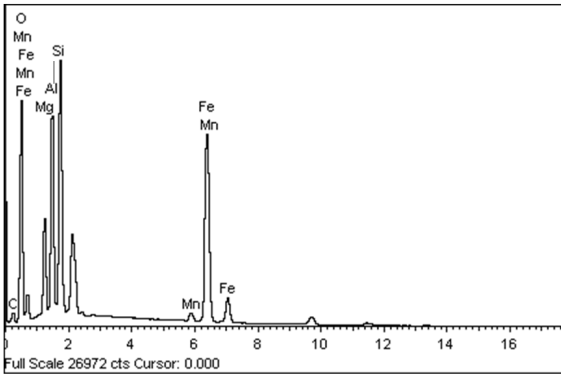

$(Si_{3.07}Al_{0.93})^{IV}$ $(Fe^{2+}_{2.33}Mg_{0.17}Mn^{2+}_{0.15\ \ 0.34})^{VI}$ $O_{10}(OH)_2$ $[Al_{1.61}Mg_{1.39}](OH)_6$ + 31.9 wt.-% $FeCO_3$

Chlorites

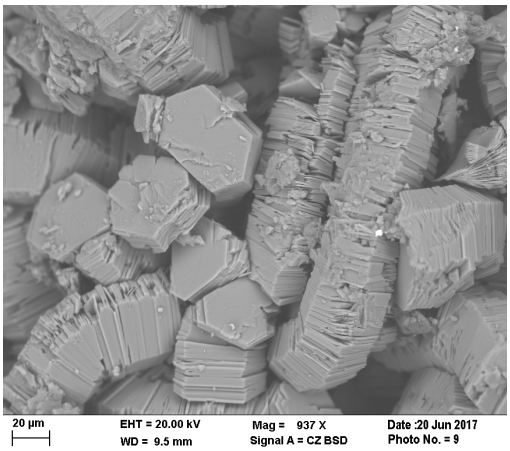

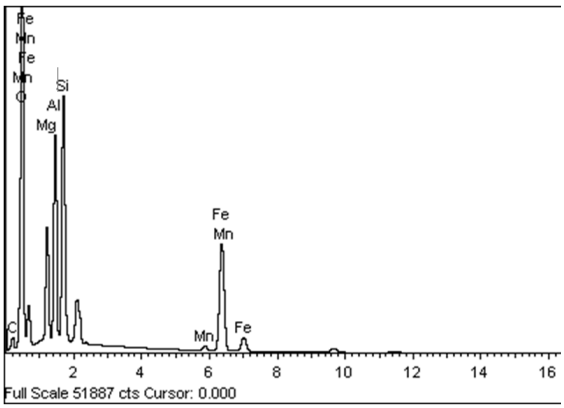

$(Si_{2.99}Al_{1.01})^{IV}$ $(Fe^{2+}_{2.47}Mg_{0.20}Mn^{2+}_{0.08\ \ 0.25})^{VI}$ $O_{10}(OH)_2$ $[Al_{1.51}Mg_{1.49}](OH)_6$

Chlorites

Fig. B-198: Cont.

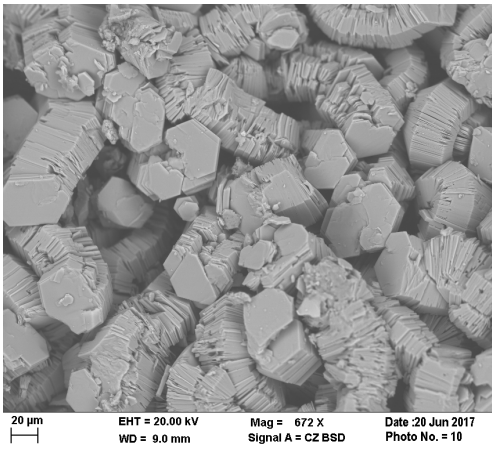

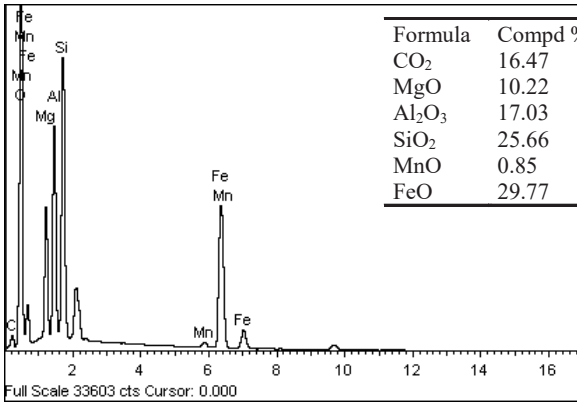

Formula	Compd %
CO_2	16.47
MgO	10.22
Al_2O_3	17.03
SiO_2	25.66
MnO	0.85
FeO	29.77

$(Si_{3.47}Al_{0.53})^{IV}$ $(Fe^{2+}_{0.83}Mg_{1.25}Mn^{2+}_{0.10\ \ 0.83})^{VI}$ $O_{10}(OH)_2$ $[Al_{2.19}Mg_{0.81}](OH)_6$ + 43.4 wt.-% $FeCO_3$

Chlorites

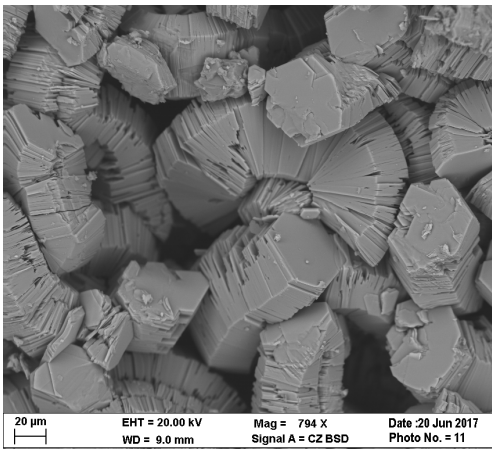

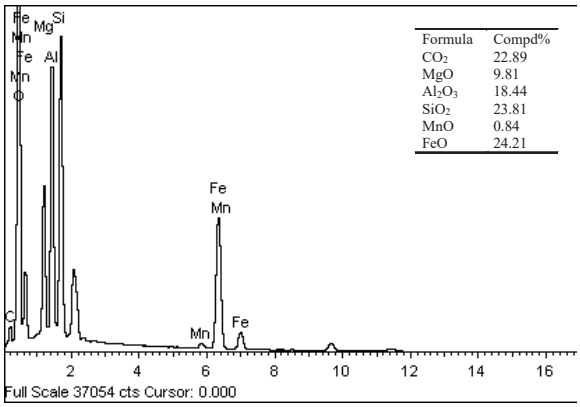

Formula	Compd%
CO_2	22.89
MgO	9.81
Al_2O_3	18.44
SiO_2	23.81
MnO	0.84
FeO	24.21

$(Si_{2.88}Al_{1.12})^{IV}$ $(Fe^{2+}_{2.45}Mg_{0.27}Mn^{2+}_{0.09\ \ 0.19})^{VI}$ $O_{10}(OH)_2$ $[Al_{1.51}Mg_{1.49}](OH)_6$

Chlorites

Fig. B-198: Cont.

Appendix C

Analytical results

Tab. C-1: Total surface area in the bentonite samples (in m^2/g)

Sample	Total SA	Average
FEBEX Ref.	682	668 ± 21
FEBEX Ref.	653	
BB47-1/1	627	625 ± 3
BB47-1/2	623	
BB47-2/1	600	598 ± 4
BB47-2/2	595	
BB47-3/1	618	611 ± 9
BB47-3/2	605	
BB47-4/1	607	599 ± 12
BB47-4/2	590	
BB47-5/1	579	584 ± 6
BB47-5/2	588	
BB47-6/1	615	615 ± 1
BB47-6/2	614	
BB47-7/1	592	594 ± 2
BB47-7/2	595	
BB47-8/1	628	630 ± 2
BB47-8/2	631	
BB47-9/1	623	629 ± 8
BB47-9/2	634	

Sample	Total SA	Average
BB53-1 1	592	577 ± 21
BB53-1 2	562	
BB53-2 1	594	590 ± 6
BB53-2 2	586	
BB53-3 1	622	616 ± 9
BB53-3 2	609	
BB53-4 1	600	605 ± 6
BB53-4 2	609	
BB53-5 1	605	597 ± 11
BB53-5 2	589	
BB53-6 1	555	550 ± 7
BB53-6 2	545	
BB53-7 1	632	631 ± 2
BB53-7 2	629	
BB53-8 1	621	616 ± 7
BB53-8 2	611	
BB53-9 Back 1	560	551 ± 13
BB53-9 Back 2	542	
BB53-9 Heater 1	528	535 ± 10
BB53-9 Heater 2	542	

Tab. C-2: Total surface area in the bentonite samples (in m^2/g). Continuation

Sample	Total SA	Average
BB59-1/1	652	653 ± 0
BB59-1/2	653	
BB59-2/1	563	566 ± 5
BB59-2/2	569	
BB59-3/1	609	621 ± 16
BB59-3/2	632	
BB59-4/1	609	605 ± 5
BB59-4/2	602	
BB59-5/1	598	612 ± 20
BB59-5/2	626	
BB59-6/1	593	588 ± 7
BB59-6/2	583	
BB59-7 1	568	572 ± 6
BB59-7 2	577	
BB59-8 1	544	547 ± 5
BB59-8 2	551	
BB59-9 1	543	538 ± 7
BB59-9 2	532	
BB59-10 1	580	576 ± 5
BB59-10 2	573	
BB59-11 1	566	565 ± 0
BB59-11 2	565	
BB59-12 1	511	517 ± 8
BB59 12 2	523	
BB59-13 1	575	575 ± 0
BB59-13 2	575	
BB59-14 1	519	522 ± 5
BB59-14 2	526	

Sample	Total SA	Average
BB36-1 1	558	556 ± 3
BB36-1 2	554	
BB36-2 1	554	558 ± 6
BB36-2 2	562	
BB36-3 Back 1	583	576 ± 11
BB36-3 Back 2	568	
BB36-3 Red 1	559	556 ± 4
BB36-3 Red 2	554	
BB36-3 Green 1	542	542 ± 1
BB36-3 Green 2	541	
BB36-4 1	600	601 ± 0
BB36-4 2	601	
BB36-5 1	593	593 ± 0
BB36-5 2	593	
BB36-6 1	572	570 ± 4
BB36-6 2	567	

Tab. C-3: CEC from bentonite as a function of the distance from the gallery axis

Sample	**Distance from the gallery axis** (cm)	**CEC** (meq/100g)
FEBEX Ref.	--	98.1 ± 2.0
BB-36-1/S1 green	107.825	94.2 ± 0.3
BB-36-1/S2	96.475	91.8 ± 1.1
BB-36-2/S1	85.125	91.5 ± 0.3
BB-36-2/S2	73.775	94.3 ± 0.8
BB-36-3/S1 back	62.425	92.0 ± 2.5
BB-36-3/S2 green	51.075	94.2 ± 0.1
BB-36-5/S1	85.125	91.5 ± 2.7
BB-36-5/S2	73.775	93.8 ± 0.0
BB-36-6/S1	62.425	94.7 ± 0.7
BB-36-6/S2	51.075	91.6 ± 0.5
BB-47-1/S1	107.825	99.6 ± 0.3
BB-47-1/S2	96.475	96.5 ± 0.5
BB-47-2/S1	85.125	96.3 ± 1.0
BB-47-2/S2	73.775	100.4 ± 0.0
BB-47-3/S1	62.425	95.6 ± 0.1
BB-47-3/S2	51.075	97.7 ± 0.3
BB-47-4/S1	107.825	97.5 ± 3.1
BB-47-4/S2	96.475	97.0 ± 1.0
BB-47-5/S1	85.125	96.2 ± 0.6
BB-47-5/S2	73.775	96.6 ± 1.4
BB-47-6/S1	62.425	99.7 ± 0.4
BB-47-6/S2	51.075	93.4 ± 0.2
BB-47-7/S1	107.825	96.0 ± 0.2
BB-47-7/S2	96.475	92.5 ± 2.1
BB-47-8/S1	85.125	95.7 ± 0.1
BB-47-8/S2	73.775	95.1 ± 1.1
BB-47-9/S1	62.425	95.6 ± 0.3
BB-47-9/S2	51.075	91.5 ± 0.1
BB-53-1/S1	107.825	93.4 ± 0.5
BB-53-1/S2	96.475	94.3 ± 0.3
BB-53-2/S1	85.125	93.7 ± 0.2
BB-53-2/S2	73.775	91.5 ± 3.8

Tab. C-3: Cont.

Sample	**Distance from the gallery axis** (cm)	**CEC** (meq/100g)
BB-53-3/S1	62.425	94.6 ± 0.5
BB-53-3/S2	51.075	95.2 ± 0.1
BB-53-4/S1	107.825	92.2 ± 0.4
BB-53-4/S2	96.475	94.4 ± 0.5
BB-53-5/S1	85.125	90.9 ± 1.6
BB-53-5/S2	73.775	91.1 ± 0.2
BB-53-6/S1	62.425	94.5 ± 0.3
BB-53-6/S2	51.075	88.8 ± 0.9
BB-53-7/S1	107.825	94.1 ± 1.1
BB-53-7/S2	96.475	94.0 ± 0.1
BB-53-8/S1	85.125	95.3 ± 0.8
BB-53-8/S2	73.775	95.9 ± 1.2
BB-53-9/S1	62.425	93.7 ± 1.6
BB-53-9/S2	51.075	93.3 ± 0.1
BB-59-1/S1	107.825	97.5 ± 0.1
BB-59-1/S2	96.475	95.8 ± 0.1
BB-59-2/S1	85.125	93.7 ± 1.0
BB-59-2/S2	73.775	95.4 ± 0.5
BB-59-3/S1	62.425	96.3 ± 0.1
BB-59-3/S2	51.075	92.2 ± 0.7
BB-59-4/S1	39.725	95.9 ± 1.3
BB-59-4/S2	28.375	98.0 ± 0.4
BB-59-5/S1	17.025	97.5 ± 0.3
BB-59-5/S2	5.675	96.4 ± 1.2
BB-59-6/S1	107.825	98.6 ± 0.1
BB-59-6/S2	96.475	94.2 ± 0.1
BB-59-7/S1	85.125	94.8 ± 0.7
BB-59-7/S2	73.775	98.0 ± 1.9
BB-59-8/S1	62.43	95.9 ± 0.9
BB-59-8/S2	51.08	93.8 ± 1.3
BB-59-9/S1	39.73	94.3 ± 1.2
BB-59-9/S2	28.38	93.9 ± 0.2

Tab. C-3: Cont.

Sample	**Distance from the gallery axis** (cm)	**CEC** (meq/100g)
BB-59-10/S1	107.825	97.9 ± 0.6
BB-59-10/S2	96.475	96.5 ± 0.9
BB-59-11/S1	85.125	98.0 ± 0.1
BB-59-11/S2	73.775	96.9 ± 0.4
BB-59-12/S1	62.425	94.4 ± 0.3
BB-59-12/S2	51.075	96.0 ± 2.9
BB-59-13/S1	39.725	93.9 ± 0.1
BB-59-13/S2	28.375	90.1 ± 1.4
BB-59-14/S1	17.025	94.4 ± 0.3
BB-59-14/S2	5.675	98.9 ± 0.2

Tab. C-4: Cation exchange population from bentonite blocks samples (by duplicate: A, B)

Cations (meq/100g)	**Na**	**K**	**Mg**	**Ca**	**Sr**	**Ba**	**Cu**	**Σ cations**
FEBEX Reference	28.00	2.85	33.1	33.2	0.37	0.01	--	97.5
BB-36-1/S1 green A	34.94	4.15	15.59	47.49	0.39	0.02	0.0001	103
BB-36-1/S1 green B	34.95	4.15	15.88	49.02	0.40	0.02	0.0008	104
BB-36-1/S2 A	35.12	4.18	14.49	50.58	0.38	0.01	0.0010	105
BB-36-1/S2 B	35.16	4.18	14.90	48.20	0.39	0.01	0.0034	103
BB-36-2/S1 A	31.44	4.11	19.75	41.35	0.36	0.01	0.0026	97
BB-36-2/S1 B	31.44	4.11	19.94	42.86	0.36	0.01	0.0072	99
BB-36-2/S2 A	31.39	4.12	24.90	42.11	0.40	0.01	0.0016	103
BB-36-2/S2 B	31.37	4.12	24.90	41.19	0.42	0.01	0.0016	102
BB-36-3/S1 back A	26.55	3.81	32.09	36.58	0.36	0.01	0.0028	99
BB-36-3/S1 back B	26.57	3.81	32.46	37.83	0.37	0.01	0.0009	101
BB-36-3/S2 red A	24.71	4.89	29.82	34.18	0.25	0.01	0.0006	94
BB-36-3/S2 red B	24.70	4.89	32.16	33.17	0.27	0.01	0.0016	95
BB-36-3/S2 green A	26.59	5.12	32.06	34.97	0.27	0.01	0.0034	99
BB-36-3/S2 green B	26.58	5.12	30.94	35.08	0.26	0.02	0.0027	98
BB-36-4/S1 A	29.48	3.74	21.71	49.32	0.38	0.03	0.0030	105
BB-36-4/S1 B	29.48	3.74	21.78	49.34	0.39	0.03	0.0059	105
BB-36-4/S2 A	29.64	3.76	14.02	53.01	0.39	0.01	0.0036	101
BB-36-4/S2 B	31.63	3.88	14.47	54.69	0.40	0.01	0.0026	105
BB-36-5/S1 A	29.44	4.70	15.70	50.70	0.39	0.01	0.0054	101
BB-36-5/S1 B	29.45	4.70	15.25	50.46	0.38	0.01	0.0006	100
BB-36-5/S2	31.93	4.29	16.37	49.91	0.39	0.01	0.0007	103
BB-36-5/S2	29.91	4.17	16.48	49.46	0.39	0.01	0.0018	100
BB-36-6/S1 A	29.01	5.48	20.03	46.77	0.35	0.01	0.0023	102
BB-36-6/S1 B	29.01	5.48	21.12	46.57	0.37	0.01	0.0062	103
BB-36-6/S2 A	26.54	5.88	23.13	43.58	0.32	0.01	0.0047	99
BB-36-6/S2 B	26.56	5.88	22.76	44.02	0.32	0.01	0.0004	100
BB-47-1/S1 A	29.91	3.84	32.47	34.70	0.32	0.02	< d.l.	101
BB-47-1/S1 B	30.37	3.13	32.86	35.91	0.34	0.01	< d.l.	103
BB-47-1/S2 A	29.68	2.93	27.88	29.03	0.28	0.01	< d.l.	90
BB-47-1/S2 B	30.56	3.28	33.91	38.18	0.37	0.01	< d.l.	106
BB-47-2/S1 A	30.34	3.00	29.70	38.21	0.37	0.01	< d.l.	102
BB-47-2/S1 B	29.19	3.36	33.17	36.06	0.42	0.01	< d.l.	102
BB-47-2/S2 A	30.43	3.03	28.85	37.53	0.39	0.01	< d.l.	100

Tab. C-4: Cation exchange population from bentonite blocks samples (by duplicate: A, B)

Cations (meq/100g)	Na	K	Mg	Ca	Sr	Ba	Cu	Σ cations
BB-47-2/S2 B	30.29	3.39	34.31	40.08	0.48	0.01	< d.l.	109
BB-47-3/S1 A	25.86	2.84	30.45	38.84	0.31	0.00	< d.l.	98
BB-47-3/S1 B	24.88	3.31	35.02	39.45	0.37	0.01	< d.l.	103
BB-47-3/S2 A	15.33	2.95	36.49	41.69	0.31	0.00	0.0006	97
BB-47-3/S2 B	15.57	3.31	39.53	39.70	0.36	0.01	< d.l.	98
BB-47-4/S1 A	31.41	3.37	32.14	35.80	0.30	0.01	< d.l.	103
BB-47-4/S1 B	30.30	3.72	33.63	34.67	0.33	0.01	< d.l.	103
BB-47-4/S2 A	31.55	3.15	28.88	35.69	0.37	0.01	< d.l.	100
BB-47-4/S2 B	30.42	3.73	36.01	39.13	0.36	0.01	< d.l.	110
BB-47-5/S1 A	31.70	3.17	30.56	34.49	0.29	0.01	< d.l.	100
BB-47-5/S1 B	31.57	3.52	31.69	34.53	0.42	0.01	< d.l.	102
BB-47-5/S2 A	29.41	2.91	31.49	35.77	0.37	0.01	< d.l.	100
BB-47-5/S2 B	29.25	3.50	31.11	34.14	0.36	0.01	< d.l.	98
BB-47-6/S1 A	26.00	2.85	33.59	39.44	0.32	0.01	< d.l.	102
BB-47-6/S1 B	25.01	3.09	33.97	37.66	0.34	0.01	< d.l.	100
BB-47-6/S2 A	11.27	3.18	41.64	41.97	0.29	0.01	< d.l.	98
BB-47-6/S2 B	12.06	3.53	41.64	42.24	0.39	0.01	< d.l.	100
BB-47-7/S1 A	30.33	3.34	31.06	36.90	0.34	0.01	< d.l.	102
BB-47-7/S1 B	30.19	3.58	32.98	34.56	0.34	0.02	< d.l.	102
BB-47-7/S2 A	30.10	3.20	31.64	36.21	0.33	0.01	< d.l.	101
BB-47-7/S2 B	28.96	3.55	31.63	36.30	0.35	0.01	< d.l.	101
BB-47-8/S1 A	28.42	3.01	29.79	35.74	0.37	0.01	< d.l.	97
BB-47-8/S1 B	29.32	3.37	32.89	38.20	0.43	0.01	< d.l.	104
BB-47-8/S2 A	27.88	2.98	29.13	39.43	0.32	0.01	0.0012	100
BB-47-8/S2 B	28.75	3.34	33.73	39.03	0.43	0.01	< d.l.	105
BB-47-9/S1 A	26.37	2.99	32.28	34.56	0.35	0.00	< d.l.	97
BB-47-9/S1 B	23.40	3.11	42.26	41.24	0.36	0.01	< d.l.	110
BB-47-9/S2 A	15.54	3.06	32.22	41.94	0.28	0.00	< d.l.	93
BB-47-9/S2 B	13.33	3.30	32.22	37.61	0.34	0.01	< d.l.	87
BB-53-1/S1 A	31.34	3.02	31.76	35.78	0.31	0.01	< d.l.	102
BB-53-1/S1 B	29.38	2.90	31.39	33.52	0.30	0.01	< d.l.	98
BB-53-1/S2 A	29.45	3.03	28.90	37.78	0.29	0.01	< d.l.	99
BB-53-1/S2 B	29.45	3.03	28.90	40.07	0.29	0.01	< d.l.	102
BB-53-2/S1 A	27.50	3.02	31.36	33.65	0.35	0.01	< d.l.	96

Tab. C-4: Cation exchange population from bentonite blocks samples (by duplicate: A, B)

Cations (meq/100g)	Na	K	Mg	Ca	Sr	Ba	Cu	Σ cations
BB-53-2/S1 B	28.75	3.03	31.47	35.14	0.37	0.01	< d.l.	99
BB-53-2/S2 A	28.49	3.01	29.77	32.67	0.35	0.01	< d.l.	94
BB-53-2/S2 B	28.32	2.99	29.63	32.87	0.35	0.01	< d.l.	94
BB-53-3/S1 A	25.53	3.04	32.29	36.97	0.33	0.01	< d.l.	98
BB-53-3/S1 B	26.02	3.28	32.37	36.60	0.36	0.01	< d.l.	99
BB-53-3/S2 A	15.20	2.84	36.60	34.88	0.30	0.01	< d.l.	90
BB-53-3/S2 B	15.61	2.84	38.89	38.08	0.30	0.01	< d.l.	96
BB-53-4/S1 A	27.60	3.15	30.07	33.59	0.30	0.01	< d.l.	95
BB-53-4/S1 B	27.58	3.04	30.07	33.58	0.29	0.01	< d.l.	95
BB-53-4/S2 A	27.59	2.92	28.96	37.82	0.30	0.01	< d.l.	98
BB-53-4/S2 B	29.57	3.04	30.46	33.22	0.32	0.01	0.0009	97
BB-53-5/S1 A	27.63	3.01	30.51	32.37	0.33	0.01	< d.l.	94
BB-53-5/S1 B	28.01	3.01	29.08	34.09	0.35	0.01	< d.l.	95
BB-53-5/S2 A	26.18	2.99	30.35	32.31	0.33	0.01	< d.l.	92
BB-53-5/S2 B	26.23	3.00	33.37	34.16	0.33	0.01	< d.l.	97
BB-53-6/S1 A	26.17	3.05	33.17	37.53	0.33	0.01	< d.l.	100
BB-53-6/S1 B	26.02	3.04	40.59	36.00	0.33	0.01	< d.l.	106
BB-53-6/S2 A	16.61	3.21	39.79	36.41	0.31	0.01	< d.l.	96
BB-53-6/S2 B	16.45	3.19	30.83	35.84	0.29	0.01	< d.l.	87
BB-53-7/S1 A	28.99	3.11	32.21	33.12	0.31	0.01	< d.l.	98
BB-53-7/S1 B	29.03	3.11	33.70	39.89	0.31	0.01	0.0004	106
BB-53-7/S2 A	29.06	3.11	31.88	39.59	0.31	0.01	< d.l.	104
BB-53-7/S2 B	29.02	3.00	32.25	41.84	0.32	0.01	< d.l.	106
BB-53-8/S1 A	29.60	3.02	29.90	33.21	0.31	0.02	< d.l.	96
BB-53-8/S1 B	29.61	3.26	31.45	33.61	0.33	0.02	< d.l.	98
BB-53-8/S2 A	27.84	3.24	32.04	35.37	0.37	0.01	< d.l.	99
BB-53-8/S2 B	27.86	3.25	32.11	35.89	0.37	0.01	< d.l.	100
BB-53-9/S1 A	25.99	3.05	31.70	36.08	0.34	0.01	< d.l.	97
BB-53-9/S1 B	26.00	3.05	43.70	34.71	0.33	0.01	< d.l.	108
BB-53-9/S2 A	12.61	3.03	44.28	39.21	0.31	0.01	< d.l.	99
BB-53-9/S2 B	12.49	3.02	29.92	39.09	0.31	0.01	< d.l.	85
BB-59-1/S1 A	28.27	3.01	36.54	41.93	0.34	0.01	< d.l.	110
BB-59-1/S1 B	28.23	3.36	37.28	34.50	0.36	0.01	< d.l.	104
BB-59-1/S2 A	30.16	3.02	36.60	38.88	0.36	0.01	< d.l.	109

Tab. C-4: Cation exchange population from bentonite blocks samples (by duplicate: A, B)

Cations (meq/100g)	Na	K	Mg	Ca	Sr	Ba	Cu	Σ cations
BB-59-1/S2 B	26.30	3.37	35.48	32.66	0.32	0.01	< d.l.	98
BB-59-2/S1 A	27.66	2.99	37.01	38.40	0.36	0.01	< d.l.	106
BB-59-2/S1 B	25.81	3.22	35.53	32.16	0.34	0.01	< d.l.	97
BB-59-2/S2 A	27.35	3.10	36.96	36.16	0.35	0.01	0.0004	104
BB-59-2/S2 B	27.31	3.45	40.66	31.75	0.37	0.01	< d.l.	104
BB-59-3/S1 A	27.20	3.02	35.09	36.71	0.33	0.01	0.0006	102
BB-59-3/S1 B	27.30	3.37	37.33	32.38	0.35	0.01	< d.l.	101
BB-59-3/S2 A	25.15	2.91	34.12	32.50	0.33	0.01	< d.l.	95
BB-59-3/S2 B	25.24	3.38	37.49	31.68	0.33	0.01	< d.l.	98
BB-59-4/S1 A	26.67	2.79	34.77	32.50	0.35	0.01	0.0004	97
BB-59-4/S1 B	24.81	3.37	37.39	32.73	0.33	0.01	< d.l.	99
BB-59-4/S2 A	24.97	2.83	34.86	32.99	0.36	5.77	< d.l.	102
BB-59-4/S2 B	24.97	3.42	37.89	33.25	0.35	0.01	< d.l.	100
BB-59-5/S1 A	26.46	2.89	35.68	32.25	0.35	0.00	< d.l.	98
BB-59-5/S1 B	26.37	3.35	37.16	34.62	0.36	0.01	< d.l.	102
BB-59-5/S2 A	26.38	2.77	34.85	32.15	0.34	0.01	0.0004	96
BB-59-5/S2 B	26.32	3.23	36.33	33.50	0.33	0.00	< d.l.	100
BB-59-6/S1 A	28.69	2.92	32.32	33.31	0.32	0.01	< d.l.	98
BB-59-6/S1 B	26.56	3.51	34.96	33.29	0.31	0.01	< d.l.	99
BB-59-6/S2 A	28.04	2.88	32.59	31.86	0.34	0.01	< d.l.	96
BB-59-6/S2 B	28.29	3.34	33.70	32.87	0.33	0.01	< d.l.	99
BB-59-7/S1 A	26.26	2.93	33.23	30.13	0.34	0.01	< d.l.	93
BB-59-7/S1 B	26.26	2.93	32.10	30.12	0.31	0.01	< d.l.	92
BB-59-7/S2 A	25.64	2.91	32.95	29.97	0.33	0.01	< d.l.	92
BB-59-7/S2 B	25.68	2.91	32.95	29.97	0.33	0.01	< d.l.	92
BB-59-8/S1 A	25.41	2.93	32.40	30.09	0.32	0.00	< d.l.	91
BB-59-8/S1 B	25.42	2.93	33.15	32.38	0.32	0.00	< d.l.	94
BB-59-8/S2 A	23.17	2.93	31.62	29.99	0.31	0.01	< d.l.	88
BB-59-8/S2 B	25.21	2.93	34.26	34.54	0.34	0.01	< d.l.	97
BB-59-9/S1 A	23.56	3.19	37.28	32.64	0.33	0.00	0.0046	97
BB-59-9/S1 B	23.67	3.19	36.91	32.75	0.32	0.00	0.0017	97
BB-59-9/S2 A	23.60	3.19	37.34	32.60	0.33	0.00	0.0027	97
BB-59-9/S2 B	23.51	3.19	36.60	32.53	0.33	0.00	0.0019	96
BB-59-10/S1 A	26.82	3.03	33.02	33.37	0.32	0.01	< d.l.	97

Tab. C-4: Cation exchange population from bentonite blocks samples (by duplicate: A, B)

Cations (meq/100g)	**Na**	**K**	**Mg**	**Ca**	**Sr**	**Ba**	**Cu**	**Σ cations**
BB-59-10/S1 B	26.82	3.03	35.65	35.63	0.35	0.01	< d.l.	101
BB-59-10/S2 A	27.46	3.26	33.37	33.25	0.34	0.01	< d.l.	98
BB-59-10/S2 B	27.39	3.14	34.53	33.23	0.36	0.01	< d.l.	99
BB-59-11/S1 A	26.27	3.15	34.89	32.38	0.34	0.01	< d.l.	97
BB-59-11/S1 B	26.27	3.15	33.77	32.38	0.34	0.01	< d.l.	96
BB-59-11/S2 A	26.02	3.16	37.61	36.65	0.38	0.01	< d.l.	104
BB-59-11/S2 B	26.04	3.16	37.61	34.36	0.37	0.01	< d.l.	102
BB-59-12/S1 A	25.83	3.04	35.35	29.74	0.31	0.01	< d.l.	94
BB-59-12/S1 B	26.11	3.03	34.48	31.86	0.33	0.01	< d.l.	96
BB-59-12/S2 A	29.82	3.47	39.46	35.62	0.36	0.02	< d.l.	109
BB-59-12/S2 B	28.00	3.20	38.04	32.97	0.33	0.01	< d.l.	103
BB-59-13/S1 A	25.80	3.01	35.01	32.17	0.33	0.01	< d.l.	96
BB-59-13/S1 B	26.24	3.01	33.57	31.27	0.33	0.01	< d.l.	94
BB-59-13/S2 A	19.08	2.98	33.14	29.78	0.31	0.01	< d.l.	85
BB-59-13/S2 B	19.12	2.98	29.52	29.84	0.31	0.01	< d.l.	82
BB-59-14/S1 A	23.88	3.23	37.03	32.96	0.34	0.00	0.0012	97
BB-59-14/S1 B	23.88	3.23	37.41	32.99	0.34	0.00	0.0014	98
BB-59-14/S2 A	24.71	3.33	38.98	35.34	0.34	0.00	0.0092	103
BB-59-14/S2 B	24.67	3.33	38.98	36.49	0.35	0.50	0.0021	104

Tab. C-5: Chemical composition of the trace elements in the total fraction (in ppm)

Samples	Ag	As	Ba	Bi	Br	Cd	Ce	Co	Cr	Cs	Cu	Ga	Ge	Hf	I	La	Mn	Mo	Nb	Nd	Ni	P	Pb
FEBEX Ref.*	< d.l.	6.8	61.6	< d.l.	1.5	< d.l.	63.5	5.7	5.2	5.1	10.0	20.6	< d.l.	7.1	1.3	35.3	--	< d.l.	11.3	25.6	12.0	--	33.7
BB-36-1	< d.l.	6.6	87.6	< d.l.	< d.l.	< d.l.	71.3	n.d.	5.5	< d.l.	13.7	19.5	2.0	4.8	< d.l.	33.7	238.1	< d.l.	11.4	29.1	16.1	119.5	31.3
BB-36-2	< d.l.	6.7	78.7	< d.l.	< d.l.	< d.l.	69.8	1.8	6.0	< d.l.	12.3	19.5	2.1	5.0	< d.l.	32.3	230.4	< d.l.	11.2	31.4	16.3	112.5	29.0
BB-36-3/1 back	< d.l.	7.1	72.0	< d.l.	n.d.	< d.l.	69.8	2.1	6.2	< d.l.	10.6	19.3	2.0	4.6	< d.l.	32.7	232.0	< d.l.	11.5	29.4	14.7	94.3	30.2
BB-36-3/2 red	< d.l.	6.2	92.3	< d.l.	n.d.	< d.l.	71.8	< d.l.	5.1	< d.l.	13.0	19.9	1.8	3.4	n.d.	30.4	210.1	n.d.	11.9	30.2	15.3	116.6	30.7
BB-36-3/2 green	< d.l.	6.3	84.2	< d.l.	n.d.	< d.l.	71.7	n.d.	6.0	< d.l.	14.3	19.7	1.9	4.5	< d.l.	34.7	199.0	< d.l.	11.7	30.3	15.0	108.9	32.0
BB-36-4	< d.l.	5.3	81.7	< d.l.	< d.l.	< d.l.	74.2	n.d.	7.5	< d.l.	13.5	19.7	2.2	4.6	< d.l.	35.1	230.4	< d.l.	11.4	31.9	16.4	105.9	29.3
BB-36-5	< d.l.	6.5	74.1	< d.l.	< d.l.	< d.l.	68.0	n.d.	7.8	< d.l.	14.2	19.7	1.9	4.3	< d.l.	35.4	233.6	< d.l.	11.6	30.9	16.2	115.9	30.6
BB-36-6	< d.l.	4.8	89.1	< d.l.	n.d.	< d.l.	75.5	n.d.	7.6	< d.l.	13.9	19.7	2.0	5.3	n.d.	32.1	236.2	< d.l.	11.3	32.5	15.3	110.5	29.8
BB-47-7	< d.l.	8.5	91.2	< d.l.	< d.l.	< d.l.	75.8	n.d.	6.8	< d.l.	13.9	20.3	2.0	4.4	< d.l.	36.0	245.0	< d.l.	11.9	32.5	19.1	102.4	32.3
BB-47-8	n.d.	6.9	95.2	< d.l.	n.d.	< d.l.	67.5	n.d.	7.8	< d.l.	12.3	19.6	2.1	6.4	< d.l.	31.3	237.6	< d.l.	11.2	29.2	15.3	111.9	30.6
BB-47-9	< d.l.	7.5	71.5	< d.l.	7.7	< d.l.	69.8	n.d.	5.1	< d.l.	13.7	19.9	1.8	5.2	n.d.	32.4	235.8	< d.l.	11.1	28.7	15.5	102.5	30.6
BB-53-4	< d.l.	7.7	87.9	n.d.	n.d.	n.d.	75.3	2.2	7.4	n.d.	13.5	19.3	1.5	3.6	< d.l.	30	237.6	n.d.	11.8	32.9	16.5	114	30.9
BB-53-5	< d.l.	6.9	78.6	n.d.	n.d.	n.d.	74.2	2.1	6.1	n.d.	14.3	19.1	1.7	3.5	< d.l.	33.3	228.9	n.d.	11.4	33.1	15.7	111.7	30.8
BB-53-6	< d.l.	4.7	69.1	n.d.	4.7	< d.l.	73.5	1.9	5.4	n.d.	14.4	18.7	1.3	4.4	< d.l.	33.1	231.7	n.d.	11.6	31.7	15.7	108.6	30.5
BB-59-1	n.d.	8.4	96.2	< d.l.	1.1	< d.l.	70.0	n.d.	7.6	< d.l.	12.2	19.2	1.9	4.4	n.d.	32.0	240.7	< d.l.	10.3	30.5	14.4	116.9	28.7
BB-59-2	< d.l.	7.2	81.1	< d.l.	1.6	< d.l.	75.2	n.d.	6.6	< d.l.	12.7	19.5	2.0	5.1	n.d.	34.5	227.9	< d.l.	11.5	31.8	16.1	116.0	30.5
BB-59-3	n.d.	6.8	69.8	< d.l.	2.1	< d.l.	75.8	n.d.	6.9	< d.l.	12.7	19.1	1.6	4.3	< d.l.	31.9	224.2	< d.l.	11.2	32.0	16.6	102.5	30.0
BB-59-4	< d.l.	8.2	66.9	< d.l.	2.6	< d.l.	68.4	n.d.	5.8	< d.l.	12.4	19.7	1.9	4.2	< d.l.	32.1	219.5	< d.l.	11.5	30.3	15.1	105.7	32.0
BB-59-5	< d.l.	6.6	86.7	< d.l.	2.4	< d.l.	73.1	n.d.	7.0	< d.l.	12.2	20.2	1.9	5.4	< d.l.	33.7	227.1	< d.l.	12.0	34.5	16.2	126.6	32.3

* Trace elements determined by XRF

Tab. C-6: Chemical composition of the trace elements in the total fraction (in ppm). Continuation

Samples	Rb	Sb	Sc	Se	Sm	Sn	Sr	Ta	Te	Th	Tl	U	V	W	Y	Yb	Zn	Zr	Cl	F	Hg	S
FEBEX Ref.*	40.4	3.2	9.6	0.1	7.2	9.4	197.0	1.3	1.1	14.3	< d.l.	0.4	15.9	1.4	25.7	1.6	59.5	183.9	236.0	--	--	--
BB-36-1	41.4	< d.l.	11.4	< d.l.	7.3	6.6	192.1	3.3	< d.l.	15.3	< d.l.	< d.l.	15.7	< d.l.	26.3	< d.l.	58.3	185.4	< d.l.	2191	n.d.	153
BB-36-2	42.0	< d.l.	11.4	n.d.	9.6	5.7	198.8	3.4	< d.l.	15.1	< d.l.	< d.l.	16.2	< d.l.	27.3	< d.l.	59.2	182.8	n.d.	2031	n.d.	459
BB-36-3/1 back	38.7	< d.l.	11.0	< d.l.	8.4	5.7	194.7	2.7	< d.l.	15.5	< d.l.	n.d.	15.1	< d.l.	25.4	n.d.	56.1	186.3	98	1965	n.d.	207
BB-36-3/2 red	44.3	n.d.	10.8	< d.l.	7.4	8.2	152.0	3.0	n.d.	16.1	< d.l.	< d.l.	15.3	< d.l.	25.2	< d.l.	57.1	188.9	138	2434	< d.l.	124
BB-36-3/2 greeen	43.6	< d.l.	11.5	< d.l.	9.3	6.4	154.0	3.1	< d.l.	15.3	< d.l.	< d.l.	13.1	< d.l.	25.9	< d.l.	57.1	185.6	113	2276	< d.l.	117
BB-36-4	42.0	< d.l.	11.5	< d.l.	6.7	6.7	199.5	3.1	n.d.	15.6	< d.l.	n.d.	16.2	< d.l.	27.9	< d.l.	59.0	184.6	< d.l.	2324	n.d.	n.d.
BB-36-5	44.5	< d.l.	11.0	< d.l.	n.d.	7.0	199.4	3.7	< d.l.	16.2	< d.l.	n.d.	16.2	< d.l.	27.8	n.d.	59.5	186.3	n.d.	1978	n.d.	235
BB-36-6	42.6	< d.l.	11.0	< d.l.	9.1	6.9	205.2	3.3	< d.l.	15.1	< d.l.	< d.l.	14.5	< d.l.	25.7	< d.l.	57.3	186.5	n.d.	2231	< d.l.	188
BB-47-7	41.8	< d.l.	11.3	n.d.	7.1	7.9	175.2	3.3	n.d.	16.0	n.d.	< d.l.	16.0	< d.l.	27.4	n.d.	60.5	194.3	< d.l.	1645	n.d.	67
BB-47-8	39.8	n.d.	10.7	< d.l.	6.9	8.7	198.5	3.9	n.d.	15.6	< d.l.	n.d.	15.5	< d.l.	25.9	n.d.	57.1	185.2	n.d.	2020	n.d.	596
BB-47-9	39.2	n.d.	10.9	< d.l.	7.8	7.5	176.5	3.7	n.d.	15.1	n.d.	1.5	14.6	< d.l.	25.9	n.d.	58.3	181.4	1931	2108	109	332
BB-53-4	41.7	n.d.	10.9	n.d.	7.8	6.7	178.4	3.3	n.d.	15	< d.l.	n.d.	17.2	n.d.	28	n.d.	57.1	187.1	n.d.	2139	n.d.	107
BB-53-5	40.3	< d.l.	10.6	n.d.	8.4	7.6	199.9	2.7	< d.l.	14.5	n.d.	< d.l.	17	n.d.	27	< d.l.	55.6	183.5	n.d.	1912	< d.l.	303
BB-53-6	38.6	n.d.	11.1	n.d.	10.2	8	179.6	3.5	< d.l.	14.9	n.d.	n.d.	15.2	n.d.	26.4	< d.l.	54.6	182.2	1053	1921	159	415
BB-59-1	42.5	< d.l.	10.2	< d.l.	9.0	6.5	194.1	2.9	< d.l.	14.1	n.d.	n.d.	14.3	< d.l.	26.8	n.d.	54.8	166.6	231	2231	n.d.	247
BB-59-2	40.4	< d.l.	12.1	< d.l.	7.4	7.0	189.2	4.6	n.d.	14.9	< d.l.	< d.l.	15.1	< d.l.	27.2	n.d.	58.8	191.1	266	2183	< d.l.	299
BB-59-3	38.4	< d.l.	11.6	< d.l.	6.4	7.8	188.4	3.5	< d.l.	15.0	< d.l.	< d.l.	15.1	< d.l.	25.7	n.d.	56.6	181.1	469	1915	< d.l.	251
BB-59-4	37.8	< d.l.	11.5	< d.l.	7.7	6.3	183.7	3.8	< d.l.	15.6	n.d.	< d.l.	14.0	< d.l.	26.8	< d.l.	56.6	186.7	547	2214	< d.l.	217
BB-59-5	40.0	n.d.	11.2	< d.l.	9.0	8.7	193.3	3.5	n.d.	16.0	< d.l.	n.d.	15.7	< d.l.	26.4	< d.l.	58.7	196.0	511	2470	< d.l.	317

* Trace elements determined by XRF

Tab. C-7: Chemical composition of the major oxides in the < 2 µm fraction of a Ba-homoionized sample (in wt.-%)

Samples	**SiO_2**	**Al_2O_3**	**Fe_2O_3**	**MnO**	**MgO**	**CaO**	**Na_2O**	**K_2O**	**TiO_2**	**P_2O_5**	**SO_3**	**Ba**	**SUM**	**LOI**
FEBEX Ref.*	52.92	16.03	3.66	0.03	4.41	1.04	0.68	0.66	0.12	0.01	< 0.01	n.d.	99.08	19.42
BB-36-1	50.30	14.97	3.27	0.04	4.13	0.06	0.27	0.72	0.28	0.02	< 0.05	8.1	99.19	17.71
BB-36-2	50.05	14.75	3.40	0.04	4.10	0.06	0.25	0.72	0.26	0.02	< 0.05	8.2	99.32	17.32
BB-36-3/1 back	50.28	15.02	3.08	0.04	4.08	0.07	0.26	0.58	0.23	0.01	< 0.05	8.0	99.04	17.29
BB-36-3/2 green	50.42	14.90	3.06	0.04	4.05	0.05	0.26	0.61	0.23	0.02	< 0.05	7.6	98.68	16.91
BB-36-3/2 red	50.09	14.76	3.87	0.04	3.98	0.07	0.26	0.70	0.25	0.02	< 0.04	8.1	99.13	17.36
BB-47-7	49.69	14.73	3.30	0.04	4.07	0.09	0.28	0.75	0.27	0.02	< 0.07	8.0	99.08	17.32
BB-47-8	49.79	14.79	3.31	0.04	4.09	0.06	0.26	0.70	0.25	0.02	< 0.05	8.1	99.15	17.65
BB-47-9	49.85	14.91	3.23	0.04	4.22	0.05	0.25	0.60	0.23	0.01	< 0.05	8.0	99.10	17.58
BB-53-4	50.06	14.89	3.25	0.04	4.17	0.06	0.27	0.68	0.23	0.02	< 0.04	8.3	99.34	17.29
BB-53-5	48.64	14.55	3.08	0.03	4.06	0.08	0.24	0.60	0.23	0.02	< 0.08	7.8	98.87	19.39
BB-53-6	48.64	14.39	3.24	0.03	3.96	0.05	0.25	0.58	0.23	0.02	< 0.05	8.1	99.14	19.57
BB-59-1	49.99	15.02	3.21	0.04	4.15	0.05	0.26	0.62	0.25	0.02	< 0.04	8.2	99.28	16.91
BB-59-2	50.41	14.91	3.37	0.04	4.13	0.06	0.25	0.68	0.25	0.02	< 0.05	8.1	99.22	16.85
BB-59-3	49.76	14.90	3.34	0.04	4.02	0.07	0.25	0.61	0.24	0.02	< 0.06	8.3	99.34	17.71
BB-59-4	49.67	14.68	3.66	0.04	3.95	0.08	0.25	0.71	0.26	0.02	< 0.05	8.0	99.09	17.65
BB-59-5	50.31	14.91	2.94	0.02	4.06	0.05	0.25	0.59	0.22	0.02	< 0.04	7.2	98.26	17.58

* Major elements determined by XRF

Tab. C-8: Chemical composition of the trace elements in the < 2 µm fraction of a Ba-homoionized sample (in ppm). Continuation

Sample	As	Cl	Co	Cr	Cu	Ga	Hf	La	Mo	Nb	Nd	Ni
FEBEX Ref.*	25.3	N.D.	6.0	2.2	N.D.	25.2	4.9	n.d.	2.3	26.9	23.7	12.8
BB-36-1	20.2	< d.l.	8.9	19.0	10.1	19.6	5.9	51.9	1.9	9.7	69.7	22.3
BB-36-2	7.4	< d.l.	6.6	17.0	17.5	20.0	6.3	51.9	1.8	3.3	64.3	17.7
BB-36-3/1 back	13.0	< d.l.	5.9	26.8	18.6	20.1	3.3	41.2	2.1	12.2	54.5	19.5
BB-36-3/2 green	5.0	< d.l.	6.9	17.3	14.8	18.0	6.8	49.8	2.0	16.4	58.7	21.5
BB-36-3/2 red	4.5	< d.l.	10.8	7.8	10.9	21.1	4.8	52.5	1.9	5.9	67.4	10.4
BB-47-7	6.2	< d.l.	10.4	21.0	14.1	21.7	5.2	57.9	1.8	9.4	63.6	17.8
BB-47-8	8.1	< d.l.	10.8	22.6	21.9	20.2	7.6	47.5	1.8	4.9	73.0	16.5
BB-47-9	< d.l.	< d.l.	10.4	18.6	13.9	19.5	5.8	50.3	2.0	9.9	59.8	14.5
BB-53-4	19.9	4.7	6.3	29.4	6.5	19.5	2.8	53.6	2.0	11.3	68.8	21.9
BB-53-5	2.8	< d.l.	6.2	44.0	20.7	19.7	6.2	60.5	2.0	13.3	62.1	16.6
BB-53-6	7.6	< d.l.	10.0	10.9	17.6	21.2	6.6	44.0	1.8	6.1	57.4	11.2
BB-59-1	1.2	< d.l.	7.8	18.4	47.7	20.2	4.9	52.6	1.8	6.4	60.5	23.7
BB-59-2	3.6	< d.l.	7.9	15.9	26.0	19.9	6.5	51.7	1.7	1.4	62.6	27.6
BB-59-3	7.3	< d.l.	5.7	71.8	23.1	21.1	6.4	47.8	2.0	6.2	59.2	23.6
BB-59-4	12.7	< d.l.	9.2	19.8	13.4	20.2	6.4	51.4	1.8	5.9	61.7	27.4
BB-59-5	N.D.	< d.l.	4.7	24.6	2.6	19.4	5.4	45.2	2.2	22.4	55.3	15.0

* Trace elements determined by XRF

Tab. C-9: Chemical composition of the trace elements in the < 2 µm fraction of a Ba-homoionized sample (in ppm). Continuation

Samples	Pb	Rb	Sc	Sm	Sr	Ta	Th	Tl	V	U	W	Y	Yb	Zn	Zr
FEBEX Ref.*	36.7	57.3	8.2	5.6	216.6	n.d.	24.5	0.8	20.9	6.2	5.1	22.8	1.5	137.1	177.2
BB-36-1	33.4	44.4	21.0	5.6	19.4	< d.l.	11.4	0.9	160.0	2.9	4.3	22.1	2.1	113.7	140.5
BB-36-2	28.8	48.2	18.0	5.7	13.8	15.0	4.4	0.8	158.0	0.0	0.7	20.0	2.1	110.6	142.1
BB-36-3/1 back	18.1	38.6	16.8	5.7	19.4	< d.l.	14.9	0.9	151.5	1.8	< d.l.	20.3	1.9	101.9	118.2
BB-36-3/2 green	23.0	36.7	17.4	5.6	18.3	4.7	17.9	0.8	160.7	4.6	2.3	20.7	1.6	105.4	111.8
BB-36-3/2 red	22.5	44.1	9.9	5.7	16.6	2.5	9.7	0.7	167.1	1.9	11.0	20.7	1.7	110.6	135.0
BB-47-7	22.2	45.6	14.5	6.5	19.2	< d.l.	10.9	0.9	163.0	1.3	2.5	22.2	1.9	109.4	136.4
BB-47-8	27.8	46.2	17.1	5.7	17.7	< d.l.	6.7	0.8	171.0	< d.l.	5.4	21.4	1.8	110.2	139.6
BB-47-9	25.4	40.0	21.0	5.5	12.3	0.8	15.4	0.7	160.4	1.2	< d.l.	19.5	2.0	104.4	120.2
BB-53-4	24.9	42.6	19.4	6.0	16.9	< d.l.	11.9	0.8	185.9	2.1	< d.l.	20.5	1.9	106.0	123.7
BB-53-5	20.5	39.0	18.1	5.6	19.7	< d.l.	12.9	0.8	166.1	3.1	< d.l.	20.5	2.1	102.3	119.6
BB-53-6	27.3	40.6	20.0	5.9	12.0	< d.l.	7.6	0.9	174.3	0.4	8.9	19.3	2.0	110.3	126.1
BB-59-1	18.2	41.7	17.5	5.7	14.1	0.8	8.4	0.9	167.8	< d.l.	< d.l.	19.6	1.9	119.3	136.2
BB-59-2	25.3	40.7	16.1	6.1	11.9	< d.l.	2.4	0.8	163.8	< d.l.	3.2	19.9	1.8	104.3	131.2
BB-59-3	29.2	43.0	14.4	6.3	14.4	1.0	9.7	0.8	159.3	1.4	7.4	19.6	1.8	112.8	128.7
BB-59-4	20.9	44.2	19.8	6.1	19.6	< d.l.	9.3	0.7	154.5	2.1	< d.l.	20.8	2.1	109.2	132.7
BB-59-5	24.1	35.1	16.6	5.7	19.4	< d.l.	23.8	0.9	145.2	5.6	6.4	21.0	1.9	99.5	103.5

* Trace elements determined by XRF

Tab. C-10: Aqueous leaching tests at 1:4 solid to liquid ratio (in mg/L)

Sample	**BB-36-1/S1 green A**	**BB-36-1/S1 green B**	**BB-36-1/S2 A**	**BB-36-1/S2 B**	**BB-36-2/S1 A**	**BB-36-2/S1 B**	**BB-36-2/S2 A**	**BB-36-2/S2 B**	**BB-36-3/S1 back A**	**BB-36-3/S1 back B**	**BB-36-3/S2 red A**	**BB-36-3/S2 red B**	**BB-36-3/S2 green A**	**BB-36-3/S2 green B**
w.c. (%)	12.78	12.78	13.48	13.48	14.78	14.78	14.99	14.99	12.99	12.99	13.90	13.90	13.70	13.70
Total mass (g)	10.0000	10.0001	10.0006	10.0001	10.0006	10.0002	10.0003	10.0004	10.0002	10.0002	10.0006	10	10.0003	10.0004
pH	9.1	9.1	9.2	9.1	9	9.1	8.8	8.8	8.7	8.7	8.7	8.7	8.8	8.7
F^-	6.9	7.6	4	4	3.3	3.3	2.4	2.2	4.1	2.5	2.6	2.5	3	2.9
Br^-	0.03	0.03	0.05	0.03	0.05	0.04	0.08	0.05	0.11	0.1	0.15	0.11	0.13	0.11
Cl^-	20	20	23	24	31	31	46	43	70	77	83	84	87	89
NO_3^-	0.52	0.86	3.6	0.56	0.85	0.97	0.49	0.57	0.71	0.98	0.67	0.55	0.43	0.57
SO_4^{2-}	45	47	81	84	119	120	298	276	174	200	114	114	119	121
$HCO_3^{-(*)}$	243.39	241.56	216.55	215.33	193.37	195.20	150.67	150.06	198.86	186.05	192.15	181.78	178.12	174.46
Al	56	67	23	24	3.7	3.1	< 0.03	0.089	< 0.03	0.22	3.5	3.1	3.2	3.3
Ca	19	17	3.6	3.6	2.1	2.1	3.9	3.8	3	3.9	3.5	3.2	3.2	3.1
Mg	57	23	7.5	8	1.8	1.6	1.5	1.5	2.2	2.3	3.1	2.9	2.9	2.9
Na	160	160	150	150	160	160	230	230	200	220	190	190	200	190
K	9.6	9	4.4	4.4	4.2	4.2	6	6.1	5.6	6.1	7.9	7.8	7.7	7.9
Sr	0.35	0.31	0.066	0.065	0.034	0.034	0.071	0.069	0.039	0.078	0.053	0.048	0.052	0.052
Fe	56	22	5.6	6	0.75	0.62	< 0.03	< 0.03	< 0.03	< 0.03	0.99	0.85	0.89	0.91
Ba	0.031	< 0.03	< 0.03	< 0.03	< 0.03	< 0.03	< 0.03	< 0.03	< 0.03	< 0.03	< 0.03	< 0.03	< 0.03	< 0.03
B	0.35	0.31	0.36	0.35	0.3	0.3	0.35	0.35	0.41	0.41	0.31	0.31	0.32	0.33
Mn	0.23	0.096	< 0.03	< 0.03	< 0.03	< 0.03	< 0.03	< 0.03	< 0.03	< 0.03	< 0.03	< 0.03	< 0.03	< 0.03
Si	59	55	38	33	26	25	16	16	19	19	22	21	20	20
Ti	1.1	0.4	0.16	0.13	< 0.03	< 0.03	< 0.03	< 0.03	< 0.03	< 0.03	< 0.03	0.035	< 0.03	< 0.03
V	< 0.03	< 0.03	< 0.03	< 0.03	< 0.03	< 0.03	< 0.03	< 0.03	0.038	< 0.03	< 0.03	< 0.03	< 0.03	< 0.03
Zn	< 0.03	< 0.03	< 0.03	< 0.03	< 0.03	< 0.03	< 0.03	< 0.03	0.038	< 0.03	< 0.03	< 0.03	< 0.03	< 0.03
S_2O_3	< 0.1	< 0.1	< 0.1	< 0.1	< 0.1	< 0.1	< 0.1	< 0.1	< 0.1	< 0.1	0.18	0.17	< 0.1	< 0.1
Acetate	< d.l.	< d.l.	< d.l.	< d.l.	< d.l.	< d.l.	< d.l.	< d.l.	0.1	2.3	19.8	25.6	18.2	23.8
Formate	2.67	1.89	1.07	1.56	0.82	0.35	0.47	< d.l.	2.52	1.31	1.94	2.27	1.6	2.33

(*) Alkalinity as HCO_3^-

Tab. C-11: Aqueous leaching tests at 1:4 solid to liquid ratio (in mg/L). Continuation

Sample	BB-36-4/S1 A	BB-36-4/S1 B	BB-36-4/S2 A	BB-36-4/S2 B	BB-36-5/S1 A	BB-36-5/S1 B	BB-36-5/S2 A	BB-36-5/S2 B	BB-36-6/S1 A	BB-36-6/S1 B	BB-36-6/S2 A	BB-36-6/S2 B
w.c. (%)	14.20	14.20	14.85	14.85	14.98	14.98	16.48	16.48	14.01	14.01	12.64	12.64
Total mass (g)	10.0005	10.0005	10.0002	10.0003	10.0002	10.0003	10.0003	10.0002	10.0005	10.0006	10.0003	10.0004
pH	8.9	8.9	9	9.1	9	9	9.1	9	8.9	8.8	9	9
F^-	4.9	5.7	3.6	3.8	3.1	3.3	3.2	3.2	3.2	3.2	4.4	4
Br^-	0.02	0.04	0.03	0.02	0.06	0.06	0.05	0.05	0.09	0.08	0.13	0.12
Cl^-	16	17	16	35	41	40	33	33	58	59	77	78
NO_3^-	1.4	0.51	0.17	0.33	0.72	1.8	1.1	0.57	0.87	1.2	0.75	0.97
SO_4^{2-}	35	32	83	88	206	150	164	163	131	118	148	150
$HCO_3^{-(*)}$	244.61	248.88	212.89	211.06	174.46	181.17	174.46	162.87	191.54	188.49	215.33	213.50
Al	30	26	12	30	0.63	4.3	3.4	3.9	1	0.47	0.44	0.85
Ca	5.8	4.1	3.1	5.3	22	3.1	2.7	2.8	8.1	2.5	4.2	4.3
Mg	9.8	8.7	4.3	9.8	0.83	1.9	1.6	1.8	1.1	0.89	1.5	1.7
Na	130	130	140	140	170	170	170	170	170	170	200	200
K	4	3.7	3.6	4.5	5.2	5.2	4.5	4.5	6.9	6.8	9.9	9.9
Sr	0.073	0.062	0.05	0.08	0.062	0.046	0.042	0.042	0.075	0.037	0.056	0.058
Fe	7.7	6.5	3.1	7.5	0.13	0.92	0.57	0.83	0.18	< 0.03	< 0.03	0.11
Ba	< 0.03	< 0.03	< 0.03	< 0.03	< 0.03	< 0.03	< 0.03	< 0.03	< 0.03	< 0.03	< 0.03	< 0.03
B	0.23	0.23	0.31	0.32	0.37	0.36	0.35	0.35	0.33	0.35	0.31	0.3
Mn	0.037	0.031	< 0.03	0.043	< 0.03	< 0.03	< 0.03	< 0.03	< 0.03	< 0.03	< 0.03	< 0.03
Si	41	38	47	42	19	28	26	26	21	18	14	13
Ti	0.18	0.16	0.091	0.18	< 0.03	0.037	< 0.03	< 0.03	< 0.03	< 0.03	< 0.03	< 0.03
V	< 0.03	< 0.03	0.048	< 0.03	< 0.03	0.047	< 0.03	0.032	< 0.03	0.052	< 0.03	< 0.03
Zn	< 0.03	< 0.03	< 0.03	< 0.03	< 0.03	< 0.03	< 0.03	< 0.03	< 0.03	< 0.03	< 0.03	< 0.03
S_2O_3	0.21	0.17	< 0.1	< 0.1	< 0.1	< 0.1	< 0.1	< 0.1	< 0.1	< 0.1	< 0.1	< 0.1
Acetate	< d.l.	< d.l.	< d.l.	< d.l.	< d.l.	< d.l.	< d.l.	< d.l.	< d.l.	< d.l.	< d.l.	< d.l.
Formate	2.67	< d.l.	2.3	< d.l.	0.62	< d.l.	0.54	< d.l.	0.34	< d.l.	0.94	0.31

* Alkalinity as HCO_3^-

Tab. C-12: Aqueous leaching tests at 1:4 solid to liquid ratio (in mg/L). Continuation

Sample	BB-47-1/S1 A	BB-47-1/S1 B	BB-47-1/S2 A	BB-47-1/S2 B	BB-47-2/S1 A	BB-47-2/S1 B	BB-47-2/S2 A	BB-47-2/S2 B	BB-47-3/S1 A	BB-47-3/S1 B	BB-47-3/S2 A	BB-47-3/S2 B	BB-47-4/S1 A	BB-47-4/S1 B	BB-47-4/S2 A	BB-47-4/S2 B
w.c. (%)	17.50	17.50	14.52	14.52	17.23	17.23	18.48	18.48	15.68	15.68	15.53	15.53	13.57	13.57	13.99	13.99
Total mass (g)	5.0006	10.0004	5.0005	10.0002	5.0005	10	5.0006	10.0025	5.0001	10.0002	5.0004	10.0003	5.0003	10.0017	5.0005	10.0013
pH	8.4	9.2	8.9	9	8.5	8.9	8.3	8.7	8.3	8.4	8	8.1	8.5	9.1	8.6	9
F^-	2.1	3.4	2.1	2.2	3.7	2.6	1.9	1.9	1	0.71	0.13	0.1	4.2	4.1	4.6	3.6
Br^-	< 0.1	< 0.1	< 0.1	< 0.1	< 0.1	< 0.1	< 0.1	< 0.1	0.38	0.32	1.6	1.6	< 0.1	< 0.1	< 0.1	< 0.1
Cl^-	16	16	17	18	22	24	36	44	197	199	726	727	19	20	17	18
NO_3^-	0.33	0.34	0.12	0.19	0.22	0.22	0.32	0.3	1.8	1.7	8.1	8	< 0.10	0.26	0.14	0.16
SO_4^{2-}	75	70	108	109	180	210	260	349	257	347	247	256	80	79	111	116
$HCO_3^{-(*)}$	251.93	220.82	273.28	227.53	248.88	190.93	172.63	142.74	152.5	116.51	82.35	75.64	296.46	260.47	299.51	239.73
Al	44	33	2.7	6	0.94	1	< 0.3	< 0.03	< 0.3	< 0.03	< 0.3	< 0.03	4.6	6.2	2.1	4.3
Ca	3.3	3.5	1.5	1.6	2.2	2.2	2.7	4.1	6.9	8.6	44	44	1.6	1.8	1.7	1.6
Mg	14.4	12	1.6	2.6	1.6	1.5	1.6	2.3	4.1	4.9	30	30	2.3	3.2	1.7	2.1
Na	140	150	160	150	190	190	210	250	290	320	500	570	150	160	160	160
K	3.4	3.4	2.6	2.8	3.4	3.3	3.8	4.4	5.6	6.3	14	15	2.9	3.1	3.2	2.9
Sr	< 0.3	0.061	< 0.3	< 0.03	< 0.3	0.039	< 0.3	0.085	< 0.3	0.14	0.8	0.69	< 0.3	< 0.03	< 0.3	< 0.03
Fe	11	8.7	0.64	1.4	< 0.3	0.24	< 0.3	< 0.03	< 0.3	< 0.03	< 0.3	< 0.03	1.1	1.5	0.49	1
Ba	< 0.3	< 0.03	< 0.3	< 0.03	< 0.3	< 0.03	< 0.3	< 0.03	< 0.3	< 0.03	< 0.3	< 0.03	< 0.3	< 0.03	< 0.3	< 0.03
B	0.44	0.32	0.37	0.29	0.29	0.23	0.3	0.21	0.35	0.3	0.69	0.61	0.3	< 0.03	0.3	0.25
Mn	< 0.3	0.074	< 0.3	< 0.03	< 0.3	< 0.03	< 0.3	< 0.03	< 0.3	< 0.03	< 0.3	0.051	< 0.3	< 0.03	< 0.3	< 0.03
Si	63	321	23	56	20	16	15	14	16	14	15	15	33	30	24	23
Ti	0.3	0.21	< 0.3	0.032	< 0.3	< 0.03	< 0.3	< 0.03	< 0.3	< 0.03	< 0.3	< 0.03	< 0.3	< 0.03	< 0.3	< 0.03
V	< 0.3	0.058	< 0.3	0.052	< 0.3	0.043	< 0.3	0.03	< 0.3	< 0.03	< 0.3	< 0.03	< 0.3	0.049	< 0.3	0.05
Zn	< 0.3	< 0.03	< 0.3	< 0.03	< 0.3	< 0.03	< 0.3	< 0.03	< 0.3	< 0.03	< 0.3	< 0.03	< 0.3	< 0.03	< 0.3	< 0.03
S_2O_3	< 0.1	< 0.1	< 0.1	< 0.1	< 0.1	< 0.1	< 0.1	< 0.1	< 0.1	< 0.1	0.1	< 0.1	0.14	< 0.1	< 0.1	< 0.1
Acetate	< 1	< 0.1	< 1	0.68	< 1	< 0.1	< 1	< 0.1	1.1	2.4	21	19.7	< 1	< 0.1	< 1	< 0.1
Formate	2	0.53	< 1	0.77	1.6	0.66	2.4	0.29	< 1	< 0.1	< 1	< 0.1	< 1	0.53	< 1	0.34

(*) Alkalinity as HCO_3^-

Tab. C-13: Aqueous leaching tests at 1:4 solid to liquid ratio (in mg/L). Continuation

Sample	BB-47-5/S1 A	BB-47-5/S1 B	BB-47-5/S2 A	BB-47-5/S2 B	BB-47-6/S1 A	BB-47-6/S1 B	BB-47-6/S2 A	BB-47-6/S2 B	BB-47-7/S1 A	BB-47-7/S1 B	BB-47-7/S2 A	BB-47-7/S2 B	BB-47-8/S1 A	BB-47-8/S1 B	BB-47-8/S2 A	BB-47-8/S2 B	BB-47-9/S1 A	BB-47-9/S1 B	BB-47-9/S2 A	BB-47-9/S2 B
w.c. (%)	14.67	14.67	13.91	13.91	16.01	16.01	15.06	15.06	16.55	16.55	15.84	15.84	17.58	17.58	16.49	16.49	16.78	16.78	15.22	15.22
Total mass (g)	5.0002	10.0006	10.0027	10.0000	5.0001	10.0002	5.0004	10.0009	5.0007	10.0001	5.0003	10.0001	5.0006	10.0002	5.0005	10.0003	5.0006	10.0004	5.0003	10.0001
pH	8.5	8.8	8.8	8.8	8.3	8.6	8	8.1	8.6	9.1	8.5	9.1	8.5	9	8.3	8.7	8.3	8.5	8	8.1
F^-	3	2.8	1.5	1.2	1.2	0.68	0.2	0.19	4.2	4.3	3.3	3.7	2.1	1.9	1.7	1.4	1.4	0.88	0.19	0.14
Br^-	< 0.1	< 0.1	< 0.1	< 0.1	0.39	0.39	1.8	1.8	< 0.1	0.1	< 0.1	< 0.1	< 0.1	< 0.1	< 0.3	0.11	0.34	0.35	1.8	1.6
Cl^-	19	20	28.7	32	185	204	875	928	8.7	9.2	12	12.3	21	19.8	48	47	178	189	769	741
NO_3^-	0.13	0.39	1	0.31	1.6	1.7	9.5	9.7	< 0.1	0.38	0.12	0.36	0.19	0.29	0.42	0.46	1.9	2.5	12	11.2
SO_4^{2-}	259	298	369	401	193	297	169	198	61	57	114	116	243	239	388	377	286	321	195	215
$HCO_3^{-(*)}$	234.24	191.54	156.465	153.72	172.02	128.1	87.23	77.47	295.24	258.64	270.84	233.63	208.62	179.95	168.97	144.57	148.84	122.61	88.45	80.52
Al	< 0.3	< 0.03	< 0.3	< 0.03	< 0.3	< 0.03	< 0.3	< 0.03	13	56	2.5	10	0.6	2.5	< 0.3	< 0.03	< 0.3	< 0.03	< 0.3	< 0.03
Ca	2.9	3	5	4.8	5.5	7.2	64	62	2	4.5	1.5	2.1	2.3	2.4	4.8	4.5	6.9	7.8	47	47
Mg	1.8	1.7	2.7	2.7	3.5	4.4	47	44	4.8	19	1.6	4.9	1.5	2	2.7	2.5	4	4.4	34	32
Na	220	230	250	280	260	310	500	580	140	140	150	150	200	190	250	250	275	300	500	530
K	4.1	4.2	4	4.8	5	6	18	19	2.8	4.1	2.8	3.1	3.5	3.5	4.8	4.7	5.7	6	15	15
Sr	< 0.3	0.058	< 0.3	0.093	< 0.3	0.11	1.2	1	< 0.3	0.078	< 0.3	0.034	< 0.3	0.039	< 0.3	0.083	< 0.3	0.12	0.8	0.74
Fe	< 0.3	< 0.03	< 0.3	< 0.03	< 0.3	< 0.03	< 0.3	0.047	3	13	0.6	3	< 0.3	0.56	< 0.3	< 0.03	< 0.3	< 0.03	< 0.3	< 0.03
Ba	< 0.3	< 0.03	< 0.3	< 0.03	< 0.3	< 0.03	< 0.3	< 0.03	< 0.3	< 0.03	< 0.3	< 0.03	< 0.3	< 0.03	< 0.3	< 0.03	< 0.3	< 0.03	< 0.3	< 0.03
B	0.3	0.23	0.4	0.26	0.4	0.38	0.6	0.52	0.3	0.25	0.3	0.21	0.3	0.2	0.3	0.19	0.34	0.26	0.56	0.52
Mn	< 0.3	< 0.03	< 0.3	< 0.03	< 0.3	< 0.03	< 0.3	0.064	< 0.3	0.11	< 0.3	< 0.03	< 0.3	< 0.03	< 0.3	< 0.03	< 0.3	< 0.03	< 0.3	0.047
Si	18	16	15	15	16	15	18	16	61	161	25	18	17	16	16	14	17	14	16	15
Ti	< 0.3	< 0.03	< 0.3	< 0.03	< 0.3	< 0.03	< 0.3	< 0.03	< 0.3	0.32	< 0.3	0.074	< 0.3	< 0.03	< 0.3	< 0.03	< 0.3	< 0.03	< 0.3	< 0.03
V	< 0.3	0.037	< 0.3	0.034	< 0.3	< 0.03	< 0.3	< 0.03	< 0.3	0.063	< 0.3	0.055	< 0.3	0.043	< 0.3	0.032	< 0.3	< 0.03	< 0.3	< 0.03
Zn	< 0.3	< 0.03	< 0.3	< 0.03	< 0.3	< 0.03	< 0.3	< 0.03	< 0.3	0.035	< 0.3	< 0.03	< 0.3	< 0.03	< 0.3	< 0.03	< 0.3	< 0.03	< 0.3	< 0.03
S_2O_3	< 0.1	< 0.1	< 1	< 0.1	0.12	< 0.1	< 0.1	< 0.1	< 0.1	< 0.1	< 0.1	< 0.1	< 0.1	< 0.1	< 0.1	< 0.1	< 0.1	< 0.1	0.11	< 0.1
Acetate	< 1	< 0.1	1	0.52	1.4	3.4	20	13.4	< 1	< 0.1	< 1	< 0.1	< 1	0.38	< 1	0.31	1	2.5	22	14.3
Formate	< 1	0.68	0.49	0.12	< 1	< 0.1	< 1	< 0.1	< 1	0.79	< 1	0.37	< 1	0.33	< 1	0.31	< 1	0.27	< 1	< 0.1

(*) Alkalinity as HCO_3^-

Tab. C-14: Aqueous leaching tests at 1:4 solid to liquid ratio (in mg/L). Continuation

Sample	BB-53-1/S1 A	BB-53-1/S1 B	BB-53-1/S2 A	BB-53-1/S2 B	BB-53-2/S1 A BIS	BB-53-2/S1 B BIS	BB-53-2/S2 A BIS	BB-53-2/S2 B BIS	BB-53-3/S1 A BIS	BB-53-3/S1 B BIS	BB-53-3/S2 A BIS	BB-53-3/S2 B BIS	BB-53-4/S1 A	BB-53-4/S1 B	BB-53-4/S2 A	BB-53-4/S2 B
w.c. (%)	13.56	13.56	14.06	14.06	14.22	14.22	13.21	13.21	14.47	14.47	16.11	16.11	14.22	14.22	14.29	14.29
Total mass (g)	10.0004	10.0006	10.0003	10.0001	10.0002	10.0003	10.0007	10.0037	10.0005	10.0088	10.0019	10.0105	10.0006	10.0006	10.0007	10.0005
pH	9	9.1	8.9	8.9	8.9	9	8.9	8.9	8.6	8.5	8.4	8.3	8.9	8.9	8.9	9
F^-	4	4	3.4	3.4	2.3	2.3	2	2	1.2	1.2	0.47	0.51	4.3	4.2	3.4	3.3
Br^-	< 0.1	< 0.1	< 0.1	< 0.1	0.11	0.1	0.13	0.13	0.5	0.51	1.7	1.7	< 0.1	< 0.1	< 0.1	< 0.1
Cl^-	25	25	33	33	47	48	58	60	200	202	570	577	20	20	21	22
NO_3^-	0.54	0.21	0.41	0.24	0.94	0.57	0.96	0.85	3.7	3.5	10.4	10.3	0.22	0.17	0.15	0.14
SO_4^{2-}	83	83	145	145	222	221	229	233	333	339	259	261	97	99	138	148
$HCO_3^{-(*)}$	237.29	240.34	220.82	222.04	171.41	171.41	172.02	167.14	126.88	125.66	86.01	81.74	245.22	247.05	225.09	219.6
Al	0.99	6.9	1.3	0.9	< 0.3	0.4	< 0.3	< 0.3	< 0.3	< 0.3	< 0.03	< 0.3	2.1	2.3	1.8	2.2
Ca	1.2	1.7	2	1.9	3.4	3.3	3.5	3.8	11	12	38	38	1.6	2.4	1.9	1.9
Mg	1.4	3	1.5	1.4	1.8	2	2	2	6.3	6.5	26	25	1.5	1.6	1.6	1.7
Na	160	160	170	170	210	210	210	210	320	320	460	450	150	150	170	170
K	3	2.7	3.2	3.2	3.4	3.4	3.4	3.6	6.3	6.3	11	11	2.9	2.9	2.9	3
Sr	< 0.03	< 0.03	< 0.03	< 0.03	< 0.3	< 0.3	< 0.3	< 0.3	< 0.3	< 0.3	0.6	0.6	< 0.03	< 0.03	< 0.03	< 0.03
Fe	0.29	1.6	0.3	0.2	< 0.3	< 0.3	< 0.3	< 0.3	< 0.3	< 0.3	< 0.3	< 0.3	0.47	0.51	0.41	0.5
Ba	< 0.03	< 0.03	< 0.03	< 0.03	< 0.3	< 0.3	< 0.3	< 0.3	< 0.3	< 0.3	< 0.3	< 0.3	< 0.03	< 0.03	< 0.03	< 0.03
B	< 0.03	0.25	0.4	0.4	0.5	0.5	0.5	0.5	0.5	0.5	0.8	0.8	0.38	0.39	0.37	0.37
Mn	< 0.03	< 0.03	< 0.03	< 0.03	< 0.3	< 0.3	< 0.3	< 0.3	< 0.3	< 0.03	< 0.3	< 0.3	< 0.03	< 0.03	< 0.03	< 0.03
Si	21	16	16	19	17	19	17	16	19	19	19	19	18	18	36	17
Ti	< 0.03	0.038	< 0.03	< 0.03	< 0.3	< 0.3	< 0.3	< 0.3	< 0.3	< 0.3	< 0.03	< 0.03	< 0.03	< 0.03	< 0.03	< 0.03
V	0.05	0.046	0.04	0.041	< 0.3	< 0.3	< 0.3	< 0.3	< 0.3	< 0.3	< 0.03	< 0.03	0.033	0.036	0.036	0.035
Zn	< 0.03	< 0.03	< 0.03	< 0.03	< 0.3	< 0.3	< 0.3	< 0.3	< 0.3	< 0.3	< 0.03	< 0.03	< 0.03	< 0.03	< 0.03	< 0.03
S_2O_3	< 0.1	< 0.1	< 0.1	< 0.1	0.98	0.98	1.27	1.24	1.42	1.42	2.48	2.46	< 0.1	< 0.1	< 0.1	< 0.1
Acetate	< 0.1	< 0.1	< 0.1	< 0.1	0.99	0.85	1.37	0.95	3.3	3.36	10.88	10.74	< 0.1	< 0.1	< 0.1	< 0.1
Formate	0.8	0.12	0.36	0.52	0.55	0.97	0.23	0.76	0.61	0.37	0.28	0.4	0.85	0.84	0.32	0.14

* Alkalinity as HCO_3^-

Tab. C-15: Aqueous leaching tests at 1:4 solid to liquid ratio (in mg/L). Continuation

Sample	BB-53-5/S1 A	BB-53-5/S1 B	BB-53-5/S2 A	BB-53-5/S2 B	BB-53-6/S1 A	BB-53-6/S1 B	BB-53-6/S2 A	BB-53-6/S2 B	BB-53-7/S1 A	BB-53-7/S1 B	BB-53-7/S2 A	BB-53-7/S2 B	BB-53-8/S1 A	BB-53-8/S1 B	BB-53-8/S2 A	BB-53-8/S2 B	BB-53-9/S1 A	BB-53-9/S1 B	BB-53-9/S2 A	BB-53-9/S2 B
w.c. (%)	13.35	13.35	13.06	13.06	14.63	14.63	12.26	12.26	12.53	12.53	12.65	12.65	14.41	14.41	13.58	13.58	14.51	14.51	14.12	14.12
Total mass (g)	10.0066	10.0006	10.0144	10.0252	10.0229	10.0353	10.0032	10.0153	10.0005	10.0001	10.0005	10.0002	10.0368	10.006	10.0101	10.0271	10.0117	10.0141	10.0202	10.051
pH	9	8.9	8.9	8.9	8.6	8.6	8.1	8	9	9	8.9	9	9.1	8.9	8.8	9	8.5	8.4	7.9	7.9
F^-	2.5	2.5	1.9	1.9	1	0.94	0.38	0.37	3.7	3.9	3.2	3.2	2.4	2.3	2.3	2.4	1.1	1	0.22	0.24
Br^-	< 0.1	< 0.1	< 0.1	< 0.1	0.51	0.51	2.6	2.3	< 0.1	< 0.1	< 0.1	< 0.1	< 0.1	< 0.1	< 0.1	< 0.1	0.52	0.51	2.6	2.5
Cl^-	24	24	31	31	225	226	975	973	35	34	37	36	34	34	42	42	249	251	1000	1000
NO_3^-	0.41	0.55	0.43	0.58	3.2	3.3	19	17	0.12	0.15	0.56	0.18	0.52	0.43	0.52	0.5	3.4	3.5	21	21
SO_4^{2-}	227	217	311	317	345	348	221	219	97	96	139	138	220	221	243	247	371	388	220	217
$HCO_3^{-(*)}$	184.83	183	161.65	161.04	115.29	122.61	71.98	77.47	244	242.78	221.43	220.82	179.34	187.27	186.05	172.02	124.44	120.78	67.1	63.44
Al	2.5	0.7	< 0.3	< 0.3	< 0.3	< 0.3	< 0.3	< 0.3	15	3	2.5	1.7	0.4	1.3	< 0.3	2.5	< 0.3	< 0.3	< 0.3	< 0.3
Ca	3.4	2.7	3.2	3.5	9.5	10	78	75	2.5	1.7	1.8	1.9	2.2	3	3.6	3.8	15	14	87	87
Mg	2.6	1.5	1.7	1.9	5.7	5.7	56	56	6.1	1.9	1.8	1.6	1.4	2	2	2.8	8.3	8	66	65
Na	190	190	210	230	330	330	540	530	160	160	170	180	190	190	210	210	360	360	540	540
K	3.5	3.4	3.9	3.9	6.4	6.4	20	19	3.4	3	3.2	3.1	3.3	3.3	3.5	3.6	6.8	6.7	19	19
Sr	< 0.3	< 0.3	< 0.3	< 0.3	< 0.3	< 0.3	1.3	1.3	0.034	< 0.03	< 0.03	< 0.03	< 0.3	< 0.3	< 0.3	< 0.3	0.3	0.3	1.4	1.4
Fe	0.8	< 0.3	< 0.3	< 0.3	< 0.3	< 0.3	< 0.3	< 0.3	3.9	0.75	0.57	0.38	< 0.3	0.4	< 0.3	0.7	< 0.3	< 0.3	< 0.3	< 0.3
Ba	< 0.3	< 0.3	< 0.3	< 0.3	< 0.3	< 0.3	< 0.3	< 0.3	< 0.03	< 0.03	< 0.03	< 0.03	< 0.3	< 0.3	< 0.3	< 0.3	< 0.3	< 0.3	< 0.3	< 0.3
B	0.5	0.4	0.4	0.4	0.5	0.5	0.7	0.7	0.38	0.4	0.4	0.41	0.4	0.5	0.5	0.5	0.5	0.5	0.8	0.8
Mn	< 0.3	< 0.3	< 0.3	< 0.3	< 0.3	< 0.3	< 0.3	< 0.3	0.031	< 0.03	< 0.03	< 0.03	< 0.3	< 0.3	< 0.3	< 0.3	< 0.3	< 0.3	< 0.3	< 0.3
Si	26	17	14	15	15	15	17	17	20	17	16	38	15	20	18	26	19	18	16	16
Ti	< 0.3	< 0.3	< 0.3	< 0.3	< 0.3	< 0.3	< 0.03	< 0.3	0.095	< 0.03	< 0.03	< 0.03	< 0.3	< 0.3	< 0.3	< 0.3	< 0.3	< 0.3	< 0.3	< 0.3
V	< 0.3	< 0.3	< 0.3	< 0.3	< 0.3	< 0.3	< 0.03	< 0.3	< 0.03	0.032	0.032	0.037	< 0.3	< 0.3	< 0.3	< 0.3	< 0.3	< 0.3	< 0.3	< 0.3
Zn	< 0.3	< 0.3	< 0.3	< 0.3	< 0.3	< 0.3	< 0.03	< 0.3	< 0.03	< 0.03	< 0.03	< 0.03	< 0.3	< 0.3	< 0.3	< 0.3	< 0.3	< 0.3	< 0.3	< 0.3
S_2O_3	0.97	0.97	1.09	1.11	2.29	2.3	3.18	3.23	< 0.1	< 0.1	< 0.1	< 0.1	1	0.99	1.12	1.15	1.73	1.73	3.55	3.54
Acetate	1.32	1.44	1.13	1.19	2.83	3.1	8.75	8.81	< 0.1	< 0.1	< 0.1	< 0.1	1.22	1.23	1.74	1.67	3.22	3.12	10.23	9.94
Formate	0.86	0.97	0.42	0.42	0.15	0.29	0.55	0.49	0.64	0.16	0.13	0.45	0.53	0.46	0.44	0.91	0.4	0.21	0.39	0.51

* Alkalinity as HCO_3^-

Tab. C-16: Aqueous leaching tests at 1:4 solid to liquid ratio (in mg/L). Continuation

Sample	BB-59-1/S1 A	BB-59-1/S1 B	BB-59-1/S2 A	BB-59-1/S2 B	BB-59-2/S1 A	BB-59-2/S1 B	BB-59-2/S2 A	BB-59-2/S2 B	BB-59-3/S1 A	BB-59-3/S1 B	BB-59-3/S2 A	BB-59-3/S2 B	BB-59-4/S1 A	BB-59-4/S1 B	BB-59-4/S2 A	BB-59-4/S2 B
w.c. (%)	13.31	13.31	13.49	13.49	12.48	12.48	12.33	12.33	13.47	13.47	13.93	13.93	13.63	13.63	15.15	15.15
Total mass (g)	10.0008	10.0006	10.0003	10.0001	10.0007	10.0000	10.0000	10.0001	10.0008	10.0003	10.0005	10.0005	10.0003	10.0004	10.0001	10
pH	8.5	8.7	8.8	8.7	8.8	8.5	8.7	8.5	8.8	8.6	8.6	8.6	8.7	8.5	8.6	8.4
F^-	3.8	2.3	3.3	2.5	2.4	2.6	2.1	2.7	2.2	2.2	1.9	2.1	1.8	1.9	1.6	2.1
Br^-	0.28	0.1	0.25	0.19	0.28	0.26	0.38	0.31	0.43	0.37	0.5	0.38	0.55	0.51	0.59	0.52
Cl^-	108	125	115	132	133	155	170	179	184	217	216	229	248	279	259	278
NO_3^-	< 1	0.3	< 1	0.4	< 1	2.1	< 1	1.9	2.9	3.2	< 1	3.2	4.8	5.4	5.1	4.3
SO_4^{2-}	137	156	182	265	208	279	256	267	194	242	186	213	178	214	163	201
$HCO_3^{-(*)}$	215.94	196.42	197.03	165.31	186.05	170.8	187.27	178.73	184.22	157.99	175.07	155.55	162.26	143.35	159.82	140.91
Al	0.17	0.2	< 0.03	< 0.03	0.04	< 0.03	< 0.03	< 0.03	< 0.03	< 0.03	< 0.3	< 0.03	< 0.3	< 0.03	< 0.3	< 0.03
Ca	3.3	3	3.9	4.3	4.2	5.3	6.2	6.1	5.8	6	6.3	6.5	6.4	7	6.4	7.3
Mg	2.2	2.1	2.5	3	2.9	3.7	4.3	4.3	4	4.4	4.4	4.7	4.6	5.1	4.5	5.3
Na	195	240	215	290	235	300	275	320	255	330	270	310	285	340	285	310
K	4	4	4.2	4.9	4.4	5.6	5.8	6	5.3	5.9	5.6	6.1	5.6	6.1	5.7	6.2
Sr	0.06	0.044	0.08	0.075	0.08	0.1	0.12	0.12	0.11	0.12	0.12	0.12	0.13	0.14	0.12	0.14
Fe	0.03	0.051	< 0.03	< 0.03	< 0.3	< 0.03	< 0.3	< 0.03	< 0.3	< 0.03	< 0.3	< 0.03	< 0.3	< 0.03	< 0.3	< 0.03
Ba	< 0.3	< 0.03	< 0.3	< 0.03	< 0.3	< 0.03	< 0.3	< 0.03	< 0.3	< 0.03	< 0.3	< 0.03	< 0.3	< 0.03	< 0.3	< 0.03
B	0.33	0.29	0.34	0.32	0.36	0.3	0.35	0.28	0.33	0.27	0.32	0.38	0.33	0.28	0.31	0.38
Mn	< 0.3	< 0.03	< 0.3	< 0.03	< 0.3	< 0.03	< 0.3	< 0.03	< 0.3	< 0.03	< 0.3	< 0.03	< 0.3	< 0.03	< 0.3	< 0.03
Si	17	16	15	14	15	15	16	16	15	15	16	13	14	13	13	13
Ti	< 0.03	< 0.03	< 0.03	< 0.03	< 0.3	< 0.03	< 0.3	< 0.03	< 0.03	< 0.03	< 0.3	< 0.03	< 0.3	< 0.03	< 0.3	< 0.3
V	0.03	< 0.03	< 0.03	< 0.03	< 0.3	< 0.03	< 0.3	< 0.03	< 0.03	< 0.03	< 0.3	< 0.03	< 0.3	< 0.03	< 0.3	< 0.3
Zn	< 0.03	< 0.03	< 0.03	< 0.03	< 0.3	< 0.03	< 0.3	< 0.03	< 0.03	< 0.03	< 0.3	< 0.03	< 0.3	< 0.03	< 0.3	< 0.3
S_2O_3	< d.l.	< 0.1	< d.l.	< 0.1	< d.l.	< 0.1	< d.l.	< 0.1	< d.l.	< 0.1	< d.l.	< 0.1	< d.l.	< 0.1	< d.l.	< 0.1
Acetate	< d.l.	0.24	< d.l.	< 0.1	< d.l.	< 0.1	< d.l.	< 0.1	< d.l.	< 0.1	< d.l.	< 0.1	< d.l.	< 0.1	< d.l.	< 0.1
Formate	< d.l.	0.26	< d.l.	0.31	< d.l.	0.21	< d.l.	0.49	< d.l.	0.22	< d.l.	< 0.1	< d.l.	0.26	< d.l.	< 0.1

(*) Alkalinity as HCO_3^-

Tab. C-17: Aqueous leaching tests at 1:4 solid to liquid ratio (in mg/L). Continuation

Sample	BB-59-5/S1 A	BB-59-5/S1 B	BB-59-5/S2 A	BB-59-5/S2 B	BB-59-6/S1 A	BB-59-6/S1 B	BB-59-6/S2 A	BB-59-6/S2 B	BB-59-7/S1 A	BB-59-7/S1 B	BB-59-7/S2 A	BB-59-7/S2 B	BB-59-8/S1 A	BB-59-8/S1 B	BB-59-8/S2 A	BB-59-8/S2 B	BB-59-9/S1 A	BB-59-9/S1 B	BB-59-9/S2 A	BB-59-9/S2 B
w.c. (%)	12.94	12.94	12.67	12.67	14.23	14.23	12.54	12.54	14.76	14.76	13.80	13.80	14.50	14.50	14.41	14.41	13.31	13.31	13.49	13.49
Total mass (g)	10.0004	10.0006	10.0001	10.0007	10.0006	10.0000	10.0002	10.0005	10.0004	10.0003	10.0000	10.0004	10.0001	10.0001	10.0002	10.0005	10.0108	10.0118	10.019	10.0017
pH	8.5	8.5	8.5	8.5	8.5	8.8	8.9	8.7	8.6	8.6	8.5	8.7	8.6	8.6	8.5	8.6	8.4	8.6	8.4	8.4
F^-	1.8	1.1	1.3	1.7	2.7	3.3	2.1	2.3	1.7	1.7	1.5	2.3	1.4	2.6	2.2	2.2	1.5	2.2	1.5	1.6
Br^-	0.58	0.49	0.61	0.47	0.25	0.18	0.28	0.18	0.26	0.24	0.32	0.3	0.39	0.38	0.43	0.45	0.41	0.43	0.33	0.41
Cl^-	252	286	265	280	92	99	109	117	148	148	182	180	221	220	243	241	250	254	261	234
NO_3^-	4.9	5.6	5.1	4	< 1	0.17	< 1	0.1	1	0.55	1.9	1.4	3	2	3.7	2.9	3.4	3.5	4.3	3.7
SO_4^{2-}	167	218	191	217	123	132	232	258	271	265	256	248	259	253	270	269	160	162	184	157
$HCO_3^{-(*)}$	176.29	148.84	162.26	143.96	237.29	204.96	188.49	167.14	173.85	169.58	169.58	161.04	174.46	159.82	159.21	145.18	163.48	162.26	161.04	164.09
Al	< 0.3	< 0.03	< 0.3	< 0.03	< 0.3	0.43	< 0.3	< 0.03	< 0.03	< 0.03	< 0.03	< 0.03	< 0.03	< 0.03	< 0.03	< 0.03	< 0.03	< 0.03	< 0.03	< 0.03
Ca	6.7	7.3	7	7.5	2.3	2.4	3.8	4.2	5.4	5.3	5.6	5.5	6.8	6.9	7.8	7.8	6.5	6.5	8	7.2
Mg	4.8	5.4	4.9	5.4	1.7	1.7	2.5	2.8	3.8	3.7	4	4	4.9	4.9	5.5	5.4	4.7	4.7	5.7	5.1
Na	285	340	300	330	190	200	235	270	290	290	300	300	340	320	340	340	300	300	310	280
K	6	6.4	5.9	6.4	3.5	3.6	4.5	4.8	5.4	5.5	5.7	5.7	6.3	6.3	6.6	6.6	5.6	5.6	6.2	5.5
Sr	0.13	0.14	0.14	0.14	0.04	0.037	0.08	0.07	0.1	0.1	0.11	0.1	0.13	0.12	0.15	0.15	0.11	0.11	0.13	0.12
Fe	< 0.3	< 0.03	< 0.3	< 0.03	< 0.3	0.11	< 0.3	< 0.03	< 0.03	< 0.03	< 0.03	< 0.03	< 0.03	< 0.03	< 0.03	< 0.03	< 0.03	< 0.03	< 0.03	< 0.03
Ba	< 0.3	< 0.03	< 0.3	< 0.03	< 0.3	< 0.03	< 0.3	< 0.03	< 0.03	< 0.03	< 0.03	< 0.03	< 0.03	< 0.03	< 0.03	< 0.03	< 0.03	< 0.03	< 0.03	< 0.03
B	0.3	0.29	0.34	0.41	0.33	0.26	0.36	0.42	0.24	0.38	0.26	0.38	0.23	0.36	0.23	0.35	0.37	0.37	0.38	0.35
Mn	< 0.3	< 0.03	< 0.3	< 0.03	< 0.3	< 0.03	< 0.3	< 0.03	< 0.03	< 0.03	< 0.03	< 0.03	< 0.03	< 0.03	< 0.03	< 0.03	< 0.03	< 0.03	< 0.03	< 0.03
Si	10	14	13	13	13	15	12	13	15	15	15	14	14	13	14	13	15	15	16	16
Ti	< 0.3	< 0.03	< 0.3	< 0.3	< 0.3	< 0.03	< 0.3	< 0.3	< 0.03	< 0.03	< 0.03	< 0.03	< 0.03	< 0.03	< 0.03	< 0.03	< 0.03	< 0.03	< 0.03	< 0.03
V	< 0.3	< 0.03	< 0.3	< 0.3	< 0.3	< 0.03	< 0.3	< 0.3	< 0.03	0.031	< 0.03	< 0.03	< 0.03	< 0.03	< 0.03	< 0.03	< 0.03	< 0.03	0.03	0.03
Zn	< 0.3	< 0.03	< 0.3	< 0.3	< 0.3	< 0.03	< 0.3	< 0.3	< 0.03	< 0.03	< 0.03	< 0.03	< 0.03	< 0.03	< 0.03	< 0.03	< 0.03	< 0.03	< 0.03	< 0.03
S_2O_3	< d.l.	< 0.1	< d.l.	< 0.1	< d.l.	< 0.1	< d.l.	< 0.1	< 0.1	< 0.1	< 0.1	< 0.1	< 0.1	< 0.1	< 0.1	< 0.1	< 0.1	< 0.1	< 0.1	< 0.1
Acetate	< d.l.	1.1	< d.l.	< 0.1	< d.l.	< 0.1	< d.l.	< 0.1	0.31	0.28	0.46	< 0.1	0.31	< 0.1	< 0.1	< 0.1	0.26	< 0.1	0.45	0.57
Formate	< d.l.	< 0.1	< d.l.	< 0.1	< d.l.	0.27	< d.l.	0.26	< 0.1	< 0.1	< 0.1	0.13	< 0.1	< 0.1	0.12	0.16	< 0.1	< 0.1	< 0.1	< 0.1

(*) Alkalinity as HCO_3^-

Tab. C-18: Aqueous leaching tests at 1:4 solid to liquid ratio (in meq/L). Continuation

Sample	BB-59-10/S1 A	BB-59-10/S1 B	BB-59-10/S2 A	BB-59-10/S2 B	BB-59-11/S1 A	BB-59-11/S1 B	BB-59-11/S2 A	BB-59-11/S2 B	BB-59-12/S1A BIS	BB-59-12/S1 B BIS	BB-59-12 2A BIS	BB-59-12/S2 B BIS	BB-59-13/S1 A BIS	BB-59-13/S1 B BIS	BB-59-13/S2 A BIS	BB-59-13/S2 B BIS	BB-59-14/S1 A	BB-59-14/S1 B	BB-59-14/S2 A	BB-59-14/S2 B
w.c. (%)	14.05	14.05	17.91	17.91	14.02	14.02	14.29	14.29	14.09	14.09	30.53	20.53	13.39	13.39	12.34	12.34	14.83	14.83	18.46	18.46
Total mass (g)	10.0000	10.0006	10.0001	10.0003	10.0003	10.0003	10.0002	10.0002	10.0236	10.0183	10.0152	10.0451	10.0302	10.0223	10.0765	10.0761	10.0000	10.0021	10.0011	10.0715
pH	8.9	8.9	8.6	8.6	8.6	8.6	8.5	8.5	8.7	8.7	8.7	8.7	8.6	8.5	8.6	8.5	8.5	8.4	8.4	8.4
F^-	3.6	3.6	2.6	2.7	1.7	1.8	1.7	2.5	2	1.9	1.8	1.8	2	1.8	1.8	1.7	2.6	2.3	1.5	3.5
Br^-	< 0.1	< 0.1	0.13	0.13	0.2	0.2	0.24	0.24	0.41	0.4	0.45	0.45	0.53	0.52	0.57	0.57	0.47	0.47	0.48	0.46
Cl^-	70	70	91	92	117	117	144	142	181	182	203	203	234	230	254	253	268	270	269	263
NO_3^-	0.33	0.14	0.15	< 0.1	0.25	0.57	0.81	1.1	2.8	0.77	< 0.1	0.11	1.9	0.1	4.3	0.79	3.8	3.7	4.5	4.9
SO_4^{2-}	120	120	281	282	252	252	303	298	251	253	264	264	237	234	214	214	182	185	175	165
$HCO_3^{-(*)}$	208.62	207.4	171.41	174.46	180.56	177.51	164.7	164.7	148.84	159.82	154.33	157.99	147.62	148.23	135.42	143.96	151.89	151.28	165.31	168.36
Al	0.95	1.3	< 0.03	< 0.03	< 0.03	< 0.03	< 0.03	< 0.03	< 0.3	< 0.3	< 0.3	< 0.3	< 0.3	< 0.3	< 0.3	< 0.3	< 0.03	< 0.03	< 0.03	< 0.03
Ca	2	1.9	4.1	4	4.2	4.3	5.9	5.8	5	5.4	6.2	6.5	6.3	6.3	7.8	8.2	7.2	7.1	7.7	7.6
Mg	1.6	1.6	2.7	2.7	2.9	3	4.1	4	3.5	3.8	4.2	4.5	4.6	4.5	5.3	5.6	5.1	5.1	5.5	5.5
Na	180	180	250	260	260	260	310	300	280	290	300	300	300	300	310	310	300	320	310	280
K	3.2	3.3	4.7	4.7	5	5	5.8	5.7	5.2	5.2	5.5	5.5	5.6	5.6	5.6	5.6	5.8	6	6.2	5.9
Sr	0.03	< 0.03	0.067	0.067	0.07	0.075	0.11	0.1	< 0.3	< 0.3	< 0.3	< 0.3	< 0.3	< 0.3	< 0.3	< 0.3	0.12	0.12	0.13	0.12
Fe	0.21	0.29	< 0.03	< 0.03	< 0.03	< 0.03	< 0.03	< 0.03	< 0.3	< 0.3	< 0.3	< 0.3	< 0.3	< 0.3	< 0.3	< 0.3	< 0.03	< 0.03	< 0.03	< 0.03
Ba	< 0.03	< 0.03	< 0.03	< 0.03	< 0.03	< 0.03	< 0.03	< 0.03	< 0.3	< 0.3	< 0.3	< 0.3	< 0.3	< 0.3	< 0.3	< 0.3	< 0.03	< 0.03	< 0.03	< 0.03
B	0.37	0.36	0.38	0.38	0.38	0.39	0.39	0.38	0.4	0.4	0.4	0.4	0.4	0.4	0.5	0.5	0.4	0.4	0.37	0.38
Mn	< 0.03	< 0.03	< 0.03	< 0.03	< 0.03	< 0.03	< 0.03	< 0.03	< 0.3	< 0.3	< 0.3	< 0.3	< 0.3	< 0.3	< 0.3	< 0.3	< 0.03	< 0.03	< 0.03	< 0.03
Si	15	15	14	14	14	14	14	14	13	13	12	13	14	14	15	15	14	14	15	16
Ti	< 0.03	< 0.03	< 0.03	< 0.03	< 0.03	< 0.03	< 0.03	< 0.03	< 0.3	< 0.3	< 0.3	< 0.3	< 0.3	< 0.3	< 0.3	< 0.3	< 0.03	< 0.03	< 0.03	< 0.03
V	0.035	0.032	< 0.03	< 0.03	0.031	< 0.03	< 0.03	< 0.03	< 0.3	< 0.3	< 0.3	< 0.3	< 0.3	< 0.3	< 0.3	< 0.3	< 0.03	< 0.03	< 0.03	< 0.03
Zn	< 0.03	< 0.03	< 0.03	< 0.03	< 0.03	< 0.03	< 0.03	< 0.03	< 0.3	< 0.3	< 0.3	< 0.3	< 0.3	< 0.3	< 0.3	< 0.3	< 0.03	< 0.03	< 0.03	< 0.03
S_2O_3	< 0.1	< 0.1	< 0.1	< 0.1	< 0.1	< 0.1	< 0.1	< 0.1	0.22	0.22	0.3	0.32	0.44	0.43	0.37	0.35	< 0.1	< 0.1	< 0.1	< 0.1
Acetate	< 0.1	< 0.1	< 0.1	< 0.1	0.68	0.46	0.23	< 0.1	0.43	0.9	0.56	1.8	< 0.1	< 0.1	< 0.1	< 0.1	< 0.1	< 0.1	< 0.1	< 0.1
Formate	0.35	0.44	0.3	0.13	0.11	0.31	< 0.1	0.26	< 0.1	< 0.1	< 0.1	< 0.1	< 0.1	< 0.1	< 0.1	< 0.1	< 0.1	< 0.1	< 0.1	< 0.1

* Alkalinity as HCO_3^-

Tab. C-19: Aqueous leaching tests at 1:4 solid to liquid ratio (in mg/L). Continuation

Reference samples	**FEBEX -1**	**FEBEX -2**	**FEBEX -3**	**FEBEX -4**	**FEBEX-5**
w.c. (%)	13.49	13.49	13.49	13.49	13.49
Total mass (g)	10.0014	10.0058	10.0055	10.005	10.0000
pH	8.8	8.7	8.4	8.5	8.73
F^-	2.5	2.7	2.4	2.2	n.d.
Br^-	0.32	0.3	0.31	0.32	n.d.
Cl^-	156	157	149	158	149.6
NO_3^-	3.7	3.9	3.4	2.8	4.4
SO_4^{2-}	197	197	139	172	200.6
$HCO_3^{-(*)}$	165.31	165.31	185.44	177.51	154.15
Al	0.3	0.1	0.3	0.05	0.52
Ca	5	4.5	3.8	3.8	4.27
Mg	3.1	3	2.5	2.6	2.86
Na	210	240	250	270	246
K	5.1	5.2	3.9	4.2	6.1
Sr	0.1	0.08	0.04	0.05	0.08
Fe	0.07	< 0.03	0.07	< 0.03	0.2
Ba	< 0.03	< 0.03	< 0.03	< 0.03	n.d.
B	0.4	0.4	0.4	0.4	n.d.
Mn	< 0.03	< 0.03	< 0.03	< 0.03	n.d.
Si	13.5	13	13	10	n.d.
Ti	< 0.03	< 0.03	< 0.03	< 0.03	n.d.
V	< 0.03	< 0.03	< 0.03	< 0.03	n.d.
Zn	< 0.03	< 0.03	< 0.03	< 0.03	n.d.
S_2O_3	0.26	0.27	< 0.5	< 0.5	n.d.
Acetate	2.3	2.6	< 0.5	< 0.5	n.d.
Formate	4.2	4.2	< 0.5	< 0.5	n.d.

* Alkalinity as HCO3-

Tab. C-20: Water adsorption isotherms from retrieved samples at heated sections after dismantling of Heater #2 and comparison with FEBEX Reference sample

mg/g dry clay	**$a_w = P/P_o$**	**BB-47-1**	**BB-47-2**	**BB-47-3**	**BB-53-1**	**BB-53-2**	**BB-53-3**	**FEBEX Ref.**	**FEBEX Ref.** (Fernandez et al. 2004)		
NaOH	0.09	--	--	--	41.1856	32.7009	39.6540	33.9341	$a_w = P/P_o$	Adsorbed water mg/g dry clay	Basal spacing d(001)
NaOH	0.09	--	--	--	40.9954	32.8162	35.3112	34.8785			
LiCl	0.11	33.9464	33.5631	39.8240	71.1673	65.2902	70.1360	70.3439	0	0	9.6
LiCl	0.11	34.2435	40.9517	39.3550	70.2900	62.1456	64.9670	68.3389	0.03	30.00	9.899
CH_3-COOK	0.23	66.1981	67.6262	62.9833	92.9047	86.2261	90.0447	90.1621	0.07	39.73	13.562
CH_3-COOK	0.23	61.9989	65.3266	65.5517	92.1373	87.9109	89.0801	89.9201	0.12	41.59	12.147
$MgCl_2$	0.33	88.4253	73.9862	90.8373	110.6303	98.5931	98.5884	102.6692	0.20	78.26	14.165
$MgCl_2$	0.33	91.4364	87.4486	88.0765	108.7991	94.7962	101.6269	105.4033	0.33	104.09	14.205
K_2CO_3	0.44	96.3071	98.0750	101.1891	135.0932	131.4235	122.0756	130.4492	0.45	130.44	15.231
K_2CO_3	0.44	96.5533	100.2973	107.4128	131.2997	131.9638	125.5281	134.4659	0.58	163.73	15.609
NaBr	0.57	127.8272	120.5093	133.6192	151.3543	152.7452	146.3849	151.6090	0.63	171.51	15.687
NaBr	0.57	126.5752	125.0285	135.7159	150.3809	151.1706	150.2955	149.4202	0.75	195.59	15.833
KI	0.72	143.7872	136.6269	161.1622	163.1684	165.3068	154.4273	161.6217	0.85	226.75	15.773
KI	0.72	142.8732	153.4512	153.7852	162.9859	165.2514	155.6667	166.7592	0.97	330.50	18.653
NaCl	0.78	154.9264	148.9507	162.2355	184.2627	193.6967	175.5514	191.9494	1.00	368.02	18.9
NaCl	0.78	156.5696	142.8248	152.3201	186.2853	189.0564	176.9666	191.5577	--	--	--
KCl	0.85	175.0336	179.0738	168.7137	229.0202	232.9165	210.7757	231.8056	--	--	--
KCl	0.85	178.2467	175.2648	170.2769	227.8829	235.1757	205.8887	226.7928	--	--	--
KNO_3	0.94	216.3073	211.0910	244.1087	306.2417	305.6646	259.7790	274.4925	--	--	--

Tab. C-20: Cont.

mg/g dry clay	**$a_w = P/P_o$**	**BB-47-1**	**BB-47-2**	**BB-47-3**	**BB-53-1**	**BB-53-2**	**BB-53-3**	**FEBEX Ref.**	**FEBEX Ref.** (Fernandez et al. 2004)		
KNO_3	0.94	216.1102	214.2210	239.4271	299.6275	308.7971	267.4225	275.4438	--	--	--
$K_2Cr_2O_7$	0.97	254.7899	267.6906	293.6319	370.2357	377.6978	321.1843	311.8752	--	--	--
$K_2Cr_2O_7$	0.97	255.0185	270.5452	292.3897	370.6309	374.0347	320.7377	311.3509	--	--	--
NaCl 0.1M	0.99	299.2258	301.0361	368.4091	382.7952	370.8557	554.4454	461.4103	--	--	--
NaCl 0.1M	0.99	298.7129	304.4362	357.9353	389.0180	385.9079	578.8767	441.6843	--	--	--
H_2O	1	407.4781	378.3815	--	--	--	--	--	--	--	--
H_2O	1	410.9451	358.3286	--	--	--	--	--	--	--	--

Tab. C-21: Water adsorption isotherms from retrieved samples at non-heated sections after dismantling of Heater #2. Comparison with the Reference sample

mg/g dry clay	$a_w = P/P_o$	BB-36-4	BB-36-5	BB-36-6	BB-59-1	BB-59-2	BB-59-3	BB-59-4	BB-59-5	FEBEX Ref.
NaOH	0.09	--	--	--	27.9867	42.8295	--	48.3669	47.1388	33.9341
NaOH	0.09	--	--	--	32.0427	42.2599	--	48.5172	46.9510	34.8785
LiCl	0.11	29.2252	41.1785	38.5610	62.0552	70.1715	34.3299	88.5731	93.2261	70.3439
LiCl	0.11	30.6366	44.6602	40.9106	57.5133	71.3555	37.8520	89.3893	93.6368	68.3389
CH_3-COOK	0.23	65.4513	78.4247	74.0072	85.6031	91.5469	67.3581	97.1481	99.7174	90.1621
CH_3-COOK	0.23	67.7119	77.6334	70.7855	81.9309	90.9605	66.8184	96.6057	100.6218	89.9201
$MgCl_2$	0.33	87.3348	101.2095	91.2667	100.3215	107.9860	88.3022	115.1267	117.7735	102.6692
$MgCl_2$	0.33	87.5945	100.5587	90.7047	100.3771	108.3465	87.5256	114.1625	116.7438	105.4033
K_2CO_3	0.44	104.1690	114.1459	106.2374	128.3132	130.7675	112.0403	141.8046	143.4856	130.4492
K_2CO_3	0.44	106.3228	113.1067	105.6765	128.1454	126.3595	114.7541	142.4838	143.7274	134.4659
NaBr	0.57	121.7712	142.7759	129.1769	149.3463	147.5502	136.5609	160.9208	163.7902	151.6090
NaBr	0.57	123.2923	139.7618	127.9239	148.3614	150.7419	130.9037	160.4448	163.1134	149.4202
KI	0.72	137.1358	156.8516	142.8412	154.5083	164.1690	147.2219	169.4435	170.9845	161.6217
KI	0.72	138.7952	157.6087	143.0644	154.4150	165.3517	149.5974	171.8466	172.1570	166.7592
NaCl	0.78	136.1885	170.0873	157.7537	183.9487	187.0504	164.6938	198.0299	200.7435	191.9494
NaCl	0.78	132.3722	170.8645	161.4133	184.7754	187.9217	168.5939	198.4361	201.3764	191.5577
KCl	0.85	160.9955	196.1119	185.2101	232.9010	230.6740	178.8975	242.0541	244.2267	231.8056
KCl	0.85	158.4964	195.8447	187.5981	239.2244	229.3165	180.8414	241.5158	246.0273	226.7928
KNO_3	0.94	212.7093	249.8288	229.2486	292.3537	299.2446	252.2409	284.4213	289.7702	274.4925
KNO_3	0.94	207.6473	251.4305	234.0329	295.0856	298.7976	248.7945	280.2807	288.0802	275.4438

Tab. C-21: Cont.

mg/g dry clay	$a_w = P/P_o$	BB-36-4	BB-36-5	BB-36-6	BB-59-1	BB-59-2	BB-59-3	BB-59-4	BB-59-5	FEBEX Ref.
$K_2Cr_2O_7$	0.97	252.5074	298.3733	308.4112	384.5641	358.6176	298.8649	422.6547	405.3993	311.8752
$K_2Cr_2O_7$	0.97	247.2751	294.1846	298.2181	389.8961	374.6637	297.7778	430.7413	408.5840	311.3509
NaCl 0.1M	0.99	304.9104	346.9272	309.5318	382.0424	329.8946	291.3714	382.4895	396.9810	461.4103
NaCl 0.1M	0.99	306.7729	347.8509	308.9768	396.3624	337.6419	285.4267	378.5892	389.0704	441.6843
H_2O	1	347.6854	448.5569	418.4039	--	--	355.7736	--	--	--
H_2O	1	342.6550	428.3273	416.3013	--	--	354.5321	--	--	--

Appendix D

Saturation indices of aqueous extracts

Tab. D-1: Saturation indices from aqueous extracts calculated with the PhreeqC program

Sample	SI Calcite	SI Dolomite	SI Strontianite	SI Gypsum	SI Celestite	SI Halite	SI Quartz	SI Chalcedony	SI Fluorite
BB-36-2 S1 A	-0.08	0.13	-1.40	-3.03	-3.06	-6.87	0.55	0.12	-1.54
BB-36-2 S1 B	0.02	0.27	-1.30	-3.04	-3.07	-6.87	0.52	0.09	-1.55
BB-36-2 S2 B	-0.08	-0.23	-1.37	-2.50	-2.49	-6.59	0.36	-0.06	-1.70
BB-36-3 S1 back A	-0.12	-0.02	-1.54	-2.76	-2.90	-6.43	0.45	0.02	-1.23
BB-36-3 S1 back B	-0.05	0.02	-1.29	-2.60	-2.55	-6.35	0.45	0.02	-1.56
BB-36-3 S2 red A	-0.11	0.07	-1.47	-2.83	-2.91	-6.37	0.51	0.08	-1.52
BB-36-3 S2 red B	-0.17	-0.03	-1.53	-2.87	-2.95	-6.37	0.49	0.06	-1.59
BB-36-3 S2 green A	-0.10	0.11	-1.43	-2.86	-2.90	-6.33	0.46	0.03	-1.44
BB-36-3 S2 green B	-0.21	-0.11	-1.53	-2.83	-2.89	-6.34	0.47	0.04	-1.48
BB-36-4 S2 A	-0.09	0.31	-1.42	-2.97	-3.01	-7.21	0.81	0.38	-1.25
BB-36-5 S1 A	0.91	0.75	-1.17	-1.84	-2.64	-6.73	0.42	-0.01	-0.62
BB-36-5 S1 B	0.03	0.19	-1.34	-2.78	-2.85	-6.74	0.58	0.16	-1.38
BB-36-5 S2 A	0.04	0.21	-1.29	-2.81	-2.86	-6.82	0.54	0.11	-1.48
BB-36-5 S2 B	-0.07	-0.03	-1.43	-2.78	-2.86	-6.82	0.55	0.12	-1.45
BB-36-6 S1 A	0.47	0.43	-1.09	-2.42	-2.70	-6.58	0.47	0.04	-0.99
BB-36-6 S1 B	-0.11	-0.31	-1.47	-2.96	-3.04	-6.57	0.42	-0.01	-1.49
BB-36-6 S2 A	0.31	0.53	-1.09	-2.69	-2.81	-6.39	0.28	-0.15	-1.04
BB-36-6 S2 B	0.31	0.57	-1.08	-2.68	-2.79	-6.38	0.25	-0.18	-1.11
BB-47-1 S2 A	-0.12	0.14	-	-3.23	-	-7.13	0.51	0.08	-2.09
BB-47-1 S2 B	-0.17	0.23	-	-3.18	-	-7.13	0.89	0.46	-2.00
BB-47-2 S1 A	-0.35	-0.49	-	-2.87	-	-6.95	0.48	0.05	-1.45
BB-47-2 S1 B	-0.12	-0.07	-1.41	-2.82	-2.82	-6.92	0.35	-0.08	-1.77
BB-47-2 S2 A	-0.61	-1.12	-	-2.64	-	-6.70	0.37	-0.06	-1.96
BB-47-2 S2 B	-0.18	-0.28	-1.41	-2.39	-2.34	-6.55	0.31	-0.11	-1.82
BB-47-3 S1 A	-0.28	-0.45	-	-2.29	-	-5.84	0.39	-0.04	-2.14
BB-47-3/S1 B	-0.24	-0.39	-1.58	-2.10	-2.16	-5.80	0.33	-0.10	-2.37
BB-47-3/S2 A	-0.09	-0.01	-1.38	-1.64	-1.64	-5.07	0.37	-0.05	-3.20
BB-47-3/S2 B	-0.04	0.09	-1.40	-1.64	-1.71	-5.01	0.37	-0.06	-0.19
BB-47-4/S1 A	-0.41	-0.32	-	-3.29	-	-7.11	0.70	0.27	-1.42
BB-47-4/S1 B	0.04	0.69	-	-3.28	-	-7.06	0.60	0.17	-1.42
BB-47-4/S2 A	-0.28	-0.21	-	-3.15	-	-7.13	0.56	0.13	-1.34
BB-47-4/S2 B	-0.10	0.27	-	-3.17	-	-7.11	0.50	0.07	-1.59
BB-47-5/S1 A	-0.27	-0.42	-	-2.63	-	-6.96	0.44	0.01	-1.55
BB-47-5/S1 B	-0.09	-0.09	-1.34	-2.58	-2.55	-6.92	0.36	-0.06	-1.61
BB-47-5/S2 A	0.02	0.11	-	-2.29	-	-6.74	0.34	-0.09	-1.95
BB-47-5/S2 B	-0.10	-0.12	-1.36	-2.29	-2.27	-6.64	0.34	-0.08	-2.18
BB-47-6/S1 A	-0.30	-0.46	-	-2.47	-	-5.91	0.39	-0.04	-2.05
BB-47-6/S1 B	-0.07	-0.03	-1.44	-2.23	-2.31	-5.80	0.35	-0.08	-2.47

Tab. D-1: Cont.

Sample	SI Calcite	SI Dolomite	SI Strontianite	SI Gypsum	SI Celestite	SI Halite	SI Quartz	SI Chalcedony	SI Fluorite
BB-47-6/S2 A	0.09	0.40	-1.18	-1.67	-1.66	-4.99	0.45	0.03	-2.68
BB-47-6/S2B	0.11	0.42	-1.23	-1.63	-1.68	-4.90	0.40	-0.03	-2.75
BB-47-7/S2 A	-0.47	-0.56	-	-3.18	-	-7.31	0.58	0.15	-1.67
BB-47-7/S2B	-0.05	0.62	-1.37	-3.04	-3.07	-7.30	0.38	-0.05	-1.44
BB-47-8/S1 A	-0.42	-0.69	-	-2.74	-	-6.96	0.41	-0.02	-1.94
BB-47-8/S1 B	-0.07	0.11	-1.40	-2.74	-2.78	-7.00	0.34	-0.09	-2.02
BB-47-8/S2 A	-0.42	-0.77	-	-2.29	-	-6.52	0.39	-0.04	-1.86
BB-47-8/S2 B	-0.14	-0.21	-1.43	-2.33	-2.33	-6.52	0.31	-0.11	-2.06
BB-47-9/S1 A	-0.30	-0.50	-	-2.25	-	-5.90	0.42	-0.01	-1.85
BB-47-9/S1 B	-0.15	-0.22	-1.52	-2.16	-2.24	-5.84	0.33	-0.10	-2.22
BB-47-9/S2 A	-0.03	0.15	-1.34	-1.71	-1.74	-5.04	0.40	-0.03	-2.84
BB-47-9/S2 B	0.03	0.23	-1.33	-1.67	-1.74	-5.03	0.37	-0.06	-3.10
BB-53-1/S1 A	-0.16	0.11	-	-3.43	-	-6.96	0.46	0.03	-1.62
BB-53-1/S1 B	-0.03	0.54	-	-3.28	-	-6.96	0.33	-0.10	-1.46
BB-53-1/S2 A	-0.08	0.06	-	-2.99	-	-6.82	0.35	-0.07	-1.56
BB-53-1/S2 B	-0.10	0.03	-	-3.02	-	-6.82	0.43	-0.00	-1.58
BB-53-2/S1 A BIS	0.38	0.85	-	-2.66	-	-6.59	0.28	-0.15	-1.74
BB-53-2/S1 B BIS	0.30	0.74	-	-2.67	-	-6.58	0.36	-0.07	-1.74
BB-53-2/S2 A BIS	0.33	0.78	-	-2.63	-	-6.5	0.31	-0.12	-1.89
BB-53-3/S1 A BIS	0.33	0.75	-	-2.02	-	-5.8	0.43	0.0	-1.82
BB-53-3/S1 B BIS	0.38	0.83	-	-1.98	-	-5.79	0.43	0.0	-1.78
BB-53-3/S2 A BIS	0.43	1.03	-0.92	-1.66	-1.73	-5.2	0.46	0.03	-2.13
BB-53-3/S2 B BIS	-0.05	0.05	-1.41	-1.65	-1.72	-5.2	0.47	0.05	-2.05
BB-53-4/S1 A	-0.12	0.08	-	-3.23	-	-7.09	0.41	-0.02	-1.43
BB-53-4/S1 B	0.05	0.28	-	-3.05	-	-7.09	0.41	-0.02	-1.27
BB-53-4/S2 A	-0.11	0.07	-	-3.03	-	-7.02	0.71	0.28	-1.57
BB-53-4/S2 B	-0.04	0.22	-	-3.01	-	-7.0	0.37	-0.06	-1.61
BB-53-5/S1 A BIS	0.36	0.95	-	-2.64	-	-6.92	0.47	0.04	-1.66
BB-53-5/S1 B BIS	0.31	0.72	-	-2.76	-	-6.92	0.28	-0.15	-1.77
BB-53-5/S2 A BIS	-0.13	-0.20	-	-2.53	-	-6.77	0.31	-0.12	-1.92
BB-53-5/S2 B BIS	0.28	0.64	-	-2.52	-	-6.74	0.26	-0.17	-1.92
BB-53-6/S1 A BIS	0.24	0.59	-	-2.08	-	-5.73	0.33	-0.1	-2.04
BB-53-6/S1B BIS	0.2	0.5	-	-2.05	-	-5.73	0.34	-0.09	-2.08
BB-53-6/S2 A BIS	0.26	0.72	-1.07	-1.5	-1.55	-4.92	0.43	0.0	-2.07
BB-53-6/S2 B BIS	0.28	0.77	-1.03	-1.52	-1.55	-4.92	0.43	0.0	-2.11
BB-53-7/S1 A	-0.17	0.39	-1.58	-3.02	-3.14	-6.81	0.44	0.01	-1.34
BB-53-7/S1 B	-0.04	0.32	-	-3.23	-	-6.83	0.37	-0.06	-1.50
BB-53-7/S2 A	-0.15	0.06	-	-3.05	-	-6.77	0.35	-0.07	-1.65
BB-53-7/S2 B	-0.04	0.2	-	-3.04	-	-6.76	0.72	0.29	-1.64

Tab. D-1: Cont.

Sample	SI Calcite	SI Dolomite	SI Strontianite	SI Gypsum	SI Celestite	SI Halite	SI Quartz	SI Chalcedony	SI Fluorite
BB-53-8/S1 A BIS	-0.14	-0.14	-	-2.80	-	-6.77	0.33	-0.10	-1.85
BB-53-8/S1 B BIS	0.28	0.74	-	-2.70	-	-6.77	0.38	-0.05	-1.78
BB-53-8/S2 A BIS	-0.43	-0.66	-	-2.51	-	-6.64	0.60	0.17	-1.60
BB-53-9/S1 A BIS	0.45	0.98	-0.79	-1.87	-1.83	-5.66	0.43	-0.00	-1.78
BB-53-9/S1 B BIS	0.41	0.91	-0.81	-1.89	-1.81	-5.65	0.40	-0.02	-1.90
BB-53-9/S2 A BIS	0.41	1.04	-0.93	-1.40	-1.46	-7.88	0.39	-0.03	-2.45
BB-53-9/S2 B BIS	0.39	0.99	-0.96	-1.41	-1.47	-7.88	0.39	-0.03	-2.37

Appendix E

TEM photomicrographs

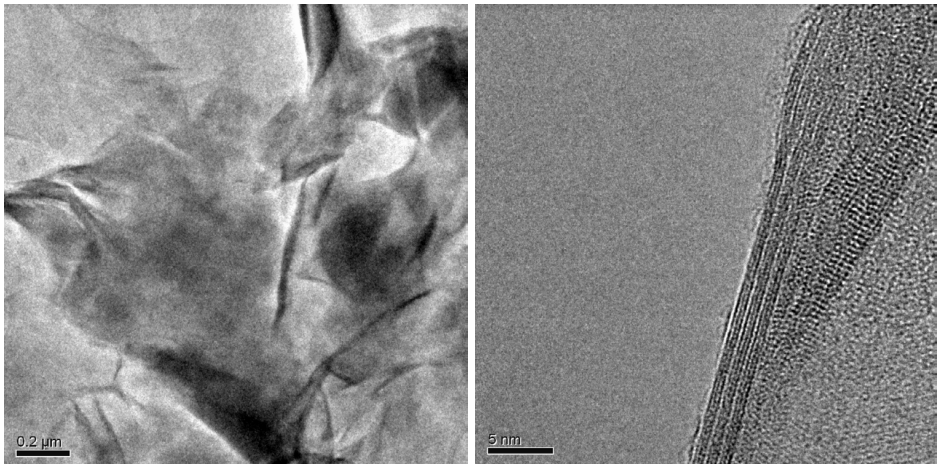

Fig. E-1: TEM images from < 2 µm clayey suspensions of the FEBEX Reference bentonite

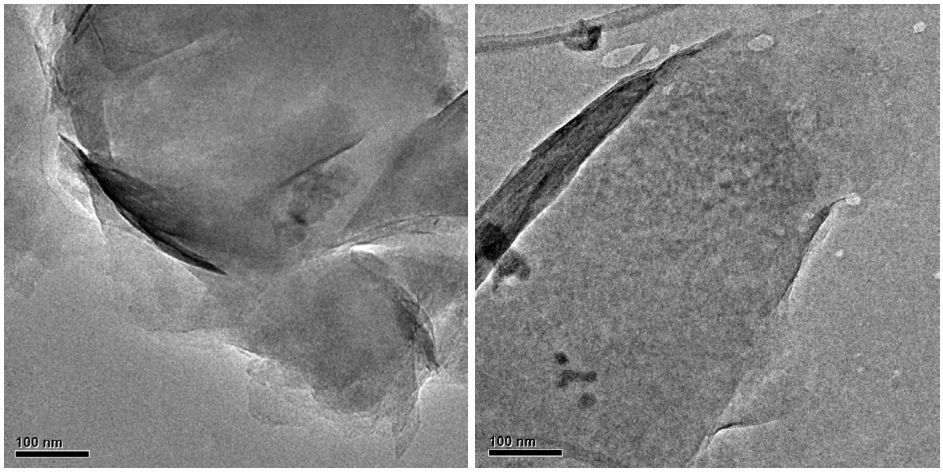

Fig. E-2: TEM images from < 2 µm clayey suspensions of the bentonite block BB-36-1

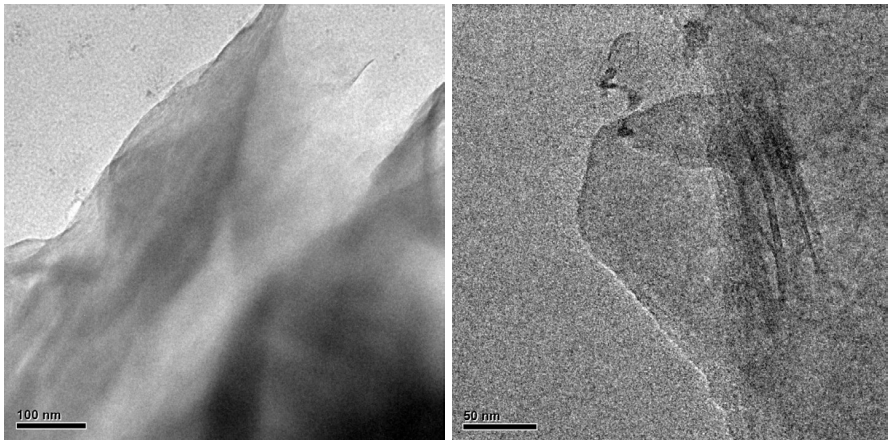

Fig. E-3: TEM images from < 2 µm clayey suspensions of the bentonite block BB-36-2: a) smectite particle; b) kaolinite type particle

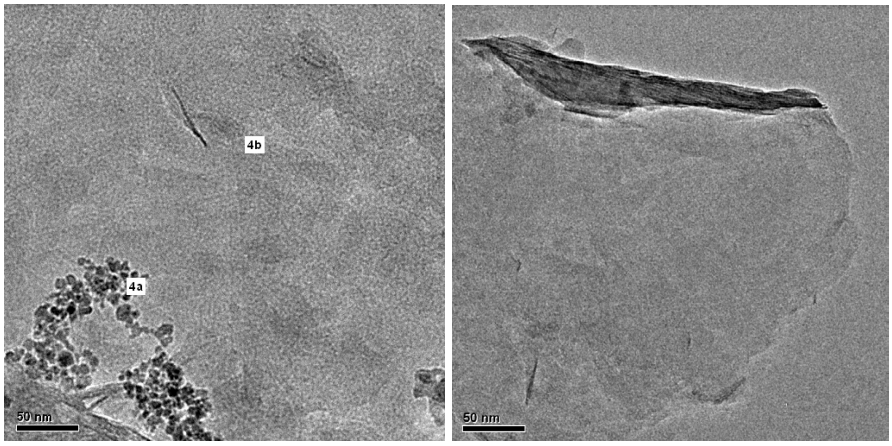

Fig. E-4: TEM images from < 2 μm clayey suspensions of the bentonite block BB-36-3 red: a) nontronite type particle and/or iron colloids (4a), smectite particle (4b); b) smectite particle

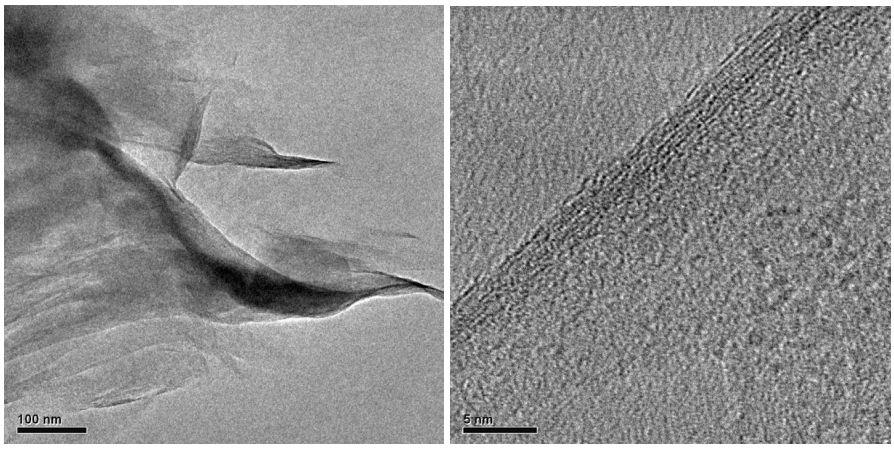

Fig. E-5: TEM images from < 2 μm clayey suspensions of the bentonite block BB-47-7

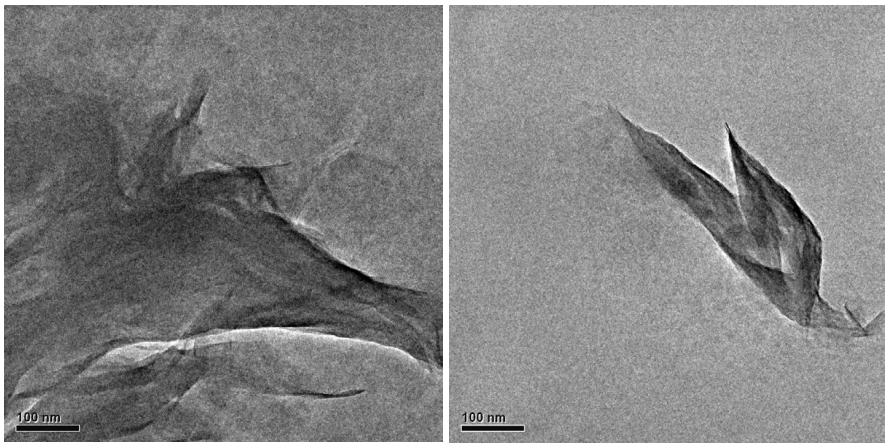

Fig. E-6: TEM images from < 2 μm clayey suspensions of the bentonite block BB-47-8

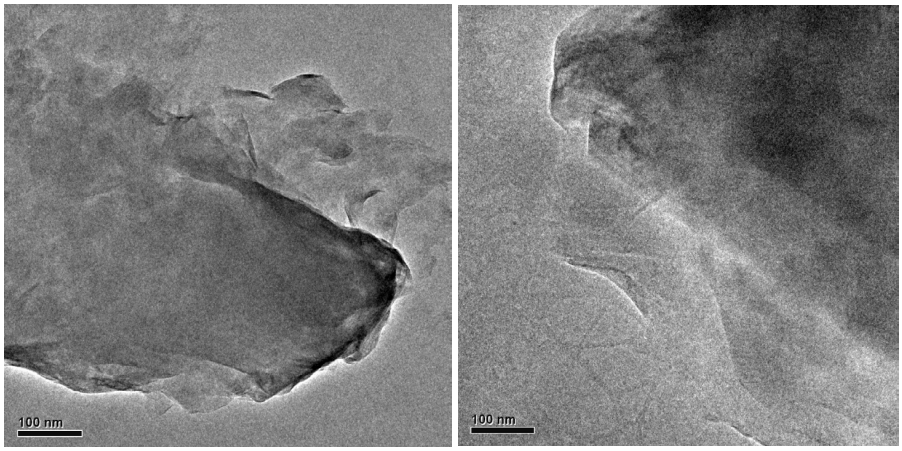

Fig. E-7: TEM images from < 2 µm clayey suspensions of the bentonite block BB-47-9: a) smectite particle; b) illite particle

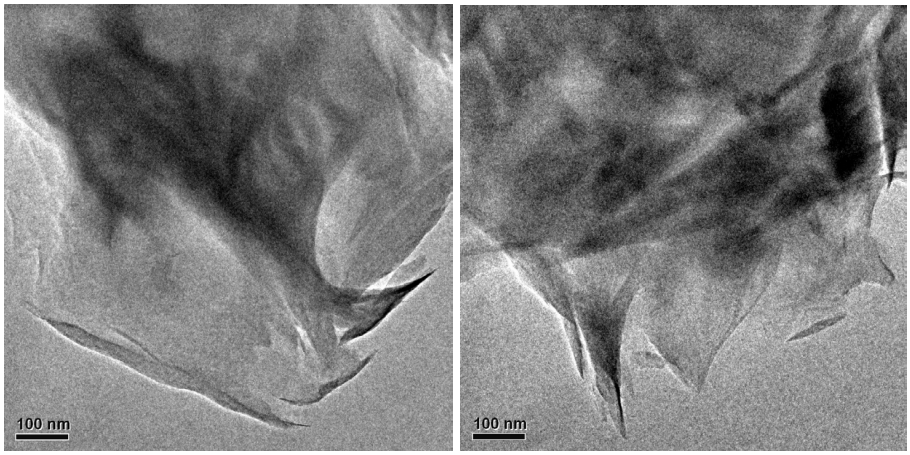

Fig. E-8: TEM images from < 2 µm clayey suspensions of the bentonite block BB-53-3

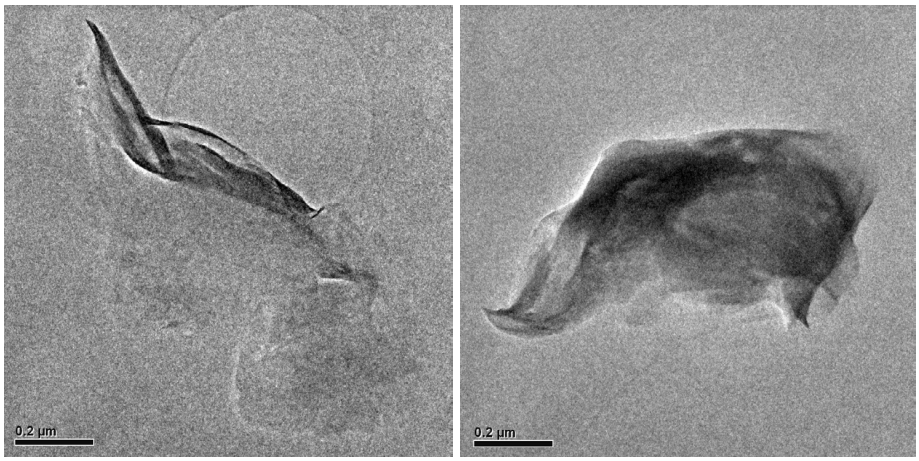

Fig. E-9: TEM images from < 2 µm clayey suspensions of the bentonite block BB-59-1

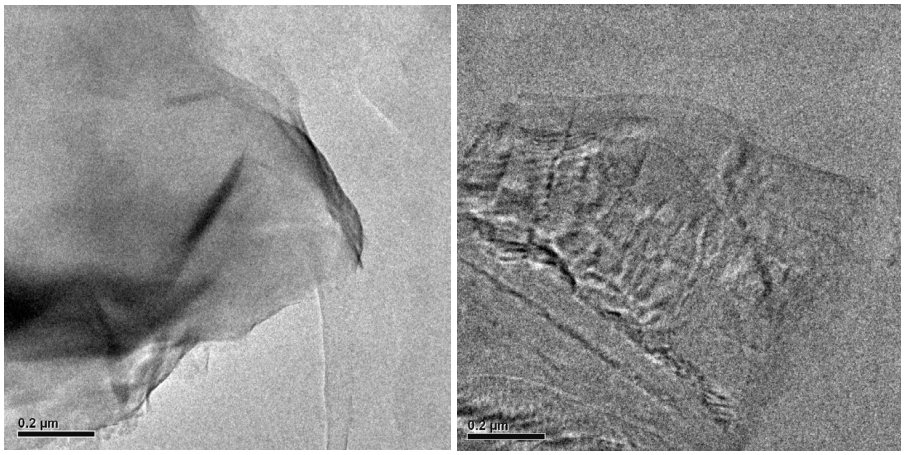

Fig. E-10: TEM images from < 2 µm clayey suspensions of the bentonite block BB-59-3: a) smectite particle; b) illite type particle

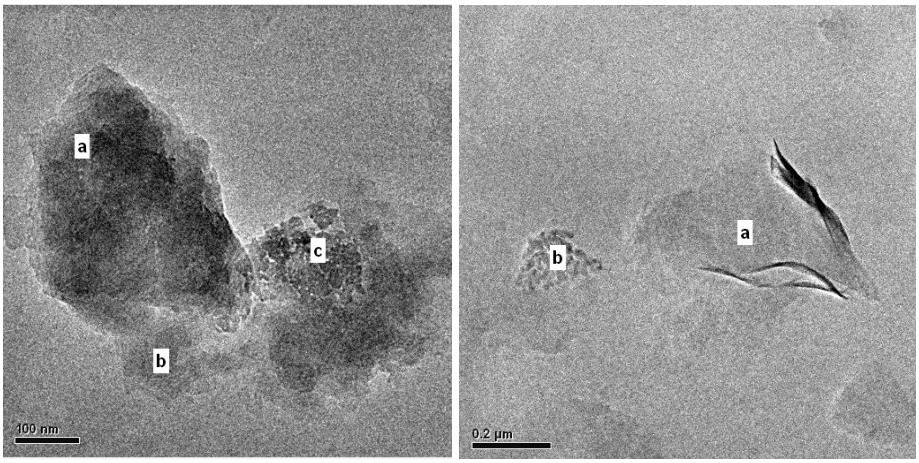

Fig. E-11: TEM images from < 2 µm clayey suspensions of the bentonite block BB-59-5: a) silica colloids (a and c); smectite particle (b); b) smectite particle (a); silica colloids (b)

Appendix F

Analysis of the samples at direct contact with the liner/Heater #2

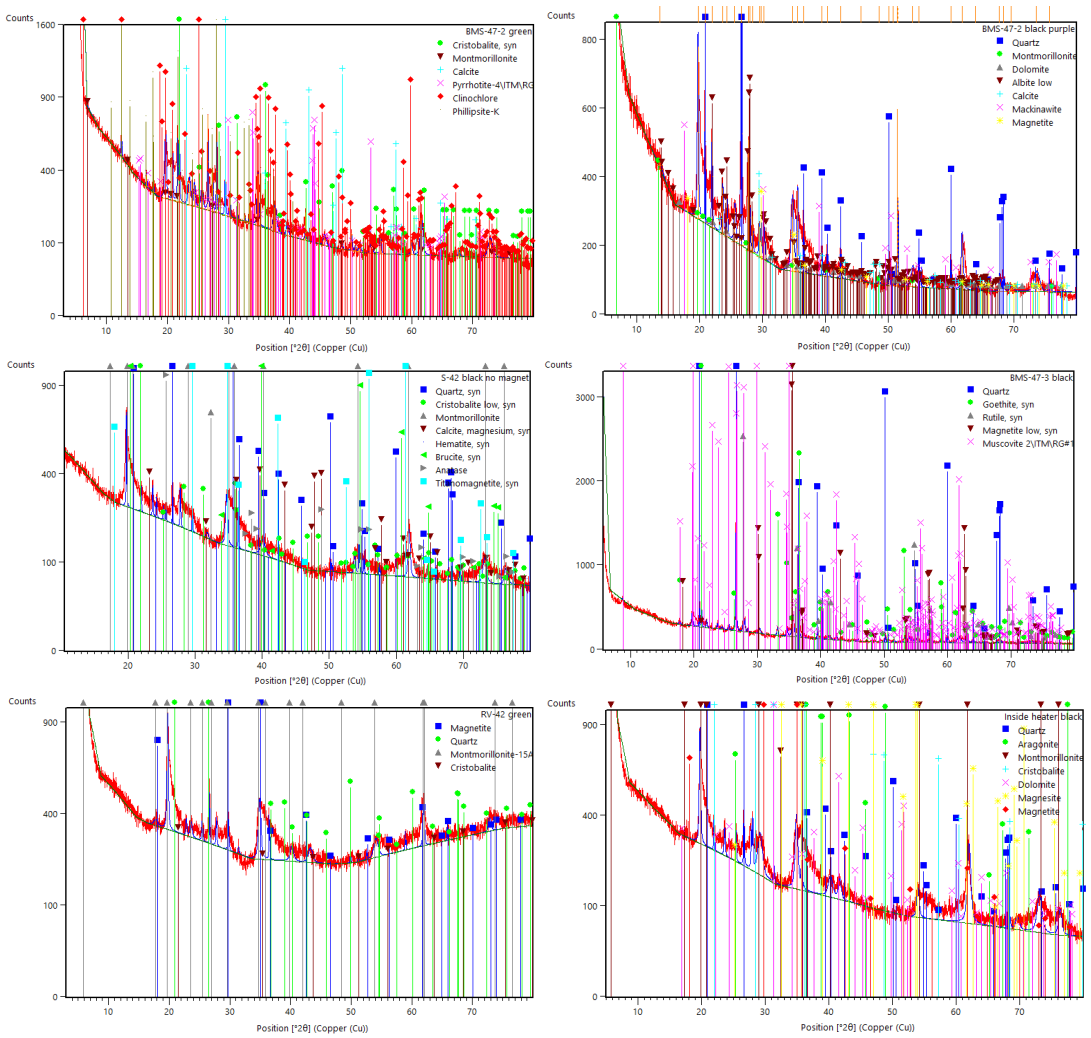

Fig. F-1: XRD pattern of bulk samples from BMS and protrusion samples located at contact with the liner/Heater #2 (feldspars are omitted)

Vertical lines: hkl reflexions of mineral (see color in the legend)

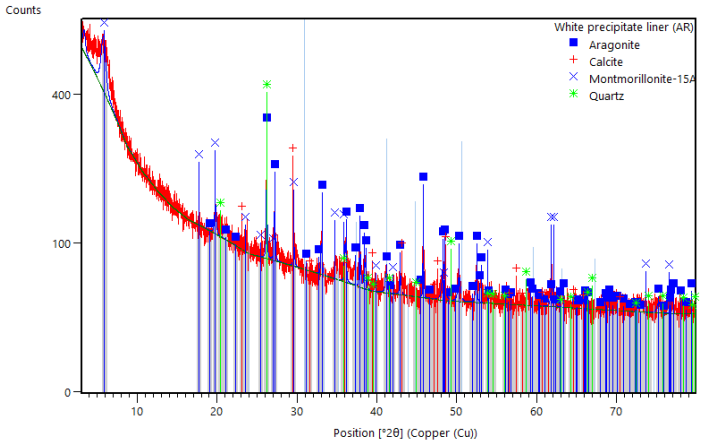

Fig. F-2: XRD pattern white scraped material from the internal part of the liner (AR sample)

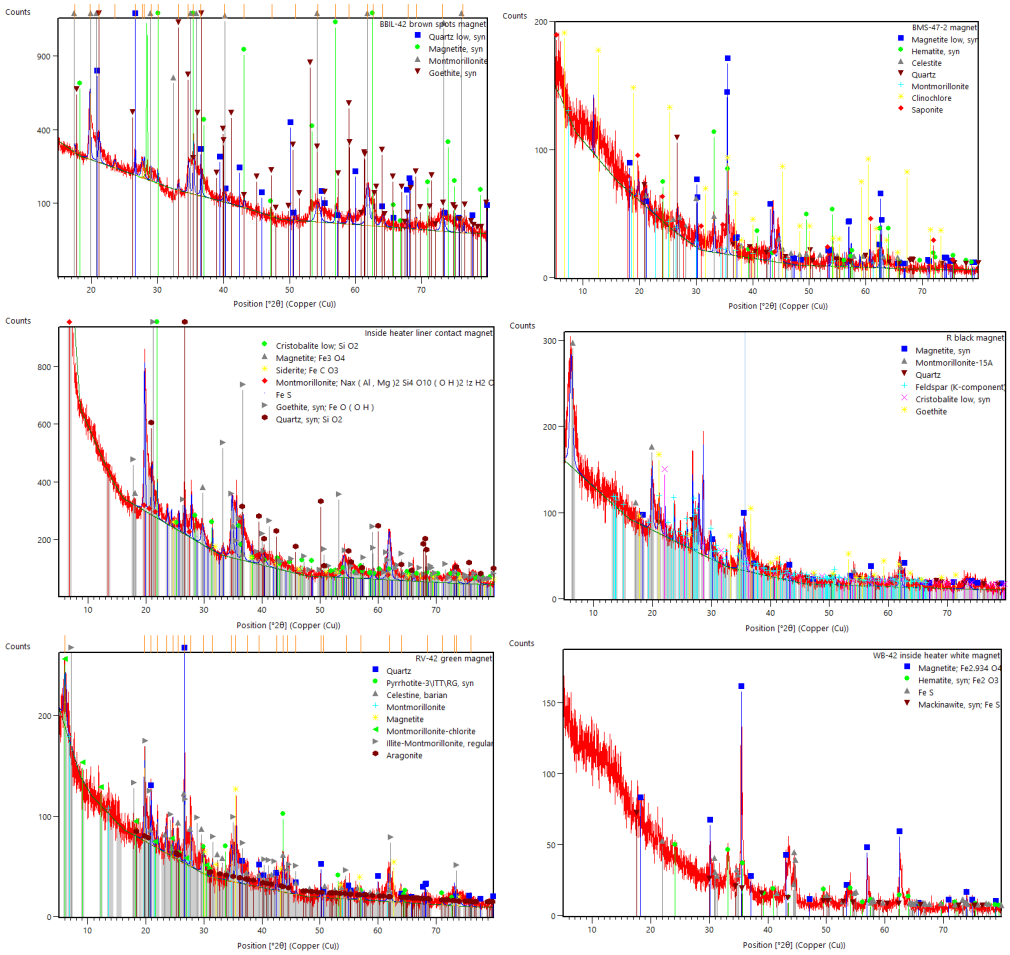

Fig. F-3: XRD patterns of BMS at Section S47 and S53 at direct contact with the liner and protrusion magnetic samples at direct contact with the liner/Heater #2 (feldspars are omitted).

Vertical lines: hkl reflexions of mineral (see color in the legend)

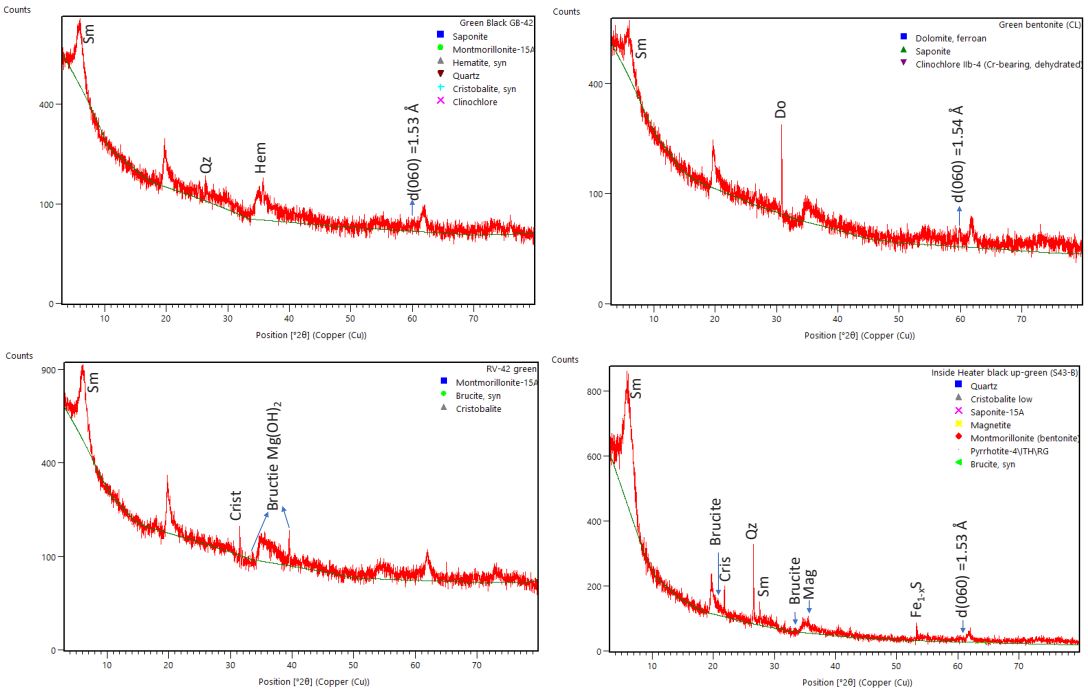

Fig. F-4: XRD pattern of the sample at direct contact with the Heater #2 (Protrusions samples): d(060) basal reflexion of trioctahedral smectites and brucite

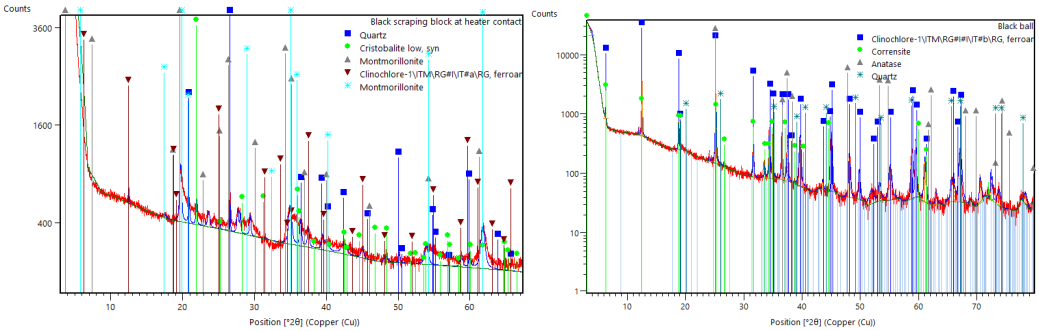

Fig. F-5: XRD pattern of the sample at direct contact with the frontal surface of Heater #2: a) black particles adhered to bentonite block (BPB), b) Black ball particle (BB): chlorite and Chl/S ML. Vertical lines: hkl reflexions of mineral (see color in the legend)

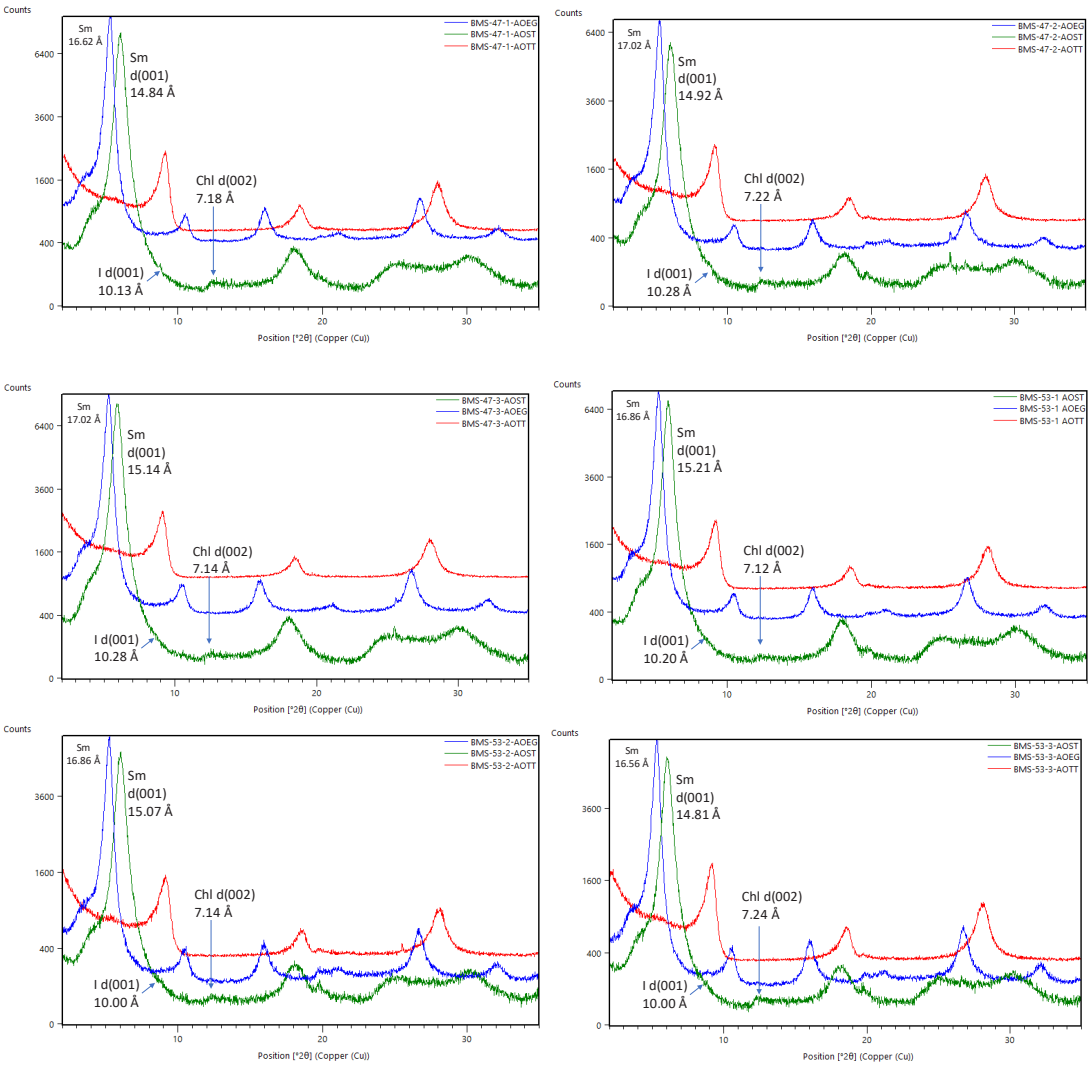

Fig. F-6: XRD patterns of oriented aggregates samples (normal, ethylene glycol solvated and heated at 550 °C): BMS samples at Section S47 and S53 at direct contact with the liner: BMS-47-1 to 3 and BMS-53-1 to 3

Y-axis units are given in counts square root.

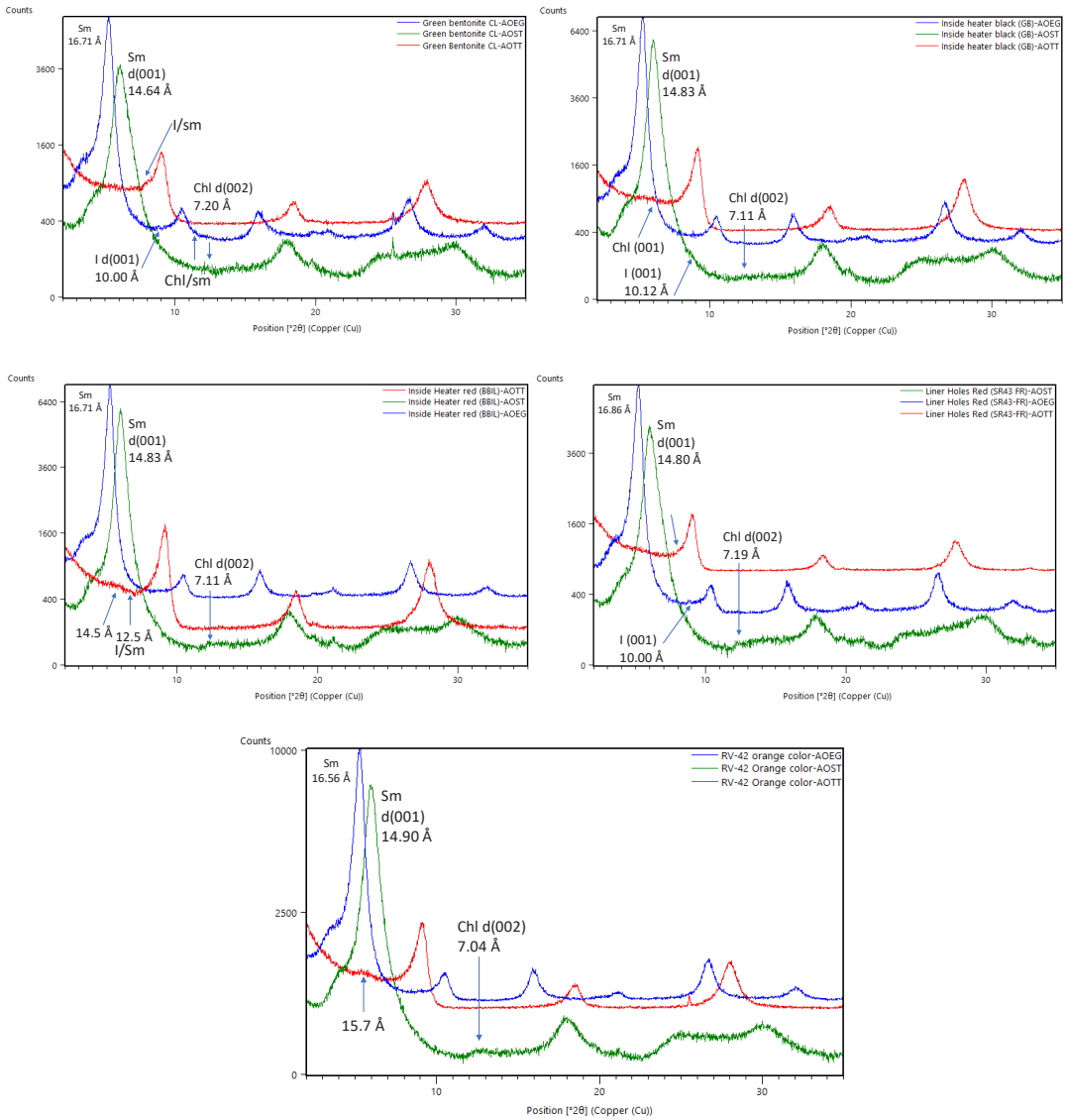

Fig. F-7: XRD patterns of oriented aggregates samples (normal, ethylene glycol solvated and heated at 550 °C): Protrusion samples at Sections S42-S43 (CL, GB, BBIL, SR43-FR, RV-42)

Y-axis units are given in counts square root.

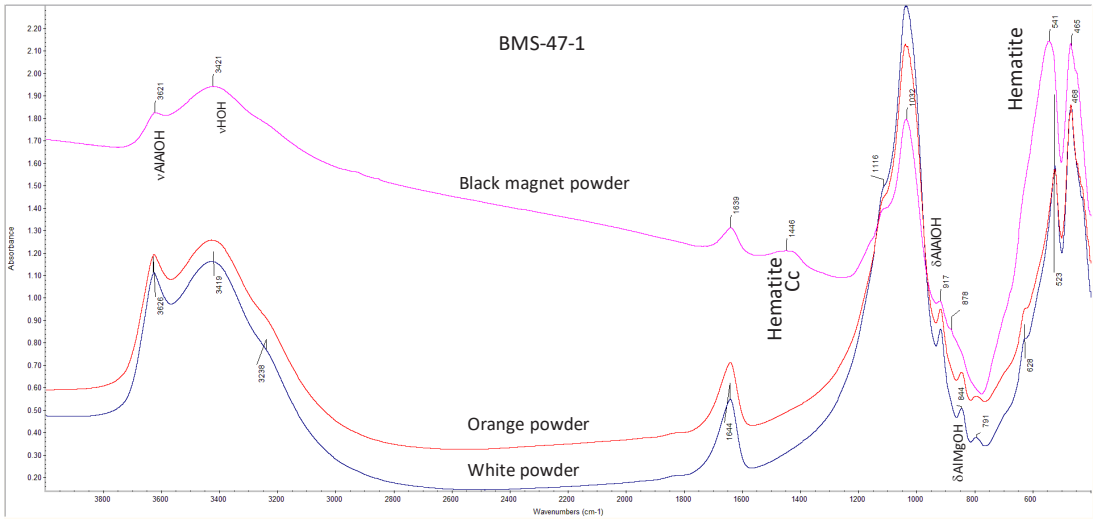

Fig. F-8: FTIR spectrum of the bentonite sample BMS-47-1 adhered to liner

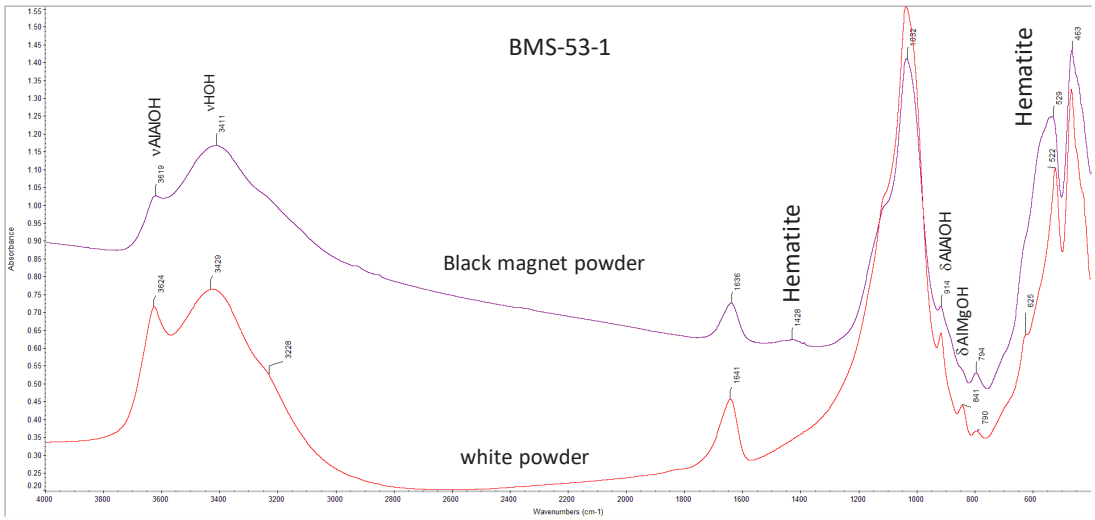

Fig. F-9: FTIR spectrum of the bentonite sample BMS-53-1 adhered to liner

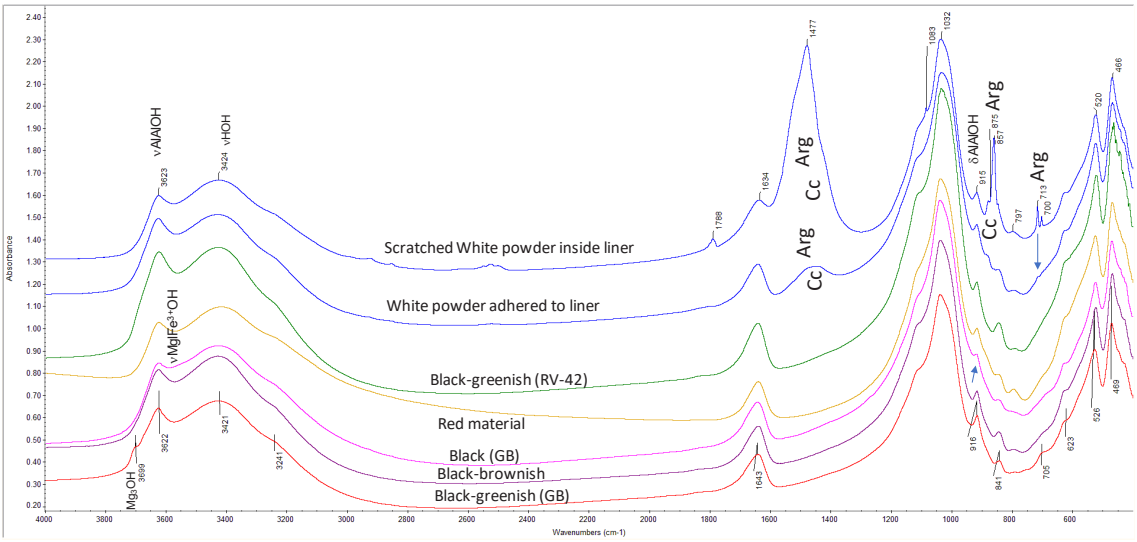

Fig. F-10: Samples from inside the liner: adhered white powder to liner (WP) and bentonite protrusions

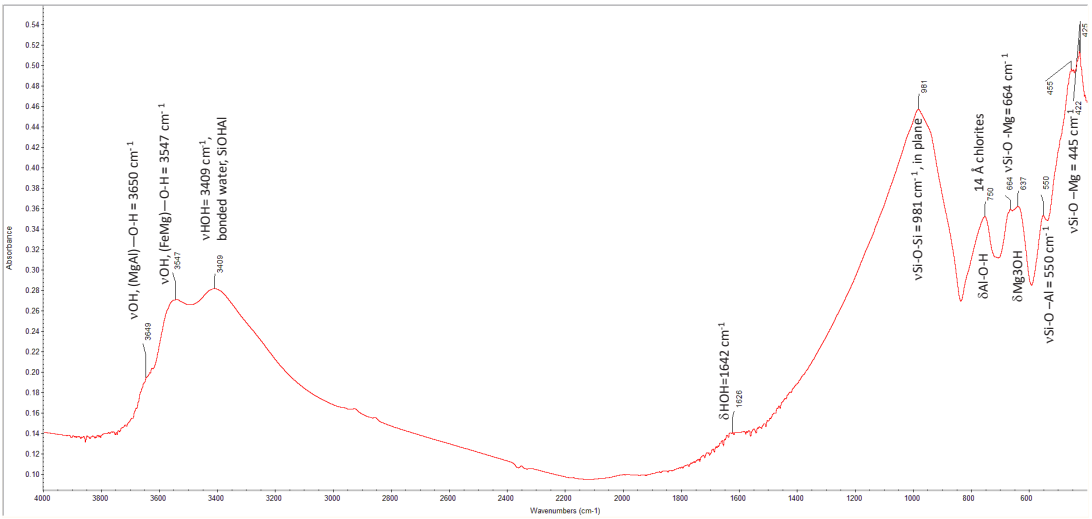

Fig. F-11: FTIR spectrum from a sample at direct contact with the frontal surface of Heater #2: Black ball particle (BB): chlorite

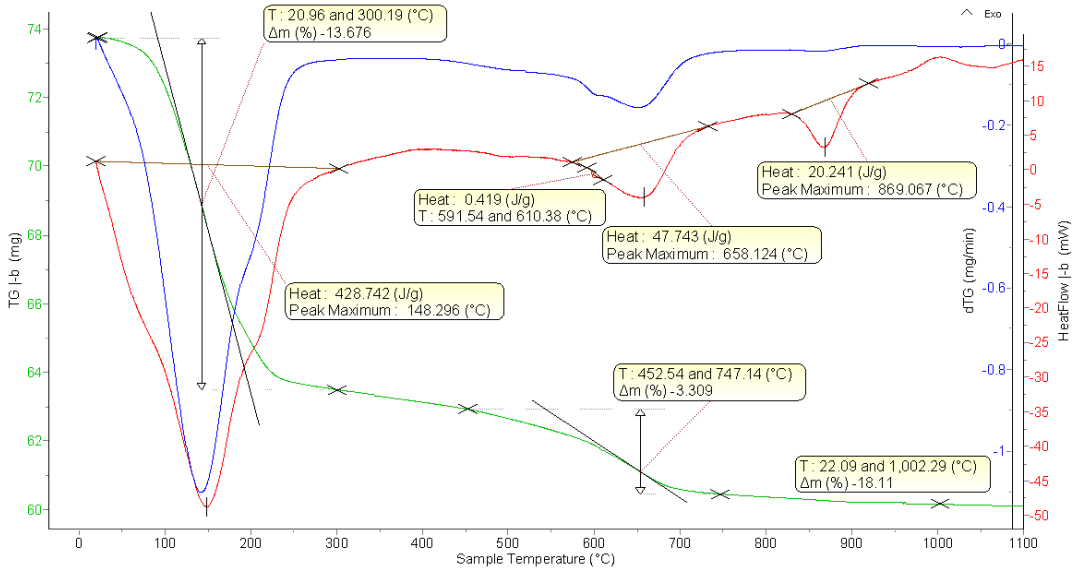

Fig. F-12: TG-DSC curves from the sample BMS-47-1 (total fraction) at direct contact with the liner

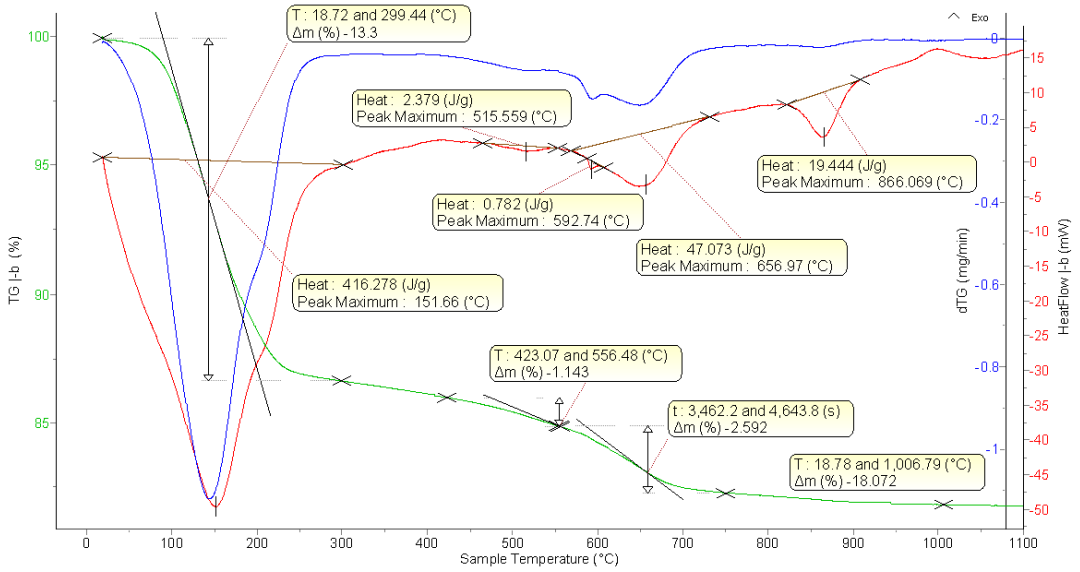

Fig. F-13: TG-DSC curves from the sample BMS-47-2 (total fraction) at direct contact with the liner

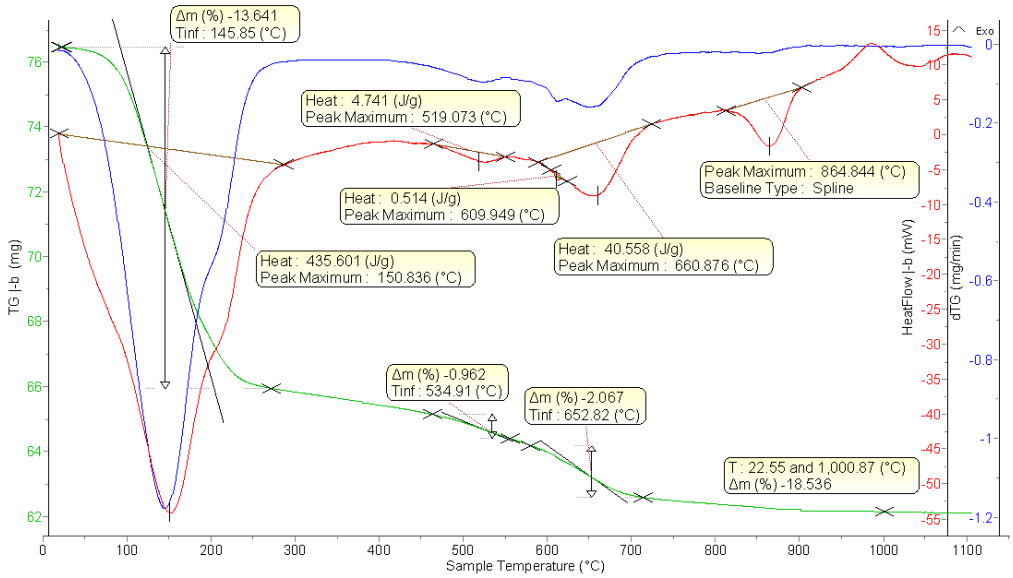

Fig. F-15: TG-DSC curves from the sample BMS-47-3 (total fraction) at direct contact with the liner

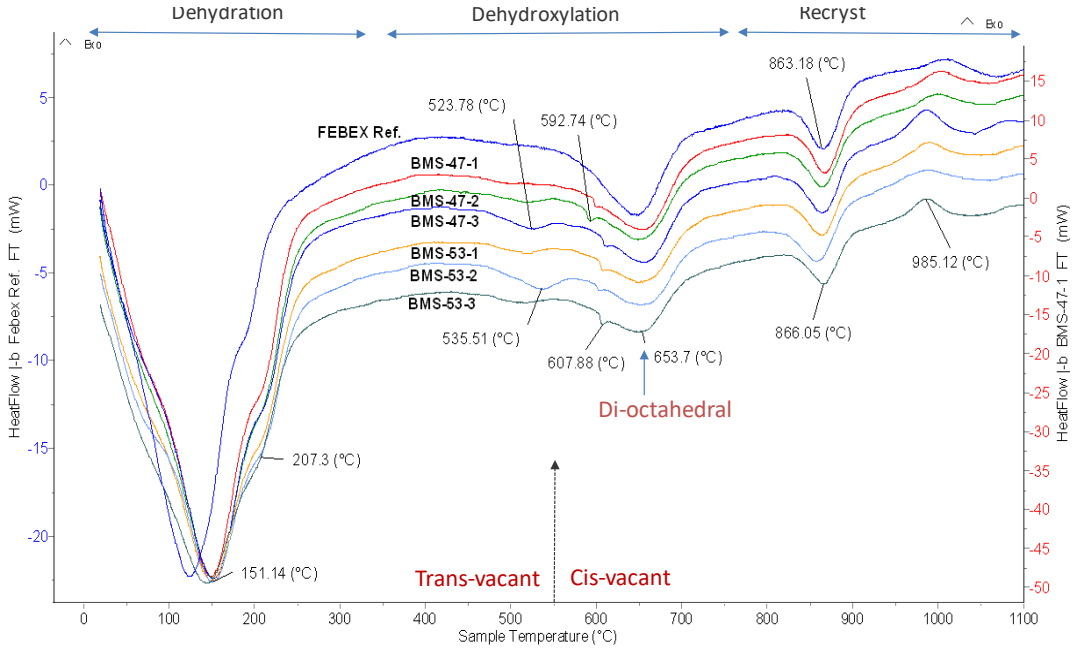

Fig. F-16: Comparison of DSC curves from the samples BMS-47-xx and BMS-53-xx (total fraction) at direct contact with the liner

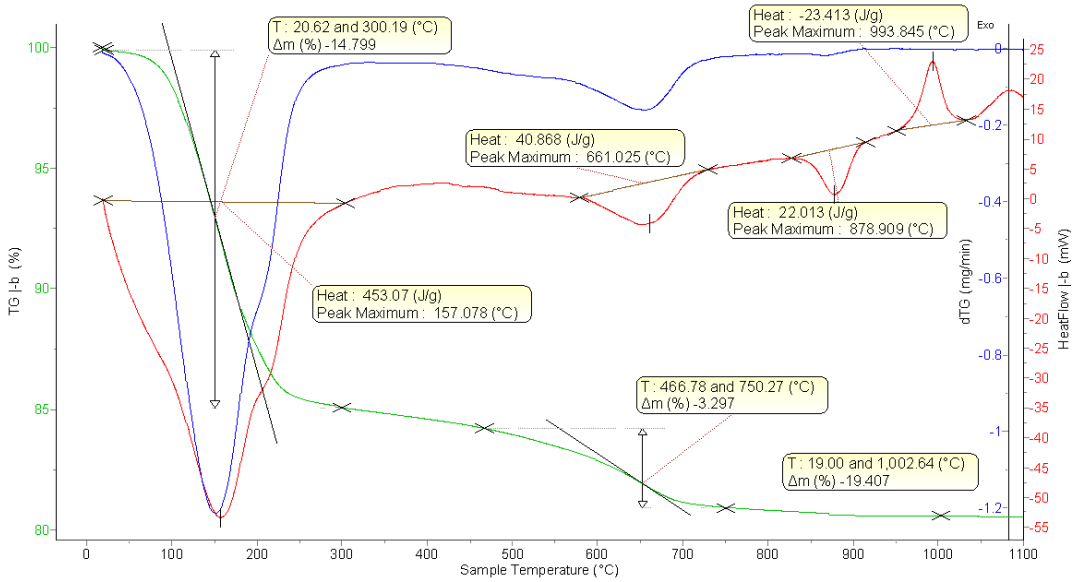

Fig. F-17: TG-DSC curves from the sample BMS-47-1 (< 2 µm fraction) at direct contact with the liner

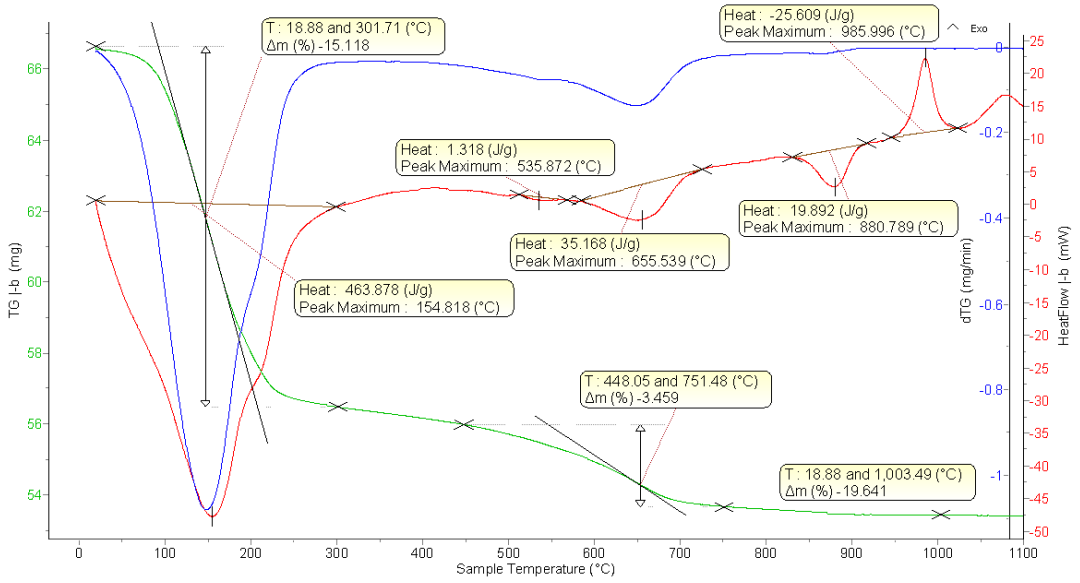

Fig. F-18: TG-DSC curves from the sample BMS-47-2 (< 2 µm fraction) at direct contact with the liner

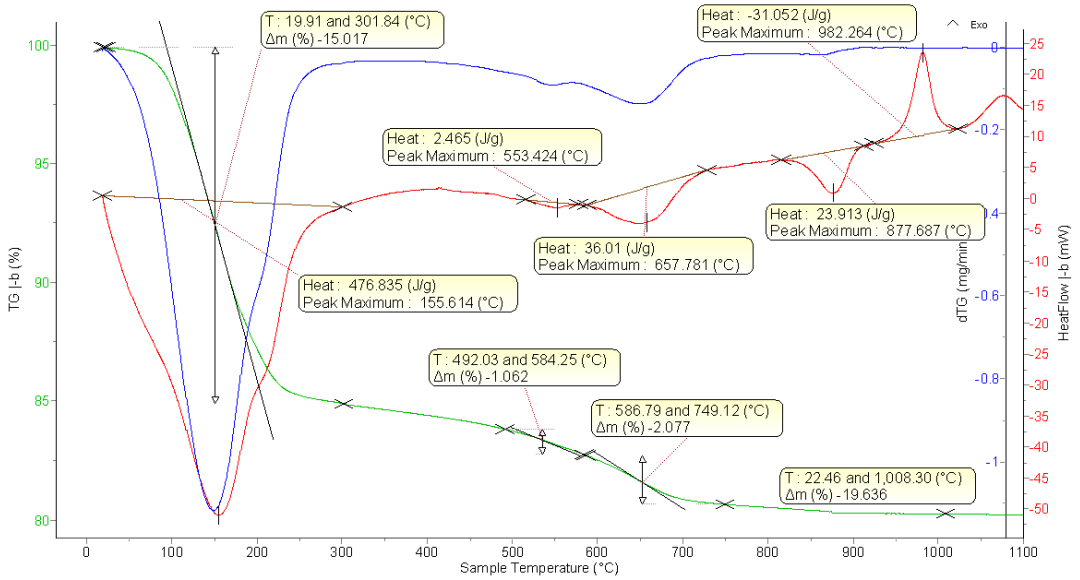

Fig. F-19: TG-DSC curves from the sample BMS-47-3 (< 2 µm fraction) at direct contact with the liner

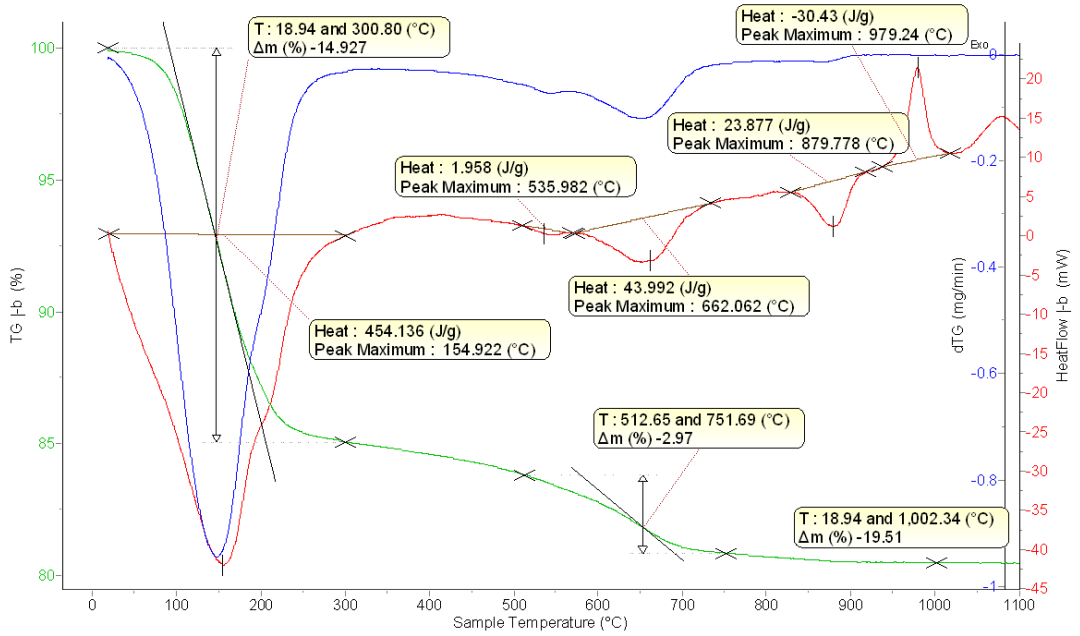

Fig. F-20: TG-DSC curves from the sample BMS-53-1 (< 2 µm fraction) at direct contact with the liner

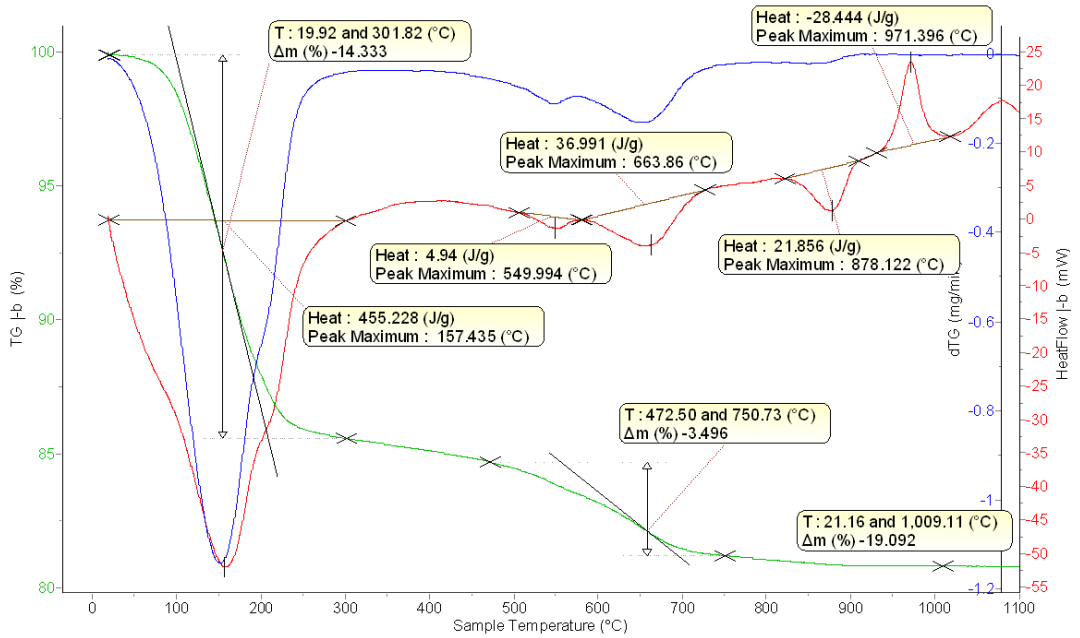

Fig. F-21: TG-DSC curves from the sample BMS-53-2 (< 2 µm fraction) at direct contact with the liner

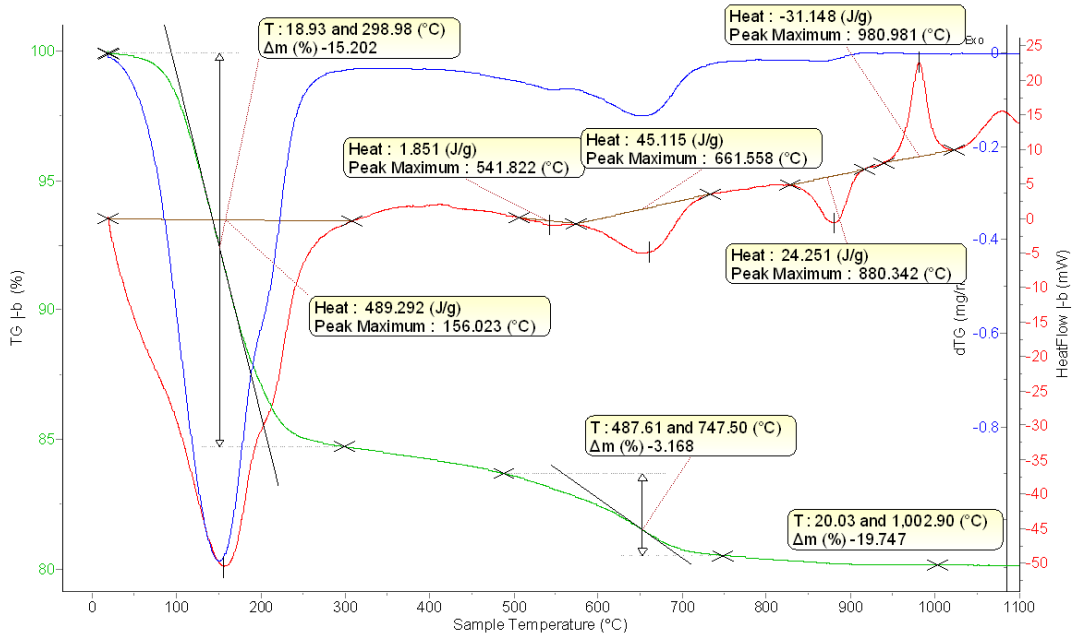

Fig. F-22: TG-DSC curves from the sample BMS-53-3 (< 2 µm fraction) at direct contact with the liner

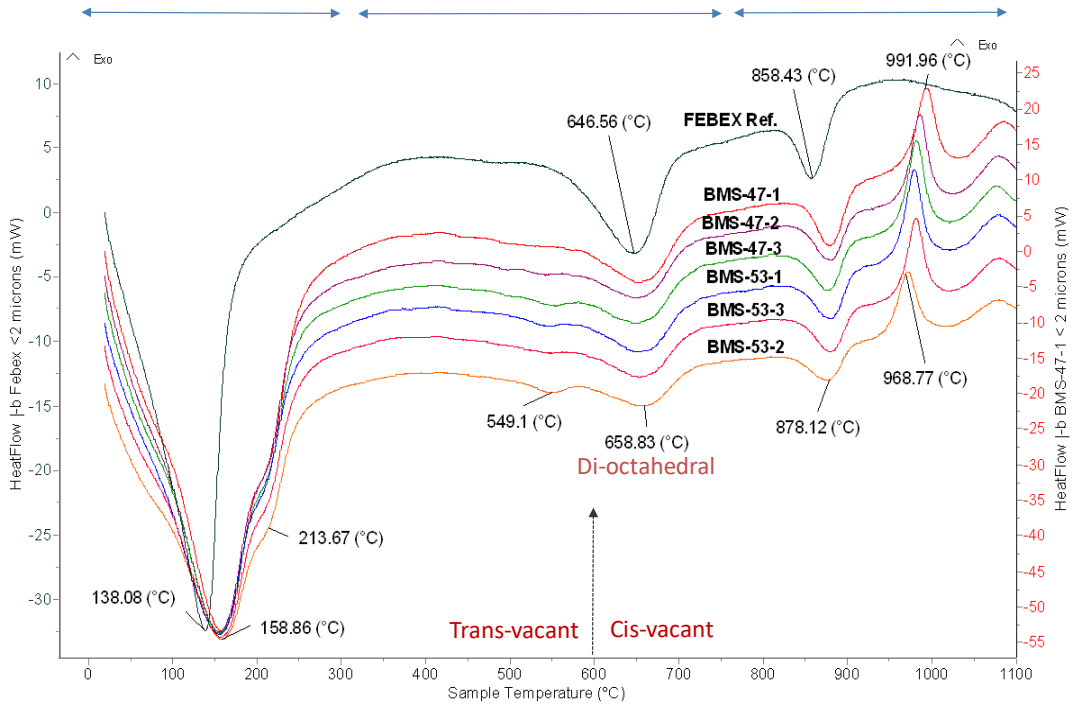

Fig. F-23: Comparison of DSC curves from the samples BMS-47-xx and BMS-53-xx (< 2 µm fraction) at direct contact with the liner

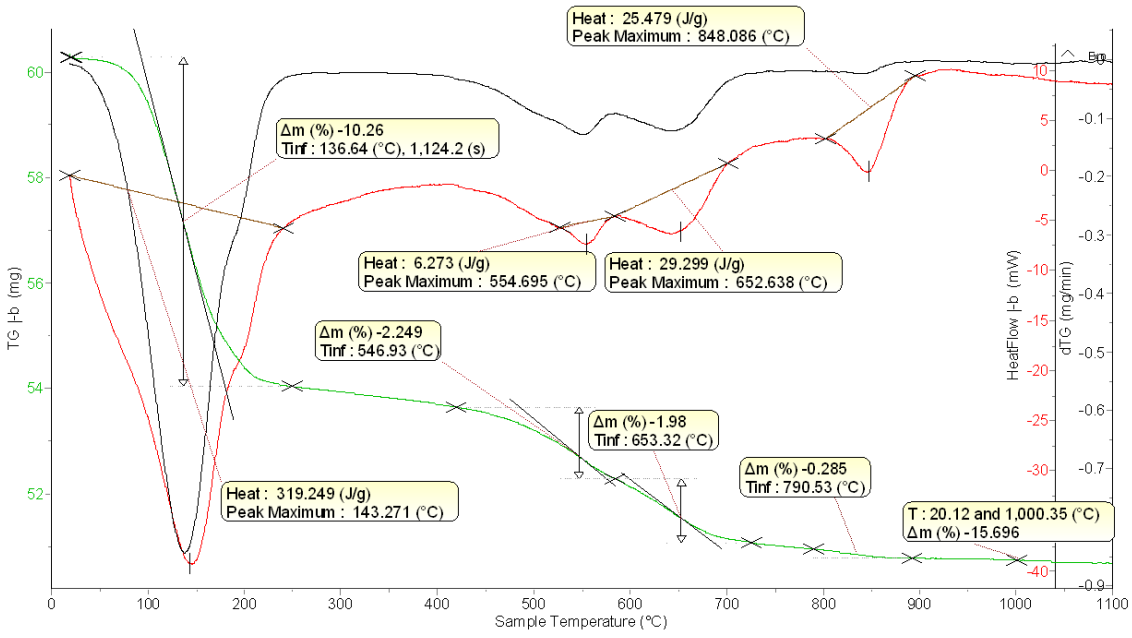

Fig. F-24: TG-DSC curves from the Green bentonite (CL) at direct contact with the frontal part of the Heater #2 (Slice 60)

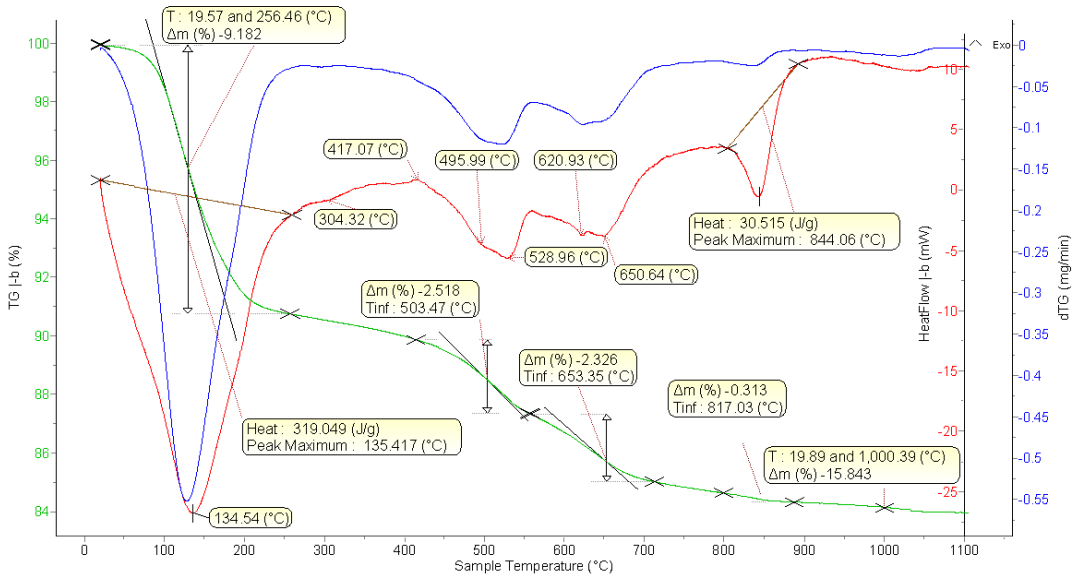

Fig. F-25: TG-DSC curves from bentonite protrusions through the liner holes towards the heater. Samples taken from the internal part of the liner at contact with the heater (bentonite slice 59/57, bentonite sampling Sections S42/S43): R-green (RV)

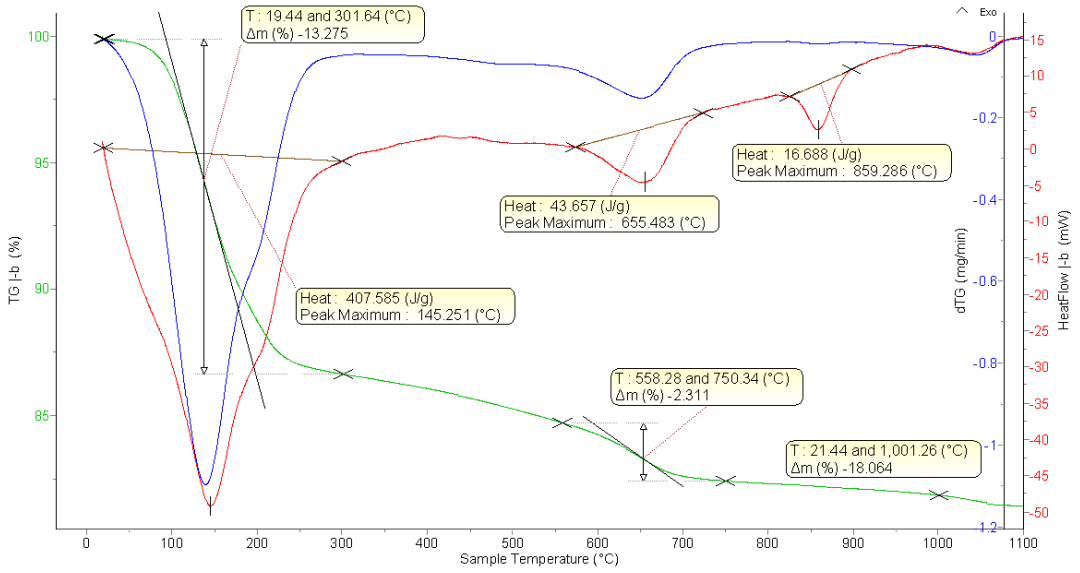

Fig. F-26: TG-DSC curves from bentonite protrusions through the liner holes towards the heater. Samples taken from the internal part of the liner at contact with the heater (bentonite slice 59/57, bentonite sampling Sections S42/S43): R-black&white (RNW42)

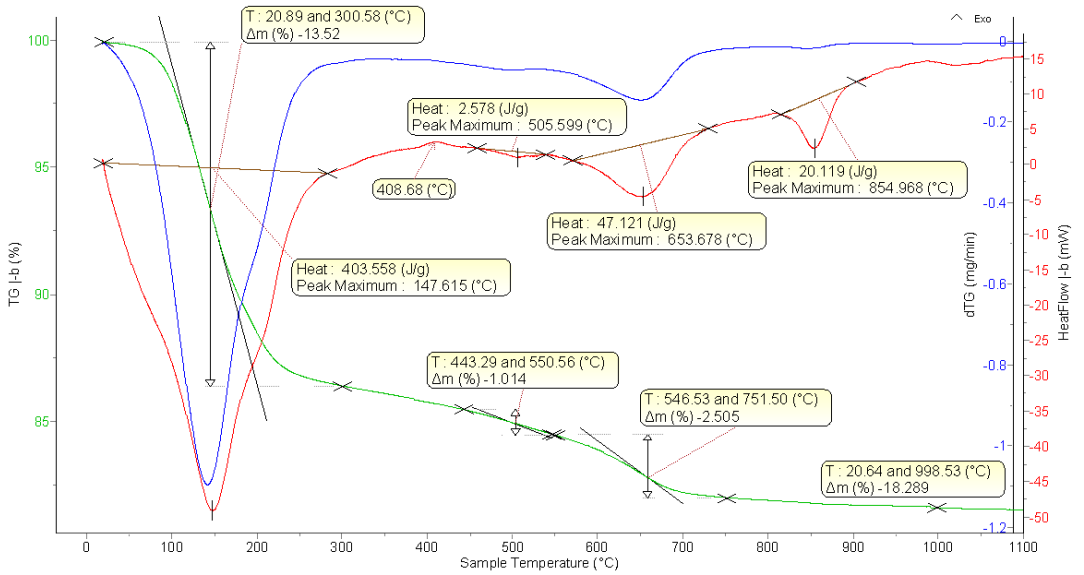

Fig. F-27: TG-DSC curves from bentonite protrusions through the liner holes towards the heater. Samples taken from the internal part of the liner at contact with the heater (bentonite slice 59/57, bentonite sampling Sections S42/S43): R-orange particles (RNW42)

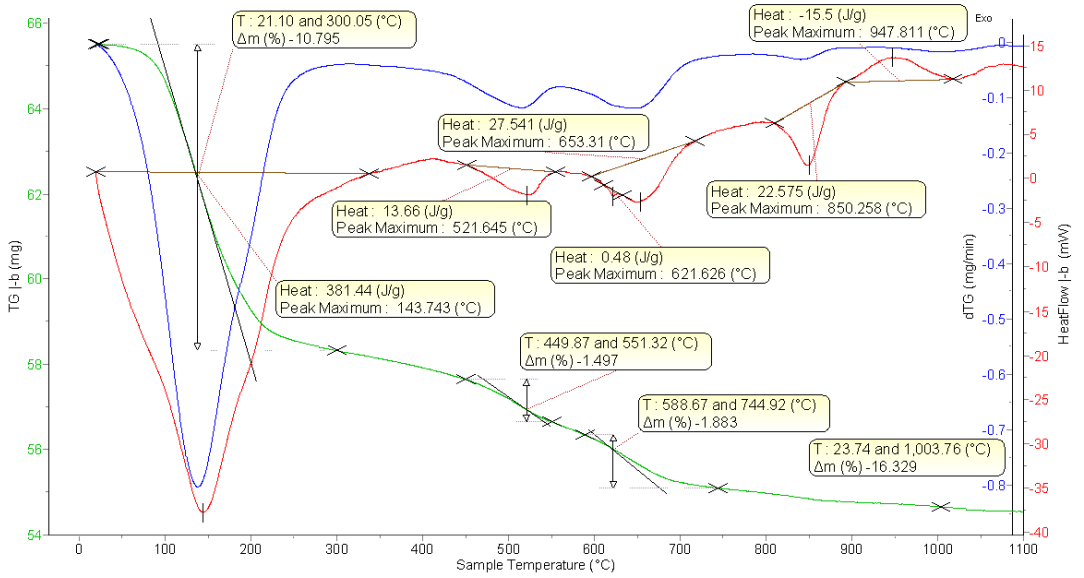

Fig. F-28: TG-DSC curves from bentonite protrusions through the liner holes towards the heater. Samples taken from the internal part of the liner at contact with the heater (bentonite slice 59/57, bentonite sampling Sections S42/S43): R-black particles (RNW42)

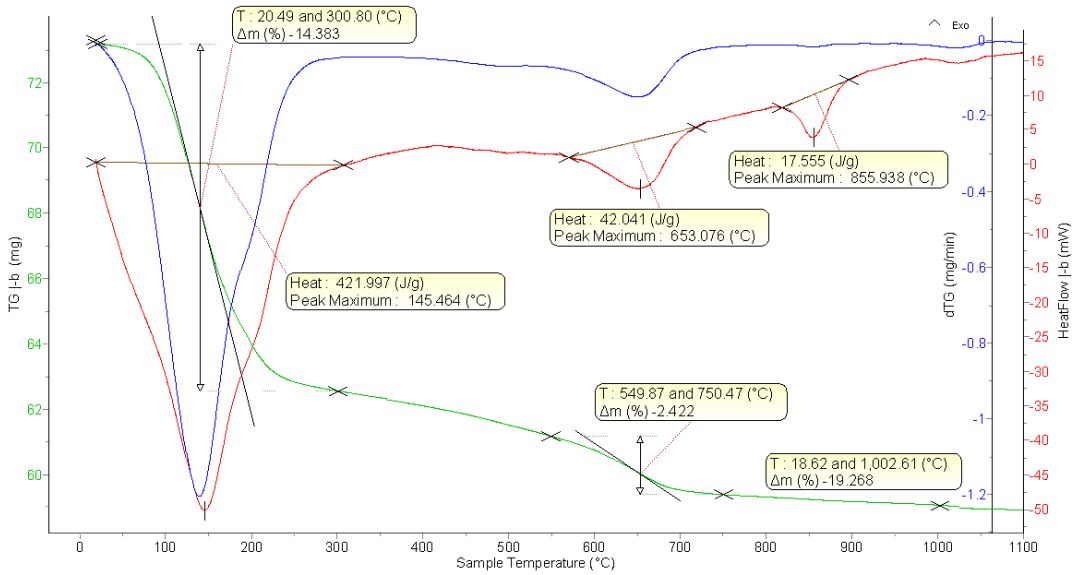

Fig. F-29: TG-DSC curves from bentonite protrusions through the liner holes towards the heater. Samples taken from the internal part of the liner at contact with the heater (bentonite slice 59/57, bentonite sampling Sections S42/S43): R-black&white interface particles (RNW42)

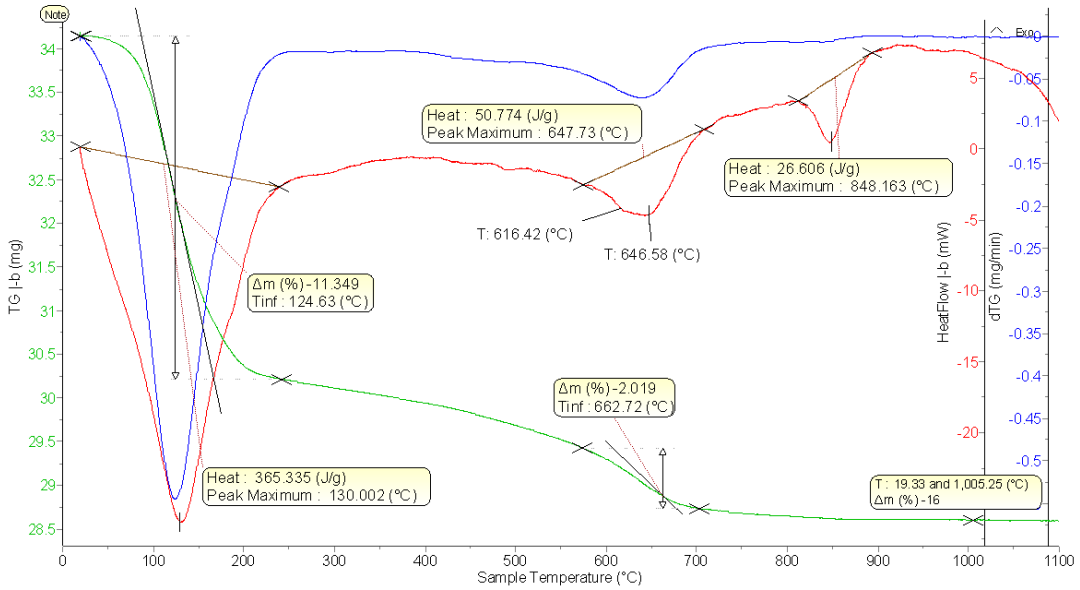

Fig. F-30: TG-DSC curves from bentonite protrusions through the liner holes towards the heater. Samples taken from the internal part of the liner at contact with the heater (bentonite slice 59/57, bentonite sampling Sections S42/S43): Black-green (GB)

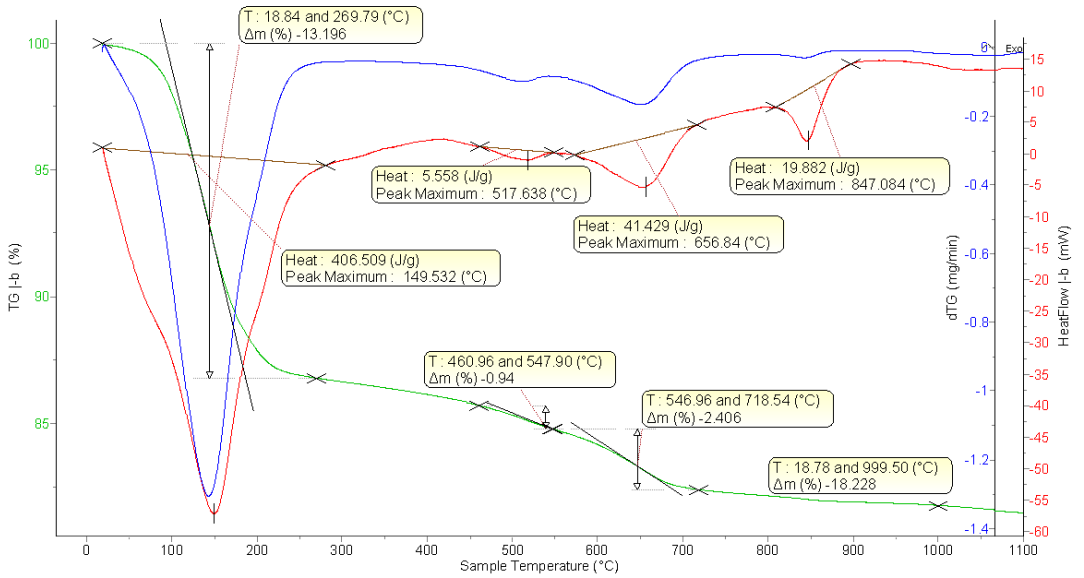

Fig. F-31: TG-DSC curves from bentonite protrusions through the liner holes towards the heater. Samples taken from the internal part of the liner at contact with the heater (bentonite slice 59/57, bentonite sampling Sections S42/S43): inside heater black (GB-42) total fraction

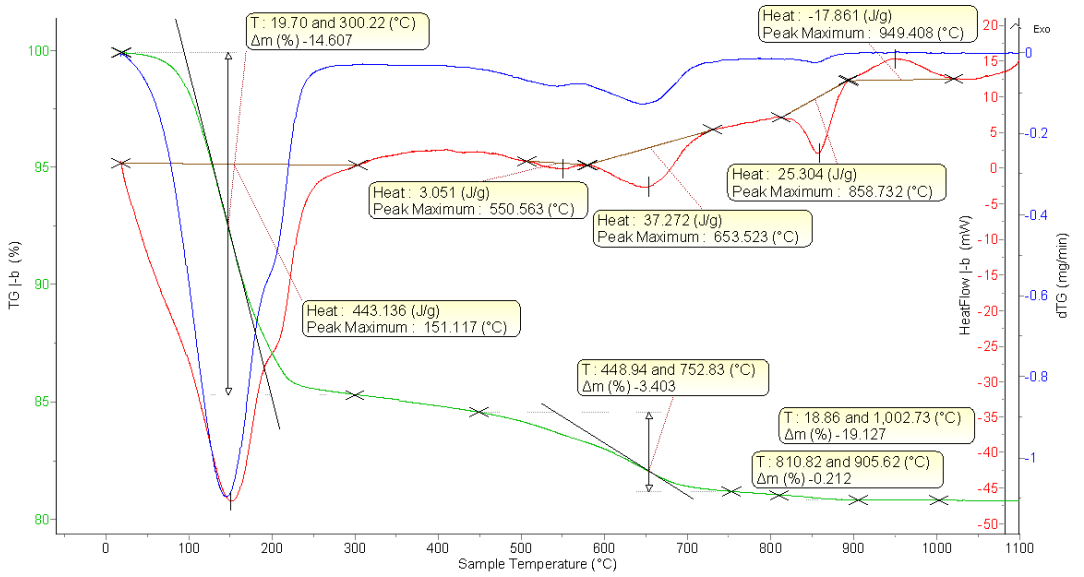

Fig. F-32: TG-DSC curves from bentonite protrusions through the liner holes towards the heater. Samples taken from the internal part of the liner at contact with the heater (bentonite slice 59/57, bentonite sampling Sections S42/S43): inside heater black (GB-42) < 2 μm fraction

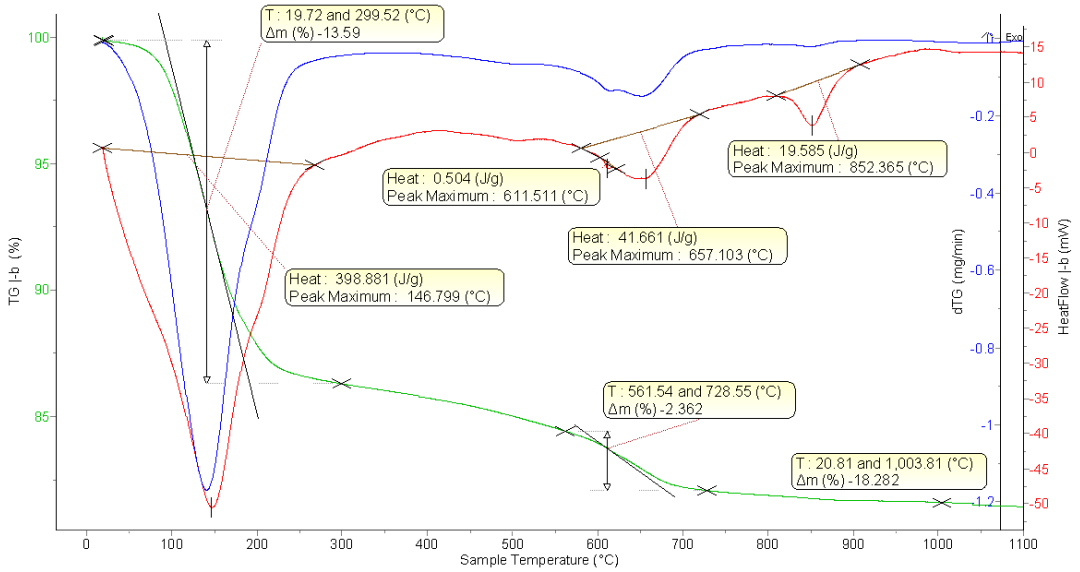

Fig. F-33: TG-DSC curves from bentonite protrusions through the liner holes towards the heater. Samples taken from the internal part of the liner at contact with the heater (bentonite slice 57, bentonite sampling Section S43): inside heater red (PS-43) total fraction

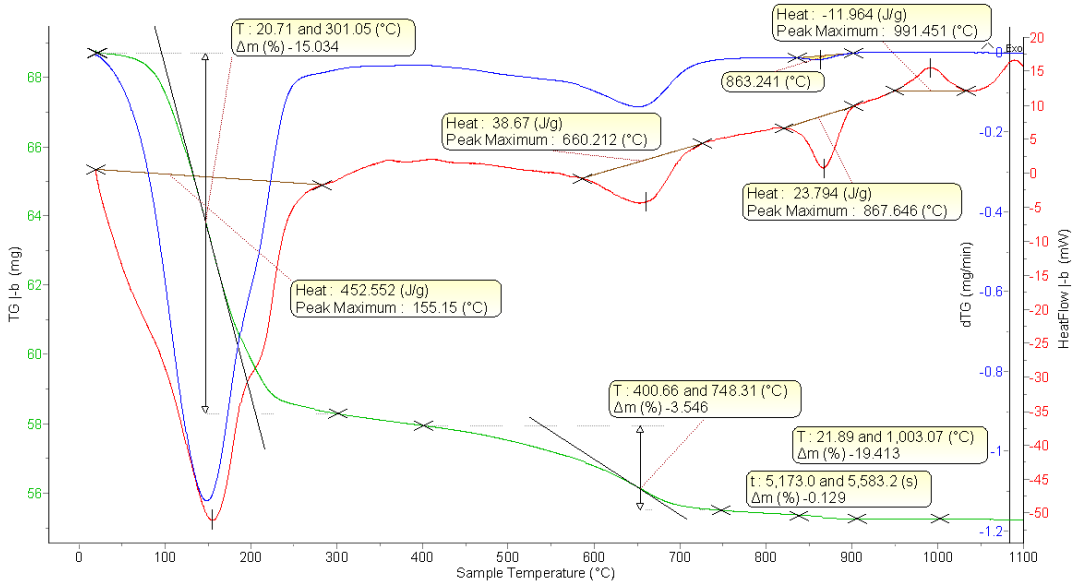

Fig. F-34: TG-DSC curves from bentonite protrusions through the liner holes towards the heater. Samples taken from the internal part of the liner at contact with the heater (bentonite slice 57, bentonite sampling Section S43): inside heater red (PS-43) < 2 µm fraction

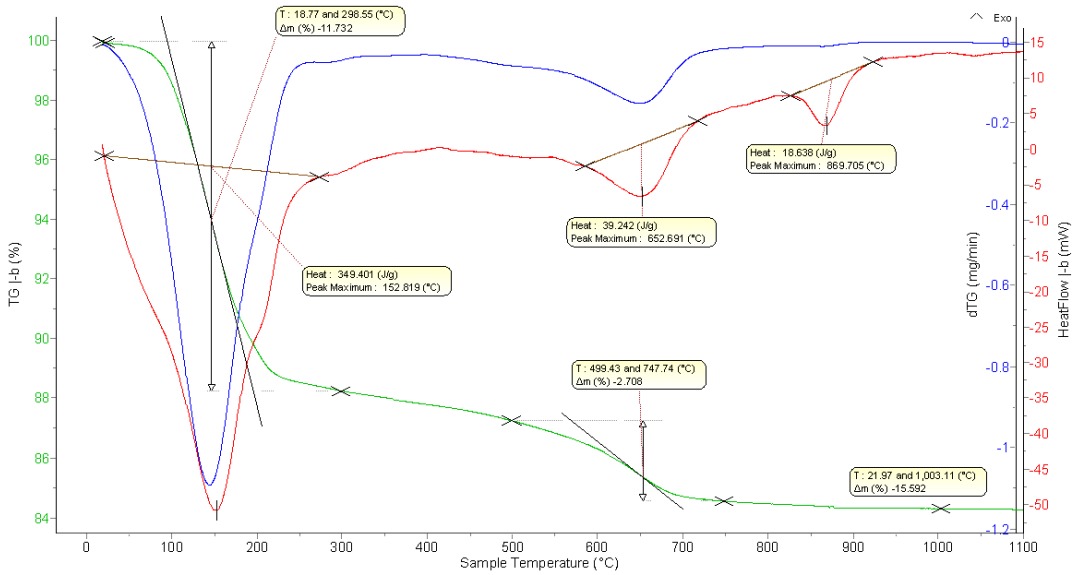

Fig. F-35: TG-DSC curves from bentonite protrusions through the liner holes towards the heater. Samples taken from the internal part of the liner at contact with the heater (bentonite slice 59, bentonite sampling Section S42): liner holes red (BBIL-42) total fraction

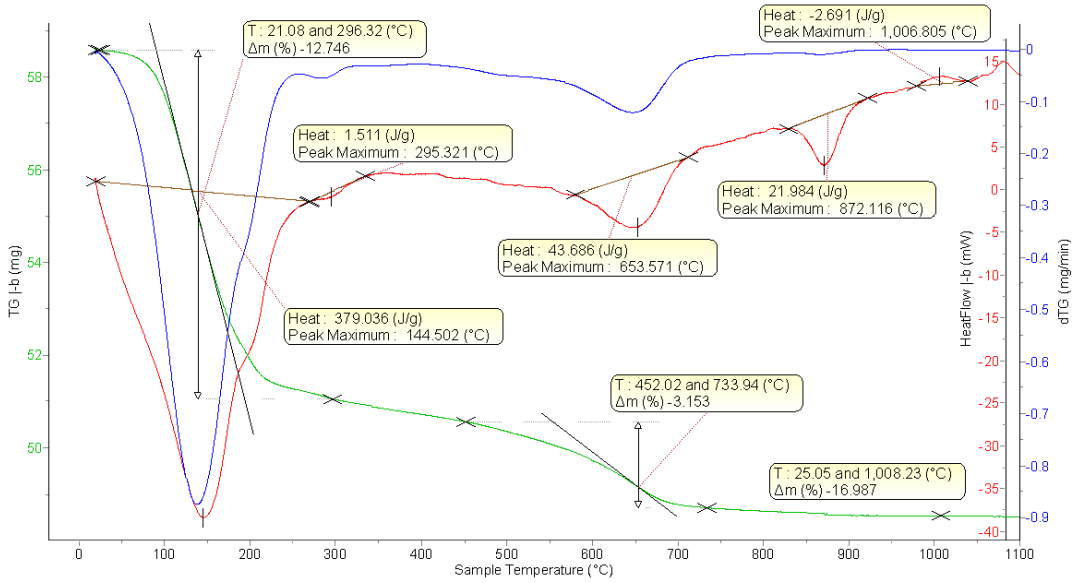

Fig. F-36: TG-DSC curves from bentonite protrusions through the liner holes towards the heater. Samples taken from the internal part of the liner at contact with the heater (bentonite slice 59, bentonite sampling Section S42): liner holes red (BBIL-42) < 2 µm fraction

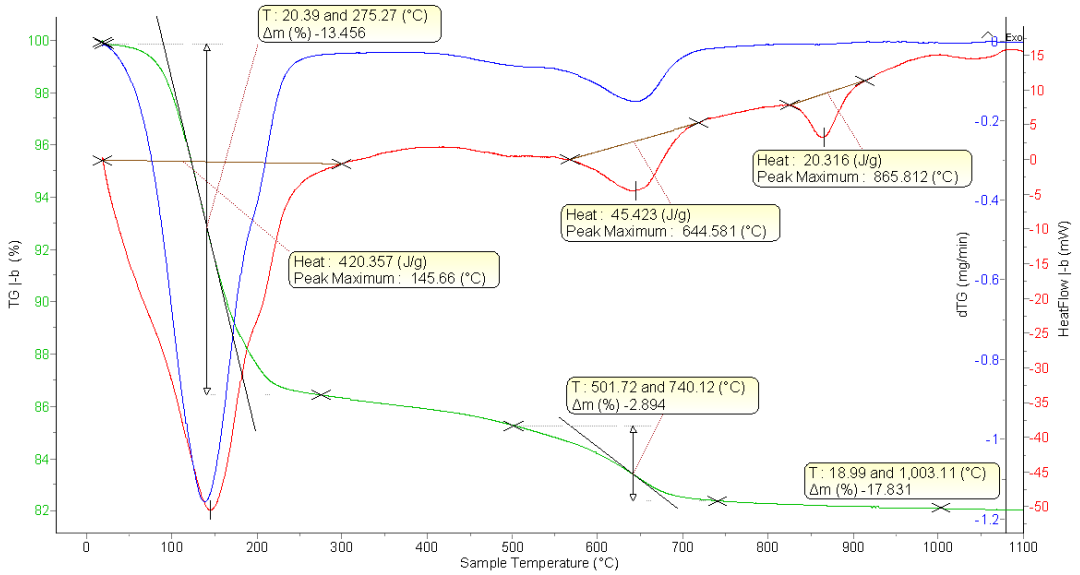

Fig. F-37: TG-DSC curves from < 2 µm bentonite sample at direct contact with Gas Pipe 3

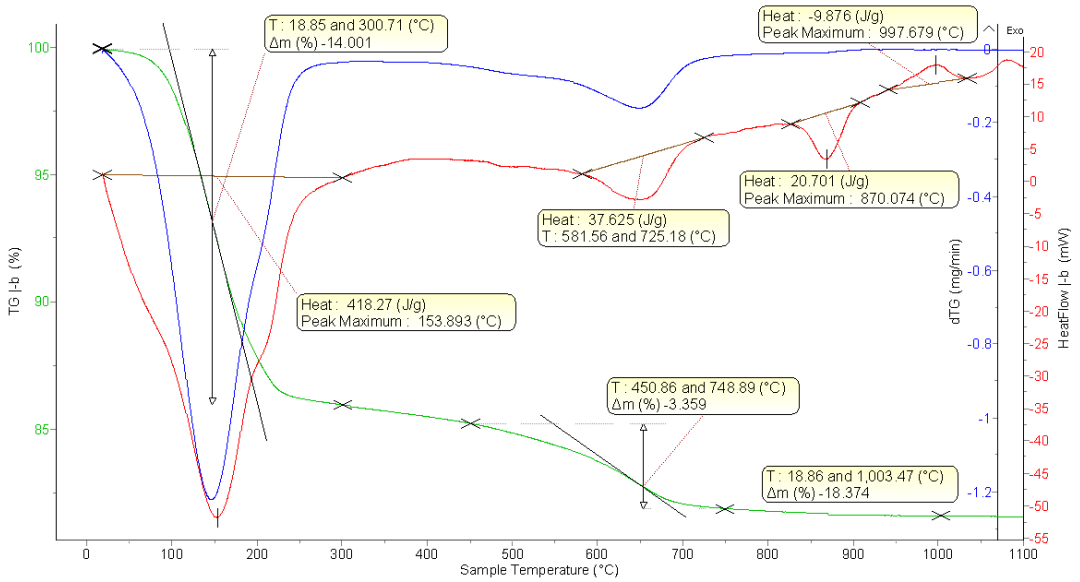

Fig. F-38: TG-DSC curves from < 2 µm bentonite sample at direct contact with Gas Pipe 3

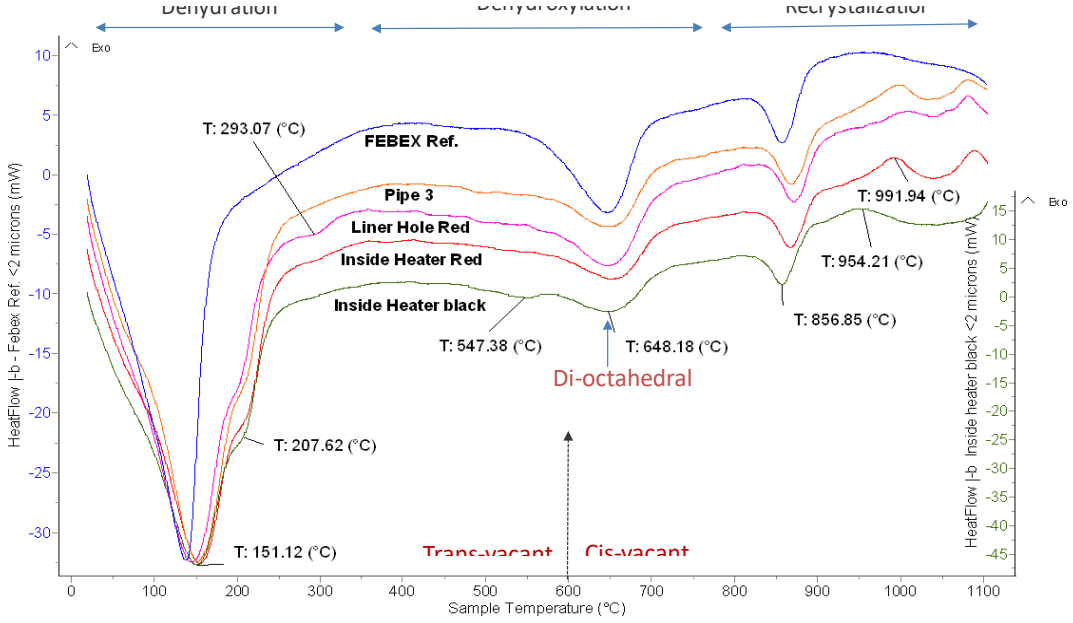

Fig. F-39: Comparison of DSC curves from the < 2 µm bentonite samples from protrusions through the liner holes towards the heater and around Gas Pipe 3